TAYLOR'S UNIVERSITY

Wisdom · Integrity · Excellence

IT'S IN YOU TO **OWN THE FUTURE**

PROCEEDINGS OF

10th eureca 2018

INTERNATIONAL ENGINEERING RESEARCH CONFERENCE

TAYLOR'S UNIVERSITY, LAKESIDE CAMPUS

27th of JUNE 2018

Proceedings of the 10th International Engineering Research Conference (10th eureca 2018)

27th June 2018

Taylor's University, Lakeside Campus

Proceedings of the 10th International Engineering Research Conference
10th eureca 2018

27th June 2018, Taylor's University

Editors

Satesh Namasivayam

Mohammad Hosseini Fouladi

Chockalingam Aravind Vaithilingam

Chew Wei Jen

Yong Leng Chuan

Chua Bee Lin	Ghafour Amouzad Mahdiraji	Hafisoh Ahmad
Kelvin Chew Wai Jin	Koay Seong Chun	Ku Pei Xuan
Lim Joon Hoong	Mohammad Taghi Hajibeigy	Mun Hou Kit
Nurhazwani Ismail	Oh Kai Siang	Phang Swee King
Rashmi Gangasa Walvekar	Reynato Andal Gamboa	Tee Lee Hong
Teh Aun Shih	Abdulkareem Shafiq Mahdi Al-Obaidi	

Published by
School of Engineering
Taylor's University

eISBN 978-967-0173-58-0

eISSN 2590-3845

© 2018 All Rights Reserved.

No print of this publication may be reproduced in any form or by any means without the prior permission of the publisher in writing.

Preface

This volume of proceedings from the 10th International Engineering Research Conference (10th eureca 2018) held at Taylor's University on the 27th of June 2018 contains a selection of refereed papers that were presented during the conference. With the ever-increasing expectations of graduates to be ready to address a variety of new world challenges, the requirements to equip the graduates, especially those in the field of engineering, science and technology, with research skills are more pressing. The aim of the conference is to provide the undergraduate engineering students an opportunity to experience a research environment and is expected to prepare them not only for careers in research but also to provide a precursor for them to use the developed research skills in their future endeavours.

The National Academy of Engineering (NAE) has identified 14 areas awaiting engineering solutions in the 21st century. Taylor's University Malaysia is the first Malaysian university to embrace grand challenges in its curriculum to enhance the student interest and increase the visibility and importance of engineering and science. Thus, the theme of this 10th eureca 2018 conference focuses on the topics from the 14 grand challenges.

For this 10th edition, we have added the 1st International Meeting on Sustainable Urbanisation (SU18) to run in conjunction with the eureca conference. This meeting is separated into several topics and is mainly for postgraduates and experienced researchers to present their findings.

As chairperson of the 10th eureca 2018, I know that this conference will not be possible without the hard work and dedication of my organising team and I would like to extend my sincerest gratitude to them. Finally, I hope to see the eureca conference under Taylor's School of Engineering carry on for many years to come and continue to have a positive impact on the research community.

DR. CHEW WEI JEN
Chairperson of the 10th eureca 2018,
School of Engineering,
Faculty of Built Environment, Engineering, Technology and Design,
Taylor’s University.

Table of Contents

No.	Paper Title	Page No.
1	**Integrated Extraction And Purification Of Anthocyanin From *Dacryodes rostrata* Peel Using Aqueous Two-Phase Extraction (ATPE)** *(Paper 2CE01)* Alawi Al-Alawi, Rajesh Nithyanandam, Tee Lee Hong	1
2	**Degradability Study of Controlled - Release Phosphorus Hydrogel** *(Paper 2CE02)* Anis Raihana Abdul Aziz and Siew Wei Phang	15
3	**Biodegradability Study of Starch Derivative Control-Released Urea** *(Paper 2CE03)* Zhe Shyi Choon, Siew Wei Phang	30
4	**Application of Eggshell as Micro-beads in Toothpaste** *(Paper 2CE04)* Rajesh Rajasekaran, and Goh Pik Yuan	39
5	**Material Flow Cost Account (MFCA)-based Approach for Synthesis and Optimisation of Wastewater Treatment Plant** *(Paper 2CE05)* Jo Yee Ho, Yoke Kin Wan, and Li Wan Yoon	53
6	**Simulation and Design for Multicyclone in Dust Removal System** *(Paper 2CE06)* Lee Sze Young, Wan Yoke Kin, Anis Suhaila Shuib, Chong Thiam Heng, Teh Khim Choon	69
7	**Antioxidant properties of Malaysian fruit and its potential to use as additives for increasing the shelf life of packaged food material** *(Paper 2CE07*) Lok Eu Lee, Rajesh Rajasekaran, and Tee Lee Hong	84
8	**Treatment of ink printing wastewater by advanced oxidation process** *(Paper 2CE08)* Maryam Sulaiman AL-Adawi, Rajesh Nithyanandam	96
9	**Potential of *Hibiscus Sabdariffa* and Jatropha curcas as the natural coagulant in the dye wastewater treatment** *(Paper 2CE09)* Ong Sin Yee, Nurhazwani Ismail	111
10	**Parametric Study of DES-Plasticised Chitosan/CMC Proton Exchange Membrane** *(Paper 2CE10)* Raja Rafidah Raja Sulaiman, Rashmi G. Walvekar, and Wong Wai Yin	123
11	**Study on the Effectiveness of Bond Strength Reduction in Separating Egg Membrane from the Shell** *(Paper 2CE11)* Revathi Kuppusamy, Rajesh Rajasekaran and Phoon Chow Lin	135
12	**Enrichment of Aerobic Sludge for Microbial Protein Production from Palm Oil Mill Effluent (POME)** *(Paper 2CE12)* Sathishkumar Nalatambi, Li Wan Yoon, Yoke Kin Wan, Adeline Seak May Chua	149
13	**Removal of pharmaceutical from wastewater by adsorption-coagulation combined system with *Hibiscus Sabdariffa* as coagulant** *(Paper 2CE13)*	161

Sharwin Raj, and Nurhazwani Ismail

14 **Degradation Pathway of Palm Oil Effluent and Sludge using Fenton Oxidation Process** *(Paper 2CE14)* 174
Ragavan Sukddesh, and Nithyanandam Rajesh

15 **Process Optimization of Bioconversion of Palm Oil Mill Effluent (POME) to Microbial Protein** *(Paper 2CE15)* 191
Chee Sing Tan, Li Wan Yoon, Yoke Kin Wan and Adeline Seak May Chua

16 **Preliminary Study for Optimisation of Pectin Extraction from Dragon Fruit Peels** *(Paper 2CE16)* 204
Tang Shin Fong and Chua Bee Lin

17 **Co-Composting of Oil Palm Empty Fruit Bunch with Partially Treated Palm Oil Mill Effluent** *(Paper 2CE17)* 212
Tang Yi Hui , Phoon Chow Lin, Yoon Li Wan

18 **Primary Recovery of Amylase from *Hylocereus Polyrhizus* Peels using Polymer/Salt Aqueous-Two Phase** *(Paper 2CE18)* 227
Then Chit Siew and Chow Yin Hui

19 **Preparation and Properties of Sea Clam Shell Filled Polylactic Acid Biocomposites** *(Paper 2CE19)* 228
Kar Yan To, Ming Meng Pang, Jiun Hor Low, Seong Chun Koay, Yose Fachmi, Kim Yeow Tshai

20 **Optimization of the Extraction of Anthocyanin from the *Dacryodes rostrata* peel** *(Paper 2CE20)* 240
Vinosyah Palaniandy, Chua Bee Lin, and Tee Lee Hong

21 **Optimization of polysaccharide extraction process from *Dioscorea Opposita*** *(Paper 2CE21)* 256
Wong Yong Yuen and Chua Bee Lin

22 **Synthesis of Nanoparticles and Characterization of Hybrid Nanofluid** *(Paper 2CE22)* 262
Tsui San Yap, , Rashmi Walvekar , Mohammad Khalid, Sumair Ahmed and Chockalingam Aravind Vaithilingam

23 **Extraction of Polyphenols from *Orthosiphon Stamineus* using Ethanol/Salt Aqueous Two Phase System** *(Paper 2CE23)* 274
Yew Kar Mun and Chow Yin Hui

24 **Production and Characterization of Nanocellulose from Chrysanthemum Stem** (*Paper 2ME01*) 275
Aaron Wong Chung Hieng , Chou Pui May

25 **Numerical Analysis on Suspended Load at Taylor's University** *(Paper 2ME02)* 286
Benny Foo Qing Hui , Chou Pui May

26 **Compact Fast and Simple Tire Lifting Device** (*Paper 2ME03*) 302
Kwan Meng Chan, Mohammad Hosseini Fouladi, Satesh Narayana Namasivayam

27 **Biodynamic modelling of human comfort in vehicle** (*Paper 2ME04*) 319
Yang Chan, and Mohd. Farid

28 **One-Stop Portable Fixture For Tire Dimension Measurement Instruments** *(Paper 2ME05)* 337
Gilbert Lim, Douglas Tong, and Jonathan Lim

29 **Mathematical Modelling of Postural Balance Associated with the Changes of Body Mass Index Classification and Skinfold Thickness in Female Young Adult during Dynamic Standing** *(Paper 2ME06)* 344
Iman Mohamad Husaini, and Ku Pei Xuan

30 **Design and Analysis of a Hybrid Rain Energy Harvesting System** *(Paper 2ME07)* 358
Kiritaran Gunasegran, and Douglas Tong Kum Tien

31 **Conceptual Design of a Compact Integrated Tire Rim Storage and Retrieval System** (*Paper 2ME08*) 374
Varen Lau Rui Hang , Chou Pui May, and Jonathan Lim Shiang Chin

32 **Comparison Study on Load Distribution of Different Involute Spline Clearance** (*Paper 2ME09*) 390
Chong Ghee Lee, Noor Zafirah Abu Bakar, Hazlan bin Meera Hussain

33 **The Influence of Winglet Configurations on the Aerodynamic Efficiency of Fixed Wing Micro Unmanned Aircraft Vehicles (MUAV)** *(Paper 2ME10)* 405
Chie Quen Leong; Abdulkareem Sh. Mahdi Al-Obaidi

34 **Improving the Efficiency of a Hybrid Photovoltaic-Thermal System Through Building Integrated Semi-transparent Photovoltaic Thermal System** (*Paper 2ME11*) 426
Chee Jit Lim, Aravind CV, Mohd Hardie Mohyi

35 **Biomimicry Inspired High Impact Absorbed Helmet** (*Paper 2ME12*) 441
Jia Qing Lim , Leng Chuan Yong, Norhabibah Mohamad, and Hui Leng Choo

36 **Preparation and Characterization of Wood Plastic Composite from Recycled Polystyrene Foam and Coconut Shell** (*Paper 2ME13*) 459
Sing Li Ling, Seong Chun Koay, Ming Meng Pang, Kim Yeow Tshai, Ming Yeng Chan, and Thevy Ratnam Chandara

37 **Properties and Characterization of Durian Husk Fiber Filled Recycled Polystyrene Foam Composites** (*Paper 2ME14*) 469
Mah Chee Hang , Koay Seong Chun, Pang Ming Meng, Kim Yeow Tshai, Ming Yeng Chan, and Chandara Thevy Ratnam

38 **Suppression of Vibration Transmission to Structures subjected to Rail-induced Vibrations** (*Paper 2ME15*) 482
Melanie Yong, Mohammad Hosseini Fouladi , and Satesh Narayana Namasivayam

39 **Autonomous Lake Monitoring System (ALMS)** (*Paper 2ME16*) 495
Mohamed Nazer, Mohammad Taghi Hajibeigy, Se Yong Eh Noum, Azadeh Ghadimi

40 **Improving Natural Frequency of an Engine Oil Pan – A structural Optimization Method** (*Paper 2ME17*) 514
Mohammad Ammar Zulsyahmi Mohd Zali, Noor Zafirah Abu Bakar, and Azmi Osman

41 **Evaluation and Assessment of whole-body vibration in passenger vehicle** (*Paper 2ME18*) 515
Mohd Ikhwan Syamil Bin Mohd Anwar, Mohd Farid Bin Aladdin

42 **A Numerical Assessment of the Effect of Surface Topography on the Dynamic Stability of Microorganisms for Biofouling Control** (*Paper 2ME19*) 531
Muhamad Sean Farof, Felicia Wong Yen Myan

43 **Mathematical Modelling of Isokinetic Testing with Energy Balance and Body Fat among Male Young Adults** (*Paper 2ME20*) 546
Muhammad Fadzrul Hafidz, and Ku Pei Xuan

44 **Preparation and Characterization of Biocomposite from PLA and Natural Fibre from Chrysanthemum Waste** (*Paper 2ME21*) 563
Koay Seong Chun, Muhammad Faiz Ishak, Chou Pui May, Chan Ming Yeng, and Albert Tshai

45 **Sintered properties of zirconia reinforced with manganese oxide (MnO_2) and stainless steel (SS-316L)** (*Paper 2ME22*) 574
K.H. Nicholas Cheong , W.J. Kelvin Chew, and S. Ramesh

46 **Biomimicry Inspired High Impact Absorbed Elbow Pad** (*Paper 2ME23*) 583
Nik Arisha Suraya, Leng Chuan Yong, Norhabibah Mohamad, and Hui Leng Choo

47 **Design and Simulation of Vehicle Simulator Structure** (*Paper 2ME24*) 598
Farid Mohd Bin Aladdin, Dr. Seong Chun Koay, and Kah Kit Phang

48 **A Numerical Study to Compare the Antifouling Potential of an Isotropic and an Anisotropic Microtopography** (*Paper 2ME25*) 615
Ramzi Bin Ab Rashid, Felicia Wong Yen Myan

49 **Design and prototyping of a new economic automatic coconut deshelling machine.** (*Paper 2ME26*) 631
Ryan Jerome Lee, Ghafour Amouzad Mahdiraji.

50 **Development of mathematical model for driveline abuse test** (*Paper 2ME27*) 649
Sheldon Vinsent , Noor Zafirah Abu Bakar , and Hazlan bin Meera Hussain

51 **Sintered Properties of Stainless Steel-doped Y-TZP Ceramics** (*Paper 2ME28*) 663
Suraj Nair, W. J. Kelvin Chew, S. Ramesh

52 **Characterization of Co-doped Zirconia** (*Paper 2ME29*) 675
Tan Wei Keong, Kelvin Chew Wai Jin, and Ramesh Singh

53 **Android device extended shield** (*Paper 2ME30*) 685
Boon Hock Teh, Mohammad Hosseini Fouladi, and Mohsen Nabipoor

54 **Optimization Of The Performance Of Vapor Compression Cycle Using Liquid Suction Line Heat Exchanger** (*Paper 2ME31*) 695
Thabit Khalifa, Ali Naif, Abdulkareem Sh. Mahdi Al-Obaidi

55 **System Protection Coordination Study For Taylor's University Electrical Distribution System** *(Paper 2EE01)* 707
Chew Ai Chin, Reynato Andal Gamboa

56 **Study on Effect of Salt Concentration in Heat Transfer Fluid on Performance of Semi-transparent Photovoltaic System** *(Paper 2EE02)* 725
Chong Meng Joe, Aravind CV1, Rashmi Walvekar

57 **Design of Double Layered Vertical Axis Wind Turbine combining Lift and Drag force** *(Paper 2EE03)* 737
Chua Chong Zhe, Chockalingam Aravind Vaithilingam

58 **Design and Analysis of Wind Powered Generator** *(Paper 2EE04)* 749
Henry Chin Tshun Fan , Aravind CV

59 **Smart City Intelligence Safety Systems On Road (S.C.I.S.S.O.R)** *(Paper 2EE05)* 761
Muhammad Hadi bin Saleh,Teh Aun Shih, and Aravind CV

60 **Comparison Of Experimental Thermophysical Properties Of Glycerol And Polyethylene Glycol 600 Based Deep Eutectic Solvents (Dess) With Des And Ils Literature Findings** *(Paper PG01)* 778
Amarpreet Singh, Rashmi Walvekar, Mohammad Khalid, Wong Wai Yin, TCSM Gupta

61 **A Comparative Study of the Effects of Dimples on Aerofoils of Horizontal Axis Wind Turbines at Laminar & Turbulent Flows** *(Paper PG02)* 791
M.K. Lee, M. Hosseini Fouladi, Satesh N.N., Manish Kumar Singh Domun

62 **A Natural Language Processing Framework For Spoken Dialogue Systems** *(Paper PG03)* 809
Praveen Edward James, Mun Hou Kit, Chockalingam Aravind Vaithilingam, Alan Tan Wee Chiat

63 **Drying Of *Clinicanthus Nutans* Leaves Using Combined Vacuum-Microwave Method: Drying Kinetics And Antioxidant Studies** *(Paper PG04)* 817
Lisa Y.W. Chua, Bee Lin Chua

64 **Detection Of Time Localised Transition In Meditation EEG Using Discrete Wavelet Transform** *(Paper PG05)* 826
Jen Looi Tee, Wei Jen Chew, Hou Kit Mun, Siew Wei Phang

65 **Impulsive Force Calibration of a Torsional Thrust Stand using Electrostatic Technique** *(Paper PG06)* 839

Lam Jiang Kai, Koay Seong Chun, Cheah Kean How

66 **Experimental And Theoretical Investigation On Displacer Topology Of A Low Temperature Gamma -Type Stirling Engine** *(Paper PG07)* 849
Kun Yong Ng, Edwin C. Y. Chung, Satesh N. Namasivayam, Douglas K. T. Tong

67 **Mathematical Modelling Simulation Analysis Of A Photovoltaic Thermal System** *(Paper PG08)* 870
Mohammad Taghi Hajibeigy, Rashmi Walvekar and Chockalingam Aravind Vaithilingam

68 **External Cathodic Protection For Above Ground Storage Tank Using Controlled Sacrificial Anodes** *(Paper PG09)* 890
Muhammad N. Jawad, Ghafour Amouzad Mahdiraji, Mohammad Taghi Hajibeigy

69 **Investigation On Polarization Losses In A Direct Carbon Fuel Cell Operating On Oil Palm Mesocarp Fiber Biochar** *(Paper PG10)* 899
Nida Jafri, Yoon Li Wan, Wong Wai Yin, Veena Doshi, Cheah Kean How

70 **Load Bearing Simulation On Lumbosacral Disc In Pre And Post-Operated Thoracic Scoliosis Patients** *(Paper PG11)* 915
P. Mohankumar, Yong Leng Chuan, Anis Suhaila Shuib, Shajan Koshy

Integrated Extraction and Purification Of Anthocyanin From *Dacryodes rostrata* Peel Using Aqueous Two-Phase Extraction (ATPE)

Alawi Al-Alawi[1], Rajesh Nithyanandam[1], Tee Lee Hong[1]*

[1]School of Engineering, Faculty of Environment, Engineering, Technology & Design, Taylor's University, Subang Jaya, Selangor, Malaysia

Abstract: *Dacryodes rostrata* fruit belongs to the family of *Buseraseae*. It is found in Sarawak, Sabah (Malaysia) and is indigenous to that region. This fruit is underutilized but is commonly used among local people as a traditional medicine to treat diseases such as malaria and skin infection. *Dacryodes restrata* is reported to be rich in oil, protein, minerals and could be a potential source of natural antioxidant such as anthocyanin. Conventionally, recovery of bioactive compounds usually need to go thourgh two separate processes which are extraction followed by purification. Aqueous Two-Phase seemed to be an ideal method to extract and purifiy anthocyanin from other such as protein and sugar in one integrated step. An Aqueous Two-phase extration formed by mixing short chain alcohol with inorganic salt. ATPE gained great attiontion in extracting bioactive materials as well as protein purification from plant materials because of its advantages such as low energy consumption, low cost of alcohol and salt and fast processing time. Therefore, this project aimed to study the feasibility of Aqueous Two-Phase System (ATPS) to extract and purify anthocyanin from *Dacryodes rostrata* peel in one single integrated step. The first stage of this project is screening of suitable ethanol-salt system (ammonium sulfate, dipotassium phosphate, potassium dihydrogen phosphate) in extraction and purification of anthocyanin from *D. rostrata* peel. Second stage is optimizing of selected ethanol-salt system using response surface methodology (RSM). Potassium dihydrogen phosphate fail to form two phase which was eliminated at the beginning of the experiment. The optimum partition coefficient for the purification of anthocyanin was obtained in the ATPE system of 30% (wt/wt) ethanol, 15% (wt/wt) dipotassium phosphate and 10% (wt/wt) feedstock. The purified anthocyanin had partition coefficient of 157.89, yield of anthocyanin in the top phase is 99.37 % and yield of anthocyanin in the top phase is 0.63 %.

Keywords: Aqueous two-phase extraction, anthocyanin, *Dacryodes rostratata*, optimization, ethanol-salt system

Introduction

Anthocyanin is a part of flavonoid group and it owns antioxidant capabilities as it scavenges free radicals. It helps in fighting DNA cleavage, lipid peroxidation and cancer [1]. It is also used as anti-carcinogenic medicine but the exact behavior of anthocyanin as anti-carcinogenic medicine is still unclear [2]. Anthocyanin is accountable for red, blue, and purple colour of fruits and vegetables. The fruits such as berries, currants, and grapes have high anthocyanin content [3]. In Malaysia, local and indigenous fruits like Dabai *(Canarium odontophyllum)* and Kembayau (*Dacryodes rostrata)* which can be found in Sarawak and Sabah (Malaysia). This fruit is underutilised but is widly used among local people as a madicane to treat diseases such as malaria and skin infuction [4]. The peels of *D. rostrata* fruit is reported to have natural antioxidants such as anthocyanin, protein, oil, and minerals, thus it will be utilize as the surce to retrieve anthocyanin in this project.

Commercial recovery of natural pigment from plant materials is usually solvent extraction after homogenization. For instance, Solvent extraction such as acidified solution of acetone, ethanol, water, methanol, and a mixture of this materials are traditionally used to extract bioactive compound from plants materials. From those methods, the extraction with acidified methanol is the most efficient. Nerveless, in food processing industry ethanol is preferred due to the toxicity of methanol. Furthermore, the extraction method needs large amount of solvent and much energy to recovering the solvent. Generally, the purification of anthocyanin is carried out by HPLC or counter-current chromatography (CCC). However, these methods are too expansive to be used. Thus, there is a need for an economical, more efficient, and large-scale biomaterial extraction method that can achieve high purity as well as high yield, while preserving the biological activity of these materials. Aqueous two-phase extraction (ATPE) is likely to be developed as one extraction method to meet the above criteria [5].

ATPE used as a primary separation method has been widely applied for the recovery of natural pigment from plant materials due its easiness for scale-up, high capacity and yield, low cost and short processing time. Furthermore, ATPE has the potential to achieve extraction and purification in a single step. Polymer has been used recently in extraction of natural pigment from plant materials. However, polymers are very expansive and not easy to recover. Therefore ATPE system composed of short chain alcohol and salt has is more preferred due to its low cost and easy to recover the solvent [6].

This paper aimed to study the effect of process parameters of salt and ethanol concentration and the amount of feedstock in the extraction and purification process of anthocyanin of the antioxidants from *Dacryodes rostrata* peels using ATPE. Followed by optimize the ATPE parameters in the extraction process using ethanol to salt systems of (20 to 40% (wt.)) for ethanol and (10 to 25% (wt.)) for salt and at the end evaluate the feasibility of ATPE system to extract and purify anthocyanin compared to conventional solid-liquid extraction according to the amount of extraction and time.

2.0 Materials and method

2.1 Chemical and reagents

Ammonium sulphate (AR grade), dipotassium phosphate (AR grade), potassium dihydrogen phosphate (AR grade), ethanol (96%) (AR grade), potassium chloride (AR grade) and sodium acetate (AR grade) were purchased from CHEMOLAB SUPPLIES SDN BHD (Selangor, Malaysia). Pierce^{TM} BCA Protein assay kit were purchased from Sigma-Aldrich (St. Louis, USA).

2.2 Materials and sample preparation

Fresh fruits of *Dacryodes rostrata* were supplied by Agricultural Research Centre, Department of Agricultural, Sarawak, Malaysia. The fruit were transported to Taylor's University in an icebox through airmail. The fruit with a good condition, shape, and colour are chosen. Then, the fruit is washed with tap water followed by distilled water and air-dried. The fruit then is peeled and the peels was dried using the freeze-drying process and subsequently pulverized using grinding machine and then sieved using 0.25 mm. The samples are stored at -20 C° for further analysis [8].

2.3 Aqueous two-phase extraction (ATPE)

Aqueous two-phase systems were consisting of a specific amount of ethanol, salt, and water in a total weight of 5 g. Different systems are prepared in range of ethanol (20% - 40% (w/w)) and salt (10%- 25% (w/w)) concentration. a pre-determined quantity of salt was dissolved in water in order to determine a specific concentration of (32% (w/w)). Three different salts were used in this experiment: ammonium sulphate, di-potassium phosphate, and potassium dihydrogen phosphate. Phase system were prepared in a 15 mL graduated centrifuge tube by weighting an appropriate amount of ethanol followed by an amount of salt and (10% (w/w)) D. *rostrate* peel powder then distillate water was added to the system to obtain a final mass of 5 g [9]. Prepared mixtures were vortexed followed by centrifugation at 5000 rpm for 10 minutes in order to promote the two-phase system [10]. Table 1 shows the different ATPE systems prepared.

Table 1 Experimental setup for the ATPE system

Ethanol %	Salt %	Water %	Feedstock %
25	20	45	10
30	15	45	10
40	10	40	10

2.4 Determination of volume ratio, partition coefficient, and recovery yield

After the two-phase had separated, the volume of the top and bottom layers were recorded. To estimate the volume ratio (R) of the ATPE, the volume of the top (V_T) and the bottom (V_B) phases are taken into account according to **Equation 1** [11]. The samples from both top and bottom phase were assayed for total anthocyanin content (TAC) and total protein content (TPC).

$$R = \frac{V_T}{V_B} \quad (1)$$

The partition coefficient (K) of the powder concentration of the top (C_T) and of the bottom (C_B) is given by **Equation 2**,

$$K = \frac{C_T}{C_B} \quad (2)$$

The yield of anthocyanin at the top (Y_T) and at the bottom (Y_B) phases is calculated according to **Equations 3** and **4**, respectively:

$$Y_T = \frac{C_T V_T}{C_T V_T + C_B V_B} \times 100\% \quad (3)$$

$$Y_B = \frac{C_B V_B}{C_T V_T + C_B V_B} \times 100\% \quad (4)$$

where,
V_T is the volume of the top phase (ml), and V_B is the volume of the bottom phase (ml).

All volumes, V_T and V_B, of the separated phases are measured directly from the test tube while the concentration, C_T and C_B, are quantified by the UV spectrophotometry method.

2.5 Analytical method

2.4.1 Estimation of total anthocyanin content (TAC)

The total anthocyanin content was determined using UV-spectrophotometer pH- differential method [21]. The sample was prepared by mixing 0.5 mL of the extract with 0.025 M potassium chloride buffer whose pH is 1.0 and volume of 4 mL and sodium acetate buffer whose pH is 4.5 and volume of 4mL. The absorbance of the mixture is measured at 520 and 700 nm using UV-spectrophotometer. Absorbance (A) will be calculated using **Equation 5,**

$$A = (A_{520}\text{-}A_{700})_{\text{at pH=1.0}}\text{-}(A_{520}\text{-}A_{700})_{\text{at pH=4.5}} \quad (5)$$

where A_{520} is the absorbance at 520 nm and A_{700} is the absorbance at 700 nm.

Additionally, the monomeric anthocyanin pigment concentration in the original sample is calculated according to **Equation 6** which can be converted to mg of total anthocyanin content per 100 g sample [12],

$$\text{Monomeric anthocyanin pigment (mg/L)} = (A \times MW \times DF \times 1000)/(\varepsilon \times 1) \quad (6)$$

where MW is the molecular weight of cyanadin-3-glucoside (MW = 449.2) and DF is the dilution factor, and ε is absorptivity ($\varepsilon = 26{,}900$).

2.4.2 Estimation of total protein content

Total protein content was determined using the standard method known as Thermo Scientific Pierce Bicinchoninic Acid (BCA) Protein Assay Kit. BCA method is a detergent-compatible formulation used to detect and quantify the amount of the total protein [13]. The working reagent (WR) was prepared by mixing 50 parts of BCA reagent A with 1 part of BCA reagent

B at a ratio of 50:1. In BCA, a pipette 10 μL of the standard or the unknown sample replicate into a microplate well (working range equals to 125-2000 μg/mL). Then, a 200 μL of WR is added to each well and mix plate on a plate shaker for 30 seconds. The contents were kept covered at 37 °C for 30 minutes. Finally, the plate was cooled down to room temperature and the absorbance is measured at 562 nm. To find the amount of protein, bovine serum albumin (BSA) was used to construct a standard curve of absorbance versus protein concentration. Total protein content was found using the formula of the line of best fit from the standard graph.

2.6 Experimental design

2.6.1 Screening of ethanol-salt systems (ATPE)

The first step of the screening process was to examine different the different salt system if it can form two phase or not and eliminate the salt that did not form two phase. Table 2 shows the concentration for ethanol and salt (ammonium sulfate, dipotassium phosphate, and potassium dihydrogen phosphate) used to examine the two phase forming.

Table 2: Concentration for salt and alcohol for examining the phase forming capability

Ethanol-Salt System		
Amount of Ethanol %	Amount of salt %	Amount of water %
20	10	50
30	15	55
40	20	40

2.5.2 *Optimization of the selected ethanol- salt system (ATPE) using RSM*

Response surface methodology is used to find the optimum condition of anthocyanin extraction process from *Dacryodes rostrata* using. In this experiment Box-Behnken design with three main factors (X_1, feedstock amount; X_2, ethanol concentration; X_3, salts concentration) and two responses (K_1: Partition coefficient of total Anthocyanin content, K_2: Partition coefficient of total Protein content). All experiments are carried out randomly according to Table 3.0 to minimize the effect of unexplained systematic errors then the results were fitted to a second order regression [14].

Table 3 RSM optimization run generated by design expert software

Run	Parameters		
	A: Ethanol concentration	B: salt Concentration	C: feedstock amount
	(%)	(%)	(%)
1	25.00	10.00	2.00
2[a]	25.00	15.00	6.00
3	20.00	10.00	6.00
4[a]	25.00	15.00	6.00
5	30.00	15.00	10.00
6[a]	25.00	15.00	6.00
7[a]	25.00	15.00	6.00
8	25.00	10.00	10.00
9	25.00	20.00	10.00
10	30.00	20.00	6.00
11	20.00	20.00	6.00
12[a]	25.00	15.00	6.00
13	20.00	15.00	2.00
14	25.00	20.00	2.00
15	30.00	10.00	6.00
16	20.00	15.00	10.00
17	30.00	15.00	2.00

3.0 Results and discussion

3.1 Aqueous two-phase extraction

The partitioning of the anthocyanin and protein was influenced by many factors such as ethanol concentration, salt concentration and amount of feedstock. In order to optimize partition behaviour of anthocyanin and protein, experiment was conducting by manipulating those parameters in multiple experiment and the results were discussed in the flowing section.

3.1.1 Screening of ethanol-salt systems

The deferential partitioning of anthocyanin and protein was studied in ATPE comprised of ethanol, different salt (ammonium sulphate, dipotassium phosphate, and potassium dihydrogen phosphate). Tow phase formation of ethanol-ammonium sulphate as well as ethanol-dipotassium phosphate could be observed. However, it was difficult to observe two-phase formation for ethanol- potassium dihydrogen phosphate as showed in Table 3.1.1 Two below. Also a system of 40% ethanol and 10 % salt did not form two-phase system which then the experiment were carried out in the range of ethanol (25%-30%) (wt/wt) and salt in the range of (20%-30%) (wt/wt).

Table 3.1.1Two phase forming screening.

Amount of Ethanol	Amount of Salt	Amount of Water	Two phase forming
Ethanol-Ammonium Sulphate			
%	%	%	YES/NO
25	20	55	YES
30	15	55	YES
40	10	50	NO
Ethanol-Dipotassium Phosphate			
%	%	%	YES/NO
25	20	55	YES
30	15	55	YES
40	10	50	NO
Ethanol- Potassium dihydrogen phosphate			
%	%	%	YES/NO
25	20	55	NO
30	15	55	NO
40	10	50	NO

3.2 Analytical method for ATPE optimization

3.2.1 Total anthocyanin content (TAC)

Total anthocyanin content was obtained using pH-deferential method which as described in section 2.4.1. Table **0** shows the total anthocyanin content in the top and bottom phase of each system. 30% Ethanol and 15% ammonium sulphate system contain the highest anthocyanin content in the both phases thus anthocyanin cannot be purified using ammonium sulphate-ethanol system. Other than that 30% ethanol and 15% dipotassium phosphate system is preferred due to the big difference in the TAC between the top and bottom phase.

Table 0 Total Anthocyanin Content (TAC).

Salt Type	Phase composition (ethanol/salt,(%w/w))	Concentration of anthocyanin in the top phase (mg GAE/mg extract)	Concentration of anthocyanin in the bottom phase (mg GAE/mg extract)
Ammonium sulphate	(25/20)	58880.26	44730.74
	(30/15)	214525	184172

Dipotassium Phosphate	(25/20)	15062.39	4792.57
	(30/15)	**136930.85**	**4336.14**

3.2.2 Total Protein Content

Total protein content is obtained using BCA method discussed in section 2.4.2. The protein content for the top and bottom phase of all system were determine as showed in Table 3.2.2

Table 3.2.2Total Protein Content (TPC).

Salt Type	Phase composition (ethanol/salt,%wt/wt)	Concentration of protein on the top phase (ug/mL)	Concentration of protein on the bottom phase (ug/mL)
Ammonium sulfate	(25/20)	0.09907	0.0993
	(30/15)	0.0988	0.099
Dipotassium Phosphate	(25/20)	0.09944	0.09881
	(30/15)	**0.0989**	**0.09913**

3.2.3 Determination of Volume Ratio, Partition Coefficient, and Recovery Yield

Table shows the partition coefficient as well as recovery yield of the top and bottom phase for all ATPE systems. It was observed that majority of the targeted anthocyanin partitioned to the top phase. The partition coefficient of ethanol dipotassium phosphate system is the highest compared to other system. The yield of the same system at the top phase is 99.37% which mean most of the anthocyanin, therefore dipotassium phosphate was utilized for response surface methodology.

Table 3.2.3 Volume Ratio, Partition Coefficient, and Recovery Yield of different ethanol-salt system.

	Phase composition (ethanol/salt,(%wt/wt)	Partition coefficient , K		Recovery yield, Y (Top)		Recovery yield, Y (bottom)	
		TAC	TPC	TAC	TPC	TAC	TPC
Ammonium Sulfate	(25/20)	9.21	6.98	90.21	87.47	9.79	12.53
	(30/15)	4.96	4.25	83.22	80.95	16.78	19.05
Dipotassium Phosphate	(25/20)	6.29	2.01	86.27	66.81	13.73	33.19
	(30/15)	157.89	4.99	99.37	83.30	0.63	16.70

3.3.1 Screening of Significant Parameters

Response surface methodology (RSM) was applied using commercial statistical package, Design Expert version 11 to identify the optimum extraction parameter in order to extract anthocyanin from *Dacryodes rostrata* peels. Analysis of two responses was performed (i.e. partition coefficient (k) for total anthocyanin content, and partition coefficient (k) for total protein content). The order of the experiments was randomized and all data was analysed using multiple regression. Quadratic equation was used to express the responses as a function of independent variable where A, B and C present ethanol concentration, salt concentration, and amount of feedstock each at two level Table The initial selection of the independent parameters and its range is based on literature review. 17 runs were carried out with 5 centre point as per the design matrix.

Table 3.2.4Factors and Levels Tested for the Extraction.

Independent Parameters	Factor levels	
	Low (-)	High (+)
Ethanol concentration (%)	20	30
Salt concentration (%)	10	20
Amount of feedstock (%)	2	10

3.3.2 Optimization of the significant factors

Based on the results discussed before three parameters such as ethanol concentration, salt concentration, and amount of feedstock were screened and two responses which are partition coefficient (k) for total anthocyanin content, and partition coefficient (k) for protein content. Box-behnken design (BBD) was used to identify the correlation between process parameters and the three responses, as well as to determine the optimum extraction condition that give higher total anthocyanin partition coefficient from *Dacryodes rostrata* peel. Box-behnken design is usually used for research propose in order to understand the effect of parameters in a system as well as it minimize the number of experiments, material resources, cost and time. A second order polynomial model was applied to predict the response variable and adequacy of the model using the regression analysis R^2 and ANOVA one-way. the relation between independent parameters and response variable was demonstrated by the response surface graph.

Table 3.3.2 Experimental Design Condition and Results.

	Factor 1	Factor 2	Factor 3	Response 1	Response 2
Run	A: ethanol %	B: salt %	C: feedstock %	K1 For TAC	K2 For TPC
1	25.00	10.00	2.00	3.55	3.56
2[a]	25.00	15.00	6.00	10.26	4.32
3	20.00	10.00	6.00	-	-
4[a]	25.00	15.00	6.00	9.56	4.01
5	30.00	15.00	10.00	86.6	10
6[a]	25.00	15.00	6.00	16.59	4.12
7[a]	25.00	15.00	6.00	12.11	4.21
8	25.00	10.00	10.00	6.05	2.67
9	25.00	20.00	10.00	56.47	9.48
10	30.00	20.00	6.00	12.68	3.51
11	20.00	20.00	6.00	4.92	3.47
12[a]	25.00	15.00	6.00	19.18	4.35
13	20.00	15.00	2.00	12.91	3.05
14	25.00	20.00	2.00	34.07	4.96
15	30.00	10.00	6.00	13.56	5.01
16	20.00	15.00	10.00	10.5	2.9
17	30.00	15.00	2.00	17.66	5.85

[a] Centre point
K: partition coefficient

The experimental design above was used to analyse the effect of the three factors (ethanol concentration, salt concentration, and amount of feedstock) in the extraction of anthocyanin from *Dacryodes rostrata* peels, all experiment runs were conducted and the responses of partition coefficient of anthocyanin as well as partition coefficient of protein were recorded as seen in Table . Experimental results were used to calculate the coefficient of the quadratic equation and ANOVA results of the model. P-value lower than 0.05 in the model indicate more significant effect on the response variables. Coefficient of multiple determination R^2 for the experiment data were 0.9574 and 0.9968 for both responses respectively, R^2 is greater than 80% the model considered to be good-fitting model and when R^2 is close to unity, it indicates that the empirical model is suitable for fitting the actual results. Also, when the R^2 shows the inappropriateness of the model to explain the relation between two variables, however adding any other variable will increase the value of R^2 even if the variable is not much important, therefore this also indicate that a large R^2 does not always imply the adequacy of the model.

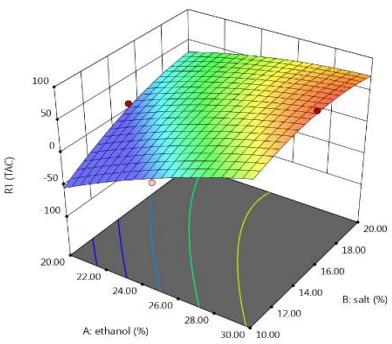
3.3.3 Response Surface Analysis for Anthocyanin Partition Coefficient

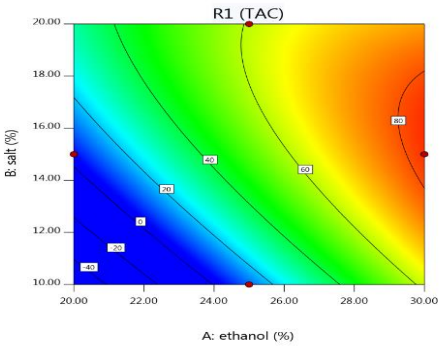
The data in Table 3.3.3 below shows the relation between petition coefficient of anthocyanin and the three extraction parameters (ethanol concentration, salt concentration, and amount of feedstock). The p-value of the model is 0.0018 which is lower than 0.05 therefore the model considered significant which mean there is an effect caused by the three parameters in the partition coefficient of anthocyanin.

Table 3.3.3 ANOVA for Quadratic Model (partition coefficient for Anthocyanin content).

Source	Sum of Squares	df	Mean Square	F-value	p-value	
Model	6867.63	9	763.07	15.00	0.0018	significant
A-ethanol	2419.25	1	2419.25	47.55	0.0005	
B-salt	1955.73	1	1955.73	38.44	0.0008	
C-feedstock	1044.93	1	1044.93	20.54	0.0040	
AB	684.78	1	684.78	13.46	0.0105	
AC	1272.71	1	1272.71	25.02	0.0024	
BC	99.00	1	99.00	1.95	0.2125	
A^2	211.24	1	211.24	4.15	0.0877	
B^2	734.39	1	734.39	14.44	0.0090	
C^2	2312.32	1	2312.32	45.45	0.0005	
Residual	305.25	6	50.87			
Lack of Fit	235.49	2	117.74	6.75	0.0522	not significant
Pure Error	69.76	4	17.44			

Figure 3.3.3A is the response surface plot and 3.3.3B is counter plot showing the effect ethanol concentration, salt concentration, and amount of feedstock on the partition coefficient of anthocyanin. From 3.3.3 A and B, it clearly seen that the parameters of ethanol concentration salt concentration and feedstock amount showed a positive linear effect which mean when ethanol concentration increases the partition coefficient of anthocyanin increases too and that revealed to the best ethanol concentration of 30%, on the other hand the partition coefficient of anthocyanin increases when the salt concentration increases until it reaches an optimum point of 15.9% then it decreases slowly. In addition to that feedstock amount shows a similar relationship as ethanol and salt concentration.





3.3.3A /3.3.3B are the Response Surface Plot and counter plot showing the effect of extraction variables (Ethanol concentration, salt concentration and the amount of feedstock) in the partition of anthocyanin content.

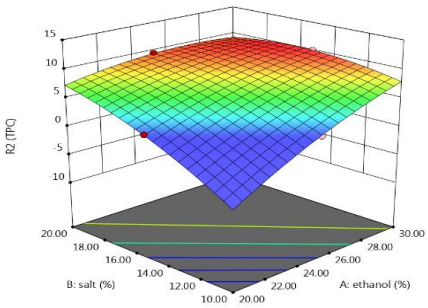
3.3.4 Response surface analysis for protein partition coefficient

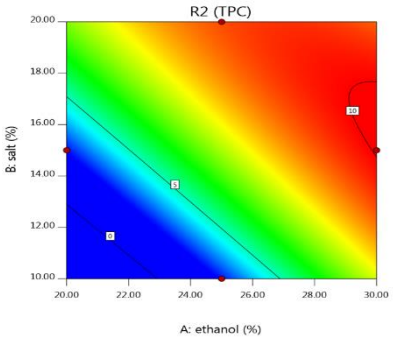
The data in Table 3.3.4 shows the relation between the partition coefficient of protein and the three independent variables (ethanol concentration, salt concentration, and amount of feedstock). Which have a regression value of 0.89. The p-value of the model is < 0.0001 which is lesser than 0.05 therefore this model is significant. Which mean all three parameters have an effect on the partition coefficient of protein.

Table 3.3.4 ANOVA for Quadratic Model (partition coefficient for protein content).

Source	Sum of Squares	df	Mean Square	F-value	p-value	
Model	67.83	9	7.54	208.07	< 0.0001	significant
A-ethanol	35.00	1	35.00	966.29	< 0.0001	
B-salt	20.61	1	20.61	568.85	< 0.0001	
C-feedstock	7.28	1	7.28	200.89	< 0.0001	
AB	13.82	1	13.82	381.52	< 0.0001	
AC	4.62	1	4.62	127.61	< 0.0001	
BC	7.32	1	7.32	201.99	< 0.0001	
A^2	4.44	1	4.44	122.57	< 0.0001	
B^2	6.88	1	6.88	189.92	< 0.0001	
C^2	19.23	1	19.23	530.96	< 0.0001	
Residual	0.2173	6	0.0362			
Lack of Fit	0.1379	2	0.0689	3.47	0.1337	not significant
Pure Error	0.0795	4	0.0199			

Figure 3.3.4A is the response surface plot and 3.3.4B is counter plot showing the effect of ethanol concentration, salt concentration, and amount of feedstock on the partition coefficient of protein. All three parameters showed a positive linear effect and quadratic negative effect to the partition coefficient of protein. Figure 3.3.4 A shows decreases of the partition coefficient of protein when salt concentration increases which can be seen 15.9% salt is an optimum concentration to make the protein content as lower as possible. On the other hand, when ethanol concentration increases the partition coefficient increases too until it reaches 30 % ethanol.





3.3.4A /3.3.4B are the Response Surface Plot and counter plot showing the effect of extraction variables (Ethanol concentration, salt concentration and the amount of feedstock) in the partition of anthocyanin content.

4.0 Conclusion

In this study, within the aim of the extraction and purification of anthocyanins from *Dacryodes rostrata* peels using ATPE, the experimental design and optimization were performed. The focus of this study provided notable information regarding to anthocyanin and their recovery from *Dacryodes rostrata* peels which no one preformed before. It was found that *D.rostrata* peel contain high amount of anthocyanin thus it can be utilized as an alternative supplement for chronic and degenerative diseases.

From the screening of different ethanol- salt system it was found that dipotassium phosphate is the most preferred salt due to its high anthocyanin yield of top and bottom phase of 83.4, 16.3 respectively as well as high partition coefficient of 158.89. Ammonium sulphate and potassium dihydrogen phosphate were ignored either because it did not form two phase or the amount of anthocyanin extracted is very low compared to that dipotassium phosphate.RSM optimization shows that the effect of the three parameters namely ethanol concentration, salt concentration as well as the amount if feedstock are important parameters to obtain the optimum extraction condition. This optimum condition is defined as the extraction process that maximise the total anthocyanin content and minimize the total protein content. 30% ethanol, 15.952% dipotassium phosphate, and 10% feedstock is the optimum extraction conditions that give anthocyanin partition coefficient of 83.016 and protein partition coefficient of 10.120.

5.0 References

[1] D. Webb, "Anthocyanins" *Today's Dietitian"*, vol.16, no.3 pp.20, 2014.
[2] H. E. Khoo, A. Azlan, S. T. Tang, and S. M. Lim, "Anthocyanidins and anthocyanins: colored pigments as food, pharmaceutical ingredients, and the potential health benefits," *Food Nutr. Res.*, vol. 61, no. 1, p. 1361779, 2017.
[3] T. Bin Zou, M. Wang, R. Y. Gan, and W. H. Ling, "Optimization of ultrasound-assisted extraction of anthocyanins from mulberry, using response surface methodology," *Int. J. Mol. Sci.*, vol. 12, no. 5, pp. 3006–3017, 2011.
[4] W. Mullen, S. C. Marks, and A. Crozier, "Evaluation of phenolic compounds in commercial fruit juices and fruit drinks," *J. Agric. Food Chem.*, vol. 55, no. 8, pp. 3148–3157,

2007.
[5] T. G. Albuquerque, M. A. Silva, M. B. P. P. Oliveira, and H. S. Costa, *Analysis, Identification, and Quantification of Anthocyanins in Fruit Juices*. 2017.
[6] W. Mullen, S. C. Marks, and A. Crozier, "Evaluation of phenolic compounds in commercial fruit juices and fruit drinks," *J. Agric. Food Chem.*, vol. 55, no. 8, pp. 3148–3157, 2007.
[7] Z.Hua, D.Yuesheng, X.Ge. L.Menglu, D.Liya, A.Lijia and X. Zhilong, "Extraction and Purification of Anthocyanins from the Fruit Residues of Vaccinium uliginosum Linn," *J Chromat Separation Technique,* vol. 4, no.2, pp.1-5, 2013.
[8] Z.Hua, D.Yuesheng, X.Ge. L.Menglu, D.Liya, A.Lijia and X. Zhilong, "Extraction and Purification of Anthocyanins from the Fruit Residues of Vaccinium uliginosum Linn," *J Chromat Separation Technique,* vol. 4, no.2, pp.1-5, 2013.
[9] Y.-C. Feng *et al.*, "Aqueous Two-Phase System as an Effective Tool for Purification of Phenolic Compounds from Fig Fruits (*Ficus carica* L.)," *Sep. Sci. Technol.*, vol. 50, no. 12, pp. 1785–1793, 2015.
[10] J. Sutharut and J. Sudarat, "Total anthocyanin content and antioxidant activity of germinated colored rice," *Int. Food Res. J.*, vol. 19, no. 1, pp. 215–221, 2012.
[11] X. Wu *et al.*, "Aqueous two-phase extraction, identification and antioxidant activity of anthocyanins from mulberry (Morus atropurpurea Roxb.)," *Food Chem.*, vol. 129, no. 2, pp. 443–453, 2011.
[12] Thermo Scientific, "User Guide: Pierce BCA Protein Assay Kit," *Pierce Biotechnol.*, vol. 0747, no. 23225, pp. 1–7, 2011.
[13] Yun-Chao Feng, Wen-Liang Li, Fa-Mei He, Tao-Tao Kong, Xiao-Wei Huang, Zhong-Hong Gao, Nai-Hao Lu, and Hai-Ling Li, "Aqueous Two-Phase System as an Effective Tool for Purification of Phenolic Compounds from Fig Fruits (*Ficus carica* L.)," *Sep Sci Technol*, vol. 50, no. 12, pp. 1785–1793, 2015.
[14] Ehsan Ghanaei, Feridun Esmaeilzadeh, Jamshid Fathi Kaljahi, and U Shiraz, "Evaluation of Activity Coefficient Models in Prediction of Wax Appearance Temperature," no. 1, pp. 1–5, 2006.

Degradability Study of Controlled - Release Phosphorus Hydrogel

*Anis Raihana Abdul Aziz[1], and Siew Wei Phang[*1,2]*

[1]School of Engineering, Faculty of Built Environment, Engineering, Technology & Design, Taylor's University, Malaysia

Abstract. A fertiliser is an essential component in the agricultural industry. Production of conventional fertiliser and soil fertilisation increases continuously over time in order to meet the ever increasing demands of ecosystem especially in the aspect of food security. However, in terms of the efficiency of nutrient use, it is relatively low. "Intelligent fertilisers" such as slow release fertilisers and controlled - release fertilisers have also been developed to reduce the negative impacts on environment and society. Controlled - release fertiliser (CRF) is a purposely designed fertiliser coated with either a natural or semi - natural macromolecule material which acts as a semi - penetrator for diffusion process. Anyhydrous calcium chloride (93% purity), diammonium hydrogen phosphate (99% purity), sodium alginate (99%) of pharmaceutical grade were and food grade of pure cassava starch (99.9%) were adopted to formulate 13 samples in order to study the effect of biodegradation of the phosphorus hydrogel into the soil over 31 days. Surface morphology of the beads were also being analysed over a period of 21 days. Ability of starch to retain water over a period of time could not be denied. Sodium alginate when incorporated with anhydrous calcium chloride had helped in further strengthening the polymer matrix of hydrogel beads by preventing starch from dissolving into the bio - soil compost. After 31 days of biodegradability test, it was determined that the best combination for an optimum result in real life application would be S3 for its moderately high content of pure cassava starch (9 w/v%) for better water retention ability, S6 for its low amount of sodium alginate (0.5 w/v%) to provide better mucoadhesion between the polymer matrix which eventually prevent the starch from dissolving at a fast rate and lastly, S13 for its high molarity of calcium chloride solution (3.5 M) for tighter network cavity.

Keywords: Controlled-release, Degradability, Hydrogel, Phosphorus

1 Introduction

A fertiliser is an essential component in the agricultural industry. Its granules possess brittle failure mode or the breaking degree and porous characteristics of various mineral compounds and edges of crystals [1]. The basic principle of fertilisation is that the amount of nutrient absorbed by the plants has to be equivalent with the amount of nutrient supplied by the fertiliser. Ammonia, nitrogen (urea), phosphorus and sodium are the common types of fertiliser used globally. Urea tops the other three fertilisers with approximately 184 million tonnes of production worldwide [2].

The production of conventional fertiliser and soil fertilisation increases continuously over time in order to meet the ever increasing demands of the ecosystem especially in the aspect of food security. However, in terms of the efficiency of nutrient use, it is relatively low. Nutrient use efficiency is defined as the biomass produced per an input of nutrient content in the fertiliser [3]. Nitrogen and potassium nutrients recorded 50 - 60% nutrient assimilation by crops in the first year, while 10 - 25% for phosphorus also in the first year of nutrient assimilation, with continuous reduction of 1 - 2% yearly [1]. Fertilisers are exposed to leaching, de - nitrification, volatilisation and fixation [4]. The amount of nutrient losses to the environment depends on the conditions of soil, the climate and the implementation of latest technologies. As a result, there will be an increment in production costs, water eutrophication, and imbalance gaseous content especially nitrous in the atmosphere, and deterioration of water, soil and food quality. Therefore, it is crucial to manage and mitigate the issues of fertilisers so as to maintain a balanced ecosystem.

Steps to boost the nutrient assimilation efficiency have been discussed thoroughly and these include production of stabilised fertiliser, liquid fertiliser, and urea super - granules. “Intelligent fertilisers” such as slow release fertilisers and controlled - release fertilisers have also been developed to reduce the negative impacts on environment and society for instance hazardous emissions, seed toxicity, changes in pH level of soil, breathing problems and dermal irritation. The development of these intelligent fertilisers eventually improves nutrient use efficiency while boosts up crop production as the fertilisers possess the ability to inhibit nutrient loss [1,5]. Henceforth, soil quality and rate of germination are enhanced.

Controlled - release fertiliser (CRF) is a purposely designed fertiliser coated with either a natural or semi - natural macromolecule material which acts as a semi - penetrator for diffusion process. The coating is known as hydrogel with the capability to retain water or saline solutions under pressure. The active nutrients in CRF will be released at a slow pace with the gradual nutrients intake of plants. A single application of CRF is able to meet the requirements of crop production [6]. Thickness of the coating determines the release longevity. The thicker the coating, the longer the longevity, the smaller the rate of application required by the crop. Surrounding temperature, moisture, soil bioactivity, wetting and drying cycles play an essential role in determining the amount of fertiliser released [5].

The coating material of the fertiliser that was prepared at 13 formulations of various pure cassava starch, sodium alginate and cross linking calcium chloride solution composition (referring to Table 2.0) would affect biodegradability or dissolution rate of nutrient. The biodegradability typically depends on the polymer chains of that are cleaved enzymatically [7]. Researchers are currently working on the possibilities of producing biodegradable polymers to make hydrogels less harmful to the environment and to apply as conditioners for the soil in order to improve access to water [8]. There are a number of driven factors that causes researchers to develop a handful of formulations. Firstly, to meet the nutrient needs of crops. Secondly, to reduce fertiliser salts leaching as this is the major contributor to nutrient losses. [9]. Leaching gets highly critical at locations where rigorous irrigation happens.

Starch, a type of superabsorbent material, has an excellent properties of water retention. Due to this, it has garnered so much attention among the researchers to include it in the formulation of controlled - release fertiliser. It took 60 days for active nutrients to be fully released, after the starch matrix was employed in the pesticide coating material [10]. Its high water absorbency has caused starch based formulation to have a high possibility to burst. Thus, an enhancement for the polymer matrix was made by adding sodium alginate which was reported to possess good gelation characteristic [11] or mucoadhesion [12] property to strengthen the matrix. Cross - linking agent, in this case, calcium chloride further improvised the porosity and molecular structure of matrix polymer to be better [11].

In short, controlled - release fertiliser is a green technology [4] that causes alteration to the nutrient release kinetics so as to meet the metabolic requirements of plants on top of reducing the rate of leaching and volatilisation.

This project aims to study the effect of different formulations of pure cassava starch, sodium alginate, diammonium hydrogen phosphate and cross linking agent (calcium chloride solution) on biodegradability of the controlled - release of phosphorus hydrogel in bio - soil compost. The project scope includes the biodegradability and surface morphology studies of the hydrogel as a continuation project from previous research of the same group [13].

2 Methodology

2.1 Material

A typical Baba 518 Planter Box and 28 liters of bio - soil compost manufactured by Impra Plant Care Solutions were purchased off the shelf from Bunga Raya Nursery, Seremban. Anyhydrous calcium chloride (93% purity), diammonium hydrogen phosphate (99% purity), sodium alginate (99%) of pharmaceutical grade were purchased from Sigma - Aldrich Corporation, USA. Food grade of Cap Kapal ABC pure cassava starch (99.9%) manufactured in Thailand was purchased from Mydin Hypermarket, Malaysia. Lastly, a pack of 100 pieces disposable filter tea bags was purchased from Daiso.

2.2 Synthesis of Starch - Alginate Hydrogel Beads

The methodology to prepare the starch - alginate hydrogel beads were extracted from B. Singh et al. and J.Y. Low [13-15]. In order to prepare 13 samples of three formulation sets as shown in Table 2.0, pure cassava starch, sodium alginate and anhydrous calcium chloride variations were used. A constant 5 w/v% of diammonium hydrogen phosphate was mixed with the components (pure cassava starch and sodium alginate) in 100 ml of distilled water. The chemicals were stirred by using a hot plate (Wise Stir MSH - 20D, Germany) at a stirring speed of 600 RPM and a temperature of 50℃ for 30 minutes so as to achieve a homogenous solution. 14.7g of anyhydrous calcium chloride was dissolved in 100 ml of distilled water to prepare 1M of calcium chloride solution. Cross linking action occurs through an extrusion method when a syringe of 1.2mm diameter was used to drop the mixture of alginate-starch-phosphorus into the calcium chloride solution. Further, distilled water was used to rinse the hydrogels and hydrogels were filtered using 200 - mesh stainless steel sphere - shaped net to allow a compact coating formation around the core material of the fertilisers. The hydrogels were then dried using tissue paper and at room temperature (24±2) ℃ in order to remove excess cross linking calcium chloride solution. This step was also used to obtain constant weight. Drying of hydrogels took place in an oven (Memmert UN75, Germany) set at a temperature of 60℃ for 24 hours. This step was essential in order for the hydrogels to achieve thermal stability. The dried samples were removed from the oven, cooled and kept in parafilm sealed bottles to inhibit

humidity. S1 to S5 differs in terms of amount of pure cassava starch, meanwhile S6 to S9 varies in terms of sodium alginate volume and variations of anhydrous calcium chloride happened in S10 to S13. Table 3.0 recorded the percentage yield of each formulation.

Table 2.0. Controlled - release Formulations.

Material Variation	Sample	Cassava Starch (w/v) %	Sodium Alginate (w/v) %	Calcium Chloride (M)
Starch	**S1**	3	1	1.5
	S2	6	1	1.5
	S3	9	1	1.5
	S4	12	1	1.5
	S5	15	1	1.5
Sodium Alginate	**S6**	12	0.5	1.5
	S7	12	1.5	1.5
	S8	12	2	1.5
	S9	12	2.5	1.5
Calcium Chloride	**S10**	12	1	2.0
	S11	12	1	2.5
	S12	12	1	3.0
	S13	12	1	3.5

2.3 Measurements of Beads Size

From each formulation, 15 completely dried hydrogel beads were taken out to measure the average size using a 150 mm AOS Digimatic Caliper CD - 6" ASX model manufactured by Mitutoyo and a measuring balance TX423L model supplied by Shimadzu.

The conditions including shapes of hydrogel beads in the teabags were also being observed from time to time for 21 days. Results were tabulated in Table 3.0.

2.4 Degradability Study of Controlled - Release of Phosphorus Hydrogel

The phosphorus hydrogel biodegradability was studied by analysing the samples mass loss for a designated period in a bio - soil compost medium. A planter box was labelled with 13 labels based on the formulations in Table 2.0. Then, 14 liters of bio - soil compost was placed into the planter box. 15 phosphorus hydrogel beads from each formulation were put in 13 labelled disposable filter tea bags prior to burying in the bio - soil compost, 5 cm from the base of the box at an ambient temperature of approximately between 30℃ to 32℃. Water was added daily to keep the water in the soil saturated. Initial weights of the hydrogel beads were weighed and denoted as W_i. After a fixed interval time of 1 hour, 2 hours, 4 hours, 28 hours (Day 1), 41 hours (Day 2), 168 hours (Day 7), 336 hours (Day 14), 360 hours (Day 15), 504 hours (Day 21) and 744 hours (Day 31), the buried samples were dug out, cleaned and weighed as W_b so as to monitor the biodegradation process.

The biodegradability test was performed through the measurement of triplicate average weight of that particular 15 phosphorus hydrogel beads for each formulation throughout the mentioned fixed intervals. Results were plotted in Figures 1, 2 and 3.

$$Biodegrdation = \frac{W_i - W_b}{W_i} \times 100\% \quad (1)$$

2.5 Sample Characterisation

2.5.1 Digital Microscope

The surface morphology of samples from each formulation was analysed under 4X magnification using Swift M10DB - MP microscope supplied by Swift Optical. Results were depicted for before and after 21 days from Figure 4a) onwards until Figure 16b).

3 Results and Discussions

3.1 Yield Percentages, Sizes and Weights of Phosphorus Hydrogel Beads

Table 3.0 depicted the percentage of yield, sizes and weights of phosphorus hydrogel beads, both fresh and after 31 days of being buried in the bio - compost soil.

The percentages production of phosphorus hydrogel beads were calculated based on the following formula:

$$\text{Yield } (\%) = \left(\frac{\text{quantity of product formed}}{\text{quantity of reactant taken}}\right) \times 100 \quad (2)$$

S1 to S5 varied in the aspect of pure cassava starch amount as stated in Table 2.0. S4 had the highest yield percentage of 75% while S3 possessed the lowest production percentage of 35.90%. Moving onto the variation of sodium alginate group from S6 to S9, S7 had the highest yield percentage of 63.57 % whereas S9 had the least yield percentage of 49.16%. From the variation of the cross linking solution which is calcium chloride, the greatest yield was S10 with a record of 72.72% and further, 26.61% was recorded for S11 that had the lowest production percentage.

As for the sizing of the hydrogel beads, a Vernier caliper was used to measure the width of 15 beads from each formulation. Data in Table 3.0 showed the average size for all 15 beads. Variation of pure cassava starch recorded S1 to have had the tiniest average size of 2.292mm and the biggest was S4 which had an average size of 3.460mm. Sodium alginate variation class recorded S9 to have possessed the largest average size of 10.379mm while the smallest average was from S7 with a record of 3.077mm. The next classification that differed in terms of the molarity of calcium chloride solution had S10 as the biggest average size of 3.161mm and S11 as the smallest with an average size of 2.751mm. Typically, as days passed, beads changed their shapes to be either in powder form, lumps or flattened out and stick onto the wall of the tea bags. Only S7, S8 and S9 had their original shapes after 21 days. Even so, the shapes were starting to change.

Further, the weights measurement was an average reading of a triplicate of 15 hydrogel beads taken from each sample formulation. The readings of samples were taken from Day 0 until Day 31 that were buried in the bio-soil compost. S4 was the heaviest with a weight of 1.6640g while S2 being the lightest with a weight of 1.0683g, for the starch variation category after 31 days. When sodium alginate composition was being manipulated, S6 recorded the lightest average weight of 1.2290g whereas S9 possessed the heaviest average weight of 2.6093g. The anhydrous calcium chloride solution variation showed S12 and S11 to be the lightest (1.8730g) and heaviest (2.3447g) respectively, after 31 days.

Table 3.0. Yield Percentages, Sizes and Weights of Phosphorus Hydrogel Beads.

Sample	Yield (%)	Initial Average Size, mm	Average Size (After 21 Days)	Initial Average Weight, g	Average Weight After 31 Days, g
S1	46.27	2.292	NA: beads became about four lumps.	0.2783	1.5763
S2	42.80	3.009	NA: beads turned into a big lump.	0.2300	1.0683
S3	35.90	2.687	NA: beads crumpled together and stick on to wall of tea bag.	0.1737	1.4353
S4	75.00	3.460	NA: beads existed as powder form, started to change shape.	0.3500	1.6640
S5	51.97	2.999	NA: beads flattened in shape and stick with each other.	0.2157	1.4567
S6	54.78	3.745	NA: beads changed shape, became powder form and flattened, sticks on to wall of tea bag.	0.1633	1.2290
S7	63.57	3.077	NA: two beads remained as they were originally whereas the rest either formed lump or degraded into soil.	0.2137	1.4420
S8	62.08	4.615	NA: beads stick with each other while still having their original powder form.	0.3720	2.0810
S9	49.16	10.379	NA: beads remained in the original powder form.	0.4290	2.6093
S10	72.72	3.161	NA: beads were not intact with each other, however flattened in shape.	0.3330	2.3433
S11	26.61	2.751	NA: beads formed lump and became flat.	0.3893	2.3447
S12	55.63	3.065	NA: powdered form beads became flat.	0.2987	1.8730
S13	34.62	3.139	NA: beads were still in shape and were stick to each other.	0.2167	2.1657

3.2 Biodegradability Test

The weights measurement for this test was an average reading of a triplicate of 15 phosphorus hydrogel beads that were buried in the bio - soil compost for 31 days as mentioned in previous section.

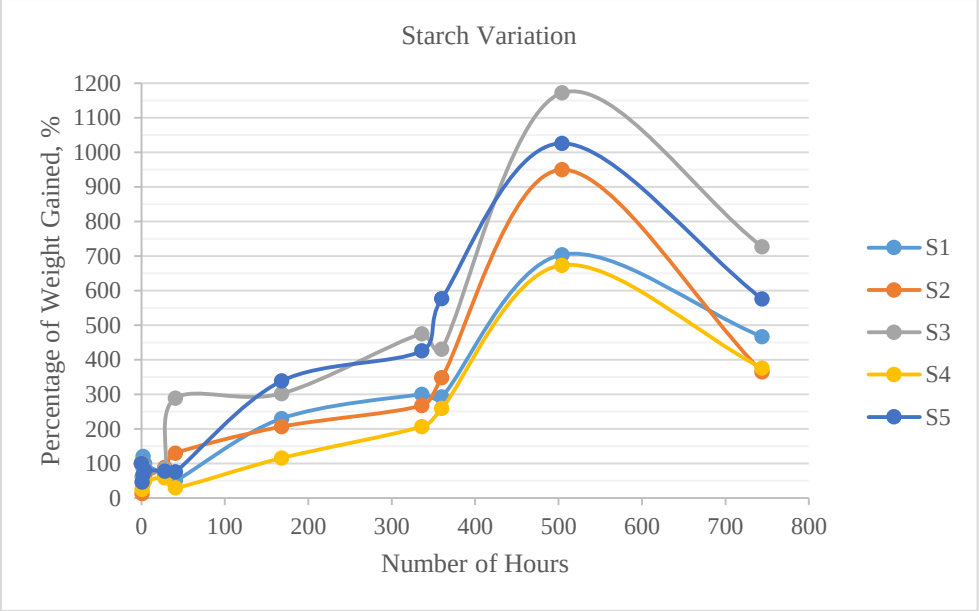


Figure 1. Starch Variation in terms of Weight Gained Percentage against Number of Hours.

Based on Figure 1, Day 2 and Day 14 showed that S3 had a greater weight gained percentage than that of S5. However, as more water was added to the pot, S5 overtook S3 on the following day. S5 possessed the most amount of starch compared to the rest of the hydrogel bead samples, thus, allowing it to be able to have the highest water retention ability until Day 15 when S3 overtook S5 and remained as the greatest ability to retain water until Day 31.

Meanwhile, S4 constantly had the lowest percentage of weight gained and shared an almost similar weight gained percentage with S2 by Day 31. Thus, establishing the fact that both had a very low water retention ability. The percentage of weight gained decreased across all 5 samples after Day 21 which could be from the result of biodegradation that took place in the compost soil.

Variation in pure cassava starch content led to the results in Figure 1 as pure cassava starch had the ability to retain water under high saline concentration, for a certain period making the medium swells. Starch suspension viscosity thus, increases. The viscosity is dependent on the continuous water uptake of the insoluble remains and solubility of starch granules [16]. Initially, water uptake and retention ability increased with the augment of starch content from 3% to 15%, however declined when the density was excessively high. The declination was an effect of a compact space of network [17] in the molecule.

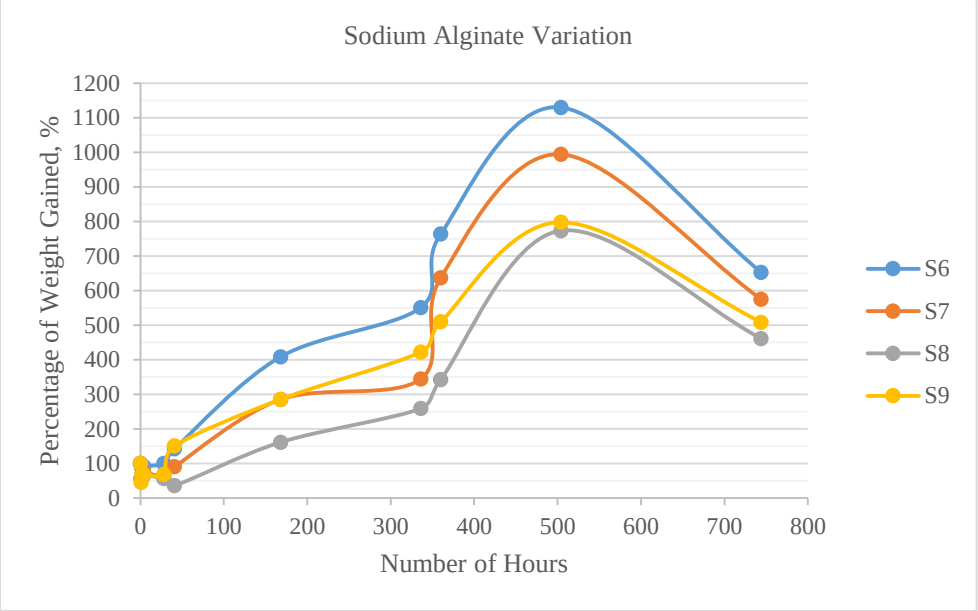


Figure 2. Sodium Alginate Variation in terms of Weight Gained Percentage against Number of Hours.

S6 to S9 varied in terms of the sodium alginate content. The trend lines in Figure 2 increased without intercepting one another as much as it was in the variation of starch. S6 depicted the largest weight gained percentage among all four samples. This was followed by S7, S9 and S8. S8 showed the least percentage of weight gained throughout the experiment. Although S9 contained the most amount of sodium alginate, making it the biggest in size, its weight gained percentage was not as much as S6 and S7. It might have happened that the space in S9 sample was enough to retain water and had achieved maximum strain of structure. Since all four samples did not have a drop on percentage of weight gained until Day 21 before they experienced percentage weight loss, it can be concluded that sodium alginate had prevented starch from dissolving into the bio - soil compost and allowed water to be retained in the coating from 0 hours up until Day 21. Day 21 onwards was where starch started to dissolve gradually, degrading the coating structure into the soil.

Sodium alginate of high concentration caused a smaller weight gained percentage and vice versa. This is attributed to the formation of the highly compact and rigid matrix which inhibiting fertiliser release [18].

Finally, the anhydrous calcium chloride solution acted as a cross linker in the formation of phosphorus hydrogel beads. There was an increasing trend in weight gained percentage as shown in Figure 3. S13 which had the highest molarity of calcium chloride solution, showed the highest percentage of weight gained over time followed by S10, S12 and S11. On Day 15, while the rest of the samples showed increments in the weight gained, S13 showed a small drop before augmented up again until Day 21 and started declining. The small drop can be explained by the gel network that was tightening. Nonetheless, when cavities made up in the polymer chain using G-blocks were vacant, calcium ions filled up the cavity until an equilibrium state was achieved [19]. High concentration of calcium ions will accelerate the gelation kinetics which then became a factor to beads stabilisation and rapid entrapment [19]. S11 was constantly having the least percentage of weight gained from the start of the experiment until Day 21 before declining a slight weight percentage.

Higher weight gained percentage was observed and obtained as the concentration of anhydrous calcium chloride solution increased. This is owing to the polymeric chains that have

greater availability of active binding sites of calcium [18]. Thus, the ability of calcium chloride to possess a higher degree of cross linking action.

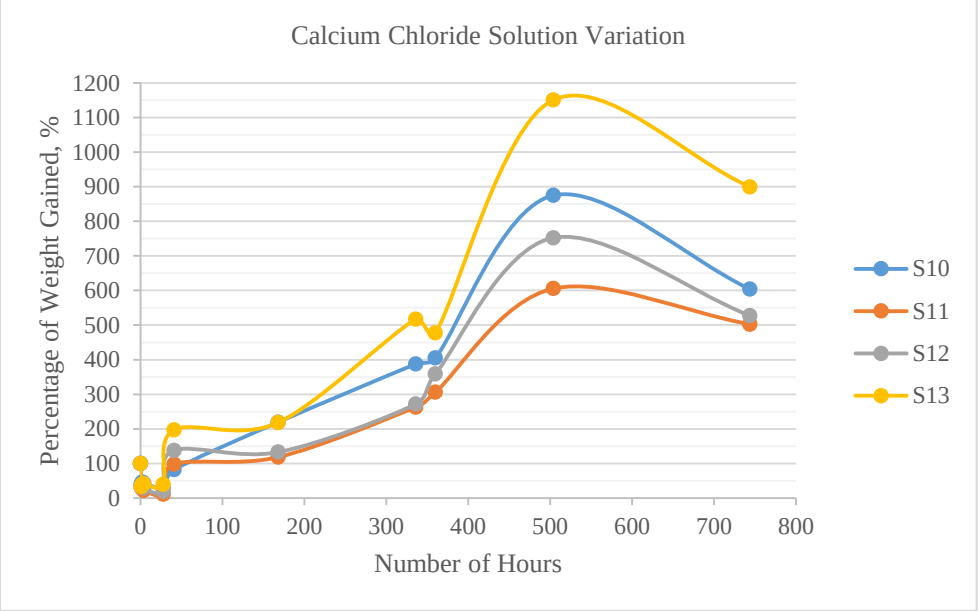


Figure 3. Calcium Chloride Solution Variation in terms of Weight Gained Percentage against Number of Hours.

3.3 Surface Morphology under the Digital Microscope

For each formulation, the surface morphologies of the hydrogel beads before (fresh sample) and after burying for 21 days in the bio - soil compost were studied under the digital microscope using 4X magnification.

Black dots in the figures below were traces of bio - soil compost that stuck on the hydrogel beads over a period of time, when degradation took place. Following figures involved the amount of starch as the manipulative variable.

From Figure 4a), the cross linking action of the chemicals could be seen clearly through the spiky - liked diagram. After 21 days, S1 lost its morphology, confirming that degradation had taken place. Figure 5a) showed that composition of chemicals for S2 formed polygon shapes. 21 days later, these polygon shapes could not be seen anymore. Fresh S3 of Figure 6a) has a similar surface to S1. However, after 21 days, the surface of S3 in Figure 6b) had not changed completely. S4 in Figure 7a) is slightly similar to the fresh S2. The surface of S4 in Figure 7b) can still be seen after 21 days which suggested that it does not retain much water. As for S5, the structure of the fresh sample looked more compact than the rest of the samples that vary in terms of starch. After 3 weeks, the surface turned darker due to its high water retention capability. This was further proven by the water movement that was present under the digital microscope.

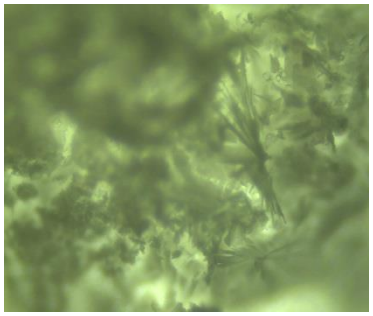


Figure 4a). Surface of fresh S1.

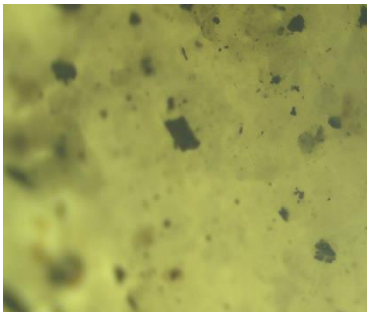


Figure 4b). Surface of S1 after 21 days.

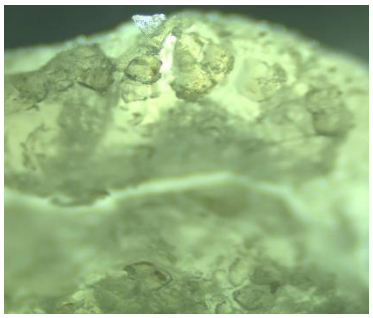


Figure 5a). Surface of fresh S2.

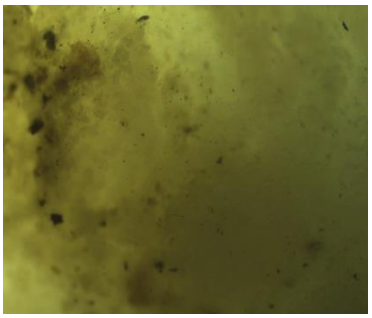


Figure 5b). Surface of S2 after 21 days.

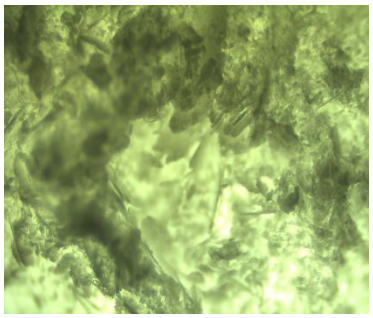


Figure 6a). Surface of fresh S3

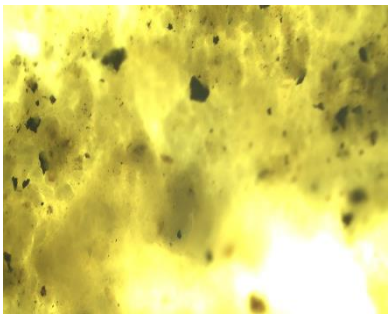


Figure 6b). Surface of S3 after 21 days.

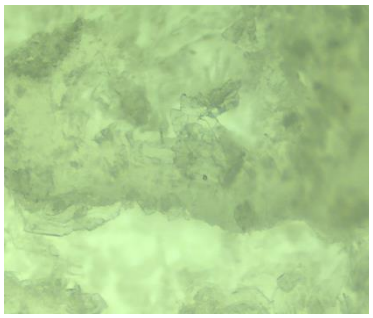


Figure 7a). Surface of fresh S4.

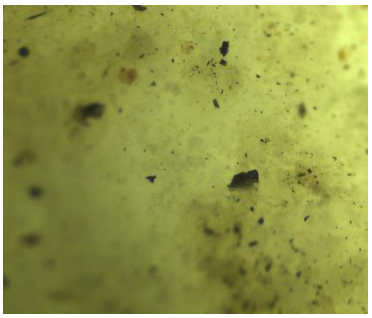


Figure 7b). Surface of S4 after 21 days.

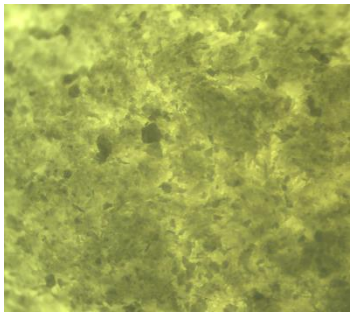


Figure 8a). Surface of fresh S5.

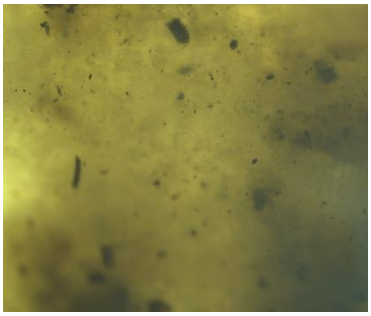


Figure 8b). Surface of S5 after 21 days.

Then, figures below discussed on the surface morphology of the hydrogel beads when the sodium alginate weight was manipulated.

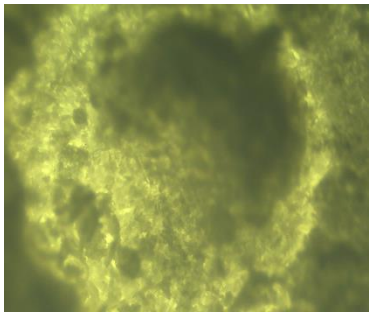


Figure 9a). Surface of fresh S6.

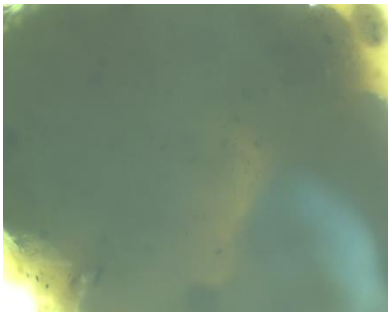


Figure 9b). Surface of S6 after 21 days.

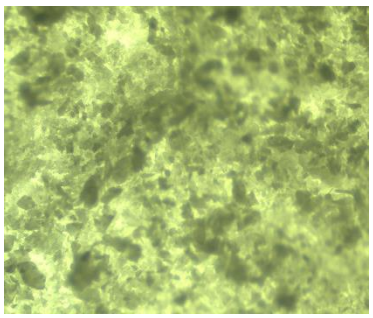


Figure 10a). Surface of fresh S7.

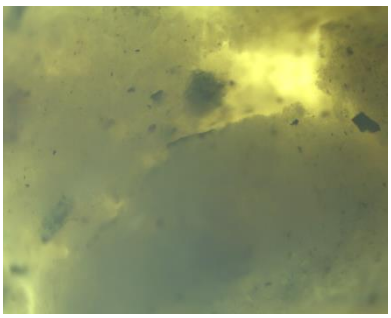


Figure 10b). Surface of S7 after 21 days.

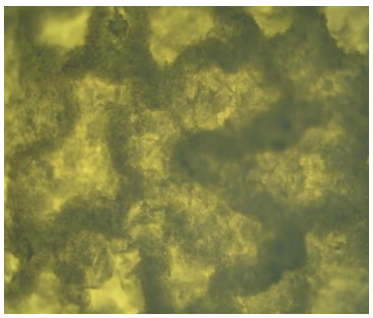


Figure 11a). Surface of fresh S8.

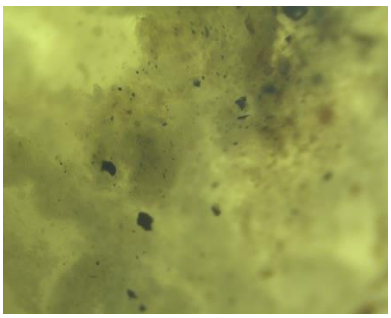


Figure 11b). Surface of S8 after 21 days.

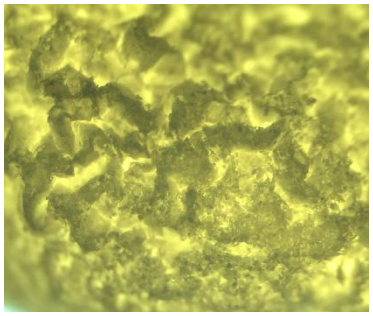


Figure 12a). Surface of fresh S9.

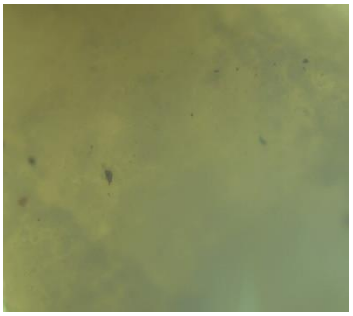


Figure 12b). Surface of S9 after 21 days.

Among these four samples, S9 had the clearest view of its structure when it was still fresh as a result of a high concentration of sodium alginate. Nevertheless, after 21 days, the digital microscope could not zoom in to the structures of S6 and S9 due to the beads being covered by the sand and the fact that starch was prevented from dissolving into the soil through the high content of sodium alginate. Structure of S7 and S8 could still be magnified after 21 days. S6 and S7 were not uniformly structured while S8 and S9 seemed to be more compact and uniform when fresh.

The last four samples varied in the aspect of calcium chloride solution.

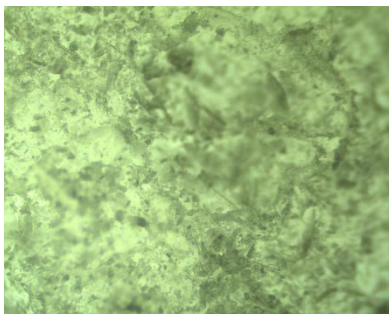


Figure 13a). Surface of fresh S10.

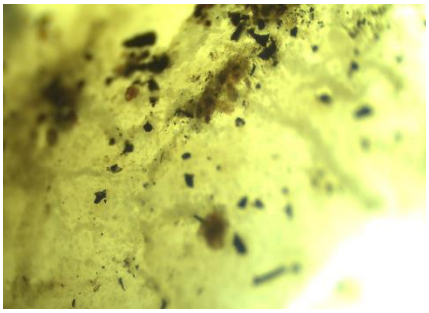


Figure 13b). Surface of S10 after 21 days.

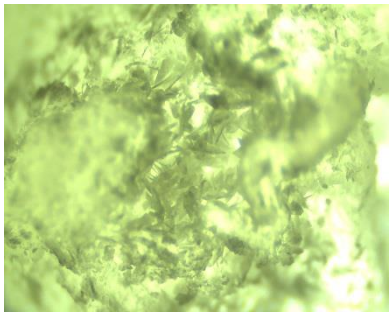


Figure 14a). Surface of fresh S11.

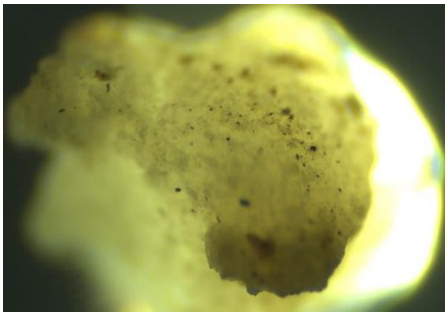


Figure 13b). Surface of S11 after 21 days.

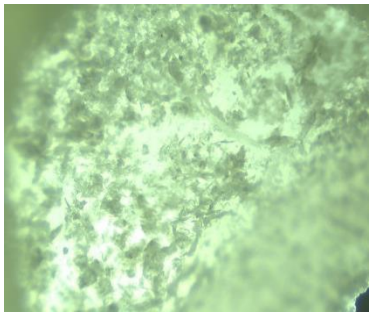


Figure 15a). Surface of fresh S12.

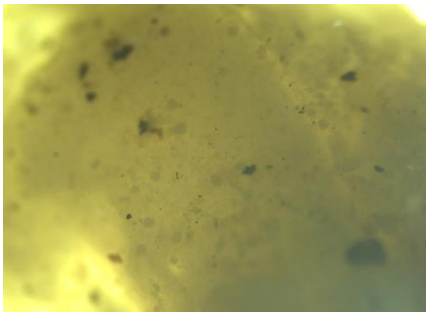


Figure 15b). Surface of S12 after 21 days.

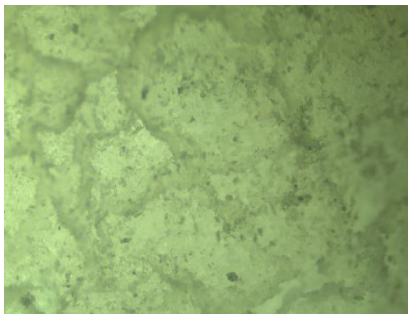


Figure 16a). Surface of fresh S13.

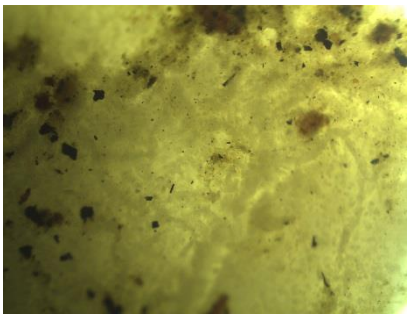


Figure 16b). Surface of S13 after 21 days.

From these 8 figures, S13 has a surface that showed a strong cross linking action that had taken place really well which led to the highest percentage of weight gained after 21 days. The surface of fresh 11 though could be seen, nonetheless, after 21 days, only a small part of the bead could be magnified while the other parts were covered either with water or bio - soil compost. The higher the molarity of calcium chloride solution, the better the porosity structure of the hydrogel beads. Therefore, stronger network of cavity was formed under the presence of bivalent calcium ion [13] through cross - linking action.

These surface morphology sections further conformed that this phosphorus hydrogel type of controlled - release fertiliser falls under a matrix type due to the dispersion of active ingredients in an originally matrix region and is further supported by diffusion across the matrix continuum to the external surroundings [3].

4 Conclusion

Degradability study of the controlled - release phosphorus hydrogel had been successfully made through the formulation of pure cassava starch - sodium alginate - diammonium hydrogen phosphate and calcium chloride as the cross - linking solution. Ability of starch to retain water over a period of time could not be denied. Sodium alginate when incorporated with anhydrous calcium chloride had helped in further strengthening the polymer matrix of hydrogel beads by preventing starch from dissolving into the bio - soil compost. The surface morphology study further conformed that calcium chloride solution played a highly essential role in forming a tight network cavity of the hydrogels surface. Fluctuated pattern of percentage of weight gained graphs could be observed for pure cassava starch and sodium alginate variations. On the other hand, anhydrous calcium chloride variation exhibited a more stable pattern. After 21 days of biodegradability testing the controlled - release fertiliser in bio – soil compost, it was determined that the best combination for an optimum result in real life application would be S3 for its moderately high content of pure cassava starch (9 w/v%) for better water retention ability, S6 for its low amount of sodium alginate (0.5 w/v%) to provide better mucoadhesion

between the polymer matrix which eventually prevent the starch from dissolving at a fast rate and lastly, S13 for its high molarity of calcium chloride solution (3.5 M) for tighter network cavity.

Future work includes the study of rate of mass change as a function of temperature using Thermal Gravimetric Analysis and analysis of functional groups of materials applied in the synthesising of the sample formulations using Fourier Transformed Infrared. To further confirmed the effectiveness of the controlled - release phosphorus hydrogel when the concentration of pure cassava starch (9 w/v%) from S3, combines with the least concentration of sodium alginate (0.5 w/v%) from S6 and the highest concentration of anhydrous calcium chloride (3.5M) from S13. This is to see if the fertiliser can possess good water retention capacity, greater mucoadhesion between polymer matrix and tighter network cavity within the hydrogel beads.

References

[1] K. Lubkowski., A. Smorowska., B. Grzmil., A. Koz#owska. (2015). "Controlled-release fertilizer prepared using a biodegradable aliphatic copolyester of poly(butylene succinate) and dimerized fatty acid," *J. Agric. Food Chem.,* pp. 2597- 2605

[2] M. M. E. Costa., E. C. M. Cabral - Albuquerque., T. L. M. Alves., J. C. Pinto., R. L. Fialho. (2013). "Use of polyhydroxybutyrate and ethyl cellulose for coating of urea granules," *J. Agric. Food Chem.,* pp. 9984 - 9991

[3] M. J. Hawkesford., S. Kopriva., L. J. De Kok. (2014). Nutrient Use Efficiency in Plants Concepts and Approaches. *Springer International Publishing*

[4] T. H. Trinh., K. Kushaari., A. S. Shuib., L. Ismail., B. Azeem. (2015). "Modelling the release of nitrogen from controlled release fertiliser: Constant and decay release," *Biosyst. Eng* (130): pp. 34 - 42

[5] B. Azeem., K. Kushaari., Z. B. Man., A. Basit., T. H. Thanh. (2014). "Review on materials & methods to produce controlled release coated urea fertilizer," *J. Controlled Release* (181): pp. 11 - 21

[6] X. Han., S. Chen., and X. Hu. (2009). "Controlled - release fertilizer encapsulated by starch/polyvinyl alcohol coating," *Desalination* (240): pp. 21 - 26

[7] R. J. Mueller. (2006). "Biological degradation of synthetic polyesters - Enzymes as potential catalysts for polyester recycling," *Process Biochem* (41) : pp. 2124 - 2128

[8] B. R. Dos Santos., F. B. Bacalhau., T. D. S. Pereira., C. F. Souza., R. Faez. (2015). "Chitosan - montmorillonite microspheres: A sustainable fertilizer delivery system," *Carbohydr. Polym* (127): pp. 340 - 346

[9] M. M. Hanafi., S. M. Eltaib., M. B. Ahmad. (2000). "Physical and chemical characteristics of controlled release compound fertiliser," *Eur. Polym. J* (36)10: pp. 2081 - 2088.

[10] Y. Cao., L. Huang., J. Chen., J. Liang., S. Long., Y. Lu. (2005). "Development of a controlled release formulation based on a starch matrix system," *Int. J. Pharm* (298): pp. 108 - 116

[11] M. E. Trenkel. (2010). Slow- and controlled – release and stabilised fertilizer: An Option for Enhancing Nutrient Use Efficiency in Agriculture. *Paris, France: IFA, International Fertilizer Industry Association*

[12] G. M. Fujiwara., R. Campos., C. K. Costa., J. F. G. Dias., O. G. Miguel., M. D. Miguel., F. A. Marques., S. M. W. Zanin. (2013). "Production and characterization of alginate – starch – chitosan microparticles containing stigamsterol through the external ionic gelation technique," *Braz. J. Pharm. Sci* (49)3: pp. 538 - 547

[13] J. Y. Low. (2016). "Preliminary Study on Controlled - Release Phosphorous - Fertilizer Encapsulated by Starch - Alginate Superabsorbent," in *7th EURECA International Engineering Research Conference*

[14] J. O'Shea., T. A. Spillane., J. F. Connolly. (1979). "New Process for Recycling Agricultural Waste as a Slow Release Fertiliser," *Conserv. Recycl* (2)" pp. 269 - 275

[15] B. Singh., D. K. Sharma., R. Kumar., A. Gupta. (2009). "Controlled release of the fungicide thiram from starch - alginate - clay based formulation," *Appl. Clay Sci* (45): pp. 76 - 82

[16] Z. Yang., S. Chaib., Q. Gu., Y. Hemar. (2017). "Impact of pressure on physiochemical properties of starch dispersions," *Food Hydrocolloids* (68): pp. 164 - 177

[17] K. Zhong., Z. T. Lin., X. L. Zheng., G. B. Jiang., Y. S. Fang., X. Y. Mao., Z. W. Liao. (2013). "Starch derivative – based superabsorbent with integration of water - retaining and controlled – release fertilizers," *Carbohydr. Polym* (92): pp. 1367 - 1376

[18] S. Mandal., S. S. Kumar., B. Krishnamoorthy., S. K. Basu. (2010). "Development and evaluation of calcium alginate beads prepared by sequential and simultaneous methods," *Braz. J. Pharm. Sci* (46)4: pp. 785 - 793

[19] B. B. Lee., P. Ravindra., E. S. Chan. (2013). "Size and Shape of Calcium Alginate Beads Produced by Extrusion Dripping," *Chem. Eng. Technol* (36)10: pp. 1627 – 164

Biodegradability Study of starch derivative Control-Released Urea

Zhe Shyi Choon [1], Siew Wei Phang[1]*

[1] School of Engineering, Taylor's University Lakeside Campus, Malaysia.
*zheshyi@gmail.com

Abstract. Due to the steady rise in the population in earth, a steady food supplied and crops are required to be sustainable. The fertilizer that are generally used in the fertilizer industry are made from non-renewable fossil fuels where the research particular in the area of renewable control-released Urea where starch and calcium alginate are used to overcome the environmental issues as the materials required no need for special disposal due to its specialty in biodegradation by nitrifying bacteria in soil [1][2]. Calcium chloride also is used to act as a crosslink to gel both calcium alginate and starch. The mixture of beads is then dried with know weight to test for degradation in soil mixture with the presence of bacteria from compost soil for 2 weeks. Weight is then tested and recorded again intervalley every 2 days and weight change in between 2 days are recorded and biodegradability rate is calculated using known equations. The research shows that the higher the concentration of urea use in the mixture in formulation of CRF causes lower biodegradation rate, same goes to the high concentration of calcium alginate. The research also shows that starch-alginate polymer uses in CRF is promising results in substituting commercial CRF made by fossil fuels, therefore more research should be carryout in extending and accessing the sustainability of starch based CRF in the fertilizer agriculture sector.

Keywords: Controlled-release fertilizers, biodegradability studies, biodegradation rate, starch-alginate beads, Urea concentration.

1.0 Introduction

1.1 Background

It is expected by research projection from the Food and Agriculture Organization (FAO) that the world's population will rise to around 10 billion in the coming 20 years. Furthermore, it is forecast that especially in the countries under-development of south east Asia region will faces a famine based on the land availability to grow sustainable source of food for nourishing the population. [3-5] This issue will in fact involves the challenges where a large demand of food sources is required to ensure the population is sustainable in the coming years. It is shown that for grain crops plays a significant role in solving the challenge as it is the most sought-after carbohydrates for consumption in the south east Asia region. However, the arable land is claimed that 12% of land is available for agricultural plantations which proves to be a limiting factor and constraint. Therefore, research regarding the fertilizer for higher and better-quality fertilizer is chosen for researched to ensure the increase in crop productivity.

Urea is an inexpensive organic compound which it appearance of a white crystal granular solid that has the Nitrogen-Phosphorus-Potassium (NPK) of 46-0-0 ratio. The high ration of nitrogen content is known to reduced activity of microbial in soil when ammonia (NH3) is oxidized to nitrates (NO_3). The urea fertilizers that are readily available for conventional used is known to increase harmful emissions that will greatly affect the environments air emissions, such as carbon dioxide, methane, nitrous oxide, which causes greenhouse effect. The overused of conventional fertilizers also causes the leaching of nitrogen into lakes or rivers which causes eutrophication process where the over-enriched algae nutrients caused algae bloom which reduces the oxygen concentration in water causing aquatic live activity to reduced and eventually died off [6-9]. Due to the easily occurring phenomenon of eutrophication, researched are being made to improve the quality of urea fertilizer while evaluation and tweak are made towards the fertilizer to reduce the environmental footprints caused by food production. Therefore, starch-based formulation of controlled release fertilizer (CRF) with the presence of urea as an active ingredient is potentially obligated to be studied in order to encounter the situation. [4]

Controlled release fertilizer (CRF)is design to released specific agriculture nutrients to a plot of land in a delayed manner over time [5]. The CRF parameters are required to optimize appropriately for its efficiency in releasing the required concentration of nutrient while complementing the required nutrient of a crop [7]. The application of CRF involves the encapsulation of fertilizer with an economical and environmental friendly material to not further worsen the state of the soil and strife to maintain the soil quality which diminish ecological and biological effects on the soil [9-11].

The downsides of the CRF includes limitations are huge quantities of polymers used are required to be removed from soil after the nutrients is fully released. The following of left overs can be improved by using biodegradable polymers such as starch and research and studies are required to improve the formulation of starched based CRF with testing the degradability. In this decade where huge concern over non-renewable fossil fuel resources, the focus of CRF with biodegradable polymers is brought to the limelight to enforce the sustainable development in the fertilizer and agricultural industry as it. This characteristic shows promised in great

biodegradability factor, less to no environmental impacts and economical viable when the CRF is produced in a large-scale production [11-13].

Due to concerns of biodegradability and economical viable factors, it is shown in justification above that starch shows a promising polymer material as it fits the expectations as a CRF for the following research. Nevertheless, the only downside as shown in previous research that the presence of hydrogen bonds in the hydroxyl groups will affect both suspension stability and mechanical properties of the starch when act as a polymer when producing a biodegradable CRF [14-15]. It is also suggested that low ratio of alginate can be used to ensure better formulation of the starch based CRF as alginate provides an anionic biopolymer that is made up of linear chains of α-L-guluronic acid and β–D-mannuronic acid residues bonds with 1, 4- glycosidic groups [8]. Furthermore, using calcium chloride between the two polymers, beads is produced as alginates reacts with the calcium ions from the calcium chloride solution. Research papers also shows that complete beads can be formed by calcium alginate with the presence of calcium ions without the addition of heating involved. The structure of the alginate and calcium ions can be shown below in figure.1.

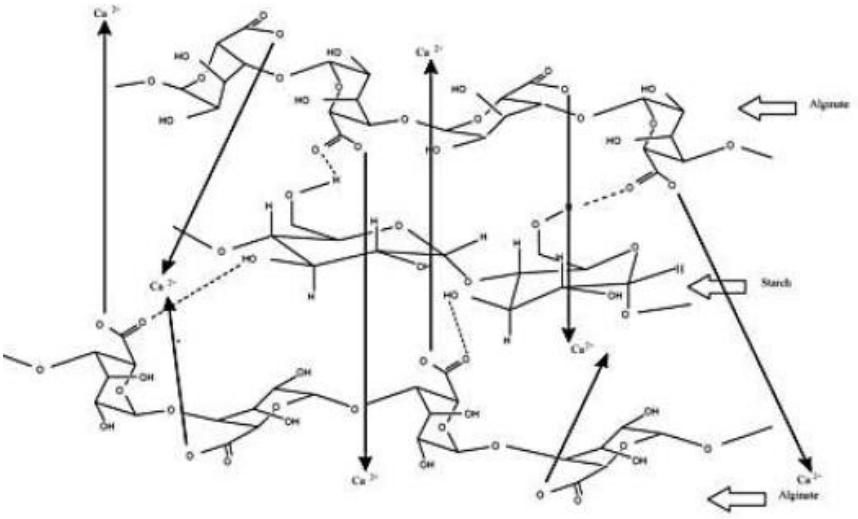


Figure 1: Chemical bonds of starch-alginate-Ca^{2+}

The amount of alginate and crosslinker, calcium chloride concentration will greatly affect the stability of the CRF formulation. [14,15] As shown in the research paper, the higher the concentration of alginate, the higher the size of the starch alginate beads formation. It is explained that the increment of size in the beads is directly affected due to the more amount of crosslinking formation between molecules instead of hydrogen bonding between starch and alginate molecules thus increasing the size and yield is not affected. On the other hand, the calcium chloride crosslink agent used for CRF formulation shows directly opposite to the calcium alginate where the higher the amount of calcium chloride solution used, the smaller the bead size and lower swelling percentage. The smaller beads size is justified as the calcium chloride crosslinker will decrease the CRF beads samples due to the bivalent bonds that causes the formation of cavities network. Although the following research shows great results in the alginate and crosslinker interaction with starch beads, the formulation of the beads involves thiram instead of urea so further experiment research is required to be carryout on urea CRF beads.

The biodegradation characteristics varied significantly with different starch content in the biodegradable polymer research. [18] Based on the research paper, two type of starch which are poly-butylene succinate, (PBS) and poly-caprolactone (PCL) was tested. Both starch materials were placed under aerobic and anaerobic conditions to test out the biodegradability. The results show that PCL in 44days is degraded by 88% while PBS in 80days only degraded 31% in aerobic conditions. With anaerobic conditions, PBS is shown that no physical change after of biodegradation test whereas PCL biodegraded a small amount. Both PBS and PCL biodegradable test for anaerobic conditions were done in the same duration of 180 days.

Other factors that are shown in affecting the biodegradation process for the starch derivative CRF than composition of starch and crosslinker concentration are bioavailability of soil, pH of soil, temperature of surrounding and the history of pollution of soil environment. The factors that are stated above were tested with alginate beads sample by measuring weight loss after a period of time after incubation in different type of soil. Furthermore, the physical properties in the research are affected using as manipulated variables for concentration parameters for starch, calcium chloride, urea and calcium alginate.

2.0 Experimental

2.1 Materials

The starch used in the experiment is obtained from Malaysian Mills Sdn. Berhad. that is manufactured in Malaysia. Calcium chloride is obtained from Export Solution Sdn. Bhd manufactured in Malaysia. The sodium alginate is obtained from Bis Chemicals Sdn. Bhd., Malaysia. The urea used is manufactured from A1 Asia Chemical Industry Sdn. Bhd., Malaysia.

2.2 Parameters for formulation of Starch-derivative-Alginate beads

Based on previous researched, formulation is made by repeating the formulation starch-alginate beads with a different quantity is used. The CRF that is designed in the following experiment can be shown in Table 1 below. 10% w/v of starched is used for all repetition of CRF formulation. Furthermore, the crosslinker material, calcium chloride solution is set at 1M. The Urea content design ranged from 5-20% w/v and 0.5-2% for sodium alginate as they act as the manipulated variables in the experiment to test for biodegradability of the starch formulated CRF.

Table 1 : Parameters for formulation of Starch-derivative-Alginate beads

Formulation	Starch % (w/v)	Urea %(w/v)	Na-Alg %(w/v)	CaCl2 (Molar)
SA1	10	5	0.5	1
SA2	10	5	1.0	1
SA3	10	5	1.5	1
SA4	10	5	2.0	1
SA5	10	10	0.5	1
SA6	10	10	1.0	1
SA7	10	10	1.5	1
SA8	10	10	2.0	1

SA9	10	15	0.5	1
SA10	10	15	1.0	1
SA11	10	15	1.5	1
SA12	10	15	2.0	1
SA13	10	20	0.5	1
SA14	10	20	1.0	1
SA15	10	20	1.5	1
SA16	10	20	2.0	1

2.3 Synthesis of Starch-derivative-Alginate beads

The starch, alginate and urea with specified quantity is first mixed into a 100mL distilled water with the conditions of 600 rpm at 50 ^{o}C for 1 hours to obtained a homogenize solution. The solution after mixing is then transferred into 1M calcium chloride solution using a 10mL syringe under constant stirring. The syringe content with the starch-alginate-urea mixture is slowly added into the solution drop by drop at the constant height of 30cm. The beads formed is then rinsed in distilled water and was placed on top of lab disposable paper towel to dry off excess water on the beads.

2.4 Starch-derivative-Alginate Bead Measurement and Drying

15 Samples of beads after drying from all samples from SA1-SA16 is taken and is measured using Vernier callipers. The beads measurement is taken before and after the bury of beads in the soil. [16]

2.5 Drying of Starch-derivative-Alginate beads

The Starch-derivative-Alginate beads is then dry using a chemical oven under the conditions of 60^{o}C over a period of time and the weight is constantly measured until no further drop in mass of the dried beads. The beads are then stored in lab plastic seal vials with the presence of silica gel pouch.

2.6 Soil Preparation

Gardening soil is first mixed with compost soil with the presence of microorganism obtained from Seremban is used for a medium to test the biodegradable of the beads formed. Soil is also dried under sunlight for 1 day after initial mixing. The beads are then placed in teabags then bury into the soil for the ease of keep tracking. The duration of beads bury in the soil is 14 days where the weight of the beads is taken in interval.

2.7 Determination of Weight Change from beads

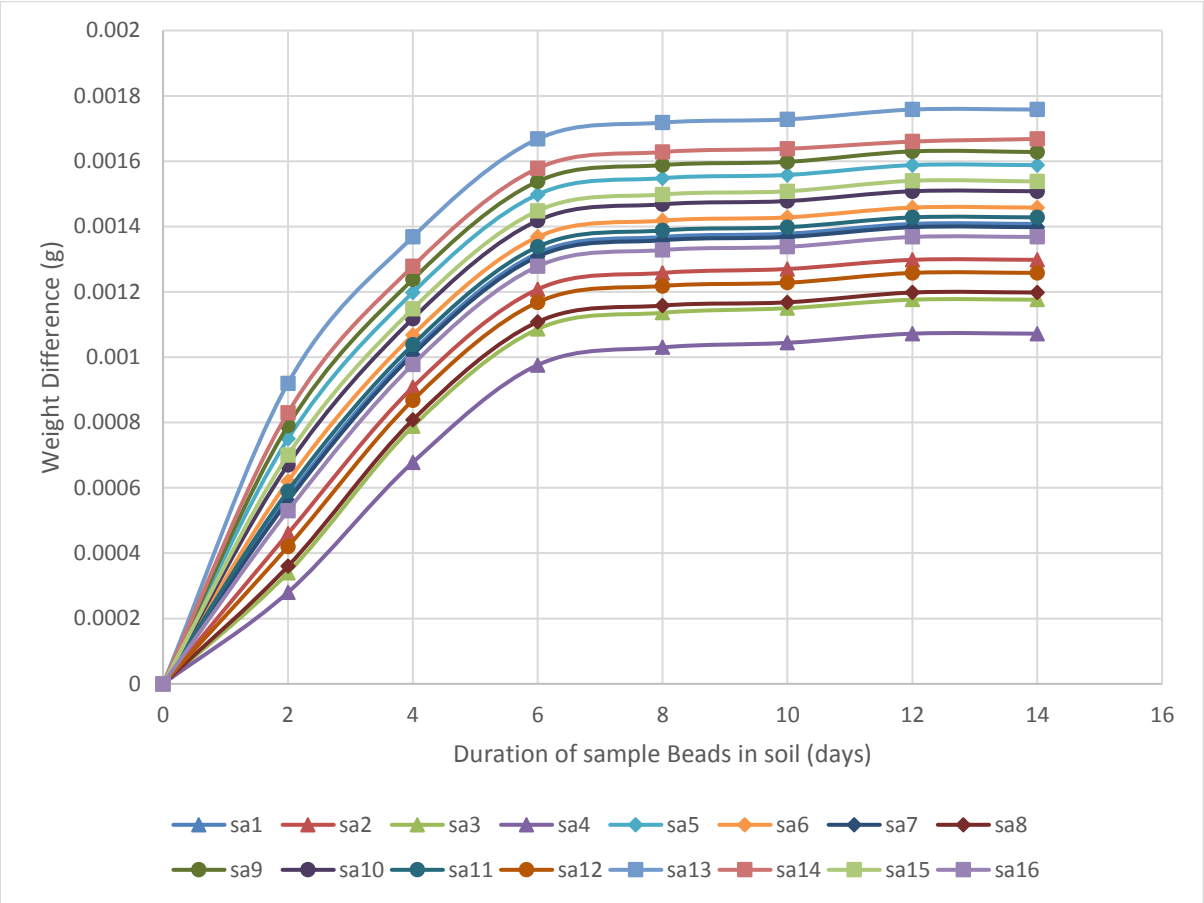
The weight change in beads before and after burying in the prepared soil is measured using the equation 1 below, [16]

$$\%\ of\ Weight\ change = \frac{M_o - M_d}{M_d} \times\ 100\% \quad (1)$$

Where M_o is the initial mass and M_d is the mass after degradation for the beads in soil.

3.0 Result and Discussion

Figure 2: Biodegradability of Sample Beads



Based on the weight difference shown above of sample in figure 2, it is shown that the microbes in the soil mixture degrades the sample beads. The trends of all sample beads show the increment of weight change sharply from 0 to 6 days of burying in soil then a slow decrease in weight difference after 7 to 8 days onwards due to the carbon or urea source depleting in the beads by the microorganisms. At the end of the experiment which is 2 weeks, the biodegradation rate sample shown by sa13 is at 92.8 %. Based on literature research, it is known that the microorganisms prefer to selective degrade materials which have amorphous are which are area with low crystalline structure of the polymer.

The higher concentration of Urea show in groups of sa 13, 14, 15 and 16 can be show a higher biodegradable rate in mass in compared to other groups which lower urea content mixture in forming the polymer beads. As in the literature, the higher the urea will result in higher density

and concentration of N-H chains to be broken down by the nitrifying microorganism present in the soil which will increase the rate of biodegradation of the beads. [16]

Samples with low calcium alginate content which are sa1, sa5, sa9 and sa13 all shows high biodegradation rate as compared to their counter part with higher calcium alginate content beads. This may due to lesser crystalline structure formed between the starch and calcium alginate which causes the beads to be more prone to be degrade by the microorganisms in the soil which results in the increment of biodegradable rate of the following sample beads. Samples of beads such as sa4, sa8, sa9 and sa16 all shows higher resistance to the microorganism's degradation from the soil due to more crosslinks formed between the calcium alginate and starch linkage. The higher presence of Ca^{2+} causes the structure of the molecule to be form higher density molecules, the ionic Ca^{2+} ion also provided by the calcium alginate which is ionic causes longer polymer between starch further strengthen the intermolecular forces between starch molecules within its own long chain, which furthers confirm the literature of higher concentration of calcium alginate bonds are more stable to form more mechanical strength and more resistance towards microorganism attack. [17]

4.0 Conclusion

In conclusion, concentration of urea and concentration of calcium alginate plays a significant role in controlling the biodegradation rate of controlled release fertilizer. The chemical bonds form by the combination of chemicals of calcium alginate, starch and calcium chloride mixture proves to be sufficient to be considered as a natural substitute for fertilizer towards fossil fuel based CRF. The experiment also shows that the highest biodegradation rate is present in the sa13 with biodegradation rate of 92.8% which the formulation of 10% w/v starch and 0.5% w/v calcium alginate with high concentration of 20% w/v urea in controlled solvent of 1M calcium chloride solution. The highest and most resistance towards degradation sample can be shown in sample sa4 with formulation of 10% starch, 2% alginate and low concentration of 5% w/v of urea in standard 1M calcium chloride solution.

Furthermore, the results shown that formulation of the starch based CRF will affect highly on the released pattern of urea from the formulated beads as it is shown that starch content will increased the released rate of urea. On the other hand, high concentration of calcium alginate will decrease the urea released rate during formulation of the CRF. As the following experiment achieved for the starch-based urea contained CRF in a controlled and sustainable which are requirement for agricultural chemicals in controlling the pollution to the environment. Hence, the starch based CRF can be used in calculated safe handling in urea released for better delivery for the agricultural sector.

References

[1] M. M. Hanafi, S. M. Eltaib, M. B. Ahmad, and S. R. Syed Omar, "Evaluation of controlled-release compound fertilizers in soil," *Commun. Soil Sci. Plant Anal.*, vol. 33, no. 7–8, pp. 1139–1156, 2002.

[2] S. Lü *et al.*, "Synthesis of a starch derivative and its application in fertilizer for slow nutrient release and water-holding," *RSC Adv.*, vol. 4, no. 93, pp. 51208–51214, 2014.

[3] J. Chen, Y. Li, A. E. Creamer, and H. Chen, "Slow-release fertilizer encapsulated by graphene oxide films," Chem. Eng. J., vol. 255, pp. 107–113, 2014

[4] K. Zhong *et al.*, "Starch derivative-based superabsorbent with integration of water-retaining and controlled-release fertilizers," *Carbohydr. Polym.*, vol. 92, no. 2, pp. 1367–1376, 2013.

[5] C. Guo, L. Zhou, and J. Lv, "Effects of expandable graphite and modified ammonium polyphosphate on the flame-retardant and mechanical properties of wood flour-polypropylene composites," *Polym. Polym. Compos.*, vol. 21, no. 7, pp. 449–456, 2013.

[6] M. Tarvainen et al., "Aqueous starch acetate dispersion as a novel coating material for controlled release products," J. Control. Release, vol. 96, no. 1, pp. 179–191, 2004.

[7] T. Jahns, H. Kaltwasser, "Mechanism of Microbial Degradation of Slow-Release Fertilizers", 2000 8: 11. 1566-2543 pp, 2000.

[8] X. Luo, J. Li, and X. Lin, "Effect of gelatinization and additives on morphology and thermal behavior of corn starch/PVA blend films," *Carbohydr. Polym.*, vol. 90, no. 4, pp. 1595–1600, 2012.

[9] Z. Zhu and R. Zhuo, "Crosslinked Quaternary Ammonium Cornstarch Matrix for Slow Release of Carboxylic Groups-containing Herbicides," *Starch-Stärke*, vol. 52, no. 2–3, pp. 58–63, 2000.

[10] F. Siepmann, J. Siepmann, M. Walther, R. J. MacRae, and R. Bodmeier, "Polymer blends for controlled release coatings," *J. Control. Release*, vol. 125, no. 1, pp. 1–15, 2008.

[11] R. Ito, B. Golman, and K. Shinohara, "Controlled release with coating layer of permeable particles," *J. Control. Release*, vol. 92, no. 3, pp. 361–368, 2003.

[12] T. Jamnongkan and S. Kaewpirom, "Controlled-release fertilizer based on chitosan hydrogel: phosphorus release kinetics," *Sci J UBU*, vol. 1, no. 1, pp. 43–50, 2010.

[13] M. E. González *et al.*, "Evaluation of biodegradable polymers as encapsulating agents for the development of a urea controlled-release fertilizer using biochar as support material," *Sci. Total Environ.*, vol. 505, pp. 446–453, 2015.

[14] B. Singh, A. Gupta "A study towards release dynamics of thiram fungicide from starch-alginate beads to control environmental and health hazards," J. Hazard. Mater., vol. 161, no. 1, pp. 208–216, 2009.

[15] B. Singh, A. Gupta "Controlled released of the fungicide thiram from starch-alginate-clay based formulation" A. Clay Science., vol. 45, no. 1, pp. 76–82.

[16] Astm, "Standard Test Method for Determining Aerobic Biodegradation of Plastic

Materials in," Astm D5988 − 12, pp. 1–6, 2014.

[17] K. P. R. Chowdary and D. U. Chandra, "Preparation and Evaluation of Cross-linked Starch Urea - A New Polymer for Controlled Release of Diclofenac," *Int. J. Chem. Sci.*, vol. 7, no. 4, pp. 2239–2245, 2009.

[18] I.M. Thakore, Sonal Desai, B.D. Sarawade, S. Devi, "Studies on biodegradability, morphology and thermomechanical properties of LDPE/modified starch blends" E. P. Journal. vol 37, pp 151-160.

Application of Eggshell as Micro-beads in Toothpaste

Rajesh Rajasekaran[1,], and Goh Pik Yuan[1]*

[1]School of Engineering, Taylor's University, 47500 Subang Jaya, Selangor, Malaysia

Abstract. Microbeads, one of the microplastics that used in the personal care and cosmetics products (PCCPs) since many years ago. The use of microbeads should be reduce or eliminate since it had been identified as source of marine and plastic pollution. Eggshell (ES), an animal by-product (ABP), was proposed as an alternative plan to replace the usage of microbeads in this study. The objective of this study was mainly focus on the investigation of the abrasive agent presence in the eggshell. Elemental and component analysis will be carried out in order to determine the presence of abrasive agent in eggshell by using Atomic Absorption Spectrometry (AAS) and High-Performance Liquid Chromatography (HPLC) respectively. In this study, 86.1% of calcium was determined in the eggshell powder with low quantities of organic components. Organic components like potassium, iron and copper were less than 1%. Abrasive agents like calcium carbonate, alumina and dicalcium phosphate dehydrate were tested by HPLC. Based on the results, abrasive agents were found to be presented in the eggshell. Hence, this study suggested that the biodegradable eggshell could be used to replace the application of micrabeads in toothpaste.

1 Introduction

'Microbeads' is being used as the name of the primary microplastic particles that present as ingreditents in personal care and cosmetic products (PCCPs) [1]. "Microbeads are plastics fragement or beads ranging in size from roughly 5 µm to 1mm. They are made from synthetic polymers including polyethylene (PE), polyactic acid (PLA), polypropylene (PP), polystrene, or polyethylene terephthalate (PET)." [2] Microbeads are used in variety of products like cosmetics, hand-cleanser, toothpaste, suncreen, face washes, body washes and so on as abrasive scrubber [1, 2].

Most of the natural exfoliating materials that found in cosmetics such as oatmeal, jojoba beads, walnut husks, pumice and apricot are being replaced by the micro-plastics [1]. The sources of micro--plastics can be generally separated into two types: (i) primary micro-plastics which are produced and will enter the environment with small sizes and (ii) secondary micro-plastics which generally come from the breakdown of larger plastic debris in the environment [3].

Cosmetics like facial scrubs are the most common PCCPs that contains harmful micro-beads as exfoliating agents. These kind of products will result in contamination of micro-plastics to the marine environment [4] because of the presence of the micro-beads in the products [2]. The main reasons for the concern on the use of micro-beads is because of this plastics will presist for years in the natural environment [5]. Generally, the small particles size of micbo-beads will be washed from the daily products like facial scrubs and toothpaste. They will escape from the filtration system and enter the aquatic enviroment and cause pollution. In addtion, plastic micro-beads might be ingested by the aquatic biota, especially those constitute the base of the food chain [6]. Researchers have found that the microbeads are usually mistaken by most of the surface feeding fish species as plankton and this ingestion of platics by aquatic organisms is one of the major deleterious environmental impacts in the marine environment [7]. The occurrence of micro-beads in aquatic environment is not merely resulted in biological impacts on marine life but for human health as well. According to Mathalon and Hill [8], the concern related to the ingestion of micro-plastics is growing due to the presence of its in the human food chain by ingestion of fish, filter feeders and shellfish, causing potential human health impacts."

The achievement of completed degradation for the plastic micro-beads has create serious issue in marine pollution. Apart from that, the removal of the micro-beads as well as the micro-plastics from the aquatic environment is difficult and costly due to their small particles size and iniquitousness in the environment [9]. Hence, minimization or elimination of the use plastic micro-beads has been concerned in order to prevent plastic pollution. The emission of micro-beads in PCCPs which are the major sources of pollution can be avoided relatively easy by replacing or removing the synthetic micro-beads from PCCPs formulas [10].

In order to minimize the use of microbeads, an alternative source to replace it in PCCPs is required. The composition of eggshell which is rich in calcium carbonate is suggested as it could have the similar characteristic as abrasives agents in toothpaste. Below is the structure of an egg (Fig. 1) and composition of eggshell (ES) and eggshell membrane (ESM) (Table 1). After the production of eggs and egg derivatives, the by-product ES represents a significant waste and will be _____

* Corresponding author: Rajesh.Rajasekaran@taylors.edu.my

disposed of for landfill. Occasionally, it will be used as the fertiliser or soil conditioner due to its high nutrition contents [11]. ES is also an environmental friendly technique that could contribute to reduce the waste disposal [12]. In addition to that, the matrix of the ES has been studied because of it calcium supplment in term of animal use [13].

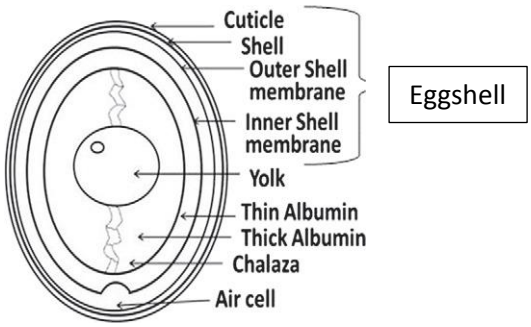


Figure 1. Egg and eggshell structure [14].

Table 1. Major constituents of the eggshell (ES) and eggshell membrane (ESM). [14]

Eggshell (ES)	**Eggshell Membrane (EMS)**	
Calcium Carbonate (94%)	Protein (59%)	Collagen (35%)
Organic Matter (4%)		Glucosamine (10%)
Calcium Phosphate (1%)		Chondoitin (9%)
Magnesium Carbonate (1%)		Hyaluronic Acid (5%)
Traces of Sodium (Na), Potassium (K), Manganese (Mn), Iron (Fe), Copper (Cu) and Strontium (Sr)	Organic Components (41%)	Calcium, Ca
		Magnesium, Mg
		Silicon, Si
		Zinc, Zn

1.1 Other applications of eggshell

Some reposts might not fit in the topics discussed so far. Technological options have been explored by the literature in order to obtain added-value commercial products from ES as well as to take the advantages of the eggshell properties. The technological options can be generally separated into two main categories which are raw materials for products manufacture and operating supplies for catalytic applications (Fig. 2).

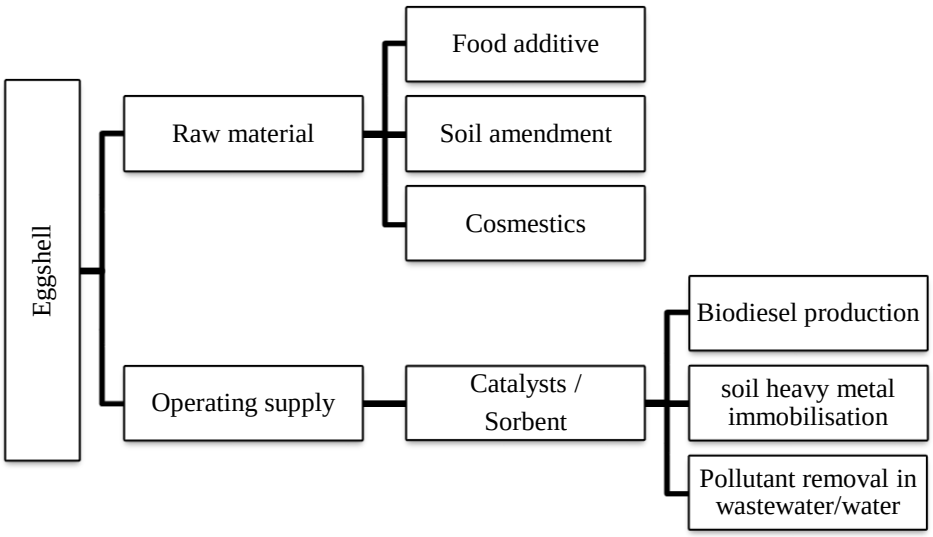


Figure 2. Classification of potential uses of Eggshell [15].

1.1.1 Food additives for animal and human

Eggshell powder has been used as the animal feed, especially as a calcium sources for laying hens [16] since it could improve the egg production as compare to ground lime [17]. As a matter of fact, the eggshell has been accepted as feed additive for both livestock and companion animals by the Association of American Feed Control Officials.

Eggshell can be used as human feed as dietary supplement because it is rich in calcium and contain low quantities of toxic elements such as Al, Hg and Pb. Researchers had reported that eggshell can be used to inhibit human needs for the calcium nutrient, especially for the osteoporosis. [18].

1.1.2 Cosmetics

One of the important ingredients in most of the cosmetics is collagen, a fibrous protein that helps in structuring proteins and cells and acts as a supporting tissue. The presence of collagen can improve the elasticity and thickness of the skin and prevents the skin wrinkles [16]. It is also found that collagen obtained from eggshell is safe to use in comparison with the collagen extracted from the other sources as it presents low allergic reactions [19]. In additional, it is also used in facial cleansers as a function of skin sebum and dust removal [16].

1.1.3 Pollutant removal

Eggshell is expected to behave like calcite, like sorbent, because it is mainly composed by calcium carbonate [20]. ES and ESM have been found as an excellent scavengers in the pollution aspects as they can remove the organic or inorganic chemicals like aromatic compounds (phenol), hazardous dyes, copper, mercury et al. effectively [14]. The carbonate group in the eggshell is the main interest in using it as a sorbent. Carbonate group have a cation

exchange properties which will rise the negative charge density of the surface as well as increase the pH, hence prompting the attraction of metallic ions with positive charge [20].

Theoretically, microbeads can be replace by the eggshell as it is rich in calcium. It is because calcium carbonate has been used as the tooth whitening agents [21] or abrasive agents in the toothpaste. To the best of author's knowledge, no research has been studied the application of eggshell as micro-beads in toothpaste. Therefore, this present research is studied with the objectives as follows:

1. To investigate the particles (abrasive agents) in the eggshell powder using Atomic Absorption Spectrometry (AAS).
2. To identify the presence of the abrasive agents in the eggshell by using High-Performance Liquid Chromatography (HPLC).

2 Methodology

2.1 Research materials

The main raw material used in this research is chicken eggshell was collected from hawker stall at Lahad Datu, Sabah. Chemicals like dicalcium phosphate ($CaHPO_4$) dehydrate and alumina (Al_2O_3) were purchase from Evergreen Engineering & Resources (Malaysia).

2.2 Preparation of eggshell powder

The eggshell collected was washed and boiled at 100^oC for 5-10 minutes in order to kill the pathogens on its. The boiled eggshell was then left to air dry. The eggshell membrane was removed from the eggshell before it was grinded. The dry eggshell were then grinded into fine powder form by using a grinding machine, Shimono Multifunctional food processor (Platinum Series Blender, Model No: SKP 1009). After that, a small kitchen use flour sieve was used to sieve the eggshell powder to separate the particle of larger size and obtain a fine powder. By using the small sieve, the size of the eggshell powder is expected to be fine enough.

2.3 Elemental analysis of eggshell

The element analysis of the eggshell was performed by using Atomic Absorption Spectrometry (Perkin Elmer, AAnalyst 400). Elements that were being tested in this research are Calcium, Potassium, Iron, Copper and Manganese. The wavelength of the light transmitted by each of the element were recommended by the AAS software which are 422.67, 766.49, 248.33, 324.75 and 279.48 respectively. The flame used was air-acetylene. Concentration of eggshell samples tested were 20 ppm and 60 ppm.

Stock solution of the element of 1000 ppm for the AAS was available in laboratory of Taylor's University Lakeside Campus. The stock solution (1000 ppm) of each element was diluted into 100 ppm before it was being further dilute into the tested concentration range in the AAS. Ultrasonic pure water was required for the dilution process. Calcium and Manganese were tested in a concentration range of 0 to 60 ppm while Potassium, Iron and Copper were tested from 0 to 20 ppm. The ultra-pure water was used as the blank solution (0 ppm) in the AAS.

The absorbance values of the five standard solutions will be plotted by the AAS software and saved. A calibration curve of standard solutions against the corresponding absorbance readings for each of the elements were plotted.

2.4 Identifying the individual components of eggshell and micro-beads

All individual components of the samples eggshell and abrasive agents like Calcium Carbonate, Dicalcium Phosphate Dihydrate and Alumina could be identified by the High-Performance Liquid Chromatography (HPLC). The components analysis of eggshell sample and chemical abrasive agents were analysed on a C-18 HPLC (Agilent Technologies, Model: LC 1220), 250 mm x 4.6 mm (long x ID). There were two mobile phase used in time gradient flow of 15 mL/min which were mobile phase A and B. The mobile phase A was merely consisted of the phosphate buffer with pH 5.4; mobile phase B was the mixture of H

PLC grade Acetonitrile:Tetrahydrofuran:: 90:10 (v/v). The temperature of the samples and column was maintained at 6^{o}C and 40^{o}C respectively. Throughout the analysis, the detector was set at 220 nm. **Table 2** below show the gradient program set for the HPLC analysis. [22]

Table 2. Gradient program of the HPLC analysis.

Sr. No	Time (min)	Mobile Phase (%)	
		A	B
1	0	100	0
2	10	100	0
3	20	85	15
4	35	15	85
5	47	100	0
6	50	100	0

All the sample, standard and mobile phase solutions were prepared by ultrapure water. Both mobile phase were undergone vacuum filtration at 0.2 µm and degas for 15 minutes after that. Five standards were prepared for each chemical from 2 ppm to 10 ppm and an eggshell sample solution of 10 ppm. The standard solutions prepared were undergone syringe filter at pore size of 045 µm.

3 Results and discussion

3.1 Chicken eggshell powder

Eggshell powder weight was 155.815 g (n = 25). A small sieve was evaluated as mechanical methods available at home compare with the laboratory sieve shaker as the standard method. The sieved chicken eggshell powder, by using the kitchen use flour sieve, was being sieved again by using the laboratory sieve shaker at 500 µm. Hence, the expected particle size of the powder was smaller than the laboratory instrument: sieve plate with opening of 500 µm. A multiphase microscope image as shown in **Figure 3.1** confirmed the range of the particle size ($p<5.2$ µm – 500 µm) of the eggshell powder. As mentioned in the introduction, the mirco-beads used was ranging from roughly 5 µm to 1 mm [2]. Therefore, the eggshell powder

prepared was in the ranging size of microbeads and could be considered as fine powder to use in the follow experiments.

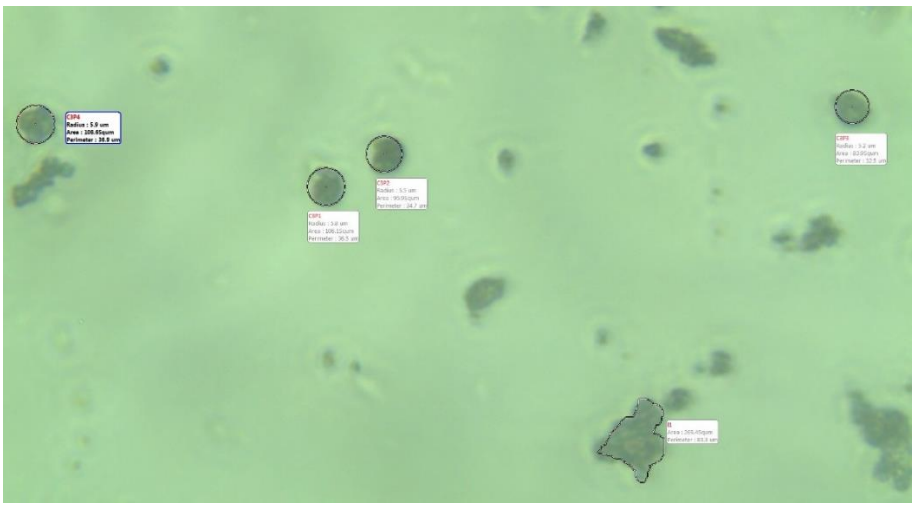


Figure 3.1 Chicken eggshell particle size (µm) under multiphase microscope.

3.2 Elemental analysis

Theoretically, the major constituents of the eggshell all around the world should be the same. However, the percentage of them might not be the same due to the different of animals feed, surrounding and so on. Hence, the chicken eggshell in Malaysia was tested in order to verify that it is rich in calcium. The calibration data obtained for calcium and potassium were shown as **Table 3** as an example table for the tested elements. Based on the obtained data from the AAS, two calibration curves were plotted as **Fig. 3.2.** The percentage of elements presence in the eggshell is calculated and summarized in **Table 4**.

As was already outlined in **Table 1**, the major constituents of the eggshell is calcium carbonate, $CaCO_3$ which is about 94 % [14] and traces amount of organic components like sodium, potassium, manganese, iron and so on. In this study, the chicken eggshell in Malaysia consists of 86.1 % of calcium (**Table 4**) which is the highest among all the tested elements. From the determined data, ES in Malaysia is rich in calcium but it contained a smaller amount of calcium in comparison with the generally data obtained from the literature. The amount of calcium found in the chicken eggshell was considered as high although it had about 8 % difference from the previous researcher studies. Hence, the eggshell can be considered as calcium rich source. Apart from that, eggshell contains not only calcium but also other elements, such as potassium, iron, copper and manganese that were tested in the research project. Despite the concentration of the other elements were low, they might contribute to the requirements and give a positive effect on bone or dental metabolism [23]. The level of other elements like Na, Mg, Cr, Zn, Se, Pb Cd and Hg were not being tested in this research project, but they were very low in content and had been determined by others [14]. The presence of the calcium element in the eggshell was validated and are applicable to the analysis of other elements.

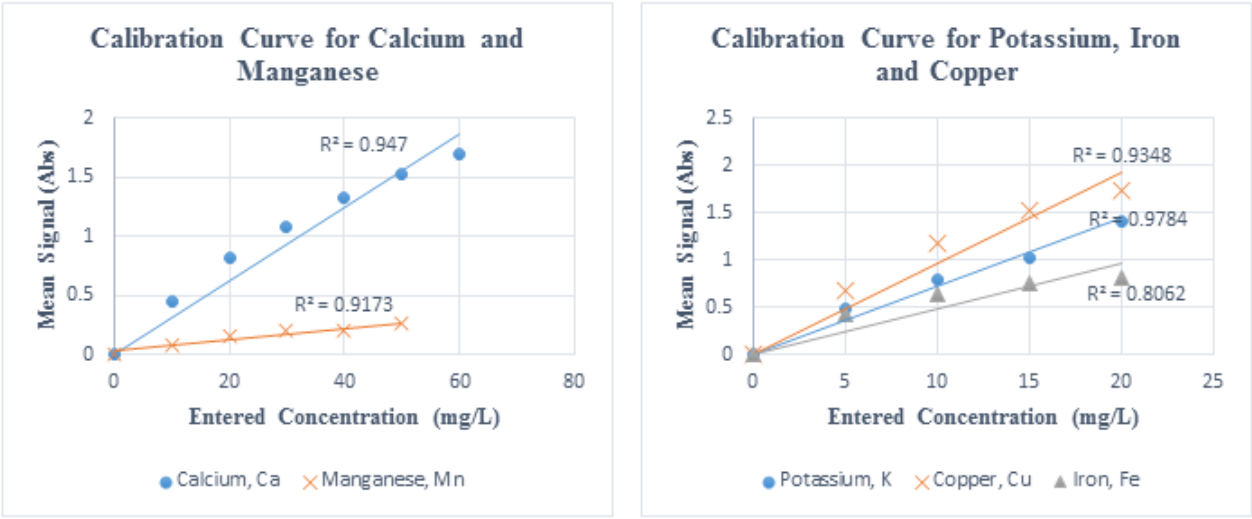
It is known that certain amount of abrasive agents is required in toothpaste as to remove the stains as well as to prevent it from forming [24]. Calcium carbonate, one of the known ingredients in the toothpaste, a tooth whitening and abrasive agent acts as the primary stain removal ingredient in toothpaste [25]. Hence, eggshell powder, a source that rich in calcium,

has the ability in replacing the micro-beads in the toothpaste. In additional, researchers found that eggshell had been used in facial cleanser [16]. This show that the utilization of eggshell powder is safe in the cosmetic product as well as in toothpaste.

Table 3. Calibration data for calcium and potassium elements.

Calibration data for Calcium, Ca with recommended wavelength of 422.67					
ID	**Mean Signal (Abs)**	**Entered Conc. (mg/L)**	**Calculated Conc. (mg/L)**	**Standard Deviation**	**% RSD[a]**
C. Blank	0.000	0.0	0.000	0.01	1.99
Calib. Std 1	0.4502	10.0	14.294	0.00	0.31
Calib. Std 2	0.8098	20.0	25.709	0.00	0.40
Calib. Std 3	1.0824	30.0	34.363	0.01	0.88
Calib. Std 4	1.3172	40.0	41.819	0.01	0.50
Calib. Std 5	1.5159	50.0	48.128	0.04	2.35
Calib. Std 6	1.6876	60.0	53.579	0.01	0.80
Correlation Coef. : 0.965663		Slope: 0.03150	Intercept: 0.0000		
Determined Mean Conc. of Ca in 20 ppm Eggshell Conc. : 22.15 mg/L					
Determined Mean Conc. of Ca in 60 ppm Eggshell Conc. : 46.12 mg/L					
Calibration data for Potassium, K with recommended wavelength of 766.49					
ID	**Mean Signal (Abs)**	**Entered Conc. (mg/L)**	**Calculated Conc. (mg/L)**	**Standard Deviation**	**% RSD[a]**
C. Blank	0.000	0.0	0.000	0.00	1.37
Calib. Std 1	0.485	5.0	6.707	0.01	1.34
Calib. Std 2	0.789	10.0	10.919	0.01	1.28
Calib. Std 3	1.020	15.0	14.119	0.01	1.06
Calib. Std 4	1.412	20.0	19.538	0.17	11.98
Correlation Coef. : 0.980819		Slope: 0.07226	Intercept: 0.0000		
Determined Mean Conc. of K in 20 ppm Eggshell Conc. : 0.025 mg/L					

[a] Relative Standard Deviation.



(a) (b)

Figure 3.2 Calibration Curve (a) calibration curve for calcium and manganese; (b) calibration curve for potassium, copper and iron.

Table 4. Summarized table for the percentage of elements presence in eggshell.

Elements		Percentage of Element in Eggshell	
		20 ppm	60ppm
Calcium	Ca	86.1 %	86.1 %
Potassium	K	0.13 %	-
Iron	Fe	0.11 %	-
Manganese	Mn	0.07 %	-
Copper	Cu	Trace	-

3.3 Eggshell components analysis (HPLC)

HPLC analysis using the High-Performance Liquid Chromatography (HPLC) method revealed the presence of a lots impurities in the calcium carbonate, alumina and dicalcium phosphate dehydrate with respect to principle peak of the eggshell sample. After running for 5 hours, standard calibration for a component can be obtained. However, there will be some error in the graph since the HPLC is a sensitive method to all the impurities in the components. **Figure 3.3** below show the retention time of all the impurities presence in the eggshell sample.

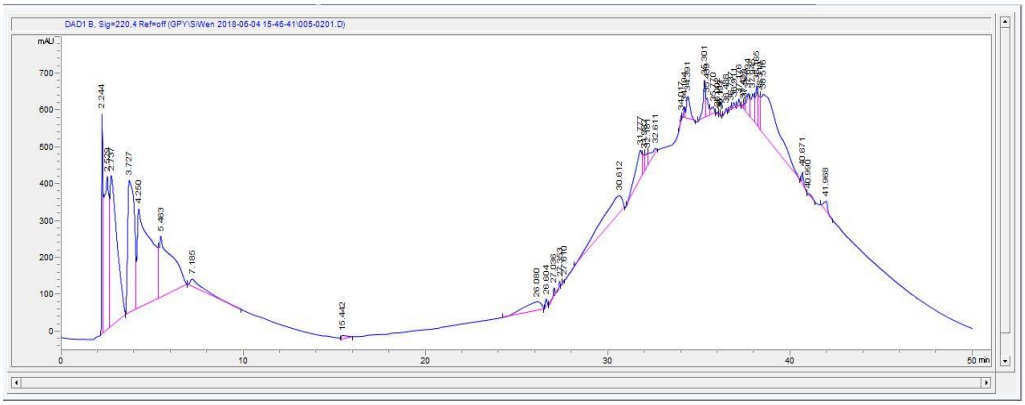


Figure 3.3 HPLC analysis of Eggshell Sample.

From the results obtained, a lot of impurities were detected. . Since there were too many noise in the chemicals calibration curve, the retention time of the specific chemicals, calcium carbonate, alumina and dicalcium phosphate, were uncertain. Thus, graph of concentration of the chemicals against the Area percentage were plotted in order to obtain the coefficient of determination, R^2 values. A table of the R^2 value obtained for the chemicals abrasive agents, calcium carbonate, alumina and dicalcium phosphate dehydrate, from the graph were tabulated as shown in **Table 5** below in order to determine the retention time of the chemicals from theirs HPLC analysis concentration calibration graph. Based on the result graph, most of the chemicals had the peak after 30 minutes. However, the retention time for calcium carbonate was taken as 26 minutes as refer to the journal of determination of atorvastatin calcium [22]. As refer to **Table 5**, the expected retention time of the three chemicals: calcium carbonate, alumina and dicalcium phosphate dehydrate were expected at around 26 min (according to the journal [22] mentioned in Literature Review, HPLC), 38.5 min and 41 min.

By comparing the retention time of the chemical with the sample (**Fig 3.3**), there were a peak at the retention time of the compound mentioned before. The data analysis of the eggshell sample show that there was the presence of the three chemical abrasive agents in the eggshell. Hence it can be conclude the eggshell can be used as an abrasive agent in toothpaste since it show the presence of them in the sample.

Table 5. R^2 value of the peak impurities evaluated over the concentration linear curve.

Sr. No.	Name of the Component		R^2 value	Retention Time (min)
1	Calcium Carbonate	$CaCO_3$	0.7518	26.0 mins
2	Alumina	Al_2O_3	0.9662	38.5 mins
3	Dicalcium Phosphate Dihydrate	$CaHPO_4$	0.9146	41.0 mins

4 Conclusion

Based on the findings of this research study, the following conclusion were drawn:

1. Since the purpose of the eggshell powder in this research study is to replace the harmful micro-beads, the particles size of the grinded eggshell should not larger than the mirco-beads. The particle size of the chicken eggshell powder can be produced in fine powder form (p<5.2µm -500 µm) which is in between the roughly ranging of the mirco-beads used.

2. Chicken eggshell powder were rich in calcium, even though the percentage of it might have a small difference from the other researchers due to the different of the growth environment, colour of the egg, thickness and so on. Eggshell powder used in this research study is local animal-by-product. It consists of 86.1 % of Calcium (Ca) and trace amount of other organic elements such as Potassium (K), Iron (Fe), Manganese (Mn) and Copper (Cu) which are 0.13 %, 0.11 %, 0.07 % and trace respectively. The presence of calcium element in the eggshell was validated and it is calcium rich. Thus it can be said that chicken eggshell has the characteristic of abrasive agent since eggshell is rich in calcium and calcium carbonate ($CaCO_3$) is known as one of the chemical abrasive agents used in toothpaste.

3. Throughout the HPLC analysis, the retention time for calcium carbonate, alumina and dicalicum phosphate dehydrate are 26, 38.5 and 41 minutes. In the calibration graph of eggshell sample, it proved that there are the presence of the three chemical abrasive agents in eggshell. Hence it can also conclude that eggshell has the abrasive properties as micro-beads in terms of the stain removal.

One of the main objectives in this research study was to analysis the elements and the compounds presence in the eggshell in term of abrasive agents. The objectives of this research project could be achieved due to the literature studies and the completed of the methods of analysis. Eggshell is a bio-mineral with a high content of calcium and it is an animal by-product. The organic matter in eggshell is low but is N-rich and high content (86.1%) of calcium. Eggshell powder will not cause pollution, biodegradable, rich in calcium element which usually used as the abrasive agent in toothpaste. Besides, the eggshell powder is used as sorbent for water as outlined in Introduction's subsection. Hence, the cheap eggshell as animal-by-product could be a suitable source to replace the widely used cheap, but harmful and non-biodegradable micro-beads presence in the toothpaste which will result in plastic pollution.

Future Work

There are some improvement that can be made to improve as well as extended further. Some of the research topics which are worth to investigate further were drawn as follow:

1. More research on the similar title or topic should be carried out although the proposed methods are limited and in-completed due to the new approach of using eggshell as microbeads.
2. Many tests and experiments have been left for the future due to lack of time like the validation of the HPLC analytical method have to continuous in the further study and future work. The HPLC requires a day to finish a single run. If possible, identify all the impurities in the eggshell will be helpful for the further study too.
3. Another essential objective, test and experiment should be taken into consideration is the effectiveness of the eggshell in term of the stain removal. The efficiency of it can

be tested by observing the surface roughness of shell before and after rubbing with the eggshell toothpaste.

5 Acknowledgement

The authors would like to acknowledge Taylor's University Lakeside for the services and facilities as well as the financial support provided for this study.

References

[1] L. S. Fendall, M. A. Sewell, Contributing to marine pollutin by washing your face: microplastics in facial cleansers, Mar. Pollut. Bull., vol. 58, 1225-1228, (2009).

[2] C. M. Rochman, S. M. Kross, J. B. Armstrong, et. al., Scientific Evidence Supports a Ban on Microbeads, Environ. Sci. Tech., **49**, 10795-10761, (2015).

[3] T. Gouin, J. Avalos, I. Brunning, et. al., Use of micro-plastics beasd in cosmetics products in Europe and their estimated emissions to the North Sea environment, SOFW, **141**, 40-46, (2015).

[4] I. E. Napper, A. Bakir, S. J. Rowland, R. C. Thompson, Characterisation, quantity and sorptive properties of microplastics extreacted from cosmetics, Mar. Pollut. Bull., **99**, 178-185, (2015).

[5] D.K. Barnes, F. Galgani, R.C. Thompson et. al., Accumulation of fragmentation of plastic debris in global environments., Philos. Trans. R. Soc. B: Biol. Sci., **364**, 1985-1998, (2009).

[6] A. Lusher, Microplastics in the Marine Environment: Distribution, Interactions and Effects., Mar. Anthropogenic Litt., 245-307, (2015).

[7] S. Baulch, C. Perry, Evaluating the impacts of marine debris on cetaceans, Mar. Pollut. Bull., **80**, 210-221, (2014).

[8] A. Mathalon, P. Hill, Microplatics fibres in the intertidal ecosystem surrounding Halifax Harbor, Nova Scotia, Mar. Pollut. Bull., **81**, 69-79, (2014).

[9] P. Sherman, E. van Sebille, Modeling marine surface microplastic transport to assess optimal removal locations, Environ, Res. Lett., **11**, 014006, (2016).

[10] P. K. Cheung, L. Fok, Evidence of microbeads from personal care product contaminating the sea, Mar. Pollut. Bull., **109**, 582-585, (2016).

[11] A. Tacon, Utilisation of chick hatchery waste: The nutritional characteristics of day-old chicks and egg shells, Agr. Wastes, **4**, 335-343, (1982).

[12] R. B. Lucas, L. Maela, A. D. Damian, et al., Chicken eggshell as suitable calcium source at home, International J. of Food Sci. and Nutrition, 1-4, (2013).

[13] R.B. Christmas, R.H. Harms, Utilization of egg shells and phosphoric acids as a sources of phosphorus and calcium in the diet of White Leghorn cockerels, Poult. Sci., **55**, 264-267, (1976).

[14] A. Mittal, M. Teotia, R. K. Soni, J. Mittal, Applications of egg shell and egg shell membrane as adsorbents: A review, J. Mol. Liq., **223**, pp. 376-387, (2016).

[15] J.Q. Margarida, A. R. S. Micaela, Rosa Quinta-Ferreira, Applications of industrial eggshell as a valuable anthropogenic resource, Resour. Conserv. Recy., **123**, 176-186, (2017).

[16] C. M. M. Cordeiro, M. T. Hincke, Recent patents on eggshell: shell andmembrane applications, Recent Pat. Food. Nutr. Agric., **3**, 1-8, (2011).

[17] J. S. Sim, L.M. Aw-Yong, D.B. Bragg, Utilization of egg shell waste by the laying hen, Poult. Sci., vol. **62**, pp. 2227-2229, (1983).

[18] A. Schaafsma, I. Pakan, G.J. Hofstede, et al., "Mineral, amino acid, and hormonal composition of chicken eggshell powder and the evaluation of its use in human nutrition," Poult Sci., **79**, 1833-1838, (2000).

[19] Y. Zhao, Y. Chi, Characterization of collagen from eggshell membrane, Biotechnology, **8**, 254-258, (2009).

[20] P.S. Guru, S. Dash, Sorption on eggshell waste-a review on ultrastructure, biomineralization and other applications., Adv. Colloid Interface Sci., **209**, 49-67, (2014).

[21] J. Andrew, Whitening toothpastes: A review of the literature, J. of Dent, **38s**, e17-e24, (2010).

[22] L. K. Gupta, Spectroscopic characterization and quantitative determination of atorvastatin calcium impurities by novel HPLC method, Spectrochimica Acta Part A: Molecular and Biomolecular Spectroscopy, **97**, 495-501, (2012).

[23] P.J. Meuniew, C. Roux, E. Seeman, et al. , The effects of strontium renelate on the risk of vertebral fracture in women with postmenopausal osteoporosis, n Engl J Med, **68**, 350-459, (2004).

[24] G. K. Stookey, T. A. Barnhard, B. R. Schemehorn, In vitro removal of stain with dentrifrices, J. of Dent. Res., **61**, 1236-1239, (1982).

[25] A. JoinerI. editor: Johansson, P. Somasundaran, The cleaning of teeth, Handbook for cleaning/ deontamination of surfaces, **1**, 371-405, (2007).

Material Flow Cost Account (MFCA)-based Approach for Synthesis and Optimisation of Wastewater Treatment Plant

Jo Yee Ho[1], Yoke Kin Wan[1], and Li Wan Yoon[1]

[1] School of Engineering, Faculty of Built Environment, Engineering, Technology & Design, Taylor's university, Lakeside Campus.

Abstract. Wastewater treatment (WWT) is a mandatory process in every manufacturing company. However, with countless WWT technologies prevailing in the market, the selection of WWT technologies are usually based on vague assumptions which results in subsidiary remittance. Material Flow Cost Accounting (MFCA) is a management tool which quantifies material flows across a production process in both physical and monetary values. As MFCA is capable to track the cost associated to each stream (hidden cost) within the process, this research aims to develop a novel MFCA-based approach primary decision-making tool in selection of wastewater treatment technologies which meets the constraint of quality of treated effluent (e.g., BOD, COD, TSS and OG). A series of mathematical equations will be formulated based on a generic superstructure of a WWT plant. To illustrate the approach, a case study on sago-based organic WWT plant has been solved in this work via an optimisation software (LINGO). The objective functions of this work is to minimise the sludge cake generation cost which will be disposed for landfill. At the end, a novel MFCA-based approach, which able to synthesise a wastewater treatment plant (WWTP) which complies with the discharged regulation and with minimum sludge cake generation cost, has been developed in this work. As results, the implementation of this approach is capable of minimising the waste generation cost as low as 5% from capital investment based on a case study on the wastewater treatment process in a sago biorefinery plant in Sarawak.

1 Introduction

Over the past decades, urbanization had rapidly increased human population and industrial advancements which leads to pleasant living pursuits. However, these urban developments were bounded with adverse impacts on the environment, including the escalating production of wastewater. According to the World Health Organization (WHO), it is forecasted that half of the world's population would suffer in restriction of clean water access in year 2025 [1] . Despite the need of conservation of water, it is globally approximated that over 80% of wastewater is discharged to the environment without appropriate treatment in year 2012 [2]. As preservation of water is crucial, myriad research studies on optimization of wastewater treatment had been adapted in recent developments to reduce consumption from natural water sources; prolonging and sustaining the water cycle. Note that the treated wastewater from manufacturing processes could be recovered for in-house use to minimize utilization of natural water sources as well as to upsurge economic performance of the manufacturing process. Earlier developments in optimization of wastewater treatment includes water recovery network with reuse/recycle streams [3, 4, 5] optimization of operating conditions in wastewater processes [6, 7] and advancements in wastewater treatment technologies. However, as wastewater technologies and parameters improvements had been established, more recent extended studies on optimization of wastewater treatment evaluates the overall performance of wastewater treatment process via various mathematical models were reviewed in this work.

For instance, Life cycle analysis (LCA) was used to evaluate the efficiency of wastewater treatment plant processes in year 2016 [8]. This approach evaluates whether all the input and output materials across a boundary meet the desired goal by listing the environmental impact or any attributes in a sequencing life cycle manner. Extended version of LCA method is the Multiple-attribute decision-making (MADM) approach which involves logical sequencing to model a framework for preference decision over a vast range of alternatives [9]. In other words, MADM approach predicts different outcomes of LCA when different attributes are applied. Nevertheless, previous research on LCA method only prioritize in selection of wastewater treatment technology at specific treatment stage boundary but could not identify the optimum combination of technologies to form a complete whole wastewater treatment process. Material Flow Analysis (MFA) is another technique used in optimizing production systems by incorporating linkage between all inlet and outlet mass flowrate within one technology equipment to another [10]. Therefore, the concept of MFA is relatively applicable as technology selection tool in wastewater treatment as contaminant balances will vary depending on both mass flowrate and removal efficiency of technology. Similarly, a more novel approach had been proposed by Turner et al. [11] is to combine both MFA and LCA methods where complex and huge wastewater treatment systems can now not only be evaluated based on the flowrate trends but also focusing on environmental perspective such as contaminant removal. Although this proposed framework is capable in synthesizing a wastewater treatment system which meet environmental effluent discharged standard, however, it does not fully optimize the sustainability of the process by also considering cost factor.

Material Flow Cost Accounting (MFCA) was first developed in year 2005 as a tool in Environmental Management Accounting (EMA) [12] and was recognized by the International Organization for Standardization (ISO) in year 2011 as ISO 14051 [13]. At early stages, MFCA was established to measure the material flow in production lines in terms of both physical and monetary values for management purpose [14]. Over time, this approach had been successfully implemented in diverse industrial fields for maximizing profit and reducing waste generation cost. Unlike MCA or LCA, MFCA does not only prevail material identification, but instead, it advance further to assessing monetary values within the stream to gauge potential pathways

for cost minimization. According to Schidmt [15], MFCA is proven to be a mathematical framework which also measures greenhouse gases emission and energy consumption based on the mass flows. One important assumption that should be considered is to assume waste streams as by-products which require additional cost for treatment in a plant process. With this assumption, it can be concluded that any initial investment cost into the process would not only be turned over by desired product cost but a partial of the investment will be forfeited for by-product (waste) production. Some actual case examples are such as Canon lens manufacturing [16], NITTO DENKO manufacturing line for adhesive tapes and electronics [17], SEKISUI chemical recovery [18], SUMIRON development of mass production [19] and Mitsubishi pharmaceutical and medical products [19]. Hence, it was proven that the implementation of MFCA had aid these leading companies in improving overall performance of the company. Nevertheless, from the reviewed application of MFCA, most applications were done on manufacturing processes. There are still limited works to incorporate the concept of MFCA into mathematical optimization approaches.

As MFCA tracks the monetary value in the streamline of a process, this concept was proposed to be incorporated into waste recovery prioritization by Wan et al. [20]. Most conventional accounting practices in industrial manufacturing process only consider operating cost (OC) such as material cost, labor cost and system cost. Thus, the overlooked novel parameters that was proposed by Wan et al. [20] were hidden cost (HC) and carry forward cost (CFC). Hidden costs are the incurred cost that was embedded in each stream. Hence, hidden costs in waste streams should be kept to minimum to prevent lost in profit. Carry forward cost is the HC that are carried forward along the stream and will be incurred in the next stage of process. Therefore, to reduce raw material consumption and waste generation cost, hidden cost was proposed to be included in manufacturing processes as implementation of waste recovery [21]. All in all, the concept of MFCA in waste recovery advocates that every independent waste stream is bounded with an associated cost which consequently accumulates throughout the whole consecutive process. These cumulated waste costs are part of the investment cost of the process, hence, it is vital to minimize these costs to increase the economic performance of the process. Based on the reviewed studies, the MFCA framework is developing and used by manufacturing companies but there are limited research works that incorporates MFCA as an optimization tool in wastewater treatment technologies. In addition, it is noted that wastewater treatment process is a process that involves combination and integration of different treatment stage technologies. However, in most previous research works, models are used to determine which technology to be used in that particular treatment stage but not as an interlink within the whole wastewater treatment process. Further to this, there are limited research which considers all affecting attributes in selecting an optimum wastewater treatment process. For instance, most research would only focus only either in contaminants removal rate or environmental impacts or cost instead of having all attributes considered. In most cases, contradiction among these attributes may occur.

Therefore, in this work, the concept of MFCA has been incorporated to develop a novel MFCA-based approach to synthesize a wastewater treatment process by considering all these attributes (e.g., cost, removal rate, and environmental impact). Removal rate and environmental impact will be used to meet the constraint (environmental discharge regulation) in this work. Furthermore, in order to accurately gauge the profit of the overall production process, hidden cost and carry-forward cost of each stream of the wastewater treatment process have also been considered in the process synthesis. Also, sludge treatment optimization which rarely being considered in previous research works has also been integrated in this work. The optimum treatment process shall satisfy the government standard quality of the discharged (e.g., Biochemical oxygen demand (BOD), chemical oxygen demand (COD), total suspended solid (TSS), and oil and grease (OG)). Since treated water from the organic wastewater could be

recovered into manufacturing process, it is not considered as waste in this work. Therefore, the waste generation cost in this case study would be the sludge generation cost as treated sludge inhibits limited monetary value. In short, the objective of this research work is to develop a MFCA-based approach for synthesis of optimum WWTP where the effect of pollutants' removal efficiency of different technologies and cost optimisation are incorporated.

2 Methodology

An overview on the methodology in developing a MFCA-based approach for synthesis of a wastewater treatment plant is as illustrated in Figure 2.1. A generic superstructure is first generated based on the general wastewater treatment process stages. Then, the constraints in the developed model is set to be the contaminant concentration to ensure the treated water from the process would comply to the standard effluent discharged regulations. Simultaneously, the objective function which governs the selection of WWTP pathways would be minimisation of sludge cake generation cost. Sludge cake that is generated from the wastewater process will be disposed to the environment eventually as it is not a renewable source to be recirculated into the process. Relatively, any incurred cost in the sludge cake generation will be minimised to reduce the profit lost or disposal cost. Hence, prioritisation is set for a pathway route which has the least cost accrued within the sludge cake generation stream at the same time, complying with the constraints of contaminant concentration. Next, a series of equations are formulated which includes flowrate balance, contaminants (e.g. COD, BOD, TSS, OG) mass balance and cost computations (e.g. material cost, labour cost, hidden cost, carried forward cost) based on the generic superstructure. To illustrate the approach, a case study superstructure on organic wastewater treatment plant has been developed and solved. Based on the available technologies, the series of formulated equations are then coded into LINGO for process optimisation. Ultimately, an optimum organic wastewater treatment plant is synthesized.

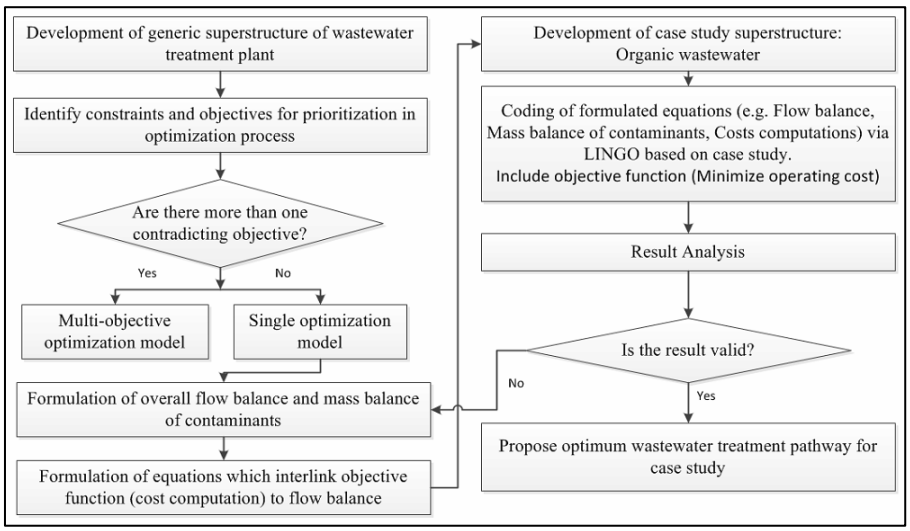


Fig. 2.1: **Methodology for development of a MFCA-based approach.**

2.1 Generic superstructure

Generic superstructure is established to project all possible pathways that could be generated based on interlinks between wastewater treatment technologies at different treatment stages. As shown **in Figure 2.2**, feed wastewater would be treated with a series of wastewater treatment; which includes, preliminary treatment $a \square A$, chemical treatment $b \square B$, biological treatment $c \square C$, tertiary treatment $d \square D$ and sludge treatment $e \square E$. As both chemical and

biological treatment would generate a certain amount of sludge, a certain amount of flowrate will diverge into the sludge treatment process. The sludge treatment process would further dehydrate the entering sludge water into sludge cake and dewatered wastewater would be recycled back into the system.

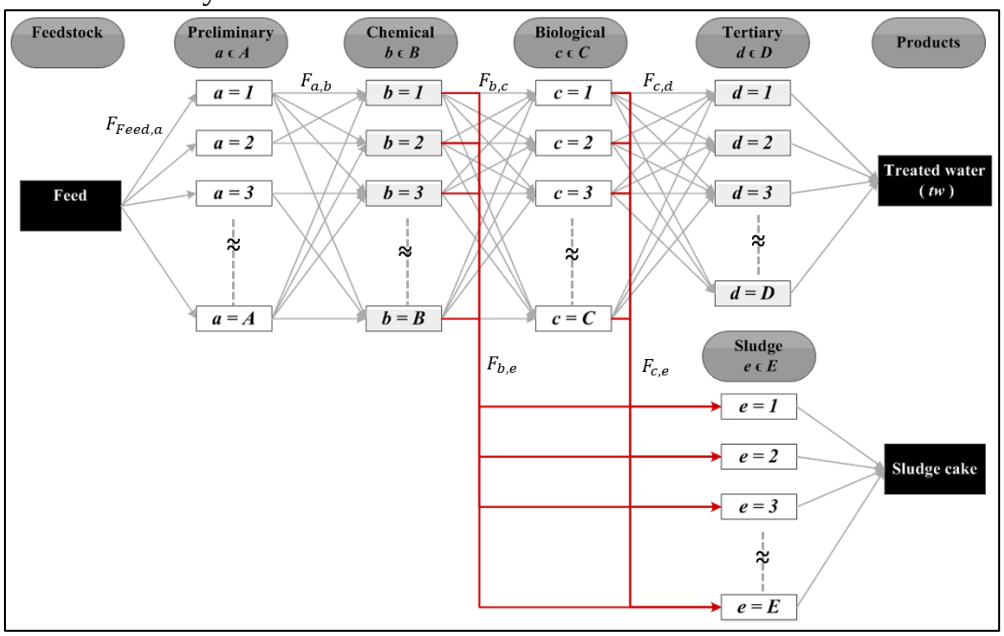


Fig. 2.2: **Generic superstructure of conventional wastewater treatment process.**

2.2 Modelling equations

2.2.1 Flowrate balance equations

Flowrate balance is first formulated as other constraints are linearly associated to the flowrate of effluent at each stream. In modelling the equations, the volumetric flowrates are represented by F ($\frac{m^3}{day}$). Flowrates flowing from one treatment stage to another are represented by an index which will be showed as subscript. For instance, the flowrate of the feed wastewater that flow to preliminary treatment a, with be represented as $F_{Feed,a}$. Then, the total flowrate in preliminary treatment a, F_a^{in} can be determined by summing up all the $F_{Feed.a}$ as shown in Eq. (1). The total flowrate that removed from preliminary treatment a is presented as F_a^{rev}. Meanwhile, the total outlet of wastewater of preliminary treatment a is presented as F_a^{out}. This outlet of wastewater will be flowing to chemical treatment b with flowrate of $F_{a,b}$. The same principle is applied to chemical treatment b where F_b^{in} is total wastewater to chemical treatment b; $F_b^{sludge,chem}$ is the flowrate of chemical sludge; F_b^{out} is the total outlet of wastewater of chemical treatment b; $F_{b,c}$ is the flowrate of wastewater that flow from chemical treatment b to biological treatment c; and $F_{b,e}$ is the sludge flowrate that flow from chemical treatment b to sludge treatment e. Similarly, this principal is also applied for biological treatment c where F_c^{in} is total wastewater to biological treatment c; $F_c^{sludge,bio}$ is the flowrate of biological sludge; F_c^{out} is the total outlet of wastewater of biological treatment c; $F_{c,d}$ is the flowrate of wastewater that flow from biological treatment c to tertiary treatment d; and $F_{c,e}$ is the sludge flowrate that flow from biological treatment c to sludge treatment e. Lastly, flowrate entering tertiary treatment d, F_d^{in} can be determined by summing up all the flowrate from biological treatment, c to tertiary treatment d, $F_{c,d}$. Thus, the total mass flowrate of treated water F_{tw} will

be identified. The formulation of equations will be arranged according to the flow of the treatment pathway projected in the generic superstructure as shown below:

Preliminary treatment (*a*):

$$F_a^{in} = \sum_{a=1}^{A} F_{Feed.a} \qquad \forall a \qquad (1)$$

$$F_a^{in} = F_a^{out} + F_a^{rev} \qquad \forall a \qquad (2)$$

$$F_a^{out} = \sum_{b=1}^{B} F_{a,b} \qquad \forall a \qquad (3)$$

Chemical treatment (*b*):

$$F_b^{in} = \sum_{a=1}^{A} F_{a,b} \qquad \forall b \qquad (4)$$

$$F_b^{in} = F_b^{out} + F_b^{sludge,chem} \qquad \forall b \qquad (5)$$

$$F_b^{out} = \sum_{c=1}^{C} F_{b,c} \qquad \forall b \qquad (6)$$

$$F_b^{sludge,chem} = \sum_{e=1}^{E} F_{b,e} \qquad \forall b \qquad (7)$$

Biological treatment (*c*):

$$F_c^{in} = \sum_{b=1}^{B} F_{b,c} \qquad \forall c \qquad (8)$$

$$F_c^{in} = F_c^{out} + F_c^{sludge,bio} \qquad \forall c \qquad (9)$$

$$F_c^{out} = \sum_{d=1}^{D} F_{c,d} \qquad \forall c \qquad (10)$$

$$F_c^{sludge,bio} = \sum_{e=1}^{E} F_{c,e} \qquad \forall c \qquad (11)$$

Tertiary treatment (*d*):

$$F_d^{in} = \sum_{c=1}^{C} F_{c,d} \qquad \forall d \qquad (12)$$

$$F_d^{in} = F_d^{out} \qquad \forall d \qquad (13)$$

$$F_d^{out} = F_{tw} \qquad \forall d \qquad (14)$$

2.2.2 Contaminant balance

COD balance

Generally, this section of formulation interlinks the mass of COD, *m* ($\frac{kg\ COD}{day}$) to the flowrate of wastewater, *F*($\frac{m^3}{day}$) by multiplying with the concentration of COD present in the wastewater, represented by C^{COD} ($\frac{kg\ COD}{m^3}$).

Preliminary treatment (*a*):

The mass of COD entering preliminary treatment *a*, $m_a^{COD,in}$ is equivalent to the concentration of COD in feed, C_{Feed}^{COD}($\frac{kg\ COD}{m^3}$) multiplying with the flowrate of feed entering *a*, $F_{Feed,a}$ ($\frac{m^3}{day}$).

$$m_a^{COD,in} = C_{Feed}^{COD}\, F_{Feed,a} \qquad \forall a \qquad (15)$$

The mass of COD removed in preliminary treatment, $m_a^{COD,rev}$ is equivalent to the COD removal efficiency of technology *a*, x_a^{COD} multiplying with the total mass to COD entering the technology, $m_a^{COD,in}$ as shown:

$$m_a^{COD,rev} = m_a^{COD,in} x_a^{COD} \qquad \forall a \qquad (16)$$

Therefore, the remaining mass of COD exiting preliminary *a*, $m_a^{COD,out}$ will be sent to chemical treatment for further removal of COD.

$$m_a^{COD,in} = m_a^{COD,rev} + m_a^{COD,out} \qquad \forall a \qquad (17)$$

$$m_a^{COD,out} = \sum_{b=1}^{B} m_{a,b}^{COD} \qquad \forall a \qquad (18)$$

The concentration of mass that is remaining in the wastewater stream entering chemical treatment *b*, C_a^{COD} is computed as shown below:

$$C_a^{COD} = \frac{m_a^{COD,out}}{F_a^{out,total}} \qquad \forall a \qquad (19)$$

Chemical treatment (*b*):

Similarly, the mass balance on COD is computed with the same concept in preliminary treatment *a*. However, the removal of COD in chemical treatment is now based on the efficiency of removal of COD by technology *b*, x_b^{COD} as computed as following:

$$m_{a,b}^{COD,in} = C_a^{COD} F_{a,b} \qquad \forall b \qquad (20)$$

$$m_b^{COD,rev} = \sum_{a=1}^{A} m_{a,b}^{COD,in} x_b^{COD} \qquad \forall b \qquad (21)$$

In chemical treatment, the dissolved solid (DS) in wastewater is removed chemically and consequently reduce the mass of COD in the wastewater. Meanwhile, the DS is being removed as sludge to sludge treatment *e*, $m_b^{COD,sludge}$. The remaining mass of COD present in the wastewater, $m_b^{COD,out}$ will be send to biological treatment, *c* as listed below:

$$\sum_{a=1}^{A} m_{a,b}^{COD,in} = m_b^{COD,sludge} + m_b^{COD,out} \qquad \forall b \qquad (22)$$

$$m_b^{COD,out} = \sum_{c=1}^{C} m_{b,c}^{COD} \qquad \forall b \qquad (23)$$

$$m_b^{COD,sludge} = \sum_{e=1}^{E} m_{b,e}^{COD} \qquad \forall b \qquad (24)$$

$$C_b^{COD} = \frac{m_b^{COD,out}}{F_b^{out,total}} \qquad \forall b \qquad (25)$$

Similar to chemical treatment, the series of formulation of COD mass balance in biological treatment *c* and tertiary treatment *d* is computed with similar principle.

Biological treatment (*c*):

$$m_{b,c}^{COD,in} = C_b^{COD} F_{b,c} \quad \forall c \quad (26)$$

$$m_c^{COD,rev} = \sum_{b=1}^{B} m_{b,c}^{COD,in} \, \mathrm{x_c^{COD}} \quad \forall c \quad (27)$$

$$\sum_{b=1}^{B} m_{b,c}^{COD,in} = m_c^{COD,sludge} + m_c^{COD,out} \quad \forall c \quad (28)$$

$$m_c^{COD,out} = \sum_{d=1}^{D} m_{c,d}^{COD} \quad \forall c \quad (29)$$

$$m_c^{COD,sludge} = \sum_{e=1}^{E} m_{c,e}^{COD} \quad \forall c \quad (30)$$

$$C_c^{COD} = \frac{m_c^{COD,out}}{F_c^{out,total}} \quad \forall c \quad (31)$$

Tertiary treatment (*d*):

$$m_{c,d}^{COD} = C_c^{COD} F_{c,d} \quad \forall d \quad (32)$$

$$m_d^{COD,in} = \sum_{c=1}^{C} m_{c,d}^{COD} \quad \forall d \quad (33)$$

$$m_d^{COD,rev} = m_d^{COD,in} \mathrm{x_d^{COD}} \quad \forall d \quad (34)$$

$$m_d^{COD,in} = m_d^{COD,rev} + m_d^{COD,out} \quad \forall d \quad (35)$$

$$m_d^{COD,out,total} = \sum_{d=1}^{D} m_d^{COD,out} \quad \forall d \quad (36)$$

$$C_{tw}^{COD} = \frac{m_d^{COD,out,total}}{F_{tw}} \quad (37)$$

To comply with the standard wastewater discharge COD concentration, $C^{std.COD}$ the COD concentration in treated water *tw*, C_{tw}^{COD} should be lesser as shown in Eq. (38):

$$C_{tw}^{COD} \leq C^{COD,Std} \quad (38)$$

BOD, TSS and OG balances

The formulation of the remaining contaminants (BOD, TSS and OG) balance is formulated according the same concept for the formulated series of equations for COD contaminant balance. The only change in these equations would be replacement of COD index to the respective indexes values.

2.2.3 Sludge treatment Mass balance

Mass of sludge present in the wastewater stream is represented by *M* ($\frac{kg\ SS}{day}$). Sludge generated in chemical treatment *b*, $M_b^{sludge,gen}$ and biological treatment *c*, $M_c^{sludge,gen}$ is directed to sludge treatment *e*, $M_e^{sludge,in}$ as computed in Eq. (39).

$$M_e^{sludge,in} = M_b^{sludge,gen} + M_c^{sludge,gen} \quad \forall e \quad (39)$$

For every mass of COD removed m^{COD} , the total mass of chemical sludge generated, $M_b^{sludge,gen}$ is corresponding to the sludge yield, $\mathrm{Y_b^{sludge,COD}}$ ($\frac{kg\ SS}{kg\ COD}$) as shown in Eq. (40). Then, the total mass flowrate of sludge generated by chemical treatment *b*, $M_b^{sludge,gen}$ will be directed to sludge treatment *e* with a total mass flowrate of $M_{b,e}^{sludge,gen}$ as shown in Eq. (41). Subsequently, the density ($\frac{kg\ SS}{m^3\ wastewater}$) of chemical sludge, $\mathrm{cSS^{chem}}$ interlinks the mass

flowrate of sludge flowing from chemical treatment *b* to sludge treatment *e*, $M_{b,e}^{sludge,gen}$with the total volumetric flowrate of wastewater from chemical treatment *b* to sludge treatment *e*, $F_{b,e}$.

$$M_b^{sludge,gen} = \mathrm{Y_b^{sludge,COD}} m_b^{COD,rev} \quad \forall b \quad (40)$$

$$M_b^{sludge,gen} = \sum_{e=1}^{E} M_{b,e}^{sludge,gen} \quad \forall b \quad (41)$$

$$M_{b,e}^{sludge,gen} = F_{b,e}\mathrm{cSS^{chem}} \quad \forall b \quad (42)$$

Same principle is applied to sludge generation from biological treatment *c* as shown below:

$$M_c^{sludge,gen} = \mathrm{Y_c^{sludge,COD}} m_c^{COD,rev} \quad \forall c \quad (42)$$

$$M_c^{sludge,gen} = \sum_{e=1}^{E} M_{c,e}^{sludge,gen} \quad \forall c \quad (43)$$

$$M_{c,e}^{sludge,gen} = F_{c,e}\mathrm{cSS^{bio}} \quad \forall c \quad (44)$$

Subsequently, the inlet and outlet flowrate of sludge treatment *e* is as following:

$$F_e^{in} = \sum_{b=1}^{B} F_{b,e} + \sum_{b=1}^{B} F_{b,e} \quad \forall e \quad (45)$$

$$F_e^{in} = F_e^{sludgecake} + F_e^{recycle} \quad \forall e \quad (46)$$

The flowrate of sludge cake produced, $F_e^{sludgecake}$ is based on the dryness ($\frac{kg}{m^3}$), $\mathrm{D_e}$ of the sludge treatment equipment and summarised as below:

$$F_e^{sludgecake} = \frac{M_e^{sludge,in}}{\mathrm{D_e}} \quad \forall e \quad (47)$$

2.2.4 Cost computation

MFCA tracks the monetary value associated to each stream. In other words, at the end of the cost computation, what is being evaluated will be the cost of wastewater and sludge cake after being processed at succeeding treatment stages. Hence, the formulation of cost computations is based on total unit cost per flowrate of wastewater. The unit operating cost for each stream, $UCost^{opt}$ ($\frac{RM}{m^3}$) are attributed to the unit material cost, $\mathrm{UCost^{mat}}$ and unit labour cost, $\mathrm{UCost^{labour}}$. Meanwhile, the actual operating cost $Cost^{opt}$ ($\frac{RM}{\mathrm{day}}$) needed for each equipment can be tracked by multiplying the unit operating cost, $UCost^{opt}$ with flowrate entering the equipment, F^{in}. Similarly, the operating cost that were generated will be associated to the outlet flowrates and will be carried forward as carried forward cost, CFC ($\frac{RM}{\mathrm{day}}$) to the next treatment stage along the stream. A series of cost computation on the preliminary treatment is as following:

Preliminary treatment (*a*):

$$UCost_a^{opt} = \mathrm{UCost_a^{mat}} + \mathrm{UCost_a^{labour}} \quad \forall a \quad (48)$$

$$Cost_a^{opt} = UCost_a^{opt} F_a^{in} \quad \forall a \quad (49)$$

$$CFC_{a,b} = UCost_a^{opt} F_{a,b} \quad \forall a \forall b \quad (50)$$

Then, the total carried forward cost entering chemical treatment *b*, CFC_b^{in} is computed by summing all carried forward cost from preliminary treatment, *a* to chemical treatment *b*, $CFC_{a,b}$. The flowrate entering chemical treatment *b*, F_b^{in} ($\frac{m^3}{day}$) is now associated with the carried forward cost, CFC_b^{in} ($\frac{RM}{\text{day}}$) . Hence, carried forward cost per unit, $UCost_b^{CFC}$ ($\frac{RM}{m^3}$) entering treatment *b* is determined as shown in Equation (52). Therefore, the actual unit operating cost, $UCost_b^{opt}$ now includes the unit material cost, $\text{UCost}_\text{b}^{\text{mat}}$, unit labour cost, $\text{UCost}_\text{b}^{\text{labour}}$, and unit carried forward cost, $UCost_b^{CFC}$. The same principle for cost is applied to biological treatment *c*, tertiary treatment *d* and sludge treatment *e*. Lastly, the hidden cost exiting tertiary treatment *d*, HC_d^{out} ($\frac{RM}{\text{day}}$) will be equals to the total cost of treated wastewater, $Cost_{tw}$ ($\frac{RM}{\text{day}}$). Similarly, the total hidden cost of sludge cake, $HC_e^{sludgecake}$ ($\frac{RM}{\text{day}}$) generated at sludge treatment *e* will be equals to the waste generation cost for sludge cake, $WGC_{sludgecake}$ ($\frac{RM}{\text{day}}$).

Chemical treatment (*b*):

$$CFC_b^{in} = \sum_{a=1}^{A} CFC_{a,b} \quad \forall b \quad (51)$$

$$UCost_b^{CFC} = \frac{CFC_b^{in}}{F_b^{in}} \quad \forall b \quad (52)$$

$$UCost_b^{opt} = \text{UCost}_\text{b}^{\text{mat}} + \text{UCost}_\text{b}^{\text{labour}} + UCost_b^{CFC} \quad \forall b \quad (53)$$

$$Cost_b^{opt} = UCost_b^{opt} F_b^{in} \quad \forall b \quad (54)$$

$$CFC_{b,c} = UCost_b^{opt} F_{b,c} \quad \forall b \forall c \quad (55)$$

$$CFC_{b,e} = UCost_b^{opt} F_{b,e} \quad \forall b \forall e \quad (56)$$

Biological treatment (*c*):

$$CFC_c^{in} = \sum_{b=1}^{B} CFC_{b,c} \quad \forall c \quad (57)$$

$$UCost_c^{CFC} = \frac{CFC_c^{in}}{F_c^{in}} \quad \forall c \quad (58)$$

$$UCost_c^{opt} = \text{UCost}_\text{c}^{\text{mat}} + \text{UCost}_\text{c}^{\text{labour}} + UCost_c^{CFC} \quad \forall c \quad (59)$$

$$Cost_c^{opt} = UCost_c^{opt} F_c^{in} \quad \forall c \quad (60)$$

$$CFC_{c,d} = UCost_c^{opt} F_{c,d} \quad \forall c \forall d \quad (61)$$

$$CFC_{c,e} = UCost_c^{opt} F_{c,e} \quad \forall c \forall e \quad (62)$$

Tertiary treatment (*d*):

$$CFC_d^{in} = \sum_{c=1}^{C} CFC_{c,d} \quad \forall d \quad (63)$$

$$UCost_d^{CFC} = \frac{CFC_d^{in}}{F_d^{in}} \quad \forall d \quad (64)$$

$$UCost_d^{opt} = \text{UCost}_\text{d}^{\text{mat}} + \text{UCost}_\text{d}^{\text{labour}} + UCost_d^{CFC} \quad \forall d \quad (65)$$

$$Cost_d^{opt} = UCost_d^{opt} F_d^{in} \quad \forall d \quad (66)$$

$$HC_d^{out} = UCost_d^{opt} F_d^{out} \quad \forall d \quad (67)$$

$$Cost_{tw} = \sum_{d=1}^{D} HC_d^{out} \quad \forall d \quad (68)$$

Sludge treatment (*e*):

$$CFC_e^{in} = \sum_{b=1}^{B} CFC_{b,e} + \sum_{c=1}^{C} CFC_{c,e} \quad \forall e \quad (69)$$

$$UCost_e^{CFC} = \frac{CFC_e^{in}}{F_e^{in}} \quad \forall e \quad (70)$$

$$UCost_e^{opt} = \mathrm{UCost_e^{mat}} + \mathrm{UCost_e^{labour}} + UCost_e^{CFC} \quad \forall e \quad (71)$$

$$Cost_e^{opt} = UCost_e^{opt} F_e^{in} \quad \forall e \quad (72)$$

$$HC_e^{sludgecake} = UCost_e^{opt} F_e^{sludgecake} \quad \forall e \quad (73)$$

$$HC_d^{recycle} = UCost_e^{opt} F_e^{recycle} \quad \forall e \quad (74)$$

$$WGC_{sludgecake} = \sum_{e=1}^{E} HC_e^{sludgecake} \quad \forall e \quad (75)$$

2.3 Case study

In this work, a case study will be evaluated on the organic wastewater treatment plant for water recovery in a sago-based biorefinery in Sarawak. Figure 2.3 illustrates the superstructure of an organic WWT plant consisting different technologies at different treatment stages. Preliminary treatment *a*, includes conventional technologies such grit screen, bar screen and oil & grease trap. Chemical treatment *b* includes dissolved air flotation (DAF) tank for removal of TSS and O&G for reduction of BOD or COD content. Biological treatment *c* includes are biological aerated filter (BAF), membrane bioreactor (MBR), sequencing batch reactor (SBR) and moving bed biofilm reactor (MBBR). Tertiary treatment *d* includes chlorination, ozone disinfection and activated carbon adsorption. Lastly, sludge treatment *e* includes filter press, belt filter press and centrifuge press.

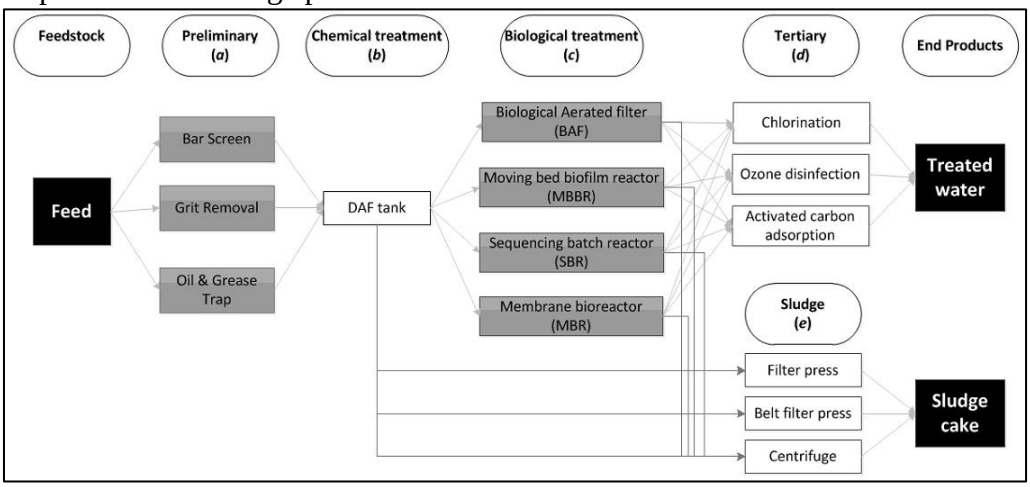


Fig. 2.3: Case study superstructure for organic wastewater treatment.

The constraint in this WWT plant is to ensure treated water exiting from the process would comply with the standard discharged regulation (Standard A) provided in Table 2.1 along with the wastewater feed provided by partnering sago mill company in Sarawak [22]. The contaminant removal efficiency of each technology is summarised in Table 2.2. In addition, Table 2.3 projects the dryness efficiency of each sludge treatment technology. Meanwhile, Table 2.4 projects the operating cost which includes the material cost and labour cost for each listed technology at each treatment stage. The labour cost is calculated by assuming an average

income of RM 15 per hour for one technician. Do noted that information regarding the specifications of technologies as well as costs were provided by industrial partner.

Table 2.1: Sago wastewater contaminants characteristic and discharged regulations.

	Concentration (ppm)			
	TSS	**COD**	**BOD**	**O&G**
Sago wastewater	4,942	7,763	3,362	**0**
Discharge regulations (Standard A) [24]	**150**	**300**	**150**	**20**

Table 2.2: Contaminant removal efficiency of wastewater treatment technologies.

		Removal efficiency (%)			
	Technologies	TSS	COD	BOD	O&G
Preliminary treatment	Bar Screen	65	0	0	0
	Grit Removal	40	0	0	0
	Oil & Grease trap	82	0	0	98
Chemical treatment	Dissolved air flotation (DAF)	86	70	65	77
Biological treatment	Biological aerated filter (BAF)	58	85	87	0
	Membrane bioreactor MBR	25	90	84	0

Table 2.2: Contaminant removal efficiency of wastewater treatment technologies (cont.)

	Sequencing batch reactor SBR	36	91	76	0
	Moving bed biofilm reactor MBBR	42	90	92	0
Tertiary treatment	Chlorination	16	56	29	0
	Ozone disinfection	35	29	15	0
	Activated carbon adsorption	58	65	18	0

Table 2.2: Dryness of sludge cake produced by each sludge treatment technology [25] [26]**.**

Technologies	Dryness (kg SS/m^3)
Filter press	25
Belt filter press	29.9
Centrifuge press	28.5

Table 2.4: Operating cost of wastewater treatment technologies [23] [27]**.**

	Technologies	Unit Cost (RM/m^3)		
		Raw material	Labour	Opt. cost
Preliminary treatment	Bar Screen	0	2.5	0
	Grit Removal	0	2.5	0
	Oil & Grease trap	0	0	0
Chemical treatment	DAF	1.50	2.50	3.00
Biological treatment	Biological aerated filter (BAF)	1.60	32.50	11.96
	Membrane bioreactor (MBR)	2.00	37.80	22.72
	Sequencing batch reactor (SBR)	1.60	45.10	11.67
	Moving bed biofilm reactor (MBBR)	1.60	35.40	9.00
Tertiary treatment	Chlorination	3.20	5.20	8.40
	Ozone disinfection	2.00	12.60	14.60
	Activated carbon adsorption	5.00	6.50	11.50
Sludge treatment	Filter press	0.5	3.26	3.76
	Belt filter press	0.5	4.74	5.24
	Centrifuge press	0.5	6.51	7.01

3 Results and Discussion

To demonstrate the developed approach, a case study on the wastewater treatment plant from a sago biorefinery plant is solved. Based on the information provided, the wastewater flowrate is 276 m^3/day with contaminant concentration as shown in Table 2.1. The contaminant concentration are the fixed variable inputs inserted into in LINGO software. Apart from this, other fixed variable inputs include the material cost, labour cost, density of chemical and biological sludge, sludge yield as well as efficiency of equipment. With the formulated equations, the results obtained from LINGO software (Version 17.0) is set with an objective function to minimise sludge cake generation cost, solved using global solver with computer specification of Intel ® Core ™ i5-6402P @ 8 Gb RAM, x64-based processor. Based on the global optimum solution results, the optimum pathway is oil and grease trap, dissolved air floatation (DAF) biological aerated filter (BAF) and belt filter press. The optimum solution proposed that there is no tertiary treatment needed in this case study wastewater treatment process to produced treated wastewater effluent which complies with the discharge regulation. Hence, this further reduces the overall operating cost of the process. Figure 3.1 illustrates the overview distribution of flowrates of the optimum wastewater treatment pathway. Figure 3.2 projects case study results showing the optimum pathway for a wastewater treatment process along with the contaminant concentration. The concentration of contaminants in the treated water are 201 ppm for COD, 5 ppm for BOD and 57 ppm for TSS which complies with the Standard A as illustrated in Table 2.1.

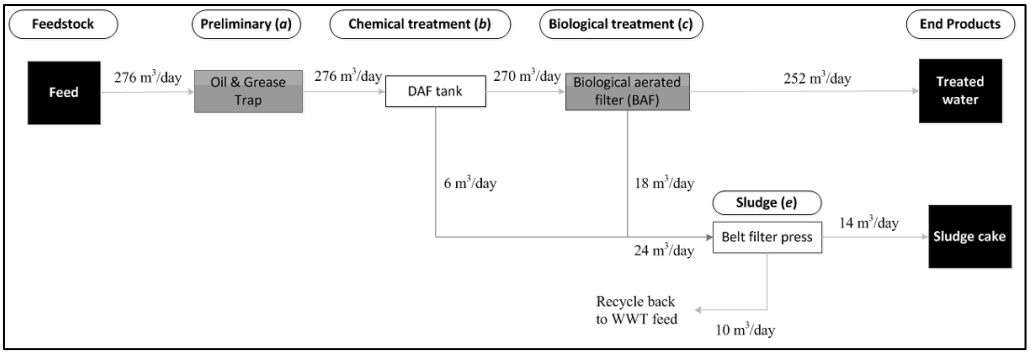


Fig. 3.1: Case study results for optimum pathway with volumetric flowrates.

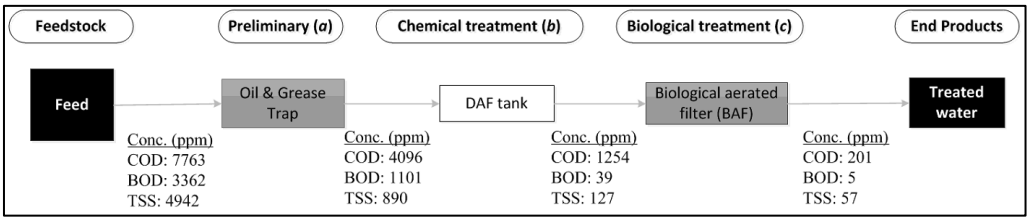


Fig. 3.2: Case study results for contaminant concentration.

Based on the flowrate distribution, the hidden cost (RM/day) which are associated to each stream can be computed based on the operating unit cost as shown in Figure 2.3. As illustrated, the hidden cost which are embedded in each stream are consecutively accumulated and carried forward to the next stage. For every RM 16,661/day spent on the wastewater treatment process, RM 814/day value of sludge cake will be disposed which is approximately 5% from the investment. Meanwhile, the remaining 95% of the investment will be utilised back into the sago biorefinery process. Therefore, it is concluded that with the application of this developed MFCA approach, the waste generation cost (sludge cake cost) can minimise up to 5% from the capital investment.

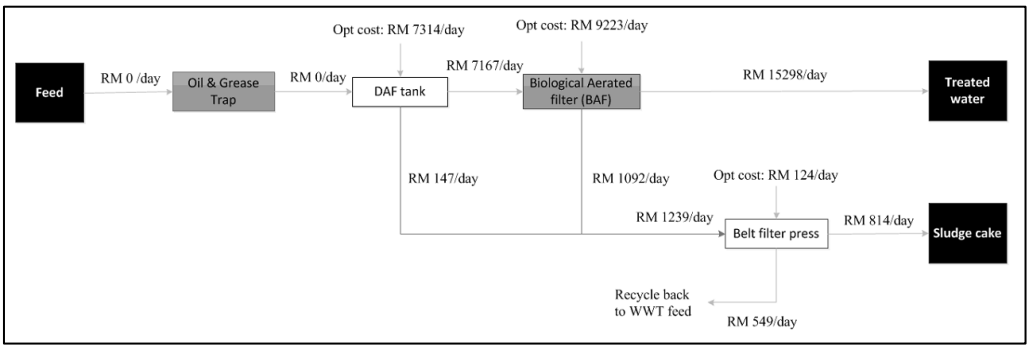


Figure 2.3: Case study results on cost computation.

4 Conclusion

In conclusion, the novel MFCA-based approach that was developed in this study is capable of synthesizing an optimum wastewater treatment which not only complies with the standard regulation of effluent discharged, but also minimises the waste generation cost, minimising the profit lost. Therefore, the significance in this work is incorporation of MFCA in wastewater treatment process which impacts the current wastewater treatment market by providing a decision-making tool in technology selection through this approach which satisfy both environmental and economic perspective. This developed approach is a flexible model which

can be easily modified for diverse field. The future work in this approach can be further extended by considering capital cost like equipment cost.

Acknowledgement: The authors would like to acknowledge LINDO Systems for providing academic licenses to conduct this research. Author would also like to gratefully acknowledge the financial support provided by the Taylor's University Research Grant Scheme (TRGS) – Emerging Researchers Funding Scheme (TRGS/ERFS/1/2017/SOE/028).

References

[1] World Health Organisation, "Drinking-Water," United Nations, Switzerland, 2017.

[2] United Nations Educational, Scientific and Cultural Organization (UNESCO), "The United Nations World Water Development Report," World Water Associated Programme, 2017.

[3] M. M. El-Hawagi, F. Gabriel and D. Harell, "Rigorous Graphical Targetting for Resource Conservation via Material Recycle/Reuse Networks," *Industrial and Chemical Engineering Research*, pp. 4319-4328, 2003.

[4] Y. P. Wang and R. Smith, "Wastewater minimisation," *Chemical Engineering Science*, pp. 981-1006, 1994.

[5] J. K. Kim, "System analysis on total water systems for water minimization," *Chemical Engineering Journal*, pp. 304-317, 2012.

[6] K. Hosni, S. B. Moussa, A. Chachi and M. B. Amor, "The removal of pottasium ion by calcium hydroxide from synthetic wastewater: Optimisation of operating conditions," *Desalination,* pp. 337-343, 2008.

[7] Q. Zhuo, H. Ma, B. Wang and F. Fan, "Degradation of methylene blue: Optimisation of operating condition through a statistical technique and environmental estimate of the treated wastewater," *Journal of Hazardous Materials*, pp. 44-51, 2008.

[8] W. Piao, Y. Kim, H. Kim, M. Kim and C. Kim, "Life cycle assessment and economic efficiency analysis of integrated management of wastewater treatment plants," *Journal of Cleaner Production,* vol. 113, pp. 325-337, 2016.

[9] G. X. Gao, Z. P. Fan and Y. Zhang, "MADM method considering attributes aspiration with an application to selection of wastewater treatment technologies," *Kybernetes*, vol. 44, no. 5, pp. 739-756, 2015.

[10] A. Allesch and P. H. Brunner, "Material Flow Analysis as a Tool to improve Waste Management Systems: The Case of Austria," *Environmental Science and Technology*, vol. 51, no. 1, pp. 540-551, 2017.

[11] D. A. Turner, I. D. Williams and S. Kemp, "Combined material flow analysis and life cycle assessment as a support tool for solid waste management decision making," *Journal of Cleaner Production,* vol. 129, pp. 234-248, 2016.

[12] International Federation of Accountants: Environmental Management Accounting, "International Guidance Document," New York, 2005.

[13] ISO 14051, "Environmental Management - Material Flow Cost Accounting," General Framework, Geneva, 2011.

[14] H. K. Katsuhiko Kokubu, "Material flow cost accounting and existing management perspective," *Journal of Cleaner Production,* vol. 108, pp. 1279-1288, 2015.

[15] M. Schmidt, "Ther interpration and extension of Material Flow Cost Accounting (MFCA) in the context of environmental material flow analysis," *Journal of Cleaner Production,* vol. 108, pp. 1310-1319, 2015.

[16] M. Schmidt and M. Nakajima, "Material Flow Cost Accounting as an Approach to Improve Resource Efficiency in Manufacturing Companies," *Resources,* vol. 2, pp. 358-369, 2013.

[17] NITTO DENKO Corporation, "Protecting our planet to pass on to future generations," NITTO DENKO Corporation, Osaka, 2015.

[18] H. Kitada and A. Higashida, "Management Control Systems for Material Flow Cost Accounting: A Case of Japanese Company," in *Industrial Engineering and Operations Management,* Kuala Lumpur, 2016.

[19] K. Kokubu, "Material Flow Cost Accounting MFCA Case Examples," Ministry of Economy, Trade and Industry (METI), Tokyo, 2013.

[20] Y. K. Wan, R. T. Ng, D. K. Ng and R. R. Tan, "Material Flow Cost Accounting (MFCA)-based approach for priortisation of waste recovery," *Journal of Cleaner Production,* vol. 107, pp. 602-614, 2015.

[21] A. Simms, S. Hammilton and W. K. Biswas, "Carbon footprint assessment of Western Australian Groundwater Recycling Scheme," *Environmental management,* vol. 59, no. 4, pp. 557-570, 2017.

[22] Y. K. Wan, R. T. Ng, D. K. Ng, K. B. Aviso and R. R. Tan, "Fuzzy multi-footprint optimisation (FMFO) for synthesis of a sustainable value chain: Malaysian sago industry," *Journal of Cleaner Production,* vol. 128, pp. 62-76, 2016.

[23] TENAGA NASIONAL Bhd., "Special Industrial TARIFF (SIT) New policy," TENAGA NASIONAL Bhd., Selangor, 2018.

[24] Department of Environment , "Environmental Requirements: A guide for investors," Ministry of Natural Resources and Environment Malaysia, Putrajaya, 2013.

[25] Faure Equipments, "Filter Presses," Germany, 2018.

[26] P. Ginisty, . F. Guei, R. Girault, J. Tosoni, J. Olivier and J. Vaxelaire, "DRYNESS LIMIT: A USEFUL PARAMETER TO ASSESS SLUDGE DEWATERING," in *FILTECH 2013*, Wiesbaden, 2013.

[27] Y. Gu, Y. Li, X. Li, P. Luo, H. Wang, X. Wang, J. We and F. Li, " self-sufficient wastewater treatment plants: feasibilities and challenges," *Procedia,* vol. 105, pp. 3741-3751, 2017.

Simulation and Design for Multicyclone in Dust Removal System

Lee Sze Young[1], Wan Yoke Kin[1], Anis Suhaila Shuib[1], Chong Thiam Heng[2], Teh Khim Choon[2]

[1] School of Engineering, Faculty of Built Environment, Engineering, Technology & Design, Taylor's University, Malaysia.
[2] Mackenzie Industries Sdn. Bhd, Malaysia.

Abstract. Recently, the Environmental Quality (Clean Air) Regulations have been revised to be more stringent where the dust or solid particles emitted shall not be exceed 150 mg/m^3 (previously was 400 mg/m^3). Therefore, in this research work, a new multicyclone system with higher dust removal performance will be designed to further reduce the dust load. Prior to the new design of multicyclone a study has been performed on the existing multicyclone design that provided by industrial partner to determine a suitable model to be used for the new design by comparing the study results with the actual industrial results. Then, a design improvement of the existing multicyclone was conducted by designing the single cyclone of the system. This is because the improvement in single cyclone will eventually improves the efficiency of multicyclone. To do that, a preliminary study of Computational Fluid Dynamics (CFD) evaluation has been performed using the suitable model to predict the collection efficiency and the pressure drop of single cyclone with different design criteria, which is the diameter of vortex finder as well as the inlet configuration. The numerical solutions were carried out using ANSYS CFD FLUENT version 18.0. In this work, the original single cyclone design of the existing multicyclone system was named as Design I. Then, for the proposed single cyclone design with different vortex finder diameters were named as Design II and Design III, which, Design I incorporate the smallest diameter and subsequently to Design III with the smallest diameter. Furthermore, two types of cyclones with tangential single inlet as well as tangential double inlets, which named as Design IV and Design V were also included in this work to study their performance. The effect of vortex finder diameter and inlet configuration on the performance parameters such as pressure drop and collection efficiency in fluid dynamics behaviour were analysed. In the CFD, the suitable model, Re-Normalisation Group (RNG) k–ε turbulence model that was used to simulate turbulence flow was applied in this work to study the flow behaviour. Apart from this, the dust particle flows were tracked via Discrete Phase Model (DPM). Based on the CFD simulation results, the collection efficiency and pressure drop of existing multicyclone was found to deviate 18.5% and 7.66% respectively from the actual industrial data provided. Relatively, the collection efficiency and the pressure drop of

multicyclone was increased by 4.86% and 8% respectively with decreasing the diameter of vortex finder by 35mm.

Keywords: Dust removal system, multicyclone, CFD, RNG k–ε model, collection efficiency

1 Introduction

The boiler system is commonly found in most of the industries to produce heat energy. In previous industrial practices, fossil fuels were used in boiler as heat generation source. This caused depletion of fossil fuel and severe impacts to the environment and human health as significant amount of greenhouse gases were emitted during the combustion process. Therefore, there is a rising call in the industries and companies from exploiting fossil fuels, but instead, investing in new energy sources in the future [1]. Biomass is one of the alternative sources for boiler system to produce heat energy instead of using fossil fuels . The types of biomass fuels that commonly used for boiler are wooden chip, rice husk, palm waste and wooden pallet [2]. However, the biomass boiler has a major drawback to the environment and human health, which is during the burning process, significant amount of particulate matter such as fly ash and dust are produced. According to the regulation stated in Part V, Section 28 in Environmental Quality (Clean Air) Regulations 1978, a stationary plant shall not emit or discharge dust or solid particles more than 400 mg/m^3 from every chimney to the environment [3]. However, in year 2014, the regulations have been revised to be more stringent where the dust or solid particles emitted shall not be exceed 150 mg/m^3 [4]. Therefore, a higher efficiency of dust removal system is necessary to be designed or modified from existing dust removal system to reduce the dust load emission as well as to comply with the new regulations.

Basically, the existing dust removal system involved different types of dust collectors such as cyclone, fabric filter, wet scrubber and electrostatic precipitator (ESP). All the dust collectors mentioned are having different operating specifications. It is mainly depending on the particle size to be removed. Table 1.0 showed the limitation on dust particle size for different types of dust collectors.

Table 2.0: The different types of dust collectors [5].

Types of Dust Collector	Particle size, µm
ESP	0.01 - 1.0
Centrifugal Separator (Cyclones)	2 - 500
Wet Scrubber	0.01 - 100
Fabric filter	0.01 - 50

The ESP is found to give the greatest dust removal performance among all the dust collectors but it also comes with the highest installation cost and maintenance cost [6]. According to James [7], the capital cost required to install an ESP was approximately between one hundred thousand US Dollar to ten million US Dollar. The wet scrubber is another type of dust collector that having high efficiency to remove the dust particle in the size between 0.01µm to 100µm. However, it generated significant amount of wastewater and subsequently created additional problems to owner (e.g., water pollution, high treatment cost, etc.) [8]. The fabric filter is another alternative for dust collector that able to remove dust particle between

0.01μm to 50μm. However, it caused high pressure drop to the system and required frequent maintenances to clean the dust particles left on fabric filter to avoid blockage in the system [5]. On the other hand, cyclone is found more sustainable in dust removal as the cyclone system is more economical, easier to maintain and produce lesser pollution to environment [9]. It works based on the principle of centrifugal forces that created due to the swirling flow occurred inside cyclone body that resulted particle separation based on its density properties. However, a simple cyclone system is only effective for dust particles more than 5μm in diameter [10]. Based on the report from industry, the size of particles that produced from biomass boiler system are between 0.38μm to 260μm [11]. In order to solve this problem, a multicyclone dust collector that consists of multiple single cyclone units in parallel arrangement within a specified capacity was introduced to the industry in past decade.

According to the monitoring results obtained by Environmental Science (M) Sdn. Bhd. in year 2015 [10], the current design of multicyclone dust removal system can only achieve a result of about 200 mg/m^3 to 300 mg/m^3, which is not complying with the new regulation. Therefore, there is a need to design multicyclone system with higher dust removal performance to further reduce the dust load. In order to validate the dust removal performance of the new design of multicyclone system, simulation is vital to be performed. Therefore, a Computational Fluid Dynamics (CFD) study has been performed in this work for the new design of multicyclone using ANSYS CFD FLUENT version 18.0. The CFD is a computational software that able to visualize the fluid flow as well as the interaction between the air flow and dust particles inside a cyclone system.

In the similar area of research, several researches have been proposed to study the effect of flow structure with the changes in geometry and to determine the collection efficiency by injecting particle to the flow in CFD simulation study [12, 13]. The CFD approach is preferably applied for incompressible to lightly compressible flows. The conservation of mass, momentum and energy in fluid flow are expressed in terms of non-linear partial differential equations that usually against the solution by analytical means. The solution from these equations successfully applied for the calculation of complicated flow models by CFD simulation [14]. Furthermore, the CFD simulation is proven to generate the accurate description of the behaviour of turbulent flow occurred in a cyclone model [13].

In ANSYS, the numerical models commonly used simulate fluid flow inside cyclone are the standard k–ε model, the RNG k–ε model, the Realizable k–ε model and the RSM model. The k–ε models involve the solution of transport equations for the kinetic energy of turbulence and its dissipation rate as well as the calculation of a turbulent allowance to the viscosity at each cell. Hence, this model cannot be optimized for strongly swirling flows that usually found in multicyclone. While the RSM includes the characteristics of anisotropic turbulence and provide the solution of transport equations for every Reynolds stress components that suitable for complex fluid flow with strong swirling motion. However, this model require an excessive computational effort than k–ε model [15]. Therefore, in order to minimize the computational effort and solving time, the RNG k–ε model can be used with a 12% deviation from experimental results [13]. The numerical study for this multicyclone system was carried out using the RNG k–ε model in order to reduce the computational effort due to the limitations on computing hardware provided.

Gimbun and his teams proposed a CFD study to predict the collection efficiency of cyclone model using the RNG k–ε model. It showed that the results obtained from CFD simulation was an accurate method to model the single tangential cyclone collection efficiency

[12]. In addition, a similar study was performed by Azadi [17] to determine the effect of cyclone size on its performance parameters using RNG k–ε model and Reynolds Stress model (RSM). Then, the particle flow behaviour in cyclone body was tracked using the Discrete Phase model (DPM). The simulation results justified the CFD modelling with RSM as a promising tool to study flow behaviour for single tangential cyclone model [17]. However, both CFD simulation studies were only performed to study the single tangential cyclone model that only effective for particle size between $2\ \mu m$ to $500\ \mu m$. Limited study is performed for multicyclone. Therefore, there is a need to perform CFD simulation study for multicyclone to determine the effect of multicyclone design on its performance parameters.

Recent study by Zhou [18] to study the effects of surface roughness on single cyclone performance using RSM model in CFD simulation. Other than that, a similar study was done by Kaya [19] to study the effect of surface roughness on the performance of tangential inlet cyclone separators using CFD simulation. This study was performed using RSM to predict continuous gas flow behaviour and the Lagrangian approach (LES) to study particle motions. Both simulation results were verified with experimental results and achieved a deviation less than 5% when compared to experimental results. However, both studies only focused on the effects of surface roughness on tangential cyclone model. Besides, the effects of cyclone geometry on separation performance were not addressed in the recent studies. Furthermore, the RSM model contains 7 different governing equations to solve the simulation that requires more CPU effort up to 2-3 times. Hence, it requires a high performance CPU to carry out flow simulation using RSM model. Therefore, in this work, the RNG k–ε model is applied in CFD simulation to analyse the performance parameters of an existing multicyclone in industry. In addition, in order to address the research gaps as mentioned above, an existing multicyclone design has been modified in this work. The dust removal efficiency and pressure drop of the modified multicyclone have also been determined. Besides, a new multicyclone system with higher dust removal efficiency has been designed in this work as well for biomass boiler system.

By carrying out such CFD study on multicyclone system will enable industry to verify and support the performance parameters such as collection efficiency and pressure drop of the multicyclone system with different cyclone designs. Hence, it could eliminated unnecessary cost and work on improving the efficiency of multicyclone system.

2 Methodology

As described previously, the existing design of multicyclone system was modified to improve its separation efficiency and then the CFD simulation was performed to determine the performance parameters of multicyclone. In order to verify the results generated from CFD simulation from new multicyclone system, a CFD simulation was carried out for existing multicyclone system and the results generated were compared with the actual results collected from site. The CFD simulations were performed with Precision T5500 2.13 GHz Dell CPU workstation with 4 MB cache memory, 6 GB RAM-memory and 500 GB hard-disc memory. According to Ozen Engineering Inc. [20], the recommended requirement for CPU RAM-memory to use CFD FLUENT for simulation of complex geometry is 16 GB. Therefore, in order to reduce the simulation effort and calculation time, an assumption was made that when there is an improvement for the collection efficiency of single cyclone, the collection efficiency of multicyclone that contained multiple of that single cyclone will increases as well. Then, a design improvement of the existing multicyclone was conducted by designing the single

cyclone of the system. This is because the improvement in single cyclone will eventually improves the efficiency of multicyclone.

Generally, engineers are interested in two performance parameters when carrying out an analysis of the design and performance of a multicyclone system. These parameters are the collection efficiency of particle and the pressure drop through multicyclone system. An accurate prediction of these parameters is very important because an inaccuracy of numerical results may result an inefficient design of multicyclone system. Therefore, the numerical study done by CFD is applied as the CFD has a great potential to predict the flow field feature and track particle inside cyclone dust removal as well as the pressure drop across [23].

2.1 Multicyclone Design

Currently, there are various types of multicyclone systems available in the market but the multicyclone with vertical inlets as shown in Figure 2.0 is most often used in boiler system [21]. In this research study, the CFD simulation dealt with a standard case of multicyclone system with contains multiple pieces of cyclone with vertical inlet which provided by industrial partner. Hence, the improvement in single cyclone will eventually improves the efficiency of multicyclone. Different vertex finder diameter of single vertical cyclones (see Figure 2.1), which labelled as Design I, II and III as well as different inlet configuration of single tangential cyclone (see Figure 2.2), which labelled as Design IV and V were included in this research work. The Design I incorporated the largest vortex diameter and subsequently to Design III with the smallest vortex diameter while the Design IV represented single inlet tangential cyclone and the Design V represented double inlet tangential cyclone. The vortex finder diameter of Design II was 35mm smaller than existing design (Design I) and subsequently another 35mm reduction from Design II for Design III. However, the detailed dimensions of all the cyclone design were not revealed in this work due to the confidential issue. All the cyclone models mentioned above were simulated in this research to compare the collection efficiency as well as the pressure drop across the system. An optimum design of cyclone that gave the greatest removal efficiency with minimal pressure drop is selected based on the simulation results among the five different designs.

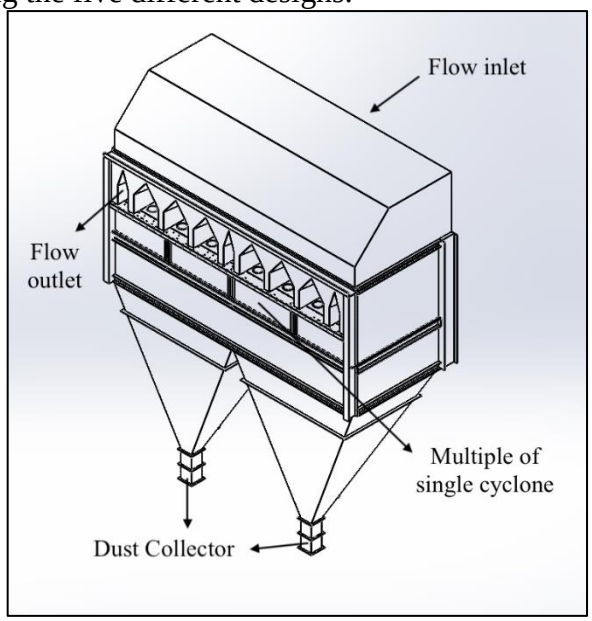


Figure 2.0: The geometry of existing multicyclone system.

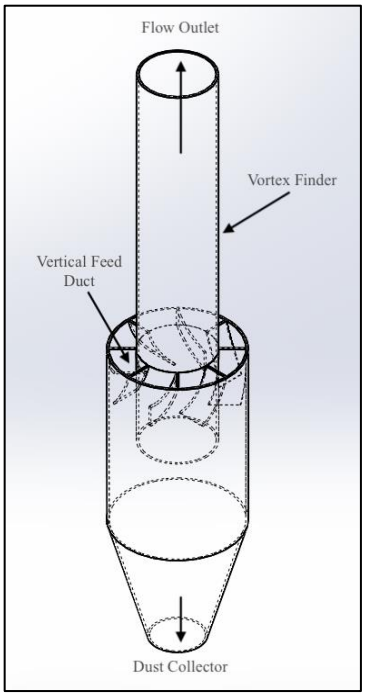


Figure 2.1: The geometry of single vertical inlet cyclone.

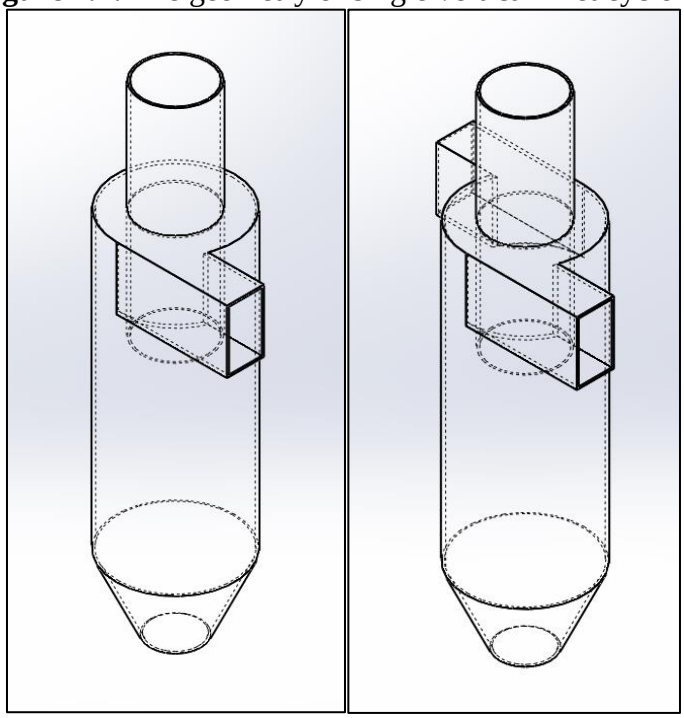


Figure 2.2: The geometry of different cyclone designs: (left) single inlet tangential cyclone; (right) double inlet tangential cyclone.

2.2 Mathematical Modelling

For the steady and incompressible fluid flow in multicyclone, the Reynolds-averaged Navier-Stokes equations (RANS) is used to model the flow in the multicyclone. The equation is expressed as below [24]:

$$\rho u_j \frac{\partial u_i}{\partial x_j} = -\frac{\partial P}{\partial x_i} + \frac{\partial}{\partial x_j}\left[\mu\left(\frac{\partial u_i}{\partial x_j} + \frac{\partial u_j}{\partial x_i}\right)\right] + \frac{\partial \tau_{ij}}{\partial x_j} \quad (1)$$

where the symbol of $u, P, \rho \; and \; \mu$ correspond to the carrying fluid velocity, operating pressure, fluid density and fluid viscosity respectively. Then, the Reynolds stress tensor, τ_{ij} is defined as below:

$$\tau_{ij} = -\rho\overline{u_i' u_j'} \tag{2}$$

The Reynolds stress tensor is known as the effects of turbulent fluctuations to the fluid flow [25]. For the continuity equation for the mean motion, it is defined as the partial differential of velocity with respect to change in distance. The equation can be expressed as:

$$\frac{\partial u_i}{\partial x_i} = 0 \tag{3}$$

where the dash mark represents the fluctuating part while the overbar mark represents a Reynolds average value. In order to solve the Reynolds stress tensor, a turbulence model is required. Hence, the numerical study for this multicyclone system was carried out using the RNG k–ε model. The numerical study carried out by Gimbun [12] reveal that the simulation with RNG k–ε model showed a 8% deviation on experimental data. Furthermore, the advantage of this model is to reduce the computational effort due to the limitations on computing hardware provided.

For the turbulent kinetic energy (k) and dissipation rate (ε) in the RNG k–ε model, the transport equations can be derived from the Navier-Stokes equations which developed using the Re-Normalisation Group (RNG) methods in order to consider the effects of minor scales motion. The derived transport equations are expressed as below [17]:

$$\rho \frac{dk}{dt} = \frac{\partial}{\partial x_i}\left(\alpha_k \mu_{eff} \frac{\partial k}{\partial x_i}\right) + G_k - \rho\epsilon \tag{4}$$

$$\rho \frac{d\epsilon}{dt} = \frac{\partial}{\partial x_i}\left(\alpha_\epsilon \mu_{eff} \frac{\partial \epsilon}{\partial x_i}\right) + C_{1\epsilon}\frac{\epsilon}{k}G_k - C_{2\epsilon}\rho\frac{\epsilon^2}{k} - R \tag{5}$$

Where the $C_{1\epsilon}$ and the $C_{2\epsilon}$ are constants that having the value of 1.42 and 1.68 respectively. The RNG k–ε model is different from the standard k–ε model as the RNG k–ε model considers an additional term of R in the dissipation rate equation.

In this research, the particles that injected into multicyclone system are fine that the size range from 0.38μm to 260μm. There are some assumptions made in this study in order to determine the trajectories of particle inside the multicyclone system [26, 27, 12]:

1. The presence of the particles does not affect the flow field.
2. The fluid obey ideal gas law.
3. The collisions between particles and the walls of the multicyclone are perfectly elastic.
4. The particle-particle collision is negligible.
5. The mass flow rate of particle is equally distributed for every single cyclone in multicyclone.

Based on the assumptions made, the Lagrangian approach is applied to calculate the trajectories of particles in flow. In Lagrangian approach, the discrete phase model (DPM) was used to track individual particles through the fluid flow across the multicyclone because it is assumed that there is no any interactions between each particle. Following this, the particle force balance equations are expressed in the x, y and z directions due to the 3D fluid flow.

$$\frac{du_p}{dt} = F_D\left(u - u_p\right) + \frac{v_p^2}{r_0} \tag{6}$$

$$\frac{dv_p}{dt} = F_D\left(v - v_p\right) - \frac{u_p v_p}{r_0} \tag{7}$$

$$\frac{dw_p}{dt} = F_D\left(w - w_p\right) - g \tag{8}$$

where, the $\frac{v_p^2}{r_0}$ and $\frac{u_p v_p}{r_0}$ stand for centrifugal and Coriolis components of particle acceleration, the u, v and w represent the fluid phase velocity in x, y and z directions and the u_p, v_p and w_p

represent the particle velocity in x, y and z directions. For the term of F_D in the equations above, it represent the drag force per unit of particle mass and it can be expressed as below:

$$F_D = \frac{18\mu}{\rho_p d_p^2} \frac{C_D Re}{24} \quad (9)$$

2.3 Computational Fluid Dynamics Approach

2.3.1 Grid System

To generate an accurate simulation result, the grid generation, also known as meshing of geometry acts as an important factor in CFD simulation. During meshing, the geometry is divided into small pieces knowns as elements and the corner of each element is called node. The calculation is performed at the nodes and then the combination of all the elements and nodes is called the mesh. Therefore, all the cyclone geometries are meshed using the unstructured meshing method. Only three different sizing relevance centre, which are coarse, medium as well as fine meshing were used to control the fineness of the meshing. in this research work, the mesh dependent numerical study was not covered due to limitation on time and scope of this research. The meshing results were evaluated based on skewness quality and orthogonal quality. The skewness quality is one of the primarily quality measures for a mesh. It determines the how close a face or a cell mesh to the ideal equilateral triangle or equiangular quadrilateral within a scale of 0 to 1, where a value of 0 represents the best quality while a value of 1 represents the worst quality [38]. For recommendation, the skewness quality of meshing must be lower than 0.98 for simulation. For the orthogonal quality of meshing, it is computed using three different vectors, which are the face normal vector, the vector from the cell centroid to the centroid of each of the adjacent cells and the vector from cell centroid to each of the faces [38]. The range of orthogonal quality is between 0 to 1, where a quality value of 1 is the best while a value of 0 is the worst. The Figure 2.1 below illustrates the geometries and grid arrangement for existing multicyclone, vertical cyclone and tangential cyclone. The meshing results are tabulated in the Appendix 1.0. Based on the meshing results, the meshing with fine relevance centre was used in this research work because it gave the best quality compared the other meshing results. A better meshing quality will results a better simulation results. Other than that, a better meshing quality also requires lesser effort for computing [21]. Additionally, the symmetrical simulation is applied in this study in order to reduce the calculation time for each case.

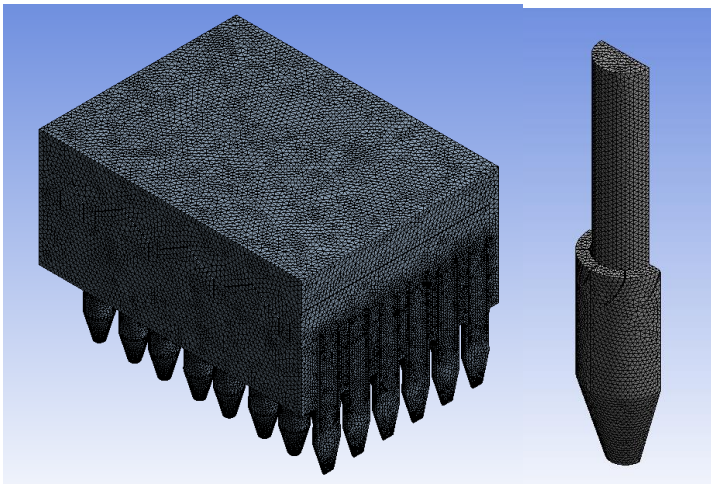


Figure 2.1: The grid system for: (left) multicyclone; (right) single vertical cyclone.

2.3.2 Solver Settings

In the present CFD simulation, the details of simulation settings are given in the Table 2.3 below. The solver setting for all the simulations present in this study were identical as described in Table 2.3 below.

Table 2.3: Solver settings for numerical study.

Turbulence model	RNG k–ε model
Solver type	Pressure based
Solver time	Steady
Near wall treatment	Standard wall function
Pressure-velocity coupling	SIMPLE
Pressure interpolation scheme	Second order upwind
Turbulent dissipation rate	Second order upwind

2.3.3 Boundary and Convergence Conditions

For the boundary condition at the flow inlet, a uniform distribution for all the dependent variables are employed. Hence, the velocity inlet condition is imposed at the inlet, where the inlet velocity can be expressed as below:

$$u_n = u_i \tag{10}$$

where, the u_n represents the normal velocity perpendicular to the inlet surface. Furthermore, for the discrete phase of particle, a number of 5000 particles is released and tracked for Design I, II and III. Each segment of the particle size distribution includes number of 1000 particles. The collection efficiency is obtained by calculating the ratio of trapped and released particles inside the fluid domain [29]. Theoretically, the more particles are injected and tracked, the more accurate collection efficiency can be obtained. However, it also results in high computing effort [30].

For the boundary condition at the fluid outlet and the particle outlet, the outflow boundary condition is imposed for both outlets. Following that, for the boundary condition at the wall, the non-slip boundary condition is imposed at the wall of multicyclone. In this CFD simulation, a steady state time solver is performed and the 10^{-3} convergence of basic accuracy is imposed for the calculation. The total number of iterations is set at 5000 and the time of iterations for each calculation is approximately 5 hours by using the computational platform mentioned above. The Table 2.4 below illustrates the operating conditions provided from industrial partner.

Table 2.4: The operating conditions for numerical study.

Operating Pressure	101325 Pa
Operating Temperature	573.15 K
Fluid (Continuous phase)	
Medium	Air
Velocity	3.043 m/s
Viscosity	1.7894×10^{-5} kg/m.s
Density	1.225 kg/m^3

Particle (Discrete phase)	
Medium	Ash solid
Flow rate	2.3124 x 10^{-4} kg/s
Velocity	3.043 m/s
Diameter range	$0.38\mu m\ to\ 260\mu m$
Mean diameter	$80\mu m$

2.4 Performance Parameters

As mentioned above, there are two parameters selected in this study in order to compare the efficiency of multicyclone with different designs, which are the collection efficiency of injected particles and the pressure drop across the multicyclone system. For the collection efficiency of particle, it is determined by calculating the ratio of trapped particles and escaped particles [31]. The collection efficiency can be expressed as below:

$$\eta = \frac{n_{p,trapped}}{n_{p,injected} - n_{p,incomplete}} \times 100\% \quad (11)$$

where the η represents the collection efficiency in percentage and the n_p represent the number of particles. Furthermore, the particles are tracked for every 10 iterations. For the pressure drop across the system, it is generally known as the difference between the inlet pressure and the average pressure at the outlet [32]. The pressure drop across the system can be computed in the post-processing stage of the CFD simulation.

3 Results and Discussion

In this numerical study, the actual results from site were provided by industrial partner for the existing multicyclone. Therefore, the results of simulations using were verified with actual results provided in the Section 3.1. Next, for the design improvement, it was done based on a single cyclone in the system because the improvement in single cyclone will eventually improves the efficiency of multicyclone. In the Section 3.2, the effect of cyclone size on the collection efficiency and pressure drop were discussed.

3.1 Validation of numerical model

In every numerical study, it is important to verify the simulation results before concluding any findings from the study. This is because without any validations on simulation model, it is impossible to say that the CFD modelling can predict promising results. Therefore, in this study, the existing multicyclone which contained multiple of single vertical cyclone with Design I was simulated based on the operating conditions on site provided by industrial partner and the simulation results were compared with the actual results provided. There are two performance parameters used to compare with the actual results, which are the collection efficiency of particle and the pressure drop across the system. The comparison between the simulation results and the actual results in terms of the collection efficiency and the pressure drop is illustrated in the Table 3.1 below.

Table 3.1: The comparison between simulation results and actual results for existing multicyclone.

Performance parameter	Actual results from site	Simulation results	Percentage error, %
Collection efficiency, %	92.00	74.98	18.50

Pressure drop, Pa	490.33	452.78	7.66

It is seen that the simulation results by using the RNG k–ε model predict an accurate results of collection efficiency and pressure drop with the deviations of 18.50% and 7.66% respectively of the actual results provided. Referred to the similar study done by Mehdi [26] using the RNG k–ε model to predict the performance of cyclone separator, a deviation of 8% from experimental results was observed. Due to the limitations on computing hardware, the finer meshing cannot be generated to give a greater meshing quality for a better simulation results. Hence, it is possible to say that the CFD modelling of this multicyclone predicts promising results although the deviation of results was greater than previous studies [41, 42].

3.2 Effect of cyclone size on collection efficiency and pressure drop

In this section, there were three different vortex diameter of single vertical cyclones provided by industrial partner, which labelled as Design I, II and III due to confidential issue, used to study the effect of cyclone size on the separation efficiency. The Design I represented the cyclone model with the greatest vortex diameter and subsequently the Design III represented the cyclone model with the smallest vortex diameter. The separation efficiency is calculated by using the Eq. (14) above. In CFD simulation of cyclone models, the particles injected were tracked and analysed by the DPM. In some studies, it showed that the collection efficiency of cyclone can be expressed in terms of cut-off diameter, which is defined as the particle size for which the collection efficiency of cyclone is 50%. However, according to the study done by Hoekstra [44], the author found that the overall collection efficiency expressed more accurate than the cut-off diameter for cyclone system. Hence, the present study dealt only with the overall collection efficiency. The trajectories of particles inside each cyclone models were arranged in the Table 3.2 below.

Table 3.3: The trajectories of particles flow inside different cyclone models.

Cyclone model	Number of particle injected, $n_{p,injected}$	Number of particle trapped, $n_{p,trapped}$	Number of incomplete particle, $n_{p,incomplete}$
Design I (Existing)	1680	419	122
Design II	1640	480	128
Design III	1650	488	127

Table 3.4: The collection efficiency and pressure drop obtained from simulation results for cyclone with different vortex finder diameters.

Cyclone model	Collection efficiency, η	Pressure drop, ΔP
Design I (Existing)	26.89 %	147.72 Pa
Design II	31.75 %	159.55 Pa
Design III	32.04 %	190.51 Pa

Based on the results above, it is noticeable that the collection efficiency of single vertical cyclone improved when the vortex finder diameter of cyclone reduced. The cyclone separates the solid particles injected based on the principle of centrifugal force. In order to separate particles, the centrifugal force must be greater than gravitational force. Furthermore, the cyclone separator works more efficiently at large entrainment space, because a large entrainment space creates a better swirling movement inside the column. When the decrease in vortex finder diameter, it increases the entrainment space as well as the particle re-entrainment

time in the underflow stream, therefore, the separation efficiency increases as well. Furthermore, the contour plot of velocity for each designs were displayed in Figure 3.1 below. It is noticed that the velocity magnitude increased near vortex finder when the diameter of vortex decreased. Therefore, the collection efficiency of cyclone increased because the swirling motion near the vortex became stronger when decreased the diameter of vortex. As compared to the study done by Derksen [45], a 9.54% of increment in collection efficiency was noted for smaller diameter of vortex finder while a 7.70% reduction in collection efficiency was observed for larger diameter of vortex finder. Therefore, this numerical study for different designs of single vertical cyclone were verified and the cyclone for Design III showed the greatest performance in terms of particle collection efficiency.

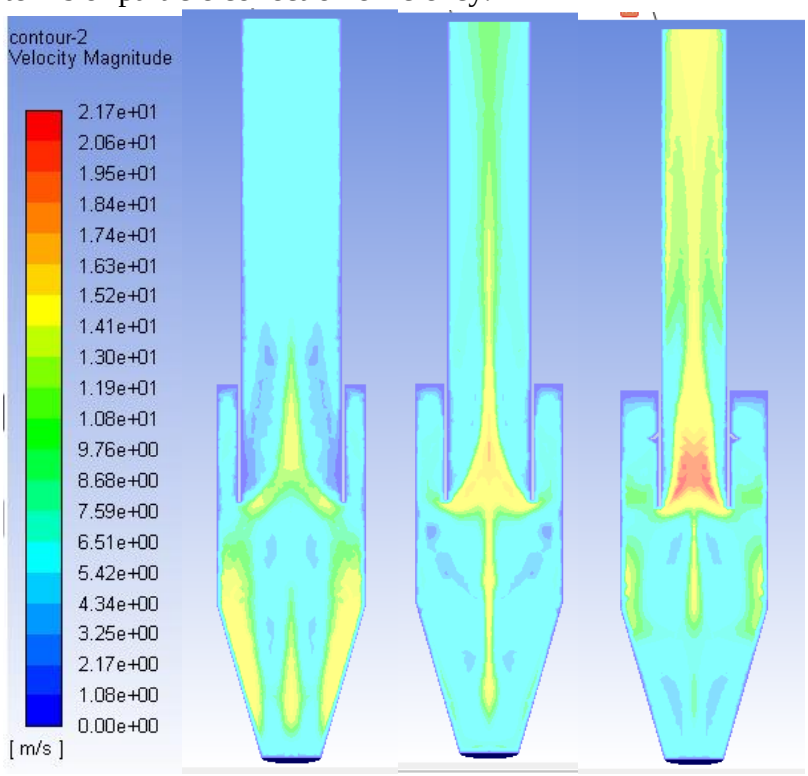


Figure 3.1: The velocity magnitude contour plot: Design I; Design II; Design III (left to right).

Moving on, the effects of cyclone size on pressure drop are reviewed in this section. Generally, the pressure drop of cyclone system can be calculated as the difference between the inlet pressure and the average pressure across the outlet [44]. As presented in Table 3.3 above, the computed pressure drops of Design I, II and III of different vortex finder diameter are compared. The simulation results showed that the pressure drop varies directly with the vortex finder diameter. The Design I of cyclone model had the lowest pressure drop across the system while the Design III of cyclone gave the greatest pressure drop across the system. In other words, the decrease in the vortex finder diameter of cyclone will results an increase in the pressure drop across the system. When the vortex finder diameter decreases, the entrainment space increases and results a better swirling movement inside the column. However, a high swirling movement will cause a high turbulence flow inside column and it will increase the air resistance. Therefore, the pressure drop inside column increases when the air resistance increased.

In overall, the Design III gave the greatest particle collection efficiency while the Design I showed the lowest collection efficiency. In reverse, Design I had the smallest pressure drop following by the Design II and lastly the Design III with the greatest pressure drop. To select

the optimum design of cyclone, both performance parameters must take into the considerations. This is because a high pressure drop across the cyclone system will results a high operating cost associated as high capacity centrifugal fan is required to overcome the pressure drop. Based on the results showed in Table 5.3, it is obvious that the improvement on collection efficiency is negligible, which is below 1% when reduce the vortex finder diameter from Design II to Design III. However, there is a huge pressure drop (up to 50 Pa) when reducing the vortex diameter from Design II to Design III. Hence, it means that reducing the vortex diameter of Design II gives insignificant improvement in collection efficiency but a great pressure drop to the system. The Design II was concluded as the optimum design in this section because the design improved the collection efficiency by 4.86% with a pressure drop of 11.83 Pa greater than existing cyclone design (Design I). Therefore, the Design II was used to study the effect of inlet configuration on the collection efficiency and pressure drop.
In this numerical study, the actual results from site were provided by industrial partner for the existing multicyclone. Therefore, the results of simulations using were verified with actual results provided.

4 Conclusion

In the nutshell, this research work presents a CFD study on predicting the effect of vortex finder diameter and inlet configuration on the collection efficiency and pressure drop of multicyclone system in order to further reduce the dust load from current multicyclone design. A design improvement from existing multicyclone was conducted by modifying the design of single cyclone in a system because the improvement in single cyclone will eventually improves the efficiency of multicyclone. To evaluate the performance of cyclone model, the RNG k–ε turbulence was used in the CFD study to predict the flow field. Then, the dust particle injected was analysed using the DPM model. This CFD modelling method predicted the collection efficiency and pressure drop of existing multicyclone system with the deviations of 18.50% and 7.66% respectively from actual results provided. It was found that a 35mm decrease in the vortex finder diameter for existing cyclone design resulted an improve of collection efficiency by 4.86% and an increase of pressure drop by 8%.

Acknowledgement

The authors would like to acknowledgement Ansys Inc. for providing the academic researches license to conduct this research. The authors would also like to acknowledgement Taylor’s University for providing the computing hardware to conduct this study.

References

[1] C. Serrano, H. Portero and E. Monedero, “Pine Chips combustion in a 50 kW domestic biomass boiler,” *Fuel,* vol. 111, pp. 564-573, 2013.

[2] R. Saidur, E. Abdelaziz, A. Demirbas, M. Hossain and S. Mekhilef, “A review on biomass as a fuel for boilers,” *Renewable and Sustainable Energy Reviews,* vol. 15, pp. 2262-2289, 31 January 2011.

[3] “Environmental Quality (Clean Air) Regualtions, 1978,” Malaysia, 1978.

[4] “Environmental Quality (Clean Air) Regulations 2014,” Attorney General's Chambers, Malaysia, 2014.

[5] D. L. W. Leong, “Air Pollution Control Study,” 2002.

[6] "Electrostatic Precipitators Information," IEEE Global Spec, [Online]. Available: http://www.globalspec.com/learnmore/manufacturing_process_equipment/air_quality/electrostatic_precipitators. [Accessed 28 September 2017].

[7] Turner, J. H., Lawless, P. A., Yamamoto, Toshiaki, Coy, D. W., G. P. Greiner, McKenna, J. D., Vatavuk and W. M., "Sizing and Costing of Electrostatic Precipitators," *Control Technology,* vol. 38, no. 5, pp. 715-726, 8 March 2012.

[8] K. C. Schifftner, "Air purification equipment and supplies," in *Air pollution control equipment selection guide,* Boca Raton, Lewis Publishers, 2002, pp. 100-126.

[9] Bondi and Andrew, "The operation and advantages of a cyclone dust collector," WoodCraft Supply LLC, 14 September 2017. [Online]. Available: https://www.woodcraft.com/blog_entries/the-operation-and-advantages-of-a-cyclone-dust-collector. [Accessed 29 September 2017].

[10] L. W. Leong, "Air Pollution Control," Malaysia, 1994.

[11] Y. S. Moi and L. C. Gee, "Particle sizing distribution for powder samples collected from biomass boiler," Malaysia, 2017.

[12] J. Gimbun, T. G. Chuah and T. S. Y. Choong, "A CFD study on the prediction of cyclone collection efficiency," *International Journal for Computational Methods in Engineering Science and Mechanics,* vol. 6, pp. 161-168, 2005.

[13] W. D. Griffiths and F. Boysan, "Computational Fluid Dynamics (CFD) and Empirical Modelling of the Performance of a Number of Cyclone Samplers," *Journal of Aerosol Science,* vol. 27, no. 2, pp. 281-304, 1996.

[14] F. Qian and M. Zhang, "Effects of the inlet section angle on the flow field of a cyclone," *Chemical Engineering & Technology,* vol. 30, no. 11, pp. 1564-1570, 2007.

[15] K. Elsayed and C. Lacor, "The effect of cyclone vortex finder dimensions on the flow pattern and performance using LES," *Computers & Fluids,* vol. 71, pp. 224-239, 2013.

[16] H. K. Versteeg and W. Malalasekera, An introduction to computational fluid dynamics - the finite volume method, Pearson Education, 2012.

[17] M. Azadi, M. Azadi and A. Mohebbi, "A CFD study of the effect of cyclone size on its performance parameters," *Journal of Hazardous Materials,* vol. 182, pp. 835-841, 2010.

[18] F. Zhou, G. Sun, Y. Zhang, H. Ci and Q. Wei, "Experimental and CFD study on the effects of surface roughness on cyclone performance," *Separation and Purification Technology,* vol. 193, pp. 175-183, 2018.

[19] F. Kaya, I. Karagoz and A. Avci, "Effects of surface roughness on the performance of tangential inlet cyclone separators," *Aerosol Science and Technology,* vol. 45, pp. 988-995, 2011.

[20] "Hardware Requirements," Ozen Engineering Inc., [Online]. Available: https://www.ozeninc.com/ansys-system-hardware-requirements/. [Accessed 16 April 2018].

[21] Y. Y. Hong and N. D. Fu, "Research and application of high-efficiency multi-cyclone dust removal," *Applied Mechanics and Materials,* vol. 109, pp. 400-404, 2011.

[22] S. Park, "Performance prediction model for deisgning a mulitple electro-cyclone system," *Journal of Residuals Science & Technology,* vol. 14, no. 1, pp. 325-331, 2017.

[23] L. Chuah, J. Gimbun, T. S. Y. Choong and A. Fakhru, "A CFD analysis on the effect of vortex finder and cylindrcal length on cyclone hydrodynamics and centrifugal forces," *Journal - The Institution of Engineers, Malaysia,* vol. 71, no. 2, pp. 51-58, 2009.

[24] B. Zhao, Y. Su and J. Zhang, "Simulation of gas flow pattern and separation efficiency in cyclone with conventional single and spiral double inlet configuration," *Chemical Engineering Research and Design,* vol. 84, pp. 1158-1165, 2006.

[25] G. S. Hui Ci, "Effects of wall roughness on the flow field and vortex length of cyclone," *Procedia Engineering,* vol. 102, pp. 1316-1325, 2015.

[26] A. Raoufi, M. Shams, M. Farzaneh and R. Ebrahimi, "Numerical simulation and optimization of fluid flow in cyclone vortex finder," *Chemical Engineering and Processing: Process Intensification,* vol. 47, no. 1, pp. 128-137, 2008.

[27] H. Safikhani, M. Akhavan-Behabadi and M. Shams, "Numerical simulation of flow field in three type of standard cyclone separators," *Advanced Powder Technology,* vol. 21, no. 4, pp. 435-442, 2010.

[28] K. Elsayed and C. Lacor, "The effect of cyclone vortex finder dimensions on the flow pattern and performance using LES," *Computers & Fluids,* vol. 71, pp. 224-239, 2013.

[29] L. S. Brar, R. P. Sharma and R. Dwivedi, "Effect of vortex finder diameter on flow field and collection efficiency of cyclone separators," *Particulate Science and Technology,* vol. 33, pp. 34-40, 2015.

[30] D. W. Stephens and K. Mohanarangam, "Turbulence model analysis of flow inside a hydrocyclone," in *Seventh International Conference on CFD in the Minerals and Process Industries*, Melbourne, 2009.

[31] L. Enliang and W. Yingmin, "A new collection theory of cyclone separators," *AIChe Journal,* vol. 35, no. 4, pp. 666-669, 1989.

[32] J. Gimbun, T. Chuah and F. Razi, "The influence of temperature and inlet velocity on cyclone pressure drop: a CFD study," *Chemical Engineering and Processing: Process Intensification,* vol. 44, no. 1, pp. 7-12, 2005.

[33] A. Hoekstra, "Gas flow field and collection efficiency of cyclone separators," A.J. Hoekstra, 2000.

[34] J. Derksen, "Separation performance predictions of a Stairmand high-efficiency cyclone," *AIChE Journal,* vol. 49, no. 6, pp. 1359-1371, 2003.

[35] B.Zhao, "A theoritical approach to pressure drop across cyclone separators," *Chemical Engineering & Technology,* vol. 27, no. 10, pp. 1105-1108, 2004.

[36] A. Khalkhali and H. Safikhani, "Pareto based multi-objective optimization of a cyclone vortex finder using CFD, GMDH type neural networks and genetic algorithms," *Engineering Optimization,* vol. 44, no. 1, pp. 105-118, 2012.

[37] Y. H. Alahmadi and A. F. Nowakowski, "Modified shear stress transport model with curvature correction for the prediction of swirling flow in a cyclone separator," *Chemical Engineering Science,* vol. 147, pp. 150-165, 2016.

Antioxidant properties of Malaysian fruit and its potential to use as additives for increasing the shelf life of packaged food material

Lok Eu Lee[1], *Rajesh Rajasekaran*[1], and *Tee Lee Hong*[1]

[1] School of Engineering, Faculty of Built Environment, Engineering, Technology & Design, Taylor's University, Subang Jaya, Selangor DE, Malaysia

Abstract. The objective of this research is to study the antioxidant potential of Malaysian fruits which are dragonfruit, mangosteen and longan. (*Hylocerues undatus, Garcinia mangostana L., Nephelium lappaceum L.*). This study involves the investigation on the total phenolic content, total flavonoid content and DPPH scavenging activity. The experiments will use the three fruits to be compared with the butylated hydroxytouluene and butylated hydroxyanisole. From the experiments. It is found that the mangosteen consist of higher % inhibition in the DPPH assay compared to the synthetic antioxidants. The % inhibition of mangosteen is 88.39% while BHA consist of 80.23% inhibition. The synthetic antioxidants however consist of a higher value in terms of total phenolic content (TPC) and total flavonoid content (TFC). The TPC and TFC for mangosteen is 4093.25 (mg GAE/100 g DW) and 345.58 (mg CE/100 g DW) respectively. The TPC and TFC value of BHA is 4093.25 (mg GAE/100 g DW) and 345.58 (mg CE/100 g DW).

1.0 Introduction

Lipid oxidation is an inevitable process which would occur to any food. The oxidation process would eventually lead a certain food to become rancid which means that the food would be not safe to be consumed. The oxidation process would be complemented with a loss of flavor of the food original taste, loss of nutritional value and even loss of color [1]. Thus, antioxidants are substances that are used in food in order to slow down the process of oxidation that would occur in food. These antioxidants act as a protection of the life span of foods as oxidation is slowed down [1].

Antioxidants are categorized into two different categories, where one of it is natural and one of it is synthetic. Synthetic antioxidants are mostly as made non-naturally as its name implies. The synthetic antioxidants are known to be cheap and a suitable counterpart to the natural antioxidants [2], however many studies shown that the synthetic antioxidants namely BHT (Butylated Hydroxytoluene) and BHA (Butylated Hydroxyanisole) are carcinogenic upon consumption. The exposure of BHT and BHA would promote the growth of cancer cells. Carcinogenic effects are observed through an experiment that was done by researchers which also reported that non-rodents such as pigs and monkeys would cause similar carcinogenic effects [3].This is further reinforced as other sources stated that a higher dose of BHA and BHT resulted in death to all animals while lower level concentrations causes tumour growth and cancer in certain species of animals [4].

In order to find replacements of these synthetic antioxidant, antioxidant content should be researched from natural sources. Antioxidants can be found in many naturals sources. According to Martin and Prior [5], strong antioxidant compounds can be found from fruit. Malaysia is a country that consist of abundant of fruits. In fact, Malaysia consist of many fruits which would have varying antioxidant values. The fruits from Malaysia can yield different antioxidant results even if the same fruit from another country would to be compared with its Malaysian counterpart. This is due to the difference in cultivar of the fruit or sub-species as well as the location of the fruit tree is being grown. The agronomic and environmental factors yield a different result of antioxidant contents of the fruit itself [6].

Thus, the demands of natural antioxidants are growing because alternative antioxidant is needed to be introduced in order to replace products that use synthetic antioxidants [7]. Thus, this project is done in order to determine antioxidants activities in Malaysian fruits to replace existing used synthetic antioxidants that is suspected to cause cancer when consumed. The source of antioxidants are the phenolic compounds that come from natural sources such as fruits. Phenolic compounds are antioxidant agents that prevent the rancidity of food. Phenolic compounds consist of the flavonoid compounds which is responsible of the colours of the fruits. Hence, it is important to study the Total Phenol Content (TPC) and Total Flavonoid Content (TFC) of fruits as having high TPC and TFC values would mean that the fruit consist of high antioxidant capabilities.

α,α-diphenyl-β-picrylhydrazyl (DPPH) is a stable free radical that consist of an unpaired valence electron at one atom of nitrogen bridge [8]. The DPPH scavenging is a popular antioxidant assay which is used to determine antioxidant in terms of using stable free radicals [9]. The assay would be based on the scavenging capacity of the antioxidants towards the DPPH free radicals. The DPPH is a free radical which is used to replicate the free radicals released from lipid oxidation. Hence, the TPC, TFC and DPPH values of the Malaysian fruit would be investigated.

2.0 RESEARCH METHODOLOGY

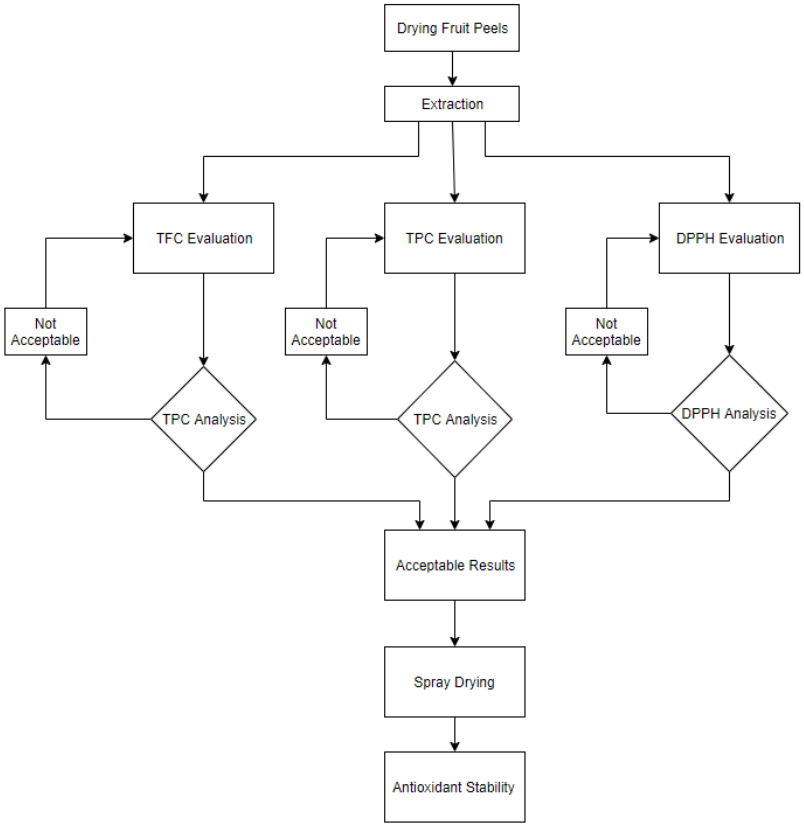


Figure 1: Design of Experiment (DOE)

The research consists of few stages which would be done during this project. Firstly it is the extraction stage which the fruit sample would be extracted. The part of the fruit also had to be taken into consideration based on the literature review. However, as peel is found to be a discarded material, cheaper than the pulp itself, and consist of high in quantity, peels of fruit would be used in this study. Besides that, the different types of extraction would also yield different outcomes at the end of the experiment. Ultrasonic-assisted extract would be used in this study as it is proven to be more effective compared to the other extract methods as said in the literature review. After extraction, the total phenolic content (TPC) and total flavonoid content (TFC) would be obtained base on the value of the fruit extract through Folin-Ciocalteu reagent which is based on a procedure by Chong [34] and procedure by Ozsoy [35] respectively. This can be done by plotting a calibration curve which can be used to identify the TPC and TFC values according to the calibration equation obtained. Next would be DPPH scavenging which involves obtaining the absorbance values of a blank solution and the absorbance of the extract using the UV-spectrophotometer. Once done, the best sample of fruit extract would be encapsulated based on a spray drying process. The spray drying product would then applied on yogurt which is a common source of food that undergoes lipid oxidation. The antioxidant stability of yogurt would be done through the DPPH scavenging test which would be carried in an interval of 7 days per sample for 28 days.

2.1 Materials

Dragonfruit, longan, and mangosteen are used in the experiment. 80% Ethanol is used in order to be used as a solvent with the fruit extract. Folin-ciocalteu reagent and 20% sodium carbonate

is used in order to obtain the TPC results. 0.075 ml 5% sodium nitrate solution and 0.15 of 10% aluminium chloride is used in the TFC assay. 1M of 0.5ml sodium hydroxide is also used in the TFC assay. 3.9 ml 60 x 10^{-5} ethanolic DPPH is used for the DPPH scavenging assay.

2.2 Extraction

The extraction method is done using the ultrasonic-assisted extraction as done by Pushpanathan [9]. Solid to solvent ratio used is 1:15 (grams to ml). Solvent used would be 80% ethanol as ethanol is found to be more effective compared to methanol. 10g of plant powder extract is placed inside a conical flask. The flask is then filled with 150ml 80% ethanol solution. The conical flask is then placed onto an ultrasonic cleaner at 45^{o}C for 45 minutes as mentioned earlier. After 45 minutes have passed, the extracts were filtered using filter paper into beakers. The extraction was done in triplicates for each solvent in order to obtain averages for more accuracy.

2.3 Total Phenolic Contents (TPC) Evaluation

The Total Phenolic Contents (TPC) can be determined by using the Folin-Ciocalteu reagent which is based on a procedure by Chong [10]. The procedure involves adding 0.2 ml of Folin-Ciocalteu reagent with the plant extract (0.1 ml). 1 ml of 20% Sodium carbonate is then adding to the mixture after 3 minutes of incubation in room temperature. The mixture is then left to be incubated for 1 hour. The absorbance value is then determined by using a UV-Spectrophotometer which is measured at 765 nm. A blank is used by replacing the fruit extract with distilled water. The same procedure would be then repeated however with gallic acid of different concentration in order to obtain a calibration curve to be compared with the fruit extract's TPC value. The absorbance value is then taken from gallic acid of different concentration which then a calibration curve can be plotted. The following equation expressed is the TPC value of the fruit extracts:

$$\text{Total Phenolic Content (mg } GAE/100\ g\ DW) = GAE \times \frac{V}{M} \times 100 \quad \textbf{(1)}$$

where GAE is the gallic acid equivalence (mg/ml) attained from the standard curve, V is total volume of solvent used during the assay (ml), and M is the mass of plants used during the assay (g). The results were expressed as miligrams of gallic acid per 100 g dried weight.

2.4 Total Flavonoid Content (TFC) Evaluation

The Total Flavonoid Content (TFC) is determined by using the procedure by Ozsoy [11]. The fruit extracts (0.25 ml) is mixed with 1.25 ml distilled water and 0.075 ml of 5% sodium nitrite solution. The mixture is then incubated at room temperature for 6 minutes. 0.15 ml of 10% aluminium chloride is then added to the mixture. After that, 1 M of sodium hydroxide (0.5 ml) is then added to the mixture with more distilled water. The absorbance is then identified using a UV-spectrophotometer which was measured at 510 nm. A blank is used by replacing the fruit extract with distilled water. The same procedure is then repeated by replacing the fruit extract with (+)-catechin of different concentrations in order to obtain a calibration curve to be compared with the TFC value. The absorbance value is obtained for every absorbance value that is gotten from the (+)-catechin of different concentration. The following equation expressed is the TFC value of the fruit extract:

$$\text{Total Flavonoid Content (mg CE/100 g DW): CE} \times \frac{V}{M} \times 100 \quad \textbf{(2)}$$

where CE is the (+)-catechin equivalence (mg/ml) attained from the standard curve, V is the total volume of solvent used during the assay (ml), and M is the mass of plants used during the assay (g). The results were expressed as miligrams of (+)-catechin per 100 g dried weight.

2.5 α, α-diphenyl-β-picrylhydrazyl (DPPH) free radical scavenging

The method used was by Saha [12] which is based on a modified assay by Tagashira and Ohtake [13]. Plant extract (0.1 ml) is added to 3.9 ml ethanolic DPPH ($60x10^{-5}$ M). The mixture is kept inside a dark place for 30 minutes duration. This is done in order to block UV light which would trigger free radicals which would disrupt the experimental results. The solution is then measured with a UV-spectrophotometer at 517 nm. The wavelength is used as results found in past experiments better inhibition % [13]. The radical scavenging activity is calculated using the following formula:

$$\% \text{ Inhibition} = \frac{Ab - Aa}{Ab} \times 100\% \quad \textbf{(3)}$$

where A_a is the absorbance of the extract while A_b is the absorbance of the blank sample.

3.0 Results and Discussion

Based on the results obtained from Table 1 to Table 3, it is seen that the mangosteen consist the highest value in all 3 assays among the fruits. However, the synthetic antioxidant namely BHA has a higher value of TPC and TFC compared to mangosteen. Mangosteen DPPH scavenging activity however yielded a higher inhibition value compared to both synthetic antioxidant. This proves that despite having a lower value of both TPC and TFC value, the scavenging activity of the mangosteen surpass the synthetic antioxidants. This is likely due to the fact that antioxidant properties differ amongst the phenols and the flavonoids. Phenolic compounds consist of many different groups [14]. Different groups would yield different antioxidant properties which indicates that a higher TPC value or TFC does not mean that the scavenging activity would be better. Hence, it can be said that the relationship of TPC to the scavenging activity is not obvious and needs to be further studied [14]. It can be seen that the all TFC value is seen to be lower when being compared to the TPC value. This is due to the fact that flavonoids are considered to be a phenol group [14]. Hence, if the TFC value will be directly proportional to the value of the TPC. However, despite the fact that the % inhibition of the DPPH assay does not directly increase due to the TPC or TFC value, there is still a relationship between them. This can be seen as dragonfruit is found to be very low in terms of TPC and TFC value. It is also further observed with a lower value of % inhibition which is elaborates that there is a relationship between the TPC and TFC values.

3.1 Total phenolic content test results

The total phenolic content is determined by using the standard curve to obtain the gallic acid equivalent of all of the components. Longan, mangosteen and dragonfruit are the three fruits used in the experiment. Besides that, both synthetic antioxidants (BHA and BHT) are also tested in order to be compared with the natural antioxidants obtained from the local fruits. Hence **Table 1** shows the results for all of the components. The experiment is done in triplicates and the average of those values are calculated.

Table 3.1: Total phenolic content obtained from the experiment.

Components	Average Absorbance Value	TPC (mg GAE/100 g DW)
Longan	2.230	1730.83
Mangosteen	4.110	3701.25
Dragonfruit	0.777	78.07
BHT	1.852	1247.61
BHA	4.469	4093.72

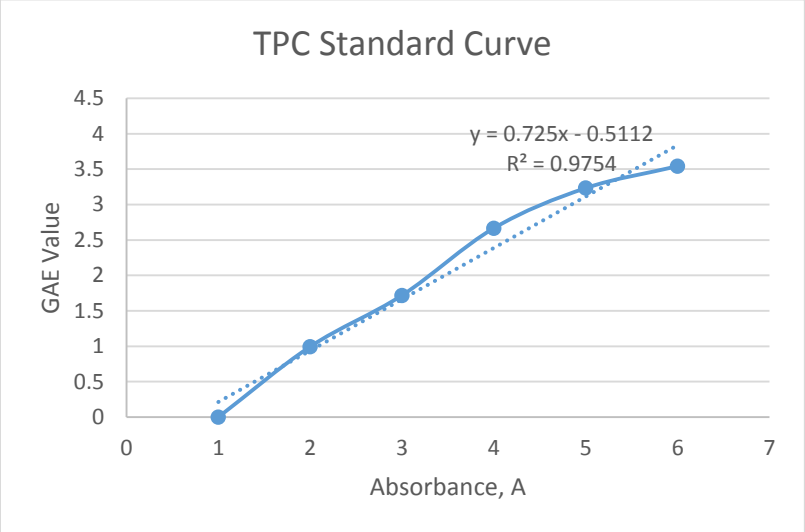


Figure 3.1: Total phenolic content standard curve.

Figure 2 is the TPC standard curve plotted in order to find the TPC value in terms of **(mg GAE/100 g DW).** The absorbance of the corresponding component is used in the linear equation that is obtained from the graph. The GAE value is then obtained which allows the TPC value to be calculated using equation (1). The highest TPC value for the local fruits would be from mangosteen where the TPC value obtained is 3701.25 (mg GAE/100 g DW). BHA however consist of a higher TPC value of 4093.25 (mg GAE/100 g DW).

3.2 Total flavonoid content test results

The total flavonoid content is determined by using the standard curve to obtain the catechin equivalent of all of the components. Similar to the TPC assay, longan, mangosteen and dragonfruit are the three fruits used in the experiment. Both synthetic antioxidants (BHA and BHT) are also tested in order to be compared with the natural antioxidants obtained from the local fruits. Thus, **Table 2** shows the results for all of the components. The experiment is done in triplicates and the average of those values are calculated.

Table 3.2: Total flavonoid content obtained from the experiment.

Components	Average Absorbance Value	TFC (mg CE/100 g DW)
Longan	0.330	95.40
Mangosteen	0.656	156.53

Dragonfruit	0.014	36.08
BHT	1.323	264.60
BHA	1.663	345.58

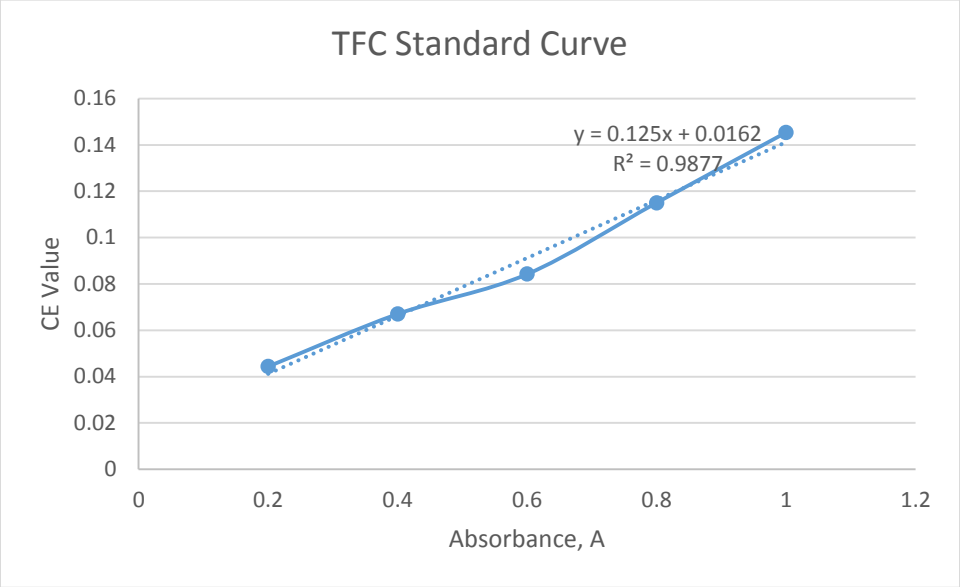


Figure 3.2: Total flavonoid content standard curve.

Figure 3 is the TFC standard curve plotted in order to find the TFC value in terms of (mg GAE/100 g DW). The absorbance of the corresponding component is used in the linear equation that is obtained from the graph which is the same as seen in the TPC calculation. The GAE value is then obtained which allows the TFC value to be calculated using equation (2). The highest TFC value for the local fruits would be from mangosteen where the TFC value obtained is 156.53 (mg GAE/100 g DW). Both synthetic antioxidant however consist of a higher TPC value where BHT yield 264.6 **(**mg CE/100 g DW) while BHA yield 345.58 (mg GAE/100 g DW).

3.3 DPPH scavenging activity test

The DPPH Scavenging Activity is determined by obtaining the absorbance value for all of the components. The absorbance value are used in equation (3). A constant is needed for the formula which is only pure ethanolic DPPH compared to the other samples which contains a portion of components in the mixture. Thus, **Table 3** shows the results for all of the components. The experiment is done in triplicates and the average of those values are calculated.

Table 3.3: DPPH scavenging activity obtained from the experiment.

Components	**Average Absorbance Value**	**DPPH (% Inhibition)**
Longan	0.2606	72.35
Mangosteen	0.1094	88.39
Dragonfruit	0.7413	21.33
BHT	0.2278	75.83
BHA	0.1863	80.23

3.4 Total Phenolic Content (TPC) result analysis

The phenols are chemical compounds that consist hydroxyl group which are bonded directly to an aromatic hydrocarbon group. These phenols are important additives to many laboratory processes, chemical processes and other processing industries. These phenols play an important role as antioxidants in food [80]. This is due to the fact that the phenols are reactive towards the oxidation process [80]. When food goes rancid, oxidation occurs. Phenol would prevent the oxidation process to occur which makes phenols to be important in terms of food storage. Therefore, the higher the TPC of the antioxidant, the better the prevention of oxidation in food rancidity.

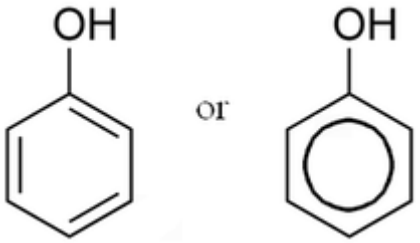


Figure 4.3: A simple phenol drawing.

Based on the results, it can be seen that the three fruits yield different TPC values. The lowest to highest of TPC value of the fruits are dragonfruit, longan and mangosteen where the values are 78.07, 1730.83 and 3701.25 (mg GAE/100 g DW**).** Based on previous findings, it can be seen that the TPC values of the three fruits are similar in terms of the order which follows the results obtained. The TPC value of the fruits of dragonfruit, longan and mangosteen of previous findings are 21.0, 680.15 and 2690 (mg GAE/100g DW) respectively. However, when compared to the synthetic antioxidant, it can be seen that BHA consist of a higher TPC value of 4093.72 (mg GAE/100g DW).

3.5 Total Flavonoid Content (TFC) result analysis

The flavonoids are the most common group in the phenolic group. They are a group which consist of two phenyl rings of plants [15]. They function as the pigments of the plant which means that the plants have their colours based on these flavonoids [16]. When rancidity of the food occurs, the colour would change from its original colour to a dark and abnormally colour. This happens because oxidation occurred which would change the colour of the fruit. Flavonoids consist of the ability to reduce free radical formation which means that they have antioxidant potential [16]. Hence the higher the TFC value, the more the oxidation can be prevented.

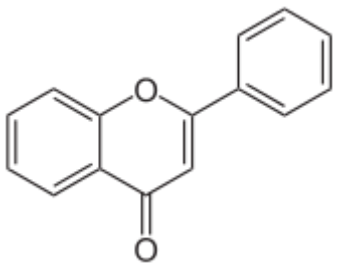


Figure 3.4: Flavone structure, a type of flavonoid.

Based on the results, it can be seen that the three fruits yield different TFC values. There are not much data regarding dragonfruit in terms of TFC. However the findings of 36.08 (mg CE/100g DW) make sense as the value is similar to the TPC as well as being lower as the TFC value should be lower than the TPC value. This is because the flavonoid group is under one of the many groups of the phenols. Based on previous findings of the other two fruits, it can be seen that the TFC values of the other three fruits are similar in terms of the order which follows the results obtained. The TFC value from the experiment are 36.08, 95.40 and 156.53 (mg CE/100 g DW). The TPC value of the fruits of longan and mangosteen of previous findings are 180.15 and 408 (mg QE/100g DW) respectively. However, when compared to the synthetic antioxidant, it can be seen that BHA consist of a higher TFC value of 345.58 (mg GAE/100g DW).

3.6 DPPH scavenging activity result analysis

The DPPH organic chemical compound is a dark-colored crystalline powder. They are made out of stable free-radical molecules similar to those released when lipid oxidation occurs. Hence, when the DPPH is in liquid form, it would be dark in colour [17]. When a sample is tested using the DPPH test, the free-radical will serve to be the free radicals released during lipid oxidation. Hence, antioxidants would donate extra electrons to the free radicals which will prevent oxidation of the food from occurring. Hence, TPC and TFC are antioxidants that will donate their electron to the free-radicals to prevent oxidation from occurring [17]. The higher the values of the TPC and TFC, the higher the % inhibition of the DPPH scavenging activity.

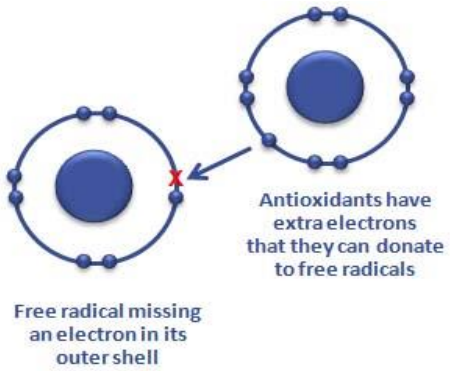


Figure 3.5: Antioxidant donating extra electron to free-radical.

The DPPH obtained from the results from the fruits are 21.33, 72.35 and 88.39 % for dragonfruit, longan and mangosteen respectively. Based on the TPC and TFC results obtained, it can be seen that the % inhibition obtain follows the TPC and TFC value. However, the synthetic antioxidant yield a lower % inhibition value of 75.83 and 80.23 for BHT and BHA respectively. BHA is found to have lower % inhibition despite having a higher TPC and TFC value compared to the mangosteen.

3.7 Deviation of value of previous findings

The previous findings are found to be have different values that varies in terms of TPC and TFC. This is due to the procedures which are different. One reasons why that there are differences is that the climate of the where the fruit is obtained. Besides that, the solvent used during the extraction stage would also influence the values obtained. Besides that, the

temperature used in the Ultrasonic-assisted extractor would also influence the result. This is due to the fact that a higher temperature can potentially denaturize the fruit extract. The solvent used for the extraction can also influence the results of the experiment.

3.8 Mangosteen against synthetic antioxidant.

The values obtained for mangosteen TPC and TPC can be found lower than BHA. However the % inhibition of the mangosteen is higher than BHA despite the results. The TPC is tested using Folin-Ciocalteu Reagent which can be one of the cause of obtaining such results. This is because the reagent does not measure only phenols that are present in the test [18]. The Folin-Ciocalteu Reagent will also react with other reducing substances that can potentially not be a phenol [18].

The TFC is also higher for both synthetic antioxidant compared to the mangosteen. It is found that most flavonoids do well as antioxidants such as vitamin C [16]. Despite that, there are not many experimental evidence that shows that all flavonoids does perform well as an antioxidant. Therefore, flavonoids can be seen to be a matter of debate due to the fact that not many experiment evidence proves that all flavonoids will help in free-radical scavenging activity [16].

DPPH % inhibition of the mangosteen is observed to be higher than the synthetic antioxidant. This is probably due to the fact that mangosteen consist of many anthocyanin. Anthocyanin are found to be one of the most recognized in terms of free-radical scavenging as well as having better antioxidant capacities. It is said that anthocyanin would increase the DPPH scavenging activity proportionally [19]. Besides that, abundant of xanthones are found in the mangosteen. Xanthones consist of the ability to activate extracellular antioxidant mechanism which can contribute into mangosteen having higher % inhibition [20]. This can be seen as past experiments show that xanthones exhibit linear relationship which illustrates that the measured antioxidant activity increases with xanthone amount [21].

BHT and BHA are synthetic antioxidants that normally have high potential in terms of anti-lipid-oxidation [22]. BHT is found to be lower compared to mangosteen are BHA due to the fact of its chemical composition, where the hydroxyl group of BHT is surrounded by two large trimethyl groups which blocks the access of free radicals [22] . Besides that, the scavenging free radical activity assay is based on an environment which is different compared to real lipid oxidation conditions [22]. Besides that, radicals have a preferential attack behavior towards a hydrogen bond that is not involve in a complex formation which may provide a lower % inhibition value for BHA and BHT [23].

4.0 Conclusion

In conclusion, the objectives of this study are to measure phenolic content, flavonoid content In conclusion, the synthetic antioxidant namely BHA has a higher value of TPC and TFC compared to mangosteen. Mangosteen DPPH scavenging activity however yielded a higher inhibition value compared to both synthetic antioxidant. This proves that despite having a lower value of both TPC and TFC value, the scavenging activity of the mangosteen surpass the synthetic antioxidants. This is likely due to the fact that antioxidant properties differ amongst the phenols and the flavonoids. Phenolic compounds consist of many different groups [14]. Hence, if the TFC value will be directly proportional to the value of the TPC. Besides that, mangosteen consist of xanthone and anthocyanin which would contribute into higher % inhibition. Besides that, BHA and BHT are complex compounds which would trigger less of the free radicals. Besides that, previous journals are found to have varying values of TPC, TFC and DPPH values. This is due to the fact that there are many variables to take into consideration

in the experiment. Things that can affect the results are the solvent used in the extraction phase, the temperature used when using the extractor as well as the place where the fruit is collected.

Mangosteen is found to be the best among the 3 fruits used in the experiment. This is due to the fact that the TPC, TFC and DPPH value is higher compared to the dragonfruit and the longan. The TPC, TFC and % inhibition of the DPPH assay of the mangosteen is 3701.25 (mg GAE/100 g DW), 156.53 (mg GAE/100 g DW) and 88.39% inhibition respectively. It is found that the TPC and TFC value does not directly influence the DPPH results. This is proven as the BHA has a higher TPC and TFC value of 4093.25 (mg GAE/100 g DW) and 345.58 (mg GAE/100 g DW) but have a lower % inhibition value of 80.23%. This is due to the fact that the TPC and TFC value does not purely influence the DPPH value. This is because the TPC consist of many groups which some of them would not influence the scavenging activity. Hence, despite having high TPC and TFC value, the DPPH value will not be directly influence by it. Thus, mangosteen has a higher % inhibition compared to the synthetic antioxidant despite having lower TPC and TFC value.

5.0 Reference

[1] Wsowicz, E., Gramza, A., Hêœ, M., Jeleñ, H. H., Korczak, J., Ma³ecka, M., & Zawirska-Wojtasiak, R. Oxidation of lipids in food. Pol J Food Nutr Sci, 13, 87-100. (2004)

[2] Sarin, A., Singh, N. P., Sarin, R., & Malhotra, R. K. Natural and synthetic antioxidants: influence on the oxidative stability of biodiesel synthesized from non-edible oil. Energy, 35(12), 4645-4648. (2010).

[3] Botterweck, A. A. M., Verhagen, H., Goldbohm, R. A., Kleinjans, J., & Van den Brandt, P. A. Intake of butylated hydroxyanisole and butylated hydroxytoluene and stomach cancer risk: results from analyses in the Netherlands cohort study. Food and Chemical Toxicology, 38(7), 599-605. (2000).

[4] Race, S. Antioxidants: The truth about BHA, BHT, TBHQ and other antioxidants used as food additives. Part, 1, 6-1. (2009).

[5] Kalt, W., Forney, C. F., Martin, A., & Prior, R. LAntioxidant capacity, vitamin C, phenolics, and anthocyanins after fresh storage of small fruits. Journal of agricultural and food chemistry, 47(11), 4638-4644. (1999).

[6] Ikram, E. H. K., Eng, K. H., Jalil, A. M. M., Ismail, A., Idris, S., Azlan, A., & Mokhtar, R. A. M. (2009). Antioxidant capacity and total phenolic content of Malaysian underutilized fruits. Journal of Food Composition and Analysis,

[7] Kanatt, S. R., Chander, R., & Sharma, A. Antioxidant potential of mint (Mentha spicata L.) in radiation-processed lamb meat. Food Chemistry, 100(2), 451-458. (2007).

[8] Eklund, P. C., Långvik, O. K., Wärnå, J. P., Salmi, T. O., Willför, S. M., & Sjöholm, R. E. Chemical studies on antioxidant mechanisms and free radical scavenging properties of lignans. Organic & biomolecular chemistry, 3(18), 3336-3347. (2005).

[9] Lim, Y. Y., Lim, T. T., & Tee, J. J. (2007). Antioxidant properties of several tropical fruits: A comparative study. Food chemistry, 103(3), 1003-1008.

[10] Mizrahi, Y., & Nerd, A. (1999). Climbing and columnar cacti: new arid land fruit crops. Horticulture, 82, 13.

[11] Ariffin, A. A., Bakar, J., Tan, C. P., Rahman, R. A., Karim, R., & Loi, C. C. (2009). Essential fatty acids of pitaya (dragon fruit) seed oil. Food Chemistry, 114(2), 561-564.

[12] Becker, L. C., Bergfeld, W. F., Belsito, D. V., Hill, R. A., Klaassen, C. D., Marks, J. G., & Andersen, F. A. (2010). Final report of the amended safety assessment of myristic

acid and its salts and esters as used in cosmetics. International journal of toxicology, 29(4 suppl), 162S-186S.

[13] Pascual, G., Avgustinova, A., Mejetta, S., Martín, M., Castellanos, A., Attolini, C. S. O., & Bescós, C. (2017). Targeting metastasis-initiating cells through the fatty acid receptor CD36. Nature, 541(7635), 41-45.

[14] Peyrat-Maillard, M. N., Cuvelier, M. E., & Berset, C. (2003). Antioxidant activity of phenolic compounds in 2, 2′-azobis (2-amidinopropane) dihydrochloride (AAPH)-induced oxidation: Synergistic and antagonistic effects. Journal of the American Oil Chemists' Society, 80(10), 1007-1012.

[15] Markham, K. R. (1982). Techniques of flavonoid identification (Vol. 31). London: Academic press.

[16] Swain, T., & Bate-Smith, E. C. (1962). Flavonoid compounds. In Comparative Biochemistry, Volume 3 (pp. 755-809).

[17] Locatelli, M., Gindro, R., Travaglia, F., Coïsson, J. D., Rinaldi, M., & Arlorio, M. (2009). Study of the DPPH-scavenging activity: Development of a free software for the correct interpretation of data. Food chemistry, 114(3), 889-897.

[18] Singleton, V. L., Orthofer, R., & Lamuela-Raventós, R. M. (1999). [14] Analysis of total phenols and other oxidation substrates and antioxidants by means of folin-ciocalteu reagent. In Methods in enzymology (Vol. 299, pp. 152-178). Academic press.

[19] Abdel-Aal, E. S. M., Hucl, P., & Rabalski, I. (2018). Compositional and antioxidant properties of anthocyanin-rich products prepared from purple wheat. Food chemistry, 254, 13-19.

[20] Ovalle-Magallanes, B., Eugenio-Pérez, D., & Pedraza-Chaverri, J. (2017). Medicinal properties of mangosteen (Garcinia mangostana L.): A comprehensive update. Food and Chemical Toxicology, 109, 102-122.

[21] Suvarnakuta, P., Chaweerungrat, C., & Devahastin, S. (2011). Effects of drying methods on assay and antioxidant activity of xanthones in mangosteen rind. Food Chemistry, 125(1), 240-247.

[22] Zhang, Y., Shen, Y., Zhu, Y., & Xu, Z. (2015). Assessment of the correlations between reducing power, scavenging DPPH activity and anti-lipid-oxidation capability of phenolic antioxidants. LWT-Food Science and Technology, 63(1), 569-574.

[23] Yehye, W. A., Rahman, N. A., Ariffin, A., Hamid, S. B. A., Alhadi, A. A., Kadir, F. A., & Yaeghoobi, M. (2015). Understanding the chemistry behind the antioxidant activities of butylated hydroxytoluene (BHT): A review. European journal of medicinal chemistry, 101, 295-312.

Treatment Of Ink Printing Wastewater By Advanced Oxidation Process

Maryam Sulaiman AL-Adawi[1], Rajesh Nithyanandam[1**]*

[1]Taylor's University

*maryam.sulaiman.19@gmail.com

**Rajesh.Rajasekaran@taylors.edu.my

Abstract. Printing ink wastewater comes from the printing ink industry. When laboratory and industrial equipment is washed out, printing ink wastewater is created. Printing ink wastewater (PIWW) has a very strong color and it is contaminated with different organic substances. The wastewater needs to be treated before it is released into the environment. Special treatment is needed for industrial wastewater because the components in the wastewater such as decomposed Acrylics pigments are non-bio-degradable. Advanced oxidation processes (AOPs) are used and the chosen effective method to treat is Fenton oxidation process. The purpose of this project is to use one of advanced oxidation processes such as the Fenton method for the treatment of printing ink wastewater. Then, the optimum concentration and molar ratio of ferrous to hydrogen peroxide (Fe^{2+}/ H_2O_2) that will give the best efficiency for treating printing ink wastewater will be found. Printing ink wastewater sample is a pure sample from the company of printing ink. In this research two treatments were used to treat the PIWW sample such as chemical treatment and physical treatment, in order to degrade the components in the sample. Chemical treatment (Fenton method) which is by using various molar ratios of $FeSO_4$ /H_2O_2 dosages at different concentrations. The physical treatment checks the effect of different range of pH and temperatures on the PIWW sample. After the treatment, the content percentage of chemical oxygen demand (COD) which is in the sample, is determined. In addition, compounds which are present in the wastewater are determined by using Gas Chromatography Mass Spectrometry (GC MS) before and after treatment of PIWW. The COD in the printing ink wastewater was reduced after the Fenton oxidation process by 52.1% when using the optimum ratio of ferrous to hydrogen peroxide which is 1:1 at 0.3M. High result of physical treatment is achieved when T=35^{o}C, pH 4 and the COD removal is 7.04%, 13.4%, respectively.

Keywords: Water based printing ink, chemical treatment, Fenton Oxidation.

1. Introduction

Water is one of the most important thing in human life. Therefore, clean water is needed to keep human species alive. Another important thing about water is that, it is used in daily human activities such as in cleaning, washing, shower, manufacturing and so many other things. The earth is covered about 71% of water and mostly is the ocean water which is 97.5% of the total water. Which means that freshwater is very little with a percentage of 2.5% but the only accessible water is 1% [1]. As it can be seen, the amount of water needed in human life, is existing with a very little amount. This amount is reducing every year.

In order to solve this issue, people generated methods to reuse the used water or wastewater by building Sewage Treatment Plant. There are two types of wastewater according to the waste type such as municipal waste that is mostly from human that contains organic matter and industrial waste which contains heavy metals and hazardous chemicals Wastewater that is released from commercial facilities, houses and institutions is treated to get rid of microorganisms and compounds that pollutes the water. The technology wastewater treatment developed to stop the diseases from spreading that comes from travelling water microbes. Also, to make the wastewater safe before releasing it to local environment or for reuse [2].

Industrial waste needs special treatment because it discharges non bio-degradable or xenobiotic compounds [3]. The dangerous waste discharged from ink printing industry is one of the major concerns these days because ink printing wastewater is non-bio-degradable. In addition, the wastewater needs to follow the standards of Environmental Protection Agency (EPA)[4]. Therefore, so many researches and different treatment methods are required for this kind of waste to meet the standards [5][6].

There are various advanced technologies for the aim of degrading non-biodegradable product. Some of the technologies include chemical oxidation which is done by activated carbon (sorption process), ozone and hydrogen peroxide and nanofiltration or reverse osmosis which are part of membrane filtration process[7][8]. One of the most important process is advanced oxidation process

Some advanced chemical oxidation processes are Fenton ($Fe^{2+}$and H_2O_2), Sonolysis and Gamma-radiolysis, Ozone (O_3) and hydrogen peroxide (H_2O_2), Photo and electron Fenton, Ozone (O_3) and ultraviolet (UV), Heterogenous photo-oxidation by titanium dioxide (TiO_2/hv), Ozone (O_3), ultraviolet (UV) and hydrogen peroxide (H_2O_2), Chelating agents assisted Fenton and photo-Fenton and Ultraviolet (UV) and hydrogen peroxide (H_2O_2).

The objectives of this research are: to treat printing ink wastewater by using physical treatment (that is by changing the applied parameters such as temperature at (25^{o}C, 30 ^{o}C, 35 ^{o}C, 40 ^{o}C, 45 ^{o}C) and the pH at (2, 4, 6, 8, 10). Also by using chemical treatment at different molarities (0.1M, 0.2M and 0.3M) of Fenton's Reagent using these ratios (1:1, 1:2, 1:3 and 1:4). In addition, also to suggest the advanced oxidation process (Fenton ($Fe^{2+}$and H_2O_2) as the main/ specific treatment of wastewater.

This project is under the scope that Fenton process conditions at 25^{o}C and 1atm. pH need to be adjusted between 2-3 and most of the processes is at pH =3. 1:1:0.3 molar ratios of COD/ Fe^{2+}/ H_2O_2 gives the best conditions for the process. Ferrous (II) sulphate is used in the process instead of FeOx because it is not toxic.

2. Materials and Methods

2.1 Materials

The experiment materials used are: 0.1M sodium hydroxide / sulphuric acid used (to adjust the wastewater pH), Iron (II) sulphate and hydrogen peroxide 6%, (20vol) for Reagent experiment were purchased from Evergreen and COD test cells from Merck.

2.2 Preparation of printing ink wastewater sample

The raw sample of printing ink wastewater was diluted by using distilled water to a ratio of (1:100). Means that, 1ml of wastewater sample plus 99ml of distilled water gives a total of 100ml volume. The (1:100) ratio was done twice to get 200ml volume in 500ml beaker. For each treatment, fresh new bunches of 200ml volume diluted sample were prepared according to the required amount. The preparation was done at room temperature $25^{O}C$. physical treatment required 10 beakers and chemical treatment 12 beakers, each beaker with 200ml of diluted sample.

200ml of prepared diluted sample without adding any chemical was gone for several tests such as measuring the pH, temperature, COD, turbidity and suspended solids. After collecting all the measurements then second part took place which is the treatment part.

2.3 Treatment

The sample of printing ink wastewater (PIWW) is directly from the printing ink company. The sample is going through two different treatments such as physical treatment and chemical treatment in order to find the percentage of COD, turbidity and total Suspended Solids in the sample. Physical treatment is to check the effect of pH, settling time and temperature at different amount contents. Chemical treatment is by using photo Fenton at different effects of FeSO4 and H_2O_2 dosages. In addition, (GC MS) Gas Chromatography Mass Spectrometry is used to analyse the compounds like (Fe S) before and after the treatment of the waste water. The colour change of the printing ink wastewater after the treatment should be near to clean water appearance.

2.3.1 Physical treatment

This treatment was done by adjusting the temperature and the pH of the sample. The Fenton reagent was not included. The reason is because in this treatment, the main purpose of doing it was to study how the changing in temperature and pH will affect the decomposition of the matters in the sample. 6 samples need to be tested with different pH starting from range 2.0 to 10 with a difference of two and one is a blank sample without changing any pH of it. At the beginning, the pH of PIWW was obtained or measured by using pH meter. Then, the sample was added with Sodium hydroxide in order to increase the pH of the printing ink wastewater sample and added with sulphuric acid to decrease the pH of the PIWW sample. The desired value of pH was achieved after the addition of alkaline/ acid. In addition, temperature changing of the wastewater sample was the second treatment. The sample went to heating process by using hot plate at different temperature ranges starting from 25 to $45^{o}C$ with increment of $5^{o}C$ temperature. The heating was until the PIWW sample reaches the desired temperature. Those,

COD, turbidity and total Suspended Solids of each sample were tested after physical treatment of each sample and best results can be determined[9]. The purpose of physical treatment is to compare between the two methods (physical and chemical treatment) by comparing the results obtained from the methods.

2.3.2 Chemical treatment

Four beakers with 1liter each were poured with 20ml of diluted PIWW sample in each beaker and the sample pH was tested. 0.05M of (H_2SO_4) sulphuric acid is added to the sample in order to adjust the pH of the sample and reduces it to pH 3, just some drops of it. As it is mentioned before that the optimum results can be obtained when the pH of Fenton is from 2 to 3. The addition of (H_2SO_4) made the sample to produce bubbles and rise. Then, the required amount of $FeSO_4$/ H_2O_2 to be added in each beaker were measured by using analytical balance to weight $FeSO_4$ and pipette for H_2O_2 volume. The calculation of the required amount are according to wanted molarity at different mole ratios such as (1:1, 1:2, 1:3 and 1:4) of Fe^{2+}/H_2O_2 . Starting with molarity of 0.1M at different mole ratio (1:1, 1:2, 1:3 and 1:4) of $Fe^{2+}/H_2O_2$is added to each beaker containing diluted sample of the printing ink wastewater. The sample produced bubbles and rose. Then, the sample was left to react for half an hour. Once the Fenton reagent is in the sample, the stopwatch starts to count the time. The compound normal degradation rate can be found within 30 min in the room conditions. That helps to know the level of COD after the treatment of printing ink wastewater. The same Fenton's Reagent experiment at the same mole ratios (1:1, 1:2, 1:3 and 1:4) of Fe^{2+}/ was repeated for molarities of 0.2M and 0.3M.

The level of COD (mg/L) in each sample is measured or tested after 30minutes of the reaction. Fenton's Reagent efficiency can be determined by using COD measurements, when chemical oxidation process was used to remove the components or organics. The reaction is exothermic and it is fast. During the whole reaction period, the sample need to be stirred for 30minuets [10].

2.4 Analysis

The measured parameters are COD, total suspended solids (TSS) and turbidity. The content of colloidal matter in water is measured by measuring the turbidity which can show how cloudiness is the water tested[11].

2.4.1 Turbidity

The turbidimeter was switched on by ON\OFF key then it went through the calibration method by pressing the CAL key. There are fore standards to be place in the sample well which were inserted one by one according to the CAL number on the screen. The standards are CAL1 (800 NTU), CAL2 (100NTU), CAL3 and CAL4. Once the calibration is done, the instrument showed STBY. That means it is ready to measure the required sample [12].

10ml of the sample was poured in a clean and dry vial up to the shown mark. Then the vial was closed tightly by black screw cap. The outside surface of vial was wiped with soft cloth to keep it dry and clean. Little amount of silicone oil was applied on outside surface of vial and was

wiped again. Then, the sample was measured by inserted the vial in the sample well meter after pressing READ/ENTER key.

Turbiditimeter (EUTECH Instruments TN-100) was used to measure the turbidity of the wastewater sample. The percentage of turbidity removal can be calculated as in Eq.1:

$$\text{Turbidity removal} = \frac{RT_c - RT}{RT_c} \times 100\ \% \quad (1)$$

Where: RT is the turbidity of the printing ink wastewater after the treatment.
RT_c is the turbidity of the printing ink wastewater before the treatment.

2.4.2 Chemical Oxygen Demand (COD)

Reaction cells were used to measure COD with the range of 300-3500 mg/L. It consists of reagents such as potassium dichromate, mercury (II) sulphate, chloride and catalyst (silver sulphate). In order to test COD: 2 mL of pre-treated sample was added to the test cells onto reagent by using pipette inside a fume hood. The reaction cell was then tightly closed with screw cap and strongly shook. It was then heated in a thermoreactor for 2 hours at 150℃. Then, all the cells were removed from thermoreactor and sort on test-tube rack for them to cool. After 30 minutes, the cells were sent to photometer (Prove 300 UV/VIS Spectrophotometer) in order to measure the COD[13].

COD removal can be calculated as in Eq.2:

$$\text{COD removal} = \frac{COD_c - COD_i}{COD_c} \times 100\ \% \quad (2)$$

Where: COD_i is the COD of the printing ink wastewater after the treatment.
COD_c is the COD of the printing ink wastewater before the treatment.

2.4.3 Total Suspended Solids (TSS) Test:

The sample trays were labelled with sample number. Filter paper (934-AH RTU glass microfibre filters) was oven dried at 103ºC for about 1 hour then was weighted on analytical balance then placed on filtration apparatus (vacuum filter/vacuum flask set-up), by using tweezers. The vacuum was turn on and 100ml of sample was poured and distributed onto filter paper. The vacuum was kept on until all the sample has drained totally through the filter paper. Filter paper was remove by using tweezers and placed it on the aluminium dish then it was left to dry in the oven at 103ºC for one hour. The dried filter paper then was kept in the desiccator for 30 minutes to cool in a moisture free environment. Finally, the filter paper then was weighed and the value of TSS can then be calculated [14] [15].

To calculate TSS in milligrams per litre can be calculated as in Eq.3:

$$TSS\ (mg/L) = \frac{[(final\ weight\ (g) - original\ weight\ (g)) * 1000000]}{(sample\ volume\ (ml))} \quad (3)$$

2.4.4 Procedure for GC-MS (Sample preparation)

25% of diluted PIWW was added to the test tube with an amount of 2ml plus 2ml of $NaSO_4$ (0.05 N) in order to take off the content moisture. The sample went for centrifugation and it was left for one day after the previous addition. Two things were obtained such as settled particles and moisture. The particles which were settled were subjected to a temperature of -17^oC for about 15 minutes then sent to high pressure vacuum filter. In addition, 2ml of methanol was added to the moisture which had less particles. The solution was mixed at a speed of 11000 rpm for 20 minutes when it was centrifuged [10]. Finally, the supernatant was subjected to GC-MS [16].

3. Results & Discussion

Table 1 shows the properties of the sprinting ink wastewater before any treatment.

Table 5: Characteristics of printing ink wastewater.

Characteristics of the sprinting ink wastewater	
Temperature (^oC)	25
pH	7.5
Turbidity (NTU)	760
TSS (mg/L)	10.204
COD (mg/L)	144800

The printing ink wastewater sample used is alkali in nature. The wastewater has a pH of 8.2 for the sample before diluting it with distilled water and after diluting the sample the pH value dropped to 7.5.

3.1 Physical treatment

3.1.1 Effect of pH

Characteristic of inorganic compounds in PIWW can be studied by pH treatment of the sample [9]. The adjustment of the pH was done by adding sodium hydroxide and sulphuric acid to the desired value without adding any Fenton reagent. As it can be seen in Table 2, the composition of inorganic compounds is slightly affected by pH because at various pH the compounds change their structures into different type of inorganic compounds. The solubility of compounds in the sample mostly increases when the pH of PIWW decreases and very thin soap layer was formed.

The overall treatment of pH has slightly reduced the level of COD to less than 14% and turbidity to less than 7% but increased the suspended solids removed to less

than 55(mg/L). The highest removal of COD 125400 (mg/L) about 13.4% was at pH 4, turbidity708 (NTU) about 6.9% at pH 2 and suspended solids reached to 50 (mg/L) at pH 2. Therefore, highest COD removal was obtained at pH 4. This sample was then sent for the GC-MS analysis.

Table 2: Characteristics of printing ink wastewater.

pH	COD (mg/L)	Turbidity (NTU)	TSS (mg/L)	
	2	135400	708	50
	4	125400	745	26.5
	6	125800	752	20
Raw (7.5)		144800	760	10.204
	8	142000	776	10.205
	10	136600	798	10.22

3.1.2 Effect of temperature

Characteristic of inorganic compounds in PIWW also was studied by temperature treatment [9]. From Table 3, it can be seen that in the temperature treatment the reduction percentage of inorganic compounds for the COD is less than 8%, turbidity is less than 2% but suspended solids removed from the treated sample reached to12.063 (mg/L). The reason is because the contained inorganic compounds in PIWW will alter its structure or decomposed into stable compound. At 35ºC, the highest removal of COD reached 134600 (mg/L) about 2.9% from the raw sample. Turbidity reduced to 745 NTU (about 2%) at 45ºC removal and suspended solids less than 10.215 (mg/L) removal were obtained. The least removal obtained for COD 143000 (mg/L) about 1.24% at 40ºC, turbidity increased to 763 NTU at 35ºC and suspended solids reduced to 10.215 (mg/L) at 30ºC.

Table 3: Characteristics of printing ink wastewater.

Temperature (ºC)	COD (mg/L)	Turbidity (NTU)	TSS (mg/L)
Raw (25)	144800	760	10.204
30	141600	763	10.215
35	134600	759	12.063
40	143000	752	10.31
45	140600	745	13.12

The degradation efficiency for physical treatments is too low especially for the temperature because then increasing the temperature of the PIWW, it does not affect the degradation in a significance way. That is because the dissolved oxygen is too less.

No studies were found for the treatment of PIWW by using only physical treatment (temperature and pH) without adding any chemical of AOPs. However, there is a study done for palm oil wastewater which addresses this treatment [10].

3.2 Chemical treatment

3.2.1 Effect of Fenton reagent concentration

PIWW was treated by adjusting Fenton reagent concentration starting from 0.1M to 0.3M. Besides, the ratio range (1:1, 1:2, 1:3 and 1:4) of iron (II) sulphate/ hydrogen peroxide were calculated regarding to mass. The mass of iron (II) sulphate required is less than hydrogen

peroxide mass needed because the major component that generated free radicals is hydrogen peroxide[10]. In addition, iron (II) sulphate was the catalyst which was performed in the Fenton experiment. Figure 1, 2 and 3 show expected results for COD, turbidity and suspended solids for the treated PIWW after conducting Fenton process. The numbers (1, 2, 3 and 4) at the x-axis in the Figures below refers to the ratio (1:4, 1:3, 1:2 and 1:1) respectively.

The sample pH was fixed at 3 when treated so that the Fenton reagent can fully utilized as mentioned in the literature. The degradation reaction took about 30 min. It can be seen that, the Fenton treatment reduced the values of COD and turbidity but suspended solids were increased for each treated sample. The generated foam in the beakers during the treatment was higher at 0.3M comparing to 0.1M.

Different molar ratio of Fe^{2+}/H_2O_2 Fenton Reagent and COD variation

From Figure 1, Fenton Reagent at 0.1M, it was observed that when Fe^{2+}/H_2O_2 Molar ratio increase the level of COD (mg/L) gradually decrease. This is because higher hydrogen peroxide amount generated more amount of hydroxyl radicals, which leads to oxidise more carbon atoms. The reduction of COD increased comparing to the original or raw sample starting from the ratio (1:4 to 1:1) because some of the inorganic components were removed by Fenton reagent. It reduced about less than 18.5% of the COD. The percentage of COD (mg/L) level reduction varied from minimum of 11.8% (at 1:4 Fe^{2+}/H_2O_2) to a maximum of 18.5% (at 1:1 Fe^{2+}/H_2O_2). The efficiency of Fenton process is too low and is not eligible because just less than 20% of PIWW was degrade and approximately 80% of organic compound was in the treated sample. The reason is because the non-degrade organic compounds maybe did not get sufficient supply or amount of hydroxyl radicals.

Fenton Reagent at 0.2M, the efficiency of Fenton degradation is higher than the concentration of 0.1M because when the Fenton reagent concentration is high leads to have more reduction of COD (mg/L) level. It reduced about less than 42.5% of the COD. The percentage of COD (mg/L) level reduction varied from minimum of 23.1% (at 1:4 Fe^{2+}/H_2O_2) to a maximum of 42.5% (at 1:1 Fe^{2+}/H_2O_2). The efficiency of Fenton process is still low and is not desirable because it only degraded approximately of 40% of PIWW and 60% of inorganic compound was still in the treated sample and the process needs more degradation time.

The most effective and most efficient concentration of Fenton reagent occurs at 0.3M. It reduced about less than 53% of the COD. The percentage of COD (mg/L) level reduction varied from minimum of 28% (at 1:4 Fe^{2+}/H_2O_2) to a maximum of 52.1% (at 1:1 Fe^{2+}/H_2O_2). The efficiency of Fenton process is not sufficient because approximately just 50% of organic compound was degraded in the treated sample. The reason is because the non-degrade organic compounds did not get sufficient supply of hydroxyl radicals and the concentration of Fenton reagent should be more than 0.3. Another cause is that, the hydrogen peroxide 6%, (20vol) is not sufficient enough.

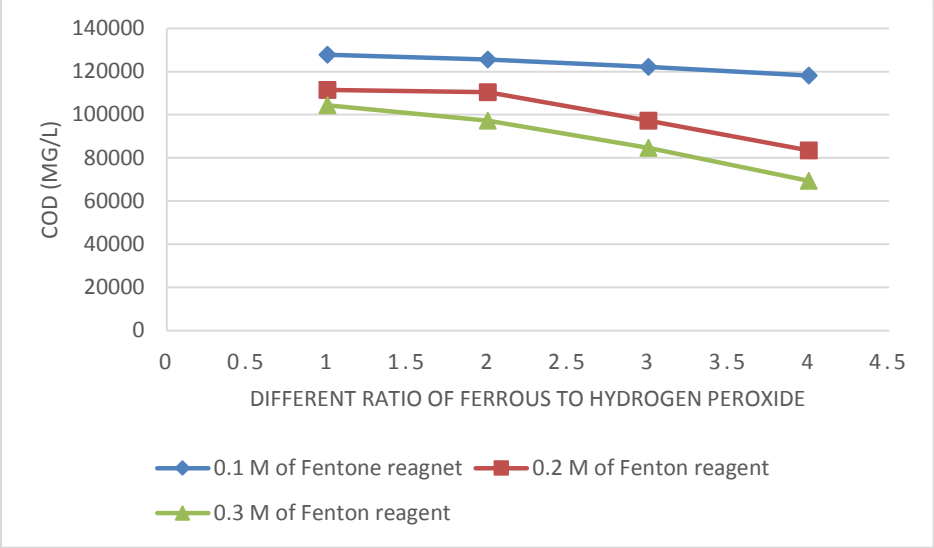


Figure 1: COD and different ratio of ferrous to hydrogen peroxide

Among all the concentrations, Fenton reagent at 0.3M ratio (1:1) removed the highest amount of COD 52.1% and at 0.1M ratio (1:4) less amount of COD 11.74% was removed in the PIWW. Studies done by [17] and [18] shows that the degradation increases when increasing the concentration of Fenton reagent [19].

Throughout the process of Fenton, organic compounds that react with the reagent in PIWW would disintegrate into water plus carbon dioxide. Therefore, BOD and COD amount in samples subsequent to treatment decreases when Fenton reagent concentration increases. Moreover, bubbles were produced during the process. The formation of gas is due to the breakdown of inorganic compounds. In addition, the decomposition of inorganic compounds will result in formation of salt and water [17].

The production of CO2, salt and water from the process of Fenton, PIWW's inorganic compounds were reduced. As a result, COD and turbidity amount in PIWW was decreased. Additionally, as Fenton reagent concentration increases, the gas formed increases too. This is due to the availability of hydroxyl radicals that are able to attack inorganic compounds easily. Thus, the level of turbidity and COD of PIWW would be decreased and amount of TSS increased because of the salts formed in the sample after the treatment[9].

Table 4: Summary of the highest values of COD.

Initial COD	144800 (mg/L)	
pH 4 COD	125400 (mg/L)	13.4%
Temperature 35ºC	134600 (mg/L)	7.04%
0.3M (1:1) COD	69400 (mg/L)	52.1%

From what was found, Fenton oxidation process can be applied or implemented after the secondary treatment in wastewater plants for ink printing industries. In addition, Fenton process only works when the pH is between 2 to 3 as it was mentioned before so further optimisations and studies should be done to get the appropriate and best working pH.

Different molar ratio of Fe^{2+}/H_2O_2 Fenton Reagent and TSS variation

From Figure 3, at 0.1M, 0.2M and 0.3M the TSS increased in the treated sample comparing to the original or raw sample starting from the ratio (1:4 to 1:1) because some of the inorganic components were removed by Fenton reagent. At 0.1M the total TSS found was less than 3000(mg/L), at 0.2M the total TSS found was less than 6100(mg/L) and at 0.3M the total TSS found was less than 11000 (mg/L). Among all the concentrations, Fenton reagent at 0.3M ratio (1:1) gave the highest value of TSS 10660 (mg/L) and at 0.1M ratio (1:4) lowest value of TSS 1170(mg/L) was found. 0.1M at Fe^{2+}/H_2O_2 ratio (1:4) is not effective similar results obtained for COD removal was not efficient.

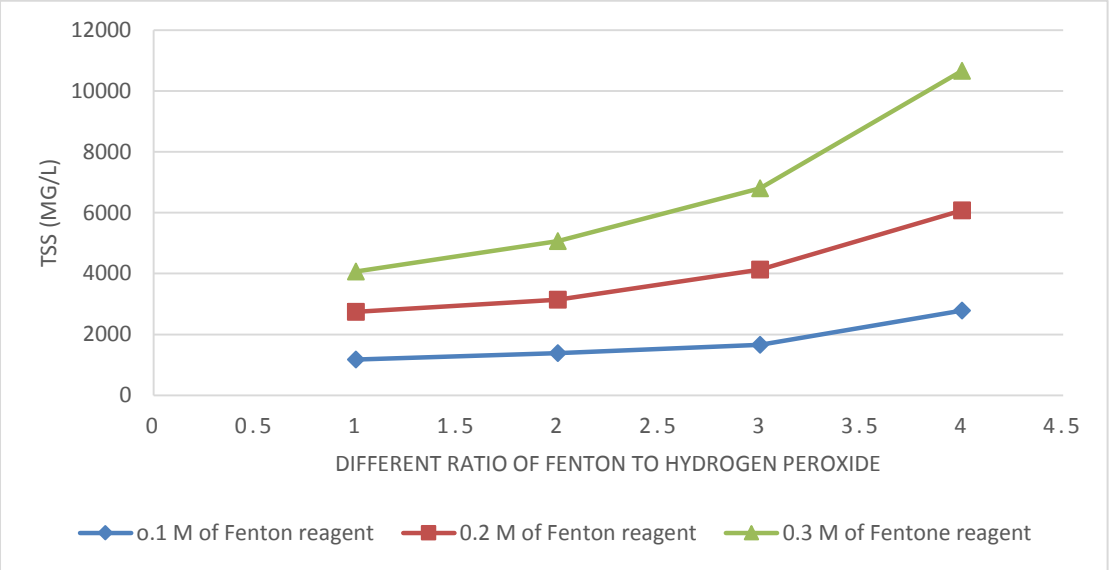


Figure 2: Total suspended solids and different ratio of ferrous to hydrogen peroxide.

In the treated sample, the amount of TSS (mg l−1) is directly affected by Fe^{2+}/H_2O_2 ratio and Fenton reagent concentration. That is because the PIWW bonds depends on the concentration of hydroxyl radicals which will attack and break the bonds that are present in the reaction. It is also depends on the kinetic rate of the reaction.

The rate constant (k = 63 l mol−1s−1) for the Fenton reaction between the hydrogen peroxide and ferrous ions that produces ferric ions and hydroxyl radicals is higher comparing to the rate constant (k = 3.1 × 10−3 l mol−1s−1) obtained the H_2O_2 reaction and Fe(II) regenerates from Fe(III). TSS is reduced at a rapidly rate when the radical concentration is high. On the other hand, the amount of sludge increases when increasing the amount of ferrous sulphate so gravity separation can be used to remove the sludge [19].

The TSS level found in the PIWW reduction increases when the inorganic compounds molecular structures have been reduced. The bonds between hydrogen and carbon atoms are attacked by the radicals then the bonds of carbon atoms are broken from larger functional groups to smaller molecular compounds of the printing ink.

Different molar ratio of Fe^{2+}/H_2O_2 Fenton Reagent and Turbidity variation

From figure 2, at 0.1M, 0.2M and 0.3M the reduction of turbidity increased comparing it to the original sample starting from the ratio (1:4 to 1:1). The turbidity reduced about less than 94.5% at 0.1M, less than 95% at 0.2M and less than 98.5% at 0.3M from the original

sample. Among all the concentrations comparing it to the raw PIWW sample, Fenton reagent at 0.3M ratio (1:1) removed the highest amount of cloudiness particles in the sample which lowered the turbidity to 98.3% from the original sample and at 0.1M ratio (1:4) highest amount of turbidity 156 NTU about 79.5% removal was found which gave more cloudiness appearance in treated wastewater.

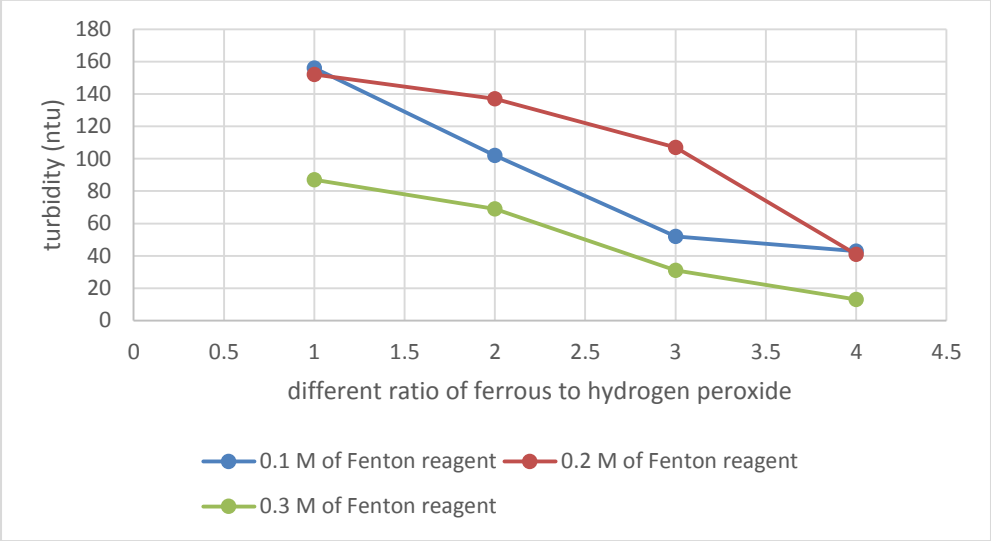


Figure 3: Turbidity and different ratio of ferrous to hydrogen peroxide.

The PIWW can effectively be treated when the concentration of Fenton reagent is 0.3M, Fe^{2+}/H_2O_2 ratio is (1:1) which leads to decrease the turbidity in the sample. The degradation activity is low at concentrations lower than 0.3M because of the less amount of free radicals in the treated sample.

3.2.2 Effect of hydrogen peroxide and iron (II) sulphate concentration

Salts deposited during the Fenton process. The ferrous ions (less reactive to hydroxyl peroxide) will be formed due to the high concentration of ferric ions but a recycling redox process between ferric ions and ferrous ions will occur when in excess. Therefore Fenton reagent's effect will decrease [17].

The concentration of iron (II) sulphate has to be monitored because ferrous ions hinder hydroxyl peroxide to turn into a radical state and decompose organic matters.

Further cost will be incurred due to the elimination of iron sludge, this is caused by the high concentration of iron which result into deposition of salt after the experiment.

For an effective Fenton process the iron concentration must be at an optimum but also the concentration hydrogen peroxide cannot be neglected as it is essential in this process. In fact hydroxyl radicals serve to decompose organic compounds but when in excess they tend to form various structures with organic compounds thus reducing their effectiveness and the COD level [9].

The mineralisation of PIWW generates carbon dioxide and water. Carbon dioxide is not good for environment even though it does not pollute the water but it is one of the greenhouse gases which affects the climate change and leads to global warming. Removing of printing ink from wastewater does not lead to any other environment problems. In order to avoid emission of carbon dioxide to air, technology such as carbon capture need to be employed. That procedure to capture the gas can be done by passing carbon dioxide out of calcium carbonate. Furthermore, Neutralisation of the treated wastewater is required after treatment because the sample is in acidic conditions so by adding sodium hydroxide the sample can be neutralised because it is alkali-based. Lastly, after 2 hours of Fenton process reaction, precipitation of Fe^{3+} will generate and sodium hydroxide is added to remove the precipitation which will produce Fe(OH) salt.

3.3 GC-MS Analysis for untreated and treated samples

The chromatogram photos shows the present compounds at different peaks for the samples before and after the treatment. At different retention times, different peaks are obtained. Which indicates various individual compounds. The analysed treated samples were according to the highest percentage of the COD removal.

There are 4 peaks for the untreated sample. Figure 0 shows the found compounds which are: Benzene, 1,2,3,5-tetramethyl, 6-Hydroxymethyl-4-methylbenzo, N-(3-Allyl-2-oxo-2,3-dihydro-1,3 and 1,2-Benzenedicarboxylic acid. The compounds were indicated at a retention time of 5.042 min, 12.080 min, 16.469 min and 22.643 min respectively.

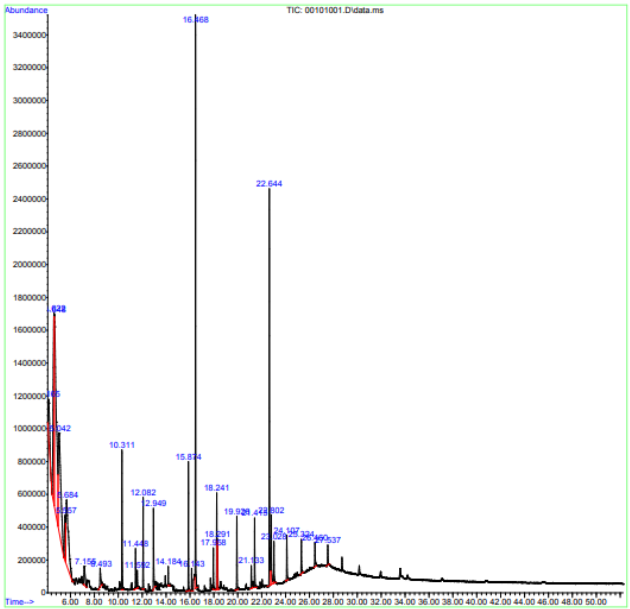


Figure 0: Library search report for the raw sample.

There are 4 peaks for the treated sample by using temperature treatment at 35ºC. Figure 5 shows the content compounds such are: benzene, 1,2,3,5-tetramethyl, 6-hydroxymethyl-4-methylbenzo, N-(3-allyl-2-oxo-2,3-dihydro-1,3 and 1,2-benzenedicarboxylic acid. The compounds were indicated at a retention time of 4.631 min, 12.945 min, 16.464 min and 22.638 min respectively. No degradation happened.

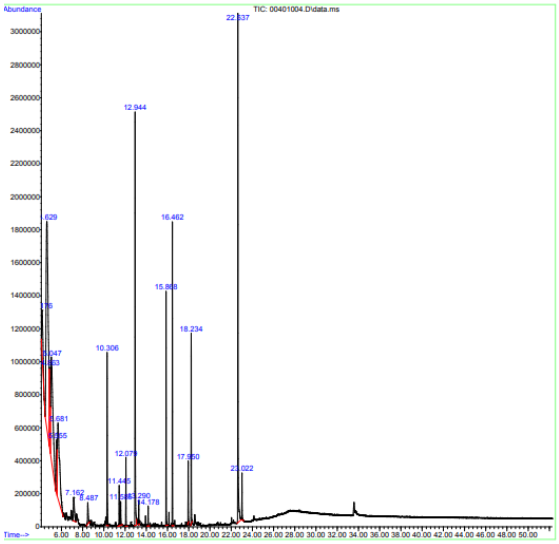


Figure1: Library search report for the treated sample by temperature.

There are 3 peaks for the treated sample by using pH treatment at pH 4. Figure 6 shows the found compounds which are: hexadecanoic acid, methyl ester, cctadecanoic acid, methyl ester and 1,2-benzenedicarboxylic acid. The compounds were indicated at a retention time of 15.869 min, 18.237 min and 22.638 min respectively. N-(3-Allyl-2-oxo-2,3-dihydro-1,3 was removed after the pH treatment and the compounds in the raw sample degraded to new compounds as which are hexadecanoic acid, methyl ester, octadecanoic acid, methyl ester but no degradation happened for 1,2-benzenedicarboxylic acid.

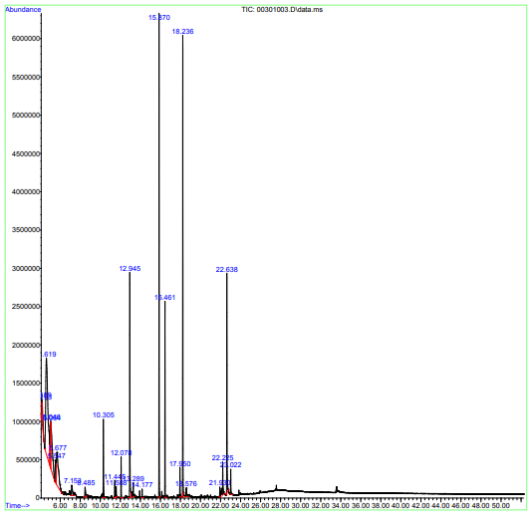


Figure 02: Library search report for the treated sample by pH.

Figure 7 shows 2 peaks of compounds which were found after the Fenton oxidation process (0.3M) at 1:1. The compounds are: hexadecanoic acid, methyl ester and octadecanoic acid, methyl ester. The compounds were indicated at a retention times of 15.874 min and 18.243 min respectively.

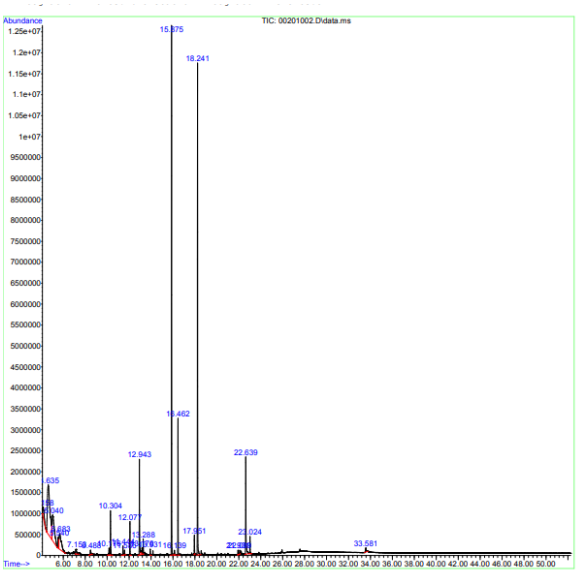


Figure 03: Library search report for the treated sample by Fenton.

Only 2 major peaks were found after the Fenton process which means that the Fenton degraded the rest of the components. It can be clearly seen from the chromatogram photos that the components which did not degrade are: hexadecanoic acid, methyl ester and acid, methyl ester. In short, COD value was affected by the compounds found in the sample which made the COD valued to be high.

The level of COD 69400 (mg/L) in the treated sample by Fenton did not reach the disposal limit according to the (MALAYSIA'S REQUIREMENTS ON INDUSTRIAL EFFLUENT TREATMENT SYSTEMS) [46]. Therefore, optimisations and further work should be done to reach the disposal limit as stated in the discussion (Fenton reagent should be more than 0.3M).

7. Conclusions

The aim of this experiment is to determine by using Advanced oxidation process (AOP) whether Fenton oxidation process have a strong effect on printing ink wastewater (PIWW) and helps to remove the printing ink from the wastewater. From the conducted research, it can be seen that (PIWW) was better treated when using Fenton oxidation process comparing to physical treatment. The reason is because that at 0.3 M and 1:1 molar ratio of (Fe^{2+}/H_2O_2) the COD in the (PIWW) reduced by 52.1% and the wastewater became less cloudiness since the color of the sample changed from dark black to light brown which reached to the turbidity of 13 NTU. Furthermore, the

Furthermore, the suspended solids in the sample increased from 10.204 mg/L to 10660 mg/L because of the degradation of (PIWW) components. The physical treatment gave high results at pH 4, T= 35^{o}C and the removal of COD was 13.4%, 7.04%, respectively. In addition, GC-MS results show that the components which did not degrade after the Fenton process are: hexadecanoic acid, methyl ester and acid, methyl ester.

References

[1] R. L. Stotler, Chasing Water: A Guide for Moving from Scarcity to Sustainability, vol. 53, no. 3. 5AD.
[2] CONDIAS, "Industrial Wastewater Treatment," vol. 4, no. Fall, pp. 29–31, 2016.
[3] D. Orhon, F. G. Babuna, and O. Karahan, Industrial Wastewater Treatment by Activated Sludge. 2009.
[4] M. B. Ishak, "Administrative and institutional set up for environmental management in Malaysia as compared with the U . K . and U . S ."
[5] M. Sellami, Z. Zarai, M. Khadhraoui, N. Jdidi, R. Leduc, and F. Ben Rebah, "Cactus juice as bioflocculant in the coagulation-flocculation process for industrial wastewater treatment: A comparative study with polyacrylamide," Water Sci. Technol., vol. 70, no. 7, pp. 1175–1181, 2014.
[6] S. Sauco, J. Gomez, F. R. Barboza, D. Lercari, and O. Defeo, "No Title," no. 1, 2013.
[7] J. Bergendahl and J. O'Shaughnessy, "Advanced oxidation processes for wastewater treatment," J. New Engl. Water Environ. Assoc., vol. 38, no. 2, pp. 179–189, 2004.
[8] M. Swaminathan, M. Manickavachagam, and M. Sillanpaa, "Advanced Oxidation Processes for Wastewater Treatment," Int. J. Photoenergy, vol. 2014, p. 216, 2013.
[9] R. N. Taylor, "Treatment of Palm Oil Refinery Effluent Using Advanced Oxidation Process," no. MAY, 2015.
[10] R. Nithyanandam and R. Saravanane, "Treatment of Pharmaceutical Sludge by Fenton Oxidation Process," Int. J. Chem. Eng. Appl., no. September 2015, pp. 359–364, 2013.
[11] S. Kumar Gupta, Y.-T. Hung, and S. Kumar Gupta, Treatment of Pharmaceutical Wastes, no. July. 2005.
[12] M. A. Sabur, A. A. Khan, and S. Safiullah, "Treatment of Textile Wastewater by Coagulation Precipitation Method," J. Sci. Res., vol. 4, no. 3, 2012.
[13] Spectroquant, "COD Cell Test," vol. 49, no. July, p. 75057, 2013.
[14] N. Standard and O. F. The, "Gb/t 11901-1989," vol. 1989, pp. 4–7, 1990.
[15] E. Significance et al., "15 . 0 Experiment on Determination of Total Dissolved and Suspended Solids in Water."
[16] A. El Nemr, M. A. Hassaan, and F. F. Madkour, "Advanced Oxidation Process (AOP) for Detoxification of Acid Red 17 Dye Solution and Degradation Mechanism," *Environ. Process.*, vol. 5, no. 1, 2018.
[17] X. J. Ma and H. L. Xia, "Treatment of water-based printing ink wastewater by Fenton process combined with coagulation," J. Hazard. Mater., vol. 162, no. 1, pp. 386–390, 2009
[18] L. Ding, Y. Chen, and J. Fan, "An overview of the treatment of print ink wastewaters," *Environ. Chem.*, vol. 3, no. 10, pp. 272–276, 2011.
[19] H. Puddoo, R. Nithyanandam, and T. Nguyenhuynh, "Degradation of the antibiotic ceftriaxone by Fenton oxidation process and compound analysis," *J. Phys. Sci.*, vol. 28, no. 3, pp. 95–114, 2017.

Potential Of *Hibiscus Sabdariffa* And *Jatropha Curcas* As The Natural Coagulant In The Dye Wastewater Treatment

Ong Sin Yee[1], Nurhazwani Ismail[2]

School of Engineering, Taylor's University, Taylor's Lakeside Campus, No.1 Jalan Taylor's, 47500, Subang Jaya, Selangor DE, Malaysia

Abstract

The coagulation process is commonly used in wastewater treatment to reduce the chemical solubility, turbidity and so on. Aluminum sulfate (alum) is the one of the most common used coagulant, however, recent studies have shown that residual aluminum in drinking water and sludge may induce Alzheimer's disease and environmental problems. As to overcome this problem, the natural coagulant have been concern instead to use the chemical coagulant. In this work, Hibiscus Sabdariffa and Jatropha curcas was studied as a natural coagulant to treat Congo Red-containing dye wastewater. The seeds were extracted with distilled water to extract the coagulant. The HS and JC seed will be mixed with different ratio, pH value, dosage concentration and concentration of dye wastewater. There is 99.95% color removal and 92.99% COD removal under operating conditions of pH 2 and 1500 mg/L coagulant dose at 400 ppm dye concentration for HS. The JC also working well under the same performance of the HS which is under pH 2, 1500 mg/l and 400 ppm which provide 99.97% color removal and 95.17% COD reduced. The combination of JC and HS which is 60% JC+ 40% HS giving 99.97% color removal and 93.77% COD reduced. Hence, the hypothesis is acceptable. And this combination is used applied to real dye wastewater which obtain from the local batik industry which also given the high performance which are 86.96% color removal and 68.82% COD reduced which the range of legal effluent discharge range which are below 310 mg/l.

1. Introduction

The synthetic dye has widely used in many industries such as textile, paper, fabric and so on. Textile industry is one of the most industry that create the most dye wastewater [1]. The industry using more than 8000 chemicals in the manufacture and a huge volume of water will be used in the dyeing and printing process. There had been estimated around 8000 kg per day of water consume by the average textile industry [1]. Many of these chemicals are poison and can harm human's health and even cause the environment pollution [1]. Mills discharged millions of gallons of this effluent into hazardous toxic waste, filled with dyed salt and salt color and organic chemicals. The presence of sulfur, naphtha, vat dyes, nitrates, and heavy metals such as copper, lead, mercury, nickel and certain auxiliary chemicals together make the effluent highly toxic. Other harmful chemicals present in the water may be formaldehyde-based dye fixing agents, hydrocarbon-based softeners and non-biodegradable dyeing chemicals [1].

Hence, to overcome this problem a lot of the treatment is carried out. Coagulation is one of the most method used in the dye wastewater treatment plant due to low cost and easily operating process [2]. The coagulation is the process that using coagulant to remove the uncertain residual material which unable to remove by using the filtration process. The coagulation is the process that using the positive charge of the coagulant to remove the negative charge of the residual material. Once the charge is neutralized, the small particles will stick together and form the flocs which is denser and easily to filter out.

The most common coagulant that used in industry is alum, ferric sulphate and so on [3]. However the coagulant that commonly used may harm the human's health such as alum. The residual aluminum was found in the treated water [4]. The aluminum ions has found out will induce Alzheimer's disease and the sludge that formed is non-biodegradable [4]. Hence, the natural coagulant have been concern in the recent year. The natural coagulant have been popular try in the world such as Moringa Oleifera, Jatropha curcas, Hibiscus Sabdariffa and so on [4]. The natural coagulant give several advantage than using the chemical coagulant which are the cost for the natural coagulant is cheaper, and is biodegradable [5]. The natural coagulant also giving the high performance in wastewater treatment which approximately 90% and above [6]. Hence, the natural coagulant is one of the potential material that can applied to the industry wastewater treatment.

In this paper, the Hibiscus Sabdariffa (HS) and Jatropha curcas (JC) have been used. The HS is one of the well know medicine plant in Malaysia. Generally, people will boiled the HS to make the juice and after that the HS will be throw as waste. JC seed contain the high oil content which is able to be the source of bio-diesel. And after extract the oil, JC press cake will be throw as waste. In this paper, the boiled HS and JC press cake will be used due to the high protein content in both plant. The protein of both plants have the high potential in wastewater treatment. The objective of the project is to find out the best combination of this two plant seeds together with the concentration wastewater and pH value which giving the high performance in dye wastewater treatment.

2. Methodology

2.1 Preparation of Hibiscus Sabdariffa as the coagulant

The seeds of the Hibiscus Sabdariffa will be boiled in 100°C for 30 minutes which is the process as the general industry making the juice of Hibiscus Sabdariffa [7]. After the boiling process, the seed will be put into the oven to dry at 60± 2°C for 2 hours. Then the dried seeds will be pulverized into powder form by using the grinder. To extract the coagulant agent from

the seed, 5g of the seed powder will be mixed with 100 ml of distilled water. The mixture will be extract by using food blender for 2 minutes. Then the mixture will be filtered through muslin cloth to remove the unreacted residual material.

2.2 Preparation of Jatropha curcas as the coagulant

The Jatropha curcas dried seed that using was already extracted the oil from the industry. The dried seeds will be pulverized into powder from by using the grinder. To extract the coagulant agent from the seed, 5g of the seed powder will be mixed with 100 ml of distilled water. The mixture will be extract by using food blender for 2 minutes. Then the mixture will be filtered through muslin cloth to remove the unreacted residual material.

2.3 Preparation of synthetic dye wastewater

The dye that using is Congo Red ($C_{32}H_{22}N_6Na_2O_6S_2$); molecular weight: 696.66 (g/mol). The stock solution will be prepared by mixing Congo Red with distilled water which has 1000 ppm concentration. The pH value of the dye wastewater will be adjusted with 1 M of hydrochloric acid and 1M of sodium hydroxide.

2.4 Preparation of mixture coagulant

The ratio of the HS seed powder and JC seed powder will be prepared as 90% HS+10% JC,80% HS+20% JC, 70% HS+30% JC, 60% HS+40% JC, 50% HS+50% JC, 40% HS+60% JC, 30% HS+70% JC, 20% HS+80% JC, and 10% HS+90% JC [8][9]. The powder will be mixed completely, then take 5 g of the HS-JC powder mixed with 100 mL of distilled water. . The mixture will be extracted by using food blender for 2 minutes. Then the mixture will be filtered through muslin cloth to remove the unreacted residual material.

2.5 Jar test

The jar test is usually used to carry out the coagulation process. 500 ml of the dye wastewater was added coagulant ad the mixture will be rapid mix under 100 rpm with 4 minutes to enhance the formation of flocs. After that, the mixing will be continued with 40 rpm with 25 minutes to allow the flocculation process. Then the mixture will allow to settle for 30 minutes. After the sedimentation, the sample will be filtered by using filtered paper. The supernatant will be collected and used the UV-Spectrophotometer to measure color removal. The percentage f the color removal will be determined by using the formula at below:-

$$\%\ of\ color\ removal = \frac{Ab_{so} - Ab_s}{Ab_{so}} \times 100$$

Where Ab_{so} is the absorbance value of dye wastewater before treatment and Ab_s is the absorbance value of dye wastewater after treatment. The calibration graph of absorbance value and dye wastewater is shown in Figure 1.

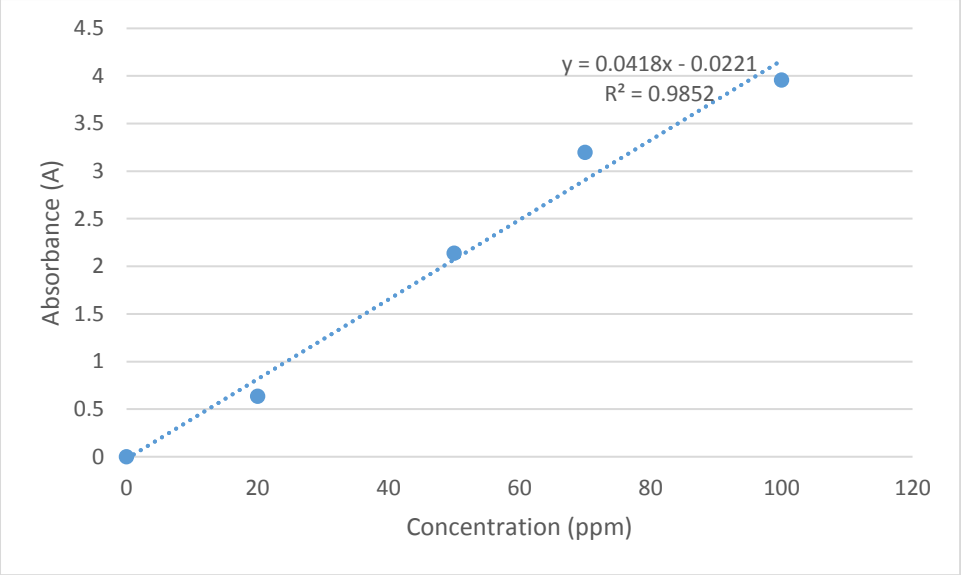


Figure 4. Calibration graph for Absorbance value (A) VS Concentration of wastewater (ppm).

2.6 Effect of coagulant dosage

According to the journal refer, the optimum pH value of the journal is 2 for HS seed and pH 3 for JC seed. Hence, the research will start with using 400 ppm of the wastewater with pH 2 and varies dosage. The dosage for HS and JC was set from 1000 to 4000 mg/l.

2.7 Effect of pH

The pH value of the dye wastewater will be adjusted from pH 2 to pH 12 by using the 1 M sodium chloride (NaCl) and 1 M sodium hydroxide (NaOH). The optimum pH value of the coagulation process will be obtained for HS seed powder, JC seed powder and HS-JC seeds powder.

2.8 Effect of concentration of synthetic dye wastewater

The experiment will be carried according to the optimum pH value and coagulant dosage for each type of coagulant. Various doses of coagulant were added to the several sample wastewater and rapidly mixed. Then the suspension was slowly mixed and left for the sedimentation to happen. The range of the concentration of dye wastewater is set between 100 to 400 ppm.

2.9 Applied to real dye wastewater

After obtain the result, the high efficiency combination of HS and JC with pH value and coagulant dosage will be applied to the real dye wastewater which obtain from the batik industry.

2.10 Chemical Oxygen Demand (COD) testing

The COD was measured using a 25-1500 mg/l reaction cell which containing sulfuric acid, potassium dichromate, and mercury (II) sulfate as reagents. 3 mL of the test sample was carefully added to the reaction cell in the fume hood. The cells were then shaken vigorously

and heated using a thermal reactor at 150°C for 2 hours. The cells were then removed and allowed to cool to room temperature. The COD was then measured using a photometer (Prove 300 UV/VIS spectrophotometer). COD removal rate is calculated according to formula below:-

$$COD\ removal = \frac{COD_i - COD_f}{COD_i} \times 100\%$$

(COD_i) is the COD of the wastewater before the coagulation, and (COD_f) is the COD after the wastewater.

3. Results and Discussion

3.1 *Hibiscus Sabdariffa*

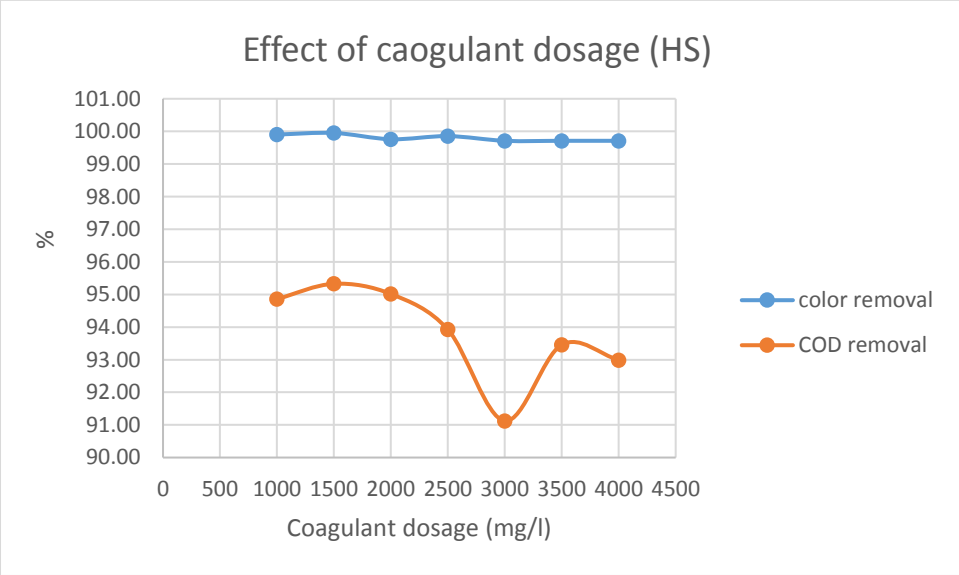


Figure 2. Effect of coagulant dosage (HS).

In this step, the dye wastewater was adjusted the pH value to 2 and the concentration of wastewater is set as 400 ppm which is refer from the journal which provide the optimum operation condition of Hibiscus Sabdariffa [10][11]. The result shown the highest color removal and COD reduced at 1500 mg/l which are 99.95% and 95.32%. The color removal from the range of 1000 to 4000 mg/l showing approximately 99.99% color removal which is high efficiency. The COD reduce from the range 1000 to 4000 mg/l is from 91 % to 95%. Which both results are showing the high efficiency of Hibiscus Sabdariffa in dye wastewater treatment. The trend line of color removal decrease from 1000 to 2000 and increase at 2500 mg/l and after that the color removal become constant. For the COD reduced, at 3000 mg/l gave the lowest COD reduced which is 91.12%. This is due to the overdosing which increase the unnecessary sludge. Hence, the Hibiscus Sabdariffa performance well under 1500 mg/l.

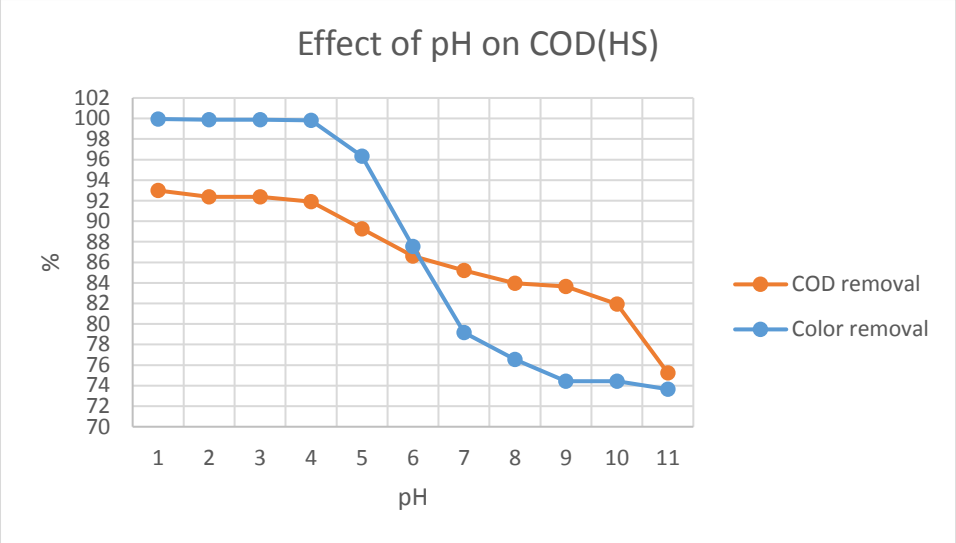


Figure 3. Effect of pH (HS).

After that, by applied 1500 mg/l and 400 ppm to various pH value. The color removal with various pH value is decrease from 99.95% to 73.65%. The COD removal with various pH value is also decrease from 92.99% to 75.23%. The Hibiscus Sabdariffa seen performance well under acidic environment than the alkaline environment. At pH 2 show the highest efficiency of color removal and COD reduced which are 99.95% and 92.99%. And at pH 12 show the low efficiency at color removal and COD reduce which are 73.65% and 75.23%. This is due to the protein content in the Hibiscus Sabdariffa seed has the isoelectric point range which is between 3.5 and 4 [12]. When the protein is subjected to pH lower then isoelectric point will give a positive net. The coagulation process is using the positive charge of the coagulant to remove the negative charge of the dye wastewater. Hence, the pH 2 is chose. Based on,

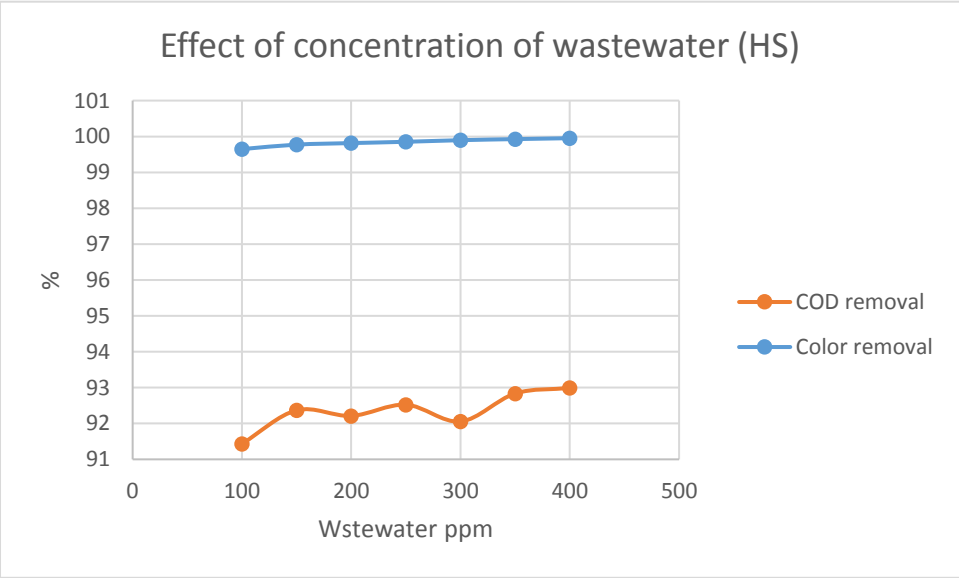


Figure 4. Effect of concentration of wastewater (HS).

In this step is to apply the pH 2 and 1500 mg/l with various concentration of synthetic dye wastewater. The range of wastewater is 100 to 400 ppm. The efficiency of color removal from the range are 99.64% to 99.95%. The COD reduced efficiency is from 91.43 to 92.99%. At 100 ppm showing the lowest result and 400 ppm showing the highest result. Hence, the 400 ppm is chose. This is due to low residual material in the dye wastewater which become the limited agent to let the coagulant to neutralize. The amount of coagulant is higher than the dye element which cause the reaction of coagulation slower and have the overdosing problem. This is due to the limited dye elements being react become flocs and the residual coagulant will become unnecessary sludge.

The Hibiscus Sabdariffa working well under pH 2, 1500 mg/l (coagulant) and 400 ppm (wastewater).

3.2 *Jatropha curcas*

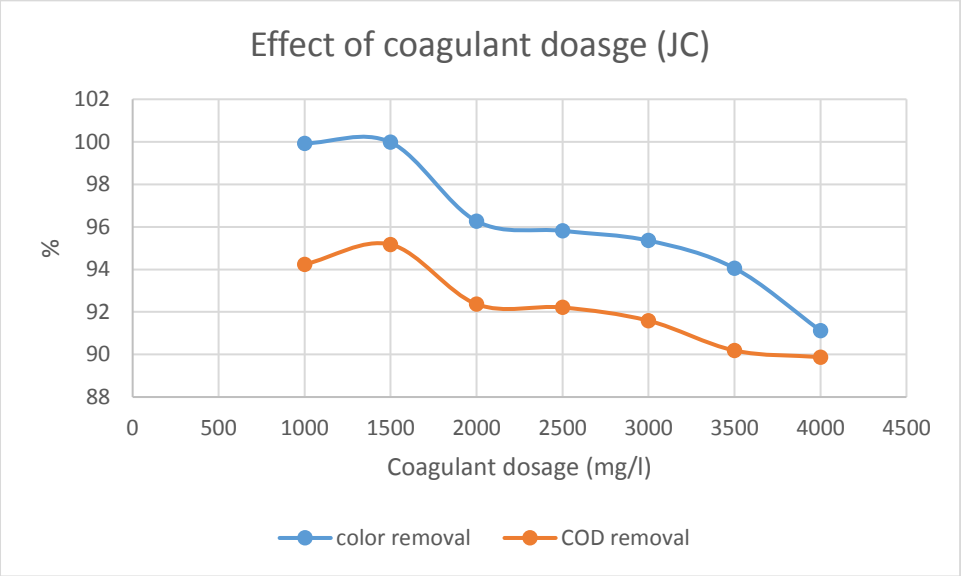


Figure 5.Effect of coagulant dosage (JC).

In this step, the dye wastewater was adjusted the pH value to 3 and the concentration of wastewater is set as 400 ppm which is refer from the journal which provide the optimum operation condition of Jatropha curcas [13][14]. The result shown the highest color removal and COD reduced at 1500 mg/l which are 99.97% and 95.17%. The trend line of color removal decrease from 1000 to 4000. For the COD reduced, at 4000 mg/l gave the lowest COD reduced which is 89.88%. The Jatropha curcas performance well under 1500 mg/l which gave 95.17% COD reduced and 99.97% color removal. Hence, the 1500 mg/l is chose to apply to next step.

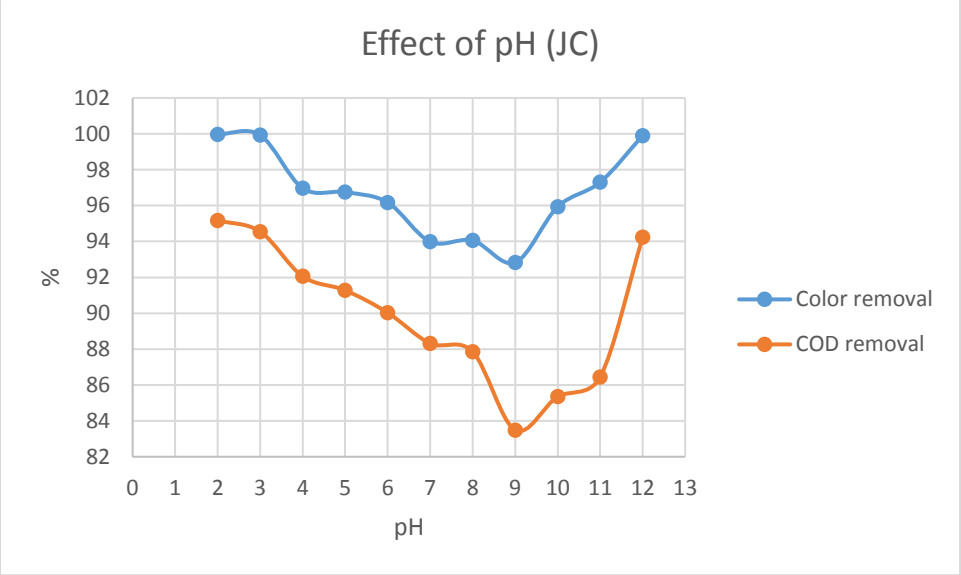


Figure 6. Effect of pH (JC).

After that, by applied 1500 mg/l and 400 ppm to various pH value. The color removal show high efficiency at pH 2, 3 and 12 which approximate 99.99%. However the optimum pH value is different with the journal that referred. At pH 2 showing the highest efficiency of color removal and COD reduced which are 99.97% and 95.17%. And at pH 12 show the increase efficiency at color removal and COD reduce which are 99.90% and 94.23% but still lower than the performance at pH 2. This is due to the majority of amino acids present in JC have isoelectric point (pH) values of around 3 to 11 [13]. Therefore, most amino acids are expected to have a positive charge at a pH of less than 3, so that the protein can performed as the well cationic coagulant. As an amphipathic molecule, the charge on a protein is depend with the pH value. When the pH is larger than 3, the mixture of the positive and negative charges for various amino acids in the protein may reduce the efficient of the solid removal in the coagulation process. Above pH 11, amino acids other than arginine show a negative charge. However, the amount of the arginine is huge in the JC protein. Therefore, this large amount of arginine may play an important role in the coagulation process at pH> 11.

Hence, pH 2 is chose.

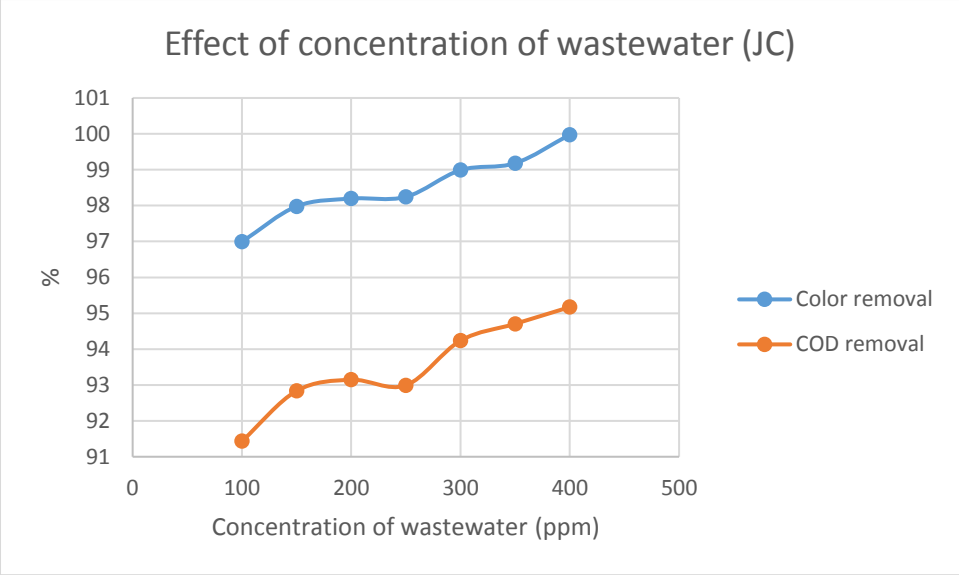


Figure 7. Effect of concentration of dye wastewater (JC).

In this step is to apply the pH 2 and 1500 mg/l with various concentration of synthetic dye wastewater. The range of wastewater is 100 to 400 ppm. The efficiency of color removal from the range are 96.99 to 99.97%. The COD reduced efficiency is from 91.43 to 95.17%. At 100 ppm showing the lowest result and 400 ppm showing the highest result. Hence, the 400 ppm is chose. The Jatropha curcas working well under pH 2, 1500 mg/l (coagulant) and 400 ppm (wastewater) which is similar with Hibiscus Sabdariffa.

3.3 Combination of HS-JC

The combination of JC and HS is set as the table below:-

Table 6.Combination of JC and HS.

90% JC + 10% HS
80% JC + 20% HS
70% JC + 30% HS
60% JC + 40% HS
50% JC + 50% HS
40% JC + 60% HS
30% JC + 70% HS

20% JC + 80% HS
10% JC + 90% HS

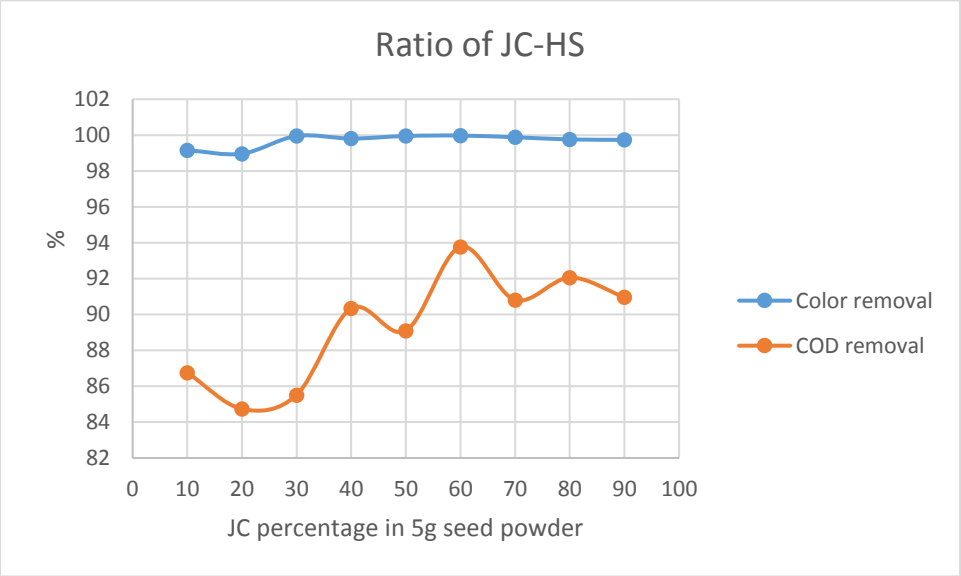


Figure 8.Effect of various combination of JC-HS.

In this process, the combination of 60% JC + 40% HS shown the highest efficiency on color removal and COD reduced which are 99.97% and 90.81%. And the combination of 20% JC + 80% HS show he lowest result which is 98.96% color removal and 84.74% COD reduced. Hence, the combination of 60% JC + 40% HS is chose to apply to real dye wastewater.

3.4 Applied to real dye wastewater

Table 7. Result of color and COD remove for real dye wastewater.

	Before	After	Removal %
Absorbance (A)	0.092	0.012	86.96
COD	263	82	68.82

The combination 60% JC + 40% HS under pH 2 and 1500 mg/l is applied to the real dye wastewater which obtain from the local batik industry. The color remove from 0.092A to 0.012A which is 86.96% color remove and the COD reduce from 263 to 82 which is 68.82%

COD reduced. The result has achieved the legal dye wastewater discharge range which are below 310 mg/l.

The concentration of this paper applied is highest than the referred journal [10][13]. This is due to the Hibiscus Sabdariffa seed have been boiled before the experiment. This is due to the common procedure of the industry making the Roselle juice is to boil the whole flower into the water instead of remove the seed before making the juice [7]. Hence, in this process some of the protein content may be denatured and this cause the performance of Hibiscus Sabdariffa in coagulation process reduce. Which means the amount of coagulant needed increase as the protein content decrease. However, the performance of the Hibiscus Sabdariffa in coagulation process is still high even though the amount of coagulant needed increase. The coagulant dosage of Jatropha curcas also vary from the journal referred. This due to the journal that referred is applied the JC into kaolin wastewater and the Congo red is used in this project. Hence, vary of dye used needed different working condition.

4.0 Conclusion

In conclusion, the hypothesis is accepted. The performance of the HS and JC provide a high efficiency in synthetic and real dye wastewater treatment. The combination 60% JC + 40% HS provided the high performance under pH 2 and 1500 mg/l of coagulant dosage. This showing the high potential of the HS and JC to invest into the real wastewater treatment. The HS and JC are cheaper than the current chemical coagulant that used in the market and is biodegradable and safety without release toxicity product.

References

[1] P. Bhatt and A. Rani, “Textile dyeing and printing industry: An environmental hazard,” *Asian Dye.*, vol. 10, no. 6, pp. 51–54, 2013.

[2] S.-T. Ong, P.-S. Keng, W.-N. Lee, S.-T. Ha, and Y.-T. Hung, “Dye Waste Treatment,” *Water*, vol. 3, no. 4, pp. 157–176, 2011.

[3] P. Presented, S. Engineer, P. Design, A. Qld, and W. Industry, “AN OPERATOR ’ S GUIDE TO WATER TREATMENT COAGULANTS Paper Presented by : Peter Gebbie Earth Tech Engineering 31st Annual Qld Water Industry Workshop – Operations Skills AN OPERATOR ’ S GUIDE TO WATER TREATMENT,” no. 14, pp. 14–20, 2006.

[4] B. a & J. M. V Renuka M S, “Application of Natural Coagulants in Water Purification,” *Int. J. Adv. Technol. Civ. Eng.*, vol. 2, no. 1, pp. 118–123, 2013.

[5] T. . V. K. Vijayaraghavan, G.; Sivakumar, “Application of Plant Based Coagulants for Waste Water Treatment,” *Int. J. Adv. Eng. Res. Stud.*, vol. 1, no. 1, pp. 88–92, 2011.

[6] A. M. Abdelaal, “Using a Natural Coagulant for Treating Wastewater,” *Eighth Int. Water Technol. Conf.*, pp. 781–792, 2004.

[7] Idolo Ifie, "Production and quality attributes of vegetable wine from Hibiscus sabdariffa Linn.," *African J. Food Sci.*, vol. 6, no. 7, pp. 212–215, 2012.

[8] I. Project, "Production of an acceptable shelf -stable roselle- pineapple juice beverage," 2005.

[9] N. E. Nwaiwu, a a Bello, W. R. Engineering, M. Ward, and B. State, "Effect of Moringa oleifera -alum Ratios on Surface Water Treatment in North East Nigeria," *Res. J. Appl. Sci. Eng. Technol.*, vol. 3, no. 6, pp. 505–512, 2011.

[10] M. Y. Yong and N. Ismail, "Optimisation of hibiscus sabdariffa as a natural coagulant to treat Congo red in wastewater," *J. Eng. Sci. Technol.*, vol. 11, no. Special Issue onthefourtheureca2015, pp. 153–165, 2016.

[11] H. Nicholas, J. Hoong, and N. Ismail, "Removal of Dye in Wastewater by Adsorption-Coagulation Combined System with Hibiscus sabdariffa as the Coagulant," vol. 01008, 2018.

[12] A. Ismail, E. Hainida, K. Ikram, H. Saadiah, and M. Nazri, "Roselle (Hibiscus sabdariffa L.) Seeds – Nutritional Composition, Protein Quality and Health Benefits," *Food*, vol. 2, no. 1, pp. 1–16, 2008.

[13] Z. Z. Abidin, N. Ismail, R. Yunus, I. S. Ahamad, and A. Idris, "A preliminary study on Jatropha curcas as coagulant in wastewater treatment," *Environ. Technol.*, vol. 32, no. 9, pp. 971–977, 2011.

[14] Z. Z. Abidin, N. S. Mohd Shamsudin, N. Madehi, and S. Sobri, "Optimisation of a method to extract the active coagulant agent from Jatropha curcas seeds for use in turbidity removal," *Ind. Crops Prod.*, vol. 41, no. 1, pp. 319–323, 2013.

Parametric Study of DES-Plasticised Chitosan/CMC Proton Exchange Membrane

Raja Rafidah Raja Sulaiman[1,1], Rashmi G. Walvekar[1] , and Wong Wai Yin[2]

[1] School of Engineering, Taylor's University, Malaysia
[2]Fuel Cell Institute, University Kebangsaan Malaysia, Malaysia

Abstract. Nafion® is a standard polymer electrolyte membrane (PEM) widely applied in fuel cells for its excellent proton conductivity, and thermal and mechanical stability. However, Nafion® is limited to its high cost. Chitosan (Ch) and carboxymethyl cellulose (CMC) are natural, bio-based polymers that are investigated for their application in synthesising a cheaper and eco-friendly proton exchange membrane for fuel cell application. Choline chloride (ChCl) and urea-based deep eutectic solvents (DES) is incorporated as a plasticiser in the chitosan/CMC biocomposite blend, in which the addition of DES would provide a more flexible, better thermal stability, and an improved proton conductivity of the membrane film. In this study, chitosan/CMC biocomposite membranes are synthesised at different volumetric ratios of chitosan to CMC (50:50, 45:55, 55:45, 40:60, and 60:40) using triflouroacetic acid (TFA) as a co-solvent, and an addition of 1 ml DES into each compositions. Membranes are formed via solution casting. Analysis is carried out by measuring the membrane's thickness, water uptake, thermal stability through Thermogravimetric Analysis (TGA), functional group study through Fourier Transform Infrared (FTIR) Spectroscopy, and proton conductivity measurements through Electrochemical Impedence Spectroscopy (EIS). DES membranes are compared with membranes without addition of DES, as well as with Nafion® 117. Percentage water uptake is the lowest for Ch :CMC(55 :45) with DES at 19.10%, and improved from the low water uptake of Nafion® 117. Thermal stability of the DES membranes at all compositions have been observed to be slightly higher than the membranes without DES, in which degradation Proton conductivity of Ch :CMC(55 :45) with DES is the highest at 0.0246 S/cm. High conductivity at lower water uptake is elaborated in terms of hydration effects on membrane and the electro-osmotic drag. Conductivity is compared with Nafion® 117 and other biocomposite membranes.

[1] Corresponding author: rajarafidahrajasulaiman@sd.taylors.edu.my

1 Introduction

The fuel cell technology is considered as a clean and effective form of power generation with applications in transportation, power stations, and in portable devices. The Proton Exchange Membrane Fuel Cell (PEMFC) is a well-known fuel cell type that operates at low temperature (< 100^{o}C) [1, 2]. The key advantages of the PEMFC are its high efficiency, silent operation due to its static nature, simple construction, and near zero emissions of harmful pollutants. In addition, it can also be made a portable source of energy, such as for the charging of mobile phones. However, the major drawback of the fuel is its high cost, which limits its commercialization [1].

The PEMFC is an electrochemical apparatus that directly converts the electrochemical energy into electricity, water and heat. The basic structure of the PEMFC is illustrated in Fig. 1.1. The main components of the fuel cell lies within the membrane electrode assemble (MEA), which consists of the electrodes and the polymer exchange membrane (PEM). Hydrogen is used as the main fuel for PEMFC, and the main reactions take place within the MEA. [2, 3]. At the anode, hydrogen is oxidised to produce hydrogen ions and electrons. The hydrogen ions (as protons) passes through the PEM while electrons flow through an external circuit. The protons then reached the cathode, where they will combine with oxygen to produce water. Therefore, the end products of the reactions are electricity, heat, and water.

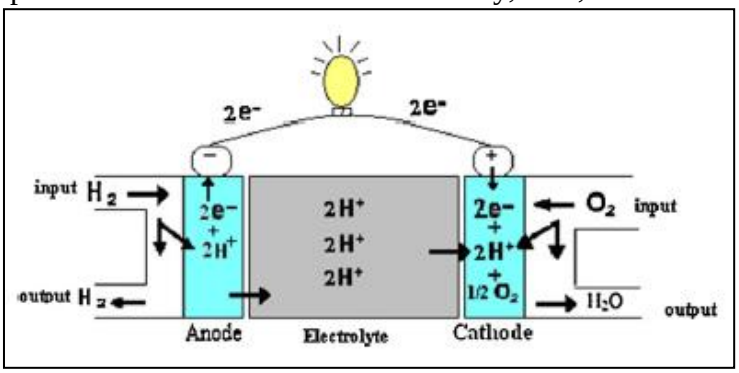


Fig. 1.1. Basic diagram of the PEMFC. [3]

The polymer electrolyte membrane is a thin layer at the center of the MEA with proton conducting ability. Desired properties of this PEM for fuel cell application includes high proton conductivity, high fuel resistance, good level of hydration, and adequate thermal, mechanical, and chemical strength [4, 5] Currently, the Nafion® membrane is commonly used as PEM in low temperature fuel cells. The membrane has a perflouronated backbone in its structure with attached sulfonic acid groups. Its common interest in use in fuel cells is due to its characteristics, in which the membrane has high proton conductivity, and good thermal, mechanical and chemical stability [1, 4, 6]. However, Nafion® is limited to its high cost, in addition to safety factors in its manufacturing and usage [4]. Therefore, extensive study has been carried out on the search for cheaper, bio-based materials that have potential in application as PEM material in fuel cells. Chitosan (Ch) and carboxymethyl cellulose (CMC) are abundant natural polymers that have been investigated for their application as biopolymer electrolyte. The structures of chitosan and CMC are shown in Figure 1.2a and 1.2b. Chitosan can be derived from shells of crustaceans and fungi. It is low cost, biodegradable and has good film forming abilities [7, 8]. Application of chitosan as PEM material has been shown by various studies such as the chitosan-sodium alginate by Smitha [9] and chitosan-europium triflate membrane by Alves [10]. CMC is a water soluble cellulose that also has film forming abilities as well as biodegradable. Studies on the proton conducting abilities of CMC is limited, but its potential was investigated in a study for its application in rechargeable proton batteries [11].

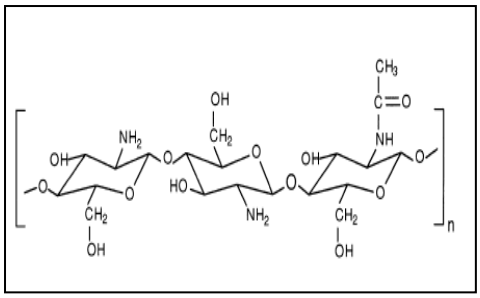


Fig. 1.2a: Structure of chitosan [12].

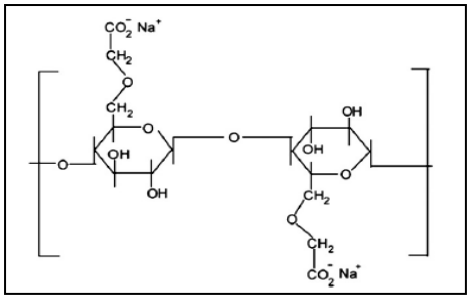


Fig. 1.2b: Structure of CMC [13].

Blending chitosan and CMC to form a single film yields several characteristics. A study of chitosan-CMC blend with zinc oxide nanoparticles by Norshivani [14] showed that the blend displays good mechanical strength and rigidity, in addition to high water uptake and good thermal stability. In this study, chitosan and CMC are blended using triflouroacetic acid (TFA) as a dissolution solvent, which would produce a clear, homogenous blend solution and transparent film, based on the works done by [15].Ionic liquids (ILs) can potentially improve the proton conductivity of the PEM, however, ILs can be toxic and harmful to the environment. Deep eutectic solvent (DES) will be added into the chitosan-CMC blend in which it will act as a plasticiser to give an amorphous, more flexible film, as well as improving its proton conductivity. The DES is an eco-friendly, non-flammable, low toxic, and biodegradable alternative form of ILs, where it can be produced by mixing quarternary ammonium or metal salts together with a hydrogen bond donor (HBD) [16]. Choline chloride/urea-based DES mixed with a ratio of choline chloride to urea of 1:2 is shown to have a good potential as a plasticiser based on studies on regenerate cellulose films done by Wang [16] and the chitosan-cellulose blend by Wong [17]. A characteristic study of the chitosan/CMC blend film with different chitosan and CMC compositions and DES as plasticiser will be described in this paper, which will include its properties in terms of film thickness, water uptake, and proton conductivity that are compared with Nafion®. In addition, thermal characteristics and internal bonding of the film are also investigated.

2 Methodology

2.1 Preparation of Chitosan and CMC Blend Solutions

The chitosan solution is prepared by dissolving 1 wt% (1 g) of chitosan powder into 100 ml of 0.1M acetic acid in a 100ml DURAN Laboratory bottle. The bottle is sealed with parafilm to prevent excess moisture from entering. The mixture is then subjected to continuous stirring on a hotplate magnetic stirrer for 4 hours at 47^{o}C until all the powder is dissolved to form a homogenous yellow solution. For CMC solution, 1 wt% (1 g) of low viscosity CMC powder is dissolved in 100 ml of deionized water in 100 ml DURAN Laboratory bottle. The mixture then undergoes continuous stirring for 4 hours under room temperature to form a homogenous, clear solution. The chitosan and CMC blends are prepared using different compositions of chitosan and CMC. Five different volumetric ratios of chitosan to CMC (50:50, 45:55, 55:45, 60:40, 40:60) are added into 250 ml DURAN Laboratory bottle respectively, which is then followed by adding 5 ml of triflouroacetic acid (TFA) into each mixture. All the mixtures undergo continuous stirring for 4 hours under room temperature until a clear solution is formed. The mixtures are then subjected to ultrasonication in an ultrasonic water bath for 30 minutes under room temperature, with a frequency of 37 Hz.

2.2 Preparation of DES

The deep eutectic solvent (DES) is prepared using choline chloride (ChCl) and urea with a ratio of choline chloride to urea of 1:2. To prepare DES at a 50 ml basis, 32.2 g of ChCl and 27.7 g of urea are weighed and added directly into a 100 ml DURAN Laboratory bottle. The weighing and mixing are carried out in a fume hood to minimize the exposure of ChCl to excess moisture, due to the salt's high sensitivity to moisture. ChCl salt must also be transferred quickly into the bottle, which is then followed by the addition of urea. The bottle is sealed with parafilm and then undergo continuous stirring on a hotplate magnetic stirrer for 4 hours at a temperature of 120^{o}C. A clear, viscous solution of DES is then obtained. It is necessary to prolong the stirring process until all the salt and urea have formed a homogenous solution. Karl-Fischer test is carried out on the obtained DES to check the moisture content, which must be in the range of under 5% to ensure that the properties of DES is not compromised by too much water.

2.3 Preparation of DES-Plasticised Chitosan/CMC Biocomposite Membranes

For each biocomposite membrane sample, 40 ml of chitosan/CMC-DES mixture solution is required. 39 ml of chitosan/CMC blend solution of each ratio is measured and transferred into a 100 ml DURAN Laboratory bottle. 1 ml of DES is then added into each of the solution. For control solutions, 40 ml of the chitosan/CMC blend is added into each bottle without the addition of DES. The bottles are sealed with parafilm. All mixtures then undergo continuous stirring for 4 hours under room temperature to obtain an even mixing of components. Ultrasonication is then carried out on all mixtures in an ultrasonic water bath at room temperature for 30 minutes, with a frequency of 37 Hz. The obtained chitosan/CMC-DES solutions at different chitosan/CMC ratios are casted onto glass petri dishes. The petri dishes containing the solutions are covered with aluminum foil poked with holes and undergo air drying under fume hood for 2-3 days to evaporate the acid solutions. The casted solutions are then placed in an oven at 60^{o}C for another 2-3 days to further evaporate the solutions and obtain a dry membrane. The dried membranes are rinsed with deionized water to remove any trace solvents and is then placed in the oven again until the membranes are completely dry. Similar step is taken for casting the solutions without DES.

2.4 Thickness Measurement and Water Uptake

Thickness of the dried membranes containing DES and those without DES are measured using a digital vernier caliper. The measurements are made in millimeters with 0.01 mm tolerance. Measurement is also made at different areas of each membrane, and the average thickness is calculated. For water uptake, each dry biocomposite membrane at approximately 2 cm in length is first weighed to obtain the dry mass. The membranes are then immersed in deionized water for 24 hours. Wet membranes are carefully removed and wiped to remove excess surface water. The membranes are then weighed to obtain the wet mass. Percentage water uptake is calculated by using the ratio of difference between wet and dry mass to the dry mass of membranes, as shown in equation below:

$$Water\ uptake\ (\%) = \frac{m_s - m_d}{m_d} \quad (1)$$

Where m_s is the wet mass of the membrane in grams and m_d is the dry mass of the membrane.

2.5 Electrochemical Impedance Spectroscopy (EIS) Analysis

The electrochemical impedance spectroscopy (EIS) (Autolab PGSTAT128N potentialstat) testing is carried out on all the membrane samples to measure the proton conductivity at room temperature and at 80^{o}C (operating temperature of PEMFC). Each sample is placed in between two stainless steel electrodes with measurement cell through alternative current (AC) mode. The frequency range is1000 kHz and signal amplitude is 0.1 V. The diameter of the circular

electrode is taken at around 1.9 cm. Resistance of each sample is measured through the potentialstat and the proton conductivity is calculated using the formula of uniform current distribution.

$$Conductivity\ \left(\frac{S}{cm}\right) = \frac{t}{R \times A} \qquad (\mathbf{2})$$

Where t is the membrane thickness (cm), R is the measured resistance and A is the area of the membrane (cm^2).

2.6 Thermogravimetric Analysis (TGA)

Thermogravimetric analysis (TGA) (PerkinElmer, TGA 8000) are carried out on all samples to study the sample's thermal stability. Approximately 5 mg of each sample is placed into a small tray within the TGA apparatus. The temperature rise is set at 10°C/min, in a range of 30°C to 500°C to degrade the components within the membrane samples. A plot of weight percentage against temperature is then obtained and analysed.

2.7 Fourier Transform Infrared Spectroscopy (FTIR)

Fourier Transform Infrared Spectroscopy (FTIR) (PerkinElmer, Spectrum 100 FTIR Spectrometer) is carried out to analyse the chemical functional groups and internal bonding in the biocomposite membrane. Wavenumber is set between 4000 cm^{-1} to 650 cm^{-1}. Percentage transmittance is measured for all samples. The plot of percentage transmittance against wavenumber is analysed from the Spectrum software.

3 Results and Discussions

3.1 Film Thickness and Texture Comparison

A digital vernier caliper is used to measure each sample at different locations. **Table 3.1** shows the resulting average thickness of the membranes obtained.

Table 3.1. Summary of thickness of the chitosan/CMC membranes with and without DES.

	Thickness (mm)	
Compositions	W DES	W/O DES
Ch:CMC (50:50)	0.335	0.072
Ch:CMC (45:55)	0.278	0.035
Ch:CMC (55:45)	0.385	0.070
Ch:CMC (40:60)	0.520	0.073
Ch:CMC (60:40)	0.528	0.073
Nafion® 117	0.2	

The chitosan/CMC membranes that are formed without the presence of DES are thinner compared to the membranes that contain DES. The DES membranes are also thicker than Nafion® 117. In terms of texture, the samples with DES are more soft and flexible, while the samples without DES are mostly rigid. The effect of the ChCl/urea-based DES giving a flexible and soft membrane is similar to the findings by Wang et al [16] in the plasticisation of cellulose films. In addition, the colour is whitish-opaque and there is some degree of fragility seen in the samples with DES. This texture is possibly contributed by the formation of lumps of urea within the DES samples. This possibility is pointed out based on Wang et al. [16], where cellulose membranes with the addition of urea alone showed an opaque, whitish appearance while having quite a weak texture. Comparison between the Ch:CMC (50:50) appearance is shown in **Figure 3.1.** Nevertheless, flexibility is maitained for the DES samples, where the membrane can be

folded to a certain extent before breaking. Samples without DES are brittle in comparison, and breaks from a slight folding.

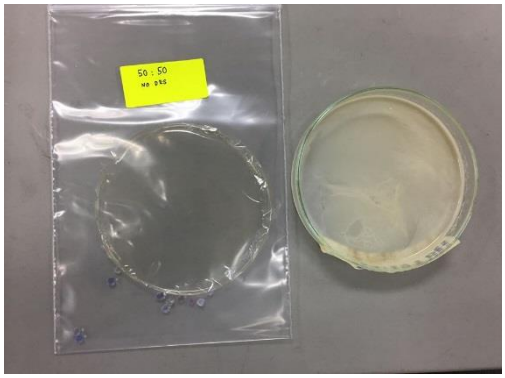


Fig. 3.1. Difference in appearance between the Ch:CMC (50:50) sample without DES (left) and with DES (right).

3.2 Water Uptake

The conductivity of the proton exchange membrane is dependent on its level of hydration. A higher water content would facilitate the movement of protons, which in turns increase the conductivity [4]. Table 3.2 shows the percentage of water uptake of all samples.

Table 3.2: Summary of the percentage water uptake for the chitosan/CMC membranes with and without DES.

	Water uptake (%)	
Compositions	W DES	W/O DES
Ch:CMC (50:50)	49.18	257.50
Ch:CMC (45:55)	61.69	244.90
Ch:CMC (55:45)	19.10	225.58
Ch:CMC (40:60)	29.14	126.98
Ch:CMC (60:40)	30.59	262.75
Nafion® 117 [20]	8.47	

A very high water uptake can be observed from the chitosan/CMC samples without DES, which means the membranes have a high level of swelling. This is due to the membranes being very thin. Rapid hydration is influenced by the reduction of membrane thickness [4]. This high water uptake also shows that the hydrophillicity of chitosan is maintained, as pointed out by Norshivani et al. [14] regarding the blending between chitosan and CMC. Hydration control is important in order to maintain the performance and durability of the PEMFC, as well as preventing flooding of membrane and reducing electro-osmotic drag [1, 4]. Adding DES into the Ch:CMC blend reduces the absorption of water and prevent excessive swelling. Nafion® 117 has quite low water uptake. Ch:CMC (55:45) with DES has the lowest uptake at 19.1%, while the Ch:CMC (50:50) and and Ch:CMC (45:55) absorbs quite a large amount.

3.3 FTIR Analysis

The FTIR spectra of chitosan/CMC biomembrane containing DES and without DES for Ch:CMC (50:50) is shown in Figure 3.3a below. Figure 3.3b shows the spectra for all chitosan/CMC samples containing DES. The characteristic bands of the chitosan and CMC can be deduced from the spectra.

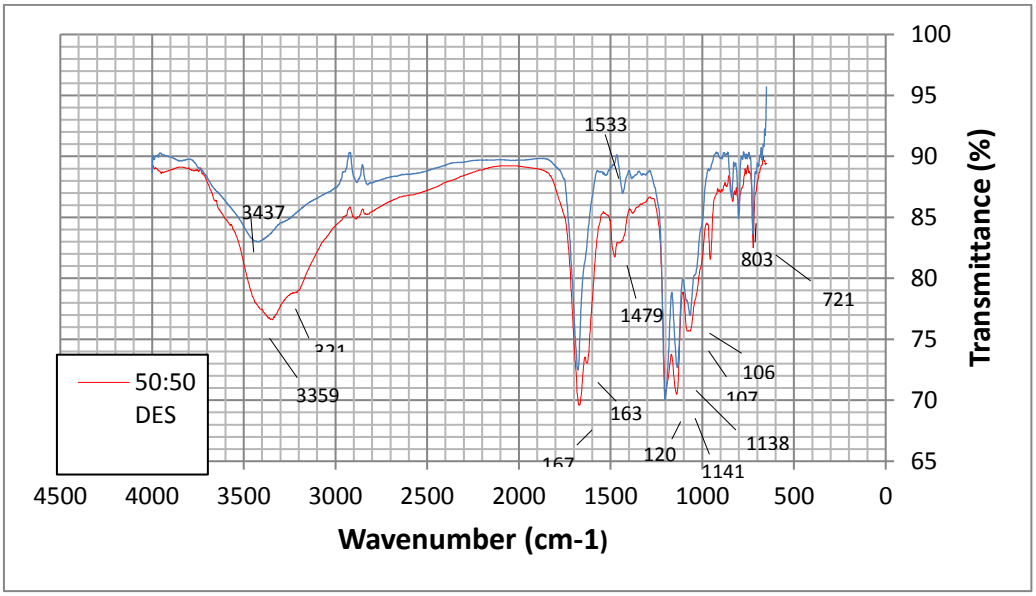


Fig. 3.3a: FTIR spectra for Ch:CMC (50:50) with and without DES.

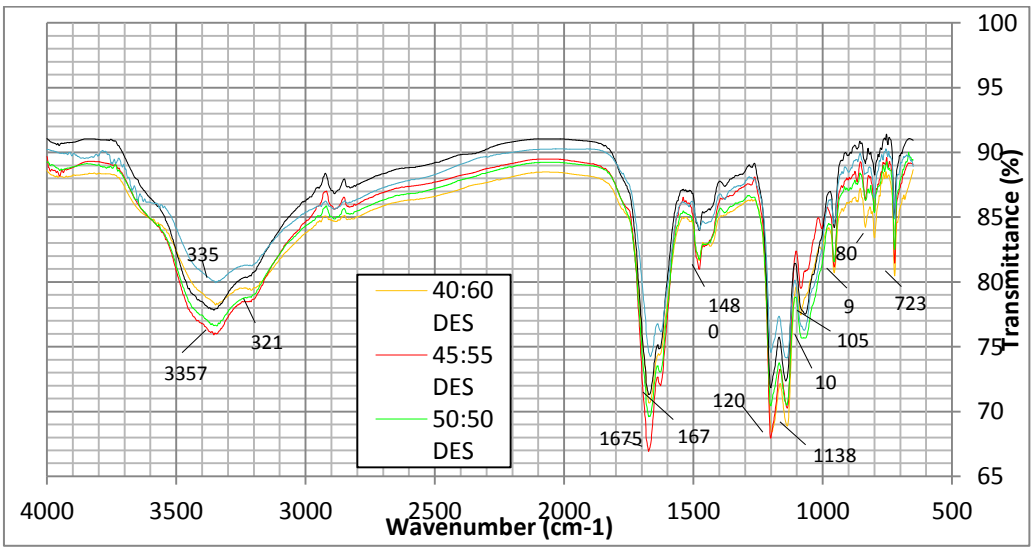


Figure 3.3b: FTIR spectra for chitosan/CMC samples of all compositions containing DES.

From Figure 3.3A, the band at 1647 cm^{-1} corresponds to the carbonyl (C=O) stretch in the amide group of chitosan. The broad transmission band showing the 3217 cm^{-1} band represents the (O-H) stretching within CMC [19]. The frequency at 3359 cm^{-1} and 3437 cm^{-1} also shows the (O-H) stretching that is present in chitosan. From Figure 3.3B, the broadening of the band at the range from 3500 cm^{-1} to 3100 $cm^{-1}$with increasing CMC content to the Ch:CMC (40:60) ratio (wide yellow band) indicates the intermolecular hydrogen bonding formed between the chitosan and CMC [19]. A small characteristic absorption band at 1533 cm^{-1} for Ch:CMC (50:50) (blue line) can be attributed to the (N-H) bending of amide and amine groups in chitosan [24]. Peak at 1141 cm^{-1} is presented as the diaryl group (C-O-C) stretching, while 1079 cm^{-1} and 1069 cm^{-1} presents the (C-O) stretching in chitosan and CMC [9]. The peak at 1479 cm^{-1} is related to the CH_2 bending of alkyl group in DES. In addition, peak at 721 cm^{-1} represents the (N-H) bending from the urea functional group within DES [21]. The spectrum for the samples containing DES and without DES show a similar pattern, but the presence of

DES can be clearly observed from the significant peaks at 1479 cm^{-1} and 721 cm^{-1} from Figure 3.3a.

3.4 Thermogravimetric Analysis (TGA)

TGA curves of the chitosan/CMC biocomposite membranes with Ch:CMC (50:50) are shown in Figure 3.4 for both samples containing DES and without DES.

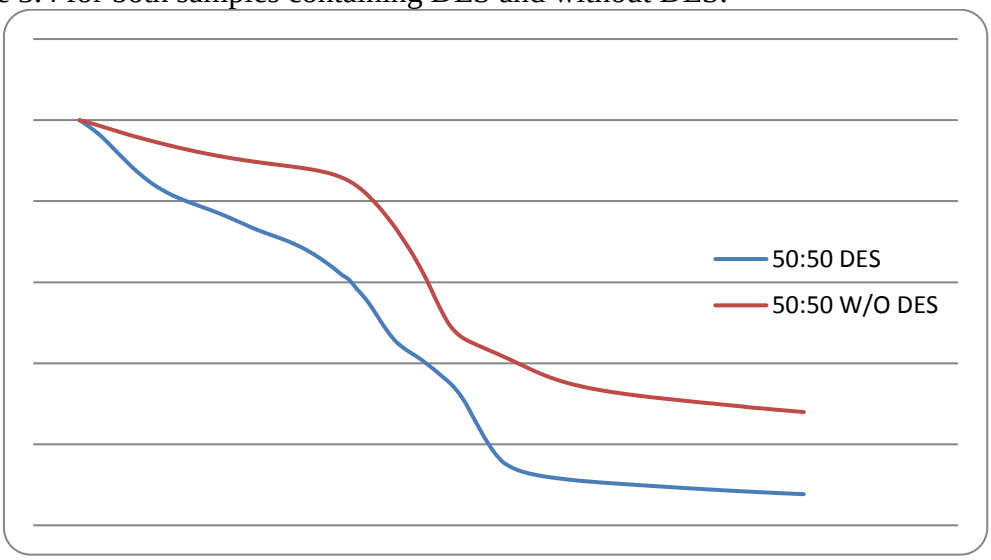


Fig. 3.4: TGA curve for Ch:CMC (50:50) samples with and without DES.

In both samples with DES and without DES, the first stage of weight loss takes place from 30°C to around 180°C, which can be attributed to the loss of water from the samples [11, 19, 22]. The percentage weight loss in DES samples in this stage is roughly 35%, while the samples without DES, the loss is around 13%. At temperature higher than 180°C, the samples would be anhydrous [22]. The higher weight loss due to water in DES sample is likely from the higher water contents of the DES membrane. The second stage decomposition occurs from 180°C to 270°C in the sample without DES, with a percentage loss of 38%. For sample with DES, the decomposition also starts from 200°C to 245°C, with percentage loss of about 18%. At this range of temperature, the weight loss is due to the degradation of the chitosan molecules and the decarboxylation of the COO^- group in CMC [11, 19]. In addition, the urea in DES also decomposes to cyanic acid and ammelide, in which the degradation temperature lies in between 130°C to 217°C [21]. The third stage of decomposition begin at around 270°C to 300°C for the sample with DES with a further loss of weight by 15%, and for the sample without DES, the decomposition from the same temperature range resulted on 7% weight loss. This weight loss is attributed to the degradation of the chitosan chains and further decarboxylation of CMC [11, 22]. Within this range, the degradation of ChCl also occurs, as its complete degradation lies in the temperature range between 252°C to 302°C [21]. The decomposition pattern of both the membranes containing and without DES is similar to that found by Hoe [20]. The findings are also similar to Hoe in terms of the higher degradation temperature for the sample with DES in second stage (from 200°C to 245°C). There is no difference in degradation temperature for third stage. Nevertheless, this indicates that addition of DES is able to increase the degradation temperature of the chitosan/CMC biocomposite membrane.

3.5 Proton Conductivity

The key desired properties for PEM in fuel cell application is high proton conductivity with minimal resistive loses [4, 6]. The membrane resistance is obtained from the Nyquist plots derived from EIS analysis, and the proton conductivity are calculated based on the formula for

uniform current distribution. Table 3.5 displays the resulting conductivity of the samples tested at room temperature (30^{o}C) and in hydrated state.

Table 3.5: Summary of proton conductivity measurements of chitosan/CMC biocomposite membranes.

	Proton conductivity (S/cm)	
Composition	W/O DES	W DES
Ch:CMC (50:50)	0.002669	0.0140
Ch:CMC (45:55)	0.001890	Breaks
Ch:CMC (55:45)	0.007637	0.0246
Ch:CMC (40:60)	0.008403	0.0194
Ch:CMC (60:40)	0.006102	Breaks
Nafion® 117	0.0856	

From **Table 3.5,** it can be observed that the proton conductivity of chitosan/CMC films with DES are higher than the ones without DES. Based on the FTIR analysis, the hydrogen bonding between the blend of chitosan and CMC promotes a rapid bond breaking and bond forming process, which facilitates the proton transport through the proton-hopping mechanism [23]. Note that the term 'Breaks' indicate that the following samples, Ch :CMC (45 :55), and Ch :CMC (60 :40) with DES were fragile and broke under the EIS apparatus, therefore, no results of conductivity could be obtained. Ch :CMC (40 :60) shows the highest conductivity at 0.008403 S/cm for sample with DES, with the lowest water uptake at 129.98%. Ch :CMC (55 :45) with DES has the highest conductivity for sample with DES, at 0.0246 S/cm. In addition, the water uptake for Ch :CMC (55 :45) is 19.10%, the lowest among the DES membranes. This interesting pattern on the membranes with low water uptake exhibiting high conductivity was also noted by Jiang et al. [22] on the study of chitosan/P(AA-AMPS) membranes. This is likely due to low resistance from the lowered water uptake, and therefore there is a decrease in electro-osmotic drag. Zadowsinki et. al [25] described that an increase in membrane resistance is due to increase in electro-osmotic drag. Water molecules were dragged along with the proton travelling across the membrane, slowing down the membrane movement due to the drag. This also demonstrated the presence of vehicular mechanism [2]. Comparing the DES membranes with Nafion® 117, the conductivities of the membrane are still low. When compared with other biocomposite membranes for PEM application, the conductivity of Ch :CMC (55 :45) with DES is close to the conductivity of chitosan-SGO by Liu et al [26]. It is also higher than the CMC-DTAB by Samsudin et al. [12], but lower than chitosan/P(AA-AMPS) by Jiang at al. [22] and chitosan-sodium alginate by Smitha et al. [9]. It is also almost similar to the chitosan/CMC with DES found by Hoe [20] at chitosan to CMC 50 :50 ratio, which was 0.0292 S/cm.

4 Conclusion

The chitosan/CMC biocomposite membranes at different ratios of chitosan and CMC have been synthesised by using triflouroacetic acid (TFA) as a co-solvent and ChCl-urea-based DES as a plasticiser. The characteristics of the biocomposite membranes were analysed in terms of its membrane thickness, water uptake, chemical functional groups through FTIR analysis, thermal stability through TGA, and the proton conductivity through EIS analysis. Resulting membranes that have been casted from the chitosan/CMC blend solutions show differing thickness between the blends containing DES and without DES. Membranes containing DES are thicker, softer and more flexible compared to the ones without DES, which are rigid and brittle, with some degree of fragility. Water uptake measurements showed that Ch:CMC (55 :45) with DES has the lowest water uptake at 19.10%, which is also improved from the

lower water uptake of Nafion® 117. It is important to have an appropriate hydration of the PEM in fuel cell to minimize flooding of membranes and maintain the durability of the fuel cell, at the same time sustaining a good proton conductivity. FTIR analysis have shown intermolecular hydrogen bonding was formed between the chitosan and CMC functional groups, that promotes a rapid bond breaking and bond forming that assists the proton transfer throughout the membrane following the proton-hopping mechanism. TGA results showed that the chitosan/CMC membranes containing DES have a slightly higher degradation temperature than those without DES, with a three stage decomposition which begins with the water loss from 30^{o}C to 180^{o}C, and degradation of chitosan, CMC and DES components from 200^{o}C to 245^{o}C, and from 270^{o}C to 300^{o}C, showing a good thermal stability of the biocomposite membranes. Conductivity of Ch :CMC (55 :45) with DES is the highest at 0.0246 S/cm. The membrane's low water uptake and high conductivity shows that there is lower resistance in the mobility of the proton due to electro-osmotic drag when there is lower level of hydration. It is also similar to the conductivity of chitosan-SGO and close to that found by Hoe [20] for chitosan/CMC membrane with DES. This shows that adding DES can have a beneficial effect on the biocomposite membrane as PEM for PEMFC application.

Acknowledgement

First and foremost, I would like to express my gratitude to my supervisors, Dr. Rashmi G. Walvekar and Dr. Wong Wai Yin for their continuous support and guidance for the completion of this project. I would also like to thank the School of Engineering, Taylor's University for providing the financial aid required for the execution of this project.

References

[1] O. Z. Sharaf and M. F. Orhan, "An overview of fuel cell technology: Fundamentals and applications," *Renewable and Sustainable Energy Reviews,* vol. 32, pp. 810-853, 2104.

[2] S. J. Peighambardoust, S. Rowshanzamir and M. Amjadi, "Review of the proton exchange membranes for fuel cell applications," *International Journal of Hydrogen Energy,* vol. 35, pp. 9349 - 9384, 2010.

[3] S. Mekhilef, R. Saidur and A. Safari, "Comparative study of different fuel cell technologies," *Renewable and Sustainable Energy Reviews,* vol. 16, pp. 981 - 989 , 2012.

[4] B. Smitha, S. Sridhar and A. A. Khan, "Solid polymer electrolyte membranes for fuel cell applications - a review," *Journal of Membrane Science,* vol. 259, pp. 10-26, 2005.

[5] Y. Wang, K. S. Chen, J. Mishler, S. C. Cho and X. C. Adroher, "A review of polymer electrolyte membrane fuel cells: Technology, applications and needs on fundamental research," *Applied Energy,* vol. 88, pp. 981 - 1007, 2011.

[6] D. Kim, M. J. Joe and S. Y. Nam, "A review of polymer-nanocomposite electrolyte membranes for fuel cell application," *Journal of Industrial and Engineering Chemistry,* vol. 21, pp. 36-52, 2015.

[7] J. Ma and Y. Sahai, "Chitosan biopolymer for fuel cell application," *Carbohydrate Polymers,* vol. 92, no. 2, pp. 955-975, 2013.

[8] J. Ramirez-Salgado, "Study of basic biopolymer as proton membrane for fuel cell systems," *Electrochimica Acta,* vol. 52, pp. 3766 - 3778, 2007.

[9] B. Smitha, S. Sridhar and A. A. Khan, "Chitosan-sodium alginate polyion complexes as fuel cell membranes," *European Polymer Journal,* vol. 41, pp. 1859-1866, 2005.

[10] R. Alves, J. .. Donoso, C. J. Magon, I. D. A. Silva, A. Pawlicka and M. M. Silva, "Solid polymer electrolytes based on chitosan and europium triflate," *Journal of Non-Crystalline Solids,* vol. 432, pp. 307-312, 2-16.

[11] A. S. Samsudin, W. M. Khairul and M. I. N. Isa, "Biopolymer Materials Based Carboxymethyl Cellulose as a Proton Conducting Biopolymer Electrolyte for Application in Rechargeable Proton Battery," *Electrochimica Acta,* vol. 129, pp. 1-13, 2014.

[12] Y. Wan, K. A. M. Creber, N. Peppley and V. T. Bui, "Ionic conductivity of chitosan membranes," *Polymer,* vol. 44, pp. 1057-1065, 2003.

[13] A. Samsudin, W. M. Khairul and M. I. N. Isa, "Characterization on the potential of carboxy methylcellulose for application as proton conducting biopolymer electrolytes," *Journal of Non-Crystalline Solds,* vol. 358, pp. 1104-1112, 2012.

[14] N. Noshirvani, B. Ghanbarzadeh, R. R. Mokarram, M. Hashemi and V. Coma, "Preparation and characterization of active emulsified films based on chitosan carboxymethul cellulose containing zinc oxide nano particles," *International Journal of Biological Macromolecules,* vol. 2017, pp. 530-538, 2017.

[15] M. Hasegawa, A. Isogai, F. Onabe and M. Usuda, "Characterization of cellulose-chitosan blend films," *Journal of Applied Polymer Science,* vol. 45, no. 10, pp. 1857 - 1863, 1992.

[16] S. W. e. al, "Choline chloride/urea as an effective plasticizer for production of cellulose films," *Carbohydrate Polymers,* vol. 117, pp. 133-139, 2015.

[17] C. Y. Wong, W. Y. Wong and R. G. Walvekar, "Application of Deep Eutectic Solvent (DES) in Chitosan-Cellulose Blend Film for Proton Exchange Membrane," in *eureca-2015,* Conference Paper, 2015.

[18] P. Mukoma, B. R. Jooste and H. C. M. Vosloo, "Synthesis and characterization of cross-linked chitosan membranes for application as alternative proton exchange membrane materials in fuel cells," *Journal of Power Sources,* vol. 136, pp. 16-23, 2004.

[19] D. Hu, H. Wang and L. Wang, "Physical properties and antibacterial activity of quaternized chitosan/carboxymethyl cellulose blend films," *LWT - Food Science and Technology,* vol. 65, pp. 398 - 405, 2016.

[20] J. G. B. Hoe, W. Y. Wong and R. G. Walvekar, "A Study of Deep Eutectic Solvent (DES) Chitosan Bio-Membrane for Proton Exchange Membrane Fuel Cell (PEMFC)," in *eureca-2016,* Conference Paper, 2016.

[21] N. Delgado-Mellado, M. Larriba, P. Navarro, V. Rigual, M. Ayuso, J. Garcia and F. Rodriguez, "Thermal stability of choline chloride deep eutectic solvents by TGA/FTIR-ATR analysis," *Journal of Molecular Liquids,* vol. 260, pp. 37-43, 2018.

[22] Z. Jiang, X. Zheng, H. Wu, J. Wang and Y. Wang, "Proton conductivity CS/P(AA-AMPS) membrane with reduced methanol permeability for DMFCs," *Journal of Power Sources,* vol. 180, pp. 143 - 153, 2008.

[23] K. Kreuer, S. J. Paddison, E. Spohr and M. Schuster, "Transport in Proton Conductors for Fuel-Cell Applications: Simulations, Elementary Reactions, and Phenomenology," *Chemical Reviews,* vol. 104, pp. 4637-4678, 2004.

[24] C. Stefanescu, W. H. Daly and I. I. Negulescu, "Biocomposite films prepared from ionic liquid solutions of chitosan and cellulose," *Carbohydrate Polymers,* vol. 87, pp. 435 - 443, 2012.

[25] T. A. Zawodzinski, J. Davey, J. Valerio and S. Gottesfeld, "The Water Content Dependence of Electro-Osmotic Drag in Proton-Conducting Polymer Electrolytes," *Electrochimica Acta,* vol. 40, pp. 297 - 302, 1995.

[26] Y. Liu, J. Wang, H. Zhang, C. Ma, J. Liu, S. Cao and X. Zhang, "Enhancement of proton conductivity of chitosan membrane enabled by sulfonated graphene oxide under both hydrated and anhydrous conditions," *Journal of Power Sources,* vol. 269, pp. 898 - 911, 2014.

Study on the Effectiveness of Bond Strength Reduction in Separating Egg Membrane from the Shell

Revathi Kuppusamy[2], Rajesh Rajasekaran[1] and Phoon Chow Lin[1]*

[1]School of Engineering, Taylor's University, Malaysia

Abstract. Chicken eggs are common source of good quality and affordable protein which is essential for human body of all ages. Malaysians consumes 36.5 million eggs per day which generates large amount of waste eggshell annually and it is normally dispose as landfills. The membrane in the waste eggshell compose amino acids and partially contain collagen which has high monetary value. Therefore, it is necessary to find a possible solution which would transform the waste eggshell into valuable product. This project focused on the effectiveness of bond strength separation of the egg membrane from the shell. Three factors were taken into consideration for separating the eggshell membrane. The eggshells were soaked in sodium chloride (NaCl) of 1wt.% to 5 wt.% and in temperature from 30℃ to 5℃. The soaking duration was taken for 3 hours and 24 hours. Statistical analysis was performed on the readings that obtained. Collected data indicated that, soaking eggshells 3 wt.% of NaCl solution at 30℃, shows significance effect on reducing the peeling strength of egg membrane from the shell. The analysis of total protein content in membrane was analysed after the pre-treatment process. The total protein was loss by 14.33 % when compared to non-treated membrane. Treating in high temperature, showed high amount of protein loss.

[2] Corresponding author: ChowLin.Phoon@taylors.edu.my

1 Introduction

Chicken eggs provides a large amount of good quality source of protein essential for human body of all ages at cheapest price comparing with meat, poultry and fish. There are many ways of consuming eggs either directly in meals or used as food emulsifying agent in mayonnaise or as a raw material for making different types of foods such as bakery products, ice-cream. Therefore, eggs are an inexpensive source of high-quality protein that being consumed all over the world.

A recent study showed that Malaysians consumes 36.5 million eggs per day which generates large amount of waste eggshell annually [1]. Most of the eggshell waste is commonly disposed in landfill without any pre-treatment process as this food waste disposal method is widely accepted, cost effective and simple [2]. Recently, the landfill site has increased in an alarming rate resulting the scarcity of land, causes an increased in the cost of landfill tremendously. Besides, these eggshell waste draw in vermin which lead to an unhealthy environment and causes sickness.

Fundamentally, the eggshells waste consists of 92 % (w/w) egg shell and 8 % (w/w) organic fibre membrane [3]. The egg shells are rich in calcium carbonate which is used as a source of calcium in animal feed. The eggshell membranes are protein fibres which has high percentage of certain amino acids such as glutamine acid, methionine, arginine, proline and cysteine. The presence of hydroxyproline in hydrolysates of membrane layers suggest that the membrane contained 10% (w/w) collagen [4]. This collagenous protein can be a beneficial source for application in foods, cosmetics and biomedical materials. Thus, the membranes contain many bioactive compounds which have higher monetary value compare to egg shell [5]. There are many applications of separated egg shell and membrane but not many when they are attached together due to strong interaction of calcium carbonate crystals with organic matrix has made of eggshell and membrane difficult to separate and it resulted in limiting the value of the waste egg shells [6].

To the best of the author's knowledge, only limited number of information is known about its interaction strength and mechanical characteristics between the egg membrane and the shell. The only exception represents the paper of A. Hussain et al [7]. which is focused on the study of peeling bond strength of the egg membrane from the shell after the eggshell treated in microwave with different power density, soaking in hot water with different temperature over different duration. The results showed that microwave treatment with higher power density and longer duration of soaking time has significantly reduces the bond strength between the egg shell and membrane [7].

Previous researcher was developed a multi-beaded knife machine to scrape the membranes, and the membranes were physically separated from the egg shell in a tank filled with water by cavitation [5] . The shell particles being heavier than the membrane particles, precipitated at the bottom of the tank, while the lighter membranes are suspended in water. After removed the shell particles, the wet membrane is then dried by removing the excessive water that presence in the membrane. Besides, previous study has developed a separation processes by dissolving collagen of the egg membrane in acid solution and Ethylenediaminetetraacetic acid (EDTA) respectively. The egg shells were then removed by centrifuge method whereby the heavier egg shells settle down at the bottom of the tank. These separation processes generate large quantity of chemical waste. Thoroski JH. used pneumatic method to separate the crushed eggshell from the membrane after the eggshells were washed to remove the presence of pathogens and bacteria, and dried to remove the excessive moisture

content [8]. It was subsequently crushed into small pieces, and air was purged through it to separate the membrane from the crushed eggshell. Outcome from all these processes, it produces wet and small membrane size or flakes, which subsequently need to be dried before packing, and generated large quantity of waste fluids.

To the best of the author's knowledge, only limited number of information is known about its interaction strength and mechanical characteristics between the egg membrane and the shell. The only exception represents the paper of A. Hussain et al. which is focused on the study of peeling bond strength of the egg membrane from the shell after the eggshell treated in microwave with different power density, soaking in hot water with different temperature over different duration. The results showed that microwave treatment with higher power density and longer duration of soaking time has significantly reduces the bond strength between the egg shell and membrane [7].

In this study, sodium chloride, heat and duration of soaking were used as factors to reduce the bond strength of the membrane and eggshell. Concentrated sodium chloride has the tendency to weaken the bond between eggshell and the membrane and it is also widely used to remove the impurities such as lipid, pigment and pathogens [9, 10]. ANOVA test was also performed to identify the significance factors that affected the peeling strength. Besides, Kjedahl method is used to analyse the total protein content (g/ g) available after the pre-treatment process. Kjedahl method is normally treated with strong acid so that it releases nitrogen which can be determined by a suitable titration technique. The amount of protein present is then calculated from nitrogen concentration of the food. This is a standard method to determining protein concentration, because the Kjedahl method does not measure the protein content directly, therefore, a conversion factor (F) is needed to convert the measured nitrogen concentration to a protein concentration [11].

2 Material and methods

A quantitative research approach on the experiment data was carried out. This involves the process of analysing the peeling strength of the eggshell membrane from the treated eggshells and the total protein content in the treated eggshell membrane.

2.1 Factors affecting the separation of eggshell membrane

Factors that commonly used to manipulate is temperature, soaking in chemical for certain duration, microwave method and pneumatic membrane removal method (pressure). In this research, prior to separation of eggshell membrane, few experimental conditions were taken into consideration to determine optimum conditions in eggshell membrane separation using soaking method. The three parameters involved were temperature, NaCl concentration and soaking duration. Temperature range used in previous research to investigate the denaturation of protein was in the range of 70℃ -90℃. As mentioned earlier in the literature review, eggshell membrane contains collagen which has high monetary value. Types of collagen that can be found is collagen type I, V and X. These types of collagens are sensitive to high temperature condition. As reported on the previous study, collagen would denature and transform into gelation when being exposed to high temperature. Temperature range that taken in this study was from 30℃ to 45℃. The collagen started to denature at 50℃ onwards [12]. Nevertheless, if the temperature goes high, denaturation of eggshell membrane protein content might happen. Hence the range of temperature chosen for this temperature was 30℃ to 50℃.

Based on previous studies by Ponkham Walaiporn et al., EDTA was selected as solvent to separate the membrane. It proved the result was significant in separation when the eggshell was

mixed with 5 L of 5 % EDTA solution at the speed of 50 rpm for 30 minutes [9]. Apart from that, similar process separation was studied but using hydrochloric acid. The concentration of hydrochloric acid was used to study at 3 levels: 3 wt.%, 4 wt.% and 5 wt.% [13]. The separation of eggshell membrane increased when the concentration of hydrochloric acid increased. Higher concentration showed the most significant result [13]. Therefore, the concentration of NaCl was set from 1 wt.% to 5 wt.%. Another factor that affects the peeling strength of the eggshell membrane is soaking duration [7].

In previous research, the soaking duration for the membrane to separate the eggshell was varied from 0 to 48 hours. Longer soaking duration tends to increase the moisture content on the eggshell and membrane. Higher moisture content gives better respond to microwaves separation of eggshell membrane method [7].On the other hand, Maojie Zhang et al. studies showed that high moisture content makes the eggshell membrane difficult to separate manually, resulting in a lower recovery rate but higher residual rate [14]. Therefore, the soaking duration range used for this experiment was 3 to 24 hours. The factors and level of NaCl concentration duration of soaking and temperature are summarised in the Table 2.7. The eggshell heating at 40 ℃ and 50 ℃ were carried out in the oven.

Table 2.1: Experimental conditions for treating the strips of eggshells

Factors	Levels
Soaking Duration (Hours)	3
	24
Temperature (℃)	30
	40
	50
NaCl Concentration (wt. %)	1
	3
	5

2.2 Preparation of eggshell samples

Commercial chicken eggs of grade A were used in all the measurements. The albumin and egg yolks were discarded by making a small hole at the bottom end of the egg. The eggshells were then cut into strips by 10mm × 30mmin dimension at the meridian equator of the shell where the eggshell curvature was minimal and uniform using a Bosch Professional GWS 18V-LI cutter. The cutting work was done in the workshop (Cowah Engineering, Puchong) shown in Figure 3.5. It was than washed thoroughly with distilled water to remove any egg white residues sticking onto the surface of the membrane. The strips of eggshell were then soaked in different concentration of NaCl solution at 30 ℃, 40 ℃ and 50 ℃ for 3 hours and 24 hours, respectively.

2.3 Preparation of sodium chloride solution

Sodium chloride solutions were prepared at three different weight percentage: 1 wt.%, 3 wt.% and 5 wt.%. 1 wt.% of NaCl solution was prepared by adding 1 gram of sodium chloride into 100ml of distilled water. Then the solution was stirred until all NaCl solute completely dissolved in the water.

$$\frac{1g\ of\ NaCl}{100ml\ of\ distilled\ water} \times 100\% = \ 1\ wt\%\ of\ NaCl \quad (1)$$

The same method was used to prepare 3 wt.% and 5 wt.% of NaCl solution. Then the eggshells strips were placed into the beaker contain respective concentration of NaCl solution.

2.4 Heat treatment of eggshell

As reported on the previous study, collagen would denature and transform into gelation when being exposed to high temperature. Temperature range that taken in this study was from 30℃ to 45℃. The collagen started to denature at 50℃ onwards [12]. Nevertheless, if the temperature goes high, denaturation of eggshell membrane protein content might happen. Hence the range of temperature chosen for this temperature was 30℃ to 50℃.

2.5 Tensile testing on the eggshell membrane

Measurements of peeling strength of egg membrane from the shells were carried using a tensile testing machine which is (Instron – 5969) controlled by a computer software (BlueHills). The holder and clip for pulling the eggshell membrane was customized. The holder is slightly curved-shaped PVC screwed to a metal plate, while, the clip is a plastic peg attached to an iron rod. The experiment was set up as shown in Figure 3.6.

The treated and cut eggshell samples were glued on the PVC holder mounted on the tensile testing machine. Then, about 5mm of the membrane from the eggshell was manually detached and attached to the plastic peg which was connected to a 50N load cell. The experiment was followed ASTM D307-98 standard. the load cell moved upwards at the constant rate of 5mm/min, while the membrane was peeled as the peg moved upwards from the shell. The time taken, extension peel, and peeling strength per width of the sample were recorded. The average value of the three replicate measurement was used in the statistical analysis. At each experimented condition, three strips of eggshell were used for three replicate measurements.

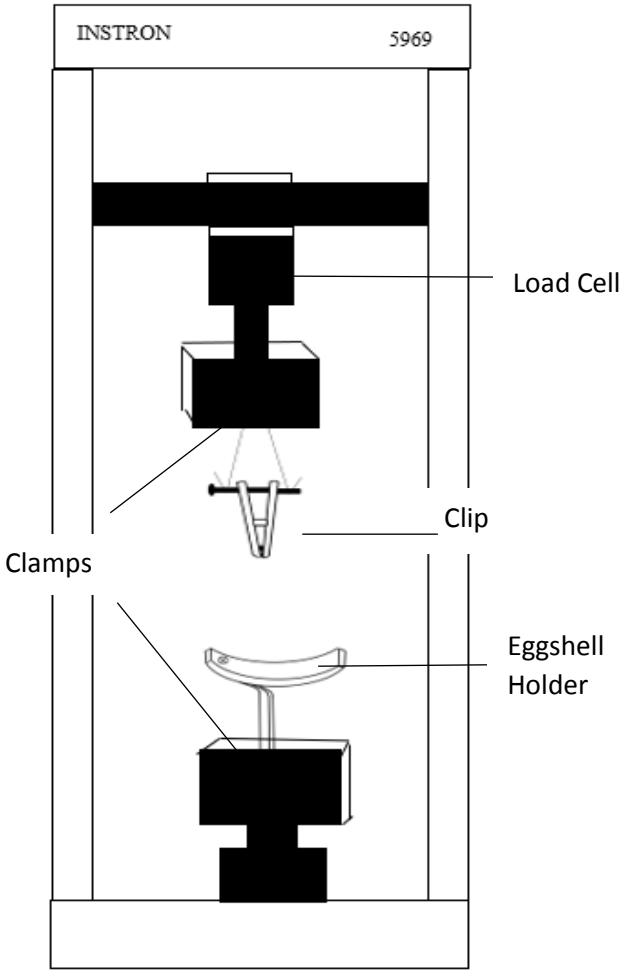


Figure 2.1. Experimental Setup for Tensile Test

2.6 Preparation for Total protein test on the treated egg membranes

Kjedahl method is normally treated with strong acid so that it releases nitrogen which can be determined by a suitable titration technique. The amount of protein present is then calculated from nitrogen concentration of the food.

This is a standard method for determining protein concentration, because the Kjedahl method does not measure the protein content directly, therefore, a conversion factor (F) is needed to convert the measured nitrogen concentration to a protein concentration[11] .

Kjedahl method was done in order to determine the total protein content in the eggshell membrane after it being treated in the sodium chloride solution. The eggshell membranes were pre-treated by following the method of Sadowska et al [15]. in order to remove the impurities such as soluble non-collagen compound, lipid, off-flavour and pigment. Four sets of samples each containing 100g of eggshell membrane were prepared.

The test was carried for temperature at 50℃ included one control sample. The membranes were soaked in 0 wt.%, 1 wt.%, 3 wt.% and 5 wt.% of NaCl solutions and all at 50℃. The control sample was not treated with NaCl solution and soaked at room temperature. Firstly, the non-collagen compounds were removed by washing in cold water. The membrane was then mixed with cold water (1:6 w/v) by using magnetic stirrer for three minutes. Then the retentate

membrane was homogenized with distilled water for (1:6 w/v) at 6000 rpm for four minutes. After that, the retentate membrane was washed with distilled water (1:6 w/v) and centrifuged at 2000 rpm, for 30 min.

3 Result and Discussion

3.1 Effect of Temperature and Concentration in 3 hours Soaking Duration

The eggshell strips were soaked in the sodium chloride solution (1 wt.%, 3 wt.%, 5 wt.% and one control sample which soaked in distilled water without adding NaCl) for 3 hours before the tensile test was carried out. Three strips of eggshell were used for three replicates measurement at each condition. The average value (N/m) of the peeling strength of three replicates measurement are presented in Table 3.1 under different NaCl concentrations and temperature conditions.

Table 3.1. Data for the peeling strength (N/m) after 3 hours of soaking

Temperature	**NaCl Concentration (wt.%)**			
(℃)	0	1	3	5
30	40.75	42.38	27.22	46.78
40	31.55	41.19	38.20	41.00
50	26.96	31.23	41.28	52.09

Based on Figure 3.1, there are rise and fall in the readings for temperature of 30℃ and 40℃. The peeling strength at 30℃ was increased from 40.75 N/m to 42.37 N/m when the NaCl increased from 0 wt.% to 1 wt.%. At NaCl concentration of 3 wt.%, the peeling force dropped dramatically from 42.37 N/m to 27.22 N/m. Then it increased back from 27.22 N/m to 46.7869 at the 5 wt.% sodium chloride concentration. The tensile readings at 40℃ also increase from 31.546 to 41.1916 when the NaCl concentration increased from 0 wt.% to 1 wt.%. Then, the peeling force reading dropped to 38.20 N/m in 3 wt.% of NaCl concentration and escalated to 41.00 N/m in 5 wt.% of NaCl concentration. The readings of temperature of 50℃ showed a gradual increase compare to the other two temperatures. The readings were increased from 26.96 N/m to 52.09 N/m.

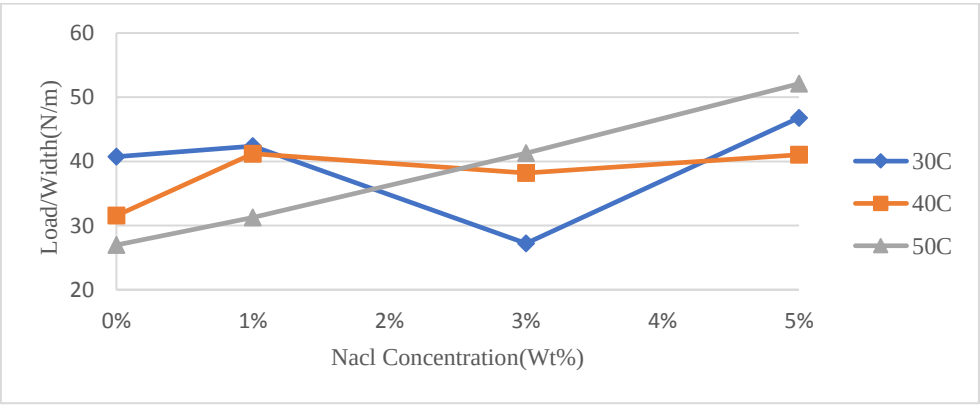


Figure 3.1. Peeling Strength against NaCl Concentration of Soaking for 3 hours

NaCl concentration have significance factor which effects the peeling strength of the eggshell membrane. Figure 3.1 showed effects of temperature after soaking for 3 hours in NaCl concentration. It is clearly shown that the NaCl concentration does influence the tensile force

for peeling the membrane from the eggshell. The concentrated NaCl penetrates through the pores of the most outer layer of the eggshell. By doing so, it tends to weaken the bond between eggshell and the membrane [10].

Based on this result, the peeling strength of the eggshell membrane at 30℃ after soaking in 3 wt.% has the lowest peeling strength value, 27.22 N/m. This indicated less force was used to peel the eggshell and membrane. The peeling strength of eggshell membrane is low when it soaked for 30℃. The heat at 30℃ is little and can be considered as surrounding temperature. Where the current surrounding temperature in Peninsula Malaysia is in the range of 29℃ to 30℃ [16]. Previous study was done on the separation of eggshell and membrane using EDTA solution at room temperature [9]. A study by Hussain et al. was proven that heat had no effect on the bond energy between eggshell and membrane and for the same reason factors of temperature was not extensively studied [7].

Analysis of Variance was performed for the temperature, concentration and the interaction between both which were shown in Table 3.2. From the statistical analysis, the temperature showed p-value is more than 0.857 which indicate insignificance. On the other side, the concentration factor was ($p < 0.01$) which was indicated as significance. This showed concentration does affects the peeling strength. Interaction between temperature and concentration shows a marginal effect on the peeling strength. This shows the temperature has effect when it interacts with concentrated NaCl solution.

Table 3.1.2 ANOVA Table of Peeling Strength after 3 hours of Soaking

Source	SS	df	MS	F	p-value
Model	1943.417	11	176.674	2.552	0.027
Intercept	53130.250	1	53130.25	767.532	0.000
Temperature	21.500	2	10.750	0.155	0.857
Concentration	934.306	3	311.435	4.499	0.010
Temperature*Concentration	987.611	6	164.602	2.378	0.060
Error	1661.33	24	69.22		
Total	56735.00	36			
R^2	0.539				
Adjusted R^2	0.328				

3.2 Effect of Temperature and Concentration at 24 hours of Soaking Duration

The eggshell strips were soaked in the sodium chloride solution (1 wt.%, 3 wt.%, 5 wt.% and one control sample which soaked in distilled water without adding NaCl) for 24 hours before the tensile test was carried out. Three strips of eggshell were used for three replicates measurement at each condition. The average value (N/m) of the peeling strength of three replicates measurement are presented in Table 3.2 under different NaCl concentrations and temperature conditions.

Table 3.2.1 Data for the peeling strength (N/m) after 24 hours of soaking

Temperature (℃)	NaCl Concentration (wt.%)			
	0	1	3	5
30	44.22	44.05	48.59	44.62
40	39.98	41.18	41.61	48.45
50	59.77	50.10	47.79	49.62

Figure 3.2. showed effects of temperature after soaking for 24 hours in NaCl concentration. The eggshell strips were soaked at 30℃, 40℃ and 50℃ and the concentration of NaCl used for soaking it is 1 wt.%, 3wt, 5 wt.% and one control which has soaked in distilled water without adding NaCl.

After the eggshell strips were soaked in the NaCl solution for 24 hours, the graph trend indicated the peeling force has a rise and fall readings as the concentration of sodium chloride increased. The readings at 40℃ shows an upward trend from 39.97 N/m to 48.45 N/m as the NaCl concentration increases from 0 wt.% to 5 wt.%. the readings for 30℃ and 50℃ were rise and fall. At 30℃ the peel force was increased from 44.21 N/m to 48.59 N/m when the NaCl concentration increased from 0 wt.% to 3 wt.%. Then it was declined at 5 wt.% and fell to 44.61N/m. The peeling strength of the eggshell membrane at 50℃ were also decreased from 59.76 N/m to 47.78N/m when the NaCl concentration was increased from 0 wt.% to 3 wt.%. Subsequently, it rose gradually from 47.78 N/m to 49.61N/m when the NaCl increased from 3 wt.% to 5 wt.%.

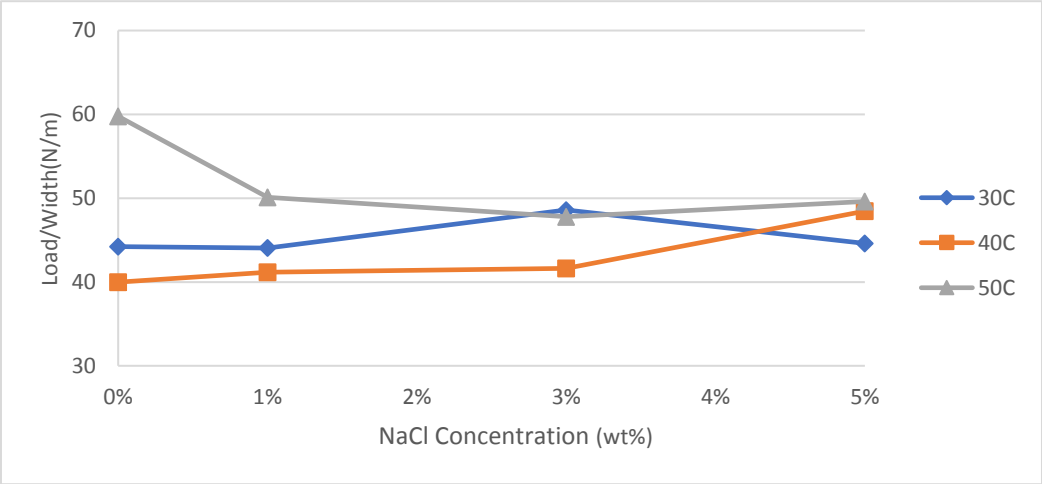


Figure: 3.2. Peeling Strength against NaCl concentration at 24 hours of Soaking

The peeling strength readings are slightly higher than the values obtain for 3 hours of soaking duration eggshell membrane. Soaking the eggshells for 24 hours tends to have high moisture content. High moisture content makes the eggshell membrane difficult to separate, resulting in a lower recovery rate but higher residual rate [14]. Also, changed the fibre structure of membrane and adhesion of membrane and shell [7].

From the ANOVA statistical analysis on all collected data, there was no significant effect of concentration, temperature and the interaction between them on the peeling strength of the membrane from the Table 3.2.2 ($p < 0.01$).

Table 3.2.2 ANOVA analysis of peeling Strength after 24 hours of soaking

Source	SS	df	MS	F	p-Value
Model	953.143	11	86.649	1.265	0.302
Intercept	78391.600	1	78391.600	1144.353	0.000
Temperature	517.318	2	258.659	3.776	0.038
Concentration	48.895	3	16.298	0.238	0.869
Temperature*Concentration	386.929	6	64.488	0.941	0.484
Error	1644.071	24	68.503		
Total	80988.815	36			
R^2	0.367				
Adjusted R^2	0.077				

3.3 Comparative study of Peel Strength between 3 hours and 24 hours

In the result, 3 hours of soaking duration showed lesser peeling strength than 24 hours of soaking duration. The peeling strength for 3 hours of soaking in concentrated NaCl solution on the eggshell strip shown the range between 25 N/m to 52 N/m, while the peeling strength for 24 hours shown the range between 40 N/m to 60 N/m. Figure 3.3a, Figure 3.3b, Figure 3.3c shows the comparison of soaking duration of 1 wt.%, 3 wt.% and 5 wt.% of NaCl concentration at different temperature conditions. This proves that soaking the eggshell strips for 24 hours changed the fibre structure of membrane and adhesion of membrane and shell, resulted in increasing the peel strength [7].

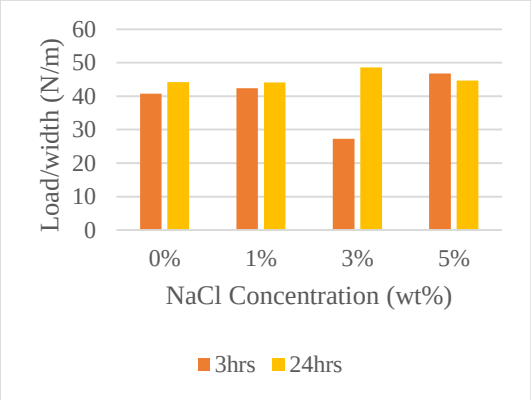


Figure 3.3a: Effect of peeling strength at 30℃

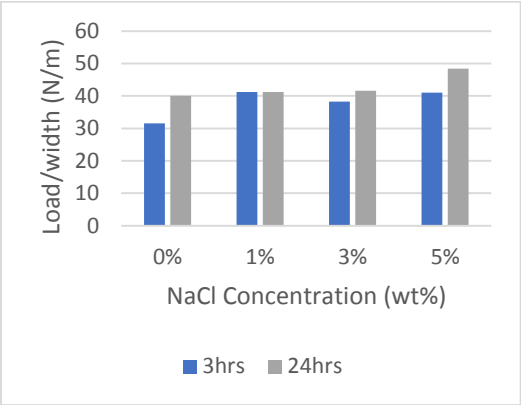


Figure 3.3b: Effect of peeling strength at 40℃

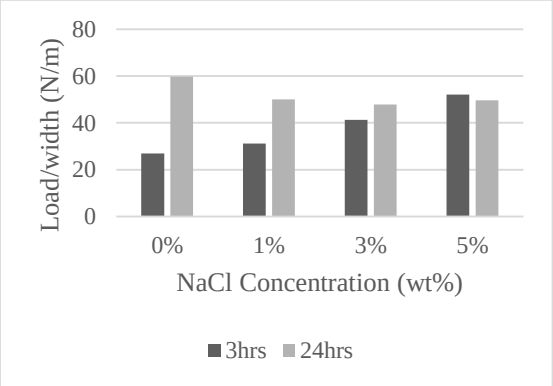


Figure 3.3c: Effect of peeling strength at 50℃

3.4 Total protein test by Kjedahl method

Total protein content test was carried out to determine the total protein that available in the membrane after treated with certain temperatures and NaCl concentration. Kjedahl method was used to determine the total protein content. Table 3.4 showed the total protein content in the eggshell membrane at different concentration of NaCl solutions and temperature.

Table 3.4 Total Protein content at different conditions

Eggshell membrane condition	Protein Content (g/100g)

30℃, 0 wt.%, 24 hours (Control Sample)	5.37
50℃, 0 wt.%, 24 hours	5.05
50℃, 1 wt.%, 24 hours	5.09
50℃, 3 wt.%, 24 hours	4.08
50℃, 5 wt.%, 24 hours	4.60

As, the eggshell membrane consists of active sites which induce the nucleation of the mineral, in consequence it has an active role in the calcite crystal growth. The calcite crystal and the active sites are bonded together even though the membrane is subjected to immersion in any solutions. This is because, some of the mineral are closely bonded with the fibres of the eggshell membrane [17]. Therefore, some protein content can be found due to the strong relationship between calcite crystal and the active sites. The total protein content at for the control sample is 5.37 g/g while the protein content at 0 wt.% at 50℃ is 5.05 g/g. Based on this result, it shown that 6 % of protein were loss after it being heated at 50℃. Besides, the total protein content at 50℃ decrease from 5.37 to 4.60 as the NaCl concentration increased from 0 wt.% to 5 wt.%. 14.33 % of protein were loss when the NaCl concentration was increased from 0 wt.% to 5 wt.%. Some protein content was loss due to the temperature. Based on previous study, Collagen Type I denatured when the temperature exceeded 50℃ [12]. This justified on the loss of the total protein content. It is proven that there is protein loss due to the temperature effect[23].

4 Conclusion

In conclusion, soaking in concentrated NaCl solution for 3 hours showed significance effect on the peeling strength. ($p<0.01$). where, the temperature does not show any significant effect on the peeling strength. However, temperature is marginally significance when it was interacting with concentration. Besides, the other set of readings of peeling strength at 24 hours of soaking in concentrated NaCl at different temperature does not showed any significance. Therefore, suitable condition to peel the membrane is at 3 hours and with soaking the eggshells in concentrated NaCl solution. Besides, Kjedahl method were used to analyse the total protein content available after the pre-treatment process. The total protein was loss by 14.33% when compared to non-treated membrane. Highest concentrated NaCl showed highest amount of protein loss. The effectiveness of peeling strength using concentrated NaCl solution were not only determines the source of revenue for egg processing industry, but it will have a significant impact on the environmental and disposal cost that associated with waste eggshells.

5 Reference

[1] Charlotte Chong, "*Teo Seng: Malaysia's egg consumption to grow at 3% to 5%*," The Edge Market, Kuala Lumpur, (2015)

[2] Mohamad Anuar Kamaruddin, Mohd Suffian Yusoff, Nurazim Ibrahim and Mohd Hafiz Zawawi, *"Resources Recovery from Municipal Solid Waste by Mechanical Heat Treatment: An Opportunity*," Resource recovery from municipal solid waste by mechanical heat treatment, (2017)

[3] Matej Balaz, *"Eggshell membrane biomaterial as a platform for application in material sciene,"* Acta Biomaterialia, **vol. 10**, no. 9, pp. 3827-3843, (2014)

[4] Zhangguo Liu, Lingzi Song and Fuming Zhang, *"Comparative proteomics of matrix fraction between pimpled and normal chicken eggshells,*" Journal Proteomics, **vol. 167**, pp. 1-11, (2017)

[5] J. H.MacNeil, *"Method and Apparatus for Separating a Protein Membrane and Shell Material in Waste Egg Shells". United State Patent US6176376B1*, (2001)

[6] Sunho Park et al., *"Eggshell membrane: Review and impact on enginnering,"* Biosystem Engineering , pp. 446-463, (2016)

[7] Hussain.A.,SRS Dev., Gariepy.Y, Ragavan.G.S.V, "*Microwave-Assisted Separation of Eggshell and Membrane,"* World Congress of the International Commision of Agricultural and Biosystem Engineering, pp. 2-10, (2010)

[8] J. H. Thoroski, *"Eggshell Processing methods and Apparatus"*. US Patent US Patent 6649203 (2004)

[9] Ponkham Walaiporn, Kullaya Limroongreungrat, Sangnark Arpathsa , *"Extraction of Collagen from Hen Eggshell Membrane by Using Organic Acids,"* International Conference on Agriculture and Agro-Industry, pp. 2-4, (2010)

[10] X.D. Chen, Y.Freeman, F. Guo And P.Chen, *"Diffusion Of Sodium Chloride Through Chicken Eggshell In Relation To An Ancient Method Of Egg Preservation,"* Food Science and Process Engineering Group, **vol. 77**, pp. 41-46, (1999)

[11] Tadau Eder da Silva, Edenio Detmann, Marcia de Oliveira Franco, Malber Nathan Nobre Palma and Gabriel Cipriano Rocha, *"Evaluation of Digestion Procedures in Kjeldahl method to quality total nitrogen in analyses applied to animal nutrition,"* Animal Science, **vol. 38**, no. 1, pp. 45-51, (2016)

[12] Wentao Liu and Guoying Li, *"Non-isothermal kinetic analysis of the thermal denaturation of type I collagen in solution using isoconventional and multivariate non-linear regression methods,"* Polymer Degradation and Stability, no. 95, pp. 2233-2240, (2010)

[13] Wunwiboon Garnjanagoonchorn and Alongkot Changpuak, *"Preparation and Partial Characterization of Eggshell Calcium Chloride,"* International Journal of Food Properties , pp. 497-503, (2007)

[14] Maojie Zhang, Ning Wang, Qi Xu, Putri Widyanti Harlina and Meihu Ma, *"An Efficient Method for CO-purification of Eggshell Matrix Protein OC-17, OC-116 and OCX-36,"* Korean J Food Sci Anim Resour, **vol. 36**, no. 6, pp. 769-778, (2016)

[15] S. e. al, *"Evolution of basal metabolic rate in bank voles from a multidirectional selection experiemnt,"* Biological Science, (2015)

[16] Fredolin T.Tangang, Liew Juneng, Ester Salimun, Kwan Meng Sei,Loh Hui Le And Halimatun Muhamad, *"Climate Change and Variability over Malaysia: Gaps in Science and Research Information,"* Science Malaysiana, no. 11, pp. 1355-1366, (2017)

[17] Adriana Torres-Mansilla et al., *"Influence of Separation Techniques with Acid Solutions on the Composition of Eggshell Membrane,"* International Journal of Poultry Science, **vol. 16**, no. 11, pp. 451-456, (2017)

[18] Msarah M. and Alsier A. , *"Protein Digestibility and Amino Acid Content of Malaysian Local Egg Preotein Prepared by Different Methods,"* Environment & Ecosystem Science, pp. 7-9, (2018)

[19] Kullaya Limroongreungrat and Arpathsra Sangnark, *"Extraction of Collogen from hen eggshell membrane by using organic acids,"* ResearchGate, pp. 1-6, (2011)

[20] H.Lin, K.Mertens,B.Kemps, T.Govaerts, B. De Ketelaere, J.De Baedemarker, E.Decuypere, *"New Approach of Testing The Effect of Heat Stress on Eggshell Quality: Mechanical and Material Properties of Eggshell and Membrane,"* British Poultry Science, pp. 476-481, (2010)

Enrichment of Aerobic Sludge for Microbial Protein Production from Palm Oil Mill Effluent (POME)

Sathishkumar Nalatambi[*], *Li Wan Yoon*[1*], *Yoke Kin Wan*[1], *Adeline Seak May Chua*[2]

[1]School of Engineering, Taylor's University, Malaysia

[2]Department of Chemical Engineering, Faculty of Engineering, University of Malaya, Malaysia

[*]sathishkumar.nalatambi@sd.taylors.edu.my

*Corresponding author: LiWan.Yoon@taylors.edu.my

Abstract. Production of microbial protein (MP) as alternative protein maintains the balance for highly nutritious protein as food and feed source, where enrichment process is necessary to yield high protein content. This research work done investigated the effect of different types and dosage of nutrients for microbial protein production through aerobically enriched sludge. Mixed culture of aerobic sludge enriched with Palm Oil Mill Effluent (POME) as carbon (C) source and ammonium chloride and potassium dihydrogen phosphate added as nitrogen (N) and phosphorus (P) source respectively. Enrichment process operated under aerobic condition and pH, temperature, aeration rate, string rate and sludge retention time (SRT) and hydraulic retention time (HRT) fix at 7,28℃, 1 vvm, 450 rpm and 2 days respectively. The operation run with different nutrients dosage, C: N: P ratio: a) 92.3: 8.4: 1 (N-50% excess), b) 92.3: 11.2: 1 (N-100% excess) and c) 92.3: 5.6: 1 (stoichiometric ratio). The process operated continuously until stable mixed liquor volatile suspended solid (MLVSS) and chemical oxygen demand (COD) observed and the protein content analysed for the first and last day of operation. All three nutrients ratio reduced the COD concentration with range of 90-92%. N-50% excess nutrient ratio produced highest protein content, 55% and followed by N-100% excess at 40%. However, both conditions have similar specific protein production rate, which is 0.0031 mg/day. N-100% excess has the highest specific substrate consumption, which is 0.08 mg/day and followed by N-50% excess and stoichiometric ratio at 0.04 mg/day and 0.03 mg/day respectively. With that being said, the finding in this report demonstrates a new effective strategy for MP production through enrichment of aerobic sludge with POME and additional nutrients sources. This strategy serves 2 purposes where POME is treated along with MP production. Apart from promotion to a more sustainable POME management, it proved to function as value added waste feedstock.

Keywords: microbial protein, enrichment, mixed culture, palm oil mill effluent (POME), activated sludge

1.Introduction

In current modernisation era, alternative protein or commonly referred as microbial protein (MP) has been receiving tremendous attention that led to a promising option as replacement of natural protein such as animal and plant based protein. Moreover, escalating global population has put immense need to find alternatives proteins for sustainable consumption of mass population. United Nation (UN) recently produced a report stating that the global population expected to increase from 7 billion to 9.6 billion by 2050 whereby the current global population as per 2017 is 7.6 billion [1]. Henchio et al [2] reported that with 7.6 billion global populations, the protein demand is approximately 202 million tonnes globally and expected incline to 206 million tonnes per year. Dependency on animal and plant based protein contributes to 12% greenhouse gas (GHG) emission and other negatives implications associated with deforestation and conversion of agriculture land [3]. In addition, plant-based proteins require acres of land for agriculture and the production is limited due to seasonal based production. These constrains contributed for MP to emerge as feasible and cost effective technology and mushrooming scholarly research have been done on MP production.

Many contemporary studies successfully derived MP production from waste materials. For instance, Khan et al [4] and Steven et al [5] produced 58.62% of protein from waste banana skin with pure yeast strain of *Saccharomyces Cerevisiae* and 40% of crude protein from potato processing waste with pure culture of *Cephalosporium Eichhorniae*. Comparative to fruit waste, agriculture waste typically high in carbon, which is necessary food source for the microorganism where Asmamaw et al [6] utilized apple pomace to produce MP. In Malaysia, palm oil industry is deemed to be one of the sustainable industries that need to ensure that its entire production and supply chain are in line with globally accepted environment requirements. Palm oil produced from fresh fruit bunch (FFB), whereby it undergoes a series of sterilization, threshing, digestion, pressing and oil purification process. Alongside palm oil production, high strength wastewater namely palm oil mill effluent (POME) produced. Typically, 2.5 tonnes of POME produced for every one-ton of palm oil production [7]. POME is a brownish acidic wastewater with extremely high chemical oxygen demand (COD) level, 22500 – 74000 ppm [8,9]. This is a clear indication of proper POME management is required. In general, POME undergoes several treatment processes including anaerobic and aerobic process with surface aerators prior to discharge. A plethora studies have been done for treatment-oriented management of POME in accordance to discharge limit but most of the studies overlooked the facts of POME as an extremely potential candidate for many waste derived products. Transformation of POME from waste to a value-added product has been continuously proven with polyhydroxyalkanoates (PHA) production from microorganism [10,11]. Nonetheless, very limited research has been done for MP production from POME.

In regard to direct MP production from POME, Onyekachi [12] reported one out seven-isolates yeast from POME yield 4.42 g/L of microbial protein. Most research methodology of MP production focused on pure culture. However, mixed culture has the tendency to yield even higher protein content and it is coupled with several advantages. Productions of MP through mixed culture will not only yield higher protein content but associated with cost reduction. Pure culture requires a specific operating condition and a single strain of microbe is far expensive than mixed culture and this concludes the reason of mixed culture being a cost-effective MP production methodology. Yadav et al [13] did a comparative study for MP

production between pure and mixed culture of yeast and mixed culture yielded additional 8% higher protein content than pure culture and this finding tally with Yunus et al [14] and Dhanasekaran et al [15] findings whereby mixed culture has the tendency to yield higher protein content. Although, mixed culture of yeast has been widely explored for MP production, there are very limited studies have been done on mixed culture of bacteria. The most common source of bacterial mixed culture is activated sludge where Honda et al [16] reported 72.7% of MP production through mixed culture of bacteria. Despite higher protein yield through mixed culture condition, the result is much robust with enrichment process adaptation.

In the context of bio-operation, enrichment is imperative to consider once the process tailored to mixed culture condition. This is due to the availability of varieties species of microbes in the mixed culture medium and due to the incompetency of certain species to produce the desired product. Through enrichment, the species that able to produce the desired product will continuously enriched and survive while the remaining will be eliminated from the system depending on the sludge retention time (SRT) and hydraulic retention time (HRT). In the available literature, enrichment process has repeatedly ameliorate the bioprocess efficiency and it is projected in polyhydroxyalkanoates (PHA) production where mixed culture aerobic sludge enriched with C: N: P ratio of 100:5:1. Chen et al [17], Mengmeng et al [18] and Valentino et al [19] enriched activated sludge with ammonium chloride as the nitrogen source and potassium dihyrogen phosphate as the phosphorus source and led greater yield of PHA. Recent novel discovery of Matassa et al [20] through production of MP with hydrogen-oxidizing bacteria showed that enrichment process resulted in 71% of protein content.

Although MP production has been receiving tremendous attention, there are several gaps that can be closed through this research. MP has been predominantly produced through either alternating anaerobic-aerobic or aerobic condition. In addition, most research on MP production was done on comparative basis of pure and mixed culture of yeasts. Comparative to other parameters, the manipulation of nutrients dosage has a greater impact of the production of microbial protein. Therefore, enrichment of mixed culture sludge with nutrients dosage variation and POME as the sole carbon source is of particular interest in this research. POME lacks with nitrogen and phosphate source, which is necessary for protein production. As such, additional of nutrients (nitrogen (N) and phosphate (P)) source has the potential to be the decisive factor to yield higher protein content. In order to evaluate the feasibility of combined component of POME and activated mixed culture sludge for MP production, the activated sludge enriched with excess nutrients dosage under aerobic condition without pH variation. Henceforth, this study investigated the effect of different types and dosage of nutrients on MP production, whereby the nutrients dosage set at a) 92.3: 5.6: 1 (stoichiometric ratio), b) 92.3: 8.4: 1 (N-50% excess) and c) 92.3: 11.2: 1 (N-100% excess).

2. Methodology

2.1 Materials

One batch (35 L) raw POME collected from local palm oil mill, Seri Ulu Langat Palm Mill. Activated sludge (5 L) collected from local sewage treatment plant, Indah Water Konsortium (IWK), Puchong. For nutrients solution preparation, ammonium chloride ($\geq 99.8\%$, Merck), potassium dihydrogen phosphate ($\geq 99.5\%$, Merck) used as nitrogen (N) and phosphate (P) source respectively as well as N-allylthiourea ($\geq 98\%$, Merck) to inhibit nitrification. In addition, iron (III) chloride hexahydrate, ethylenediamine tetra acetic acid (EDTA), potassium

iodide, boric acid, cobalt (II) chloride hexahydrate, manganese (II) chloride tetrahydrate, zinc sulphate heptahydrate, sodium molybdate dehydrate and copper (II) sulphate pentahydrate purchased from Merck for trace nutrients preparation.

2.2 Characterization of POME

Upon collection of POME, it was placed in chiller and preserved at 4℃ for 24 h in order to prevent biodegradation of POME due to microorganism activities and promote conventional gravitational solid settling to reduce its solid content. Through settling phase, the supernatant separated from raw POME and remained preserved at 4℃ for enrichment process. Samples from both raw POME and supernatant of settled POME characterized for pH, soluble chemical oxygen demand (sCOD), total chemical oxygen demand (TCOD), total suspended solids (TSS) and volatile suspended solids (VSS).

2.3 Enrichment of Aerobic Sludge with POME

2.3.1 Operation of Aerobic Sludge Enrichment

An aerobic operating sequencing batch reactor (SBR, working volume of 0.6 L) was used for enrichment of aerobic sludge for microbial protein production from POME at room temperature $(30℃ \pm 1℃)$ and pH of 7. The reactor was inoculated with re-suspended activated sludge with nutrients solution at 3000 mg/L and POME with 3000 mg (COD basis) /L. Air was supplied to the reactor at 1 vvm. The reactor operated at 24 h per cycle. Each cycle consisted of 2 phases: (a) 10-min of simultaneous feeding of 0.15 L of POME (carbon substrate) and 0.15 L of nutrient solution (N and P source) and purging of 0.3 L through peristaltic pump (Cole Parmer/ Masterflex/ USA), (b) 23.8-h of aerobic reaction phase. There was no settling phase involved and resulting in equal sludge retention time (SRT) and hydraulic retention time (HRT) of 2 days and the reactor continuously stirred at 450 rpm. The enrichment process started with stoichiometric ratio with C: N: P ratio of 92.3: 5.6:1. Ammonium chloride and potassium dihydrogen phosphate used as nitrogen (N) and phosphate (P) source respectively. Magnesium sulphate was added at fixed concentration of 660 mg/L while N-Allylthiourea added at fixed concentration of 50 mg/L to prevent nitrification. Alongside macronutrients, trace element adapted from Ong et al [20] was added in to provide additional supplements for microbial growth. The trace element consisted of (concentration in mg/L): EDTA (14400 mg/L), $FeCl_3 \cdot 6H_2O$ (2160 mg/L), KI (260 mg/L), H_3BO_3 (220 mg/L), $CoCl_2 \cdot 6H_2O$ (220 mg/L), $MnCl_2 \cdot 4H_2O$ (170 mg/L), $ZnSO_4 \cdot 7H_2O$ (170 mg/L), $Na_2MoO_4 \cdot 2H_2O$ (80 mg/L), $CuSO_4 \cdot 5H_2O$ (50 mg/L). The process was run continuously until stable COD and mixed liquor volatile suspended solids (MLVSS) were achieved where sample was taken at intervals of 2 days. At the end of enrichment operation, the sample was also subjected to Kjeldahl nitrogen content to evaluate the protein content as well as ammoniacal-nitrogen content.

2.3.2 MP production at different nutrients dosage

In order to yield higher protein content under similar condition, the effect of different nutrients dosage was investigated. Henceforth, under similar condition as section 2.3.1 without remaining parameters alterations the nutrients dosage (C: N: P) was varied at 2 high levels: (a) 92.3:8.4:1 (N-50% excess), (b) 92.3: 11.2: 1 (N-100% excess). The enrichment process was started with nutrient dosage of 92.3:8.4:1 (N-50% excess) and new batch of re-suspended activated sludge. Upon stable condition, the enrichment process was continued with nutrient dosage of 92.3: 11.2: 1 (N-100% excess). Both conditions were operated one after another

continuously until stable COD and MLVSS were achieved where samples were withdrawn at intervals of 2 days. At the end of enrichment operation, the sample was also subjected to Kjeldahl nitrogen content to evaluate the protein content as well as ammoniacal-nitrogen content.

2.4 Analytical Methods

Mixed liquor suspended solid (MLSS) and mixed liquor volatile suspended solid (MLVSS) were determined based on American Public Health Association (APHA, 1992) standard method [21]. For MLSS analysis, samples were filtered and heated with oven (Jouan/ Strarts Scientific/ Malaysia) at $103℃ \pm 2℃$ for 1 h. On the other hand, MLVSS analysis was heated at $550℃ \pm 50℃$ with furnace (Thermconcept/ Fisher Scientific/ Malaysia) for 15 min.

COD was determined with COD test kit (Merck/ Rance: 25-1000 mg/L) where 3 ml of filtered samples mixed with the test kit and heated for 2 h with thermo reactor. Once that, the COD measured with photometer (Merck/ Spectroquant Prove 300/ Germany). For protein analysis, Kjeldhal nitrogen content was adapted, where sample mixed with sulphuric acid and heated to $350℃ - 380℃$. Upon digestion, samples was cooled down to room temperature and diluted with ultrapure water and transferred to distillation unit in which, ammonium ion converted to ammonia through addition of alkaline solution. Once that, the captured ammonium ion undergoes titration and the amount of ammonia was evaluated. Ion chromatography (861 Advanced Compact IC, Metrohm, Switzerland) with Metrosep C4-150/4 column was used to determine ammonium concentration.

2.5 Performance Evaluation

The MP production through enrichment process was evaluated based on Equation (1):

$$\text{Protein content} = \frac{\text{Protein}}{\text{MLVSS}} \times 100\% \quad (1)$$

On the other hand, specific substrate consumption rate $(-q_s)$, specific protein production rate $(q_{protein})$, specific and percentage COD reduction were computed based on Equation (2)-(4) respectively. The cell concentration was taken as the difference in concentration between MLVSS and protein [22].

$$-\mathrm{q_s} = \frac{\text{sCOD consumed}}{\text{initial cell concentration} \times \text{duration of experiment}} = \frac{\mathrm{sCOD_{initial} - sCOD_{final}}}{\mathrm{X_{initial} \times time}} \quad (2)$$

$$\mathrm{q_{protein}} = \frac{\text{protein produced}}{\text{initial cell concentration} \times \text{duration of experiment}} = \frac{\mathrm{Protein_{final} - Protein_{initial}}}{\mathrm{X_{initial} \times time}} \quad (3)$$

$$\%\ \text{COD reduction} = \frac{\mathrm{sCOD_{initial} - sCOD_{final}}}{\mathrm{sCOD_{initial}}} \times 100\% \quad (4)$$

The protein and biomass yields on the substrate consumed were computed based on Equation (5)-(6).

$$\left(\mathrm{Y_{protein/substrate}}\right) = \frac{\text{Protein produced}}{\text{Substrate consumed}} = \frac{\mathrm{Protein_{final} - Protein_{initial}}}{\mathrm{sCOD_{initial} - sCOD_{final}}} \quad (5)$$

$$\left(Y_{mlvss/substrate}\right) = \frac{\text{Cell produced}}{\text{Substrate consumed}} = \frac{X_{final} - X_{initial}}{sCOD_{initial} - sCOD_{final}} \quad (6)$$

3. Results and Discussion

3.1 Characterization of POME

The characteristics of raw and supernatant of settled POME are presented in Table 1. Based on Table 1, it can be said that POME is an acidic wastewater rich in organic matter that contains lots of suspended solids. The reduction of suspended solids was achieved with 24 h of gravitational solid settling. This result was reflected with TSS value of raw and supernatant of settled POME. It was found that 91% of TSS was removed with simple yet conventional settling technique and resulting in final TSS concentration of 1450 mg/L.

Table 8. Characterization of POME and supernatant of settled POME.

Parameters	Raw POME	Supernatant of Settled POME
pH	4.6 ± 0.2	4.6 ± 0.2
TSS (mg/L)	15510 ± 2163	1450 ± 183
VSS (mg/L)	13780 ± 1951	1020 ± 141
TCOD (mg/L)	70950 ± 2474	40250 ± 1767
sCOD (mg/L)	34350 ± 1484	37350 ± 1484
sCOD/TCOD	0.48 ± 0.004	0.92 ± 0.078
Ammoniacal-Nitrogen (mg/L)	109.31	95.43

The resultant effect of TSS reduction was observed alongside with TCOD reduction, where it was reduced from 70950 mg/L to 40250 mg/L. Regardless of such reduction, the value is still high enough to consider as suitable food source for MP production as it remained rich with organic matter. In addition, most organic matter is soluble as indicated by supernatant of settled POME sCOD/TCOD ratio of 0.92. This ratio is almost double as it sCOD/TCOD ratio of POME that is 0.48. The high fraction of soluble organic matters in the supernatant of settled POME is highly privileged to microorganism as they could easily attain and consume the rich organic matters for MP production.

3.2 Feasibility of direct application of activated sludge and POME for MP production

In this study, activated sludge from local sewage treatment plant was cultivated for MP production with POME. Prior for MP production, activated sludge was subjected to initial protein content and POME for nitrogen content. The results showed that raw POME and supernatant of settled POME has ammoniacal nitrogen content of 109.31 mg/L and 95.43 mg/L respectively as presented in Table 1. This is an indication that sole reliance of POME, as nitrogen source for MP production is not feasible. In addition, activated sludge showed an initial protein content of 10.4%. Henceforth, additional nitrogen source under excess condition will help to boast the MP production with high protein yield.

3.3 Enrichment of activated sludge

In order to enrich activated sludge with POME and additional nutrient sources for MP production, an aerobic enrichment operating SBR was established. The process was operated at 30℃ with SRT and HRT of equal 2 days as no settling phase involved. Besides that, air was

supplied at 1 vvm without any dissolved oxygen (DO) control and pH was set at 7 without continuous pH control. POME and nutrients feed daily into the reactor at a combined volume of 0.3 L. The first enrichment process started with stoichiometric C: N: P ratio, which is 92.3: 5.6:1 and lasted for 23 days. This ratio is well within recommended ratio for active biomass growth [23].

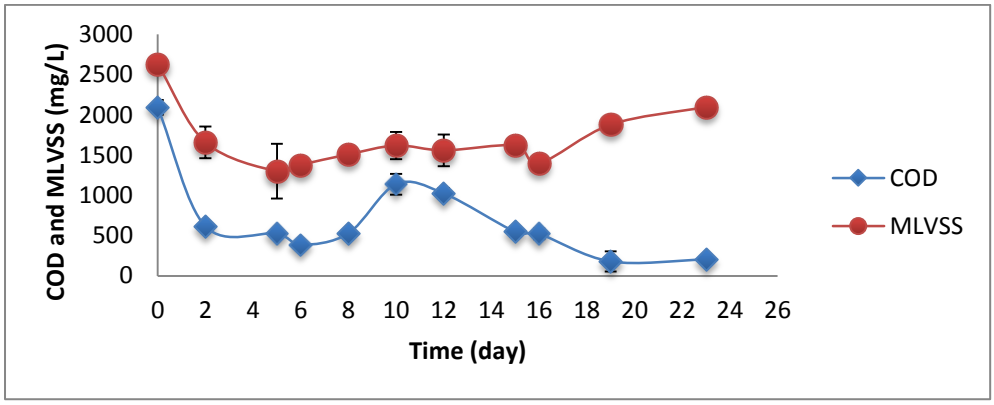


Figure 5. Concentration profiles of COD and MLVSS based on stoichiometric nutrients ratio (92.3: 5.6: 1).

Fig 1 displays the concentration profiles of COD and MLVSS of the enrichment operation based on stoichiometric ratio. On the 0th day, the influent COD and MLVSS to the SBR was at 2095 mg (COD)/L and 2630 mg/L respectively. Drastic drop of COD at 615 mg/L was noticed on day 2 onwards based on the initial COD concentration and similar trend was noticed on MLVSS trend. From 2nd to 8th day onwards, the COD concentration profile remained at a considerably steady level within the range of 615 mg/L to 530 mg/L. The immense decline of COD within short period of time (2 day) explained with the facts that the bacteria consumed about 71% of the initial influent COD and continuously retained the COD consumption rate within the range until the 8th day. Similarly, the MLVSS reduced from 2630 mg/L to 1300 mg/L within 5 days. The tremendous reduction in MLVSS concentration is due short SRT of 2 days that would have washed out the entire slow grower from the system. Short SRT generally reduced the number of surviving species on the system. This implies the facts that on the first 5 days, the system was not dominated with MP producing species of bacteria. Similar findings were reported by Lee et al [24] under similar operating condition. However, 5th day onwards until 10th day a stable increment of MLVSS concentration was noticed and remained steady until day 15th. There was a notable COD increment from 8th to 10th day and the concentration progressively reduced to 203 mg/L. The continuous steady state consumption and reduction of COD concentration promoted the growth of microbes and new cells where it is reflected through the increment of MLVSS concentration. The increment of MLVSS concentration upon progressive drop of COD concentration from the 10th day onwards showed that MP producing organism had dominated the system. The enrichment operation was stopped upon stable COD concentration achieved on day 19th onwards. Toward end operation, total of 90% COD reduction was achieved with continuous progression of MLVSS concentration. Nevertheless, if the system was cultivated for even longer period of time, there are possibilities for the MLVSS to continuously increase and reach steady state alongside constant COD consumption rate.

3.4 Enrichment of activated sludge with excess nutrients dosage

A comparative study was done under similar condition, where nutrients dosage of nitrogen source was varied in excess of 50% and 100%. The enrichment process was started with nutrients dosage of 92.3: 8.4: 1 (N-50% excess) and upon stable condition, the process continued with nutrients dosage of 92.3: 11.2: 1 (N-100% excess).

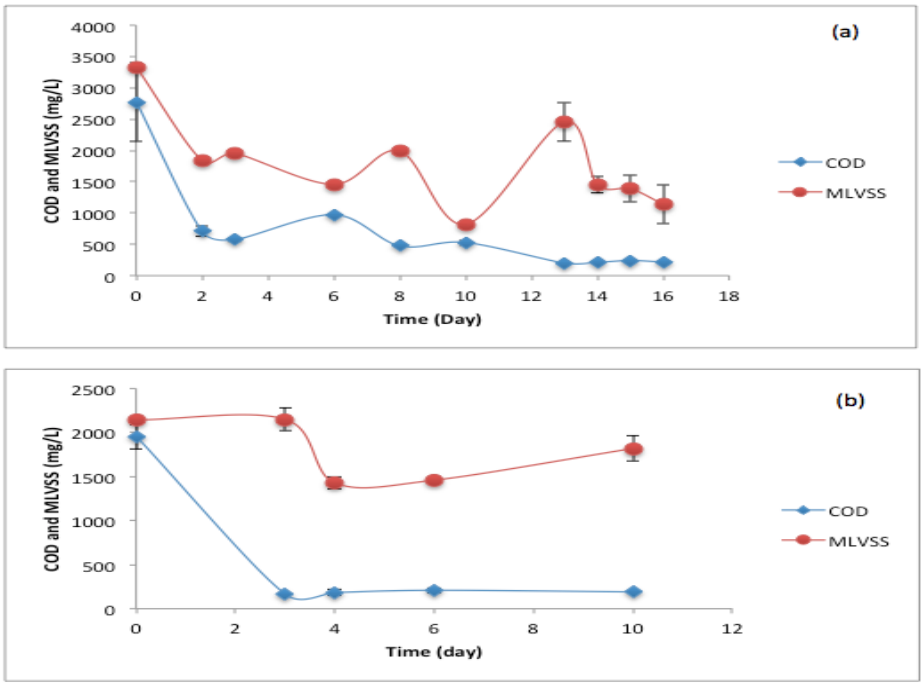


Figure 6. Concentration profiles of COD and MLVSS at excess nutrients dosage: (b) N-50% excess, (c) N-100% excess.

Fig 2 (b) is the concentration profiles of COD and MLVSS at N-50% excess nutrients dosage and Fig 2 (c) is the concentration profiles of COD and MLVSS at N-100% excess nutrients dosage. In the available literature, limited nutrients dosage has the tendency to suppress microbial growth for MP production and favours towards PHA production. Thus, excess nutrients dosage expected to yield higher protein content. Comparative to enrichment based on stoichiometric nutrients dosage, the COD and MLVSS concentration profile trend of N-50% excess enrichment processes through excess nutrients dosage is more or less the same. The relationship between COD and MLVSS concentration profiles for both conditions are much apparent in contrast to stoichiometric nutrients dosage. Generally, with presence of biodegradable COD heterotrophic bacteria consume oxygen to oxidize the biodegradable COD in order to generate energy and build up new cells [25]. Production of new cells deduced based on the increased of MLVSS concentration.

On day 0, the influent COD and MLVSS to the SBR was at 2760 mg (COD)/L and 3325 mg/L respectively for N-50% excess. Meanwhile for N-100% excess the influent COD and MLVSS is at 1950 mg (COD)/L, 2151 mg/L respectively. For both conditions, the COD concentration dropped progressively until 3rd day, where 79% and 91% of COD was consumed respectively for N-50% and N-100% excess. For N-50% excess, the COD concentration slowly decreased from 975 mg (COD)/L to 218 mg (COD)/L. Alongside the decrement, the MLVSS concentration continuously fluctuate with COD concentration and remained stable on day 14th onwards. The operation was stopped on day 16th continues with N-100% excess condition. Disparity to N-50% excess condition, the COD and MLVSS profile is slightly different. The

enriched sludge from N-50% excess condition was used for N-100% excess condition. Henceforth, this has reduced the acclimatization period for the system to reach fast steady state system. This is proven with constant COD consumption from 3rd day onwards and MLVSS concentrations augment linearly from 4th day onwards. Nevertheless, if the system was cultivated for even longer period of time, there are possibilities for the MLVSS to continuously increase and reach steady state alongside constant COD consumption rate. Towards the end, both condition reached total COD reduction of 92% and 90% respectively.

3.5 MP Production at different nutrients dosage

Towards the end of each enrichment process, samples were withdrawn and subjected to performance evaluation for MP production. Protein content, specific protein production rate $(q_{protein})$, specific substrate consumption $(-q_s)$, biomass yield $(Y_{X/S})$ and protein yield$(Y_{protein/S})$ were evaluated and tabulated in Table 2.

Table 9. Performance evaluation of MP production.

Nutrients Dosage	$-q_s$(mg COD/mg X/h)	$q_{protein}$(mg protein/ mg X/h)	$Y_{X/S}$	$Y_{Protein/S}$	Protein content (%)
92.3:8.4:1 (N-50% excess)	0.0477	0.0031	0.8595	0.0641	55
92.3: 11.2:1 (N-100% excess)	0.0818	0.0031	0.1876	0.0375	40
92.3:5.6:1 (N-stoichiometric)	0.0312	0.0010	0.2801	0.0349	22

Based on Table 11, N-50% excess resulted a higher protein content compared to N-100% excess and N- stoichiometric, which is 55%, 40% and 22 respectively. Comparatively, similar protein content of 54.5% was reported by Rajoka et al [52] through mixed culture of *C.utilis* and *Brevibacterium lactofermentum*. At initial stage, activated sludge was tested for protein content and the results indicated approximately 11% of protein content. This shows that enrichment at N-stoichiometric ratio alone had doubled the protein content. Similarly, enrichment through excess nitrogen source based on the stoichiometric ratio had doubled the protein content.

However, the specific protein production rate for N-50% is slightly higher than N-100% excess, which is 0.0031 mg protein/ mg X/d and 0.0027 mg protein/ mg X/d . The possibilities of such results are as explained in section 4.3, where N-50% excess condition was continuously run until stable COD was noticed alongside with stable MLVSS concentration. Stable MLVSS concentration is an indication of maximum protein content production. Hence, it can be concluded that N-50% excess has the ability to produce 55% of protein content. Comparative to N-50% excess, N-100% excess and N-stoichiometric has protein content of 40% and 22% respectively. However, the system only stabled with COD concentration but the MLVSS concentration still increases constantly. Thus, 40% and 22% protein content is only measured on the final day for N-100% excess and N-stoichiometric and there are possibilities that the

protein content to increase even higher than 50% for N-100% excess if the system was enriched and cultivated for even longer period with constant MLVSS concentration observed as well. This protein content results tally alongside with protein yield where N-50% and N-100% excess is 0.0641 mg protein/ mg substrate and 0.0375 mg protein/ mg substrate.

Meanwhile, the specific substrate consumption is the highest for N-100% excess doubled compared to N-50% excess. In the available literature, it was proven that the initial COD concentration greatly affects the biomass yield [53]. High substrate COD concentration expected to lower the biomass yield. Based on observation, the biomass yield for N-50% excess is far greater than N-100% excess, where the yield is 0.8595 mg (VSS)/ mg (COD) and 0.1876 mg (VSS)/ mg (COD). At a stable MLVSS concentration, the biomass yield approximated at 0.3 ± 0.03 mg (VSS)/ mg (COD). Henceforth, the biomass yield for N-50% excess is acceptable. Comparatively, the biomass yield for N-100% excess and N-stoichiometric is lower than theoretical value as the MLVSS concentration has not stabled. Similar findings were reported by Lim et al [53], where the biomass yield is higher for initial COD of 2310 mg/L than 1040 mg/L. Hitherto, the biomass yield calculation was done on assumption that the complete substrate consumption results on biomass growth. In reality, the substrate consumption by microbes is not only for biomass growth but also for non-growth-related processes where portion of substrate consumed by microbe used for cellular maintenance [54]. Thus, the biomass yield based on biomass growth only is underestimated. Although lower yield obtained for N-100% excess, 90% COD reduction within a short period of time and the objective was achieved, 90% COD reduction within a short period of time and the objective was achieved.

Conclusion

This work demonstrated an effective strategy for enrichment of aerobic sludge with POME as carbon source and additional nitrogen source for higher MP production. Throughout the enrichment process, all three nutrients ratio reduced the COD concentration to 90%, 92% and 90% for stoichiometric, N-50% excess and N-100% excess nutrients ratio respectively. However, the MLVSS concentration noticed to continuously increased for N-stoichiometric and N-100% excess nutrient ratio despite constant COD consumption. In contrast, N-50% excess conditions reached constant MLVSS and COD concentration and resulted in 55% protein content while N-100% excess and N-stoichiometric resulted in 40% and 22% protein content respectively. On the other hand, protein yield for N-50% is twice compared to N-100% excess and N-stoichiometric. In future work, cheaper nitrogen sources that are abundant in waste could be investigated in order to reduce more production cost as well as higher protein yield.

References

[1] United Nation, “World Population Prospects 2017 Revision”, Department of Economic and Social Affairs, New York, (2017)

[2] M. Henchion, M. Hayes, A. Mullen, M. Fenelon and B. Tiwari, “Future Protein Supply and Demand: Strategies and Factors Influencing a Sustainable Equilibrium”, Foods, **6**, no. 7, p. 53, (2017)

[3] H. van Zanten, H. Mollenhorst, C. Klootwijk, C. van Middelaar and I. de Boer, "Global food supply: land use efficiency of livestock systems", The International Journal of Life Cycle Assessment, **21**, no. 5, pp. 747-758, (2015).

[4] M. Khan, S. Khan, Z. Ahmed and A. Tanveer, "Production of Single Cell Protein from *Saccharomyces Cerevisiae* by utilizing Fruit Waste", **1**,no. 2, pp. 95-178, (2010)

[5] C. Stevens and K. Gregory, " Production of Microbial Biomass Protein from Potato Processing Wastes by *Cephalosporium Eichhorniae*", Applied and Environmental Microbiology, **2**, no.53, pp. 284-291, (1986).

[6] T. Asmamaw and A. Fassil, "Co-culture: A great promising method in single cell protein production", Biotechnology and Molecular Biology Reviews, **9**, no. 2, pp. 12- 20, (2014)

[7] A. Latif Ahmad, S. Ismail and S. Bhatia, "Water recycling from palm oil mill effluent (POME) using membrane technology", Desalination, **157**, no. 1-3, pp. 87-95, (2003)

[8] M. Chin, P. Poh, B. Tey, E. Chan and K. Chin, "Biogas from palm oil mill effluent (POME): Opportunities and challenges from Malaysia's perspective", Renewable and Sustainable Energy Reviews, **26**, pp. 717-726, (2013)

[9] Y. Chin, S. Loh and C. Fong, " Palm Oil Potential", (2017)

[10]W. Lee, A. Chua, H. Yeoh and G. Ngoh, "Influence of temperature on the bioconversion of palm oil mill effluent into volatile fatty acids as precursor to the production of polyhydroxyalkanoates", Journal of Chemical Technology & Biotechnology, **89**, no. 7, pp. 1038-1043, (2013)

[11]M. Md. Din, P. Mohanadoss, Z. Ujang, M. van Loosdrecht, S. Yunus, S. Chelliapan, V. Zambare and G. Olsson, "Development of Bio-PORec® system for polyhydroxyalkanoates (PHA) production and its storage in mixed cultures of palm oil mill effluent (POME)", Bioresource Technology, **124**, pp. 208-216, (2012)

[12]I. Onyekachi, "Treatment and Valorization Palm Oil Mill Effluent (POME) through Production of Microbial Biomass", University of Nigeria, (2015)

[13]J. Yadav, S. Yan, C. Ajila, J. Bezawada, R. Tyagi and R. Surampalli, "Food-grade single-cell protein production, characterization and ultrafiltration recovery of residual fermented whey proteins from whey", Food and Bioproducts Processing, **9**, pp.156- 165, (2016)

[14]F. Yunus, M. Nadeem and F. Rashid, "Single-cell protein production through microbial conversion of lignocellulosic residue (wheat bran) for animal feed", Journal of the Institute of Brewing, **121**, no. 4, pp. 553-557, (2015)

[15]D. Dhanasekaran, S. Lawanya, S. Saha, N. Thajuddin and A. Pannerselvam," Production of Single Cell Protein from Pineapple Waste using Yeast", Innovative Romanian Food Biotechnology, **8**, pp. 26-32, (2011)

[16]R. Honda, K. Fukushi and K. Yamamoto, "Optimization of wastewater feeding for single-cell protein production in an anaerobic wastewater treatment process utilizing purple non-sulfur bacteria in mixed culture condition", Journal of Biotechnology, **125**, no. 4, pp. 565-573, (2006)

[17]Z. Chen, L. Huang, Q. Wen, H. Zhang and Z. Guo, "Effects of sludge retention time, carbon and initial biomass concentrations on selection process: From activated sludge to polyhydroxyalkanoate accumulating cultures", Journal of Environmental Sciences, **52**, pp. 76-84, (2017)

[18]C. Mengmeng, C. Hong, Z. Qingliang, S. Shirley and R. Jie, "Optimal production of polyhydroxyalkanoates (PHA) in activated sludge fed by volatile fatty acids (VFAs) generated from alkaline excess sludge fermentation", Bioresource Technology, **100**, no. 3, pp. 1399-1405, (2009)

[19]F. Valentino, L. Karabegovic, M. Majone, F. Morgan-Sagastume and A. Werker, "Polyhydroxyalkanoate (PHA) storage within a mixed-culture biomass with

simultaneous growth as a function of accumulation substrate nitrogen and phosphorus levels", Water Research, **77**, pp. 49-63, (2015)

[20]Y. Ong, A. Chua, B. Lee, G. Ngoh and M. Hashim, "An Observation on Sludge Granulation in an Enhanced Biological Phosphorus Removal Process", Water Environment Research, **84**, no. 1, pp. 3-8, (2012)

[21]APHA, Standard Methods for the Examination of Water and Wastewater, 18th edn. APHA, USA (1992).

[22]M. Albuquerque, V. Martino, E. Pollet, L. Avérous and M. Reis, "Mixed culture polyhydroxyalkanoate (PHA) production from volatile fatty acid (VFA)-rich streams: Effect of substrate composition and feeding regime on PHA productivity, composition and properties", Journal of Biotechnology, **151**, no. 1, pp. 66-76, (2011)

[23]J. Willey, L. Sherwood, C. Woolverton and L. Prescott, Prescott's principles of microbiology. New York: McGraw-Hill, (2012)

[24]W. Lee, A. Chua, H. Yeoh, T. Nittami and G. Ngoh, "Strategy for the biotransformation of fermented palm oil mill effluent into biodegradable polyhydroxyalkanoates by activated sludge", Chemical Engineering Journal, **269**, pp. 288-297, (2015)

[25]Y. Hung, L. Wang and N. Shammas, Handbook of environment and waste management. Singapore: World Scientific Pub. Co., (2012)

[26]M. Rajoka, S. Ahmed, A. Hashmi and M. Athar, "Production of microbial biomass protein from mixed substrates by sequential culture fermentation of Candida utilis and Brevibacterium lactofermentum", Annals of Microbiology, **62**, no. 3, pp. 1173-1179, (2011)

[27]J. Lim and V. Vadivelu, "Treatment of agro based industrial wastewater in sequencing batch reactor: Performance evaluation and growth kinetics of aerobic biomass", Journal of Environmental Management, **146**, pp. 217-225, (2014)

[28]G. Bitton, Wastewater microbiology. New Delhi: John Wiley & Sons, (2013)

EURECA 2018 – Conference Paper
Paper number 2CE13

Removal of pharmaceutical from wastewater by adsorption-coagulation combined system with *Hibiscus Sabdariffa* as coagulant

Sharwin Raj[1], and Nurhazwani Ismail[1]*

[1] School of Engineering, Faculty of Built Environment, Engineering, Technology & Design, Taylor's
University, Subang Jaya, Selangor DE, Malaysia

Abstract. With the ever growing environmental and health threats that are present in the form of pharmaceutical waste, there is a dire need in efficient wastewater treatment process. Hence, this study is aimed at the determination of the optimum operating conditions of the 2 most dominant wastewater treatment processes which are adsorption and the coagulation process individually as well as the optimum operating condition of the combination of the both processes. The study of coagulation will involves the use of Hibiscus Sabdariffa as it proved to have coagulative traits and also a much cheaper alternative than the existing coagulants that are readily used nowadays and also it is a natural coagulant proving to be a more environmental friendly alternative as well. The study of the adsorption process however will involve the use of activated carbon due to heavy commercial practice of it. In the determination of the optimum operating condition for the coagulation process, it was found that Hibiscus Sabdariffa works best at pH 2, coagulant dosage of 160mg/l where the turbidity removal is at 40%. Besides, under those specifications as well, the COD level decreased by 30%. Activated carbon was found to work best at pH 2 and at an adsorbent dosage of 2000 mg/l as whereby under these conditions, turbidity removal of up till 50 % and decrease in COD level of 32%. Consecutively, study will need to be done to determine the optimum operating condition for the combination of both processes since it is a more economically viable process to integrate both of these processes rather than operating them individually. This study also proves that natural coagulants can be used in the treatment of pharmaceutical wastewater.

1 Introduction

In this ever growing world that is filled with vast and upcoming industries of various sorts, environmental threats are at the peak. This is such where these industries regardless of the goods that they provide the world with has a dark side effect which is more often than not overlooked. Hence, it then begs for governmental acts to be established in order to maintain environmental stability in an act to preserve lives on earth. With such acts even in the existence, it is still the industries responsibility to uphold proper treatment regiments in ensuring the wastewater released to the environment complies with the environmental regulations.

This study however is aimed towards the wastewater treatment that exists within the pharmaceutical industries due to there being a dire need for it as pharmaceutical companies are reportedly typical of leaving a wide range of products in the wastewaters due to them often carrying out their processes in a batch manner [1]. Pharmaceutical waste are also increasingly found in soil and water nowadays worldwide based on the research done by scientists [1]. There are two main manners in which pharmaceutical can be present in soil and water which is the form of disposal and excretion. However, with the increase in the pharmaceutical use nowadays, the amount of unused drugs being found in septic tanks also start to increase. Consecutively, there are larger pharmaceutical wastes in wastewater which tends to cause more environmental hazards. Conclusively, due to the excessive growth and environmental hazard caused by pharmaceutical waste inside wastewater, optimum conditions for the treatment of the pharmaceutical wastewater needs to be identified [1].

In such cases of doing so, companies tend to use various sort of coagulants in attempts of getting rid of the contaminants that lie within the wastewater. Coagulation is a process which is done before the sedimentation process takes place where the coagulation process helps with the settling of the contaminants inside the wastewater [2]. This is possible where this process which is usually combined with the flocculation process helps the contaminants to become neutrally charged which then promotes the combining of the contaminants which then renders it a larger particle as a whole. Consecutively, this makes the settling of the contaminants an easier task [3]. Conclusively, this process enables the removal of colloidal particles from the wastewater.

With that being said, the type of chemicals used in industries as coagulants varies due to various aspects such as the severity of the treatment that needs to be done as well as the cost of the coagulant in itself. One major potential coagulant based on recent studies would be the Hibiscus Sabdariffa or also known as Roselle. Recent researches have shown that the involvement of the Hibiscus Sabdariffa has been able to reduce the pH value in a wastewater tested for. Hence, it was recommended that its sensory attributes has to be further improved before being used commercially as a coagulant in wastewater treatments [4] [5]. However that this maybe so, the coagulation process has factors in which betters or deters the process as a whole. Such factors that would be discussed in this study are the coagulant dosage and the pH value of the wastewater [4].

Another key processes to be considered in the wastewater treatment is the adsorption process which is of utmost importance in the separation of the contaminants from the wastewater. The adsorption process itself has several contributing factors which as a result will make the adsorption process quicker. The factors that will be discussed in this study are such as the the

pH value of the wastewater with the added adsorbent as well as the adsorbent dosage[6]. These factors based on recent studies has proved to be able to affect the outcome of the adsorption process with regards to the quickness of the adsorption process.

Other treatment processes such as advance oxidation process is not considered in this study due to its severe disadvantages which includes it being very expensive, requiring pre-treatment in some cases before undergoing this treatment process as well as it needing the use of expensive reactants [3]. Biological treatment process is also not discussed because of the consideration towards an economical standpoint [6].

As a whole, this study is aimed at not only determining the optimum condition for each parameter discussed for either the coagulation process or even the adsorption process but instead this study is also tasked to determine the optimum combination for both the processes. This is a dire need to be researched and also has been done in the past due to the importance of these two processes in the treating of wastewater. With these two processes operating at its optimum conditions, the cost of wastewater treatment will be reduced [7]. These two factors are the contributing forces towards the effectiveness of the wastewater treatment process.

2 Materials and Methods

This experiment contains a few stages of which would be done during the span of this study as shown in **Figure 1** below.

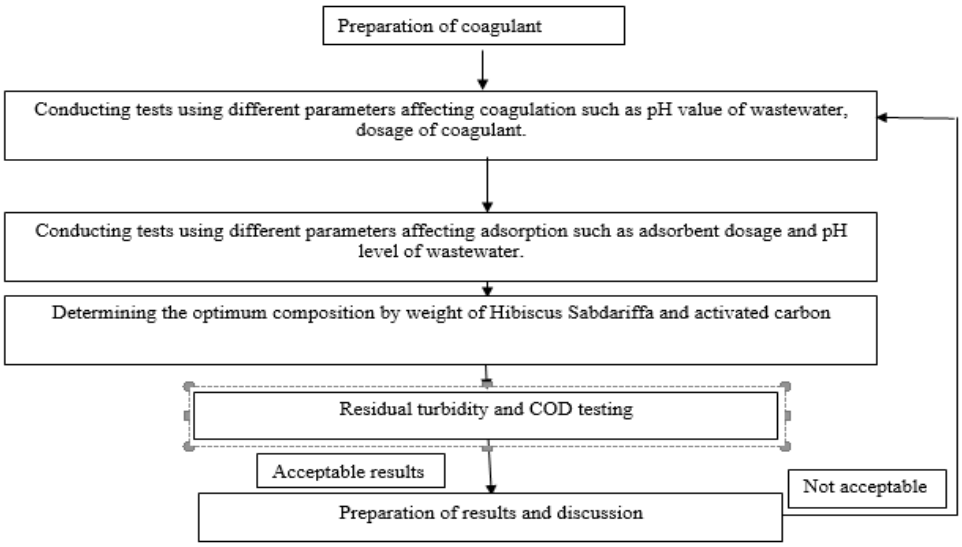


Figure 1: Design of Experiment

2.1 Materials

This experiment included the use of materials such as Hibiscuss Sabdariffa's dry seeds, activated carbon, pharmaceutical wastewater as well as 1M sodium hydroxide and 1M hydrochloric acid (used to adjust the pH value of the wastewater).

2.2 Preparation of the *H. Sabdariffa* seed powder

The roselle seeds were washed initially in order to remove any sort of impurities on the seeds using tap waters. Only the good seeds were selected to be used in this study. These washed seeds were then dried in the oven for 2 hours at a temperature of 60 ± 2℃. This was done in order to remove the remaining moisture content inside the seeds. Consecutively, the seeds were then grinded into powder form using a blender.

2.3 Preparation of the H. Sabdariffa as coagulant

In order to attain the coagulants, distilled water was used as the solvent for the extraction purpose of proteins from the powdered Hibiscus Sabdariffa seeds. In doing so, 0.5 g of the seeds were added into 100 ml of distilled water and then was stirred at room temperature and 200 rpm for 3 minutes using a hot plate. Consecutively, the solution was then filtered using a filter paper where the following jar tests then used the resulting filtrate obtained from the filtered solution.

2.4 Jar Tests Experiment

With regards to the coagulation process that uses the Hibiscus Sabdariffa extracts as coagulant, the tests were carried out by manipulating the pH and the coagulant dosage. The pH of the wastewater was altered at a range of 2 to 12. The coagulant dosage was varied at a range of 40 to 200 mg/L. The mixing rates were kept constant at 100 rpm (rapid mixing). The temperature of the wastewater was also kept constant during the tests at room temperature.

Jar test was the method used in order to carry out these tests whereby 500 mL of pharmaceutical wastewater was filled into six beakers each and placed in the jar test. Initially, in order to determine the optimum pH value of the wastewater, the pH value for each of the 6 beakers were varied at the range as mentioned previously. During this testing, the coagulant dosage was kept constant for each of the beaker which was at 40mg/l. The mixtures were then stirred at 40 rpm for 25 minutes. After doing so, the mixtures were then allowed to settle for an hour to enable the sedimentation process to take place. Sedimentation process was key in order to let the flocs that have been formed to settle at the bottom of the beaker. Consecutively, the mixture was then filtered using a filter paper to separate the mixture from the flocs that have been formed. The resulting filtrate was then measure for its residual turbidity as well as COD removal to determine the optimum pH value of the wastewater.

These steps were then repeated for the tests that involved varying coagulant dosages whereby this time the pH value of the wastewater was kept at its optimum value that was obtained from previous step. The resulting residual turbidity as well as the COD were measured for each of the mixtures in order to determine the optimum dosage of coagulant.

The steps were then repeated again for the mixing rates where one underwent slow mixing of 40 rpm and the other rapid mixing of 100 rpm. Rapid mixing is essentially to enable collision between the coagulants as well as the pharmaceuticals. However, the slow mixing is in order to promote the growth of the flocs.

With regards to the adsorption process however that uses activated carbon as the adsorbent, the tests were carried out by manipulating the pH value of the wastewater, as well as the adsorbent dosage. The pH of the wastewater was altered at a range of 2 to 12. The dosage was varied at a range of 2000 to 1800 mg/L. The mixing rate of the jar test of each of this testing was kept at a constant of 100 rpm. The temperature was also kept constant which was at room temperature.

The steps were done similarly for the adsorption testing as they were for the coagulation testing whereby the resulting filtrate of the mixture will undergo the residual turbidity and COD testing in order to determine the optimum conditions for each of the factor being studied.

Lastly, with regards to the combination of both the processes, samples were created with wastewater being added with different amount of composition of Hibiscus Sabdariffa to activated carbon at a range by weight. And the resulting filtrate was then of the mixture did undergo the residual turbidity and COD testing in order to determine the optimum composition of each respective material to be added into the wastewater for treatment purposes.

2.5 Analytical Method

With regards to wastewater study, there are several features that may be considered as a better alternative in order to gauge the characteristics of the specific wastewater. Those features as mentioned are such as COD, pH, Biological Oxygen Demand (BOD), residual turbidity, total suspended solids as well as total dissolved solids [8].

Turbidity is the measure of cloudiness of a certain sample. Considering that both the coagulation process and the adsorption process is to promote the removal of the colloidal particles within a certain sample, turbidity is a good testing to be carried out as it is able to determine the amount of colloidal particle left within the sample.

COD is another test that is selected simply because a drop in COD value is highly desirable during a coagulation process and an adsorption process in commercial application of these processes in wastewater treatment industries [9]. This is because, these processes tend to take place before biological treatment where there is activated sludge from microbial activity. Hence, a lower COD is desired in order for less sludge to be produced . Conclusively, the two tests that are carried out to determine the optimum condition of the processes are the residual turbidity as well as the COD.

Turbidity

With regards to the residual turbidity removal, the value was measured using a turbiditimeter. The percentage of turbidity removal was then measured using the equation as follows:

$$\text{Turbidity removal} = \frac{RT_c - RT}{RT_c} \times 100\ \% \quad (1)$$

Where;

RT_c = turbidity of the wastewater before the coagulation process

RT = turbidity of the wastewater after the coagulation process.

Chemical Oxygen Demand (COD)

With regards to the COD testing, the samples were measured for using reaction cells COD was measured using reaction cells of range 25-1500 mg/L. These reaction cells contained potassium dichromate as well as mercury (II) sulphate as reagents. In order to carry out the testing, 3 mL of the sample being tested for will be gently added into the reaction cells within an enclosed fume hood. After being added, the reaction cells are then closed with the lid and shaken vigorously. Consecutively, the reaction cells are then placed in the thermoreactor to be heated for 2 hours at 150 ℃ . The reaction cells were then let to cool down at room temperature for 30 minutes. The COD for the samples were then measured using the spectrophotometer. The percentage of COD removal is calculated based on the equation as follows:

$$\text{COD removal} = \frac{COD_c - COD_i}{COD_c} \times 100\ \% \quad (2)$$

Where;

COD_c = COD of the wastewater before coagulation and adsorption process

COD_i= COD of the wastewater after the coagulation and adsorption process.

3 Results & Discussion

The wastewater obtained from the pharmaceutical industry contains properties as shown below in **Table 1:**

Table 1: Characteristics of wastewater.

Characteristics of the synthetic wastewater	
Temperature (℃)	30
pH	4
Turbidity (NTU)	70.5
COD (mg/L)	665

3.1 Coagulation activity using Hibiscus Sabdariffa

3.1.1 Effect of pH on coagulation activity

The effect of pH on the turbidity as well as the COD level of the wastewater is as shown below in Figure 2 and Figure 3. The solubility of a certain particle in a solution is highly dependent on the pH value of the wastewater which renders the pH an important factor [10]. As mentioned earlier, the pH value is varied at a range of 2-12 whereby the coagulant dosage is kept constant at 200mg/l. The results obtain shows that pH 2 has the best turbidity removal as well as decrease in COD. This then complies with study that has been done before which states that Hibiscus Sabdariffa is highly effective in acidic conditions where in this case, pH value of 2 means an acidic condition [10]. The percentage of turbidity removal at pH 2 is 34.47% whereas the COD level drops by 38.3%.

This is such due to the fact of the isoelectric points of the amino acids that are present in the Hibiscus Sabdariffa seeds. Acidic amino acids are present in the seeds which are the coagulative agent in the seeds which consists of glutamic acid and aspartic acid [11]. Furthermore, the seeds contain a number of other amino acids with isoelectric points ranging from 3 to 6. Thus, this is why the coagulative traits of the seeds works best in acidic conditions.

Furthermore, it can also be seen how the turbidity is relatively lower in the acidic regions than that compared to the alkalinity regions. This then further promotes the fact of the seeds possessing better coagulative traits in acidic conditions.

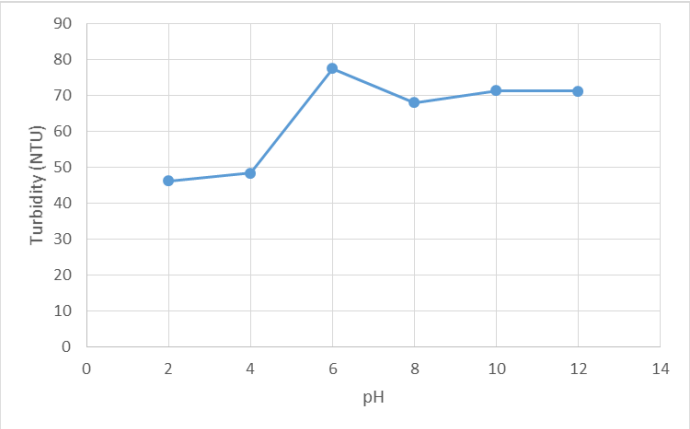


Figure 2 The effect of pH on the turbidity of the wastewater after coagulation.

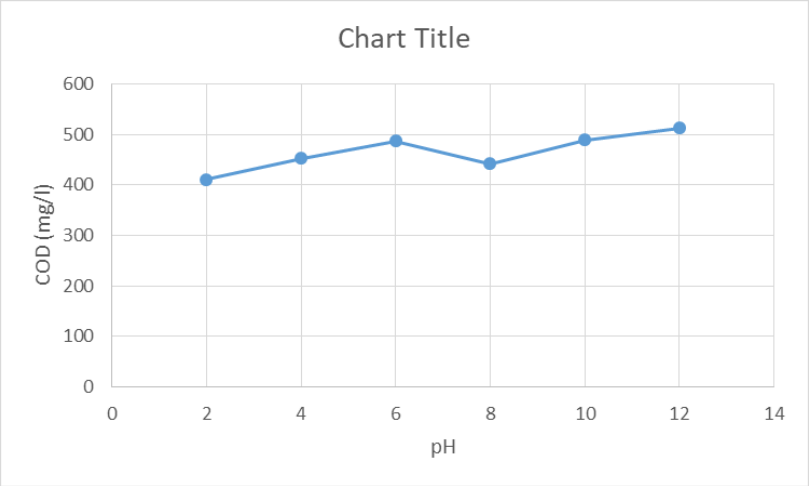


Figure 3 The trend in COD when varying the pH of the wastewater after coagulation.

Figure 2 and Figure 3 shows the relationship of pH with the turbidity removal and COD removal rate respectively.

3.1.2 Effect of coagulant dosage on coagulation activity

The coagulant dosage plays an important role in the formation of the flocs which is crucial in the removal of colloidal particles from a certain solution. Furthermore, the forces of attraction and repulsion between particles is what that affects the strength of the floc. Thus, there isn't sufficient energy to form flocs when the dosage is lower which then renders the formation of weaker and smaller flocs [12]. However, overdosing may also occur in an event of too much of coagulant dosage whereby the performance of the coagulation process os rather unsatisfactory and formation of sludge occurs [13]. As mentioned earlier, the coagulant dosage range will be varied from 40 to 200 mg/L.

As it can be seen from Figure 4, 160mg/l proves to give the highest amount of turbidty removal of 40%. From Figure 5 it can also be seen that 160 mg/l gives the best COD decrease of 30%. This then comes to show that the turbidity removal is lesser at lower dosages as weaker flocs are formed.

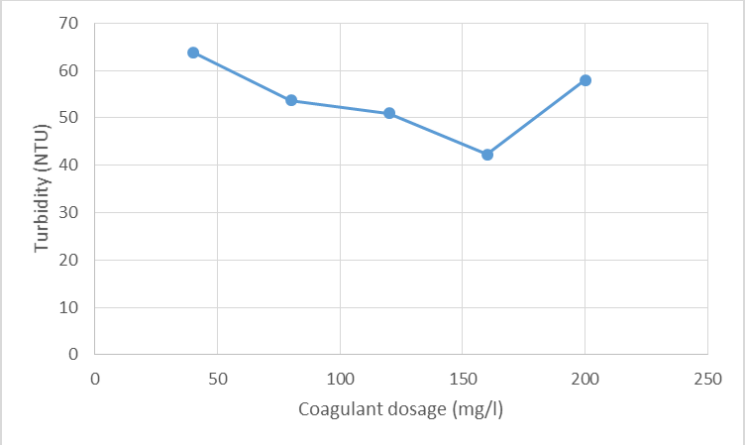


Figure 4 The trend in turbidity with varying coagulant dosage

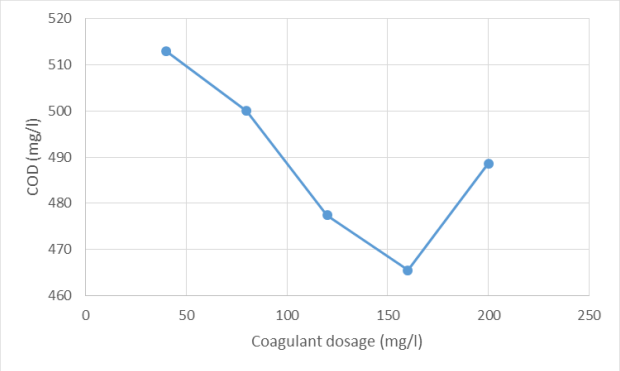


Figure 5 The trend in COD with varying coagulant dosage

3.2 Adsorption activity using activated carbon

3.2.1 Effect of pH on adsorption activity

Figure 6 and Figure 7 does show a similar trend as that seen in the pH affecting coagulation process. The lowest turbidity or rather the highest turbidity removal rate of 45.67%. Furthermore it can also be seen that the COD had a bigger drop at pH 2 of about 28.38%. This then comes to show that the adsorption process is more condusive in an acidic environment.

This is such due to the fact that the number of negatively charged sites increases as the pH increases. This then leaves lesser room for the positively charged sites. Adsorption is not favoured in the case of a negatively charged surface on the site of the adsorbent due electrostatic repulsion with there being anions present inside the wastewater. Thus, this is why as the pH increases, the removal rate of contaminants decreases [14].

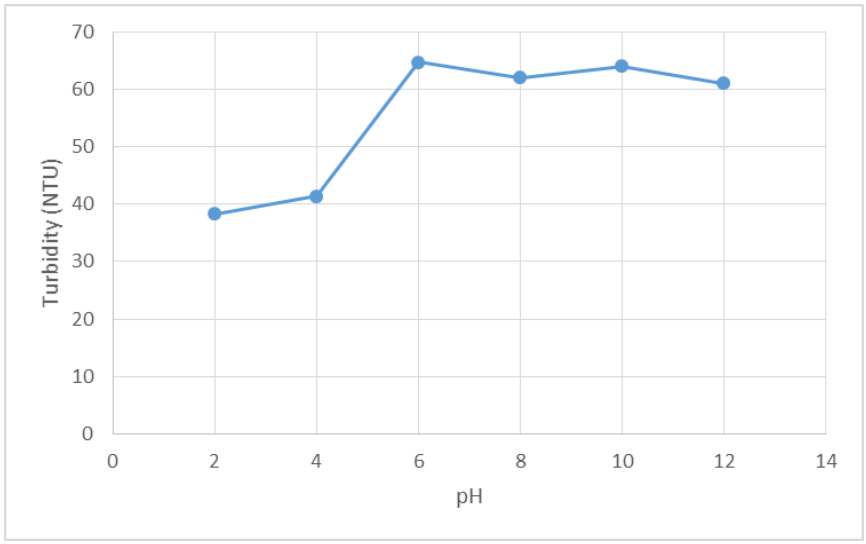


Figure 6 The effect of pH on the turbidity of the wastewater after adsorption.

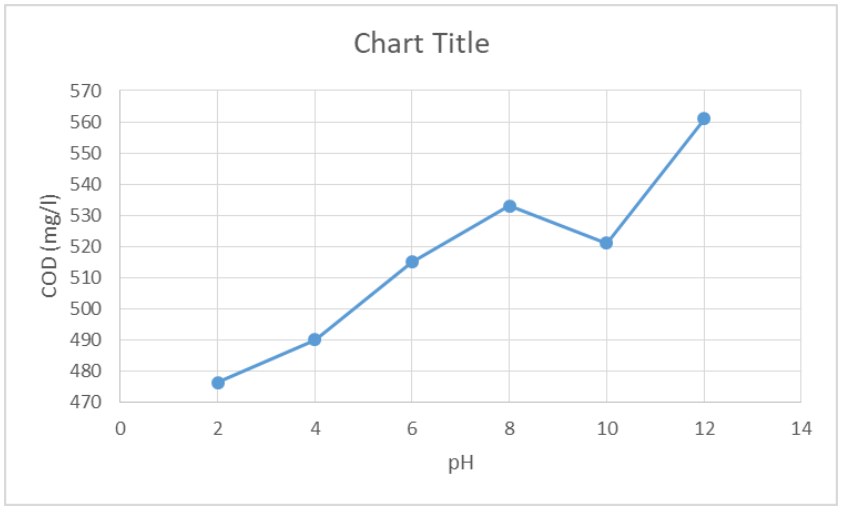


Figure 7 The effect of pH on the COD of the wastewater after adsorption.

3.2.2 Effect of adsorption dosage on adsorption activity

As it can be seen from Figure 8 and Figure 9 that the adsorbent dosage does indeed affect the rate of removal of contaminats from the wastewater. That is why at an adsorbent dosage of 10000mg/l the removal rate of residual turbidity ids the highest of 50% removal rate and also the COD removal was at 32%.

This happens due to the fact that with an increase in adsorbent dosage there is an increase in adsorbent surface area which means more room for the contaminants to be attracted to. However, in the event of overdosing, that means there is more room then there are contaminants within the wastewater, whereby the activated carbon becomes part of the contaminant within the wastewater. Hence, the contaminant removal rate decreases as the adsorbent dosage increases beyond 10000 mg/l.

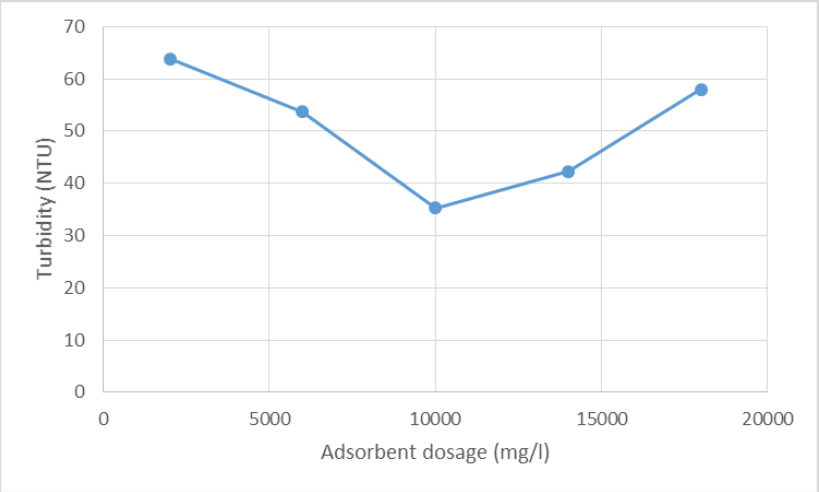


Figure 8 The trend of turbidity with adsorbent dosage

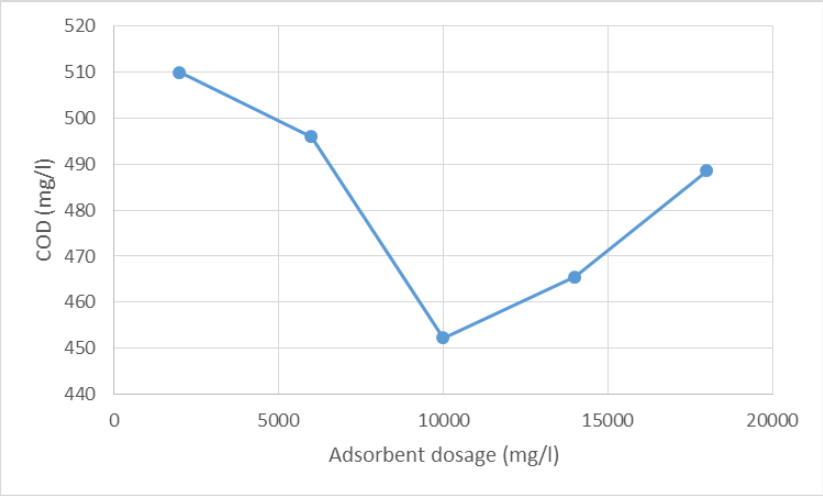


Figure 9 The trend of COD with adsorbent dosage

3.3 Combination of adsorption and coagulation process

The study done shows that both the processes work best in acidic environments wher in the event of the integration of both of the processes, the pH will be set at 2 since that is when both of these components carry out their process the best. The optimum dosage will also be set based on the study that has been done. Thus, the combination will use an equal amount Hibiscus Sabdariffa and activated carbon by weight.

4 Conclusion

From carrying out this study, it can be seen that Hibiscus sabdariffa does indeed possess cagulative traits and can be used in the removal of pharmaceuticals from wastewater. It

was also seen that both of these processes work more conducive in a rather acidic environment or rather at a lower pH value.

It is also seen that as the dosage increases, so does the effectiveness of the process whereby the coagulation process is more effective when the coagulant dosage increases as the same goes for the effectiveness of the adsorption process with regards to the adsorbent dosage. However, it was noted that in an event of an overdosage a poor performance is expected from both of the processes.

Integration of the both processes should be done in order to determine the optimum operating conditions for this combination. This is vital as the integration of these two processes are much more economically viable than a standalone process.

Furthermore, the use of High Performance Liquid Chromatography could also be inculcated in the testing of the samples in order to determine the pharmaceuticals present in the wastewater both prior and after the respective coagulation and adsorption process. This can be done in order to know what pharmaceuticals are heavily affected by each of the process.

Acknowledgements

I would like to thank my supervisor, Ms.Nurhazwani Binti Ismail for her continued guidance and support throughout this study. My deepest gratitude also go forth towards the lab assistance for their guidance in assisting me to use the lab equipment.

Thanks also goes out to my friends who have been very supportive of me over this course of period by encouraging me to always do well during the tough times.

Finally, I would like to sincerely thank my family for their role in making sure I have all the necessities required so that I don’t have to worry much during this period of course.

References

[1] Industrial &Engineering Chemistry Research, "Pharmaceutical Industry Wastewater:Review of the technologies for Water Treatment and Reuse," American Chemical Society, Cantabria, 2014.
[2] Islamic University of Gaza- Environmental Engineering Department, "Coagulation and Flocculation," Dr. Fahid Rabah, 2015.
[3] Felicien Mazille, "Sustainable Sanitation and Water Management," 2003. [Online]. Available: http://www.sswm.info/content/coagulation-flocculation. [Accessed 30 11 2011].
[4] Pakistan Journal of Nutrition, "Effect of Hibiscus Sabdariffa Extract on Biochemical and Organoleptic Propperties of Yogurt," p. 172, 2007.
[5] N. Mun Y.Yong, "Optimistaion of Hibiscus Sabdariffa as a Natural Coagulant," pp. 153-165, 2016.
[6] L. Lorenzen, "Factors affecting the mechanism of the adsorption of arsenic species on activated carbon," vol. 8, no. 4-5, pp. 557-569, 1995.I.G.Bantcheva, "Study On The

Factors Affecting Coagulation And Flocculation In Treatment Of Industrial Effluents," 2001.

[7] I.G.Bantcheva, "Study On The Factors Affecting Coagulation And Flocculation In Treatment Of Industrial Effluents," 2001.

[8] Z. Z. Abidin, N. S. Mohd Shamsudin, N. Madehi, and S. Sobri, "Optimisation of a method to extract the active coagulant agent from Jatropha curcas seeds for use in turbidity removal," *Ind. Crops Prod.*, **vol. 41**, no. 1, pp. 319–323, (2013).

[9] Hlthman, "Waste water treatment 2 2.1," *Waste Water*, **vol. 20,** no. 30, pp. 1–18, (2002).

[10] N. Fathinatul and R. Nithyanandam, "Wastewater Treatment by using Natural Coagulant," (2014).

[11] K. I. E. Hainida, I. Amin, H. Normah, and N. Mohd.-Esa, "Nutritional and amino acid contents of differently treated Roselle (Hibiscus sabdariffa L.) seeds," *Food Chem.*, **vol. 111**, no. 4, pp. 906–911, (2008).

[12] Z. Ma, J.-J. Qin, C.-X. Liou, L. Zhang, and S. Valiyaveettil, "Effects of Coagulation, pH and Mixing Conditions on Characteristics of Flocs in Surface Water Treatment," National University of Singapore, (2012).

[13] H. Patel and R. T. Vashi, "Removal of Congo Red dye from its aqueous solution using natural coagulants," *J. Saudi Chem. Soc.*, **vol. 16**, no. 2, pp. 131–136, (2012).

[14] C.Namasivayam, "Removal of Congo Red from water by adsorption onto activated cabon prepared from coir puth, an agricultural solid waste," *Dyes and Pigments*, vol.54, no.1, pp.47-58,2002

Degradation Pathway of Palm Oil Effluent and Sludge using Fenton Oxidation Process

Ragavan Sukddesh[1,], and Nithyanandam Rajesh[1]*

[1]School of Engineering, Faculty of Built Environment, Engineering, Technology and Design

Abstract. Fenton oxidation is used to degrade the palm oil refinery effluent (PORE) and sludge which contains chemical oxygen demand (COD) and biological oxygen demand (BOD) of 70,300 mg l^{-1} and 7436.3 mg l^{-1} respectively. Physical and chemical treatment methods were applied to the wastewater to determine the best condition for the degradation process as well as to determine the optimal concentration of the Fenton reagent which is prepared using iron (II) sulphate and hydrogen peroxide. The Fenton reagent was prepared in terms of different ratios with ferrous ions (Fe^{2+}) to hydrogen peroxide (H_2O_2) with different molar concentration respectively. Ratios and molar concentration varied for Fenton reagent are (1:2, 1:4 and 1:6) and (0.4M, 0.6M, 0.8M and 1.0M) respectively. Physical treatment comprises experimental temperatures of (35ºC, 45ºC and 55ºC and 65ºC) and pH of (2, 6, 8 and 10) where Fenton reagent is not involved in this treatment. Findings from the experiments proved that COD values of the wastewater was reduced in all three treatments where the reduction percentage for pH was 65.4% (pH 10), temperature was 68.8% (45ºC) and the highest reduction was by Fenton reaction which was 87.3% (1:6, 0.8M) from the raw sample COD value. Furthermore, xenobiotic compounds and iron were identified for both raw and reacted effluent using GC-MS and atomic absorption spectroscopy (AAS) analysis respectively. It was found that 53% of xenobiotic compounds (octadecanoic and methyl ester) were removed successfully by Fenton process (1:6, 0.8M) and the findings in AAS shows that the highest concentration of iron were found in the Fenton's sample (1:6, 0.8M) with a concentration of 23.65mg/l.

Keywords: Palm Oil Refinery Effluent (PORE), chemical treatment, physical treatment, Fenton Process, Xenobiotic

1.0 Introduction

Malaysia is a country that is diverse and fruitfully rich with natural resources and plantations. It is known to this day that Malaysia is the biggest producer and world's largest exporter of palm oil. Malaysia accounts for 39% of the world's palm oil production and 44% of the world's palm oil exports [1]. In the year 2012, there was approximately 6,037,200 m^3 of palm oil refinery effluent (PORE) generated across Malaysia [2]. Current technologies are trying to develop a method efficient enough to treat the effluent and sludge of the palm of refinery to reduce environmental effect towards the nature and living organisms upon discharging to the Malaysian waters and inland waters accordingly based on the regulations of the environmental department.

Palm oil industry produces palm oil refinery effluent (PORE) and sludge in character and quantity depending on the palm oil mill process which contains recalcitrant compounds which are harmful to the environment if released to the inland waters without being treated [3]. According to Wu et al., it takes about 5 to 7.5 tons of water to process one ton of crude palm oil [4]. In addition to this, Ahmad et al., stated that about 50% of the water will end up as wastewater which has to be treated before discharging to the inland waters [5]. However, based on the chemical equilibrium principle the organic compounds present in the effluent will also be found in the sludge. PORE and sludge has COD and BOD value of 70,300 mg l^{-1} and 7436.3 mg l^{-1} respectively. Hence, wastes like this has to undergo necessary chemical treatment such as AOP (Advanced Oxidation Process).

In today's world, biological treatment using open ponding system is widely used for PORE treatments [6-7]. It is basically treated with the presence of microorganism which helps to breakdown the structure and organic matters of PORE. Microorganisms are very sensitive towards the environment, especially temperature which makes the sustainability of microorganisms in the treatment process to be challenging. Therefore, discharged effluent have to be stored at 4^{o}C as common biological treatment will be occur under mesophilic range [8]. Temperature as such can be achieved by storing effluents in chiller. Besides temperature, the pH level along the treatment has to be strictly controlled depending on the microorganism's adaptability toward the environment. Although biological treatments are able to reduce the concentration of recalcitrant compounds (xenobiotic or non-biodegradable compounds), it requires very long retention time and large space yet failing to meet the criteria of the discharge regulation [9].

Besides biological treatment, several other methods have been practiced to treat recalcitrant compound but they end up ineffective and fail to meet the discharge standard. Based on literature, it is found that a more conventional and adaptable method is available to treat recalcitrant compound which is the advance oxidation process (AOP) method discovered by H.J.H Fenton in the year 1894. AOP consists of Fenton process, ozonation process, hydrogen peroxide oxidation process, photocatalytic oxidation process. In this research, the Fenton process is chosen which consists of iron (II) sulphate and hydrogen peroxide as the Fenton reagent [10]. The reason Fenton process is chosen because it has high efficiency in reducing COD and BOD levels in wastewater hence treating recalcitrant compounds [11].

Fenton process is being widely used in many industries to treat wastewater such as pharmaceutical industries, dye industries, paper industries and manufacturing industries [12]. Hydrogen peroxide as the part of the reagent has high oxidative power that has the potential of 2.8eV to remove organic matters from the production OH radicals. Iron (II) sulphate plays a

role as the catalyst in the Fenton process which enhances the production of OH radicles [10]. The rate of hydroxyl radicals produced is directly proportional to the time taken to degrade the organic compounds in discharged effluent [13]. The greater the production rate of hydroxyl radicals, the shorter the time taken for degradation of discharged effluent.

Among the types of AOP, Fenton process is the most efficient process so far as it complies advantages such as short reaction time, cheap and non-toxic chemicals involved ($FeSO_4$ and H_2O_2), no mass transfer limitation as Fenton process has homogenous catalytic nature, no catalyst required and it is easy to handle [8]. However, Fenton process is considered technical as the pH of the sample being tested must be in the range of 2-3 for a smooth reaction to occur [14]. This research will be conducted by using chemical and physical process to study the degradation of PORE and sludge. Chemical process is the Fenton process chosen from AOP. The experiment will be done by varying the concentration of Fenton reagent with respect to the ratio of ferrous ions (Fe^{2+}) to hydrogen peroxide (H_2O_2) to degrade recalcitrant compounds in PORE and sludge.

Physical treatment is the process the varies the temperature and pH of samples without involving Fenton reagent. The reason to vary samples based on these two parameters is to determine the effectiveness of the Fenton process by comparing the amount of reduction of COD and BOD levels for each treatment respectively. Therefore, by applying Fenton process for this research, the organic compounds can be degraded as well as the level of COD and BOD can be reduced before discharging to the environment. By doing so, the concentration of recalcitrant compounds can be reduced. In a nutshell, this research aims to determine the suitable concentration and ratio of Fenton reagent to degrade the recalcitrant compounds in PORE and sludge and reduce the COD and BOD levels simultaneously, determine the percentage of reduction of COD and BOD for both Fenton process (Chemical treatment) and by varying pH and temperature of PORE samples (Physical treatment) and study the presence of iron compound through elemental analysis (AAS) and the percentage of reduction of xenobiotic compounds by comparing the samples before and after the treatment using GC-MS.

2.0 Materials and methods

2.1 PORE and sludge

The sample was collected from a palm oil mill, Tuan Mee Oil Palm Mill, Ijok, Selangor. The sample was collected in a 5-liter container and stored in a chiller at the lab in the university. It was made sure that the temperature of the chiller set to 4^{o}C in order to avoid any biodegradation of sample. Since the sample was highly concentrated, a dilution factor of 1:10 was used to obtained more accurate data throughout the experiment. The sample are diluted by 1:10 factor by extracting 1 ml of raw sample and adding 9ml of ultrapure water. The reason ultrapure water was used is because it contains less amount of impurities which will aid in delivery accurate data when doing sample analysis.

2.2 Chemicals and analytical test kits

Ferrous sulphate heptahydrate ($FeSO_4.7H_2O$) and hydrogen peroxide (6 wt%) were purchased from Evergreen Engineering and Resource, Malaysia. COD and BOD cell test kits and BOD nutrient salts were purchased from Merck Malaysia.

2.3 Analytical methods

2.3.1 pH measurement

pH measurement for every sample was measured using an electronic pH meter with pH probe (Eutech Instruments PC 700).

2.3.2 Chemical oxygen demand

COD was tested for both raw and treated sample. Before beginning any treatment, the sample is diluted to a factor of 1:10 ratio in order to obtain values within the range of the COD cell test kit. 2ml of the sample were extracted using a micropipette and deposited inside the COD cell. The screw cap was tightly attached and the cell was mixed vigorously by holding on the screw cap. The cell was then placed in the pre-heated thermoreactor (VELP ECO 8 Thermoreactor) at 150^{o}C for 120 minutes. After heating, the cells are placed onto a test tube holder to cool for 30 minutes where for the first 10 minute of the cooling phase the cell was swirled. The cell was placed in the photometer (Merck Spectroquant Prove 300) to determine the COD value. As a precaution, the addition of sample into the COD cell was done inside a fume hood while wearing a respirator as COD is potentially harmful if inhaled.

2.3.3 Biological oxygen demand

BOD was tested for both raw and treated sample. Before beginning any treatment, the sample is diluted to a factor of 1:10 ratio in order to obtain values within the range of the BOD cell test kit. BOD nutrient salt was prepared by means of number if samples being tested. 1 vial is subjected to be dissolved in 1 litre of water inclusive of 20ml raw sample. Two batch of samples was prepared together with two batch of blank sample (nutrient salt solution) and stored in oxygen reaction bottles. One bottle of sample and one bottle of blank solution was kept in an incubator at temperature of 21^{o}C for 5 days to determine the BOD level as mentioned below. The other two bottles were tested for current BOD values. Reagent 1K, 2K and 3K was mixed

into the bottles according to the BOD procedure and both the solutions were filled in BOD cell test to be tested using the photometer (Merck Spectroquant Prove 300). The BOD values will then be calculated.

2.3.4 Total suspended solids

Total suspended solids for all the samples were done according to APHA Standard Methods for the Examination of Water and Wastewater (Method 2540D). Whattman filter paper was used. The filter paper was treated by washing with ultrapure water then drying it in the oven for 1 hour at 103^{o}C. The filter paper was then weight on an analytical balance to determine blank weight. The filter paper then was placed in a vacuum filter set. 200ml of sample was run through the filter paper. The collected suspended solids on the filter paper were placed in the oven for 1 hour at 103^{o}C. After drying, the filter paper was placed in the desiccator to cool down to room temperature. The filter paper was then weight to determine weight of the suspended solids to be calculated. In order to determine accurate data, the weighing process is repeated until consistent reading was obtained.

2.3.5 Turbidity

Turbidity of the raw and treated samples were measured using the Eutech Instruments TN 100 turbidity meter. The turbidity meter was required to be calibrated using the available kit samples with turbidity values of 0.02NTU, 20NTU, 100NTU and 800NTU. After calibration, the PORE sample was filled in the vial up to the mark that is obtained from the turbidity meter. The outer surface of the vial was wiped using the KIMTECH Science tissue with silicon oil before measuring the turbidity. It was ensured that the top of the measuring areas was covered with a black opaque cap to avoid disturbance in the reading of the infrared light source.

2.4 Experimental methods

2.4.1 Fenton oxidation process (Chemical Treatment)

200ml of diluted sample was prepared for the Fenton oxidation process. The pH of the sample was adjusted to be in the range of 2-3 because Fenton process reaction is more favourable in acidic environment. The pH of the diluted sample was 4.8. The pH was adjusted using 2M H_2SO_4. Drops of H_2SO_4 were added to the sample until the pH reaches the desired value. After the pH value was regulated, the sample was filled into a 5 litre beaker. Fenton process was carried out with molarity of 0.4M, 0.6M, 0.8M and 1M with ratio of ferrous ions (Fe^{2+}) to hydrogen peroxide (H_2O_2) of 1:2, 1:4 and 1:6 for all samples respectively.

The mass and volume of iron (II) sulphate and hydrogen peroxide required were calculated based on the molarity and ratio being tested. The iron (II) sulphate was added first followed by the hydrogen peroxide into the beaker containing the sample. The reaction time was 30 minutes. Based on observation, the sample's color changed into reddish orange and there was formation of foam on the top layer of the sample. The sample was mixed from time to time during the reaction period. The reaction was exothermic at room temperature of 30^{o}C. The reacted sample was then immediately tested for COD, BOD, turbidity, pH and suspended solids to determine the efficiency of Fenton oxidation process.

2.4.2 Variation of pH and temperature (Physical Treatment)

Raw sample of PORE was diluted to 1:10 factor to prepare 200ml of diluted sample. The prepared diluted samples were treated using the physical treatment by varying pH and temperature. Physical treatment does not involve Fenton process. pH treatment was done in the of pH 2,6,8 and 10. The pH of samples were adjusted using 2M H_2SO_4 and 5M NaOH respectively. After each samples prepared based on the pH values, the COD, BOD, turbidity and suspended solids were tested. Temperature treatment was done for prepared sample with temperatures of 35^{o}C, 45^{o}C and 55^{o}C and 65^{o}C. Samples were heated using a magnetic hotplate and stirred using a magnetic stirrer. After samples reaching desired temperature, each samples were tested for COD, BOD, turbidity, pH and suspended solids.

2.5 Elemental analysis

2.5.1 Procedure for Atomic Absorption Spectroscopy (AAS)

AAS instrument (Perkin Elmer AAnalyst 400) was used as an elemental analyzer to detect the amount of iron presence in the raw sample, pH and temperature treated samples and Fenton oxidation reacted samples. AAS is a complex and technical instrument that requires the specific bulb of the component being tested. The samples were filtered using a filter paper to avoid any solids being injected into the AAS inlet. The filtered samples were stored in centrifuge tubes. AAS requires several stages of calibration before it is able to detect the presence of iron in samples.

Initially, iron standard solution was prepared with concentration of 100ppm from the raw iron standard solution (100ppm) for 50ml using ultrapure. Then, 5 different concentration of iron standard solution were prepared by extracting from the prepared 100ppm iron standard solution. All extraction was done using a micropipette to obtain precise volume. An analytical balance was used to weigh the centrifuge tube and was set to zero before adding the extracted volume from the 100ppm solution. After adding the extracted solution to the centrifuge tube, the remaining volume was added with ultrapure water until the weight scale showed 50g which is equivalent to 50ml. The same method was used to prepared all the other solution with desired concentration.

The AAS instrument were start up using the Winlab 32 AA Flame software on the computer. The method of testing for the component was chosen and the details of the calibration iron standard solution was registered. A blank sample of ultrapure water was registered as well to be the reference in plotting the calibration curve. The Fe bulb was turn on to be heated for 15 minutes and the energy level was recorded. The flame was started as the inlet tube was placed in the blank solution. The calibration graph was started and the reading was made zero after a stable value of the blank solution was detected. The 2ppm iron standard solution was tested for concentration to determine the accuracy of the results that will be obtained for the PORE sample.

Final stage of calibration involved the blank solution once again and the other solutions of 5ppm-20ppm in sequence before testing the presence of iron in the PORE samples. Finally, the samples were tested for iron concentration and the result was printed on the software notepad.

2.6 Compound analysis

2.6.1 GC-MS Analysis

Sample Preparation

2 ml of POME samples (treated & untreated) was taken in different test tubes respectively. 0.05 N of $NaSO_4$ (2ml) was added to remove the moisture content in each test tubes. Then, the samples were kept for 1 day. Next, the samples were centrifuged at 4000RPM. The settled particles for each samples were subjected to high pressure vacuum filter. Then, the settled particles were kept at -17°C in the freezer for 15 min and then subjected to high pressure vacuum filter again. Then the moisture less compound was subject to the addition of methanol (2ml). Finally, the solution was centrifuged at 10000 rpm for 30 min. Supernatant for each samples were extracted and filtered once again through 0.22-μm nylon membrane prior to the analysis. Then a methanol blank solution was made and the samples were then subjected to GC-MS (AGILENT Technologies) for analysis.

Equipment Preparation

Table 10: Condition For GC-MS

GC: Agilent Technologies 6890	
Inlet	Splitless
Mode	Pulsed splitless/ 1μL injected
Inlet Temp (°C)	300
Pressure, psi	13
Total Flow, mL/min	34.6
Gas type	Helium
Oven Temp (°C)	325
Column: HP-5MS	
Length, m	30
Diameter, μm	250
Film thickness, μm	0.25

3.0 Results and discussion

3.1 Characterization of Palm Oil Refinery Effluent and sludge

Table 11: Characteristics of PORE and sludge from Tuan Mee Palm Oil Mill with multiplication of dilution factor

No	Characteristics	Value
1	pH	4.84
2	COD, mg/l	70,300
3	BOD, mg/l	9350.4
4	Turbidity, NTU	446
5	Total Suspended Solids, mg/l	13,000

3.2 COD and total suspended solid variation for molar concentrations of Fenton reagent and ratios of Fe^{2+} to H_2O_2

PORE and sludge was treated using different ratio of Fe^{2+}/H_2O_2 with different concentrations respectively. The Fenton reaction lasted for 30 minutes. During experiment, the sample reacting with Fenton concentration of 0.4M of ratio 1:4 and 1:6 Fe^{2+}/H_2O_2 had minimal reaction. The foam generated in the beaker during reaction was the least among the other samples reacting with higher Fenton concentration and ratio. Although the COD of the samples were lower than the raw sample, the samples still had the highest COD among all the other ratio and concentration of Fenton tested samples. This is due to lack of hydroxyl radicals in these particular molar ratios hence the high COD was contributed by the unreacted ferrous sulphate and insufficient concentration of hydrogen peroxide. The total suspended solid was the lowest lowest for ratio 1:6 Fe^{2+}/H_2O_2 (0.4M) compared to other samples.

Fenton reagent at 0.6M delivered better results compared to 0.4M as the COD value reasonable enough as it slightly reduced. As the previous result of 0.4M, the most foam was formed in the ratio of 1:6 Fe^{2+}/H_2O_2. However, the total suspended solid increased for 0.6M generally and the lowest value recorded was for ratio 1:6 Fe^{2+}/H_2O_2.

At 0.8M, the foam generation was the largest for all three ratios. The highest was for 0.8M, 1:6 Fe^{2+}/H_2O_2. On top of that, 0.8M with ratio 1:6 Fe^{2+}/H_2O_2 obtained the lowest COD level compared to all the Fenton reacted samples. Almost 87% of the COD was reduced compared to the raw sample in 0.8M with ratio 1:6 Fe^{2+}/H_2O_2. The total suspended solid fairly increased more compared to both 0.4M and 0.6M and the highest recorded was for 1:2 Fe^{2+}/H_2O_2.

At 1M, foam generated was lesser than than 0.8M but significantly higher than 0.4M and 0.6M. The total suspended solid increased for 0.8M generally and the lowest value recorded was for ratio 1:6 Fe^{2+}/H_2O_2. The highest value for total suspended solid overall was for 1M with ratio 1:2 Fe^{2+}/H_2O_2. The lowest COD recorded was for ratio 1:6 Fe^{2+}/H_2O_2 but the value was slightly higher compared to 0.8M. In comparison, about 86% of COD was reduced compared to the raw sample.

The foam generation was generally the highest for ratio 1:6 Fe^{2+}/H_2O_2 and heat energy was release proving that the reaction is exothermic. The COD level for 1M is higher compared to 0.8M due to large amount of hydroxyl radical generation which eventually consumes the dissolved oxygen in the samples [14]. Therefore, the efficiency in degradation of recalcitrant compounds will reduce and excess of ferrous sulphate. The results discussed above is portrayed as per graphs below:

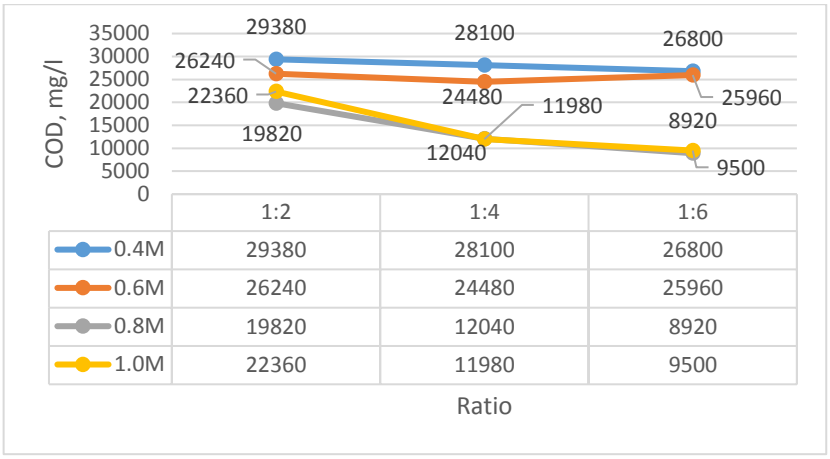


Fig 7: COD reduction with different ratio of Fe^{2+}/H_2O_2 with corresponding molarity

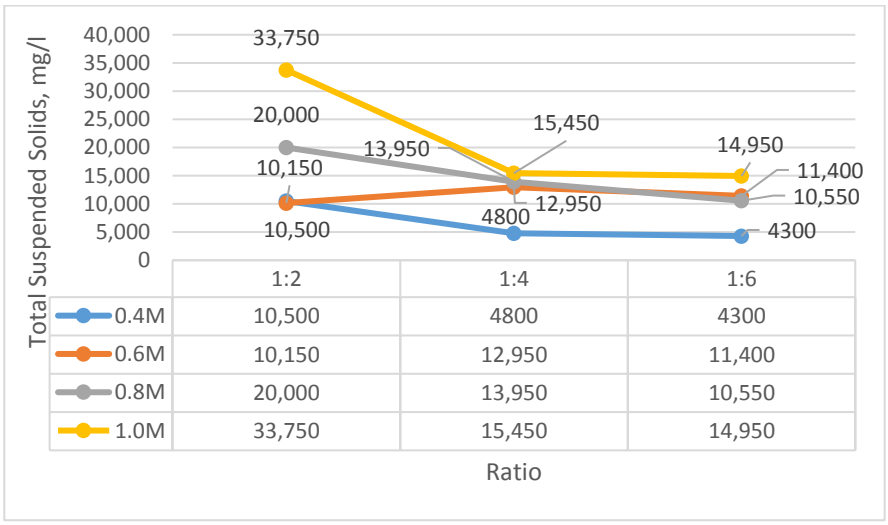


Fig 8: Total suspended solids reduction with different ratio of Fe^{2+}/H_2O_2 with corresponding molarity

3.3 COD reduction by Physical Treatment

Physical treatment is done to study the characteristics of PORE. There are four major fatty acids that contains in crude palm oil which are palmitic acid, oleic acid, linoleic acid and stearic acid [15]. The fatty acid sensitive towards pH and temperature changes in which the bonds of the fatty acids will break down and it will degrade into a new compound. Therefore, the physical treatment is done to compare the efficiency of degradation of organic compounds comparing to Fenton process. The physical treatment conducted were variation of pH and temperature. Raw samples were prepared for each rounds of test for both temperature and pH

treatment. Physical treatment is the treatment that does not involve Fenton treatment in the same samples. Samples prepared for Fenton treatment are a different batch. After the physical treatment, COD and BOD level were tested as shown in the tables below.

Table 12: pH treatment

pH Physical Treatment				
Parameter pH	**COD, mg/l**	**BOD, mg/l**	**Suspended Solids, mg/l**	**Turbidity, NTU**
2	25660	2815.1	3000	246
6	24760	2695.7	4000	208
8	25180	2712.4	4500	207
10	24300	2670	5000	217

pH treatment was conducted by adjusting the pH of the samples. The pH was adjusted by using 2M H_2SO_4 and 5M NaOH. The pH values applied were 2, 6, 8 and 10. pH 4 was not tested because the pH of the raw sample lies in the range and the results of COD and BOD of that particular sample can be assumed as the raw sample results. No Fenton reagent was added on the physical treatment as mentioned earlier. pH treatment conducted does effect the reading of COD and BOD levels because the organic compounds will change structure when it at different pH. The pH of PORE increases, organic compounds would also increase the solubility and forms a layer of 'soap' [16]. Based on table 3, the trend of data shows that high pH value results in lower COD and BOD levels. Besides, changes of pH would cause organic compounds to change its structure into another type of organic compound as well [17].

Table 13: Temperature Treatment

Temperature Physical Treatment					
Parameter / **Temperature, ^oC**	**COD, mg/l**	**BOD, mg/l**	**Suspended Solids, mg/l**	**Turbidity, NTU**	**pH**
35	22820	2503.5	667	256	4.78
45	21960	2395.2	1333	237	4.78
55	22900	2528.9	2667	233	4.78
65	25200	2715.6	4000	213	4.78

Temperature treatment was done by applying heat to samples based on the manipulated temperatures as shown in Table 4. The temperature of PORE samples is increased using a hotplate with a magnetic stirrer. Each samples were heated to the subjected temperature for 30 minutes. The best result was obtained for 45^{o}C as seen on the table above. The worst result was for the highest temperature. This is because oleic acid will decompose and change its structure into stearic acid when at high temperature. N. Zhang et al. (2013) stated that oleic acid poses weak stability due to the double bond structure [18]. Besides, R. Pearcy (1978) also reported that organic compounds could decompose into different type of organic compounds when the temperature is high [19]. For example, according to R. Pearcy studies, composition of linoleic acid has decreases about 15% when temperature was increased. Hence, this will increase the saturated organic compounds. This will result in simultaneously for the increase of stearic acid as there is reduction in linoleic acid. Below are the graphical analysis of both pH and temperature treatment.

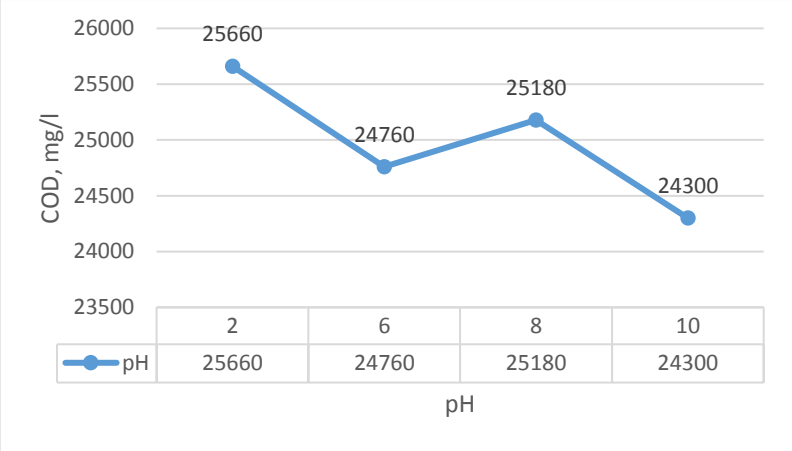


Fig 9: COD reduction by varying pH

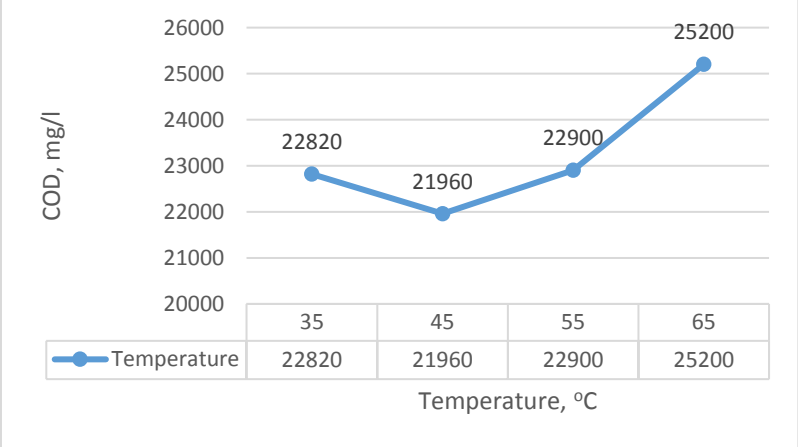


Fig 10: COD reduction by varying temperature

Figure 3 and 4 shows the graphical analysis of the physical treatment on PORE and sludge. The temperature and pH were manipulated to determine the percentage of reduction of COD. Based on the results, pH 10 gives the lowest COD for pH treatment which is a 65% reduction of COD and for the temperature treatment, 45°C gives the lowest COD which is a 69% reduction of COD compared to the raw sample.

Table 14: PORE and Sludge characteristic before and after treatment

No	Characteristics	Value (Before)	Value (After)
1	pH	4.84	2.28
2	COD, mg/l	70,300	8920
3	BOD, mg/l	9350.4	195.4
4	Turbidity, NTU	446	50.9
5	Total Suspended Solids, mg/l	13,000	10,550

Based on Table 5, sample used was diluted to 1:10 factor before undergoing treatment. The values for after reaction was chosen from the sample that reacted at 0.8M with ratio 1:6 $Fe^{2+/}H_2O_2$ as it has the best COD among all the other samples. It is noticeable that there is drastic reduction in COD, BOD and turbidity. In addition, there is also minor reduction for total

suspended solids. However, the main aim of the experiment is to reduce the COD and BOD levels of the raw sample. Both the values were successfully reduced by 87% and 98% respectively compared to the raw sample.

3.4 Experimental Analysis

3.4.1 Elemental Analysis

Atomic Absorption Spectroscopy Analysis for treated and untreated samples

AAS was used for elemental analysis to detect the concentration of iron in treated and untreated sample. Based on the results, it was clear that iron increased from the raw sample to the Fenton treated sample.
Below are the results obtained from the AAS instrument.

Table 15: Concentration of Iron in treated and untreated sample

Treatment	Concentration of Iron, mg/l
Raw Sample	10.03
Temperature (45^{o}C)	10.67
pH (pH 10)	10.76
Fenton (0.8M-1:6)	23.65

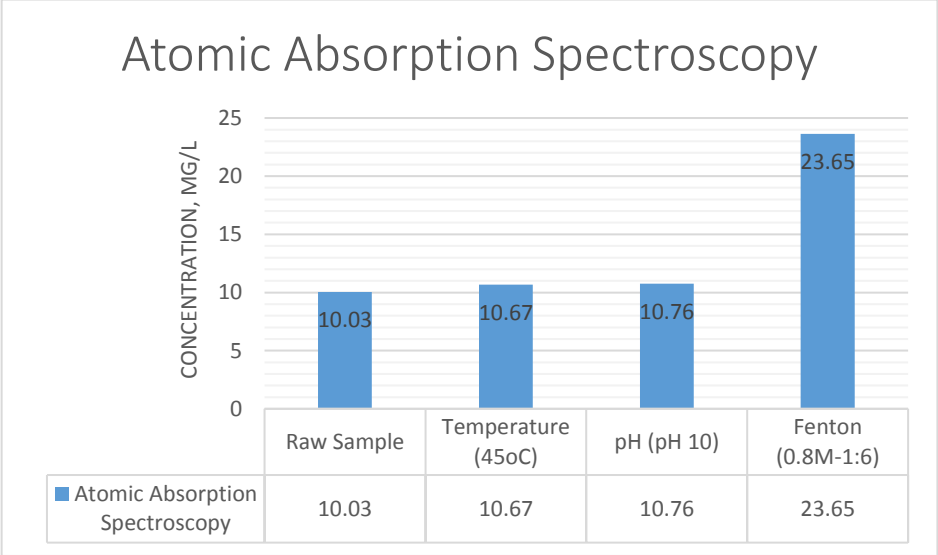


Fig 11: Concentration of Iron in treated and untreated sample

The highest content of iron was present in the Fenton sample which was 23.65 mg/l where it is twice more than all the samples. However, the concentration of iron can be reduced by adding sodium hydroxide [20]. One of the contribution for the high concentration of iron is because of the low concentration sodium hydroxide used which then resulted in unreacted ferrous sulphate [14]. One of the other reason Fenton process has the highest concentration of iron detected because of the iron salts precipitate. The formation of salts caused by the high concentration of Fe^{2+} will produce Fe^{3+} (ferrous ions) that are less reactive towards hydroxyl peroxide. Moreover, Brillas et al. (2009) research shows that there will be recycling redox process between ferric ions and ferrous ions when it has overdosed. So, the effectiveness of Fenton reagent will reduce as well. Based on the process mechanism, hydroxyl peroxide has to compete with ferrous ions in order to become radical state so that it will be able to degrade organic compounds. Hence, this explains that high concentration of Fenton reagent will result in higher amount of salt deposition. Therefore, this shows that Fenton process requires further

treatment and this can be considered as the disadvantage of this process as it requires additional cost to get rid of the iron precipitate in Fenton process.

3.4.2 Compound Analysis

Gas Chromatography-Mass Spectroscopy Analysis

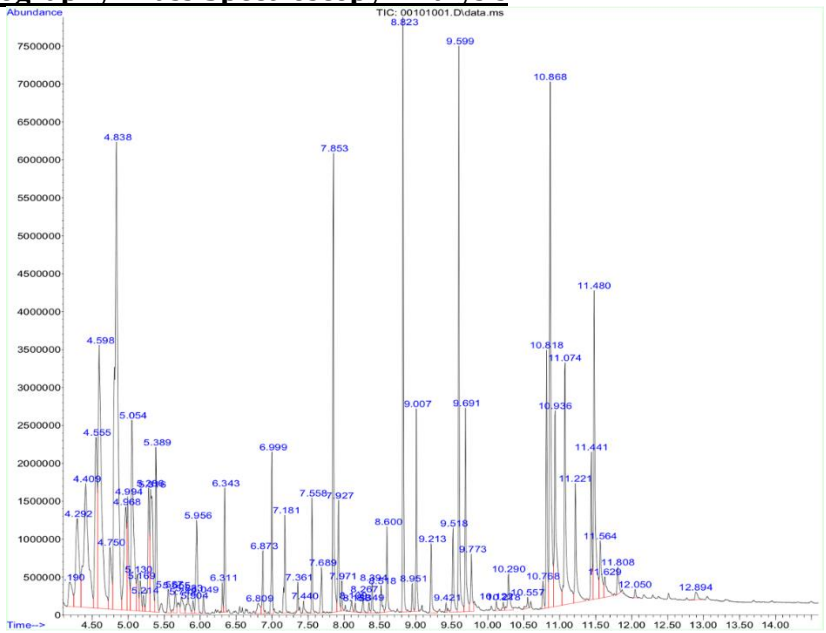


Fig 12: GC-MS Analysis for Raw Sample

Figure 6 shows the analysis obtained for Raw sample using GC-MS. According to Figure 6, there are two highest peak among the entire graph which shows the amount of abundance of particular organic compound in the specific residence time detected. Table below shows the results of organic compounds found in the two peaks.

Table 16: Organic Compounds founds with respect to time in GC-MS analysis

Time (min)	Organic compounds	Quality
8.823	Hexadecanoic acid	97
	Methyl Ester	97
9.599	Octadecanoic acid	98
	Methyl Ester	98

Table 7 shows the tabulated data of the organic compounds found in the respected time during the analysis run. It is found that, at time 8.823 min hexadecanoic acid and methyl ester were found with 97% quality matching with both the NIST08 and Wiley library. The abundance recorded for both this compounds were above 7500000 based on Figure 6. At time 9.599 min, octadecanoic acid and methyl acid were found with 98% quality matching with both the NIST08 and Wiley library. The abundance recorded for both this compounds were 7500000 based on Figure 6.

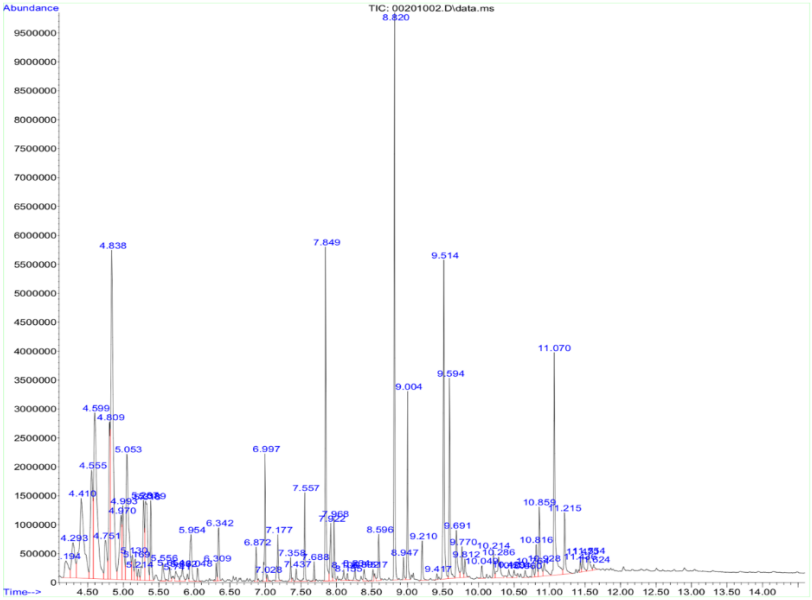


Fig 13: GC-MS Analysis for Fenton Process

Figure 7 shows the analysis obtained for Fenton process sample using GC-MS. The Fenton sample tested was with ratio 1:6 with 0.8M because it was the only Fenton reagent delivery the best result in terms of COD and BOD values. According to Figure 7, there are two highest peak among the entire graph which shows the amount of abundance of particular organic compound in the specific residence time detected. Table below shows the results of organic compounds found in the two peaks that has the similar timing as the raw sample analysis to compare and discuss the results.

Table 17: GC-MS Analysis for Fenton Sample

Time (min)	Organic compounds	Quality
8.820	Hexadecanoic acid	96
	Methyl Ester	96
9.594	Octadecanoic acid	99
	Methyl Ester	99

Table 8 shows the tabulated data of the organic compounds found in the respected time during the analysis run. It is found that, at time 8.820 min hexadecanoic acid and methyl ester were found with 96% quality matching with both the NIST08 and Wiley library. The abundance recorded for both this compounds were above 9500000 based on Figure 7. At time 9.594 min, octadecanoic acid and methyl acid were found with 99% quality matching with both the NIST08 and Wiley library. The abundance recorded for both this compounds were 3500000 based on Figure 7. Therefore, this shows that the organic compounds hexadecanoic acid and methyl ester were not degraded by Fenton process. This may be due to the low concentration of hydrogen peroxide (6wt%) which resulted in lesser production of hydroxyl radicals which eventually reduce the efficiency of the degradation process. Hence, higher concentration of hydrogen peroxide must be used to test the efficiency of the Fenton degradation process. On the other hand, the organic compounds octadecanoic acid and methyl ester were degraded by 53% based on the abundance value mentioned earlier.

4.0 Conclusion

From the application of Fenton Oxidation process, the presence of hydroxyl radicals had effectively degraded the recalcitrant compounds present in PORE and sludge. The 30 minutes Fenton reaction applied to the samples prepared was tested with Fenton reagent having ratio of 1:2, 1:4 and 1:6 and concentration 0.4M, 0.6M, 0.8M and 1.0M respectively to determine the COD, BOD, pH, total suspended solids and turbidity. It was found that the sample reacted in ratio 1:6 with Fenton reagent concentration of 0.8M had the best result overall in terms of COD and BOD mainly emphasized. This Fenton reagent ratio and concentration is said to be the best preparation as it managed to reduce 87% of COD and 97% of BOD compared to the raw sample.

Physical treatment was done without adding any chemicals. Temperature and pH that was varied in the physical treatment resulted in a reasonable COD reduction of 69% (45^{o}C) and 65% (pH 10) compared to the raw sample respectively. BOD level for temperature and pH treatment was reduced by 74% (45^{o}C) and 71% (pH 10) respectively. Based on the Atomic Absorption Spectroscopy instrument, it was found that the highest concentration of iron was from the Fenton sample with value of 23.65 mg/l whereas the lowest concentration of iron was found in the raw sample with value of 10.03 mg/l. The elemental analysis to determine the presence of compounds before and after treatment was determined using GC-MS. About 53% of octadecanoic acid and methyl acid were degraded based on the abundance as compared to Figure 6 and 7 for the Fenton process sample.

There is always room for improvement hence some recommendations are recommended for the future work of this project. First recommendation is the concentration of hydrogen peroxide could be fixed higher for example to 30wt%, 60wt% and 98wt% to study the effectiveness of Fenton process in degradation of recalcitrant compounds. Besides, the limitation of Fenton reagent could be studied by manipulating concentration of chemicals required for Fenton reagent and higher pH values tested for pH treatment as the highest pH resulted in the best result based on Table 3. Furthermore, more testing could be done such as HPLC and FID testing in order to determine the content of PORE before and after the treatment and effectiveness of Fenton reagent can be further study as well.

Apart from that, more research must be done to study to improve the mechanism of Fenton process on the PORE in order to scale up the Fenton process for PORE treatment process in industries scale. Fenton process would be an ideal process to be applied for an industrial scale as results obtained from experiments are very significant and promising. Besides, there are very less application of Fenton process up to industrial scale as most of them are being tested in a lab scale. Lastly, studies have to be done to reduce formation of iron salts precipitate in order to optimized the Fenton process.

ACKNOWLEDGEMENT

First and foremost, the completion of my thesis project entitled “Degradation Pathway of Palm Oil Effluent and Sludge Using Fenton Oxidation Process” would never been able to finish without the guidance from my supervisor, laboratory officers, family and friends.

I would like to express my deepest thank to my supervisor, Dr. Rajesh Rajasekaran for his excellent guidance, patience and supervision throughout my two semesters of completing this final thesis. I would also like to thank laboratory officers, Miss Lithnes Kalaivani Palniandy, Miss Nur Farihah Abdul Malik and Miss Puteri Farah Wahida who took the responsibility in assisting and providing me a good atmosphere in the lab during my research. They were willing to teach and guide me during the handling of lab equipment and materials

to ensure the ongoing of my research. My research would not have been possible without their helps.

I would like to thank my friends who as good friends were always willing to give a hand and suggestions that were constructive for my project. Last but not least, I would also like to thank to Miss Nurhazwani Ismail for being an excellent module coordinator. Thank you.

Reference:

[1] A. S. A. Ferdous Alam, A. C. Er, and Halima Begum, *Malaysian oil palm industry: Prospect and problem*, (2015).

[2] S. Kaman, I. Tan and L. Lim, Palm oil mill effluent treatment using coconut shell – based activated carbon: Adsorption equilibrium and isotherm, *MATEC Web of Conferences*, **vol. 87**, p. 03009, 2016.

[3] Y.J. Chan, M.F. Chong, C.L. Law, (2010). *Biological treatment of anaerobically digested palm oil mill effluent (POME) using a Lab-Scale Sequencing Batch Reactor (SBR)*. J. Environ. Manag. **91,** 1738e1746. http://dx.doi.org/10.1016/j.jenvman.2010.03.021.

[4] T.Y. Wu, A.W. Muhammad, J. Jahim, N. Anuar, (2009). *A holistic approach to managing palm oil mill effluent (POME): biotechnological advances in the sustainable reuse of POME*. Biotechnol. Adv. **27**, 40e52. http://dx.doi.org/10.1016/j.biotechadv.2008.08.005.

[5] A.L. Ahmad, C.Y. Chan, S.R.A. Shukor, M.D. Mashitah, (2008a). *Recovery of oil and carotenes from palm oil mill effluent (POME)*. Chem. Eng. J. **141**, 383e386. http://dx.doi.org/10.1016/j.cej.2008.03.005.

[6] P.E. Poh, W.J. Yong, M.F. Chong, (2010). *Palm oil mill effluent (POME) characteristic in high crop season and the applicability of high-rate anaerobic bioreactors for the treatment of pome*. Ind. Eng. Chem. Res. **49**, 11732e11740. http://dx.doi.org/10.1021/ie101486w.

[7] Z. Yejian, Y. Li, Q. Xiangli, C. Lina, N. Xiangjun, M. Zhijian, Z. Zhenjia, (2008). Integration of biological method and membrane technology in treating palm oil mill effluent. J. Environ. Sci. 20, 558e564.

[8] W. Eckenfelder, *Industrial water pollution control*, **3rd ed**. Boston: McGraw-Hill, (2000), pp. 240-245.

[9] M. Bello and A. Abdul Raman, *Trend and current practices of palm oil mill effluent polishing: Application of advanced oxidation processes and their future perspectives*, Journal of Environmental Management, **vol. 198**, pp. 170-182, (2017).

[10] M. Oturan and J. Aaron, *Advanced Oxidation Processes in Water/Wastewater Treatment: Principles and Applications. A Review*, Critical Reviews in Environmental Science and Technology, **Vol. 44**, No. 23, Pp. 2577-2641, (2014).

[11] J. Blanco, F. Torrades, M. Morón, M. Brouta-Agnésa and J. García-Montaño, *Photo-Fenton and sequencing batch reactor coupled to photo-Fenton processes for textile wastewater reclamation: Feasibility of reuse in dyeing processes*, *Chemical Engineering Journal*, **vol. 240**, pp. 469-475, (2014).

[12] B. Grote, *Application of Advanced Oxidation Processes (AOP) In Water Treatment*, In 37th Annual Qld Water Industry Operations Workshop, Parklands, Gold Coast, (2012), Pp. 17-23.

[13] J. Wang and L. Xu, *Advanced Oxidation Processes for Wastewater Treatment: Formation of Hydroxyl Radical and Application*, Critical Reviews in Environmental Science and Technology, **Vol. 42**, No. 3, Pp. 251-325, (2012).

[14] R. Nithyanandam and R. Saravanane, *Treatment of Pharmaceutical Sludge by Fenton Oxidation Process*, International Journal of Chemical Engineering and Applications, **vol. 4**, pp. 359-364, (2013).

[15] F. Kamp and J. Hamilton, *'How fatty acids of different chain length enter and leave cells by free diffusion', Prostaglandins, Leukotrienes and Essential Fatty Acids*, **vol. 75**, no. 3, pp. 149-159, 2006.

[16] Wolf, B. A, Pasquale, S. M., and Turk, J. (1991) Biochemistry 30,6372-6379 SES, (1994). *'The UV/Oxidation Handbook'*. Solarcham environment system, Markham, Ontario, Canada.

[17] N. Zhang, S. Sui, Z. Wang and Z. Ma, *'Thermal Stability of Soybean Protein Isolate-Based Oleic Acid/Stearic Acid Blend Edible Films'*, *AMM*, **vol. 469**, pp. 171-174, 2013.

[18] R. Pearcy, *'Effect of Growth Temperature on the Fatty Acid Composition of the Leaf Lipids in Atriplex lentiformis (Torr.) Wats.'*, *PLANT PHYSIOLOGY*, **vol. 61**, no. 4, pp. 484-486, 1978.

[19] M. Neff, S. Bhavsar, E. Braekevelt and M. Arts, *'Effects of different cooking methods on fatty acid profiles in four freshwater fishes from the Laurentian Great Lakes region'*, Food Chemistry, **vol. 164**, pp. 544-550, 2014.

[20] Palmoilworld.org, *'Welcome to the Malaysian Palm Oil Board // About Palm Oil // Washington, DC // 1-202-572-9768'*, 2014. [Online]. Available: http://www.palmoilworld.org/about_palmoil.html. [Accessed: 01- JUN- 2018].

Process Optimization of Bioconversion of Palm Oil Mill Effluent (POME) to Microbial Protein

Chee Shing Tan[1], *Li Wan Yoon*[1‡], *Yoke Kin Wan*[1], and *Adeline Seak May Chua*[2]

[1]School of Engineering, Faculty of Built Environment, Engineering, Technology and Design, Taylor's University, Malaysia

[2]Department of Chemical Engineering, Faculty of Engineering, University of Malaya, Lembah Pantai, 50603 Kuala Lumpur, Malaysia

Abstract. Technological advancements on microbial protein production via waste recovery method has reached its maturity recently. This study proposes a new aerobic approach on utilizing activated sludge in POME to simultaneously remove waste and produce microbial protein by optimizing sludge retention time (SRT 2, SRT 6, SRT 10) and oxygen supply rate (DO 1.0, DO 1.5, DO 2.0). Sequencing batch reactors (SBRs) were operated to examine effects of SRT and DO on nutrient removal, biomass yield, and protein production. Every setting is capable to achieve chemical oxygen demand (COD) removal efficiency of 90%. SRT 2 has the highest biomass concentration at 1.14 mg/L, and the highest biomass yield at 0.86 and protein content at 37.34%. DO 2.0 has the highest biomass and protein content as more oxygen are consumed to synthesize protein as storage. Operating the bioreactor at SRT 2 days at DO 2.0 is the best approach to achieve high and constant yield of microbial protein. Process parameters such as pH and temperature should be optimized to further enhance the protein synthesis capability.

‡ *Corresponding author: Li Wan Yoon, Taylor's University. Email: liwan.yoon@taylors.edu.my*

1 Introduction

The oil palm industry has been widely recognized as one of the major economic source for Malaysia since the 1960s. Over the past decade, Malaysia's palm oil mill has doubled its production, resulting in Malaysia accounting for half of the global palm oil production. However, with great benefit also comes great disadvantage. The palm oil industry is one of the most polluting industrial sector owing to its massive generation of palm oil mill effluent (POME) in the process of refining the oil. For every tone of fresh fruit bunch (FFB) produced, 0.67 tonnes of POME is generated [1]. With the annual production of 25 tonnes FFB per hektar [2], a total amount of 16.75 tonnes of POME is generated per hektar.

POME is an brownish yellow colloidal suspension which is often acidic the th pH value of 4 – 6 and a chemical oxygen demand (COD) range 35 000 – 57 000 mg L^{-1} [3]. POME are mainly produced from the sterilization of fresh fruit bunches, clarification of palm oil and effluent from hydrocyclone operations [4]. The exceptionally high organic content in POME also brings along high chemical and biochemical oxygen demand (COD/BOD), which can lead to serious environmental pollution, particularly in the water resources and the ambient air [5, 6]. Direct disposal of untreated POME can cause huge amount of organic particles to seep into the water courses and soil, which adversely affect aquatic life, domestic water supply and land uses [7]; On the other hand, temporary storage of POME can have equal polluting capability when the design of the tank does not accommodate to the proper collection of methane, which can progresseively cause air pollution by the means of greenhouse gas emission when the methane escape into the atmosphere. Several attempts on the wastewater treatment has been devised, with the most common ones being the anaerobic treatment owing to its cheap cost and low maintenance, but the open emission of the methane gas can add on another layer of harm to the current state of the environmnent [8, 9].

Current technologies has proven that wastewater advancement does not limit to the field of treatment technology, but also in resource recovery. Recent research has shown that the aerobic treatment of POME via yeast strains of *Candida Utilis sp.* shows promising results on reducing the carbonaceous content, and at the same time recovers most of the nutrients (mainly nitrogen and phosphorus) in the form of microbial protein (MP) in the cell body [10]. However, the culturing, seeding, acclimatizing, and build-up of the species colonies demands for ample amount of time and cost [3]. Owing to this, most company in the industry does not favour this high investment, but considerably low return rate technological advancement. The production of MP through algae on the other hand has a much simpler, scalable and less energy intensive compared to the application on yeast and bacteria [11]. Different species of algae such as *Chlorella sp.* and *Spirulina sp.* had been study to justify the economic potential, and to a certain degree proven as a reliable food source for human consumption owing to its plant-like nature. However, comparing to other MP producing organisms, algae demands large areas with considerable sunlight radiation. Moreover, macroscopic algae in most cases is only classified as a food source, but seldom categorized as MP due to its low protein content [12]. Comparing to yeast, bacteria also has a stance in the MP world, with the former focusing on human consumption, while the latter for the application of agricultural feed [13]. The restriction of the application of bacterial MP on human consumption is largely because of its bacterial nature which could be detrimental to human health such as development of gout, plus the high content

of nucleic acid and the components of cell wall, which limits the protein intake when ingested [14].

Several literature has highlighted the approach to optimization of bioreactor is through the control of operating conditions. SRT and DO are the most important factors in terms of biomass yield. In the case of POME treatment, the right sludge age is highly essential in order to obtain high nutrients recovery, high organic matter utilization, as well as high biomass yield. The concern of POME in terms of aerobic treatment is the potential of nitrification and denitrification conditions that release nitrogen compound in the form of nitrogen instead of protein synthesis [15]. High SRT settings is most common to encounter nitrification because nitrifiers are slow growing microorganism species. Moreover, old sludge is undesirable as food source as more compounds that are undesirable exist in their biomass. Aeration rate of the aerobic treatment also plays a major part in the control of biomass yield. According to Ge et.al [15], usual COD treatment scheme demands for very high aeration rate at the DO level of 4 mg/L for high strength waste effluent that contain fats, which corresponds to high energy and cost demand. Thus, high rate activated sludge process with short hydraulic and sludge retention could strategically convert organic matter into microbial protein and therefore minimizes aeration period and intensities.

In this study, lab-scale SBR process were operated to study the operating performance at different SRTs and DO rate, including nutrients removal, biomass yield and sludge protein content, with the aim to optimize the nutrients recovery approach of POME. These factors will be used to identify the best condition and parameter for MP production, and therefore open up the market of MP production as the major treatment for industrial effluent.

2 Materials and Methods

2.1 Characterization of POME

Raw POME was collected from a local palm oil plantation Seri Ulu Langat Plantation, Jalan Banting, Dengkil, 43800, Selangor Malaysia. The raw POME will be collected in vessel of 5 L, and were allowed to settle for 24 hours at the temperature of 4 ^{o}C in order to separate the supernatant from the residual solid in the POME. Both raw POME and its supernatant products were characterized for parameters such as pH, soluble chemical oxygen demand (sCOD), total ammoniacal nitrogen content (NH_4-N), total suspended solids (TSS), and volatile suspended solids (VSS). The POME is then stored in chiller at 4 ^{o}C for further use.

2.2 Setup of Bioreactor

The lab scale configuration for the aerobic oxidation of POME for simultaneous waste minimization and protein production was simulated by employing sequencing batch reactors (SBRs) at 1 L capacity operating in fed-batch mode. Before the operation of SBR, activated mixed culture sludge retrieved from the secondary clarifier of the local municipal waste management body, *Indah Water Konsortium*, which was stored at 4 ^{o}C is first reactivated by continuous aeration for 1 day. The sludge is then centrifuged (Scanspeed 1236, Labogene, Demark) at 6000 rpm for 10 minutes to remove the supernatant before seeding it into the aeration tank with diluted POME of 3000 mg C/L. Additional nutrients solution consisting of

ammonium chloride (≥99.8%, Merck), monopotassium phosphate (≥99.5%, Merck), magnesium sulphate (99.5%, R&M Chemicals) N-Allylthiourea (≥98%, Merck) and trace elements is supplemented with a C:N:P ratio at 92.3:5.59:1. This concoction of the trace element is adapted from the work of Ong et al [7]. The ratio of activated sludge to POME and nutrients solutions was fixed at 1:9 in volume on order to achieve a MLSS concentration of approximately 3000 mg/L. The initial pH will be adjusted to 7 ± 0.2 with the addition of 5M sulphuric acid. Different SRT and DO level were investigated to optimize the production of microbial protein. The mixed liquor suspended solid (MLSS) at the outlet of the process is analyzed through the APHA protocol [14] to define the effectiveness of the aerobic process of POME to produce microbial protein. Table 1 lays out the trace elements used as nutrients for the bioreactor.

Table 1 - Trace element essential for the growth of activated sludge in the form of microbial protein.

Trace Chemical	Concentration (mg/L)
Ethylenediamine tetraacetic acid	12.0
Iron (III) chloride hexahydrate	1.8
Potassium iodide	0.22
Boric acid	0.18
Cobalt (II) chloride hexahydrate	0.18
Manganese (II) chloride tetrahydrate	0.14
Zinc sulfate heptahydrate	0.14
Sodium molybdate dehydrate	0.07
Copper (II) sulfate pentahydrate	0.04

2.3 Process Optimization if aerobic oxidation of POME

2.3.1 Operation of the aerobic reactors at different sludge retention time (SRT)

The investigation of the variation of SRT (SRT = 2 days, SRT = 5 days, SRT = 10 days) is conducted in the aerobic reactor (with a working volume of 600 ml) in fed-batch mode. The operating temperature of the SBR is kept constant at ambient T = 30 ± 1^{o}C [3] using a heat jacket-insulated bioreactor. The aerobic condition is achieved by supplying air at the aeration rate at 1 vvm. Air diffuser was attached at the end of the air tube to ensure proper oxygen distribution. The magnetic stirrer is set to rotate at 600 rpm to ensure homogenous mixing. In this study, the bioreactor was operated under fed-batch mode at the feeding interval of 24 hours, with the feeding rate as according to the SRT duration. The POME feed and the nutrients solution described in section 2.2 are added in equal quantity per feeding phase, and equal amount of MLSS were also pumped out of the reactor to prevent sludge accumulation. The transport of both feed and purge were automated with the help of peristaltic pump (Cole Parmer, Masterflex, USA). Sampling (30 ml MLSS) is done at the interval of 2 days to analyze the effluent and sludge characteristics. The experimental setup is shown in Figure 1.

2.3.2 Operation of the aerobic reactors at different aeration rate (DO)

The effect of DO on MP production was also investigated to understand the correlation between dissolved oxygen to the biomass growth rate. Three levels of DO level were studied, which were 1.0 vvm, 1.5 vvm and 2.0 vvm. The employment of the reactor configuration is similar with that mentioned in section 2.3.1 of the SBRs. Similar approach on analyzing the effect of aeration rate and the growth of biomass was apply.

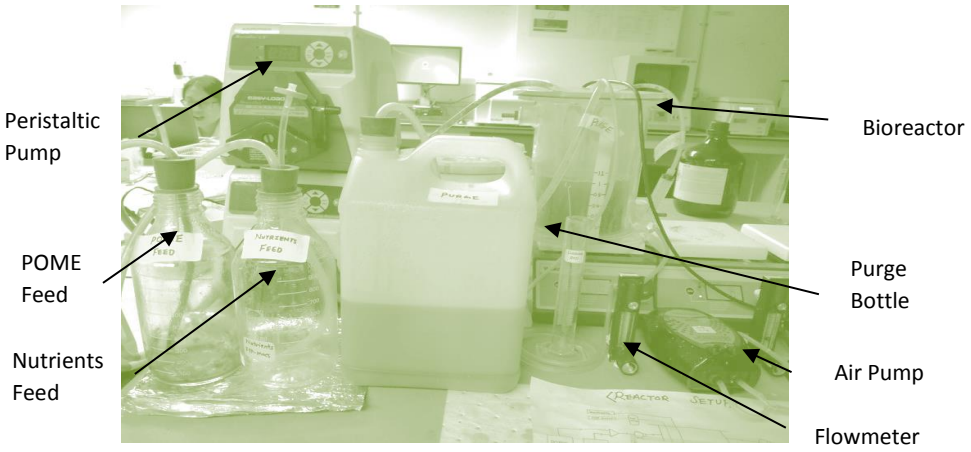


Figure 1 – Experimental setup of the bioconverion of POME into MP.

2.4 Analytical Methods

The COD of the sample was determined in accordance to the COD test kit procedure (Method: Photometric 25 – 1500 mg L^{-1}, Spectroquant, Merck, Germany), which requires 2 hours of digestion in a thermoreactor. The COD concentration was measured using a photometer (Spectroquant Prove 300, Merck, Germany). The TSS and VSS were determined following the standard APHA method for SS protocol. The weighing steps in the APHA method is carried out using a weigh balance (Mettler Toledo, MS204, Switzerland). The protein content was studied through the analysis of total Kjedahl Nitrogen (TKN). TKN was determined through the Kjedahl method, which is outsourced to PERMULAB Sdn. Bhd. The dissolved oxygen level of the mixed liquor is measured using a portable dissolved oxygen meter (Mettler Toledo, FIVEGO^{TM} F4, Switzerland), which is used to study the slope of the change in DO level during the feeding phase.

2.5 Performance Evaluation

As defined in the scope of this study, two key performance were evaluated, which is waste minimization justified by the specific substrate consumption rate ($-q_{POME}$), and the nutrients recovery justified by the protein production rate ($-q_{PRT}$). COD removal efficiency is a straightforward method to justify the performance of the waste treatment, which compares the initial and final COD level to justify COD removed, as seen in Equation (1).

$$\%\Delta\, COD = \frac{sCOD_o - sCOD_f}{sCOD_o} \times 100\% \quad (1)$$

The COD reduction was further computed into the specific substrate consumption rate, to understand the rate of utilization of COD present in the POME to carry out microbial activity. The specific substrate consumption rate was then computed through Equation (2).

$$-q_{POME} = \frac{COD\ Reduction}{Biomass\ Concentration \times time} = \frac{sCOD_o - sCOD_f}{X_o \times t} \times 100\% \quad (2)$$

The protein content in the biomass was obtained through the ratio of protein to the sludge dry weight, which can be seen in Equation (3). In this study, all the total Kjedahl nitrogen are assumed to convert into protein, which is calculated with the conversion factor of 6.25 as done in previous studies [120, 121].

$$\%\ Protein = \frac{Mass\ of\ Protein}{Sludge\ Dry\ Weight} = \frac{N_{KJ} \times 6.25}{VSS} \times 100\% \quad (3)$$

Similarly, the percentage protein can be analyzed to understand the specific protein production rate of the activated sludge over a fixed period of time, as shown in Equation (4).

$$-q_{PRT} = \frac{Protein\ Increment}{Biomass\ Concentration \times time} = \frac{M_{PRT,f} - M_{PRT,o}}{X_o \times t} \times 100\% \quad (4)$$

The yield of cell mass and protein was analyzed through Equation (5) and Equation (6).

$$Y_{X/S} = \frac{Cell\ Mass\ Increment}{COD\ Reduction} = -\frac{\Delta X}{\Delta S} \quad (5)$$

$$Y_{P/S} = \frac{Protein\ Increment}{COD\ Reduction} = -\frac{\Delta P}{\Delta S} \quad (6)$$

3 Results and Discussion

3.1 Characteristics of POME

The characteristics of both the raw POME and supernatant are measured and acquired from the mentioned analytical methods, and then compared side-by-side in Table 2.

Table 2 - Characteristics of raw POME and supernatant POME after settling for at least 24 hours at 4 C (standard deviation due to different containers.

Parameters	*Raw POME*	*Supernatant POME*
pH	4.23 ± 0.035	4.16 ± 0.035
TCOD (mg L^{-1})	70,950 ± 17.5	40,250 ± 12.5
sCOD (mg L^{-1})	34,350 ± 10.5	37,350 ± 10.5
TSS (mg L^{-1})	15,510 ± 1530	1,450 ± 130
VSS (mg L^{-1})	13,780 ± 1380	1,020 ± 100
NH_4-N (mg L^{-1})	109.31 ± 0.50	95.43 ± 0.50
sCOD/TCOD	0.484 ± 0.03	0.928 ± 0.03

Judging from the pH value obtained, it can be deduced that raw POME and supernatant POME are acidic wastewater. Compared to the DOE effluent discharge standard of 5.5-9.0 for Standard B [19], POME was consider a high-level pollutant and thus needed wastewater treatment procedure before discharging. TCOD accounts for both soluble and insoluble organic compound in the content. Comparing the TCOD value between raw POME and supernatant POME, it can be seen that a great fraction of TCOD is removed from the raw POME by merely separating the supernatant from the suspended solids. From the nutrients point of view, this is non-essential for bacterial growth as food was deprived from supply. However, most microorganism can only utilize soluble organic matter in the wastewater for microbial activity, hence feeding raw and supernatant POME would have similar food fraction available for the utilization of microorganism.

In this case, supernatant POME would be a more suitable source of feed for protein production since there are more readily available food that consist of fraction of sCOD/TCOD of 0.93 compared to the raw POME at only 0.48. This ratio has been proven by Lee et.al [3] to be strategic for the maximum utilization of POME into value-added product, which includes protein. Besides that, this characterization study has also proven that the ammoniacal nitrogen available in POME is a great source of monomer in the synthesis of protein. However, as the C to N ratio for optimum cell growth rate has to be theoretically 92.3 : 5.59, it can be seen that the ammonium concentration present in the reactor is not sufficient to meet the ideal ratio. A simple calculation was done to prove that at the COD loading of 37,350 mg L^{-1}, the ammoniacal nitrogen should have the concentration of approximately 2,262 mg L^{-1}. Henceforth, this give rise to the strategy of supplying nitrogen in the form of ammonium chloride in order to meet the dietary requirement for healthy activated sludge growth.

3.2 Influence of sludge retention time variation on nutrients recovery

Three fed-batches of SBR has been employed consecutively at SRT 2 days, SRT 6 days and SRT 10 days. Their COD removal trend has been plotted in Figure 2.

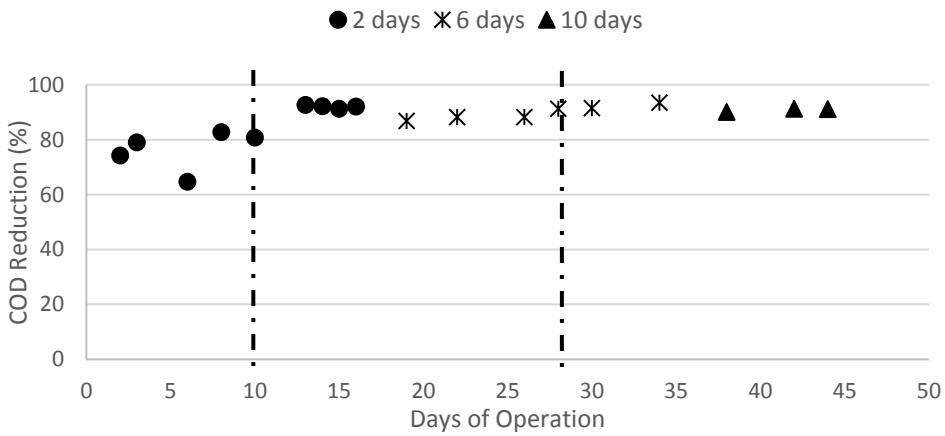


Figure 2- Percentage of COD reduction in the aerobic treatment of POME at SRT 2, SRT 6 and SRT 9. The vertical dash lines represents the switch to new SRT setting

In the first setting, SRT 2 days can be seen having lower COD reduction efficiency in the first 4 days, with a sudden sharp drop of COD on the 5th day down to 68%. Following that, the

COD removal rate remain relatively low at around 80%, which lasted until day 11 before high removal efficiency of 90% and above is reached. This phenomenon can be most likely due to the organic shock of the POME feed. When suddenly exposed to a high carbon content wastewater of 3000 mg L^{-1}, a shock response can be witnessed where the COD removal will be seen reducing and fluctuates at a slightly low value. Several studies has also proven this phenomenon [20], and all has concluded that the effect of shock were always short and the reactor efficiency resume within a short period. Nonetheless, the SRT 2 settings only took a total of 11 days to adjust to the new organic loading. Explanation by K. Vijayaraghavan and Wun [21, 22] instead mentions that fluctuation of COD removal often happens during the acclimatization phase. A study has achieved similar results of total maximum COD reduction of raw POME by 90% [23] through aerobic treatment, and thus, justifying the process capability of SRT 2.

SRT 6 days on the other hand shows the evidence where the bacterial colonies have acclimatized to the new organic loading, and henceforth achieving 88% COD removal efficiency within 3 day, and successively reaches 91% removal efficiency in 12 days. Similar to SRT 6 days, SRT 10 days directly achieves a total removal efficiency of 92% in the matter of 4 days. This indicates the acclimatization period of the activated sludge has passed and the activated sludge has become efficient in treating high strength POME. After studying the waste minimization trend, the biomass growth trend is analysed. The VSS/TSS ratio was acquired for each sample and the change of the ratio is documented in Figure 3.

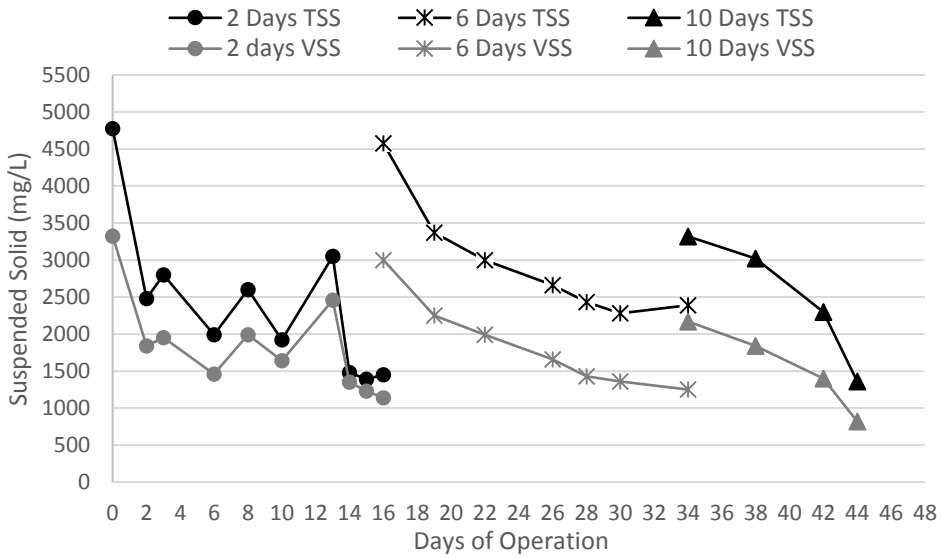


Figure 3 - VSS to TSS ratio in the aerobic treatment of POME at SRT 2, SRT 6 and SRT 10. The dashed lines indicates their linear best-fit line.

As a general rule of thumb by the DOE of Malaysia, a functional treatment system should have an optimum organic removal of wastewater to achieve a VSS/TSS ratio of 0.8 and above [22]. Higher VSS/TSS ratio indicates a higher bacterial activity in the bioreactor, meaning a better biomass health to carry out bacterial metabolism according to Selvam et.al [24]. Henceforth, the aerobic microbial protein production performance can be based and justified on their VSS/TSS trend, with a higher ratio indicates a better biomass concentration. Initially,

it can be seen that all 3 settings has the biomass at the start off point at 0.67± 0.02, which is based on the initial loading of 3000 mg L^{-1} sCOD and 3000 mg L^{-1} activated sludge. Judging from the trend line, SRT 2 days has an increasing VSS/TSS ratio, while SRT 6 days and SRT 10 days are decreasing.

From Figure 3, SRT 2 days has an increasing trend in the VSS/TSS ratio at a positive gradient of 0.0106 increment per day. The average ratio of this system is 0.79 ± 0.07, which is already at the borderline limit in reaching the optimal operating ratio. From there, the system has experience continuous increment in the VSS/TSS ratio. This could potentially means that the available substrate is highly utilized by the activated sludge to form new cells. As mentioned by J.S.S. Yadav [14], protein concentration increase when the total solids in the system increase. This indicates that aside forming new cell; the activated sludge is also utilizing available substrates to form proteins.

Similarly, the SRT 6 days setting also has an exponential decreasing trend for both TSS and VSS. Starting off at 4575 ± 35 mg/L and 3000 ± 70 mg/L and then exponentially decreases to 2390 ± 35 mg/L and 1250 ± 70 mg/L respectively at the course of 18 days. From their ratio perspective, the first and highest point of the graph is 0.66 ± 0.02, and finally ends at 0.52 ± 0.02 where the system acclimatize. This system shows a decreasing trend in VSS to TSS ratio. Graphically, the decreasing trend shown in for TSS and VSS are almost parallel to each other, indicating very low cell biomass increment rate. Several studies before has also shown the correlation of low sludge yield at high SRT. Sherrard and Schroeder compared the sludge production between 2 days and 18 days to found out 63% reduction [57].

Compared to the SRT 6 days settings, SRT 10 days on the other hand starts off the TSS and VSS at 3320 ± 35 mg/L and 2170 ± 70 mg/L, and experience a logarithmic decrease to 1360 ± 35 mg/L and 820 ± 70 mg/L respectively. The VSS/TSS ratio trend can be seen rather stable starting from 0.65 ± 0.02 and ends at 0.60 ± 0.02, experiencing a decrease. The SRT 10 days setting is the continuation from the SRT 6 days setting, which explains the slight reduction of initial biomass concentration. The reducing trend of both TSS and VSS could be due to the low loading of substrate into the bioreactor. At the configuration of SRT 10 days, the substrate loading creates the condition of substrate/biomass ratio (F/M) of only 0.1 kg COD/(kg SS.d), which is much lower than the conventional activated sludge process of 0.5 [51]. According Ouyang and Liu whom studied the relationship between SRT and biomass concentration, low substrate loading could cause endogenous respiration state in the cells, which pauses their physiological growth [59].

The protein data also shows similar trend in terms of biomass production and protein content. Total Kjedahl Nitrogen (TKN) which is obtained from PERMULAB Sdn. Bhd. is an indicator to gauge the amount of protein synthesized by the system. The biomass concentration can be seen in Figure 4, while the protein content in Table 3.

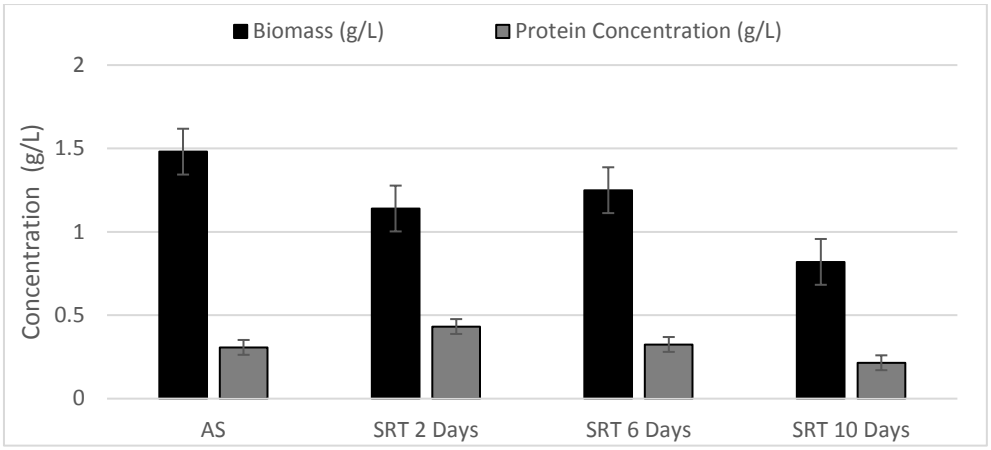


Figure 4 - (a) Correlation of TKN, final biomass concentration, and protein concentration for Activated Sludge, and sludge from SRT 2, SRT 6 and SRT 10. (b) Protein content in each sludge

Table 3 - Data of total Kjedahl nitrogen (TKN), protein concentration and percentage.

SRT	TKN (g/100g SS)	Protein (g/L)	Protein content (%)
Activated Sludge	3.32	0.307	20.75
2 d	6.07	0.432	37.94
6 d	4.16	0.325	26.00
10 d	4.2	0.215	26.25

Protein content can be witnessed to experience a significant surge in the SRT 2 days from the activated sludge inoculum. Comparing the biomass and protein concentration in Figure 4, it is easy to notice that the SRT 2 days setting has a high fraction of protein compared to the other two settings. Moreover in Table 3, it can be clearly seen that protein content surged from 20.75% to 37.94% in the SRT 2 days setting even though the biomass concentration experiences a reduction. This proves the occurrence of microbial protein to form protein for storage. SRT 6 days and SRT 10 days has shown a lower but relatively stable protein content at 26% and 26.25%. Judging from the reduction of biomass and protein concentration in SRT 10 days, cell lysis might has occurred and therefore reduction of the biomass controls the food uptake by the bacteria. Protein reduction is due to the lack of food in the first place, and henceforth no storage of nutrients as intracellular granules nor EPS. From the COD reduction trend analyzed above in SRT 10 days, it can be seen that the utilization of food is mainly for the survival of the cell. Low SRT also gives the condition of high food to microorganism (F/M) ratio, which encourages the storage of excess carbon substrates to convert into intracellular storage granules and certain fraction of EPS [60]. High SRT on the other hand has low F/M ratio, which indicates the low production of EPS. As protein is the dominant component in EPS, high SRT inhibits the formation of protein due to lack of food. The protein production performances are laid out in Table 4.

Table 4 - The production performances of cell mass and protein for SRT 2, SRT 6, and SRT 10

SRT	Cell mass yield (mg SS/mg COD)	Protein yield (mg protein/mg COD)	$-q_{POME}$ (mg COD/mg SS/d)	$-q_{PRT}$ (mg protein/mg SS/d)
2 d	0.8596	0.0079	0.1394	0.4156
6 d	0.6220	0.0008	0.1483	0.3113
10 d	0.7962	-0.0087	0.2068	0.1778

From the data obtained above, the best performance for cell mass and protein yield on the overall is SRT 2 days with the cell mass yield of 0.8596 mg biomass/mg COD consumed at the protein yield of 0.0079 mg protein/mg COD consumed. This high performance is explained earlier, where low SRT provides high FM ratio condition in the bioreactor for the production of cell mass. On the other hand, the SRT 6 days has a relatively low cell mass yield and protein yield This phenomenon can be seen where substrate are mostly utilized for the cell reproduction and not for protein synthesis nor cell growth owing to low food to microorganism ratio for storage [58]. Lastly, SRT 10 has a relatively high biomass yield at 0.7962 mg SS/mg COD, but instead consumes protein in the process, leading to negative yield of protein at -0.0087 mg protein/mg COD. This is caused by the endogenous respiration where the lack of food for the cell causes catabolism of stored cell structure to be broken down in order to carry out cell respiration [59]. Hence, from the analysis above, the setting of SRT 2 days is the most optimum setting for the simultaneous operation of COD reduction and biomass with protein synthesis.

4 Conclusion

This study demonstrated that operating aerobic treatment of POME at the SRT of 2 days would produce higher biomass yield and protein concentration compared to the SRT 6 and SRT 10 settings. SRT 2 days can achieve a total sludge protein content of 37.94%, which is higher by sewage activated sludge by 17.19%. SRT 6 and SRT 10 is only capable to enrich the sludge to 26% and 26.25%, which is the increment of only approximately 5%. The waste minimization capabilities were proven to be non-affected by the variation of SRT as long as enough acclimatization period is given to the activated sludge to enriched itself with suitable bacterial colonies. Low aeration rate at DO 1.0 vvm has also been proven to be more effective thatn DO 1.5 vvm and DO 2.0 vvm. Low aeration rate achieves a more stable increase of SOUR, indicating constant utilization of nutrients, whereas high aeration rate finishes the nutrients too quickly, and therefore create the feast and famine phase with endogenous respiration. The protein content can be further enhanced if more process parameters are taken into consideration, such as pH, temperature and organic loading rate.

References

[1] S. Yacob, M. A. Hassan, Y. Shirai, M. Wakisaka and S. Subash, "Baseline study of methane emission from open digesting tanks of palm oil mill elffluent treatment," *Chemosphere,* pp. 1575-1581, 2005.

[2] I. Comte, F. Colin, J. K. Whalen and J. -P. Caliman, "Agricultural Practices in Oil Palm Plantations and Their Impact on Hydrological Changes, Nutrient Fluxes and Water Quality in Indonesia. A Review.," *Advances in Agronomy,* vol. 1, no. 1, pp. 116:71-122, 2012.

[3] W. S. Lee, A. S. M. Chua, H. K. Yeoh and G. C. Ngoh, "Influence of temperature on the bioconversionof palm oil mill effluent into volatile fatty acid as precursor to the production of polyhydroxyalkanoates," *J Chemical Technology Biotechnology,* vol. 1, no. 1, 2013.

[4] A. Ahmad, A. Buang and A. H. Bhat, "Renewable and sustainable bioenergy production from microalgal co-cultivation with palm oil mill effluent (POME): A review," *Renewable and Sustainable Energy Reviews,* vol. 65, no. 1, pp. 214-234, 2016.

[5] S. S. Mahmod, J. M. Jahim and P. M. Abdul, "Pretreatment conditions of palm oil mill effluent (POME) for thermophilic biohydrogen production by mixed culture," *International Journal of Hydrogen Energy,* vol. 42, no. 45, pp. 27512-27522, 2017.

[6] Y. Y. Choong, K. W. Chou and I. Norli, "Strategies for improving biogas production of palm oil mill effluent (POME) anaerobic digestion: A critical review," *Renewable and Sustainable Energy Reviews,* vol. 1, no. 1, p. 1, 2017.

[7] O. Awotoye, A. C. Dada and G. A. O. Arawomo, "Impact of Palm Oil Processing Effluent Discharge on the Quality of Receiving Soil and River in South Western Nigeria," *Journal of Applied Sciences Research,* vol. 7, no. 2, pp. 111-118, 2011.

[8] S. J. Arceivala, in *Wastewater Treatment for Pollution Control* , New Delhi, Tata McGrawHill, 2000, p. 2nd Ed.

[9] E. a. Metcalf, in *Wastewater Engineering: Treatment, Disposal, Reuse* , New Delhi, Tata McGrawHill, 2003, p. 4th Ed..

[10] J. O. I. a. J. O. Ugwuanyi, "Treatment and Valorization of Palm Oil Mill Effluent through Production of Food Grade Yeast Biomass," *Journal of Waste Management,* vol. 1, no. 1, p. 9, 2014.

[11] D. M. Mahapatra, H. N. Chanakya and T. V. Ramachandra, "Chapter 15 – Algae Derived Single-Cell Proteins: Economic Cost Analysis and Future Prospects," *Protein Byproducts,* vol. 1, no. 1, pp. 275-301, 2016.

[12] M. G. Garibay, L. G. Ruiz and A. C. G. E. Barzana, "SINGLE CELL PROTEIN | The Algae," *Encyclopedia of Food Microbiology (Second Edition),* vol. 1, no. 1, pp. 425-430, 2014.

[13] M. G. Garibay, L. G. Ruiz and A. C. G. E. Barzana, "SINGLE CELL PROTEIN | Yeasts and Bacteria," *Encyclopedia of Food Microbiology (Second Edition),* vol. 1, no. 1, pp. 431-438, 2014.

[14] J. S. S. Yadav, J. Bezawada, C. M. Ajila, S. Yan, R. D. Tyagi and R. Y. Surampalli, "Food-grade single-cell protein production, characterization and ultrafiltration recovery of residual fermented whey proteins from whey," *Food and Bioproducts Processing,* vol. 99, no. 1, pp. 156-165, 2016.

[15] H. Ge, D. J. Batstone and J. Keller, "Operating aerobic wastewater treatment at very short sludge ages enables treatment and energy recovery through anaerobic sludge digestion," *Water Research,* vol. 47, no. 17, pp. 6546-6557, 2013.

[16] S. Matassa, W. Verstrate, I. Pikaar and N. Boon, "Autotrophic nitrogen assimilation and carbon capture for microbial protein production by a novel enrichment of hydrogen-oxidizing bacteria," *Water Reasearch,* vol. 1, no. I, pp. 137-146, 2016.

[17] H. K. Maehre, L. Dalheim, G. K. Edvinsen, E. O. Elvevoll and I.-J. Jensen, "Protein Determination-Method Matters," *foods,* vol. 1, no. I, pp. 1-11, 2018.

[18] Mercer University, "INTRODUCTION TO ENVIRONMENTAL ENGINEERING LABORATORY," Mercer University, Columbus, 2018.

[19] Department of Environment Malaysia, "A Guide for Investors," Department of Environment Malaysia, Kuala Lumpur, 2009.

[20] L. G. Mendoza-Espinosa and T. Stephenson, "Organic and Hydraulic Shock Loadings on a Biological Aerated FIlter," *Environmental Technology,* vol. 22, no. I, pp. 321-330, 2001.

[21] K. Vijayaraghavan, D. Ahmad and E. M. Abdul Aziz, "Aerobic treatment of palm oil mill effluent," *Journal of Environment Management,* vol. 82, no. I, pp. 24-31, 2007.

[22] W. L. Wun, G. K. Chua, S. Y. Chin and S. Y. Chin, "Effect of Palm Oil Mill Effluent (POME) Treatment by Activated Sludge," *Journal CleanWAS,* vol. 1, no. 2, pp. 06-69, 2017.

[23] Y. J. Chan, "Optimization on Thermophilic Aerobic Treatment of Anaerobically Digested Palm Oil Mill Effluent (POME)," *Biochemical Engineering Journal,* vol. 55, no. I, pp. 193-198, 2011.

[24] S. B. Selvam, S. Chelliapan and M. F. Md Din, "The effect of Mesophilic and Thermophilic Temperature on the Performance if an Up-Flow Anaerobic Sludge Bed (UASB) Reactor," *Research Journal of Pharmaceutical, Biological, and Chemical Sciences,* vol. 6, no. 4, pp. 984-989, 2015.

[25] J. H. Sherrad and E. D. Schroeder, "Cell Yield and Growth Rate in Activated Sludge," *Journal (water Pollution Control Federation,* vol. 45, no. 9, pp. 1889-1897, 1973.

[26] B. Li and G. Wu, "Effects of SLudge Retention TImes on Nutrient Removal and Nitrous Oxide Emission in Biological Nutrient Removal Processes," *International Journal of Environmental Research and Public Health,* vol. 11, no. 4, pp. 3553-3569, 2014.

[27] X. Huang, P. Gui and Y. Qian, "Effect of Sludge REtention Time on Microbial Behaviour in a Submerged Membrane Reactor," *PROCESS BIOCHEMISTRY,* vol. 36, no. 10, pp. 1001-1006, 2001.

[28] WWF, "THE PALM OIL INDUSTRY IN MALAYSIA," WWF, Petaling Jaya, 2002.

[29] C. G. Choong and A. McKay, "Sustainability in the Malaysian palm oil industry," *Journal of Cleaner Production,* vol. 85, no. 1, pp. 258-264, 2014.

[30] G. L. Karia and R. A. Christian, "10: Anaerobic Biological Wastewater Treatment," in *Wastewater Treatment Concepts and Design Approach*, New Delhi, Prentice-Hall of India Private Limited, 2006, pp. 291-293.

[31] W. Verstraete and S. E. Vlaeminck, "ZeroWasteWater: short-cycling of wastewater resources for sustainable cities of the future," *Int. J. Sustain. Dev. World Ecol.*, vol. 18, no. 1, pp. 253-264, 2011.

Preliminary Study for Optimisation of Pectin Extraction from Dragon Fruit Peels

Tang Shin Fong[1], and *Chua Bee Lin*[1§]

[1] School of Engineering, Taylor's University, 47500 Subang Jaya, Selangor, Malaysia

Abstract. *Hycocerus polyrhizus*, also known as dragon fruit is locally abundant in Malaysia and it is found to have high content of pectin that is comparable with the commercial sources of pectin. Pectin is widely used as stabilizer and thickening in food industry and its disease preventing potentials has gained interests of researchers for its usage in pharmaceutical industry. This research was a preliminary study to suggest the initial ranges of ultrasound-assisted extraction (UAE) extraction conditions for three extraction parameters (extraction time, extraction temperature and solid-liquid ratio). These ranges were identified through the study of single factor experimental design and further to be optimized using response surface methodology (RSM) optimization in order to maximize pectin extraction from dragon fruit peel. Qualitative test such as degree of esterification was carried out in this study to characterize the extracted pectin. Based on single factor experimental design, the ranges of process parameters were found to be 65°C-85°C for extraction temperature, 25min to 35min for sonication time, and 1:30-1:40 g/ml for solid-liquid ratio.

§ Corresponding author: beelin.chua@taylors.edu.my

1 Introduction

Dragon fruit is claimed to have a number of health benefits such as its ability to strengthen the immune system and helps prevent cancer and heart disease [1]. Due to its huge demands in the market, it is now widely grown in Asian countries such as Malaysia and Thailand. In 2013, the production of dragon fruit in Malaysia has reached 8577 metric tons and the value is still growing over years as the impact of using it as a source of nutritional juice [2,3]. The disposal of dragon fruit peels as a waste will leads to environmental problem. Hence, waste recovery of dragon fruit peels is always a continuous study for the researchers and approximately 11-13% of valuable pectin yield was found in dragon fruit peel [4].

Pectin is a heterogenous complex polysaccharide, which consists of esterified D-galaturonic acid in α(1,4) chain and forms 35% of the cell wall of the dragon fruit [5]. It is widely used in food industry as a gelling agent to produce jellies or jams for bakery line and a fat substitute in ice cream and spreads [6]. Pectin also having enhancing effect on cardiovascular health and reduces the risk of chronic diseases [7]. The gel properties of pectin are influence by the degree of esterification (DE). Pectin with DE more than 50%, it is classified as high methoxyl pectin (HMP) and pectin with DE less than 50% is classified as low methoxyl pectin (LMP) [8]. LMP can forms physical gels in the presence of calcium while HMP requires high sugar content (65%) and pH less than 3.5 to form physical gels [9]. Therefore, DE is important to classify the pectin and its applications in food and pharmaceutical industry.

The first step of pectin extraction is drying process of dragon fruit peel. There is several drying methods such as sun drying [5], oven drying [10,11] and freeze drying, but the most commonly used method is oven drying for the pre-extraction stage [12]. This pre-treatment process is important to keep the peels in low moisture content as it could preserve the peels as well as affects the quality of the extracted pectin such as antioxidant activity of the pectin [13–15]. In this research, oven drying was applied as it is not time consuming as compared to sun-drying and is not as costly as freeze drying for a large-scale production.

After the preliminary drying process, the pectin will be extracted with citric acid as solvent under ultrasound-assisted extraction (UAE) and microwave-assisted extraction (MAE). Ultrasound-assisted extraction has recently drawn much attention these years as compared to conventional method which is time consuming [17]. It was proven as a proficient extraction technique that can enhance the mass transfer across the cell membranes which leads to a higher extraction efficiency [18,16,19]. Limited research has been conducted to optimize the extraction process of dragon fruit peels using UAE [18,19]. With respect to this, UAE was selected to extract the pectin from the dragon fruit peels in this study. The optimization process of extraction typically involved response surface methodology (RSM) which known as a useful statistical techniques for developing and optimizing a process, in which a response of interest is influenced by independent variables such as extraction time, temperature and solid-liquid ratio [20,21]. The extraction process of pectin is a physical-chemical process in which hydrolysis and extraction of pectin macromolecules from plant take place continuously under the influences of temperature, solid-liquid ratio and sonication time [18,22]

However, limited studies were found to be relating to the identification of the practical ranges of extraction conditions of dragon fruit peels prior to RSM optimization to increase the extraction yield of pectin. Hence, this research objective is to suggest and identify the preliminary ranges of extraction parameters such as extraction temperature, sonication time and solid-liquid ratio prior to RSM optimization process.

2 Methodology

2.1 Pre-treatment of dragon fruit peels

Dragon fruit were collected from Soon Seng Ever Fresh Fruits Store in ss15, Subang Jaya, Selangor, Malaysia. 500g of dragon fruit peels were cleaned with distilled water to remove any impurities and dirt. The peels were then cut into smaller pieces using a knife.

2.2 Drying of dragon fruit peels

In this research, the dragon fruit peels were dried under 45°C though oven drying as shown in **Figure 1**. Moisture analyser (Model XM50, Precisa Gravimetrics AG, Switzerland) was utilized to measure the initial moisture content of the dragon fruit peels. With this data, the bone-dry weight of the peels can be estimated and bone dry weight is needed to calculate the moisture content of sample at respective time. The samples were placed evenly on an aluminium tray to avoid any overlapping that would reduce the efficiency of drying. The peels were dried in an oven (Model UN75, Memmert, Germany) under 45°C until constant weight of the samples had attained [12]. After drying, the dried dragon fruit peels were grinded into powder and the powdered peels were kept in polyethylene bag and stored at a desiccator for further analysis.

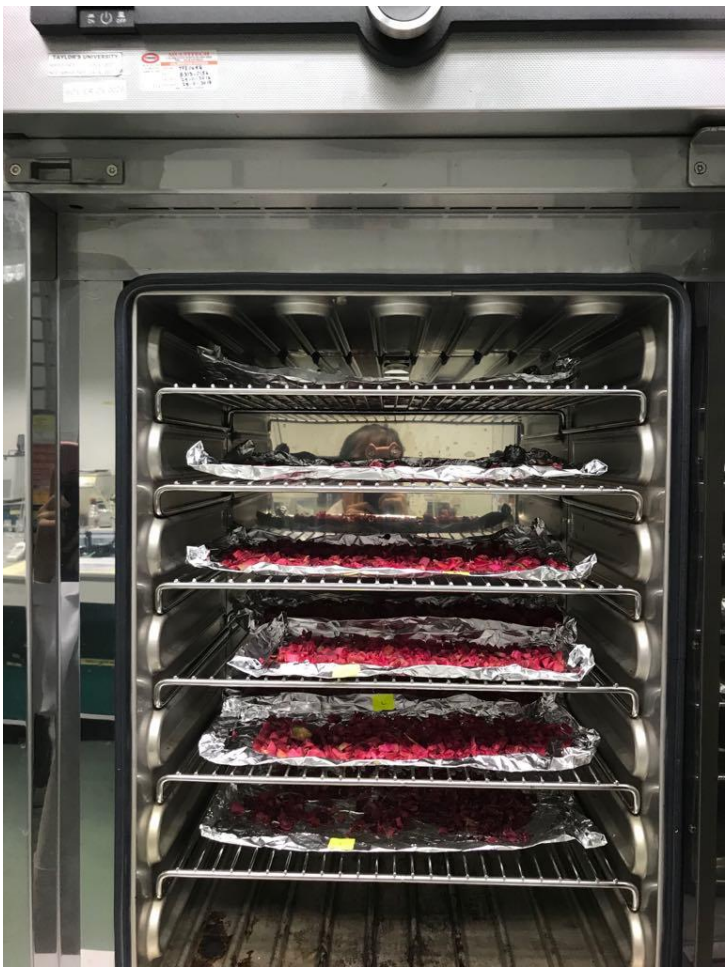


Figure 1. Drying of Dragon Fruit Peel

2.3 Pectin Extraction using Ultrasound-assisted Extraction (UAE)

The extraction of pectin was carried out based on previous findings with minor modifications [23]. Sonicator water bath (Elmasonic P120H, Elma, Germany) with power and frequency of 100 W and 37 kHz was used to extract the pectin from the dragon fruit peels. 3 gram of dragon fruit peels powder was first mixed with 0.1M citric acid solution with solid-liquid ratio of 1:20 g/ml and pH of 2.0. The solution was then placed in a universal bottle and then put inside the ultrasonic bath (Elmasonic P120H, Elma, Germany) with temperature of 65˚C for 25 min for the extraction to take place. The supernatant of the mixture was centrifuged out using a centrifuge (Scanspeed 1236MG, LaboGene, Denmark). The filtrated solution was then precipitated using 95% ethanol (ethanol-to-filtrate ratio, 2:1 v/v) as shown in **Figure 2**. The precipitate was then separated out using centrifuge at 7500 rpm for about 20 min. the wet pectin was rinsed with 95% ethanol for three respective times to remove the impurities and then dried in an oven operated at 50˚C overnight. The pectin yield extracted from the powdered dragon fruit peels was calculated using Eq. (1).

$$\text{Pectin yield (\%)} = \frac{\text{weight of dried pectin (g)}}{\text{weight of powdered dried peels (g)}} \times 100\% \qquad (1)$$

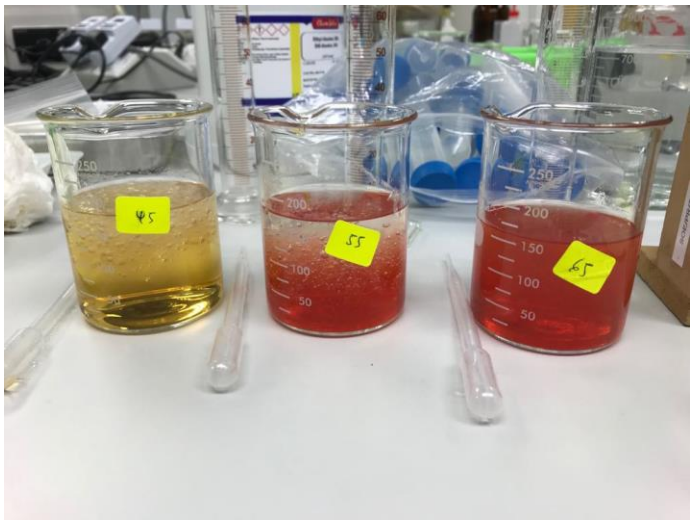


Figure 2. Precipitation process of dragon fruit pectin



Figure 3. Wet Pectin obtained after centrifugation.

2.4 Single Factor Experimental Design

Single factor experimental design was conducted by changing one parameter at a time while keeping all others constant. Therefore, the single factor experimental design with five levels was employed in this research and aimed as the preliminary tests to determine the optimal experimental range for each of the extraction parameters for the desired response, namely extraction yield of pectin.

Three extraction parameters (X_1: extraction temperature, X_2: extraction time and X_3: solid - liquid ratio) were identified using single factor experimental design. Table 1 shows the single factor experiment design pectin yield as the response.

The effects for the above-mentioned extraction parameters on the response (pectin yield) were plotted individually by varying one factor while keeping another two factors at their center points in each experiment. Based on the results of the single factor experimental design, the optimal ranges of these three factors were determined and could be applied subsequently in response surface methodology.

Table 1. Single factor experimental design

Run	**Extraction parameters**			**Response**
	Sonication time (min)	**Extraction temperature (**°C)	**SL ratio (g/ml)**	**Pectin Yield (%)**
1	15	65	1:20	
2	20			
3	25			
4	30			
5	35			
6	25	45	1:20	
7		55		
8		65		
9		75		
10		85		
11	25	65	1:10	
12			1:15	
13			1:20	
14			1:25	
15			1:30	

3 Results and discussion

3.1 Single Factor Experimental Design Analysis

Fifteen experiments runs were carried out according to the single factor design conditions arranged as shown in Table 1. Three significant factors, each with respective ranges that found in most research were employed in this study. Based on Figures 4 to 6, ranges for each parameter were further narrowed down from five variables to three variables based on highest pectin yield result.

Sonication time is an important extraction process parameter as it associated with mass transfer effect. Based on Figure 4, it was found that, the pectin yield increased with increasing the sonication time in ultrasound bath up to 30 min and it then decreased after 30 min. this is probably due to providing more time for the mass transfer of pectin from the dragon fruit peels to solution [8]. However, excessive exposure to ultrasonic waves caused the structural decomposition and pectin will be destructed, thus reduces the pectin yield of extraction [21]. It was found that the extraction time has a reverse effect on DE. This result was expected as similar result was found in [8]. As the result, the range of sonication time was limited to 25min to 35min with the central level at 30min.

The pectin yield is greatly influenced by the extraction temperature [21]. On the increasing extraction temperature from 45°C to 75°C as shown in Figure 5, the pectin yield from dragon fruit peels powder was found to be increased and then it decrease on further increment of temperature at 85°C. The diffusivity of pectin from the plant materials was found to increase with increase of temperature but high temperature would change the surface tension and viscosity of the acid solvent which result in changes of ultrasonic cavitation and causes pectin degradation, thus low pectin yield was found on further increment of temperature after 75°C [21]. Therefore, the range for extraction temperature to be further ultilised in RSM was 65°C to 85°C with central level at 75°C.

The condition of solid-liquid ratio for pectin extraction was usually in between 1:10 g/ml to 1:30g/ml from precious study. Referring to Figure 6, it was found that the pectin yield increased with the increase of solid-liquid ratio and there was no reduce in pectin yield for solid-liquid ratio up to 1:30 g/ml. Theoretically, higher solid-liquid ratio will leads to higher pectin yield due to the enhancement of penetration rate of solvent into plant matrix but further increment of solid-liquid ratio will causes reduction in the intensity of cavitation, thus reduces the pectin extraction yield [21]. Based on the result, the pectin yield is still increasing at solid liquid ratio of 1:30g/ml, thus the range of solid liquid ratio for RSM optimization were 1:30-1:40 with the central level of 1:35g/ml.

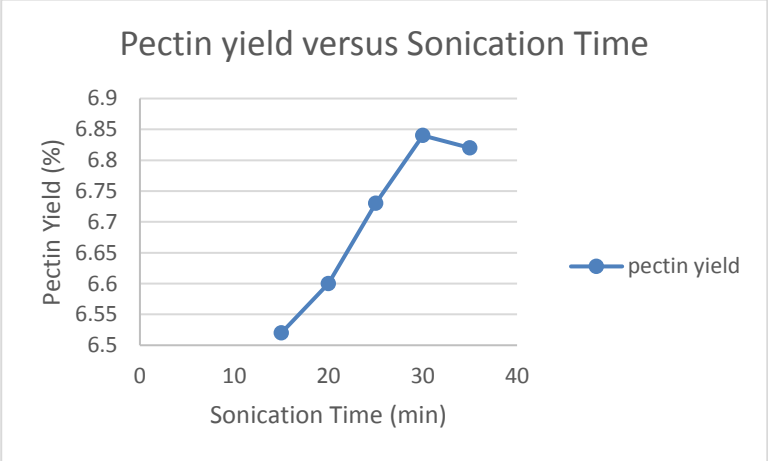


Figure 4. Influence of Sonication Time on Pectin Yield

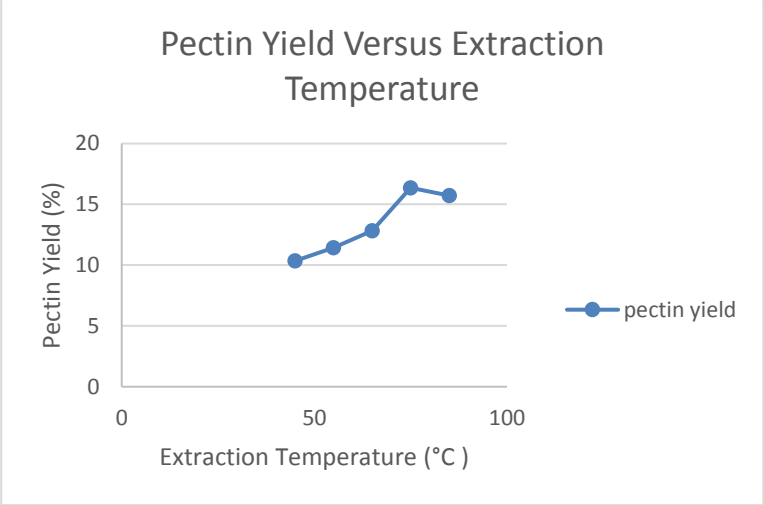


Figure 5. Influence of Extraction Temperature on Pectin Yield

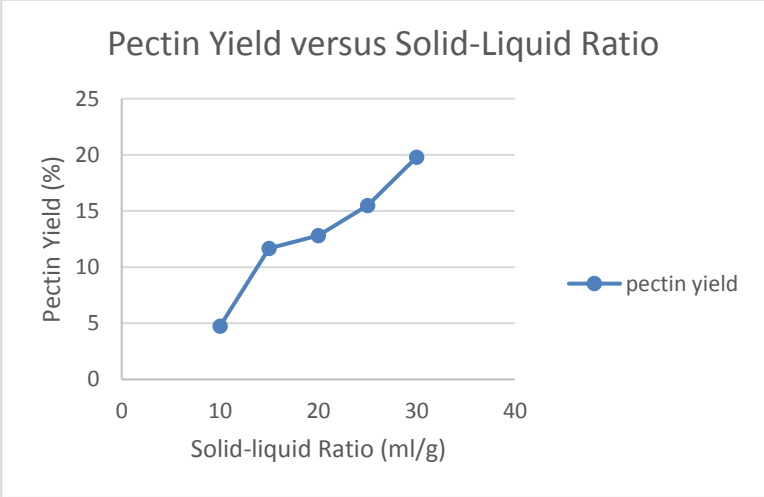


Figure 6. Influence of Solid-Liquid Ratio on Pectin Yield

4 Conclusion

In this research work, the preliminary ranges of each process parameters for RSM optimization using single factor experimental design were identified as 25min to 35min for sonication time, 1:30g/ml to 1:40 g/ml for solid liquid extraction and 65°C to 85°C for extraction temperature by using single factor experiment design. These ranges can be further optimised using RSM-optimization in order to determine the optimum extraction conditions for a highest pectin yield extract.

References

[1] S. Rahmati, A. Abdullah, E. Momeny, O.L. Kang, Int. Food Res. J. **22**, 233 (2015)

[2] K. Muhammad, N.I. Nur, S.P. Gannasin, N. Mohd. Adzahan, J. Bakar, Food Hydrocoll. **42**, 289 (2014)

[3] M. Zainudin, B.A. Hafiz, Status of Dragon Fruit Production in Malaysia, Malaysia, n.d.

[4] P.Y. Tang, C.J. Wong, K.K. Woo, Asian J. Biol. Sci. (2011)

[5] B.L. Chua, Y.C. Chong, MATEC Web Conf. **152**, (2018)

[6] K. Thirugnanasambandham, V. Sivakumar, J. Prakash Maran, J.P. Maran, Carbohydr.

Polym. **112**, 622 (2014)

[7] L.R. Adetunji, A. Adekunle, V. Orsat, V. Raghavan, Food Hydrocoll. **62**, 239 (2017)

[8] B. Pasandide, F. Khodaiyan, Z.E. Mousavi, S.S. Hosseini, Carbohydr. Polym. **178**, 27 (2017)

[9] F. Jafari, F. Khodaiyan, H. Kiani, S.S. Hosseini, Carbohydr. Polym. **157**, 1315 (2017)

[10] B.L. Chua, Z. Abdullah, K.Y. Pin, L.C. Abdullah, T.S.Y. Choong, U.K. Yusof, Res. J. Pharm. Biol. Chem. Sci. **6**, (2015)

[11] B.L. Chua, Z. Abdullah, K.Y. Pin, L.C. Abdullah, T.S.Y. Choong, U.K. Yusof, J. Eng. Sci. Technol. **12**, (2017)

[12] W. Wang, X. Ma, Y. Xu, Y. Cao, Z. Jiang, T. Ding, Food Chem. **178**, 106 (2015)

[13] N.S. Ramli, P. Ismail, A. Rahmat, Sci. World J. **2014**, (2014)

[14] A.S.M.K. Dayang Norulfairuz Abang Zaidal, Jamaeyah Md Rashid, Nurul Hazirah Hamidon, Liza Md. Salleh, Extraction and characterization of pectin from dragon fruit (Hylocereus polyrhizus) peels, Vol. 56, 2017

[15] A. Ali, C. Chong, S. Mah, L. Abdullah, T. Choong, B.L. Chua, Molecules **23**, 484 (2018)

[16] B.L. Chua, Y.L. Chen, MATEC Web Conf. **152**, (2018)

[17] H. Bagherian, F. Zokaee Ashtiani, A. Fouladitajar, M. Mohtashamy, Chem. Eng. Process. Process Intensif. **50**, 1237 (2011)

[18] A. Ali, X.Y. Lim, C.H. Chong, S.H. Mah, B.L. Chua, Sep. Sci. Technol. (2018)

[19] A. Ali, X.Y. Lim, C.H. Chong, S.H. Mah, B.L. Chua, LWT - Food Sci. Technol. **89**, 681 (2017)

[20] C.B. Lin, C.Y. Cze, MATEC Web of Conferences, 14AD, p. 2018

[21] C.S. Moorthy, I.G.; Maran, J.P.; Surya, S.M.; Naganyashree S.; Shivamathi, Int. J. Biol. Macromol., **72**, 1323 (2015)

[22] P. Methacanon, J. Krongsin, C. Gamonpilas, Food Hydrocoll. **35**, 383 (2014)

[23] N. Medina-Torres, T. Ayora-Talavera, H. Espinosa-Andrews, A. Sánchez-Contreras, N. Pacheco, Agronomy **7**, 47 (2017)

[24] W. Liaotrakoon, P. dr. ir. K. Dewettinck, Characterization of dragon fruit (Hylocereus spp.) components with valorization potential, Vol. PhD, 2013

[25] S.Q. Liew, N.L. Chin, Y.A. Yusof, Agric. Agric. Sci. Procedia **2**, 231 (2014)

[26] K.. Woo, Y.Y. Chong, S.K. Li Hiong, P.Y. Tang, J. Biol. Sci. (2010)

Co-Composting of Oil Palm Empty Fruit Bunch with Partially Treated Palm Oil Mill Effluent

Tang Yi Hui, Phoon Chow Lin*, Yoon Li Wan*

School of Engineering, Taylor's University, Malaysia

* yihui.tang@sd.taylors.edu.my

*Corresponding author: chowlin.phoon@taylors.edu.my

Abstract. With the rapid growth of palm oil industry globally, Malaysia being the world's second largest palm oil producer has been largely contributing in the production of palm oil. Following the tremendous amount of production, wastes generation such as empty fruit bunches (EFB) and palm oil mill effluent (POME) are being constantly produced in abundance until an extend where it starts to deteriorate the environment, leading to major environmental pollution when the wastes are not being properly managed before disposing. Therefore, the objective of this research work is to co-compost EFB with POME, having the aim of expediting the entire composting process. This can be achieved by reducing the size of EFB and homogenizing the compost mixture with sufficient aeration, converting the two major wastes into a value-added product. The formation of final compost would contribute to the oil palm industry as it can be turned into a value-added fertilizer which could solve more environmental problems, at the same time enhancing the economical benefits. In this research project, POME was added onto EFB with a weight ratio of 3:1 respectively, and the compost mixture undergone a rotation process using a constructed manual rotating drum at 2-3 days interval to provide sufficient aeration while maximising the homogenization of the compost mixture under aerobic condition. Throughout the co-composting period, temperature, pH level and moisture content were monitored and recorded at different depth of the compost mixture randomly at every 2-3 days interval to monitor the composting condition and aids in identifying the maturity level of the compost. Meanwhile, another important test of carbon to nitrogen (C/N) ratio was identified before and after the composting process. The final experimental result was found that the reducing in size of EFB with periodic rotation of compost pile would be the best combination for the co-composting of EFB and POME which resulted in lowest C/N ratio, final temperature falls within the range of 30 – 35 °C, pH level within the alkaline range while the moisture content remained within 60 – 75%.

Keywords: Empty fruit bunch, palm oil mill effluent, composting, rotating drum

1 Introduction

Among the 17 major oils and fats production in the world, palm oil has successfully secured its value by topping the production rate globally for many years. The tremendous production rate of palm oil is due to the high oil yield which is almost 13 times greater than soybean, 8 times greater than sunflower and 6.5 times greater than rapeseed [1]. Growing of oil palm has soon became a trend in many tropical regions in Southeast Asia upon realising the growing demand and value of palm oil. Malaysia being the world's second largest palm oil producer has successfully transform the palm oil industry from an agriculture commodity into a well-diversified industry which has been benefiting the economic growth for the country. The palm oil production rate in Malaysia was seen to have a flying growth over years from 4 million tonnes in 1985 to 18.8 million tonnes in 2012 [1]. Palm oil had since become the most important product in Malaysia which magnificently changed the scenario of the agriculture sector while boosting the economy. However, with the incredible amount of palm oil productivity being executed, the amount of wastes generated during the processing of palm oil was in excess up to a point that it is hardly negligible as it has extensively deteriorated the environment.

Corresponding to the extraordinary growth rate of palm oil industry, massive volume of solid wastes is generated including empty fruit bunch (EFB), palm pressed fibre (PPF), oil palm fronds (OPF), oil palm trunks (OPT) and palm kernel shells (PKS). Yet, the production of EFB had been worrisome as it was being constantly produced in large quantity. Knowing that EFB was produced after removing the fruits from fresh fruit bunches (FFB), for every 100 tonnes of FFB being processed, 20 – 22 tonnes of EFB were produced [2]. In 2005, the estimated annual production of EFB in Malaysia held a percentage of 53% among the 26.7 million tonnes of solid wastes produced; whereas in 2012, it was reported that more than 50 million tonnes of EFB was produced worldwide [134], [4]. This significant amount will not halt at this stage and is foreseen to increase with the continuous rising demand of palm oil in various applications, mainly for cooking oil, margarine, detergent, soap and cosmetics. In the past, due to the high calorific value of EFB, it was being used as fuel to generate steam through burning while the ash formed will be used as soil conditioner or fertilizer. This method was being commonly practiced by mill operators back then due to the constraint in technical utilization for proper EFB treatment. However, burning was later banned due to the emission of large amount of smoke which increases the carbon footprint and provide negative impacts to the environment [5].

Apart from solid wastes, palm oil mill effluent (POME) is another waste generated in abundance from the palm oil industry. POME refers to the effluent produced from the final stage of palm oil production. Approximately 5 – 7.5 tonnes of water are required for each ton of crude palm oil produced while more than 50% of the water eventually become waste water and ended up as POME [6]. Due to the hazardous characteristic of POME which is high in temperature, highly acidic, contains high level of biological oxygen demand (BOD) and chemical oxygen demand (COD), it is still considered as the most difficult and expensive waste to manage [138], [8]. When raw or partially treated POME is illegally discharged into nearby rivers without meeting the criteria of BOD and COD level set by the Department of

Environment (DOE), the hazardous content of POME could ended up killing the vegetation, leading to the blockage of filtration and causes water-logging, finally resulting in anaerobic condition in the river which not only suffocate the aquatic life but contaminating the drinking water for human [6]. Without proper management of POME, the sludge could become a major source of environmental pollution due to methane emission.

While realization on the potential environmental hazards caused by the wastes produced from the palm oil industry has increased, proper actions are highly desired to overcome the undesirable impacts towards the environment. With the fast pace of development and advancement in current technology, the industries are devoted in the co-composting of EFB and POME as a predominant approach to fully utilize the abundant wastes produced from the palm oil production as a solution to diminish the negative environmental impact [6], [9]. As EFB is known to be rich in carbon content while POME has high nitrogen content, the co-composting process can be performed by adding POME onto EFB as a source of nutrient for the enrichment of EFB. The high nitrogen content of POME favours the growth of microorganisms and assists the breaking down of cellulose and hemicellulose in EFB hereby leads to an advantage of shortening the co-composting period [10]. The final compost will be turned into a value-added product which is suitable to be used as fertilizer and soil amendment for the agriculture which benefits both palm oil industry and environment.

Henceforth, this study investigated on the effect of particle size of EFB and aeration condition. This can be evaluated based on the co-composting period and quality of compost with different form of EFB whereby the shredded EFB was further cut into shorter length to reduce the size of the shredded EFB. Meanwhile, a manual rotating drum was set up to provide proper rotation to ensure the compost receive sufficient aeration during the co-composting process. To identify the maturity of final compost, the carbon to nitrogen (C/N) ratio of composts were determined before and after the co-composting period, whereby temperature, pH value and moisture content were measured on a basis of 2-3 days intervals.

2 Materials and Methods

2.1 Pre-Treatment of Empty Fruit Bunch

The composting materials, EFB and partially treated POME were collected from Tuan Mee Oil Palm Mill which is located at Sungai Buloh, Selangor, Malaysia. Upon collecting the raw materials, the collected EFB undergone a series of pre-treatment process before starting with the composting process. The EFB was shredded into long fibre using a shredding machine, followed by drying in oven at 65 °C for at least 6 hours to ease the cutting process. The EFB was refined by cutting into shorter length of approximate 0.5 – 1.0 cm using a fibre cutting machine [11]. The entire shredding, drying and cutting processes were done at the Forest Research Institute Malaysia (FRIM). With such, the total exposing area of EFB fibres were increased, hence increasing the total contact surface with the microorganisms during aerobic digestion and speeds up the composting period.

2.2 Setting up of Different Batch of Composting Piles

Four different batches of compost piles aligning to the research objectives were set up as shown in **Table 2.1** below.

Table 2.1 Batches of Compost piles.

Group A **(Different form of EFB)**	**Group B** **(Different aeration condition)**
Cut EFB + Rotation (Compost pile A)	Cut EFB + Rotation (Compost pile A)
Uncut EFB + Rotation (Compost pile B)	Cut EFB + No Rotation (Compost pile C)

The first two batches of compost mixture were prepared by having one batch using the cut EFB while the second batch using the uncut EFB. This is to compare the difference between the compost maturity and period of co-composting process with different level of surface exposure due to different size of EFB. Likewise, the following two batches of compost mixture were prepared by having one batch of compost mixture undergo the aeration process by using the manual rotating drum while the other batch did not involve in any aeration process using manual rotating drum. Instead, occasionally the compost pile was manually flipped for homogenization purpose. This is to monitor the difference in the effect of aeration on the period of co-composting process. However, by referring to **Table 2.1** above, compost pile A was seen to duplicate in both areas, hence there were only three compost piles were set up to carry out the co-composting process. All the compost piles have the EFB mixed with POME at a weight ratio of 1:3, whereby each compost pile consists of 4 kg of EFB and 12 kg of POME respectively.

2.3 Design and Manufacturing of Manual Rotating Drum

Throughout the composting process, the compost piles require a turning process to maintain sufficient aeration and proper mixing of compost mixture to ensure the homogenization, good temperature control and moisture content on the compost mixture. However, one of the drawback was that there might be certain areas that were not being mixed thoroughly, leading to uneven mixing and temperature build up at certain parts of the compost pile, causing a poor aeration process to be carried out. Therefore, a manual rotating drum is set up to replace the physical turning process. Conducting a proper rotation is capable of providing sufficient aeration, thus enabling the reduction of compaction within the compost pile, at the same time creating a channel that allows the penetration of water, oxygen and nutrients into the compost pile. Nevertheless, proper rotation could provide homogenize mixing while maintaining even distribution of moisture content within the compost piles.

In this study, the compost mixtures were left to co-compost and it was then collected and placed into the rotating drum at an interval of every 2-3 days while the drum is rotated manually. The intervals between the rotating period was standardized to 3 rounds with 100 rotations per round as to allow the microbial activities of microorganism being carried out during the composting period without receiving external disturbance [12].

2.3.1 Detail Specification of Manual Rotating Drum

The rotating drum was set up using a recycled hydraulic drum of metal material with a standard drum capacity of 200 litres. The purpose of using metal as the material for the drum body is to ease the manual rotation process by having a firm and strong outer structure to hold the load after filling up the drum with the EFB and POME mixture. The rotating mechanism is function by fixing bearings on each end of the drum connected with a shaft, whereby one end of the shaft is extended into a handle used for rotation purpose. Besides, an opening on the central drum body allows the filling up and removing the compost mixture, which can be closed using a window cover and was held in place using metal hinge and latches. The side of the window opening is fixed with layers of rubber to avoid any leakage during the rotation. The drum is completely sealed when the cover is closed, hence creating an anaerobic condition inside the drum. Such condition can be overcome by opening the window opening after every 50 turns to allow the flow of air to enter the drum. With this, the aerobic condition was introduced and proper aeration on the co-compost material is achieved while improving the aeration intensity. A schematic drawing as shown in **Figure 2.1 (a)** below has illustrated the design of the manual rotating drum while **Figure 2.1 (b)** shows the actual manufactured manual rotating drum.

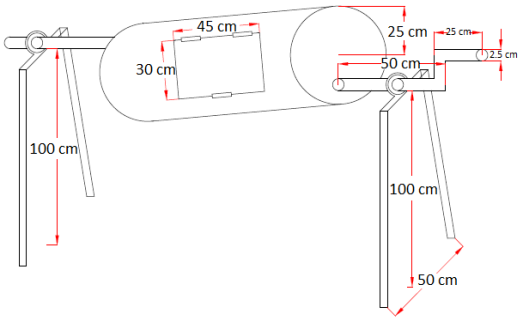


Fig. 2.1(a). Schematic drawing of manual rotating drum.



Fig. 2.1(b). Actual Manufactured Manual Rotating Drum.



Fig. 2.2. Internal mixer fixed inside the manual rotating drum.

As shown in **Figure 2.1 (a)** above, the manual rotating drum can be seen to be connected diagonally from one end to another end using a shaft. While the drum is being connected diagonally, it allows the mixing of compost in both horizontal and vertical direction in the drum, hence maximizing the homogenization of the compost mixture. Meanwhile, a total of six

internal mixers were installed as shown in **Figure 2.2** above, with three each at both ends in the drum to further assist in separating the fibrous compost structure. This would help in improving the homogenization of compost during rotation. To allow the rotation to happen, two ball bearings were installed at each end of the drum while the shaft is directly connected onto the bearing. The sizing of bearing is calculated based on the weight of total load being added into the drum. **Table 2.2** below shows the breakdown of the weight of each added load, as well as the diameter of shaft in order to determine the type and size of bearing according to the pillow block bearing specification provided by NSK Bearing Company that is suitable to handle the total weight in order to carry out the rotation smoothly.

Table 2.2. Detail Breakdown of Weight of Each Load, Shaft Diameter and Bearing Code.

Weight of Empty Metal Drum (kg)	Weight of EFB (kg)	Weight of POME (kg)	Total weight (kg)	Shaft Diameter (mm)	Pillow Block Bearing Code
18	4	12	34	25	UCP 205

2.4 Compost Data Analysis

The application of compost aids to increase the nutrient level and water retention of soil, providing a porous medium which allows the growth of roots, controlling the disease pathogens as well as decreasing the penetration resistance of soil [13]. Therefore, it is utmost important to identify the maturity level of compost to meet the specific criteria to be used as an effective fertilizer. During the entire composting process, there are several parameters that assist in determining the maturity level of the final compost product, and the parameters were temperature, C/N ratio, pH level and moisture content.

At the end of the co-composting process, several tests were carried out to identify the maturity level of the final compost. The carbon and nitrogen content of the composts were tested using the CHNS analyser, and finally obtaining the C/N ratio of the final compost. Meanwhile, to monitor the progress of the co-composting process, temperature and pH value of each compost pile were measured on site using a thermometer and a portable pH probe respectively, while the moisture content was measured in the laboratory using the XM-50 moisture analyser on a basis of 2 - 3 days intervals.

CNHS analyzer is a common tool to determine the carbon, nitrogen, hydrogen and sulphur content in organic materials. To carry out the analysis, samples will be freeze-dried and crushed, weighed and mixed with oxidizer in a tin capsule, followed by a combustion process which takes place in a reactor at high temperature of 1000 °C. During the combustion process, carbon will be converted into carbon dioxide; hydrogen to water; nitrogen to nitrogen oxide and sulphur to sulphur dioxide. These products formed during combustion will be swept out of the reactor by helium as carrier gas and passed through a heated high purity copper. The function of copper is to remove the unconsumed oxygen and finally converting nitrogen oxide to nitrogen gas. Then, the gases can be detected via three different ways which are: (i) GC separation followed by quantification using thermal conductivity detection; (ii) Partial separation by GC followed by thermal conductivity detection for C, H, N only, and (iii) A

series of separate infrared and thermal conductivity cells to detect individual components. Calibration is required for the quantification of each element through high purity "micro-analytical standard" compounds [14], [15].

As for the moisture analyser, it is an instrument used to determine the moisture content of various types of samples. To obtain the moisture content of each compost pile, samples were collected randomly at different depth and placed evenly on the tray in the moisture analyser. Firstly, the moisture analyser weight the sample, followed by heating and drying of sample at 100 °C for approximately 60 minutes. Finally, the dried sample is weighed again. This is a standard method used to measure the moisture content, which is known as Loss on Drying (LOD).

3 Results and Discussion

3.1 Characterization of EFB and POME

The initial Carbon (C), Hydrogen (H) and Nitrogen (N) compositions of EFB and POME before composting were tested using the CHNS analyser and the results were tabulated in **Table 3.1** below.

Table 3.1. Initial C, H, N Compositions of EFB and POME.

Samples	Unit	Parameters			
		Carbon, C	**Hydrogen, H**	**Nitrogen, N**	**C/N**
EFB	%	40.99	6.29	0.57	83.85
POME	%	32.55	5.28	1.78	21.32

Based on the results obtained above, EFB was found to have a comparatively higher carbon content and lower nitrogen content than POME. Meanwhile, the nitrogen content of POME was seen to be almost triple of EFB, indicating the presence of rich nitrogen source to be provided for the microbial activity which help in the protein generation inside the bodies of microorganisms during the composting process. This will eventually help in accelerating the composting period. Besides, the carbon-to-nitrogen (C/N) ratio represents another key factor indicating the maturity level of the compost. Knowing that EFB is naturally rich in carbon content, hence the initial C/N ratio of the compost is high. While the nitrogen-rich POME being added onto the shredded EFB, it aids in lowering the C/N ratio of compost to a more acceptable level. During the composting period, the carbon content of the compost materials was required to decrease gradually, showing that the microorganisms being actively carrying out microbial activity by consuming the cellulosic substrate and nitrogen from the compost piles, hence increasing the microbial protein and humic substances [16]. At the end of the composting process, a C/N ratio below 20 is considered as a satisfactory maturity level with C/N ratio between 12 – 15 would be the optimum range as the indication of matured compost [16], [17]. Therefore, from the result above, the C/N ratio of EFB and POME was 83.85 and 21.32 respectively, implying that none of these materials could be used directly as nitrogen source for plantation as the C/N ratio has yet to reach the satisfactory level of below 20.

3.2 Temperature Variation

Temperature is one of the important parameter to be taken into consideration throughout the co-composting period to indicate the efficiency and performance of the entire process [18]. The ambient temperature of the composting surrounding was measured to be approximately 26 – 29 °C during the composting period. In the present study, temperature was measured at multiple depth and spots randomly to obtain the mean temperature of each compost pile. When the high nitrogen content POME was added and mixed with EFB, the compost pile generated more heat due to the respiration of the microorganisms. All batches of compost piles started off at a mean temperature of 30 °C, and the temperature in each compost pile was seen to be gradually increasing at a slow rate, indicating the existence of microbial activity. The temperature profile of each compost pile throughout the composting period was illustrated in **Figure 3.1** below.

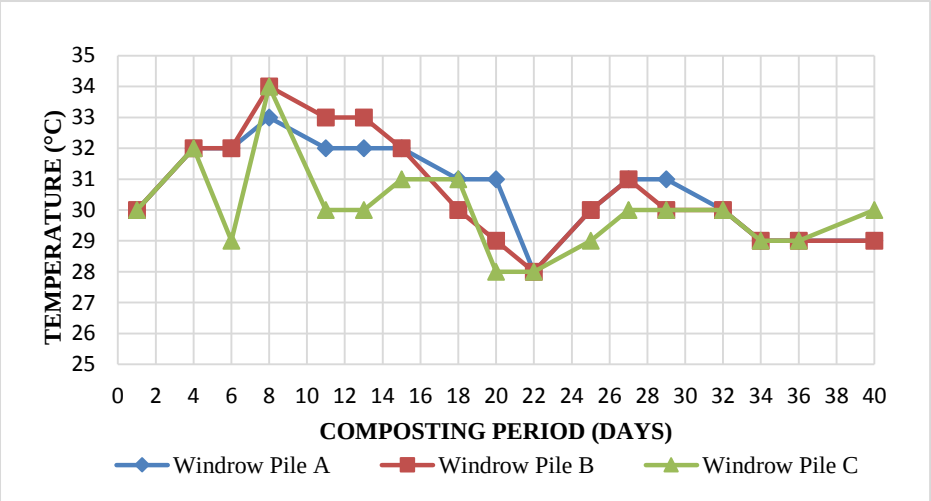


Fig. 3.1. Temperature profile for different co-composting batches of EFB + POME.

As shown in **Figure 3.1** above, it was observed that the mean temperature of all compost piles was at peak during Day 8, with compost pile A having a mean temperature of 33°C while both compost pile B and C was found to have a mean temperature of 34°C respectively. The phenomenon of rising in temperature occurred at random spots on each compost pile and the temperature was found to decrease slightly after every rotation done on both compost pile A and B. Up until Day 18, the mean temperature of each compost pile was found to be fluctuating within a range of 1 – 2 °C. After Day 18, the mean temperature was found to be gradually decreasing and finally reaching a constant temperature of 29 °C for all compost piles.

Despite the similar fluctuation in temperature profile for all compost piles, it was noticed that compost pile C shows a slightly different temperature profile trend as compared to compost pile A and B. Referring back to **Figure 3.1** above, it was found that on the Day 6 of composting, the mean temperature of compost pile C was seen to have a drastic drop from 32°C to 29 °C while both compost pile A and B remained constant at 32 °C. Similarly, compost pile C was seen to have a comparatively lower temperature than both compost pile A and B during Day 11 and Day 13. This phenomenon can be explained whereby insufficient aeration within the compost pile seemed to affect the microbial activity. This was because without sufficient

aeration, penetration of oxygen became limited due to the compaction of compost pile, thus resulting in low oxygen level available within the compost pile for the microorganisms to carry out aerobic digestion. Without active microbial activity being conducted, temperature of compost pile will remain constant and eventually decreases instead of increasing.

At the end of the composting period of 40 days, the temperature in each compost pile was not seen to rise until the optimum temperature range of 45 – 55 °C which was suitable for the activity of microorganisms to maximize the biodegradation process. This had indicated that the microorganisms in the compost piles were not able to reach thermophilic phase and decompose the materials actively [13], [16]. Instead, the microorganisms available within all compost piles have maintained at the mesophilic stage throughout the entire composting period. This condition reflected that all the compost piles have yet to reach maturity.

However, this does not imply the absence of decomposition from happening in the compost piles. The progress of the decomposition can still be observed via physical changes [16]. There was a change in colour in all compost piles from light brown to dark brown, as well as the fibrous EFB was seen to decompose at a slow rate and eventually forming lumps in various sizes. **Figure 3.2** below illustrated the physical changes on compost pile A.



Figure 3.2: Physical changes of colour and lump formation for compost pile A during composting; (a) Day 1 and (b) Day 40.

Through observing the physical changes of all compost piles, it was found that the formation of lump from compost pile A with cut-EFB and undergone periodic rotation progressed faster as compared to compost pile B which did not have the EFB being cut, as well as compost pile C which did not undergo periodic rotation. With this, it can be concluded that reducing the size of EFB with sufficient aeration shows a more promising composting rate as compost pile A shows the most significant difference as compared to compost pile B and C.

3.3 Moisture Content Distribution Analysis

Moisture content is not a parameter used to indicate the maturity level of compost, yet it is critical to be well-monitored throughout the composting process as it will directly determine the rate of decomposition along the composting period. It is highly essential to have the moisture content maintained between 60 – 75% as it contributes to high bioactivity level for the microorganisms as well as providing a good aeration capacity. While periodical turning of

the compost and the increasing in temperature during the process might lead to evaporation of water, necessity amount of moisture is added from POME to replenish the water loss as to sustain the microbial activities. The moisture content profile for all three compost piles that were subjected to three different methods of co-composting was illustrated as shown in **Figure 3.3** below.

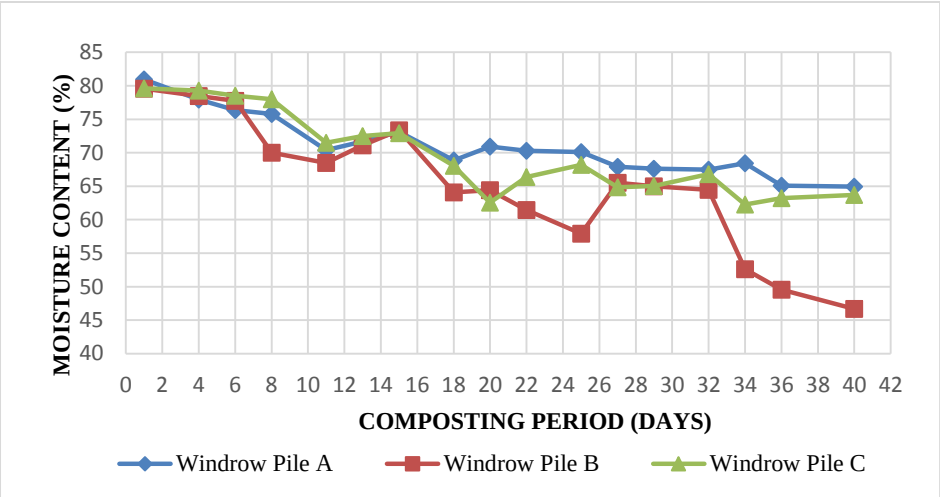


Fig. 3.3. Moisture content profile for different co-composting batches of EFB + POME.

Generally, the moisture content for all compost piles decreases along the composting period. It can be observed that there were days where the moisture content bounced back after losing some of the content. This was because additional POME had been added into all compost piles to maintain the moisture content level throughout the composting period, at the same time sustaining the nitrogen source as nutrient which will enhance the composting process. Referring to **Figure 4.3** above, it can be seen that compost pile A and C had similar trend in terms of the changes in moisture content profile while both compost piles managed to maintain its moisture content within 60 – 75% throughout the composting period. However, compost pile B was seen to have the most drastic fluctuation in terms of the lost in moisture, especially from Day 32 onwards until the end of the composting period. This is presumably because of the bulk structure formed by the uncut EFB which had a poor exposed surface area to retain the available moisture, leading to the non-uniform distribution of moisture which eventually explained the drastic loss of moisture content. Comparatively, compost pile A was seen to be able to absorb a relatively higher percent of moisture content as compared to compost pile B and C throughout the composting period. This explains why the rate of formation of lump was faster in compost pile A as the presence of additional moisture can enhance the microbial activities and the rate of decomposition.

Trisakti et al. [12] reported that the turning frequency of compost at an average interval of 2 – 3 days give the best moisture content value. Besides, Baharuddin et al. [16] has also reported that a moisture content between the range of 60 – 75% provides the best moisture content condition for composting. If the moisture content level is too high, the excess moisture will fill up the air cavity, resulting in the anaerobic condition within the compost pile. This will not only inhibit the growth of microorganisms but kills the aerobic microorganisms due to the deficiency of oxygen [12], [19]. Conversely, if the moisture content is too low, it will slow down the rate of decomposition and causes early dehydration for the compost pile. Such

condition will negatively affect the biological process and resulted in the degradation of final compost quality [20].

Therefore, it could be deduced that reducing the size of EFB with periodic rotation managed to enhance the composting process better than that of those without cutting the EFB and without undergoing periodic rotation. This is because reducing the size of EFB is able for the fibrous structure to have a better retention on the available moisture while periodic rotation managed to distribute the moisture evenly within the compost pile. Yet, all three compost piles managed to have the level of moisture content well maintained within the proposed range throughout the composting period, providing a good aeration condition as well as a high bioactivity level for the microorganisms.

3.4 Effect of pH

The pH value represents another indicator to identify the maturity level of a compost. During the initial stage of the composting process, the pH level was expected to be slightly acidic and slowly increased towards a slightly alkaline condition with the rise in temperature. This may due to the amount of ammonia being produced from the microbial activities related to nitrogen-containing matters. Additionally, the presence of POME enriching the compost also contributes to the slightly alkaline condition. When the compost has reached its maturity level, the pH level will normally at approximately 8 – 9 [16], [21]. The trend of the pH fluctuations in this study was illustrated in **Figure 3.4** below.

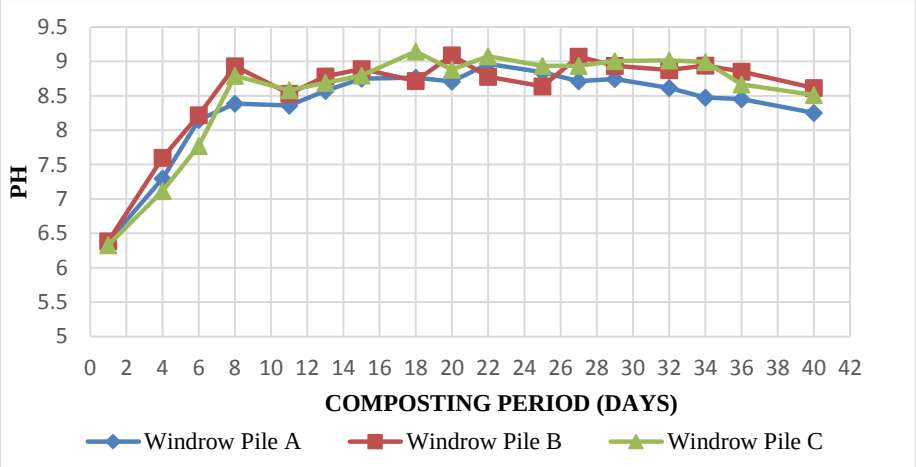


Fig. 3.4. Profile of pH value for different co-composting batches of EFB + POME.

As shown in **Figure 3.4** above, the initial pH value of each compost pile started off at a slightly acidic condition due to the addition of POME which is acidic in nature, giving a pH value of 6.38, 6.39 and 6.33 for compost pile A, B and C respectively. In the following days, the pH values for all compost piles were seemed to increase gradually with a similar trend, creating an alkaline condition within the compost pile. The occurrence of alkaline condition was mainly resulted from the rotating process on compost pile A and B as well as the flipping process on compost pile C. This was because frequent rotation and flipping of the compost pile would help in emitting carbon dioxide gases that were produced from the microbial activities and trapped within the empty spaces among the particles of composting materials. The removal

of carbon dioxide gases will prevent the formation of acidic conditions, hence inhibiting the growth of microorganisms which would degrade the composting process [12], [22]. Besides, the amount of ammonia being produced from the microbial activities due to the existence of nitrogen content would also contributes to the alkaline condition within the compost piles. Hence, pH control was not required in this study as the alkaline condition was able to remain as long as the microbial activities continue to take place.

At the end of the composting period, compost pile A, B and C showed a pH value of 8.25, 8.62 and 8.51 respectively, which was within the pH range for matured compost. This phenomenon was in agreement with Yahya et al. [23] that reported on fully developed composting process, the pH value of compost entering maturity phase often increases to a range of 8 – 9, with a mean pH value of 8.5. This indicated that the mesophilic phase was dominated by bacteria, hence there will be of minor acidity tolerance [16], [21].

3.5 Final Carbon, Hydrogen and Nitrogen Composition of Compost Materials

Samples from each batch of compost piles were taken randomly on the 40th day of composting period and sent for the determination of final C, H, N composition. The final results were tabulated in **Table 3.2** below.

Table 3.2. Final C, H, N Compositions of EFB and POME Composts.

Samples	**Unit**	**Parameters**			
		Carbon, C	**Hydrogen, H**	**Nitrogen, N**	**C/N**
Compost Pile A	%	37.41	5.76	1.7	22.01
Compost Pile B	%	38.01	6.05	1.22	31.16
Compost Pile C	%	38.10	5.96	1.37	27.81

Based on the results obtained, the C/N ratio for each sample were calculated to determine whether the compost has reach its maturity level and is ready to be used as fertilizer for plantation. It was found that the C/N ratio for compost pile A, B and C were 22.01, 31.16 and 27.81 respectively. From the result, it can be concluded that compost pile A turned out to have the best rate of decomposition due to the lowest final C/N ratio, followed by compost pile C and finally compost pile B having the slowest rate of decomposition due to the highest final C/N ratio. The results obtained indicated that the reducing in size of EFB with sufficient aeration created a significant difference in terms of composting condition for the microorganisms during the co-composting process. With this combination, a more favourable composting condition was provided to the microorganisms to carry out the microbial activities.

Despite the decrease in C/N ratio of all final compost pile compared to the original C/N ratio of EFB, the results showed that none of the final compost piles have reached their maturity level as the final C/N ratio did not drop below 20. One of the reason that cause such phenomenon may be due to the drying process of EFB before composting. While one of the experimental parameter was the reducing in size of EFB, it requires the EFB to be thoroughly dried in order to proceed with the cutting process using the cutting machine. The drying process has now been assumed to have killed the existing microorganisms that would be very much needed in the co-composting process. When the microorganisms in the EFB were mostly killed

under high temperature, the available microorganisms to carry out the decomposition would have come from POME only, which is insufficient to speed up the entire process. This explained why the temperature were not increasing in the compost piles and there were only mesophilic phase occurring throughout the process, which eventually slows down the rate of decomposition. But, the process of decomposition was still happening as the moisture content and pH value in all compost piles had reflected the ongoing process. Although all three compost piles have yet to reach their maturity level, compost pile A was found to be the closest to reach maturity as the C/N ratio was about to drop below 20 [16], [17].

4 Conclusion

The outcome of this experimental study shows that the reducing in size of EFB with periodic rotation of compost pile would be the best combination for the co-composting of EFB and POME which resulted in the final C/N ratio of 22.01 for compost pile A. This combination shows a comparatively better rate of co-composting as reflected in the changes in colour and formation of lumps, whereby the physical changes on compost piles which did not undergone both reduced size of EFB and rotation were not as significant. This is because the increase in area of exposure of EFB to nitrogen source as well as sufficient aeration would stimulate the microbial activity and results in better rate of decomposition. Although the expedition of composting period to lesser than 40 days has yet to be achieved, still it has a high possibility to be accomplished if the microorganisms on the EFB were well conserved at the beginning of the process.

The future work that can be focused on would be the improvement on the pre-treatment method of EFB. While drying of shredded EFB was the main concern in this research work whereby the high temperature during the drying process had probably killed the existing microorganisms in the EFB, resulting in the inefficient of microbial activity. To avoid such phenomenon from happening in the future, drying of EFB shall not be conducted before any composting process. However, the reducing in size of EFB has been proven to bring significant effect onto the co-composting process. Therefore, research on alternative method of cutting huge amount of EFB into shorter length of 0.5 – 1.0 cm without drying should be carried out. This would help in preserving the microorganism community within the EFB while cutting the EFB efficiently.

Apart from that, the future work on introducing automation onto the current manual rotating drum could be done. As automation is applied to the rotating drum, it will help in increasing the frequency and consistency of rotation. This will create positive impact on the aeration of compost pile by increasing the oxygen level so that the microorganisms will be able to carry out the aerobic digestion actively and efficiently.

References

[1] S. H. Chang, "An overview of empty fruit bunch from palm oil as feedstock for bio-oil production," Biomass & Bioenergy, **62**, pp. 174 - 181 (2014)

[2] K. Somrat and L. Krongkaew, "Renewable Energy from Palm Oil Empty Fruit Bunch," Renewable Energy - Trends and Applications, **1**, pp. 123 - 150 (2011)

[3] S. Yacob, M. A. Hassan, Y. Shirai, M. Wakisaka and S. Subash, "Baseline study of methane emission from open digesting tanks of palm oil mill effluent treatment," Chemosphere, **59**, no. 11, pp. 1575 - 1581 (2005)

[4] A. Arya, "Forming Process Analysis in Environmentally-Friendly Composite Production from Fibres of Oil Palm Empty Fruit Bunches," Tropical Agriculture Science, **40**, no. 1, pp. 203 - 214 (2017)

[5] N. Abdullah and F. Sulaiman, "The Oil Palm Wastes in Malaysia," Biomass Now – Sustainable Growth and Use , pp. 75 - 100 (2013)

[6] Y. W. Ta, W. M. Abdul, M. J. Jamaliah and A. Nurina, "A holistic approach to managing palm oil mill effluent (POME): Biotechnological advances in the sustainable reuse of POME," Biotechnology Advances, **27**, pp. 40 - 52 (2009)

[7] F. Sulaiman, N. Abdullah, H. Gerhauser and A. Shariff, "An outlook of Malaysian energy, oil palm industry and its utilization of wastes as useful resources," Biomass and Bioenergy, **35**, pp. 3775 - 3786 (2011)

[8] M. J. Chin, P. E. Poh, B. T. Tey, E. S. Chan and K. L. Chin, "Biogas from palm oil mill effluent (POME): Opportunities and challenges from Malaysia's perspective," Renewable and Sustainable Energy Reviews, **26**, pp. 717 - 726 (2013)

[9] S. Tabassum, Y. J. Zhang and Z. J. Zhang, "An integrated method for palm oil mill effluent (POME) treatment for achieving zero liquid discharge – A pilot study," Journal of Cleaner Production, **95**, pp. 148 - 155 (2015)

[10] Y. Krishnan, C. C. B. Phun, N. F. Azman, Z. Zakaria, N. A. Othman, N. Abdullah, S. H. Chin, T. L. Chew, S. B. Hansen and H. Hara, "Co-composting of palm empty fruit bunch and palm oil mill effluent: Microbial diversity and potential mitigation of greenhouse gas emission," Journal of Cleaner Production, **146**, pp. 94 - 100 (2017)

[11] N. F. Ishak, A. L. Ahmad and S. Ismail, "Feasibility of Anaerobic Co-composting Empty Fruit Bunch with Activated Sludge from Palm Oil Mil Wastes for Soil Conditioner," Physical Science, **25**, no. 1, pp. 77 - 92 (2014)

[12] B. Trisakti, J. Lubis, T. Husaini and Irvan, "Effect of Turning Frequency on Composting of Empty Fruit Bunches Mixed with Activated Liquid Organic Fertilizer," IOP Conference Series: Materials Science and Engineering, **180**, pp. 1-9 (2017)

[13] P. O. Oviasogie, N. O. Aisueni and G. E. Brown, "Oil palm composted biomass: A review of the preparation, utilization, handling and storage," African Journal of Agricultural Research, **5**, no. 13, pp. 1553 - 1571 (2010)

[14] M. Thompson, "AMC Technical Brief - CHNS Elemental Analysers," Analytical Methods Committee, The Royal Society of Chemistry (2008)

[15] K. Fujine, "FlashEA 1112 Elemental Analyzer (CHNS): User Guide," International Ocean Discovery Program (2014)

[16] A. S. Baharudin, M. Wakisaka, Y. Shirai, S. Abd-Aziz, N. A. Abdul Rahman and M. A. Hassan, "Co-Composting of Empty Fruit Bunch and Partially Treated Palm Oil Mill Eflluent in Pilot Scale," International Journal of Agriculture Research, **4**, no. 2, pp. 69 - 78 (2009)

[17] I. V. Heerden, C. Cronje, S. H. Swart and J. M. Kotze, "Microbial, chemical and physical aspects of citrus waste composting," Bioresource Technology, **81**, pp. 71 - 76 (2002)

[18] X. J. Li, R. H. Zhang and Y. Z. Pang, "Characteristics of dairy manure composting with rice straw," Bioresource Technology, **99**, no. 2, pp. 359 - 367 (2008)

[19] Y. J. Shen, L. M. Ren, G. X. Li, T. B. Chen and R. Guo, "Influence of aeration on CH4, N2O and NH3 emissions during aerobic composting of a chicken manure and high C/N waste mixture," Waste Management, **31**, no. 1, pp. 33 - 38 (2011)

[20] A. Makan, O. Assobhei and M. Mountadar, "Effect of initial moisture content on the in-vessel composting under air pressure of organic fraction of municipal solid waste in Morocco," Iranian Journal of Environmental Health Sciences & Engineering, **10**, no. 3 (2013)

[21] C. Sundberg, S. Smars and S. Jonsson, "Low pH as an inhibiting factor in the transition from mesophilic to thermophilic phase in composting," Bioresource Technology, **95**, pp. 145 - 150, (2004)

[22] H. T. Liu and L. Cai, "Effect of Sewage Sludge Addition on the Completion of Aerobic Composting of Thermally Hydrolyzed Kitchen Biogas Residue," Bioresources, **9**, no. 3, pp. 4862-4872, (2014)

[23] A. Yahya, P. S. Chong, T. A. Ishola and H. Suryanto, "Effect of adding palm oil mill decanter cake slurry with regular turning operation on the composting process and quality of compost from oil palm empty fruit bunches," Bioresource Technology, **101**, pp. 8736 - 8741 (2010)

Primary Recovery of Amylase from *Hylocereus Polyrhizus* Peels using Polymer/Salt Aqueous-Two Phase

Then Chit Siew[1,], and Chow Yin Hui[1]*

[1]School of Engineering, Taylor's University, 47500 Subang Jaya, Selangor, Malaysia

Abstract. The extraction of the amylase from the *Hylocereus Polyrhizus* peels or normally known as the red pitaya peels was investigated using the PEG/phosphate salt in aqueous two phase system (ATPS). Different parameters such as the type of salts, effect of molecular weight of PEG, and the concentrations of both the PEG and the salt were studied on the amylase partitioning behaviour. Using this ATPS method, the amylase was satisfactorily partitioning towards the PEG-rich top phase. The highest partition coefficient and purification factor of 4.28 and 1.52 respectively were achieved in the ATPS composed of 17.50 w/w% of PEG 4000 and 10.40 w/w% of potassium phosphate salt. The amylase yield recovered was 81.88% which is considered satisfactorily high**.**

Preparation and Properties of Sea Clam Shell Filled Polylactic Acid Biocomposites

Kar Yan To[1], Ming Meng Pang[1,], Jiun Hor Low[1], Seong Chun Koay[2], Yose Fachmi[3], Kim Yeow Tshai[4]*

[1]Chemical Engineering Programme, School of Engineering, Faculty of Built Environment, Engineering, Technology & Design, Taylor's University Lakeside Campus, No. 1 Jalan Taylor's, 47500 Subang Jaya, Selangor, Malaysia.
[2]Mechanical Engineering Programme, School of Engineering, Faculty of Built Environment, Engineering, Technology & Design, Taylor's University Lakeside Campus, No. 1 Jalan Taylor's, 47500 Subang Jaya, Selangor, Malaysia.
[3]Department of Manufacturing and Materials Engineering, International Islamic University Malaysia (IIUM), Jalan Gombak, 53100 Kuala Lumpur, Malaysia.
[4]Faculty of Engineering, The University of Nottingham, 43500 Semenyih, Malaysia.

Abstract. Polylactic acid (PLA) is a bioplastic derived from renewable resources, but its high cost and brittleness limited its application. Hence, economical natural filler is added to reduce the production cost and improve the properties of PLA. This research aims to produce a PLA biocomposite with sea clam shell (SCS) and expanded graphite (EG) flakes. This paper focuses on effect of SCS and EG on tensile and thermal properties of PLA. Results show that no enhancement in tensile strength with the addition of SCS into PLA matrix. This could be attributed to poor dispersion and filler-matrix adhesion for 5-10 wt.% SCS content since SCS is a stiff particle. Besides, the tensile modulus increased up to 10 wt.% SCS content and then decreased at 20 wt.% as high SCS content promotes agglomeration and specimen can break easily due to improper filler-matrix bonding. The EG showed no significant improvement on the tensile properties of the composites. DSC results showed the glass transition temperature shifted to higher point after addition of 5 – 10 wt.% SCS. SCS acted as nucleating agent in promoting the crystallization of PLA, while EG exhibited immobilizing effect on the PLA matrix. However, the presence of EG as conductive filler decreased the electrical resistivity of the composites.

* Corresponding author: MingMeng.Pang@taylors.edu.my

1 Introduction

Nowadays, plastics are being used so commonly in packaging goods, for example bottles, containers, protection packaging and many more. Formerly, plastics are made from petroleum which is a non-renewable resource. They are chemically stable and do not biodegrade easily in the nature. Hence, the disposes of used plastic products will bring great harm to the environment. In year 2017, a statistic shows that 79% of 8.3 billion metric tons of the plastic that has been produced is now accumulating in landfills and scattered around as trash [1]. With this arising awareness, people are encouraged to use bioplastic packaging material which is biodegradable, in order to solve the issue of scattering plastic waste. Polylactic acid (PLA) is an example of bioplastic, which is derived from renewable resources, such as corn starch and sugarcane. PLA is non-toxic and possesses a good mechanical properties [2], which leads to the increased market demand of bioplastic for applications like food packaging, textile, and automobile industries. For instance, SelfEco manufacturer has produced various types of PLA product like tableware and garden pots. Although bioplastic shows a lot of benefits compared to petroleum based plastic, but the usage of bioplastic is still lagging behind petroleum based plastic, which can be seen from the bioplastic production rate of 750000 tons/year compared to petroleum based plastics' 200 million tons/year in year 2008 [3]. The main reason is because the production cost of bioplastic is much higher (2 to 10 times more expensive) than the conventional petroleum based plastic [4]. For PLA, the high cost and brittleness with less than 10% elongation at break [5] became the reason for industries to not take it as the first preference material. One of the efforts that can be made to enhance the usage of PLA is to blend it with an economical natural filler in order to reduce the production cost and improve the properties of PLA.

Biocomposite is a material composed of bio-based polymer as matrix and a natural filler. The natural filler can be sourced from plant fibers (e.g., leaf, seed and wood), animals (e.g., chicken feather and snail shell), or mollusks (e.g., shell of aquatic creatures) [6]. Biocomposite has recently received a lot of attention from the mass public due to its low cost, availability, recyclability and degradability features [7]. In this regard, the market size of natural fiber-reinforced polymeric composites are expected to increase from 155 million US dollar to 1.38 billion US dollar by 2025 [8], where the demand of biocomposite is expected to increase annually. Currently, there are a lot of biocomposite products in the market. For instance, ZESPRI© has produced a spoon-knife made from PLA and kiwifruit waste, which is a biodegradable utensil for cutting and scooping kiwifruit. Besides, there is an iPhone casing brand called RE-case, that is produced with rice husk waste and post-consumer thermoplastics obtained from used car bumpers, bottle caps, CD containers and others.

Fillers are solid materials that ground into powder and blended with the polymer matrix to reduce overall production cost and improve the properties of polymer [9]. In the past decade, mineral fillers like calcium carbonate, kaolin, silica and talc were used more often than natural sourced fillers in compositing with plastic material to reduce production cost, as well as to improve the properties of the polymer such as strength, hardness and modulus [10]. In general, mineral fillers are extracted from the ground by mining operation and being sold to industries for further processing into fine powder. For plastic industry, mineral filler like calcium carbonate is not only used as filler, but it is also used as white colour pigment for plastic compound. The role of colour pigment is to provide particular colour on plastic product. Other than that, the present of colour pigment may also helps in preventing the degradation of plastic. Nowadays, plastic industry prefer to use calcium carbonate derived from natural resources as white pigment, because they are more environmental friendly and cost less.

In present, some common natural fillers can be obtained from mollusk wastes, for example the shell of aquatic creatures. Shells usually contain mainly mineral like calcium carbonate, which is similar to mineral based calcium carbonate. *Venerupis Philippinarum*, also called the Manila clam is a species of sea clam that has been highly cultivated due to high popularity in seafood restaurants. Nearly 5 million metric tonnes of clams are cultured each year on global scale, and Manila clam occupied 81% to the annual global yields of clams [11]. The Manila clam shell is one of the waste materials generated by restaurant daily. They are treated as waste after consumed by human and are mostly dumped into the sea, sent for landfills or landspreading, which is considered an environment hazard because of the unpleasant fishy smell. In order to reduce these practices, these sea clam shells should be utilized instead of disposing after the removal of their soft edible part.

Typically, a shell is composed of more than 90% of calcium carbonate by weight [12-13], hence it is suitable to substitute mineral based calcium carbonate as natural filler in compositing with plastic materials. Compared to the mineral based calcium carbonate, natural sea clam shells are a more abundant resource as they can be obtained from many seafood restaurants, which substantially saves some cost for the production of composite. Also, they make the production of biocomposite more environmental friendly because they are biodegradable. The utilization of discarded sea clam shells is a good way to recycle waste from seafood industry. Since Manila clam shell is widely available in Malaysia, this research is proposed to utilize Manila clam shell as natural filler in producing PLA based biocomposite.

Other than natural and mineral filler, there is another type of filler called conductive filler. It is a material used to add in polymer to give conductivity. Conductive fillers can be very useful depending on their electrical conductivity. For example, high conductive (low resistance) fillers are normally applied in electrodes, conductive wiring and electrical contact materials. Whereas, those with low conductivity (high resistance) are usesd as resistant materials, which can be found in electrical wires, heating elements, or materials that prevent static electricity. Polymers are poor electrical conductors, therefore, the addition of conductive fillers allow them to gain electrical characteristic.

Conductive fillers can be sourced from few types of materials, namely carbon, graphite and metal. In the basis of good strength properties, graphite has been used as the conductive filler for plastics to possess some good properties. Because of the layered structure of graphite, small molecules can be introduced between the carbon layers, and hence produced a compound called expanded graphite. Expanded graphite (EG) has been proven to have an excellent balance of properties in aspect of mechanical, thermal, electrical conductivity and fire resistance etc. [14]. Hence, it is used for a wide field of applications, for instance, carpets, plastic foils, pipe closing systems and rubber products like conveyer belts. By incorporating EG with sea clam shell (SCS) and PLA, the composite is believed to be more valuable.

The study focused on the development of PLA biocomposite by using Manila clam shell as the natural filler. The dose varying was ranged from 0, 5, 10 and 20 wt.% of SCS added into PLA to form biocomposite. Besides, EG was added as conductive filler to impart electrical conductivity characteristic on the PLA/SCS biocomposite. The EG dose was varying at 0, 1, 5 and 8 wt.%, added into a fixed amount of 10 wt.% SCS/PLA composites. The composition effect of the Manila clam shell and EG flakes on the fabricated PLA biocomposites were evaluated in terms of tensile properties, thermal stability, electrical resistivity and morphological properties. It is expected that this research will diversify the use of Manila clam shell and EG flakes whilst develop a new class of PLA biocomposite.

2 Methodology

2.1 Research Materials

PLA used for this research was supplied by NatureWorks®. The sea clam shells (Manila clam) was collected from a Chinese restaurant named Kar Hiong, which is located at SS18, Subang Jaya (Selangor). Expanded graphite (EG) flakes was supplied by gk-graphite.

2.2 Preparation of Sea Clam Shell

The collected Manila clam shell were washed with tap water and cleaned using a brush. Then, they were dried in the oven at 100°C for 1 hour to remove the moisture content. After drying, they were ground using a grinder and sieved using a 600-micron mesh size sieve to obtain homogenous size of fine powder.

2.3 Preparation of PLA/SCS/EG Biocomposites

The PLA/SCS/EG biocomposites were compounded using Haake Rheomix 600p at SIRIM Sdn. Bhd. Shah Alam, Malaysia. The biocomposites were prepared with few different formulations as shown in Table 1 below. The processing temperature was set at 190°C and 70 rpm rotor speed [15]. The compounding procedure was: i) PLA resin was added into the mixing chamber for 1 minute; ii) SCS powder / EG was added into the melted PLA and compounded for 5 minutes; iii) Lastly, the compound was removed from mixing chamber.

Table 1. Formulations of PLA/SCS/EG biocomposites.

Sample No.	PLA Content (wt%)	SCS Content (wt%)	EG Content (wt%)
1	100	0	-
2	95	5	-
3	90	10	-
4	80	20	-
5	89	10	1
6	85	10	5
7	82	10	8

The PLA/SCS/EG biocomposites were then moulded into a thin sheet with 1mm thickness using a hotpress machine (model Moore). The processing temperature was set at 190°C. The moulding procedure was: i) the compound was preheated for 2 minutes; ii) the compound was being fully compressed under 150MPa pressure for 1 minute; iii) Lastly, the compressed sheet was let to cool under the same pressure for 20 minutes. The biocomposite sheets were cut into tensile specimen based on ASTM D638.

2.4 Testing and Characterization

Dynamic light scattering method was used to analyse the particle size of SCS. The particle size of SCS was determined by Zetasizer software.

The tensile test was carried out using Instron Universal Testing Machine (Model 5569) according to ASTM D638 standard. The cross-head speed of the machine was set at 5mm/min and the selected load cell was 15kN. Effect of the filler content on tensile properties namely tensile strength and tensile modulus were determined by Bluehill 3 software.

Electrical resistivity test was conducted using an electrometer (Prostat PRS-801 Resistance System Set). Test voltage of 100V was selected to test the electrical resistivity of the compressed biocomposite sheets. The measurements were repeated three times to obtain the average electrical resistivity for one sheet.

Differential Scanning Calorimetry (DSC) analysis was conducted using DSC 8500 (Perkin Elmer). The specimen was prepared in granular size and weighted 8mg, then placed in a closed aluminium pan. With nitrogen gas flow rate of 20ml/min, the specimen was heated from 30°C to 220°C to break the polymer chains, cooled from 220°C to 30°C for crystallization, and heated up again from 30°C to 220°C. Both heating and cooling rate were set at 10°C/min. The glass transition temperature of the specimens was determined. The percent crystallinity of biocomposites (X_c) was determined using the Eqn. (1) below:

$$X_c = \frac{\Delta H}{\Delta H_m^{\circ}\left(1-\frac{W_f}{100}\right)} \times 100\% \quad (1)$$

where $\Delta H\ \left(\frac{J}{g}\right) = \Delta H_m - \Delta H_c$ and ΔH_m° is the melting enthalpy for 100% crystalline PLA ($\Delta H_{100} = 93 J/g$).

3 Results and Discussion

3.1 Particle Size Analysis

Determining the particle size of SCS is important as it matters for the filler particle dispersion in PLA matrix, where big particle raise the potential to result in poor dispersion of filler in the polymer matrix, while smaller particles will disperse more homogenously. The measurement of particle size for SCS powder using intensity is shown in Figure 1. It can be seen that the peak occurred at around 400 – 500 d.nm, which indicates the range of diameter of the particles. The highest peak is at 429.5 d.nm. Hence, the particle size of the SCS is determined to be 429.5 d.nm.

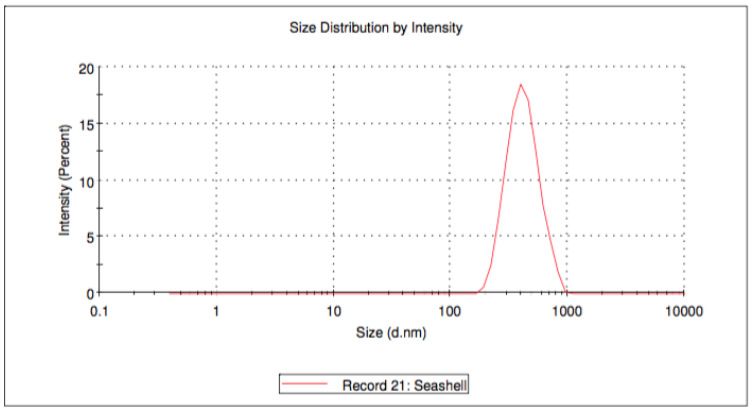


Fig. 1. Size distribution by intensity.

3.2 Effect of SCS Loading on Properties of PLA

3.2.1 Tensile Properties Test

Tensile strength of the PLA reduced along with the increment of SCS filler content as seen in Figure 2. Normally, mollusc shells exhibit a much lower tensile strength compared to most plastic materials. Previous studies reported that the tensile strength of clam shell is displayed to be in a range of 2.5MPa to 3.6MPa as compared to neat PLA with much higher tensile strength (~20MPa) [16]. Hence, the addition of SCS might reduce the resistance to breaking when the tensile load was subjected to the PLA matrix. Furthermore, decrement of the strength was also caused by poor dispersion and filler-matrix adhesion between SCS and PLA, where the poor stress transfer on the weak interfacial bonding decreased the strength of biocomposites. Similar results were reported by Ashok et al. [17].

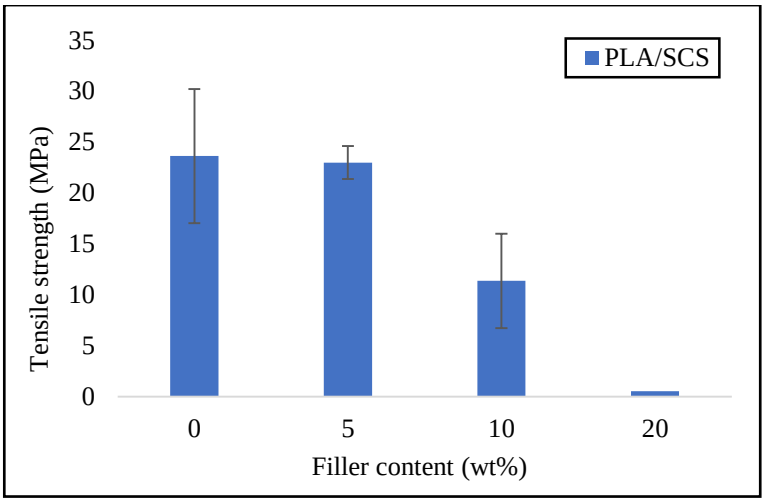


Fig. 2. Tensile strength of PLA with different loading of SCS content.

The effect of SCS filler content on the tensile modulus of PLA is presented in Figure 3. From the result trend, it is observed that the tensile modulus increased at 5 – 10 wt.% of SCS content and decreased at 20 wt.%. This discontinuity may be associated with the result that the SCS powder still existed in an agglomerate structure with poor filler dispersion. Thus, the interfacial adhesion between EG and PLA matrix was very poor. Similar result trend has been reported

by Ashok et al. [17].

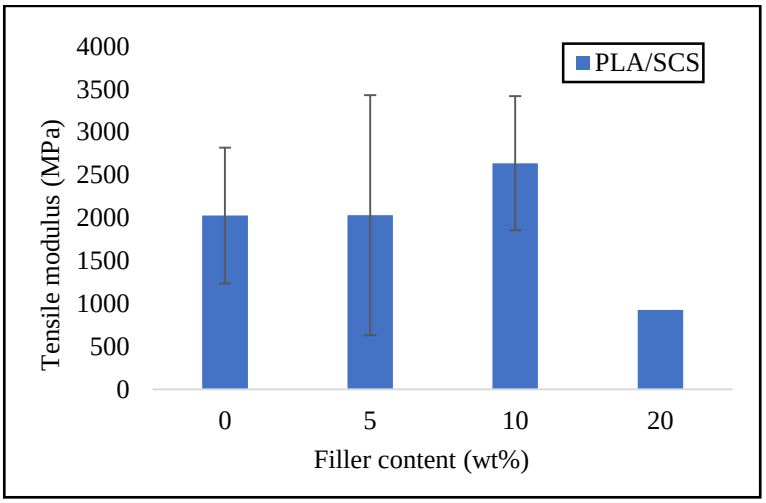


Fig. 3. Tensile modulus of PLA with different loading of SCS content.

3.2.2 Differential Scanning Calorimetry Analysis (DSC)

Differential scanning calorimetry (DSC) curves for the biocomposites at different SCS filler content are shown in Figure 4. Whereas, the DSC data is shown in Table 2. The glass transition temperature (T_g) of the PLA/SCS biocomposite increased at 5 wt.% and 10 wt.% SCS content. This explained the presence of SCS gives stiffening effect to the PLA matrix, thus restricted the polymer long chain mobility. However, once the SCS content increased to 20 wt.%, it caused particle-particle interaction instead of particle-polymer interaction, which makes it failed to form homogenous polymer matrix and break apart easily, thus T_g decreased. Besides, the melting temperature (T_m) varied in a range of 145 – 157°C. The crystallization temperature (T_c) at 5 wt.% - 10 wt.% SCS was observed to be higher than the neat PLA. This suggests the SCS had nucleation effect on PLA matrix. However, the decrement in T_c at 20 wt.% was associated with poor filler-matrix adhesion. It is observed that the effect of SCS on degree of crystallinity (X_c) of PLA/SCS composites was inconsistent with the SCS content. This may be due to the agglomeration of filler particles within the PLA.

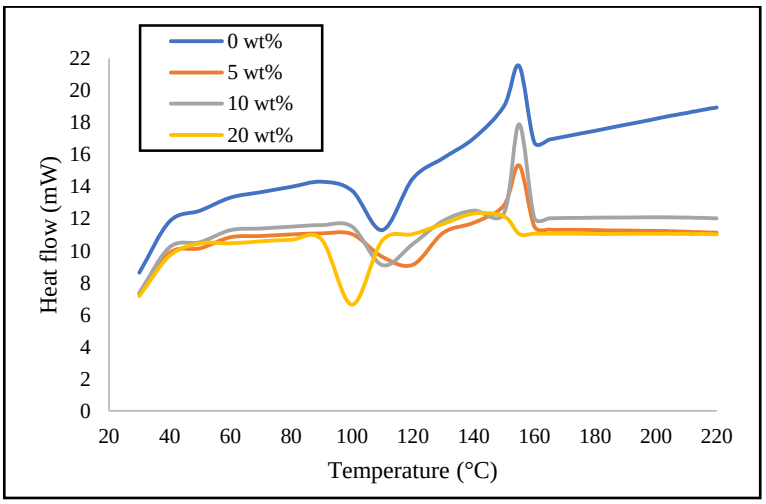


Fig. 4. DSC curves of PLA with different loading of SCS content.

Table 2. DSC data for PLA/SCS biocomposites.

Samples (wt.%)	T_g (°C)	T_c (°C)	T_m (°C)	X_c (%)
PLA/SCS: 100/0	51.32	108.46	153.76	76.07
PLA/SCS: 95/5	53.92	115.79	156.43	72.79
PLA/SCS: 90/10	54.07	113.65	155.43	77.76
PLA/SCS: 80/20	46.88	101.22	145.09	61.49

3.3 Effect of EG Loading on Properties of PLA/SCS Biocomposites

3.3.1 Tensile Properties Test

The effect of EG content on the tensile strength of PLA/SCS biocomposite is shown in Figure 5. Tensile strength of the PLA/SCS biocomposite slightly increased at 1 wt.% EG then decreased along with the increment of EG filler content. It was found that graphite layers still existed in an aggregate structure with poor filler dispersion, hence causing the poor interfacial adhesion between EG and PLA, which is the reason why the composites break easily. Also, the effect of poor stress transfer on the weak interfacial bonding was appeared to be more distinct when EG flakes were incorporated into the PLA matrix.

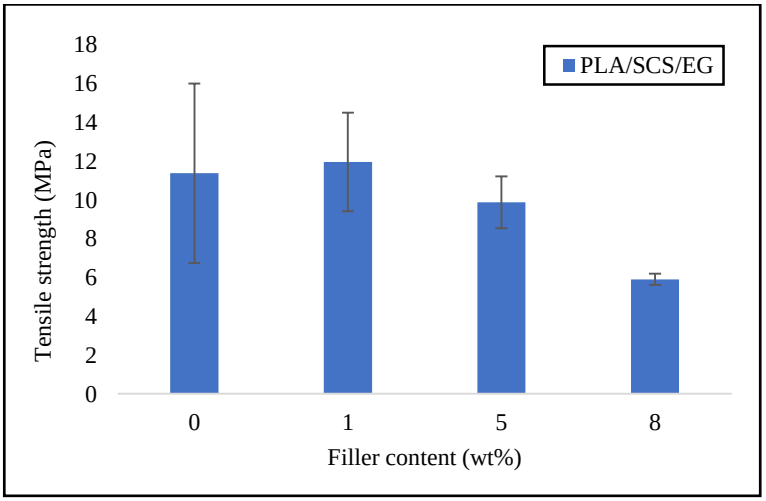


Fig. 5. Tensile modulus of PLA/SCS biocomposites with different loading of EG content.

The effect of EG filler content on the tensile modulus of PLA/SCS biocomposites is presented in Figure 6. The modulus decreased up to 5 wt.% EG and then increased at 8 wt.%. Normally, the composites should show higher modulus than the neat PLA when EG is being added, as reported by Kim and Jeong [18]. The inconsistency in the tensile modulus result could be due to the poor dispersion of both the EG and SCS filler into the PLA. The compound formed is not homogenous, thus, the result is also inconsistent.

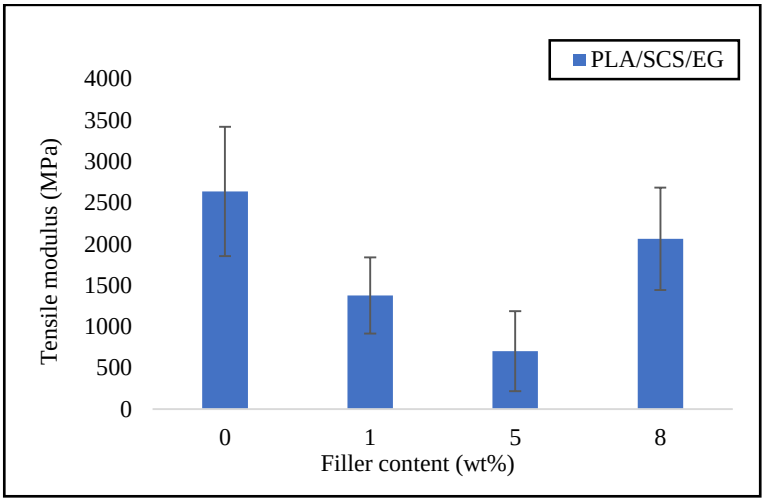


Fig. 6. Tensile modulus of PLA/SCS biocomposites with different loading of EG content.

3.3.2 Differential Scanning Calorimetry Analysis (DSC)

Differential scanning calorimetry (DSC) curves for PLA/SCS biocomposites at different EG filler content are shown in Figure 7. Whereas, the DSC data is shown in Table 3. The glass transition temperature (T_g) decreased at 1 wt.% and then increased with addition of EG. This can be explained as that the EG gives a slightly stiffening effect to the PLA, hence reducing the mobility of polymer chains. Besides, the melting temperature (T_m) varied in a range of 151 – 156°C. The crystallization temperature (T_c) could not be detected when EG filler was incorporated with the PLA/SCS composites, because the EG flakes have restricted the crystallization process of the composites. Similar findings were reported by Zheng et al. [19]. The addition of EG filler brought negative effect to the degree of crystallinity of the composites, where the values dropped drastically at 1 wt.% filler and increased slightly at 8 wt.% filler. This reduction effect was probably due to poor compatibility of EG with PLA and lack of uniform dispersion of EG within the PLA matrix, hence causing poor filler-matrix interfacial adhesion.

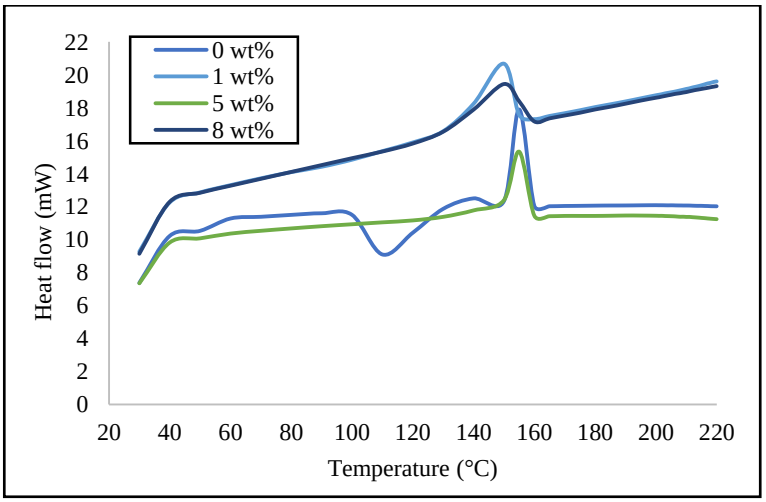


Fig. 7. DSC curves of PLA/SCS biocomposites with different loading of EG content.

Table 3. DSC data for PLA/SCS/EG biocomposites.

Samples (wt%)	T_g (°C)	T_c (°C)	T_m (°C)	X_c (%)
PLA/SCS/EG: 90/10/0	54.07	113.65	155.43	77.76
PLA/SCS/EG: 89/10/1	47.66	-	151.03	36.01
PLA/SCS/EG: 85/10/5	52.07	-	156.03	30.58
PLA/SCS/EG: 82/10/8	54.62	-	152.44	41.14

3.3.3 Electrical Resistivity

Figure 8 shows the changes of electrical resistivity of PLA/SCS biocomposites as a function of EG filler content. Since the biocomposites incorporated with EG contained constant SCS loading of 10 wt.%, the biocomposite (90 wt.% PLA / 10 wt.% SCS) was taken as control and its electrical resistivity was evaluated to be $1.60 \times 10^{12}\Omega$. Result shows that the electrical resistivity of PLA/SCS biocomposites decreased slightly at the EG content between 1 wt.% to 5 wt.%, and then decreased drastically at 8 wt.%. It is believed that this decrement is associated with the result that the EG flakes contained free electrons, and these electrons can move through the graphite particles, carrying charge from one place to another and allowing it to conduct electricity. Kim and Jeong [18] have also reported that the increment of EG leads to decrement of electrical resistivity of the PLA composites. The typical region for conductive material falls below $1 \times 10^{5}\Omega$. In this study, electrical resistivity of $1 \times 10^{11}\Omega$ is still considered as insulative region.

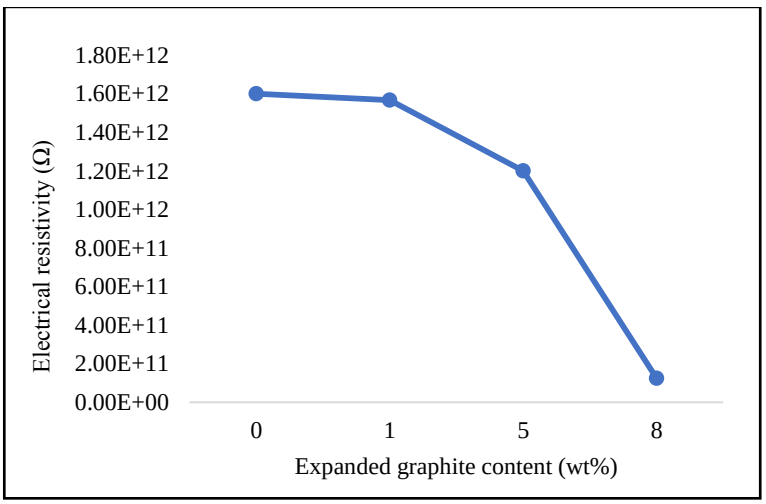


Fig. 8. Electrical resistivity of PLA/SCS/EG biocomposite with different expanded graphite content.

4 Conclusion

The average particle size of the SCS used in this research was 429.5 d.nm. The increment of SCS and EG filler content decreased the tensile properties like tensile strength and modulus of PLA. The PLA/SCS and PLA/SCS/EG biocomposites displayed lower strength and modulus compared to virgin PLA. However, the average strength of biocomposites still exhibit 11MPa, which is still comparable with the commercial plastic materials like low density polyethylene (LDPE) that can be used as material for plastic bags and plastic wraps. Thermal stability is reflected by TGA. But in this paper, TGA is not included. The addition of SCS (5 – 10 wt.%) shifted the T_g of PLA composites to higher temperature. However, when higher dose of 20 wt.% was added, agglomeration formed and caused poor interfacial adhesion, which subsequently reduced the T_g of the composites. The addition of EG into the PLA/SCS composites exhibited lower T_g and crystallinity, which is attributed to the poor dispersion of the conductive filler and poor interaction between filer and matrix. EG did not show enhancement on tensile and thermal performance, but it allowed the composites to be slightly electrical conductive. However, the overall degree of crystallinity decreased with the addition of SCS and EG fillers. Therefore, it is concluded that the overall enhancement was not impressive due to the fact that the filler-matrix interface was not optimized in the melt-blending process.

5 Acknowledgement

This research was financially supported by the Taylor's University, Malaysia (Grant: TRGS/ERFS/1/2017/SOE/031).

References

[1] L. Parker, "A Whopping 91% of Plastic Isn't Recycled," *National Geographic*, 2017. [Online]. Available: http://news.nationalgeographic.com/2017/07/plastic-produced-recycling-waste-ocean-trash-debris-environment/.

[2] K. Hamad, M. Kaseem, H. W. Yang, F. Deri, and Y. G. Ko, "Properties and medical applications of polylactic acid: A review," *Express Polym. Lett.*, vol. 9, no. 5, pp. 435–455, 2015.

[3] F. Gironi and V. Piemonte, "Bioplastics and petroleum-based plastics: Strengths and weaknesses," *Energy Sources, Part A Recover. Util. Environ. Eff.*, vol. 33, no. 21, pp. 1949–1959, 2011.

[4] J. H. Song, R. J. Murphy, R. Narayan, and G. B. H. Davies, "Biodegradable and compostable alternatives to conventional plastics," *Philos. Trans. R. Soc. B Biol. Sci.*, vol. 364, no. 1526, pp. 2127–2139, 2009.

[5] R. M. Rasal, A. V. Janorkar, and D. E. Hirt, "Poly(lactic acid) modifications," *Progress in Polymer Science (Oxford)*, vol. 35, no. 3. pp. 338–356, 2010.

[6] S. K. Ramamoorthy, M. Skrifvars, and A. Persson, "A review of natural fibers used in biocomposites: Plant, animal and regenerated cellulose fibers," *Polymer Reviews*, vol. 55, no. 1. pp. 107–162, 2015.

[7] Faris M. AL-Oqla and Mohammad A. Omari, "Sustainable biocomposites: challenges, potential and barriers for development," *Green Compos.*, vol. 7, no. November, pp. 13–29, 2017.

[8] M. P. M. Dicker, P. F. Duckworth, A. B. Baker, G. Francois, M. K. Hazzard, and P. M.

Weaver, “Green composites: A review of material attributes and complementary applications,” *Composites Part A: Applied Science and Manufacturing*, vol. 56. pp. 280–289, 2014.

[9] A. B. Strong, *Fundamentals of Composites Manufacturing Materials, Methods, and Applications. 2nd ed.*, vol. 2, no. 1. 2008.

[10] M. Tasdemir and S. Ersoy, “Mechanical , Morphological and Thermal Properties of Hdpe Polymer Composites Filled With Talc , Calcium Carbonate,” *J. Mater.*, vol. 45, no. 2, pp. 147–154, 2015.

[11] E. Gosling, “Bivalve Culture,” *Bivalve molluscs Biol. Ecol. Cult.*, pp. 284–332, 2003.

[12] G. L. Yoon, B. T. Kim, B. O. Kim, and S. H. Han, “Chemical-mechanical characteristics of crushed oyster-shell,” *Waste Manag.*, vol. 23, no. 9, pp. 825–834, 2003.

[13] P. Ballester, I. Mármol, J. Morales, and L. Sánchez, “Use of limestone obtained from waste of the mussel cannery industry for the production of mortars,” *Cem. Concr. Res.*, vol. 37, no. 4, pp. 559–564, 2007.

[14] S. Jia, D. Yu, Y. Zhu, Z. Wang, L. Chen, and L. Fu, “Morphology, crystallization and thermal behaviors of PLA-based composites: Wonderful effects of hybrid GO/PEG via dynamic impregnating,” *Polymers (Basel).*, vol. 9, no. 10, 2017.

[15] K. Piekarska, E. Piorkowska, and J. Bojda, “The influence of matrix crystallinity, filler grain size and modification on properties of PLA/calcium carbonate composites,” *Polym. Test.*, vol. 62, pp. 203–209, 2017.

[16] W. A. S. Bin Wan Mohammad, N. H. Othman, M. H. Wan Ibrahim, M. A. Rahim, S. Shahidan, and R. A. Rahman, “A review on seashells ash as partial cement replacement,” *IOP Conf. Ser. Mater. Sci. Eng.*, vol. 271, no. 1, 2017.

[17] B. Ashok *et al.*, “Tensile and Thermal Properties of Poly(lactic acid)/Eggshell Powder Composite Films,” *Int. J. Polym. Anal. Charact.*, vol. 19, no. 3, pp. 245–255, 2014.

[18] I. H. Kim and Y. G. Jeong, “Polylactide/exfoliated graphite nanocomposites with enhanced thermal stability, mechanical modulus, and electrical conductivity,” *J. Polym. Sci. Part B Polym. Phys.*, vol. 48, no. 8, pp. 850–858, 2010.

[19] W. Zheng, X. Lu, and S. C. Wong, “Electrical and mechanical properties of expanded graphite-reinforced high-density polyethylene,” *J. Appl. Polym. Sci.*, vol. 91, no. 5, pp. 2781–2788, 2004.

Optimization of the Extraction of Anthocyanin from the *Dacryodes rostrata* peel

Vinosyah Palaniandy[1], Chua Bee Lin[1], and Tee Lee Hong[1]*

[1]School of Engineering, Faculty of Built Environment, Engineering, Technology and Design, Taylor's University, Malaysia

Abstract. In Synthetic antioxidants were widely used as antioxidants until strict legislation on usage of those carcinogenic antioxidants have caused the attention of manufactures incline towards natural antioxidants. In the previous, antioxidant activities and prominent content in *Dacryodes rostrata* is consumed by human as a source of energy and minerals. Although epidemiologic studies suggest that the consumption of this fruit enhances health, anthocyanin concentration were still low as most of the anthocyanin content in its peel is thrown away as waste. The aim of this study is to optimize the solid-liquid extraction of anthocyanin from *Dacryodes rostrata* peel using Response Surface Methodology (RSM). The effects of several SLE on the total anthocyanin contents (TAC) and the DPPH (2,2-diphenyl-1-picrylhydrazyl) radical scavenging activity on *D. rostrata* peel were studied. Temperature, extraction time, liquid/solid ratio, pH condition and solvent concentration have been investigated as independent variables in two-level full factorial design. Among the examined variables, extraction time, pH condition and liquid/solid ratios were significant factors for the extraction of anthocyanin from *D. rostrata* peel. The three significant factors were then subjected to optimization using Box-Behnken design (BBD) of RSM. The optimal SLE conditions in extracting anthocyanin with desirability of 1.0 were pH 4.2 with liquid/solid ratio of 1:94 for 104 minutes, resulting TAC of 38295.92 mg CGE/100 g dw and DPPH of 91.17 %. The validation experiment was proven resulting small error difference less than 10 % which confirm the validity of the optimization. The antioxidant activity of *D. rostrata* peel after optimization was higher than antioxidant activity of BHT, 84.71 % and BHA, 77.73 %. Therefore, *D. rostrata* peels can be used as an alternative source of natural antioxidant activity.

1 Introduction

Traditional medicine has been used widely for diseases treatment since the awareness of synthetic drug side effects increased and many begun utilizing medicinal plants to overcome this healthcare challenge. Almost 80 % of the population take medical plants as their primary healthcare [1]. The importance of medicinal plants and traditional health systems has been captivating in the recent times, contributing to the phenomenal growth in research of natural antioxidants. Many synthetic and natural food antioxidants are used in foods and health supplement to protect them against oxidation. Synthetic antioxidants such as butylated hydroxytoluene (BHT) and butylated hydroxyanisole (BHA) are widely used as antioxidants in cosmetics, food industry and therapeutic industry. However, BHT and BHA are carcinogenic and strict legislation on its usage of some synthetic antioxidants have caused the attention of manufactures incline towards natural antioxidants. Therefore, a global trend toward the use of natural substance present in medicinal plants and dietary plants as an alternative is increasing. Lately, it has been drawing much attention especially in the medical industry such as controlling Type II diabetes, reduction of coronary heart disease and prevention of cancer [156].

In a tropical country like Malaysia, amongst many fruits and herbs that contribute to the medicinal value, *Dacryodes* species contains high content of antioxidant and polyphenols [157]. *Dacryodes rostrata*, normally found in wild forests of Southeast Asia is also known as *kembayau* or *kedondong kerut* in Malaysia. The attribution of *D. rostrata* bioactivities are evident with its antioxidant components like flavonoids, phenolics and anthocyanin. Anthocyanin are known as the largest and most important category of water-soluble pigments in nature that are responsible for the blue, purple, red, and orange colours in many fruits and vegetables [158]. As the peel can be a potential source to retrieve its anthocyanin, this study can convert waste into useful product having the extracted anthocyanin being used in health supplement/nutraceutical industry.

In order to retrieve the bioactive compounds from natural sources, extraction process has to be done. The best extraction method must provide high extraction rates and should be time saving with high quality. Each technique has its own advantage and disadvantage, however, for preliminary study on the anthocyanin extraction from *D. rostrata* peel, solid-liquid extraction (SLE) is used. SLE method is more accurate in obtaining non-destructed results with varying parameters as the procedure varied for different antioxidants and different fruits. Extraction efficiency is influenced by several factors such as such as concentration of solvent, liquid/solid ratio, time, temperature, pH, etc. However, there are some limitations for this research work. Although many non-conventional methods had been developed in the extraction techniques, SLE was used in this research as one of the reference method to compare the success of newly developed methodology. Its ease of operation, low cost and wide range of use also ensures SLE to be the most convenient and common method for initial researches.

The optimization of anthocyanin yield and antioxidant activity from the *D. rostrata* peel was not widely developed. The findings on the fruit's peel is even less, thus it is important for this research to prove the potential of *D. rostrata* peel to become an alternative natural antioxidant. However, previous studies only show the influence of a single factor on the extraction of anthocyanin and not the interactions between the factors. Therefore, to optimize the extraction conditions, factorial design is used to allow the simultaneous study the effects of several factors. It also allows measuring the interaction between each factor to achieve the best overall optimization. Many studies have reported extraction of anthocyanin from different plant material, but literature data concerning optimization of anthocyanin from *D. rostrata* peel is very few [5].Although previous research of optimum extraction of anthocyanin from other

fruits such as grapes and citrus have been succesful, the analytical results are insuffient to justify that if the extraction of anthocyanin from the *D. rostrata* peel would give similar results.

In the present study, the influence of five factors (time, liquid/solid ratio, temperature, pH, solvent concentration) on the extraction were initially screened to identify three significant factors that would extract the highest anthocyanin content and have a high antioxidant activity by DPPH radicals scavenging activities. Response Surface Methodology (RSM) using the Box-Behnken design was applied due to its high efficiency and less number of experiments were required, thus reducing the total cost to optimize the extraction of anthocyanin from *D. rostrata* peel.

2 Materials and Methods

2.1 Chemicals

Ethanol 96% (AR), sodium acetate, acetic acid, 96% hexane, pure methanol (HPLC grade) and potassium chloride (AR) was purchased from Friendemann Schmidt. 2,2-diphenyl-picrylhydrazyl (DPPH) and 1M sodium hydroxide solution were obtained from R & M Chemicals while 1M hydrochloric acid from Merck.

2.2 Sample material and preparation.

Fresh *D. rostrata* fruits was collected from indigenous areas in Sarawak, Malaysia and then transported in an icebox through airmail to Taylor's University lab. The fruits without physical damage, with uniform shape and colour were chosen. It was then cleaned with tap water and air dried before subjected for lyophilization. The lyophilized samples were grounded into fine powder using a laboratory grinder and sieved through a 0.1 mm to maintain the consistency of sample sizes. At the ratio of 1:4, the samples were defatted using hexane and filtered using a vacuum filter before being subjected for oven drying at 35℃ to remove the remaining solvent. The sample powder was stored in a sealed bag and kept in a freezer at -20 ºC until used [6].

2.3 Solid-liquid extraction of anthocyanin from *D. rostrata* peel

The solid-liquid extraction was carried out in an incubator shaker at 150rpm based on the combination of parameters as dictated by experimental design shown in Table 1. The extraction time, temperature, ethanol concentration, pH and solid to solvent proportion were based on the experimental design generated by Design Expert trial version 11.0 (State Ease, Inc.) The extract was centrifuges at 8000 rpm for 15 min to obtain the supernatant. The extract was then kept in 15ml centrifuge tubes at -20 ºC before analysis. The total anthocyanin content and DPPH assay were carried out in triplicates and the results were evaluated to determine conditions for RSM.

2.4 Experimental design

2.4.1. Preliminary factorial screening

A 2^3 fractional factorial design was used to investigate the effect and choose the significant parameters that influence the total anthocyanin content and DPPH radical scavenging ability. Each factor was studied on three levels to generate an experimental design with 37 runs using Design Expert 11.0 trial version as presented in Table 1. Although all factors showed significance in the TAC analysis, extraction temperature and ethanol concentration were found insignificant in the model for DPPH analysis.

Table 1. Experimental design for screening of factors influencing total anthocyanin content and DPPH radical scavenging ability

Factors	Level (-)	Level (0)	Level (+)
Temperature (℃)	40	60	80
Extraction time (min)	30	105	180
pH value	2	4	6
Ethanol concentration (%)	20	50	80
Liquid/solid ratio (g/ml)	1:100	1:55	1:10

2.4.2 Response surface methodology using the Box-Behnken design

The Box-Behnken design (BBD) for RSM was used to optimize the three most significant extraction parameters with the help of Design Expert Software Trial Version 11.0 (Stat-Ease Inc, Minneapolis, USA) to create the design of experiments. The three independent variables were coded at three levels (low: -1, 0, high: +1) as shown in Table 2. The response was fitted to the following second order polynomial model equation in Eq. (1) to study the relationship between the responses and the independent variables.

$$Y = \beta_0 + \sum_{i=1}^{k} \beta_i X_i + \sum_{i=1}^{k} \beta_{ii} X_{ii}^2 + \sum_{i}^{k-1} \sum_{j}^{k} \beta_{ij} X_i X_j \quad (1)$$

where the response of the model is expressed as Y; β_0 is the constant coefficient; β_i , β_{ii} and β_{ij} are the linear, quadratic, and cross-product coefficient of the variables respectively; X_i and X_j were the independent variables.

The optimization process was carried out to determine the optimum extraction condition with the most desirable properties by using graphical and numerical optimization procedures. Graphical optimization was done by drawing three-dimensional (3D) response surface plot for visualizing the significant ($p \leq 0.05$) interaction effects of the parameters on the target responses.

Table 2. Experimental design for optimization of extraction using Box-Behnken design

Factor levels	Independent variable		
	Extraction time (min)	pH value	Liquid/solid ratio
-1	30	2	1:10
0	105	4	1:55
+1	180	6	1:100

2.5. Analytical method

2.5.1. Determination of total anthocyanin content (TAC)

TAC in the samples was estimated using the pH-differential method using two buffers, namely potassium chloride buffer (0.025M, pH 1.0) and sodium acetate buffer (0.4M, pH 4.5). About 0.5 ml of fruit extract was diluted with potassium chloride (pH 1.0) and measured at 520 nm until the extract absorbance was within the range of 0.2-1.4. Similarly, 0.5ml of extract was diluted with sodium acetate (pH 4.5) in the same dilution factor. The absorbance was recorded

using a UV-spectrophotometer and distilled water was used as a blank for calibration. TAC was expressed as mg cyanidin-3-glucoside equivalent per 100 g dry weight (mg CGE/100 g dw) of fruit sample according to Eq. (2) [7] [8].

$$\text{TAC (mg CGE/100g dw)} = \Delta A \times MW \times df \times 10^3 \times \frac{100}{\varepsilon} \times L \quad (2)$$

where, $\Delta A = [(A520nm - A700nm)pH1.0 - (A520nm - A700\ nm)pH\ 4.5]$
MW = molecular weight (449.2 g/mol of cyanidin 3-glucoside)
df = dilution factor
L= path length in cm = 1 cm
ε= 26,900 M extinction coefficient in L $mol^{-1}cm^{-1}$for cyanidin 3-glucoside
10^3 = factor for conversion from gram to milligram

2.5.2 DPPH radical scavenging activity

A solution of 0.2mM of 2,2-diphenyl-1-picryhydrazyl (DDPH) was prepared by adding 3.98mg of DPPH into 50ml of HPLC grade pure methanol. Extract (1ml) was added to 3 ml of DPPH solution, mixed vigorously and kept in the dark for 30 min. The absorbance was measured at 520nm against a blank without sample using a UV-VIS spectrophotometer. The following equation was used to calculate the scavenging activity ability:

$$\text{DPPH} = \frac{A-B}{A} \times 100 \quad (3)$$

where, A is the absorbance of DPPH minus the absorbance of blank solution and B is the absorbance of DPPH solution containing the extract. The determination of the radical activity of fruit peel extract was done in triplicate and the results were expressed as %.

2.6 Validation of the model

The optimization process was carried out to determine the optimum extraction condition with the most desirable properties by using graphical and numerical optimization procedures. Graphical optimization was done by drawing three-dimensional (3D) response surface plot for visualizing the significant ($p \leq 0.05$) interaction effects of the parameters on the target responses. Simultaneously, an overlaid contour plot was applied to demonstrate how the yield and antioxidant activity were affected by the interaction effects of three variables, while the two remaining independent variables was kept constant at the middle level. The validation process was done to determine the adequacy of the final reduced model and recommended optimum conditions. Then the predicted optimum extraction condition was practically applied to obtain the most desirable *D. rostrata* peel extract. Finally, the experimental and predicted values of each response was compared for error difference (%). The insignificant difference ($\leq 10\%$) observed between the experimental data and predicted values confirmed the validity of the final reduced model.

3 Results and discussion

3.1 Analysis of Preliminary Factorial Screening.

2^{6-1} fractional factorial design experiment was conducted with 37 experimental runs to determine the significant factors that affect the extraction of anthocyanin from *D. rostrata* peel. TAC and antioxidant activity by DPPH extracted from *D. rostrata* peel was performed using solid-liquid extraction with ethanol as solvent. The solubility of anthocyanins was studied by varying the solvent concentration (20, 50, 80 %), extraction time (30,105,180 min), temperature (40,60,80 ℃), pH condition (2,4 and 6) and liquid/solid ratio (1:100, 1:55, 1:10). Table 3 shows the p-value and the percentage contribution for both response where extraction time, pH condition and liquid/solid ratio was the most significant factors in extraction TAC and DPPH radical scavenging activity. The significance of each factor on the total anthocyanin extracted and DPPH radical scavenging activity were further discussed.

Table 3. *p*-value and percentage contribution of responses against factor and their interaction

Factor	***p*-value**		**% Contribution**	
Response	TAC	DPPH	TAC	DPPH
Model	< 0.0001*	< 0.0001*	-	-
A	< 0.0001*	0.6807	5.10	0.00
B	< 0.0001*	< 0.0001*	10.91	45.81
C	< 0.0001*	0.0011*	2.92	0.79
D	< 0.0001*	0.0594	0.92	0.01
E	< 0.0001*	0.0002*	1.12	2.22
AB	< 0.0001*	0.0336*	4.15	0.12
AC	< 0.0001*	0.3194	8.80	0.01
AD	< 0.0001*	0.0004*	1.31	1.38
AE	< 0.0001*	0.0002*	1.23	1.79
BC	< 0.0001*	0.0010*	3.86	0.87
BD	< 0.0001*	0.0034*	0.24	0.45
BE	< 0.0001*	< 0.0001*	0.53	6.97
CD	< 0.0001*	0.0158*	2.30	0.19
CE	< 0.0001*	0.1475	1.51	0.04
DE	< 0.0001*	0.0003*	7.54	1.65

***A, B, C, D and E* represent temperature, extraction time, pH condition, ethanol concentration, liquid/solid ratio, respectively**
***Significant at $p < 0.05$**

3.1.1 Extraction time as a significant factor on extraction of TAC yield and antioxidant activity

Extraction time was very significant in contributing to a higher yield of TAC and antioxidant activity ($p < 0.0001$) with 10.91 and 45.81 % contribution respectively. Not only it exhibits the largest contribution but also has significant interaction with other factors. All the interaction of extraction time with another factors has a *p* value lesser than 0.05. TAC and antioxidant activity increased with extraction time due to their contact time with the *D. rostrata* peel in aqueous ethanol. An increase in TAC yield was also reported in extraction from *Sparganii rhizome* and mulberry for a 100 min extraction time [9, 10]. The longer extraction time helps on breaking the bonding of phenolic-matrix and impact the membrane chemical structure of plant tissues that increase the TAC yield.

The interaction between liquid/solid ratio and temperature is also very good. In SLE, an increase in temperature usually leads to higher recoveries of bioactive compounds such as anthocyanin. On the other hand, high temperature can also cause higher degradation rates of anthocyanins [11]. However, liquid/solid ratio balances the limitation of temperature in this

research, similar to previous research on the extraction of eggplant (*Solanum melongena L.)* peel. The antioxidant activity also improves at longer extraction time as the saturation of anthocyanin in the solvent is higher.

3.1.2 Liquid/solid ratios as a significant factor on extraction of TAC yield and antioxidant activity

Liquid/solid ratio was another significant factor ($p < 0.05$); contributing 1.12 % and 2.22 % in the extraction of TAC and DPPH radical scavenging activity respectively. The higher liquid/solid ratio was an important factor in increasing yield as it would promote the access to the solid to the solvent. This was due to a series of mechanical effects, such as particle collisions and cell wall disruption will occur during cavitation which facilitates penetration of solvent into the sample and increase the mass transfer rates of anthocyanins [12]. At lower ratio of liquid/solid, the solvent can get saturated during the extraction. The interaction between liquid/solid ratio and ethanol concentration also showed significant ($p < 0.0001$) effect on TAC yield. Previous research on TAC extraction from milled berries also showed that increasing liquid/solid ratio provides higher diffusion coefficient [13]. The change in activity coefficient due to solvent composition also affects the solubility of compounds [8].
DPPH radical scavenging activity also increased with high liquid/solid ratio because more solvent was in contact with the solid. This is consistent with the principles of mass transfer; the driving force during mass transfer is the concentration gradient between the solid and the bulk of the liquid, which is greater when a higher liquid/solid ratio is used. Previous study in antioxidant activity on almond hulls (*Prunes amygdalus*) and pine sawdust (*Pines pinaster*) also corresponds to this research [14, 15]. The interaction between the extraction time and pH condition was also very significant ($p < 0.0001$) as shown in Table 4. The results are similar to the findings in *Feronia limonio* (wood apple) extraction and grape extract who reports the high antioxidant activity dependency on the liquid/solid ratio [16, 17].

3.1.3 pH condition as a significant factor on extraction of TAC yield and antioxidant activity

The third significant factor affecting the extraction of anthocyanin from *D. rostrata* peel is the pH condition ($p < 0.0001$) on both responses: TAC and DPPH scavenging activity with 2.92 % and 0.79 % contribution respectively. Changes in pH may alter the solubility and polarity of the polyphenols by dissociation of the –OH groups and thus directly affecting the TAC yield and its antioxidant capacity. Based on previous researches, it is proven on *Jabuticaba* peel that anthocyanins are more stable in acidic pH [18]. This is because an increase in pH may result in reduction of antioxidant properties stability [19]. Extraction temperature and ethanol concentration does not contribute significantly towards the antioxidant activity ($p > 0.05$). From the results obtained, liquid/solid ratio and extraction time were very significant in obtaining higher yield of TAC and DPPH radical scavenging activity. pH was also significant in contributing to the TAC yield and antioxidant activity, thus was also selected for optimization. These factors were used to determine the optimum extraction condition with the aid of response surface methodology.

3.2 Analysis of Response Surface methodology

The experimental modelling results for TAC and DPPH using the Box-Behnken design (BBD) were shown in Table 4. The experimental results for TAC and DPPH in the fruit peel extracts varied from 1353.17 to 36178.13 mg CGE/100g dw and 28.65 to 90.84 % respectively.

Table 4. Box-Behnken design (BBD) experimental design with the independent variable and experimental data for both response.

Run	Extraction conditions			Experimental results	
	Liquid/solid ratio (g/ml)	Time (min)	pH	TAC (mg CGE/100g dw)	DPPH (%)
1	55	105	4	25599.39	64.79
2	10	180	4	1809.05	41.26
3	10	105	6	2730.94	58.36
4	100	105	2	34436.44	81.67
5	100	105	6	35546.92	86.87
6	100	180	4	31256.97	79.90
7	100	30	4	36178.13	90.84
8	55	105	4	18211.80	77.79
9	55	105	4	17381.87	77.21
10	55	180	6	11309.04	74.15
11	55	30	6	14810.24	84.08
12	10	30	4	1353.17	28.65
13	55	105	4	23507.02	85.64
14	55	30	2	6552.64	50.86
15	55	105	4	23121.28	85.30
16	10	105	2	8439.62	46.72
17	55	180	2	2267.71	54.38

3.2.1 ANOVA for total anthocyanin content

The R^2 value, F value and *p*-value were used for analysing the model and evaluating the mutual interaction of the independent and dependant variable for total anthocyanin content in Table 5.

The experimental result for total anthocyanin content was highly fitted to the quadratic model due to its low *p*-value at 0.0007. The lack of fit of the model was also calculated using Design Expert software to analyse the error in the model. The value of lack of fit of this quadratic model was 0.305, which is more than 0.05. It can be said that the quadratic model was very close to the responses of the TAC yield. A second order polynomial model, Eq.1 was fitted the experimental data well, with R^2 value of 0.9533 for TAC. The second-order polynomial Eq. (4) described the relationship between liquid/solid ratio (X_1), extraction time (X_2) and pH (X_3).

$$TAC = -25690.2 + 100.4889X_1 + 285.0081X_2 + 9805.042X_3 - 0.3983X_1X_2 + 18.9421X_1X_3 + 1.30622X_2X_3 + 1.88608X_1^2 - 1.37498\,X_2^2 - 1273.78X_3^2 \quad (4)$$

3.2.2 ANOVA for DPPH radical scavenging activity

The R^2 value, F value and *p*-value were used for analysing the model and evaluating the mutual interaction of the independent and dependant variable for total anthocyanin content in Table 5.

The experimental result for DPPH radical scavenging activity was highly fitted to the quadratic model due to its low *p*-value at 0.0132. The lack of fit of the model was also

calculated using Design Expert software to analyse the error in the model. The value of lack of fit of this quadratic model was 0.3205, which is more than 0.05. It can be said that the quadratic model was very close to the responses of the DPPH radical scavenging activity. A second order polynomial model, Eq. 1 were fitted the experimental data well, with R^2 value of 0.8867 for DPPH radical scavenging activity. The second-order polynomial Eq. (5) described the relationship between liquid/solid ratio (X_1), extraction time (X_2) and pH (X_3).

$$DPPH = -26.7286 + 1.1307X_1 + 0.560809X_2 + 11.73609X_3 - 0.00175X_1X_2 - 0.01788X_1X_3 - 0.02242X_2X_3 - 0.00382X_1^2 - 0.00182\,X_2^2 - 0.50421X_3^2 \quad (5)$$

3.2.3 Effect of extraction parameter on optimization of TAC and antioxidant activity

From the developed second order polynomial model in Eq.4 and Eq.5, three-dimensional response surface plots were constructed to illustrate the main and interactive effect of independent process parameters on a response variable. Figure 1 and Figure 2 shows the response surface plots for total anthocyanin content from *D. rostrata* peel and its antioxidant activity respectively.

Effect of liquid/solid ratio

Liquid/solid ratio is one of the dominant factors in extraction of anthocyanin from *D. rostrata* peel using solid liquid extraction method. As shown in Table 5, the TAC extraction yield was more significantly affected by liquid/solid ratio and pH condition compared to the extraction time. From the surface plots (Fig 1A, B and Fig .2A, B), the liquid/solid ratio showed significant positive effect on both responses. Previous research by J.E. Cacace and G. Mazzaon showed that TAC extraction from milled berries also showed that increasing liquid/solid ratio provides higher diffusion coefficient [13]. DPPH radical scavenging activity also increased with high liquid/solid ratio because more solvent was in contact with the solid.

This is consistent with the principles of mass transfer; the driving force during mass transfer is the concentration gradient between the solid and the bulk of the liquid, which is greater when a higher liquid/solid ratio is used. Previous study in antioxidant activity by M. Pinelo et al. on almond hulls (*Prunes amygdalus*) and J.A. Michiels et al. on pine sawdust (*Pines pinaster*) also corresponds to this research [14, 15]. The results obtained in this research are similar to the findings by N. Ilaiyaraja et al. in *Feronia limonio* (wood apple) extraction who reports the high antioxidant activity dependency on the liquid/solid ratio [16].

Effect of pH condition

Based on Table 5, the linear effect of pH was significant on DPPH radical scavenging activity but not on the total anthocyanin content. However, its quadratic effect on the total anthocyanin was significant as shown in Table 5. From the surface plots (Fig 1B, C and Fig 2B, C), the total anthocyanin content increases at the optimum around pH 4 then decreases with pH until pH 6. This agrees with previous research by A.R.C. Braga et al., anthocyanins are more easily extracted in acidic condition [18]. This is because at acidic condition, hydrolysis mechanism may occur to disintegrate the compounds that bound to their polymers or cell wall membrane. When pH increases, it can increase solubility of the compound as the polarity increases by dissociation of the mainly acidic phenolic –OH groups [19].

However, decreasing pH will facilitate the oxidation process of anthocyanins which reflects in the low TAC extract yield and low antioxidant activity at pH 2. Based on Fig 2B and

C, a higher pH condition significantly increases the antioxidant activity by DPPH. This is because, anthocyanins are distinguished from other flavonoids by their re-arrangement in response to pH changes. A decrease in pH condition being more acidic may result in reduction of antioxidant properties stability [18]. Similarly, previous research on pH condition effect on *L. sativa* by A. Altunkaya et al. also proved that acidic pH condition increase of the antioxidant activity due to an increase of their electron-donating ability upon deprotonation and to their stabilization in alkaline solutions leading to polymerization reaction [20].

Effect of extraction time

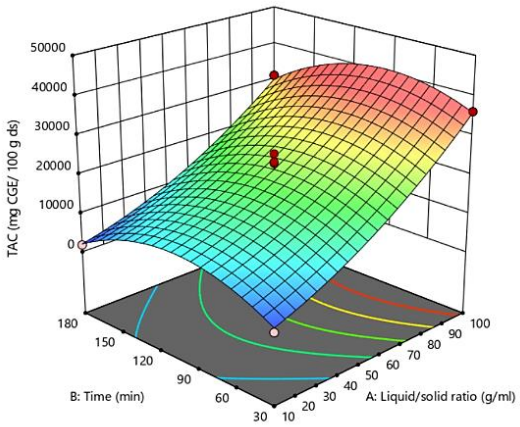
Based on Fig 1A, C and Fig.2A, C, longer extraction time also assists in the extraction of anthocyanin using SLE method as it gives more time in contact of the solid and solvent [21]. TAC and antioxidant activity increased with extraction time due to their contact time with the *D. rostrata* peel in aqueous ethanol. Similarly, E. Espada-Bellido et al. reported that an increase in TAC yield in extraction from *Sparganii rhizome* and mulberry for a 100 min extraction time [10]. The longer extraction time helps on breaking the bonding of phenolic-matrix and impact the membrane chemical structure of plant tissues that increase the TAC yield. Similarly, TAC decreased proportionally with extraction time as low as 30 min at any pH condition (Fig. 1A and C). The antioxidant activity also improves at longer extraction time as the saturation of anthocyanin in the solvent is higher. Although non-conventional methods claim that extraction time is negligible in extraction, it was significant in SLE method of extracting anthocyanin from *D. rostrata* peel [21].

Table 5. ANOVA for response surface model of all independent variables on TAC and DPPH.

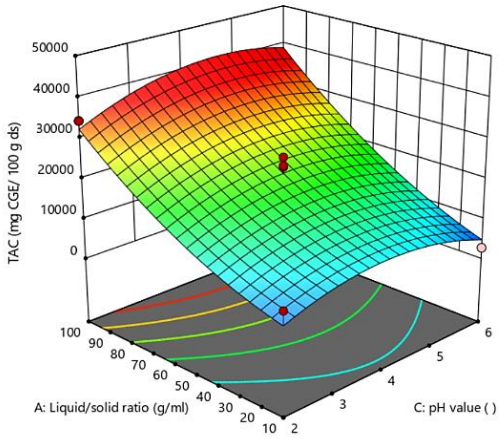
Factor	` TAC					DPPH				
	SS	DF	MS	*F*-value	*p*-value	SS	DF	MS	*F*-value	*p*-value
Model	2.37×10^9	9	2.64×10^8	15.87	0.0007*	4950.75	9	550.08	6.09	0.0132*
Linear term										
X_1	1.89×10^9	1	1.89×10^9	114.03	< 0.0001*	3373.61	1	3373.61	37.32	0.0005*
X_2	1.88×10^7	1	1.88×10^7	1.13	0.3231	2.81	1	2.81	0.0311	0.8651
X_3	2.02×10^7	1	2.02×10^7	1.21	0.307	609.78	1	609.78	6.75	0.0356*
Quadratic										
X_1^2	6.14×10^7	1	6.14×10^7	3.7	0.0959	251.26	1	251.26	2.78	0.1394
X_2^2	2.52×10^8	1	2.52×10^8	15.17	0.0059	443.32	1	443.32	4.9	0.0624
X_3^2	1.09×10^8	1	1.09×10^8	6.58	0.0373	17.13	1	17.13	0.1895	0.6765

Interactions											
X_1X_2	7.23×10^6	1	7.23×10^6	0.4352	0.5305	138.72	1	138.72	1.53	0.2553
X_1X_3	1.16×10^7	1	1.16×10^7	0.7	0.4304	10.36	1	10.36	0.1146	0.7449
X_2X_3	1.54×10^5	1	1.54×10^5	0.0092	0.9261	45.22	1	45.22	0.5003	0.5022
Lack of fit	6.50×10^7	3	2.17×10^7	1.69	0.305**	346.1	3	115.37	1.61	0.3205**
Pure error	5.12×10^7	4	1.28×10^7			286.61	4	71.65		
CV %	23.52					13.83				
R^2	0.9533					0.8867				

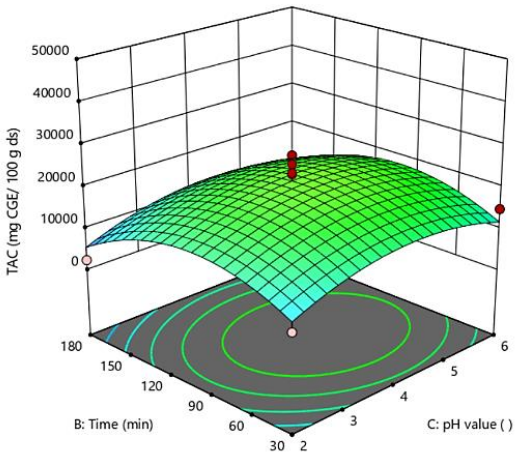
X_1, X_2, X_3 represent liquid/solid ratio, extraction time, pH, respectively; SS, DF, MS and CV represent sum of squares, degree of freedom, mean square, coefficient of variation, respectively.
*Significant at $p < 0.05$
** Not significant at $p > 0.05$



A

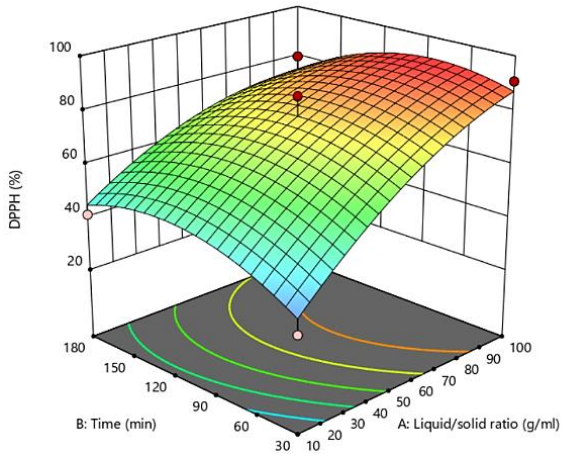


B

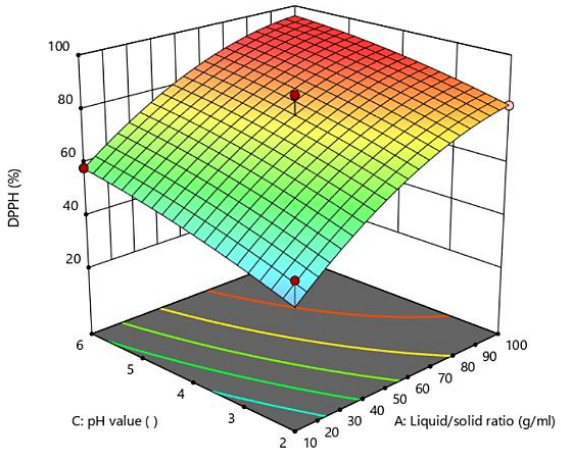


C

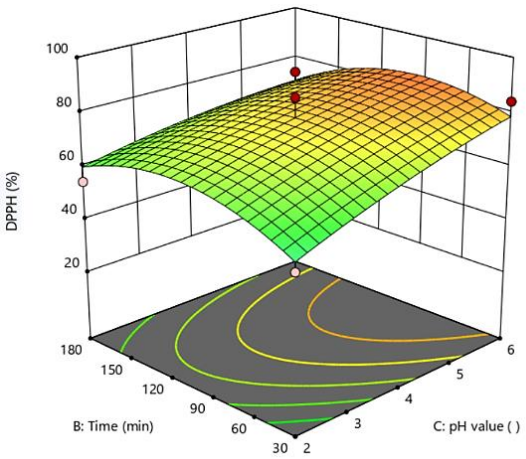
Figure 1. Response surface plots for interactions between three extraction parameters on extraction yields of total anthocyanin (TAC, in mg CGE/100g dw).



A



B



C

Figure 2. Response surface plot for interactions between three extraction parameters on extraction yields of DPPH scavenging activity ability (in %).

3.3 Verification of the predicted optimal conditions

The optimum condition for extraction process of TAC from *D. rostrata* peel were determined based on Eq. 4 and Eq.5 to obtain the highest yield of TAC and DPPH radical scavenging activity. By analysing the experimental data of RSM using Design Expert Software Trial Version 11.0 (Stat-Ease Inc, Minneapolis, USA), the optimized conditions were determined

and shown in Table 4.5. The optimum TAC yield was predicted to be 38295.92 mg CGE/100 dw and antioxidant activity was 91 % with desirability of 1.0.

Table 6. Optimized conditions for the extraction process for TAC

Extraction parameter	Optimized condition
Liquid/solid ratio	1:94 g/ml
Extraction time	104 min
pH condition	4.2

The reliability of the models was verified by performing an experiment under the reduced model optimal conditions discussed in earlier section. The comparison of the experimental and predicted extraction yields for TAC and DPPH are as shown in Table 7.

Table 7. Validation of extraction under optimum parameters.

Response	TAC (mg CGE/100 dw)	DPPH (%)
Predicted	38295.92	91.17 %
Experimental	35067.66	88.59 %
Error deviation	8.43 %	2.84 %

Using the optimal condition, the experimental anthocyanin content extracted was 35067.66 mg CGE/100 dw which was not much different with the predicted yield of 38295.92 mg CGE/100 dw. The validation was achieved as the difference between the predicted values and experimental values were only 8.43 % for TAC and 2.84 % which is less than 10 %, validating the adequacy of the model. Thus, the regression models obtained by RSM could predict the TAC and DPPH extraction yields for any combination of liquid/solid ratio, extraction time and pH condition. In addition, to study if the *D. rostrata* peel have the potential to be an alternative natural antioxidant, the antioxidant activity of D. *rostrata* peel after optimization was compared to the commercial antioxidants, Butylated Hydroxytoluene (BHT) and Butylated Hydroxyanisole (BHA) [22]. The antioxidant activity of *D. rostrata* peel after optimization was higher than antioxidant activity of BHT, 84.71 % and BHA, 77.73 %. Therefore, *D. rostrata* peels can be used as an alternative source of natural antioxidant.

4 Conclusions

In this research *D. rostrata* peel were proven to have high antioxidant activity and they are suitable to be used as natural antioxidants. The optimised conditions to extract total anthocyanin content from *D. rostrata* peel were determined using Box-Behnken Design in response surface methodology.

The optimum value for liquid-solid ratio, extraction time and pH condition were 1:94 g/ml, 104 min and 4.2 respectively. Using the optimal condition, the experimental anthocyanin content extracted was 35067.66 mg CGE/100 dw which was not much different with the predicted yield of 38295.92 mg CGE/100 dw. The experimental DPPH radical scavenging activity was found to be 88.59 % compared to the predicted value of 91.17 %. Both response validated the research with error difference less than 10 %.

.

References

[1] M. Ekor, Frontiers in Pharmacology, **4**, 1-10, (2014).

[2] A. Sinela et al., Food Chem., **214**, 234-241, (2017).
[3] L.H. Tee et al, Food Chem.,**165**, 247-255, (2014).
[4] M. G. Miguel, J. Appl. Pharm. Sci.,**06**, 07-15, (2014).
[5] L.H. Tee et.al, Med.Chem., **4**, 23-27, (2015).
[6] K. W. Kong et al., Food Research Int. **44**, 2332-2338, (2011).
[7] Lee, J., Drust, R. W.,& Wrolstad, R.E.,J. AOAC Int. **88**, 1269-1278, (2005).
[8] T.Belwal,et al. Food. Chem. **207**, 115-124, (2016).
[9] X. Wang et al. , Ultrasonics Sonochemistry, **20**, 846-854, (2013).
[10] E. Espada-Bellido et al. , Food Chem., **219**, 23-32, (2017).
[11] F. Dranca, M. Oroian, Ultrasonics Sonochemistry ,**31**, 637-646, (2016).
[12] F. Chemat., Ultrasonic Sonochemistry, **18**, 813-835, (2011).
[13] J.E. Cacace; G. Mazza, J. Food Eng. **59**, 379-389, (2003).
[14] M. Pinelo et al. Food. Chem. , **85**, 267-273, (2004).
[15] J.A. Michiels et al. , Food. Chem., **130,** 986-993, (2015).
[16] N. Ilaiyaraja et al. , Food Chem., **173**, 348-354, (2015).
[17] E. Karacabey; G. Mazza , Food Chem., **119**, 343-348, (2010).
[18] A.R.C. Braga et al., J. Food Comp. Analysis,**68,** 31-40 (2017).
[19] N. T. A. F. Erdogdu, J. Food Eng. **76**, 579-583, (2006).
[20] A. Altunkaya et al. , Food Chem. , **190,** 25-32, (2016).
[21] S. Sai-Ut, et al., Food Sci. Tech. **64**, 742-749, (2015).
[22] W. Wang et al., Environ. Research , **151**, 339-343, (2016).
[23] Tee, L.H. et.al; Food Chem., **165**, 247-255, (2014).
[24] M. Miguel, J. Appl. Pharm. Sci. **06**, 07-15, (2014).
[25] G. Burgos, J. Food Comp. Analy. **30**, 6-12, (2013).
[26] E.N. Bridgers, Industrial Crops. Prod., **32**, 613-620, (2010).
[27] Y.J. Kang, Food Sci. Biotechnol. **23**, 97-106, (2014).
[28] G.Patil, Chem. Eng. Processes, **48**, 364-369, (2009).
[29] A. Sinela, N. Rawat et al., Food Chem., **214**, 234-241, (2017).
[30] H. Wang, J. Agric. Food Chem. **44**, 701-705, (1996).

Optimization of polysaccharide extraction process from *Dioscorea Opposita*

Wong Yong Yuen[1], and *Chua Bee Lin*[5*]

[1]School of Engineering, Faculty of Build Environment, Engineering, Technology and Design, Taylor's University, Malaysia

Abstract. In this studies, polysaccharide from *dioscorea opposita* also known as Chinese Yam is known to have antioxidant, anti- inflammatory and anti-tumour properties. Although epidemiologic studies have proven the consumption of Chinese yam do enhance in health but most of the countries do not have access to such medicine. Ultrasound assisted extraction (UAE) method was used to extract the polysaccharide in this research. The aim of this study is to identify the preliminary range of extraction parameters (extraction temperature, extraction duration and solid liquid ratio) prior to response surface methodology optimisation to maximise the extraction yield of polysaccharide from *Dioscorea opposita.*

[5] Corresponding author: beelin.chua@taylors.edu.my

1.0 INTRODUCTION

Dioscorea Opposita also known as "*Shan Yao*" or Chinese Yam, classified as one of the genus of Dioscoreaceae [1]. It was believed to be a traditional medicinal plant where it is edible and available throughout China and was recognized to contribute towards medical purpose. Physical appearance of a *Dioscorea Opposita* does look like a common potato. However, one physical characteristic that can been seen in *Dioscorea Opposita* is that when it was cut or smash, it exuded a white vicious liquid or gum [2]. Previous studies show that *Dioscorea Opposita* has strong anti-oxidative capacity and a high comprehensive utilization value that is effective in removing free radicals.

Polysaccharides play as one of the important roles in developing in pharmaceutical and biodegradable packing materials. Polysaccharides had a low molecular weight and a chemical with low molecular weight are closely related to human health [3]. Since 1970s, polysaccharides from *Dioscorea Opposita* consists of unique physiological properties and it was believe that it might become an alternative source for cancer treatment [4]. *Dioscorea Opposita* is proven rich in polysaccharides where it is widely used in food application, medical purpose and emulsion stabilizer [5]. Hence, extraction process was performed on *Dioscorea Opposita* for study and research to further improve the potential of polysaccharide from *Dioscorea Opposita* towards the society.

There are few extraction methods such as maceration with and without thermal treatment [6,7] and ultrasound-assisted extraction (UAE) [8–12] frequently used to extract bioactive compounds from medicinal plants. Hot water extraction technique was frequently used for extraction of polysaccharide but this method is time consuming with higher energy consumption. Ultrasound-assisted extraction (UAE) is one of the alternative method when comes to polysaccharides extraction process. UAE of food and medical product was always involved with low molecular weight chemical compounds such as polysaccharides [13].

Until recently, most of the research method done on extraction process is slowly moving to UAE from water bath. This was due to functionality ultrasound-assisted extraction by applying high intensity sound wave to accelerate and speed up the extraction process. However, based on literature review, most research on UAE extraction method was involving extraction of polysaccharides on fruits as material where research on UAE extraction of *Dioscorea Opposita* were limited which it became a great opportunity to fill up the research gap.

For research purpose, it is better to perform optimisation on extraction process of polysaccharide as it do help most of the researcher to perform better understanding and have a more efficient experiment. Prior to this, the identification of preliminary range to be applied in RSM optimisation is crucial as these ranges will be further optimised using Optimiser in Design Expert Software to finally identify the optimum extraction conditions that give to highest extraction yield of polysaccharide from *Dioscorea Opposita*.

Hence, the ranges of extraction conditions such as extraction time, extraction temperature and solid liquid ratio of solvent prior to RSM optimisation will be identified in this research.

2.0 RESEARCH METHODOLOGY

2.1 Collection of Raw materials and Chemicals.

Chinese Yam, *Dioscorea opposita* was purchased and collected from a local groceries store. Chemical and reagents were been through analytical grading and available at Taylor's University.

2.2 Drying process of *Dioscorea Opposita*

Weight of *Dioscorea opposita* samples was measured using weighing balance (Model TX423L, Shimadzu, Japan). Samples of *Dioscorea opposita* with constant dimension and weight were prepared before drying process. *Dioscorea opposita* samples were dried in oven (Model UN75, Memmert, Germany) and the drying process was completed when constant weight of *Dioscorea* was obtained. The dried *Dioscorea opposita* samples were cooled down and further grinded into powder form using grinder (Model BL-1525BG, OEM, China). For storage purpose, the powder samples are kept in separated polyethylene bag in room temperature.

2.3 Extraction and Precipitation process of Polysaccharide from *Dioscorea Opposita*

Ultrasound-assisted extraction (UAE) method was conducted based on [14,15] with few modifications. 2 g of powdered *dioscorea opposita* was added into 40 ml of citric acid (solid to liquid ratio of 1:10 to 1:50 g/mL). The input power of ultrasonic bath (Model: Elmasonic P120H, Elma, Germany) was set to 80% with 37 Hz frequency. The extraction temperature was set at 50℃ and extraction time was set at 60 min. After extraction process, the experiment was further preceded to alcohol-precipitation stage. The extracted polysaccharides were then centrifuged at 5000 rpm for 15 min using a centrifuge (Model Scanspeed 1236MG, LaboGene, Denmark). The supernatant collected wax was mixed with 100 ml of ethanol and kept under 4℃ for more than 12 hours. The crude polysaccharide was formed and further centrifuged at 9000 rpm for 15 min. The crude polysaccharide was collected and underwent drying process for more than 12 hours. The polysaccharide collected was then quantified.

2.4 Single factor experimental design

Single factor experiment was used to reduce the gap of the experimental range of each of the extraction conditions prior to RSM optimisation. Three extraction parameters (extraction temperature, extraction time and solid to liquid ratio) were identified using single factor experimental design. Table 1 shows the single factor experiment design and polysaccharide was selected as the response.

The effects for the above-mentioned extraction parameters on the response (polysaccharide yield) were plotted individually by varying one factor while keeping another two factors at their center points in each experiment. Based on the results of the single factor experimental design, the optimal ranges of these three factors were identified.

Table 1. Single factor experimental design

Process Parameter			
Extraction Temperature (℃)	Extraction Time (min)	SL ratio (g/ml)	Yield of polysaccharide (%)
40	120	1:20	
50			
60			
70			
80			
70	90	1:20	
	120		
	150		
	180		
	210		
120	70	1:10	
		1:20	
		1:30	
		1:40	
		1:50	

3 Results and discussion

3.1 Single Factor Experimental Design Analysis

Fifteen experiments runs were carried out based on single factor design conditions shown in Table 1. Three process parameters, each with respective range found from research journal were employed into this study. Each process parameters were further narrow down from five levels to three levels based on higher polysaccharide yield at shown in Figure 4 to 6.

Extraction time or sonification time is a significant variable due to it associated with mass transfer effect. From Figure 4, it can be observe that the polysaccharide yield increased along with increasing extraction time in UAE until the time of 150min and it will start decreasing. This is because excessive ultrasound wave will lead to structural decomposition and destroyed the polysaccharide, in the end polysaccharide yield reduced [8]. Hence, the range of sonification time was set between 120 min to 180 min with central point of 150 min.

The extraction temperature do also play a significant role when comes to polysaccharide yield. The polysaccharide yield do show increasing trend when extraction temperature increasing but it starts to decrease once pass 60°C. This can be explained by increasing temperature will change the surface tension and viscosity of the solvent which lead to polysaccharide degradation, in the end decrease in polysaccharide yield. Therefore, the range of polysaccharide extraction temperature was selected between 50 to 70°C.

In addition to that, solid liquid ratio for polysaccharide extraction process do make a differences in polysaccharide yield Based on research study, increase in solid liquid ratio leads to a high polysaccharide yield due to enhance in penetration rate of solvent into sample but will cause reduction in intensity of cavitation due to excessive in solid liquid ratio. Based on result, the polysaccharide yield is increasing until 1:30 g/ml but start to show decreasing trend after that. Thus, the range for solid liquid ratio was set around 1:10 to 1:30 g/ml.

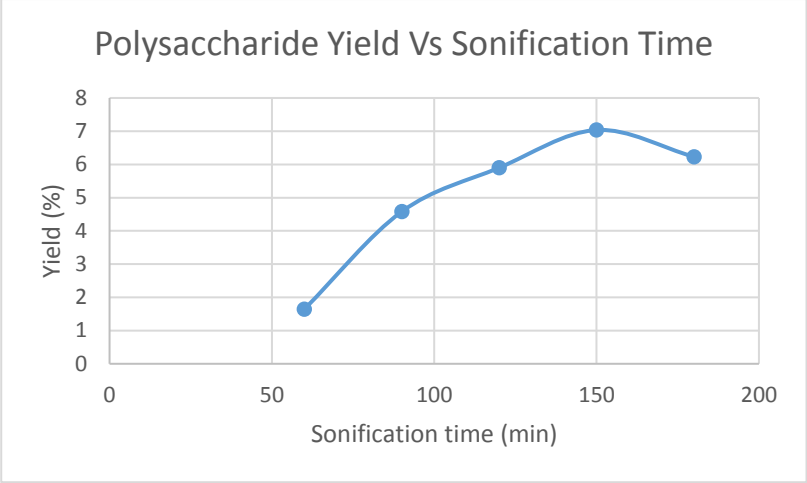


Figure 4. Impact trend of sonication time on polysaccharide yield.

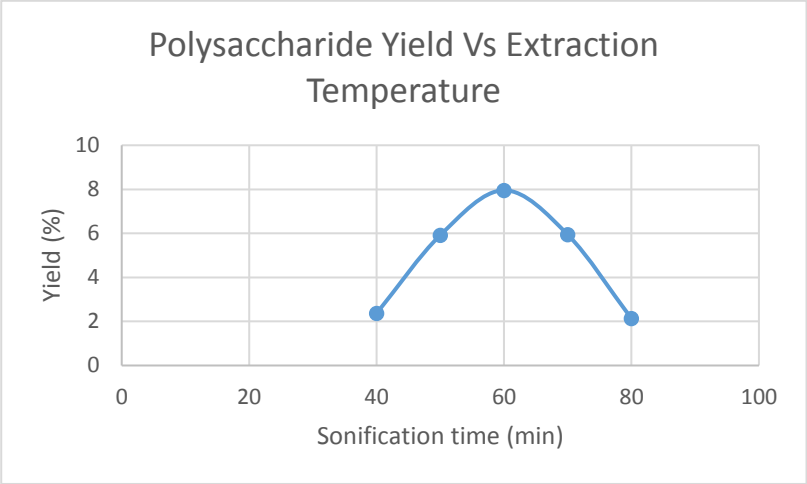


Figure 5. Impact trend of extraction temperature on polysaccharide yield.

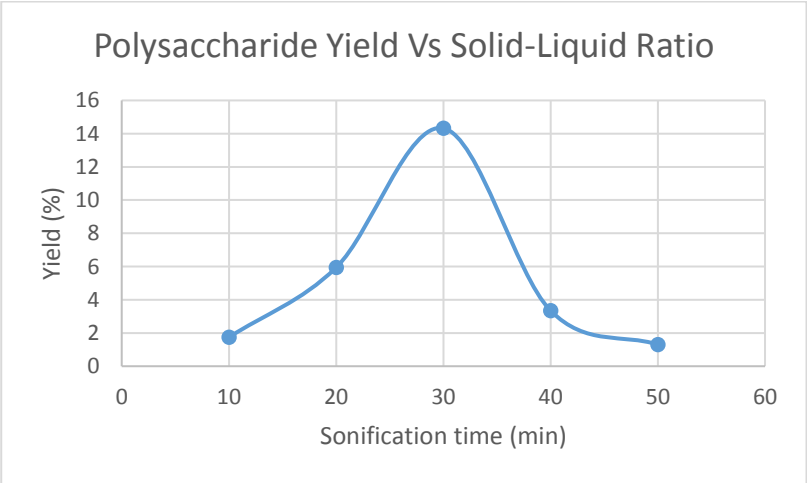


Figure 6. Impact trend of solid-liquid ratio on polysaccharide yield.

4.0 CONCLUSIONS

In this research work, the preliminary ranges of extraction parameters prior to RSM optimization using single factor experimental design were identified as 120 min to 180 min, 1:20 to 1:40 g/ml and 50 to 70 °C for extraction temperature. These ranges can be further optimised using RSM-optimization in order to determine the optimum extraction conditions for the highest polysaccharide yield

REFERENCES

1. A. Pengelly, K. Bennett, Appalach. Plant Monogr. 1 (2011)
2. G. Zhao, J. Kan, Z. Li, Z. Chen, Carbohydr. Polym. **61**, 125 (2005)
3. W. Yang, Y. Wang, X. Li, P. Yu, Carbohydr. Polym. **117**, 1021 (2015)
4. L. Gao, Y. Di, J. Wu, M. Shi, F. Zheng, J. Spectrosc. **2014**, 1 (2014)
5. F. Ma, Y. Zhang, Y. Yao, Y. Wen, W. Hu, J. Zhang, X. Liu, A.E. Bell, C. Tikkanen-Kaukanen, Food Chem. **228**, 315 (2017)
6. B.L. Chua, Z. Abdullah, K.Y. Pin, L.C. Abdullah, T.S.Y. Choong, U.K. Yusof, J. Eng. Sci. Technol. **12**, (2017)
7. B.L. Chua, Z. Abdullah, K.Y. Pin, L.C. Abdullah, T.S.Y. Choong, U.K. Yusof, Res. J. Pharm. Biol. Chem. Sci. **6**, (2015)
8. A. Ali, X.Y. Lim, C.H. Chong, S.H. Mah, B.L. Chua, Sep. Sci. Technol. (2018)
9. A. Ali, C. Chong, S. Mah, L. Abdullah, T. Choong, B.L. Chua, Molecules **23**, 484 (2018)
10. B.L. Chua, Y.L. Chen, MATEC Web Conf. **152**, (2018)
11. B.L. Chua, Y.C. Chong, MATEC Web Conf. **152**, (2018)
12. A. Ali, X.Y. Lim, C.H. Chong, S.H. Mah, B.L. Chua, LWT - Food Sci. Technol. **89**, 681 (2017)
13. Y.C. Cheung, K.C. Siu, J.Y. Wu, Food Bioprocess Technol. **6**, 2659 (2013)
14. L. Zhang, M. Wang, Int. J. Biol. Macromol. **95**, 675 (2017)
15. T. Yılmaz, Ş. Tavman, Rev. Agaroquimica Y Tecnol. Aliment. **22**, 112 (2016)

Synthesis of Nanoparticles and Characterization of Hybrid Nanofluid

Tsui San Yap[1,††], Rashmi Walvekar[1] , Mohammad Khalid[2], Sumair Ahmed[3] and Chockalingam Aravind Vaithilingam[1]

[1]School of Engineering, Faculty of Built Environment, Engineering, Technology & Design, Taylor's University, Lakeside Campus, No. 1 Jalan Taylor's, 47500 Subang Jaya, Selangor, Malaysia

[2]Sunway University, No. 5 Jalan University, Bandar Sunway, 47500 Subang Jaya, Selangor, Malaysia

[3]TECSOL Power and Control System, India

Abstract. The burning of fossil fuels to generate energy in the form of power is one of the main contributor to global warming due to the large amounts of carbon dioxide (CO_2) released into the atmosphere. Therefore, the efficient utilization renewable energy sources, especially solar energy, is widely considered to be a promising solution to global warming. Solar panels utilize thermal energy storage (TES) to contain solar energy in thermal energy form while heat from solar irradiation is collected by a thermal energy carrier also known as heat transfer fluid (HTF). Recent studies have shown that eutectic salts exhibit excellent thermal properties and can be utilized as HTF. With the advancement in nanotechnology, the addition of nanoparticles into eutectic salts can be carried out to enhance its thermo-physical properties. The aim of this research is to synthesize and study a new class of working fluids and mateiral that have improved physical and thermochemical characteristics that is able to operate at higher temperature range with minimal impact to the total cost of the system. Graphene oxide was synthesized through the conventional Hummer's method. Eutectic salt was synthesized from nitrate salt mixture of sodium, potassium, lithium, cesium, and calcium while the synthesis of TiO_2-graphene nanocomposites was prepared using the sol-gel method. Eutectic salt was then combined with the nanocomposites to produce a hybrid nanofluid and characterized thermally. The characterization of hybrid nanofluid that was carried out through TGA and it was found that the degradation temperature of hybrid nanofluid was ~680°C while the addition of GO nanoparticles did not cause a significant change in the thermal stability of the salt mixture. FTIR results showed that there were no noticeable structural change in organic compounds after the additions

†† Corresponding author: tsuisan83@gmail.com

of GO nanoparticles and TiO_2/graphene nanocomposites indicating that there was no chemical reaction between GO and the salt mixture.

1 Introduction

The burning of fossil fuels, such as coal and natural gas, to generate energy in the form of power is one of the main contributor to global warming and climate change due to the large amounts of carbon dioxide (CO_2) released into the atmosphere [1]. Many countries, including Malaysia, is highly dependent on fossil fuels to generate energy in the industry to ensure sustainable social and economic development. In 2012, the recorded increase in energy consumption in Malaysia was 7.5% with expectations to rise further in the range of 6-8% in the following years [2]. This rise in energy demand will most likely increase the need for more fossil fuels which will also result in an increase in CO_2 emissions.

The Malaysian government has taken the initiative to address this issue by introducing and encouraging the implementation of renewable energy (RE), such as solar energy, in the 8th Malaysia Plan during 2001 [3]. Solar energy is advantageous in Malaysia because the country experiences hot and humid weather all year round due to its location being near the equator [3]. The efficient utilization renewable energy sources, especially solar energy, is widely considered to be a promising solution to global warming. With noticeable impact as a source of power generation, solar energy has contributed to more than 20% of the development of global power in 2016 [4]. In the year 2016, solar power generation had experienced a rapid growth rate of 29.6% and its capacity has more than trebled over the past four years [4]. The annual increase of the global solar energy capacity is depicted in **Figure 14** below.

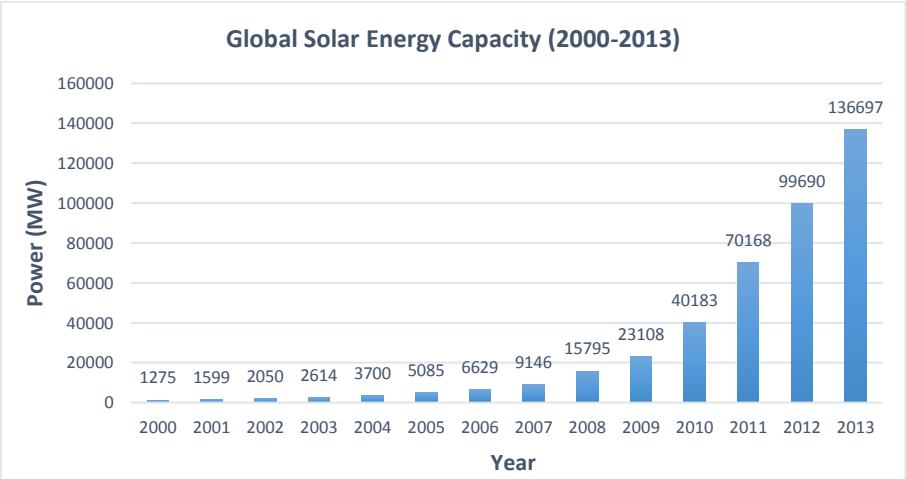


***Figure 14. Global Trend of Solar Energy Capacity from Year 2000 to 2013** [5].*

Solar panels or collectors utilize thermal energy storage (TES) to contain solar energy in thermal energy form. Heat from solar irradiation is collected by a thermal energy carrier also known as heat transfer fluid (HTF) [6]. A common limiting factor present in any form of solar-based energy conversion technology is the intermittent nature of solar irradiation which inhibits them from fulfilling the continuous energy needed [7]. Nevertheless, hot HTF can be kept in an insulated tank for power generation whenever sunlight is unavailable. Typically, HTF is required in large amounts for a solar plant to maximize its performance. However, the drawbacks of utilizing the conventional HTF as TES include the high cost and low efficiency of the fluid.

Recent studies have shown that molten salts do not only cost less than the conventional HTF, but also exhibit excellent thermal properties and are utilized in various industrial applications that relate to heat transfer [8]. Molten salts, also known as eutectic salts, are considered as phase change material that consist of a mixture of salts at specific compositions. Due to the large amount of individual salt species and salt mixtures, the possibility for combination arrangement of eutectic salts is enormous. Comparatively to the conventional HTF such as mineral oils, eutectic salts tend to have high working temperatures and heat capacity, lower vapour pressure and corrosivity, as well as have good thermal and physical properties at high temperatures [9]. However, eutectic salts tend to decompose when operating temperatures are higher than their thermal stability which causes corrosion effects [10].

With the advancement in nanotechnology, the addition of nanoparticles into eutectic salts can be carried out to enhance its thermo-physical properties [11]. Titania (TiO_2) nanoparticles have been a favourable choice due to its high photocatalytic abilities, chemical stability, low toxicity, and low cost [12]. However, TiO_2 on its own has a large bang gap which reduces the amount of solar spectrum absorption, making it not feasible for solar energy applications [12]. Therefore, modifications such as doping these nanoparticles to produce hybrid nanoparticles help mitigate these issues. Carbon-doped TiO_2 showed the most promising results as it is less costly, shows good conductivity, and has strong light absorption capabilities.

One of the most well-known two-dimensional (2D) graphite carbon material is graphene, which exhibit superior physical and chemical properties. Composites based on graphene, graphene oxide and nano-powders of metal oxides tend to be promising raw products for fabricating new materials with a variety of end use such as thermal energy storage solar cells. The ultra-dispersed powder of graphene or graphene oxide can be prepared through various methods such as the sol-gel method, hydrothermal method, solvothermal method, self-assembly, etc. [13]. These methods are usually preferred because they are environmentally friendly, have low operating temperatures, and is technically feasible [13].

To overcome the challenges mentioned, energy capacity of solar energy can be improved while reducing overall cost of the technology by utilizing eutectic salts as HTF because of their promising thermal properties. Additionally, to further enhance the thermo-physical properties of eutectic salts, additional materials such as carbon-doped nanoparticles are required to be added. Therefore, the aim of this research is to study a new class of working fluids and material that have improved physical and thermochemical characteristics that is able to operate at higher temperature range with minimal impact to the total cost of the system. The research will contain the synthesis and characterization of a hybrid nanofluid to determine its corresponding parameters. The scopes of this research work focus on mixing nitrate salts at specific compositions to produce eutectic salt and to study the effects of mixing additives such as GO and TiO_2/GO nanocomposite into the salt mixture.

2 Methodology

2.1 Materials

The required materials that were utilized for sample synthesis were listed in **Table 18** while **Table 2** shows the list of equipment utilized to carry out this research along with its intended purpose.

Table 18. Materials Required for the Synthesis of Eutectic Salt & Graphene Oxide.

Purpose	Materials Required
Synthesis of graphene oxide	Graphite, $NaNO_3$, H_2SO_4, $KMnO_4$, H_2O_2
Synthesis of eutectic salt	$NaNO_3$, KNO_3, $LiNO_3$, $CsNO_3$, $CaNO_3 \cdot 4H_2O$
Synthesis of hybrid nanocomposite	GO, $Ti(OBu)_4$, C_2H_5OH
Adjusting of pH values	HCl, NaOH

Table 19. Required Equipment and Purpose.

Equipment List	Abbv.	Usage
Thermogravimetric Analysis	TGA	To determine the degradation temperature of synthesized samples
Fourier Transform Infrared Spectroscopy	FTIR	To determine compounds present within a sample at its initial and final stages of the process as well as its chemical structure.
Kd2-Pro	-	To determine the thermal conductivity of synthesized samples.
Oven	-	To carry out corrosion test on copper and aluminium strips when immersed into samples.

2.2 Synthesis of Eutectic Salt

As mentioned earlier, the scope of study focuses on utilizing nitrate salts for the synthesis of eutectic salt. Hence, the synthesis of eutectic salt will be based on procedures and nitrate salt mixtures as reported by Ahmed et al [13]. The type of nitrate salt and its composition by mass required to formulate eutectic salt are as shown in **Table 20**. The salt mixture was dissolved completely in 50 ml of deionized water under continuous stirring with the aid of a magnetic stirrer and plate set at 125 RPM at room temperature. These salt ratios were able to synthesize an approximate amount of 10 gram of molten salt.

Table 20. Individual Amount of Nitrate Salt [14].

Type of Salt	Amount (gm)
$NaNO_3$	0.566
KNO_3	2.125
$LiNO_3$	0.734
$CsNO_3$	4.1
$CaNO_3$	2.475

2.3 Synthesis of Graphene Oxide

The Hummers method is a common method utilized to produce Graphene oxide (GO) from graphite. Hence, GO was synthesized using the Hummers method as reported by Contreras and Briones [14]. The synthesis begun with preparation of an ice bath and maintaining its temperature at 5°C. Graphite (1 g), sodium nitrate ($NaNO_3$, 0.50 g) and concentrated sulphuric acid (H_2SO_4, 23 ml) were added into a 500 ml flask and placed into the ice bath where the mixture underwent continuous stirring for 5 minutes. Then, potassium permanganate ($KMnO_4$, 3 g) was added slowly in small amounts into the flask to prevent any strong reaction at local points. The reaction mixture was maintained at 5°C for 2 hours then allowed to slowly increase to 35°C and kept for another 30 minutes under vigorous stirring. Distilled water (46 ml) was added into the suspension. This resulted in an increment of temperature to 98°C due to the hydration heat released. The bath was kept at this temperature for 30 minutes under continuous stirring.

To complete the reaction, distilled water (140 ml) and hydrogen peroxide (H_2O_2, 10% v/v, 10 ml) were added into the flask containing the mixture. As a result, a brown-yellowish colour product was produced and separated from the solution using a centrifuge. The resulting product was washed with diluted hydrochloric acid (HCl, 5%) solution and warm (70°C) distilled water to remove the remnant Mn ions and acid respectively. The resulting product was allowed to dry in air for 12 hours at 60°C using an oven. **Figure 15** shows the synthesized GO before and after drying.

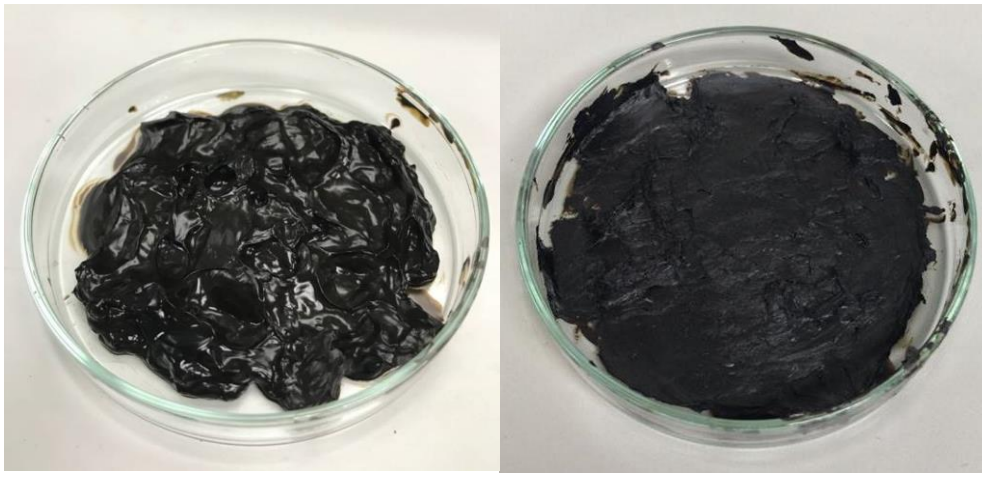


Figure 15. Synthesized Graphene Oxide (GO) Before and After Drying.

2.4 Synthesis of TiO_2/Graphene Oxide Nanocomposites

The synthesis of TiO_2/graphene nanocomposites was prepared by a modified sol-gel method as reported by Atout et al [16]. Firstly, the desired amount of graphene oxide (GO) was disperse in deionized water and allowed to undergo mechanical stirring for 1 hour. Then, ultrasonication was proceed for another hour. The pH of the dispersion will be adjusted to 1.5 by adding 0.025 M of HNO_3 drop by drop. A second solution was prepared by mixing 4.5g of tetrabutyl titanate ($Ti(OC_4H_9)_4$) and 18 ml of ethanol. The mixture was stirred for 1 hour. Then, the required amount of GO dispersion, which can be determined through calculations depending on the desired amount of GO content in the final composite, was added into the tetrabutyl titanate mixture in a drop wise action. The obtained solution was transferred into a 100 ml Teflon-

sealed hydrothermal vessel and maintained temperature at 120°C for 5 hours. The resulting product with deionized was washed with distilled water and ethanol, and allowed to dry for 15 hours at 60°C in an oven. **Figure 16** shows the synthesized TiO_2/graphene oxide nanocomposites (0.2 wt.%, 0.6 wt.%, 1.0 wt.%) before drying in the oven.

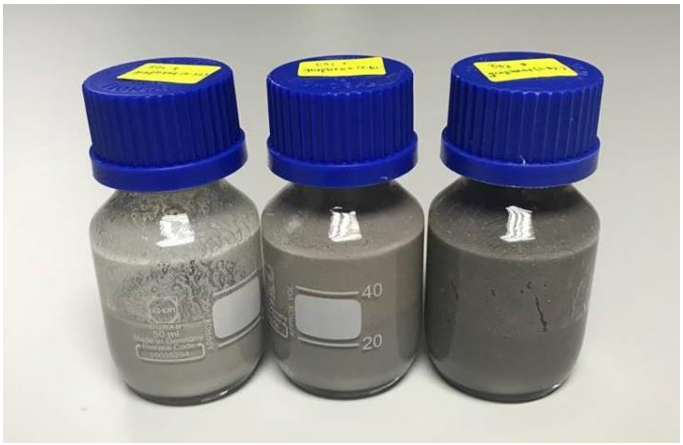


Figure 16. Synthesized Graphene Oxide/TiO_2 Nanocomposite before Drying.

2.5 Synthesis of Hybrid Nanofluid

The synthesis of hybrid nanofluid began with grinding the synthesized graphene oxide into powder using a grinder. The powder GO was measured and added into the eutectic salt at different weight percentages (0.2 wt.%, 0.6 wt.%, and 1.0 wt.%). The resulting mixture was allowed to undergo ultrasonication for 3 hours at 65°C to ensure nanoparticles were dispersed homogeneously.

2.6 Characterization of Hybrid Nanofluid

The characterization of hybrid nanofluid is carried out to determine its HTF and TES capabilities based on its thermal physical properties. The thermal physical properties to be considered are thermal stability, thermal conductivity, and structural changes. Each parameter is to be measured with a specific test using a specific equipment. **Table 4** summarizes the tests required to determine the required parameters as well as its designated equipment.

Table 4. Equipment and Required for the Characterization.

Thermal Properties	Tests	Equipment
Degradation Temperature	TGA	Perkin Elmer TGA 8000
Thermal Conductivity	KD 2 Pro	KD2 Pro

2.6.1 Thermogravimetric Analysis (TGA)

TGA analysis was conducted to monitor the weight of the sample as a function of increasing temperature, or isothermally as function of time, when the sample is placed in a controlled atmosphere filled with either inert or reactive gas. Approximately 10 mg of sample was placed onto the TGA sample holder and the analysis was performed at room temperature up to 800°C with the increment of 10°C per minute under nitrogen environment. The degradation temperature of the samples were then observed from the graph generate from the Pyris software. It was expected the first few weight percentage reading with respect to change in temperature, a steep decrease of slope will be produced. This point indicates the water loss from samples during heating process. The next steep slope that occurs due to the sudden decrease of mass indicates the degradation temperature of the sample whereby when utilized in solar energy applications, such temperature should be avoided to prevent any inefficiency to the process.

2.6.2 Thermal Conductivity Analysis

The thermal conductivity analysis begun by immersing the sensor into pure glycerol and comparing thermal conductivity result with value stated on the bottle to verify that the KD2 Pro equipment was working correctly and maintaining its accuracy. Then the sensor was then cleaned with some acetone and a thin layer of paste was applied onto the surface of the sensor to improve thermal conductivity between samples and sensor. The sensor was then fully immersed into samples and readings were recorded at 5 minute intervals until a total of 5 readings were obtained. During this stage, it was recommended to avoid touching the sensor to prevent any forced convection from occurring. Also, the sensor should be kept straight still at all times when analysis is being carried out to prevent any inaccuracy of data.

2.6.3 Fourier Transform Infrared (FTIR) Analysis

The fourier transform infrared (FTIR) spectrometer was utilized to analyse the structural changes occurred due to degradation of samples, by verifying its peaks. Hence, data collection was conducted for eutectic salt before and after the addition of any nanomaterials whereby the representation of data results were based on the graph the FTIR generates. A background reference was taken before measuring the spectrum of samples to ensure there are no interferences. The data was measured and collected within the frequency range of 4000 to 650 cm^{-1}.

3 Results and Discussion

3.1 Characterization of Eutectic Salt/Graphene Oxide

3.1.1 Thermogravimetric Analysis (TGA)

The short-term thermal stability of the eutectic salt and the hybrid nanofluid (eutectic salt + GO) was determined using the TGA apparatus. **Figure 17** shows the results for change in weight percentage of the salt mixture as a function to temperature. The steep slope occurring from temperature range of 30°C to approximately 87°C was the result of removal of residual moisture that was absorbed by the sample during preparation phase. This agreed with the assumption made earlier that the first steep slope was the result of moisture loss from the sample. The results show that salt mixture is stable below the temperature of 580°C, and its decomposition level would gradually deepen past 580°C.

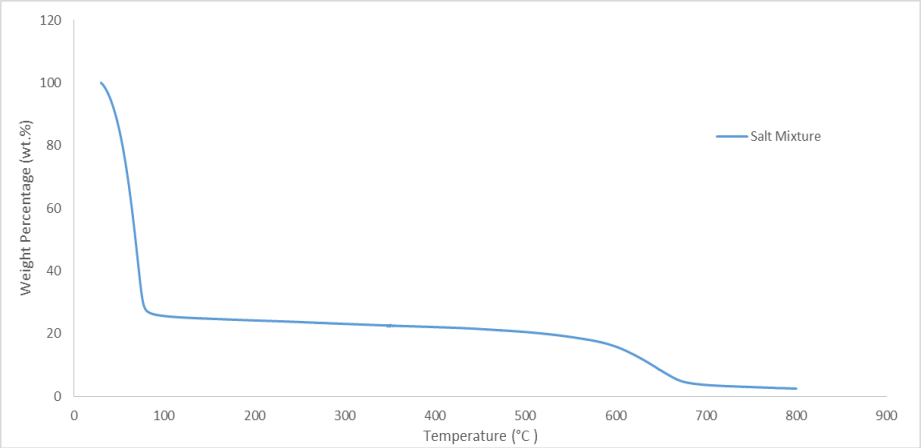


Figure 17. TGA Analysis for Salt Mixture.

A comparative study was conducted between the formulated salt mixture with other types of HTFs. **Table 21** shows the degradation temperature of different types of HTFs obtained from establish studies. From the table, conventional commercialized HTFs such as synthetic oil and mineral exhibit degradation temperatures of 400°C and 300°C respectively. The binary nitrate salt mixture (KNO_3-$Ca(NO_3)_2$) has the highest degradation temperature among the 3 types of salt mixture. The ternary nitrate salt mixture (KNO_3-$LiNO_3$,-$(CaNO_3)_2$) has a higher degradation temperature compared to the chloride salt mixture (NaCl-$CaCl_2$-$MgCl_2$). However, all HTFs shown in the table still exhibit lower degradation temperatures compared to the formulated salt mixture. This indicates that the formulated salt mixture is more stable and can withstand higher operating temperatures.

Table 21. Degradation Temperature of Different Types of Heat Transfer Fluids.

Author	Salt Mixture	Degradation Temperature (°C)
Pacheco et al. [17]	Synthetic oil (Therminol)	400
Pacheco et al. [17]	Mineral oil (Xceltherm)	300
Zhao and Wu [18]	KNO_3-$LiNO_3$,-$(CaNO_3)_2$	450
Du et al. [19]	NaCl-$CaCl_2$-$MgCl_2$	400
Wu et al. [20]	KNO_3-$Ca(NO_3)_2$	569.7

Figure 18 shows the results for change in weight percentage of the salt mixture and GO-dispersed salt mixture at different concentrations as a function to temperature. Results show that GO-dispersed salt mixture at concentrations of 0.2 wt.% and 1.0 wt.% showed a slight decrease in degradation temperature of eutectic salt after the addition of GO nanoparticles at 510°C and 595°C. For GO-dispersed salt mixture at concentration of 0.2 wt.%, the fluctuation of data occurring from 30°C to approximately 200°C could be cause by noise occurring from the surrounding atmosphere when the test was being carried out. Overall, this does not affect the analysis to determine the degradation temperature of sample.

Figure 7 shows the results obtained from hybrid nanofluid samples. With the addition of TiO_2/graphene nanocomposites at constant TiO_2 compositions and varied graphene compositions of 0.2 wt.% and 0.6 wt.%, it was found that the degradation temperature for both samples were similar at ~680°C, which is significantly higher than the degradation temperature of eutectic salt. Hence, it can be said the addition of TiO_2/graphene nanocomposites enhances the thermal degradation temperature of the eutectic salt. This enhancement also indicates that the hybrid nanofluid has a higher operating temperature and is suitable for TES in solar energy applications as typical operating temperatures are around 500°C and above [12].

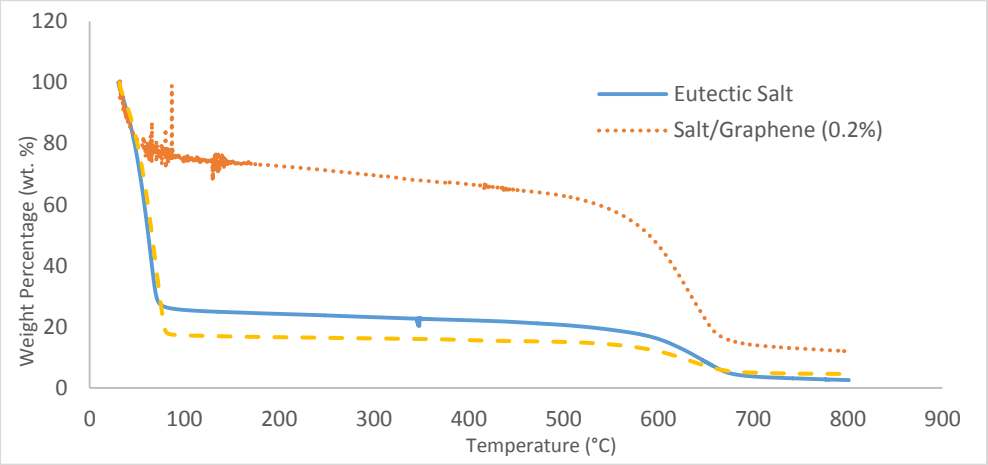


Figure 18. TGA Analysis for Salt Mixture & GO-dispersed Salt Mixture.

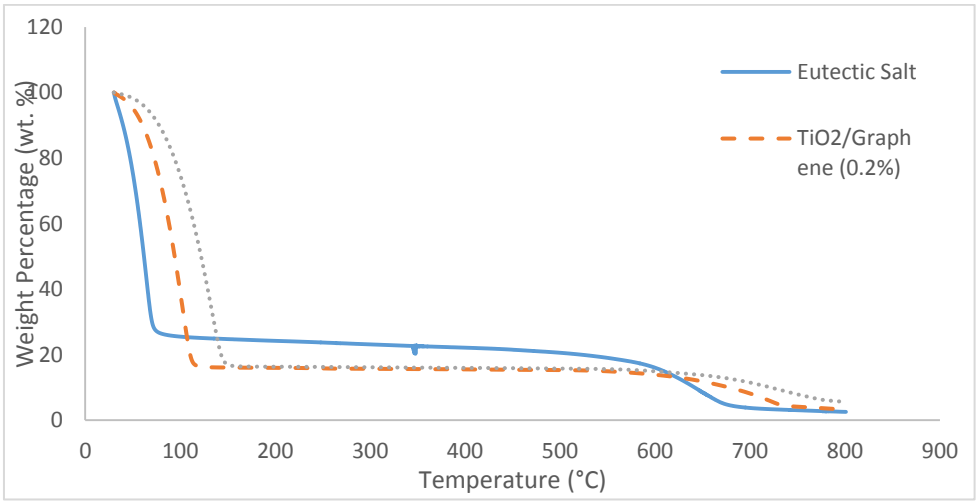


Figure 7. TGA Analysis for Salt Mixture &TiO_2/GO-dispersed Salt Mixture.

3.1.2 Fourier Transform Infrared (FTIR) Analysis

Figure 8 and **Figure 9** shows FTIR spectrum of salt mixture and different weight percentage of dispersed GO along with TiO_2/GO dispersed salt mixture. Both figures show a similar trend in result indicating that bonds present in all samples were identical. This could be caused by FTIR only being able to detect change in organic compounds whereas TiO_2 and GO are not considered as organic compounds. From the figures, it can be observed that all nitrates are present at band of 1358 cm^{-1}. The presence of angular deformation band of $–COO^{–}$ vibrations was observed 1300 cm^{-1}. Also, vibrational bands appear around 1634 cm^{-1} that match up with

C=N stretching. Salt mixture with no dispersed amount of GO showed identical spectrum to all concentrations of GO-dispersed salt mixture. These spectra agree with previous established results [14]. The addition of GO only increases the viscosity of the fluid and does not affect the degradation of the compound.

Table 22. FTIR Frequency Assignments [14].

Spectra (cm^{-1})	Functional Group
3400-3640	-OH
2850-2960	C-H stretching
1050-1150	C–O stretching
2210-2260	C=N stretching
1334	NO_3 stretching
1343-1240	$–COO^-$ vibrations
825-850	O–N–O group bending
760	$–COO^-$ in-plane bending

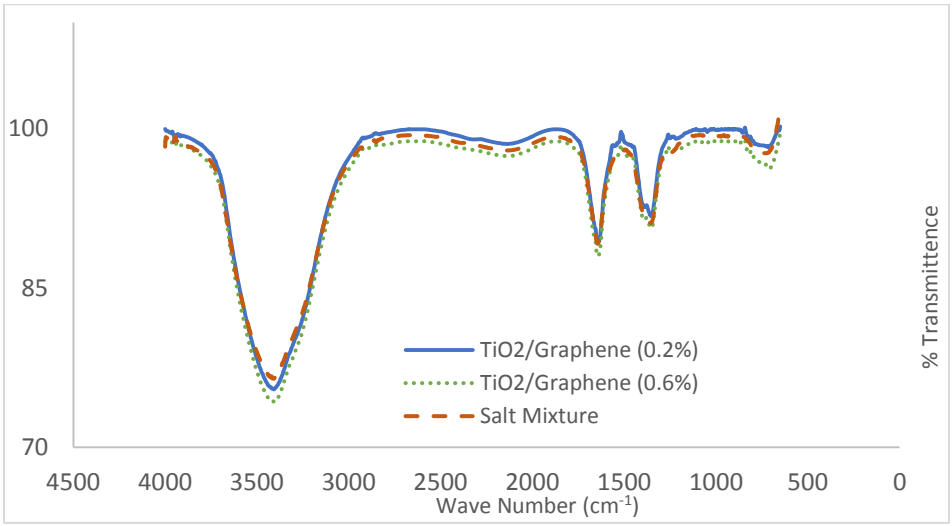


Figure 8. FTIR Spectrum of Salt Mixture and GO-dispersed Salt Mixture.

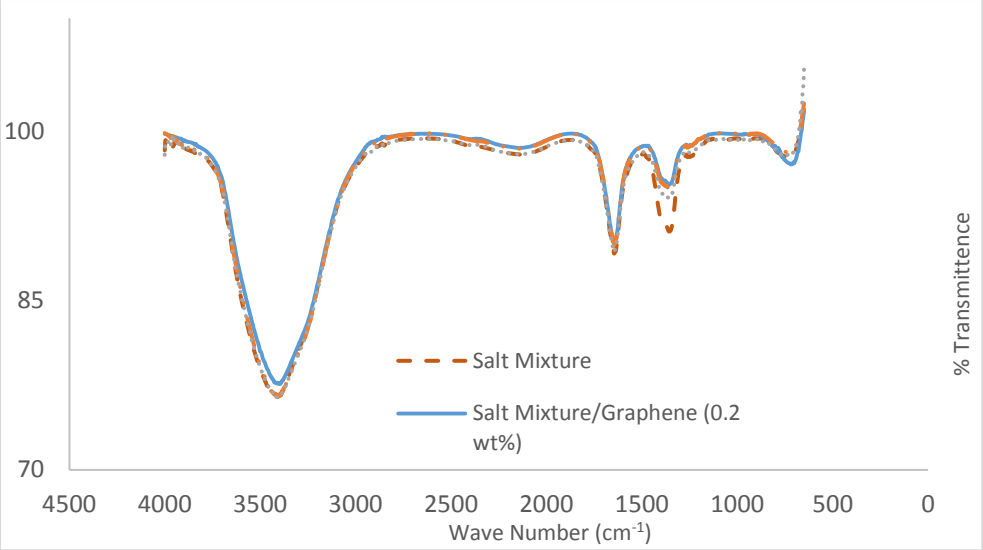


Figure 9. FTIR Spectrum of Salt Mixture and TiO_2/GO-dispersed Salt Mixture.

4 Conclusion

In this study, GO nanoparticles and TiO_2/graphene oxide nanocomposites were synthesized through the Hummers method and sol-gel method respectively. Also, the characterization of eutectic salt/graphene oxide was carried out where thermal stability and structural changes of hybrid nanofluid were measured and observed. From the thermal stability analysis, it was concluded that the salt mixture has a degradation temperature of 680°C, which was higher than the conventional HTF used in solar panels. It was also concluded that the addition of GO nanoparticles does not affect the degradation temperature. The structural changes caused by degradation were observed through the FTIR spectrometer. From the FTIR analysis, it was concluded that there was no chemical reaction between GO and salt mixture molecules.

5 Acknowledgement

The authors would like to acknowledge the support of the project partially by the Taylor's Flagship Research Grand TUFR/2017/001/01.

References

1. IPCC *Intergovernmental Panel on Climate Change*, New York (2014).
2. Tenaga Suruhanjaya, *National Energy Balance*," *Energy Commission*, Putrajaya, (2014).
3. T. H. Oh, M. Hasanuzzaman, J. Selvaraj, S. C. Teo and S. C. Chua, *Energy Policy and Alt. Energy in Malaysia: Issues and Challenges of Sustainable Growth - An Update*, Renewable and Sustainable Eenrgy Reviews, pp. 1-11 (2017).
4. BP Global, *Statistical Review of World Energy: Solar Eenrgy*, (2017).
5. J. Petinrin and M. Shaaban, *Renewable Energy for Continuous Energy Sustainability in Malaysia*, Renewable and Sus. Energy Reviews, no. 50, pp. 967-981 (2015).

6. K. Vignarooban, X. Xu, A. Arvay, K. Hsu and A. Kannan, *Heat Transfer Fluids for Concentrating Solar Power Systems - A Review*, Appl. Energy, pp. 384-394 (2015).
7. Z. L. Bin, L. R. Yuan, T. Bo and W. Peng, *Solar-thermal Conver and thermal Energy Storage of Graphene Foam-based Composites*, Nanoscale, no. 30, pp. 1-8 (2016).
8. D. Zhou and P. Eames, *A Study of A Eutectic Salt of Lithium Nitrate and sodium Chloride (87-13%) for Latent Heat Storage*, Sol. Energy Mater. Sol. Cells, **167**, pp. 157-161 (2017).
9. Q. Peng, X. Yang, J. Ding, X. Wei and J. Yang, *Design of New Molten Salt Thermal Energy Storage Material for Solar Thermal Power Plant*, Appl. Energy, **112**, pp. 682-689 (2013).
10. L. Du, J. Ding, H. Tian, W. Wang, X. Wei and M. Song, *Thermal Properties and Thermal Stability of the Ternary Eutectic Salt NaCL-CaCl2-MhCl2 used in High-Temperature Thermal Energy Storage Process*, Appl. Energy, **204**, pp. 1225-1230 (2017).
11. D. Bharath and D. Shin, *Effect of Nanoparticle Dispersion on Specific Heat capacity of a Binary Nitrate Salt Eutectic for Concentrated Solar Power Applicaitons*, Int. J. of Thermal Sci., pp. 37-42 (2013).
12. H. Li, Y. He, Z. Liu, B. Jiang and Y. Huang, *Rapid Synthesis of Broadband Ag@TiO_2 Core-Shell Nanoparticles for Solar Energy Conversion*, Sol. Energy Mater. Sol. Cells, **166**, pp. 52-60 (2017).
13. B. Benabdallah, Z. Edfouf, A. Lallaoui, I. Saadounne, M. Abd-Lefdil, F. C. El Moursli, *Improved Electrochemical Properties of Sol-gel Prepared ZnO/Graphene Composite*, Solid State Ionics, pp. 7-12 (2016).
14. S. F. Ahmed, M. Khalid, N. Amin, W. Rashmi, *Investigation of Rheological and Corrosion Properties of Grapehen-Based Eutectic Salt*, J. Mater. Sci., **51**, pp 1-18 (2016).
15. J. G. Contreras, F. C. Briones, *Grapehen Oxdie Powders with Different Oxidation Degree, Prepared by Synthesis Variations of the Hummers Method*, Mater. Chem. Phys., **153**, pp. 209-220 (2015).
16. F. Wu, W. Liu, J. Q, J. Li, W. Zhou, Y. Fang, S. Zhang, X. Li, *Enhanced Photocatalytic Degradation and Adsorption of Methylene Blue via TiO_2 Nanocrystals Supported on Graphene-like Bamboo Charcoal*, Appl. Surf. Sci., **358**, pp. 425-435 (2015).
17. X. Xu, G. Dehghani, J. Ning, P. Li, *Basic Properties of Eutectic Chloride Salts NaCl-KCl-$ZnCl_2$ and NaCl-KCl-$MgCl_2$ as HTFs and Thermal Storage Media Measured Using Simultaneous DSC-TGA*, Sol. Energy, vol. 162, pp 431-441 (2018).
18. L. Du, J. Ding, H. Tian, W. Wang, X. Wei, M. Song, *Thermal Properties and Thermal stability of the Ternary Eutectic Salt NaCl-$CaCl_2$-$MgCl_2$ Used in High-Temperature Thermal Energy Storage Process*, Appl. Energy, **204**, pp. 1225-1230 (2017).
19. L. Du, J. Ding, H. Tian, W. Wang, X. Wei, M. Song, *Thermal Stability of the Eutectic Composition in NaCl-$CaCl_2$-$MgCl_2$ Ternary System Used for Thermal Energy Storage Applications*, Energy, **105**, pp. 4185-4191 (2017).
20. Y. Wu, Y. Li, Y. Lu, H. Wang, C. Ma, *Novel Low Melting Point Binary Nitrates for Thermal Energy Storage Applications*, Sol. Energy Mater. Sol. Cells, **164**, pp. 114-121 (2017).

EURECA 2018 – Conference Paper
Paper number 2CE23

Extraction of Polyphenols from *Orthosiphon Stamineus* using Ethanol/Salt Aqueous Two Phase System

Yew Kar Mun[1] and *Chow* Yin Hui*[1]

[1]School of Engineering, Taylor's University, 47500, Subang Jaya, Selangor, Malaysia.

Abstract. Ethanol/ammonium sulphate aqueous two phase system (ATPS) is used to extract total phenolic compounds from *Orthosiphon Stamineus* leaves. *Orthosiphon Stamineus* consist of many phenolic compounds and flavonoids which are beneficial to human's health. This research aim is to study the effect of ATPS parameters such as concentration ethanol and salt on the partition coefficient, recovery percentage and yield of the phenolic compounds. The Fast Blue BB assay and DPPH free scavenging activity assay were used to determine the total phenolic content and scavenging activity respectively. In this study, the most suitable bottom phase phase-forming component was ammonium sulphate salt. The best extraction conditions can be achieved with 24% (w/w) ethanol, 21% (w/w) ammonium sulphate. At this maximum ATPS conditions, the maximum partition coefficient, recovery efficiency and yield of total phenolic contents were 39.35, 97.2%, 143.2 mg GAE/g respectively. Results showed that the ethanol/ammonium sulphate ATPS can serve as a promising extraction tool for the extraction of the phenolic compounds from *Orthosiphon Stamineus* leaves, giving the yield of phenolic compounds higher than the conventional extraction method. Some future works can be done based on this study such as recycling of the bottom phase component and the purification of the extracted phenolic compounds from *Orthosiphon Stamineus* leaves.

Production and Characterization of Nanocellulose from Chrysanthemum Stem

Aaron Wong Chung Hieng[1], *Chou Pui May*[27]

[1,2] School of Engineering, Faculty of Built Environment, Engineering, Technology & Design, Taylor's University, Lakeside Campus, No.1, Jalan Taylor's, 47500 Subang Jaya, Selangor Darul Ehsan, Malaysia

Abstract. Nanocellulose has received increasing interest to be used as a renewable and advanced material for many applications, owing to its excellent properties such as renewability, biocompatibility and biodegradability. Nevertheless, it is very challenging to extract nanocellulose from agricultural waste as agricultural waste is made up of three biopolymers (*i.e.,* cellulose, hemicellulose and lignin). Thus, the main aim of the present study is to produce nano-sized cellulose from chrysanthemum stem. Herein, the influence of reaction time and temperature on the yield and thermal properties of the synthesized nanocellulose were reported. In this work, nanocellulose was successfully extracted from the chrysanthemum stem via acid hydrolysis method. Acid hydrolysis was performed using sulfuric acid (64 wt%) at different reaction times (*i.e.,* 30, 60, 90 and 120 minutes) and different reaction temperatures (*i.e.,* 45, 60, 75 and 90°C). Characterization of the synthesized nanocellulose was carried out using Fourier transform infrared spectroscopy (FTIR) and thermogravimetric analysis (TGA). Based on the result obtained, the yield and thermal stability of the synthesized nanocellulose was decreasing as decreased the reaction time and temperature during the extraction stage. The nanocellulose exhibited yield up to 17.7% and high thermal stability up to 329 °C of onset temperature. The preliminary results clearly showed that chrysanthemum stem is one of the promising agricultural waste to produce nanocellulose that has a great potential to be used as a reinforcing filler for nanocomposites.

Keywords; Nanocellulose, Renewable, Acid hydrolysis, Morphology, Chrysanthemum

[7] Corresponding author: PuiMay.Chou@taylors.edu.my

1. Introduction

As the nanotechnology emerges and develops, nanocellulose attracts a lot of attention as a new nanomaterial produced from cellulose, the most abundant natural polymer on earth. Nanocellulose is a renewable and advanced material for wide range of applications due to its exceptional characteristics and excellent properties. The term 'nanocellulose' refers to cellulose in nano-size or structure. Nanocellulose can be extracted from any cellulosic source material such as plants, bacteria, algae or even invertebrate animals like tunicates [1]. Basically, nanocellulose can be categorized in three forms; *i.e.*, cellulose nanocrystal (CNC), cellulose nanofibril (CNF) and bacterial cellulose (BC) [2]. Different methods such as acid hydrolysis, high-pressure homogenization and (2,2,6,6-Tetramethylpiperidin-1-yl)oxyl (TEMPO)-mediated oxidation are used for the extraction of nanocellulose. As a result, nanocellulose with variety of crystallinities, surface chemistries, and mechanical properties were produced.

Nanocellulose has been discovered since 1980s in which wood is the main source for extraction of nanocellulose using high-pressure homogenization. Nevertheless, commercialization of nanocellulose was not successful back to 1980s due to the energy intensive production process involved. Besides, challenge is also faced in which the wood cannot be obtained at reasonable price as insufficient wood supply caused by the competition between different sectors such as furniture industry, paper and pulp industry and construction industry [3]. This circumstance results in the discovery of agricultural crops and by-products to become additional sources for producing nanocellulose through the years. For instance, the crops include sisal, flax, and hemp whereas the agricultural by-products include those obtained from the cultivation of sugarcane, banana, corn and pineapple [3].

Nanocellulose has outstanding characteristics identical to Kevlar, a light-weight material used for manufacturing high-strength and durable materials [4]. Furthermore, nanocellulose is totally renewable when compared to Kevlar. Its tensile strength is also very high which is eight times greater than of steel. Besides, its crystalline form is transparent and gas impermeable. It shows high absorbency of water which allows it to be used for making aerogels or foams. Last but not least, it is non-toxic and electrically conductive as well. These properties of nanocellulose make it an attractive option for use in dozens of industries, fields and disciplines around the world. There is a wide variety of applications for nanocellulose. For instance, it can be used as barrier material in food packaging, strengthening agent for paper, oil recovery, pharmaceutical and medical industries as well as many other existing and potential applications.

Nevertheless, there are considerable challenges remain to be solved despite the exceptional characteristics and properties of nanocellulose. For instance, the cost should be reduced as upscale in production and standardization for nanocellulose are expected due to high potential of research and development [5]. Furthermore, systematic characterization of nanocellulose sources, properties and behaviours are still lacking in literature. For instance, the surface, rheological, mechanical properties as well as the interaction between nanocellulose and living tissues require more developments. In addition, there are still many potential sources and applications of nanocellulose have not been fully discovered due to the limitations, such as availability and cost. Therefore, the main objective of the present study is to produce nanocellulose from chrysanthemum stem using a rapid and effective extraction method. This

research study was conducted to investigate the effect of different parameters such as reaction temperature, and time in the production of nanocellulose from chrysanthemum stem. The yield, chemical structure, and thermal properties of nanocellulose by manipulating the aforementioned parameters have been investigated in detail. Nevertheless, production of nanocellulose is significant for the expansion of potential applications in various industries as exploitation of cellulose was hindered by its stiff structure.

2. Experimental

2.1 Materials

Chrysanthemum stems (CS) was collected by from a flower stall in Puchong, Selangor, Malaysia. Ethanol (95%, Grade AR, *R&M* Chemicals), sodium hydroxide (NaOH, pellet, *R&M* Chemicals), hydrogen peroxide (H_2O_2, 30%, Grade AR, *R&M* Chemicals), sulfuric acid (H_2SO_4, 95-97%, Grade AR, FRIENDEMANN SCHMIDT CHEMICAL), were obtained from the laboratory of School of Engineering in Taylor's Univeristy, Malaysia. All the chemicals were utilized as received. Distilled water used was produced by FAVORIT W4L water stills. Whatman No. 1 filter paper was utilized during the filtration process.

2.2 Production of cellulose and nanocellulose from chrysanthemum stem

2.2.1 Cellulose production

The chrysanthemum stems collected were dried in the oven with temperature of 70 °C for 24 hours after removing the leaves and flowers. The dried chrysanthemum stems were cut into small pieces and ground into powder using grinder (Model JK-SG-160). The ground CS was first extracted with ethanol in a Soxhlet apparatus for 5 hours to remove wax, pigments and oils followed by drying process at 70 °C for 24 hours. 10g of dewaxed chrysanthemum stem powder was treated with 300 ml NaOH solution of 5% concentration at room temperature for 24 hours followed by heating at 90 °C for 5 hours [6]. The treated powder was filtered and washed with distilled water and ethanol. The powder was then dried at 70 °C for 24 hours. The solid treated by NaOH was added into 200 mL of 4% H_2O_2 while using NaOH to adjust the pH to 11.5 at 45 °C for 6 hours [6]. Filtration and washing with distilled water were conducted again for the treated powder followed by drying process at 70 °C for 24 hours. The pure cellulose produced was referred as CL.

2.2.2 Nanocellulose production

The pure cellulose obtained from the sodium hydroxide/hydrogen peroxide treatment was going through acid hydrolysis process to get nanocellulose. Cellulose was added into sulfuric acid solution (64 wt%) at cellulose to acid ratio of 1 g : 20 ml. [6,7]. The acid hydrolysis was carried out at 45 °C under continuous stirring for 30 minutes followed by quenching with 10-fold cold water to stop the reaction. Centrifugation was conducted for the suspension at 5000 rpm and 15 minutes for the removal of excess sulfuric acid. Washing against distilled water was conducted for the suspension until neutral condition was achieved. The nanocellulose suspension was then going through sonication process for 5 minutes at 80 Hz frequency for

disruption of large nanocellulose aggregates. The nanocellulose suspension was kept at 4 °C in a refrigerator for future characterization. Acid hydrolysis was conducted for the cellulose under different reaction time and temperature which the nanocellulose produced was coded as NC with numbering as shown in Table 1.

Table 1. Nanocellulose produced under different acid hydrolysis condition.

Sample code	Reaction time (mins)	Temperature (°C)
NC 1	30	45
NC 2	60	45
NC 3	90	45
NC 4	120	45
NC 5	30	45
NC 6	30	60
NC 7	30	75
NC 8	30	90

2.3 Characterization

Chemical bonding and thermal stability of the nanocellulose samples were characterized using Fourier transform infrared spectrometry and thermogravimetric analysis. The procedure of characterization is presented in the following section.

2.3.1 Fourier transform infrared spectrometry (FTIR)

The freeze-dried samples were ground and blended with potassium bromide (KBr) at sample to KBr ratio of 1:100 (w/w) followed by compressing into thin pellets. FTIR spectra of cellulose and nanocellulose samples were recorded by PerkinElmer Spectrum 100 FTIR spectrometer in range of 4000 –400 cm^{-1} with resolution of 4 cm^{-1} and 20 scans were conducted for each sample.

2.3.2 Thermogravimetric analysis (TGA)

The freeze-dried nanocellulose was was analysed using PerkinElmer Thermogravimetric Analyzer TGA 8000. 5 mg of sample was evaluated under nitrogen atmosphere with a gas flow rate of 20 mL/min, heating temperature range from 30 °C to 500 °C and heating rate of 10 °C/min.

3. Result and discussion

The effect of hydrolysis time on the yield, chemical bonding and thermal stability of the prepared nanocellulose, is discussed in the following section.

3.1 Yield of nanocellulose from chrysanthemum stems

Nanocellulose with different yield was produced after going through different reaction time of acid hydrolysis as shown in table 2. All the yield value of nanocellulose was calculated based on its weight over the weight of pure cellulose in percentage. It is observed that nanocellulose produced under different reaction time with highest yield is NC 1 with 15.4%, followed by NC 2, NC 3 and NC 4 with 13.2%, 11.8% and 11.3% yield, respectively. The yield of the nanocellulose decreased from 15.4% to 11.3% as the reaction time of acid hydrolysis increased from 30 minutes to 90 minutes. These results were attributed to the concentrated acid which further hydrolysed the amorphous cellulosic regions as the time increased and caused the cellulose to hydrolyse into glucose while another possible reason could be the degradation of the crystalline domains [8, 9]. For the nanocellulose produced under different temperature, the yield increased from 15.4% to 17.7% for NC 5 until NC 7 and then decreased to 14.6% in NC 8. The acid hydrolysis process accelerates as the temperature rises and increases the yield. However, further increase in temperature caused decrement in yield as higher temperature caused the cleavage in glycosidic bonds of the cellulose molecules which then decreased the degree of polymerization and released single crystals [10]. In addition, glucose is produced when temperature is too high as cellulose experienced further hydrolysis, resulting in reduced yield.

Table 2. Yield of nanocellulose under different acid hydrolysis reaction conditions.

Sample Code	Yield (%)
NC 1	15.4
NC 2	13.2
NC 3	11.8
NC 4	11.3
NC 5	15.4
NC 6	16.8
NC 7	17.7
NC 8	14.6

3.2 Chemical bonding of the prepared nanocellulose

FTIR analysis was conduceted to investigate the chemical composition and changes in the chemical structure of cellulose and nanocellulose samples produced after acid hydrolysis. Fig. 1 and Fig.2 demonstrates the FTIR spectra of cellulose and nanocellulose produced under different acid hydrolysis reaction time and temperature. A wide absorption band was shown between 3400 and 3200 cm^{-1} in all spectra corresponded to O–H stretching vibration of OH

groups in cellulose molecules and demonstrated the H-bonding interactions in these materials [11]. The peaks around 2900 cm^{-1} was ascribed to the C–H stretching. There was a shoulder shown in the spectra of CL at around 1700 cm^{-1} indicated that the acetyl or uronic ester groups of the hemicelluloses while the shoulder disappeared in spectra of nanocellulose samples as the hemicelluloses were removed [12, 14]. Besides, the peaks at around 1610 cm^{-1} were ascribed to the O–H stretching vibration of absorbed water [11, 14]. Peaks at approximately 1450 and 900 cm^{-1} could be seen in the spectra of all samples were attributed to the bending of the $-CH_2$ groups and C–O–C stretching vibrations of the characteristic β (1→4)-glycosidic linkages respectively [11, 13]. The peaks at around 1070 cm^{-1} in all of spectra demonstrated the occurenece of C–O–C pyranose ring skeletal vibration. Similar result for FTIR was reported in other sources [6, 11, 13]. Based on the spectra of nanocellulose samples, there is no much change in the chemical structure of the samples as all the function groups were presented in the similar region which implied that the chemical group of the samples were stable. However, it could be observed that there were some smaller bands that appeared at region after 900 cm^{-1} in some of the spectra was due to the noise or residues from previous samples, or contaminants such as impurities in KBr.

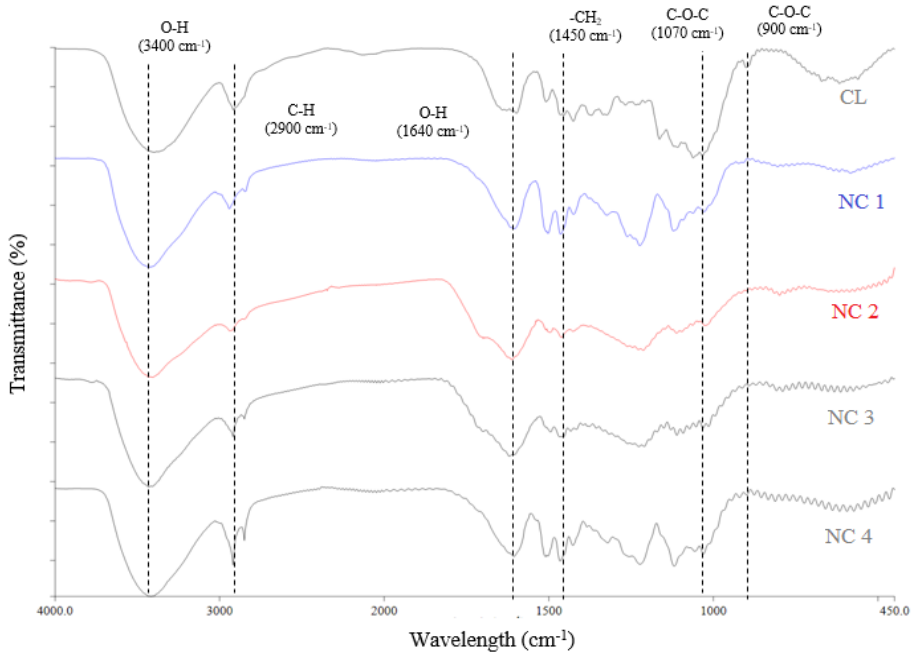


Fig. 1. FTIR spectra of cellulose and nanocellulose samples produced under different reaction time.

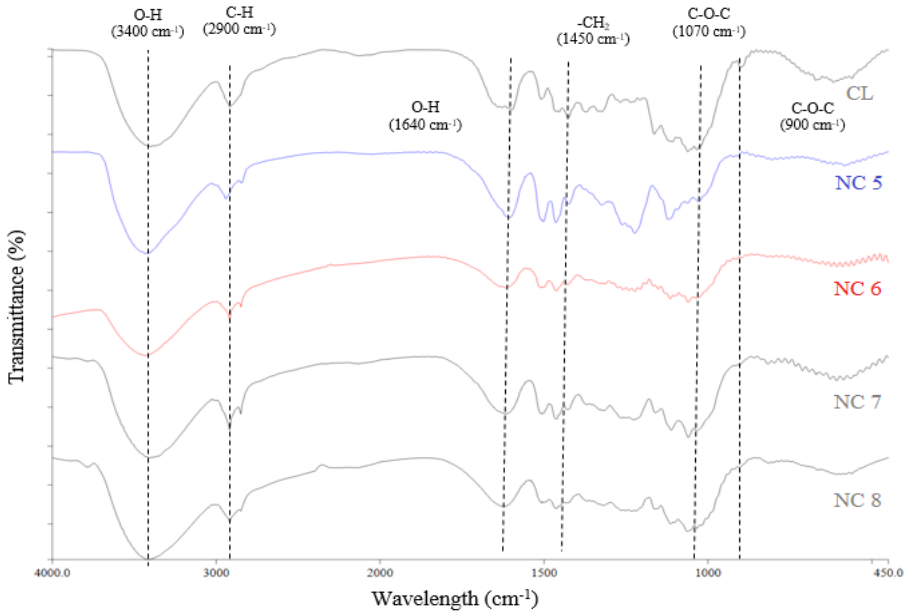


Fig. 2. FTIR spectra of cellulose and nanocellulose samples produced under different temperature.

3.3 Thermogravimetric analysis (TGA)

TGA was conducted to investigate the thermal stabilities of nanocellulose for evaluating its potential usage in applications that can withstand high temperature. The thermogravimetric (TG) and derivative thermogravimetric (DTG) curves of nanocellulose samples produced under different acid hydrolysis condition were demonstrated in Fig. 3, Fig. 4, Fig. 5 and Fig. 6, respectively. The thermal degradation onset temperature and maximum thermal degradation temperature of nanocellulose samples were recorded in Table 3. A small percentage of weight loss which is around 13% was found before 100 °C as shown in TG curves is due to the evaporation of moisture from the nanocellulose. The weight loss was also verified with the endothermic peak in the DTG curves before 100 °C. The onset temperature of NC 1, NC 2, NC 3 and NC 4 is 307 °C, 313 °C, 329 °C and 258 °C while the maximum degradation temperature is 381 °C, 392 °C, 423 °C and 291 °C respectively. The onset temperature and maximum degradation temperature of the nanocellulose increased as the acid hydrolysis reaction time increased from 30 minutes to 90 minutes but decreased from 90 minutes to 120 minutes. This is because that the formation of sulfate groups was promoted by increased acid hydrolysis time which caused dehydration reaction, resulting in decline of thermal stability. These findings were consistent with prior reports on nanocellulose from other sources [8, 15]. In addition, decrease in the thermal stability of nanocellulose may be attributed to the increased amount of short cellulose chains, which was caused by increased acid hydrolysis time that produced nanocellulose with high specific surface area and free end chains while the decomposition of these end chains began at lower temperature [8]. In addition, the DTG curves showed the nanocellulose samples with char residues yield of 39.3%, 49.3%, 56.7% and 37.36% at 500 °C. It was found that the char residues increased with reaction time of acid hydrolysis as well. This

was because of the increment of sulphated groups which acted as flame retardants when hydrolysis time increased [8]. For nanocellulose produced under different acid hydrolysis temperature, it could be observed that the onset temperature and maximum degradation temperature decreased as the acid hydrolysis temperature increased from 45 °C to 90 °C. Nanocellulose with greater thermal stability could be ascribed to the elimination of amorphous regions of cellulose and residual lignin as well as its higher crystallinity index [6]. The crystalline region was damaged by the concentrated acid during the acid hydrolysis as the temperature increased and thus caused lower thermal stability. However, it could be seen that there were some fluctuations in the DTG curves in Fig. 6, which were attributed to the disturbances during analysis such as noise and vibration. Among all the nanocellulose samples, NC 3 exhibited the best thermal stability with the highest onset temperature and maximum degradation temperature.

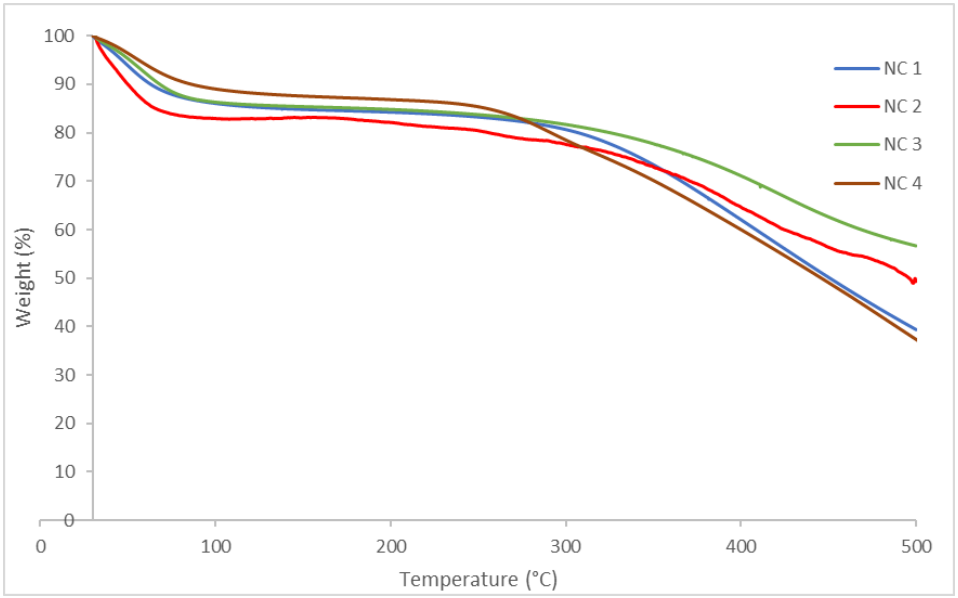


Fig. 3. TG curves of nanocellulose samples produced under different reaction time.

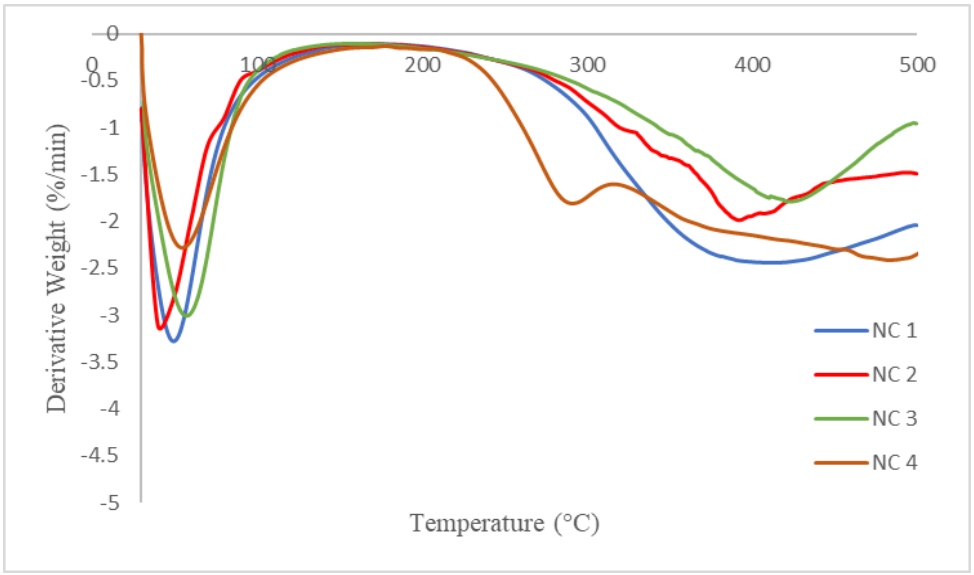


Fig. 4. DTG curves of nanocellulose samples produced under different reaction time

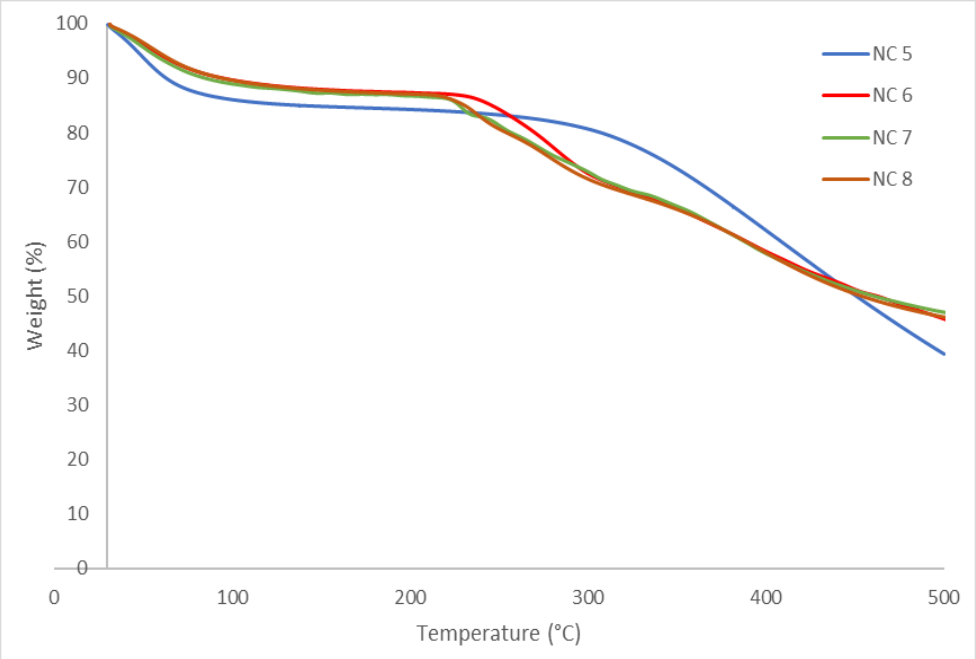


Fig. 5. TG curves of nanocellulose samples produced under different temperature.

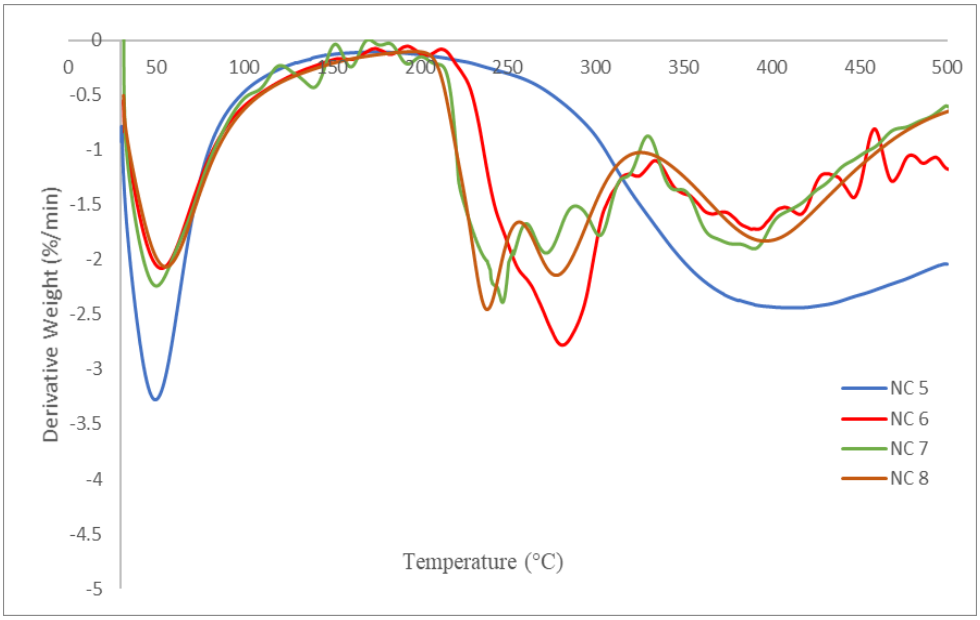


Fig. 6. DTG curves of nanocellulose samples produced under different temperature.

Table 3. Onset temperature and maximum thermal degradation temperature of nanocellulose samples.

Sample code	Onset temperature (°C)	Maximum degradation temperature (°C)
NC 1	307	381
NC 2	313	392
NC 3	329	423
NC 4	258	291
NC 5	307	381
NC 6	245	283
NC 7	225	247
NC 8	223	241

4. Conclusion

The production and characterization of nanocellulose from chrysanthemum stems had been demonstrated using sulfuric acid hydrolysis. Nanocellulose (NC 7) produced from acid hydrolysis (75 °C, 30 mins) has the highest yield of 17.7% while the nanocellulose (NC 3) produced from acid hydrolysis (45 °C, 90 mins) has the highest thermal stability with onset temperature and maximum degradation temperature up to 329 °C and 423 °C, respectively. Thus, the optimum conditions of acid hydrolysis used for producing nanocellulose from chrysanthemum stem is 64 wt% H_2SO_4, 90 minutes and 45 °C in this research. The study shows that chrysanthemum stem is a promising agricultural waste for the production of nanocellulose and highly potential to be used as a reinforcing filler for nanocomposites.

Acknowledgement

The author would like to acknowledge the School of Engineering and School of Bioscience at Taylor's University for the analyses as well as offering the equipment and laboratories for researching the project.

References

[1] A. H.P.S, C. Saurabh, A. A.S., M. Nurul Fazita, M. Syakir, Y. Davoudpour, M. Rafatullah, C. Abdullah, M. M. Haafiz and R. Dungani, "A review on chitosan-cellulose blends and nanocellulose reinforced chitosan biocomposites: Properties and their applications", *Carbohydrate Polymers*, vol. 150, pp. 216-226, 2016.

[2] N. Lin and A. Dufresne, "Nanocellulose in biomedicine: Current status and future prospect", *European Polymer Journal*, vol. 59, pp. 302-325, 2014.

[3] M. Islam, M. Alam, A. Patrucco, A. Montarsolo and M. Zoccola, "Preparation of Nanocellulose: A Review", *AATCC Journal of Research*, vol. 1, no. 5, pp.17-23, 2014.

[4] J. Rusmirović, J. Ivanović, V. Pavlović, V. Rakić, M. Rančić, V. Djokić and A. Marinković, "Novel modified nanocellulose applicable as reinforcement in high-performance nanocomposites", *Carbohydrate Polymers*, vol. 164, pp. 64-74, 2017.

[5] D. Milanez, R. Amaral, L. Faria and J. Gregolin, "Assessing nanocellulose developments using science and technology indicators", *Materials Research*, vol. 16, no. 3, pp. 635-641, 2013.

[6] F. Jiang and Y. Hsieh, "Cellulose nanocrystal isolation from tomato peels and assembled nanofibers", *Carbohydrate Polymers*, vol. 122, pp. 60-68, 2015.

[7] C. Liu, B. Li, H. Du, D. Lv, Y. Zhang, G. Yu, X. Mu and H. Peng, "Properties of nanocellulose isolated from corncob residue using sulfuric acid, formic acid, oxidative and mechanical methods", *Carbohydrate Polymers*, vol. 151, pp. 716-724, 2016.

[8] H. Kargarzadeh, I. Ahmad, I. Abdullah, A. Dufresne, S. Zainudin and R. Sheltami, "Effects of hydrolysis conditions on the morphology, crystallinity, and thermal stability of cellulose nanocrystals extracted from kenaf bast fibers", *Cellulose*, vol. 19, no. 3, pp. 855-866, 2012.

[9] M. Martínez-Sanz, A. Lopez-Rubio and J. Lagaron, "Optimization of the nanofabrication by acid hydrolysis of bacterial cellulose nanowhiskers", *Carbohydrate Polymers*, vol. 85, no. 1, pp. 228-236, 2011.

[10] B. Hong, F. Chen, and G. Xue, "Preparation and Characterization of Cellulose Nanocrystals from Bamboo Pulp", *Cellulose Chemistry and Technology*, vol. 50, no. 2, pp. 225-23, 2016.

[11] P. Nascimento, R. Marim, G. Carvalho and S. Mali, "Nanocellulose Produced from Rice Hulls and its Effect on the Properties of Biodegradable Starch Films", *Material Research*, vol. 19, no.1, 2016.

[12] N. Johar, I. Ahmad and A. Dufresne, "Extraction, preparation and characterization of cellulose fibres and nanocrystals from rice husk", *Industrial Crops and Products*, vol. 37, no. 1, pp. 93-99, 2012.

[13] W. Chen, Q. Li, Y. Wang, X. Yi, J. Zeng, H. Yu, Y. Liu and J. Li, "Comparative Study of Aerogels Obtained from Differently Prepared Nanocellulose Fibers", *ChemSusChem*, vol. 7, no. 1, pp. 154-161, 2014.

[14] B. Li, H. Mou, Y. Li and Y. Ni. (2013). Synthesis and Thermal Decomposition Behavior of B. Li, H. Mou, Y. Li and Y. Ni, "Synthesis and Thermal Decomposition Behavior of Zircoaluminate Coupling Agents", *Industrial & Engineering Chemistry Research*, vol. 52, no. 34, pp. 11980-11987, 2013.

[15] Y. Chen, C. Liu, P. Chang, X. Cao and D. Anderson, "Bionanocomposites based on pea starch and cellulose nanowhiskers hydrolyzed from pea hull fiber: Effect of hydrolysis time", *Carbohydrate Polymers*, vol. 76, no. 4, pp. 607-615, 2009.

Numerical Analysis on Suspended Load at Taylor's University

Benny Foo Qing Hui[1,8,] *Chou Pui May*[2]

[1,2] School of Engineering, Taylor's University, Malaysia

Abstract. The project was about a high beam light acted as a risk suspended load which at times can lead to serious injury or death. The objectives of the present study were to determine whether the nine types of suspended loads at Taylor's University are safe and will not to fall down. Durability of the suspended loads was determined using ANSYS simulation. For theoretical knowledge part, structural optimization was included with sizing, shape and topology optimizations. A theoretical analysis on the factor of safety was performed. The best results of each suspended load had been chosen and discussed in detailed. Factor of safety for each suspended load was obtained in order to verify whether the suspended load is safe to be used. Comparison between theoretical and experimental factor of safeties had been obtained. For factor of safety, all the experimental readings were higher than theoretical readings which mean the suspended loads were all considered as safe in static condition.

Keywords: Suspended load; Structural analysis; Factor of safety

[8] Corresponding author: bennyqinghui.foo@sd.taylors.edu.my

1. Introduction

1.1 Theoretical background

Taylor's University Lakeside Campus has 45 years of history in education and still undergoes its continued commitment to self-development. There are some issues about the quality and durability of suspended loads built at Taylor's University. There is a total of nine suspended loads to be analysed in the present study.

To consider a suspended load acts as an assembly of structural elements for undergoing a specific load or load combination, the effectiveness of the suspended load aims at creating in a way that the sustainable load can be worked with the best performance based on certain criteria. Static structural analysis regulates displacements, deformations, stresses, strains, forces and other effects in the components or structures, which are caused by loads without any damping or inertia significances. Assumptions are commonly made by steady loading and various response conditions according to the load or structure's response varying slowly with respect to time. In the present study, static structural analysis of all the suspended loads was performed using ANSYS Workbench software. Normally the type of loading applied in the static structural analysis includes the external applied forces that have gained mechanical energy. During the process of optimization, some of the items or part of the components are expected to be maximized or minimized. Some of the items or part components could be considered both as advantageous objective. The structural optimization challenges were commonly formulated by choosing one of the part components as objectives function and some others had picked as constrains. The objective function for each suspended load analysis was the maximization and minimization as the goal, such as deformation and stress [1].

1.2 Suspended Load

For allowable stress design, safety of a structure is achieved by specifying a safety factor against the uncertainties based on arbitrary experience and judgment like 1/3 decrease of allowable stresses. The probabilistic codes for limit state design take into proper account of the uncertainties of variables like material and load in shape of load and resistance factors. Structural design is based on load and resistance variables which are random in nature. In working stress design, resistance is divided by a factor of safety based on experience [2]. Bilal reports that uncertainty using deterministic factors of safety could lead to inconsistent reliability producing conservative design. Uncertainties in capacity or member strength occur due to variability in material strength or geometric inconsistencies [3]. This is due to the limitation of engineering theories to predict the component and system response and capacity. Factors of safety are used for these uncertainties and they provide the increased safety margins against future structural damage, deterioration or an addition of scope of work due to future expansion of project [4].

Component fails when it is not capable to resist the loads and the failure occurs due to yielding, deflection or buckling. In case of joints, the failure modes may be compression, tension, in-plane bending or out-plane bending. The characteristics of structural design are also dependent on load uncertainties which are more specifically related to environmental loads. The safety factors play a major role for avoiding failure. Environmental load factors are proposed after determining characteristic values of the random variables. Jacket platforms are designed as per component and joint based design codes and the end product is structural system [5]. Modelling uncertainties are introduced by all the physical models used to predict the load and structural response effects [6]. Characteristic resistance should have low probability of being exceeded at any specified design life of Jacket. It is defined as that value below which not more than 5% of the test results of large number of test would fall [7]. Characteristic strength should be equal to guaranteed yield strength but shall not exceed 0.8 times the guaranteed tensile strength or minimum of upper yield strength [8].

1.3 ANSYS Workbench Static Structural Analysis

ANSYS Workbench is powerful platform software that is the backbone for an integrated, comprehensive simulation system. This chapter describes how to operate ANSYS Workbench to carry out structural or stress analyses of a fundamental type of component parts for demonstrating elementary use of the software [9].

Overview of ANSYS structure had commonly guided with steps by steps of various vital stages in the analysis. The analysis begins with launching the programme (naming the project, saving it in an appropriate directory, using various menus available and exiting the programme), pre-processing stage (construction of the model, selection of material, element type, meshing), the solution stage (setting up boundary conditions, applying loads, and running the solution), and finally the post-processing stage (the general postprocessor, displaying results, error estimation) [10].

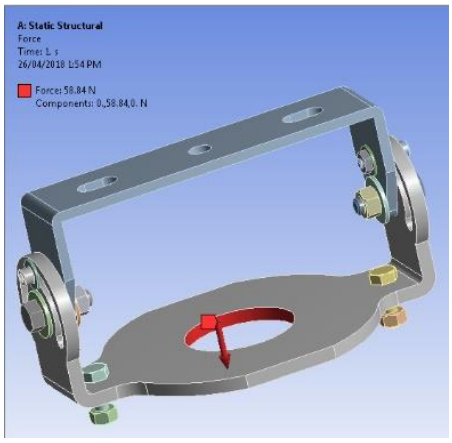


Fig. 7. Topology optimization of a high beam light.

1.2 Factor of safety analysis

Every object has a stress limit depending on the material and other criteria used which is presented as ultimate strengths or material yield strength. If there is an external loading acting against an object, there will be a stress occurred and it might be failed when the stress is too high. Stress in a body will be the function of load applied and cross-section, whereas strength is a property of the body material from manufacturing process. A graph of material stress-strain curve had been shown by extracting the deformation data and plotting in the function of loading data, as figure below13

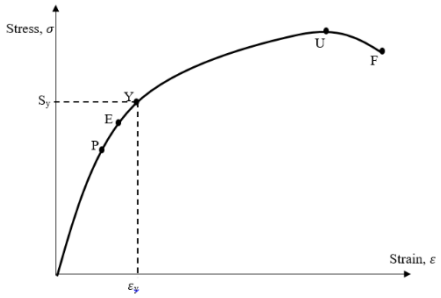


Fig. 8. Stress-Strain curve.

where P is proportional limit, defined by Hooke's law

E is elastic limit, letting material to behave elastically

Y is yield point, corresponding yield strength of the material

U is maximum stress, corresponding ultimate tensile strength

F is fracture point, representing point the failure

Normally points E and Y could be coincided together depending the materials used, such as ferrous material like iron. The yield point is generally obtained by an offset method, which considered to be an intersection of the offset line, acting parallel to the linear portion of the Stress-Strain curve at particular axial strain and the plastic portion of the curve [11]. As the ratio of maximum allowable stress to equivalent (Von-Mises) stress, the factor of safety must be at least 1 in order to consider as acceptable design. If the factor of safety is less than 1, means there is permanent deformation occurred on the design. For instance, a steel had an ultimate strength of 300 MPa, any stresses (tension or compression) above the ultimate strength limit could lead to failure in a form of permanent deformation. If the object is not supposed to be designed to deform permanently undergoing yield, the maximum allowable stress will be 300 MPa. In static structural analysis, equivalent (Von-Mises) stress results provides red or blue signs, meaning high or low value of stress in certain areas. Factor of safety shows area of potential yield. The level of tolerable risk is decided by a target on the factor of safety, which considered the probability of the occurrence of design loads as well as the strength of material that can take a risk based on the factor of safety approached [12].

$$Factor\ of\ safety = Strength_{ult} / Stress_{max} = 310MPa/21.55MPa \quad (1)$$

= 14.385 (Extremely safe)

To know whether the material is safe, a design margin over theoretical design capacity can be used to allow for uncertainty in the design process. Factor of safety is recommended by the conditions over which the designer has no control, which is to account for the uncertainties involved in the design process, by defining the ratio between the ultimate tensile strength of material and the maximum tensile stress.

Table 1. Factor of Safety marginal design effect [].

Factor of Safety Margin	**Description**
Less than 1	The material is not viable and will represent likely failure.
1	The material is essential that it is safe for people to use.
1.25 – 1.5	Material properties known in detail. Operating conditions known in detail. Loads and resultant stresses and strains known with high degree of certainty. Material test certificates, proof loading, regular inspection and maintenance. Low weight is important to design.
1.5 - 2	Known materials with certification under reasonably constant environmental conditions, subjected to loads and stresses that can be determined using qualified design procedures. Proof tests, regular inspection and maintenance required.
2 – 2.5	Materials obtained for reputable suppliers to relevant standards operated in normal environments and subjected to loads and stresses that can be determined using checked calculations.

2.5 - 3	For less tried materials or for brittle materials under average conditions of environment, load and stress
3 - 4	For untried materials used under average conditions of environment, load and stress. Should also be used with better-known materials that are to be used in uncertain environments or subject to uncertain stresses.

2. Experimental

2.1 Methodology

An overall research methodology has been arranged into three parts of stages within one year term of period. For Part 1, all the related investigation of project had been conducted including research questions, project objectives, hypothesis and literature review. Decision making had been obtained to know whether all literature reviews were fully supportive with the project-based contents, trimming or deduction had been taken to cut down unnecessary data or collection. For Part 2, field researches had been separated into three division, which were observation, random (question and answer) and survey researches. A secondary case study and life history had been obtained in order to go for more comprehensive and detailed to the point of views, such as reinvestigate cross sectional collection of data for intensive suspended load analysis. For Part 3, several types of technical approvals had been conducted especially ethical issue, legalization from OSHA (Occupational Safety and Health Administration) and conductive issues. Data collection had been constructed and analysed by interpret all findings using quantitative and qualitative data analysis with validation of findings against prior research. Implications of research and identification of putting findings had been utilized into evidence-based practices. After finishing all the experiment, statement of purpose, findings and relevance of research activity, all the details had been fully written and disseminated by distributing copies of dissertation or thesis. A final consultation with supervisor will be revised as pre-presentation preparation in order to have a final process of formal discourse, recommendation and conclusion. If there was none of final testing, re-construction improvement to be modified, the presentation shall be ready to be conducted for conference or seminar.

A summary of experimental methodology had been shown as a flow chart in the thesis. A SolidWorks drawing file had been imputed into ANSYS software (Parasolid, STEP, STL and IGES). After importing material properties into

engineering data, a boundary condition had been specified before selecting the meshing method. Justification for meshing method had been selected, such as Automatic, Tetrahedrons, Hex Dominant, et cetera. Simulation results and discussion had been compared and modification was improved to have detailed discussion about the refinement [14].

In the static structural analysis, considered a set of components including mount, hex nuts, hex bolt which were located on the body as shown in figure.

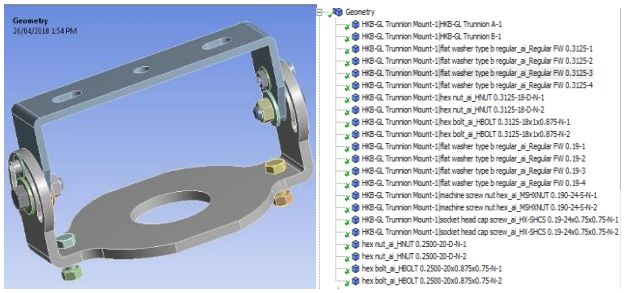


Fig. 9. Geometry of high beam light C1D1-2 - C2D1-2.

2.2 Engineering data

The material of the high beam light was Aluminum 6061-T6. According to Larson Electronics, high beam light C1D1-2 - C2D1-2 had a fixture constructed of extruded corrosion resistant. For the material used, Aluminum 6061-T6 had been selected and putting into the ANSYS content as engineering data. In the engineering data outline, the properties included with density, tensile yield strength, tensile ultimate strength and isotropic elasticity which had consisted of young's modulus, Poisson's ratio, bulk modulus and shear modulus. Considering the scenario of static condition, there is no hardness, fatigue and elongation at break due to the high beam light does not change in shape, size or any impact causes. Therefore, the other mechanical properties were neglected in the engineering data [15].



Fig. 10. Name of material used.

Properties of Outline Row 3: Aluminum 6061-T6

	A	B	C
1	Property	Value	Unit
2	Material Field Variables	Table	
3	Density	2698.8	kg m^-3
4	Isotropic Elasticity		
5	Derive from	Young's Modulus and Poisson...	
6	Young's Modulus	6.89E+10	Pa
7	Poisson's Ratio	0.33	
8	Bulk Modulus	6.7549E+10	Pa
9	Shear Modulus	2.5902E+10	Pa
10	Tensile Yield Strength	2.76E+08	Pa
11	Tensile Ultimate Strength	3.1E+08	Pa

Fig. 11. Properties of Aluminum 6061-T6.

2.3 Boundary condition

2.3.1 Fixed support condition

A fixed support had been made on three inner surfaces of nut and bolt holes which is located on upper shaft as illustrated in Figure in order to imitate the appearance of supporting condition in the exact moment of contact. In the static condition, the fixed support was considered none of rotation occurred by the upper shaft [16].

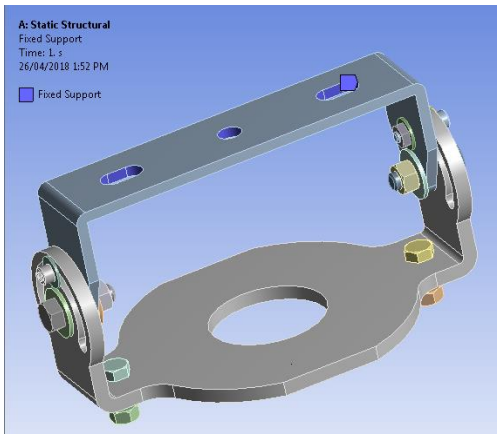


Fig. 12. Fixed support at three inner surfaces of supper shaft.

2.3.2 Loading condition

Considering the topology optimization, a 58.84N of force was acted as center gravitational force on the whole body of high beam light. The center of gravity of the high beam light was pointed at which weight was evenly distributed and all sides were in balance [17].

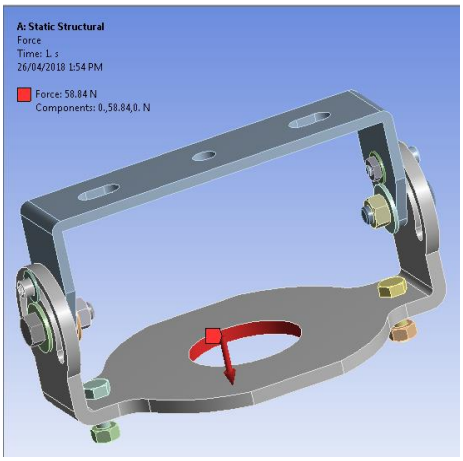
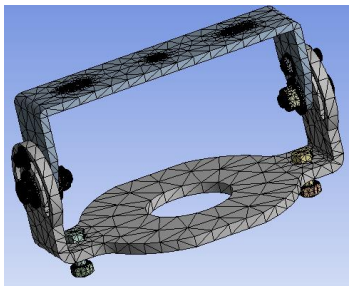
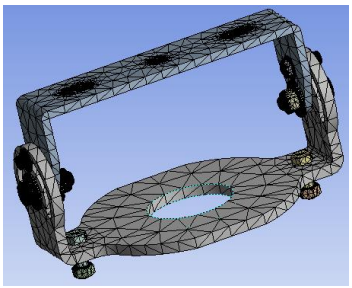
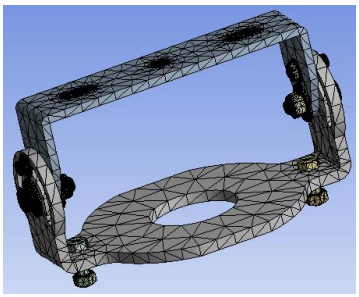
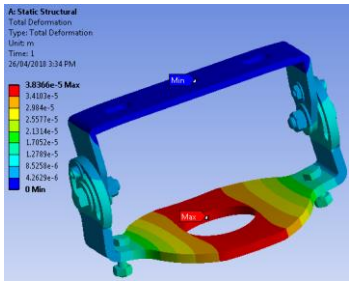
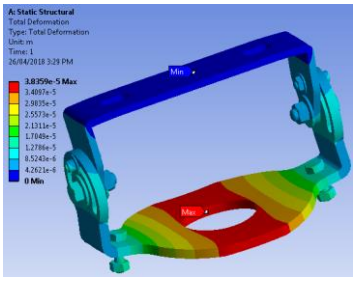
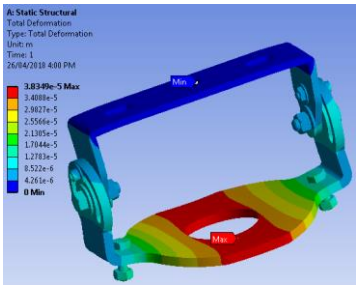


Fig. 13. Center of gravity on the high beam light body.

2.4 Meshing Methods

For the meshing methods, there were two methods had been conducted in the experiments, which were Automatic Meshing Method and Tetrahedrons Meshing Method. Based on the ANSYS software, meshing processes were performed using both methods based on the shape of model, loadings and constrains. The size of elements in minimum size limit section had been manipulated and variably adjusted in order to get the best results. For each meshing method, fixed support and loading conditions had been defined and assumed before meshing process. **Table 2** and **3** had shown a sample of each meshing method which had been demonstrated using size of element concerns. Each meshing method had been operated at least 3 solutions and the best results of the meshing had been chosen. Best results was decided by considering the maximum allowable total deformation, maximum allowable equivalent stress, number of element, number of nodes element quality and skewness [18].

Table 2. Automatic Meshing Method.

Mesh 1	**Mesh 2** **(Best result)**	**Mesh 3**
Sizing = 0.69mm 	Sizing = 0.70mm 	Sizing = 0.71mm 
Max total deformation = 0.038366mm 	Max total deformation = 0.038359mm 	Max total deformation = 0.038349mm 
Max equivalent stress = 20.446Mpa	Max equivalent stress = 21.155Mpa	Max equivalent stress = 18.914Mpa

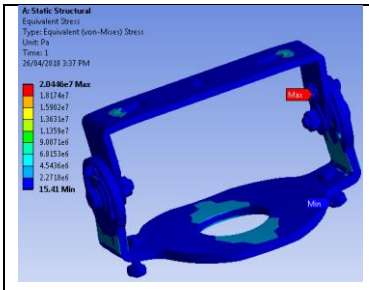
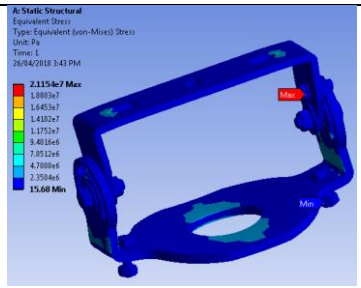
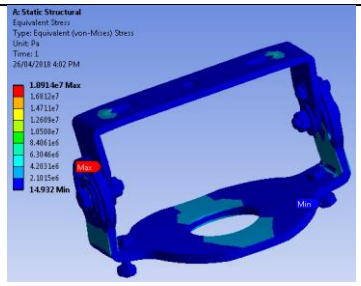
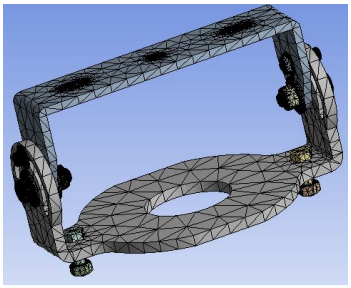
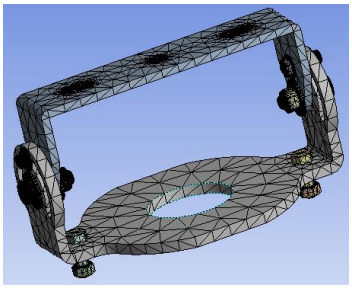
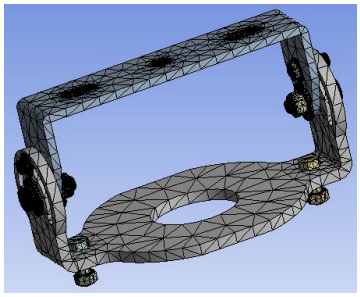
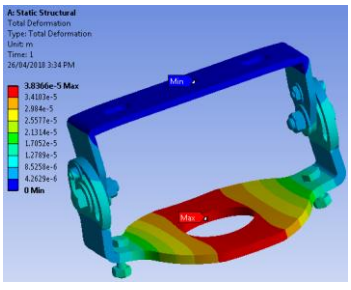
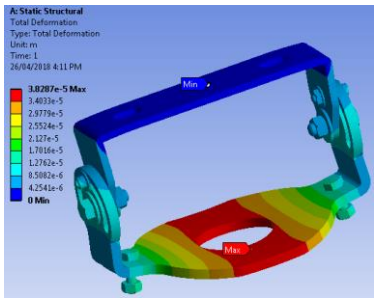
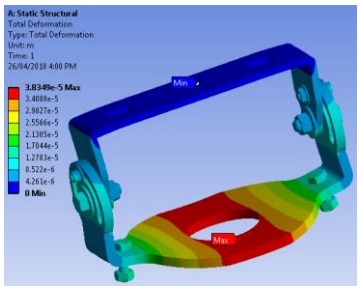
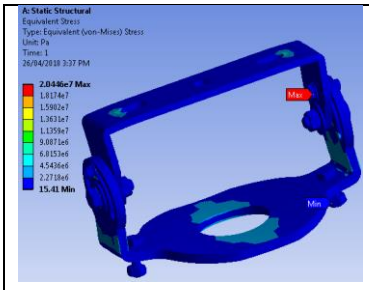
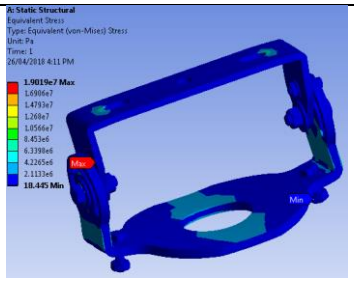
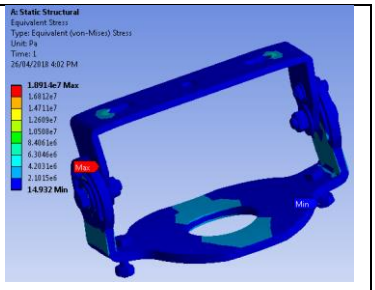
		
No. of elements = 103065 No. of nodes = 224921	No. of elements = 100335 No. of nodes = 319357	No. of elements = 98951 No. of nodes = 216592
Element quality = 0.7255 Skewness = 0.40207	Element quality = 0.72645 Skewness = 0.39853	Element quality = 0.72569 Skewness = 0.39934

Table 3. Tetrahedrons Meshing Method.

Mesh 1	**Mesh 2** **(Best result)**	**Mesh 3**
Sizing = 0.69mm 	Sizing = 0.70mm 	Sizing = 0.71mm 
Max total deformation = 0.038325mm 	Max total deformation = 0.038318mm 	Max total deformation = 0.038287mm 
Max equivalent stress = 20.608Mpa	Max equivalent stress = 21.302Mpa	Max equivalent stress = 19.019Mpa

		
No. of elements = 105772 No. of nodes = 190595	No. of elements = 101723 No. of nodes = 180341	No. of elements = 99896 No. of nodes = 180344
Element quality = 0.67561 Skewness = 0.47707	Element quality = 0.67371 Skewness = 0.47756	Element quality = 0.67255 Skewness = 0.47872

3. Result and discussion

3.1 Total Deformation

As observed in **Fig. 14**, the maximum deformation of the high beam light can afford the center of gravity is 0.038359mm using 0.70mm of element sizing. The reading is considered as successful since the body of high beam light only deformed such a small distorting process. The total deformation has been considered as the vector sum of all directional displacements of the systems that had evaluated. The fixed support had successfully prevented the deformation becoming larger [19].

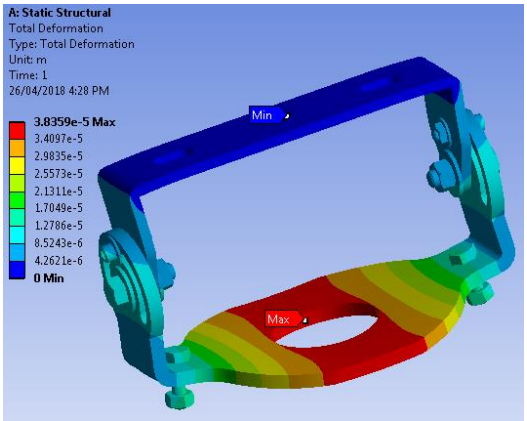


Fig. 14. Total deformation of high beam light in final analysis (Best result).

3.2 Equivalent (Von-Mises) Stress

Fig. 15 shows the maximum allowable stress of the high beam light can afford is 21.15MPa. The areas of stress region were mostly on the surface of fixed support, upper and side surfaces on trunnion body part. Both sides of nut and bolt holes have the high possibility to get maximum stress at the point of view. Based on first

principal theory, the value of stress that is normal to the plane in which shear stress is considered as zero, therefore the reading is reflected the plasticity theory which applies the best to ductile material, such as Aluminum. When Aluminum 6061-T6 was under tension, the gravitational force acted on the whole body to stretch the material which had occurred 21.55MPa of maximum allowable stress [20].

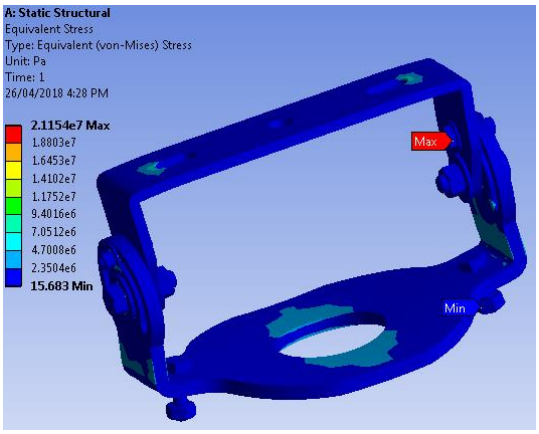


Fig. 15. Equivalent (Von-Mises) stress in final analysis (Best result).

3.3 Number of Elements, Number of Nodes, Element Quality and Skewness

According to **Table 4**, the number of elements and nodes are 100335 and 319357. Considering the element quality and skewness of meshing results, the responding values are positive which are 0.72645 and 0.39853. The element quality provides theoretically with a composite quality metric that ranges between 0 and 1, therefore 0.72645 of experimental element quality had proven as a good meshing result. According to the definition of skewness, a value of 0 represents an equilateral cell (best) and a value of 1 represents a degenerate cell (worst), therefore 0.39853 of experimental skewness reading is good and acceptable, compared with Table 3.

Table 4. Theoretical skewness value and cell quality [21].

Value of Skewness	Cell Quality
1	Degenerate
0.9 — <1	Bad (silver)
0.75 — 0.9	Poor
0.5 — 0.75	Fair
0.25 — 0.5	good

>0 — 0.25	Excellent
0	Equilateral

3.4 Safety Factor

Most of the industries have different codes of practices for factor of safety or margins of safety according to a design employment. The level of risk toleration is a target deciding on the factor of safety. Therefore, the probability of the appearance of design loads as well as the strength of material could take a risk based approach to calculate the factor of safety. To account for imperfections in Aluminium 6061-T6, a factor of safety, also known as safety factor had been obtained into calculation in order to ensure the high beam light is safe. Referring to ultimate tensile strength of Aluminium 6061-T6 from figure, the strength had been divided with the maximum allowable stress in order to find the factor of safety.

$$Factor\ of\ safety = Strength_{ult} / Stress_{max} = 310\text{MPa}/21.55\text{MPa} \quad (1)$$

$$= 14.385 \text{ (Extremely safe)}$$

To evaluate the experimental factor of safety, a theoretical table had been shown as below, regarding the ideal margin of safety factor which are commonly published in technical standards [8]. According theoretical factor of safety for bolts The Engineering Toolbox, the theoretical reading is 8.5. The experimental factor of safety, 14.385 is almost double as much as the theoretical reading. The experimental results had shown that the high beam light is considered extremely safe to be hanged on the ceiling at the grand hall and corridor.

Table 5. Typical overall factor of safety [22].

Equipment	**Factor of Safety**
Aircraft compounds	1.5 – 2.5
Boilers	3.5 – 6
Bolts	8.5
Cast-iron wheels	20
Engine components	6 – 8
Heavy duty shafting	10 – 12

Lifting equipment	8 – 9
Pressure vessels	3.5 - 6
Turbine components (static)	6 – 8
Turbine components (rotating)	2 – 3
Spring, large heavy-duty	4.5
Structural steel work (buildings)	4 – 6
Structural steel work (bridges)	5 – 7
Wire ropes	8 - 9

4. Conclusion

The analyses were performed successfully. In this report, some of the findings that have been drawn through extensive process of research, were expressed with general ideas. Most of the general statements, thoughts and theories from literature review, journals and other book sources were referred and moved forward more focused and complex ideas. All the suspended loads were successfully analysed and the factor of safety for each suspended load was calculated. The comparison between theoretical and experimental factor of safety was obtained. All the experimental readings for factor of safety are higher than theoretical readings, which indicates that the suspended loads were all considered as safe in static condition.

To elaborate the details of findings and expected outcomes, analyses were well framed to be revealed from the researches. Expected outcomes were indicated and happened. Student has gained the experience in structural analysis using ANSYS software. Using the software, most of the complex structural engineering challenges could be solved with better, faster design decisions by optimizing all the suspended loads.

Acknowledgement

The author appreciates the assistances from School of Engineering, Facilities Operation & Engineering and Facilities EHS (Sustainability, Events & Building Services) at Taylor's University for the experiment analyses as well as providing data collection and laboratories for project researches purposes.

References

[1] M. Rezazadeh and R. Delavar, "*Production cost reduction through optimization of machine component*," Diva-Portal. [Online]. Available: https://www.diva-portal.org/smash/get/diva2:750029/FULLTEXT01.pdf. [Accessed: 01-May-2018].

[2] M.C. Ferguson, "A comparative study using API RP2A-LRFD", *Proceedings of the Offshore Technology Conference*, OTC 6308, 1990

[3] M.A. Bilal, "Development of Reliability-based load and resistance factor design (LRFD) methods for piping", *ASME*, 2007.

[4] F. Moses, "Reliability based design of offshore structures", *American Petroleum Institute*, 1981.

[5] D.J. Wisch, "Fixed Steel Standard: IS0 & API Developments", IS0 TC 671SC 7NVG 3, presented at the Offshore Technology Conference OTC 8423, Houston, 1997.

[6] Y. Guenard, J. Goyet, J. Labeyrie, "Structural safety evaluation of steel jacket platforms", *Proceedings of the Marine Structural Reliabilty Symposium*, Virginia, pp. 169–183, 1987.

[7] C.J. Billington, I.F. Tebbett, "The basis for new design formula of grouted Jacket to pile connections", *Proceedings of the Offshore Technology Conference*, OTC3788, Houston, 1980.

[8] I. Holland, "Norwegian Regulations for Design of Offshore Structures", *Offshore Technology Conference*, 2-5 May, Houston, OTC 2863, pp. 449–453, 1977.

[9] Engineeringtoolbox.com. (2018). *Factors of Safety*. [online] Available at: https://www.engineeringtoolbox.com/factors-safety-fos-d_1624.html [Accessed 8 May 2018].

[10] Mohamad, M., Rahman, M., Khan, S., Basha, M., Adom, A. and Hashim, M. (2017). Design and static structural analysis of a race car chassis for Formula Society of Automotive Engineers (FSAE) event. *Journal of Physics: Conference Series*, 908, p.012042.

[11] Taranath, B. (2011). *Structural Analysis and Design of Tall Buildings*. 1st ed. Boca Raton.

[12] Choi, H., Kim, J. and Pak, D. (2014). Comparison of pretreatment of fallen leaves for application evaluation by Bio-ethanol raw material. *Journal of Energy Engineering*, 23(3), pp.241-246.

[13] T. Stolarski, Y. Nakasone and S. Yoshimoto, "Using ANSYS workbench for structural analysis", *Engineering Analysis with ANSYS Software*, pp. 37-39, 2018.

[14] P. Christensen and A. Klarbring, *An introduction to structural optimization*. [Dordrecht]: Springer, 2009.

[15] "Meshing Methods (ANSYS Meshing)", Everyone is Number One, 2018. [Online]. Available: https://deust.wordpress.com/2013/04/23/meshing-methods-ansys-meshing/. [Accessed: 05- May- 2018].

[16] N. Pereira and X. Romão, "Material strength safety factors for the seismic safety assessment of existing RC buildings", *Construction and Building Materials*, vol. 119, pp. 319-328, 2016.

[17] A. Bavafa, A. Mahdiyar and A. Marsono, "Identifying and assessing the critical factors for effective implementation of safety programs in construction projects", *Safety Science*, vol. 106, pp. 47-56, 2018.

[18] P. Shenoy, *Dynamic load analysis and optimization of connecting rod*. AISI, university of Toledo, May 2004, ppi-393.

[19] A. Fatemi, J. Williams and F. Montazersadgh, "Fatigue Performance Evaluation of Forged Steel versus Ductile Cast Iron Crankshaft", *A Comparative Study*, university of Toledo, August 2007.

[20] P. Thejasree, G. Dileep Kumar and S. Leela Prasanna Lakshmi, "Modelling and Analysis of Crankshaft for passenger car using ANSYS", *Materials Today: Proceedings*, vol. 4, no. 10, pp. 11292-11299, 2017.

[21] O. Singh, Vikas and S. Sharma, "Analysis and Comparison of Total Deformation of Welded Plates in Tensile and Fatigue Tests using ANSYS", *Materials Today: Proceedings*, vol. 4, no. 8, pp. 8409-8417, 2017.

[22] A. Eswara Kumar, R. Krishna Santosh, S. Ravi Teja and E. Abishek, "Static and Dynamic Analysis of Pressure Vessels With Various Stiffeners", *Materials Today: Proceedings*, vol. 5, no. 2, pp. 5039-5048, 2018.

EURECA 2018 – Conference Paper
Paper number 2ME03

Compact Fast and Simple Tire Lifting Device

Kwan Meng Chan[*]*, Mohammad Hosseini Fouladi, Satesh Narayana Namasivayam*

School of Engineering, Taylor's University, No. 1 Jalan Taylor's,
47500 Subang Jaya, Selangor DE, Malaysia

Abstract. Tire lifting device is an equipment that used for lifting and transporting tire from a place to another place. However, the current design of the device has some limitations, for instances, the portability is low due to the wire or horse length which are referring the pneumatic or electrical design. Furthermore, the design with battery powered has limitation of operational sustainability because of limited battery life. Apart from that, the current design is unable to rotate tire in different orientations for tire replacement purpose. Therefore, this project aims to innovate a design with compact, portable and non-electrical operated to lift and place tire in different orientations. Besides, the purpose of the research is to study various mechanisms and comparing each of them. The design can be distributed as three types of mechanism which are lifting mechanism, base structure and clamping mechanism. As a result, the hydraulic cylinder was chosen as lifting mechanism Once the design is selected, 3D modelling will be designed and analysed by using ANSYS software. In conclusion, a human powered mechanism for lifting and placing tire in different orientations will be designed and verified by using ANSYS software in terms of feasibility, reliability, robustness and portability.

Keywords: Tire lifting device, Human powered mechanism, Tire mounting

1. Introduction

Tire lifting device is an equipment that used for lifting tire from ground and installing it onto the car during replacement of old tire. The designs of tire lifting device in current existing market that are compact and portable device such as pneumatic, electrical and battery powered. However, there are some limitations of current design of tire lifting device. The portability is considered as low due to the hose or wire length. Besides that, the operational sustainability is limited as well by the limited battery life or fix carriage design. Apart from that, the fix carriage is not able to service the process which requires the tire to be in different orientations for instances as do balancing and installation with one device and improve ergonomic and safety at work as well. Therefore, an innovative design of tire lifting device must be invented to reduce the work load from human.

The objective of this project is to design an innovative human-powered single carriage mechanism for lifting and placing tire in different orientation. Besides, the feasibility and reliability of the design as well as robustness and portability are required to evaluate. Some hypothesis of the project are made as well based on the literature review. First of all, the flexible link was assumed as straight before it deformed during analyzing the multi-link. Furthermore, the thermal expansion of holes for the bolts and screws can be neglected in simulation as the product will be used in ambient temperature mostly. Hence, the design shall include the below considerations:

1) Considerations in the aspect of suitability and economics must be taken into account during the preliminary design stage.

2) Conduct mechanism feasibility and reliability check, with support of computer simulation.

3) Prepare complete set of part and assembly drawings.

Throughout this project, the numerical analysis of the design of tire lifting device will be conducted and done by using ANSYS software. The research of this project is limited to the design of the tire lifting device with only powered by human. Other types of external power source such as pneumatic, battery or electrical powered are excluded in the design of the product. Besides that, clamping mechanism should be able to carry different size of tire and place the tire in different orientation. Since there are too many types of tire in market, we are only focus the sizes of passenger tire where it is between 14” and 18”. Apart from that, the structural analysis of the design is required to be done for safety purpose and to prove the feasibility of the design from the simulation results.

2 Literature review

The dynamics properties for multi-link spatial flexible manipulator arm was determined such as the bending, torsional and shear effect on the links [1]. Each flexible join was treated as a linearly elastic torsional spring and their mass were taken in account in calculations. Hence, the dynamic stiffening effect are considered in the dynamic modelling. During the analysis of the multi links, the flexible joint can be simplified as an Euler-Bernoulli beam in order to ignore the shear deformation. Then the flexible link is also assumed as straight before it deformed.

Rashid *et al.* [2] had validated the Scissors lift structure which manufactured by AEREX, UMW. The scissors lift structure is used to hoist the catering hi-lift for aircraft servicing. Deflection is always happened on the scissor lift while heavy load applied on it. Some manufacturers found out the maximum deflection exceeds the allowable range and the structure didn’t meet the safety requirement. Therefore, the structure was analyzed by using computer simulation to prove that it is safe to use by the author

An optimized hydraulic scissor lift was designed and analyzed by Manaharrao [3]. If the action of loading and unloading is repeated frequently, the chances of getting fatigue failure increases. Moreover, the cases of deformation in hydraulic scissor lift is increased when the lifting mechanism is used to lift heavier object. Therefore, the mechanism was converted to 3D model in computer in order to analyse the mechanism by using ANSYS software. From the result, the hydraulic scissor lift was optimized by reducing the thickness of ribs as well as plate and increasing proper channels on the support. The cycle of life of the mechanism was also determined to prevent the fatigue failure happen.

Sainath *et al*. [4] had designed a mechanical hydraulic jack for lifting purpose. There are two types of jacks which can be distinguished in term of operation: mechanical and hydraulic. For instances, mechanical jacks are used to lift heavy loads by employing screw thread to lift heavy load such as car jack and house jack. As for hydraulic jack, it tends to be stronger and able to lift heavier loads which includes floor jack and bottle jack. If a force is applied on a cylinder, equal pressure is produced in both cylinders (a large and a small one where they are connected). This mechanism is applying the principle of "Pascal's law". As the larger the area of cylinder, the greater force is generated. Besides that, there is a plunger connected to the small cylinder. The plunger is used to control the position of valve which draws the oil into cylinder chamber from external discharge check valve. When the plunger is pushed down, the oil moves to the cylinder chamber to produce external pressure so that the platform of large cylinder will be lifted.

Compbell [5] had design a tire lifting and mounting tool. The device can transport the tire and mount the tire on vehicle during installation. It has the ability of mounting the tire on the spot without lifting the entire vehicle. Apart from that, tire can be transported easily due to the two small wheels. The tire is lifted when push the handle downward and then transports tire to the destination point. This method is like the lever mechanism and the wheels indicates the pivot points where are located at the center position. Nonetheless, these two wheels structure might not suitable for our tire lifting device because the lifting mechanism and clamping mechanism are heavy. So that humans needs to exert more forces to overcome the weight of those mechanism.

Naeem [6] had innovated a new design of worm pair self-locking system. The efficiency of the novel design is around 90% whereas the conventional worm pair system is only about 40%. It stated that the efficiency is affected by two factors which are the lead angle and coefficient of friction. He found out that high percentage of efficiency can be achieved when the lead angle is designed in the range between 15° and 30°. Therefore, the recommended lead angle will be applied in the analysis of worm gear jack.

Aleksandar *et al*. [7] had studied about the power losses of worm gear pairs. There are the losses that exist in the worm gear box such as bearing losses, sealing losses, gearing losses and oil churning power losses in the transmission. The worm and worm gear coupling have the highest power losses compared to other losses in gearing. Therefore, the efficiency of worm gear pairs is lower than other types of gear. Nevertheless, its efficiency can be improved by using appropriate combination of materials and gear ratio. According to their results, the lead angle between 10° and 20° with coefficient of factor between 0.02 and 0.04 will able to obtain efficiency of around 90%. Besides that, worm made of hardening steel and for worm gear made of phosphor bronze has lower coefficient of friction when compared to worm pairs made of cast iron.

3 Research methodology

In order to execute the analysis in a well-organized manner, the process flow is defined in a way such that each stage is clearly defined. Initially, the literature studied are needed to be done for conceiving the ideas and understanding those mechanism that may apply in future

design. Three potential designs that from literature reviews will be selected and compared them in terms of their advantages and disadvantages. Selection of potential designs must be able to lift and place tire in different orientations as well as it is only powered by human. Besides that, the efficiency of those potential designs of lifting mechanism will be calculated manually before proceeds to 3D modelling. Every mechanism will be designed to achieve their best efficiency and those mechanisms are then compared to each other. Therefore, the most suitable mechanism will be selected from the result as an equitable method of selecting a good design is demonstrated.

Once the most potential design is decided, the design will be modelled by using 3D drawing software such as SOLIDWORK and SPACECLAIM. The 3D model is then exported into ANSYS Workbench 18.0 for further analysis and simulation. The design will be divided into three mechanisms for instance as clamping mechanism, lifting mechanism and base structure, each mechanism will be analyzed respectively. Before analyzing the design, the 3D model will proceed to meshing stage. The element size of focusing part will be adjusted into smaller in order to obtain accurate result. The analysis of the design will be focusing on total deformation, equivalent strain and equivalent stress. After the simulation is accomplished, the optimization of design will be proceeded to improve and refine the design. Last but not least, the result will be analyzed in terms of feasibility, reliability, robustness as well as portability.

3.1 Lifting Mechanism

According to the objectives of research, design of lifting mechanism must be only powered by manual force alone. Hence, the concepts of car jack are implemented into our design which it is using mechanical advantage to allow a human to lift heavy equipment. There are several types of lifting mechanism which can be classified as hydraulic jack and worm gear jack, and rack and pinion jack and scissor lift. However, the scissor lift is not taken into consideration in conceive stage because this mechanism doesn't satisfy the objective of this project which is compact design. The advantages and disadvantages of each lifting mechanism are listed in Table 1 and they will be compared to each other.

Table 23. Advantages and disadvantages of each lifting mechanism.

	Hydraulic Cylinder	Worm and Gear Jack	Rack and Pinion Jack
Advantages	1. Large amount of force generated with small force applied. 2. Constant force is provided. 3. Movement of force is in vertical axis 4. Easy to use	1. It has the ability of self-locking and braking. (reverse movement is restricted) 2. It consists worm gear and worm wheel only, hence compact size can be achieved. 3. Operating silently.	1. Cheap manufacturing cost. 2. Compact gearset. 3. Converts rotation to linear motion. 4. High robustness.

		4. High speed reduction can be obtained.	
Disadvantages	1. Oil leakage is the major failure. 2. Difficult to predict oil leakage.	1. Manufacturing cost is high due to two different metals made. 2. Efficiency is low at high gear ratio. 3. They have high power losses due to the characteristic of self-locking system. 4. Requires frequent maintenance (lubrication) as it has heavy power losses. 5. Lots of heat will be produced in large reduction of speed ratio.	1. It works only in certain levels of friction. The gears undergo process of wear if high friction is produced. 2. Lubrication is needed to perform often. 3. Efficiency is low due to overcome the friction force in contacting gears.

3.2 Base structure

Base structure is built for combining the lifting mechanism and clamping mechanism into one body. Referring to the objectives of this project, the mobility of the device is one of the criteria needed to be concerned while designing the base structure. As the device will be using in industry area, the surface of floor is uneven sometimes. So different designs of wheel are studied and compared in
Table **24**. Besides that, the material of base structure must able to afford heavy load to prevent highly deformation on structural. If the maximum stress that applied on the structure exceeds the yield strength of the material, the structure would undergo deformation process. Hence, either changing the thickness of structure or replacing it with another material that has stronger hardness are the way to solve the challenge.

Table 24. Different designs of wheel.

	Three Wheels (2 big at rear, 1 small at front)	Four Wheels (4 small)
Advantages	1. Able to cross over a small bump. 2. Easy to control direction.	1. Higher stability of base structure as it isn't tipping over easily.

	3. less weight (lesser material). 4. Has greater manoeuvrability because of their tighter turning radius.	2. Able to use at outdoor rough and uneven surface.
Disadvantages	1. Lower stability. 2. Unable to withstand heavy load.	1. Turning radius is not as tight as 3 wheels 2. Heavier weight (more material). 3. It unlikely to fit in narrow corridor due to the base area is wider,

Based on the table above, both designs have each its advantages and disadvantages. By combining their advantages, a new design is carried out with two big wheels with two small wheels. The two big wheels are located at the rear part, so the device can be moved on uneven surface easily and has greater efficiency to cross over small bumps. Moreover, the material of the base structure will be mild steel because it is inexpensive and commonly used in huge equipment.

3.3 Clamping mechanism

Clamping mechanism is defined as a mechanism that clamping or holding tire in order to transport it from a place to another. There are 2 types of clamping mechanism which includes external clamp and internal clamp. The difference between them are shown in Table 25.

By comparing both designs, external clamp is more suitable in clamping mechanism. Reason being one of the objective of this project is to able to locate the tire in different orientations at the same time to maintain the shape of tire. Therefore, external clamp is chosen and stress analysis on the structure will be carried out.

Table 25. Difference between external clamp and internal clamp

	External Clamp	Internal Clamp
Advantages	1. Able to place tire in two degrees of freedom (horizontal & vertical) 2. Able to transfer tire from device to mounting tire machine.	1. It is commonly used in clamping tire 2. Easy to clamp tire. 3. The stability of device can be controlled as it is moving up and down only.

	3. Able to clamp tire whether with rim or without rim.	
Disadvantages	1. Stability of device is lower while increasing degree of freedom. 2. Geometry design is more complex.	1. It damages the shape of tire. 2. Can be used for only one design either tire with rim or without rim. 3. Difficult to transport tire from device to mounting tire machine in horizontal position.

4 Results and discussion

4.1 Manual calculation of lifting mechanism

4.1.1 Force analysis on hydraulic cylinder

Figure below shows the simplified force diagram for calculation manually. Table 4 demonstrates the set values for hydraulic cylinder.

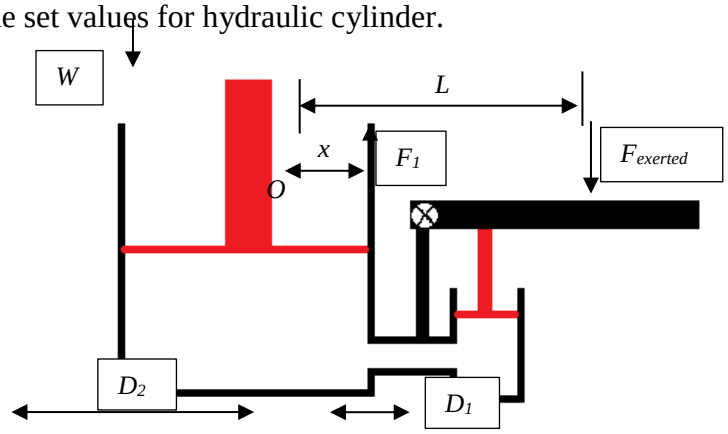


Fig. 1. Simplified force diagram of hydraulic cylinder.

Table 26. Information for force analysis on hydraulic cylinder.

Weight of object, *W*	294.3 N
Diameter of small cylinder, D_1	12 mm
Diameter of large diameter, D_2	45.08 mm
Length of handle, *L*	0.30 m
Distance between point *O* and F_1, *x*	0.03 m
Hydraulic force, F_1	unknown
Force required to push handle, $F_{exerted}$	unknown

As this is a closed system, the internal pressure will be the same due to the principle of "Pascal's law". Therefore, the F_1 can be calculated as shown below:

$$P_1 = P_2 \quad (1)$$

$$\frac{F_1}{A_1} = \frac{F_2}{A_2} \quad (2)$$

$$\frac{F_1}{\frac{\pi}{4}(0.012^2)} = \frac{294.3}{\frac{\pi}{4}(0.04508^2)}$$

$$F_1 = 20.854 \text{ N}$$

Therefore, the force required to push down the handle can be calculated by using summation of moment about point O is equal to zero.

$$+\circlearrowleft \sum M_O = 0 \quad (3)$$

$$F_{exerted} \cdot L - F_1 \cdot x = 0$$

$$F_{exerted} \cdot 0.3 - 20.854 \cdot 0.03 = 0$$

$$F_{exerted} = 2.085 \text{ N} \quad (4)$$

Furthermore, the mechanical advantage of this system is determined by using following equation:

$$\text{Mechanical advatange}, MA = \frac{\text{Force produced by the machine}}{\text{Force applied}} \quad (5)$$

$$MA = \frac{294.3}{2.085} = 141.15$$

4.1.2 Force analysis on rack and pinion jack

The ratio of output gear to the input gear is defined as gear ratio. When the gear ratio increases, the output torque will be improved. Therefore, the gear ratio of 5:1 is selected due to the length of gearbox is set as 18 cm. The formula of gear ratio is shown below.

$$\text{Gear Ratio} = \frac{\text{Number of teeth of output gear}}{\text{Number of teeth of input gear}} \quad (6)$$

Besides that, the module of two connected gears are same so that the reference diameter for both can be calculated when the gear ratio is given. The relationship between the diameters of two gears can be expressed as:

$$\text{Module} = \frac{\text{Reference Diameter}}{\text{Number of teeth}} \quad (7)$$

$$\therefore \text{Gear Ratio} = \frac{\text{Reference Diameter of output gear}}{\text{Reference Diameter of input gear}} \quad (8)$$

Moreover, the force required to lift 30kg can be determined by using following equations.

$$\text{Force} = \frac{\text{Torque}}{\text{Radius of gear}} \quad (9)$$

$$\text{Work done} = \text{Force} \times \text{Displacement} \quad (10)$$

Table 27 below shows the several information needed to calculate the force exerted on the handle to lift a 30 kg of object. The weight is set as 30 kg by approximating the sum of the weight of tire and the clamping mechanism.

Table 27. Information for force analysis on spur gear.

Weight of object, F_a	294.3 N
Lifting Displacement, S	0.40 m
Gear Ratio	5:1
Length of handle, L	0.20 m

By using Eq. (10) to calculate the work done by the rack

$$W = F_a \times S$$

$$W = 294.3 \times 0.4$$

$$W = 117.72 \text{ Nm}$$

The work done from linear motion is converted to rotation motion. Hence, the torque of driven shaft is equal to the work done.

$$\text{Output Torque}, T_{output} = \text{Work done by rack}, W$$

$$T_{output} = 117.72 \text{ Nm}$$

The magnitude of tangential force on driven gear is equal to the tangential force on driver gear, but the direction of force will be opposite. Hence, the minimum torque required to lift the object is calculated as shown below:

$$\frac{T_{input}}{R_{input}} = \frac{117.72}{R_{output}}$$

$$T_{input} = 117.72 \cdot \frac{1}{5}$$

$$T_{input} = 23.544 \text{ Nm}$$

By substitutes the length of handle and T_{input} in Eq. (9), the minimum force exerted by human to rotate the input shaft is:

$$F_{exerted} = \frac{23.544}{0.4} = 58.86 \text{ N}$$

The mechanical advantage of this system is investigated by using Eq. (5).

$$MA = \frac{294.3}{58.86} = 5$$

4.1.3 Force analysis on worm and gear jack

Based on the force analysis diagram of worm gear [8], F_s indicates the separating, or radial, force on for both the worm and gear, F_{wt} indicates the tangential force on worm whereas F_{gt} represents tangential force on worm wheel and γ is lead angle. The relationship between tangential force on worm and tangential force on worm wheel can be expressed below [8]:

$$F_{wt} = F_{gt} \cdot \frac{\cos\alpha_n \times \sin\gamma + \mu\cos\gamma}{\cos\alpha_n \times \cos\gamma - \mu\sin\gamma} \quad (11)$$

Where

F_{wt} = Tangential force on worm
F_{gt} = Tangential force on worm wheel (worm gear)
α_n = Normal pressure angle
γ = Lead angle of worm

Moreover, lead angle of worm gear pairs can be investigated by using following equation:

$$\gamma = \sin^{-1}\frac{m \cdot z}{d} \quad (12)$$

Where

m = Module
z = Number of thread of worm gear
d = Diameter of worm gear

Furthermore, the coefficient of friction can be obtained from the figure of influence of lead angle [7]. Table 28 below shows the several information needed to determine the minimum force required to lift. The gear ratio of 5:1 is selected from the figure of influence of transmission ratio on overall efficiency as the highest efficiency can be achieved [7]. Besides

that, the ability of self-locking is only occurred when the worm lead angle is in the range of 2° to 8° [6]. Moreover, the pressure angle is set as 14.5° as the lead angle is between 0° and 15° [8].

Table 28. Information for force analysis on worm and gear.

Weight of object, F_a	294.3 N
Lifting Displacement, S	0.40 m
Material of worm gear [7]	Tin bronze
Gear Ratio [7]	5:1
Diameter of worm gear, d_1 [9]	44 mm
Module, m [9]	3
Number of thread of worm gear, z_1 [9]	Double
Length of handle, L	0.20 m
Pressure angle, α [8]	14.5°
Coefficient of friction, μ [7]	0.03
Lead angle, γ	7.837°

The lead angle can be determined by using Eq. (12).

$$\gamma = \sin^{-1}\frac{3 \cdot 2}{44} = 7.837°$$

The value of coefficient of friction is 0.03 approximately when lead angle is 7.837° as well as the efficiency is around 84% which it can be obtained from the figure of influence of lead angle [7].

The output torque is equal to the work done by the rack as the worm wheel is connecting to the rack to lift an object. So, the output torque is 117.72 Nm. The diameter of worm wheel can be calculated by using Eq. (6).

$$\frac{5}{1} = \frac{\text{diameter of worm wheel, } d_2}{0.044}$$

$$d_2 = 0.22 \text{ m}$$

By using Eq. (9) the tangential force on worm wheel can be expressed as:

$$F_{gt} = \frac{T_{output}}{R_{output}}$$

$$F_{gt} = \frac{117.72}{0.22/2}$$

$$F_{gt} = 1070.182 \text{ N}$$

In order to determine the input torque, the tangential force on worm gear needed to be calculated first by using Eq. (11).

$$F_{wt} = 1070.182 \cdot \frac{\cos 14.5° \times \sin 7.873° + 0.03\cos 7.873°}{\cos 14.5° \times \cos 7.873° - 0.03\sin 7.873°}$$

$$F_{wt} = 182.96 \text{ N}$$

Then, the input torque can be calculated by using Eq.(9) as shown below:

$$T_{input} = 182.96 \cdot \frac{0.044}{2} = 4.025 \text{ Nm}$$

Besides that, the minimum force exerted on the handle is determined by using Eq. (9).

$$F_{exerted} = 20.125 \text{ N}$$

Moreover, the mechanical advantage of worm and gear jack is calculated by using Eq. (5).

$$MA = \frac{294.3}{20.125} = 14.62$$

The calculated results are tabulated and shown in Table 29.

Table 29. Results of Lifting Mechanism.

	Weight of object (N)	Minimum force exerted (N)	Mechanical Advantages, *MA*
Hydraulic Cylinder	294.3	3.27	141.15
Rack and Pinion Jack	294.3	58.86	5.00
Worm and Gear Jack	294.3	20.13	14.62

4.2 Discussion

4.2.1 Lifting mechanism

As seen from the Table 30, hydraulic cylinder was chosen as the most suitable mechanism for lifting purpose. The weightage given on mechanical advantage of the system is the highest because it is designed to reduce burden of human while using the device that without any electronic assistance. Moreover, the price needs to be concerned after the mechanical advantage due to high competitive market. The product has higher advantage in existing market when the product is cheaper than the other similar products. Other than that, the manufacturability of the design needs to be taken into account so that the manufacturers are able to save manufacturing cost and to produce mass amount in a short period. As for design complexity, the weightage is the lowest among the other criteria. This is because design drawing requires to be done in once only.

Table 30. Decision Matrix of Lifting Mechanism.

Criteria	Weightage	Hydraulic Cylinder	Rack and Pinion Jack	Worm and Gear Jack
Mechanical advantage	4	3	1	2
Price	3	3	1	2
Design Complexity	1	1	3	2
Manufacturability	2	1	3	2
Total		24	16	20

4.2.2 Force analysis on Part 1

As seen from figure below, the forces applied and the moment on the hydraulic cylinder can be determined by using equations below.

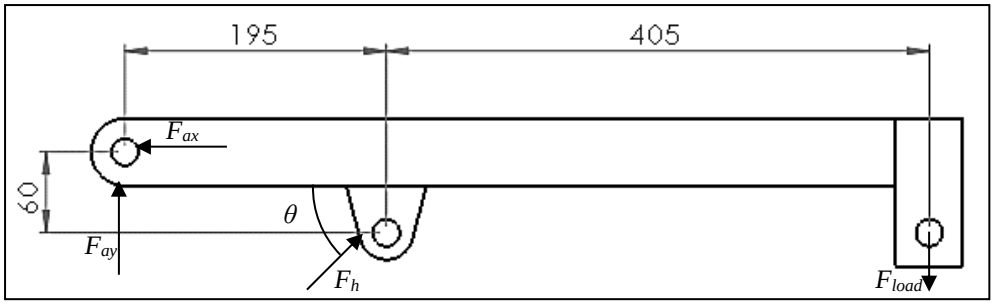


Fig. 2. Free body diagram of Part 1 in horizontal.

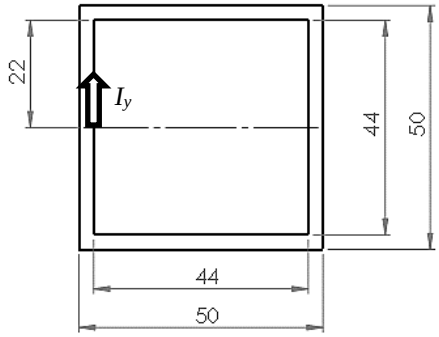


Fig. 3. Cross section of Part 1.

$$\sum F_y = 0$$

$$F_{ay} + F_h \sin\theta - F_{load} = 0 \quad (13)$$

$$\sum F_x = 0$$

$$-F_{ax} + F_h \cos\theta = 0 \quad (14)$$

$$\sum M_a = 0$$

$$F_h \cos\theta\,(L_1) + F_h \sin\theta\,(L_2) - F_{load}(L) = 0 \quad (15)$$

Loading condition parameters:

$$\theta = 78.83°, F_{load} = 850\ \text{N}, L_1 = 60\ \text{mm}, L_2 = 195\ \text{mm}, L = 600\ \text{mm}$$

Referring to Eq. (15), the F_h can be found approximately 2513 N and then the value will be using in simulation. After that, the maximum stress is determined by using the following equation:

$$\sigma_{max} = \frac{M \cdot c}{I_y} \quad (16)$$

Table 31. Identified variables of calculating maximum stress.

Length of bar, L (m)	0.6
F_{load} (N)	850
Distance between support and F_h, L_1 (m)	0.195
F_h (N)	2463.582
Moment of inertia, I_y (m^4)	2.0849×10^{-7}
Center distance, C (m)	0.022

Therefore, the maximum stress, σ_{max} will be

$$\sigma_{max} = \frac{[(2463.582\times0.195)+(850\times0.6)]\times0.022}{2.0849\times10^{-7}}$$

$$\sigma_{max} = 1.045 \times 10^{8}\ \text{Pa}$$

Table 32. Percentage error of Part 1.

Manual calculation, Pa	FE simulation, Pa	Percentage error, %
$1.045\text{x}10^{8}$	$1.30328\text{x}10^{8}$	19.81

For the above manual calculation, two forces were acting on the part which are hydraulic force and the weight of tire with clamping mechanism. Thus, there are two bending moments included in the calculation part. When comparing the simulation result and manual calculation, we see that there is percentage error of 19.81% which is considered as slightly high. Reason being the geometries were different while doing manual calculation. The geometry in manual calculation was simplified to only rectangular beam but in simulation we were using the exact model. Therefore, we can conclude that the simulation result is acceptable as it has better approach with result of manual calculation.

4.3 Finite element analysis

4.3.1 Geometry of tire lifting device

Design of tire lifting device is designed as shown figure below. The concepts of the design are based on the decision made in previous sections. After the 3D model is designed in SOLIDWORK, it will proceed to ANSYS software for further analysis. The 3D model is designed in scale 1:1.

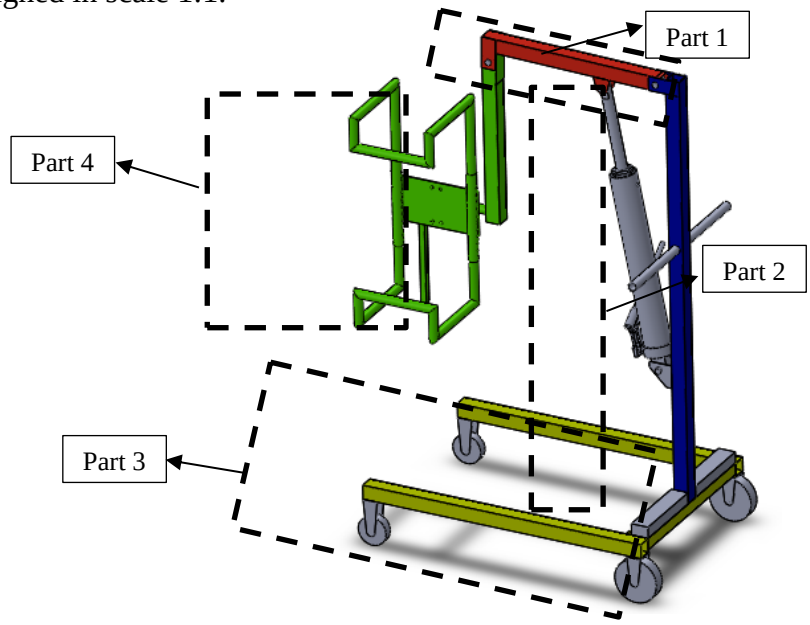


Fig. 4. 3D model of tire lifting device.

Before the 3D model undergone simulation, several assumptions were made.

1. Treat the lifting mechanism (hydraulic cylinder) as a rigid part. In real life, the fluid inside the hydraulic cylinder couldn't be compressed, hence we assume it the internal force can be transferred without any losses.

2. The counter weights were assumed as 200N to prevent the center of mass of the design locates at out of the support point.
3. The weight of tire was set as 700N to limit the weight that can be sustained by the device.
4. Treat all the component connections between parts as bonded except Part 1 with Part 2 and Part 1 with Part 4. This is simulating welding or secured by bolt and nut in real life.
5. Exclude the assembly of entire device and Part 4(clamping mechanism) due to limitation of computing power and license to run the simulation. Hence, the design was distributed as few parts to allow the computer to do simulation.

4.3.2 3D meshing

The accuracy of simulation results depends on the mesh quality. The higher the quality of mesh, the more accurate the simulation result. If the orthogonal quality is close to 1 or the skewness is close to zero, the meshing result is considered as a good meshing. The mesh quality of each part is shown in Table 33. Since the mesh quality of each part is considered as good meshing where their skewness is below 0.1, high accuracy of simulation result can be obtained.

Table 33. Comparison between Before and After Refined for each part.

		Before refined	**After refined**
Part 1	Mesh sizing (m)	Default	0.003
	Average of orthogonal quality	0.1502	0.947
	Average of skewness	0.8640	0.0081
Part 2	Mesh sizing (m)	Default	0.003
	Average of orthogonal quality	0.1267	0.9920
	Average of skewness	0.8931	0.0058
Part 3	Mesh sizing (m)	Default	0.003
	Average of orthogonal quality	0.6506	0.98483
	Average of skewness	0.5470	0.0062

4.3.3 ANSYS simulation result

The parts that analysed in ANSYS are shown in from Fig. 5and Fig. 6. The rest of the results were tabulated and shown as below.

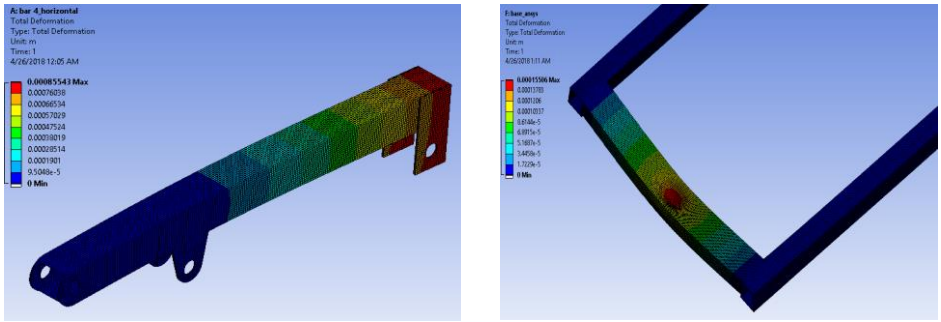


Fig. 5. Simulation result of Part 1 (total deformation) on left side whereas Part 3 on right side.

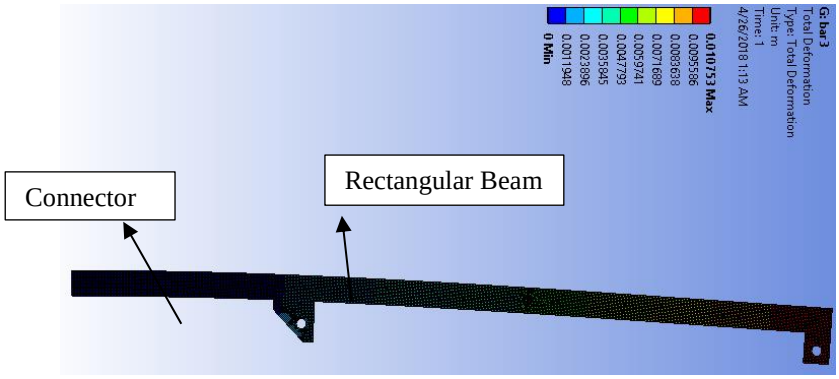


Fig. 6. Simulation result of Part 2 (total deformation).

Table 34. Results of each part.

Part number	Total deformation, m	Maximum equivalent elastic strain	Maximum equivalent stress, Pa	Safety factor
1	0.000855	0.0006520	1.30×10^8	1.9183
2	0.010753	0.0012996	2.60×10^8	0.9618
3	0.000155	0.0003982	7.97×10^7	3.1388

4.3.4 Optimization of design

The simulation result was obtained from ANSYS solution. Referring to

Table **34**, the safety factor of few parts is lower than 1.5 which means that the device would lead the user to hazardous situation. Reason being the maximum stress that produced on the structure exceeds the yield strength of the material where the yield strength of mild steel is 2.6×10^8 Pa. If the maximum stress was greater than the yield strength of the material, the process of deformation on the structure would occur. Thus, refinement of the design should be conducted to prevent structural failure happens on that device. The part that required to redesign is Part 2.

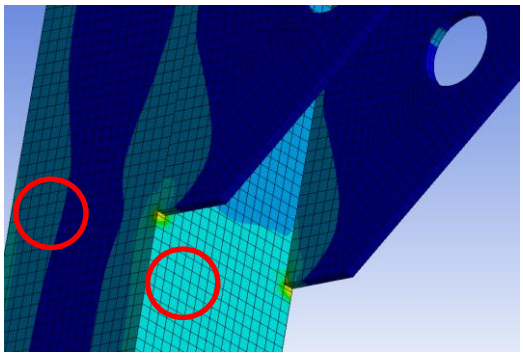


Fig. 7. Stress concentration of Part 2.

As seen the figure above, the high stress concentration occurred at the red circle area. It indicates that the area has the highest possibility of encounters plastic deformation. Based on this statement, we could know that the relative parts that requires to be improved. Hence, different thickness of the relative parts was analysed and the simulation results was tabulated in Table 35.

Table 35. Simulation results of redesign of Part 2.

Thickness	Total deformation, m	Maximum equivalent elastic strain	Maximum equivalent stress, Pa	Safety factor
Rectangular beam 3mm, connector 3mm	0.0107530	0.0012996	2.60×10^8	0.962
Rectangular beam 4mm, connector 3mm	0.0085845	0.0013667	2.73×10^8	0.915
Rectangular beam 5mm, connector 4mm	0.0072894	0.0009621	1.92×10^8	1.299
Rectangular beam 5mm, connector 5mm	0.0072734	0.0007931	1.59×10^8	1.576

According to the table above, increasing the thickness of rectangular beam would have smaller safety factor. It means that the maximum stress was distributed on connector but not the beam. However, the total deformation of it was decreased to about 8.5mm as the thickness of the beam increased. Therefore, the thickness of the connector will be modified as it has the highest stress and affecting the safety factor. Besides that, the maximum equivalent stress on redesigned of the beam and the connector are less than the yield strength of structural steel of 2.6×10^8 Pa. It implies that plastic deformation doesn't occur on that part. Since the safety factor of the redesign of Part 2 meets the minimum requirement of 1.5 when the thickness of rectangular beam and the connector are 5 mm, the redesign part was considered as acceptable and would be applied in final design.

5 Conclusion

In conclusion, a human-powered tire lifting device for lifting and placing tire in different orientations is designed. Reason being there is a shaft connected to the back of the clamping mechanism to allow the entire clamper to rotate 90 degrees. As seen from the geometry, there is no any components that requires electrical power or pneumatic system. Moreover, the feasibility and reliability of the design as well as the robustness and portability are analyzed and verified by using ANSYS. During simulating the design, the safety factor and maximum equivalent stress are the important criteria to determine whether the device is safe to be used and the limitation of it. Based on simulation result, the maximum weight of tire that can be hold is below 70 kg where it is indicating the limitation of the device. In the future, the researcher may build the prototype to test the feasibility of the design. This is because the challenge sometimes will only be figured out after carrying out some physical testing on that design. Hence, the simulation results can be proved when run some testing on the prototype.

References

[1] S. Chen , D. Zhang and JunLiu, Theoretical and Applied Mechanics, **2**, (2012)

[2] Helmi Rashid, M. K. A. Mohd Ariffin, M. H. Mohd Noh, A. H. Abdullah, A. H. Abdul Hamid, M. A. Mat Jusoh and Akbar Othman, Procedia Engineering, **41**, 1696-1701, (2012)

[3] S. A. Manoharrao, "Analysis & Optimization of Hydraulic Scissor Lift," International Journal of Engineering Development and Research, **4**, 329-347, (2016)

[4] K.Sainath, M. Salahuddin, MohdJibranBaig, M. A. Farooky, M. S. Ahmed, MohdRiyazUddin, F. U. R. Azhar and M. Shaffi, International Organization of Scientific Research Journal of Engineering, **4**, 15-28, (2014)

[5] S. A. Compbell, *Tire lifting and mounting tool*. United State Patent US 7699576 B2, (2007)

[6] N. B. Tamboli, International Journal of Innovations In Engineering Research and Technology, **2**, (2015)

[7] A. Skulić, D. Krsmanović, S. Radosavljević, L. Ivanović and B. Stojanović, Acta Technical Corviniensis-Bulletin of Engineering, (2017)

[8] Richard G. Budynas and Keith J. Nisbett, Shigley's *Mechanical Engineering Design 9th Edition*, (2010)

[9] "Khkgears," Kohara Gear Industry Co.,Ltd., 2015. [Online]. Available: http://khkgears.net/gear-knowledge/introduction-to-gears/pressure-angle/. [Accessed 11 November 2017].

Biodynamic modelling of human comfort in vehicle

Yang Chan[*1], and Mohd. Farid*[2]

[1] School of Engineering, Taylor's University, 1, Jalan Taylors, 47500 Subang Jaya, Selangor, Malaysia, cy3006@hotmail.com
[2] School of Engineering, Taylor's University, 1, Jalan Taylors, 47500 Subang Jaya, Selangor, Malaysia, mohdfarid.aladdin@taylors.edu.my
* Corresponding author

Abstract

Whole-body vibration which is due to the low frequency vibration in vehicle had a long term effect and eventually caused serious health issues to human. Researches have shown that drivers that were overexpose to vibration level had a very high chance of getting musculoskeletal issues. Continuous exposure to whole-body vibration also caused lower back pain among drivers. Different DOF models were simulated in this study to show that greater DOF models are able to predict the human body more accurately compared to lower DOF models. The challenge to be solved in this study is the simulation of human sample exposed to vertical vibration of frequencies ranging from 3 to 20 Hz as well as the measurement, evaluation and assessment of the collected data through experiments. The experiment was carried out in STRIDE and by placing the accelerometer at the head of the human subject, the vibration magnitudes of all selected frequencies were determined. A model with greater DOF is expected to be more predictable and representable towards human body compared to lower DOF models. To predict human body under vertical vibration even better, modification was done on the 3 DOF model where the configuration of mass segments are altered. From the results, the hypothesis is proven correct where greater DOF models are more identical to the human sample compared to low DOF models, provided that the frequency is beyond 16 Hz. However, the modified model failed to show that the new arrangement of the mass segments is better compared to the original model.

1.0 Introduction

Low frequency vibration in vehicle could cause serious health issues to human being especially on a long drive. It was well aware that the harmful effects of unwanted vibration to human body could lead to fatigue and discomfort. Furthermore, tremendous vibration could cause neck and spine injuries. Through research, it is shown that the lower back pain in drivers is directly related to continuous exposure to whole body vibration [1]. Based on ISO 2631, drivers that are expose to vibration level exceeds the exposure limit are placing their musculoskeletal system at risk. The transmission of vibration to human body does not only depends on frequency and magnitude of a motion, but also the independent factors such as dynamic interaction between the body and points of contact with the motion. The posture of the body could also influence the transmission of vibration to body.

In order to understand human biodynamic response and effects of low vibration better, a variety of statistical and analytical studies have been carried out by many researchers. Statistical studies involve measuring of the kinetic and biodynamic responses of human body. The biodynamic reponse functions can be classified into three characteristics which are seat-to-head transmissibility (STHT), driving point mechanical impedance (IM) and apparent mass (AP) [10]. In this project, the focus will be on STHT. It is defined as the ratio of head output vibration level to the seat input vibration level at specific range of frequency. The simulation can be in the form of displacement, velocity or acceleration. According to international standard, there are no supporting evidence to show that time depending vibration effects on human comfort in vehicle. Therefore, the RMS value of acceleration for the head in vertical direction should be measure. To estimate the comfort level of human in vehicle under condition where the vibration level is fluctuating, the distribution of RMS values can be applied.

The dangers that emerge from WBV were predicted using frequency weightings which could indicate how vibration frequencies can affect the human sensitivity towards vibration [9]. For a seated human experiencing vibration in z-axis direction, the weighting W_k should be applied [17]. In this study, since the model is a representation of a seated human and the direction of vibration is vertical, weighting W_k is used in the simulation in MATLAB software to determine the weighted r.m.s acceleration.

1.1 Research Questions

The study of biodynamic modelling involves the measurement of vibration level and dynamic discomfort of human.

1. How does the vibration level affects human comfort in vehicle?
2. How to analyse the dynamic discomfort of human body exposed to vertical vibration in vehicle?

1.2 Objectives

1. To develop a mathematical model of seated human exposed to whole body vertical vibration in vehicle
2. To predict the biodynamic discomfort of human experiencing low frequency vibration in vehicle

1.3 Hypothesis

1. Higher degree of freedom (DOF) models produce more accurate and inclusive results
2. The higher DOF model is able to predict and represent human body more accurately compared to lower DOF model

1.4 Project scope

This project involves studies and simulation of seated-human body with upright posture towards different level of whole-body vertical vibration and the biodynamic response is focus on seat-to-head transmissibility (STHT). The type of vehicles in this study is fixed to be sedan cars such as the Toyota Vios.

2.0 Research Methodology

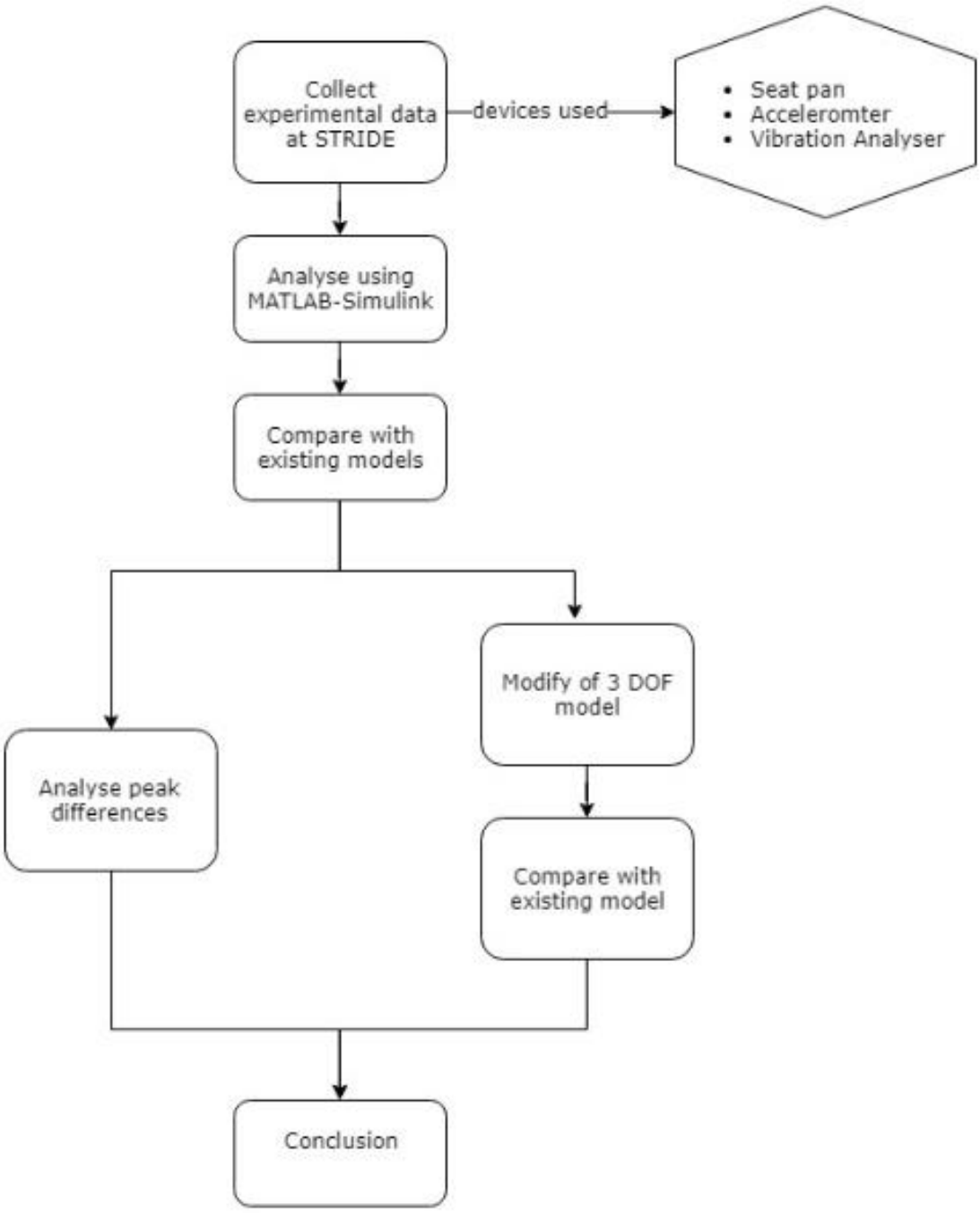


Figure 19 : Timeline of project

The approach that had been taken in this study is shown in Figure 19. The experiment data was conducted in STRIDE as there were many difficulties encountered and restriction of the law when collecting data in the vehicle. A total of three participants have been involved in this experiment with the tasks such as human sample, data collection and vibration shaker control.

The aim of this experiment is to record and analyse the vertical vibration signal of different frequencies experienced by human body. The apparatus and materials that were used in the experiment are such as :

- Seat pan
- VA
- Acceleromter
- Vibration shaker machine
- Safety helmet
- Strong adhesive tape

The procedures of the experiment are as follow :

1. The accelerometer was mounted to the frame of safety helmet by using strong adhesive tape.
2. The safety helmet was wore by the human sample.
3. The vibration analyser was configured and the vibration magnitude was set to 0.1 m/s^2.
4. The vibration shaker machine was switched on and the vibrating frequency was set to 3 Hz.
5. The human sample sat on the vibration shaker machine in upright position while holding the vibration analyser.
6. The seatbelt on the machine was fasten as a safety precaution.
7. The vibration analyser and vibration shaker machine was activated for a period of 30 seconds.
8. Step 4 to 7 were repeated with frequency of 4, 5, 7, 10, 16, 20 Hz and random.



Figure 20 : Position of human sample on vibration shaker machine

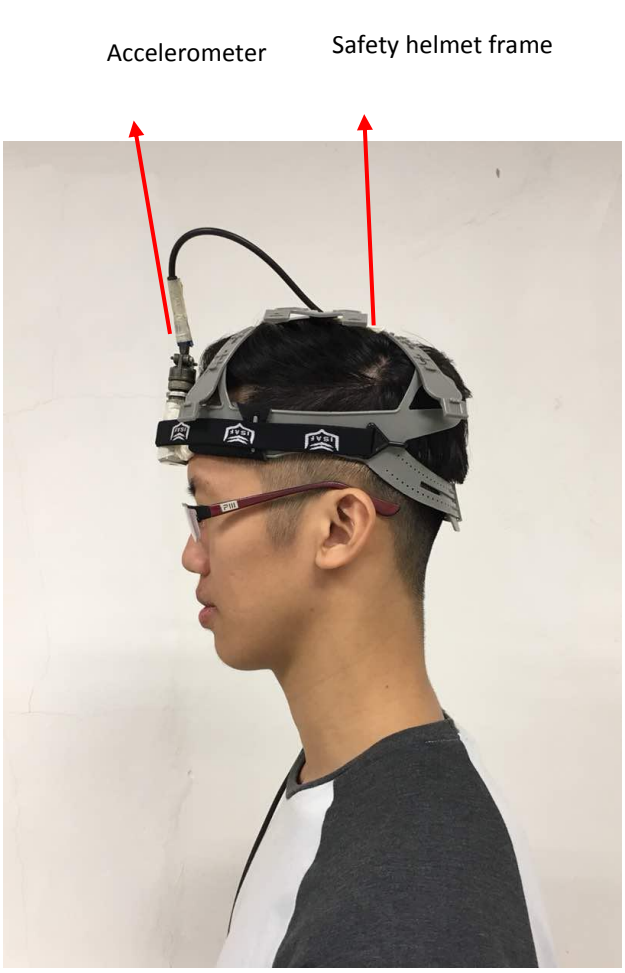


Figure 21 : Position of accelerometer mounted to head of human sample

To imitate a human sitting in vehicle, the vibration level was measured from the human sample sitting on the vibration shaker machine as shown in Figure 20. The testing subject was seated in upright position. The vibration frequency was manipulated ranging from 3 Hz up to 20 Hz. The data collection can be divided into mainly 3 frameworks which are measurement, evaluation and assessment. The measurement stage started off with the collecting of the acceleration at the head where it was measured using an accelerometer. The accelerometer which could detect acceleration in three directions (x, y and z) was mounted to the head of the passenger by using the frame of a safety helmet as shown in Figure 21. Evaluation stage involved the processing of the signal collected where the results were further analysed in MATLAB software. At the assessment stage, the experiment results were compared with the simulation results and modification was made in attempt to show that the prediction could be improved through arrangement of the configuration of lumped parameters mass-spring-damper system. The magnitude of the vibration throughout the experiment was fixed to 0.1 m/s^2. Frequencies ranging from 3 to 20 Hz were used and the duration of the human sample undergone vibration was set to 30 seconds.



Figure 22 : Vibration analyser



Figure 23 : Accelerometer properties



Figure 24 : Seat pan



Figure 25 : Accelerometer

Figure 22 shows the vibration analyser that was used to record the vibration signal during the experiment. The accelerometer used was manufactured by DYTRAN Instruments Inc. as shown in Figure 23. It has sensitivities of 101.51, 103.16 and 99.99 mV/g in the x, y and z direction respectively. To imitate the situation of a human. A seat pan as shown in Figure 24 was sat on by the human sample to measure the vibration level at the seat. The accelerometer in Figure 25 was connected to the vibration analyser to give input of vibration signal measured. It was attached to the frame of safety helmet and worn by the human sample.

After the vibration data was collected, it was analysed using MATLAB-Simulink software to compare with the existing models. Apart from that, modification was made to the existing 3 DOF model to improve the prediction of human comfort under vibration. A

conclusion was drawn from both results which is after modification, the higher DOF model is able to predict human comfort better compared to lower DOF models.

3.0 Results and Discussion

3.1 Simulink

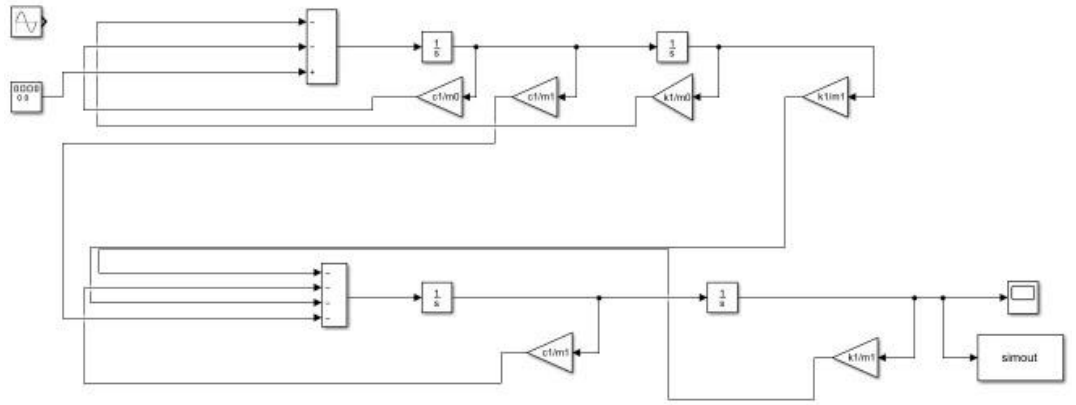


Figure 26 : 1 DOF

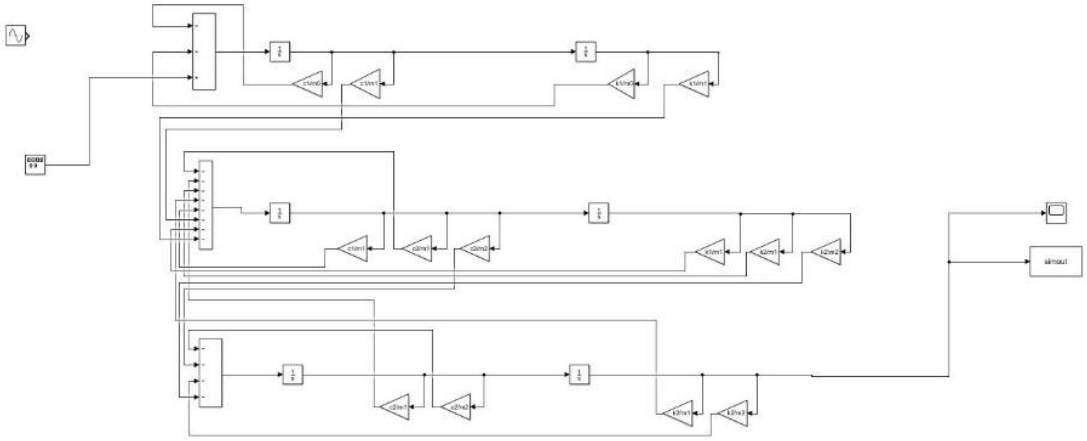


Figure 27 : 2 DOF

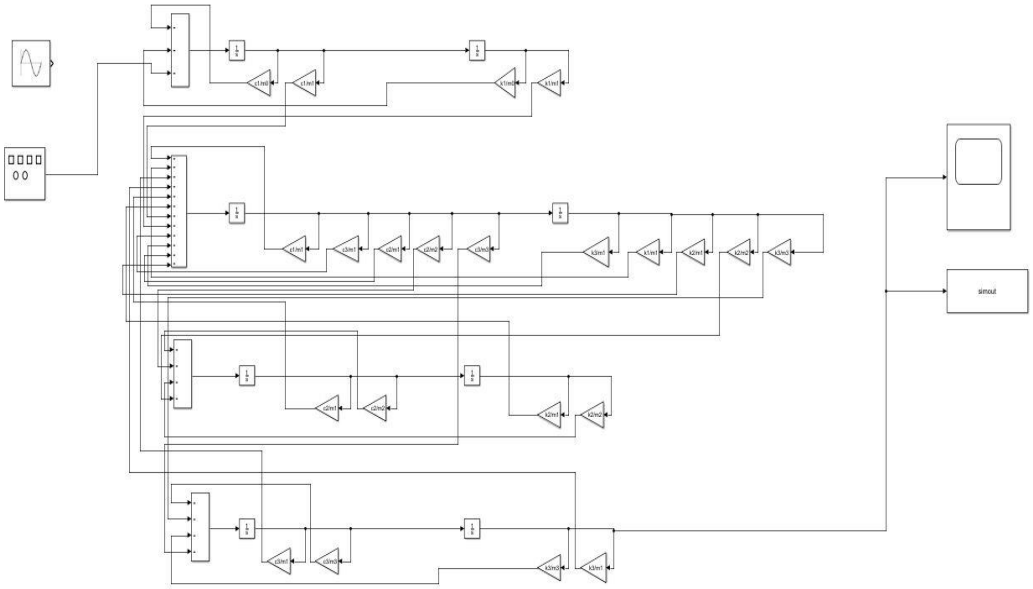


Figure 28 : 3 DOF

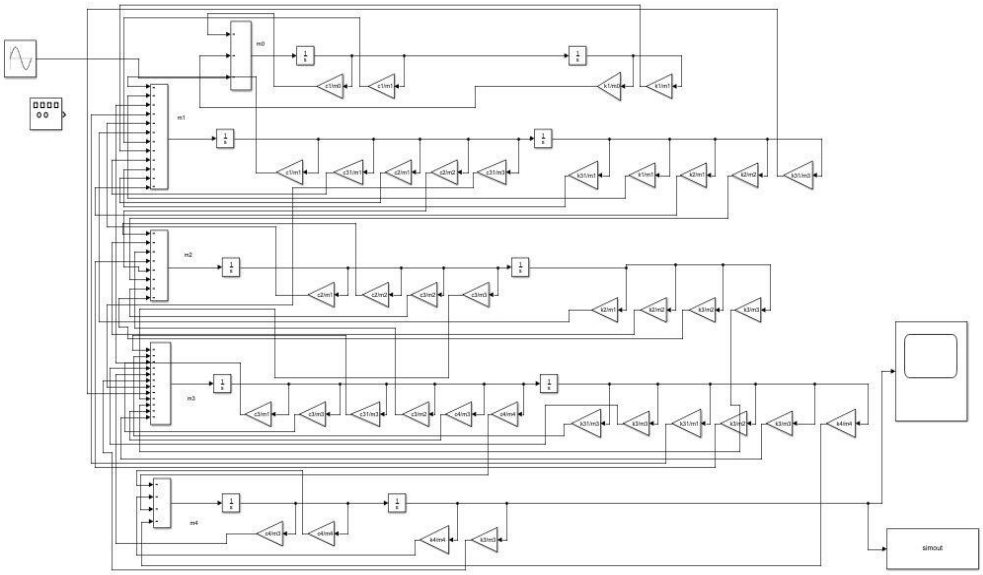
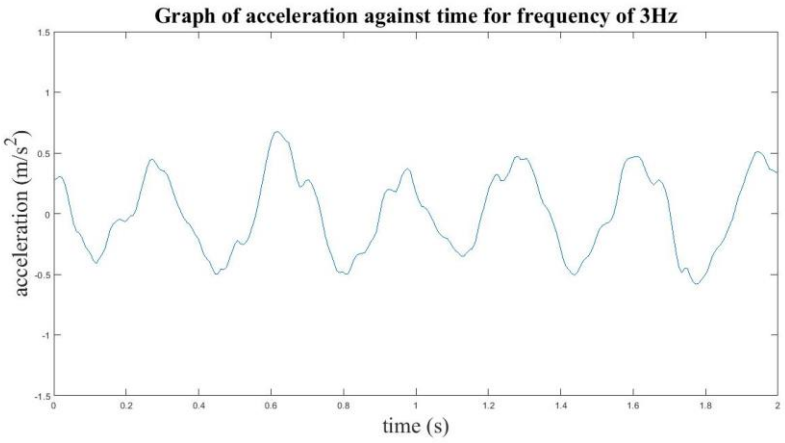


Figure 29 : 4 DOF

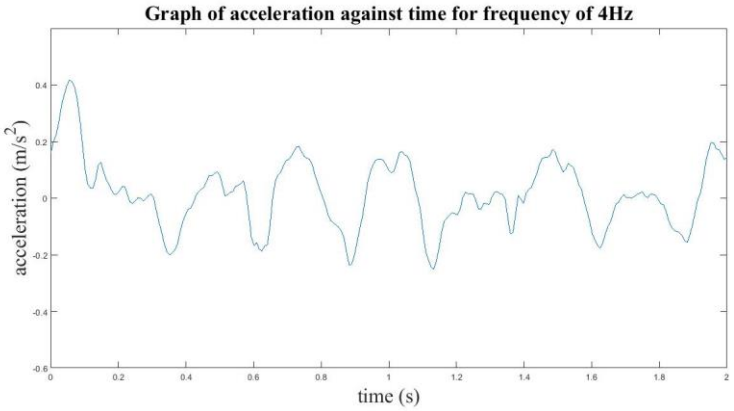
Existing models were simulated to make comparison with the experimental data. Figure 26 to Figure 29 show the block diagrams of 1 to 4 DOF models respectively, developed by using MATLAB-Simulink. Each block diagram was simulated with all the interested frequencies in this study. The frequency of the block diagram was altered by changing to input value of the sine wave generator block.

3.2 Experimental results

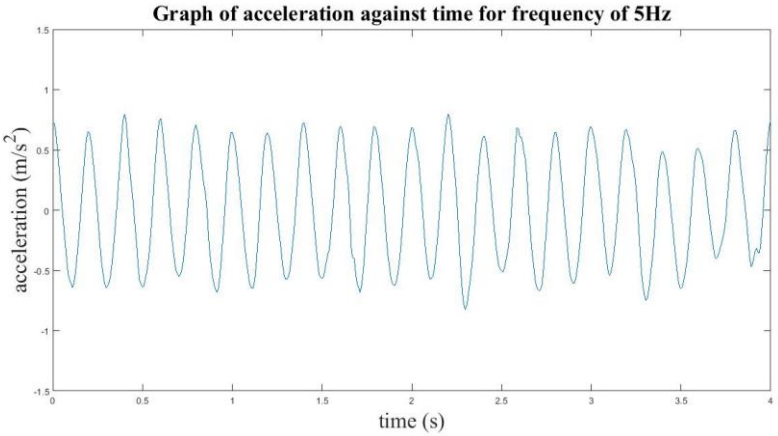
Table 36 : Experimental result

Frequency	Results
3	

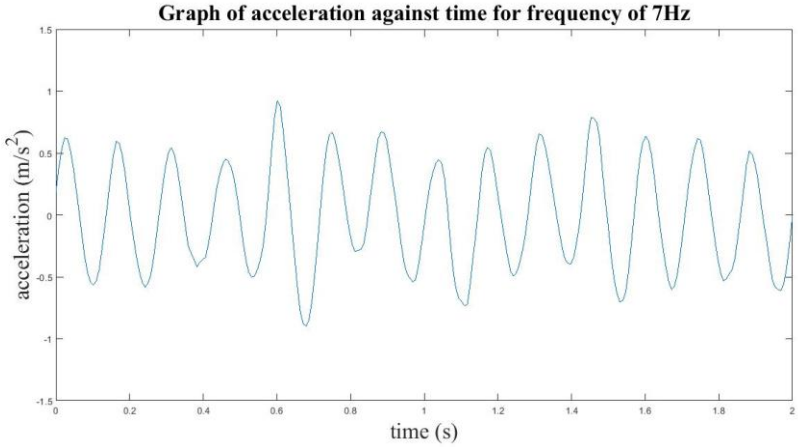
4


Graph of acceleration against time for frequency of 4Hz
acceleration (m/s^2)
time (s)

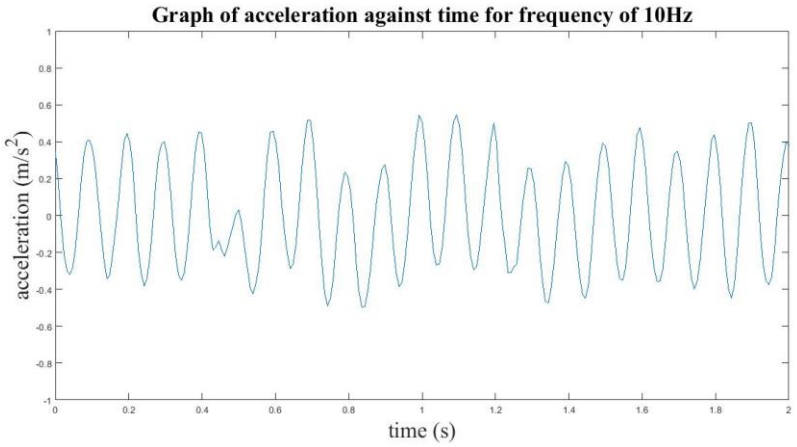
5


Graph of acceleration against time for frequency of 5Hz
acceleration (m/s^2)
time (s)

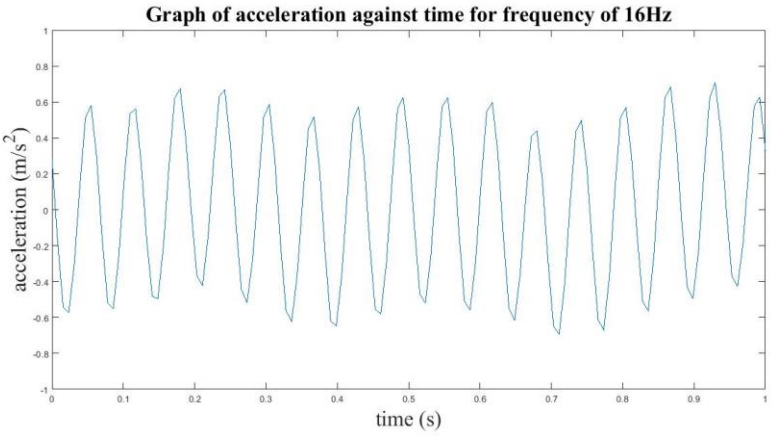
7


Graph of acceleration against time for frequency of 7Hz
acceleration (m/s^2)
time (s)

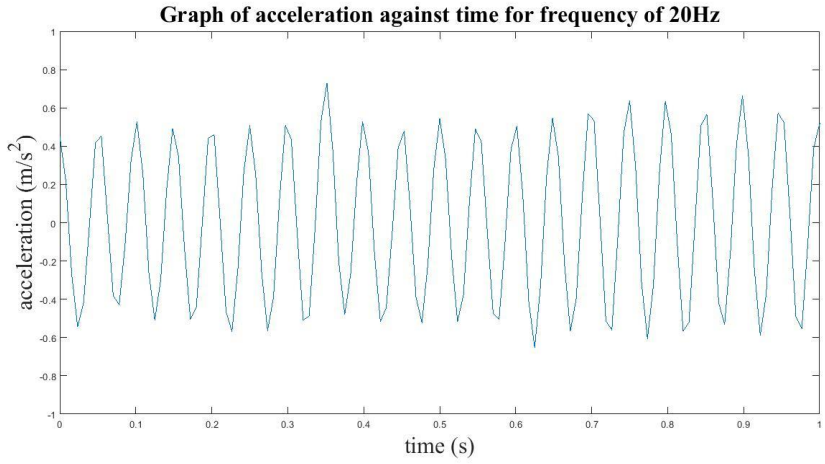
10


Graph of acceleration against time for frequency of 10Hz
acceleration (m/s^2)
time (s)

16


Graph of acceleration against time for frequency of 16Hz
acceleration (m/s^2)
time (s)

20


Graph of acceleration against time for frequency of 20Hz
acceleration (m/s^2)
time (s)

Random

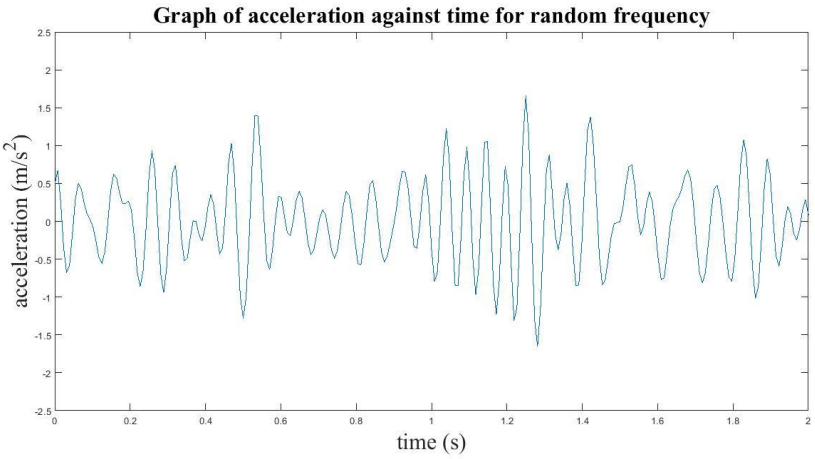


Table 36 shows the results from the experiment where the human sample has undergone a period of 30 seconds experiencing low frequencies of vertical vibration. Low frequencies such as 3 and 4 Hz show an unstable condition as the acceleration was not uniform and fluctuations occurred in every cycle of the vibrations. From frequency of 5 Hz and above, the acceleration recorded at the head of human sample was shown to be quite reasonable and acceptable as there were no obvious fluctuations happened throughout the period of vibration. For the random vibration, there was no identical peak amplitude and the value of each crest was completely different from one another.

3.3 Comparison of results between simulation and experimental data

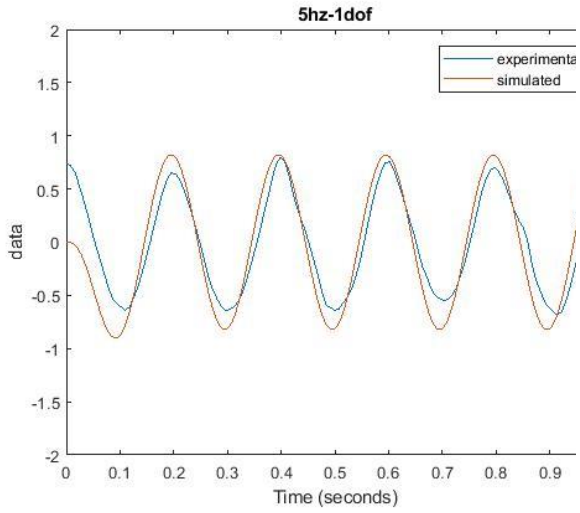


Figure 30 : 5Hz 1 DOF

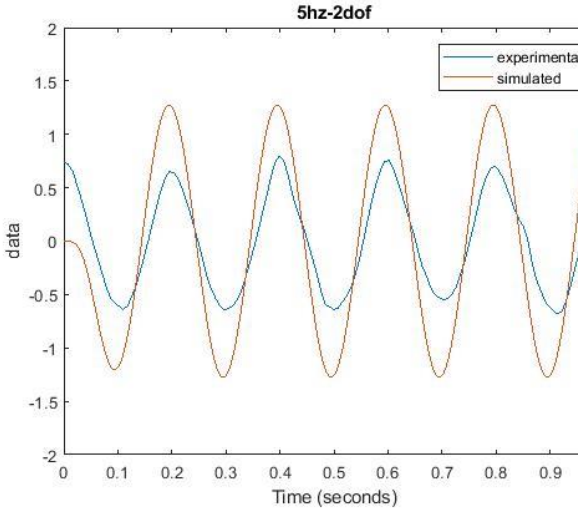


Figure 31 : 5Hz 2 DOF

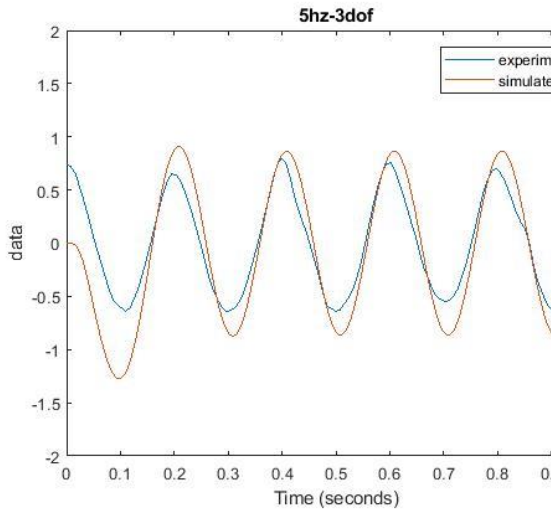


Figure 32 : 5Hz 3 DOF

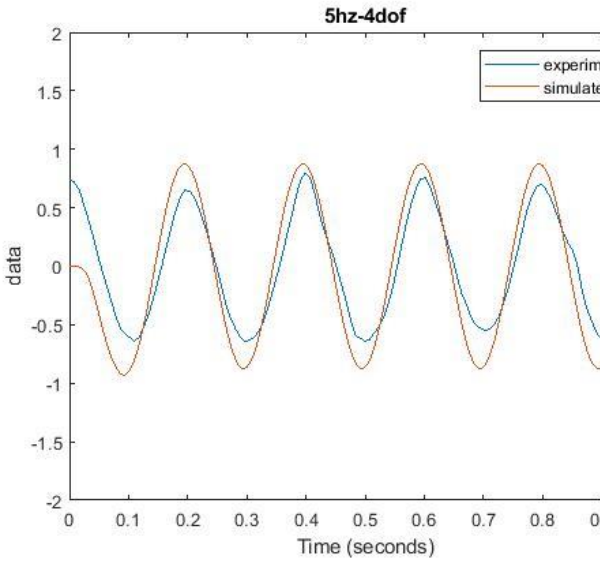


Figure 33 : 5Hz 4 DOF

The existing models were simulated to show how well they could represent a human body under vibration. **Fig. 12** to **Error! Reference source not found.** shown are the comparison of both experiment and simulation results. From 1 DOF up to 4 DOF, it can be seen that the simulation result was predictable towards the human sample as both graphs were fitted very closely. The comparison was done on frequencies of 3, 4, 5, 7, 10, 16 and 20 Hz. To compare both cases even more, the peak amplitudes of both graphs are compared and was named as the peak difference. The peak differences for all frequencies and DOFs were plotted as a graph as shown in Fig. 16

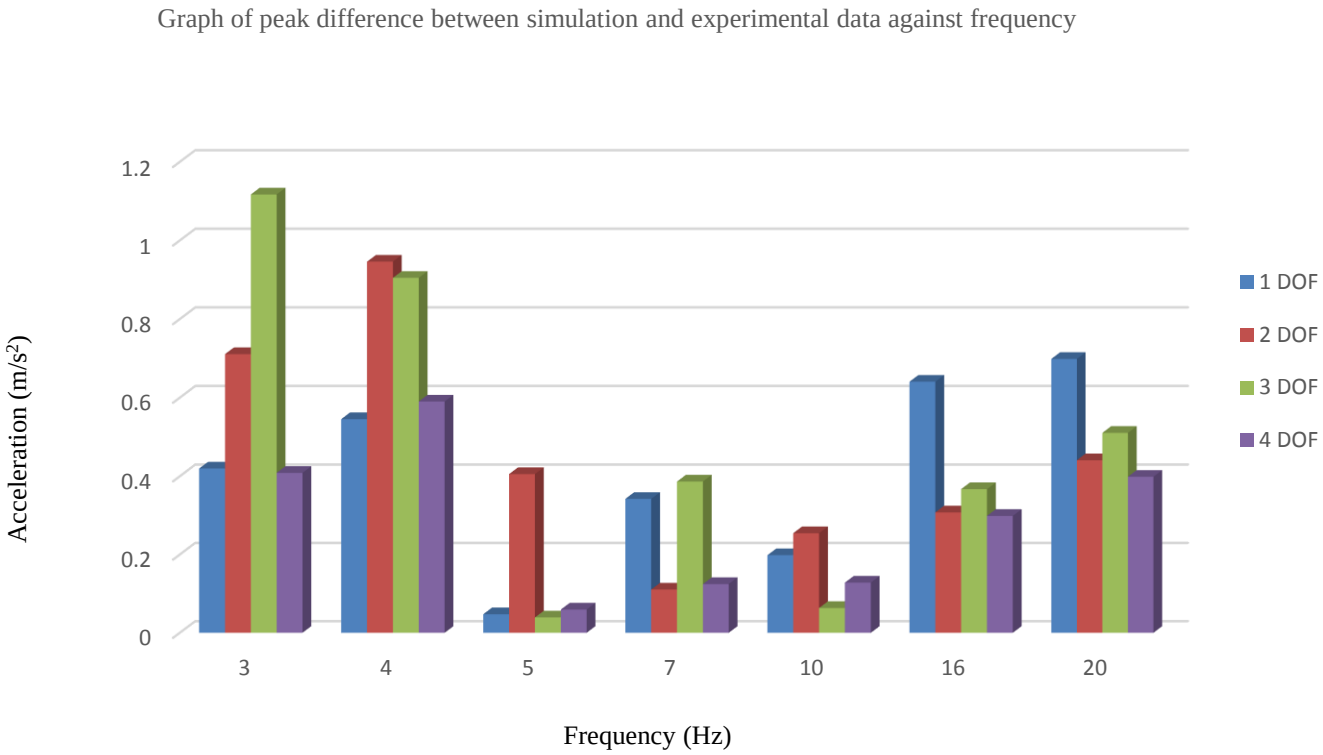


Figure above shows the comparison between both simulation and experimental data for all four DOF models. From frequency of 3Hz to 10Hz, the peak amplitude difference varies with the number of DOF because the model could not perfectly model and represent the human sample at low frequency. However, at frequency 16 and 20 Hz, the peak amplitude difference decreases as the number of DOF increases. Therefore, the greater the DOF, the more accurately it can predict the human body in seated position, provided that the frequency is above 16 Hz.

3.4 Comparison of modified and existing model

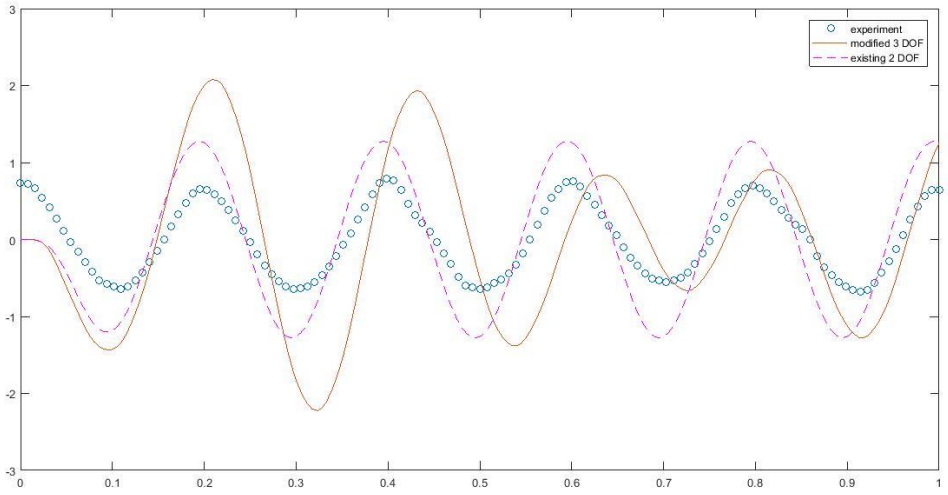


Figure 34 : Graph of experimental data, existing 2 DOF and modified 3 DOF model against time

The modified model was compared to the existing 2 DOF model to show that it could still predict the experimental data well. From Figure 34, the modified model eventually closed up the gap with the experimental data. Although before the settling time of approximately 0.5 second, the 2 DOF model has shown a better and more accurate result, but as the duration of vibration increased, the modified 3 DOF model was able to settle and predict the human sample experiencing vertical vibration more accurately.

4.0 Conclusions and Expected Outcomes

The drivers of vehicles especially tractors and trucks are constantly exposed to high level of vibration which leads to injuries and disorders. Through this study, the response of human body towards WBV can be analysed and evaluated using genetic algorithms and through modelling human body into a mass-spring-damper system with various DOF. The simulation through Matlab Simulink software is compared with the experimental data graph to obtain the accuracy between the both. As the DOF level increased, the difference of peak amplitude between both results decreases. It can be concluded that when the vibration frequency increases beyond 16 Hz, greater DOF models are able to represent and predict the human sample in seated position undergoing vertical translational vibration better.

5.0 References

[1] A. M. G.B. Kamalakar, "Development and Analysis of Human Biodynamic Model Seated on a Driver Seat Exposure to Whole Body Vibration," *IOSR Journal of Mechanical Engineering.*

[2] A. F. Abercromby, "Vibration Exposure and Biodynamic Responses during Whole Body Vibration Training," *PubMed*, 2007.

[3] Y. Q. a. M. J. Griffin, "Biodynamic Responses of the Seated Human Body to Single-axis and Dual-axis vibration," *Industrial Health*, pp. 615-627, 2010.

[4] J. Deshaw, "Effect of head-neck posture on human discomfort during whole-body vibration," *IOWA Research Online*, 2010.

[5] S. Rakheja, R. Dong, S. Patra, P. Boileau, P. Marcotte and C. Warren, "Biodynamics of the human body under whole-body vibration: Synthesis of the reported data", *International Journal of Industrial Ergonomics*, vol. 40, no. 6, pp. 710-732, 2010.

[6] N. J.Mansfield, Human Response to Vibration, London: CRC Press, 2005.

[7] J. Deshaw, "New methodologies for evaluating human biodynamic response and discomfort during seated whole-body vibration considering multiple postures," *IOWA Resesarch Online*, 2013.

[8] Z. Gan, A. Hillis and J. Darling, "Adaptive control of an active seat for occupant vibration reduction", *Journal of Sound and Vibration*, vol. 349, pp. 39-55, 2015.

[9] Y. QIU and M. GRIFFIN, "Biodynamic Response of the Seated Human Body to Single-axis and Dual-axis Vibration: Effect of Backrest and Non-linearity", *Industrial Health*, vol. 50, no. 1, pp. 37-51, 2012.

[10] W. Abbas, O. Abouelatta, M. El-Azab, M. Elsaidy and A. Megahed, "Optimization of Biodynamic Seated Human Models Using Genetic Algorithms", *Engineering*, vol. 02, no. 09, pp. 710-719, 2010.

[11] C. Liang and C. Chiang, "A study on biodynamic models of seated human subjects exposed to vertical vibration", *International Journal of Industrial Ergonomics*, vol. 36, no. 10, pp. 869-890, 2006.

[12] Y. Wan and J. M. Schimmels, "A Simple Model that Captures the Essential Dynamics of a Seated Human Exposed to Whole Body Vibration," Advances in Bioengineering, ASME, Vol. 31, 1995, pp. 333-334.

[13] F. Lu, Y. Ishikawa, H. Kitazawa and T. Satake, "Effect of vehicle speed on shock and vibration levels in truck transport", *Packaging Technology and Science*, p. n/a-n/a, 2010.

[14] X. Zhao and C. Schindler, "Evaluation of whole-body vibration exposure experienced by operators of a compact wheel loader according to ISO 2631-1:1997 and ISO 2631-5:2004", *International Journal of Industrial Ergonomics*, vol. 44, no. 6, pp. 840-850, 2014.

[15] S. Harsha, M. Desta, A. Prashanth and V. Saran, "Measurement and bio-dynamic model development of seated human subjects exposed to low frequency vibration environment", *International Journal of Vehicle Noise and Vibration*, vol. 10, no. 12, p. 1, 2014.

[16] R. Jack, M. Oliver, J. Dickey, S. Cation, G. Hayward and N. Lee-Shee, "Six-degree-of-freedom whole-body vibration exposure levels during routine skidder operations", *Ergonomics*, vol. 53, no. 5, pp. 696-715, 2010.

[17] INTERNATIONAL ORGANIZATION FOR STANDARDIZATION. ISO 2631-1:1997, Mechanical Vibration and Shock—Evaluation of Human Exposure to Whole-Body vibration, Part 1, General Requirements. Geneva, Switzerland: International Organization for Standardization, 1997.

EURECA 2018 – Conference Paper
Paper number 2ME05

One-Stop Portable Fixture For Tire Dimension Measurement Instruments

Gilbert Lim, Douglas Tong[1], and Jonathan Lim[2]

[1]Taylor's University, School of Engineering
[2]Continental Tire Technology Centre Malaysia Sdn. Bhd.

Abstract. The research details design concepts of a fixture that will be used to take measurements of conventional passenger car tires. Engineering design techniques were studied and implemented in this research. Several design concepts were drawn using 3D CAD software Solidworks and the aspects of designs will be evaluated based on feasibility, manufacturability, cost and ergonomics.

1 Introduction

1.1 Background

Tires are an important component of all land vehicles used in this modern day and age. Stability of the vehicle, fuel economy, comfort of the passengers and braking distance safety are some of the features of a well-designed tire. More than a billion tires are produced annually by several tire manufacturing companies such as Michelin, Bridgestone, Goodyear, Pirelli and Continental Tires.

A fixture as defined in the manufacturing industry, is a support device used for securely holding and positioning/orienting a workpiece relative to the tools, which in this case is a car tire and the tools being the measuring instruments. The use of fixtures improves economy of production because it allows smoother and faster operations with conformity. [1]

The fixture in this project, is a car tire lift with some modifications. The tire which is installed onto its' respective sized rim, will be mounted to the fixture on the centre hub of the wheel. There are two fixtures which have been made, one being an electrical lift and the other being a hydraulic lift. An image of these 2 fixtures with a tyre mounted are shown in figure 1.

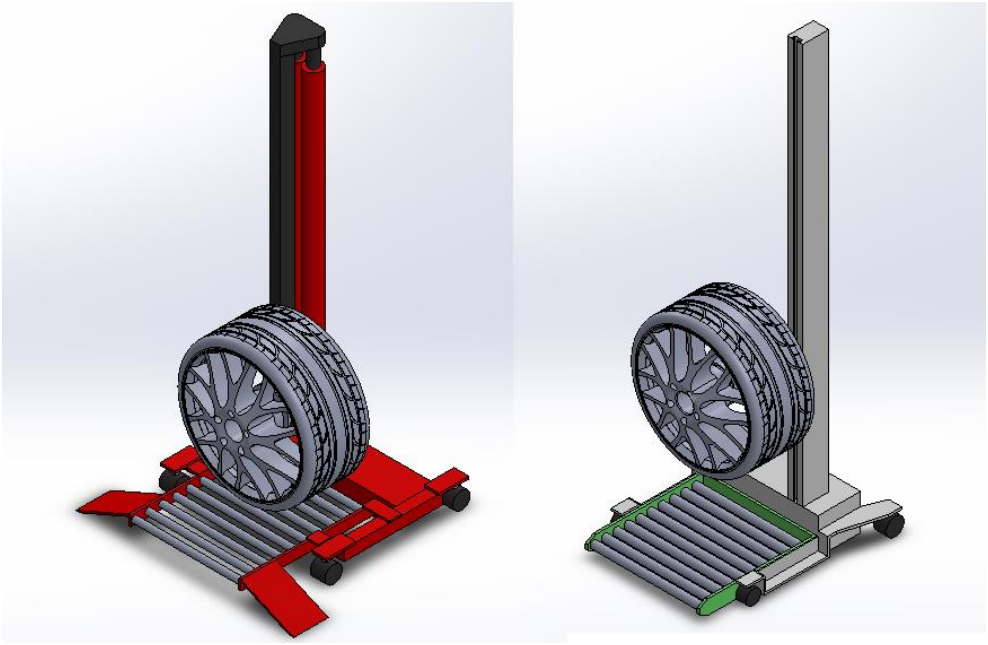


Fig. 1: 3D Part Assembly of the hydraulic fixture (left) and the electric fixture (right)

1.2 Tire Manufacturing Process

The first step in the tire manufacturing process is the mixing of raw materials to form rubber compounds. Large quantities of natural and synthetic rubber, carbon black, zinc oxide, sulfur, and other chemicals and oils are all delivered to factory site and are stored until needed. Automated computer control systems contain various recipes and can measure out specific weight portions of rubber and chemicals for mixing. These mixtures will undergo milling with heating to soften the batch and undergo mixing again with additional chemicals before being

cooled and rolled into rubber slabs for the following processes. There are 3 separate processes to prepare the components of the tire using this rubber compound.

The extrusion process applies heat to the rubber compound, mixed with additional chemicals and extruded into sheets and before being precisely weighed, cut and cooled. The tire components made form the extrusion process are the sidewall and the tire treads. The calendering process is where the rubber compound is rolled into thin sheets. Fabric calendering coats and adheres the fabric cords between layers of rubber sheets and rolled to form multiple layers. The process is similar with steel calendering, using steel cords instead. The body plies, inner liner and belt package are produced from this process. The bead building process is where a coil of steel bead wire is uncoiled, coated with rubber and coiled up again.

The subsequent process is the creation of the basic tire shape using a tire building machine. The manufactured parts from all the previous processes are delivered to a skilled assembler at the tire building machine. The centre of the machine is a collapsible rotating drum which holds the tire's parts. The tire assembler begins building a tire by wrapping the rubber-covered fabric plies around the machine drum. The ends of these plies are joined with glue, after which, the loops of beads are added and locked into place with additional tire body plies laid over the beads. The assembler then uses special power tools to shape the edges of the tire plies. Finally, the extruded rubber layers of the sidewalls and tread are glued into place, and the assembled tire, called a 'green tire', is removed from the tire-building machine.

The 'green tire' is then sent to the curing press, where tires attain their final shape and tread pattern. The curing machine is a large metal mold, inside which is an expandable balloon like component called a 'bladder'. The molds are engraved with the tread pattern and sidewall markings. The green tire is fitted onto the 'bladder' and the mold closes. The bladder fills with a recirculating heat transfer medium such as steam or inert gas, and expands to shape the tire, forcing the blank tread rubber against the interior of the mold, which is also heated up in the process. Tires are cured at above 100 degrees Celsius within 10 – 30 minutes, depending on their size. The heating from the curing process strengthens the rubber compound by forming the cross link, the chemical bond that links one polymer chain to another similar to rubber vulcanization without the use of sulfur. At the end of curing the press swings open, the tires are popped from their molds and onto a long conveyor that carries them for inspection and testing.[2]

The final stage of the tire manufacturing is testing and inspections. Each tire is thoroughly inspected visually for flaws such as bubbles or voids in the rubber of the tread, sidewall, and interior of the tire. The tire is also placed on a test wheel where it is inflated and spun. Sensors in the test wheel measures the balance of the tire and determines if the tire runs in a straight line. Tires are rarely rejected because of the competent design and assembly process of a modern tire. Once the tire has been inspected and run on the test wheel, it is moved to a warehouse for distribution. Some of the tires are sampled from the production line and X-rayed to detect hidden weaknesses or internal failures.

1.4 Tire measurements and significance of research

There are several categorised dimensions of the car tire and wheel rim which is shown in figure 2. The dimensions that define the size of a car tire and the rim that will fit it will be printed on the sidewall of the tire as a code. An example of this code is: 205/55 R16 V where 205 is the

tire's width measured in millimetres, 55 is the percentage ratio of the sidewall height to tire's width, and 16 is the wheel diameter measured in inches. The letters R and V represent the tire's construction and speed index.

The three measurements of the tire that the fixture will help measure are the tire's width, circumference and tread depth. The circumference of the tire is used to determine the tire's overall diameter. These three measurements are taken to determine first and foremost, whether the tire meets the specified tolerances based on a Manual of Standards. [3]

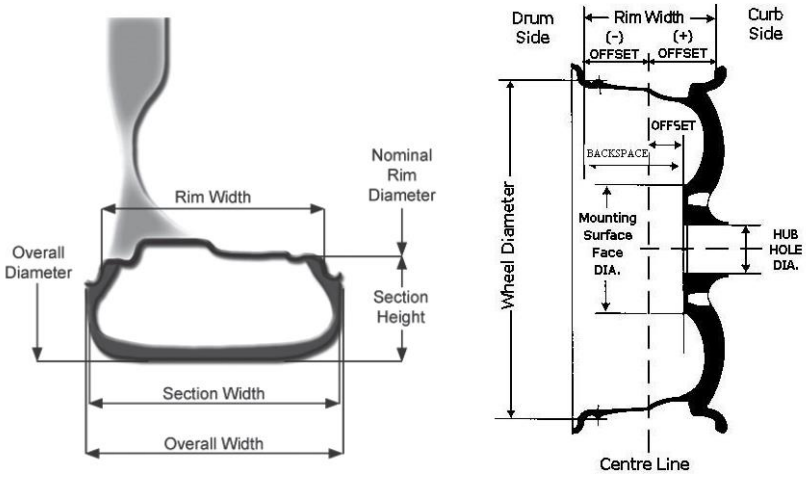


Fig. 2: Dimensions of a tire (left) and dimensions of a wheel rim (right)

The portable fixture for tire dimension measurement instruments will be used in the final stage of the tire manufacturing industry, during testing and inspection. The measurement data is important for tire manufacturers to ensure the tire meets specifications and dimension standards, assess the quality of their assembly processes and machines, and identify trends in data with new changes to the processes or machinery equipment. With such a large volume of tire production, it would benefit the tire industry if the measurement processes can be made more efficient.

1.4 Objectives

The main objective is to design a mechanism that will be built onto the fixture that will help an operator take the tire's three measurements of circumference, tire overall width and tread depth, easily and quickly. The design should be structurally sound and able to be used repetitively without failing. Additionally, the design must be adaptable for a range of car tire sizes, limited only to passenger car tires.

2 Literature Review

2.1 Alternative Tire Measuring Methods and Devices

Initial research was conducted to determine the measuring tools and methods currently available for tire measurements. Contactless measurement methods were found to be one of the more popular and recent advancement. A science journal published in 2015 details the use

of electronic sensors to measure the circumference of the tires during the industrial manufacturing stage. The paper discusses measurement methods that include the use of capacititive sensors, ultrasonic sensors, inductive sensors and optoelectric sensors.[4] Another contactless measurement device was developed by Sigmavision which patented a laser measurement device for measuring the tire tread depth, and is now being used in Hunter Engineering Company's 'QuickTread®' and Nokian® Tire's 'SnapSkan®' products.[5] The technology developed is able to be used as a handheld device or even driven over a steel housing with the device within. The system measures an estimated 2 inch segment of the car tire, which will generate a 'point cloud', a 3D image of the segment with the groove depth accurately calculated. The major advantage is it's ability to detect irregular tire wear.

2.2 Measuring Instruments

The measuring instruments that are used to measure the tire are researched thoroughly to understand their working principles and capabilities, associated terminologies, variety in design and shape and size.

2.2.1 Vernier Calipers

The Vernier calipers is a precise instrument that can be used to measure both internal and external distances accurately with the use of the Vernier scale. It is also able to measure depth using the depth measuring blade which extends from the bottom of the sliding jaw. The use of the Vernier scale allows the precision of down to 0.01 millimetres (10 micrometres) or 1/1000. The calipers common flaw is the 'zero-point error' in which the calipers do not read 0.000cm when it's jaws are fully closed.

The modern calipers developed and now commonly used is the Digital Calipers which is similar in form and function to the Vernier calipers with the addition of an electronic body attached to the jaw in the place of the Vernier scale. The electronic body is equipped with a small converter and a digital display while the sliding body of the calipers is fitted with an incremental capacitance transducer. The incremental capacitance transducer is fabricated from a foil-like dielectric material that is adhered along the entire length of the caliper's body. [6] The advantages of this unit is the ability to save the measurement last taken, extremely helpful when taking measurements of an object in a confined space that is impossible to read the measurements of the Vernier scale. Newer models are equipped with bluetooth wireless technology able to transmit the measurement data to an external device for easy records. Other minor advantages include the ability to read measurements in bad lighting because of the display, immediate conversion of units and a zero setting to be able to read relative measurements.

2.2.1 Tread depth gage

The tread depth gage is used to measure the tire's tread depth. The tread depth gage is a small handheld device which consists of the body, the protruding depth bar, which is a thin rod and the scaled rod protruding from the other end of the body. The depth bar or 'plunger' and the scaled rod are a single piece. The body of the depth gage will usually have a screw pin to tighten and prevent the depth bar from moving. The tread depth gauge may also have a zero-point error where the scaled rod does not read exactly zero when it's base is compressed against a flat

surface. The digital tread depth gage is similar to the digital caliper, having similar benefits when compared with a mechanical one.

2.2.3 Measuring Tape

Measuring tape or tape measure is a common measuring tool able to measure great lengths easily, measure around corners and curves, and able to roll up compactly. Measuring tapes are designed for specific uses such as tailoring, carpentry or construction. Measuring tapes may be made of cloth, plastic, fibre glass or as a steel or metal strip. The more common retractable measuring tape that is made of steel used for carpentry and construction is not suitable because of it's rigid shape which is unable to curve around the tire. The measuring tape that will be used is a thinner and more flexible steel strip which does not have the

3 Design Parts

3.1 Support and Base

The support and base are the components which must be securely attached to the tire lift fixture's base or on it's standing body. The design of the support structure will complement the design of the joint component. A simple support structure would be a hollow steel beam or a rod.

3.2 Joint

The joint is the component that will connect the mechanical arm to the support structure. As a result of the different sizes of car tires and different operator's working height, the tire lift will be used to raise the tire to various heights. The joint component must be able to raise or lower the mechanical arm to the height of the tire easily. The joint component must also be fool-proof in the event an operator raises the tyre and collides upwards into the mechanical arm. Designs of hinges or elbows are incorporated into the joint for this reason. Examples are shown in the figure 3 below.

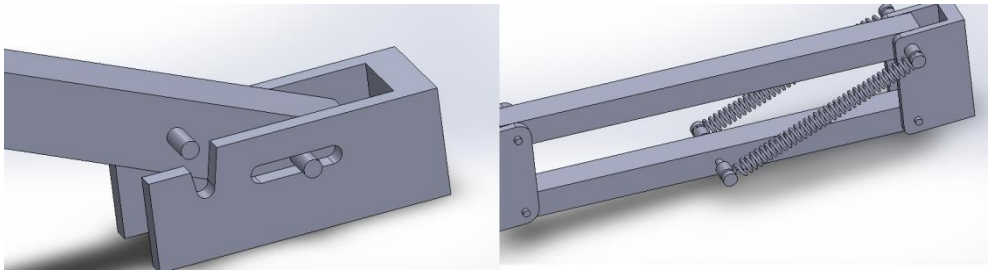


Fig. 3: Designs of joints with the safety feature

3.3 Mechanical Arm

The mechanical arm will be the component which will house all the measuring instruments ready for use. The most direct and simplest method for this is to position the Vernier calipers and measuring tape above the tire. It will position the Vernier calipers such that it is as close to the tire tread as possible or even touching it, with both jaws of the calipers clamping onto the tire sidewall. The measuring tape will be secured to the mechanical arm with the operator able to draw out the tape at approximately the centre of the tire's width. One of the designs of a mechanical arm is shown in figure 4.

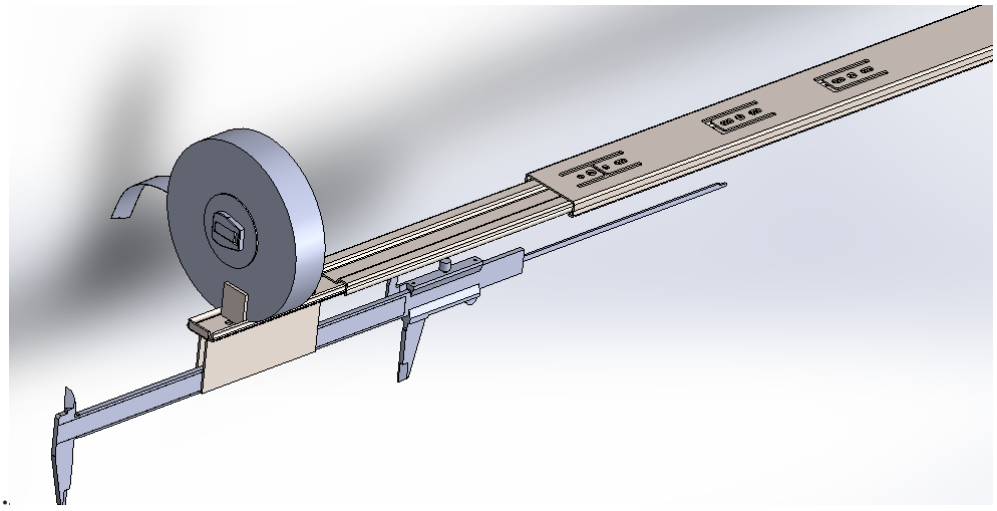


Fig. 4: Sliding mechanical arm with the Vernier calipers and measuring tape attached

References

[1] E. K. Henriksen, "Jig and Fixture Design Manual." 1973.

[2] B. (Periyar U. Balachandran, "A study on financial performance of select tyre industry in India," Periyar University, 2016.

[3] "European Tyre and Rim Technical Organisation (ETRTO) Manual 2018.PDF." .

[4] M. Navrátil and J. Zdražil, "Automatic contactless measurement of tyre circumference in industrial conditions," *Procedia Eng.*, vol. 100, no. January, pp. 408–417, 2015.

[5] S. Corporation, "(12) Patent Application Publication (10) Pub . No .: US 2006 / 0283920 A1," 2006.

[6] M. I. Etingof, "Modern vernier caliper," vol. 55, no. 8, pp. 29–30, 2012.

Mathematical Modelling of Postural Balance Associated with the Changes of Body Mass Index Classification and Skinfold Thickness in Female Young Adult during Dynamic Standing

Iman Mohamad Husaini[1,9] and Ku Pei Xuan[1]

[1]Mechanical Engineering, School of Engineering, Taylor's University, Malaysia

Abstract. Risks of falls and obesity have been closely related to poor postural balance in previous studies. Postural studies can be tested in so many ways however, physical methods are insufficient. The aim of the present study is to develop a mathematical modelling to determine the correlation between Body Mass Index (BMI) with postural balance during dynamic standing, Body Mass Index with skinfold thickness and Body Mass Index with postural balance during dynamic standing and skinfold thickness. A number of 20 healthy random female adolescents aged 18-25 subjected to postural stability (levels 5 and 12 with eyes closed and opened) and limits of stability, LOS (level 5, medium level difficulty) tests during dynamic standing with both legs using the Biodex Balance System. The skinfold measurement was measured using skinfold caliper to determine the approximate total body fat at four different body sites on the right side with the subject's consent. The final finding for this study is the mathematical equation relating three variables of BMI, postural balance and skinfold thickness which result to is $f(x,y) = p00 + p10x + p01y$ with coefficient of 95 % confidence interval p00= 0.4089 (-1.457, 2.275), p10= 0.06089 (-0.005794, 0.1276), p01= -0.04111 (-0.1367, 0.05445) relating the three variables of BMI, percentage of body fat and postural balance. Future research is needed to determine the correlations using other physical tests available using the Biodex Balance System with Body Mass Index and skinfold measurement to identify correlation to reduce the percentage of falls and obesity. .

[9]Corresponding author: imanmohamadhusaini@gmail.com

1 Introduction

Falls, trips and slips are incidents that occur frequently in general industries and contribute 646000 cases of all reported fatal accidents leading to death worldwide. Every year, economic and human losses occur caused by injurious falls [1]. This comes second after the fatalities caused by road traffic accidents. Fatal falls occur more than 80% in countries with low and middle incomes. The regions include South East Asia and Western Pacific mounting up to 60% of deaths [2]. Incidents caused by falls would generally take away 10 days off from work [3] and approximately 3.2 million non-fatal accidents at the workplace is reported within the European countries to entail to a full four day absence from work in 2014. Fatal accidents within the European countries summed up to 3739 cases and the ratio is 850 cases of non-fatal incidents for every fatal incident. The economy activities and the number of workers employed for a certain year is comprehensively related to the number of accidents occurred at the workplace. This is proven by an analysis based on the development history. In 2009, the reduction of workplace incidents is caused by the stagnation or contraction of economic crisis and global financial related activities [4].

Postural instability increases the likeliness of slips and falls at the workplace. A balanced posture while standing requires constant effort from the vestibular, musculoskeletal and visual systems. The loss of postural stability leads to imbalance, commonly evaluated in the centre of pressure (COP) and directly associated with a high probability of falling. Postural instability could be affected by the environmental workplace, tasks or even personal factors. If one or more from the vestibular, musculoskeletal and visual systems interfere with these factors, the potential of getting injured caused by postural imbalance increases [3].

The boundaries of postural stability in healthy adults are limited by environmental and personal characteristics. The mechanical factors such as body characteristics influence the postural stability besides gender and age [5] [6]. One of the factors in the increment of fall risks among Japanese women is the limited body height [7]. In addition to the factors of poor postural stability is the low body mass and foot deformities [1]. The variation in body characteristics altogether impacts the postural stability and this variation also influences the type of motor strategies chosen to sustain postural stability.

The study of shapes and sizes in biological formation components is known as anthropometry [8]. Anthropometric characteristics in adults can be defined using a metric known as the Body Mass Index (BMI) and can be classified into groups of underweight, overweight and obesity. It can be defined as the weight of an individual in kg divided by the squared of height in meters. BMI is widely interpreted as an index that represents the fatness of an individual and commonly used to dictate and acts as a prevalence of specific health issues. Nonetheless, BMI is also known to be inaccurate as it doesn't include the fat mass on other sites of the body such as the bone tissue and cartilage [9]. Central obesity can be marked using the measurement of waist circumference in children and adolescents. The waist circumference is one of the most highly sensitive anthropometric indicators. However, the ratio of waist to hip is an inaccurate marker to determine the youth's abdominal obesity as the connection

between the ratio and central adiposity is weak [10]. The high sensitivity of skinfold thickness measurements can indicate obesity as it exhibits the indirect approximation of body fat and is recommended to be used as an index to monitor obesity in both children and adolescents [11].

Many similar studies had been done but with different methods. In this research study, the Biodex Balance System will be used to test postural balance during dynamic standing through two types of tests known as the limits of stability and postural stability. The estimated total body fat percentage will be collected through skinfold thickness measurement at four different sites of the body and converted into percentage of body fat using a formula known as the Durnin and Womersly (1974), in equation [1]:

Female: Density = 1.1369-0.0598 (LOG sum of 4 skinfolds). (1)

The data from skinfold measurement will be evaluated and compared with BMI [12].

Risks of fall are closely related to weak postural balance and are affected by individual factors such as obesity and environmental factors such as the type of tasks at the workplace. In order to reduce the risks of fall and postural imbalance, the Body Mass Index (BMI) and skinfold measurement are used to indicate the estimated total body fat. A number of 5 related articles are summarized and reviewed for each of the subsections that include skinfold measurement, Body Mass Index and tests conducted on postural balance during dynamic standing.

The study is carried out to reduce the risks of falls and the rate of obesity thus to consider it as a success, the following objectives need to be achieved:

1. To determine the relationship between BMI and skinfold thickness in young female adult.

2. To study the pattern of postural balance during dynamic standing based on visual conditions in young female adult.

3. To design a mathematical modeling based on the relationship between postural balance, BMI and skinfold thickness in young female adult.

Literature Review

1.1 Methods on determining body fat percentage

Rashid (2017) states that Malaysia has been reported to have the highest obesity rate at 13.3 % among other regions in the Southeast Asia. The overweight rate is slightly higher mounting up to 38.5 % in Malaysia [13]. Studies on assessing the accuracy of determining the body fat percentage are insufficient. There are many methods to determine the body fat percentage and that includes skinfold thickness measurement, novel ultrasound, waist circumference, bio-impedence and dual X-ray absorptiometry (DXA). Patel (2015) states that the DXA method is

widely known to provide an accurate measure of total body fat but the method is too expensive to be used frequently [14]. However most recent studies compare the other methods with the results obtained from DXA. The body fat percentage obtained from skinfold thickness measurement method shows the highest correlation with DXA followed by BMI followed by waist circumference as claimed by Wohlfahrt-Veje et al (2013)[15].

1.2 The validity of BMI to determine total body fat percentage

Commonly, BMI has been used to monitor the rate of obesity as it could lead to future risks of fractures, falls and postural imbalance. The range of BMI can be classified in Table 1.

Table 1: Classifications of BMI [16]

Classification	**BMI (kg/m^2)**	
	Principal cut-off points	**Additional cut-off points**
Underweight	<18.50	<18.50
Severe thinness	<16.00	<16.00
Moderate thinness	16.00-16.99	16.00-16.99
Mild thinness	17.00-18.49	17.00-18.49
Normal range	18.50-24.99	18.50- 22.99
		23.00-24.99
Overweight	≥ 25.00	≥ 25.00
Pre-obese	25.00-29.99	25.00-27.49
		27.50-29.99
Obese	≥ 30.00	≥ 30.00
Obese Class I	30.00-34.99	30.00-32.49
		32.50-34.99
Obese Class II	35.00-39.99	35.00-37.49
		37.50-39.99
Obese Class III	≥ 40.00	≥ 40.00

The BMI values are independent of age and can be used for both genders. An individual with a low BMI value is prone to be at risk for ostopeorotic fracture which is the reduction of quality and bone density as claimed by Shiel Jr. (2017) as well as hip fracture while a high BMI value is at risk of fracture at the upperarm [17]. However, Johansson et al (2014) claimed that a low BMI can prevent fracture at the lower leg [18].

Body proportions vary in different populations, thus BMI may not correlate with the estimated total body fat at the same level. In the past years, researchers have different views on the possibility to develop a separate BMI cut-off points for different ethnics. This is because the verification relating body fat distribution, BMI and body fat percentage vary over the populations as claimed by World Health Organization (2017) [19]. Other than that, Nuttal (2015) stated that adopting BMI to determine the total body fat percentage is inaccurate as the index does not differentiate body fat and lean masses [9]. Thus an individual with a high BMI might have a low body fat mass and contrariwise.

1.3 Factors affecting postural balance

Over the ages, anthropometric measurements have been used to evaluate the patterns of human changes and the relationship with diseases. In previous studies, anthropometric measurements used are height, weight, height from the knee and hip from the ground and foot measurements as illustrated in Figure 1.

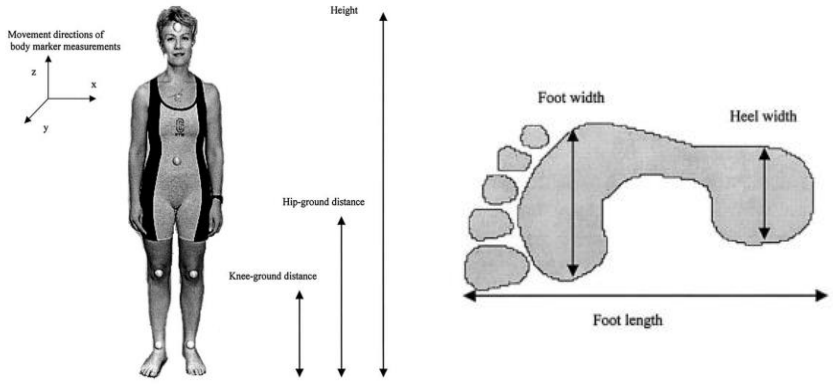


Figure 1: Anthropometric measurements [1]

Different methods have been used in previous postural balance studies and one of the factors affecting postural balance is the anthropometric measurements. The increase in postural sway when a participant is trying to balance herself is mostly influenced by increasing height and the data collected can be normalized based on the body height as stated by Alonso et al (2015) [20]. Alonso et al also claims that postural sway and anthropometric factors showed limited correlation although height is the highest factor that affects postural sway followed by the centre of pressure and the length of trunk head located at the axial region of the body. Kejonen et al (2003) also found that there are no relationships between the anthropometric measurements and the value of total body dynamics but he claimed the results from the female population shows 14.5% variation of total navel movement affected by foot width as shown in Figure 1 [1]. Increasing height affects the displacements of ankle location and gastrocnemius response as stated by Berger et al (1992) [21]. Lee and Lin (2007) claim that individuals who are lanky have higher postural sway due to the position of center of mass that is higher in comparison to endomorph individuals [22]. Postural stability is inversely associated with position of center of gravity thus anthropometric factors do affect posturography as stated by Berger et al.(2007) and Kejonen et al.(2003) [9][1]. The lack in correlations of the factors is possibly due to the difference in balance measurement apparatus and different views of dynamic analysis.

The body mass and postural balance are highly correlated thus it can be concluded that in order to maintain balance, a large force from the musculoskeletal is needed to balance the body mass inertia in opposed to centre of gravity.

2 Methodology

2.1Target population

The qualitative study population consists of 20 healthy young female adolescents aged 18 to 25 years old, chosen randomly from different local public universities among the Malay, Chinese and Indian ethnicities. Participants' health states are self-reported without any lower limb disorder. Consent letter was handed out to the participants and informed beforehand on the objectives and procedures of the experiment. The experiment is done after 2 p.m. to ensure that the participants are not dehydrated and takes approximately one hour for each participant to complete the experiment cycle.

2.2 Instruments

The instruments required in order to conduct the experiments include the Biodex Balance System in Figure 2 and skinfold caliper as shown in Figure 3. The instruments are available at Faculty of Engineering, University of Malaya. The data is analyzed using IBM SPSS after data collection for preliminary test and proceed the data analyzing cal modeling using Matlab software for mathematical modelling, available at Taylor's University's computer lab



Figure 2: An example of a participant on the Biodex Balance System during limits of stability test



Figure 3: Skinfold caliper to measure skinfold thickness

2.3 Anthropometric measurements

The height and weight measurements are measured using patient weighing scale with height rod. The participant is advised to wear light clothing and remove any shoes, lose items or jewelleries during the conduction of the experiment, long sleeves will need to be removed or raised if it's not tight during the skinfold measurement. There will be a female lab assistant during the periods of physical contact between participant and researcher. The skinfold measurement will be conducted in a private room to prevent embarrassment. The BMI is calculated by dividing the weight in kilogram by the square of the height in meters as shown in equation (2):

$$\text{BMI, kgm}^{-2} = \frac{\text{weight, kg}}{\text{Height} \times \text{height, m}^2} \quad (2)$$

The skinfold thickness is measured at four sites on the right side of the body which are the triceps, biceps, subscapula and suprailiac using the skinfold caliper. Each site is measured for three times in a chronological order of the first site to the fourth to ensure the accuracy.

2.4 Postural balance tests

The postural balance was measured using the Biodex Balance System that is able to measure the participant's postural balance during static and dynamic surfaces from level 1 to 12. Two types of tests were chosen to measure the postural balance of the participants during dynamic standing which were the limits of stability (LOS) and postural stability. The tests required the participants to stand static on the platform with both hands on the sides on the body. The platform was set at a level 5, defining moderately stable and level 12 being the most stable for dynamic surface. The levels of platform set indicate the degree of inclination. The first test conducted was the limits of stability (LOS) that required the participants to stand on both feet and try to aim for the target circle that lights up in red for approximately 2 seconds until another target around it lights up in random order as shown in Figure 4.

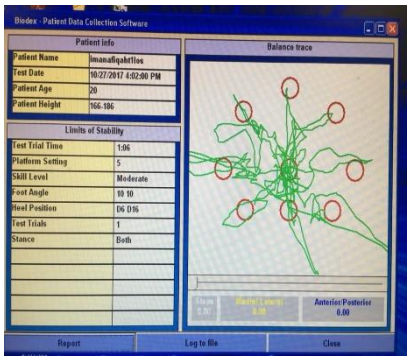


Figure 4: The sample of data collected for Limits of Stability test

The platform surface was set at level 5 and the distance of the target circles are set at medium or moderate level indicating 75% skill level difficulty. In this test, the participants' balancing skill is challenged as the platform will tilt and the participants have to try to keep their sway envelope consistent regardless of the movement pattern. The ability to control the centre of gravity within the participants' support base area is known as the sway envelope. A total of 16 sway degrees have been set vertically defining 8 degrees each on both sides and another total of 12 sway degrees defining 4 sway degrees backwards and 8 degrees forward. The results of LOS is in percentage indicates the precision of moving to the direction of the targets within their time of completion.

The platform is set at levels 5 and 12 for the second test of postural stability and this test required the participants to balance their body for 20 seconds on the same spot indicated by the black dot on the screen as shown in Figure 5.



Figure 5**: The sample data collected .for Postural Stability test**

.

This test is done with both eyes closed and repeated with opened eyes. The target point is marked in the middle of the screen grid. The postural stability test is developed to analyze a detailed pattern of the participants' movement to balance themselves based on the inclination set. The results of the postural stability test indicate the frequency of the participant to hit the target within 20 seconds. The limits of stability and postural stability tests are repeated for three times to ensure accuracy with 10 seconds of rest in between the trials. Each consecutive test is done with three trials separately hence another set of two data will be used to calculate the average value of stability and analyzed using t-test.

2.5 Procedures

The procedures of skinfold testing, limits of stability and postural stability tests are as follows:

2.5.1: Before the experiments

Before the experiments are conducted, the letter of consent was handed out to the participants with the objectives and requirements of the experiments. The name, age and phone number of the participant were taken down in case of any further procedures regarding the experiment. The weight and height of the participant with light clothing and without shoes were measured.

2.5.2 Test 1: Limits of Stability

1. The participant was instructed to stand static on the platform without shoes with their hands on the sides of the body.
2. Location of the participant's feet on the platform was recorded.
3. Testing mode and 'Limits of Stability' were chosen on the screen.
4. The user setup information on the screen (name: imantrial1, gender, height, weight and age) were filled up for the first trial.
5. Level 5 of the platform with medium skill was set.
6. The results were saved in the Biodex Balance System.

7. Steps 1 to 6 were repeated for another two trials but with a different code name (imantrial2).

2.5.3 Test 2: Postural Stability

The participant was instructed to stand static on the platform without shoes with their hands on the sides of the body. Location of the participant's feet on the platform was recorded. Testing mode and 'Limits of Stability' were chosen on the screen. The user setup information on the screen (name: imantrial1, gender, height, weight and age) were filled up for the first trial. Level 5 of the platform was set and with participant's eyes closed. The first trial of the experiment lasted for 20 seconds and the results were saved in the Biodex Balance System. Steps 1 to 5 were repeated with the participant's eyes opened. Steps 1 to 4 and 6 were repeated with the platform level set at 12 and the participant's eyes are closed. Step 8 was repeated with the participant's eyes opened.

2.5.4 Test 3: Skinfold measurement

a) Triceps skinfold

The triceps on the right side of the body was accurately located which is on the posterior midline of the upper arm and marked with a marker pen. Participant's arms were held freely on the sides of the body. A fold of the subject's skin was firmly grasped vertically between the thumb and index finger and lifted up. The skinfold was lifted up approximately 1 cm and measured vertically. The muscle or fascia should not be included as the skinfold thickness only includes skin and subcutaneous fat. The contact surface of the caliper was placed at approximately 90 ° to the skinfold and below the fingers. The pressure between the fingers was slightly released but the skinfold was remained held so that a greater pressure is applied by the caliper. The needle was read to the nearest 0.1mm approximately 4 seconds after the pressure was released.

b) Biceps skinfold

The biceps was located accurately on the right side of the body which is over the biceps muscle (approximately 1cm higher than the level used to mark the triceps site), on the anterior midline of the upper arm. Steps 2 to 8 in experiment a) were repeated.

c) Subscapula skinfold

The subscapula was located accurately on the right side of the body which is approximately in the range of 1 to 2 cm below the shoulder blade, also known as the scapula. Steps 2 to 8 in experiment a) were repeated but the skinfold was firmly grasped and diagonally measured.

d) Suprailiac skinfold

The suprailiac was located accurately on the right side of the body by poking firmly through thick subcutaneous fat. The suprailiac was located 1 cm above the top of the hip bone that is also known as anterior superior iliac crest. Steps 2 to 8 in experiment a) were repeated.

Experiments a), b), c) and d) are repeated for another two trials accordingly from experiment a) to d)

The limitation for the postural balance test is that the participants were restless after a few trials as the tests took a long duration of standing thus decreasing their attention span. Other than that, participants' sensitivity levels are different at different sites of the body leading to a shorter time of skinfold measurement..

2.5.5 Statistical analysis

The justification of the sample size of 20 would allow us an adequate observation to take the benefits of the Central Limit Theorem. A bell shape curve will be generated according to the results if the data is normally distributed. If the data is not normally distributed, non-parametric methods will be looked into to minimize the sample determination for statistical issues. G-Power 3.1 is used to determine the sample size and statistical power analyses.

The participants' BMI were calculated using the average data of height and weight using equation 2. The average value for each site of the skinfold measurement was added up and converted to percentage body fat using equation 1. The strength and direction of relationship between BMI and percentage body fat were analyzed using the Pearson's regression test. A scatter plot was developed from the regression test to assess the strength and direction relationship between these two variables. The postural balance results for each test were averaged and tabulated. Independent t-test was used to identify the most significant postural balance test to use in the mathematical modeling. All data assessments were conducted using IBM SPSS Subscription Trial (Version 25) for Windows and a significance level of 0.05 was used.

2.5.6 *Mathematical modelling*

BMI, percentage of body fat and postural balance test result were tabulated and imported into Matlab R2018A version. The mathematical modeling was generated using curve fitting toolbox. Two levels of polynomial degree were assessed to identify the higher R-squared value.

3 Results and Discussion

The most significant test for postural balance is when the participant's eyes are opened and the relationship between postural balance with BMI classification and percentage of body fat is shown in Figure 6. The best fit line of the three variables indicates the relationship between them. The equation generated from the mathematical modelling is shown in equation (3):

$$f(x,y) = p00 + p10x + p01y \quad (3)$$

Coefficients (with 95% confidence interval):

p00= 0.4089 (-1.457, 2.275)

p10= 0.06089 (-0.005794, 0.1276)

p01= -0.04111 (-0.1367, 0.05445)

where, x is defined as BMI, y is defined as percentage of body fat and z is the postural balance test for level 5 when the participants eyes are opened.

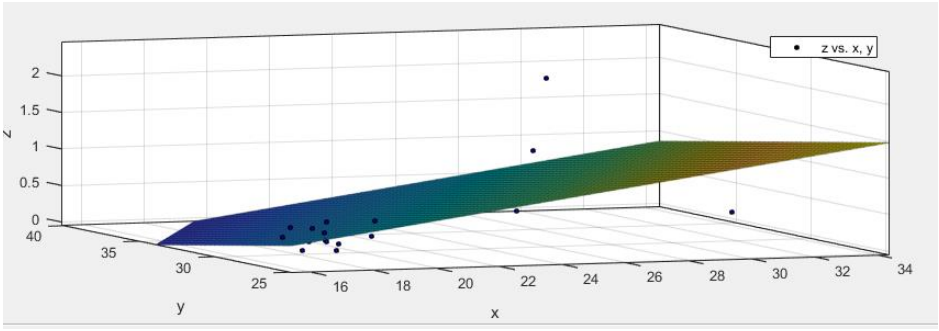


Figure 6: Mathematical model of the three variables

The R-squared value is 0.2198 which is significant thus the three variables are related through equation (3).

In this research study, 20 participants chosen randomly were assessed using three experiments. The research is designed to evaluate the relationship between BMI, percentage of body fat and postural balance in female young adults. In order to understand the pattern between the changes of these three variables, a mathematical modeling is developed. It is observed that the relationship between the variables is significant, however the R-squared value is low proving that the relationship is not strong. A second degree of polynomial is tried and resulted in a higher R-squared value, however, random fittings of the polynomial degree can be misapplied in the assessment of polynomial[23]. The relationship between BMI and skinfold is significantly high as of the value of Pearson's regression is close to 1 based on the scattered plot of data using the two variables. Other than that, the postural balance test chosen for the mathematical modeling is based on the significance between the tests using Biodex Balance System. It is expected that the mean group of participants who closed their eyes with an inclination surface of level 5 is the highest as the test indicates the number of times the target is being touched within 20 seconds. This is because their degree of sway is higher thus the imbalance caused the target to hit many times in comparison to the other tests tat allowed the participants to have a higher control of their balance as they will be static at one point within the 20 seconds. This decreases the amount of times the target is being touched on the screen. This experiment was designed to evaluate the number of times the target is being touched rather than the amount of time the participant is able to stand at the target point.

The limitation of this research study is that participants are self reportedly healthy. However, having the experiments done to a controlled age range helped in giving better results

4 Conclusion

The outcome of this study is the generation of improvised equations that relates the postural balance, BMI and skinfold thickness. The generated mathematical modeling is aimed to ease

the study in clinical and sports injuries review where the pattern of the data and results could be generated just by using the equations. This study could benefit in clinical rehabilitation process of reducing the rate of falls and obesity by observing the results of the postural tests, BMI and skinfold thickness. In the future, a refined mathematical modeling on specific BMI classifications should be generated as the risk of obesity and fall are increasing among female young adult in Malaysia.

References

[1] P. Kejonen, K. Kauranen, and H. Vanharanta, "The Relationship Between Anthropometric Factors and Body-Balancing Movements in Postural Balance."

[2] "WHO | Falls," *WHO*, 2017. [Online]. Available: http://www.who.int/mediacentre/factsheets/fs344/en/. [Accessed: 20-Nov-2017].

[3] S. Park, K. Lee, T. Lockhart, and S. Kim, "Effects of Sound on Postural Stability during Quiet Standing," *J. Neuroeng. Rehabil.*, vol. 8, no. 1, p. 67, Dec. 2011.

[4] "Accidents at work statistics - Statistics Explained." [Online]. Available: http://ec.europa.eu/eurostat/statistics-explained/index.php/Accidents_at_work_statistics. [Accessed: 20-Nov-2017].

[5] J. W. Błaszczyk, M. Beck, and D. Sadowska, "Assessment of postural stability in young healthy subjects based on directional features of posturographic data: vision and gender effects.," *Acta Neurobiol. Exp. (Wars).*, vol. 74, no. 4, pp. 433–42, 2014.

[6] T. B. Palmer, R. M. Thiele, and B. J. Thompson, "Age-Related Differences in Maximal and Rapid Torque Characteristics of the Hip Extensors and Dynamic Postural Balance in Healthy Young and Old Females," *J. Strength Cond. Res.*, vol. 31, no. 2, p. 1, May 2016.

[7] H. Matsumoto, H. Hagino, T. Wada, and E. Kobayashi, "Locomotive syndrome presents a risk for falls and fractures in the elderly Japanese population," *Osteoporos. Sarcopenia*, vol. 2, pp. 156–163, 2016.

[8] N. Utkualp and I. Ercan, "Anthropometric Measurements Usage in Medical Sciences," *Biomed Res. Int.*, vol. 2015, pp. 1–7, Aug. 2015.

[9] F. Q. Nuttall, "Body Mass Index: Obesity, BMI, and Health: A Critical Review.," *Nutr. Today*, vol. 50, no. 3, pp. 117–128, May 2015.

[10] R. W. Taylor, I. E. Jones, S. M. Williams, and A. Goulding, "Evaluation of waist circumference, waist-to-hip ratio, and the conicity index as screening tools for high trunk fat mass, as measured by dual-energy X-ray absorptiometry, in children aged 3-19 y.," *Am. J. Clin. Nutr.*, vol. 72, no. 2, pp. 490–5, Aug. 2000.

[11] W. Klimek-Piotrowska *et al.*, "Anthropometry and Body Composition of Adolescents in Cracow, Poland," *PLoS One*, vol. 10, no. 3, p. e0122274, Mar. 2015.

[12] G. Rodríguez *et al.*, "Body fat measurement in adolescents: comparison of skinfold thickness equations with dual-energy X-ray absorptiometry," *Eur. J. Clin. Nutr.*, vol. 59,

no. 10, pp. 1158–1166, Oct. 2005.

[13] F. H. Rashid, "Malaysians most obese in region | New Straits Times | Malaysia General Business Sports and Lifestyle News," *New Straits Times*. [Online]. Available: https://www.nst.com.my/news/nation/2017/06/246538/malaysians-most-obese-region. [Accessed: 23-Nov-2017].

[14] K. Patel, "Measuring body fat percentage: It's an accuracy thing | Examine.com," *Examine .com*, 2015. [Online]. Available: https://examine.com/nutrition/an-accuracy-thing-measuring-body-fat-percentage/. [Accessed: 23-Nov-2017].

[15] C. Wohlfahrt-Veje *et al.*, "Body fat throughout childhood in 2647 healthy Danish children: agreement of BMI, waist circumference, skinfolds with dual X-ray absorptiometry," *Eur. J. Clin. Nutr.*, vol. 68, no. 6, pp. 664–670, Jun. 2014.

[16] "Hungary To Be The World's No.1 With Hamburger Tax - Xpatloop.com - Expat Life In Budapest, Hungary - Health & wellness," *XpatLoop*, 2010. [Online]. Available: http://www.xpatloop.com/news/hungary_to_be_the_worlds_no1_with_hamburger_tax. [Accessed: 24-Nov-2017].

[17] W. C. Shiel Jr., "Osteoporosis Causes, Symptoms, Signs, Treatment & Diet," *MedicineNet.com*. [Online]. Available: https://www.medicinenet.com/osteoporosis/article.htm. [Accessed: 23-Nov-2017].

[18] H. Johansson *et al.*, "A Meta-Analysis of the Association of Fracture Risk and Body Mass Index in Women," *J. Bone Miner. Res.*, vol. 29, no. 1, pp. 223–233, Jan. 2014.

[19] "Weblet Importer." [Online]. Available: http://www.pitt.edu/~super1/lecture/lec38711/005.htm. [Accessed: 24-Nov-2017].

[20] A. C. Alonso, L. Mochizuki, N. M. Silva Luna, S. Ayama, A. C. Canonica, and J. M. D. A. Greve, "Relation between the Sensory and Anthropometric Variables in the Quiet Standing Postural Control: Is the Inverted Pendulum Important for the Static Balance Control?," *Biomed Res. Int.*, vol. 2015, pp. 1–5, 2015.

[21] W. Berger, M. Trippel, M. Discher, and V. Dietz, "Influence of Subjects' Height on the Stabilization of Posture," *Acta Otolaryngol.*, vol. 112, no. 1, pp. 22–30, Jan. 1992.

[22] A. J. Y. Lee and W.-H. Lin, "The Influence of Gender and Somatotype on Single-Leg Upright Standing Postural Stability in Children," *J. Appl. Biomech.*, vol. 23, no. 3, pp. 173–179, Aug. 2007.

EURECA 2018 – Conference Paper
Paper number 2ME07

Design and Analysis of a Hybrid Rain Energy Harvesting System

Kiritaran Gunasegran[1] and Douglas Tong Kum Tien[1,]*

[1]School of Engineering, Faculty of Built Environment, Engineering, Technology and Design, Taylor's University, Malaysia.

Abstract. The increase in cost of non-renewable energies have kickstarted the race to find a cheaper and clean alternative energy source. Being in the equatorial region, Malaysia is blessed with abundance of rainfall which have yet been tapped as a form of renewable energy. The kinetic and potential energy from the rain can be harvested via piezoelectric crystals and via mini-hydro turbines respectively. Energy generation potential of the hybrid rain energy harvesting system in residential and commercial buildings is evaluated. A study on the piezoelectric was done on existing journals to create the optimal design which give the highest yield. Simulations through Computational Fluid Dynamics (CFD) and Excel were carried out for the mini-turbines on both residential and commercial buildings. The results attained showed that residential buildings were able to generate power up to 30 kW while commercial buildings were able to generate power up to 3102 kW. The power generation potential in buildings have been shown.

Introduction

In the 21st century, a 20-fold increase of energy consumption has been realized. This phenomenon can be closely affiliated to the dramatic increase of the human population [1]. The International Energy Agency (IEA) predicts that the thirst for energy will rise by approximately 52 % in 20 years' time while the World Energy Council estimates an increase by 100 %. In addition, more than 80 % of the world's energy is contributed by fossil fuels in the form of coal, crude oil, gas and nuclear energy [2]. As a counter measure, the European Union (EU) have revised their policy to shift the energy generation away from fossil fuels by focusing on renewable energy resources, biomass-waste, hydroelectric, solar, wind and geothermal [3]. Renewable energy arises as the only key to fight climate change and rapid depletion of resources [4]."The problem is not that we are running out of energy. It's that we have nearly run out of the low-cost energy that has fueled the industrial development of today's rich countries and has shaped the expectations of the poor ones", the phrase clearly depicts the lives of humans whom are dependent on energy [5]. In a report released by the World Energy Council on 2016, fuel and coal accounts to 32.9 % and 30 % of the total global energy consumption as they are way cheaper compared to the other sources [6]. These energy sources contribute to huge amount of air pollution and high rate of carbon dioxide emissions. The Energy Council clarifies that the rate of improvements towards cleaner sources of energy is very slow. [6] In Malaysia, renewable energy source contributes 15 % to the annual electric power supplied. Based on the data obtained from Energy Commission Malaysia, 14 % of the power comes from hydropower [7]. Harvesting energy from rainfall however is a potential that was not tapped in Malaysia. Can energy from rainfall be harvested in Malaysia? How efficient will it be? Malaysia is blessed with abundance of rainfall; at instances reaching up to 400 mm monthly. Based on the data obtained from the Metrological Department of Malaysia, the average rainfall accumulates to 250 mm monthly [8]. The kinetic and potential energy from the rain can be harvested via piezoelectric and mini-hydro turbines respectively. Figure 1 shows the integration of the kinetic energy and potential energy that will be harvested.

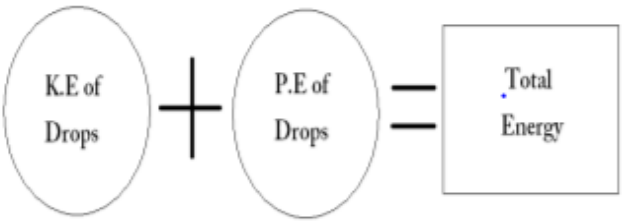


Figure 1: Energy Conversion [9]

Integration of piezoelectric and micro-hydro turbines into a system will enable to maximize the current generated from the rainfall. Commercial and residential buildings can be fixed with the system so that everyone is able to micro generate electricity during the rain.

Miceli et al. [10] have conducted a study on the effect of rainfall on the piezoelectric transducers. The aim of the experiment is to create a complete characterization on the supplied power from a drop of rain. The Polyvinylidene Difluoride (PVDF) easily undergoes elastic deformation compared to the Lead Zirconate Titanate (PZT). The higher the deformation rate, the higher the current output. Viola et al. [11] conducted an experiment to limit the optimistic

forecast of rain pattern and the behavior of transducers; piezoelectric plate. Viola claimed that the highest recorded voltage generated was 6V while the height of rainfall was not disclosed. Wong et al. [12] conducted a study on the intensity of rain and how it affects the energy generated by the piezoelectric plate. The intensity of rain was simulated in three ways; light, moderate and heavy. The different rains produced 38.89 µJ, 52.05 µJ, and 114.68 µJ respectively. For the period of 5 minutes, the maximum energy produced was about 115 µJ [12]. Ong et al. [13] has proposed a new design for maximizing the rainfall energy through piezoelectric beams. The rain rate at 33 mm/h and 99 mm/h shows an improvement by more than 400% while the others show more than 200%. Wong et al [14] has conducted a similar study on the performance of a piezoelectric energy harvester in an actual rain to provide practical insights on the implementation. This was an extension study based on his previous works in Wong et al. [12] and Ong et al. [13]. The experiment was conducted in three different rain timing which were 250min, 204min and 301min. The energy attained from these experiments were 155µJ, 438.9µJ, and 2076 µJ respectively. Paish [15] has published a journal on the different types of turbines, the new innovation and the challenges for further developments. For systems that have a higher head or height, the Pelton or Turgo turbine will be ideal. Shaleen Martin et al. [16] had conducted a research to harness the potential energy of the rainfall in his city, Maharastra. The study proved to be feasible as the multi-story analysed could produce 5KW of power. Chen et al. [17] conducted study on vertical axis turbines for power generation in water pipelines. Based on the initial design, he made a prototype via 3D printing and simulated in a pipe system. The flow rate of the pipe system was at 81 cubic meters per hour and the new design was able to generate 88.2 W.

Harnessing electricity from raindrops is a very delicate process. Piezoelectric crystals consist of Pi-elements which convert the kinetic energy of the raindrops to electricity when a force is applied on it. The compression of the molecular shell creates a magnetic field which causes an imbalance thus causing the flow of electrons [18]. There are multiple challenges that have to be overcome in order to successfully implement the piezoelectric plates into the system. The first challenge lies in identifying the right piezo with the ideal sensitivity. Different Pi-elements and stacking arrangement determines the maximum efficiency of energy harvested from the rain drops [19]. The next challenge is to identify the position and angle of the piezoelectric plates in order to cover a large surface area to maximize the collisions of the raindrops. Finally, the greatest challenge lies in successfully harnessing the electricity from a group of piezoelectric plates that are placed on the roofs of buildings. The next way to harness energy from rain is through potential energy. Commercial and residential buildings can act as reservoirs to store the rain water on the roof. Slanted roof designed homes and building can incorporate a gutter tank system in order to accumulate the run-off water on the top of the building. Height and the area of the infrastructure plays a vital role in the amount of energy that can be harvested. The accumulated water can be released when an ideal level of water is accumulated; micro-dam system. Micro-hydro turbines will be placed in the gutter drain pipes and will generate electricity as water hits the turbine blades [20]. Higher tank location equates to higher potential energy thus harvested energy increases. The integration of both piezo and hydro components in the system classifies it as a hybrid system. The primary target for the hybrid rain energy harvesting system is to investigate the potential of power generation in residential and commercial buildings.

Research Methodology

2.1 Piezo System

Piezo transducers functions as an energy converter where kinetic energy of a mass is converted to electrical energy. There are a few factors that have to be taken into consideration to increase the efficiency of the system.

2.1.1 Material Selection

The PI-ceramic cannot be created from base due to limited resources available in the country and also due to cost restraints. The creation of the element requires background knowledge on electrical and chemical engineering. Material selections for the ideal piezoelectric transducer is done based on extensive journal researches and on ready-available market materials.

Table 1:Piezoelectric Materials and Shapes Comparison

Research	Material	Setup	Area (mm^2)	Result
Ilyas et al. [21]	PVDF	Rectangular	325	2.5µW
Viola et al. [11]	PVDF	Cantilever Beam	500	4.5 µW
Jager et al. [19]	PVDF	Bridge Beam	300	12mW
Grinspan et al. [22]	PVDF	Solid Film	2800	0.1V
Vatansever et al. [23]	PVDF	Cantilever Beam	64	12V
Lee et al. [24]	PVDF	Cantilever Beam	1095	72.2 µW
Ahmad et al. [25]	PZT	Cantilever Beam	75	23 µW
Wong et al. [12]	PZT	Rectangular Plate	1706	3.85mW

Based on the observation of Table 1, the Polyvinylidene Difluoride (PVDF) material has been used in various researches compared to the Lead Zirconate Titanate (PZT). The PVDF material

is more commercially available compared to its counterpart, the PZT. The PVDF is also more cost effective and eco-friendly compared to the PZT as the PZT release harmful toxins over a certain period [10]. Lead are usually highly toxic where poisoning can cause body aches and affect the central nervous system [26]. Thus, it is not ideal to place in a residential and commercial buildings. Besides that, the power generated per area is also considered. Research done by Jager et al. [19] which uses PVDF is found to be the best for power generation.

2.1.2 Piezo Design

Based on Table 1, it is deduced that the Bridge Beam design is the most efficient for power generation. The bridge beam structure means that the material is supported on two sides as to the cantilever structure which is only supported on one side. The power generation is higher for the bridge design as the double support reduces the vibration of the beam when a force is acted upon it. As the first water droplet hits the beam, the bridge structure rapidly reduces its vibration which is ideal to absorb the energy from the upcoming droplets. The cantilever beam continues to vibrate after the first droplet, which causes the energy transfer from the upcoming droplets to be inefficient.

Figure 2 shows the setup of the intended piezo design. The position of the piezoelectric beam is very important as it is one-directional. This means that droplets that fall on the Z-Axis direction will generate power. Any other direction of droplets approaching the beam will least or not generate power. Surface area of the beam is also an important factor to be taken into consideration as higher exposed surface area will generate higher power during the rain.

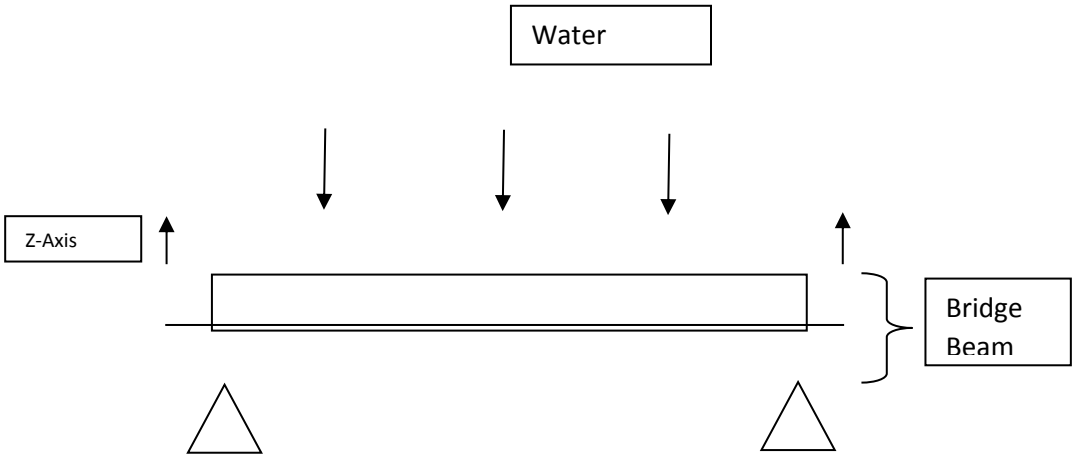


Figure 2: Bridge Beam Structure (Side View)

2.2 Turbine System

The turbine system a part of the project and it is the most important as it has the higher potential to generate more power. The turbine converts potential energy of water into electrical energy. For this system, the turbine will be used to generate energy from water flowing down the drain

pipe. There are many considerations made to choose the ideal turbine for the residential and commercial buildings. Besides that, a detailed study have been done on the system

2.1.1 Turbine Selection

Turbines can be generally classified into two different categories. One of them are reaction turbines where the turbines have better efficiency and performance in low head and high-volume flow of water. This means that the turbines are significantly effective for slow moving water which has a high discharge. Francis, Propeller and the Kaplan turbines are considered as reaction turbines. The next category of turbines is the impulse turbines. Impulse turbines are used for medium to high head water flow scenarios. Thus, the turbines depend on the velocity of flow to drive the system. Pelton, Crossflow and Turgo turbines are under this category. Figure 3 below shows the range of the turbines.

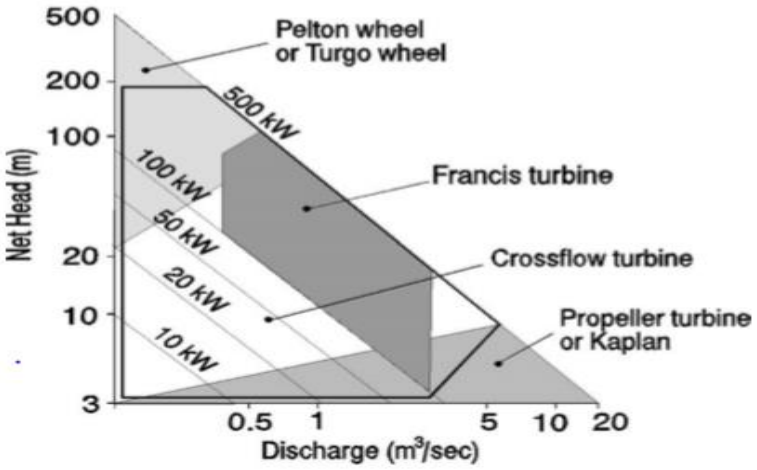


Figure 3: Turbines Selection [27]

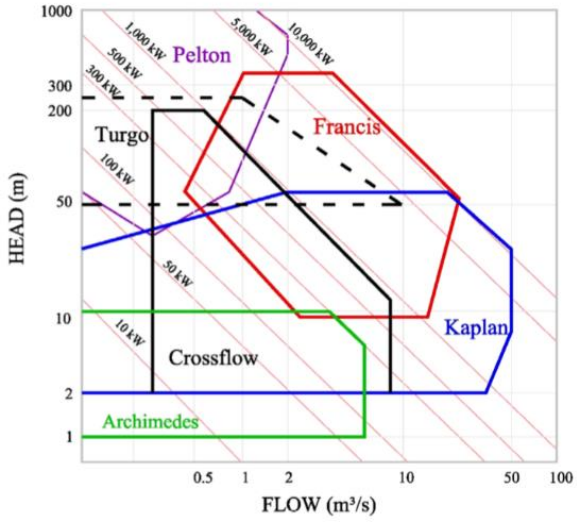


Figure 4: Head and flow rate for turbine selection [28]

For this research two different building category was investigated which are residential and commercial buildings. Data on the head of the system has been attained through extensive research along with some assumptions being made. The heights of the buildings will be taken for both residential and commercial buildings.

The values of Table 2 and Table 3 were attained through online sources and serves as a range to identify the ideal turbine type. By contrasting the height of the building alone with Figure 3, it can be concluded that the Turgo type turbine is ideal for the residential buildings (<200m) and the Pelton design turbine can be used for commercial buildings (>200). This assumption made will be validated in the results section.

Table 2: Average Residential Building Heights in Malaysia

Type of Residential Building	Height (m)
Single-storey	4.88
Double-storey	7.62
Apartment	40

Table 3: Selected Commercial Building Heights in Malaysia

Type of Commercial Building	Height (m)
Pavilion Hotel	178
Telekom Tower	310
The Exchange 106	492

2.2.1 Simulation Setup

Simulation is required for this section as there are many variables and unknowns that affect the outcome of the power generated by the turbine system. The application used to conduct the simulation are WorkBench 19, and Excel 2016. The first part of this system requires Fluent (CFD) where the outlet water velocity of the downspout pipe is calculated. The lengths of the downspout pipe (heights of residential and commercial buildings) are the manipulated variable while the constant variable that are set as in Table 4.

Based on the information from Table 2, Table 3 and Table 4, 3D models were created in the Fluent (CFD) system. The meshing done are set to smooth and the orthogonal quality of the mesh are adjusted to be more than 0.9 since the perfect quality is 1. Multizone meshing are done on the faces of the model and also inflation was applied to the inlet and outlet flow of the model.

Table 4: Constant Variable and Dimensions

Constants	Dimensions (m)
Gutter Depth (Water storage)	0.0762
Downspout Pipe Diameter	0.0762
Roughness Height of Polyvinyl chloride (PVC)	0.0015×10^{-3}

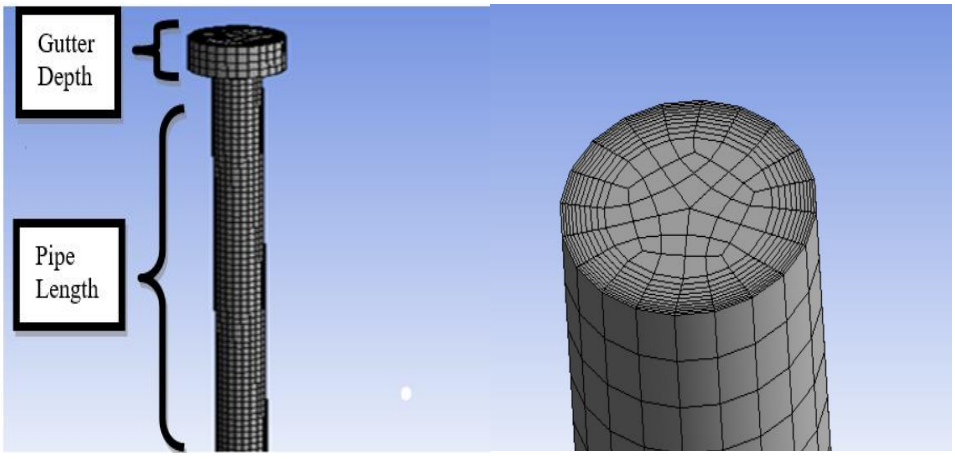


Figure 5: Multizonal and Inflation Mesh

Simulations are done based on k-epsilon model which is ideal for turbulent flow model. Continuity equation of 3D dimensional flow is used to conduct iterations. The average velocity values are then tabulated and placed in Excel for turbine equation simulation.

2.1.3 Design

Figure 6 and 7, shows the design concept of the turbine system. The dimensions used are the single-storey residential building from Table 3 and Table 4. Rain water accumulates at the gutter of a roof during the rain, once a certain height of water level is achieved, the water will be drained through the drainage pipe. The high velocity flow collides with the turbine blades and causes them to rotate and in turn generating power.

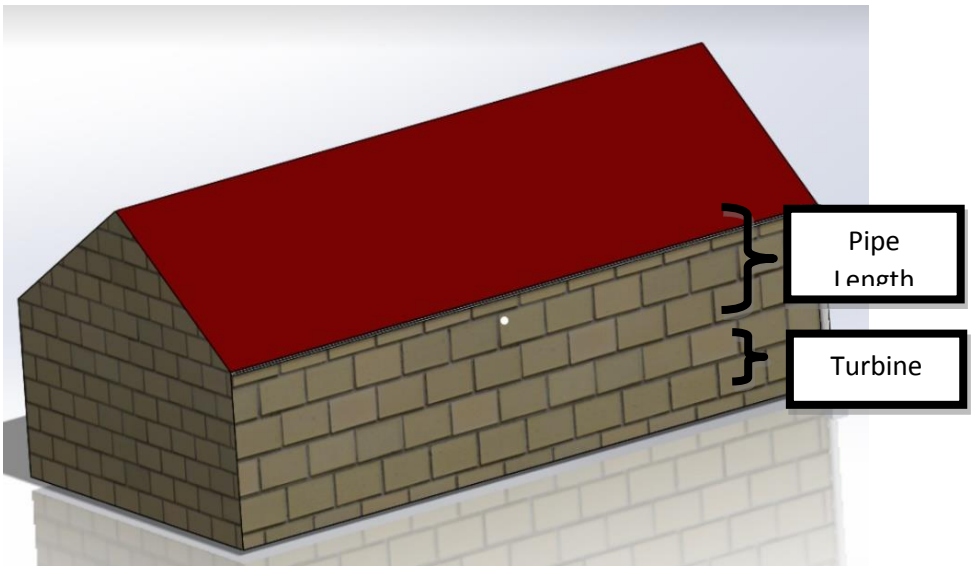


Figure 6: Turbine Placement Design on Residential Buildings

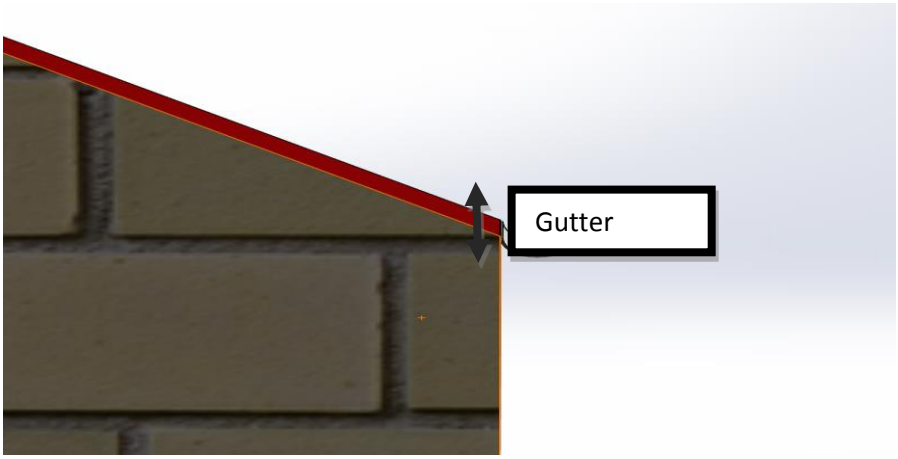


Figure 7: Gutter Design for Residential Buildings

Results and Discussion

3.1 Piezo Analysis and Power

By observation of Table 1, it was known that Jager's PVDF bridge structure piezo generated the most power in W. The piezoelectric transducer generated 12 mW over a 300 mm^2 surface area. It is assumed that the surface area of roofs is equivalent to the built area of the buildings. Thus, a simple calculation of W over area was also done.

Table 5 : Power Generation by Piezo

Type of Residential Building	Built Area (m^2)	Power Generated (W)
Single-storey	100	400
Double-storey	143	572
Apartment	325	1300
Type of Commercial Building		
Pavilion Hotel & Mall	127,000	5.08×10^5
Telekom Tower	150,000	6×10^5
The Exchange 106	453,835	1.82×10^6

The power generation in Table 5 is the maximum power that can be generated instantaneously. A few assumptions have been made in order to calculate the piezo power generation capabilities. One of the assumptions are that the built area is covered by the piezoceramics. Besides that, the intensity of rain and the mass of each droplets are assumed to be constants as there are no accurate data nor calculations to prove them. In addition, the power generation is assumed to be equivalent throughout the piezo surface area.

3.2 Turbine Analysis and Power

CFD simulation have been done in order to calculate the average velocities of water heading out the from the drain pipes. The results are tabulated and projected in graphs.

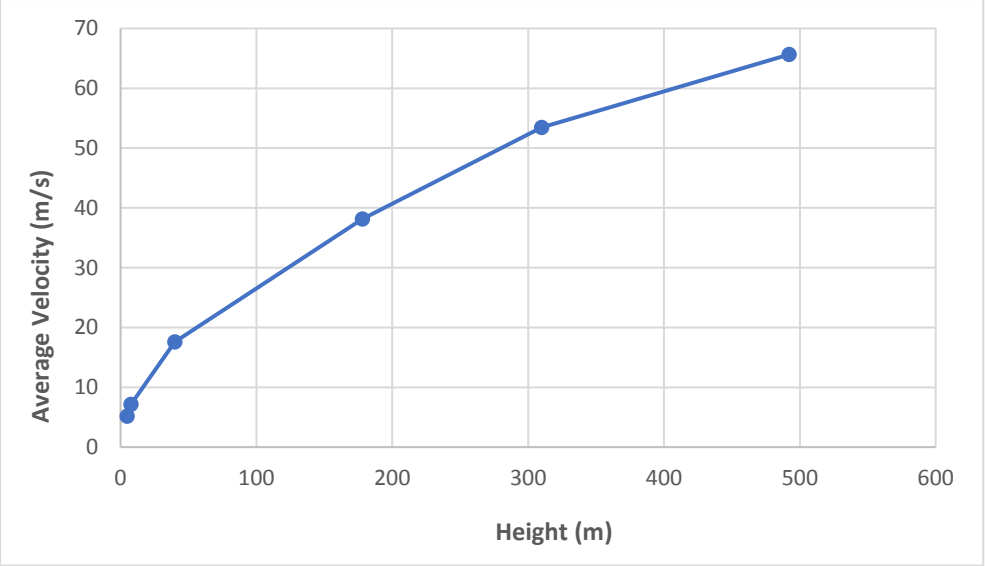


Figure 8: Graph of Average Velocity (CFD) against Height

Based on the graph above, a trend is noticed where the exiting outlet velocity of water from the drain pipe increases as length of the pipe (building height) increases. The single-storey and double-storey houses were able to generate water velocity up to 5 m/s and 7m/s. The taller commercial buildings were able to generate water velocities ranging from 38 m/s till 65 m/s.

The next value that was found was the volume flow rate. The equation of the volume flow rate is:

$$Q = \pi \times \frac{1}{4} \times (D)^2 \times V_{avg} \quad (1)$$

where Q is the flow rate, D is the diameter of downspout pipe, and ***v*** is the average velocity of the water.

The volume flow rate is required to identify the ideal type of turbine to be used for the residential and commercial buildings. As summarized from the turbine design part above, the Pelton and Turgo type are the suitable ones. Figure 2 and 3 is used to identify the ideal turbine which is either the Pelton or Turgo.

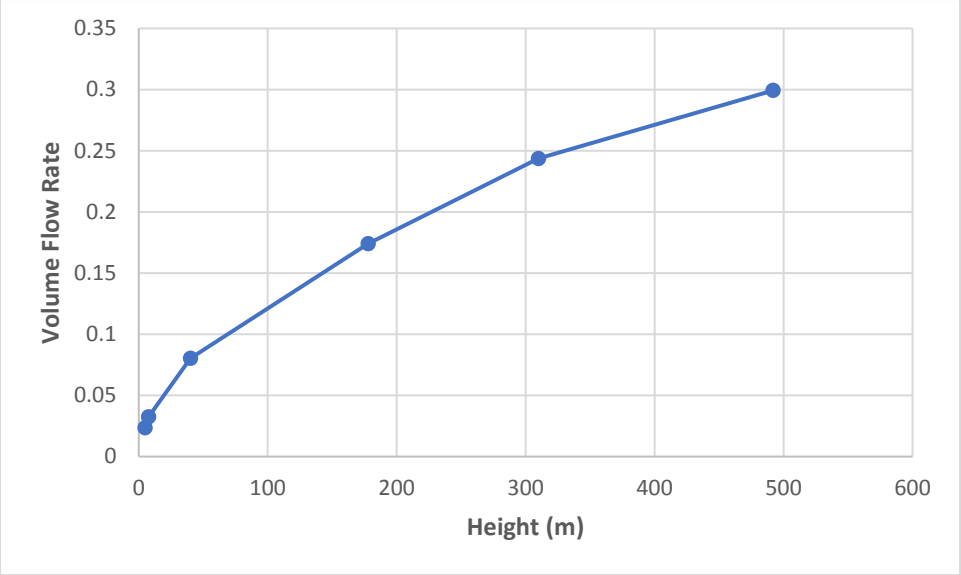


Figure 9: Graph of Volume Flow Rate against Height

Based on Figure 8, it can be observed that the volume flow rate also known as discharge rate, increases along with the height. This can be justified as the volume flow rate is affected by the outlet average velocity. Since the highest flow rate is about 0.3m^3/s, the Pelton type turbine is the most ideal turbine to be used for the Hybrid Rain Energy Harvesting System.

Power calculations were made by using the turbine power equation which is:

$$P = \eta \times \rho \times g \times Q \times h \qquad (2)$$

where P is the power generated (W), η is the efficiency of the Pelton turbine,

g is the gravitational acceleration, Q is the flow rate and h is the height.

The efficiency value of the Pelton turbine was attained from a journal that have done a performance study on Pelton micro-turbines. The Pelton turbine varies in performance due to the unsteady flow in rotating buckets in time and space [29-30]. Stamatelos et al. [31] conducted a study on the performance characteristic of a micro-hydropower Pelton turbine model in which the prototype achieved an efficiency of 86 %. Thus, the value of 86% efficiency is used for this research. The density of water used is 1000 kg/m^3 while the gravitational acceleration is 9.81 m/s^2.

The highest power generated is 1300 kW at 492 meters while the lowest generated power is 1.01kW at 4.88 meters. The potential of the energy generation in residential and commercial building can be viewed from Figure 10.

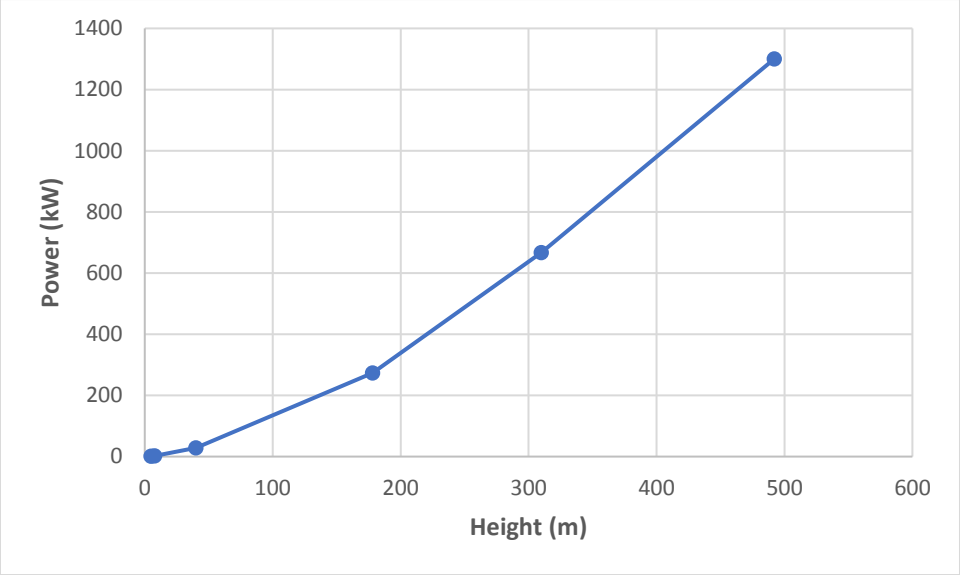


Figure 10: Graph of Power against Height

3.3 Total Power Generation

The total power that can be generated from the residential and commercial buildings with the use of the Hybrid Rain Energy Harvesting System (HREHS).

Piezoelectric Power + Turbine Power = Total Power Generation

Based on Table 6, the common residential buildings, single and double storey houses are able to generate 1.4 and 2.76 kilowatts respectively. The apartment is able to generate higher power due to its height. From Table 7, it can be deduced that the power generation in commercial buildings are very high. The values that were attained however are instantaneous. Thus, it depends on the duration and the intensity of the rain.

Table 6 : Total Power Generation in Residential Buildings

Type of Residential Building	Piezoelectric Power (kW)	Turbine Power (kW)	Total Power Generation (kW)
Single-storey	0.4	1.01	1.41
Double-storey	0.572	2.19	2.76
Apartment	1.3	28.3	29.6

Table 7: Total Power Generation in Commercial Buildings

Type of Commercial Building	Piezoelectric Power (kW)	Turbine Power (kW)	Total Power Generation (kW)
Pavilion Hotel	508	273	781
Telekom Tower	600	667	1267
The Exchange 106	1820	1300	3120

Conclusion

The cost of energy increases at an alarming rate due to high demand. This is a setback to the growth of technology and human populations. In certain countries around the world, they still lack the basic necessity supply of electricity which causes poverty among people and slow development of infrastructures. In Malaysia, the citizens are blessed with having a steady supply of electricity at a considerably low cost compared to some countries. This however does not mean that we are ensured of considerable supply of electricity in the future. The cost of power is increasing yearly as supplies are depleting. For this study, it can be concluded that microgeneration is possible in residential and commercial buildings

The aim of this study is to investigate whether integrate the piezoelectric and mini-hydro turbines components into a single functioning system and the potential of microgeneration with rain can generate power in residential and commercial buildings which have been achieved. The feasible and cost study will be carried out in further elaboration of the study.

Acknowledgements

The authors would like to deliver their sincere appreciation to the lecturers of the School of Engineering and to Taylor's University, Malaysia.

References

[1] M. Obrecht, "Evaluation and Analysis of Renewable Energy Sources Potential in Slovenia and its Compatibility Examination with Slovenian National Renewable Energy Action Plan," World Renewable Energy Congress–Sweden, (2011).

[2] M. Richter, "Utilities Business Models for Renewable Energy: Sustainability Management (CSM)," World Renewable Energy Congress- Sweden, (2011).

[3] Y. Krozer, "Cost and Benefit of Renewable Energy in Europe," pp. 60-68, (2011).

[4] W. S. Alan, C. Brent, " Development of the Sustainable Technology Balance Sheet (STBS) - A Generic Method to Assess the Sustainability of Renewable Energy Technologies," (2011).

[5] J. P. Holdren, "Population and the Energy Problem Population and Environment: A Journal of Interdisciplinary Studies," vol. **3**. (1991)

[6] "World Energy Resources", World Energy Council. (2016)

[7] "Small Renewable Energy Program," Energy Commission of Malaysia. (2011)

[8] "Malaysian Meteorological Department," [Online]. Available: http://www.met.gov.my/in/web/metmalaysia/climate/climatechange/climateinformation/monthlyrainfallreview. [Accessed Monday August 2017].

[9] E. Jacquelin, S. Adhikari, "A piezoelectric device for impact energy harvesting". (2011)

10] R. Miceli, P. Romano, C. Spataro, F. Viola, "Performances of Rainfall Energy Harvester," Department of Energy, Information Engineering and Mathematical Models University of Palermo, Italy. (2010)

[11] F. Viola, P. Romano, R. Miceli, G. Acciari, "Piezoelectric Model of Rainfall Energy Harvester," Ninth International Conference on Ecological Vehicles and Renewable Energies (EVER). (2014)

[12] V.K Wong, J.H Ho, A.B Chai, "Piezoelectric Energy Harvesting in Varying Simulated Rain Conditions," ARPN Journal of Engineering and Applied Sciences, vol. **11**. (2016)

[13] Z.Z Ong, V.K Wong, J.H Ho, "Performance Enhancement of a Piezoelectric Rain Energy Harvester," Sensor and Actuators A, Physical, Department of Mechanical, Materials and Manufacturing Engineering, Nottingham University, Malaysia. (2016)

[14] V. K. Wong, J.H. Ho, A.B Chai, "Performance of a Piezoelectric Energy Harvester in Actual Rain," Energy Journal, Department of Mechanical, Materials and Manufacturing Engineering, Nottingham University, Malaysia. (2017)

[15] O. Paish, "Small Hydro Power: Technology and Current Status," Renewable and Sustainable Energy Reviews, vol **6**. (2002)

[16] M. Sharleen, K. Shrivastava, "Feasibility of Rainwater Harvesting in High Rise Building for Power Generation". (2010)

[17] J. Chen, M. Lo, "A Novel Vertical Axis Water Turbine for Power Generation from Water Pipelines." Energy Journal. (2012)

[18] T. Jager, R. Guigon, J. Chaillout, "Harvesting raindrop energy: theory". (2008)

[19] T. Jager, R. Guigon, J. Chaillout, G. Despesse, "Harvesting raindrop energy: experimental study". (2008)

[20] R. Nathan, "Reconnaissance Study to Identify Micro Hydro Potential Sites in Malaysia," Department of Mechanical Engineering Universiti Tenaga Nasional. (2010)

[21] M.A. Ilyas, Jonathan Swingler, "Piezoelectric Energy Harvesting from Raindrop Impacts", Energy Journal, School of Engineering and Physical Sciences, Heriot-Watt University, United Kingdom. (2017)

[22]. A. S Grinspan and R. Gnanamoorthy, Colloids Surf. A 356, 162 (2010).

[23] D. Vatansever, R.L. Hadimani, T. Shah, and E. Siores, Smart Mater. Struct. 20, (2011).

[24] Y.R. Lee, J.H. Shin, I.S. Park, and S.K. Chung, IEEE 27th International Conference on MENS (2014).

[25] M. Al Ahmad, JEM **43**, 452–458 (2014).

[26] Gordon JN, Taylor A, Bennette PN, Br J Clin Pharmacol, **53**:451 (2002)

[27] L. Barelli, L Liucci, A. Ottaviano, D. Valigi, "Mini-hydro: a design approach in case of torrential rivers", Energy. (2013)

[28] P. Fraenkel, O. Paish, V. Bokalders, A. Harvey, A. Brown, R. Edwards, "Micro-hydro power: a guide for development workers", London: IT Publications.

[29] SJ Williamson, BH Stark, JD Booker, "Performance of a low-head pico-hydro turgo turbine. Appl. Energy,**102**:1114–26. (2013)

[30] SJ Williamson, BH Stark, JD Booker, “Experimental optimisation of a low-head pico hydro turgo turbine”, IEEE international conference on sustainable energy technologies;

p. 322–7. (2013)

[31] FG Stamatelos, JS Anagnostopoulos, DE Papantonis, “Performance measurements on a Pelton turbine model”. Proc Inst Mech Eng Part A: J Power Energy p 225-351. (2011)

Conceptual Design of a Compact Integrated Tire Rim Storage and Retrieval System

Varen Lau Rui Hang[10], *Chou Pui May*[1], *and Jonathan Lim Shiang Chin*[2]

[1]School of Engineering, Taylor's University Lakeside Campus, 46500, Malaysia
[2]Head of Department, Continental Tyre Technology Centre, 46050, Malaysia

Abstract

Manual Retrieval of tire rim poses a risk of injury especially to the backbone of the operators. Moreover, manual handling requires more workers and thus increases labour cost. The main objective of the present study is to design and develop a conceptual design of a compact rim storage system that can improve accessibility and safety. SolidWorks was used to produce 3D design model of the retrieval system. The feasibility and reliability of the retrieval system were check through numerical simulation (ANSYS) to ensure that the design is safe to be used. The results obtained from static analyses were used to identify the retrieval model that fits the retrieval criteria include safety and sustainable.

Keywords: Retrieval system, Lifting mechanism, safe

[10] Corresponding author: varenlau24@gmail.com

1 Introduction

There are five types of warehouse storage systems, namely pallet racking, multi-tier racking, shelving, mezzanine flooring and mobile shelving. Amongst all the storage systems, pallet rack is the most common rack used in warehouse to store pallets. The main advantage of using steel pallet rack is space-saving. Due to its design in vertical space, it does not occupy much space and thus results in a greater storage capacity. By vertical space, the pallets can be easily store and placed down by using forklifts. Another advantage of using pallet rack is the increase in productivity due to the convenience to retrieve and place down with lifting devices [1].

In the late 1915s, forklift has been announced [2]. In terms of warehouse and pallet rack, the forklift becomes popular which mostly used in warehouse storage application. The forklift concept is widely used in the first quarter of the 20th century. With presence of forklifts, majority of the pallets can be moved regardless to the weight of each individual box. This promotes fast loading and unloading of pallets, and subsequently increases the productivity. Instead of carrying each individual product manually by the workers, the forklift is capable of lifting the entire pallets in a shorter time. As technology advanced, the forklift is capable of lifting products up to several meters in height. Nonetheless, forklift is not suitable to be used in narrow aisle space as it requires ample space to move and change direction.

As modern technology continuously growth in 1950s, an automated storage and retrieval system (AS/RS) are introduced in warehouse to retrieve products in storage and production environments [3]. AS/RS is normally installed around the rack served by cranes moving through aisle between racks. This AS/RS system is fully automated, thus it does not require operator to control it [3]. The advantages of using AS/RS include the reduction in labour cost, and the increase in efficiency and productivity. However, it AS/RS is not commonly used in every industry due to its high investment cost.

Currently, there are two methods to retrieve or placed down tyre rim, that are either using overhead hoist or manually retrieval. The use of overhead hoist requires electricity to run the motor if there is any power failure, manual handling will take place. On the other hand, manual handling requires more workers and thus increasing the labour cost. Moreover, current retrieval system is inconvenience to the user and poses hazardous risk. The maximum weight of a normal tire rim is 70 kg, which difficulty for the operators to retrieve from the rack.

The main objective is to develop a conceptual design of a compact rim storage and retrieval system that can improve the accessibility. The outcome of customized retrieval system has to be convenient, user-friendly and safe. The feasibility and reliability of the design were investigated numerical analysis (ANSYS). In addition, analytical calculations were included to ensure the efficiency of the lifting mechanism. Risk can be minimized through engineering theory and simulation

2 Research Methodology

Background study on storage rack system was performed to identify each specification and limitation. The theoretical efficiency for each lifting mechanism was calculated and compared its characteristics. The 3D model of retrieval system was created through SolidWorks software. The selected lifting mechanism was applied in designing the retrieval system model. Further, the current rack design was modified through SolidWorks software.

The static structural analysis of the model was conducted using ANSYS 18.0. The model development was accomplished through six stages, namely material selection, geometry, meshing, boundary conditions, loading and output analysis. In numerical simulation, the geometry of the rack was tested in terms of total deformation, equivalent stress and strain. The

location of maximum stress or deformation induced in each geometry was identified through the ability of contour. The simulation includes a quantitative study whilst the results should meet the expectation. If the numerical results prove and satisfied, the design ready for finalized.

2.1 Lifting Mechanisms

There are few criteria to be considered in selecting lifting mechanism as the main operator in retrieval system to solve the current challenges. The advantages and disadvantages of each lifting mechanism are tabulated in Table 1. Decision matrix is tabulated in Table 2 to determine the best lifting mechanism. The rating of each criteria ranges from 1 (less performances) to 3 (high performances). The criteria included cost, efficiency, user friendly, safety and sustainability which used to finalized the lifting mechanisms.

Table *1*: Advantage and disadvantage of lifting mechanisms

	Hydraulic Lift	**Worm Gear**	**Rack and Pinion**
Advantage	-allow to lift heavy machinery -durable -lessen operating time	-self-locking -speed reducer -compact size	-inexpensive -compact -robust
Disadvantage	-contain high pressure fluid (flammable)	-high gearing friction -gearing mechanism will produce noise	-more required force to operate -constant wear

Table *2*: Decision matrix of lifting mechanisms

Criteria	**Hydraulic Lift**	**Worm Gear**	**Rack and Pinion**
Cost	2	1	3
Efficiency	3	2	1
User Friendly	2	3	1
Safety	1	3	2
Sustainability	2	3	1
TOTAL	**10**	**12**	**8**

The functionality of worm gear has self-locking ability which prevents gear in back driving. By having this ability, lifted load can be avoided from sliding down from high position. For worm gear and rack and pinion have to consistency add lubricant between gear tooth to

minimized friction in gearing. Moreover, hydraulic lift has lessened operating time and able to lift heavy machinery. However, inside piston has pressurized fluid which easier to explode and not recommended used in warehouse. Hydraulic lift has less sustainable due to pressurized fluid have to renew to ensure there is no cavitation and maintain viscosity. Rack and pinion has less operating cost however it has larger friction therefore more effort required. Due to friction, constant wear high possibility happened and needing replacement after a certain time.

Each lifting mechanism was rated based on each functionality, as listed in Table 2. The lifting mechanism with the highest rating was selected and used it as main operator for retrieval system. To summarize, worm gear is preferable as lifting device because it exhibits higher performance compact to other ideas. Through the project, theoretical calculation of each lifting mechanisms was carried out to analyze the performance of lifting mechanisms. Through theoretical lifting mechanisms calculation, the output analysis included mechanical advantage and minimum effort.

2.2 Fork Simulations

2.2.1 Effect of fork's blades

Table *3*: Advantage and disadvantage of fork's blades

	2 blades	**3 blades**
Advantage	-low manufacturing cost -light weight	-more stability during handling -available to handle small dimension objects -Less induced stress applied on surface
Disadvantage	-unavailable handling small dimension objects -higher chance of fatigue fracture due to vibration	-heavy -high manufacturing cost

A good parameter and fork design provides safety during retrieving. In this experiment, two types of blade geometry, *i.e.,* 2-bladed and 3-bladed fork were simulated and compared. Based on Table 3, 3-bladed has preferable due to it greater stability during handling, capability to handle small object and less induced stress. Although 2-bladed fork is lighter in weight but it is unable to handle small object whilst resulting in a higher chance of fatigue fracture due to vibration.

The geometry of the fork's blade was designed through SolidWorks and put inside ANSYS 18.0 for numerical simulation. The objective of this experiment is to identify the equivalent stress and total deformation of each type of fork. In meshing, the mesh method using tetrahedral elements of several element size, with refinement applied at the edge of fork surface.

This differential meshing will increase the efficiency and thus reduces computational time. In addition, as stated in finite element theory, using different sizing element would cause different results. In order to solve the challenges, there are 10 sets of element size to prove accurate output analysis.

The maximum weight of a tire rim is 70 kg which applies a force of 686.7 N distributed on both the forks evenly. In the end of experiment, total deformation, equivalent stress, equivalent strain and safety factor were examined on solving the model. Color contour plots, numerical tabulation and graphs were developed to assists in the evaluation of data output.

2.2.2 Effect of fork thickness

There are total five different fork thickness which are 5mm, 10mm, 15mm, 20mm and 25mm used for numerical simulation. All the forks have using structural steel as material in numerical simulation. The objective of this experiment is to identify equivalent stress and total deformation on different fork thickness. In meshing, the mesh method using tetrahedral elements of several element size, with refinement applied at the edge of fork surface. This differential meshing will increase the efficiency and thus reduces computational time. In order to improve results accuracy, there are 10 sets of element size to prove accurate output analysis.

In this experiment, the loading condition remains the same which applies a force of 686.7 N on both the forks evenly. In the end of experiment, the output analysis should contain total deformation, equivalent stress, equivalent strain and safety factor in order on solving the model. There are two common failures in fork: sudden fracture due to heavy load and fatigue fracture due to vibration during the travelling. Therefore, the equivalent stress analysis will mainly target in this experiment.

2.2.3 Effect of fork material

Table *4*: Advantage and disadvantage of different materials

	Stainless Steel	**Structural Steel**	**Aluminum Alloy**
Advantage	-durable	-flexible	-light weight
	-resistance to water damage	-relatively cheap	-high corrosion resistant
	-nonporous	-durable	-non-magnetic
		-withstand external pressure	-better heat dissipation/conduction
Disadvantage	-expensive	-easier to corrosion	-expensive
	-inability to attach magnet	-high maintenance	-abrasive to tooling
			-difficult to reshape if damage

-high efficiency in conducting heat	costs (re-painted) -high expansion rates

In this experiment, there are three types of materials have been simulating to determine materials efficiency in retrieval system. Besides numerical results from ANSYS, the criteria of selecting materials for fork has been consider in manufacturing cost and material physical properties. Material selection is important in design stage, a failure might happen through bad quality or properties of fork's material. Table 4 shows the pro and cons of different material as a guidance before goes to numerical analysis.

Three different fork materials, namely stainless steel, structural steel and aluminum alloy used for numerical simulation. The dimension of the fork geometry remaining the same. The objective of this experiment is to identify the equivalent stress and total deformation on effect of materials. In meshing, the mesh method using tetrahedral elements of several element size, with refinement applied at the edge of fork surface. This differential meshing will increase the efficiency and thus reduces computational time. In order to improve results accuracy, there are 10 sets of element size to capture the accuracy results.

In this experiment, the loading condition remains the same which applies a force of 686.7 N on both the forks evenly. In the end of experiment, the output analysis should contain total deformation, equivalent stress, equivalent strain and safety factor in order on solving the model.

2.3 Modified Rack Simulations

2.3.1 Hook analysis

There are two types of hook surface have been simulating to determine which surface has more efficient in handling tire rim which are circular and rectangle surface. A normal rim has 225 mm x 410 mm as reference dimension, the hook model design in half circular shape in order to fit rim tire. Each tire rim handle by a pair of hook. In addition, the hook has mobility function therefore it can used for different rim size. The drawings can be created through SolidWorks in terms of part and assemblies.

The objective of this experiment is to identify equivalent stress and total deformation on effect of hook surface. The location of maximum stress and strain induced can determined through the contour. In this experiment, the loading condition remain same which applies a force of 686.7 N on both hook evenly. Both circular and rectangle hook applied structural steel as materials. In the end of experiment, the output analysis should contain total deformation, equivalent stress, equivalent strain and safety factor in order on solving the model.

3 Results and Discussions

Section 3.1 presents the calculation for determining the efficiency of worm gear design at different lead angles. On the other hand, the calculations for the designed worm gear which is used as lifting mechanism, are presented in Section 3.2. Section 3.3 presents numerical analysis of different compartment of the design included lifting device and rack through ANSYS 18.0 software.

3.1 Theoretical analysis on worm gear as lifting mechanism

3.1.1 Calculation of efficiency at 5° lead angle

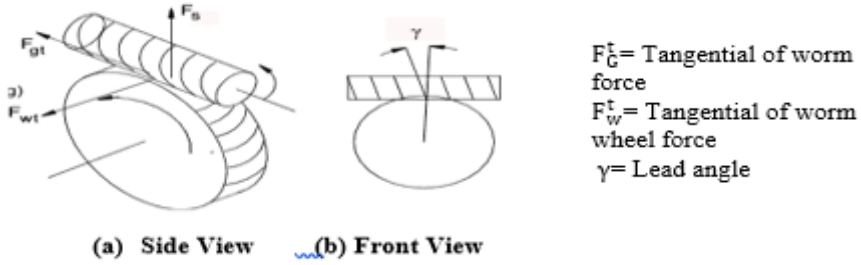


Figure 1: Forces acting on worm and worm wheel [4]

Table*5*: Parameter used for calculation

Worm diameter, d	120 mm / 4.716 in [4]
Rotating speed, n_w	18 rpm [4]
Normal pressure angle, $\emptyset_n$	20°
Lead angle, γ	5° , 25°

The sliding velocity of the worm at the pitch cylinder:

$$V_s = \frac{\pi d n_w}{12 \cos \gamma} \quad (1)$$

$$V_s = \frac{\pi \times 4.716 \times 18}{12 \cos 5°}$$

$$V_s = 22.3 \text{ ft min}^{-1}$$

The coefficient of friction calculated from Eq. (2):

$$f = 0.103e[-0.110(V_s)^{0.45}] + 0.012 \quad (2)$$

$$f = 0.103e[-0.11(22.3)^{0.45}] + 0.012$$

$$f = 0.078$$

The efficiency of worm gear at 5° lead angle calculated from Eq. (3):

$$\eta = \frac{\cos \emptyset_n - f \tan \gamma}{\cos \emptyset_n + f \cot \gamma} \quad (3)$$

$$\eta = \frac{\cos 20° - 0.078 \tan 5°}{\cos 20° + 0.078 \cot 5°}$$

$$\eta = 0.51$$

3.1.2 Calculation of efficiency at 25°

The sliding velocity of the worm at the pitch cylinder calculated from Eq. (4):

$$V_s = \frac{\pi d n_w}{12 \cos \gamma} \quad (4)$$

$$V_s = \frac{\pi \times 4.72 \times 18}{12 \cos 25°}$$

$$V_s = 24.5 \text{ ft min}^{-1}$$

The coefficient of friction from Eq. (2):

$$f = 0.103e[-0.11(24.5)^{0.45}] + 0.012$$

$$f = 0.076$$

The efficiency of worm gear at 25° lead angle is given by:

$$\eta = \frac{\cos 20° - 0.076 \tan 25°}{\cos 20° + 0.076 \cot 25°}$$

$$\eta = 0.82$$

The parameter was referenced from Tamboli (2015) and used to calculate gear performance as shown in Table 6. To justify its statement, 5° and 25° of lead angle chosen to calculate efficiency. There is standard normal pressure angle of 20° used in calculation. 5° of lead angle has efficiency of 0.51 while 25° of lead angle given efficiency of 0.82.

Therefore, the efficiency of worm gear depends on the lead angle and coefficient of friction. It concludes that in order to achieve high efficiency of worm gear, it is recommended to use lead angle between 15° to 30° [5]. By comparing two different lead angles, efficiency equation shows the 25° lead angle has higher efficiency than 5° which prove the journal statement. Therefore, lead angle will choose between 15° to 30° to design gear system.

It's has proposed that the self-locking property can be achieved through a pair of worm gear which connected to each other in mesh pattern [5]. The advantage of mesh connection is simple and robust in construction. The efficiency of worm pair mesh pattern results in 90% whereas the conventional system efficiency only 40% [5]. Therefore, the efficiency of worm gear depends on the lead angle and coefficient of friction.

3.2 Analysis on designed worm gear

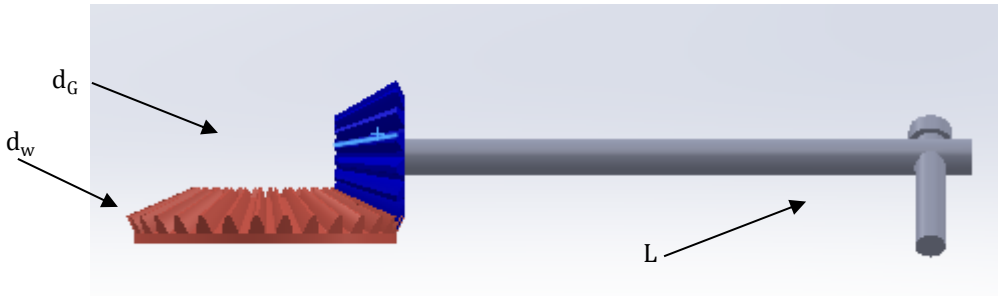


Figure *2*: Design of worm gear

Table *6*: Design parameters

Diameter of worm wheel, d_W	0.26 m
Diameter of worm, d_G	0.16 m
Load, m	70 kg
Length of handle, L	1.1 m
Lead angle, γ	25°
Normal pressure angle, $\emptyset_n$	20°

To calculate torque on worm wheel by using Eq. (5):

$$\mathrm{T} = \mathrm{Force} \times \mathrm{distance} \tag{5}$$

$$\mathrm{T} = (70 \times 9.81) \times \frac{0.26}{2}$$

$$\mathrm{T} = 89.27\ \mathrm{Nm}$$

To calculate minimum force to rotate worm by using Eq. (6):

$$\mathrm{Torque\ of\ worm} = \mathrm{Torque\ of\ worm\ wheel}$$

$$89.27 = \mathrm{F_{min}} \times \frac{1.1}{2}$$

$$\mathrm{F_{min}} = 162.31\ \mathrm{N}$$

Mechanical advantage:

$$\mathrm{MA} = \frac{686.7\ \mathrm{N}}{162.31\ \mathrm{N}}$$

$$\mathrm{MA} = 4.23$$

The results show mechanical advantage of worm gear is 4.23 which has greater benefits in lifting device. In addition, mechanical advantage greater than 1 indicates little muscle effort required to lift heavy load. The effort required to lift 70 kg load is 162.31 N. The effort and torque have optimized by varying each component parameter in numerical analysis section.

Worm gear used in most lifting devices due to its advantage over other lifting system such as higher efficiency, simple construction and compactness. Furthermore, it has ability of self-locking system which allows the input member (worm) to rotate output member (worm wheel) in either direction however it doesn't allow the output member to rotate or generate input member when input member removed [6]. This self-locking ability ensured operator safety during lifting and it can prevents lifted load falling from height when force applied on the input member is removed. To prevent lifted load moving in reverse direction (back driving), self -locking gears recommended. Besides that, another function of this mechanism is able to convert rotary motion into rectilinear motion.

3.3 Numerical Analysis on Design

3.3.1 Modelling of design using SolidWorks

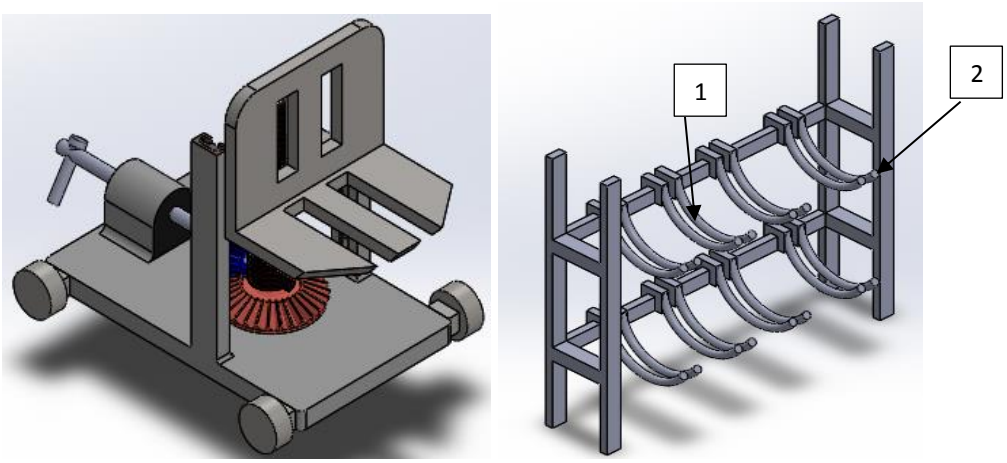


Figure *3.* Design of retrieval system & modified rack

Figure 3 shows the assembly of fork with lifting mechanism. The sharp edges of blades design are filtered out to reduce stress-concentration. The inner heel is given a fillet radius than the outer heel in order to achieve greater rigidity. The modified rack used to handle tire rim, each tire rim has holding by a pair of hook. Part 1 represents movable hook design whilst part 2 represents rack's frame which design in hollow and solid shape for numerical analyzed.

3.3.2 Effect of fork blades

Table *9* Results of different fork's blades

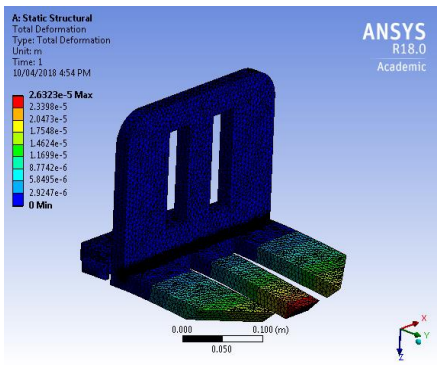
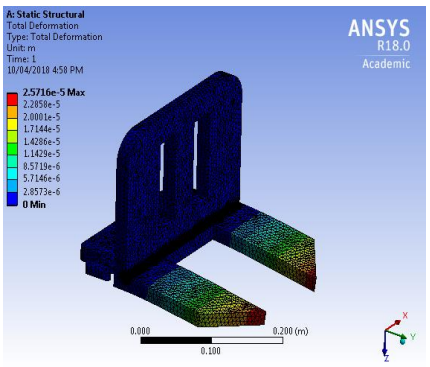
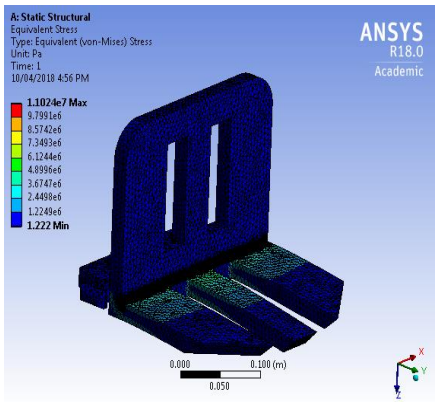
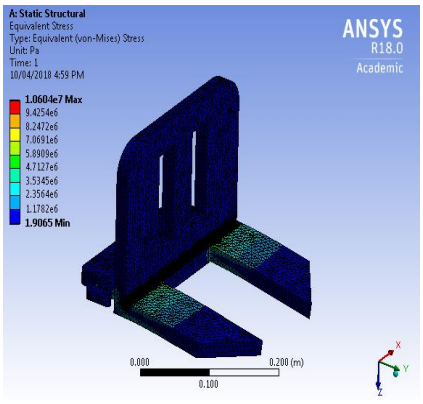
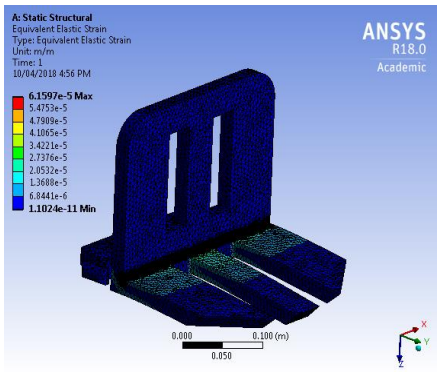
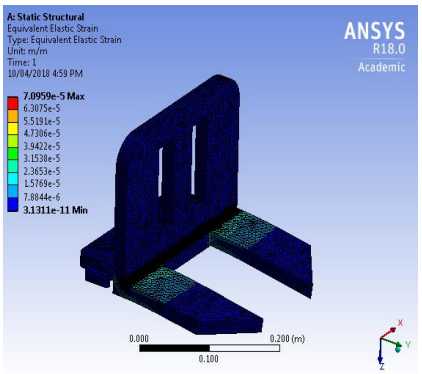
	3-bladed	2-bladed
Total deformation		
	Max Total Deformation =2.626 x 10^{-5} m	Max Total Deformation =2.56 x 10^{-5} m
Equivalent stress		
	Max Equivalent Stress = 49.09 MPa	Max Equivalent Stress = 61.83 MPa
Elastic strain		
	Max Elastic Strain = 5.988 x 10^{-5} m/m	Max Elastic Strain = 6.447 x 10^{-5} m/m

Table 9 presents the total deformation, equivalent stress & elastic strain of 3-blade & 2-bladed fork designs, when a 70 kg load was applied on the blade surface. Maximum stress was observed at the heel of fork where fracture will normally occur. The remaining areas are

relatively stress free. Maximum deformation was found at the far end of the blades. There was little strain observed at the heel of fork for both cases.

The results show that 3-bladed has less equivalent stress than 2-bladed which may minimize fatigue fracture when traveling, as expected. The maximum equivalent stress of 3 blades was 49.09 MPa. In addition, the maximum total deformation was observed to be 2.6262 x 10^{-5} m and maximum elastic strain was 5.988 x 10^{-5} m/m for 3-bladed. The elastic strain for 3-bladed less than 2-bladed. 3-bladed was selected due to lesser equivalent stress during handling a 70 kg tire rim. In addition, 3-bladed use as reference geometry for coming numerical analysis.

3.3.3 Effect of fork thickness

Table *10*: Results of fork thickness

Change in thickness, (mm)	Equivalent stress, (MPa)	Equivalent Strain, (m/m)	Total Deformation, (m)	Safety Factor
5	85.09	5.988 x 10^{-5}	2.626 x 10^{-6}	2.17
10	58.45	3.599 x 10^{-5}	8.333 x 10^{-6}	2.29
15	49.09	2.735 x 10^{-5}	3.751 x 10^{-6}	2.64
20	46.15	2.353 x 10^{-5}	2.381 x 10^{-6}	2.81
25	42.44	2.151 x 10^{-5}	2.084 x 10^{-6}	2.94

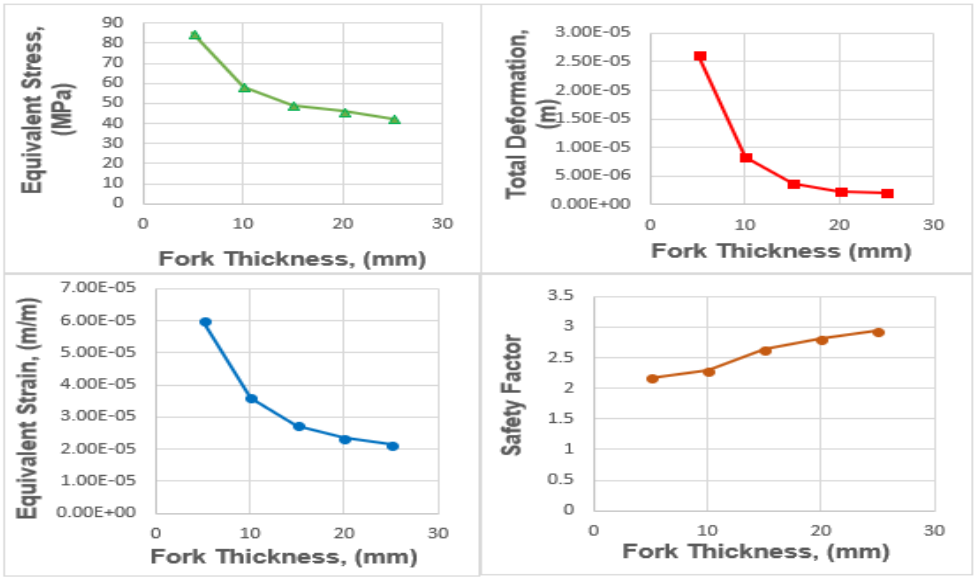


Figure 35: Effect of variable in fork thickness on the results observed (data taken from table 10)

The thickness of the fork is an important criterion to consider in designing stage. From Figure 4, as the thickness increases, strain, stress and total deformation decreases. But increases in thickness will increases weight therefore the manufacturing cost of the fork increases. The smaller thickness might happen sudden fracture during handling. The thickness of fork increase, the equivalent stress has less than ultimate tensile strength.

Factor of safety increases gradually when increases fork thickness. Table 10 shows the range of safety factor around 2.1 to 2.94 which are safe. Thus, it might be better and beneficial to go for a greater thickness which would provide reliability, sustainability even though the cost would be higher.

3.3.4 Effect of fork materials

Table *11*: Comparison of stainless steel, aluminum alloy and structural steel with all dimensions of the folk remaining same

Material	Equivalent stress, (MPa)	Total deformation, (m)	Elastic strain, (m/m)
Structural Steel	49.09	2.6262×10^{-5}	5.988×10^{-5}
Aluminum Alloy	96.83	7.3735×10^{-5}	1.6519×10^{-4}
Stainless Steel	49.63	2.7215×10^{-5}	6.1637×10^{-5}

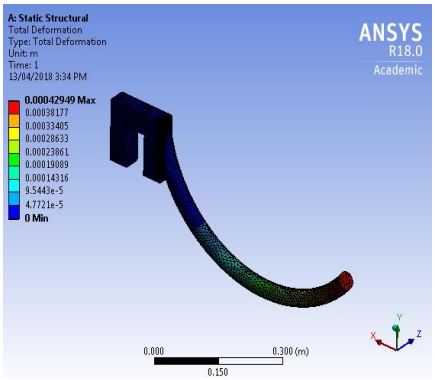
Table 11 shows the fork has been analyzed through different materials which are structural steel, aluminum alloy and stainless steel. The results state structural steel has least equivalent stress (49.086 MPa) and smallest total deformation (2.6262×10^{-5} m) among other materials. In addition, the structural steel has least elastic strain (5.988×10^{-5}m/m). Aluminum alloy has highest equivalent stress among other materials which has 96.832 MPa. Moreover, aluminum alloy has highest total deformation compared to others. Aluminum alloy is light and easier to machine while structural steel and stainless steel are heavier. Despite of aluminum alloy was cost effectiveness among all the materials but it has highest induced stress and total deformation. Therefore, structural steel will preferable as fork materials.

3.3.5 Effect of hook surface

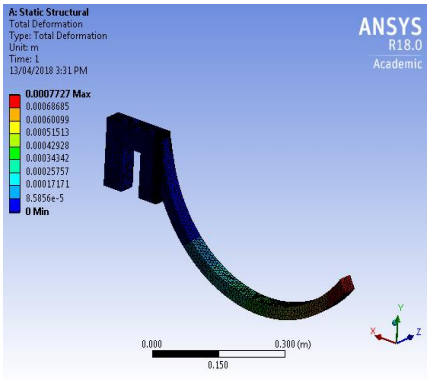
Table *12*: Results of circular and rectangular hook surface

Circular	Rectangular

Total deformation

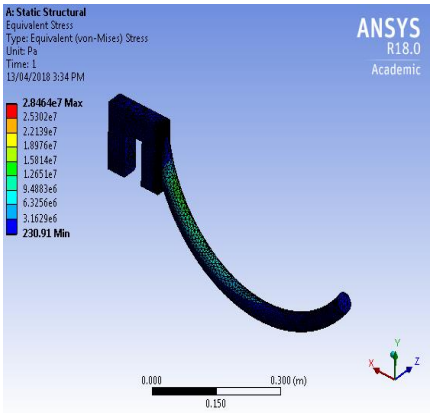


Max Deformation = 4.1570 x 10^{-4} m

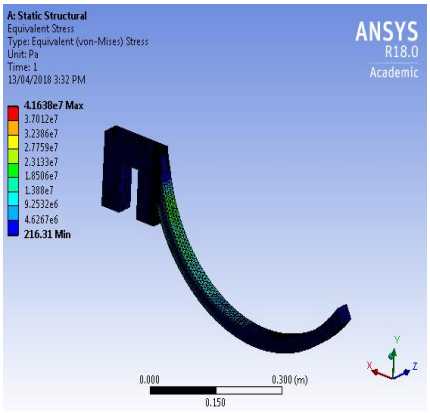


Max Deformation = 7.4590 x 10^{-4} m

Equivalent stress

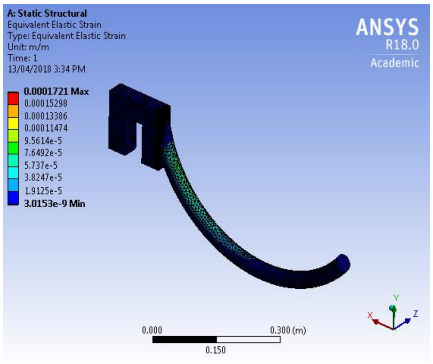


Max Equivalent Stress = 30.85 MPa

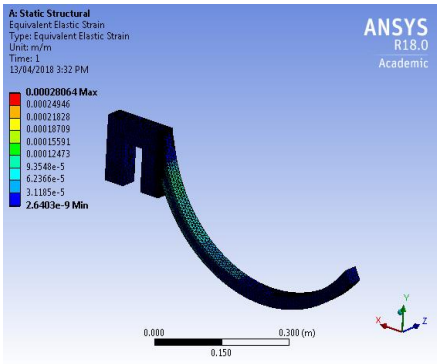


Max Equivalent Stress = 38.95 MPa

Elastic strain



Max Elastic Strain = 2.1387 x 10^{-4} m/m



Max Elastic Strain = 2.7032 x 10^{-4} m/m

From Table 12, rectangular has more equivalent stress, elastic strain and total deformation than circular. In this experiment, there is 70 kg loading applied eventually in pair of hook therefore each individually hook have 35 kg loading. The total deformation of circular hook shape has 4.157 x 10^{-4} m and equivalent stress has 30.85 MPa. Maximum stress was observed at the heel of hook where fracture will normally occur. The remaining areas are relatively stress free. On the other hand, the elastic strain for circular hook shape has 2.1387 x 10^{-4} m/m. There was little strain observed at the heel of hook for both cases too. The total deformation was found to be at the far end of the hook.

For 35 kg loading the stress induced in circular and rectangular hook surface are below the allowable stresses. The stress induced in circular is less than rectangular when 70 kg loading applied on the hook surface therefore circular hook surface offers good results for optimal hook design.

4 Conclusion

Current retrieval system has a high risk of injuries which might pose health. The operation of the new retrieval system is rather safe and simple. The retrieval system has more efficient than current retrieval system. To ensure the design is safe to use, numerical analysis of design geometry has taken place. Therefore, the possibility of injuries has minimized. This project has two design geometry included retrieval system and modified rack.

This project deal with the structural analysis of forks in lifting tire rim weighing 70 kg. There are several parameters that define fork were analysed to design the fork effectively, while considering safety factor and cost. Fork with 3-bladed was preferable as it has least induced stress, strain and deformation. The thickness of fork inversely proportional to induced stress. The material suggested for the fork was structural steel because of less induced stress and deformation thus less fracture possibility.

The outcome of tire rim rack is safety and efficient. The hook is mobility for different tire rim size. Circular hook surface was preferable because of minimal induced stress when 70 kg loading applied. In addition, the induced stress has lower than allowable stress therefore fatigue fracture would not happen. Furthermore, it present higher safety factor in circular hook than rectangular hook.

References

[1] J.Jurechko, "Drive-In Pallet Rack". United States of America Patent 2,968,409, 17 January (2007).

[2] A. Agarwal and A. Madan, "A Review of Analytical Travel Time Models in Automated Storage and Retrieval Systems," *Basic and Applied Engineering Research*, vol. **2**, pp. 1-5, (2015).

[3] K. J. Roodbergen and I. F. Vis, "A survey of literature on automated storage and," *Europen Journal of Operational Research*, vol. **2**, pp. 5-11, (2009).

[4] R. Tripathi, R. Yadav, R. K. Singh and R. Dodamani, "Design and Fabrication of Hand Operated Lift," *International Journal for Scientific Research & Development*, vol. **5**, no. 4, pp. 1-8, (2017).

[5] M. N. B. Tamboli and P. A. S.Todkar, "Modeling, Design, Development, Testing & Analysis Of Dual Worm Self Locking System For Improved Transmission Efficiency & Deceleration Locking Property," *International Journal Of Innovations In Engineering Research And Technology*, vol. **2**, no. 12, pp. 1-12, (2015).

[6] M. H. Pujari, P. Khandagale and Prof.N.S.Mane, "Review On Application Of Twin Worm Gear Arrangement In Load Lifting Devices," *International Conference on Recent Innovations in Engineering and Management*, pp. 37-45, (2016).

EURECA 2018 – Conference Paper
Paper number 2ME09

Comparison Study on Load Distribution of Different Involute Spline Clearance

Chong Ghee Lee, Noor Zafirah Abu Bakar, Hazlan bin Meera Hussain*

School of Engineering, Taylor's University, No. 1 Jalan Taylor's,
47500 Subang Jaya, Selangor DE, Malaysia

Abstract. – A spline coupling consists of a gear with external teeth inserted into another gear with internal teeth and the gap that exists in between the spline teeth is called the gap clearance. A few cases have been reported, to the car companies, in which splines have failed. An understanding of why these splines are failing and what can be done to eliminate the problem would be highly useful as it can be avoided much earlier by implementing a better tolerance of gap clearance. This research aims to find out the load distribution of different involute spline clearance along with the output torque and possible failures that different involute spline clearance carries. The project involves modelling an actual involute splines coupling into two models that are identical in all dimensions except for the tolerance in the gap clearance. A finite element analysis will be conducted on the two models to find out their load distribution along the tooth profile. The results of the simulation show a greater stress value on the spline coupling with maximum gap clearance. The spline coupling material's stress versus number of cycles-to-failure (S-N) curve was used to determine the structural durability of each gap clearances under different torque input. The spline coupling with zero gap clearance was found experiencing an infinite life, whereby an infinite number of cycles applied onto the spline coupling will not cause any failure to occur. On the other hand, the results of the simulation show that the spline coupling with max gap clearance will fail after a number of cycles applied to it.

Keyword: Load distribution, involute spline, gap clearance, structural durability, finite element analysis, S-N curve.

List of Technical Terms

Diametral Pitch, P - The number of spline teeth per inch of pitch diameter.

Pitch Diameter, D - The diameter of the pitch circle, which is determined as the ratio of the number of teeth to the diametral pitch.

Pitch Point - The intersection of the spline tooth profile with the pitch circle.

Circular Pitch, p - The distance along the pitch circle between corresponding points of adjacent spline teeth.

Pressure Angle, ϕ – The angle between a line tangent to an involute and radial line through the point of tangency.

Base Circle - The circle from which involute spline tooth profiles are constructed.

Base Diameter, D_b - The diameter of the base circle.

Major Circle - The circle formed by the outer-most surface of the spline. It is the outside circle (tooth tip circle) of the external spline or the root circle of the internal spline (commonly referred to the Addendum Circle in gear teeth).

Major Diameter, D_o, D_{ri} - The diameter of the major circle.

Minor Circle - The circle formed by the inner-most surface of the spline. It is the root circle of the external spline or the inside circle (tooth tip circle) of the internal spline.

Minor Diameter, D_{re}, D_i - The diameter of the minor circle.

Form Circle - The circle which defines the deepest points of involute form control of the tooth profile. This circle along with the tooth tip circle determines the limits of tooth profile requiring control. It is located near the major circle on the internal spline and near the minor circle on the external spline.

Form Diameter, D_{Fe}, D_{Fi} - The diameter of the form circle.

Depth of Engagement - The radial distance from the minor circle of the internal spline to the major circle of the external spline.

Actual Space Width, s - The circular width on the pitch circle of any single space considering an infinitely thin increment of axial spline length.

Effective Space Width, s_v - The effective space width of an internal spline is equal to the circular tooth thickness on the pitch circle of an imaginary perfect external spline which would fit the internal spline without looseness or considering engagement of the entire axial length of the spline.

Actual Tooth Thickness, t - The circular thickness on the pitch circle of any single tooth considering an infinitely thin increment of axial spline.

Effective tooth Thickness, t_v - The effective tooth thickness of an external spline is equal to the cicular space width on the pitch circle of an imaginary perfect internal spline which would fit the external spline without looseness or interference, considering engagement of the entire axial length of the spline.

Effective Clearance, c_v - The effective space width of the internal spline minus the effective tooth thickness of the mating external spline.

Form Clearance, c_F - The radial depth of involute profile beyond the depth of engagement with the mating part. It allows for looseness between mating splines and eccentricities between the minor circle (internal), the major circle (external), and their respective pitch circles.

1 Introduction

In mechanical transmission system, splines are often used to transfer rotary motion and torsion produced from the internal combustion engine to the transmission box, or normally term as, the gear box. The internal combustion engine and the transmission box are connected through a flywheel with a spline coupling that exist in the middle of it. The spline coupling has an involute tooth profile instead of a cycloidal tooth profile due to a few advantages that the former has over the latter. An involute tooth profile offers advantages such as smoother gear and less wear over time, simplicity in manufacturing, and more flexibility in assembly due to having a larger tolerance in manufacturing.

The involute spline coupling consists of an output shaft with external teeth inserted into a driven shaft with internal teeth both along the same rotational axis. Rotational movement and torsion is transmitted by the means of the internal and external teeth engaging with each other. The distance between the flanks of the internal and external teeth is called gap clearance and different manufacturers have different preferences on the tolerance of the gap clearance. Figure 1 below shows involute splines with (a) maximum gap clearance and (b) zero-gap clearance along with their terminology.

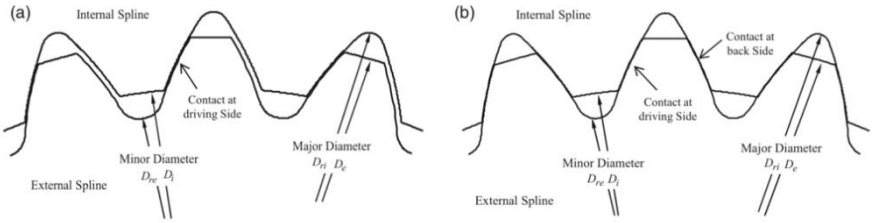


Fig.1. Schematic side views of segments of (a) a side-fit spline, and (b) a side-fit spline having back side contact [1].

The best tolerance for the gap clearance in between the spline teeth is still unknown to all, with different manufacturers making different claims for their own preferences. Some manufacturer claims that the best tolerance is to have no gap, while some prefers a certain gap. Picking the right tolerance for the gap clearance is crucial as it will able to mitigate or even prevent many issues from arising on the spline couplings. A few cases have been reported in which splines have failed. Examination of the failed parts shows that the gear tooth started wearing out at a very fast rate and begins to fail in the early stage of the gear life. An understanding of why these splines are failing and what can be done to eliminate the problem would be highly useful. Failure can be avoided much earlier, and a better tolerance of gap clearance can be implemented, which results in longer operational life of spline couplings, if the load distribution of different involute spline gap clearance is known.

Every material has mechanical properties that explains their characteristic. For instance, when a material is experiencing stress that exceeds its tensile yield strength, yielding of the material will naturally occur. Moreover, if the stress increases further towards exceeding its tensile ultimate strength, the material will break. Hence, the safety factor of the spline coupling will be taken into consideration when comparing the load distribution between the spline coupling with zero-gap and certain gap clearance.

Most journal articles focus on zero-gap clearance, or normally term as clearance-fit spline joints, as the base of their research, and the issues and failures that they discussed and analysed are not related to the different in gap clearance. Hence, this research will tackle the subject of,

how does the load distribution of the spline teeth contribute to the possible failures of a certain gap clearance and compare it with the load distribution of the zero-gap clearance. Issues and failures caused by both the zero-gap and certain gap clearance case will be discussed and analysed in this research.

Issues and failures experienced by the spline coupling cannot be thoroughly understood unless its load distribution along the spline teeth are known [4]. Different tolerance for the gap clearance may bring about different load distribution on the spline teeth. Hence, a comprehensive study on comparing the load distribution and output torque of different gap clearance of spline teeth is to be carried out in this research by using the finite element analysis method. The comparison study of load distribution will be between two spline couplings with different gap clearance conditions. With that said, two spline couplings with the same dimensions but different gap clearance, such as maximum and zero gap clearance condition, is to be modelled in this project.

The objectives of the project are stated as following;

i. To develop surface integral contact analysis model and conduct finite element analysis on the load distribution in different spline clearance conditions.
ii. To analyse the spline material's Stress versus Number of cycles-to-failure (S-N) curve for each gap clearance conditions.

2. Research Methodology

The research methodology of this project follows the Conceive, Design, Implement and Operate framework.

2.1 Conceive, Background Study

Background studies and research was carried out in the conceive stage of this project. Related journals and articles was studied to gain better understanding of the project title. The objective of the project is to develop surface integral contact analysis model and conduct finite element analysis on the load distribution of different involute spline clearance. Hence, an in depth understanding of the relationship between load distribution and different involute spline clearance was studied. It can be said that different involute spline clearance may produce different load distribution.

Furthermore, this project also requires analyzing the output torque and potential failures that comes along with the load distribution of different involute spline clearance. Hence, background studies and research will be carried out regarding the effect on the output torque of the involute spline couplings when there are different load distributions. Multiple variables such as wear, and friction caused by the different load distributions will be included in the analysis.

2.2 Design, Involute Spline Design

Two 3D models of the involute spline were drawn using the 3D modeling software, SolidWorks. Both involute spline model was identical in dimensions except for the tolerance in the gap clearance. Both involute spline model will be put into simulations using the finite

analysis method to analyze the load distribution of different tolerance in gap clearance. The software, ANSYS, was used to carry out the simulation of both involute spline models. The two models of the involute spline were designed accordingly to the design parameters from the standard DIN 5480-1 [5] shown in the Table 1 below.

Table 1: Design parameters from DIN 5480-1 [5]

	External Teeth	Internal Teeth
Number of Teeth, z	25	
Pitch Circle Diameter, D_{ref}, (mm)	26.458	
Pressure Angle, ϕ	30°	
Base Diameter, D_b, (mm)	22.9136	
Module, m	1.0538	
Major Diameter, D_o / D_{r_i}, (mm)	27.400	28.590
Minor Diameter, D_{r_e} / D_i, (mm)	23.876	25.400
Form Diameter, D_{f_e} / D_{f_i}, (mm)	25.298	-
Tooth thickness effective, t_v, (mm)	1.641	
Space Width effective, s_v, (mm)	1.661	

The involute spline was drawn by using the parametric involute curve equation, shown below, was used in generating the involute curve on the gear teeth when modelling in SolidWorks [6].

$$0.5 \times D_b \times [t \times cos(t \times \pi) + t \times sin(t \times \pi)] \qquad (1)\ [6]$$

$$0.5 \times D_b \times [t \times sin(t \times \pi) - t \times cos(t \times \pi)] \qquad (2)\ [6]$$

Where;

- D_b = Diameter of the base circle
- t = Sweep parameter of the involute curve

The Eq. (1) and (2) above is the parametric involute curve equations used to create the involute curve for a gear tooth in SolidWorks, respectively. The equations were inserted when drawing an equation driven line. Under the parametric option, Eq. (1) and (2) will be keyed in as $x(t)$ and $x(t)$, respectively. The sweep parameter of the involute curve ranges from 0 to 1 with t_1 being 0 and t_2 being a value from 0 to 1. The greater the value of t_2, the further the involute curve line is generated beyond the major diameter of gear. Hence, in this case, t_2 was

set to 1 as it does not affect the drawing as long as the involute line intersects the major diameter of the gear.

The research objective of this project is to develop a surface integral contact analysis model and conduct finite element analysis on the load distribution of different spline clearance conditions. Thus, two models of the involute spline will be design in which, one of them will have no gap clearance and the other to have a certain gap clearance. Effective clearance is another name for the gap clearance and it can be calculated by deducting the effective tooth thickness from the effective space width of the spline teeth. It can be seen from Table 1 above, that the effective space width and tooth thickness are 1.661mm and 1.641mm, respectively. Thus, the effective clearance for the maximum gap case will be 0.02mm. As for the no gap clearance case, the gear teeth will be a clearance-fit design whereby, the effective tooth thickness is the same as the effective space width, hence making the effective clearance between the internal and external spline teeth a 0 mm.

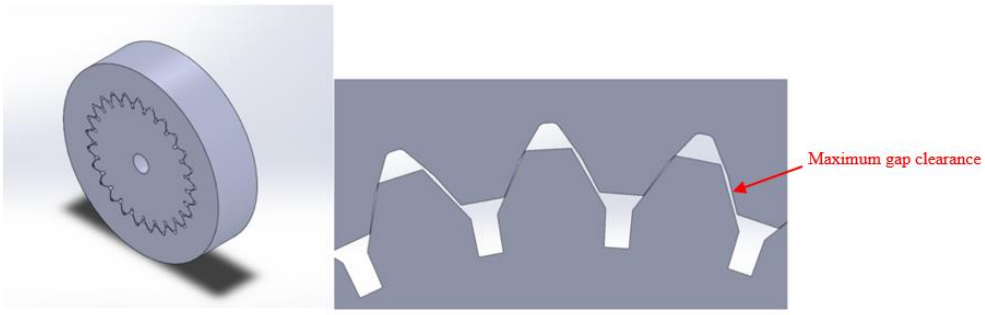


Fig.2. Involute spline coupling with maximum gap clearance.

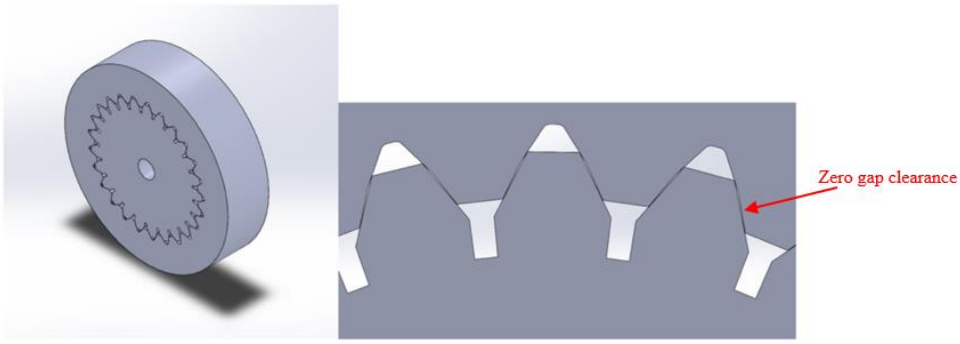


Fig.3. Involute spline coupling with zero-gap clearance.

The gap clearance of the spline coupling is the space in between the flanks of the spline teeth as marked as seen in Figure 3.1 and 3.2 above.

2.2 Implement, Analysis Method

Simulations was carried out on the two involute spline couplings using the finite element analysis method with the ANSYS software to analyze the load distributions along the spline teeth of each cases of spline gap clearance. Since the involute spline couplings was designed to have the exact same dimension as the actual spline coupling currently being used in cars transmissions, the torque input into the simulation will naturally be the same as the actual

torque. This is being done so to obtain and analyze the load distribution that is as close as possible to the actual scenario.

2.2.1 ANSYS Set up

One of the expected outcome of this project is to relate the load distribution to the wear damage on spline couplings. The transient structural solver was used in this case because wear damage occurs over-time, so time has to be one of the variables in the simulation.

The material of the spline coupling is SCM 435 Alloy steel and it has a density of $7700\ kg/m^3$. The Young's modulus and Poisson's ratio of the alloy steel is 200GPa and 0.27. SCM435 has an ultimate tensile strength of 991MPa and an ultimate yield strength of 902MPa.

Two types of connections were added into the transient structural analysis. The first connection was bonded contacts where both internal and external spline teeth come into contact with each other and the second connection was a revolute joint that tells the simulation that the gears are rotating about an axis.

A few mesh settings were applied onto the internal and external spline to increase the accuracy of the simulation results. The refinement of the mesh can be validated by the average element quality and skewness of the mesh shown in the simulation. The closer the value of the average element quality to 1, the better it is in term of the quality of the mesh. On the other hand, the quality of the mesh improves as the average skewness value gets closer to 0.

For refinement, the mesh method was changed from automatic to tetrahedral method as it shows and improvement of mesh quality as in Table 2 below. Other than that, a contact sizing was added to refine the mesh on the spline teeth of both external and internal spline gear where they are in contact with each other. The element size for the contact sizing was set to 0.0005 mm.

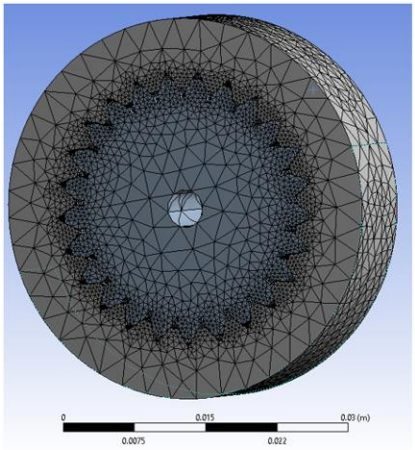


Fig. 4. Meshing of spline coupling.

Table 2: Mesh Metric of Involute Spline with Maximum and Zero Gap Clearance

Spline Coupling with Max Gap		Spline Coupling with Zero gap	
Auto generated	Refined	Auto generated	Refined

Average Element Quality	0.50590	0.70797	0.46511	0.70969
Skewness	0.38280	0.41124	0.39268	0.41959
Number of Elements	4116	125208	4721	130153
Number of Nodes	22846	210289	25867	218035

The simulation of each spline gap condition produced three sets of results due to the internal spline gear being applied with moment force of 110 Nm, 155 Nm and 205 Nm. This is because when a car is in idle state, the torque input is at 110 Nm and the maximum torque input from the internal combustion engine to the flywheel is at 205 Nm. A moment force of 155 Nm was added as a control variable in this simulation. On the other hand, a fixed support was added to the external spline to study the load distribution on both spline gears once the driver gear meets the driven gear with the specific moment force. Besides, a standard earth gravity of -9.8066 m/s^2 was also applied to both spline gears

2.3 Operate/ Project Plan

Throughout the whole final year project, the objective of this project is to develop surface integral contact analysis model and conduct finite element analysis on the load distribution in different spline clearance conditions and study the output torque and potential failures of the spline during both conditions based on the load distribution results.

This project was separated into two parts as final year project 1 and 2. Final year project 1 focused on background study, choosing design parameters and designing two models of spline couplings with different tolerance of gap clearance. The two models of involute spline coupling were put into simulation to find out the load distribution along the teeth in final year project 2. Results of the simulation was compared against each other and the load distribution and output torque for each case will be discussed as well. There is no fabrication of products required in this project and no budget was given.

3. Results

3.1 Simulation Results of Involute Spline Coupling with Max-Gap Clearance

The spline coupling with maximum gap clearance was put into a static structural simulation with an applied moment to the internal spline gear. The moment that was applied onto the internal gear are 205 Nm.

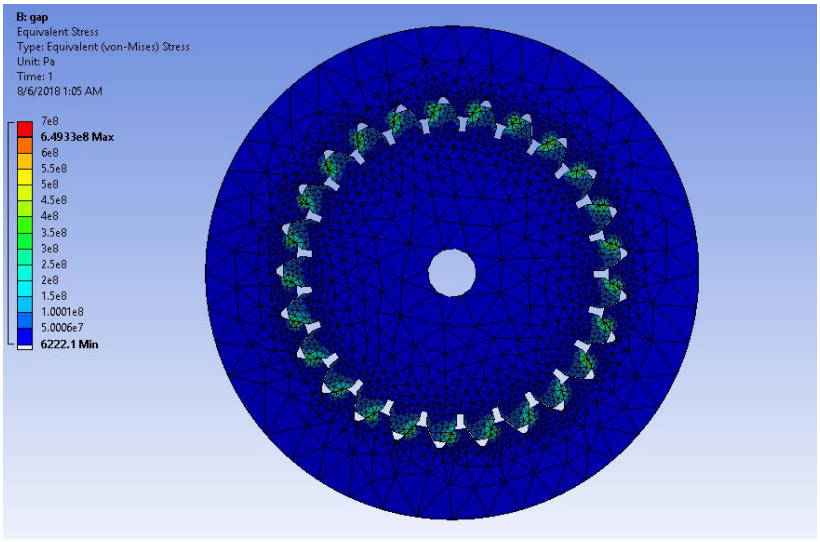


Fig.3.1: Front view of stress distribution of spline coupling with max gap clearance under 205 Nm torque

The stress distribution of the spline coupling with maximum gap clearance under the applied moment force of 220 Nm, as seen in Figure 3.1 above. 220 Nm is the maximum torque that comes from the internal combustion engine. The maximum and minimum stress that the spline coupling with maximum gap clearance is experiencing, under 205 Nm torque, is 649 MPa and 6.2 KPa, respectively. Due to the maximum gap clearance in between teeth, the stress distribution is highly concentrated at the region of the side of the teeth where the internal gear meets the external gear. The other side of the spline teeth that is not in contact with each other during operation has a lower stress concentration when compared to the other side.

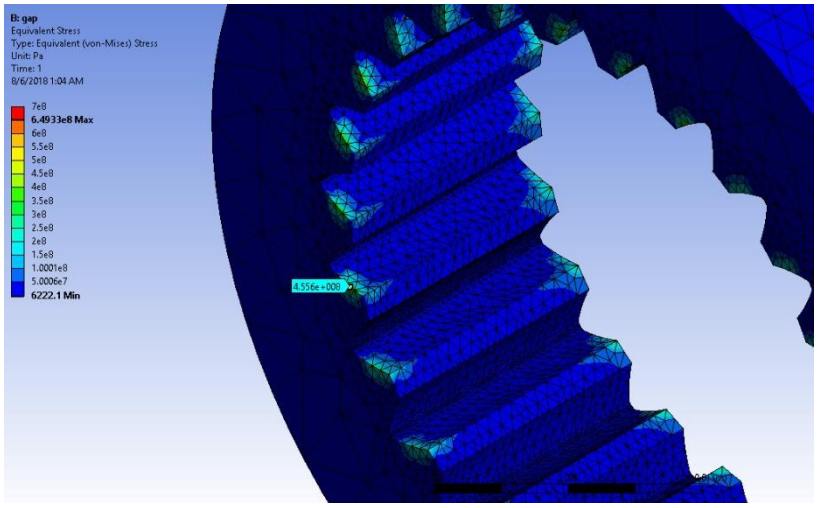


Fig.3.2: Stress distribution of max gap clearance internal spline gear under 205 Nm torque

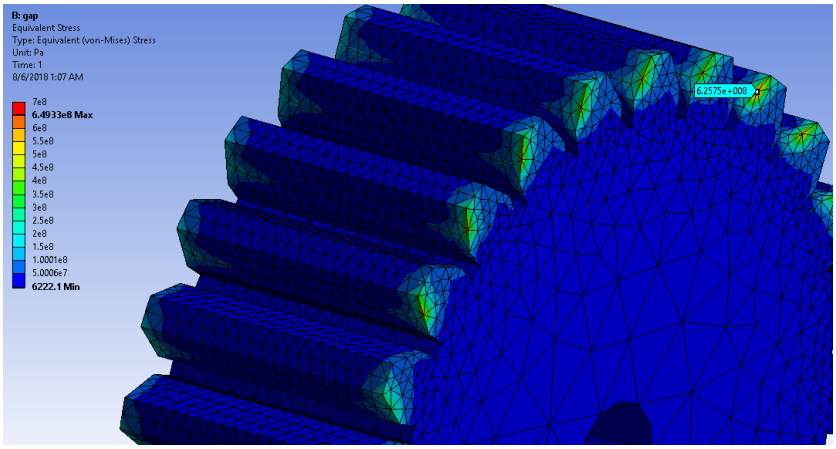


Fig.3.3: Stress distribution of max gap clearance external spline gear under 205 Nm torque

The stress distribution at the internal and external spline gear was shown in Figure 3.2 and 3.3, respectively. High stress intensity can be seen at both the edges of the spline gear teeth. This means that that region will undergo shortening of material life faster than the other region.

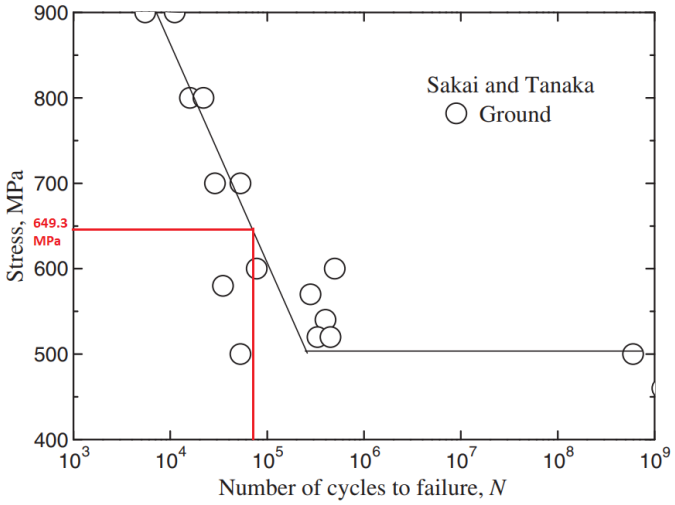


Fig.3.4: S-n curve for spline coupling with max gap clearance under 205 Nm torque

The S-n curve in Figure 3.4 shows that the spline coupling with max gap clearance under 205 Nm will have failure after 8×10^4 number of cycles. This means that once 8×10^4 number of cycles of the 649.3 MPa is applied to the material, failure will start to occur.

3.2 Simulation Results of Involute Spline Coupling with Zero-Gap Clearance

The spline coupling with zero gap clearance was also put into a static structural simulation with an applied moment to the internal spline gear. The moment that was applied onto the internal gear are 205 Nm.

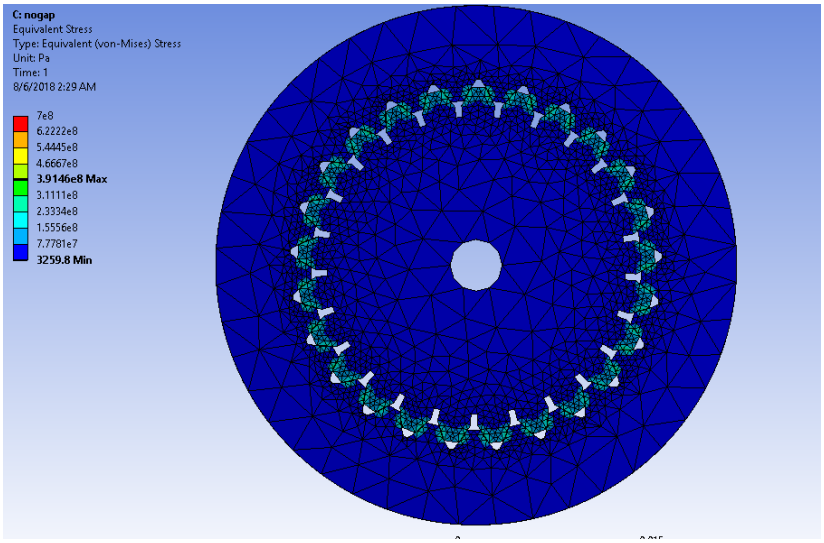


Fig.3.5: Front view of stress distribution of spline coupling with zero gap clearance under 205 Nm torque

The stress distribution of the spline coupling with zero gap clearance in Figure 3.5 shows a uniform distribution across both side of the spline teeth. This is mainly because both side of the spline teeth are in contact with each other. The maximum and minimum stress experienced by the spline coupling with zero gap clearance when being applied with 205 Nm of torque are 391.4 MPa and 3.26 kPA, respectively.

Figure 3.6 and 3.7 below also shows the stress distribution of the spline coupling with zero-gap clearance to have high concentration of stress at both edges of the spline teeth. This points to faster material life shortening that that region. The edges of the spline tooth flank do not have as high intensity of stress concentration as the edges. Hence, the edges of the spline tooth flank will not experience shortening of material life as quickly as the other edges of the spline tooth.

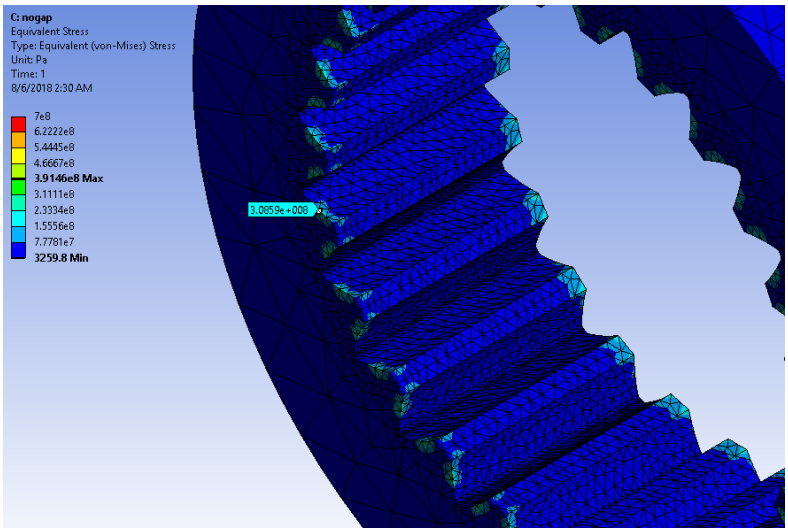


Fig. 3.6: Stress distribution of zero gap clearance internal spline gear under 205 Nm torque

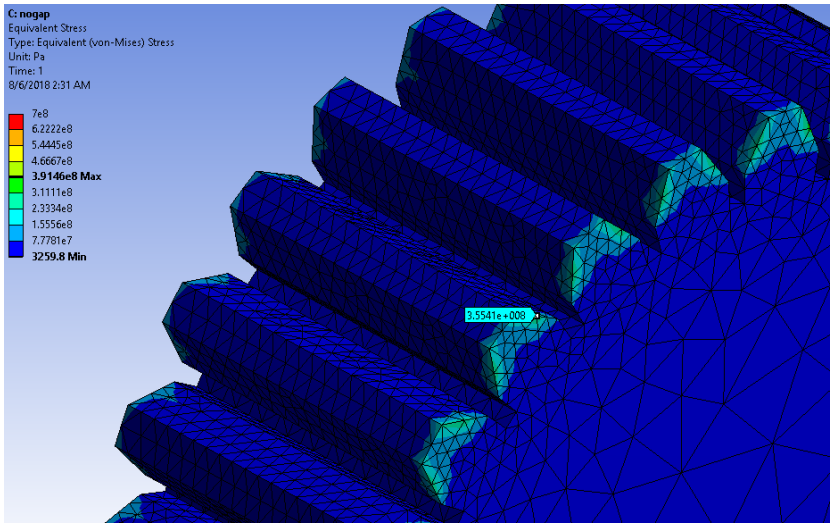


Fig. 3.7: Stress distribution of zero gap clearance external spline gear under 205 Nm torque

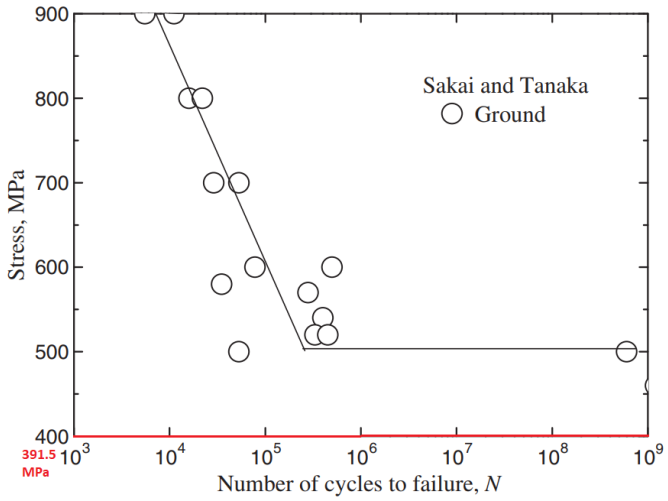


Fig.3.8.: S-n curve for spline coupling with zero gap clearance under 205 Nm torque

The S-n curve in Figure 3.8 also shows the spline coupling with zero gap clearance under 205 Nm torque falling into the infinite life region. This means that an infinite number of cycles can be applied to the material without failing.

3.3 Discussion

Table 3.1: Results of Simulation

		Maximum gap clearance		Zero gap clearance		Increase in percentage between zero and maximum gap clearance, %
		Maximum stress, MPa	Minimum stress, kPa	Maximum stress, MPa	Minimum stress, kPa	
	110	347.0	3.31	209.9	2.63	65.3

Torque input, Nm	155	490.1	4.68	296.0	3.11	65.6
	205	649.3	6.22	391.5	3.26	65.8

As seen in the Table 3.1 above, for the spline coupling with maximum gap clearance, the maximum stress it experienced increases along with the input torque. When the input torque increase from 110 Nm to 155 Nm, the maximum stress experienced by the spline coupling with maximum gap clearance increased 41%. When the input torque increases from 155 Nm to 205 Nm, an increase of 33% in maximum stress experienced by the spline coupling occurs. Whereas, for the spline coupling with zero gap clearance, the maximum stress it experienced also increased 41% when the torque input increases from 110 Nm to 155 Nm. When the torque input increases again to 205 Nm, the maximum stress experienced by the spline coupling increased for 32%, which is still very close to the increase of maximum stress, in percentage, for the spline coupling with maximum gap clearance.

It can also be seen that the maximum stress experienced by the spline coupling with maximum gap clearance are higher in all three torque input cases when compared with the maximum stress experienced by the spline coupling with zero gap clearance. Table 3.1 also shows that the maximum stress experienced by the spline coupling with zero gap clearance has an increase of around 65%, for all three torque input cases. Thus, the hypothesis that mentioned the spline coupling with zero gap clearance having a higher stress than the max gap clearance has been rejected.

However, the hypothesis that mentioned that the load distribution on the spline coupling with zero gap clearance will have a more uniform distribution when compared to the spline coupling with max gap clearance can be accepted. Figure 3.1 and 3.5 clearly shows that the stress distribution on the spline with maximum gap clearance has high stress concentration at the contact side of the spline gear teeth, whereas the spline with zero gap clearance has a more uniform stress concentration at both contact side of the spline gear teeth.

Besides, high intensity of stress is seen to be concentrated at both edges of the spline gear at both the internal and external spline teeth. This means that the edge region will undergo a faster shortening of material life than the other region, where there is not that high intensity of stress distribution. The simulation was further proven accurate as car companies have been receiving reports that shows the wearing and breaking of the same edge region of the spline teeth.

Table 3.2: Structural Durability of Spline Coupling with different Gap Clearance

	Torque input, Nm	Number of cycles to failure
Spline coupling with maximum gap clearance	110	Infinite life
	155	Infinite life
	205	8×10^4
Spline coupling with zero gap clearance	110	Infinite life
	155	Infinite life
	205	Infinite life

Table 3.2 above shows the number of cycles to failure for each torque input applied onto the spline coupling with maximum and zero gap clearance. It can be seen that only the spline coupling with maximum gap clearance that is under 205 Nm of torque will have a limited number of cycles to failure and that is 8×10^4. This shows that the stress experienced by the spline coupling with zero gap clearance will have infinite life throughout all three torque input cases. On the other hand, the spline coupling with maximum gap clearance also has two torque input cases that shows the result of infinite number of cycles to failure. However, when the torque input increases up to 205 Nm, the region of highly concentrated of stress will experience failure after a number of cycles.

4. Conclusions and Recommendations

To conclude, the load distribution of spline coupling with maximum gap clearances are much greater than the load distribution of spline coupling with zero gap clearances. Since the maximum gap clearance experience greater stress distribution, the rate of material life shortening is much faster when compared to the zero-gap clearance condition. Also, the spline coupling with maximum gap clearances are more prone to experience failure at a certain torque input after a number of cycles whereas, the spline coupling with zero gap clearances experiences infinite life with the current torque input. Thus, it can be concluded that the spline coupling with zero gap clearance has the longer operational life compared to the maximum gap clearance

There are a few ways that this project can proceed to the next stage and the first one is to include more loadings on the external spline shaft. The external spline shaft is connected to the gear box, in which there are a lot of gears on the external spline shaft itself. Including these gears means including axial loading into the project as all the other gears on the external spline shaft all has weights. The weights will become a form of resistance that goes against the driver gear. This would lead to an even higher load distribution on the spline coupling. The higher load distribution can then be related to issues such as fatigue wear, and even angular misalignment.

The second way is to proceed with this project is to continue studying the structural durability of the spline coupling in terms of mileage. This would require additional simulation software that could be provided by the car companies themselves.

More gap clearance condition could also be included in the study to find out which gap clearance suits the best. Other than that, the material of internal and external spline in this project is the same. A change in material could open up possibilities of achieving better load distribution for spline couplings

5. Acknowledgement

The author expresses his utmost gratitude towards the continuous support of effort of Noor Zafirah for providing her time and guidance to mentor the author of this project. Other than that, the author would also like to express his utmost gratitude towards Hazlan bin Meera Hussain and Mr Shukri for providing their time in their busy schedule and guidance from their technical expertise in Proton Sdn. Bhd.

6. Reference List

[1] J. Hong, D. Talbot and a. A. Kahraman, "Proc. Inst. Mech. Eng. Part CJ. Mech. Eng. Sci.," *A generalized semi-analytical load distribution mode for clearance-fit, major-fit, minor-fit and mismatch splines*, **230**, 1126-1138, (2015)

[2] A. M. a. F. A. F. Curà, "Procedia Struct. Integr.," *Fatigue damage in spline couplings: numerical simulations and experimental validation*, **5**, 1326-1333, (2017)

[3] S. M. a. V. Olver, "Proc. Inst. Mech. Eng. Part J J. Eng. Tribol.," *An analysis of misalighned spline couplings*, v**216**, 269-278, (2002)

[4] D. T. a. A. K. J. Hong, "Mech. Mach. Theory," *A semi-analytical load distribution model for side-fit involute splines*, **76**, 39-55, (2014)

[5] E. Directorate, *STANDARD DIN-5480-1 Spline Connections with Involute Splines based on Reference Diameters*, 1-8, (2014)

[6] V. B. a. A. Tsegaw, "African Res. Rev.," *Involute Spur Gear Template Development by Parametric Technique Using Computer Aided Design*, **3**, 415-429, (2009)

[7] Engineering ToolBox, (2010) *Factors of Safety*. [Online]. Available: https://www.engineeringtoolbox.com/factors-safety-fos-d_1624.html. [Accessed 20 May 2018].

[8] S. W. a. B. L. X. Xue, "Wear," *Modification methodology of fretting wear in involute spline*, **368-369**, 435-444, (2016)

EURECA 2018 – Conference Paper
Paper number 2ME10

The Influence of Winglet Configurations on the Aerodynamic Efficiency of Fixed Wing Micro Unmanned Aircraft Vehicles (MUAV)

Chie Quen Leong; Abdulkareem Sh. Mahdi Al-Obaidi

Abstract.

The idea of having wings to curl upwards at the wingtips is not novel. The development of winglet progressed significantly during the 1973 oil crisis. In modern days, winglets can be commonly seen in large commercial aeroplanes. This is because the installation of winglets can reduce fuel consumption, thereby saving fuel cost that may accumulate up to few million USD over the life time of an aeroplane. This raise a question whether it is beneficial to install winglets on to a micro unmanned aircraft vehicle (MUAV). The aim of this research is to investigate the effect of winglets' geometry, span, and sweep angle on the lift-to-drag ratio of a fixed wing MUAV as well as to Select the most suitable winglets configuration to be utilized on a fixed wing MUAV. NACA 0012 aerofoil will be used to design the winglets and the winglets will be attached on to a baseline rectangular wing. A total of 7 winglet configurations are created using SolidWorks 2017. All the winglet configurations will be analysed numerically through computational fluid dynamics (CFD) at various angle of attack using ANSYS v18.0. The numerical results obtained from the computational fluid dynamics will then be validated with experimental results obtained from the wind tunnel experiments. According to the analyses done by this research, wing with triangular winglet has the largest numerical and experimental maximum lift-to-drag ratio. In addition to that, percentage error of lift coefficient has higher precision, whereas percentage error of drag coefficient has higher accuracy.

Keywords. Winglets; Micro unmanned aircraft/aerial vehicles (MUAVs); Aerodynamic efficiency; Lift-to-drag ratio; Sweep angle; Subsonic

1 Introduction

1.1 Background

Winglet is a device that is mounted/jointed to the tip of an aeroplane. Winglets can also be embodied in the design of wings of an aeroplane. Figure 1.1 shows the schematic of winglets on an aeroplane.

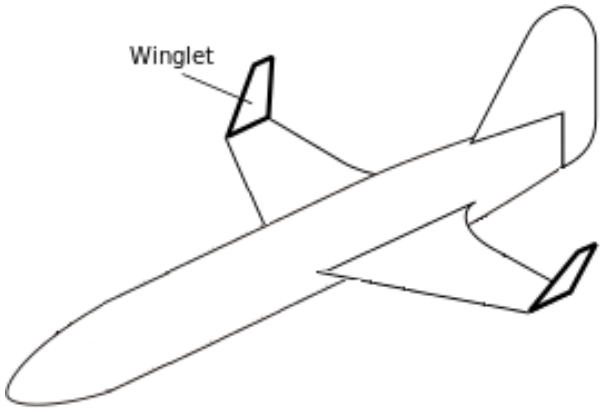


Figure 1.1: Schematic of winglets

Just like every other extension devices for aeroplanes, the main intention of winglets is to improve aerodynamic efficiency, which is the lift-to-drag ratio, of aeroplanes. This is achieved by reducing the magnitude of wingtips vortices, which are rotating air flowing in circular patterns at the wingtips as the wings are generating lift.

The idea of having wings to curl upwards at the wingtips is not novel. In 1897, Frederick William Lanchester patented the concept of vertical end plates. As the name suggests, the plates are installed vertically to the end of the wings. Experimental investigations show that such method significantly reduces the wingtips vortices. During this time, the term winglet still does not exist [1]. The development of winglet progressed significantly during the 1973 oil crisis. In October 1973, the Arab members of the Organization of the Petroleum Exporting Countries (OPEC) placed an oil embargo to the United States of America (USA). The reason for the oil embargo is because of the USA involvement in the Yom Kippur/Ramadan/October War by supplying military weapons to Israel 6 days after Egypt and Syria launched a surprise attack on Israel. The severe decrease in oil supply in the USA causes the price of oil to skyrocket.

This force engineers to work heavily on subjects that are related to reduction in fuel consumption. During the period of the 1973 oil crisis, Richard Travis Whitcomb contributed his wingtip vortices analysis. According to Whitcomb's analysis [1], air that is flowing at the wingtip of a particular aeroplane is directed inward above the wingtip and outward below the wingtip. Whitcomb hypothesized that a properly designed wingtip, which is angled nearly vertical above the wingtip (known as the cant angle as shown in Figure 1.2), will significantly reduce the induced drag, which in turn reduces fuel consumption of a particular aeroplane. The hypothesis was verified by experimental investigations. However, the adoption of winglets is relatively slow in the aircraft industry.

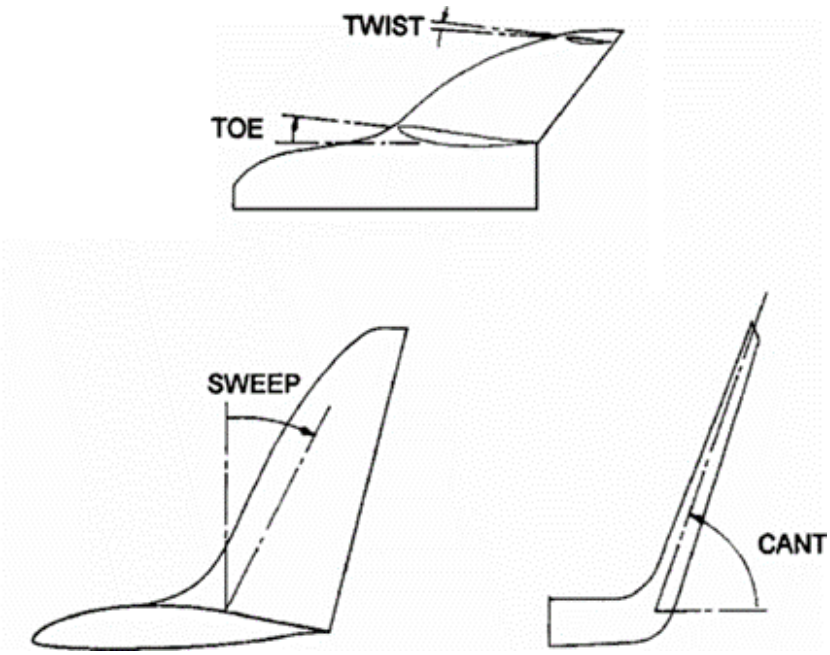


Figure 1.2: Cant (front view), sweep (left view), toe, and twist angles (top view) [2]

Whitcomb's effort in winglets began to took off after nearly 3 decades. In modern days, winglets can be commonly seen in large commercial aeroplanes. This is because the installation of winglets can reduce fuel consumption, thereby saving fuel cost that may accumulate up to few million USD over the life time of an aeroplane. In other words, a small investment on the cost of installation and maintenance of winglets can be worth in the long run.

1.2 Research Questions

At this point, one can ask whether smaller aeroplanes benefit from the installation of winglets. Whitcomb repeatedly emphasized that the design of winglets requires a lot attention as a badly design winglets can impose negative effects. Therefore, the advantages and disadvantages of different types of winglet configuration must be researched and tested thoroughly before the winglets are installed on to the wings of an aeroplane. With that being said, one may specifically ask whether it is beneficial to install winglets on to a micro unmanned aircraft vehicle (MUAV). Various questions have been raised as shown below.

1) How does winglets' geometry, span, sweep angle affect the lift-to-drag ratio of a fixed wing MUAV?
2) What is the most suitable winglets configuration to be utilized on a fixed wing MUAV?

1.3 Research Objectives

The aim of this research is to study whether it is relevant to install winglets on to a fixed wing MUAV. Based on the questions asked previously, the specific objectives of this research are shown below.

1) Investigate the effect of winglets' geometry, span, and sweep angle on the lift-to-drag ratio of a fixed wing MUAV.
2) Compare the lift-to-drag ratio of a fixed wing MUAV with different winglets configurations.

3) Select the most suitable winglets configuration to be utilized on a fixed wing MUAV.

2 Literature Review

2.1 Overview of Winglets Design

Maughmer [3] mentioned that the most paramount parameters that must be considered in the course of designing winglets are aerofoil, chord distribution, height, twist angle, sweep angle, and toe angle. Maughmer stated that every wings and winglets combination should have a specifically designed aerofoil. However, the aerofoil depends on the winglets geometry. Thus, the process in designing the winglets and its aerofoil are iterative. At low speed flight the winglets must not stall, which is the condition whereby further increasing the angle of attack will decrease the lift, before the wings. However, it is difficult to design the winglets, especially aerofoil with narrow chords as well as winglets operating at low Reynolds number. There will always be a trade-off between one and another. Maughmer indicated that winglets with very small chord may not be able to generate the required lift coefficient at low flight speed, which cause the winglets to be ineffective. Maughmer mentioned that the lift coefficient is unique for every different combination of wings and winglets. Maughmer also indicated that based on past methods for designing winglets, there will always be a trade-off between profile drag and induced drag. Therefore, it is crucial to keep in mind that the winglets must be able to decrease induced drag, but at the same time maintaining a reasonable increase in profile drag.

Heyson et al. [4] mentioned that winglets with toe-in angle increases induced drag slightly. However, despite the slight increment in induced drag, winglets with toe-in angle can achieve large percentage of reduction in root bending moment. Heyson et al. also stated that winglets benefit the most when the wind loads are heavies at the wingtips. The favourable effect of winglets, which is to decrease the magnitude of wingtips vortices, reduces for wings with washout angle. Nevertheless, for wings with washout angle, the gain from winglets increases with lift coefficient because of the increased wind loads near the wingtips. In addition to that, Heyson et al. also indicated that the induced drag and root bending moment increases with the increment of winglets length and cant angle.

2.2 Overview of Numerical and/or Experimental Analyses

Murayama and Yamamoto [5] carried out numerical and experimental analyses to study the effect of structured and unstructured meshes on a 2-dimensional NLF 7301 aerofoil, as shown in Fig 2.1, and 3-dimensional (3D) wing attached on a fuselage at high lift condition. Both the structured and unstructured meshes were further divided into 3 different types of sizing; namely coarse, medium, and fine. Murayama and Yamamoto concluded that for the 2-dimensional NLF 7301 aerofoil, the numerical lift and drag coefficients obtained from the unstructured meshes are comparable with the numerical lift and drag coefficients obtained from the structured meshes, provided that the unstructured meshes are generated properly. Similarly, Murayama and Yamamoto also concluded that for the3-dimensional wing attached on a fuselage, the numerical lift and drag coefficients obtained from the unstructured meshes are comparable with the numerical lift and drag coefficients obtained from the structured meshes, provided that the unstructured meshes are generated properly.

Gaffuri and Brezillon [6] studied the reliability of unstructured meshes for flow over a low aspect ratio wing under low speed. The numerical results of unstructured meshes are then

validated with the numerical results of structured meshes as well as experimental results of wind tunnel experiments. Gaffuri and Brezillon concluded that hybrid meshes, which consists of both structured and unstructured meshes, are suitable for complex cases, such as a highly swept delta wing at high angle of attack. The numerical results of hybrid meshes are accurately predicted at approximately $10x10^6$ nodes. Nevertheless, Gaffuri and Brezillon mentioned that a thick prism layer is required for accurate prediction of vortices. In addition to that, lift and drag can also be predicted with similar accuracy of structured meshes.

Lutton [7] studied the effect of O- and C- grids on a NACA 0012 aerofoil. Lutton concluded that both grids are suitable for general application. However, each grid has its own advantageous and disadvantageous. O-grid shows superior numerical stability as compared with C-grid. C-grid is much easier to generate as compared with O-grid. In addition to that, O- and C- grids produced similar results at the leading edge of NACA 0012 aerofoil.

Komarabathini et al. [8] studied the effect of C-, O-, and H- grids, as shown in Figure 2.1, on a NACA 0012 aerofoil. Komarabathini et al. concluded that the numerical results obtained using C- and O- grids are reasonably accurate. In addition to that, Komarabathini et al. also mentioned that at $1.2x10^6$ nodes, obtaining convergence is very difficult as it requires a lot of memory and time.

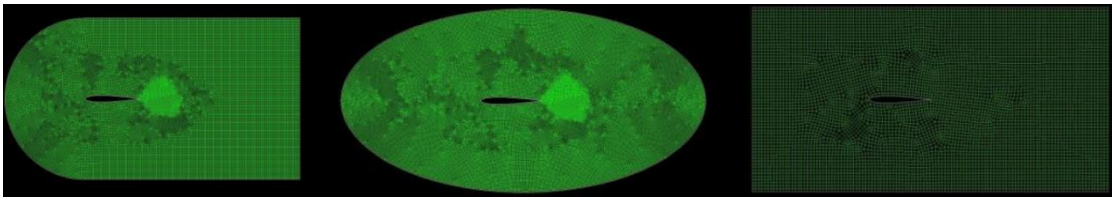


Figure 2.1: C-grid (left), O-grid (centre), and H-grid (right)

At the 1st phase of the study, Panagiatou et al. [2] investigated the air flow around the winglets of a medium altitude long endurance (MALE) unmanned aircraft vehicle. A total of 6 different types of winglet configurations, including a conventional wing without winglet, were examined numerically using computational fluid dynamics. Spalart-Allmaras turbulence model, a 1 equation model based on Reynolds-Averaged-Navier-Stokes (RANS) equations, was utilized. The lift and drag coefficients as well as lift-to-drag ratio were determined. In general, the results show that by installing the optimal design on to the medium altitude long endurance unmanned aircraft vehicle, the lift-to-drag ratio of the medium altitude long endurance unmanned aircraft vehicle increases. Besides that, the results also show that the lift-to-drag ratio increases as the cant angle of the winglet increases, regardless of the winglet configurations. Panagiatou et al. explained that this is because installation of the winglet incidentally increases the span of the wing slightly. Panagiatou et al. also concluded that the improvement in lift-to-drag ratio is mainly due to the increase in lift, rather than the decrease in drag. According to Panagiatou et al., the performance of winglets depends heavily on the types of aeroplane the winglets are attached to. The author suggested that this may be because different aeroplanes have different wings configurations, and hence, different winglets configurations should be installed on to the particular aeroplane. In other words, the most favourable design of winglets for 1 particular aeroplane may not be suitable for another aeroplane.

Azlin et al. [9] stated that a winglet increases the effective aspect ratio of a wing without greatly increases the wing span. Azlin et al. carried out a numerical analysis using computational fluid

dynamics, based on finite volume method (FVM), on a 660 mm span and 121 mm chord rectangular wing of NACA 653218 aerofoil with 2 different winglet geometries, which are elliptical and semi-circular. The lift and drag coefficients as well as the lift-to-drag ratio were determined for both winglet configurations by manipulating the winglet's cant angle to 0 °, 45 °, and 60 °. The numerical analysis was performed at low subsonic region with variation in angle of attack using Spalart-Allmaras turbulence model. The results show that lift coefficient and lift-to-drag ratio improve with the addition of winglets, regardless of its geometries. According to Azlin et al., the elliptical winglet at 45 ° cant angle is the most favourable design, which has an increment of 8 % in both lift coefficient and lift-to-drag ratio.

Dinesh et al. [10] investigated the effects of winglets on an ONERA M4 model numerically using computational fluid dynamics. Dinesh et al. achieved this by comparing the pressure, velocity, and vorticity of 2 equivalent ONERA M4 models, 1 with winglets at 28° cant angle and another 1 without winglets. Spalart-Allmaras turbulence model with a convergence factor of 0.0001 is adopted for both models. The models are simulated under steady state condition, at a low subsonic speed of 20 m/s and an angle of attack of 0 °. The results show that usage of winglets reduces the wingtips vortices, which in turn lead to a reduction in induced drag.

Myilsamy et al. [11] conducted a numerical analysis of a subsonic aeroplane with swept back wings and blended winglets of various cant angle in order to determine the best lift-to-drag coefficient. NACA 4412 aerofoil is used for the swept back wings as well as the blended winglets. The cant angles of the blended winglets are manipulated to be 0 °, 30 °, and 90 °. The models are simulated at different angle of attack, ranging from -2 ° to 10 °. $k-\omega$ turbulence model, a 1 equation model based on Reynolds-Averaged-Navier-Stokes equations, was used. The results show that wings with winglets produce higher lift-to-drag coefficient as compared with wings without winglets.

Whitcomb [12] conducted an experimental analysis of winglets mounted on the wing of a 1st generation narrow-body jet airliner using wind tunnel. Whitcomb reported that adding winglets to the wings, which has lift coefficient of approximately 0.44, at Mach number 0.78 reduces the induced drag by approximately 20 % and increases the wings lift-to-drag ratio by approximately 9 %. The improvement in lift-to-drag ratio using winglets is twice of the improvement in lift-to-drag ratio using wingtip extension. Whitcomb also stated that the overall performance of winglets is heavily dependent on the angle of incidence of the upper winglets.

Cosin et al. [13] performed an experimental analysis of multi-winglets on a half-body aeroplane model, which has a rectangular wing with a dihedral angle of 1.5 ° and washout angle of 1.25 ° using wind tunnel. A total of 6 different types of multi-winglets configurations, including a baseline wing, were tested at Reynolds number of $4x10^5$. The results show that the optimal multi-winglets configuration lead to a 7.3 % gain in lift-to-force ratio. In addition to that, each multi-winglets configurations show improvement in lift coefficient as well as clear and significant reduction in induced drag. However, the benefits of multi-winglets are outweighed by the parasite drag at low lift coefficient conditions. Cosin et al. explained that it is largely due to the separation regions at the winglets root. Cosin et al. also claimed that such phenomenon also occurs on single winglet as the separation region at the winglet root causes large drag. Besides that, Cosin et al. stated that separations are more critical at low Reynolds number.

2.3 Summary of Literature Review

To summarize the literature that were reviewed, the performance of winglets depends heavily on the types of aeroplane the winglets are attached to. Usually, addition of wingtip devices will improve the lift-to-drag ratio. Winglets improve lift-to-drag ratio by increasing lift rather than decreasing drag. Utilization of winglets effectively increases the wing span. There will always be a trade-off between induced drag and profile drag. Nevertheless, it is worth to have a significant reduction in induced drag with a small unavoidable increment in profile drag. In general, increasing the cant angle of the winglets will increase the lift coefficient and lift-to-drag ratio of the aeroplane, regardless of the winglets' geometry. However, the beneficial effect of winglet vanishes as the cant angle increases further beyond a critical point.

Most of the literatures focused on the effect of winglets' cant angle on the lift-to-drag ratio of large sized aeroplanes. There are very little mentioned about the effect of winglet's cant angle on the lift-to-drag ratio of MUAV. Moreover, there are no mentioned about the effect of winglet's geometry, span, sweep, toe, and twist angle etc. on the lift-to-drag ratio based on the literatures reviewed by the author.

3 Research Methodology

3.1 Overview of Research Methodology

Figure 3.1 shows the research methodology that will be followed in this research.

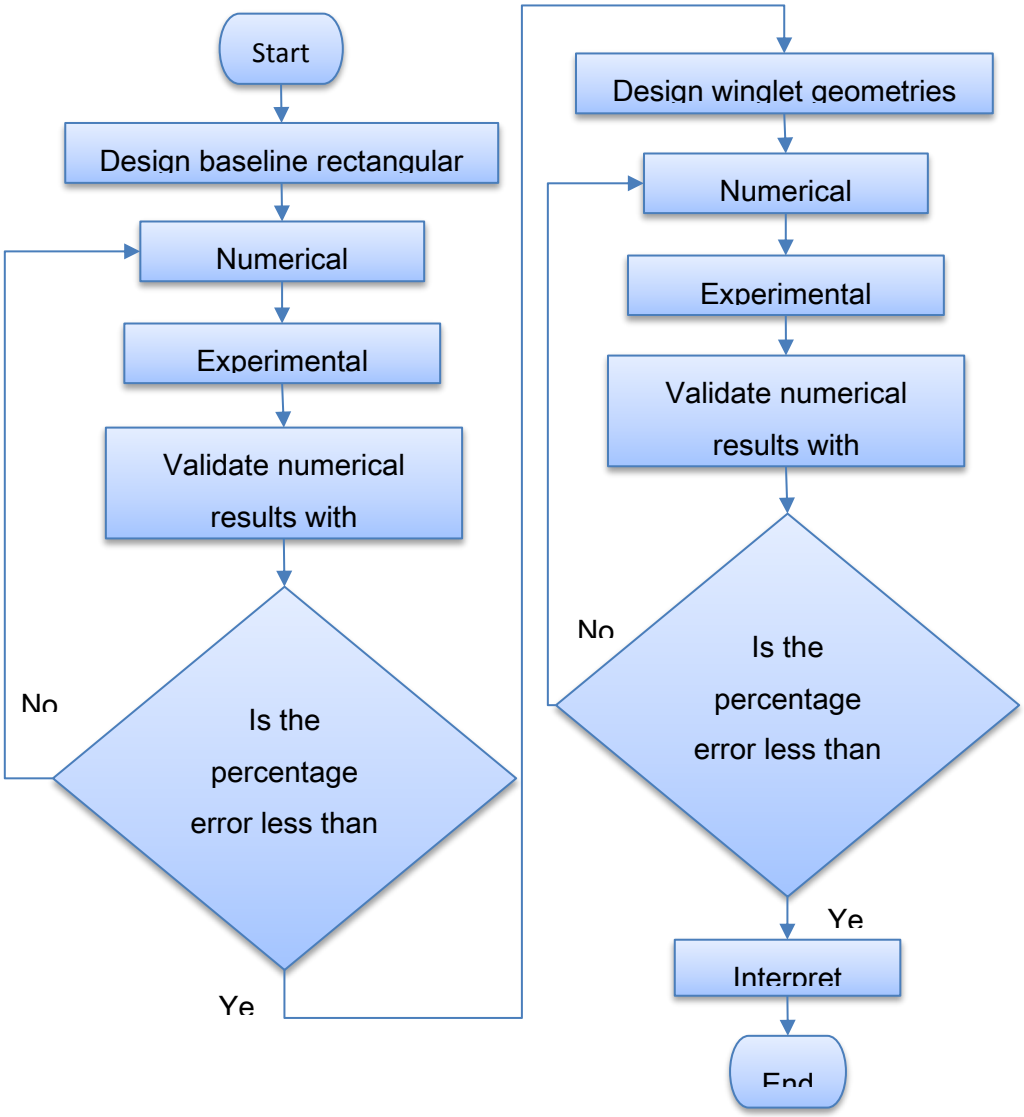


Figure 3.1: Research methodology

3.1.1 Design Synthesis

NACA 0012 aerofoil will be used to design the winglets as it is one of the most commonly used aerofoils among other researchers according to Michos et al. [14]. The winglets will be attached on to a baseline rectangular wing; which have chord of 0.25 m, span of 0.5 m, and aspect ratio of 2; of NACA 0012 aerofoil. The dimension of the rectangular wing closely resembles to the Zala 421-04 micro unmanned aircraft vehicle, which is also used by Karakas et al. [15]. A total of 7 winglet configurations; 3 with different shapes but same area, 2 with different spans but same aspect ratio; and 2 with different sweep angles; are created using SolidWorks 2017. Figure 3.2 and Figure 3.3 shows the geometries in isometric and side views.

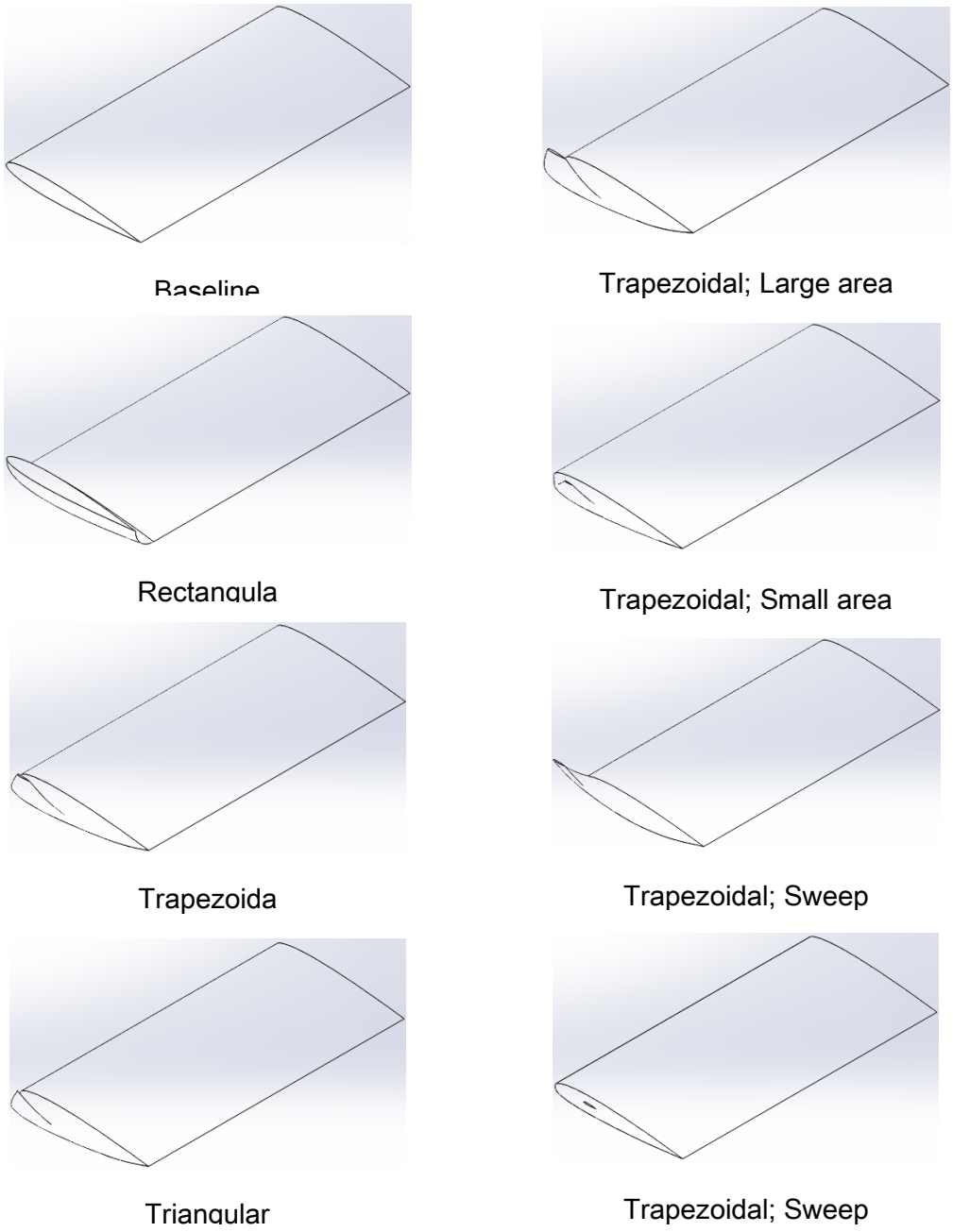


Figure 3.2: Geometries (isometric view)

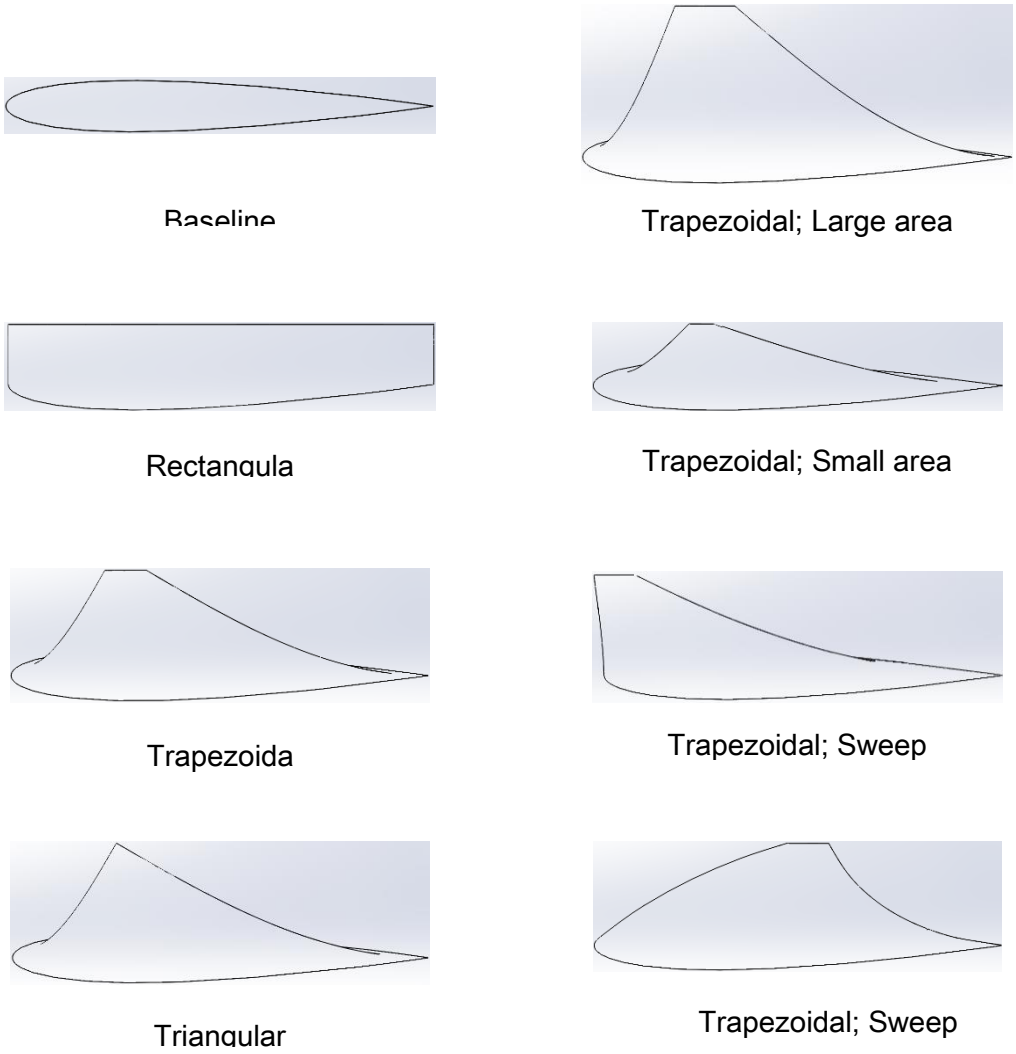


Figure 3.3: Geometries (side view)

3.2 Numerical Analysis

Each winglet configurations will be analysed numerically through computational fluid dynamic at $-20\,°$, $-15\,°$, $-10\,°$, $-5\,°$, $0\,°$, $5\,°$, $10\,°$, $15\,°$, and $20\,°$ angles of attack using ANSYS v18.0.

The process of the computational fluid dynamic can be divided into 3 phases; namely pre-processing, processing, and post-processing phases. In the pre-processing phase, firstly, the fluid domains are defined. After that, the fluid domains are discretized through meshing. Subsequently, the turbulence model, materials, and boundary conditions are set before referencing the appropriate values, which are length and area of the geometries, to calculate the numerical results, which are the lift and drag coefficients. In the processing phase, the solver methods and types of initialization are specified appropriately. Eventually, the number of iterations is set at a value that achieves convergence. In the post-processing phase, evaluation of the lift and drag coefficients is carried out reasonably.

In order to reduce the required computational power to calculate the lift and drag coefficients, the geometries of rectangular wing with and without winglet will be simplified. After that, the

fluid domains will be created using Design Modeler v18.0. Since the fluid is unconfined and flowing over a surface, it is an external flow. Therefore, the fluid domains will be constructed over the surface. The shape of the fluid domains requires careful consideration as it heavily affects many factors, such as the time required to generate the mesh. ANSYS [16] also mentioned that the fluid domains must be large enough to ensure that there will be no significant pressure gradients across the boundary of the fluid domains. Figure 3.4 shows the C-shaped fluid domain.

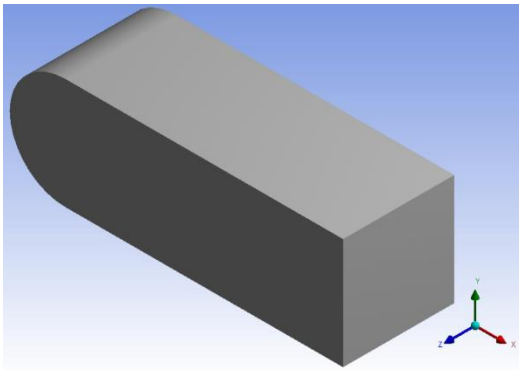


Figure 3.4: C-shaped fluid domain (isometric view)

The mesh of the fluid domains is created using Meshing v18.0. The fluid domains resemble a structured grid. In addition to that, NACA 0012 aerofoil is symmetrical and not complex in terms of geometry. Therefore, for 3-dimensional cases, hexahedron-shaped cells are the most suitable choice. This is to ensure that the connection among the centre of the nodes are regular. As a result, it significantly reduces the numerical error. In order to improve the mesh quality, the mesh is biased towards the surface as the region of interest is the surrounding of the surface. This is done by using cells of very small size. However, obtaining a full hexahedron-shaped cells is extremely difficult, especially for 3-dimensional cases. Therefore, a combination of hexahedron-, prism-, and tetrahedron- shaped cells are utilized for the fluid domains. Figure 3.5, **Error! Reference source not found.** and **Error! Reference source not found.** show the mesh of the fluid domains. It can be clearly seen that the change in cell size near the surface is very smooth. In addition to that, there is no abrupt change in cell size.

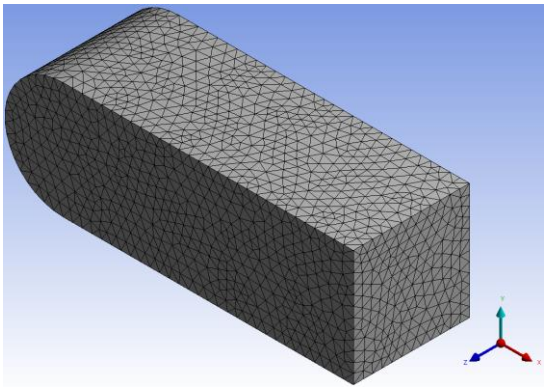


Figure 3.5: Mesh of fluid domains (isometric view)

A finite volume method (FVM) based solver, which is Fluent v18.0, is being utilized. By applying finite volume method, the general transport equation.

$$\int_V \frac{\partial(\phi_m \rho)}{\partial t} dV + \int_V \nabla.(\rho \vec{v} \phi_m)\, dV = \int_V \nabla.(\Gamma \nabla \phi_m)\, dV + \int_V s_V\, dV$$

According to ANSYS [17], shear stress transport $k-\omega$ turbulence model is suitable for complex boundary layer flows involving adverse pressure gradient. The adverse pressure gradient occurred upon reaching the separation point. The separation point moves towards the leading edge as the angle of attack increases. Therefore, shear stress transport $k-\omega$ turbulence model, a 2 equations model based on Reynolds-Averaged-Navier-Stokes equations, which means that 2 general transport equations are used, are utilized.

Since the flow is within the subsonic region, whereby $Ma < 1$, the effect of compressibility of air is negligible and can be ignored. Because of this, the flow can be modelled as incompressible. Thus, the properties of air can be set as a constant magnitude as shown in Table 3.1.

Table 3.1: Properties of air

Property	Magnitude
Density, ρ (kg/m^3)	1.225
Dynamic viscosity, μ (kg/ms)	$1.7894x10^{-5}$

Figure 3.6 shows the boundary conditions. The types of boundary condition used are tabulated in Table 3.2.

Table 3.2: Boundary conditions

	Type	Description
Inlet	Velocity inlet	$v_{absolute} = 8.7644 m/s$
Outlet	Pressure outlet	$P_{absolute} = 101325\ Pa$
Surface	Wall	Wall motion: Stationary wall Shear condition: No slip Wall roughness model: Standard

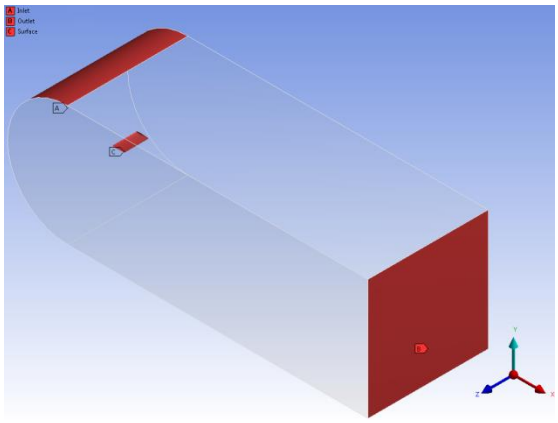


Figure 3.6: Boundary conditions

3.3 Experimental Analysis

The numerical results obtained from the computational fluid dynamics will be validated with the experimental results obtained from the wind tunnel experiments in order to ensure that the

numerical results are accurate. The wind tunnel experiments will be conducted using Taylor's University's wind tunnel apparatus.

Each configuration will be manufactured through additive manufacturing using 3D printing machine. The 3D printed models will then be mounted on to a M8 mounting rod in order to be used in the wind tunnel experiment to collect the experimental data. However, scaling factor is required to be taken into consideration before manufacturing to ensure that the 3D printed models are able to fit into the test section of the wind tunnel. The 3D printed models are scaled down by a factor of 2.5 based on the actual model.

In order to validate the numerical results with the experimental results, both numerical and experimental analyses must be performed under the same Reynolds number of $1.5x10^5$. Such Reynolds number is within the capability of Taylor's University's wind tunnel apparatus. The experimental data obtained from the wind tunnel experiment are in terms of forces and moments. Therefore, in order to obtain the experimental coefficients of lift and drag, certain calculations are required to be performed.

$$F_{L,total} = \frac{1}{2} c_{L,total} \rho v^2 A_{ref,total}$$

Whereby,
$F_{L,total}$ is the lift acting on the 3-dimensional printed model and the mounting rod,
$c_{L,model}$ is the total lift coefficient,
ρ is the density of air,
v is the velocity of air,
$A_{ref,total}$ is the total reference area.

$$F_{D,total} = \frac{1}{2} c_{D,total} \rho v^2 A_{ref,total}$$

Whereby,
$F_{D,total}$ is the drag acting on the 3-dimensional printed model and the mounting rod,
$c_{D,total}$ is the total drag coefficient,
ρ is the density of air,
v is the velocity of air,
$A_{ref,total}$ is the total reference area.

4 Result & Discussion

Figure 4.1 and Figure 4.2 show the numerical lift and drag coefficients against angle of attack, whereas Figure 4.3 shows the numerical polar diagram.

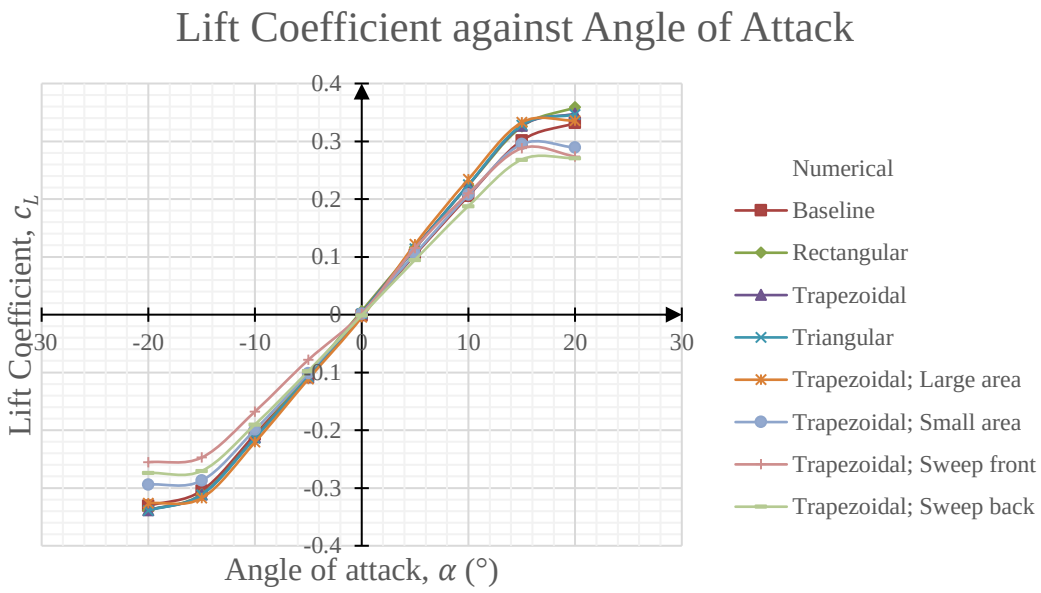


Figure 4.1: Numerical lift coefficient against angle of attack

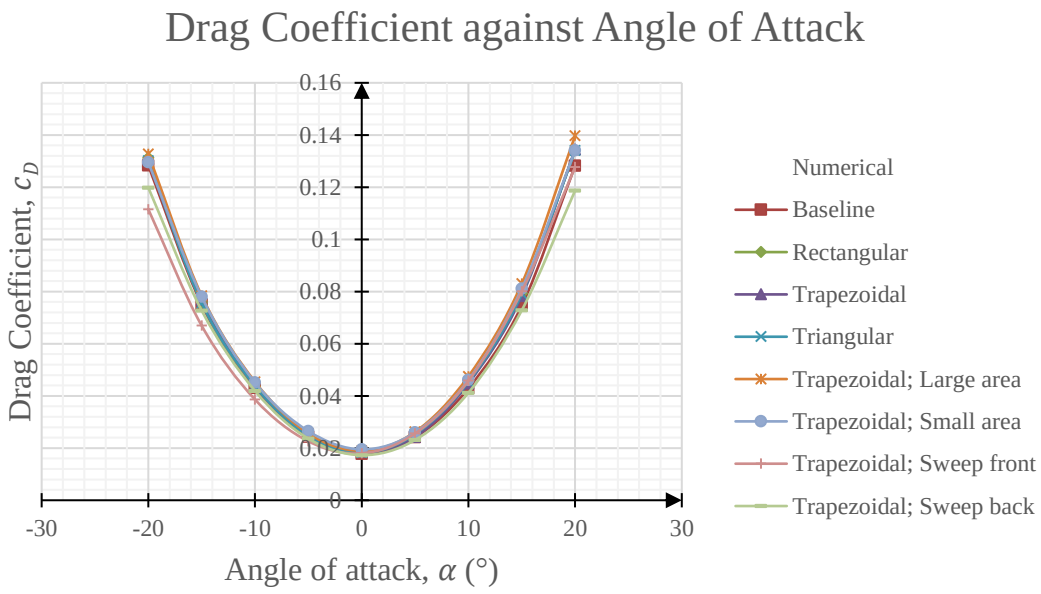


Figure 4.2: Numerical drag coefficient against angle of attack

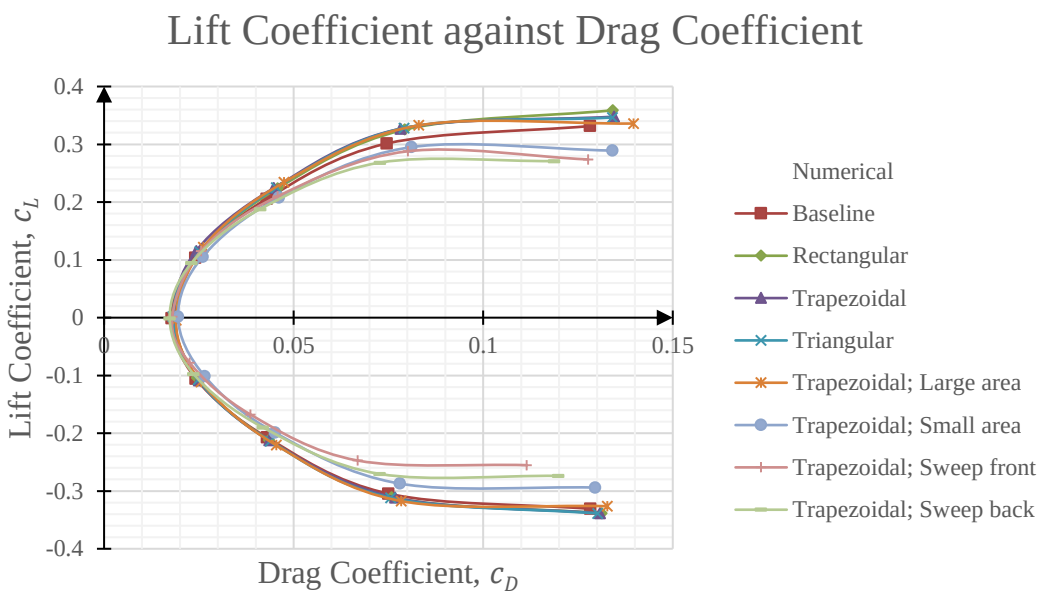


Figure 4.3: Numerical lift coefficient against numerical drag coefficient

Based on Figure 4.1, it can be clearly see that the lift coefficient increases as the angle of attack increases. The lines are also relatively close to each other despite having different configurations.

However, only some of the lift coefficient is maximum at approximately 15 ° angle of attack, whereas most of the lift coefficient continue to increase beyond this critical angle of attack. This is expected as the numerical analysis is an approximation to the experimental analysis. Despite of that, the stalling condition should occur between 20 ° to 25 ° angle of attack. In addition to that, wing with winglet has larger lift coefficient between 5 ° and 11 ° angle of attack, excluding wing with trapezoidal sweep back winglet.

A similar but opposite trend is observed. The lift coefficient decreases as the angle of attack decreases. This is also expected as the NACA 0012 aerofoil is symmetrical.

Likewise, the stalling condition does not occur at the critical angle of attack. Also, not all wings with winglet have smaller lift coefficient before the critical angle of attack. The configurations that show such trend are wings with trapezoidal small area, trapezoidal sweep front, and trapezoidal sweep back winglet.

Based on Figure 4.2, it is clear that the drag coefficient increases as the angle of attack increases. Similarly, the lines are relatively close to each other despite having different configurations. The drag coefficient at small angle of attack is smaller as compared with the drag coefficient at large angle of attack.

All wings with winglet have higher drag coefficient between 8 ° and 18 ° angle of attack, excluding wing with trapezoidal sweep back winglet. At 20 ° angle of attack, wing with trapezoidal sweep back winglet has the smallest drag coefficient.

However, the drag coefficient also increases as the angle of attack decreases. This means that the drag coefficient is always a positive value regardless of the angle of attack. The drag

coefficient at small angle of attack is also smaller as compared with the drag coefficient at large angle of attack.

Wings with trapezoidal sweep front and trapezoidal sweep back winglet have the most noticeable drag coefficient. The drag coefficient is significantly smaller as compared with other wings with winglet.

By referring to Figure 4.3, it obvious that the lines resemble a C-shaped, which is the common shape of NACA 0012 aerofoil on a polar diagram.

All wings with and without winglet have very small lift coefficient regardless of the sign, which is either positive or negative value, at 0 ° angle of attack. Besides that, wing with trapezoidal large area winglet has the largest maximum lift coefficient and wing without winglet has the smallest minimum drag coefficient. Despite of that, wing with triangular winglet has the largest maximum lift-to-drag ratio.

Figure 4.4 and Figure 4.5 show the experimental lift and drag coefficients against angle of attack, whereas Figure 4.6 shows the experimental polar diagram.

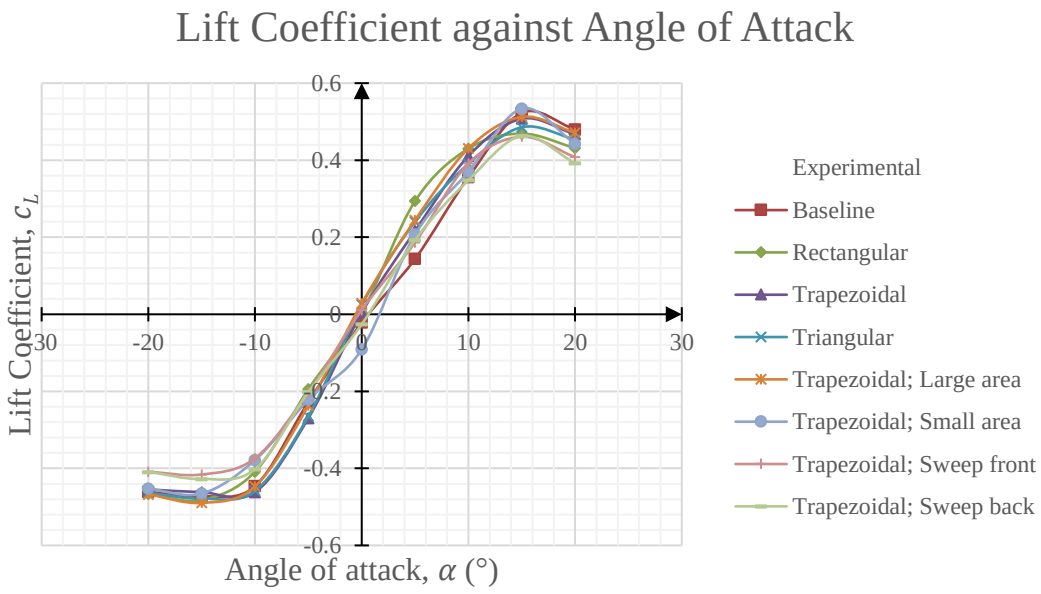


Figure 4.4: Experimental lift coefficient against angle of attack

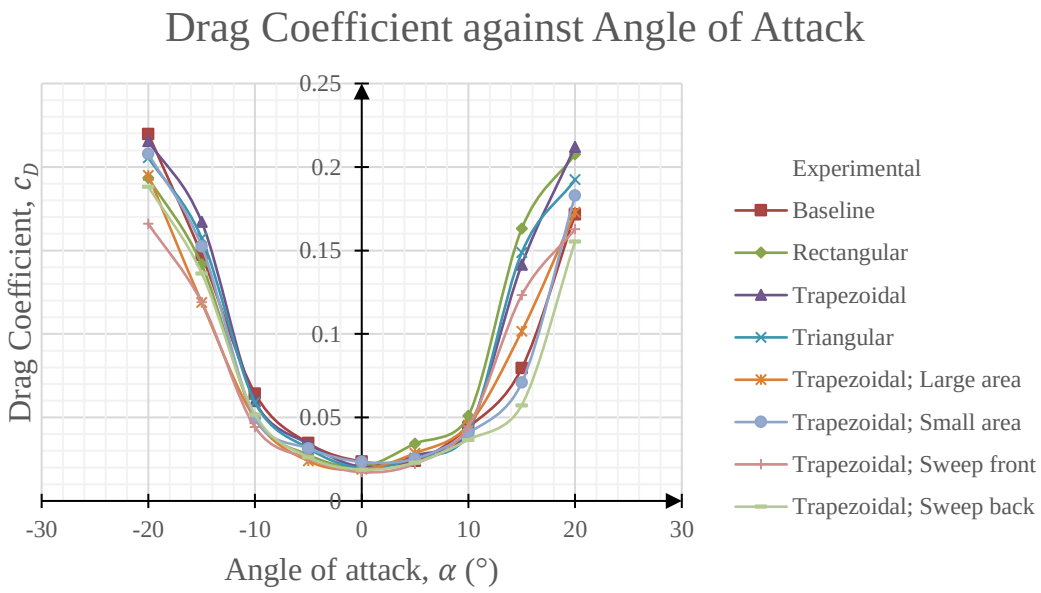


Figure 4.5: Experimental drag coefficient against angle of attack

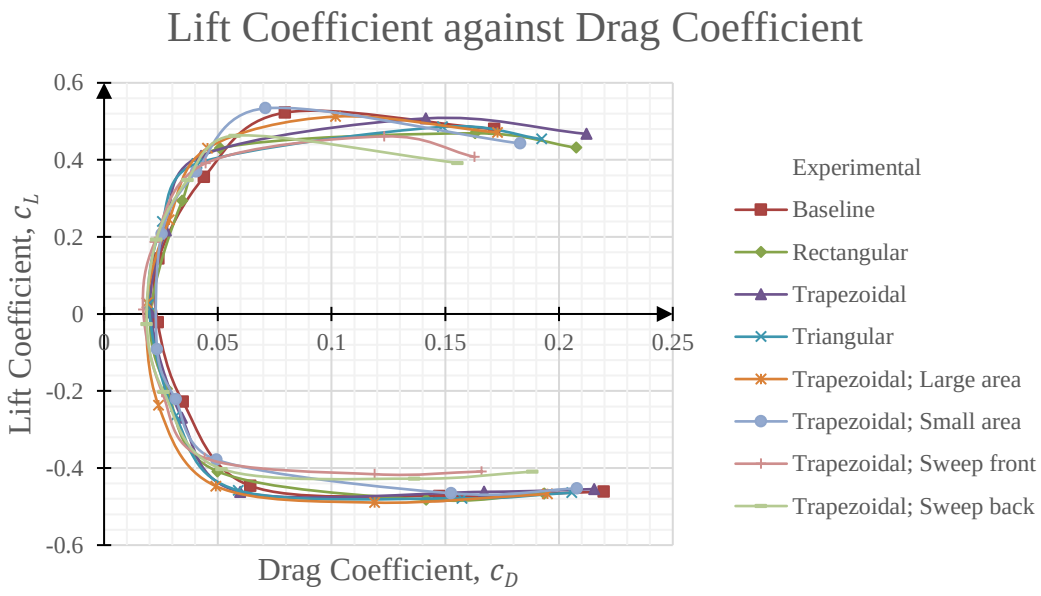


Figure 4.6: Experimental lift coefficient against experimental drag coefficient

Based on Figure 4.4, it is clear that as the angle of attack increases, the lift coefficient also increases. The lift coefficient is maximum at approximately 15 ° angle of attack. However, beyond this critical angle of attack, the lift coefficient starts to decrease despite the increase in angle of attack. This is due to the fact that stalling condition occurs. In addition to that, the critical angle of attack is independent of the configurations.

Nevertheless, wings with winglet have larger lift coefficient between 2 ° and 10 ° angle of attack regardless of its configurations. Upon reaching the critical angle of attack, wings with winglet have smaller lift coefficient, excluding the trapezoidal small area winglet. Beyond the critical angle of attack, all wings with winglet have smaller lift coefficient.

A similar but opposite trend is also observed. As the angle of attack decreases, the lift coefficient also decreases. The lift coefficient is minimum at approximately $-15\,°$ angle of attack. Such trend is expected as NACA 0012 aerofoil are symmetrical.

However, not all wings with winglet have smaller lift coefficient before the critical angle of attack. Wings with trapezoidal small area, trapezoidal sweep front, trapezoidal sweep back, and rectangular winglets are among the most noticeable ones. In addition to that, not all wings with winglet have smaller lift coefficient at the critical angle of attack and beyond.

Based on Figure 4.5, it can be clearly see that as the angle of attack increases, the drag coefficient also increases. The drag coefficient at large angle of attack is significantly higher as compared with the drag coefficient at small angle of attack. This is due to the fact that separation point moves further up to the leading edge, which in turns create a wake region. As a result, the induced drag increases.

Nevertheless, wings with winglet have higher drag coefficient between $12\,°$ and $18\,°$ angle of attack, excluding trapezoidal small area and trapezoidal sweep front winglets. Apart from that, not all wings with winglet have larger drag coefficient at large angle of attack.

As the angle of attack decreases, the drag coefficient increases. In other words, the drag coefficient is always a positive value regardless of the angle of attack. Similarly, the drag coefficient at small angle of attack is significantly higher as compared with the drag coefficient at large angle of attack.

However, all wings with winglet have smaller drag coefficient at small angle of attack. This is because the magnitude of wingtip vortices is reduced.

By referring to Figure 4.6, it can be clearly seen that the lines resemble a C-shaped, which is the common shape of NACA 0012 aerofoil on a polar diagram.

At $0\,°$ angle of attack, all wings with and without winglet have very small lift coefficient regardless of the sign, which is either positive or negative value. Other than that, wing with trapezoidal small area winglet has the largest maximum lift coefficient and wing with trapezoidal sweep front winglet has the smallest minimum drag coefficient. Nonetheless, wing with triangular winglet has the largest maximum lift-to-drag ratio.

Figure 4.7 and Figure 4.8 show the percentage error of lift and drag coefficients against angle of attack.

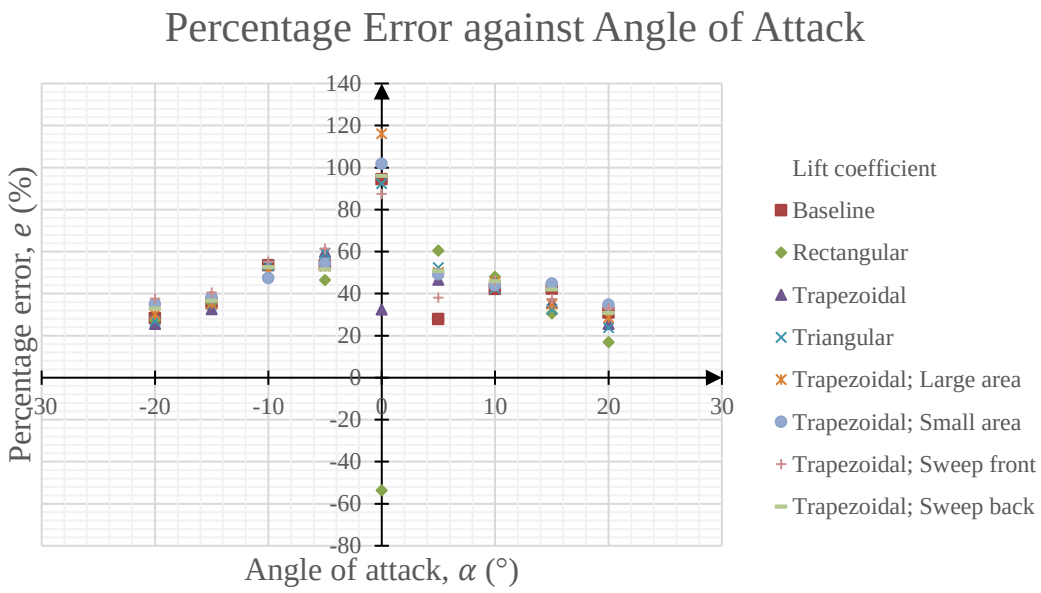


Figure 4.7: Percentage error of lift coefficient against angle of attack

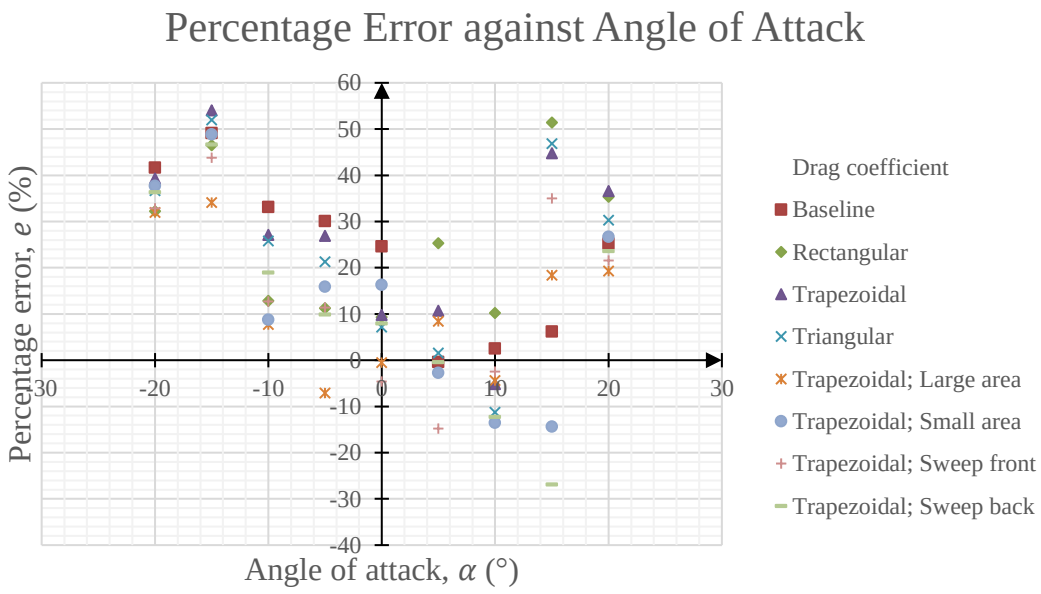


Figure 4.8: Percentage error of drag coefficient against angle of attack

By comparing Figure 4.7 and Figure 4.8, it can be clearly see that the percentage error of drag coefficient has higher accuracy as compared with the percentage error of lift coefficient, especially at small angle of attack. This is expected due to the coarse mesh used in the numerical analysis. Nevertheless, the percentage error of lift coefficient has higher precision as compared with the percentage error of drag coefficient.

Based on Figure 4.7, in general, most of the percentage error of lift coefficient lies between 20 % to 60 %. Besides that, almost all of the percentage error of lift coefficient at 0 ° angle of attack is higher than 50 %. However, both the numerical and experimental lift coefficients at 0 ° angle of attack is still approximately 0 regardless of its sign.

Based on Figure 4.8, in general, most of the percentage error of drag coefficient lies between -20 % and 30 %, more specifically between -10 ° and 10 ° angle of attack. At 15 ° angle of attack and beyond, the percentage error of drag coefficient starts to increase.

5 Conclusion

In conclusion, the aim of this research is to investigate the effect of winglets' shape, span, and sweep angle on the lift-to-drag ratio of a fixed wing micro unmanned aircraft vehicle as well as to select the most suitable winglets configuration to be utilized on a fixed wing micro unmanned aircraft vehicle.

According to the analyses done by this research, the following conclusion can be drawn.

1) The trend of the experimental results of baseline rectangular wing is similar to the trend of the published experimental results.
2) Wing with triangular winglet has the largest numerical and experimental maximum lift-to-drag ratio.
3) Wing with trapezoidal large area winglet has the largest numerical maximum lift coefficient, whereas wing with trapezoidal small area winglet has the largest experimental maximum lift coefficient.
4) Wing without winglet has the smallest numerical minimum drag coefficient, whereas wing with trapezoidal sweep front winglet has the smallest experimental minimum drag coefficient.
5) Percentage error of lift coefficient has higher precision, whereas percentage error of drag coefficient has higher accuracy.
6) Percentage error of lift coefficient lies between 20 % to 60 %, whereas percentage error of lift coefficient lies between -20 % to 30 %.

6 References

[1] J. R. Chambers, "Concept to Reality: Contributions of the NASA Langley Reserach Center to U.S. Civil Aircraft of the 1990s," National Aeronautics and Space Administration, Washington, D.C, 2002.

[2] P. Panagiatou, P. Kaparos and K. Yakinthos, "Winglet Design and Optimization for a MALE UAV Using CFD," *Aerospace Science and Technology,* vol. 39, pp. 190-205, 2014.

[3] M. D. Maughmer, "The Design of Winglets for High-Performance Sailplanes," *Journal of Aircraft,* vol. 40, no. 6, pp. 1099-1106, 2003.

[4] H. H. Heyson, G. D. Riebe and C. L. Fulton, "Theoretical Parametric Study of the Relative Advantages of Winglets and Wing-Tip Extensions," National Aeronautics and Space Administration, Hampton, 1977.

[5] M. Murayama and K. Yamamoto, "Numerical Simulation of High Lift Configurations using Unstructured Mesh Method," in *24th International Congress of the Aeronautical Sciences*, Yokohama, 2004.

[6] M. Gaffuri and J. Brezillon, "Unstructured Mesh Capabilities for Supersonic Wing Design at Low Speed Conditions," in *European Community on Computational Methods in Applied Sciences Thematic Conference*, Antalya, 2011.

[7] M. J. Lutton, "Comparison of C- and O- Grid Generation Methods Using a NACA 0012 Airfoil," Air University, Dayton, 1989.

[8] B. K. Komarabathini, D. Kancharla, K. Monika, P. K. Chikoti and K. Pasala, "Study of Rate of Convergence of Different Types of Grid in CFD Analysis," *International Journal of Current Engineering and Technology,* vol. 1, no. 2, pp. 520-524, 2014.

[9] M. A. Azlin, C. F. M. Taib, S. Kasolang and F. H. Muhammad, "CFD Analysis of Winglets at Low Subsonic Flow," *Proceedings of the World Congress on Engineering 2011,* vol. 1, pp. 87-91, 2011.

[10] M. Dinesh, P. P. S., J. S. Rao and C. Senthilkumar, "Performance Analysis of Winglets Using CFD Simulation," in *Altair Technology Conference,* Pune, 2013.

[11] D. Myilsamy, Y. Thirumalai and P. P. S., "Performance Investigation of an Aircraft Wing at Various Cant Angles of Winglets Using CFD Simulation," in *Altair Technology Conference,* Pune, 2015.

[12] R. T. Whitcomb, "A Design Approach and Selected Wind-Tunnel Results at High Subsonic Speeds for Wing-Tip Mounted Winglets," National Aeronautics and Space Administration, Washington, D.C., 1976.

[13] R. Cosin, F. Catalano, L. Correa and R. Entz, "Aerodynamic Analysis of Multi-Winglets for Low-Speed Aircraft," *27th Congress of the International Council of the Aeronautical Sciences 2010,* vol. 2, pp. 1622-1631, 2010.

[14] A. Michos, N. Athanassiadis and G. Bergeles, "Aerodynamic Characteristics of NACA 0012 Airfoil in Relation to Wind Generators," *Wind Engineering,* vol. 7, no. 4, pp. 247-262, 1983.

[15] H. Karakas, E. Koyuncu and G. Inalha, "ITU Tailless UAV Design," *Journal of Intelligent and Robotic Systems,* vol. 69, pp. 131-146, 2013.

[16] ANSYS, "Introduction to ANSYS Fluent-Lecture 3: Cell Zone and Boundary Conditions," ANSYS, Inc., Canonsburg, 2015.

[17] ANSYS, "Introduction to ANSYS Fluent-Lecture 7: Turbulence Modeling," ANSYS, Inc., Canonsburg, 2014.

[18] G. Narayan and B. John, "Effect of Winglets Induced Tip Vortex Structure on the Performance of Subsonic Wings," *Aerospace Science and Technology,* vol. 58, no. 1, pp. 328-340, 2016.

[19] M. J. Smith, N. Komerath, R. Ames, O. Wong and J. Pearson, "Performance Analysis of a Wing with Multiple Winglets," in *19th American Institute of Aeronautics and Astronautics Applied Aerodynamics Conference,* Anaheim, 2001.

[20] B. R. Rao and R. Sahitya, "Numerical and Experimental Investigation of the Flow Field around NACA 0012 Aerofoil," *International Journal on Theoretical and Applied Research in Mechanical Engineering (IJTARME),* vol. 4, no. 4, pp. 2319-3182, 2015.

[21] M. R. Soltani, A. H. Birjandi and M. S. Mooranic, "Effect of Surface Contamination on the Performance of a Section of a Wind Turbine Blade," *Scientia Iranica,* vol. 18, no. 3, pp. 349-357, 2011.

[22] A. Karimi and M. Tadjfar, "Cross-Wind Influence on Low Aspect Ratio Wings at Low Reynolds Numbers," in *American Society of Mechanical Engineers (ASME) 2013 Fluids Engineering Division Summer Meeting,* 2013.

EURECA 2018 – Conference Paper
Paper number 2ME11

Improving the Efficiency of a Hybrid Photovoltaic-Thermal System Through Building Integrated Semi-transparent Photovoltaic Thermal System

Chee Jit Lim[1], Aravind CV[1], Mohd Hardie Mohyi[1]*

[1]School of Engineering, Taylor's University, Malaysia.

Abstract

A study has been conducted on a new design for a Building Integrated Semi-Transparent Photovoltaic-Thermal system which promotes building self-sufficiency by providing additional electricity generation and external heat insulation. Insulating heat from the external decreases the heat infiltrating into the building itself, leading to a cooler and comfortable living space, hence reducing energy consumption for cooling system such as air conditioning systems. Mathematical and computational study has been conducted and discussed in this report, where the results which are expressed as the temperature difference between the outer most surface to the inner most, yielded 14.65°C and 6.74°C respectively which has a percentage error of 51% with a correlation of 2.04. Based on mathematical and CFD analysis, the temperature difference of the proposed system had 16.28 times and 16.44 times of improvement respectively when compared to a control setup.

*Corresponding author: aravindcv@ieee.org

1. Introduction

The development of solar energy has been strongly encouraged by the National Academy of Engineers (United States), as one of the Grand Challenge of the 21st Century is to make solar energy economical. Solar energy available on Earth is approximately 10,000 times more than what is used today, but solar energy only represents 1% of the global energy market share [1]. In Malaysia only 0.7% (226MW from 22,810MW) of the total energy generation by the nation are from renewable energy, based on the National Energy Balance 2015 statistics [2].

The focus of harvesting solar energy for this report is through the method of a Building Integrated Semi-Transparent Photovoltaic-Thermal system (BiSTPVT). A BiSTPVT system is an electric generation system in a form of a semi-transparent photovoltaic panel which exists with the building itself during the construction process instead of as additional equipment (such system is called B-Adapted-STPVT), for example, roofing or windows [3, 4, 5]. An example of a STPV panel is shown in BiSTPVT benefits the buildings by harvesting electrical energy by itself, which reduces the demand from the national electricity grid, ultimately reducing its electrical consumption cost and improve its sustainability.

While the system requires sunlight to generate electricity, the system will be heated up as well which would decrease its electricity generation efficiency. As temperature of the system gets too hot, the efficiency would be so low that the electricity generated is insufficient to benefit the building at all. BiSTPVT system counters this problem by harvesting the thermal energy which are built up in the panel. By harvesting the thermal energy of the system, the system will be cooled down thus regaining its efficiency, and the heat removed can be used for space heating purposes.

However, space heating is not applicable in hot countries such as Malaysia, but cooling will not only improve comfort but also reduce cooling loads of the building such as heat ventilation and air conditioning system (HVAC), which make up a huge part of the total cost of a building. According to the National Energy Commission as depicted in Figure, HVAC system makes up to 14% of the total consumption of a residential building annually. Decreasing this consumption cost will improve the economics of the building, while at the same time preserving energy for the country.

1.1. Research Theory

A BiSTPVT system is proposed that will be integrated into buildings as windows. The reason for this is that windows are crucial for allowing sunlight to enter the building improving visual perception, comfort and reducing the need for additional lighting which incur additional costs [6]. As BiSTPVT systems are semi-transparent, while a partial of light are used for electricity generation, a partial of it will still pass through it.

The source of heat of a building is mainly from the exterior atmosphere which gets transferred into the building through convection, conduction and radiation from the sun. Reducing this heat transfer will effectively reduce the heat into the building, this can be achieved through means of heat insulation. Every material has thermal properties for heat transfer which can be expressed by a coefficient of heat conduction or coefficient of heat convection. By selecting the appropriate materials, heat transfer can be reduced drastically. Gaseous objects are the best heat insulation material as it discourages heat transfer due to its freely moving particles, a gap of air will significantly reduce incoming heat.

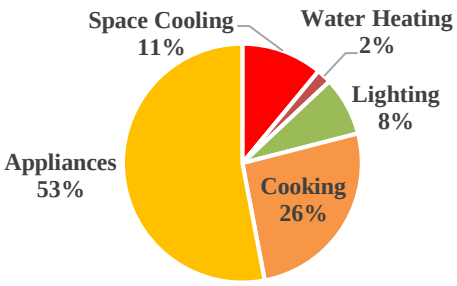


Figure 1: Energy consumption breakdown in residential sector in year 2015 [2].

To ensure that the STPV remains cool and maintains its electrical generation efficiency, heat needs to be removed, which can be done by the means of heat sink or heat fins (the term heat fins will be used in this report). Figure 2 shows the contrast between the issue of a typical condition of a building and the proposed BiSTPVT system design and its effect [7].

To summarize this work, an STPV has been converted into a BiSTPVT system by using them as a substitute for windows. This system would be able to generate electricity while at the same time reduce the transfer of heat from the exterior ambient temperature into the building, thus reducing the building temperature which simultaneously provide an economical solution to reduce the building's energy consumption cost. The design, concept and methods will be discussed thoroughly in this report, along with results from mathematical and computational analysis.

2. System Description

A flow chart depicts the methodology of this study which is shown in Figure 3. This paper discusses the flow up until comparison of results of mathematical and CFD analysis. The setup for experimental analysis will be discussed without the results for the meantime.

2.1. Research design

To ensure that the building's space is cool, the heat transfer from the exterior into the building must be reduced. A double-glazed window design which sandwiches a layer of air (named as an air gap in this report) will greatly decrease the transfer of heat. This is due to convection is a bad mode of heat transfer compared to conduction, the temperature of the surface inside the building will be a lot cooler compared to the outer surface.

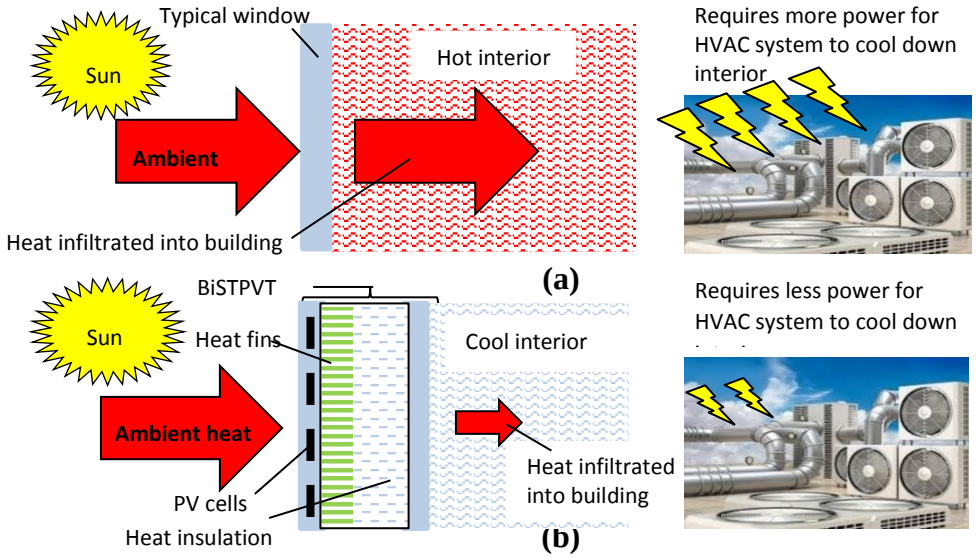


Figure 2: Current issue (a). Proposed BiSTPVT system (b).

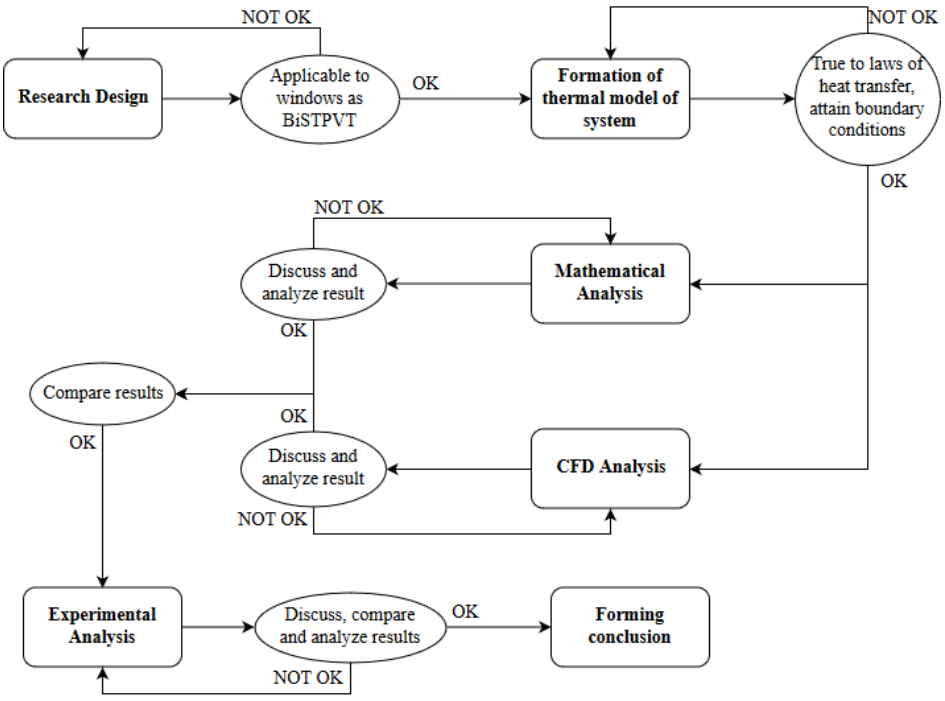


Figure 3: Flow chart of study.

However, having an air gap does not solve the issue of the decreased electrical power generation efficiency of STPV when it starts to heat up by the hot external temperature. To cool the STPV, heat fins can be installed adjacent to the STPV hence dissipating heat off the STPV hence cooling it down, which will restore its efficiency. The heat transfer from the STPV to the heat fin is a mode of conduction which can be expressed as Eq 1, where $\dot{Q}$ is the rate of heat transfer, k is the heat transfer coefficient, x is the thickness of the material while T is the temperature.

$$\dot{Q} = \sum \frac{kA}{x}(dT) \quad (1)$$

In this research, *A* is chosen to be the variable studied and varied to maximise $\dot{Q}$. From Eq 1, an increase in *A* will increase $\dot{Q}$, however, a conflict arises in maximising *A*. As this would ultimately be a window, light must be allowed thorough it. The more light enters the building, the lesser additional lighting is required thus saving energy. Therefore, a heat fin has been designed to enable both good heat dissipation and allowing light to pass through.

2.2. Proposed Design and Mathematical Modelling

Honeycomb heat fins are multiple hexagons compactly arranged next to one another which can easily be visualized by the form of a beehive. Hexagonal shapes can be easily compacted together in a uniform order compared to other irregular shapes while having a constant wall thickness throughout the entire sheet. Hexagonal shapes also provide a benefit of larger surface area coverage to promote heat dissipation [8]. Figure shows a comparison of the different shapes of a heat fin and the effect of each. Circular fins cannot be compacted uniformly leaving a non-uniform wall thickness. Triangular and square shaped fins can be compacted uniformly however, the surface area coverage lacks hexagonal shaped fins.

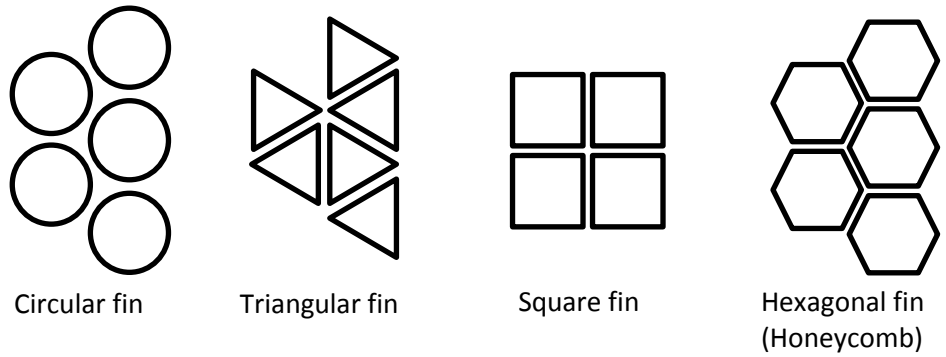


Figure 4: Comparison of different shaped heat fins.

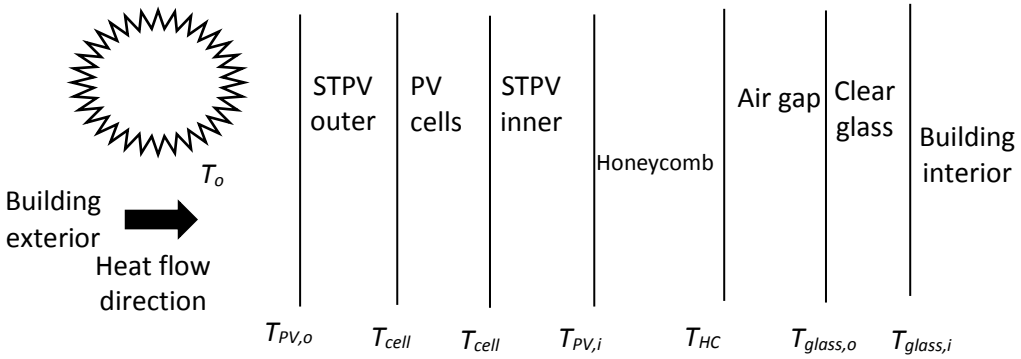


Figure 5: Simplified thermal model of the system.

The system can be analysed mathematically for its heat transfer ability using heat transfer equations of conduction, convection and radiation. It should be noted that due to the complexity of radiation from the sun, specifically the long wave radiation that are reflected off nearby surfaces, it is neglected in this study, only the main radiation from the sun is included in this study.

A simplified thermal model of the system is formed and shown as Figure to simplify the calculations of heat transfer. The subscripts "o" signifies the outer surface which faces the exterior of the building while subscript "i" signifies the inner surface. The subscripts PV, cell, HC, glass are the STPV, PV cell, honeycomb heat fin and clear glass respectively.

To simplify the analysis, the heat flux will be calculated which neglects the area of the system, which are shown by Eq 2.

$$\dot{q} = -k\frac{dT}{dx} \tag{2}$$

Starting from the exterior surface, the heat transfer are mainly due to radiation and convection onto the outer STPV surface, which can be modelled as Eq 3. Conduction coefficient, *k* and thickness, *t* of any of the equations are defined as of Table 1 and Table 2,

where the design specifications and constant values of material property.

$$h_{c,o}\left(T_{PV,o} - T_o\right) = \frac{k_{PV}}{t_{PV}}\left(T_{PV,o} - T_{cell}\right) \tag{3}$$

The ambient convection coefficient, $h_{c,o}$ can be determined as Eq 4, where v_w is the wind speed.

$$h_{c,o} = 5.7 + 3.8v_w \tag{4}$$

Table 1: Design Specifications

Part	Material	Parameter	Value
STPV, clear glass	Glass	Thickness, t_{pv}, t_{glass}	6.8mm
		Dimension (W×H)	1100mm × 1400mm
PV cell	Amorphous silicon	Thickness, t_{cell}	3×10^{-3} mm
Honeycomb heat fin	Aluminium	Thickness of fin, t_{al}	10 mm
		Thickness of cell wall	0.60 mm
		Cell side length, a	15mm
		Cell cross sectional area	$900mm^2$
Air gap	Air	Thickness, t_{gap}	33 mm

Table 2: Material Properties

Component	Properties			
	Density, ρ (kgm^{-3})	Thermal conductivity, k ($Wm^{-1}K^{-1}$)	Refractive index, $\dot{n}$	Extinction coefficient, K (m^{-1})
Clear glass [9]	2500	0.76	1.526	4
Amorphous thin film silicon, a-Si [10, 11, 12]	2330	0.25	2.000	1.639

Aluminium sheet [13]	2719	202.4	-	-
Air [13]	1.225	0.242	1.000	-

This heat will be conducted into the PV cells in the centre of the STPV along with the radiation from the sun as the STPV is transparent. As part of the sunlight is reflected away by the STPV before actually landing on the PV cells, the transmittance coefficient at the centre of the STPV, $\tau_{pv,mid}$ and the absorption coefficient of the cell, α_{cell} is taken into account. The sum of the heat flux is then conducted towards the inner surface of the STPV (Eq 5).

$$G\tau_{PV,mid}\alpha_{cell} + \frac{k_{PV}}{t_{PV}}\left(T_{cell} - T_{PV,o}\right) = \frac{k_{PV}}{t_{PV}}\left(T_{cell} - T_{PV,i}\right) + P_{PV} \quad (5)$$

$\tau_{pv,mid}$ and α_{cell} can be calculated through Eq 6 to 10, where τ_1 and τ_2 are the reflection and absorption losses by the surface, Φ is the general reflectance of light of a particular surface, K is the extinction coefficient and $\dot{n}$ is the reflective index which can be obtained from Table 2 [14].

$$\tau = \tau_1\tau_2 \quad (6)$$

$$\alpha = 1 - \tau_2 \quad (7)$$

$$\tau_1 = \frac{1-\Phi}{1+\Phi} \quad (8)$$

$$\tau_2 = exp(-\frac{Kt_j}{\cos\theta_r}) \quad (9)$$

$$\Phi = \left(\frac{\dot{n}_{air}-\dot{n}_j}{\dot{n}_{air}+\dot{n}_j}\right)^2 \quad (10)$$

The heat transfer continues where the heat from the inner surface of the STPV is transferred to the honeycomb through conduction and convection also considering any radiation from the sun that passes through the STPV that is transferred to the 0olhoneycomb fin. The mathematical equation for this heat transfer is shown as Eq 11, where A_c is the cross-sectional area of a cell and a is the cell side length, which can be referred to Table 1 [15].

$$G\tau_{PV,inner}\tau_{cell}\alpha_{PV,inner} + \frac{k_{PV}}{t_{Pv}}\left(T_{cell} - T_{PV,i}\right) = \frac{k_{Al}}{t_{Al}}\left(T_{PV,i} - T_{Al,i}\right)\frac{A_c}{6a} + h_{c,gap}\left(T_{PV,i} - T_{Al,i}\right) \quad (11)$$

$h_{c,gap}$ can be determined by using Eq 12, where Nusselt's number, Nu is calculated by Eq 13. Ra is the Rayleigh number of the air flow within the gap, which is assumed to be 15,000 in this study [16, 17].

$$h_{c,gap} = \frac{Nuk_{air}}{t_{air}} \quad (12)$$

$$Nu = 0.54 \times Ra^{0.25} \quad (13)$$

The heat will then get transferred through the air gap onto the outer surface of the clear glass which is then conducted to the inner surface (Eq 14). The convection due to the interior air is taken into account with the convection coefficient of $h_{c,i,}$ at a room temperature of T_i [18].

$$h_{c,gap}\left(T_{Al,i} - T_{glass,o}\right) = \frac{k_{glass}}{t_{glass}}\left(T_{glass,o} - T_{glass,i}\right) - h_{c,i}(T_{glass,i} - T_i) \quad (14) \text{ [18]}$$

The heat transfer is then completed and the temperature difference from the outer surface of the STPV and the inner surface of the clear glass can be related to the efficiency of the system to achieve a cooler temperature in the building interior. The larger the temperature difference, the cooler the building interior will be, therefore more savings on energy consumption for HVAC system.

2.3. Computational Analysis (CFD) Design

A CFD model is constructed based on the design. RNG k-ϵ using Coupled with Pseudo transient enabled to compute for its equation as it is proven to be reliable according to previous studies on similar double-glazed window design [17, 19, 20]. The system can be simplified into a scaled down 2D analysis for an efficient computation as the system is vertically symmetrical. Figure 6 shows the final meshing of the model.

Boundary conditions are set similarly to the mathematical analysis where $T_{PV,o}$ is 36.7°C and a convection heat transfer on the clear glass surface (shown in blue of Figure 6). Coupled wall interfaces have been set to all the adjacent walls of each layer, which are shown in yellow in Figure 6. The top of the air gap (shown in red in Figure 6) is declared as an outflow, where hot air can exit the system and cools down the system. The other edges in white are non-permeable walls, where the heat transfer by these surfaces are neglected in this study. These interfaces allow heat to be properly transferred in between layers to obtain an accurate result.

The air gap density has been specified as a boussines with specified operating density enabled and a room temperature of 27°C. This allows for air flow within the gap which will provide a result that closely mimics the reality.

To test the proposed system, an experimental analysis will be performed. A Solidworks model has been produced along with the system built in Taylor's University is shown in Figure 7. The dimensions for the honeycomb are illustrated in Figure 8 as a clarification.

2.4 Coefficient of Correlation of Analysis

A correlation can be found by analysing the ratio of the result from mathematical and computational analysis (experimental results are neglected in this paper), where it can be expressed as Eq 15

$$\gamma = \frac{\Delta T_{system,mathematical}}{\Delta T_{system,CFD}} \tag{15}$$

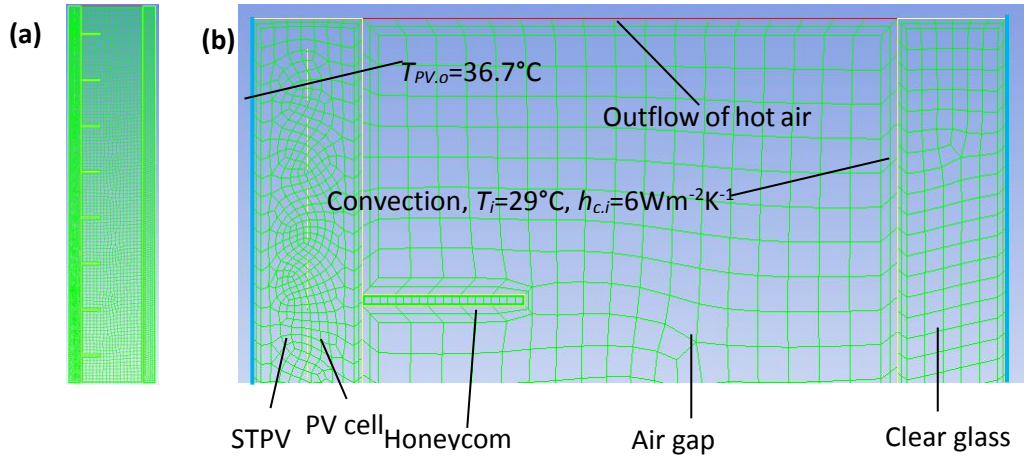


Figure 6: CFD 2D thermal model (a). Close-up of the boundary conditions set in CFD labelled (b).

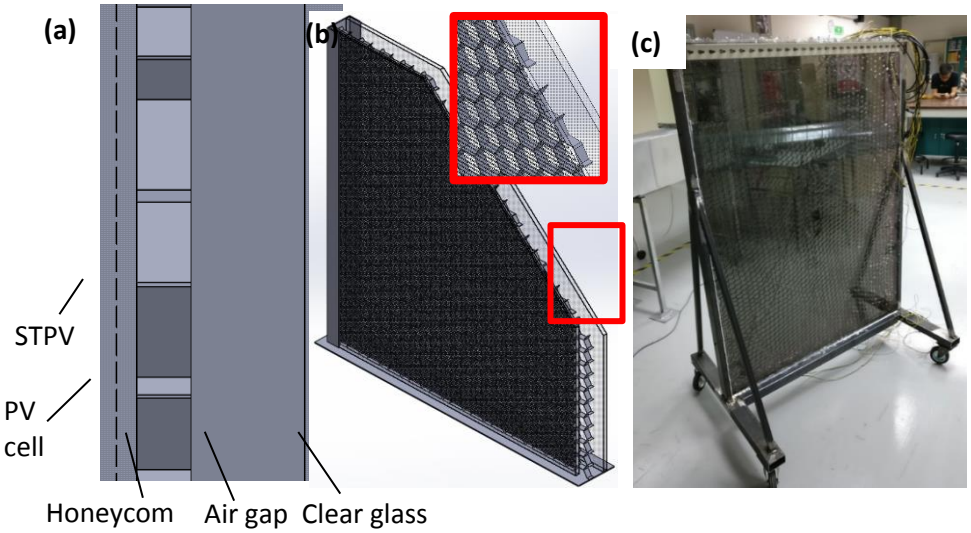


Figure 7: Cross sectional view of the system (a). Isometric view of quarter section of proposed BiSTPVT system with a close up shown in red box (b). The actual system built in Taylor's University (c).

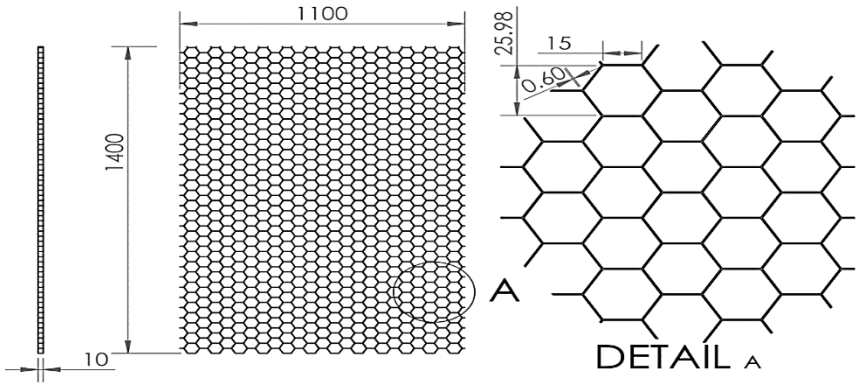


Figure 8: Clarification of honeycomb heat fin dimensions. Units are in mm.

A difference should exist in between the mathematical and computational analysis due to the difference in equations and calculation methods used by the two. However, the most significant factor that affect the difference in the two result is the complexity of air flow in the air gap of

the system. Mathematical calculation fails to include air flow pattern and assume that the layer within the air gap are stagnant and a compact layer, which in reality is not the case. Air flow affects the heat transfer drastically, which can be simulated using CFD hence it is predicted that the results from CFD will be much more accurate. γ is important as it relates to the difference between the results, which signifies the accuracy of this experiment. If γ remain constant for while carrying out similar calculation methods for both mathematical and computational for different situations (eg. Boundary conditions), then the analysis method for both in this study is strong and credible.

2.5 Control System

To compare and analyse the improvement that is produced by this system, a control system is required. Using typical windows in buildings (illustrated as Figure 2 (a)), a typical temperature difference from the exterior and interior of a building can be calculated by altering Eq 3 and Eq 14 into Eq 16.

$$h_{c,o}\left(T_{control,o} - T_o\right) = \frac{k_{control}}{t_{control}}\left(T_{control,o} - T_{control,i}\right) - h_{c,i}(T_{control,i} - T_i) \quad (16)$$

Assuming similar boundary conditions, the resulting inner surface temperature of the control setup is 35.90°C which gives a very small difference of $\Delta T_{system,control}$ 0.80°C across a typical system (Eq 17).

$$\Delta T_{system} = T_{PV,o} - T_{glass,i} \quad (17)$$

A CFD analysis on a typical system yields a temperature contour plot in Figure 9, where the inner surface temperature is 36.31°C, thus the ΔT_{system} of the control design yields 0.39°C. As expected, a difference is present between the mathematical and CFD results, hence $\gamma_{control}$ is calculated and found to be 2.05. This would be the benchmark for the study on the proposed system, if γ_{actual} is the same as 2.05, then the mathematical and CFD analysis do share a correlation which strengthens the accuracy of this study.

3. Results and Discussion

In this report, the mathematical and computational analysis will be focused on. Both approaches have produced results which are discussed in this section. Boundary values are determined to successfully analyse the system. The values are obtained from credible sources and preliminarily experiment, such as v_w and solar irradiance, G is obtained from the Malaysian Meteorological Department, published by meteoblue.com. The value of $h_{c,i}$ is taken from a study undergo by Mohebbi and Sellier [21]. T_o, T_i, $T_{PV,o}$ and P_{PV} are obtained from measurements conducted in Taylor's University. The values of τ, α and $h_{c,o}$, are calculated using Eq 6 to 10 and Eq 4 respectively.

3.1. Mathematical Analysis

The surface temperature of each layer of the system can be calculated using Eq 3 to 14 to with reference to Table 1, Table 2 and Table 3. The results from mathematical analysis shows that the surface temperature for the cell temperature, inner surface of the STPV, inner surface of the honeycomb, outer surface of the clear glass and inner surface of the clear glass are 36.49°C, 35.30°C, 32.54°C, 26.19°C and 22.95°C respectively. This gives a temperature difference of the system, $\Delta T_{system,mathematical}$ from the outer surface of the STPV to the inner surface of the clear glass of 13.95°C (Eq 17).

Table 3: Summary of Boundary Values

Property	Value
Wind velocity, v_w [22]	0.6994 ms^{-1}
Ambient temperature, T_o	31°C
Interior room temperature, T_i	29°C
Temperature outer STPV, $T_{PV,o}$	36.7°C
Solar irradiance, G [23, 22]	436.389 Wm^{-2}
Interior heat convection coefficient, $h_{c,I}$ [21]	$6W^{-2}K^{-1}$
Power generated by PV cell, P_{PV}	2.571 W
Solar transmittance coefficient (mid-section of STPV), $\tau_{PV,mid}$	0.9045
Solar absorbance coefficient (mid-section of STPV), $\alpha_{PV,mid}$	0.0135
Solar transmittance coefficient (back of STPV), $\tau_{PV,mid}$	0.8923
Solar absorbance coefficient (back of STPV), $\alpha_{PV,mid}$	0.0268
Solar absorbance coefficient (PV cells), α_{cells}	0.8
Ambient heat convection coefficient, $h_{c,o}$	$8.339Wm^{-2}K^{-1}$

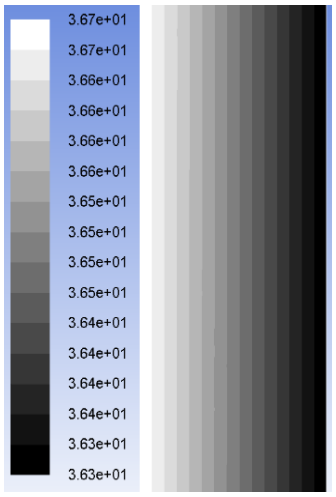


Figure 9: Resulting CFD temperature plot of the control system. Units are in °C.

Comparing this difference to the control setup, the proposed BiSTPVT brings an improvement of 17.31 times However, the mathematical analysis does not consider the air flow condition which exist within the air gap. This air flow is very complex to be determined through mathematical analysis, as the varying temperature of the system will affect the flow conditions, which will then affect the final temperature of the system. Therefore, CFD analysis will be used to further verify this result.

3.2. Computational Analysis (CFD)

The results of the CFD analysis has been shown in a temperature contour plot illustrated in Figure . According to the plot, the temperature at the inner surface of the clear glass has a range of 29.38°C to 30.54°C, which gives an average surface temperature of $T_{glass,i}$ =29.96°C. Calculating for the temperature difference across the system using Eq 17 yields a result of $\Delta T_{system,CFD}$ = 6.74°C. Comparing this to the control system CFD analysis, gives an improvement of 16.44 times.

Analysing Figure 10, the temperature of the honeycomb heat fin has a 2°C temperature difference compared to the STPV. This supports that the honeycomb can cool the system at a

much more rapid pace compared to without one. The honeycomb fin at the centre has been neglected due to meshing errors of the model. This is due to the inflation meshing method

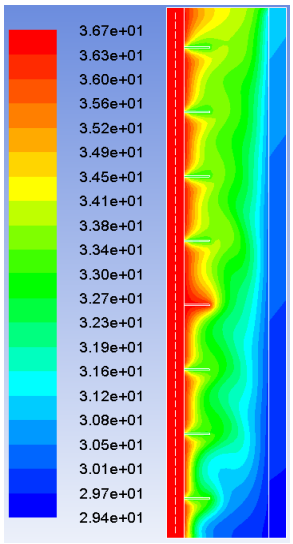


Figure 10: Resulting temperature plot of CFD analysis of the system. Units is in °C.

that commonly occurs for thin and long shapes (etc. plates), as the mesh provides more details on the edges of the object (in this care the edges of the air gap) but on the other side squishes and distorts meshes at the centre. However, inflation meshing method is important, as the edges are keys for an accurate heat transfer study.

Based on Figure 10, it has consistent pattern with the study conducted by Giorji *et al*. The cooler temperatures will be concentrated at the bottom of the system while, hotter temperatures will be at the top. This proves that the CFD result is logical and strong.

The results from both mathematical and CFD analysis have been tabulated into Table 4 and graphed into Figure 11.The distance, x is the distance across the system starting from the outer surface of the STPV. The percentage difference for each of the layer has been determined.

Table 4: Results from CFD and Mathematical Analysis

Layer	Distance, x (mm)	CFD surface temperature, (°C)	Mathematical surface temperature, (°C)	Percentage difference
Outer surface, STPV, $T_{PV,o}$	0	36.70	36.70	-
PV cell, T_{cell}	3.4	36.33	36.49	0.43%
Inner surface, STPV, $T_{PV,i}$	6.8	35.58	35.30	0.80%
Honeycomb heat fin, T_{Al}	16.8	32.63	32.54	0.27%
Outer surface, clear glass, $T_{glass,o}$	39.8	30.41	26.19	16.10%

Inner surface, clear glass, $T_{glass,i}$	46.6	29.96	22.95	30.57%
Total temperature difference, ΔT_{system}	-	6.74	13.75	51.00%

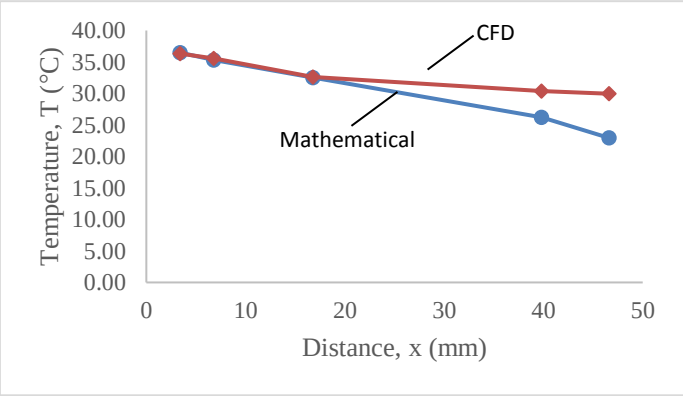


Figure 11: Graph of surface temperature from CFD and mathematical analysis against distance from the outer surface of STPV.

Referring to Table 4 and Figure 11, the percentage difference of surface temperature between both analysis spikes starting from $T_{glass,o}$, while the percentage difference before this layer are minimal. As mentioned in the mathematical analysis section, this proves that the air flow of the air gap is indeed complex to be determined through mathematical calculation. As it can be seen from Eq 14, the heat transferred through convection by the air gap is significant for $T_{glass,o}$ to be calculated. Also, more evidence from Figure 10 shows the most significant temperature change exists in the air gap, signifies the effect of air flow on resulting ΔT_{system}.

The percentage error of ΔT_{system} can be calculated through Eq 18, which gives a result of 51%.

$$\text{Percentage error} = \left| \frac{\Delta T_{system,CFD} - \Delta T_{system,mathematical}}{\Delta T_{system,mathematical}} \right| \times 100\% \qquad (18)$$

Despite the significant percentage error, the contour plot shares similarity in Giorji's study on a double-glazed system, where cooler temperatures are at the bottom while hotter at the top [17]. The temperature shift or gradient has a smooth transition across the system, and sudden shifts are absent in the plot, showing that the contour plot may be accurate to reality. Therefore, the CFD result seemed to be more credible and strong that can be used to check with an experimental study in the future.

The correlation of the two results can be obtained from Eq 15, where it is found that γ_{actual} = 2.04. With the small difference between both γ (0.01), the result from this study is strong and accurate. This can be proven with an experimental study in the future.

The usage of honeycomb fins into a BiSTPVT system has never been researched before and it is proven to be efficient until now in the study. ΔT_{system} has been analysed to reach up to 6.74°C or 13.95°C in CFD and mathematical analysis respectively. The uncertainty of the actual value can be determined by carrying out an experimental study, however both values differs far from

typical windows that is found to only provide a temperature difference of 0.39°C or 0.80°C, an improvement of 16.44 times or 16.28 times calculated by CFD and mathematically respectively.

4. Conclusion

This study successfully shows that the proposed BiSTPVT can provide good heat insulation from the hot external environment. This is proven as the temperature difference of a typical situation is below 1°C, comparing to the proposed system which has a large temperature difference of up to 13.85°C for mathematical analysis and 6.74°C for CFD analysis, which is 16.44 times and 16.28 times improvement. Although the mathematical and computational result is different, the coefficient of correlation of the two is found to be consistently at 2.05 using the same method of calculation or computation, showing that the results are not random hence credible. With this large temperature difference, the interior of the building will be cooler with the proposed system, thus reducing power consumption for HVAC system. The cooling effect of honeycomb heat fins has successfully been visualized in the temperature contour plot from CFD, where more significant temperature drops were seen at the heat fins. In the future, experimental study needs to be conducted to verify all findings from this study.

Acknowledgement

The authors acknowledge the support for the project from the Taylor's University flagship research grant TUFR/2017/001/01, 2017- 2020.

References

[1] W. Perry, NAE Grand Challenges For Engineering, National Academy of Engineering, 2017.

[2] National Energy Balance (NEB) 2015, Putrajaya: Suruhanjaya Tenaga (Energy Commision), 2015.

[3] N. Astea, C. D. Peroa and F. Leonforte, "Water PVT collectors performance comparison," *Energy Procedia,* vol. 105, pp. 961-966, 2017.

[4] A. Khelifa and K. Touafek, "Analysis of a Hybrid Solar Collector Photovoltaic Thermal (PVT)," *Energy Procedia,* no. 74, pp. 835-843, 2015.

[5] M. Proell and M. Hilt, "The Significance of the Fluid to PV Thermal Coupling in a CPC PVT Collector," *Energy Procedia,* no. 57, pp. 3120-3129, 2014.

[6] I. Acosta, M. Ángel, C. Juan and F. Molina, "Window design in architecture: Analysis of energy savings for lighting and visual comfort in residential spaces," *Applied Energy,* vol. 168, pp. 493-506, 2016.

[7] C. Y. Yong, M. T. Hajibeigy, C. A. Vatalingam and R. G. Walvekar, "Characteristics Study of Photovoltaic Thermal System with Emphasis on Energy Efficiency," *MATEC Web of Conferences,* vol. 152, 2018.

[8] M. Y. Othman, F. Hussain, K. Sopian, B. Yatim and H. Ruslan, "Performance Study of Air-based Photovoltaic-thermal (PV/T) Collector with Different Designs of Heat Exchanger," *Sains Malaysiana,* vol. 42, no. 9, pp. 1319-1325, 2013.

[9] R. Lehman, *Overview of Glass Properties: Glass Engineering 150:312,* New Jersey: Rutgers University.

[10] AmpleSun, "China Supplies: 20% Transparent Colored Solar Panels Amorphous Silicon Thin Film," China.cn, [Online]. Available: https://wap.china.cn/pharmaceutical/151431566.html?t=description. [Accessed 25 October 2017].

[11] A. Ghahremani and A. Fathy, "A three-dimensional multiphysics modeling of thin-film amorphous silicon solar cells," *Energy Science & Engineering,* vol. 6, no. 3, pp. 520-534, 2015.

[12] L. Huang, Q. Jin, X. Qu, J. Jin, C. Jiang, W. Yang, L. Wang and W. Shi, "Characterization and simulation on antireflective coating of amorphous silicon oxide thin films with gradient refractive index," *Superlattices and Microstructures,* vol. 96, pp. 198-204, 2016.

[13] ANSYS®, *Workbench 18.1, Material Database,* ANSYS® Inc.

[14] I. L. Wong and P. Eames, "A method for calculating the solar transmittance, absorptance and reflectance of a transparent insulation system," *Solar Energy,* vol. 111, pp. 418-425, 2015.

[15] Q. Li, Z. Wang, F. Bai, S. Chu and B. Yang, "Thermal Analysis of Honeycomb Ceramic Air Receiver," *SolarPACES,* vol. 1850, pp. 1-8, 2017.

[16] D.Roncati, "Iterative calculation of the heat transfer coefficient," Progettazione Ottica Roncati, Ferrara, 2013.

[17] L. D. Giorgi, V. Bertola and E. Cafaro, "Thermal convection in double glazed windows with structured gap," *Energy and Buildings,* vol. 43, pp. 2034-2038, 2011.

[18] N. Skandalos and D. Karamanis, "Investigation of thermal performance of semi-transparent PV technologies," *Energy and Buildings,* vol. 124, pp. 19-34, 2016.

[19] N. Safer, M. Woloszyn and J. J. Roux, "Three-dimensional simulation with a CFD tool of the airflow phenomena in single floor double-skin facade equipped with a venetian blind," *Solar Energy,* vol. 79, pp. 193-203, 2005.

[20] P. Kohnke, *ANSYS Theory Reference,* Pennsylvania: ANSYS.

[21] F. Mohebbi and M. Sellier, "Identification of space- and temperature-dependent heat transfer coefficient," *International Journal of Thermal Sciences,* vol. 128, pp. 28-37, 2018.

[22] Meteoblue, "Meteoblue: Weather archive Subang Jaya," Meteoblue, 2017. [Online]. Available: https://www.meteoblue.com/en/weather/forecast/archive/subang-jaya_malaysia_8504423. [Accessed 2 November 2017].

[23] SEDA, "Sustainable Energy Development Authority Malysia (SEDA)," SEDA Malaysia, [Online]. Available: http://seda.gov.my/. [Accessed 1 November 2017].

EURECA 2018 – Conference Paper
Paper number 2ME12

Biomimicry Inspired High Impact Absorbed Helmet

Jia Qing Lim[1], Leng Chuan Yong[1], Norhabibah Mohamad[1,] and Hui Leng Choo[1]

[1]School of Engineering, Taylor's University, Malaysia.

Abstract. Biomimicry is a process which most of the innovations inspired by nature and contributes in solving complex engineering challenges. The design of lattice structure is a new approach to create a high impact absorbed helmet for the sake of further absorbing impact energy which will reduce the damage to head skull even brain. Among shapes of lattice structure, triangular lattice structure has been proven that showing the best performance. Tensile test and impact test are performed in order to obtain the Effective Young's Modulus, E^* and toughness from stress-strain curve and impact energy absorbed. Other than experimental results, FEA analysis is conducted and compared with experimental results for verification. It has been found out that E^*, toughness and impact energy absorbed increase with the increase of the relative density of lattice structure. However, there are some errors happened in the tensile test which causes the error in stress strain curves therefore affect the results of 1.7mm thickness. Further improvements will be done to eliminate the error. Thus, in order to achieve the highest impact energy absorption, highest relative density of lattice structure is preferable in application of high impact energy absorbed helmet.

Keywords: Biomimicry; Hedgehog Spines; High Impact Absorption

1. Introduction

Concussion, a form of traumatic and invisible sign of brain injuries that motive by way of the bump or hit to the pinnacle. This robust impact knocks on a person's head skull and inflicting the brain experiences a surprising motion together with bouncing around, twisting and turning within the head skull. These actions will then purpose a severe injury to the brain which adverse the brain cells.
By taking into account the seriousness of brain concussion, statistic regarding brain concussions was acquire and statistic shows that the death rate of brain concussion increase slowly from year to year [1]. In overall, throughout these years, the total brain concussion injuries and death rate has spiked bit by bit and it can be seen that the case of brain concussion is indeed a prime concern if not a worsening concern among society.

There are several ways to get a concussion, commonly fighting, falling down, car crashes and bike accidents. Not only that, concussion also happened commonly in any sports or activities [1] such as football, boxing, soccer and skiing. Accidents happen unpredictably, during these activities, especially American football, there will be a higher chance for the football players to bump their head either with each other or falling to the ground. Hence, possibilities of having concussion get higher and consequently leading to higher death rate from these cases.

Currently, most of the sports required some safety gear to protect the players from injuries, such as elbow pad, knee pad and helmet for bicycle or skateboard players. Moreover, for American football, helmet is the basic safety gear which is indispensable for every football players. The contribution of helmets to American football players is to decrease the risk of Traumatic Brain Injury (TBI) [2]. According to Dr. T. Blaine Hoshizaki and Suan E. Brien [2], there are two helmet designs which work for different activities, which are "crash helmets" and "multiple-impact helmets". Crash helmets are essentially designed to manage single critical impact, for example during motor sports, cycling or skating. As this type of helmets is able to resist a large impact, therefore, they have to be replaced after one impact in order to maintain their performance. On the other hand, multiple-impact helmets are specifically designed to withstand multiple impacts without dropping in performance. Hence, multiple-impact helmets are more suitable in some sports activities such as American football, ice hockey and lacrosse activities [3].

Hence, a big leap in innovative trend is achieved by approaching Biomimicry, which is a process of innovations inspired by nature and contributes in solving most of the complex engineering challenges. Based on observation on hedgehog, it is believed that spines of hedgehog possess a high potential to be mimicked in the innovation of high impact absorbed helmet.

This biomimicking process is inspired from the arrangement and structure of hedgehog spines which able to absorb most of the impact energy without failure [4]. Notice that hedgehog usually tend to fall out from tree where approximately 9 meters high. However, sometimes they fall by accident or they fall on behalf of evading from a predator which falling is much faster than climbing down. As a hedgehog fall down toward the ground, hedgehog usually rolls into a ball, contracting the muscles and the spines surrounded itself will also roll outwards and hence forming an impact absorbed "barrier" to protect its soft belly [4].

This impact absorbed helmet consists of three layers, which are outer layer made from polycarbonate, middle layer which biomimics the hedgehog spines structure, and inner layer which consists of foam for a further impact energy absorption.

In short, current helmet designs successfully reduce the brain injuries by absorbing more impact energy generated from impact. Unfortunately, the risk of brain concussion is still a threat for public as these helmets are still having a room of improvements. However, it has been found out that the performance of helmet can be improved by biomimicking the hedgehog spines as they are able to absorb the impact way better than current materials used such as VN, EPP, Expanded Polyethylene or other cross-linked polyethylene foam [2].

Results show that the major contribution in absorbing such high impact energy is due to the inner structure of the hedgehog spines. According to Vincent and P. Owers, the hedgehog spines will tend to undergoes buckling when impact energy is applied to it. During buckling effect, there's possibility where the spines undergoes local buckling "Brazier Ovalisation" [5].

"Brazier Effect" [6] is a situation happens whenever a long, thin and mostly hollow cylindrical tube which subjected to bending moment and some compression load, the cross-section of the cylindrical tubes will change in a shape into oval shape and reduce in its second moment of area, which we called as "Ovalisation". Ovalisation is related to the curvature of the cylindrical shell and bending moment. Moreover, depends on the final curvature, initial radius, and wall thickness of the cylindrical shells and Poisson's ratio of the shells [7].

Fortunately, according to G.N. Karam and L.J. Gibson [8], the inner structures of hedgehog spines consist of honeycomb like structure which greatly reduce and overcome this Ovalisation effect and providing support against local buckling in the cylindrical shells. Nevertheless, these honeycomb structures are able to increase the buckling resistance of cylindrical shell in both axial compression load and bending moment which exert on the shell.

By evaluate the mechanical efficiency of the natural cylindrical shells with foam cores, calculation of the ratio of axial buckling load and local buckling moment to those hollow cylinder under constant parameters (mass and radius) are required. Under axial load, buckling resistance of hedgehog spine is approximately 50% higher than the hollow cylinder; under bending, most of the hedgehog spines and quills have a better buckling resistance than the hollow cylinder. Moreover, hedgehog spines from two species of hedgehog (*Erinaceus* and *Hemiechinus*) have the best improvements of more than 300% than hollow cylinder due to their honeycomb core structure inside the spines [8].

On the other hand, according to Hui Leng Choo and Jie Niu [9], there are several of lattice structures with different mechanical performances. Triangular, square and hexagonal lattice structures were designed and each mechanical performance is being compared. All lattice structures are being tested with tensile test in order to obtain the stress-strain curve and calculate the energy absorbed ability of each lattice structure. Through the excellent agreement between FEA results and experimental results, it can be concluded that triangular lattice structure possess the highest mechanical performances among all.

It was found out that Young's Modulus of the lattice structure is proportional to its relative density. Relative density of the lattice structure can be controlled by its dimension. Several dimensions with different thickness, length and height of lattice structure are modified in order to obtain different relative density.

Fabrication of 3D lattice structure was done using 3D printing technique. This 3D lattice structure model will be analysed using ANSYS software to obtain numerical results. Moreover, tensile and impact test will be performed and thus experimental results will be compared with numerical results for further data verification.

In this paper, the effect of relative density on Effective Young's Modulus, *E**, toughness and impact energy absorption is focused and studied. Hence, by obtaining the best mechanical performance of that specific dimension of lattice structure, inner structure of hedgehog spines will be replaced with this lattice structure and achieving the highest impact energy absorption.

2. Geometric Modelling

2.1 3D model of lattice structure

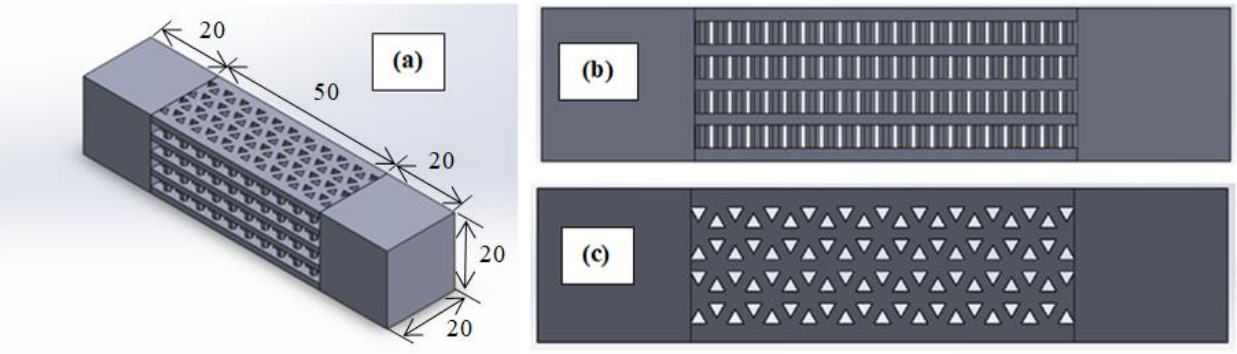


Fig. 8. 3D modeling of lattice structure, (a) Isometric View, (b) Side View, (c) Top View. Units: mm.

Fig. 8 shows the 3D lattice structure model in isometric, top, and side view. Solidworks is used to generate the 3D model of the lattice structure during the design phase. Dimensions of the lattice structure are stated in Fig. 8 as well. The dimension of the entire lattice structure is 20mm x 20mm x 90mm. Triangular lattice structure will be filed with a total of 50mm length and 20 mm of solid cap is attached to it. The purpose of the cap at both ends of the model is to allow the holding of model during tensile testing. Instead of holding the triangular lattice, machine will hold the both cap at the end to prevent from damaging the triangular lattice unit.

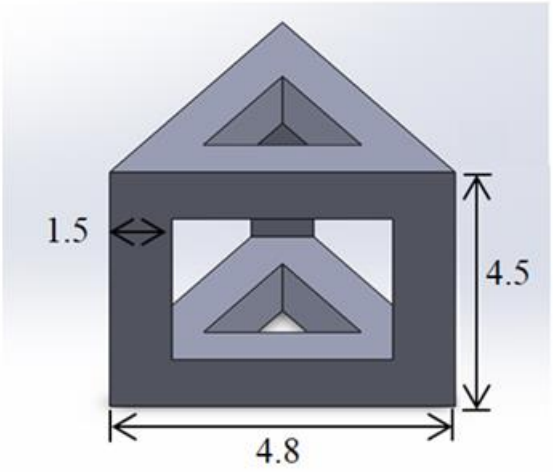


Fig. 9. Triangular unit cell of lattice structure. Units: mm

Fig. 9 shows the single unit of triangular lattice structure. Before proceeding to the whole lattice model, basic unit cell was first created according to the dimension required. Then, by using linear patterning, this basic unit cell will then further combine and form a single layer of triangular lattice structure. Moreover, this single layer will be pattern repeated for 4 times

above it. Therefore, it's considered less time consuming in generating the whole lattice structure model. Same goes to different dimension design as well, the model is generated basically using the linear patterned technique which built-in by Solidworks.

Table 1. Dimension of Triangular Lattice Structure

Lattice structure	Length, L (mm)	Thickness, t (mm)	Height, h (mm)	Relative Density, RD (%)
Triangular	4.8	1.5	4.5	66.14
		1.5	4.6	65.32
		1.5	4.7	64.53
		1.6	4.5	67.99
		1.6	4.6	67.17
		1.6	4.7	66.36
		1.7	4.5	69.89
		1.7	4.6	69.05
		1.7	4.7	68.23

Table 1 shows the dimension of the triangular lattice structure which is going to be fabricated and analyse the effect of dimension in impact absorption ability, toughness and Effective Young's Modulus.

2.2 Materials

By selecting the material between ABS, PLA, and PVA, the final material selected to fabricate the lattice structure is PLA. By comparing among these 3 materials, PLA has the highest advantage in mechanical properties, which is the highest strength and modulus.

Instead of using other rubbery materials, plastic material is used due to some of the constraints. First of all, since this fabrication process will be done using 3D printer, therefore, plastic polymer is the best choice of material. Moreover, since it is still for 1st stage prototyping purpose, it's more suitable to use plastic polymer rather than other higher cost material such as rubbery material. Table shows the mechanical properties of PLA.

Table 2. Mechanical Properties of PLA. [10]

Mechanical Properties	**Value**	**Units**
Density	1.26	g/cm^3
Young's Modulus	2346.12	MPa
Ultimate tensile strength	50	MPa
Poisson ratio	0.36	-

2.3 Fabrication of Lattice Structure

3D printer is used in the fabrication of the 3D lattice structure model which shown in Fig. 10. For these complex geometrical models, 3D printing technique is the simplest and best method to fabricate. By converting the CAD file to STL file, which can be read by 3D printer built-in software, most of the complex geometries are able to be printed. This method requires the material filament. In this case, PLA filament is required and during the printing process, PLA filament will be melted at the tip of the nozzle at approximately 210°C temperature [11]. Fig. 11 shows the completed specimen fabricated using 3D printer.

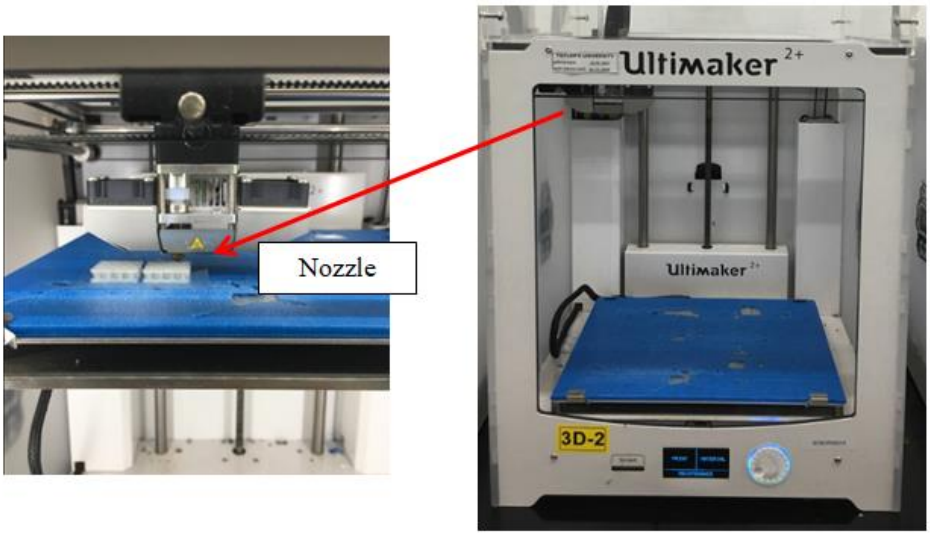


Fig. 10. Illustration of 3D printer.

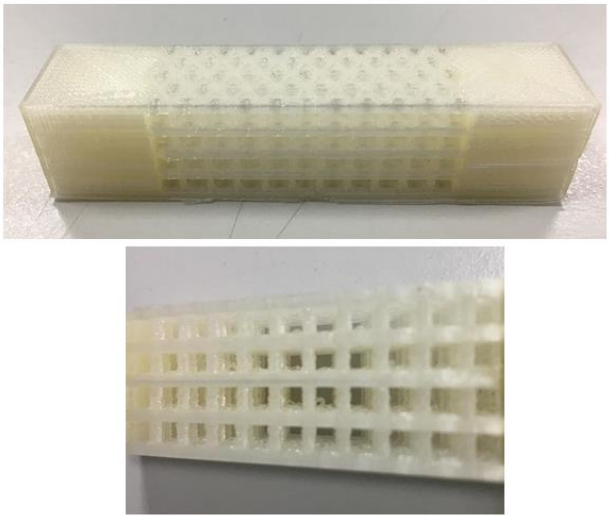


Fig. 11. Specimen sample fabricated by 3D printer.

3. Experimental Test

3.1 Tensile Test

Objective of performing tensile test is to identify the mechanical performances of each lattice structure with different dimension, which are Effective Young's Modulus, E^* and toughness. All these data are able to obtain by plotting stress-strain curve after the tensile experiment. Fig. 12 shows the experimental setup of tensile machine INSTRON 5969. Lattice structure will be clamped vertically with 2 holders at both ends as shown in Fig. 12.

It has few conveniences by using INSTRON 5969 instead of other tensile tester machine. First, it can be considered as semi-auto machine. Instead of applying tensile force manually, INSTRON 5969 allows user to setting the optimum strain rate and the force are able to be applied uniformly. Here, the strain rate is set to 0.25mm/s. Moreover, by using INSTRON 5969,

stress-strain curve can be plotted and calculation of tensile stress and tensile strain can be done by software of INSTRON 5969.

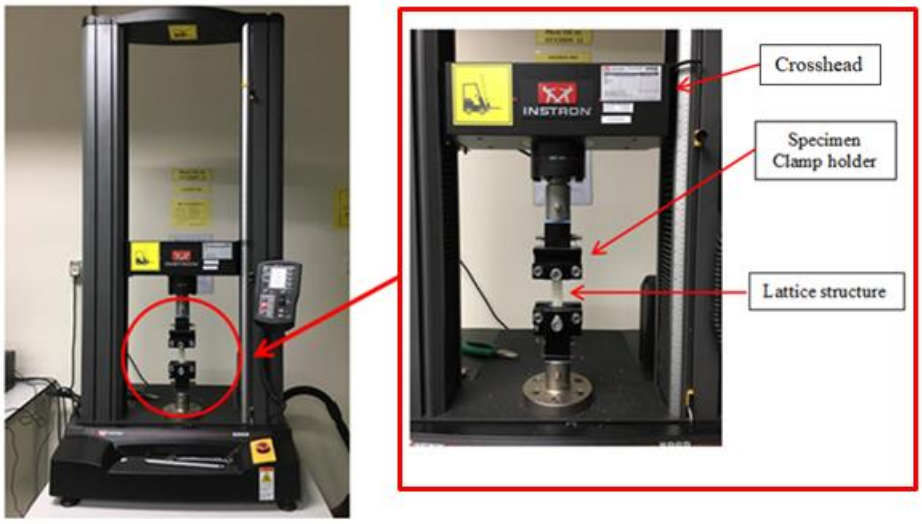


Fig. 12. Experimental setup of INSTRON 5969.

3.2 Impact Test

Besides tensile test, impact test will be performed in order to observe the impact energy absorption of the lattice structure. This impact tester consists of a swinging pendulum which acts as a source of impact force, hitting the specimen which has been placed at the specimen holder.

At the beginning of the experiment, the pendulum is positioned at the highest position and being locked by a pin and safety catch. This is to prevent the pendulum from letting go from its position and damaging user. Once lattice structure specimen has been placed on the specimen holder, the pendulum will be released by unlocking the safety pin. Pendulum will then hit on the lattice structure and impact absorbed will be showed on the scale.

During the entire impact testing, conversion of energy is the main concept in obtaining the energy absorbed by the specimen. At the beginning when the pendulum is positioned at the highest point, it storing potential energy. Next, when the pendulum is released from its original position, the potential energy is converted into kinetic energy and the kinetic energy reaches maximum at the lowest point before hitting the specimen. Once the pendulum hit the specimen, part of the kinetic energy will be loss to break the specimen. Therefore, the energy loss in breaking the specimen can be identified as the impact energy absorbed by the specimen.

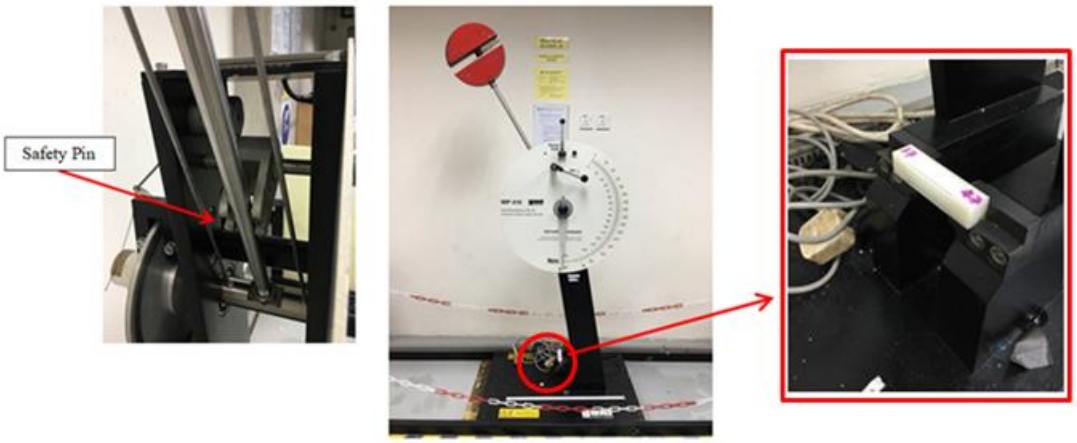


Fig. 13. Experimental Setup of WP 410 Pendulum Impact Tester.

4. Finite Element Analysis (Simulation)

4.1 Meshing Generation

In FEA analysis, meshing of geometry is significant as meshing can determine the accuracy of the simulation results. There are multiple meshing method such as, automatic, hex dominant, multizone, and tetrahedral meshing. However, hex dominant is selected in geometry meshing. The major reason is this geometry is undergoing tensile test which the tensile force is applied in direction normal to the cross-section of this geometry. Therefore, all the meshing elements will be normal to the direction of tensile force and results will be generated more accurately. And also this geometry is basically rectangular shape and without any curvature, thus, hex dominant will be more suitable in geometry meshing.

Based on Fig. 14, it can be seen that at the middle lattice part of the entire model, the meshing if relatively fine compared to the solid part at the both end. This is because this part is more critical as the deformation and stress concentration is significant here. Accuracy of the results is dependent on the number of meshing element and therefore a finer meshing element is required to obtain a better accuracy results.

On the other hand, the deformation and stress concentration at the solid part at the both end of lattice structure is not significant and any deformation at that part is assumes to be negligible. Therefore, the element size at the solid part is larger than the lattice structure part at the middle part. This is to reduce the number of element and thereby reduce the duration of FEA analysis.

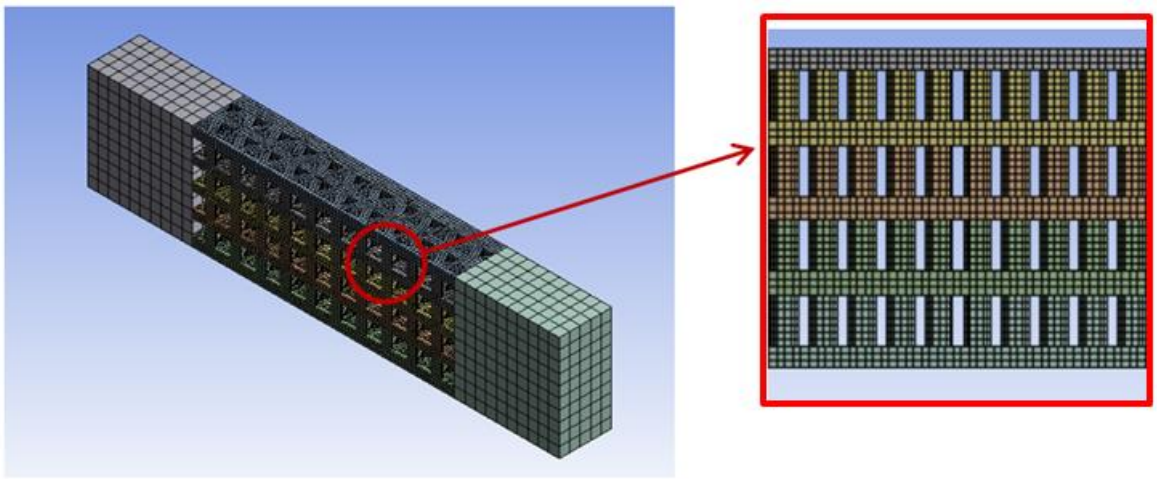


Fig. 14. Geometry meshing of lattice structure.

4.2 Boundary Conditions

As shown in Fig. 15, the bottom holder will be a fixed support and remain at its position, yet, the upper holder will moving upward and pulling the lattice structure while performing tensile test.

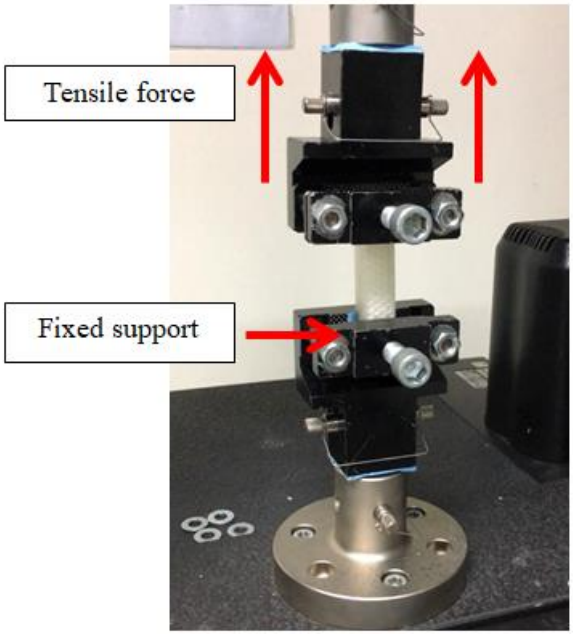


Fig. 15. Illustration of tensile testing process.

In FEA, boundary condition is to simulate the situation or condition where the geometry will be placed. Fig. 16 shows the boundary conditions applying to the geometry during FEA simulation. As previously mentioned in Fig. 12, during the tensile testing, the specimen is clamped at the specimen holder at the both end. One end of the specimen is fixed in its position and the other end is being pulled by the tensile machine. Therefore, in ANSYS simulation, one end of the solid part is applied to be a fixed support and force is applied at other end of the specimen. In this case, force of 2000N is applied to the geometry in x-direction.

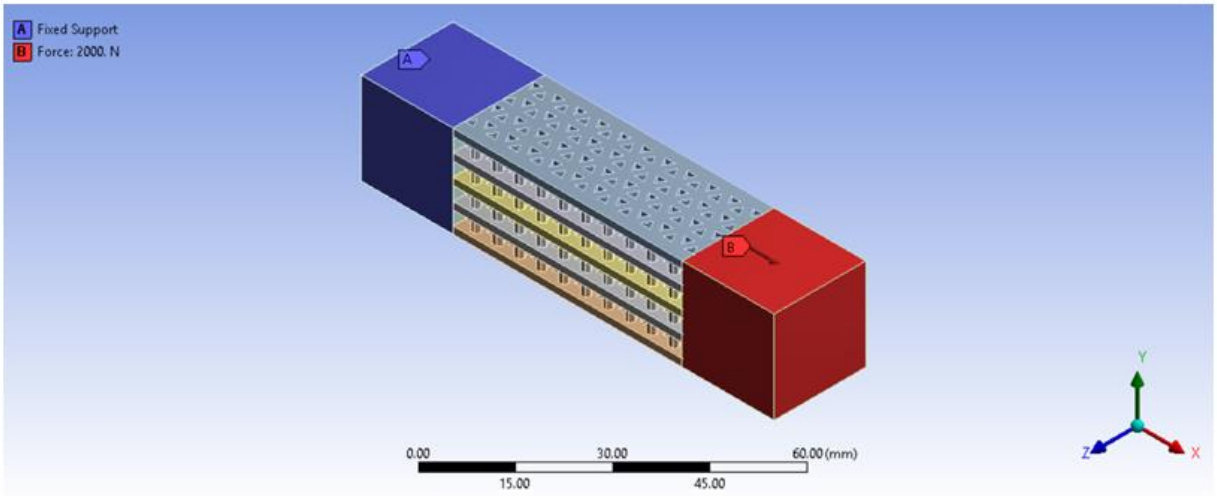


Fig. 16. Boundary conditions applied to geometry.

5. Results and Discussion

5.1 Tensile Test

Based on Table , there are total of 9 different dimensions designed to compare the mechanical performances. Besides that, relative density of lattice structure is calculated by measuring using the built-in tools from Solidworks which density of lattice structure is generated automatically. Different lattice structure's dimension will have different relative density and relative density is defined by using Equation 1.

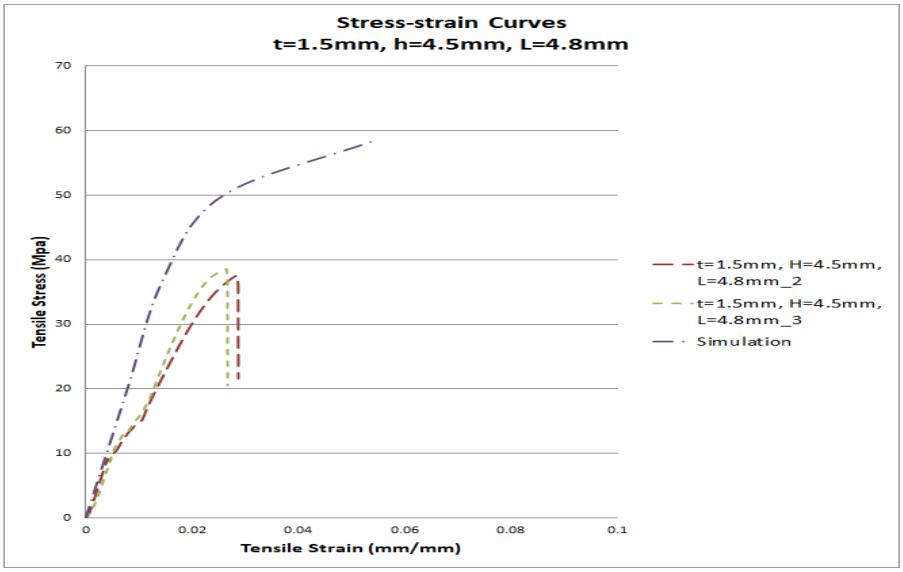
$$RD = \frac{\rho^*}{\rho_m} \times 100\% \quad (1)$$

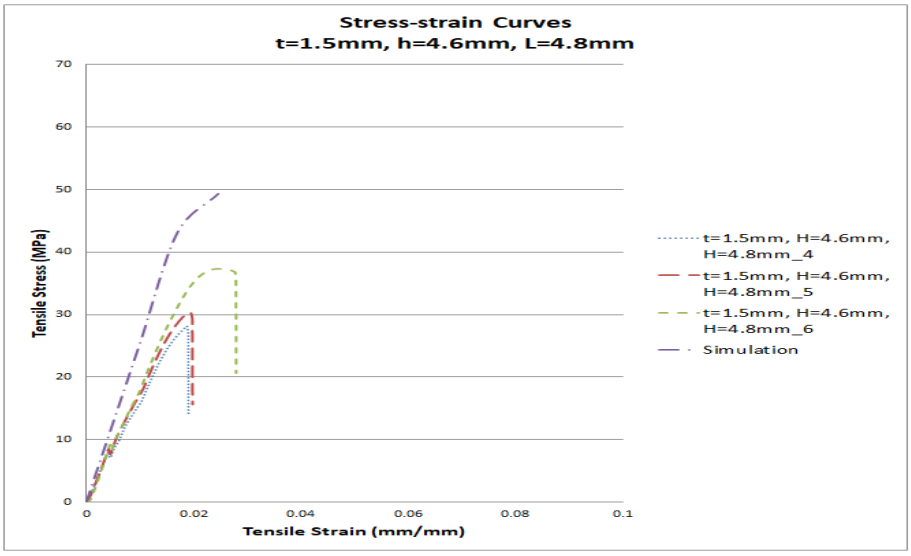
On the other hand, it is found out that the relative density of the lattice structure decrease with increase of strut's height. This is due to the increase in the strut's height will increase the hollow part of the lattice structure, which can be called as porosity. On the other hand, porosity is inversely proportional to the density of the material and the relationship between porosity and density of material using Equation 3.

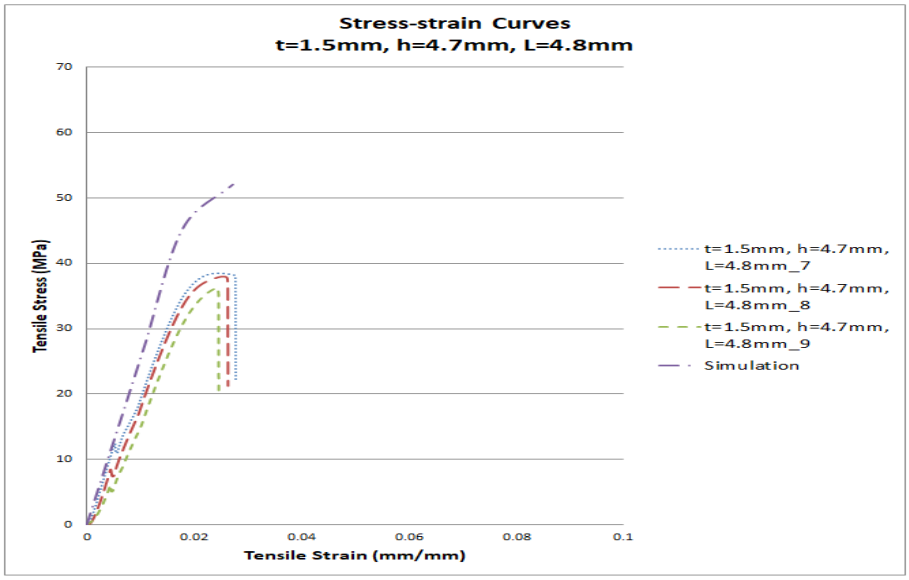
$$\alpha = 1 - \frac{\rho^*}{\rho_m} \quad (2)\ [12]$$

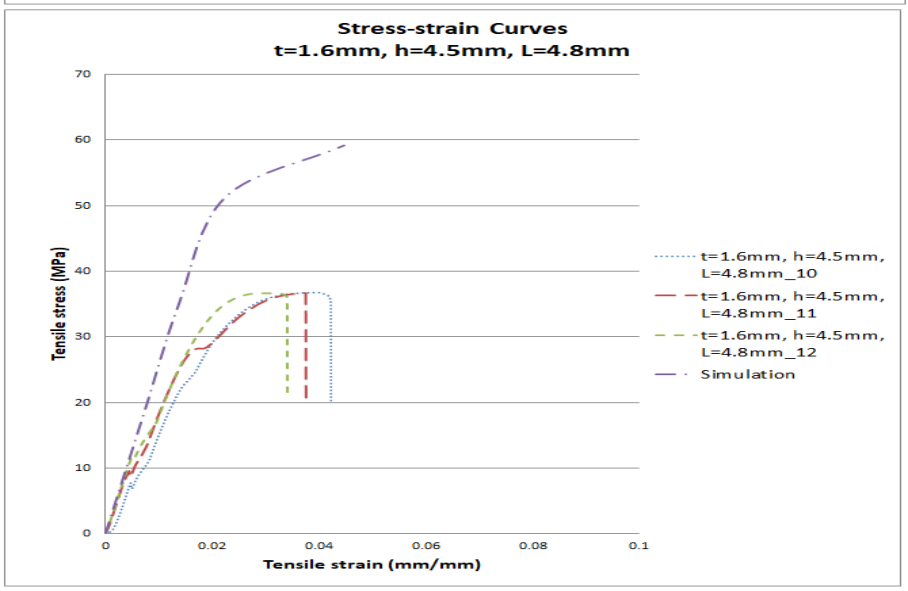
$$\frac{\rho^*}{\rho_m} = 1 - \alpha \quad (3)$$

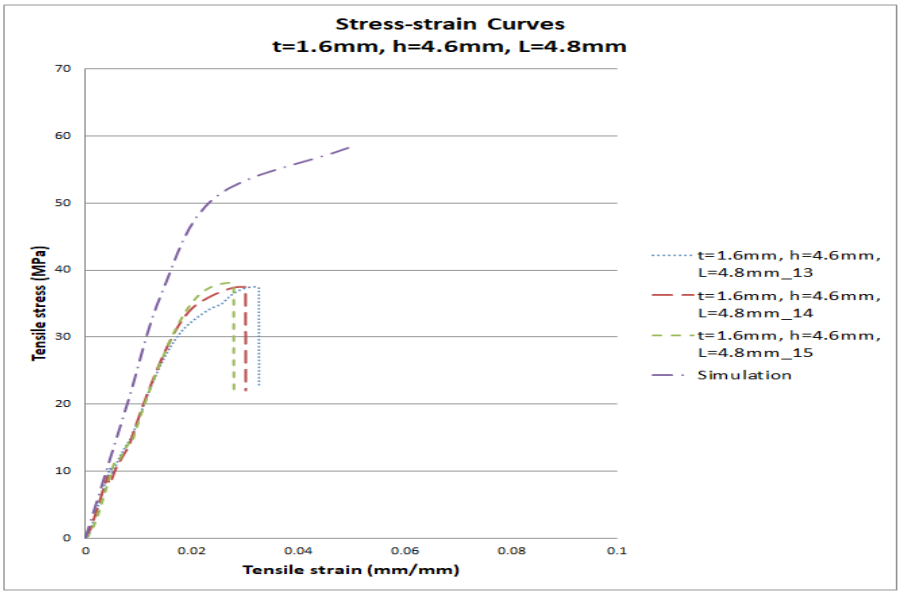
Where α is the porosity, $\rho*$ is the relative density of the lattice structure, and ρ_m is the exact density of the solid model. Therefore, with the increasing of porosity, the relative density of the lattice structure decrease.

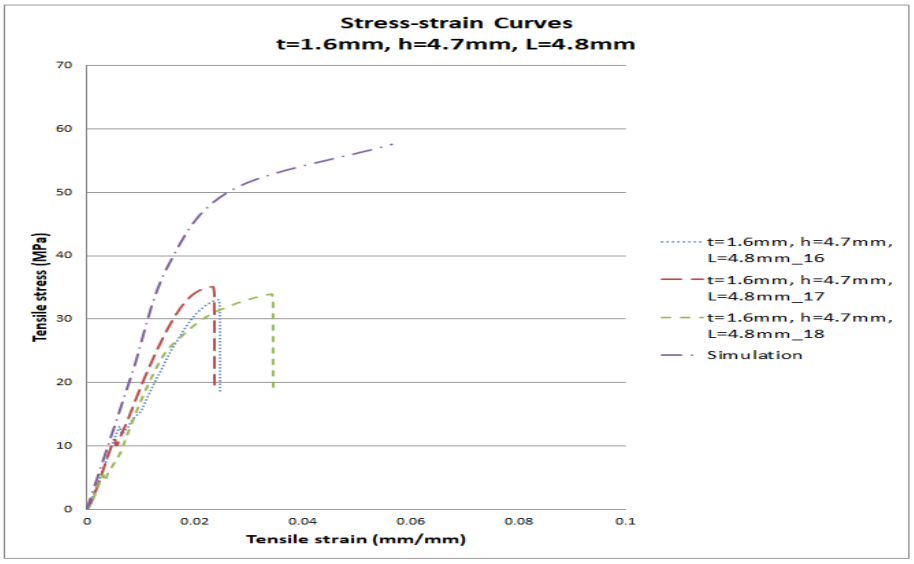


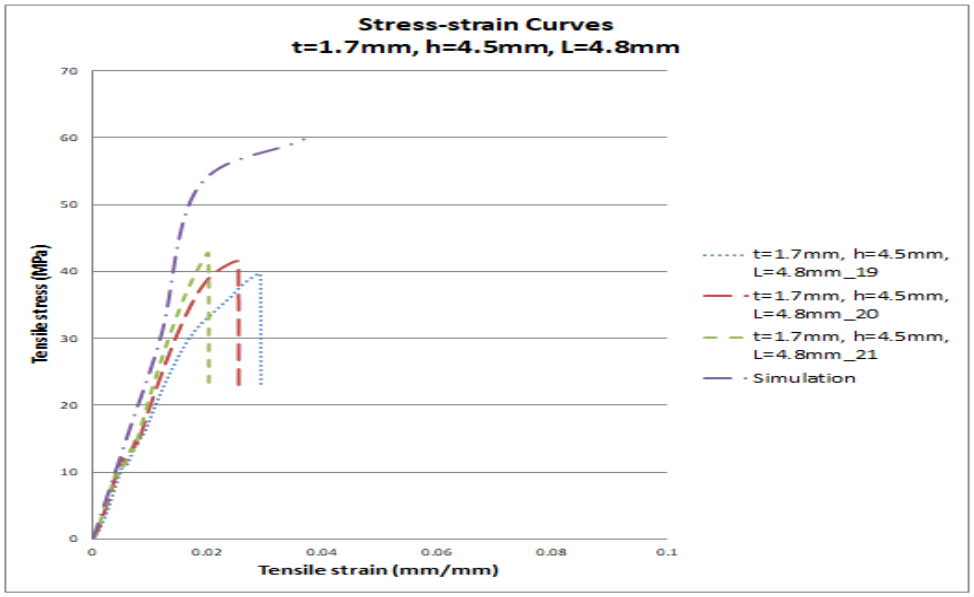

Stress-strain Curves
t=1.5mm, h=4.6mm, L=4.8mm
Tensile Stress (MPa)
Tensile Strain (mm/mm)
t=1.5mm, H=4.6mm, H=4.8mm_4
t=1.5mm, H=4.6mm, H=4.8mm_5
t=1.5mm, H=4.6mm, H=4.8mm_6
Simulation


Stress-strain Curves
t=1.5mm, h=4.7mm, L=4.8mm
Tensile Stress (MPa)
Tensile Strain (mm/mm)
t=1.5mm, h=4.7mm, L=4.8mm_7
t=1.5mm, h=4.7mm, L=4.8mm_8
t=1.5mm, h=4.7mm, L=4.8mm_9
Simulation


Stress-strain Curves
t=1.6mm, h=4.5mm, L=4.8mm
Tensile stress (MPa)
Tensile strain (mm/mm)
t=1.6mm, h=4.5mm, L=4.8mm_10
t=1.6mm, h=4.5mm, L=4.8mm_11
t=1.6mm, h=4.5mm, L=4.8mm_12
Simulation


Stress-strain Curves
t=1.6mm, h=4.6mm, L=4.8mm
Tensile stress (MPa)
Tensile strain (mm/mm)
t=1.6mm, h=4.6mm, L=4.8mm_13
t=1.6mm, h=4.6mm, L=4.8mm_14
t=1.6mm, h=4.6mm, L=4.8mm_15
Simulation


Stress-strain Curves
t=1.6mm, h=4.7mm, L=4.8mm
Tensile stress (MPa)
Tensile strain (mm/mm)
t=1.6mm, h=4.7mm, L=4.8mm_16
t=1.6mm, h=4.7mm, L=4.8mm_17
t=1.6mm, h=4.7mm, L=4.8mm_18
Simulation


Stress-strain Curves
t=1.7mm, h=4.5mm, L=4.8mm
Tensile stress (MPa)
Tensile strain (mm/mm)
t=1.7mm, h=4.5mm, L=4.8mm_19
t=1.7mm, h=4.5mm, L=4.8mm_20
t=1.7mm, h=4.5mm, L=4.8mm_21
Simulation

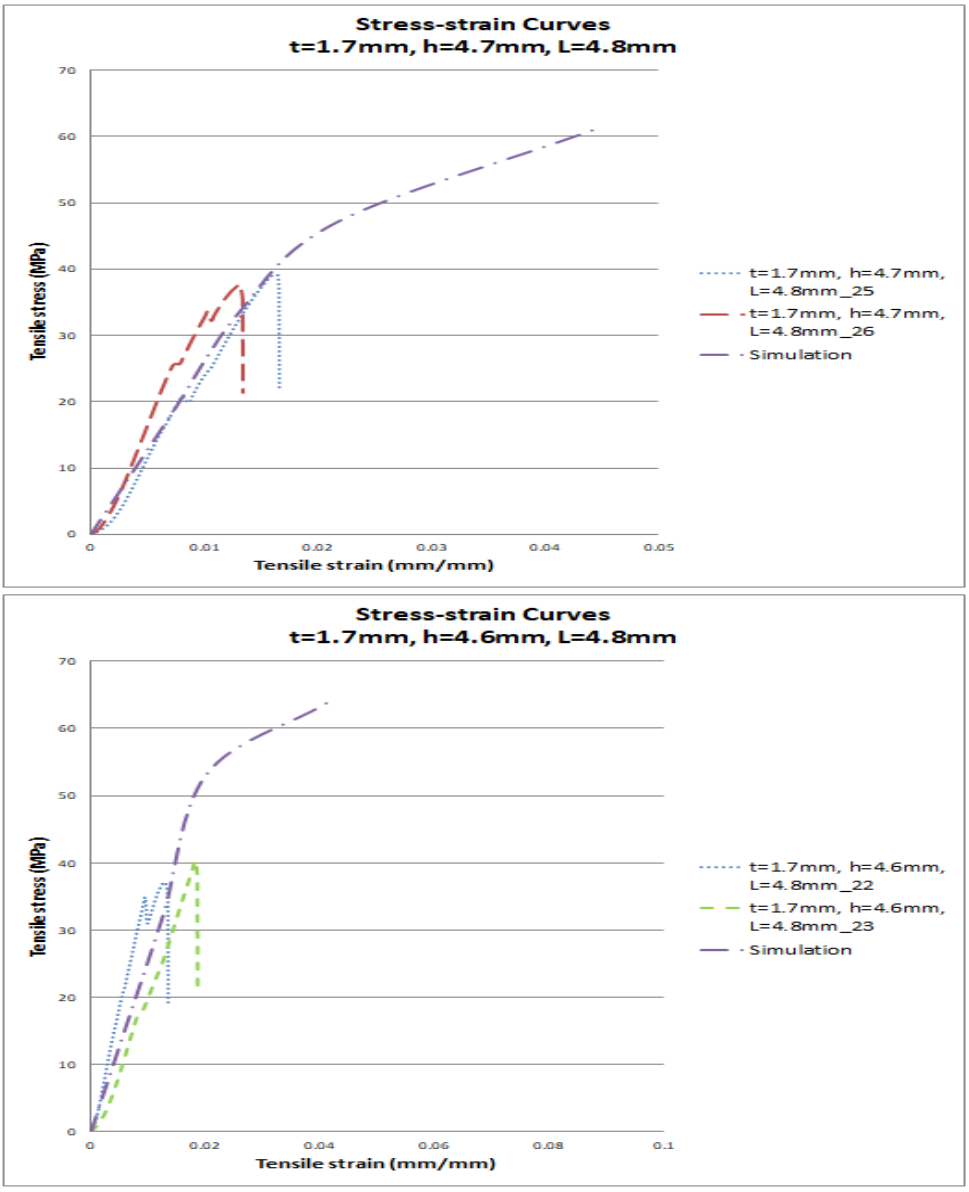


Fig. 17. Stress-strain curves for different dimension of lattice structure.

Fig. 17 shows the stress-strain curve for lattice structure of thickness of 1.5, 1.6 and 1.7mm. For one dimension of lattice structure, multiple tests were performed to observe the stability of the experimental data.

Table shows the mechanical performances of each lattice structure of different dimension after tensile test. Effective Young's Modulus, E^* and toughness will be discussed and compared within each other.

Table 3. Mechanical performances of lattice structure with different dimension.

Thickness, t (mm)	Height, h (mm)	Experimental Effective Young's Modulus, E^* (MPa)	Toughness, T (kJ/m^3)
1.5	4.5	2330	571.8
	4.6	2298	473.1
	4.7	2231	336.9
1.6	4.5	2432	869.8

	4.6	2364	795.1
	4.7	2262	785.3
1.7	4.5	1385	523.2
	4.6	1562	139.8
	4.7	2091	125.9

*5.1.1 Effective Young's Modulus, E**

It is known that Young's Modulus, *E* is the stiffness of the full solid geometry or also the resistance to resist the permanent deformation when a force is applied to it. Yet, there is a slightly difference from Effective Young's Modulus. Unlike Young's Modulus, Effective Young's Modulus, E^* is the Young Modulus of the lattice structure with respective to the relative density of the lattice structure. Therefore, the higher the Young's Modulus will cause the stiffer the geometry and higher resistance to permanent deformation.
First of all, based on Table , by taking thickness of 1.5mm, E^* of the lattice structure decreases from 2330 Mpa to 2231 Mpa while the height of the strut increase from 4.5mm to 4.7mm. Therefore, under a constant thickness, it can be observed that E^* of the lattice structure decrease with the increase in the height of the strut of the lattice structure for all three different thickness.

Besides that, it is also found out that when the thickness increase from 1.5mm to 1.6mm, E^* has been increased from 2330 MPa to 2432 MPa due to the increase in the relative density of the lattice structure.

Moreover, a relation between the relative density and Young's Modulus can be shown in Equation 4.

$$\frac{E^*}{E_m} = \left(\frac{\rho^*}{\rho_m}\right)^2 \quad (4)\ [13]$$

Where E^* is the Young's Modulus of lattice structure and E_m is the Young's Modulus of solid model. Based on Equation 4, as E_m and ρ_m are constant variables, the Young's Modulus of lattice structure is directly proportional to the relative density of lattice structure. This is due to the higher relative density will make the lattice structure become stiffer and stiffer material will need a higher force to deform compared to less stiff material. Hence, the decrement of Young's Modulus of lattice structure with the increment of porosity is valid.

5.1.2 Toughness

Toughness is an ability of a material that allows it to absorb the energy from elastic region until plastic region yet before fracture. It can also be defined as the area under the stress-strain curve plotted from tensile test or compression test. Here, stress-strain curves for each lattice structure are plotted and therefore toughness can be obtained from the graphs.

$$T = \int_{\varepsilon_1}^{\varepsilon_2} \sigma \, d\varepsilon \quad (5)$$

Equation 5 shows the formula for calculation of toughness which is the integration of the stress-strain curves before fracture. Based on Table 3, it is found out that the toughness decrease with the increasing of strut's height of lattice structure. However, for 1.7mm thickness, toughness of lattice structure is 523.2 Mpa, which is lower than toughness of 1.5m and 1.6mm thickness. Then, toughness drops until 125.9 Mpa while the strut's height increases to 4.7mm. It is believed that toughness of the lattice structure with 1.7mm thickness is supposed to be the highest compared to thickness of 1.5 and 1.6mm due to the highest relative density. Hence, it

can be claimed that there are some errors happened during the tensile testing and this error will be further justified afterwards.

Again, this will be similar to the effect of relative density on E^* which the toughness is affected by the relative density of the lattice structure. The higher the relative density of lattice structure, the higher the toughness of the lattice structure. This is because the higher relative density will cause the lattice structure to become stiffer and tougher since the solid material occupied the major portion and only minor portion of holes exist in the lattice structure. Therefore, a higher load is required to deform and even break the tougher lattice structure and the stress exerted on the lattice structure will be higher due to higher force required. Hence, the stress will be higher due to higher force required and this result in the higher stress increment with low strain rate and thus the area under stress strain curve is higher for a higher relative density.

5.2 Impact Test

Table 4 shows the impact energy absorbed by the lattice structure with different dimension. Impact energy absorbed of 1.5mm thickness varies from 7.3 to 6.4 Nm while the height increases from 4.5 to 4.6mm. Besides that, for 1.6mm thickness, while the height increases from 4.5 to 4.6mm, the impact energy absorbed drops from 9.8 to 8.5mm. Last but not the least, for t1.7mm thickness, the impact energy absorbed is the highest among other thickness which at the range of 11.9 to 15.1 Nm.

It can be see that different thickness and strut's height absorb different amount of energy. However, with the same thickness, it has a trend that increase in the height will lower the impact energy absorbed due to the increase in the porosity of the lattice structure.

Table 4. Impact Energy Absorption of Lattice Structure

Thickness, t (mm)	Height, h (mm)	Impact Energy Absorbed, J (Nm)
1.5	4.5	7.3
	4.6	6.8
	4.7	6.4
1.6	4.5	9.8
	4.6	8.5
	4.7	7.6
1.7	4.5	15.1
	4.6	13.8
	4.7	11.9

6. Error Analysis

Table 5. Comparison between Experiment Results and Numerical Results

Thickness, t (mm)	Height, h (mm)	Experimental Effective Young's Modulus, E^* (MPa)	Numerical Effective Young's Modulus, E^* (MPa)	Percentage Error (%)
1.5	4.5	2330	2541	9.06
	4.6	2298	2539	10.49
	4.7	2231	2537	13.68
1.6	4.5	2432	2548	2.66
	4.6	2364	2545	4.66
	4.7	2262	2340	3.43
1.7	4.5	2519	2587	2.76
	4.6	2497	2552	2.20
	4.7	2461	2551	3.57

Table 5 shows the comparison between experimental results and numerical results. Based on Table 5, it can be see that the percentage error of E^* for 1.5 and 1.6mm thickness are approximately around 3-14%. Thus, experimental results are proven that reliable and credible. However, percentage error of E^* for the thickness of 1.7mm are relatively higher which at the range of 36% and 56%. According to numerical results, E^* of thickness 1.7mm lattice structure is the highest among other thickness due to the higher relative density and the value of E^* decrease with the increment of the strut height. Thus, numerical results is fulfilling the theory where Young's Modulus increase with relative density.

Yet, experimental results show the other way where E^* decrease with the increment of strut height. Hence, it could be due to some experimental setting error happened during tensile test and this error could be come from the specimen holder.

During tensile test, the grip force provided by the specimen holder to hold the specimen is unstable and causes slip of the specimen from the specimen holder while the specimen is being pulled by the machine. Also the extension and strain measured by the machine is based on the position of the crosshead. Fig. 18 shows the condition of the specimen holder which cause the slip of specimen during tensile test.

Therefore, due to the existence of the slip condition, strain is affected and thereby affects the value of E^*. In order to eliminate the error, extensometer is required to be placed on the specimen in order to obtain a more accurate extension results.

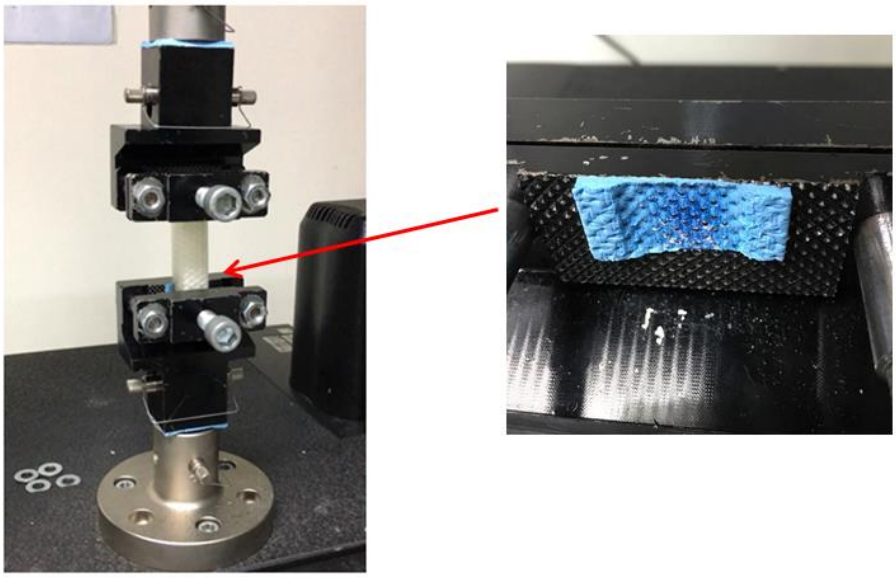


Fig. 18. Condition of specimen holder which cause slip of specimen.

Conclusion

In short, this study shows the impact energy absorption of lattice structure is depend on the relative density of the lattice structure. Different combination of lattice structure's thickness and height of structure's height will have different magnitude of relative density of lattice structure. With different relative density, it will affect the Effective Young's Modulus, E^*, toughness and also impact energy absorption. With the aid of comparison with numerical results, it has been proven that increase in the relative density, the lattice structure becomes stiffer and tougher than lattice structure with lower relative density. From the lowest relative density, which is the combination of 1.5mm thickness and 4.7mm strut height, E^* and toughness is the lowest with the value of 2231.3945 MPa and 336887.98 Nm respectively. However, for 1.7mm thickness, due to the errors during tensile test, E^* and toughness is much lower than the 1.5mm thickness. It is supposed to have a highest value of E^* and toughness for 1.7mm thickness. Yet, it's not able to obtain the results due to the slip of the specimen during tensile test and hence affects the strain results and stress strain curve. Therefore, an extensometer is suggested to used and placed on the lattice structure to measure the real tensile strain to eliminate the errors.

Therefore, in order to achieve higher impact energy absorption, lattice structure with a higher relative density is more suitable and preferable in the application of high impact energy absorbed helmet for the sake of reducing the risk of brain damage due to the higher impact.

References

[1] E. E. Andersson, R. Sejdhage and V. Wage, "Mild traumatic brain injuries in children between 0–16 years of age," *Developmental Neurorehabilitation,* vol. I, no. 15, pp. 26-30, 2012.

[2] T. B. Hoshizaki and S. E. Brien, "The Science and Design of Head Protection in Sport," *Neurosurgery,* vol. 55, pp. 956-967, 2004.

[3] K. M. Breedlove, E. L. Breedlove, T. G. Bowman and E. A. Nauman, "Impact Attenuation Capabilities of Football and Lacrosse Helmets," *Journal of Biomechanics,* vol. 49, no. 13, pp. 2838-2844, 2016.

[4] Margolin and Madison, "Inverse Innovation," 29 December 2016. [Online]. Available: https://www.inverse.com/article/25760-hedgehog-spine-quills-hedgemon-helmet-concussion. [Accessed 24 September 2017].

[5] G. Karam and L. Gibson, "Elastic Buckling of Cylindrical Shells with Elastic Cores- I. Analysis," *Int. J. Solids Structures,* vol. 32, pp. 1259-1283, 1995.

[6] L. Brazier, "On Flexure of Thin Cylindrical Shellsand Other Thin Sections," *Proceedings of the Royal Series of London Series A,* vol. 116, pp. 104-114, 1927.

[7] G. N. Karam, "On the Ovalisation in Bending of Nylon and Plastic Tubes," *Int. J. Pres. Ves & Piping,* vol. 58, pp. 147-149, 1994.

[8] G. Karam and L. Gibson, "Biomimicking of Animal Quills and Plant Stems: Natural Cylindrical Shells with Foam Cores," *Material Sience and Engineering C,* pp. 113-132, 1994.

[9] J. Niu, H. L. Choo and W. Shun, "Finite Element Analysis and Experimental Study of Plastic Laattice Structures Manufactured by Selective Laser Sintering," *Journal of Material Design and Application,* vol. 23, pp. 171-178, 2017.

[10] J. Torres, J. Cotelo, J. Karl and A. P.Gordon, "Mechanical Property of Optimization of FDM PLA in Shear with Multiple Objectives," *The Minerals, metal & Materials Society,* vol. 67, no. 5, pp. 1183-1193, 2015.

[11] "Ultimaker B.V," Ultimaker, 2018. [Online]. Available: https://ultimaker.com/en/resources/22225-how-to-print-with-ultimaker-pla. [Accessed 7 June 2018].

[12] W. J. Sun, S. Kothari and C. C. Sun, "The Relationship Among Tensile Strength, Young's Modulus, and Indentation Hardness of Pharmaceutical Compacts," *Powder Technology,* vol. 331, pp. 1-6, 2018.

[13] F. Han, Z. Zhu and J. Gao, "Compressive Deformation and Energy Absorbing Characteristic of Foamed Aluminum," *Metallurgcal and Materials Transactions A,* vol. 29, no. 10, pp. 2497-2502, 1998.

EURECA 2018 – Conference Paper
Paper number 2ME13

Preparation and Characterization of Wood Plastic Composite from Recycled Polystyrene Foam and Coconut Shell

Sing Li Ling[1], Seong Chun Koay[1], Ming Meng Pang[1], Kim Yeow Tshai [2], Ming Yeng Chan[3], and Thevy Ratnam Chandara[4]*

[1] School of Engineering, Taylor's University, Malaysia.
[2] Faculty of Engineering, The University of Nottingham, Malaysia.
[3] Centre for Engineering Programmes, HELP College of Art and Technology, Malaysia.
[4] Radiation Technology Processing Division, Nuclear Agency, Malaysia.

Abstract. Polystyrene foam (PS) is widely used as food packaging and containers. However, it generates a lot of wastes annually due to the PS being bulky and hard to recycle. Coconut is planted in all over Malaysia and its coconut shell can be used as activated carbon and as filler in wood plastic composites due to its high amount of lignin that is suitable to manufacture composites. Thus, wood plastic composites (WPC) were produced by incorporating coconut shell (CS) with recycled polystyrene foam (rPS). The effect of filler content on mechanical properties that comprises of tensile strength and tensile modulus as well as thermal properties were investigated. The increment of filler content of CS has decreased the tensile strength of the composite whereas increment of filler content of CS has increased the tensile modulus. The tensile strength at 60 phr is 11.83 MPa. For thermalgravimetric analysis (TGA), the addition of more CS content from 30 phr to 60 phr also increased the $T_{d50\%}$ of composites and higher content of char residue from 7.5% to 10.43%. For DSC analysis, glass transition temperature decreased with increasing filler content from 30 to 60 phr.

1 Introduction

Polystyrene (PS) foam is a lightweight and portable material that consists of about 98% of air with 2% of plastic and also low in cost [1]. Thus, it is among the materials extensively being used in various applications for instance as food packaging, containers, sport utility (e.g, surfboards), building and construction (e.g. bricks) [2-3]. The PS foam for packaging applications usually has a short service life. After the usage of PS foam by consumers, it will be thrown away as waste. Although the usage of PS foam increased annually, the recycling rate of PS foam is very low and expensive to recycle [4]. For this reason, there are about 3 million tons of PS foam wastes generated annually in the world [5]. Most of the PS foam wastes are sent to landfill and it contributes to environment pollution as it is non-biodegradable [6]. The recycling industries have less interest to recycle PS foam because PS foam wastes are bulky, and take up storage space as well as costly for transportation [4]. Thus, there is very little amount of PS foam that are actually recycled. Apart from that, recycled PS often cannot be utilized for food packaging again due to health concerns [7]. Hence, this research is proposed to utilize the PS foam wastes as matrix for wood plastic composite (WPC). This will highly reduce the PS foam wastes and also provide a cost advantage on WPC materials.

Fine wood is typically used as filler to produce WPC, but now there are many different types of natural filler made from agricultural wastes can be an alternative material for fine wood. For example, rice husk, kenaf fiber, wood flour, jute fiber, and coconut shell [8-11]. Coconut (*Cocosnucifera)* is widely planted in Malaysia as the country located at tropical region. In industry, the coconut kernel is used to extract the coconut milk, coconut oil and the coconut water for refreshing beverage [12]. However, the coconut shell husk is an unwanted by-product from the industry and it produces about 3.18 million tons of coconut shell annually [13]. Nowadays, coconut shell is mainly used as a raw material to product phenolic adhesive, charcoal, and activated carbon [14-15]. Moreover, some literatures reported that the coconut shell also used as filler to produce WPC [16]. Thus, this research also utilised coconut shell to produce WPC.

WPC is defined as composite materials having lignocellulosic or fine wood particles mixed together with either synthetic thermoplastic polymers such as polyethylene, polypropylene, and polystyrene, or thermoset polymers, such as polyester [17]. Nowadays, WPC also can be produced from recycled plastic and agricultural waste [18]. The market demand of WPC is increasing annually. Based on findings, the market of WPC is valued at about 3.3 billion US dollar in year 2014 and expected to reach 6 billion US dollars by year 2020 [19]. The main reason WPC materials have high market demand is because it has high and stiffness-to-density ratio which proves that it is a useful material that is vastly used to replace wood in furniture, decking and so on with vast range of finishes and appearance which are the keys to market growth [20]. Other reasons would be due to the low costs result from the huge extent of availability of natural fibers from agricultural waste being used [21]. With the high demand of WPC in many years to come, WPC will be the most environmental friendly material to replace the application of real wood and it will help in reducing the number of logging and saving the forest.

This paper is focused on the effect of filler content on the tensile and thermal properties of coconut shell filled recycled polystyrene foam composites.

2 Methodology

2.1 Research Materials

The PS foam used in this experiment were collected from electronic shops. The collected PS foam wastes were cut into smaller size and transferred to oven at 70°C. After 15 minutes in oven, the PS foams were shrinked into size that is 95% smaller than the its original size. Then, the recycled PS (rPS) was stored and ready to use for producing WPC. Coconut shell (CS) with 100 mesh size was obtained from Sekimdi Industries Sdn. Bhd. The maleic anhydride grafted polystyrene (MAPS) used in this experiment as a coupling agent to the composite was supplied by Sigma Aldrich Malaysia.

2.2 Preparation of rPS/CS composites

The rPS/CS composites were compounded using Haake Rheomix 600p that was located at SIRIM Malaysia in Shah Alam. The composites were prepared with various filler content from 15, 30, 45 and 60 phr (part per hundred resin). Processing temperature was set at 190°C and the rotor speed of 80 rpm.

The compounding procedures are as follow:

(i) rPS and 3 phr of MAPS premixed then added into the mixing chamber for 1 minute to melt the resin.
(ii) After that, CS was added into the mixing chamber and compounded for 9 minutes.
(iii) Then, the composites compound was removed from the chamber and placed in sealed, labelled plastic bags accordingly.

The rPS/CS composites were then molded into sheet of 2mm thickness. The hot press machine used was Moore model with temperature set at 190°C and pressure of 100 Bar. The rPS/CS composite sheets were then cut into tensile specimen and dimension in accordance to ASTM D638.

The molding procedures are as follow:

(i) The compound was preheated for 2 minutes to soften it.
(ii) The compound was then fully compressed under pressure of 100 Bar for 1 minute.
(iii) The compound was cooled for 20 minutes before taking it out from the machine.

2.3 Testing and Characterization

The tensile testing of rPS/CS composites were carried out using Instron universal testing machine model 5569 which was available at the laboratory in School of Engineering, Taylor's University. The standard test method used was ASTM D638. Crosshead speed was set to 5 mm/min and specimen was tested under standard room temperature with 15 kN of load cell. The tensile strength and tensile modulus of the specimens were tested and recorded by Bluehill 3 software. The minimum number of specimens tested out for every formulated composite was 7.

Thermogravimetric analysis (TGA) was conducted using Pyris Diamond TGA (Perkin-Elmer) to determine the thermal stability temperature of the WPC. Specimens were cut in small size weighing between 5 and 8 mg and put into a ceramic pan. The specimens were then heated from 30°C to 600°C at a heating rate of 10°C/min. TGA was carried out under nitrogen atmosphere utilizing gas flow rate of 20 ml/mm.

Thermal analysis was conducted using the differential scanning calorimetry (DSC) model Perkin-Elmer that was available at the laboratory in School of Bioscience, Taylor's University. The specimens were cut in small size as well weighing between 5 and 8 mg. The specimens were heated up from 30°C to 150°C then left to cool back to 30°C and then heated up again till 150°C at a heating or cooling rate of 10°C/min. The gas flow rate was set at 20 ml/min. This testing was carried out to determine the glass transition temperature (T_g) of WPC.

3 Results and Discussion

3.1 Effect of filler content on tensile and thermal properties of recycled polystyrene foam/coconut shell composites

3.1.1 Tensile Properties

The effect of filler content on the tensile strength of rPS/CS composites are shown in Figure 1. From Figure 1, the tensile strength of rPS/CS composites decreased as the CS content increases from 15 to 60 phr. Decrement of tensile strength of WPC usually due to following reason: i) poor adhesion between filler and matrix; ii) geometrical factor of filler; iii) aspect ratio of filler [22]. In this case, the MAPS was added as a coupling agent to the composites. The adhesion between the filler and matrix would not be the main reason causing the decrement of mechanical strength. However, the CS used in this experiment was in particle form, and

irregular in shape. The particle filler typically has lower aspect ratio compared to fiber. Then, the ability of CS to act as load bearing in this composites is low. Thus, the addition of more CS content in composites reduced in average of 55.2% tensile strength compared to neat rPS. Salmah *et al*. [23] also reported that the geometry of coconut shell was irregular and low aspect ratio. Thus, CS was unable to share the applied load hence the tensile strength of polylactic acid (PLA)/CS composites decreased with increasing filler content.

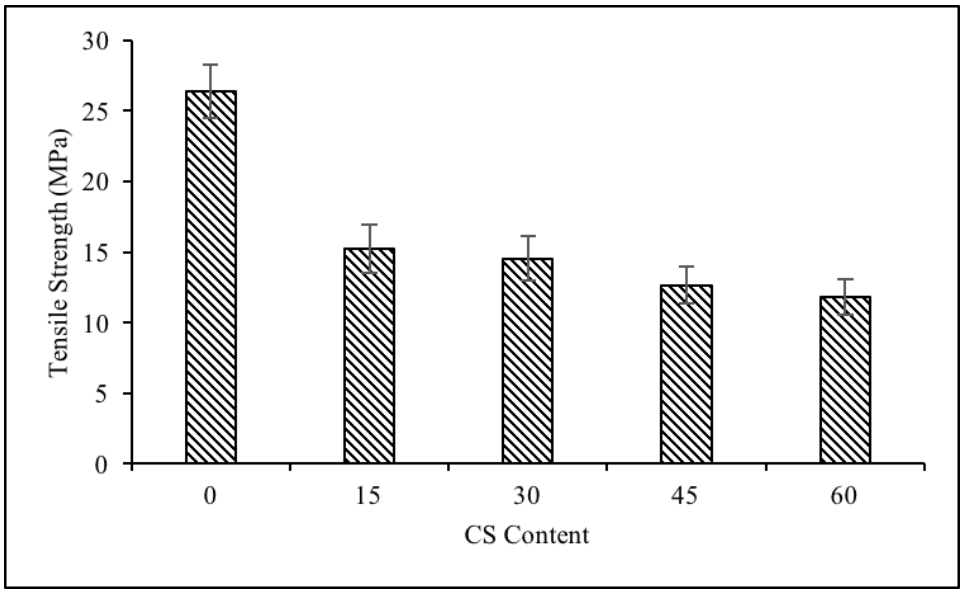


Fig. 1. Effect of filler content on tensile strength of rPS/CS composites treated with MAPS.

Figure 2 demonstrates the effect of filler content on tensile modulus of rPS/CS composites. As the filler content of CS increases, the tensile modulus of composites increases. In average, the tensile modulus increases about 29.0% from 0 to 60 phr of CS content. The CS particles are stiff and rigid than plastic material [24] and it present as rigid components in this WPC. Thus, it is normal trend if addition of stiff and rigid component in WPC will increase the modulus. Besides, the chains mobility of rPS matrix is also restricted the presence of CS and interfacial bonding due to the addition of coupling agent. Sarki *et al.* [25] also claimed that the greater surface area of coconut shell filler in polymer matrix resulted in higher quality of interfacial bonding that leads to increment of tensile modulus with increasing filler content.

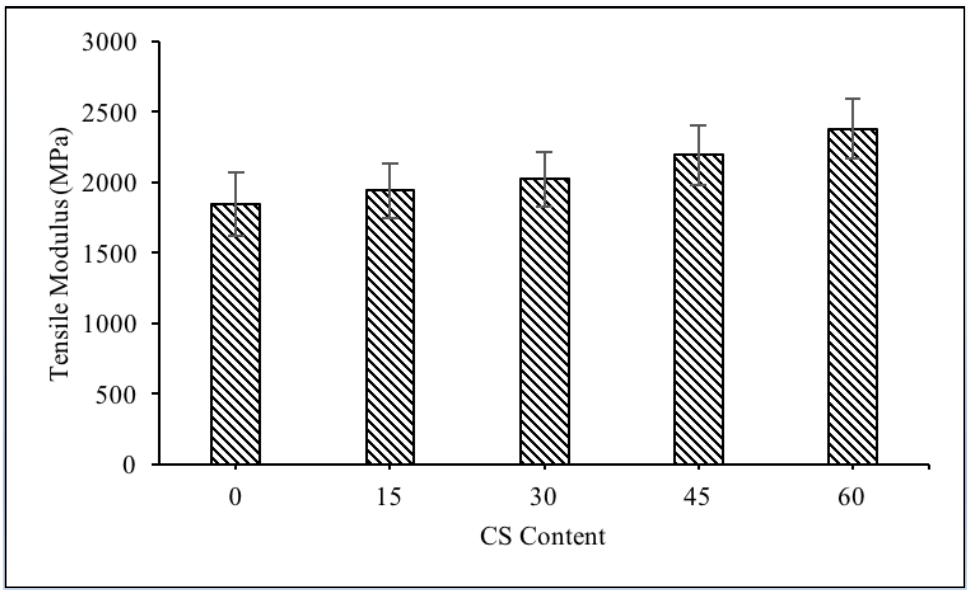


Fig. 2. Effect of filler content on tensile modulus of rPS/CS composites treated with MAPS.

3.1.2 Thermalgravimetric Analysis (TGA)

Figure 3 displays the TGA curves of rPS/CS composites with selected filler content, neat rPS and CS. All the data were recorded and tabulated in Table 1. Referring to temperature at $T_{d5\%}$, CS have undergone thermal degradation earlier than rPS. The weight loss of CS at $T_{d5\%}$ was due to removing of moisture and volatile compound [26]. According to $T_{d50\%}$, the CS also thermally degraded faster than rPS. This is because part of the lignin and hemicellulose from CS were degraded at temperature above temperature 300ºC. Then, the thermal degradation of lignin has yielded high amount of char residue. The $T_{d5\%}$ of rPS/CS/MAPS composites were lower compared to rPS and it decreased as the filler content increased. The earlier thermal degradation occurred on composites was obviously caused by the components from CS. However, the addition of more CS content from 30 to 60 phr also increased the $T_{d50\%}$ of composites and content of char residue. The presence of high char residue provided the thermal shielding effects on composites. Hence, the thermal degradation process of the remaining composites was delayed and it showed higher thermal stability at temperature above 300ºC. The similar finding was reported by Chun *et al.* [27].

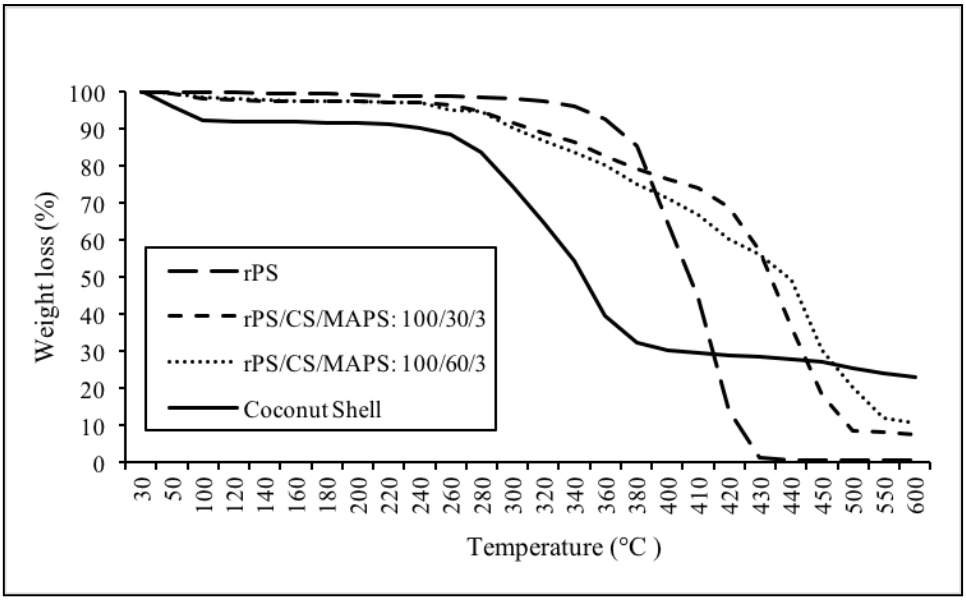


Fig. 3. TGA curves of rPS/CS composites treated with MAPS.

Table 1. Table of thermal degradation temperature at 5% and 50% weight loss and char residue at 600°C.

Samples	Temperature at 5% weight loss ($T_{d5\%}$, °C)	Temperature at 50% weight loss ($T_{d50\%}$, °C)	Char residue at 600°C (%)
rPS	347.2	406.9	0.7
CS	64.4	345.8	22.8
rPS/CS/MAPS: 100/30/3	276.0	433.4	7.5
rPS/CS/MAPS: 100/60/3	275.7	431.2	10.43

3.1.3 Differential scanning calorimetry (DSC)

The DSC curves of rPS/CS composites at selected filler content as well as neat rPS are showed in Figure 4. The DSC data of the composites and neat rPS are tabulated in Table 2. The T_g of composites were lower compared to neat rPS due to the addition of MAPS. The MAPS is a lower molecular weight co-polymer and it might provide lubricating effect to the rPS matrix. For this reason, the composites exhibited lower T_g than neat rPS. This observation was agreed with the finding reported by Chun *et al.* [28]. The T_g of composites was slightly increased with

addition of more CS content. This is because the addition of more CS restricts the chain mobility of the rPS matrix. This was agreed by Chen *et al.* [29] whereby the addition of more filler which was the wood flour restricted the chain mobility of the matrix.

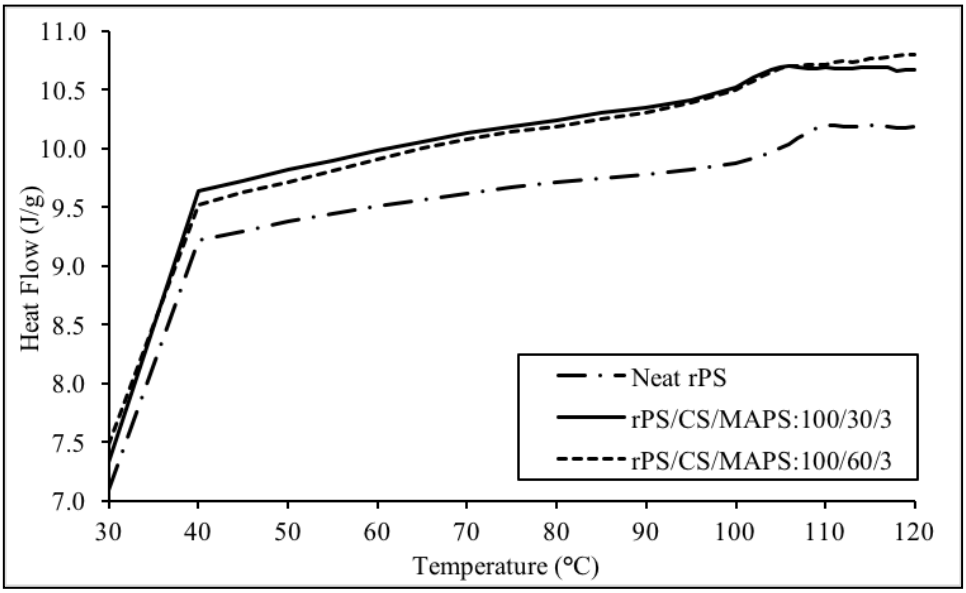


Fig. 4. DSC curves of treated rPS/CS with MAPS with different filler content.

Table 2. Table of DSC data of rPS/CS with MAPS composites.

Samples	Glass transition temperature, T_g (°C)
rPS	105.43
rPS/CS/MAPS: 100/30/3	101.45
rPS/CS/MAPS: 100/60/3	102.15

4 Conclusion

The tensile strength decreases by 55.2% with increasing CS content from 0 to 60 phr in the rPS/CS composites whereas the tensile modulus increases by 29.0%. The rPS/CS composite has relatively low tensile strength compared to neat rPS however the composite still possesses 11.83 MPa at 60 phr. The presence of MAPS has helped in better interfacial bonding between filler-matrix interaction. The TGA results have also shown that the percentage of char residue increases with increasing filler content and reaches up to 10.5%. The presence of char residue has highly improved the thermal stability of composites especially at higher temperature. The T_g increases with increasing CS content however it is lower compared to neat rPS itself. Thus, it is more beneficial with lower T_g as it will be easier for processing and mixing.

References

[1] G. Wang, X. Che, P. Liu, and S. Bai, J. Appl. Polym. Sci. **134**, 1-9 (2017)

[2] M. B. Baker, R. Abendeh, Z. A. Salem, and T. Khedaywi, Int. J. Appl. Envi. Sci. **11**, 183-192 (2016)

[3] S. Veiseh and A. A. Yousefi, Iran. Polym. J. **12**, 323-329 (2003)

[4] S. N. Kole, and S. R. Suryawanshi, Int. J. Eng. Sci. Comp. **7**, 45-53 (2017)

[5] K. Hearon, L. D. Nash, J. N. Rodriguez, A. T. Lonnecker, J. E. Raymond, T. S. Wilson, K. L. Wooley, and D. J. Maitland, Adv. Mat. **26**, 1552-1558 (2014)

[6] S. ABinaya, M. Clement, and D. S. Shanmugam, Int. R. J. Eng. Tech. **3**, 2468-2472 (2016)

[7] S. Doroudiani and H. Omidian, Build. Env. **45**, 647-654 (2010)

[8] M. Jamil, M. N. N. Khan, M. R. Karim, A. B. M. A. Kaish, and M. F. M. Zain, Const. Build. Mat. 128, 185-198 (2016)

[9] A. Kaymakci, T. Gulec, S. K. Hosseinihashemi, and N. Ayrilmis, Maderas. Cien. Tec. **19**, 339-348 (2017)

[10] T. Mukherjee, and N. Kao, J. Polym. Env. **19**, 714-725 (2011)

[11] K. S. Chun, S. Husseinsyah, and H. Osman, J. Polym. Res. **19**, 1-8 (2012)

[12] P. Appaiah, L. Sunil, P. K. Prasanth Kumar, and A. G. Gopala Krishna, J. Ame. O. Chem. Soc. **91**, 917-924 (2014)

[13] T. Lay Ting, R. Putra Jaya, N. Abdul Hassan, H. Yaacob, and D. Sri Jayanti, J. Tech. **76**, 121-125 (2015)

[14] T. U. Ganiron, J. Eng. Sci. Tech. Rev. **6**, 7-14 (2013)

[15] A. R. Hidayu and N. Muda, Pro. Eng. **148**, 106-113 (2016)

[16] S. Husseinsyah and M. M. @ Zakaria, Mal. Polym. J. **6**, 87-97 (2011)

[17] D. J. Gardner, Y. Han, and L. Wang, C. For. Rep. **1**, 139–150 (2015)

[18] M. A. Binhussain, and M. M. El-Tonsy, Const. Build. Mat. **47**, 1431-1435 (2013)

[19] R. Gupta, A. Noraziah, A. Gupta, and A. N. Abdalla, Ind. J. Sci. Tech. **10**, 1-5 (2017)

[20] L. Thomson, Derek; Hansen, Eric; Knowles, Chris; Muzynski, Bio. **5**, 1336-1352 (2010)

[21] M. A. Flores-Hernandez, J. G. Torres-Rendon, R. M. Jimenez-Amezcua, M. G. Lomeli-Ramirez, F. J. Fuentes-Talavera, J. A. Silva-Guzman, and S. G. Enriquez, Bio. **12**, 6392-6404 (2017)

[22] K. S. Chun, S. Husseinsyah, and F. N. Azizia, P.P. Tech. Eng. **52**, 287-294 (2013)

[23] H. Salmah, S. Koay, and O. Hakimah, J. Thermo. Comp. Mat. **26**, 809-819 (2012)

[24] O. O. Obiukwu, M. N. Uchechukwu, and M. C. Nwaogwugwu, Futo J. S. **2**, 43-55 (2016)

[25] J. Sarki, S. B. Hassan, V. S. Aigbodion, and J. E. Oghenevweta, J. All. Comp. **509**, 2381-2385 (2011)

[26] I. O. Oladele and L. O. Kupolusi, Ame. J. Eng. Tech. Res. **16**, 51-67 (2016)

[27] K. S. Chun, S. Husseinsyah, and H. Osman, Polym. Eng. Sci. **53**, 1109-1116 (2013)

[28] K. S. Chun, S. Husseinsyah, and H. Osman, Adv. Mat. Res. **747**, 645-648 (2013)

[29] C. H. Chen, C. L. Chiang, W. J. Chen, and M. Y. Sben, Polym Comp. **26,** 45-58 (2018)

EURECA 2018 – Conference Paper
Paper number 2ME14

Properties and Characterization of Durian Husk Fiber Filled Recycled Polystyrene Foam Composites

Mah Chee Hang[1], Koay Seong Chun[1], Pang Ming Meng[1], Kim Yeow Tshai[2], Ming Yeng Chan[3], and Chandara Thevy Ratnam[4]*

[1]School of Engineering, Faculty of Built Environment, Engineering, Technology and Design, Taylor's University Lakeside Campus, 47500 Subang Jaya, Malaysia
[2] Faculty of Engineering, Taylor's University, Malaysia.
[3]Centre for Engineering Programmes, HELP College of Art and Technology, Malaysia.
[4] Radiation Technology Processing Division, Nuclear Agency, Malaysia.

Abstract. Polystyrene (PS) is a foamed form polymer that is being widely used nowadays. It is formed by a bunched of styrene group organic compound through polymerization. In this research, polystyrene will be recycled and use as a raw material to produce wood plastic composite (WPC). Durian husk fiber (DHF) was chose as the natural filler in this research due to its similar composition with wood fiber. But due to the different natural behaviour of both material, coupling agent will be added to the composite to improve the interfacial adhesion of the material. This paper is focus on the effect of different formulation of coupling agent and processing aid on the mechanical properties and thermal properties of rPS/DHF composite. The results found that the tensile strength and tensile modulus improved when appropriate amounts of MAPS were added into the composite. The optimum results tensile strength recorded was near to 20MPa. Whereas, thermal stability of the composite improved with the increment of MAPS added into the composite. Moreover, addition of processing aid in the composite could further improve the properties of the composite.

1 Introduction

Expanded polystyrene foam (EPS) or commonly named as Styrofoam is a type of expanded polystyrene that commonly seen in the market. It is widely used as packaging material in many different industries, for instance as container for food and fruit, enclosure and endcap packaging for electronic goods and furniture. The broadly use of EPS is due to the fact that it is relatively rigid, light weight and cheap [1]. From research, it shows that the capacity and production of EPS has an increment around 7% growth annually in China from 2010 to 2015 [2]. Despite the high demand, recycling rate of EPS is relatively disappointing. This is because for recycling industries, recycling of EPS is not economic. EPS is thermoplastic foam consisting of 95% air bubbles in the structure. The high capacity of air is the reasons EPS has such great properties such as lightweight and low cost. But due to these properties, EPS is bulky and will fill up large volume of space with very little weight. For this reason, transportation expenses of EPS waste to processing plant is not worthy and gain low attention among recycling industries. In general, most of the EPS wastes will be sent to landfill [3]. However, there are still large number of unmanaged EPS wastes disposed into ocean and contaminate the marine environment. Hence, this research is proposed to utilize the EPS waste as a part of material to produce wood plastic composite. This will be an alternate way to gain the interested of people for recycling of EPS and reduce the EPS wastes.

Wood Plastic Composite (WPC) is a type of composite material being widely used in recent years. It is obtained by mixing wood fiber and thermoplastic resin [4]. According to Yadav et.al [5], WPC became a very crucial material to use for the past ten years and it involved in varies engineering applications. This is because of the attractive properties the material offers. The material has high specific strength and modulus, renewability, low density and also low cost [4]. Furthermore, WPC has emerged as a green material to replace real wood. Thus, WPC are used mostly in various indoor applications such as decking, flooring, railing, furniture, and fencing [5]. From researches**Error! Reference source not found.**, global market of WPC has been increased annually. [6] Besides, the global market of WPC was valued at 4.06 million US dollar in year 2015 and the market value is expected to reach 9.77 million US dollar by year 2024. Due to high market potential of WPC, this research is planned to focus on producing new WPC from difference recycling plastic and agricultural waste. *Durio Zibethinus Murray* or commonly called as durian and it is a type of tropical fruit that commonly found among Southeast Asia countries such as Malaysia, Thailand and Indonesia. Malaysia is one of the biggest distributor in ASEAN region producsing largest amount of durian. In year 2015, Malaysia produced about 400, 000 tons of durian and the production of the durian keep increasing annually [7]. Durian fruit usually grows with a shell and seeds. For each durian fruit, only 25-40% of its content is flesh, whereas the remaining are shell and seed which treated as waste. [8] This means for every 10 tons of durian produced will generate about 6 tons of durian husk and seeds as wastes. Such agricultural waste are expect to keep increase in the future if don't have better solution to dispose them. To turn the durian husk into something beneficial, in this research, durian husk was selected as replacement of wood fiber in production of WPC. In addition, the durian husk consists of 15.45% of lignin, 13.09% of hemicellulose and 71.46% of cellulose and the content is likely similar to wood fiber [9-10].

In fact, combining wood fiber and synthetic thermoplastic is usually difficult. This is due to the difference in natural behavior of both material, thermoplastic polymers are typically hydrophobic, whereas wood fibers are usually hydrophilic. The combination of wood fiber and

thermoplastic usually is incompatible and cause poor mechanical strength due to weak interfacial adhesion. Nowadays, various types of additive are use to overcome the incompatibility between wood fiber and thermoplastic. For example, maleated polypropylene (MAPP) is a type of functionalized co-polymer that usually uses as coupling agent in WPC. The function of MAPP is able to improve the interfacial adhesion between wood fiber and thermoplastic. Besides, melt fracture is another common issue occurs in WPC process. In order to improve the processability of WPC, processing aid will be add to WPC during the compounding process. Generally, processing aid contains fluoropolymers or polyolefin which able to promote better acts as internal and external lubricant for any plastic compound. For WPC, processing aid is crucial to eliminate the melt fracture phenomena of the compound when process at higher shear rates [11-12]. In this project, coupling agent and processing aid will be used to enhance the properties of WPC.

This research is to study the to prepare wood plastic composites from recycled polystyrene foam and durian husk fiber using melt compounding technique. At the same time, it is to investigate the effect of coupling agent and processing aid on tensile and thermal properties of rPS/DHF composite.

2 Methodology

2.1 Preparation of Durian Husk

After collected the durian husk, the durian husk waste was clean thoroughly to remove any adhering dust and particles. The rotten parts of the durian husk was also be removed. The durian husk was then be chopped into small pieces and send to oven to dried at temperature around 70^{o}C for an hour. Next, it was be ground into short fiber. The durian husk fiber was sieved into uniform size before compounding process.

2.2 Preparation of Recycled Polystyrene

Polystyrene foam obtained was cut into small pieces. The polystyrene foam pieces were then wrapped by aluminum foil before placed in oven at temperature at around 70^{o}C. The polystyrene foam was heat for 15 mins before taken out from oven for compounding process.

2.3 Preparation of Wood-Plastic Composites

Wood-Plastic composites were compounded using Haake internal mixer. The process was conducted at SIRIM Sdn. Bhd, Shah Alam, Malaysia. The formulation of rPS/DHF composites is as shown in Table

Table 1 **Formulation of rPS/DHF composites with and without processing aid and coupling agent**

Material	DHF (phr)	rPS (phr)	Coupling Agent (phr)	Processing Aid (phr)

rPS/DHF with different coupling agent content	60	100	0, 1, 3, 5	0
rPS/DHF with different processing aid content	60	100	3	0, 1, 3, 5

The composites were mixed at temperature around 190^{o}C with rotor speed fixed at 80rpm. The compounding process included: First, added in Polystyrene resin in the mixing chamfer and blend it for 1 minute to melt the resin; Then, coupling agent was added and let it blend for 10 seconds; Next, the durian husk fiber (DHF) was added into the melted resin and further mixed for 5 minutes; After that, removed the compound from mixing chamber.

After that, the mixture was moulded into 1mm thickness sheet using Moore compression moulding machine under temperature of 190^{o}C. To complete the whole moulding process, it involves three steps; First, the compound was pre-heat to soften for 4 min; Then, the compound was send to fully compressed under 100 psi pressure for 1 min; Lastly, the compound underwent cooling until the temperature drop to room temperature. The tensile specimen was cut from the sheet and the dimension of tensile specimen is according to ASTM D638 standard.

2.4 Testing and Characterization

Instron universal testing machine (model 5569) was used to evaluate the tensile properties of rPS/DHF composite. The tensile test was carried out following testing standard ASTM D638. The testing will be conduct at room temperature (25 ± 3^{o}C) with 5 mm/min crosshead speed and 15kN load cell. The specimen was shaped into size 8cm x 1.5cm. Tensile strength and tensile modulus of the samples will be recorded.

Whereas, Thermogravimetric analysis (TGA) was carried out by using Pyris Diamond TGA (brand: Perkin-Elmer). To conduct the analysis, specimen was prepared in small size with weight from 6 to 8mg. The specimen was then placed in a ceramic pan. After that, the specimen was undergone thermal scan from 30^{o}C to 700^{o}C with heating rate 10^{o}C/min and nitrogen gas flow rate 20ml/min.

3 Results and Discussion

3.1 Effect of Coupling agent on Tensile Properties

Figure illustrates the effect of different MAPS content on the tensile strength of the rPS/DHF composites. The addition of 1 phr of MAPS has significantly increased the tensile strength of the composites. The increment is about 22.5%. However, the strength of composites was gradually decreased if the content of MAPS increased from 3 to 5 phr. Usually, the bonding between hydrophilic filler and hydrophobic matrix is weak because the diffrence in natural behaviour obstruct the formation of good adhesion. This weak bonding will resulted with a poor mechanical strenght. Figure shows the schematic reaction between MAPS, fiber

and matrix and Figure shows the effect of MAPS. The present of MAPS might chemicaly reacts with hydroxyl groups of fiber and forms covalent bonding. Thus, the MAPS able to attached on the fiber surface and lefting the PS chains on fiber surface as well. The PS chains from MAPS also entangled with rPS chain from the matrix. Thus, the fiber is able to form strong interfacial bonding with matrix. In this case, this phenomenon was occurred on rPS/DHF composites with 1 phr of MAPS. For this reason, the strenght of this composites have increased. On the other hand, 3 to 5 phr of MAPS was excessed, the part of the MAPS might not able to form bonding fiber and it would stayed at interface region. The excessive MAPS might hindered the MAPS that attached on fiber from entangled with rPS matrix. Hence, the interfacial bonding at interface region will be weaken. This observation was similar to finding reported by other researchers [13-14].

Figure shows the effect of different MAPS content on tensile modulus of rPS/MAPS composite. Tensile modulus for 60phr DHF of rPS/DHF composite without coupling agent was around 2800MPa.The results shows the tensile modulus of composites was at optimum when added with 1phr of MAPS. Then, the tensile modulus of composites were dropped with further increment of MAPS content. From previous found the fiber was higher modulus compared to rPS matrix and additon of fiber usually increased the modulus of composites. However, this also depending of interfacial bonding of composites [1]. As discussed earlier, the addition of 1 phr of MAPS was improved the interfacial bonding between fiber and matrix. Thus, the tensile modulus of composites also increased. In contrast, the excessive amount of MAPS in the rPS/DHF composite might also lead to a lubricating effect on the composites. This statement also agreed by other researches[1,13,15].

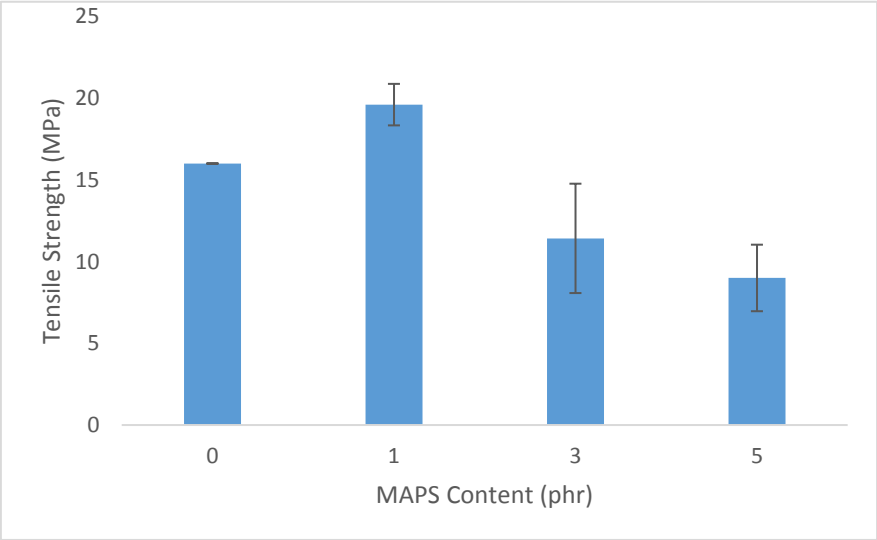


Figure 1 Tensile strength of rPS/DHF composites with different MAPS content

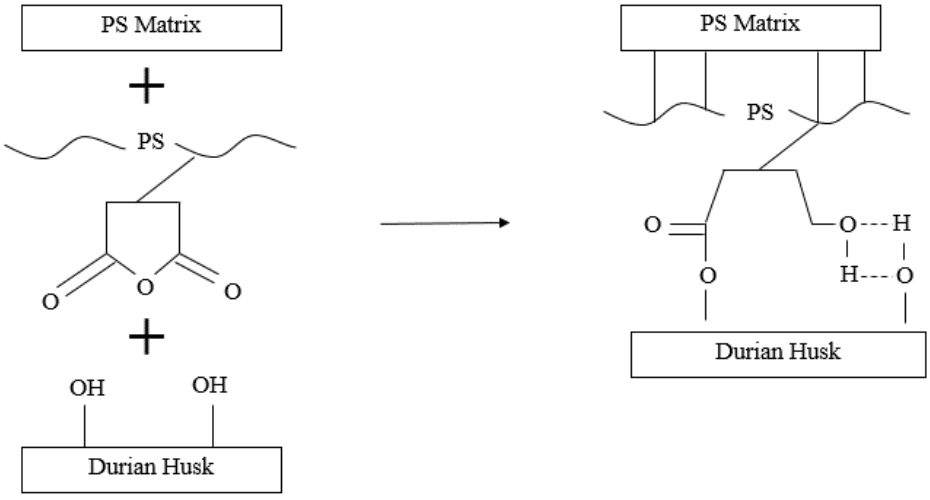


Figure 2 **Schematic reaction between rPS, DHF and MAPS**

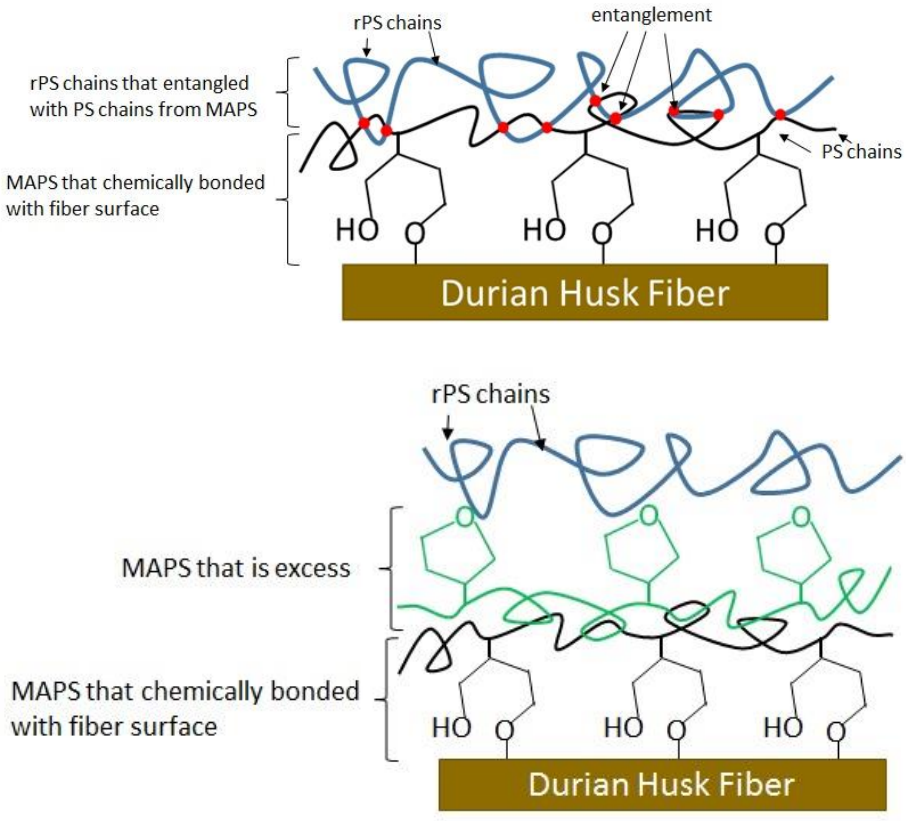


Figure 3 **Top: Effect of MAPS; Bottom: Effect of excessive MAPS**

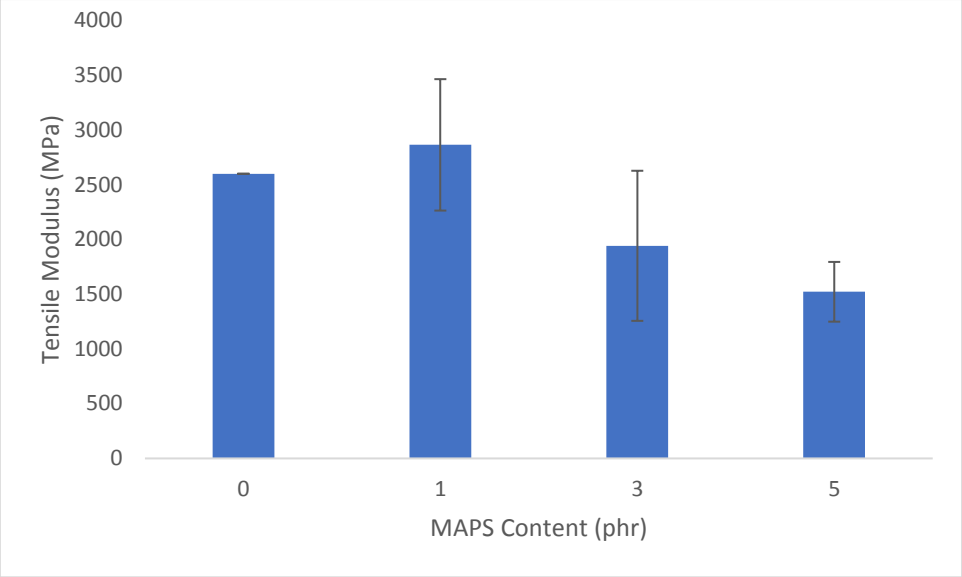


Figure 4 **Tensile modulus of rPS/DHF composites with different MAPS content**

3.2 Effect of coupling agent on Thermogravimetric Analysis (TGA)

Figure showed the TGA curves of composites with different MAPS content. Whereas, Table lists the data obtained from TGA curves. The $T_{d5\%}$ and $T_{d50\%}$ of rPS/DHF composites increased with the increasing of MAPS content. From previous study, the rPS/DHF undergone earlier thermal degradation where the $T_{d5\%}$ of composites was lower compared to neat rPS [1]. In this case, the addition of MAPS has coated the fibre and protected it from undergoing earlier thermal degradation. For this reason, the $T_{d5\%}$ of the composites increased. The $T_{d50\%}$ of composites increases due to effect of char formation. At temperature above 400^{o}C, hemicellulose and part of lignin were thermally degradation and left certain amount char. The remaining char would provide shielding effect on composites. Besides, the thermally degraded MAPS also yield small amount of char. Thus, the addition of more MAPS increased the char residue of composites. Due to increase of char content, the thermal stability of composites also improved. This result is like some studies by other researchers [16-18].

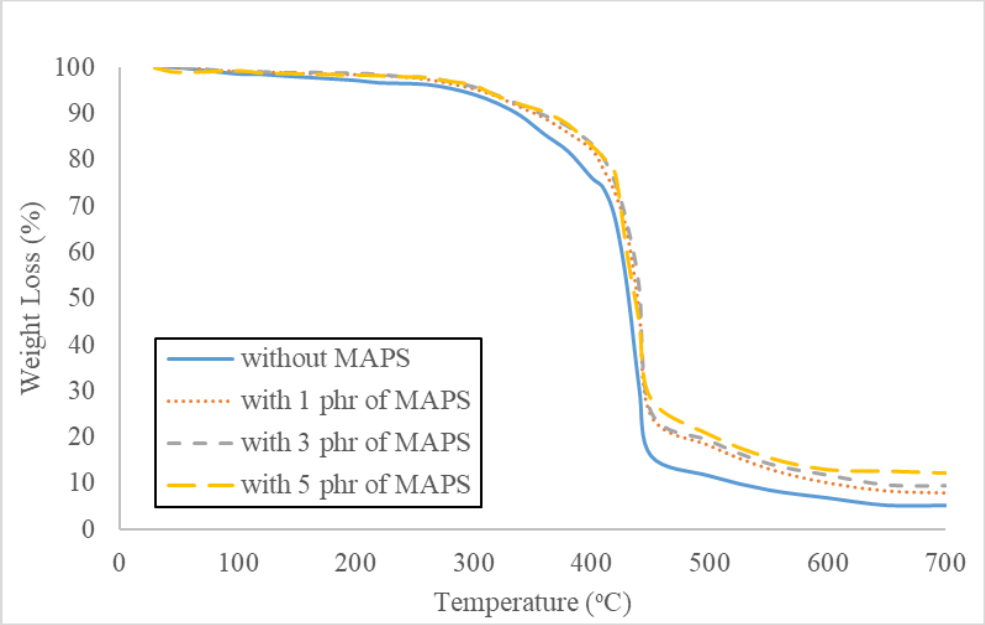


Figure 5 **TGA curves of specimen with different MAPS content**

Table 6 **TGA data of specimen with different MAPS content**

Sample	Temperature at 5% Weight Loss	Temperature at 50% Weight Loss	Char residue at 700C (%)
Without MAPS	293.3	431.77	5.183
With 1phr of MAPS	301.2	437.11	7.9345
with 3phr of MAPS	305.6	439.14	9.5704
with 5phr of MAPS	309.4	440.12	12.2192

3.3 Effect of Processing Aid on Tensile Properties

Figure illustrates the effect of processing aid (Ultra-Plast XP-519) content on the tensile strength of the composite compounded. For this experiment, 3phr of MAPS content was set as constant variable and the controlled variable was the Ultra-Plast XP-519 content. From the result, the optimum tensile strength obtained was with 1phr of Ultra-Plast XP-519. The processing aid, Ultra-Plast XP-519 was a fatty acid amide compounds. This Ultra-Plast XP-519 might easily attached on filler surface via amide groups as shown in Figure . This increment obtained was due to the utilization of XP-519 improved the fiber dispersion and further enhanced the fiber-matrix bonding. The existence of processing aid lead to a significant improvement in strength. This effect of processing aid on improving tensile properties has also been reported by another researcher [19]. However, further increment of processing aid in the composite resulting with a further dropped in tensile strength. The decrement was due to the excessive Ultra-Plast XP-519 might diffuse to interface between of MAPS and rPS matrix. The presents of excessive processing aid will be further hindered the MAPS and rPS chains from

entanglement. As result, the interfacial bonding of composites was weakened. For this reason, the tensile strength of composites with higher MAPS content was significantly reduced.

Figure 9 indicate the effect of processing aid (Ultra Plast XP-519) on tensile modulus of the rPS/DHF composite. Same with the results obtained for tensile strength, with addition of processing aid, tensile modulus obtained had a significant improvement. The optimum results obtained was 3119.19Mpa with 3phr of MAPS and 1phr of XP-519. Similar with explanation above, if amount processing aid excessed, the layer of processing aid will act as lubricant, weakening the interfacial bonding dropped, thus modulus drop.

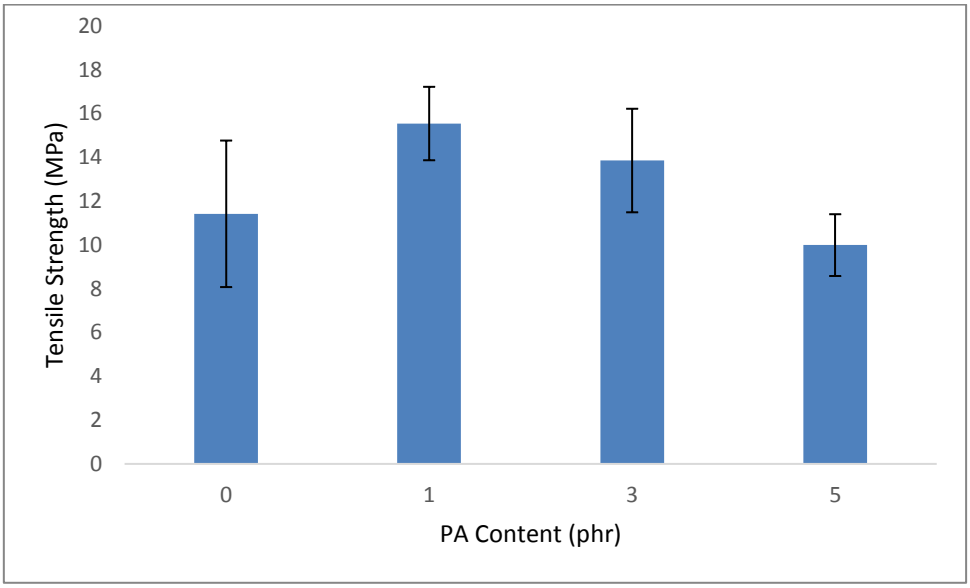


Figure 6 **Tensile strength of rPS/DHF composites with different PA content**

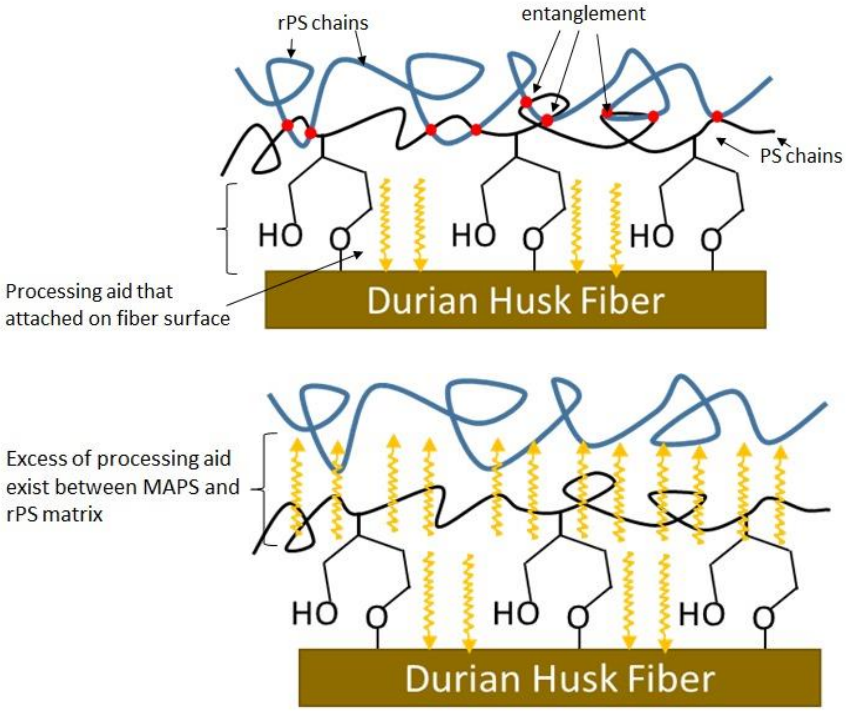


Figure 7 **Top: Effect of Processing Aid; Bottom: Effect of excessive Processing Aid**

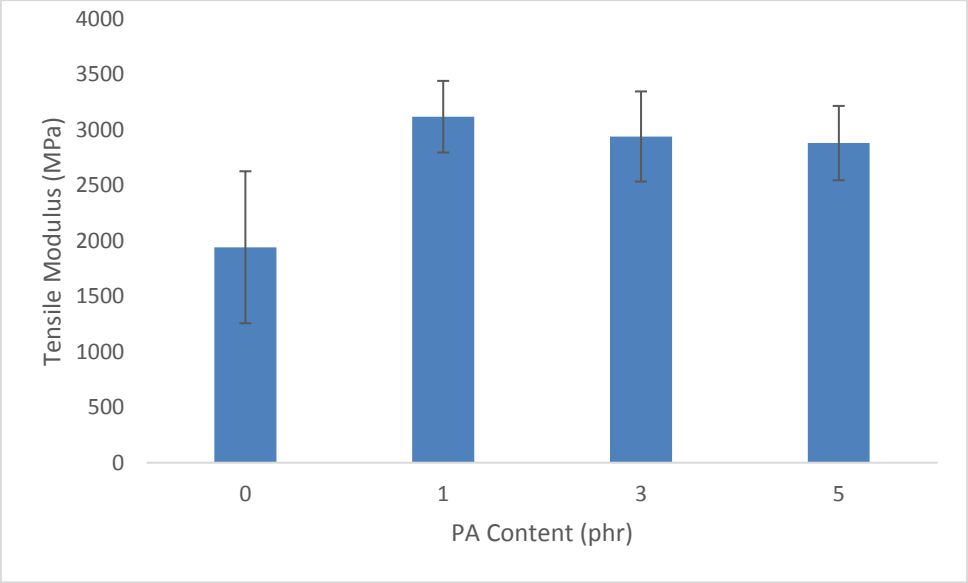


Figure 9 **Tensile modulus of rPS/DHF composites with different PA content**

3.4 Effect of Processing Aid on Thermogravimetric Analysis (TGA)

Figure illustrated the TGA curves of composites with different PA content. The results obtained was compared with the results of composite formed without PA, but with 3phr of MAPS. Data obtained from the results was tabulated in Table . From the results, compared to the TGA data for composite without Ultra Plast XP-519, the temperature recorded for 5% ($T_{d5\%}$) and 50% ($T_{d50\%}$) weight loss of composites was shifted to lower temperature. This shown that the composite thermal degraded earlier at low temperature when processing aid were added. However, the composite recorded with no significant improvement when comparing the char residue of specimen at 700^{o}C. Without the addition of processing aid, 9.5704% of char residue were recorded. The char residue of specimen recorded with a minor improvement with the increment of processing aid. This indicates that Ultra Plast XP-519 improve the resistivity of composite to thermal degradation but the improvement was neglectable. This result obtain is similar with another researcher that also studied the effect of processing aid on thermal behaviour of composite [20].

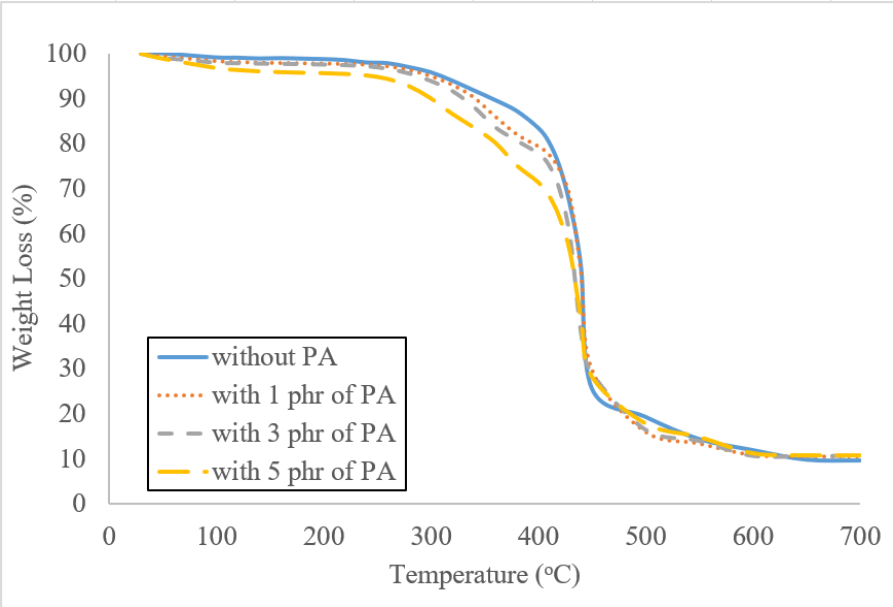


Figure 8 **TGA curves of specimen with different PA content**

Table 7 **TGA data of specimen with different PA content**

Sample	Temperature at 5% Weight Loss	Temperature at 50% Weight Loss	Char residue at 700C (%)
Without PA	305.6	439.14	9.5704
With 1phr of PA	300.2	437.96	10.3936
with 3phr of PA	288.02	438.13	10.47261
with 5phr of PA	269.82	438.93	10.67258

4 CONCLUSIONS

In conclusion, the addition of MAPS as coupling agent in rPS/DHF composite help improve the tensile strength and tensile modulus. But this improvement could only sustain with appropriate amount added. Excessive MAPS in the composite will lead to opposite effect. Moreover, the tensile properties of the composite could be further improve with appropriate amount of processing aid Ultra Plast XP-519. Next, with addition of MAPS in WPC compounded, it improved the thermal properties of the composite. Thermal stability of composite increase significantly follows the increment of MAPS. This result was proved using thermogravimetric analysis. Furthermore, the addition of Ultra Plast XP-519 could further improve the thermal properties of WPC formed, but the improvement recorded were not significant. These results indicate that the addition of MAPS and Ultra Plast XP-519 in rPS/DHF composite could make the composite a potential new WPC material, but further improvement was needed to improve the strength of the composite as the material formed was too brittle.

References

[1] S.C.Koay, S.Varnesh, M.Y.Chan, M.M.Pang, K.Y.Tsai and K.H.Cheah, "Preparation and Characterization of Wood Plastic Composite Made Up of Durian Husk Fiber and Recycled Polystyrene Foam," *Journal of Polymer Research,* pp. 1-7, 2017.

[2] M.Chang, "Analysis of 2015 & Prospects," *Polystyrene Market in China,* pp. 17-19, 2016.

[3] T.Maharana; Y.S.Negi; B.Mohanty, "Polymer-Plastics Technology and Engineering," *Recycling of Polystyrene,* pp. 729-734, 2007.

[4] M.Poletto, "Effect of using a coupling agent derived from a renewable resource," *Polypropylene based wood plastic composites,* vol. 19, pp. 265-272, 2017.

[5] S.M. Yadav; K.B. Yusoh, "Strength and sorption properties of bamboo wood-plastic composites," *Agriculture, Foresty and Plantation,* pp. 1-10, 2015.

[6] Grand View Research, "Wood Plastic Composite (WPC) Market By Type (Polyethylene, Polyvinylchloride, Polypropylene, Others)," 2016.

[7] T. Leong, *Thorny Times for durian orchards in Malaysia,* Strait Times, 2017.

[8] N. Aimi, H.Anuar, M. Manshor, W. W. Nazri and S. Sapuan, "Optimizing the parameters in durian skin fiber reinforced polypropylene composites by response surface methodology," *Industrial Crops and Products,* vol. 54, pp. 291-295, 2014.

[9] M. Salit, "Composite Material," in *Composite Materials: Concurrent Engineering Approach,* Elsevier Science & Technology Books, 2017, pp. 57-58.

[10] A. Klyosov, Wood Plastic Composites, John Wiley & Sons, Inc, 2007.

[11] H.Pirayesh, T.Tabarsa and H.Khanjanzadeh, "Manufacturing of Wood-Plastic Composite from Completely Recycled Material," *Key Engineering Material,* Vols. 47-472, pp. 62-65, 2011.

[12] S.M.Yadav and K.B.Yusoh, "Mechanical and physical properties of wood-plastic composites made of polypropylene, wood flour and nanoclay," *Kuala Lumpur International Agriculture, Foresty and Plantation,* pp. 1-10, 2015.

[13] A. El-Sabbagh, "Effect of coupling agent on natural fibre in natural fibre/polypropylene composites on mechanical and thermal behaviour," *Composites,* pp. 126-135, 2013.

[14] S. Mohanty, S. Nayak, S. Verma and S. Tripathy, "Effect of MAPP as a Coupling Agent on the Performance of Jute–PP Composites," *Reinforced Plastics and Composites,* pp. 624-637, 2004.

[15] M.R.Islam and M. Beg, "Effect of Coupling Agent On Mechanical Properties of Composite From Kenaf and Recycled Polypropylene," *Mechanical Engineering Research and Postgraduate Studies,* pp. 871-876, 2010.

[16] J.R.Araujo, W.R.Waldman and M. Paoli, "Thermal properties of high density polyethylene composites with natural fibres: Coupling agent effect," *Polymer Degradation and Stability,* pp. 1770-1775, 20008.

[17] S.C.Koay, H.Salmah and N.A.Fatin, "Characterization and Properties of Recycled Polypropylene/Coconut Shell Powder Composites: Effect of Sodium Dodecyl Sulfate Modification," *Polymer-Plastics Technology and Engineering,* vol. 52, pp. 287-294, 2013.

[18] S.C.Koay, H.Salmah and M.Y.Chan, "Green composites from kapok husk and recycled polypropylene: Processing torque, tensile, thermal, and morphological properties," *Thermoplastic Composite Materials,* pp. 1-19, 2015.

[19] M. Rasidi, S. Husseinsyah and T. Leng, "The Effect of Filler Content and UltraPlast TP01 of Nypa Fruticans Fiber-Filled Polylactic Acid/Recycled Low Density Polyethylene Biocomposites on Tensile Properties and Morphology," *Polymer-Plastics Technology and Engineering,* pp. 253-258, 2014.

[20] M. Rasidi, H. Salmah and P. Teh, "Thermal Properties of Nypa Fruticans Fiber Filled Polylactic Acid/Recycled Low Density Polyethylene Biocomposites : Effect Compatibilization with Ultra-Plast TP01," *Advances in Civil, Environmental, and Materials Research,* pp. 1-9, 2014.

Suppression of Vibration Transmission to Structures subjected to Rail-induced Vibrations

Melanie Yong, Mohammad Hosseini Fouladi[11], and Satesh Narayana Namasivayam

School of Engineering, Taylor's University, 47500 Subang Jaya, Selangor, Malaysia

Abstract.

This paper studies the transmission of ground-borne vibrations from railways into building foundations to optimize a method to reduce the possibility of long-term effects in multi-level structures. The increasing need for vibration isolation from railway tracks is due to the growing density of urban areas which require buildings to be built in close proximity to them. Ground-induced vibrations from railways may contribute to faster deterioration of buildings in the long term and also psychologically affect its occupants. Finite element analysis in ANSYS of a low-cost apartment in Selangor, Malaysia with piled raft foundation yielded a vibration response of 25.2 mm/s at 28.2 Hz which is above the minor damage limits of Malaysian vibration standards for structural steady-state response. To decrease the vibration response of the structure below the minor damage threshold of 5 mm/s, it was proposed to simultaneously increase the thickness of the raft to 2.5 m and the damping ratio to 0.107 by the increment of volume of the concrete raft foundation and installation of damping system such as High Damping Rubber Bearing in the structure. Finite element analysis results compared with the analytical calculations yielded an acceptable percentage difference of 1.19% for velocity amplitude 6 % for resonant frequency, showing that the analytical model proposed was acceptable.

Keywords: train-induced vibrations, vibration isolation, building foundations, Malaysian buildings.

[11] Corresponding author: mfoolady@gmail.com

1 Introduction

1.1 Background

The exponential growth in density of urban areas over the last few decades has caused stress on the fundamental systems of society such as transport infrastructure. Public transport plays a significant role in these areas as private vehicles may not be an economical or sustainable method of transport in large cities such as Singapore and Tokyo. Yang *et al.* [1] stated that it is unavoidable in the modern world that such railways may pass through residential or other vibration-sensitive areas and hence there is a growing interest in methods of vibration isolation. This research project aligns to the 21st century global challenge of "Restore and Improve Urban Infrastructure" proposed by the National Academy of Engineering [2].

Vogiatzis and Kouroussis [3] stated that previous focus of research in vibration transmission from railways were mostly on high-speed trains in the environment. However, the amplitude of the vibration transmission even in soft soil is found to attenuate rapidly as distance between the track and nearby buildings were typically large. This differs significantly with the situation in urban transits as the distance between structures and railways are close enough to induce localized vibrations. Urban tramways in general generates low amplitude vibrations while underground trains generate higher frequency vibrations [4]. Both sources of vibrations that are transmitted through the soil then spread through the load-bearing structures of a building foundation as shown in Fig. 19.

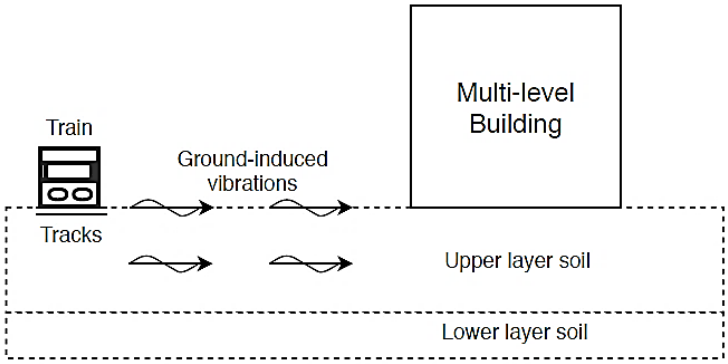


Fig. 19: Transmission of ground-induced vibrations from nearby railways.

The isolation of vibrations can be accomplished at the source, the transmission medium or at the building structure itself. Dudkin *et al.* [5] stated that methods implemented at the source include installation of vibration mat and rail lubrication systems. For the transmission medium, Cacciola *et al.* [6] suggested the implementation of a vibrating barrier. Yang *et al.* [1] studied the reduction of vibrations with the implementation of filled and open trenches. However, in dense areas there may not be enough space between the railways and buildings to implement barriers or trenches. Hence, methods of isolating buildings have to be considered as in there has been recent cases where it is required in a project but there is lack of analysis on such mitigation measures [7].

Ground-borne vibration has been expected to contribute to long term deterioration of buildings over time, which has been a major concern to areas where there may be historical and cultural sites due to low-intensity steady vibrations [8]. Eitzenberger [9] outlined that resonance may occur if the vibration frequency is near the natural frequency of the building.

However, train-induced vibrations are not likely the sole cause of damage but an acceleration of the process in buildings and is usually in combination with other factors such as thermal effects or chemical affects.

Hence, the objectives of this research are to identify parameters that affect transmission of ground vibrations produced from building base to structure and design a foundation that can minimize the vibrations. The feasibility and manufacturability of the foundation design are to be assessed based on the Malaysian context.

1.2 Existing methods to reduce vibration transmission in structures

Existing methods of vibration reduction methods in literature are investigated and summarized in Table 3 to understand the parameters that may affect the transmission of vibration into buildings. Passive base isolators which protects the intrument from the effects of the source were considered as it is a more economically sustainable option for the present study.

Table 3: Reduction of vibration transmission in literature.

Authors	Method of reduction	Conclusion
Ulgen *et al.* [10]	Wire meshes with helical springs.	Sensitive to rocking displacements due to low natural frequency.
Sanayei and Zhao [11]	Thickening of the lower floor.	Vibrations were reduced significantly in the predictive model. Experimental investigation validates that vibration to upper levels were reduced. Increment of 1 m further reduced vibration level.
Persson *et al.* [12]	Increase weight of building.	Less ground response is observed with higher weight. Vibration of structure itself was less than ground vibration due to high damping.
Persson *et al.* [13]	Stabilize soil.	Mixing soil with binder minimized vibration but resonant behaviour was detected at certain wavelengths.

1.3 Types of building foundations in Malaysia

Through this study, the building foundations commonly utilized in the construction of multi-level buildings especially in Malaysia were studied to determine the type of foundation to be considered in the design of the base isolator due to the different methodology of modelling for each in the subsequent vibration study.

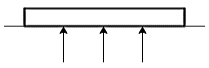
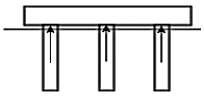
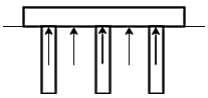
Pail and Chander [14] stated that the selection of the foundation type is influenced by the strength and compressibility of the surface soil and layers beneath. Thornton *et al.* [15] stated that concrete barrettes of pile foundations were used in the construction of KLCC with friction elements to distribute the load gradually in the Kenny Hill residual soil which is the type of

soil most found in Kuala Lumpur. The barrettes were longer where the eroded limestone bedrock beneath was thicker to even out the soil settlements.

Yean-Chin and Chee-Meng [16] stated that in Malaysia high-rise buildings are generally supported by piles. However, due to the growing unavailability of land, there has been construction in areas with very soft soils where the bedrock is usually very deep. Hence, piled-raft are usually preferred due to the upper soil layer's low bearing capacity and large soil settlement. By selecting the suitable locations of the piles, the design can be optimized. For example, the concentration of piles should be higher in the heavily loaded areas. The Burj Dubai utilizes a piled raft foundation which sits on deep deposits of carbonate roils and rocks [17].

The different types of building foundations were analysed in terms of advantages and disadvantages for each and summarized in Table . From the literature review and summary, it was then decided that the piled-raft foundation was to be considered in the design as feasible and economically sustainable designs that can be implemented in Malaysia are to be considered in the present study.

Table 1: Types of building foundations.

	Mat [14]	Piled [18]	Piled-raft [14]
Diagram			
Soil Condition	Surface soils sufficiently strong and stiff to support the imposed loads.	Upper strata too weak or compressible. Bedrock below the upper strata with higher stiffness.	Upper strata too weak or compressible. Consist of stiff clays and dense sands [19].
Materials	Concrete	Steel, concrete and timber.	Concrete raft with steel/concrete pile
Advantages	• Simple procedure for construction • Affordable cost. • Wide availability of material. • Integrate into on-grab slab.	• Resist lateral and overturning forces. • Anchor structures against uplifting forces.	• Reduced settlement compared to just mat foundation. • Less costly than purely piled foundation.
Disadvantages	• May have higher settlement.	• More costly than mat foundations. • Pile driving is noisy and send	• More costly than purely mat foundation.

	• Heavy reinforcement in certain regions.	shockwaves which may cause damage in neighbouring structures.

2 Methodology

2.1 Analytical model of harmonic excitation

2.1.1 Mathematical model of piled-raft foundation

The parameters in the transmission of ground-borne vibrations were first identified to create a mathematical model of the system. Based on the literature review conducted, the parameters expected to affect the transmission of ground vibrations from the building foundation to the multi-level structure are soil-structure interaction where soil stiffness and damping characteristics have to be considered together with the foundation stiffness and damping characteristics. Hence, the suppression of ground-borne vibrations are based on the assumption that these characteristics can be controlled.

The building foundation model to be studied is the piled-raft foundation which is shown in Fig. 20. The multi-level structure is supported by a raft which is directly in contact with the ground, which contain the driven piles and the upper layers of soil. According to the Winkler idealization [20], the soil medium can be considered as a number of linearly elastic springs that are closely spaced in the medium. Hence, the driven piles and upper layer of soil can be modelled as a viscously damped spring-mass system, which both soil and pile having their own stiffness and damping characteristics based on material properties. The soil-pile are assumed as parallel springs which have the same amount of deflection when the load is applied vertically.

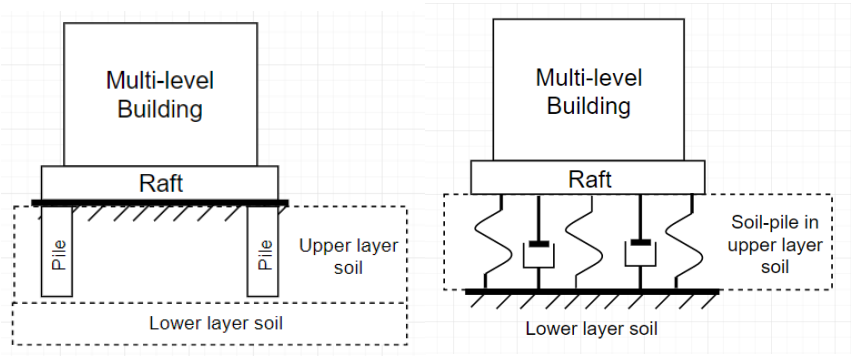


Fig. 20. Modelling of piled-raft system for multi-level building.

The superstructure which is the multi-level building and raft can be simplified as a single large mass with single degree of freedom such as shown in Fig. 21. The soil and piles in parallel springs can be idealized as a single spring and single damper with equivalent stiffness and damping. This method is demonstrated in the study by Wen *et al.* [21] where in the study of a base-isolated four-story structure with pile foundation of a group of multiple piles can be simplified as one equivalent pile to predict dynamic response especially at low frequencies.

This is based on the assumption of soil-structure interaction where the soil is homogenous while the foundation remains in close contact with the soil without slippage.

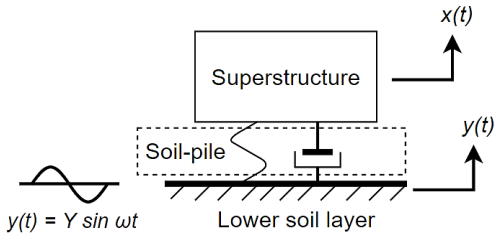


Fig. 21. Damped vibration model under harmonic base excitation.

The rail-induced vibrations from nearby railways will be the source of excitation from the system. Sanayei *et al.* [22] concluded in an experimental study that vertical vibrations is a more vital consideration in the reduction of transmission in multi-level buildings as the maximum vertical velocities were higher at a range of 63 to 70 VdB than the horizontal vibrations which were at 51 to 57 VdB. Therefore, the scope of this study is limited to only vertical vibration levels of harmonic type.

The majority of the vibration that reaches the base of buildings are below 100 Hz due to attenuation during transmission [4]. The amplitude of the ground excitation is assumed to be 0.0127 mm based on experimental investigation on the significant vertical displacement due to rail-induced vibrations in a free field [22]. The base excitation from the ground-borne vibration from railways *y(t)* will be assumed to be harmonic which will have a sinusoidal motion. From Fig. 21, the force transmitted to the base is based on the Newton's Second law which can be described in Eq. (1). The relative displacement of the system is represented as the net elongation of spring and damper *(x-y)* while the relative velocity of the motion between the two ends is (*ẋ-ẏ).*

$$F = k(x - y) + c(\dot{x} - \dot{y}) = -m\ddot{x} \qquad (1)$$

By solving the equation of motion, the relation between input force and output displacement can be related by the displacement transmissibility T_d which is the ratio of the amplitude of the steady-state response to the amplitude of the base motion which is expressed in Eq. (2) [23].

$$T_d = \frac{X}{Y} = \left[\frac{1+(2r\zeta)^2}{(1-r^2)^2+(2r\zeta)^2}\right]^{\frac{1}{2}} \qquad (2)$$

where r is the frequency ratio and ζ is the damping ratio.

2.1.2 Formulation of stiffness and damping constants for soil and pile

For the purpose of the present study, a reference geometry of a square of 10-meter length on each side is taken for the raft foundation in the calculation of soil stiffness. Gazetas [24] stated a formulation for vertical spring stiffness of soil which can be expressed in Eq. (3).

$$k_{soil} = \frac{E_s L_R}{2(1-\nu)(1+\nu)} \qquad (3)$$

where E_s is the elastic modulus of the soil, L_R is the length of the raft foundation and ν is the Poisson's ratio for soil. Hence, the soil stiffness is obtained as the following Table 2 with values from literature and calculation.

The stiffness of the pile k_{pile} is obtained as in the case of rod under an axial load as shown in Eq. (4) [23].

$$k_{pile} = \frac{E_p A_p}{L_p} \quad (4)$$

where E_p is the elastic modulus of the pile, A_p is the cross-sectional area of the pile and L_p is the length of the pile. The reference geometry and material data for a typical concrete pile and soft soil is used to calculate the pile stiffness is as shown in Table .

Table 2: Soil and pile parameters obtained from literature [20].

Material	Concrete	Soil
Elastic modulus, E_s (GPa)	21.78	0.5
Poisson's ratio, v_s	0.17	0.4
Density, ρ (kg/m^3)	2400	1733

Hence, the equivalent stiffness of the system k_{eq} can be found by the summation of the stiffness of soil and pile.

2.2 Numerical analysis with ANSYS Mechanical

2.2.1 Geometry and meshing

A piled-raft foundation is designed according to the analytical model in ANSYS Workbench as shown in Fig. 22. The geometry is based on a residential block that is located in Klang, Selangor, Malaysia that is constructed over soft soil [25]. The model consists of spring-mass system with the material data assigned as from Table . Soil at a depth of 20 m was modelled as a spring for direct input of k_{soil} calculated in analytical model. Based on BS6399: Part 1:1 1996 [26], a residential building with five floors would have a design load of 1.5 kN/m^2 for each floor. The concrete raft is of 0.2 m thickness. The total lumped mass is represented by a superstructure resembling a five-floor building at dimensions of 10 m (L) x 10 m (W) x 16 m (H). The distances between each pile, D_{p1} and D_{p2} are 2 m. The 20 m depth pile is a square with 0.2 m sides.

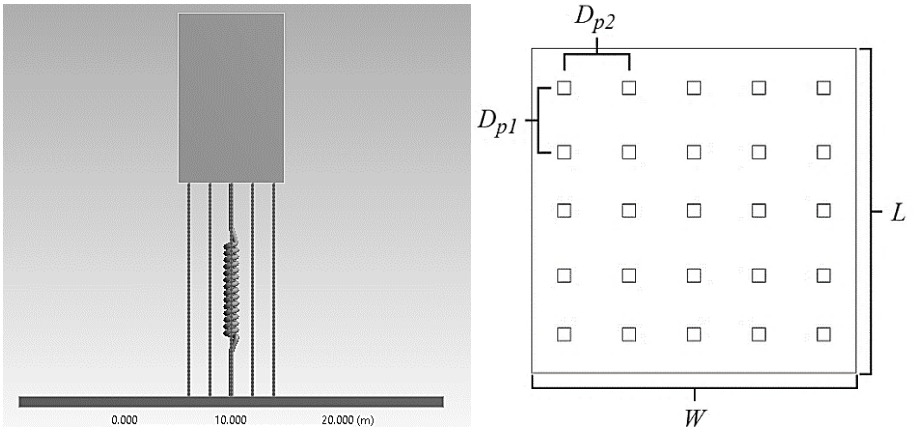


Fig. 22: Piled raft foundation design and layout.

Due to the simple geometry, structured grids are used for the mesh for good accuracy with less mesh elements. Hexahedral mesh was chosen in the Automatic method for soil and superstructure. The piles were meshed in hexahedral using Multizone with 0.2 m sizing. The number of nodes for the mesh nodes and elements were 43574 and 4424 respectively.

2.2.2 Boundary conditions and solution method

The solution method selected for the current analysis is the Full method, which obtains the displacements in the system by solving the simultaneous equations of motion derived from Eq. (1) for each node directly. The range of 0 Hz to 100 Hz was selected with a constant damping ratio of 0.05 entered as a global variable. The top face of the superstructure was selected to obtain the displacement and velocity solutions transmitted from the harmonic base excitation. A displacement of 0.0127 mm is applied on the bottom face of the soil in the upwards *Y* direction. The whole model is constrained in the *X* and *Z* components while leaving *Y* free to allow only vertical displacements.

2.3 Optimization of vibration suppression in structure

By evaluating the design of the piled-raft foundation analytically and through finite element analysis, a reasonable validation can be achieved when both results are in agreement. Suppression of vibration transmission to the superstructure are to be proposed if the vibration response is beyond the vibration limits set by Malaysian standards. Based on the guidelines published by The Department of Environment (DOE) [27], the recommended limits for risk of damage in structures from steady state vibrations is less than 3 mm/s for frequencies of 10 to 100 Hz. Above this value up to 5 mm/s is considered cautionary, while beyond that would be minor damage up to 30 mm/s.

3 Results and Discussion

3.1 Numerical analysis results and comparison to analytical method

The comparison of the analytical results to the results obtained from ANSYS is shown in Fig. 23 for the displacement amplitudes obtained. Both results from analytical and ANSYS follow the same trend of a peak displacement at the resonant frequency of the system. However, as the frequency approaches the resonant frequency, the difference of displacement amplitudes in both graphs increased. The resonant frequency for analytical calculation was 28.6 Hz while the numerical solution was 28.2 Hz which a percentage error of 1.4 %, and hence show that both methods are in good agreement for predicting the resonant frequency.

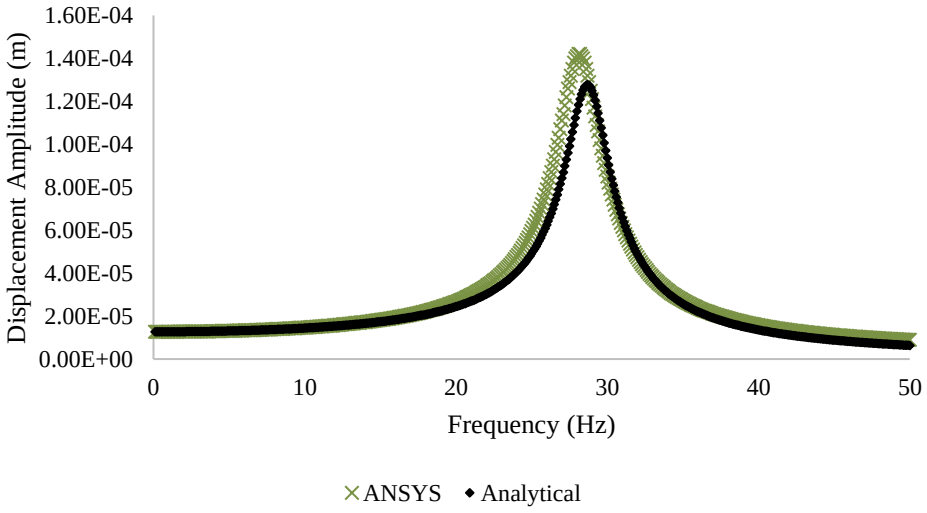


Fig. 23. Amplitude of displacements from numerical analysis and analytical calculations.

Fig. 24 shows the velocity of the vibration levels transmitted to the superstructure. Based on Fig. 24, the velocity amplitudes are beyond the recommended limits from 19.3 Hz to 46.8 Hz and 64.9 Hz to 91.7 Hz based on the Malaysian standards of vibration limits. The velocities are below the major damage limit but are above the minor damage limits. Hence, two methods can be suggested to reduce a risk of minor damage to the building structure over an extended period of time.

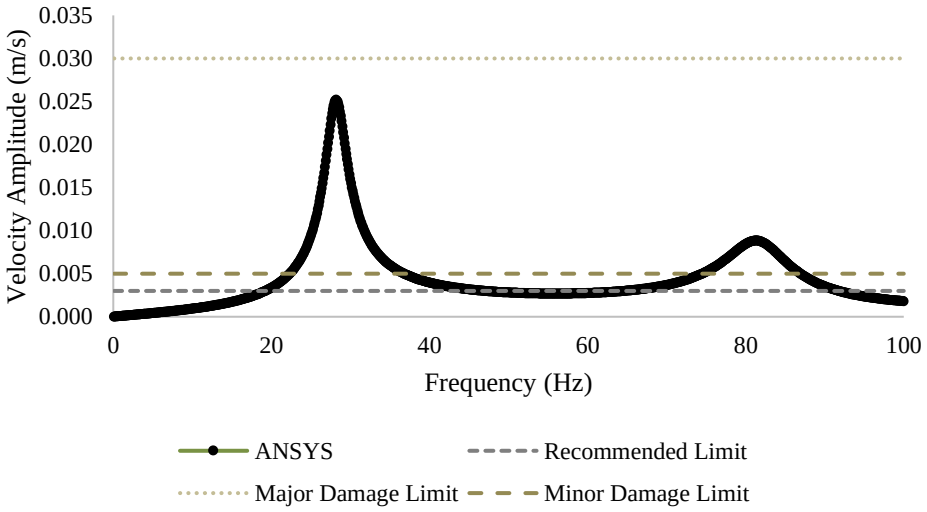


Fig. 24: Frequency response graph for velocity from numerical analysis.

3.2 Response of superstructure to increment of damping ratio or raft thickness

When the damping ratio is increased in the soil-pile system, the response of the superstructure decreases. The vibration limits can only be reduced to below the minor damage limit if the damping ratio is increased to 0.25 due to the diminishing returns of continuous increment. Hence, the installation of materials such as elastomers with a high damping factor is required if the method of increasing of damping ratio is considered alone. This is similar in the case of the increment of raft thickness alone in reducing the response of superstructure as the total

mass of the system is increased. Thickness of the concrete raft has to be increased to a large thickness of 6 m to be able to approach threshold of minor damage limit. This increases the volume of concrete required by 30 times which directly affects the cost of construction.

Therefore, it is more feasible to optimize on both methods together. By using a higher damping ratio, the required thickness of the raft would be lower as shown in Fig. 25. At ζ = 0.1, the raft thickness required is 2.5 m which is less than half of the thickness at ζ = 0.05. At ζ = 0.15, the raft thickness required is further reduced to 1 m.

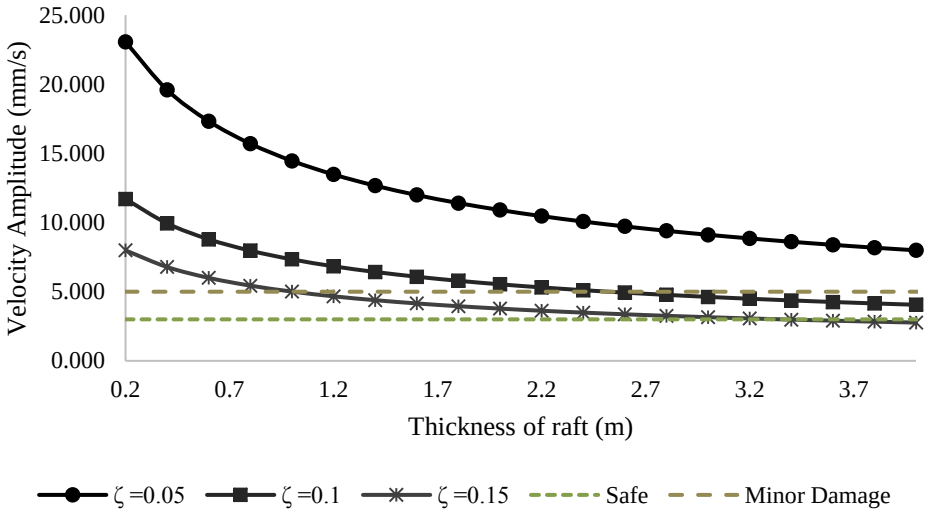


Fig. 25: Velocity amplitudes of transmission against thickness of rafts at increasing damping ratios.

3.3 Selection of material for increased damping in structure

One of the common structural damping materials are elastomeric bearings which are placed under each load-bearing column between the soil and the raft foundation. Such structural rubber bearings typically are made of specialised rubber compound and reinforced steel plates. Yong Yuan *et al.* [28] stated that commonly used materials for base isolation in structures especially for seismic response applications are high damping natural rubber bearings (HDRB) and super high damping rubber bearings (SHDRB). Among the two, HDRB has been applied in the usage of base isolation on a 3-story concrete frame building in East Malaysia and had been found to be the simplest and most cost effective method of isolation [29]. Due to the damping requirement in the present study, HDRB would be suitable to be implemented in the structure to increase the damping ratio to 10 %. As HDRB are made from natural rubber which is one of the main export products in Malaysia, it also benefits the local industry of rubber plantations and processing.

The implementation of the HDRB in parallel with raft foundation would cause the damping ratio to be increased to 10% with 2.5 m raft thickness. The results from the analytical calculations and ANSYS results for the building velocity amplitude is as shown in Fig. 26 and are found to be below the minor damage limit from DOE guidelines [27]. Both results differed by 1.19 % for velocity amplitude and 6 % for resonant frequency and hence both results are in good agreement and the analytical calculation is validated.

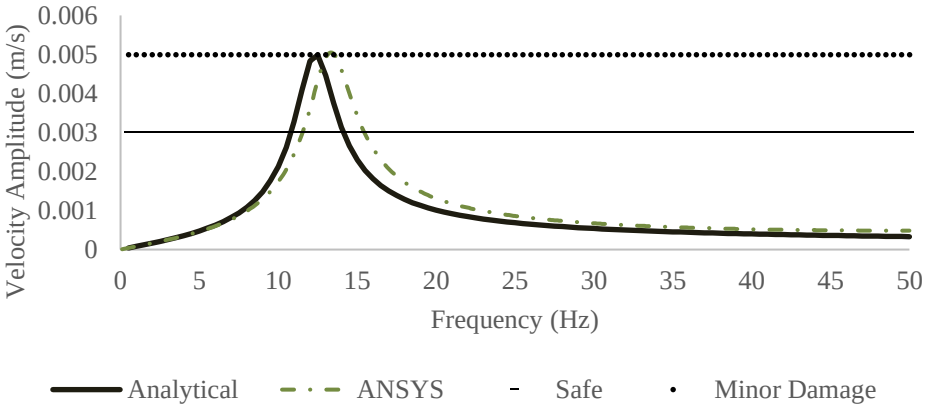


Fig. 26: Velocity amplitudes of piled-raft foundation with HDRB from numerical analysis and analytical calculations.

4 Conclusion

The parameters relating to the transmissibility of the base were identified and developed into an analytical model to find the displacement amplitude of the superstructure due to harmonic base excitation. The significance of rail-induced vibrations was identified to be detrimental to nearby structures as they contribute to the deterioration of buildings over a long time, even more so in dense urban areas where other methods of isolation are not possible. There vibrations also cause psychological health issues in people and may interfere with the function of vibration-sensitive equipment.

Hence, an analytical model of base excitation was developed to find the displacement amplitude of the superstructure due to harmonic base excitation from railways. The analytical model was validated with a numerical model developed in ANSYS Workbench based on geometry of a residential building in Selangor, Malaysia with piled-raft foundation. FEA yielded a vibration response of 25.2 mm/s at 28.2 Hz which is above the minor damage limits of Malaysian vibration standards for structural steady-state response which is 5 mm/s. The velocity amplitudes were minimized to below 5 mm/s criteria line via the increment of mass by thickening the raft to 2.5 m and increasing the damping ratio to 0.107 via installation of damping system in parallel with raft foundation. In the modified case with HDRB, the numerical and analytical results were compared for error analysis and found to be 1.19 % for velocity amplitude and 6% for the resonant frequency which are acceptable percentage differences.

References

[1] Y. B. Yang, P. Ge, Q. Li, X. Liang, and Y. Wu, "2.5D vibration of railway-side buildings mitigated by open or infilled trenches considering rail irregularity," *Soil Dyn. Earthq. Eng.*, vol. 106, pp. 204–214 (2018).
[2] American Society of Civil Engineers, *American Infrastructure | 2013 Report Card for America's Infrastructure*, no. (2013).
[3] K. Vogiatzis and G. Kouroussis, "Airborne and Ground-Borne Noise and Vibration from Urban Rail Transit Systems," in *Urban Transport Systems*, InTech, pp. 63-87 (2017).
[4] D. P. Connolly, G. Kouroussis, O. Laghrouche, C. L. Ho, and M. C. Forde, "Benchmarking railway vibrations - Track, vehicle, ground and building effects," *Constr. Build. Mater.*, vol. 92, pp. 64–81 (2015).
[5] E. P. Dudkin, L. A. Andreeva, and N. N. Sultanov, "Methods of Noise and Vibration Protection on Urban Rail Transport," in *Procedia Engineering*, vol. 189, pp. 829–835 (2017).
[6] P. Cacciola, N. Banjanac, and A. Tombari, "Vibration Control of an existing building through the Vibrating Barrier," in *Procedia Engineering*, vol. 199, pp. 1598–1603, (2017).
[7] J. LoVerde and D. W. Dong, "Isolation of residential buildings from ground vibration from railroad," *J. Acoust. Soc. Am.*, vol. 140, no. 4, pp. 3281–3281, (2016).
[8] J. Sadeghi and M. H. Esmaeili, "Safe distance of cultural and historical buildings from subway lines," *Soil Dyn. Earthq. Eng.*, vol. 96, no. January, pp. 89–103 (2017).
[9] A. Eitzenberger, "Train-induced Vibrations in Tunnels – A Review" (2008).
[10] D. Ulgen, O. L. Ertugrul, and M. Y. Ozkan, "Measurement of ground borne vibrations for foundation design and vibration isolation of a high-precision instrument," *Meas. J. Int. Meas. Confed.*, vol. 93, pp. 385–396 (2016).
[11] M. Sanayei, N. Zhao, P. Maurya, J. A. Moore, J. A. Zapfe, and E. M. Hines, "Prediction and Mitigation of Building Floor Vibrations Using a Blocking Floor," *J. Struct. Eng.*, vol. 138, no. 10, pp. 1181–1192 (2012).
[12] P. Persson, L. V. Andersen, K. Persson, and P. Bucinskas, "Effect of structural design on traffic-induced building vibrations," *Procedia Eng.*, vol. 199, pp. 2711–2716 (2017).
[13] P. Persson, K. Persson, and G. Sandberg, "Numerical study on reducing building vibrations by foundation improvement," *Eng. Struct.*, vol. 124, pp. 361–375 (2016).
[14] D. S. Patil and A. S. Chander, "Cost Effectiveness of Several Types of Foundation," vol. 2, no. 1, pp. 1–8 (2016).
[15] C. H. Thornton, U. Hungspruke, and L. M. Joseph, "Design of the World's Tallest Buildings-Petronas Twin Towers at Kuala Lumpus City Centre," *Struct. Des. Tall Build.*, vol. 6, no. 4, pp. 245–262 (1997).
[16] T. Yean-Chin and C. Chee-Meng, "Current and future trends of geotechnical engineering in Malaysia – a consultant's perspective (2009)," *Semin. Stateof-the-art Technol. Exp. Geotech. Eng.* Malaysia Hong Kong, p. 14 (2009).
[17] H. G. Poulos, "Foundation Design for the Burj Dubai – the World ' S Tallest Building," *Proc. 6th Int. Conf. Case Hist. Geotech. Eng.*, vol. 1, no. 1, pp. 1–16 (2008).
[18] J. H. Leow, "A Study of Building Foundations in Malaysia," (2005).
[19] Poulos, "The Design of High-Rise Building Foundations," *Geotech Hanoi, Oct. 2011-ISBN 978-604-82-000-8*, no. 1994 (2011).
[20] B. Das, R. Saha, and S. Haldar, "Effect of in-situ variability of soil on seismic design of piled raft supported structure incorporating dynamic soil-structure-interaction," Soil Dyn. Earthq. Eng., vol. 84, pp. 251–268 (2016).

[21] X. Wen, F. Zhou, N. Fukuwa, and H. Zhu, "Computers and Geotechnics A simplified method for impedance and foundation input motion of a foundation supported by pile groups and its application," *Comput. Geotech.*, vol. 69, pp. 301–319 (2015).
[22] M. Sanayei, P. Maurya, and J. A. Moore, "Measurement of building foundation and ground-borne vibrations due to surface trains and subways," *Eng. Struct.*, vol. 53, pp. 102–111 (2013).
[23] S. S. Rao, *Mechanical Vibrations*, vol. 6 (2010).
[24] G. Gazetas, "Formulas and charts for impedances of surface and embedded foundations," *J. Geotech. Eng.*, vol. 117, no. 9, pp. 1363–1381 (1991).
[25] Y. C. Tan, S. W. Cheah, and M. R. Taha, "Methodology for Design of Piled Raft for 5-Story Buildings on Very Soft Clay," in *Foundation Analysis and Design*, pp. 226–233, (2006)
[26] BS6399-1, "Loading for Buildings" (1996).
[27] Jabatan Alam Sekitar Malaysia, "The Planning Guideline for Vibration Limit and Control in the Environment," (2007).
[28] Y. Yuan, W. Wei, A. Igarashi, P. Tan, H. Iemura, and H. Zhu, "Experimental and analytical studies of seismic response of highway bridges isolated by rate-dependent rubber bearings," *Eng. Struct.*, vol. 150, pp. 288–299 (2017).
[29] K. A. Malek and K. B. Basir, "Design and characteristics of high damping natural rubber bearings for base isolation," vol. **57** (2001).

EURECA 2018 – Conference Paper
Paper number 2ME16

Autonomous Lake Monitoring System (ALMS)

Mohamed Nazer[1], Mohammad Taghi Hajibeigy[2], Se Yong Eh Noum[1], Azadeh Ghadimi[1]*

[1]Mechanical Engineering, School of Engineering
[2]Electrical and Electronic Engineering, School of Engineering
Taylor's University, 47500 Subang Jaya, Selangor, Malaysia

Abstract

Water pollution is rapidly increasing throughout the world due to a sky-rocketing demand for the consumption of water due the rapid urbanization and growing population. To withstand the demand of safe drinking water, the quality of the water has to be monitored day in day out. This paper is based on a research to develop a sustainable real-time water quality monitoring system using IOT (internet of the thing). The system will be utilizing different kind of sensors to measure both physical and chemical parameters of the water. There are five main parameters that has to be monitored, temperature, pH, dissolved oxygen, salinity content and lastly turbidity. All he sensors will be controlled using a microprocessor, the data collected by the sensors will be transferred to the internet using a Wi-Fi module to have a real-time monitoring. Other than sending data to the internet the whole system will be move from one point to another using GPS guidance by connecting a GPS sensor to the Arduino, other than that the whole system will be avoiding any incoming obstacles by using several ultrasonic sensors which also be controlled using an Arduino. In order to make the system self-sustainable the system will be attached to solar panels so that it would not ran out of power quickly.

Keywords: Lake monitoring, Arduino, Lake pollution

1 Introduction

It is very essential to maintain the quality of the water in rivers and streams, this will help to maintain a good ecosystem for both humans and aquatic life. Water is one of the important element to sustain life. Causing any imbalance to the water quality will backfire on the health of both humans and the ecological balance among the species [1]. Therefore, it is very important to balance the quality of the water.

Water pollution is a major factor in contribution of declining ecological and ecosystem around the world. Australia is facing a huge challenge in maintain the water quality of their fresh water system in the state of Victoria. It has been estimated that 80% of the Victoria's waterways are in the poor to moderate range and the improvement from the previous years is very little [2]. One of the main reason for a slow improvement is difficulty in diagnosing the cause of environment degradation. As for now only a low-resolution water quality monitoring has been conducted, this is done by collecting water samples from a certain area and send it for lab testing. There are many disadvantages by doing this type water quality monitoring:

- The collected data is not continuous process therefore the pollution pattern on the waterways will not be cleared.
- To increase the clarity of the data more water samples has to be collected and send in for laboratory testing, this will be more time-consuming and at the same more man power is needed which will increase the cost of the process.
- To improve the quality of the data some of the reading has to take onsite. Transporting the water samples will reduce the accuracy of the data.

There are different type of water quality monitoring system. JC Stevens is the first person to invent the first ever real-time water level monitoring system which is shown in figure 1, this lets the user to continuously monitor the water level continuously [3], in the past few years few other companies catch up catch up the real-time monitoring system. The two major companies are well known for this autonomous system is Libelium [4] and YSI [5] which are shown in figure 2 and figure 3. All three people Stevens , Libelium and YSI is capable of real time water quality monitoring system. But the drawback with this type of monitoring system is that the water quality values will be different at different position of the lake since the value of the parameters at a static water will be different [6].



Fig 1. Stevens water quality sensor [3].



Fig 2. YSI water quality sensor [4].



Fig 3. Libelium Water quality sensor [5].

Comparing all the companies above the one disadvantage of the system is all of the system only measure the water quality in static water on the lake, this type of system only give the data on the specific region of the lake, to get the data throughout the whole lake will consume a lot of time and also money, the sensors from the three major company mentioned earlier will cost around Rm 2,000 all the way up to Rm 25,000 [3] [4] [5].

Figure 4 show the other most common solution for lake monitoring is by collecting water samples from different region of the lake and do a lab test to determine the quality of the water [7]. Same as the previous solution this type of monitoring will consume a lot of time and also requires a lot of manpower, which increase the cost of the water quality monitoring.



Fig 4. Collecting water sample through a pump [7]

Simultaneous water quality surveillance across multiple tributaries allows catchment managers to detect spatial trends in water conditions in real-time. Higher resolution data would allow instant diagnosis of pollution sources and greatly assist catchment managers in assessing the impact of remediation efforts, but the expense of deploying current monitoring technology at multiple sites is prohibitive. Therefore, there is a need for real-time, on-site, water quality monitoring systems which can deliver continuous data of high quality at an acceptable cost

In summary, the project is based on building a low-cost autonomous lake monitoring system that helps to measure real-time data of the quality of the lake which will be send to the internet to manually monitor each parameters of the water to suit the marine life. The project will be divided into 3 parts, collecting data and transferring to the cloud, building an autonomous system to choose the location of the data collection together with obstacle avoidance system and lastly to build a self-sustainable system using solar panels.

2 Materials and equipment

2.1 Data collection

There are various type of data that has to be collected to monitor the water quality table 2 shows the type of sensors needed to collect each type of data, all the sensors will be connected to the Arduino to send the data to the internet. The Arduino has to be coded in a way to automatically transfer the data to internet, the Arduino will be sending the data to a website called Thingspeak, this website will provide a personal IP address to store the data and monitor the water quality 24/7.

From the research it has been found out that there are five sensors that will be used to monitor the parameters of water quality starting from temperature (LM35) to record to the of water temperature, the pH sensor is used to record the Ph value of the lake, DO sensor is used to record the dissolve oxygen concentration this will show the oxygen concentration of the lake, and lastly conductivity sensor will be used to record the salinity value of the water.

Table 1. Parameters needed for data collection

	Parameters	What does it indicate?	Range
1	pH	How acidic is the lake	0 – 14
2	Dissolved Oxygen (DO)	Amount of oxygen in the water	0 -20 mg/L
3	Conductivity	Amount of organic pollutant in the water	-20000 - +130000 uS/cm
4	Temperature	Temperature of the water	-55 to 150 ℃
5	Turbidity	Small solid particle which remain in the water	0 – 5000 NTU

2.1.1 Overall design for data transmission

Figure 5 shows the overall design of the data collection it consists of 5 different sensors and one microcontroller (Arduino) to obtain data. The gateway system for transmitting data to the cloud will be further discussed below.

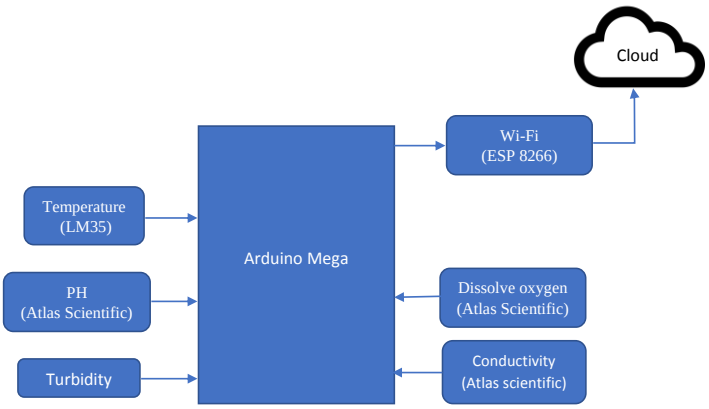


Fig 5. Overview design of data collection

2.1.2 Arduino

Arduino Mega 2560 [8] has been chosen to be used as a microcontroller in this paper. For the data transfer it acts as a sensor node to extract the data from the sensors to it. The main reason for choosing Arduino is due to its cost, it is an inexpensive open source product. The main processor is Atmel's ATmega 2560 micro controller with a clock speed of 16MHz and also a 256kB of storage, the chip has enough clock speed and memory to process the data to the cloud.

2.1.3 pH

To record the pH of the water I pH sensor from phidgets is used. It can read the pH value from 0 to 14 and can be operated from a temperature range of 0 to 80 ℃. The sensor use a BNC connection to transmit data. The signal from the sensor has to be converted to an analog voltage signal in order for the Arduino to store the data

2.1.4 Temperature

The temperature sensor used to detect the temperature of the water is a standard LM35 [9]. This sensor can read a temperature range from -55 ℃ to 150 ℃, the main reason for choosing the temperature is due to its accuracy at a normal condition and the temperature in the lake would rarely go to an extreme range. The accuracy of the sensor at a normal condition is at 0.5 ℃. Since the sensor is directly calibrated in Celsius, the Arduino can easily collect the data from the sensor using a pulse-width modulation (PWM).

2.1.5 Electrical Conductivity

To measure the conductivity of the lake a conductivity sensor is used. The sensor has a range of conductance of 5 µS/cm to 200,000 µS/cm. The sensor uses the same BNC connector as the pH sensor that were previously discussed, therefore the signal from the sensor has to be converted to an analog voltage signal in order for the Arduino to store the data. The sensor can go as deep as 343 meters before it malfunctions.

2.1.6 Dissolved Oxygen

To measure the oxygen content of the water a dissolve oxygen is used. The sensor has range of 0 – 20 mg/l. The maximum operating temperature of the sensor is 50 ℃ and also the maximum operating depth of 343 meters.

2.1.7 Decision matrix to choose the best option for data transfer

The decision matrix table (Table 1) to choose the most suitable option for data transfer. The criteria rating is given based of the priorities for the system, since it has to cover the whole surface area of the lake the coverage area is the most important criteria for the system followed by the data transfer speed of the data since it has to send signals from six sensors continuously to the internet, the faster the data is transferred the more accurate the quality analysis will be, this will give an accurate value of the index at the precise place. Other than coverage area and transfer speed the third most important criteria is the amount of power consumption, since the whole system will be autonomous the total power consumption of the whole system has to be very minimal as possible to last longer on a single charge. To increase the time taken for it to last on a single charge self-sustainable energy such as solar panels will be used.

From the decision matrix table 2 it can be seen that data transfer through Wi-Fi is more suitable, this is due to Wi-Fi having a promising coverage area and high data transfer rate, higher speed and longer direct transmission range correlate with higher power usage and thus shorter battery life this is where it contributes less points. To overcome this issue the system will be equipped with solar panels so that it won't run out of power.

Table 2**.** Decision matrix for choosing the best option for data transfer

	Criteria rating	Bluetooth	Zigbee	Wi-Fi	LoRaWan
Coverage area	4	2	1	3	4
Transfer rate	3	3	1	4	2
Power consumption	2	3	4	2	1
Cost	1	4	2	3	1
Total		27	17	31	25

As mentioned earlier the all the collected data will be transfer to internet via Wi-Fi, the most reliable Wi-Fi module for this project is ESP8266 Wi-Fi serial module, this is due to its cost effectiveness, reliabilities and lastly its low power consumptions.

Figure 6 shows the electrical schematic of the overall data collection, the Arduino will be powered using a Li-Po battery

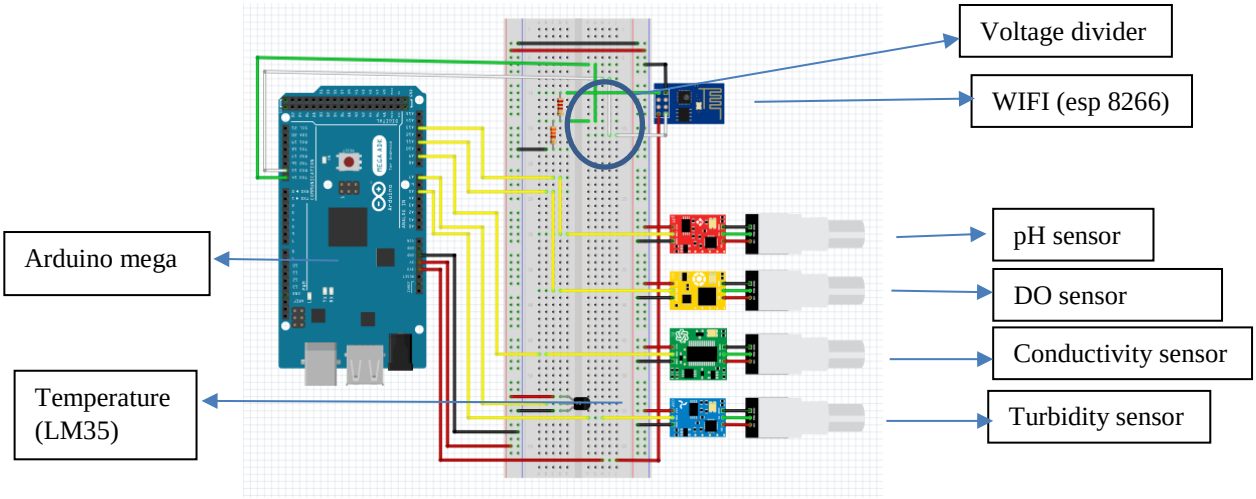


Fig 6**.** Electrical schematic for data collection

2.2 Autonomous

Figure 7 show the overall design for the autonomous system. The system consist of four main components an Arduino mega, a GPS sensor for navigation, motor controller to control the DC motor and lastly an ultrasonic sensor to detect obstacles.

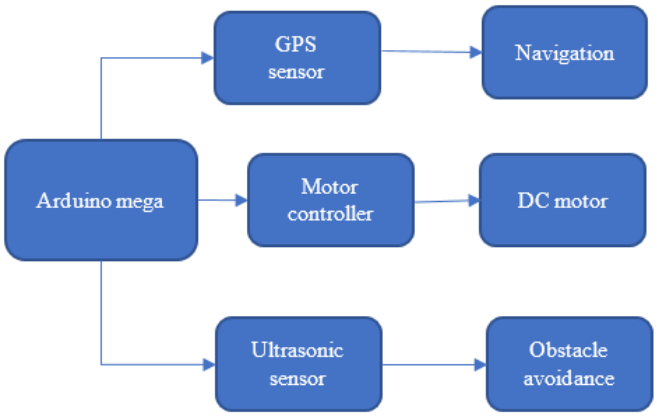


Fig 7**. Overall design of autonomous system**

2.2.1 GPS

This Grove - GPS module is a cost-efficient and field-programmable gadget armed with a SIM28 and serial communication configuration. It features 22 tracking / 66 acquisition channel GPS receiver. The sensitivity of tracking and acquisition both reach up to -160dBm, making it a great choice for personal navigation projects and location services, as well as an outstanding one among products of the same price class. Apart from that the GPS sensor only requires a

voltage between 3.3 to 5 V, this will reduce the overall power consumption of the system. Lastly the GPS has a baud rate range from 9600 to 115200 this will let the GPS and the WiFi module to communicate if it is needed.

2.2.2 Motor controller

To control the DC motor using the Arduino a L298N motor controller was used. L298N is equipped with a dual H bridge motor driver and can drive up to 2 bidirectional DC motor, this will help to control the 2 DC motor attached to the boat to be controlled individually. It requires minimum voltage of 5 V to be operated, therefore it can be directly connected to the Arduino since Arduino only transmit signals in 5 V

2.2.3 Obstacle detection

To detect an obstacle continuedly the distance between the boat and the obstacle will be measured. To measure the distance of the obstacle an HC-SR04 ultrasonic sensor was used, the main reason this sensor has been chosen due to its accuracy and low power consumption, the sensor can be measured up to 1 meter with an accuracy of 0.3 cm, it can detect obstacle in a range of 45° angle and has a higher accuracy at 15° angle.

Figure 8 show a complete electrical schematic diagram for the autonomous sensor. From the figure it can be seen that there are 3 ultrasonic sensors, this the sensors will detect the obstacle from the front, left and right. The LiPo battery will be connected to the motor controller and the Arduino will be connected to the motor controller through a PWM pin.

2.2.4 DC Motors

Figure 8 illustrated the electrical schematic diagram for the autonomous system two DC motor will be used to power the propellers in order to manure the system in the water, before determining the specification of the motor the total weight of the system has to be determined. A high torque and low speed motor will be used propel the system in the water, once the weight is determined the torque of the motor will be determined using the calculation from Martenhoff's powerboat handbook [12]. The motor will be controlled using a motor controller, LN298 that will be controlled using an Arduino. The propellers will be 3d printed and it will connect to the shaft of the motor

The boat will be equipped with two 12V DC motor with 111 rpm and 92 mA to propel, the motor will be attached to the rear end of the boat as illustrated in the design in figure8. It is estimated that the whole system will weigh around 5 Kg. The motor will provide a high torque of 3 Kg-cm and low speed, the specification of the motor is chosen based on from Martenhoff's powerboat handbook as mentioned earlier a power to weight ratio for an average $13 ms^{-1}$ is calculated below.

$$Power\ to\ weight\ ratio = \ Power/Kg$$

$$13\ ms^{-1} = \frac{54.82}{Kg} = 1300\ cms^{-1}$$

The maximum desired speed is $15\ cms^{-1}$. Therefore, the power to weight ratio of a motor to drive $15\ cms^{-1}$ is:

$$\frac{54.82\ W}{Kg}\ X\ \frac{15}{1300} = \frac{0.633\ W}{Kg}$$

The estimated weight of the boat is around 5 Kg, the power of a motor to drive 15 cms^{-1} including a factor of safety of 20% is;

$$0.633\ W\ /\ Kg\ X\ 5\ Kg\ X\ 120\% = 3.8\ W$$

From the technical specification of motor provided, the maximum power of the motor provided is [11],

12V x 1.2 A X 80% = 11.5 W

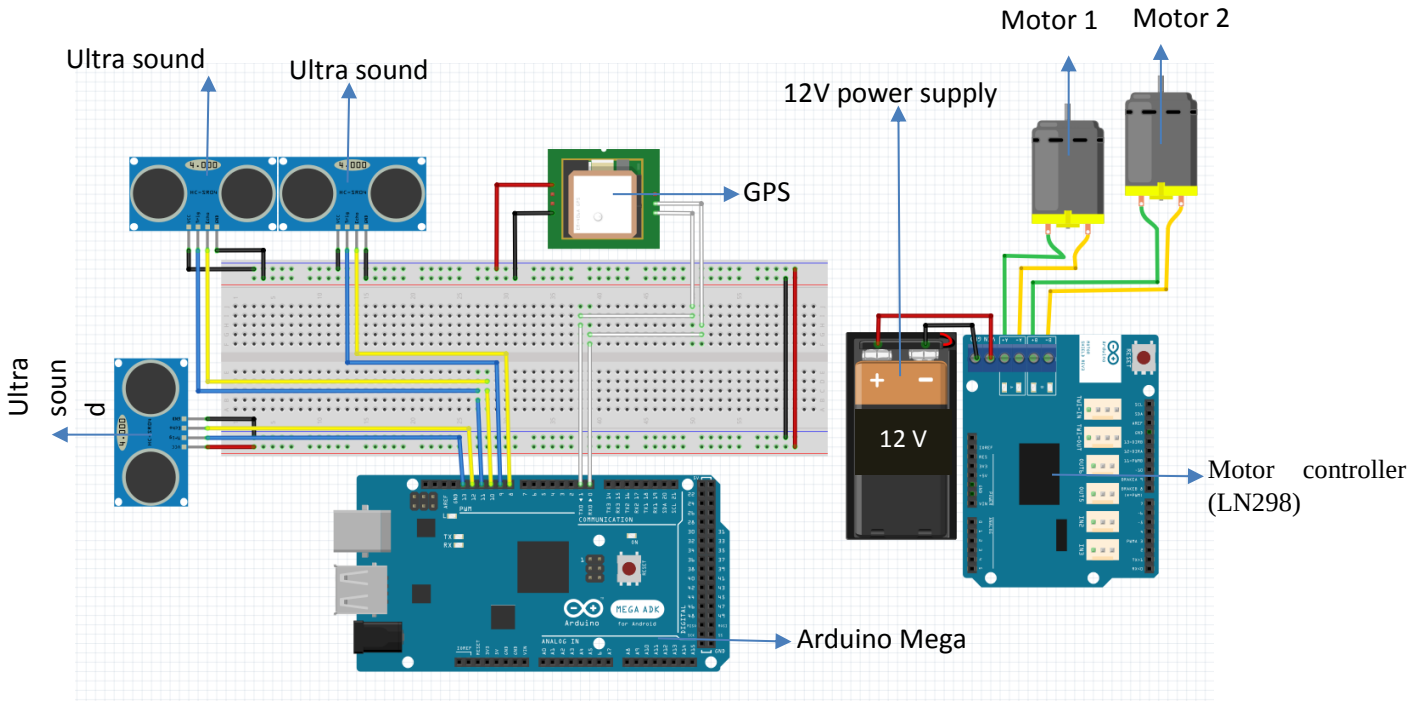


Fig 8. Electrical schematic of autonomous system

2.3 Design

Figure 9 represent the overall design of the boat all the sensors for the data collection will be fitted through the hole which are placed at the bottom of the boat and the electronics of the data collection will be placed in the right compartment of the boat. Where else in the right compartment of the boat the solar charger converter and the LiPo battery will be placed, this is to increase the ease of the maintenance. 3 ultrasonic sensors will be place on the boat front, left and right, the reason behind the placement of the ultrasonic sensor is further explained in the

flowchart (3.2). 6 solar panels 3 each side will be connected in parallel and will be placed on top of the compartment to cover the compartment.

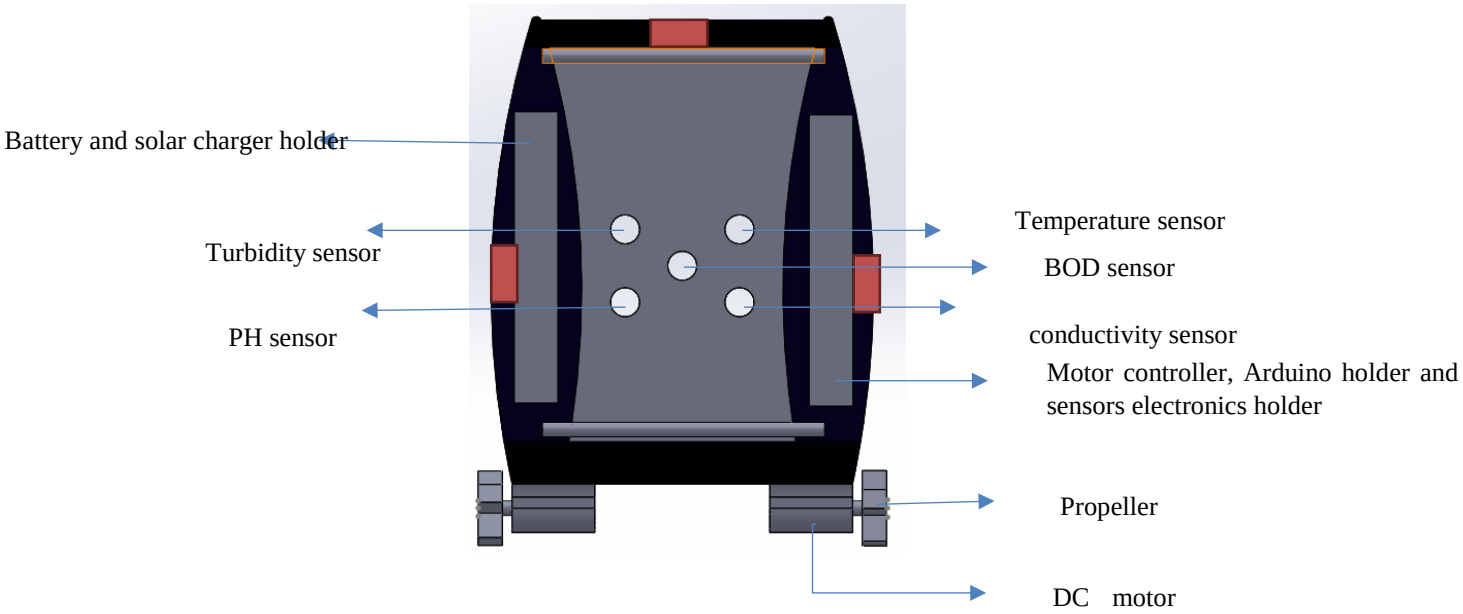


Fig 9**.** Overall Design of the boat

3. Experiment

3.1 Flow chart for data transfer

There are three stages to transmit the data from the Arduino to the cloud (Thingspeak), figure 10 shows the flowchart for the data transmission. From the flow chart it can be seen that the first stage is to collect the data from the sensors to the Arduino, once all the data has been collected the second stage will be started which is to connect the Arduino to the internet, at the beginning the user has to manually key in the SSID name and the password of a WIFI, this will let the Arduino to connect to the internet, once the Arduino is connected to the internet the last stage will be started which is to transmit the data from the Arduino to the internet. Thingspeak was chosen due to its versatility of choosing different number channels and each channel will be given an IP address to send the data individually or in group.

3.2 Flowchart for autonomous system

The autonomous part can be divided into to two parts, maneuvering using GPS sensor so set a path and obstacle avoidance using ultrasonic sensors. The ultrasonic sensors and the GPS sensors will be working simultaneously to make the boat fully autonomous. Figure 11 illustrated the flowchart of the whole system. From the figure it can be seen that the system starts with initialising the GPS sensor. Once the GPS has been initialised a connection between the sensors and the satellite has to be establishes. The user can key in multiple coordinate (longitude and latitude) to create a path for the boat, from the flow chart it can be seen that the

boat will autocorrect its direction to follow the new coordinates. As the boat identify its new path the ultrasonic sensors will be initialised for obstacle avoidance. The obstacle avoidance is based on a three-ultrasonic setup, front, left and right. The primary sensor is the front ultrasonic sensor since most of the movement is in the forward direction. A safe distance of one meter has been fixed for the boat to avoid obstacle.

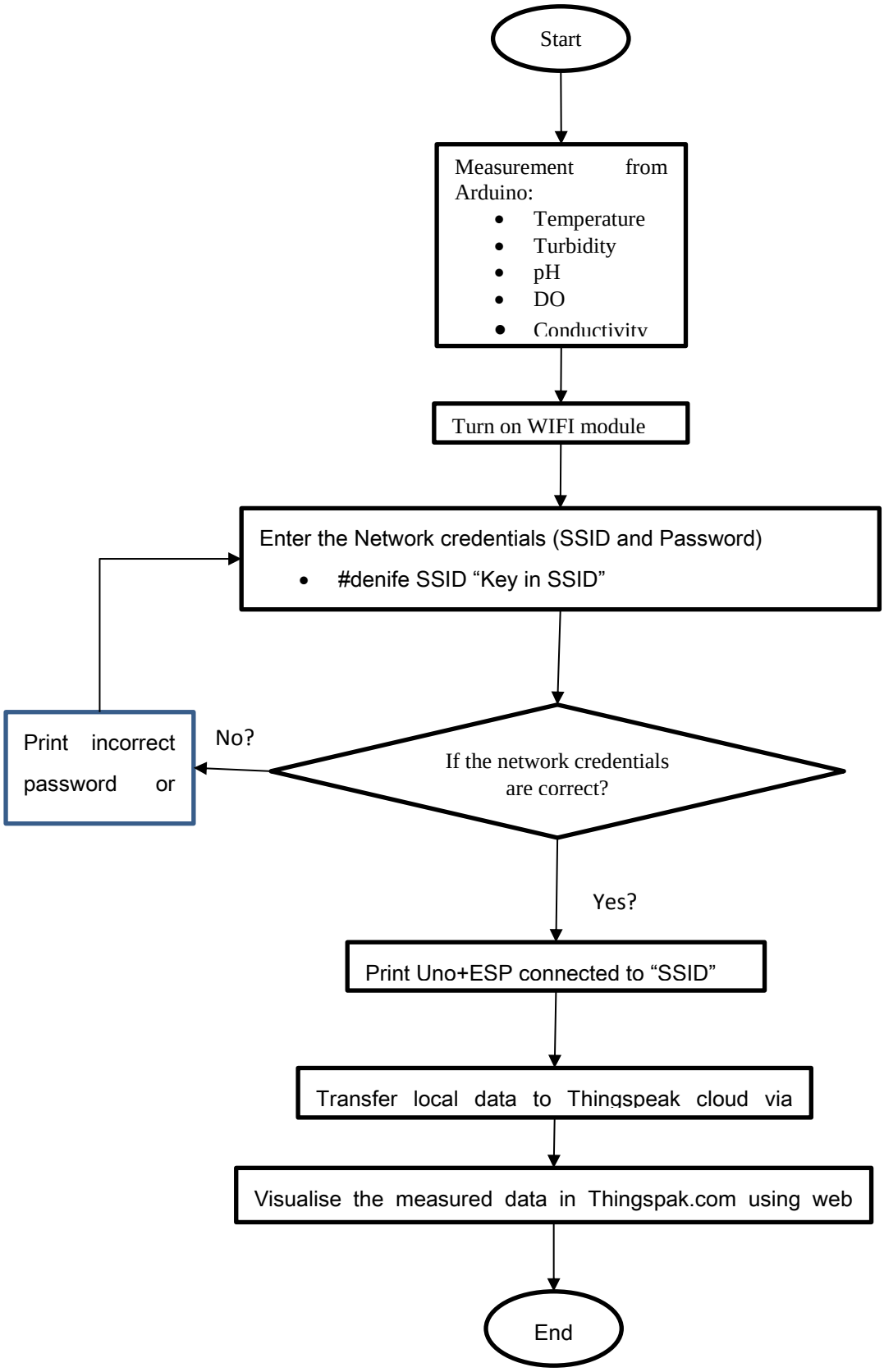


Fig 10. Flow chart for data collection

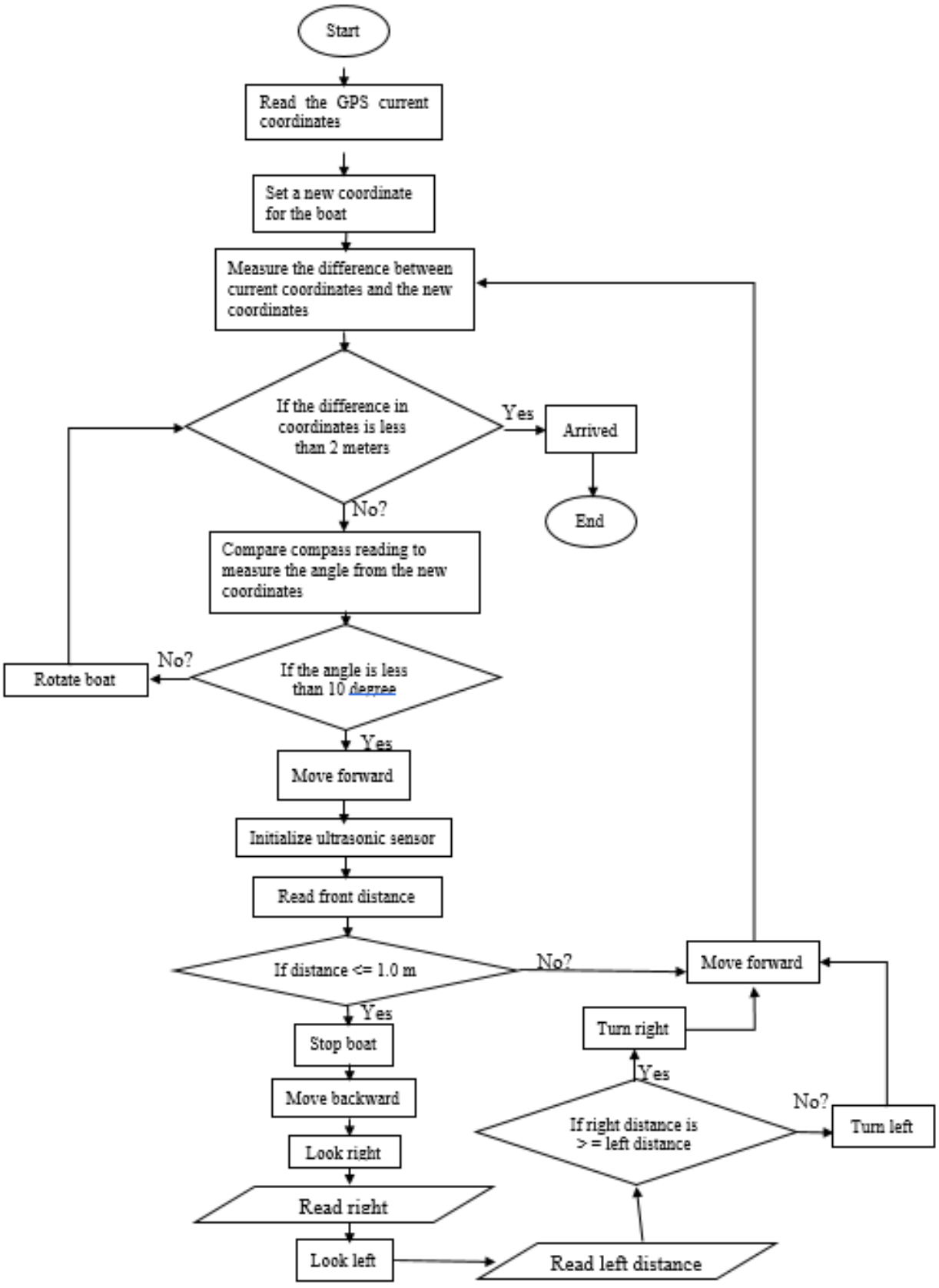


Fig 11. Flow chart for Autonomous systems.

3 Experiment

3.1 Data collection from Taylor's lake

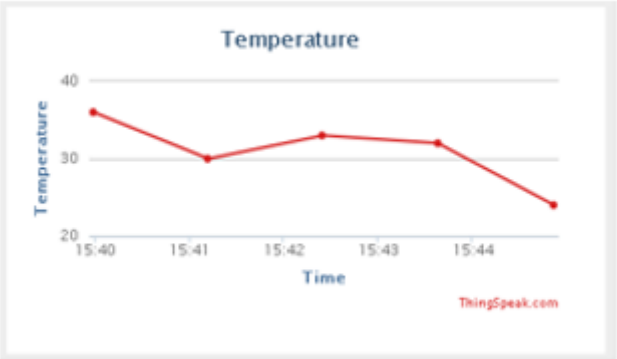


Fig 12: Temperature obtained from Taylor's lake

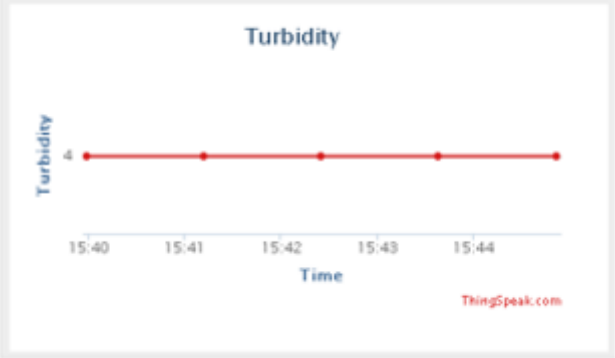


Fig 13. Turbidity obtained from Taylor's lake

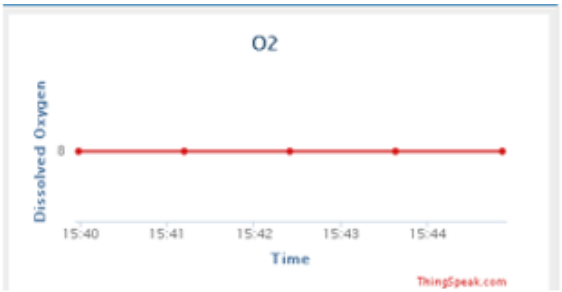


Fig 14. Dissolve oxygen obtained from Taylor's lake

Table 4. Experimental data for charging rate using solar panels

Time / hr	0	35	48	60	85	100	120	150
Voltage / V	9.45	10.72	11.06	11.13	11.24	11.25	11.23	11.25

Table 5. Experimental data od discharging rate

Time / hr	0	1	2	3	4	5	6	7	8	9	10	11	12	12.4
Voltage / V	12.5	12.35	12.1	11.9	11.8	11.55	11.43	11.36	11.2	11.22	11.15	11.04	10.94	10.79

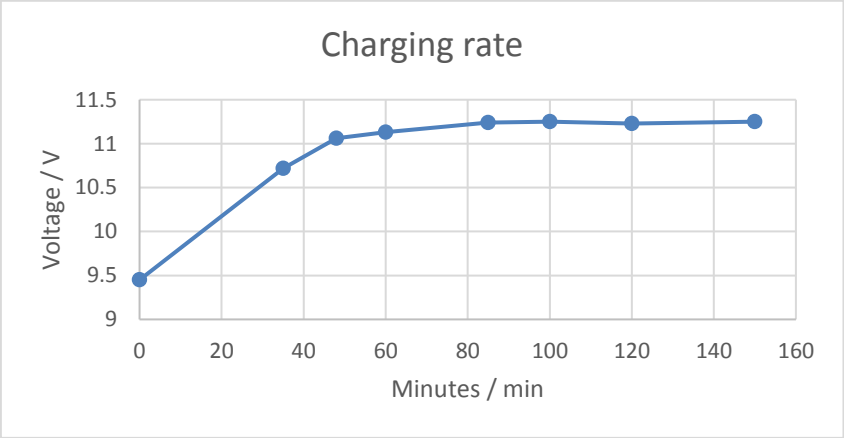


Fig 15. Battery voltage against time (Charging)

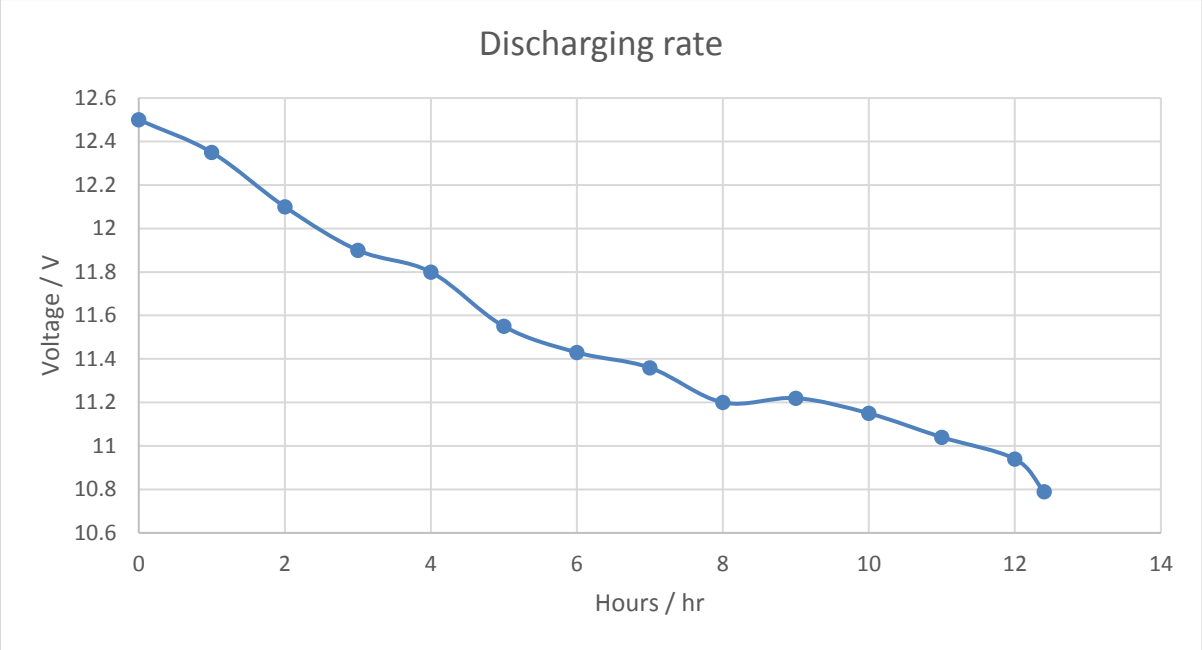


Fig 16. Battery voltage against time (Discharging)

4 Discussion

4.1 Data collection

To justify the condition of the lake the data obtained from half throttle speed will be used. Table 6 shows comparison between the data at half throttle speed and the optimum condition of the lake previously discussed in the literature review section.

Table 6: Summary of finding for collected data

Parameters	Taylor's Lake	Optimum condition
Turbidity / NTU	27.9	5 -55 [13]
DO / mg/L	8.8	More than 8 []14]
pH	8.5	6.5 – 8.5 [15]
Conductivity / uS/cm	246.3	150 – 500 [16]
Temperature / ℃	28.4	25 [17]

From the table above, it can be seen that all the parameters obtained from the lake falls within the optimum range except the temperature of the lake. The optimum temperature of the lake was set with respect to the Dissolve oxygen as previously discussed, from the literature review the to obtain a dissolve oxygen of 8mg/L and above the temperature must be less than 25 ℃, from the table it can be seen that the even though the temperature of the lake was slightly higher the dissolve oxygen is still more than 8 mg/L. Apart from the temperature it can be seen that the pH of the lake is at the edge of the maximum requirement level, this increment can again reflect to the temperature where as previously discussed in the literature review as the temperature increases the hydrogen ions will also increases therefore, the pH of the lake will shift to left but the acidity of the lake remains the same or vise versa. Therefore, comparing to the standard temperature of 25 ℃ the lake should have a higher pH than the optimum condition.

4.2 Solar Charging and Discharge Rate

Figure 16 represent the charging rate of the LiP0o battery using 6 solar panels which are connected in parallel. From the figure it is shown that it takes roughly about 2 hours for the voltage to stabilise from 9.45 V to 11.25 V. The maximum voltage the 6 parallel solar panels can only produce around 11.74 V under an optimum condition. The solar panels did not achieve the maximum voltage due to lack of availability of sunlight during the test day. When connected to power socket it was measured that the maximum voltage the LiPo battery can take in was at 12.5 V. This show that the solar panels does not produce enough voltage to fully charge the LiPo battery. The value obtained is still acceptable since the system will not be running for the entire day and also as the battery is discharging the solar panels will be continuously charging the battery.

Figure 17 shows the discharge rate of the battery when the 2 DC motor are running, by referring to figure 16 it can be concluded that it takes about 12 hours and 15 minutes to drop the voltage from 12.5 V to all the way to 10.94 V. Once the battery reaches 10.94 V the DC motors stops operating, this is due to the requirement of the DC motors. A 12 V DC motors requires a minimum of 10.94 V of voltage supply to operate, where else at this point the data collection will be still operation since all the sensors and the Arduino requires a 5 V supply.

In addition, by referring to figure 16 it can also be seen that the voltage drops ranges from 0.23 V to 0.06 V per hour. The decrement of voltage slows down to a minimum between 11.55 V and 11.22 V. Despite that, the voltage decreases tremendously from 10.94 V to 10.79V within 15 minutes. Other than that figure 17 shows that there are some fluctuation on the discharging rate, this can be due to two factors, the battery might be faulty therefore it is not giving a steady discharge rate or there might be some unwanted internal friction when the motor is rotating.

In summary by comparing both figure 16 and figure 17 it can be conclude that the minimum voltage required to run the DC motors is 10.94 V and therefore the total operational hors of the system is around 12 hours The discharge test was done by running the DC motors on air, as in real life the operational hour will be less due to friction of the water and the thrust required to move the boat. On the bright side the charging rate was about 2 hours using the solar panels therefore this will increase the operational hours of the system.

To predict the overall power consumption of the system the additional power consumption of the sensors, probes and microcontrollers as well as additional force due to drag by the water must be included. Table 7 below summarizes the power consumption of all components.

Table 7**.** Power usage of each components except motor based on technical specifications

Components	**Power usage (W)**
GPS	0.1500 [18]
3 Ultrasonic sensors	0.2250 [19]
Temperature probe	0.0500 [20]
Dissolved Oxygen probe	0.0675 [21]
Turbidity probe	0.2000 [22]
Arduino Mega	0.2500 [23]
Motor Controller	0.1800 [24]
Total	**1.1225**

According to the previous calculation each DC motor requires 4 W, using this information the total power consumption of the system can be calculated. The power consumption between all other components relative to the motors is calculated below, This shows that apart from the DC motors 14% of the total power is being used to power the sensors and the Arduino.

$$\frac{1.1225\ \text{W}}{8\ \text{W}} \times 100\% = 14.03\%$$

5 Conclusion

In conclusion, the autonomous water quality monitoring system will be energy sustainable with the help of solar panels, this will increase the charge time compared to the discharge rate therefore it will keep the system powered on more longer compared to system without solar panels. The system will can move autonomously in a fixed coordinate pattern while avoid any incoming obstacle automatically, all the data will be measured when the system comes to halt and it is uploaded to ThingSpeak through Wi-Fi data transfer with the help of esp Wi-Fi module connected to the Arduino. To minimize the complexity of the technical part of the boat the data

collection and the autonomous part of the boat will be working independently, both the data collection and the autonomous part will be using individual Arduino. The data collection and the autonomous part can be linked by the time of the data collection and the coordinate of the GPS at a given time. Separating both the system will increase the ease of maintenance of the boat since it is easy to identify the problem when there is a malfunction.

6 Reference

[1] Schmidt, W., Raymond, D., Parish, D., Ashton, I., Miller, P., Campos, C. and Shutler, J. (2018). *Design and operation of a low-cost and compact autonomous buoy system for use in coastal aquaculture and water quality monitoring*. Aquacultural Engineering, 80, pp.28-36.

[2] V. D. of *Sustainability and Environment*, "Monitoring and reporting -results," April 2012. [Online]. Available: http://www.water.vic.gov.au/monitoring/river-health/isc/results

[3] *Stevens Water Monitoring Systems Inc*., "About Us | Stevens Water." [Online]. Available: http://www.stevenswater.com/aboutus/.

[4] Libelium, "Fish farm monitoring in Vietnam by controlling water quality in ponds and tanks | Libelium," 2016. [Online]. Available: http://www.libelium.com/fish-farm-monitoring-in-vietnam-by-controlling-water-quality-in-ponds-and-tanks/?utm_source=NewsletterLB&utm_medium=Email&utm_campaign=NLB-290816.

[5] YSI, "YSI | Water Quality Sampling and Monitoring Meters and Instruments." [Online]. Available: https://www.ysi.com/.

[6] S. Dlamini, I. Nhapi, W. Gumindoga, T. Nhiwatiwa, and T. Dube, "*Assessing the feasibility of integrating remote sensing and in-situ measurements in monitoring water quality status of Lake Chivero, Zimbabwe*," *Phys. Chem. Earth*, vol. 93, pp. 2–11, 2016.

[7] "water quality", *Lake Champlain Basin Program, 2017*. [Online]. Available: http://www.lcbp.org/water-environment/water-quality/.

[8] Arduino, "Arduno mega 2560," April 2013. [Online]. Available:http://Arduino.cc/en/Main/ArduinoBoardMega2560

[9] "Phidgets," April 2013. [Online]. Available: http://www.phidgets.com/

[10] MacCallum, S. and Merchant, C. (2012). *Surface water temperature observations of large lakes by optimal estimation*. Canadian Journal of Remote Sensing, 38(1), pp.25-45.

[11] Fondriest Environmental, Inc. "*Dissolved Oxygen." Fundamentals of Environmental Measurements*. 19 Nov. 2013. Web. < http://www.fondriest.com/environmental-measurements/parameters/water-quality/dissolved-oxygen/ >.

[12] J. Martenhoff, *The Powerboat Handbook*. Winchester Press, 1975.

[13] J. J. Barrony, C. Ashton and L. Gear, "The Effects of Temperature on pH Measurement", Technical Services Department, 2018.

[14] M. Hayashi, "Temperature-Electrical Conductivity Relation of Water for Environmental Monitoring and Geophysical Data Inversion", Environmental Monitoring and Assessment, vol. 96, no. 1-3, pp. 119-128, 2004.

[15] R. Johnson, "SALINITY OF INTERSTITIAL WATER IN A SANDY BEACH", Limnology and Oceanography, vol. 12, no. 1, pp. 1-7, 1967.

[16] T. Panswad and B. Chan-narong, "Turbidity removal by the up-flow pelletisation process for low turbidity water", Journal of Water Supply: Research and Technology—AQUA, vol. 47, no. 1, pp. 36-40, 1998.
[17] Dissolved Oxygen and Temperature. 2018.
[18] QQ Online Tradings, "*DC Geared Motor GB37 [12V] Speed 17rpm ~ 500rpm*." [Online]. Available: http://qqtrading.com.my/dc-geared-motor-gb37?search=12V Dc motor.
[19] V. ke. Electronics, "*Vk2828U7G5Lf*." [Online]. Available: https://github.com/CainZ/V.KEL-GPS/blob/master/VK2828U7G5LF Data Sheet 20150902.pdf
[20] ElecFreaks, "*Ultrasonic Ranging Module HC -SR04*." [Online]. Available: http://www.micropik.com/PDF/HCSR04.pdf
[21] T. Instrument, "*LM35 Precision Centigrade Temperature Sensors*," 2013. [Online]. Available: http://www.ti.com/lit/ds/symlink/lm35.pdf.
[22] Atlas Scientific Environment, "*Dissolved Oxygen Probe*." [Online]. Available: https://www.atlas-scientific.com/_files/_datasheets/_probe/DO_probe.pdf
[23] DFrobot, "*Turbidity sensor SKU: SEN0189*." [Online]. Available: https://www.dfrobot.com/wiki/index.php/Turbidity_sensor_SKU:_SEN0189
[24] Arduino, "Arduino Mega," 2017. [Online]. Available: https://www.Arduino.cc/en/Main/ArduinoBoardMega
[25] STMicroelectronics, "*L298N Motor Controller Datasheet*," 2000. [Online]. Available: http://www.geeetech.com/Documents/L298N datasheet.pdf

EURECA 2018 – Conference Paper
Paper number 2ME17

Improving Natural Frequency of an Engine Oil Pan – A structural Optimization Method

*Mohammad Ammar Zulsyahmi Mohd Zali[1, *], Noor Zafirah Abu Bakar[2], and Azmi Osman[1]*

Abstract. Powertrain has highest contribution to vehicle noise and vibration. The engine's oil pan contributes 32% of the overall powertrain vibration particularly during idling and full load acceleration due to the thin wall structure. Designing an oil pan that optimally fulfills requirements in terms of structural, natural frequency, weight, costs and packaging space for vehicles can be challenging. These requirements often compromise one another if the design has imbalanced priorities. Current solution suggest structural optimization to increase the natural frequency of an oil pan to avoid resonance but compromise with addition of weight. This paper discuss a new structural optimization combination to address this gap. Using the intended method, natural frequency can be as high as 1273Hz (70.7% improvement) with weight as low as 2.78kg (42.3% weight reduction).

Keywords: oil pan, natural frequency, modal analysis, FEM, vibration, NVH

EURECA 2018 – Conference Paper
Paper number 2ME18

Evaluation and Assessment of whole-body vibration in passenger vehicle

Mohd Ikhwan Syamil Bin Mohd Anwar and Mohd Farid Bin Aladdin

Mechanical Engineering, School of Engineering
Taylor's University

Abstract. Over the past several years, various researches have been performed to detect the variation of vibrations occurring inside a vehicle. The variations in vibrations could occur due to results of certain factors. By applying both applicable standards that were established beforehand, which are the ISO 2631-1(International Organizational Standardization) and the BS 6841(British Standards), any data analyzation could be compared as to what can be referred to as the ideal standard value of the vibration occurs inside a vehicle. For the gap that there are in the ways to reduce the effect of vibrations of human body, limitless factors could be the major reasons towards the comfortability of a human body.[1] There are several ways to determine the discomfort levels in human body by having to calculate the root mean square value of vibration acceleration of a passenger inside a vehicle. This average value should determine the frequency of the vibrations towards an extent the average value should not be higher than the average value. This has to do with the seat amplitude transmissibility of the data gathered as to weightings needs to be applied into account. For the experiment, three types of variation of vehicles will be used as to compare the different types of cars with the occurring vibrations towards the comfortability of the passenger.

1 Introduction

The main objective of the project is to assess the discomfort level of passenger in motor vehicle. By implying several variables into account of the human response towards vibrations, data of frequency against the velocity of passenger's seat vibration is taken to compare the end root mean square of velocity of each of the factors. Then the weighted vibration magnitude is then compared between the different variables to know which type of vehicle incurred the most of the comfort level following the standardized values. Thus, the research objectives could be specified into meeting the aim of the project:

1. Comparing three different types of car variations in which commonly used in Malaysia in the assessment and evaluation of the passenger's seat whole body vibrations.
2. Identify the suitable factors to take into account of experiment such as the placement of the accelerometer, types of vehicles, severity of vibrations, duration of the vibration exposure and velocity of vehicles.

The secondary aim of this project is to know the severity of the assessment done earlier with the effect it held against a human body in a period of time. All the analysis will be brought up to certain graphs and tables as to compare different severity of whole body vibrations. A series of equations to calculate the data has to be precise and according to standards given. In order to know the severity of the examined factors, we should try to focus on the frequency analysis of the vibration signals, which will indicate the effects of vibration on health and discomfort. Then the third objective should be:

3. Identify the perception of discomfort in the human's body that human would starts to react when an exposure of vibrations is held on for such a duration.

1.1 Frequency Weightings

The data accumulated from the accelerometer device is in the form of time histories of frequency-weighted using the weightings defined for evaluating the exposures of seated persons to vertical vibration. The frequency weightings of Wb and Wk differences have been explained by Griffin.[2] As in general, the weightings are the vibration in vertical vibration produced by the frequency of the direction. However, applying these weightings comes with an axis multiplier as to get the value of weightings thus move on to the next steps of vibration does values calculations.

Table 1: Table of axis multiplier for the axis of pan

Position	Application	Measurement location	Axis	Axis Multiplier
Seated	Health	Seat Pan	X Y	1.4 1.4

			Z	1
	Comfort	Seat pan	X	1
			Y	1
			Z	1
		Seat back	X	0.8
			Y	0.5
			Z	0.4
		Floor	X	0.25
			Y	0.25
			Z	0.4
	Perception	Seat pan		1
				1
				1

1.2 Root mean square

As mentioned by Mansfield[3], the root mean square is vibration that oscillates about a fixed point. Assuming there is no translation. The mean value of the vibration signal will be in theory be zero. Thus, mean of acceleration will not indicate the magnitude of signal. The root mean square is a problem-solving solution to take value of every signal by squaring them, taking the mean and square root of every data.

$$r.m.s, (\frac{m}{s^2}) = [\frac{1}{T} \int a^2(t)dt]^{\frac{1}{2}} \quad (1)$$

As the r.m.s. is known, then it will be calculated and multiplied with the axis multiplier as mentioned in the table 2 of axis multiplier of axis pan. This is then combined with the total of individual axes to give a total weighted r.m.s. acceleration value:

$$a_y = \sqrt{({k_x}^2 . {a_{wx}}^2)} + \sqrt{({k_y}^2 . {a_{wy}}^2)} + \sqrt{({k_z}^2 . {a_{wz}}^2)}$$

(2)

1.3 Vibration Dose Value

the VDV will be multiplied with the axis multiplier and using appropriate frequency, weightings, the VDV will give a total exposure of vibration by taking account the magnitude, frequency and exposure durations.

$$\mathrm{VDV} = \left(\int_0^T a^4(t)dt \right)^{1/4}$$

(3)

Thus, the total VDV could also be calculated using the formula as similar to the multi-axis multiplier for rms value but as for the VDV value, it will be to the power of 4 instead to the power of 2. However, the total axis multiplier is neglected in the series making it to the total of calculations of power for each and every value of VDV.

The vibration dose value is in the unit of $m/s^{1.75}$. where (a)t is the frequency weighted acceleration and T is the total measurement of the period in seconds. As this is all depends on the value of crest factor, if the crest factor is above 6[4] the VDV equations then can be used as the substitute. Or else, the amount should have implied in the situation would be the equation of eVDV. In this value of calculation then we can determine the comfort of the vibration based on the reference of BS6841 and ISO 2631.

1.4 PSD Graph

The PSD (power spectral density) graph is a graph in referring to the energy distribution that would be found per unit time of data unit. In order to know the resonance frequency of the data plotted from calculating both rms and VDV value of weighted and unweighted acceleration, the highest peak of resonance of the PSD graph is needed to determine the dominant frequency of a car vibration to which frequency exerting the most outcome out of all the frequency gathered. The aim is to have a PSD peak of lower than 10 Hz in which the cushion from every vehicles should be cancelling out the vibrations of high frequency value. From the weighted data after applying coding for root mean square of the acceleration time graph, the y-axis data is taken into determining the dominant frequency of each speed of car types.

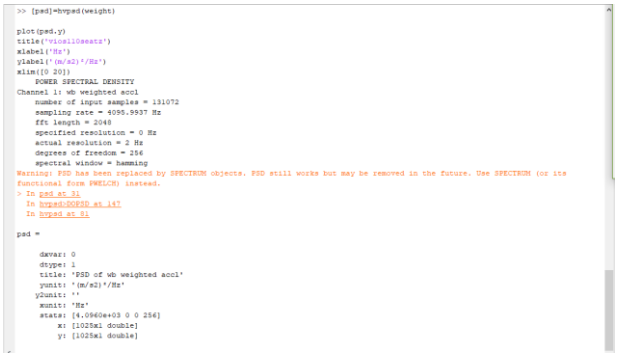


Figure 17- Function call out to find PSD value of weighted data and PSD graph plot

2 Methodology
Assessment and Evaluation of Car Seating

In the first stage of the experiment, it is basically the process of thorough research on the type of car that the project is going to be handled. All the methodology is being set up in this stage where all the equipment and tools for the data collection are being assembled and attached to its position and place. As for the project's experiment, by comparing the three different types of cars which in this case are the car of commonly used in daily life of Malaysian. These cars are Perodua Myvi as in representation of a compact car, Toyota Vios as a representation of sedan car and Perodua Alza as a representation of MPV (Multi-purpose Vehicle). As for the first part of the project, only Perdoua Myvi is being tested as for comparison with another car. The speed of testing of comparison is also capped to a derivation of 40, 60, 90 and 110 km/h. Location of the measurement are predetermined and setup of equipment are being held into procedure. As for the device, a Piezo resistive accelerometer is being used as a tool to measure the vibration in axis of x, y and z direction of the human passenger



Fig. 1. Pie resistive accelerometer

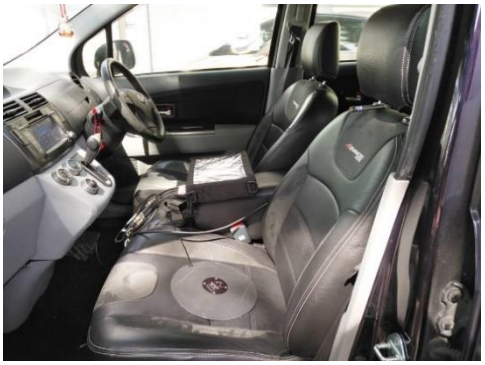


Fig. 2. The position of accelerometer for the Seat position



Fig. 3. The position of the accelerometer in back and feet position

As according to ISO 10326-part 1, The parts that are being tested for the vibration are in position of Seating, back and also feet. This to ensure the gathering of SEAT value in which is the measuring of how well the transmissibility of a seat spectrum of vibration entering a seat.[5] The value of SEAT could be obtained from a series of equation which will be later on introduced in the next stage. The reason of choosing the three position of seating direction of back, feet and seating is because of referring to Standard Handbook of Biomedical Engineering and Design. The biodynamics of design basicentric coordinate axes of translational are referred to diagram from the Handbook.[6]

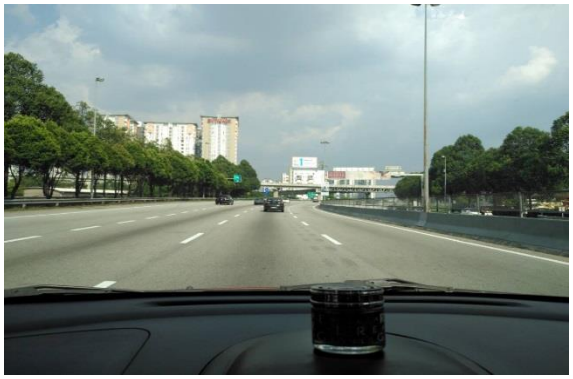


Fig. 4. Condition of the route the accelerometer is tested

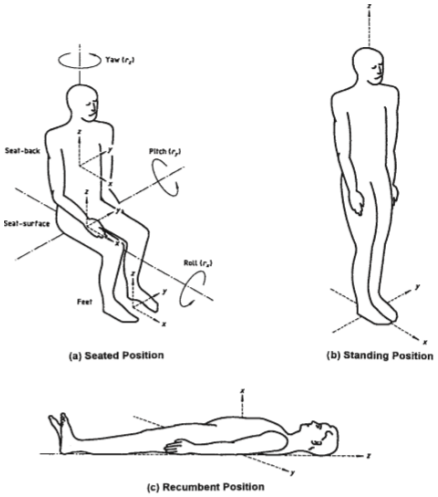


Fig. 5. Coordinate axes of seating position for translational (x, y, and z) of whole body vibration

For the project experiment, the data should be derived from the accelerometer should be on different speed of cruising as to monitor the difference in between the speeds with correlation of types of car. This is to simulate the speed of normal driving speed as in cruising through the city, normal driving speed and a speeding driving on highway speed. As for the first part of the experiment, the usage of only one type of car is persistent with the speed of constant 60 km/h on a highway of same route of testing. This has to be capped at the same variable as to reduce the uncertainties that could be happening during the data collection. The route of choosing of the data collection is the KESAS highway located near to Subang Jaya.

As the accelerometer is a digital unit which are able to connect with different sensors at the same time in different orders, the accuracy of the data tend to be neglected. To ensure every data has to be precise in the way that the unit of experimentation is accurate and sensitivity of the sensors are in sync with the accelerometer, a pre-steps of sensitivity input are necessary for each of the sensors used for the devices. As for the case of the data collection in the seating pan, back rest and feet, the tools used which is the accelerometer has a sensitivity of each and every angle of focus. The sensitivity has to be keyed in into the specific program of tools as to create a more relevant and accurate data sets.

Table 2: The axis sensitivity of each accelerometer sensors connected

Axis	Sensitivity(mV/g)
X-axis reference sensitivity	90.30
Y-axis reference sensitivity	89.50
Z-axis reference sensitivity	100.30

A series of results could be generated directly from downloading the data files of the accelerometer. As the experiment held for 32 seconds for the entire experiment to be done for

all the axes and types of cars, thus a series of coding should be applied into the accommodation provided by Matlab calculation series.

```
function [dasHw] = hvweighting(strWtg, fscale, pmode, fmin, fmax)

error(HVFUNSTART([strWtg, ' FREQUENCY WEIGHTING'])); % show header and check for global parameters
global HV; % allow access to global parameter structure

% Create output data structure
% ----------------------------
if nargin < 5; fmax = 1/(2 * HV.TINCREMENT); end
if nargin < 4; fmin = HV.FINCREMENT; end

if nargin < 3; pmode = 0; end
if nargin < 2; fscale = 1; end
if fscale > 1
    xvar = 1; %variable increment
else
    xvar = 0; %constant increment
end
if pmode == 1
    dasHw = HVMAKESTRUCT(['PSD weighting ', strWtg], [], 'Hz', 1, xvar); %mode 1 == real data
else
    dasHw = HVMAKESTRUCT(['frequency weighting ', strWtg], [], 'Hz', 2, xvar); %mode 2 == complex data
end

% Generate frequency points
% -------------------------
flimit = fmax;
fincr = max(fmin, flimit / 1024);
switch fscale
    case 2
        dasHw.x = Thirdoct_fscale(fincr, flimit);
        HVFUNPAR('frequency resolution = exact third octaves');
    case 3
        dasHw.x = Nomthirdoct_fscale(fincr, flimit);
        HVFUNPAR('frequency resolution = nominal third octaves');
    otherwise                       %i.e. case 0
        dasHw.x = Const_fscale(fincr, flimit);
        HVFUNPAR('frequency resolution', fincr, 'Hz');
end
HVFUNPAR('maximum frequency', fmax, 'Hz');

% Generate frequency weighting
% ----------------------------
qc = 1 / sqrt(2);
errWtg = 1;
```

Fig. 6. The coding for calculation of root mean square values

```
function [sdval, maxval, minval, meanval, rmsval, duration] = hvstats(dasInarr)

error(HVFUNSTART('STATISTICS OF DATA STRUCTURE', dasInarr)); % show header and abort if input is not a valid structure

for k = 1:length(dasInarr)
    if ~HVISEMPTY(k, dasInarr(k)) % return results only for non-empty array elements
        error(HVISVALID(dasInarr(k)));
        [sdval(k), maxval(k), minval(k), meanval(k), rmsval(k), duration(k)] = STATS(dasInarr(k)); % compute stats
    end
end
return
% ============================================================
% compute statistics of single workspace data structure
function [sdval, maxval, minval, meanval, rmsval, xlen] = STATS(dasIn)

if dasIn.dtype == 1; HVFUNPAR('number of real samples', length(dasIn.y)); end
if dasIn.dtype == 2; HVFUNPAR('number of complex samples', length(dasIn.y)); end
if dasIn.dtype == 3; HVFUNPAR('number of modulus & phase pairs', length(dasIn.y)); end
if dasIn.dxvar == 0
    HVFUNPAR('sampling increment', dasIn.x(2) - dasIn.x(1), dasIn.xunit);
    xlen = max(dasIn.x) - min(dasIn.x);
    HVFUNPAR('length of x-axis', max(dasIn.x) - min(dasIn.x), dasIn.xunit);
else
    xlen = max(dasIn.x);
    HVFUNPAR('limit of x-axis', xlen, dasIn.xunit);
end
meanval = mean(dasIn.y);
rmsval = sqrt(mean(dasIn.y .^2));
%rmsval = sqrt(sqrt(mean(dasIn.y .^4)));
sdval = std(dasIn.y,1);
maxval = max(dasIn.y);
minval = min(dasIn.y);
HVFUNPAR('mean value', meanval, dasIn.yunit);
HVFUNPAR('r.m.s. value', rmsval, dasIn.yunit);
HVFUNPAR('standard deviation', sdval, dasIn.yunit);
HVFUNPAR('maximum value', maxval, dasIn.yunit);
HVFUNPAR('minimum value', minval, dasIn.yunit);
if dasIn.dtype == 3
    meanval = meanval(1);
    rmsval = rmsval(1);
    sdval = sdval(1);
    maxval = maxval(1);
    minval = minval(1);
end
```

Fig. 7. The coding for frequency resolutions determined by weightings

3 Results and Discussions

3.1 Compact Car

Table 3 – Weighted root mean square and VDV value for compact car

Axis	Weighted root mean square(rms) (ISO 2631)								
	Seat-back			Seat-feet			Seat		
	x	y	z	x	y	z	x	y	z
Speed									
40	0.0983	0.0739	0.0771	0.1293	0.208	0.3256	0.0652	0.0455	0.2421
60	0.1255	0.106	0.1083	0.1328	0.1429	0.3055	0.0703	0.0444	0.1976
90	0.0919	0.2165	0.1867	0.1266	0.1277	0.2694	0.1586	0.0564	0.2651
110	0.2616	0.3407	0.2245	0.1848	0.1693	0.5076	0.1835	0.0873	0.4004
	Vibration dose value(VDV)								
Speed									
40	0.3526	0.2362	0.2452	0.44	0.6614	1.089	0.2079	0.1556	0.8274
60	0.4792	0.3646	0.3999	0.4313	0.4579	0.9667	0.2235	0.1417	0.6775
90	0.2816	0.6729	0.5945	0.4122	0.4118	0.8758	0.489	0.1751	0.9768
110	0.8661	1.0358	0.6921	0.6141	0.5335	1.6612	0.5906	0.3018	1.5049
	Weighted root mean square(rms) (BS 6841)								
Speed									
40				0.1407	0.2104	0.2555			0.321
60				0.1416	0.1482	0.2043			0.3011
90				0.1362	0.1345	0.2974			0.2689
110				0.1958	0.1784	0.4481			0.4808

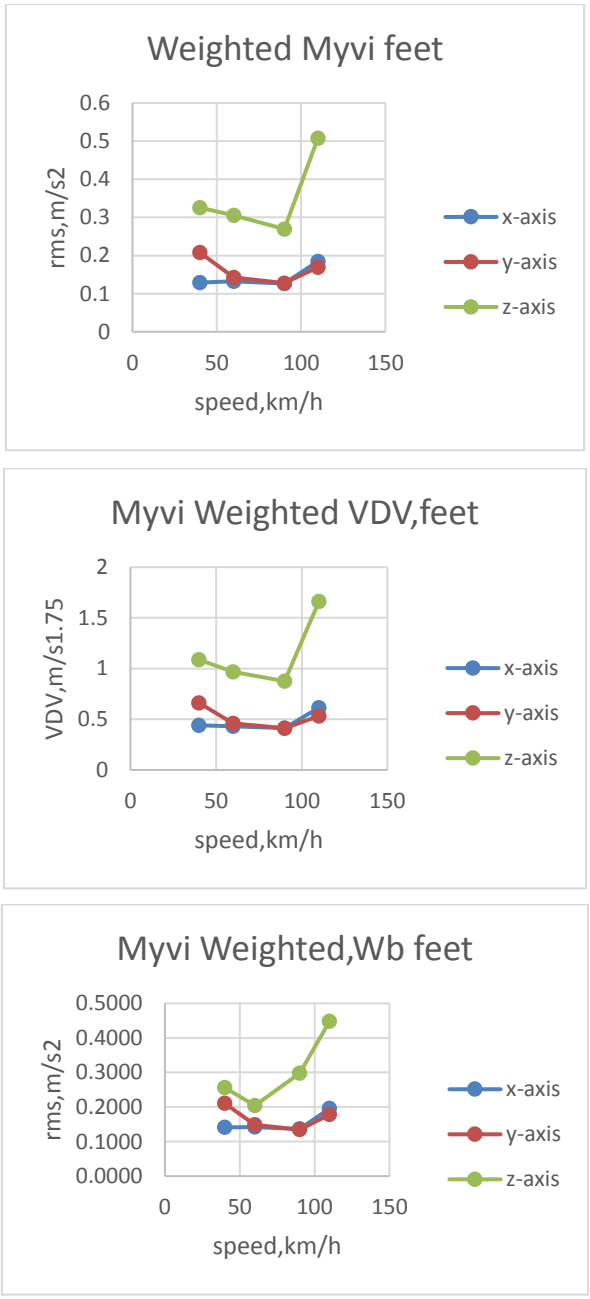


Fig. 8. Vibration magnitude (ms^{-2} r.m.s.) and VDV value ($ms^{1.75}$) of seating position for translational (x, y, and z) axes of whole body vibration with average r.m.s. for each accelerometer placement of compact car at different speed.

Based on table 3, the root mean square of the axes could be determined by both standard of ISO 2631-1,Wk or BS 6841,Wb. In the case, the standard of Wk is used to produce value of r.m.s. of each axis. As can be observed from both table 3 and graph of figure 10, at back position, the magnitude of severe axis located at the z-axis. Predominantly shown from all the weighted graph of weighted rms, it can be observed that with the higher increase in speed of the vehicle, the number of root mean square would also increase with time. But the interesting fact is the z-axis dominantly has the highest of all axis value where comes all the vibration acceleration as compared to the other axes. The back value of the compact car has the highest value in y-axis is due to because the strapping of the accelerometer to be horizontal because logically,

from research methodology, the axis should be swapped due to the placement of the sensor. Thus, this truly shows the dominant of the z-axis of the vibration inside a vehicle. Following the graph again, the highest value can be obtained from the feet as the closest part to the ground and source of vibration is where the vibration is severe the most.

3.2 Sedan Car

Table 4 – Weighted root mean square and VDV value for sedan car

Axis	Weighted root mean square(rms) (ISO 2631)								
	Seat-back			Seat-feet			Seat		
	x	y	z	x	y	z	x	y	z
Speed									
40	0.1051	0.106	0.0742	0.1135	0.1849	0.3336	0.0745	0.0485	0.2875
60	0.1448	0.096	0.0738	0.1818	0.2888	0.4652	0.079	0.0513	0.2694
90	0.1289	0.1267	0.0866	0.1653	0.1776	0.3705	0.1303	0.0656	0.3896
110	0.1944	0.2175	0.2183	0.2044	0.2141	0.4439	0.1803	0.1037	0.3613
	Vibration dose value(VDV)								
Speed									
40	0.3517	0.3218	0.2274	0.3578	0.5844	1.0326	0.2374	0.1522	0.8744
60	0.508	0.3011	0.2641	0.6091	0.9574	1.4524	0.2514	0.1591	0.8079
90	0.4121	0.4345	0.2966	0.524	0.5633	0.3532	0.4291	0.2134	1.2305
110	0.6247	0.6816	0.7869	0.6603	0.7043	1.4183	0.5666	0.3459	1.2251
	Weighted root mean square(rms) (BS 6841)								
Speed									
40				0.1203	0.1951	0.3168			0.2631
60				0.1842	0.3267	0.4538			0.2517
90				0.1663	0.1850	1.1488			0.3752
110				0.2078	0.2249	0.4124			0.3254

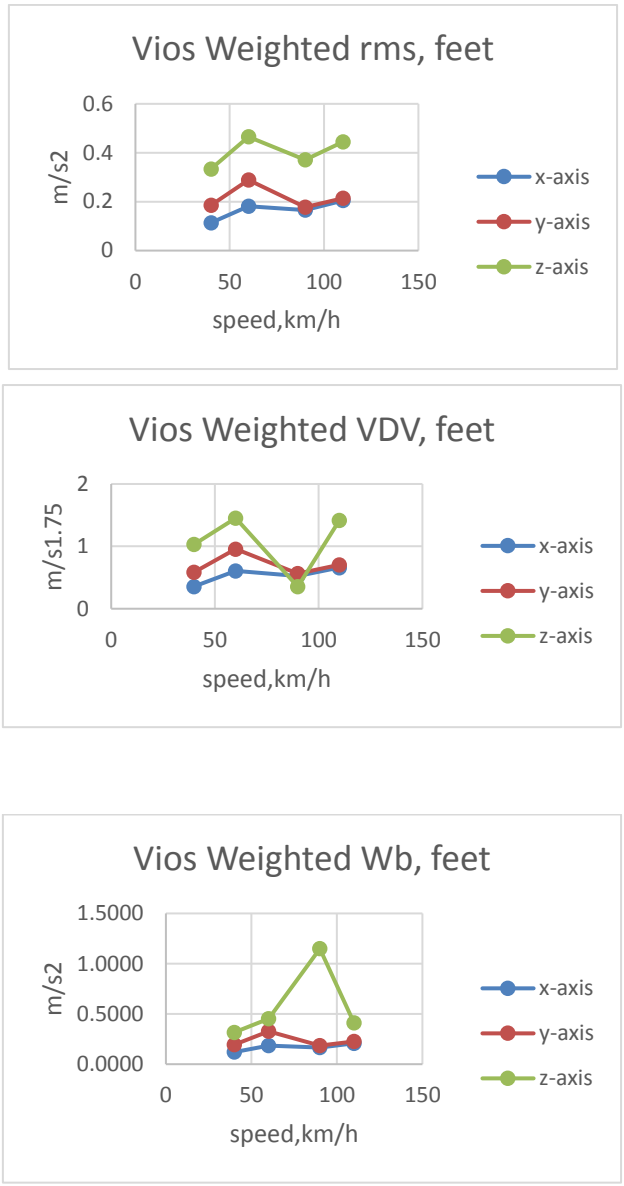


Fig. 9. Vibration magnitude (ms^{-2} r.m.s.) and VDV value ($ms^{1.75}$) of seating position for translational (x, y, and z) axes of whole body vibration with average r.m.s. for each accelerometer placement of sedan car at different speed.

From the VDV value of the product from the data of sedan car type, at the input to where the crest factor to be lesser than the crest factor of value 6, the amount of estimated vibration dose value might need to be considered as solution. From observations, the vibration dose values of the sedan car have significance increases in speed also although the types of car are differed than prior test. Though there are some downside of data in graph at higher speed acceleration, it can be due to cause of inconsistent speeding of the acceleration of the car since the highway used may be packed with traffic and there thus a slight mistreatment of speed constant in the way of experimentation. Other than that, the most severe seems to be the z-axis of feet position with the highest value of 1.4 m/s1.75. This is in the middle range of comfortability since the value is average in the range of between fairly uncomfortable and uncomfortable.

3.3 MPV Car

Table 5: Weighted root mean square and VDV value for MPV car

Axis	Weighted root mean square(rms) (ISO 2631)								
	Seat-back			Seat-feet			Seat		
	x	y	z	x	y	z	x	y	z
Speed									
40	0.1184	0.1307	0.1308	0.0861	0.1303	0.255	0.0576	0.0407	0.2616
60	0.1486	0.1537	0.1381	0.0948	0.1842	0.2589	0.0512	0.0388	0.2035
90	0.1486	0.246	0.1909	0.2064	0.1684	0.4419	0.1233	0.0512	0.2636
110	0.185	0.4528	0.394	0.268	0.2066	0.8255	0.1659	0.0607	0.4292
	Vibration dose value(VDV)								
Speed									
40	0.4043	0.4395	0.4708	0.2769	0.4217	0.7909	0.1861	0.1334	0.8325
60	0.5101	0.4757	0.4306	0.3405	0.5651	0.8516	0.1666	0.1219	0.6571
90	0.4822	0.8238	0.6459	0.6596	0.5662	1.4181	0.4108	0.1751	0.8842
110	0.6195	1.4395	1.1153	0.8525	0.6455	2.629	0.5118	0.1882	1.3746
	Weighted root mean square(rms) (BS 6841)								
Speed									
40				0.0952	0.1337	0.2457			0.2443
60				0.1029	0.1850	0.2492			0.1918
90				0.2094	0.1739	0.4179			0.2368
110				0.2861	0.2137	0.8118			0.4047

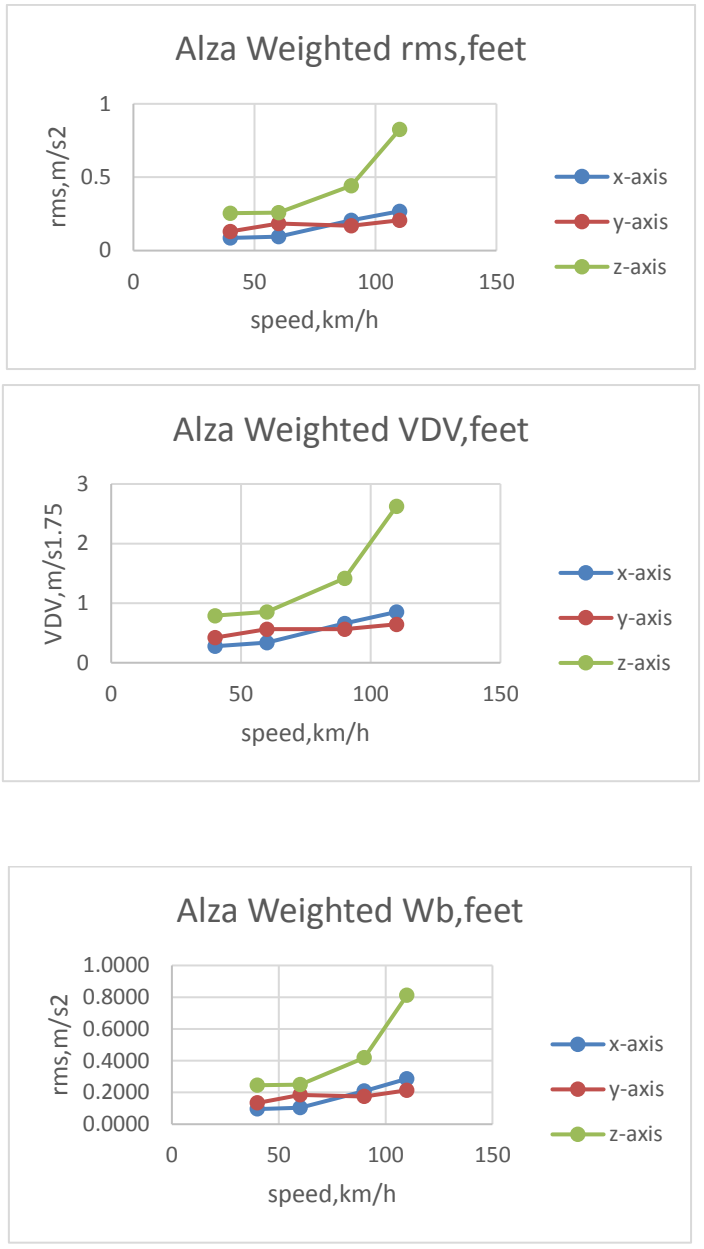


Fig. 10 Vibration magnitude (ms^{-2} r.m.s.) and VDV value ($ms^{1.75}$) of seating position for translational (x, y, and z) axes of whole body vibration with average r.m.s. for each accelerometer placement of MPV car at different speed.

Among all three types of cars examined, the MPV car type has the highest values in both weighted and unweighted root mean square and vibration dose values. The average values in term of r.m.s. in the Perodua Alza has a slight significant in increment of value although cruising at the same speed at the same road of experiment. As most z-axis is highest and most severe axis of the root mean square values, it can be say that the axis has the most severe impact towards the passenger. But with the change in speed of the car, the root mean square of the weighted data has also increased.

3.4 PSD Graph

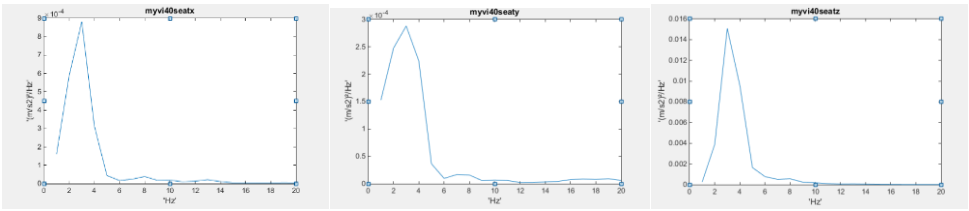


Figure **11** - PSD graph to show dominant frequency at 40 km/h seat position

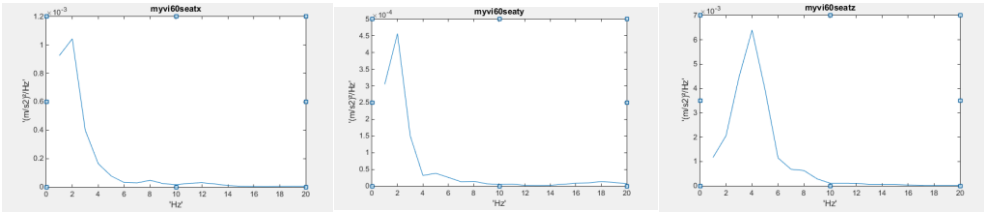


Figure **12** - PSD graph to show dominant frequency at **6**0 km/h seat **position**

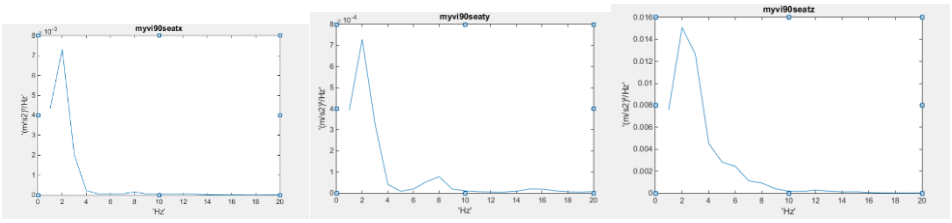


Figure **13** - PSD graph to show dominant frequency at 90 km/h seat position

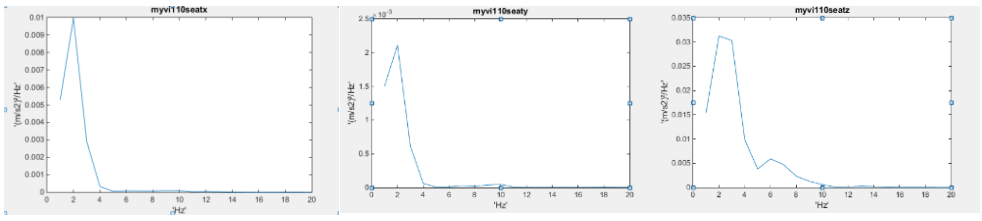


Figure **14** - PSD graph to show dominant frequency at 110 km/h

Taking into account the resonance at the highest peak available using the PSD diagram, we could observe a significance increase in the power spectral density value as the frequency of vibration in the increases. But as it reaches the maximum point, the spectral density would then decrease over frequency as the high frequency from the whole-body vibration is cancelled and soothes by the comfort of the cushion or seat. The category of high frequency could be categorized in this case as frequency of greater than 10 Hz. From the PSD graph also, we can observe the frequency of dominant is located mostly at 2 Hz where a human-body would not notice until a long exposure of time happens. It clearly unwise to assume the measurement of

the vibration in a single vehicle represents the entire car in the world. That is why the variables of the car types is taken into consideration to know whether there are variations in severity in types of car that are commonly used by the community in Malaysia.

4 Conclusions

This is conducted to research and investigate the effects of vibration on the passenger of a vehicle based on different types of vehicle using different standards of procedure with different speeds of velocity. The transmission of vibration data towards the passengers are taken from three different positioning of the accelerometer of feet, seat and back. Four different speeds were considered for the test. The speed variations indicate the variation of speeds undergoes by passengers in a typical daily route in Malaysia route. It was shown that for each and every type of cars, at different speed, the VDV values as related with the rms value, increases with the increase of speed. The sedan car is suspected to be having least amount of vibrations as compared to MPV-type of car and compact car type. Higher speeds would also indicate the higher VDV and rms values which in context, consequently effect the comfortability of a ride for a passenger. Evaluations by using different standards of operations also indicates that variation at different velocities over different speeds shows that according to ISO 2631, would give a lower amount of total VDV and rms as compared to significant other standards of BS 6841.

References

[1] M. J. Griffin and J. Erdreich, "Handbook of Human Vibration," *The Journal of the Acoustical Society of America*. 1991.

[2] G. S. PADDAN and M. J. GRIFFIN, "EVALUATION OF WHOLE-BODY VIBRATION IN VEHICLES," *J. Sound Vib.*, 2002.

[3] J. Griffin, H. Factors, R. Unit, and V. Research, "Human response to vibration," *J. Sound Vib.*, vol. 256, pp. 999–1002, 2002.

[4] Standard, "ISO 2631-1 - Mechanical vibration and shock- Evaluation of human exposure to whole-body vibration," vol. 1: General, pp. 1–30, 1997.

[5] G. S. PADDAN and M. J. GRIFFIN, "EFFECT OF SEATING ON EXPOSURES TO WHOLE-BODY VIBRATION IN VEHICLES," *J. Sound Vib.*, 2002.

[6] A. J. Brammer and D. R. Peterson, "VIBRATION, MECHANICAL SHOCK, AND IMPACT."

EURECA 2018 – Conference Paper
Paper number 2ME19

A Numerical Assessment of the Effect of Surface Topography on the Dynamic Stability of Microorganisms for Biofouling Control

Muhamad Sean Farof [1], Felicia Wong Yen Myan[2]*

[1]Bachelor of Mechanical Engineering, Taylors University Lakeside Campus,
47500 Subang Jaya, Malaysia
[2]Department of Mechanical Engineering, School of Engineering, Taylor's University Lakeside Campus,
47500 Subang Jaya, Malaysia

Abstract

Biofouling is the undesirable settlement of organism and microorganisms onto any surface that has been submerged in the water for a period of time. This phenomenon starts with the formation of a biofilm layer and consists of mixture or microorganisms and other materials in an extracellular polymeric substance. The negative impact of this phenomenon has caused affected industries to spend a lot of money on maintenance, repairs and antifoulants to control this issue. Over the years, numerous approaches to curb biofouling have been introduce to the market and one of the most effective approaches is by using *Tributylin* (TBT). TBT was proven to be the best approach until it was banned back in 2008 for its toxic content which was detrimental to aquatic environment. This lead to current research effort to develop non-toxin antifouling solutions and one such approach is by manipulating surface topography features.

Previous research into antifouling topography has determined that the physical attributes (i.e. topography size, geometry, etc.) of surface topography affects the surface's antifouling efficacy. However, there has been less effort to understand the effect of these topographies on fluid flow in its surroundings. It is possible that the hydrodynamic variations induced by antifouling topographies could have contributed to the surface's antifouling potential. This project aims to understand the hydrodynamic variations induced by antifouling topography and how these variations could have affected the dynamic stability of the microorganisms in the vicinity of the surface. This study was conducted with the aid of ANSYS Fluent, a Computational Fluid Dynamics (CFD) software package and Solidworks for the three-dimensional (3D) modelling of topography

designs. ANSYS Fluent used the analytical tool that simulates fluid flow over (3D) models of topographies and indicates regions on the topography that is likely to mitigate biofouling settlement. Parameters of interest for this project such as shear stresses and velocity magnitude will aid in the analysis of determining if the surface topography has potential for antifouling applications.

Prior studies by Min et al. (2017) and Wei et al. (2017) have determined optimum topography size and geometry with optimum antifouling potential. This project will go a step further by determining the effects of a physically optimised topography on a microorganism swimming in the vicinity of the topography.

Keywords: Biofouling, Antifouling, Topography, Numerical analysis, Computational fluid dynamics.

**Corresponding Author: FeliciaYenMyan.Wong@sd.taylors.edu.my*

1.0 Introduction

Biofouling is a phenomenon of unwanted deposition of organism and microorganism settles onto any surface that has been submerged for a period of time in water. Biofouling begins with the formation of biofilm. Biofilm which consists of adherent cells that sticks to a surface and forms complex extracellular polymeric substances (EPS)[1]. This natural process has significant impact to various industries. For example, the fouling of ship hulls causes drag and friction to increase as the ship glides through water which leads to the increment of fuel consumption. The United State spent an estimate of US$ 960 to US$ 1280 million on antifouling equipment in the oil and gas sector[2]. Besides, an additional US$ 1.5 to US$ 3 billion is spent yearly on antifoulants, repairs and maintenance to handle this phenomenon [3]. This is an indication that further research is necessary to overcome this issue.

There are various approaches to prevent biofouling but all approaches have exhibited flaws or weaknesses. In the past, Tributylin (TBT) was a chemical approach that proved to be the most effective against biofouling. This method was effective but had detrimental effects towards the aquatic environment which caused this method to be banned back in 2008 [2]. With a gap presented with the banning of TBT, there was a need to develop antifouling measures that were not harmful to the environment.

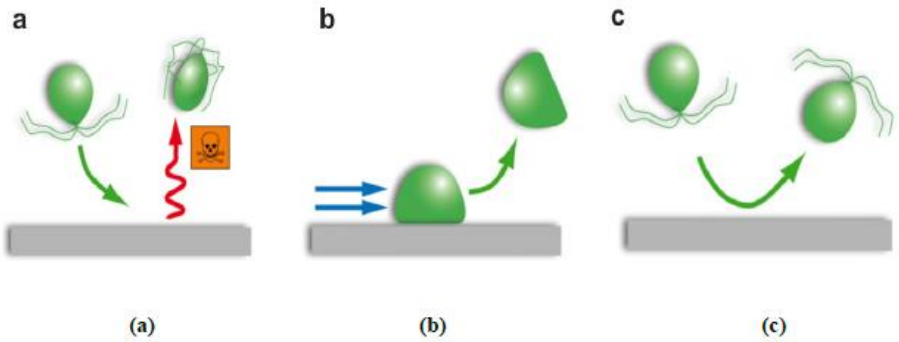
Many other methods were introduced to replace the usage of TBT. One of the few are non-toxic antifouling coatings or also known as foul-release coating (FRC). This includes hydrogel coatings, hydrolysis binder coatings and silicone based coating [4]. Upon application to a surface, the surface becomes slippery, with significantly reduce friction making it difficult for organisms to settle on the surface. Aside from that, these coatings are biocide free. The issue with these coatings would be its high costs and low lifespan which means that surfaces will need to be recoated often incurring further additional costs too [5].

Another approach to prevent fouling or settlement of organisms onto surfaces is by manipulating the topography features. Organism is less likely to settle onto a smaller size topographies than on larger topographies due to the organism having insufficient contact with smaller size topography [2]. Surface topography roughness and tortuosity of the surface are also factors that contribute to reducing microorganism settlement. It is noted that topographies by itself will not be able to completely inhibit biofouling [6]. Studies have suggested that a synergistic approach which combines chemical and physical antifouling methods would be more effective towards biofouling [2].

Nonetheless, the main objective of this project is to understand the effects of antifouling topography on the dynamic stability of microorganism that are proximal to the topography surface. Previous studies have mostly focused on the effect of topography size and geometry in relation to biofouling control. However there has yet to be a significant number of studies about an optimum configuration of a topography which can be considered to be highly effective against antifouling.

Therefore, this report will mainly focus on the dynamic stability of the microorganism based on the most optimum topography size and topography geometry that was found by two individual research study. The optimum topography that was found will be used to design the topography which being used in this project. The result obtain from the outcome were analysed to understand the effect of optimised topographies on the dynamic stability of the microorganism.

This project will use Computational Fluid Dynamics (CFD) to analyse fluid flow over



the surface, shear on the wall, etc. An advantage of this method is that there is no need to build physical prototypes that are high in costs. Numerical simulations are a suitable substitute to understand the antifouling potential of topographies

Figure 18: Different approaches against biofouling: (a) toxic antifouling, (b) foul release, (c) foul inhibition [7].

2.0 Research Methodology

Despite various approach towards antifouling technology development, a non-toxic approach is preferable. Moreover, most research that had been done are mostly field studies and lab experiment. This methods are time consuming and equipment used are costly. Hence, throughout this project, simulation of the flow over topography geometry in relation to the topography size will be analyse via ANSYS fluent.

2.1 Topography design and modeling

This idea came about based on living organism which prevent fouling in the nature. For the anti-fouling topography surface which was mainly inspired by lotus leaf, pilot whales rigid pores and shark skin riblets that has the ability to prevent any organism from settling or settling on the surface of it.

After determining the surface specific of the topography, a 3D CAD topography geometry and channel was than drawn with the aid of SolidWorks. The dimension and other detail used throughout the research are based on previous finding and journal articles. Moreover, as for the simulation which is also another vital part in obtaining an accurate result, a good mesh is required. The meshing is completed using a CFD software (ANSYS Fluent). Furthermore, boundary and mesh types was then completed using ANSYS fluent. A mesh convergence analysis was also conducted to ensure that the quality of the meshes are optimised. The result of this analysis is presented in sub-section 3.1. The fluid flow over the topography is then simulated via CFD by applying appropriate boundary condition and simulation setup.

Furthermore, at the start of the project essential research was carried out to have better understanding on biofouling towards a surface topography. Information that was obtain from multiple of article and also result from past senior result outcome help to acknowledge the combination of size and geometry type which will be most effective for antifouling application. This stage was crucial because as discussed, this will be the starting point towards this research study. This study will entirely be focused on doing so as mention in the literature review section. Therefore, based on findings done by Min et al. (2017) and Wei et al. (2017), the optimum

combination of topography geometry and topography size from their findings will be analysed to see if it will produce a higher antifouling performance.

The size of the topography will be fixed to 250 µm for simulation as it is believe to be the most optimum topography size for antifouling performance [7]. In addition, uniform dimension will be applied towards the simulation to induced higher wall shear for an ideal analysis [7]. Furthermore, as for the topography geometry pillars will be the choice of shape. Pillars exhibits the highest wall shear stress in comparison to the other type of topography geometry [1].

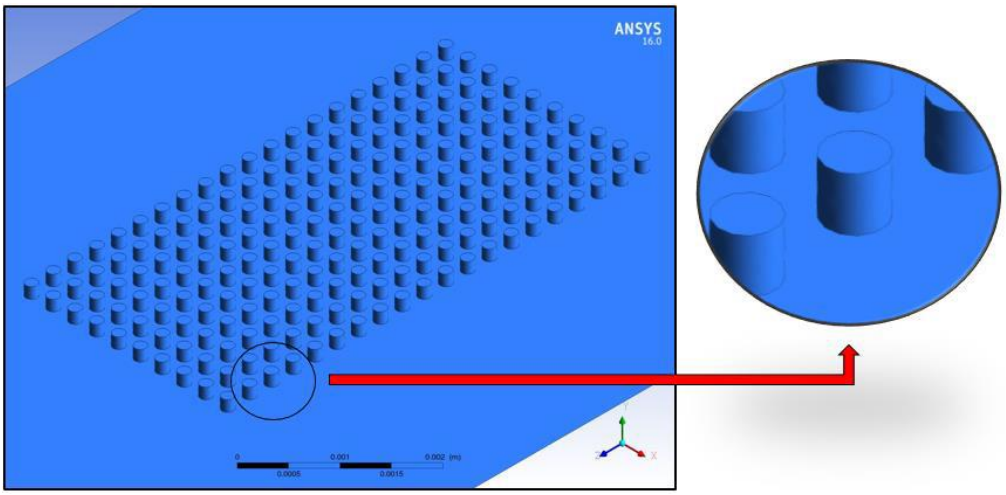


Figure 2: 250 µm topography pillars

The software used to obtain the 3D model as shown in Figure 2 is by computer aided design (CAD) software SOLIDWORKS. As mention above uniform dimension will induce a more ideal analysis, hence the height, width and gaps in between the pillars are all set to 250 µm. Hence, ANSYS was used as it is a cheaper and faster alternative in comparison to a field study.

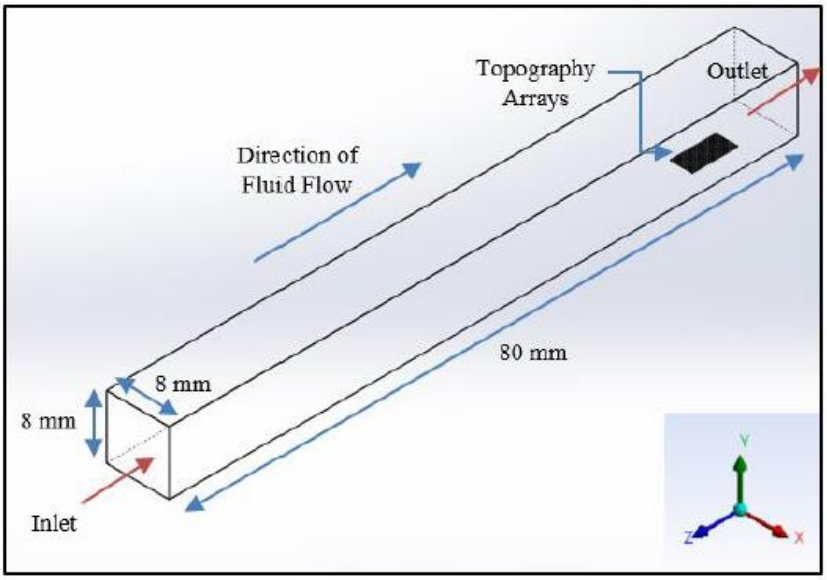


Figure 3: Wire diagram of pillar fluid domain with geometry dimension and topography position [1].

2.2 Meshing Method

The mesh quality of the model will determine the result generated by ANSYS. Appropriate meshing method will be selected for a higher accuracy in end result. Once the skewness and quality of mesh is good (skewness <1, Orthogonal quality >1), but simulation time will increase due to the fact that there are more number of element and time taken for it to converge will also increase. Moreover, ANSYS fluent is used in creating the meshing model of the topography. Firstly, the entire model is meshed with tetrahedral shape elements. Tetrahedral shape element are the primary element in the module because the elements are more versatile and suitable for further refinement especially at the edges and curvatures. This shape provides finer mesh around curvature and edges, which is important especially the model consist of multi-curvature topography features. The face sizing was used at the topography array at the bottom plane. A Sphere of influence was also define around the topography. This sphere allows focused mesh refinement around the topography array without affecting the rest of the fluid domain. Thus, produce better accuracy reading around the topography.

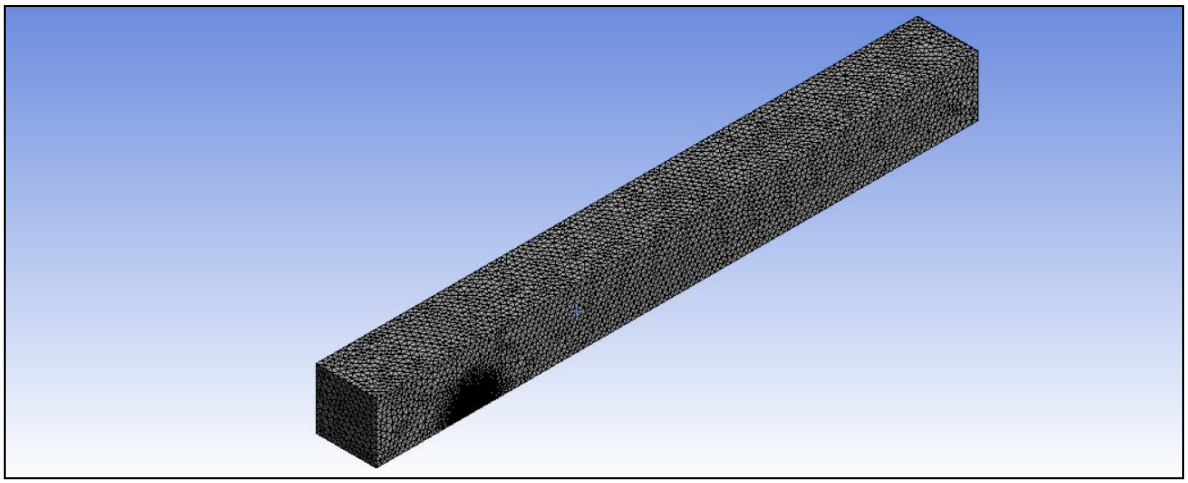


Figure 4: Mesh refinement

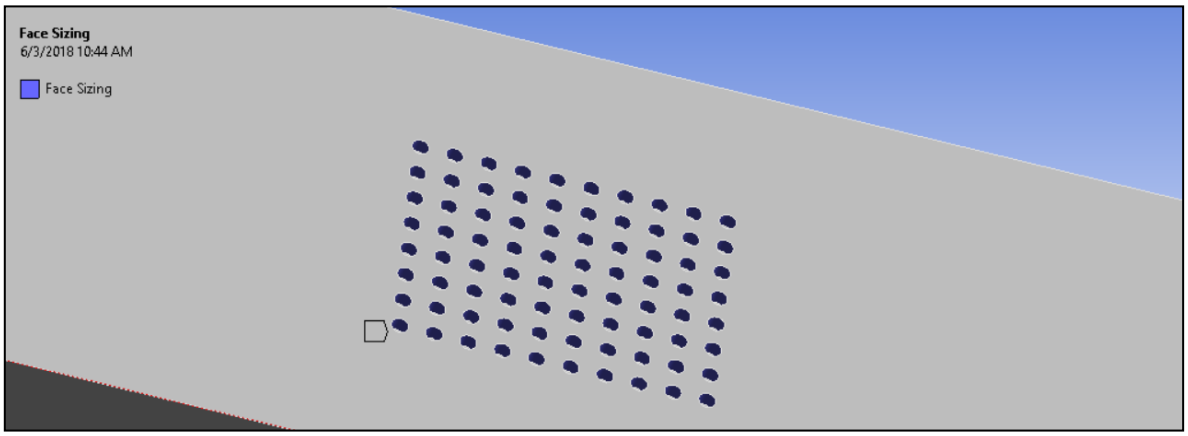


Figure 5: Face Sizing

Wall shear stress is a key parameter that is considered in this study. Therefore, hence inflation layer around the walls are created with 10 layers inflation of elements size 0.1mm. The resulting mesh are as shown in Figure 5. Furthermore, figure 6 shows the close up view of the mesh topography. The boundary conditions in CFD, the inlet, outlet and bottom plane topography was named respectively. This will help the when setting up the simulation, and makes viewing results easier.

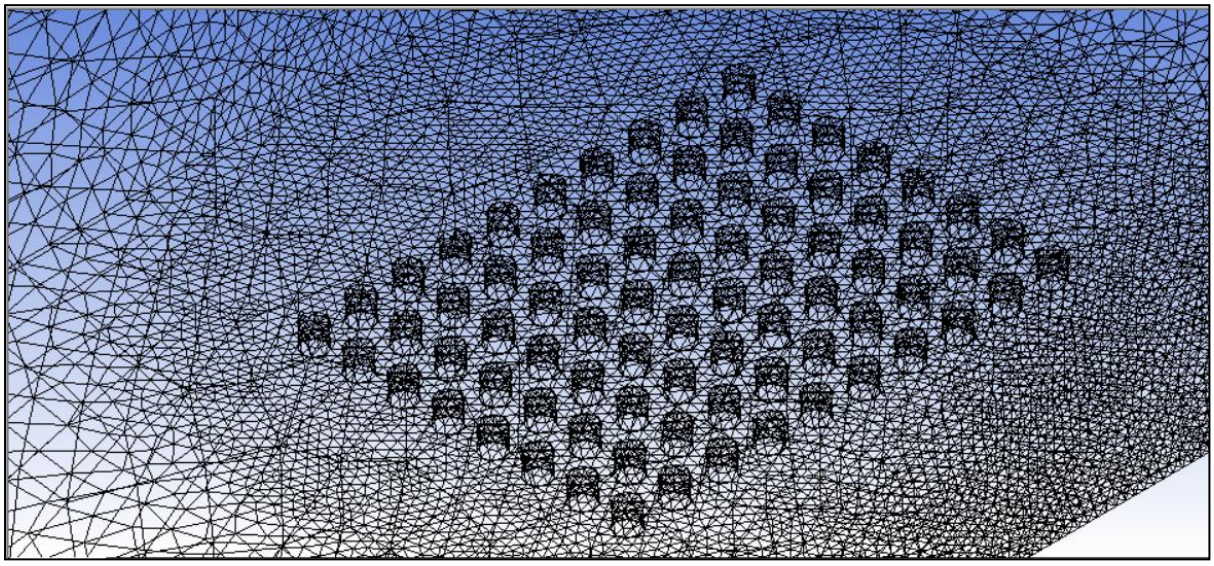


Figure 6: Close view of topography pillar

Next, this project simulation will be carried out using ANSYS Fluent. Parameters and boundary condition of the flow will be fixed based on the research done by Myan et al. (2016), Wei et al. (2017) and Min et al. (2017). Result from the simulation will specify if further optimization toward topography design is necessary to obtain optimum result (project objective). However, the selection for geometry and size will be repeated if the simulation result are not reasonable.

The CFD-software which will be used for this simulation has various equation that comes with the ANSYS Fluent package. The numerous equation presence in the program aids user to produce a result quicker. Among all the various equation, the equation that will be applied to this project would be conservation of mass and moment equation (Eq.3) and the Navier-Strokes equation (Eq.4, Eq.5 and Eq.6) [7].

$$\frac{\delta\rho}{\delta t} + \nabla \cdot (\rho V) = 0 \tag{3}$$

$$\frac{\delta\rho u}{\delta t} + \nabla \cdot \rho u V = -\frac{\delta\rho}{\delta x} + \nabla \cdot (\mu \nabla x) + S_{m,x} \tag{4}$$

$$\frac{\delta\rho v}{\delta t} + \nabla \cdot \rho v V = -\frac{\delta\rho}{\delta y} + \nabla \cdot (\mu \nabla v) + S_{m,y} \tag{5}$$

$$\frac{\delta \rho w}{\delta t} + \nabla \cdot \rho w V = -\frac{\delta p}{\delta z} + \nabla \cdot (\mu \nabla w) + S_{m,z} \quad (6)$$

From the equations, *u*, *v*, and *w* represent the velocity in *x*, *y*, and *z* axis. μ and ρ on the other hand represent the fluid dynamic viscosity and density, P is the pressure and Sm,x, Sm,y, and Sm,z are the source term for the three different axis.

3.0 RESULTS AND DISCUSSION

The hydrodynamic variable that will be analyse from this project will be the wall shear stress, velocity. By doing so, the wall shear on the topography will represent the force or stress induce by the solid boundaries of the topography. Velocity on the other hand represent the flow inside the channel through the topography array and the microorganism. Furthermore, vector shear will show the direction and magnitude of fluid flow. The CFD simulation will be computed with a sample microorganism inserted to replicate an actual event as shown in Figure 7.

Figure 7 indicates how the data of the variable was obtain from the topography array. From the diagram there are three different colored lines. Each line were place at a different location to obtain a more accurate result. Reading was taken from three different level of position because different position will experience different shear stress, velocity and also shear strain which will vary the data collected.

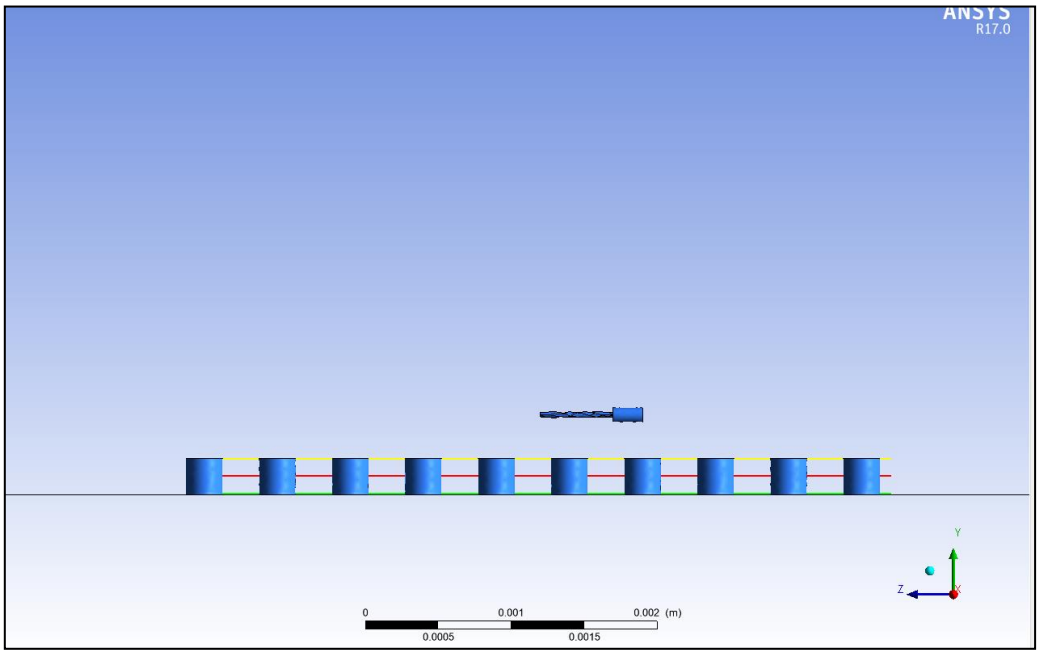


Figure 7: Side view of topography pillar and microorganism.

The yellow line is set to the top of the topography, the red line was set in the middle of the topography and the green line is set to the base of the topography. Thus by doing so, this will help to obtain data from the peak, middle and the bottom of the topography array to provide a better average reading on the variables.

3.1 Grid Independence Analysis

In each individual case, the number of element meshed has been optimized with mesh convergence analysis. By doing so this will help make sure the computational time is minimum without disrupting the quality of the outcome. As meshing with a high element number does not always result in better quality simulation. The following analysis was based on mesh convergence which monitor the flow over the micro-pillars topography [2].

Based on Partha Halder's research, by increasing the mesh element and also simulation of mesh refinement for each individual model. The percentage difference of the wall shear stress will then be tabulated to obtain the percentage of relative error. The mesh will be considered to be optimum when relative error of the wall shear stress is less than 5%. In addition, the incremental in number of element is said to be not worth the computational time if the relative error has a small difference [7].

Table 1 shows the result obtain from this analysis. The model which produce the lowest relative error less than 5% and with the least number of mesh element will be chosen as an optimum model for comparison.

Table 1: Optimum Mesh Element

Number of mesh element	Orthogonal Quality	Skewness (average)	Wall Shear (average)	Relative Error (%)
1670386	0.85736	0.25135	2.38e-02	5.6%
2766623	**0.87051**	**0.22602**	**2.52e-02**	
4226391	0.87446	0.21604	2.58e-02	**2.4%**
5087518	0.87579	0.21437	2.61e-02	1.2%

As observe from Table 1, relative error have significantly reduce as the number of mesh element was increased. Model of 1.6 million was compared to 2.7 million element (relative error was 5.6%). The error obtain is above 5%, whereas when model of 2.7 million was compared to 4.2 million (relative error was 2.4%). The relative error is below borderline, hence the error is smaller compared to 5.6% relative error and it is acceptable for an optimum model selection. Moreover, model of 4.2 million was compared to 5.0 million element (relative error had an increment of 1.2%). From the relative error pattern we can deduce that as the number of mesh element increase, the relative error decreases. Therefore, model with 2.7 million mesh element will be the ideal model selection for this simulation. Reason being 2.7 million mesh element has relative error is below 5% and computational time is less compared to 4.2 million or 5.0 million of mesh element.

3.2 Fluid flow in the fluid domain

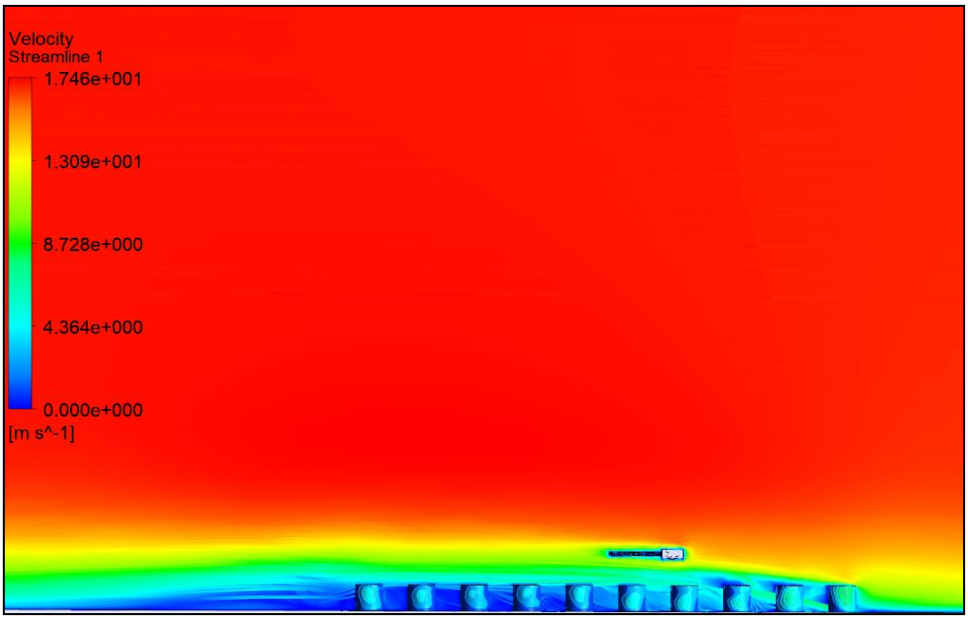


Figure 8: Velocity of fluid flow with the direction of flow moving from the right to the left

Figure 8 shows the velocity contour plot of the fluid flow from the inlet of the fluid domain. The contour plot indicates that velocity in the vicinity of the topography is slower than that or the flow in the main stream above the topography. The topography is a hurdle to fluid flow and the velocity reduces further as fluid moves through the topography array. From Figure 8, it can be observe that the velocity present at the first few topography pillars are higher and the velocity that flows on the top end of the topography pillars are higher. Region which experience a higher velocity will unlikely have high settlement because shear exerted from higher velocity regions will disrupt the stability of the microorganism's movements making it difficult for settlement to take place.

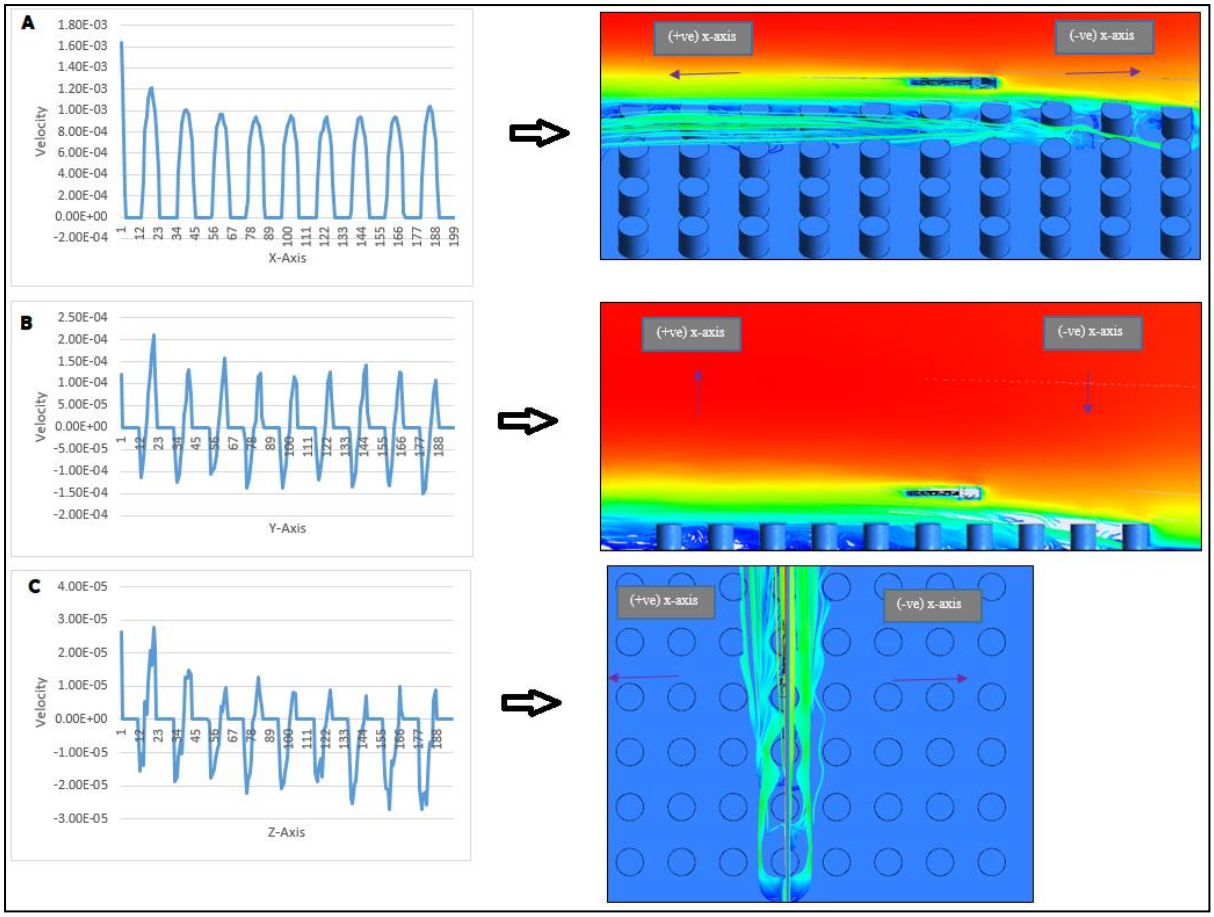


Figure 19: Graph of velocity plot (A) x-axis (B) y -axis (C) z-axis.

Figure 9 is the data exported from the simulation. The graph shows the velocity of fluid particles in the x, y and z direction. The data was collected from the velocity plot on line 1. On the x-axis the graph illustrate a looping like figure that indicate the flow pattern moving in and out through the topography on the x-axis which can be seen from Figure 8. Moreover, on the y-axis show the flow pattern in the fluid domain moving up and down throughout the fluid domain. The positive value indicates the high velocity experienced by the upper region and the negative value at the bottom region. The positive and negative values in the graphs indicate direction of movement of the fluid particles. In the case for velocity in the x direction, positive values are indicative of fluid moving in the forward direction (i.e. from the inlet to the outlet) while negative values mean that fluid is moving backwards. The z-axis represents the fluid flow moving across the breadth of the fluid domain. These are depicted in Figure 9, where the flow can be observe moving through the organism.

3.3 Presence of topography towards wall shear

The presence of wall shear induced by the flow of the fluid over the topographies is likely to contribute to the antifouling properties of the surface. As was stated earlier in the research paper that presences of wall shear on the topography will inhibit microorganism from settling onto the surface. The greater the shear the more difficult it is likely to be for organisms to adhere effectively to the surface. This section discusses results on wall shear that were obtained from the simulations and compares wall shears between 2 models. One with the topography and the other without.

Table 10 shows average wall shear measured at line 1 for the models with and without the topography. There was no wall shear without the presence of the topography which means that the likelihood for organisms to settle on such surfaces is high. This has been affirmed by multiple studies that have conducted experiments and field test and concluded that surfaces without any geometrical features are always more susceptible to fouling [8, 9, 10]. In contrast to the unpatterned surface, the model with the topography presents and average wall shear reading which points to the probability to inhibit organism settlement.

Table 2: Wall Shear Average (Topography)

Wall Shear without Topography	Wall Shear with Topography
-	3.45e-02

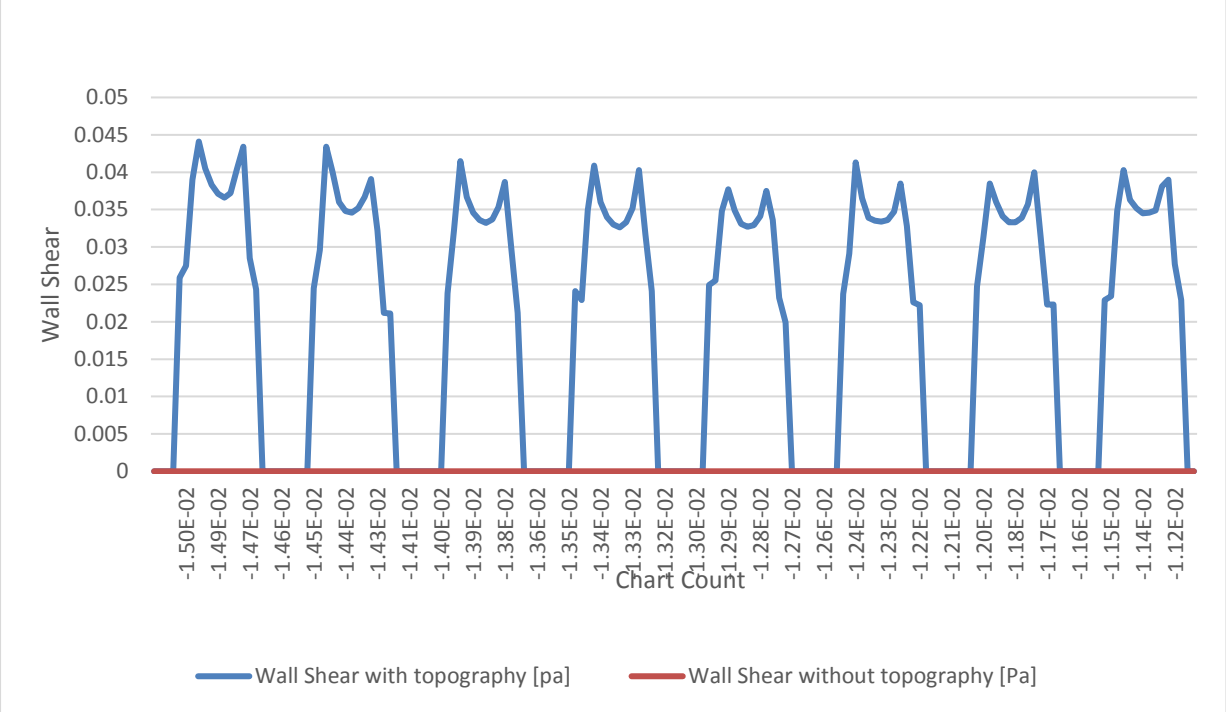


Figure 10: Graph of wall shear with and without topography.

Figure 10 shows the graph that was tabulated from the data obtain via ANSYS fluent and as observe the graph will show the characteristic of the wall shear on both the models. Model that does not have topography is said to be absence of wall shear, hence the straight line plotted on the graph. However, the model with the topography exhibit periodical spike in shear throughout the chart count. This illustrate the presence of the wall shear on the topography pillars with shear being higher at particular points along the topography. The gaps in-between spikes implies that there is a gap between each pillars to the next. Figure 11 complements the readings shown in Figure 10. Spikes in wall shear that are seen in Figure 10 coincide with higher shear stresses (i.e. indicated by the red and yellow regions) at the edges of the pillars as shown in Figure 11. The fluctuations show in Figure 10 also means that there are constant changes in the hydrodynamic conditions near the topography which would make it more difficult for any organism to settle to the surface.

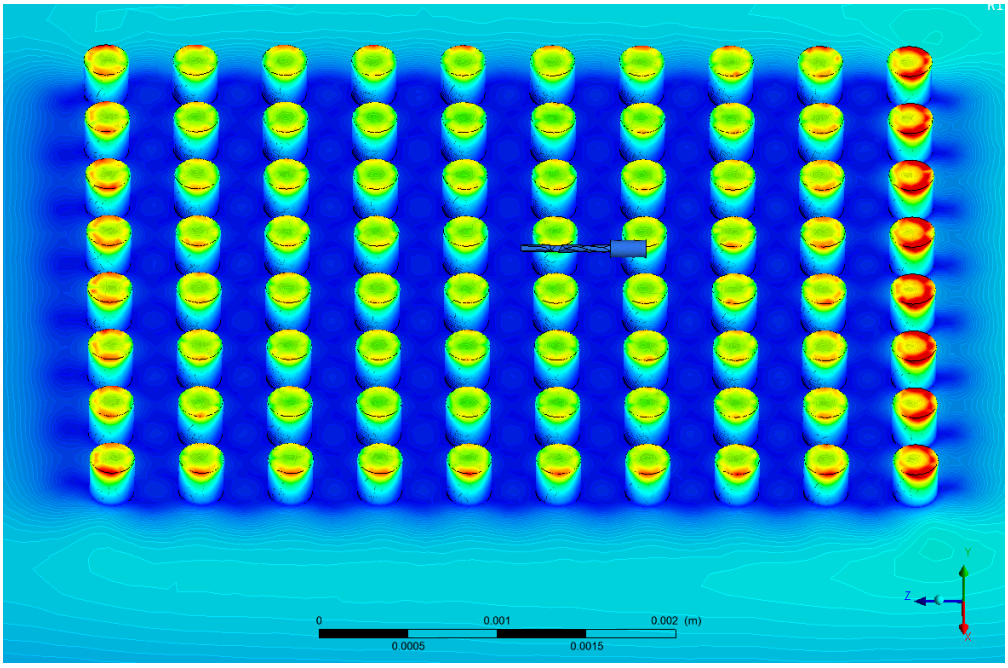


Figure 11: Wall shear contour of topography model.

In addition, Figure 12 illustrates the wall shear experience around the microorganism with and without the presence of topography. The wall shear was absent without the presence of topography which indicates that the possibility for organism settlement onto the surface is high. However, wall shear is presence and gradually increasing with the present of the topography as shown in Figure 12. Table 3 shows the average reading obtain from the simulation where the presence of topography result in much higher stress in comparison to the absent of topography. Hence, this proves that presence of topography is crucial towards optimized antifouling potential.

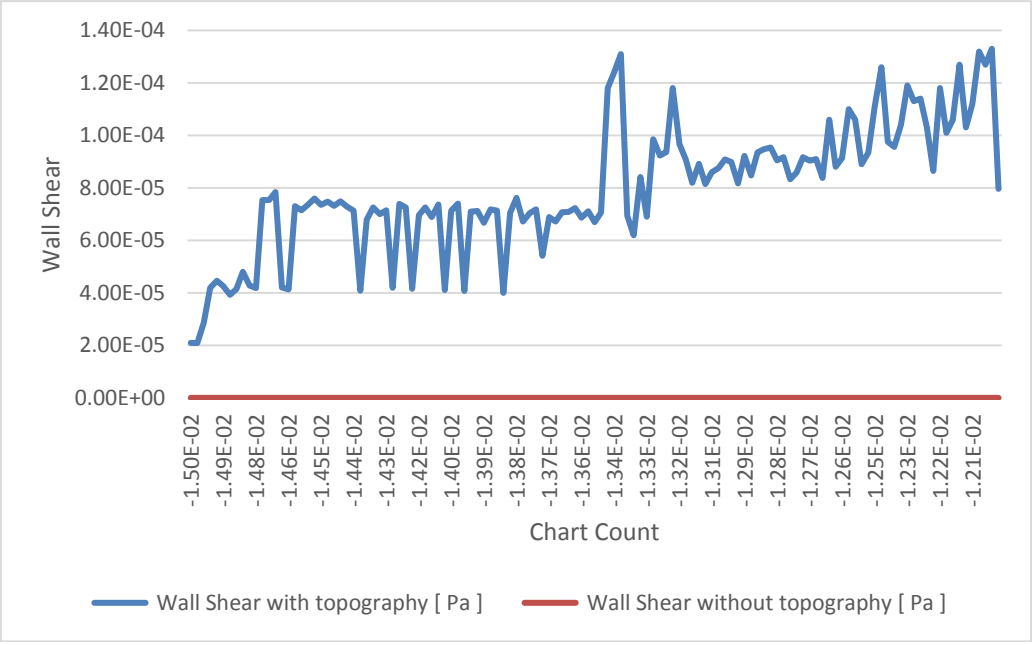


Figure 20: Wall shear around the microorganism

Table 3: Wall Shear Average (Microorganism)

Wall Shear without Topography	Wall Shear with Topography
-	7.96e-05

4.0. Conclusions

This research aimed is to determine the outcome between the combination of optimum topography geometry and optimum topography size towards antifouling potential. This research was completed with the aid of numerical analysis (ANSYS Fluent with k-ω model). The simulation that was carried out exhibit the hydrodynamic flow around the topography surface. The flow at the peak of the topography is said to experience higher stress which indicate the opportunity to reduce settlement. Whereas the middle region and the lower region have a calmer flow which makes it a better tendency for settlement. However the possibility can be reduce as the presence of vortices in between topography pillars increases. Presence of high vortices will prevent the microorganism from getting a firm hold.

Multiple studies have been done before this on antifouling topography which mostly highlight the physical characteristic such as their size, shape, height and distance in-between. However, this study shows the outcome when optimum topography geometry and optimum topography size is combined to produce an antifouling topography surface. By doing so, it has been noted that the combination between optimum size and optimum geometry resulted in a fairly good positive outcome. The outcome can be seen from the result produce by the simulation. The result shows good antifouling potential towards microorganism settlement.

As for this research, it is noted that study will not be able to imitate an actual marine environment. However, the numerical analysis (ANSYS Fluent) method that was used during this study is sufficient to gain knowledge and understanding of the flow characteristic and also the variable that was selected as region of study. In addition, there are still various research and study towards antifouling potential besides the optimum topography geometry and optimum topography size. In conclusion, further studies should be carried out toward antifouling topography. As this method to prevent biofouling will be very beneficial to the users and the environment. Future studies should include nano-sized topography and a more advance simulation which also include field test for a more realistic and better antifouling performance.

Therefore, to summarize this research topography with size of 250 μm and pillar geometry exhibit good antifouling potential and optimized topography surface exhibits antifouling potential via the dynamic stability of the microorganism.

5.0 Reference

[1] L. K. M. F. W. Myan, L. C. Hong, “A Numerical Assessment of microtopographies with Varied Geometries in Relation to Biofouling Controlo Title,” *Proc. 8th Eureca 2017*, p. 56, 2017.

[2] F. W. Y. Myan, J. Walker, and O. Paramor, “The interaction of marine fouling organisms with topography of varied scale and geometry: a review,” *Biointerphases*, vol. 8, no. 1, p. 30, Nov. 2013.

[3] I. Fitridge, T. Dempster, J. Guenther, and R. de Nys, “The impact and control of biofouling in marine aquaculture: a review,” *Biofouling*, vol. 28, 2012.

[4] M. Lejars, A. Margaillan, and C. Bressy, “Fouling release coatings: a nontoxic alternative to Biocidal antifouling coatings,” *Chem Rev*, vol. 112, 2012.

[5] M. Wouters, C. Rentrop, and P. Willemsen, “Surface structuring and coating performance: novel biocidefree nanocomposite coatings with anti-fouling and fouling-release properties,” *Prog Org Coat*, vol. 68, 2010.

[6] H. Zhang, R. Lamb, and J. Lewis, “Engineering nanoscale roughness on hydrophobic surface---preliminary assessment of fouling behaviour,” *Sci Technol Adv Mat*, vol. 6, 2005.

[7] Y. Y. W. F. W. Myan, L. C. Hong, “Assessing Flow Over Patterned Surfaces of Varied Sizes in Relation to Biofouling Controle,” *Proc. 8th Eureca 2017*, p. 67, 2017.

[8] L. J. Walters and D. S. Wethey, “Settlement, refuges, and adult body form in colonial marine invertebrates: a field experiment,” *Biol Bull*, vol. 180, 1991.

[9] J. F. Schumacher *et al.*, “Species-specific engineered antifouling topographies: correlations between the settlement of algal zoospores and barnacle cyprids,” *Biofouling*, vol. 23, 2007.

[10] L. J. Walters and D. S. Wethey, “Settlement and early post-settlement survival of sessile marine invertebrates on topographically complex surfaces: The importance of refuge dimensions and adult morphology,” *Mar Ecol Prog Ser*, vol. 137, 1996.

EURECA 2018 – Conference Paper
Paper number 2ME20

Mathematical Modelling of Isokinetic Testing with Energy Balance and Body Fat among Male Young Adults

Muhammad Fadzrul Hafidz[1,], and Ku Pei Xuan[1]*

[1]Department of Mechanical Engineering, Taylor's University, 47500 Subang Jaya, Selangor, Malaysia

Abstract It is believed that body fat plays in influence in affecting a person's absolute strength. The higher the amount of body fat in a person will enable him to exert greater force or torque when it comes to exercise, showing that a person with higher amounts of body fat have higher strength levels compared to their counterpart with lower amounts of body fat. However, it is important to note that possessing very high levels of body fat (obesity) show negative implications, and places the person at higher risk of major health problems such as heart disease and diabetes. This research aims to correlate the relationship between a person's body fat level and their energy balance (strength levels), where it is tested in an isokinetic testing experiment which tests the extension of the quadriceps muscle to determine the average peak torque, with the correlation then being formulated into a mathematical model. 40 male young adults (mean age = 22.75 ± 2.10 years; mean height = 1.71 ± 0.05 m; mean weight = 69.36 ± 3.26 kg; mean BMI = 23.67 ± 4.15) participated in this study. The participants are split into three groups, classified as: underweight, normal, and overweight. One-way ANOVA analysis was used to evaluate the differences in the values of the average peak torque between the three groups. It is shown that the average peak torque values of the overweight group is higher (APT = 226.23±31.10Nm) than that of the normal (APT = 210.43±24.56Nm) or underweight (APT = 167.63±24.87Nm) groups, thereby showing that those with higher amounts of body fat have greater strength compared to their normal or underweight counterparts. It is thought that this difference is due to extra weight carried by overweight people which acts as an energy source which provides higher amount of energy during vigorous exercise, thus improving muscle performance.

Keywords: isokinetic testing, energy balance, body fat, mathematical modelling, peak torque

1. Introduction

The prevalence of obesity is proving to be a growing health problem across the world, especially in that of developed and developing countries [1]. A study from the National Health and Morbidity Survey in the year 2015 among Malaysian adults have reported that a staggering 51.2% of Malaysian adults are either classified as overweight or obese [2]. It was also reported that the prevalence of obesity in Malaysia is more than three to four times higher than several other Asian countries, such as Japan, China, India, and Taiwan, and Malaysia is also recognised as the country with the highest obesity rate in South East Asia. Obesity is acknowledged as the cause of several major health complications, such as diabetes mellitus, cardiovascular problems, cancer, as well as respiratory problems [3]. Furthermore, an obese person is more functionally limited when compared to a non-obese person.

The Body Mass Index (BMI), also known as the Quetelet Index, is the most common index used for obesity, and it classifies a person with a BMI of 25-29.9 as overweight and a person with BMI >30 as obese. It is postulated that a high BMI has a negative effect on fitness level in terms of endurance in studies which involve people who are overweight or obese. On the other end of the spectrum, however, a very low BMI also has a negative effect on fitness, where people with low BMI perform poorly in tests involving muscle strength. This is in due to the fact that people with lower BMI have lower amounts of muscle mass.

Strength wise, however, it is theorised that obese or overweight adults perform better in fitness strength tests, and have been shown to generate higher amounts of torque and power in muscles of the lower extremity such as the knee when compared to their counterparts. This is perhaps due to the higher amounts of fat free mass in overweight people, as well as having higher energy storage in the body. This can be demonstrated in isokinetic or isometric testing, especially that of the knee extensors of the quadriceps muscle.

Isokinetic testing is a computerized testing for measure of muscle function and is one of the most useful methods for assessing muscle strength, and is conducted with an isokinetic dynamometer. Isokinetic dynamometers enable dynamic exercises to be carried out according to a predetermined angular velocity and resistance where subjects are required to perform maximal contraction with full range of motion throughout the testing duration [4]. Owing to its potential for enabling maximal effort in a safe manner in a control environment has considered isokinetic testing to be the gold standard in strength testing, and its use has been encouraged in training, evaluation and analyzation of musculoskeletal function as well as rehabilitation from injuries. The isokinetic dynamometer comes with differing angular velocities, with the angular velocities most commonly being used being 60°/s, 180°/s and 300°/s.

The aim of this study is to compare the relationship in absolute strength between overweight and non-overweight individuals in young adults aged 18-30 years old leading sedentary lifestyles, while also considering other parameters such as BMI, weight, height, and age to formulate a mathematical model which best describes the relationship.

2. Research Methodology

2.1 Gathering and recruitment of participants

A total of 40 healthy male young adults (mean age = 22.75±2.10 years; height = 1.71±0.05 m; weight = 69.36±13.26 kg; BMI = 23.67±4.15) have agreed to volunteer and participate in the study. As per the inclusion criteria, participants are between the ages of 18 to 30 years old, are healthy and of sedentary and moderately active lifestyles, not actively taking part in sports or weightlifting, and favouring the right limb as the dominant limb. All participants have agreed and signed a written informed consent form to participate in the study, and this procedure conducted is in accordance to the Human Ethics Policy set by Taylor's University, as well as by the University of Malaya.

Table 1. Inclusion and exclusion criteria for participants

Inclusion criteria	**Exclusion criteria**
Male Aged between 18-30 years old Right foot and hand dominant Engage in little to no physical activity (no more than 2 hours per week maximum)	Athletic background Chronic or previous injuries which affect physical performance Frequently engage in physical activity Mental or physical limitations which can affect performance

2.2 Instrumentation

The isokinetic testing experiment is conducted using the Cybex HUMAC NORM Isokinetic Dynamometer in the Sports Centre of University of Malaya. The isokinetic dynamometer is used to measure the average peak torque of flexion and extension in concentric motion for the quadriceps muscle. The isokinetic dynamometer consists of a head unit which acts as an interface between the user and the system, which also displays the appropriate data on the computer screen. The dynamometer also comes fitted with a seat which can be rotated 360°**,** and is also horizontally and vertically adjustable to accommodate to the user's anthropometric criteria such as height. In addition, a skinfold caliper was used to measure the percentage of body fat by measuring the thickness of the skin at three sites of the body, which are: chest, abdomen, and thigh.



Fig. 1. HUMAC NORM isokinetic dynamometer

2.2 Obtainment of anthropometric measurements

Anthropometric measurements regarding the participants, such as age, weight, height, and sex are recorded and entered into the system. The person's weight was measured to the nearest 0.1kg using an electronic weighing scale, and height was measured using a standing stadiometer accurate to the nearest 0.01m. In order to obtain the most accurate reading of weight and height, the readings were taken without shoes and any heavy clothing, such as jackets, were taken off. After the participant's weight and height are obtained, body mass index (BMI) can then be calculated using the formula below:

$$\text{BMI} = \frac{\text{Weight (kg)}}{\text{Height}^2\,(\text{m}^2)} \quad \text{(eq. 1)}$$

In addition, the participant's skinfold measurements was taken using calipers, accurate to the nearest 1mm, with measurements taken at three sites of the body, namely the chest, abdominals, and thighs, before conducting the test. The measurements for each site were taken a total of 3 times to obtain an average value. The measurements obtained were substituted into Jackson and Pollock's formula for calculating body density (B.D.) which is listed below:

$$\text{B.D.} = 1.1093800 - 0.0008267\,(X_1) + 0.0000016\,(X_1)^2 - 0.0002574\,(X_2) \quad \text{(eq. 2)}$$ [5]

Where:

B.D. = body density

X_1 = sum of skinfold measurements (chest, abdomen, thigh)

X_2 = age of test subject

By obtaining the B.D., the subject's body fat percentage can then be calculated using Siri's formula, given below:

$$\text{Body fat \%} = [(\frac{4.95}{B.D.}) - 4.5]\ 100 \quad \text{(eq. 3)}$$

After obtaining the anthropometric data of the participants, participants were then split into three groups, which are: underweight (BMI<18.5), normal (18.5-24.9), and overweight (>25) for analysis and comparison purposes.

Table 2. Anthropometrical data for the three subject groups

	Underweight (n=8)	**Normal (n-=18)**	**Overweight (n=14)**
Age (years)	23 ± 3.25	22.33 ± 1.41	23.14 ± 2.11
Height (m)	1.67 ± 0.06	1.72 ± 0.06	1.71 ± 0.06
Weight (kg)	52.75 ± 5.85	66.59 ± 5.93	82.41 ± 9.96
BMI (kg/m^2)	19.02 ± 1.86	22.18 ± 1.58	28.23 ± 2.82
Body Fat (%)	9.53 ± 2.33	13.26 ± 2.96	23.09 ± 6.54

Values are stated in mean ± SD

BMI = body mass index

2.3 Dynamic warm up exercises and ergometer cycling

Prior to beginning the experiment, a few dynamic stretching exercises were done to loosen the muscles of the body and to improve blood flow to the muscles. Three dynamic exercises, which are the squat, high knee, and the leg extend, with 10 repetitions done for each exercise. Following which, the participants warm up by cycling on the ergometer bicycle for 5 minutes at medium speed.

2.4 Experimental Procedure

The HUMAC NORM isokinetic dynamometer is appropriately calibrated based on the required parameters of the procedure, such as

a. speed which is set to an angular velocity of 60°/s
b. range of motion (ROM) which is set to 90° extension
c. concentric contraction of the muscles

The experiment is then conducted with the participant in a seated position complying with the principles of positioning which are:

a) the limb is aligned parallel to the lever arm of the dynamometer
b) the anatomical axis of rotation for knee and elbow joint are aligned with the rotational axis of the dynamometer
c) the proximal joints, eg chest, thigh, and ankle were properly stabilized using straps, and the participants held on to the handles on both sides for better stabilization

To test the quadriceps muscle, the isokinetic dynamometer was set up according to the instructions on the manual of the device in accordance to knee extension. The positioning of the seating was adjusted based on the participant's body size, the seat was adjusted to place the knee of the participant level with the center of the load cell, and the chest, pelvis, and thigh were then stabilized in order to eliminate secondary muscle involvement. To secure the participant to the seat, and to minimize body movements during the procedure, which can cause the contribution of other muscles to the contraction other than the knee, the participant is strapped across the shoulder, pelvis, as well as the middle part of the thigh.

The procedure begins with the participant seated at 90° flexion of the knee. The participant is required to perform full maximal contractions of the quadriceps muscle for a total of five repetitions obtain the reading of maximum peak torque. The procedure is conducted with a total of five trials, with five repetitions (contractions) per trial, with a rest period of 1 minute between trials. The highest reading of each trial was recorded, and was then used to find the average reading.



Fig. 2. Participant conducting the isokinetic testing experiment

2.5 Statistical Analysis

The experimental results obtained are expressed in values of mean ± standard deviation. Normality test using the Kolmogorov-Smirnov test was done to identify if the the data obtained is normally distributed, where it is confirmed to be normally distributed. For the purpose of statistical analysis, the participants were categorised into three groups according to their respective body mass index, which are: underweight (BMI <18.5), healthy (BMI 18.5-24.9), and overweight (BMI >25). One-way ANOVA was used to analyse and examine the differences associated between the readings of the peak torque and BMI between the 3 groups. The significance level was set to $P<0.05$, or 5%, with a value of less than 0.05 indicating statistical significance in the data, proving that the results obtained are not due to chance or coincidence. Statistical analysis of data is done using the IBM SPSS v23 software for Windows.

2.7 Mathematical Modelling

Based on the results obtained, stepwise regression analysis of the parameters such as body fat, BMI, weight, height, and age was conducted to determine the suitable predictors and its significance to the response, where predictors which are not significant to the response are removed until on the suitable predictors remain, where the final model can then be obtained and formulated. The mathematical model formulated was then analysed using MATLAB R2017b software using regression analysis application, where the Predicted versus Actual plot, and Response plot is generated to evaluate the suitability of the model created.

3. Results and Discussions

Table 3. Average peak torque readings for all three groups

Group	N	Mean APT	Std Deviation	P value
Underweight (BMI <18.5)	8	167.63	24.87	<0.001
Normal (BMI 18.5-24.9)	18	210.43	24.56	<0.001
Overweight (BMI >25)	14	226.4	33.95	<0.001

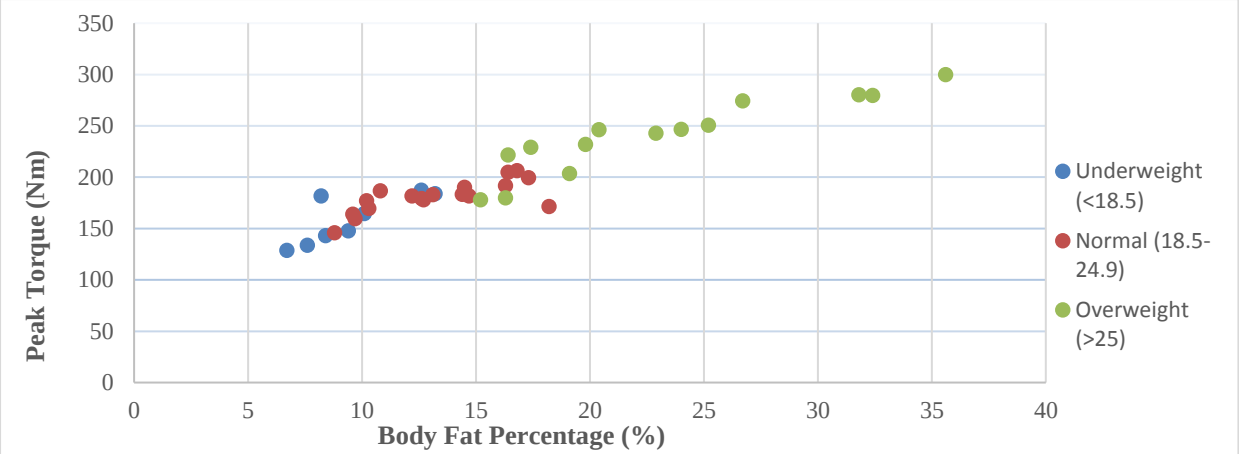


Fig. 3. Correlation of body fat percentage (%) against peak torque (Nm)

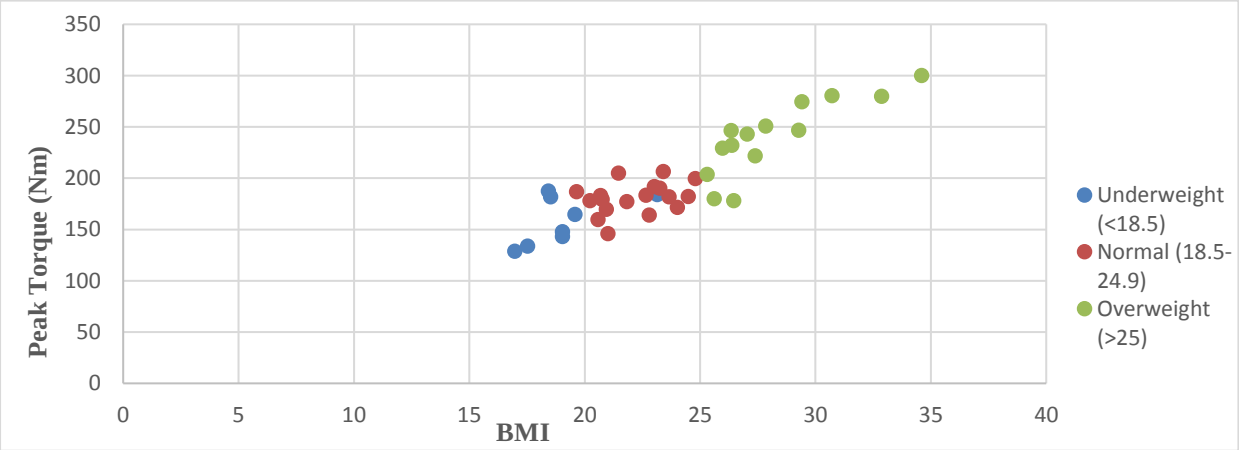


Fig. 4. Correlation of BMI against Peak Torque (Nm)

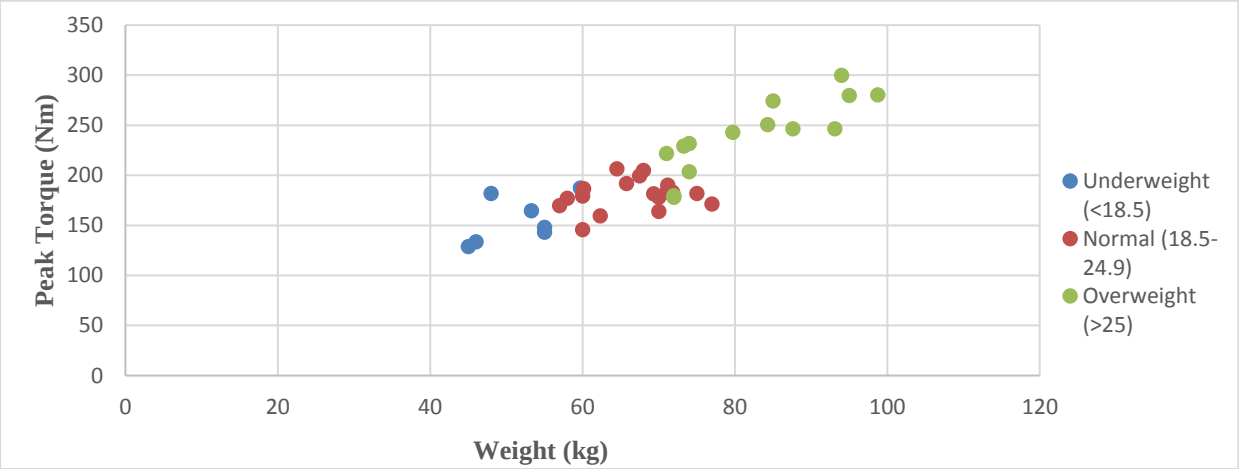


Fig. 5. Correlation of (kg) against peak torque (Nm)

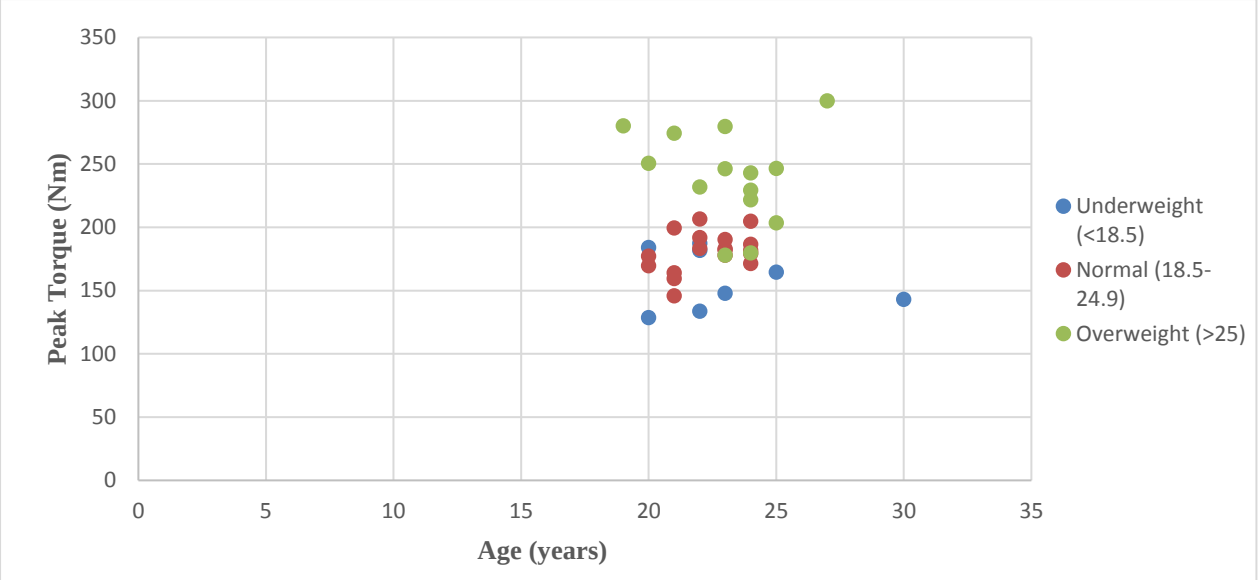


Fig. 6. Correlation of age (years) against peak torque (Nm)

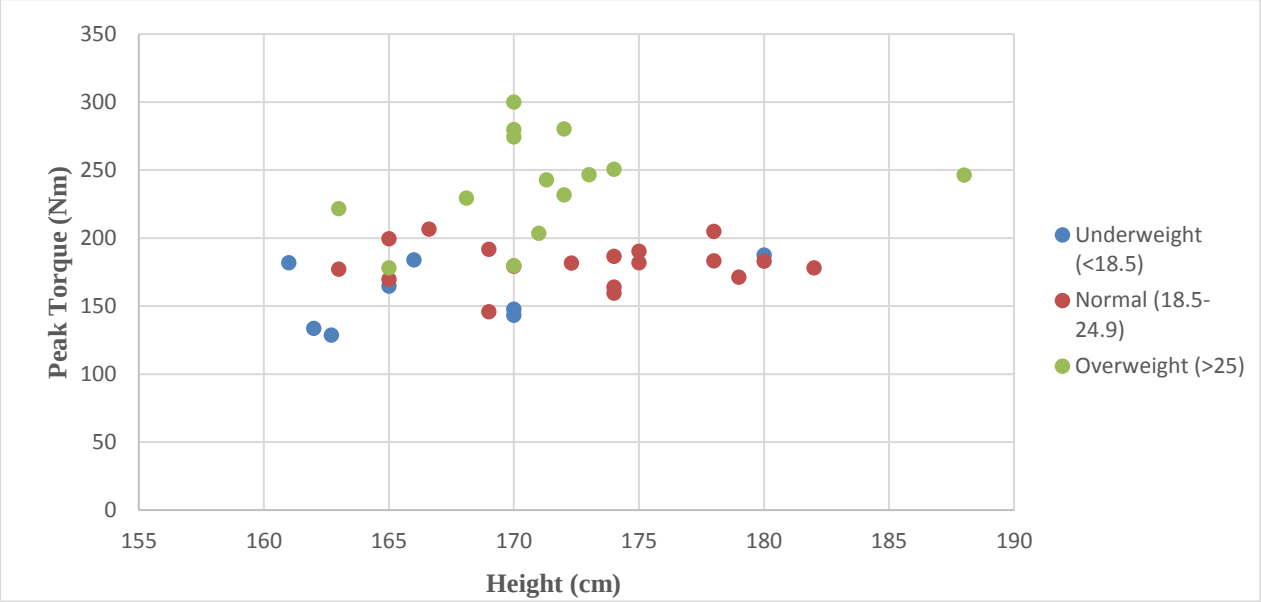


Fig. 7. Correlation of height (cm) against peak torque (Nm)

The readings from the experiment are obtained, and a graph correlating the relationship between a person's body fat percentage and their peak torque readings from maximal contraction is plotted in figure 3. By referring to the graph plotted, it can be seen that the readings of average peak torque generally increase with an increase in body fat percentage, showing a trend of positive correlation between body fat and maximal strength. It can also be seen that the values of average peak torque between the three groups show a significant difference, which is validated using SPSS. Results show that the average readings of peak torque for the overweight group are higher than those of the normal and underweight groups, with the average readings of participants below 15% body fat ranging from below 150-200 Nm. As the body fat percentage of participants go from the 15-25 % range, it can be generally seen

that the average peak torque readings range from around 200-250 Nm, whereas participants with body fat percentages above 25% showing even higher readings ranging from above 250-300 Nm.

Despite the fact that there is an increasing trend between body fat percentage and maximal strength, there are several readings which lie slightly outside of the trend, where it displays a higher or lower reading when compared to the trend. For example, some participants with a higher body fat percentage have a lower average peak torque reading compared to those with a lower body fat, and some instances where the opposite occurs is also observed. This is analyzed and is concluded to be due to several reasons. In experimentation involving human participants, the different human characteristics will influence their performance in the experiment. One such characteristic is the fact that different people have different natural strength levels. Due to reasons such as genetics, there are some people who are simply naturally physically stronger when compared to other people of the same anthropometric criteria. Thus, it is possible that a person who has a lower body fat can be stronger compared to a person who has a higher body fat percentage, and vice versa. Although another possibility may be due to the fact that the participant does not apply his maximal force during the experiment.

Similar results and trend can be seen in the figures 4 and 5 which correlate the relationships between BMI and weight with its effect on average peak torque, where it shows that an increase in BMI or weight will result in a linear increase in the peak torque produced. However, even though body fat percentage and BMI both have a linear effect towards maximal strength, it should be noted that both parameters have a different effect on the maximal strength. BMI takes into account the total weight of a person in relation to his height, and does not take into account the body fat percentage. For instance, people with very high levels of physical fitness, such as athletes, soldiers, and bodybuilders, generally have very low levels of body fat but have average to high BMI due to the amount of muscle mass possessed by the person which adds to his total mass.

These findings corroborate and support the findings of several previous studies, such as a study previously conducted by Maffiuletti et al. [6]. The study which analyzed the effects of obesity in muscle strength of adolescents reported that obese adolescents generated higher absolute contraction during testing. The study was done in similar conditions where the participants did not partake in rigorous physical activity and are generally only moderately active individuals. This is important to note because the amount of physical activity done seemingly has an effect towards increasing strength in the muscles of the lower limb which can affect the results during testing, as indicated by a previous work by Blimkie et al. [7] which reports that there are no major differences in absolute isometric knee strength between obese and non-obese individuals, however Blimkie et al. did not take into account for physical activity levels, which might be the cause of the differences in the results of the two studies mentioned.

Another study by Maffiuletti et al. [8], this time conducted on young adults as well as adults, have reported similar results compared to those of adolescents, with obese adults having 16% higher absolute isometric torque and 20% absolute isokinetic torque, as well as having higher torque on all angles and velocities. This shows that, compared to adolescents, adults do not

appear to favor a specific muscle length, whereas adolescents show higher absolute strength when tested at shorter muscle lengths.

Lafortuna et al. [9] and Tomlinson et al. have both reported that, in the 18-49 years old population, the increase of BMI and adiposity is associated with the increase of muscle volume, explaining the rise in strength in obese people [10].

These greater readings in the overweight group when compared to their normal or underweight counterparts can be due to several reasons. Overweight people carry extra weight in their bodies functions as an energy store, therefore they have higher energy storage which serve as a favorable muscle stimulus when it comes to exerting and generating force during strenuous activity, thus improving muscle performance. Due to higher energy capacity, a higher amount of force is generated, which is reflected in the results.

Even though it seems to be a positive finding that people with higher body fat levels have higher maximal strength, it should be noted that accumulating very high amounts of body fat can lead to severe health issues. Maffiuletti et al. [11] has reported that a very high amount of body fat is associated with postural instability in obese males, which increases the possibility of falls occurring when performing daily activities. In addition, obese people are also functionally limited when it comes to performing simple everyday tasks such as standing up from a sofa, or picking something up from the floor. Furthermore, overweight and obese people do not have the muscle endurance compared to people with normal body fat levels to undergo vigorous training for a prolonged period of time.

By analyzing figure 6 and 7, it can be seen that the factors of age and height do not play a significant role in affecting the average peak torque readings for this study. It is analyzed that the age difference between all participants is too small for it to affect maximal strength as the range is only of the young adult population. As a person ages, muscle loss and function is experienced, in what is known as sarcopenia [12]. Lemmer et al. [13] has shown that participants within the 20-30 years old range have significantly greater 1RM strength when compared to participants within the 65-75 years old range, indicating that age is negatively associated with strength in different age groups. Keller et al. [14] has stated in a study that muscle and strength loss is accelerated as a person approaches the age of 40.

In a study conducted by Miyatake et al. [15] which investigates the relationship between anthropometric parameters and muscle strength in adolescents, it is found that height is significantly correlated with muscle strength, particularly that of the leg. This differs with the findings obtained from this study where it is shown that height does not play a significant role in affecting muscle strength. However, the study from Miyatake et al. did not take into account the physical activity levels of the participants, thus the participants could be more diverse in terms of physical activity, unlike this study where all participants are required to be of a sedentary lifestyle.

Based on the analysis done on the parameters, multiple regression analysis is done to evaluate the effect of the parameters such as height, weight, age, BMI, and body fat percentage on the maximal strength. The five variables were analyzed using multiple regression backward

elimination analysis, and each redundant parameter was removed until only the relevant parameters remain to form the mathematical model.

Table 4. Regression statistics for 5 variables

Regression Statistics	
Multiple R	0.947289462
R Square	0.897357324
Adjusted R Square	0.882262813
Standard Error	14.33408557
Observations	40

Table 5. Regression values for 5 variables

	df	**SS**	**MS**	**F**	**Significance F**
Regression	5	61073.99759	12214.79952	59.44924698	7.83993E-16
Residual	34	6985.844308	205.4660091		
Total	39	68059.8419			

Table 6. Significance level for 5 variables

	Coefficients	**Standard Error**	**P-value**
Intercept	35.99779285	177.2481845	0.840273228
BF%	5.115562531	1.003414439	1.28138E-05
Age	-0.877734408	1.18373227	0.463483209
Weight	-0.364567418	1.208771035	0.764792756
Height	0.457635635	1.109590033	0.682608508
BMI	1.968977217	3.405772915	0.566986593

To determine the relevant parameters, the P-value of the parameters were observed. Following the $P < 0.05$ value for statistically significant values, the values which are not statistically significant are removed from the model as it indicates redundancy for inclusion into the mathematical model. Based on the observed P-values, it can be seen that the age, weight, height, and BMI parameters have a value higher than 0.05, and thus are removed from

the equation. The backward elimination regression is conducted again, this time with only the relevant parameters, in this case the body fat percentage.

Table 7. Regression statistic for one variable

Regression Statistics	
Multiple R	0.945806876
R Square	0.894550647
Adjusted R Square	0.891775665
Standard Error	13.74281273
Observations	40

Table 8. Regression values for 1 variable

	df	**SS**	**MS**	**F**	**Significance F**
Regression	1	60882.97564	60882.97564	322.362573	3.71494E-20
Residual	38	7176.866261	188.8649016		
Total	39	68059.8419			

Table 9. Significance level for 1 variable

	Coefficients	**Standard Error**	**P-value**
Intercept	107.3580723	5.456623894	1.59608E-21
BF%	5.634245118	0.31380758	3.71494E-20

Through backward elimination method, the parameters BMI, weight, height, and age is found to not be significant in affecting the maximal strength in this case, and only body fat is shown to be the significant predictor. Thus, the mathematical model is formulated which correlates the relationship and is shown in the equation created below:

$$y = 107.36 + 5.63\,(x) \qquad \text{(eq. 4)}$$

Where:

y = maximal strength

x = body fat percentage

Regression is done again where body fat and APT, was plotted into MATLAB R2017b using the regression learner application, where a predicted vs actual plot, and a residual plot were obtained. The plots obtained were analyzed in order to evaluate the suitability of the model used, and are plotted below:

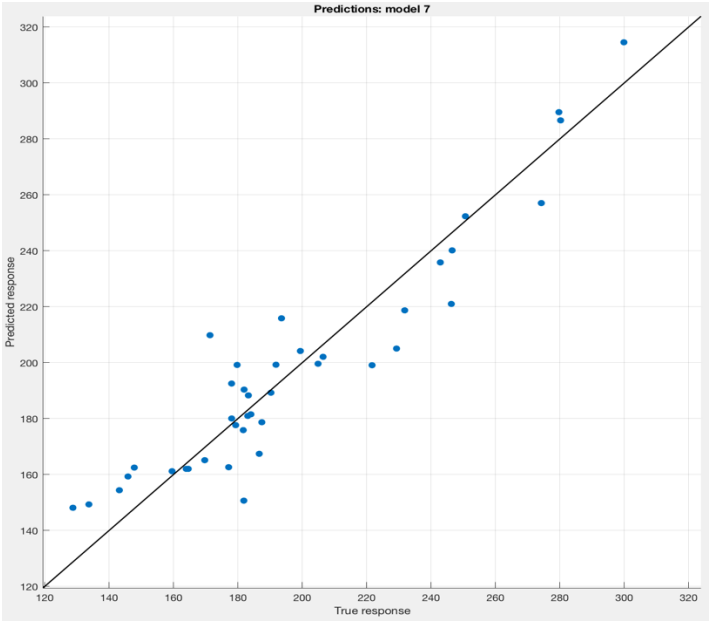


Fig. 8. Plot of predicted versus actual values

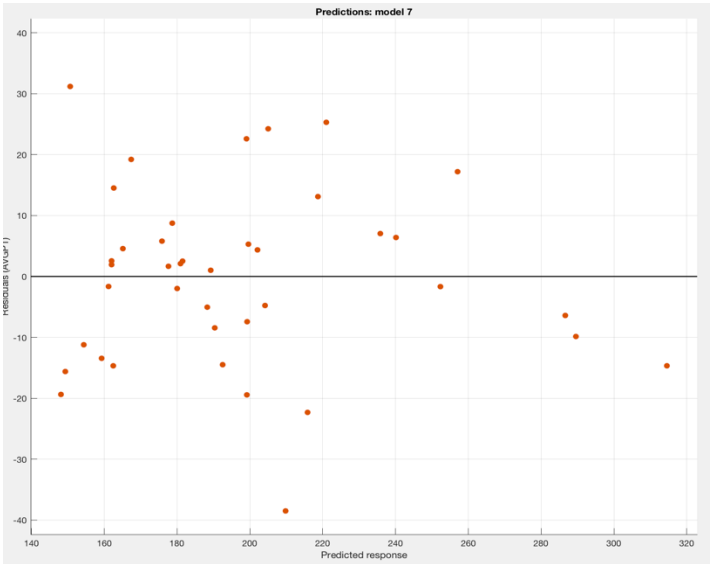


Fig. 9. Residual plot

By observing the plot of predicted versus actual values in figure 8, it can be seen that most data points are distributed along the regression line. This shows that there is a strong correlation between the predicted values of the model and the actual values. In addition, the plot has an r-squared value of 0.88, which is a measure of the closeness of the data values to the fitted regression line. Values of r-squared run from 0 to 1, with a value closer to 1 is accepted as the better value as it indicates a better fit of the data values to the regression line. Thus, this shows that the model formulated is suitable to be used.

Figure 9 shows the residual plot of the model. Residual is the difference between the observed value and the predicted value of the variables. It can be seen that the data points on the residual plot seem to be randomly symmetrically distributed and clustered towards the centre of the residual plot, which indicates that the predictions of the model is on target. Thus, this shows that the model created is of at least satisfactory condition.

The creation of this mathematical model will play a huge role in contributing to sustainable development as a guide to researchers in helping to understand and predict the behavior and correlation between body fat levels and how it affects maximal strength. Furthermore, the creation of this mathematical model will serve people in terms of providing knowledge and education towards the relationship between these two parameters and how they affect each other.

It should be noted that this study does have several limitations. Firstly, it can be considered that the sample size used for the experiment is fairly small, and the demographic of the study is also limited to young adults with sedentary lifestyles, which may not be representing that of the general population, such as the eldery demographic, or athletes. This study is also not conducted on the female gender, where it would be interesting to note the effects of gender differences on the results of this study. In addition, a separate mathematical model for females can also be formulated, as the model formulated in this study is only for that of males. A similar study on creating a mathematical model for females should strongly be considered for future research purposes to accompany this research so that a mathematical model is generated for both genders.

4. Conclusions

To conclude, the findings of this study show that the sample of overweight young adults demonstrate higher absolute isokinetic strength when compared with the normal or underweight samples. The overweight group shows a higher average peak torque reading of 226.23±31.10Nm when compared to the normal and underweight groups, where the average readings of peak torque are 210.43±24.56Nm and 167.63±24.87Nm respectively. It can be suggested that the extra weight carried by overweight people acts as excess energy storage which improves muscle performance in vigorous tasks.

Sincere gratitude and appreciated is given to the lab assistants at the Sports Centre of University of Malaya for providing permission as well as the proper guidance in utilizing the facilities provided, such as the isokinetic dynamometer. In addition, sincere and great appreciation to be given to all of the participants who have agreed to volunteer in the experiment, and also for their effort and patience during the experiment.

References

[1] Tomlinson, D., Erskine, R., Morse, C., Winwood, K. and Onambélé-Pearson, G. (2015). The impact of obesity on skeletal muscle strength and structure through adolescence to old age. *Biogerontology*, 17(3), pp.467-483.

[2] Chan, Y., Lim, K., Lim, K., Teh, C., Kee, C., Cheong, S., Khoo, Y., Baharudin, A., Ling, M., Omar, M. and Ahmad, N. (2017). Physical activity and overweight/obesity among Malaysian adults: findings from the 2015 National Health and morbidity survey (NHMS). *BMC Public Health*, 17(1).

[3] Lim, K. (2016). A Review of Adult Obesity Research in Malaysia. *Med J Malaysia*, 71(1).

[4] J. Araujo Ribeiro Alvares, R. Rodrigues, R. Azevedo Franke, B. Silva, R. Pinto, M. Vaz and B. Baroni, "Inter-machine reliability of the Biodex and Cyber isokinetic dynamometers for knew flexor/extensor isometric, concentric and eccentric tests", *Physical Therapy in Sport*, vol. 16, no. 2015, pp. 59-65, 2014.

[5] Jackson, A. and Pollock, M. (1978). Generalized equations for predicting body density of men. *British Journal of Nutrition*, 40(03), p.497.

[6] Maffiuletti, N., Jubeau, M., Agosti, F., De Col, A. and Sartorio, A. (2008). Quadriceps muscle function characteristics in severely obese and nonobese adolescents. *European Journal of Applied Physiology*, 103(4), pp.481-484.

[7] Blimkie, C., Sale, D. and Bar-Or, O. (1990). Voluntary strength, evoked twitch contractile properties and motor unit activation of knee extensors in obese and non-obese adolescent males. *European Journal of Applied Physiology and Occupational Physiology*, 61(3-4), pp.313-318.

[8] Maffiuletti, N., Jubeau, M., Munzinger, U., Bizzini, M., Agosti, F., De Col, A., Lafortuna, C. and Sartorio, A. (2007). Differences in quadriceps muscle strength and fatigue between lean and obese subjects. *European Journal of Applied Physiology*, 101(1), pp.51-59.

[9] Lafortuna, C., Tresoldi, D. and Rizzo, G. (2013). Influence of body adiposity on structural characteristics of skeletal muscle in men and women. *Clinical Physiology and Functional Imaging*, 34(1), pp.47-55.

[10] Tomlinson, D., Erskine, R., Winwood, K., Morse, C. and Onambélé, G. (2014). The impact of obesity on skeletal muscle architecture in untrained young vs. old women. *Journal of Anatomy*, 225(6), pp.675-684.

[11] Maffiuletti, N., Agosti, F., Proietti, M., Riva, D., Resnik, M., Lafortuna, C. and Sartorio, A. (2005). Postural instability of extremely obese individuals improves after a body weight reduction program entailing specific balance training. *Journal of Endocrinological Investigation*, 28(3), pp.2-7.

[12] Narici, M. and Maffulli, N. (2010). Sarcopenia: characteristics, mechanisms and functional significance. *British Medical Bulletin*, 95(1), pp.139-159.

[13] LEMMER, J., HURLBUT, D., MARTEL, G., TRACY, B., EY, F., METTER, E., FOZARD, J., FLEG, J. and HURLEY, B. (2000). Age and gender responses to

strength training and detraining. *Medicine & Science in Sports & Exercise*, 32(8), pp.1505-1512.

[14] Keller, K. and Engelhardt, M. (2013). Strength and muscle mass loss with aging process. Age and strength loss. *Muscles, Ligaments and Tendons Journal*, 3(3), pp.346-350.

[15] Miyatake, N., Miyachi, M., Tabata, I., Sakano, N., Hirao, T. and Numata, T. (2012). Relationship between muscle strength and anthropometric, body composition parameters in Japanese adolescents. *Health*, 04(01), pp.1-5.

EURECA 2018 – Conference Paper
Paper number 2ME21

Preparation and Characterization of Biocomposite from PLA and Natural Fibre from Chrysanthemum Waste

Koay Seong Chun[1,12], Muhammad Faiz Ishak[1] , Chou Pui May[1], Chan Ming Yeng[2], and Albert Tshai[3]

[1]School of Engineering, Faculty of Built Environment, Engineering, Technology and Design, Taylor's University Lakeside Campus, 47500 Subang Jaya, Selangor
[2]Centre of Engineering Programmes, HELP College of Arts and Technology, 55200 Kuala Lumpur, Malaysia
[3]Faculty of Engineering, The University of Nottingham, 43500 Semenyih, Selangor

Abstract. Polylactic acid (PLA) is a form of bioplastic that is derived from renewable resources. However, its high application cost limits its market potential. Hence, the introduction of natural filler could effectively reduce the cost of PLA. In this research, natural fibre utilised from chrysanthemum waste was used to make the PLA biocomposite. This paper focuses on the effect of fibre content and addition of coupling agent to the composite material on the tensile and thermal properties of PLA/Chrysanthemum waste (CW) biocomposites. The PLA/CW biocomposite is produced through melt compounding process using Haake internal mixer at varying part per hundred resin (phr) value. In this study, mixture of 30 phr and 60 phr of fibre was made in addition to 1, 3, and 5 phr of Maleic Anhydrided Grafted Polyethylene (MAPE) was used for testing on tensile and thermal properties. The tensile properties of the biocomposites that were tested were tensile strength and tensile modulus. The thermal properties of the biocomposite was tested for its thermal stability and weight loss %. The tensile properties of the biocomposite increases with fiber content. When MAPE is added, the tensile properties of the biocomposite was further improved but decreases after 1 phr composition. The thermal stability of the biocomposite reduces with fiber content but improved when MAPE is added to the mixture.

[12] Corresponding author: SeongChun.Koay@taylors.edu.my

1 Introduction

Plastic is a type of polymers that are derived from the polymerization of petroleum product which contains long chains of monomers [1]. The development of plastic industry since its introduction in 1940s saw the annual production of plastics increasing exponentially from 1.5 million tonnes (1950) to 300 million tonnes (2013) [1]. The dramatic increase of plastic industry poses hazard towards the environment as petroleum-based plastic have long life span to degrade naturally. In recent years, bioplastic material has been introduced to partially replace plastic derived from petroleum to reduce plastic consumption thus reducing its carbon footprints. Polylactic acid (PLA) is a form of thermoplastic polymers derived from renewable resources such as sugarcane and corn starch [2]. PLA could potentially replace plastic materials for daily usage due to its good mechanical properties, non-toxicity, biodegradable and has short life span [3-4]. It was reported in 2014 that the production of bioplastic globally amounted to 1.7 million tonnes and expected to grow to 6.2 million tonnes in 2018 [5]. Figure 1 shows the breakdown of bioplastic production in 2014. Unfortunately, the usage of bioplastic is still in small percentage when compared to global plastic consumption (207,400 tonnes vs 300 million tonnes). The main reason why bioplastic materials was not widely used by the industry is due to its pricing, as the cost of PLA resin is substantially higher than petroleum-based plastic which inhibits industry to fully adapt the technology [6].

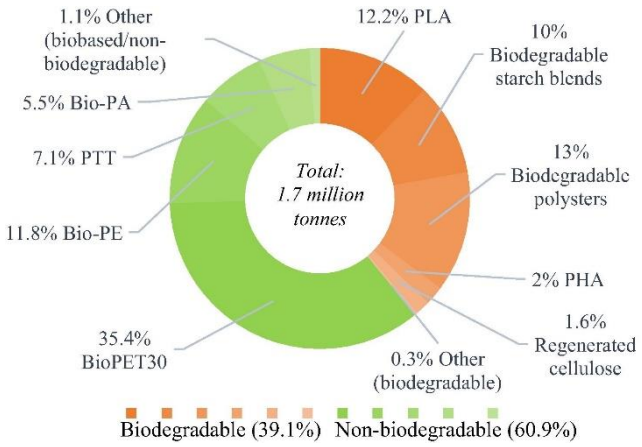


Figure 21: Percentage of bioplastic production in 2014

To offset the high production cost of PLA resin, natural filler could be introduced to PLA by partially replacing the PLA resin. The natural filler can be used to reinforce the polymer matrix in the composite materials. Natural fillers such as hemp, jute, bamboo, flax, and kenaf could be used as substitute to the PLA polymer content [11]. The main benefit of natural filler is that it is recyclable, biodegradable, have good mechanical properties and less abrasive to equipment compared to synthetic fibres, which could help in cost reductions [7]. Hence, by introducing natural filler into the PLA resin, the final cost of the biocomposite could be significantly reduced. *Chrysanthemum Indicum*, also known as chrysanthemum has been used for several centuries as traditional Chinese herbal medicine to dispel heat and wind, calming the liver and detoxifying [8]. In Chinese medicine, the flower part of the plant is simmered with boiling water to make chrysanthemum tea. Besides that, chrysanthemum flower

is also used as ornaments during weddings and ritual ceremony. However, only the flower part of the plant is used which leads to other parts of the plant being discarded to the landfill. Isha Yadav et. al [9] reported that flower waste from temples in India amounted to 3.5-4 tonnes per day. The flower waste is discarded and take up spaces in landfills which is a concern as the plant could be recycled into natural fibres for biocomposite production. Furthermore, chrysanthemum plant is composed of high concentration of cellulose, hemicellulose and lignin (42.5%, 27.5%, and 17.5%, respectively) which can be used as the fibre to enhance the performance of PLA [10]. This research is undergone to utilize the usage of natural fibre from chrysanthemum waste with PLA resin to produce a novel biocomposite.

The present research focuses on the effect of fibre content and coupling agent on the tensile and thermal properties of biocomposite made from chrysanthemum waste fibre and PLA resin.

2 Methodology

2.1 Research Materials

PLA and Maleic Anhydride Grafted Polyethylene (MAPE) used in this study was supplied by TT Biotechnologies Sdn. Bhd. (Malaysia) while the chrysanthemum waste was collected from a temple in PJS 7, Subang Jaya, Selangor.

2.2 Preparation of Chrysanthemum Waste Fibre

The chrysanthemum waste obtained from temple was firstly thoroughly cleaned by running it with tap water. The chrysanthemum waste was then dried under direct sunlight before being cut into smaller pieces. Next, the chrysanthemum waste was further dried using circulated forced convection oven at 70°C for 24 hours until it is completely dried. Then, the chrysanthemum waste was grounded into short fibres using mechanical surface grinder. The chrysanthemum fibre was then sieved using 600 μm mesh size to get homogenous fibre size. The chrysanthemum fibre was further dried using the circulated air oven before the compounding process. Figure 2 shows the flowchart of the preparation of chrysanthemum waste fibre.

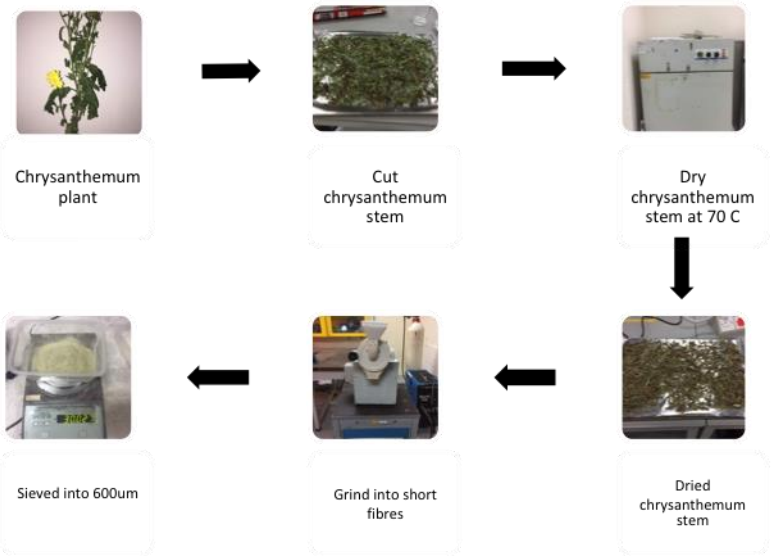


Figure 22: Preparation of chrysanthemum waste fibre

2.3 Preparation of PLA/CWF biocomposite

The PLA/CWF biocomposite were produced using melt compounding process. Haake Rheomix twin screw internal mixer was used to compound the PLA/CWF mixture at SIRIM Shah Alam, Malaysia. The biocomposites were prepared with multiple fibre content of part per hundred resin (phr) value of 30 phr and 60 phr. Besides, the biocomposites were also prepared with addition of MAPP coupling agent of 1 phr, 3 phr and 5 phr. The processing temperature of the internal mixer was set at 180°C and rotor speed of 80 rpm. The PLA resin was firstly transferred into the mixing chamber of the internal mixer for 1 minute to completely melt the resin. Next, CWF was added into the mixer and compounded for another 4 minutes. The mixed biocomposite was then removed from the internal mixer and let to rest for another 2 minutes. Table 1 shows the phr composition of the biocomposite with different fiber content and different MAPE content.

Table 6: phr composition of biocomposite

Samples	PLA (phr)	CWF (phr)	MAPE (phr)
PLA/CWF without MAPE	100	0, 30, 60	-
PLA/CWF with MAPE	100	60	1, 3, 5

The PLA/CWF biocomposites were then moulded into sheets of 2mm thickness. The biocomposites were moulded using Moore hotpress machine at 180°C at 150 bar pressure. The biocomposite was first placed into the hotpress mould at 180 °C. The biocomposite was let to pre-heat inside the hotpress for 4 minutes to soften the biocomposite before compression starts.

The compound was then compressed into sheet under 150 bar pressure for 1 minute. Next, the specimen was let to cool down under pressure for 15 minutes until the temperature of the hotpress plate reaches 50 °C. Lastly, all of the biocomposites were cut into seven to nine identical specimens where the dimensions are in accordance to American Society of Testing and Materials (ASTM) D638 standard.

2.4 Testing and Characterization

Tensile properties of the biocomposite was performed using Instron Universal Testing Machine (Model 5969). The tensile test was done according to ASTM D638 standard in which the cross-head speed of the machine was set at 5mm/min and 15kN load cell was used elongate the specimen until it reaches its breaking point. The experiment was done at room temperature with deviation of 2°C. Bluehill 3 software was used to record the tensile strength and tensile modulus of the biocomposites. For each composition, seven identical samples of tensile properties were used for tensile test. The formula used to calculate the tensile strength and tensile modulus are as follows:

$$\text{Tensile Strength} = \frac{load\ at\ break}{(original\ width)(original\ thickness)} \quad (1)$$

$$\text{Tensile Modulus} = \frac{\frac{(load\ at\ point\ on\ tangent)}{(original\ width)(original\ thickness)}}{\frac{(elongation\ at\ point\ on\ tangent)}{(initial\ gage\ length)}} \quad (2)$$

Thermogravimetric analysis (TGA) was carried out using Perkin-Elmer Thermogravimetric Analyzer. The specimen prepared in a ceramic pan at varying weights ranging from 5 to 7 mg. Thermal scan was subjected to the specimen at 30°C to 700°C at heating rate value of 10°C/min. The specimen was subjected under nitrogen gas atmosphere with gas flow rate of 20ml/min for the analysis. TGA analysis was done to investigate the thermal stability and char residual weight loss when the specimen is subjected under varying temperatures.

3 Results and Discussion

3.1 Tensile Properties

The mechanical performance of biocomposite mainly depends on few factors, namely the physical properties of the components, the interaction between the fiber and matrix, and the orientation of the reinforcing fiber. The nature of fiber which is polar and hydrophilic inhibits strong bond between the fiber and polymer matrix which is non-polar and hydrophobic in nature. Thus, this might lead to poor stress transfer which result in the reduce in mechanical performance of the biocomposite. Besides, the fiber tend to agglomerate and not disperse well during manufacturing process, preventing from optimize performance to be achieved. This is because the performance of biocomposite is also depended on the orientation of the fibers in the compound [13].

Figure 3 illustrate the tensile strength of PLA/CWF biocomposite at different filler content. The tensile strength of the biocomposite shows an increase in tensile strength with fiber content and reduces after 1 phr MAPE. This is mainly due to the characteristic of natural fiber which usually display higher mechanical strength compared to plastic materials [15]. Thus, the addition of CWF fiber to replace the PLA resin might contribute to increase in tensile strength. However, the tensile strength exhibited by PLA/CWF biocomposite is less than neat PLA. Study by Chun et al. [12] found that the tensile strength of neat PLA to be about 54 MPa. This is because the CWF used in the experiment was short fiber which might induces agglomeration of fiber to happen during manufacturing process. The randomly orientation of the fibers which are perpendicular to the direction of applied load might contribute to the low performance of the biocomposite at lower composition. However, the presence of more fiber which is parallel to the direction of applied load at higher fiber content resulted in increase in tensile strength of the composite. Similar findings was also recorded. Nevertheless, the introduction of MAPE increases the tensile strength of PLA/CWF composite. The highest tensile strength recorded was at 1 phr composition. This was mainly due to the improved in the interfacial bond between matrix-filler region. When MAPE is added to the PLA/CWF, the MAPE improved the dispersion of filler in compound. Besides that, the nature of MAPE which provide an interphase later between the hydrophobic-hydrophilic interfacial region helps to increase the strength of the material. The increase in tensile strength was due to the maleic anhydride group reacting with the hydroxyl group of the cellulose surface, forming stronger chemical bond [14]. This behaviour was also found in by Husseinsyah et al. [16]. At 3 phr onwards, the tensile strength of the composite started to decrease. This may have been due to the change in properties of biocomposite from ductile to brittle fracture behaviour. This can be explained by the excess of MAPE which give the compound a plasticizing effect. Similar result was also observed by Osman et al. [15].

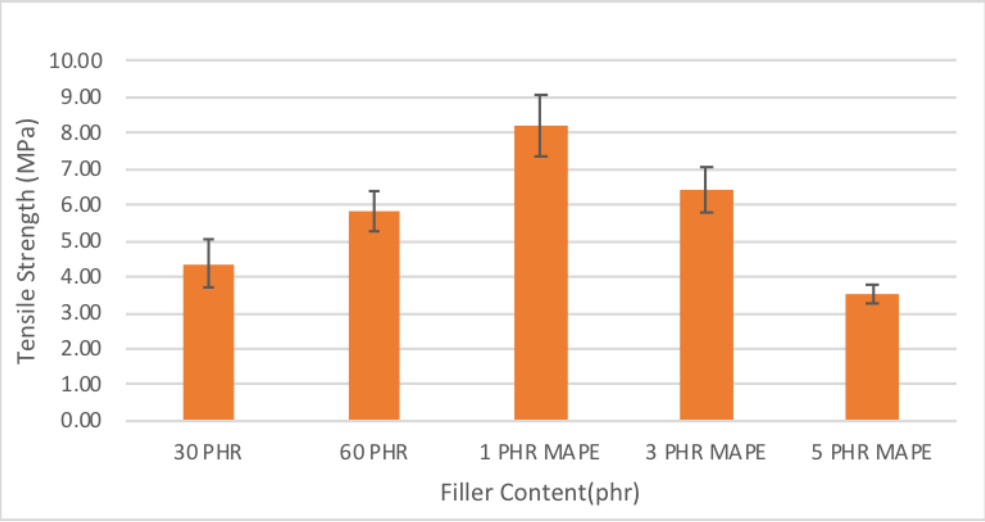


Figure 23: Tensile strength of PLA/CWF biocomposite at different composition. PLA : polylactic acid ; MAPE : maleic anhydride grafted polyethylene ; phr : part per hundred resin

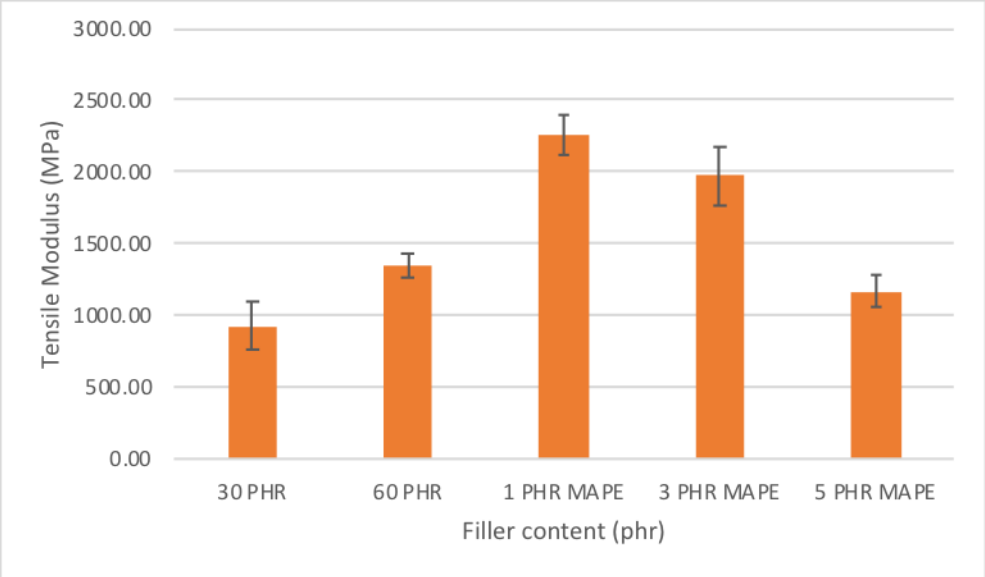


Figure 24: Tensile modulus of PLA/CWF biocomposite at different composition. PLA : polylactic acid ; MAPE : maleic anhydride grafted polyethylene ; phr : part per hundred resin

Figure 4 illustrate the tensile modulus of the biocomposite at different fiber content. The tensile modulus of the biocomposite shows similar trend as tensile strength. This was mainly due to the effect of higher filler content at 60 phr and the addition of MAPE. The addition of CWF reduces the chain mobility of the PLA matrix, thus increasing the stiffness of the PLA/CWF composites. The further increase in tensile modulus at 1 phr is due to MAPE enhancing the filler-matrix interaction. The reduced in tensile modulus at 3 phr MAPE was due to the plasticizing effect as excessive MAPE is added to the mixture, as discussed earlier.

3.2 Thermal Properties

3.2.1 Effect of different fiber content

Thermogravimetric Analysis (TGA) curves for neat PLA and CWF as well as PLA/CWF composite at different fiber content are illustrated in Figure 5. Data obtained from the TGA curves are tabulated in Table 2. From the graph illustrated, it can be seen that the CWF decompose faster than other components and yields highest char residue at 600 °C. The early thermal degradation of CWF was mainly due to the removal of moisture and other votatile compounds. Besides, the CWF undergone two stages of thermal decomposition of hemicellulose and lignocellulose at temperature 250-300 °C and 350-400 °C, respectively [16]. Tbe thermal decomposition of hemicellulose and lignocellulose contributes to the high char formation. The neat PLA and neat MAPE exhibits single stage of thermal decomposition at temperature above 350 °C. The thermal stability of PLA/CWF biocomposite reduces with filler content. This can be seen by the weight loss curves in which the curves shifted to the left, indicating earlier thermal degradation at higher fiber content. This can be further examined by the presence of higher char residue at 60 phr. This is because the higher fiber content degrade faster, thus resulting in lower thermal stability of the biocomposite. This foundings were also agreed by other researchers [17].

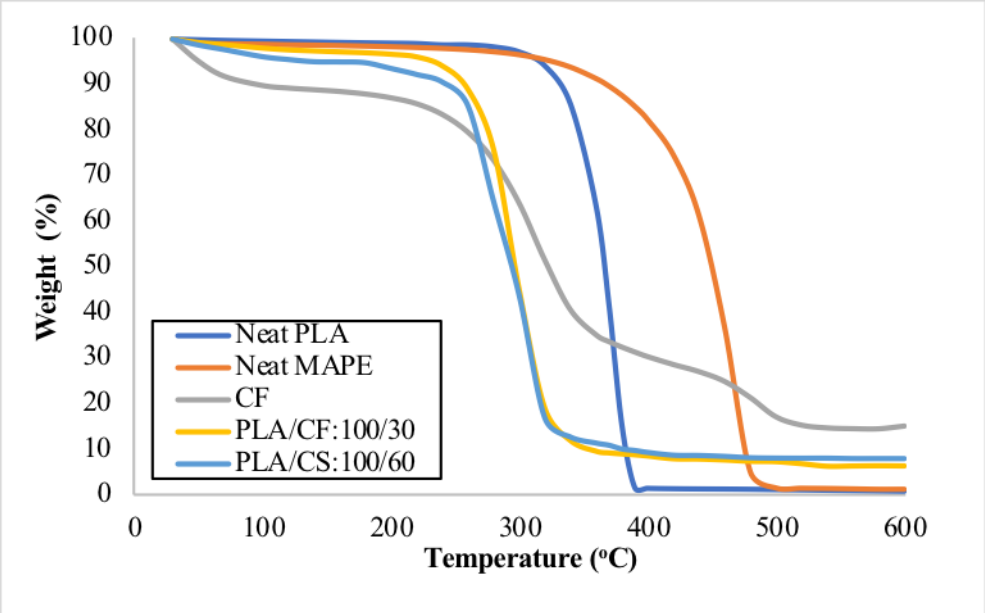


Figure 25: TGA curves of neat PLA, neat MAPE, CF as well as PLA/CWF biocomposites with filler content of 30 and 60 phr

Table 7 : Sample weight loss % at different temperature

Sample	**Weight loss at selected temperature (%)**			**Char Residue at 600°C (%)**
Temperature (°C)	**200**	**400**	**600**	
Neat PLA	0.89	98.65	99.27	0.73
Neat MAPE	1.67	69.79	98.59	1.41
CWF	12.91	69.79	85.06	14.94
PLA/CWF: 100/30	3.33	91.55	93.74	6.26
PLA/CWF: 100/60	6.43	90.55	91.91	8.09

3.2.2 Effect of different MAPE content

TGA curves for PLA/CWF at different MAPE content is illustrated in Figure 6 while table 3 shows the sample weight loss % at different temperature. The thermal stability of the biocomposite was enhanced with MAPE addition. It can be seen by the thermal decomposition curves which was shift to the right at higher temperature with MAPE content. This phenomenon can be explained by the presence of MAPE which induces good interfacial bond between filler-matrix which acts as a barrier to delay the release of volatile gases during thermal degradation. Besides, the presence of MAPE also improved the agglomeration of fiber in the composite. Thus, the existence of MAPE enabled a better thermal protecting and stronger filler-matrix interaction, which ultimately increases the thermal stability of the biocomposite. It could also be seen that the char residue increases with MAPE content. This can be explained by the enhanced filler-matrix dispersion which ultimately results in a more homogenous formation of char layer which provide better thermal protection. Similar observations was also found by [12].

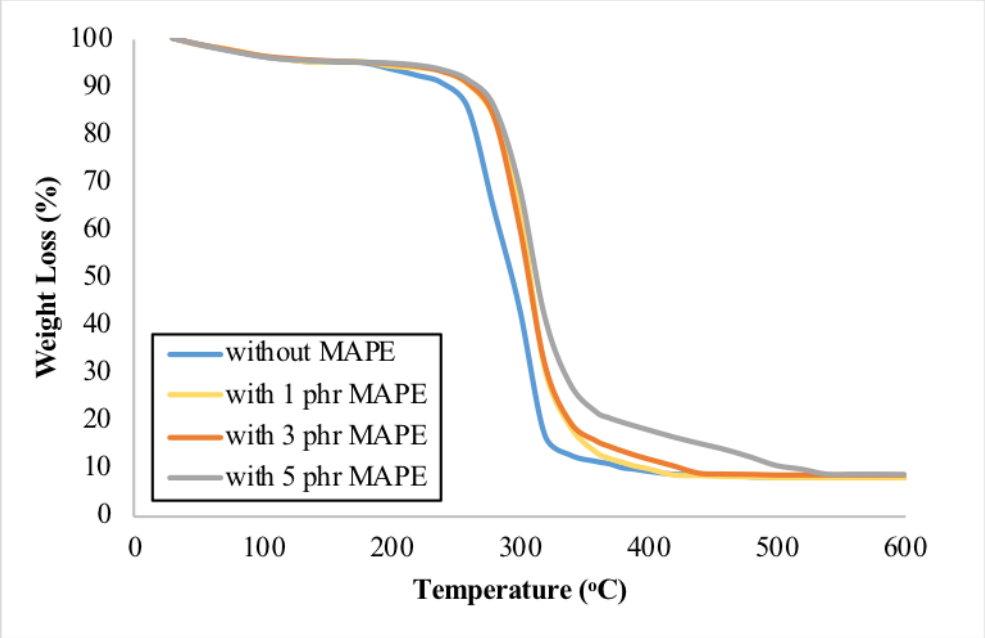


Figure 26 : TGA curves of PLA/CWF biocomposite at different fiber content

Table 8: weight loss % at different MAPE content

Sample	**Weight loss at selected temperature (%)**			**Char Residue at 600°C (%)**
Temperature (°C)	**200**	**400**	**600**	
Without MAPE	6.43	90.55	91.91	8.09

With 1 phr MAPE	5.82	89.86	91.77	8.23
With 3 phr MAPE	5.39	88.29	91.69	8.31
With 5 phr MAPE	5.21	81.76	91.14	8.86

Conclusion

It was found that the increase of CWF content increases the tensile strength and tensile modulus of PLA/CWF biocomposite. The tensile strength and tensile modulus of the biocomposite was further increased when 1 phr of MAPE was added. The incorporation of MAPE provide a coupling effect to the PLA/CWF biocomposite. This was mainly due to better dispersion of filler and enhancement of filler-matrix interaction. However, the tensile strength and tensile modulus starts to decrease when more MAPE is added. This is due to the plasticizing effect when excessive MAPE is incorporated in the compound. Besides, the thermal stability of the biocomposite was observed to decrease with fiber content due to early thermal degradation of CWF fibers. However, the thermal stability is improved when MAPE is added. The presence of MAPE enhances the filler-matrix bond and provide a thermal barrier which delay the decomposition of the composite.

References

[1] K. Chidambarampadmavathy, "Sustainable bio-plastic production through landfill methane recycling," *Renewable and Sustainable Energy Reviews,* vol. 71, pp. 555-562, May 2017.

[2] A. K. Mohanty, M. Misra and L. T. Drzal, Natural Fibers, Biopolymers, and Biocomposites, London: CRC Press, 2005, p. 809.

[3] M. J. John and S. Thomas, "Biofibres and Biocomposites," *Carbohydrate Polymers,* vol. 71, no. 3, pp. 343-364, 2008.

[4] T. Gurunathan, S. Mohanty and S. K. Nayak, "A review of the recent developments in biocomposites based on natural fibres and their application perspectives," *Composites Part A: Applied Science and Manufacturing,* vol. 77, pp. 1-25, 2015.

[5] S. M. Emedian, T. T. Onay and B. Demirel, "Biodegradation of bioplastics in natural environments," *Waste Management,* vol. 59, pp. 526-536, 2017.

[6] V. Nagarajan, A. K. Mohanty and M. Misra , "Perspective on Polylactic Acid (PLA) based Sustainable Materials for Durable Applications: Focus on Toughness and Heat Resistance," *ACS Sustainable Chemistry & Engineering,* vol. 4, no. 6, pp. 2899-2916, 2016.

[7] M. R. Fazita, K. Jayaraman, D. Bhattacharyya, M. K. Mohamad Haafiz, C. Saurabh, M. Hussin and A. H.P.S., "Green Composites Made of Bamboo Fabric and Poly (Lactic) Acid for Packaging Applications—A Review," *Materials*, vol. 9, no. 6, p. 435, 2016.

[8] K. Ming, Y. Chen, J. Shi, J. Yang, F. Yao, H. Du, W. Zhang, J. Bai and J. Liu, "Effects of Chrysanthemum indicum polysaccharide and its phosphate on anti-duck hepatitis a virus and alleviating hepatic injury," *International Journal of Biological Macromolecules*, vol. 102, pp. 813-821, 2017.

[9] I. Yadav, S. K. Juneja and S. Chauhan, "Temple Waste Utilization and Management: A Review," *International Journal of Engineering Technology Science and Research,* vol. 2, pp. 14-19, September 2015.

[10] B. Quevedo-Hidalgo, P. C. Narvaéz-Rincón, A. M. Pedroza-Rodríguez and M. E. Velásquez-Lozano, "Degradation of Chrysanthemum (Dendranthema grandiflora) wastes by Pleurotus ostreatus for the production of reducing sugars," *Biotechnology and Bioprocess Engineering,* vol. 17, no. 5, pp. 1103-1112, 2012.

[11] N. Saba, F. Mohammad, M. Pervaiz, M. Jawaid, O. Alothman and M. Sain, "Mechanical, morphological and structural properties of cellulose nanofibers reinforced epoxy composites," *International Journal of Biological Macromolecules,* vol. 97, pp. 190-200, 2017.

[12] K. S. Chun and S. Husseinsyah, "Polylactic acid/corn cob eco-composites: Effect of new organic coupling agent," *Thermoplastic Composite Material,* pp. 1-12, 2013.

[13] L. Zhang, J. Zhong and X. Ren, "Natural Fiber-Based Biocomposites," *Green Energy and Technology,* pp. 31-63, 2017.

[14] A. G. Supri, H. Ismail and S. Shuhadah, "Effect of Polyethylene-Grafted Maleic Anhydride (PE-g-MAH) on Properties of Low Density Polyethylene/Eggshell Powder (LDPE/ESP) Composites," *Polymer-Plastics Technology and Engineering,* pp. 347-352, 2010.

[15] H. Osman, K. S. Chun and S. Husseinsyah, "Tensile Properties of Polypropylene/Cocoa Pod Husk Biocomposites: Effect of Maleated Polypropylene," *Advanced Materials Research,* vol. 747, pp. 645-648, 2013.

[16] K. S. Chun, S. Husseinsyah and H. Osman, "Mechanical and thermal properties of coconut shell powder filled polylactic acid biocomposites: Effects of the filler content and silane coupling agent," *Journal of Polymer Research 19(5),* 2014.

[17] K. S. Chun, S. Husseinsyah and N. Syazwani, "Properties of kapok husk-filled linear low-density polyethylene ecocomposites: Effect of polyethylene-grafted acrylic acid," *Journal of Thermoplastic Composite Materials 29(12),* pp. 1-13, 2015.

EURECA 2018 – Conference Paper
Paper number 2ME22

Sintered properties of zirconia reinforced with manganese oxide (MnO_2) and stainless steel (SS-316L)

K.H. Nicholas Cheong[13], *W.J. Kelvin* Chew[1], and *S. Ramesh*[2]

[1] Department of Mechanical Engineering, Taylors University Lakeside Campus, 47500 Subang Jaya, Selangor
[2] Department of Mechanical Engineering, University of Malaya, 50603 Kuala Lumpur, Malaysia

Abstract. The sintered properties of yttria-tetragonal zirconia polycrystals (Y-TZP) was investigated when reinforced with manganese oxide (MnO_2) and stainless steel (SS-316L). Samples were evaluated on mechanical properties such as bulk density, Vickers hardness and fracture toughness at sintering temperature range of 1250°C-1500°C. The addition of 0.5% MnO_2 and 0.05% SS-316L shown the most effective in improving the density compared to addition of only 0.5% MnO_2 at 1350°C. However, as for the Vickers hardness and fracture toughness, the undoped sample still possess the better qualities at high sintering temperature at 1350°C and above. As concluded, the addition of manganese oxide and stainless steel to the Y-TZP do provide improvements, best quality at sintering temperature of 1200°C.

Keywords: Manganese oxide; Stainless steel; Sintered; Y-TZP; Co-doped

* Corresponding author:
E-mail address: nicholaskahhoe.cheong@sd.taylors.edu.my

1.0 Introduction

In this modern era, appearance is so important that it affects many situations in our daily life. Among all the facial characteristic, teeth have emerged into one of the most important part which allows dentistry to be so important and being emphasize to everyone to take care of. With the current technology, numerous treatment can be performed to achieve desirable results as in crown and bridge, inlays, orthodontic and implants. Most of these treatments were achieved by using material like the zirconia ceramic due to the properties. Besides dentistry, zirconia is often used in orthopaedic as joints replacements but was recently happened to have an alarm call due to low temperature degradation causing deterioration of fracture toughness. This has brought up the concern of scientist across the world to collaborate and determine the root cause of this failure. With months or even years of experimenting, an outcome was found which is to stabilize the zirconia with yttria which results in the material of yttria-stabilized tetragonal zirconia polycrystalline (Y-TZP ceramic).

One of the reason that zirconia is widely used in medical field due to the biocompatibility with bone tissues as well as aesthetically and excellent mechanical properties. However, ceramic has a lower toughness as compared to the metals, toughening process by addition of metal oxides will be needed to improve the weakness. Besides that, metal oxides were also serve as a stabilizing agent to the zirconia phases under low temperature [1]. Besides that, the toughening process allows the monoclinic phase of the Y-TZP of increase in volume by 3-5% where it induces compressive stress in crack area resulting in prevention of crack propagation. [2,3]. With the addition, properties such as strength and corrosion resistance will also be enhanced. With the research done in the past, it has shown that the doping of zirconia with other metal oxides will improve the mechanical properties such as hardness and toughness of the ceramic. [4-6] The conclusion was supported with the evidence of several experiment on the mechanical properties at a considerable low sintering temperature [7,8]. Due to the lack of insights and research on co-doping zirconia with two additives especially using metal oxides of manganese and stainless steel of grade 316L, this leads to the curiosity and selection towards this research topic. The purpose of this research study is to study the effect of two sintering additives of stainless steel grade 316L and manganese oxides on the ageing resistance of the zirconia ceramics. The motivation and goal of the findings is to provide better solution by improving the properties of the zirconia ceramic to be able to use in medical field as well as compatibility of zirconia ceramics in other applications.

2.0 Experimental Procedure

2.1 Sample Preparation

3mol% yttria-stabilized zirconia, 99.9% purity of manganese oxide, MnO_2 and stainless steel of grade 316L, SS316L powders were used in this study. Combinations of weight percentage of MnO_2 and SS316L powders were shown in Table 4. These combinations of powders were measure according to the weight percentage according to table 1 below. Then, 200ml of ethanol was added to the powder mixtures as mixing medium for the powders. The slurry then undergone stirring and mixing in the ultrasonic bath to allow better mixing to achieve the state of homogeneous. Before drying the slurry, it was poured into an attritor mill to further breaking down the particles for 30minutes at 500rpm. The slurry then placed in an oven for drying at temperature of 60°C for 12 hours. The dried mixture was then undergone filtration process by using a stainless steel sieve of 212μm mesh to ensure fine composition.

Table 1: Composition of based material and dopants powder.

Y-TZP	MnO_2	SS316L
100.0wt%	-	-
99.5wt%	0.5wt%	-
99.45wt%	0.5wt%	0.05wt%

99.0t%	0.5wt%	0.5wt%

The dried mixture then was pressed through a hydraulic bench press to be form into circular shaped pellets and rectangle bar samples, then subsequently subjected to cold isostatic press (CIP) with a configuration of 200 MPa for 1 minutes. The dimensions of the pellets are 15 mm in diameter and 3 mm in thickness and 4 X 13 X 32 mm for the rectangle bar. Then, the samples were placed into the furnace for sintering at temperature of 1200°C, 1300°C, 1450°C for 2 hours of holding time. All the sintered samples were ground with grinding paper with different granularity in sequence of 240, 600, 800 and 1200, and polished with synthetic diamond paste of grade 0.6μm then 0.1μm to obtain an optically reflective surface prior to testing.

2.2 Characterization

2.2.1 Bulk Density

Water immersion method based on Archimedes principle was used to determine the bulk densities of the sample pellets by using a standard Mettler Toledo balance. Distilled water was used as immersion medium for the pellets. However, for pellets with lower than 95% of theoretical density, the bulk density will be obtained by using the sample mass and measurements of geometric dimensions because of the ability of water to penetrate the pores which will results in overestimating value for the sample density. Relative density will be calculated by using the theoretical density of Y-TZP as 6.1 gcm^{-3}. Equation (1) will be used to calculate the bulk density.

$$\rho = \frac{W_a}{W_a - W_w}\rho_w \quad (1)$$

Where
ρ = Bulk density of sample, g/cm^3
W_a = Weight of the sample in air, g
W_w = Weight of the sample in water, g
ρ_w = Density of distilled water, g/cm^3

2.2.2 Vickers Hardness & Fracture Toughness

This test will be done to ascertain the hardness of sintered samples. The testing method will be using a pyramidal diamond indenter to perform indentation to samples with an applied load of 10kg. The load will be applied in an increasing and slow fashion without having impact. Two diagonal impressions will be visible after the load is removed, then they will be measured with microscope with filar micrometer built in. The Vickers hardness (H_v) will then be calculated using the surface area of the indent with equation (2) [10-12]

$$H_v = \frac{1.854P}{(D)^2} \quad (2)$$

Where
P = Applied load, kg
D =Average Diagonals = $\frac{D_1 + D_2}{2}$, cm

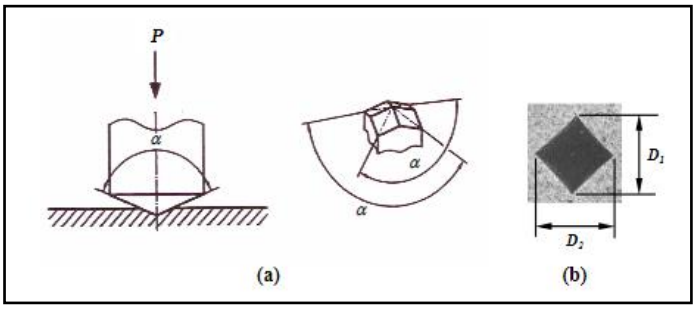


Figure 1: (a) shape of Vickers indenter (α = 136° ± 0.5°, angle between vertex of opposite faces) and (b) shaped of properly formed indentation. [12]

The fracture toughness, K_{Ic}, of the samples can also be determined with this test by measuring the cracks of each corner from the indentation. Equation (3) will be utilized to obtain the fracture toughness.

$$\left(\frac{K_{Ic}\phi}{H_v\alpha^{\frac{1}{2}}}\right)\left(\frac{H_v}{E\phi}\right)^{\frac{2}{5}} = 0.035\left(\frac{L}{\alpha}\right)^{-\frac{1}{2}} \quad (3)$$

Where

K_{Ic} = Fracture toughness

H_v = Vickers hardness

E = Young's modulus

α = Half-length of average diagonal, cm

L = Average crack length = $\frac{L_1+L_2+L_3+L_4}{4}$, cm

Φ = Constraint factor which is taken as 3

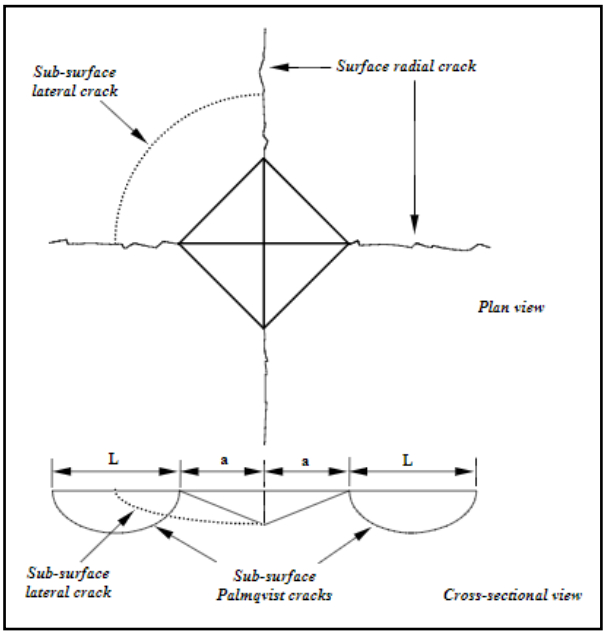


Figure 2: Schematic diagram of a typical indentation from Vickers test where L refers to the crack length and 2a is equivalent to D_1 or D_2 in equation (4) [12]

3.0 Results and Discussion

3.1 Bulk Density

The effect of sintering temperature to bulk density of different composition of samples were presented in figure 3. At the temperature of 1200°C, Y-TZP co-doped with 0.5% MnO_2 and 0.05% SS-316L possessed the highest bulk density followed by doped with 0.5% MnO_2, co-doped with 0.5% MnO_2 + 0.5% SS-316L and undoped sample. At 1350°C, all the bulk density increased by small amount while undoped sample increase by a significant amount and possessed the highest bulk density among all. The bulk density of sample from undoped and doped with 0.5% MnO_2 increase while the density of samples that were co-doped decreases. the finding shows that the samples that were co-doped does not improved in density at temperature higher than 1350°C. The optimum density that were obtained for the co-doped samples were at 1350°C.

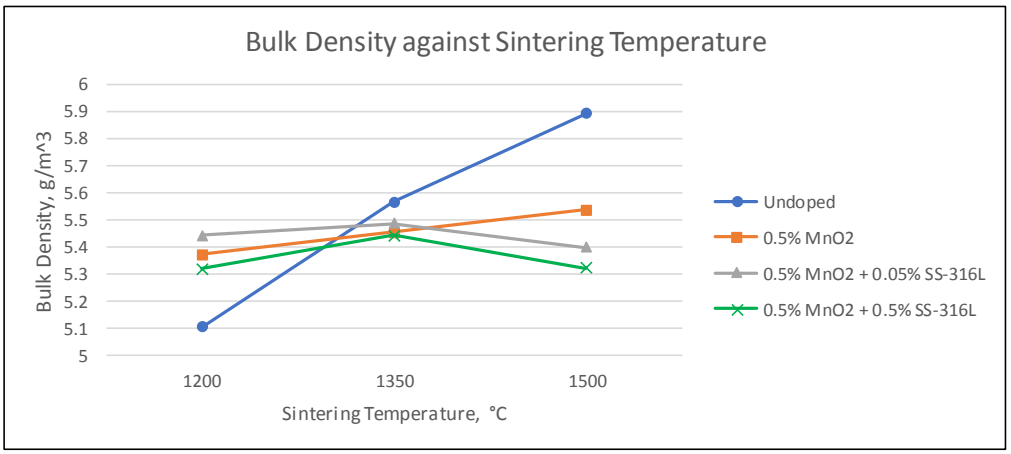


Figure 3: Graph of relative density against sintering temperature.

The effect of weight percentage of dopants against the bulk density were shown in the figure below, as the increasing of dopants in the samples, the bulk density of the samples decreases for the temperature of 1350°C and 1500°C. As in for 1200°C, the density increases along with the amount dopants except for the sample of co-doped with 0.5% MnO_2 + 0.5% SS-316L. this shows that, the

increasing of dopants does not necessarily improve the density of sample. The co-doped samples obtained the highest density at 1350°C while lowest at 1500°C.

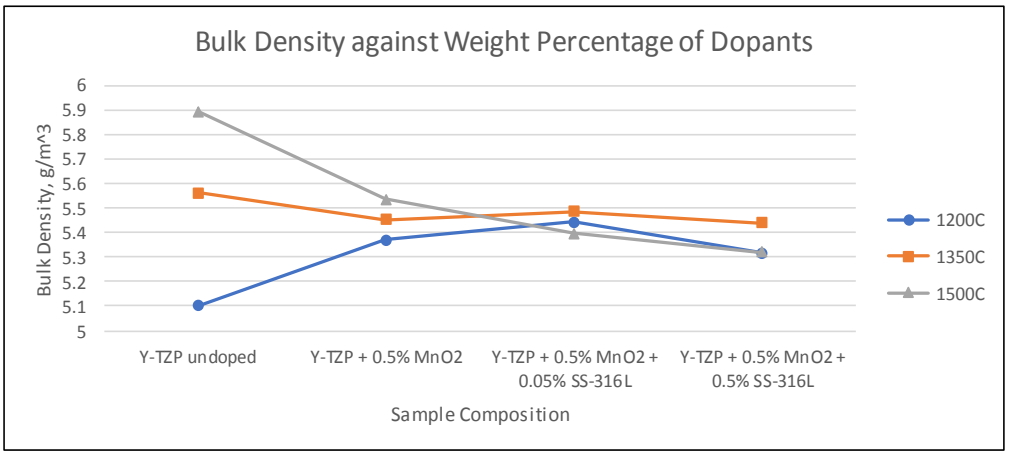


Figure 4: Graph of relative density against weight percentage of dopants.

3.2 Vickers Hardness

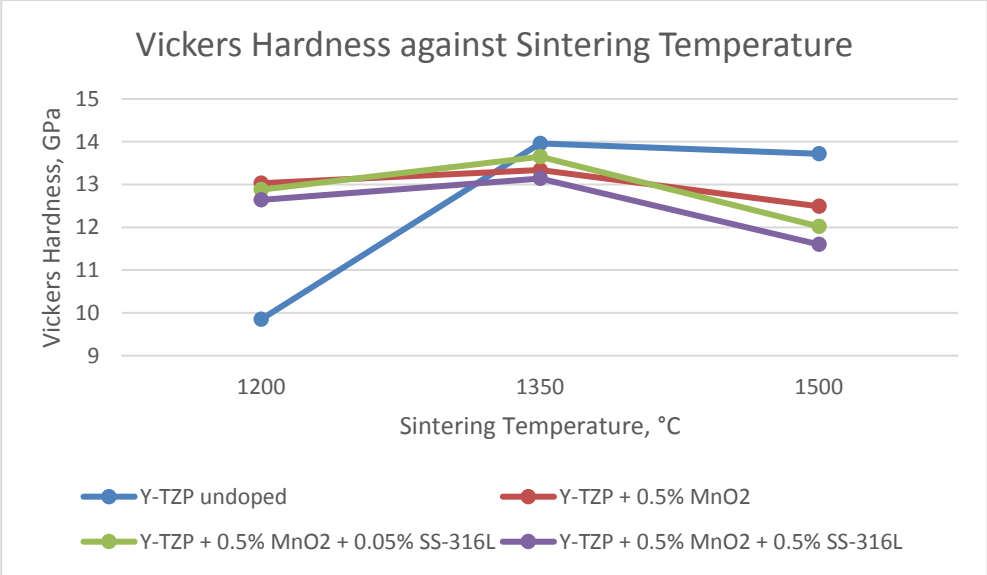


Figure 5: Graph of vickers hardness against sintering temperature.

From the result obtained, were plotted into the figure above. The doping of metal oxides into Y-TZP shows relatively high of value in Vickers hardness at sintering temperature of 1200°C compared to the undoped sample. At the temperature of 1350°C, all samples show the increase in hardness while the undoped sample increases the most and became the highest in hardness among the samples. However, at 1500°C of sintering temperature, all samples show the deterioration in hardness especially for the doped samples. This can be related to the increase of bulk density at high temperature which resulting the grain coarsening that was caused by the transformation into cubic phases.

3.3 Fracture Toughness

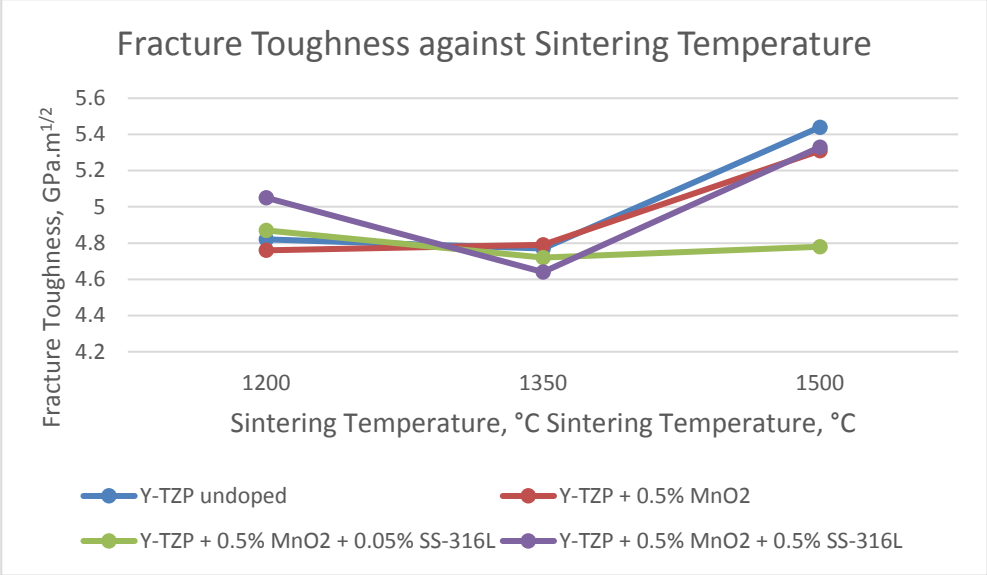


Figure 6: Graph of fracture toughness against sintering temperature.

The figure above shows the graph of fracture toughness against sintering temperature from 1200°C to 1500°C. At 1350°C the co-doped samples show deterioration in fracture toughness while the other samples show some improvements. The samples possess the highest value for fracture toughness at 1500°C, except for Y-TZP + 0.5% MnO_2 + 0.05% SS-316L which does not show much improvements from 1350°C and rather deterioration from 1200°C. The co-doped samples were the best samples at 1200°C while the undoped and Y-TZP + 0.5% MnO_2 + 0.5 SS-316L were the better sample at 1500°C.

4.0 Conclusions

In this present work, it shows that the co-doping of manganese oxide and stainless steel was beneficial as the increase in bulk density which is higher than doping with manganese oxide only. The increase in amount of stainless steel in samples do degrade the density at high sintering temperature above 1350°C. The Vickers hardness of the co-doped samples do show sign of improvements at 1350°C but rather deterioration at 1500°C. However, for fracture toughness, the co-doped samples show rather deterioration at 1350°C. Overall, the co-doping of manganese oxide and stainless steel to Y-TZP shows improvement from undoped Y-TZP in bulk density, Vickers hardness and fracture toughness at 1200°C of sintering temperature but not in all the cases at high temperature of sintering temperature. As conclusion, the Co-doping of manganese oxide and stainless steel do improve the qualities of the Y-TZP at low sintering temperature.

References

[1] P. Pandoleon, E. Kontonasaki, N. Kantiranis, N. Pliatsikas, P. Patsalas, L. Papadopoulou, T. Zorba, K. Paraskevopoulos and P. Koidis, "Aging of 3Y-TZP dental zirconia and yttrium depletion", *Dental Materials*, vol. **33**, no. 11, pp. e385-e392, 2017.

[2] D. Ćorić, M. Majić Renjo and L. Ćurković, "Vickers indentation fracture toughness of Y-TZP dental ceramics", *International Journal of Refractory Metals and Hard Materials*, vol. **64**, pp. 14-19, 2017.

[3] J. Roa Rovira and M. Rubi, *"Recent advances in ceramic materials research,"* Nova Science Publishers, Inc., 2013, pp. 71-86.

[4] J.-J. Kim, S.-Y. Yang, J.-H. Lee and J.-S. Lee, "Sintering behavior of Y-doped ZrO2 ceramics: the effect of Al2O3 and Nb2O5 addition," *Solid State Ionic,* vol. **172,** pp. 413-416, 2003.

[5] O. Agac, M. Gozutok, H. T. Sasmazel, A. Ozturk and J. Park, "Mechanical and biological properties of Al2O3 and TiO2 co-doped zirconia ceramics," *Ceramic International*, vol. **43**, pp. 10434-10441, 2017.

[6] A. Samodurova, A. Kocjan, M. V. Swain and T. Kosmacˇ, "The combined effect of alumina and silica co-doping on the ageing resistance of 3Y-TZP bioceramics," *Acta Biomaterialia*, vol. **11**, pp. 477- 487, 2015.

[7] S.M. Kwa, S. Ramesh, L.T. Bang, Y.H. Wong, W.J. Kelvin Chew, C.Y. Tan, J. Purbolaksono, H. Misran and W.D. Teng, "Effect of sintering holding time on the properties and low-temperature degradation behaviour of manganese oxide-doped Y-TZP ceramic", *Journal of Ceramic Processing Research*, vol. **16,** no. 2, pp. 193-198, 2015.

[8] M. Amiriyan, M. Satgunam, S. Sivakumar, R. Singh and R. Tolouei, "Sinterability and Mechanical Properties of MnO2-doped Y-TZP: the Effects of Holding Time Variations", *Applied Mechanics and Materials*, vol. **110-116**, pp. 1284-1288, 2012.

[9] ASTM E1876-97 (1998), "Standard Test Method for Dynamic Young's Modulus, Shear Modulus and Poisson's Ratio by Impulse Excitation of Vibration," Annual Book of ASTM Standards.

[10] Musikant, S., In *What Every Engineer Should Know about Ceramics*, (Marcel Dekker, Inc., 1991) pp. 104-105.

[11] ASTM E384-99 (1999), *"Standard Test Method for Microindentation Hardness of Materials,"* Annual Book of ASTM Standards.

[12] ISO 14705 (2000), *"Fine ceramics (advanced ceramics, advanced technical ceramics) – Test method for hardness of monolithic ceramics at room temperature".*

[13] R.N. Katz, "Applications of High Performance Ceramics in Heat Engine Design," *Mater. Sci. Eng.*, **71** (1985) 227-249.

[14] S. Ramesh and C. Gill, "Environmental degradation of CuO-doped Y-TZP ceramics", *Ceramics International*, vol. **27**, no. 6, pp. 705-711, 2001.

[15] Niihara, K., Morena, R. & Hasselman, D. P. H., "Evaluation of K_{Ic} of Brittle Solids by the Indentation Method with Low Crack-to-Indent Ratios," *J. Mater. Sci. Letts.*, **1** (1982) 13-16.

[16] ASTM E112-96 (2004), *"Standard Test Methods for Determining Average Grain Size,"* Annual Book of ASTM Standards.

[17] Mendelson, M. I., "Average Grain Size in Polycrystalline Ceramics," *J. Am. Ceram. Soc.*, **52** (1969) 443-446.

[18] Cullity, B. D. & Stock, S. R., In *Elements of X-Ray Diffraction*, 3rd edition (Prentice Hall, Inc., 2001) pp. 167-170.

[19] Toraya, H., Yoshimura, M. & Somiya, S., "Calibration Curve for Quantitative Analysis of the Monoclinic-Tetragonal ZrO_2 System by X-Ray Diffraction," *J. Am. Ceram. Soc.*, **67** (1984) C-119 - C-121.

[20] A.A. Nogiwa-Valdez, W.M. Rainforth, P. Zeng and I.M. Ross, "Deceleration of hydrothermal degradation of 3Y-TZP by alumina and lanthana co-doping," *Acta Biomaterialia*, vol. **9**, pp. 6226-6235, 2013.

[21] G. Pereira, A. Venturini, T. Silvestri, K. Dapieve, A. Montagner, F. Soares and L. Valandro, "Low-temperature degradation of Y-TZP ceramics: A systematic review and meta-analysis", *Journal of the Mechanical Behavior of Biomedical Materials*, vol. **55**, pp. 151-163, 2016.

[22] O. Agac, M. Gozutok, H. Sasmazel, A. Ozturk and J. Park, "Mechanical and biological properties of Al 2 O 3 and TiO 2 co-doped zirconia ceramics", *Ceramics International*, vol. **43**, no. 13, pp. 10434-10441, 2017.

Biomimicry Inspired High Impact Absorbed Elbow Pad

Nik Arisha Suraya[1,14], Leng Chuan Yong[1], Norhabibah Mohamad[1], and Hui Leng Choo[1]

[1]Department of Mechanical Engineering, School of Engineering, Taylor's University, Malaysia.

Abstract. Biomimicry can be defined as a study of mimicking living things and it is a powerful tool to create a new innovation that can solve human challenges. The biomimicry approach is applied in this study in order to design a high impact absorbed elbow pad inspired by the core structure of hedgehog spines which is the honeycomb structure. The nature morphology of the hedgehog spines are very unique as it consist of triangular honeycomb cellular structures as its core to prevent the spines from buckling and undergoes major breakage as the spines have a capability to absorb impact or shock. The bio-inspired material with additive manufacturing has the potential to enhance the material's performance by modifying the design geometry using biomimicry approach. The usage of the commercial 3D-printer filaments such as acrylonitrile butadiene styrene (ABS) and polylactic acid (PLA) in the fabrication of high impact absorbed elbow pad allows comparative study to be done on the materials for lightweight impact absorbing application. All the materials were 3D-printed and tested under impact and tension load in order to determine the mechanical behaviours of the lattice structure materials which has the relative density of 76 percent. Besides, the mechanical behaviours of the lattice structure were further investigated using ANSYS Workbench simulation software for results validation. From the comparative study, it was found that ABS exhibits ductile fracture and has higher energy absorption compared to PLA.

Keywords. Lattice structure, additive manufacturing, biomimicry, impact test, tensile test

[14] Author: arishasurayanikismail.nik@sd.taylors.edu.my

1. Introduction

In this modern world, the demands for a lightweight and strong materials are enormous due to the new sophisticated technology and tools. The advent of additive manufacturing has helped the engineers to design and manufacture new complex products in a short time with low cost manufacturing. The additive manufacturing is also a very reliable technology for rapid prototyping in order to test and verify the concept modelling prior to the production.

Not only that, biomimicry has become a very popular and powerful approach for innovation. Biomimicry can be defined as the study of imitating or mimicking nature where it helps the engineers to find ideas and inspirations for new creation. Most of the engineers used this approach to study about the nature such as animals, plants and microbes to create an innovation product that can solve human challenges. For instance, the invention of airplane was actually inspired by birds using biomimicry approach. The Wright Brothers have spent ample of time to observe the birds in flight and study about the bird's wings when they fly against the wind. From biomimicry studies of the birds, the Wright Brothers have successfully designed and produced the first airplane in 1903.

Thus, this shows that the combination of bio-inspired method with additive manufacturing has the potential to create new products and also to enhance the performance of the materials by modifying the design geometry using inspiration from the nature [1]. Therefore, this research covers a comparative study on the 3D-printer materials used in fabricating high impact absorbed elbow pad such as acrylonitrile butadiene styrene (ABS) and polylactic acid (PLA) inspired by the core structure of the hedgehog spines. The comparative study among these materials were done in order to determine the most appropriate choice of 3D-printer material for lightweight impact absorbing application.

The honeycomb lattice structure is one of the most effectual structure that is able to absorb impact energy compared to the other materials such as polymeric or metal foams [2]. Honeycomb core structures application is very popular in automobile and aerospace industries due to its unique properties where it has high energy absorption and high strength to weight ratio. To prove its unique properties, many researchers have studied the performance of the honeycomb structures under various cases such as quasi-static and dynamic loads. However, different honeycomb configurations such as hexagonal, orthogonal, hexagonal-chiral, anti-tetrachiral and tetrachiral will results in different energy absorption due to different Poisson's ratio [3]. Tiwari et al [4] has done an experiment and simulation in order to study the behavior of the honeycomb core structure under axial compressive load. The crushing method was conducted on the honeycomb using the compressive testing machine and the experimental results data was then being compared to the numerical simulation results. From the study, it was found that the reinforcement on the honeycomb structure materials as shown in Figure and varying the wall thickness can increased its density, strength and also the capability to absorb the impact energy [4]**.**

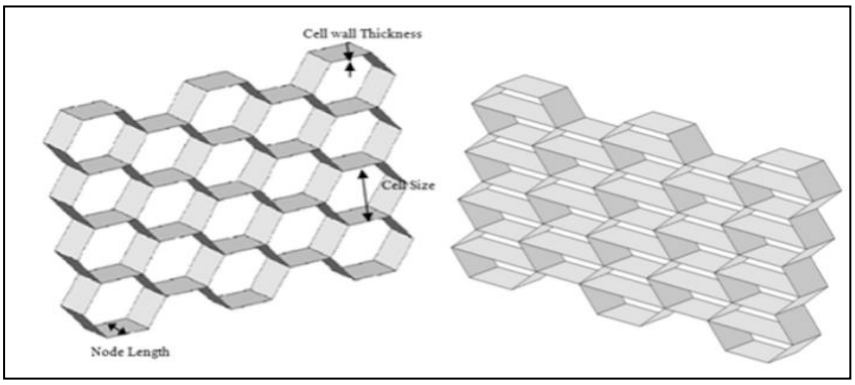


Figure 1. The cell structure of honeycombs [4]**.**

Other than that, honeycomb core is also applied in the design of safety gears such as helmet due to the high energy absorption. The capability of the honeycomb structure to absorb high impact energy has grab many researcher's attention nowadays. Kholoosi and Galehdari [5] have done a study on the design and analyzed the honeycomb structure under impact that was applied to the helmet and they claimed that by implementing a graded honeycomb structure to the helmet can enhance the energy absorption thus can reduce the injury due to the impact from the collisions.

From the research done by Vincent and Owers, it was found that the core structure of the hedgehog spines consist of triangular cells honeycomb structure [6], thus the three-dimensional of triangular prism cellular structure is implemented to the design structure of the high impact absorbed elbow pad. The mechanical behavior of this structure can be studied by observing the response of structure material towards the load applied. According to Hucko and Faria [7], they stated that the cellular structure will exhibits three different stages in uniaxial test such as linear elastic, plateau and densification as shown in

Figure 2.

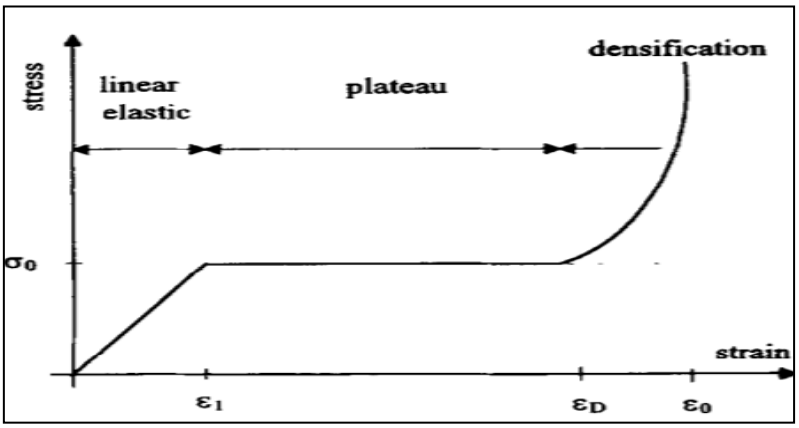


Figure 2. Stress-strain curve for cellular structure under uniaxial tension.

According to Ju and Summer [8], from the research it was found that triangular cell structure has better stiffness compared to hexagonal cell structure under the same axial stress. Not only that, the triangular cell structure also can withstand shear force as it exhibits lower value of normalized shear strain-shear strength. Based on the study done by Niu et al [9], it was found from numerical results that the triangular cell structure has higher value of Young's Modulus compared to the cubic and hexagonal cell structure with the same relative density due to the maximum stiffness-to-mass-ratio. The triangular cell structures also has a high strength as it has the lowest stress level under the uniaxial

tension force. Niu et al also stated that the cellular structure with a high relative density will have a high energy absorption meaning the porosity of the lattice structure needs to be minimized. Besides, the effective Young's Modulus of the cellular structure also increases with relative density.

A research has been done on the PLA for its mechanical response of unidirectional 3D-printing by Fusion Deposition Method (FDM) which is at the angle of 0^o and 90^o extrusion. Based on the results, it was found that the PLA has better mechanical strength compared to other plastic polymers such as ABS, polypropylene, polycarbonate and polyethyleneimine (PEI) [10]. However, the comparisons between ABS and PLA based on their energy absorption performance can be very complex as the materials are dependent on the base polymer, density and the stress and strain behavior.

Thus, the aims of this study to choose the most appropriate 3D printed filament material that can absorb high amount of impact energy for high impact absorbed elbow pad. In this article, the mechanical properties such us effective Young's Modulus, E^*, stress and strain and mechanical behavior of the 3D-printed triangular lattice structure were studied by carried out testing such as tensile test and impact test. The experimental results were then further investigated and compared with simulation results collected from ANSYS Workbench for finite element analysis (FEA).

2. Research Methodology

2.1 3-D Geometry Modelling

The 3D model of the lattice structure inspired by the hedgehog for the high impact absorbed elbow pad is designed using SolidWorks. The in-depth study on the core structure of the hedgehog spines which is the honeycomb showed that the spines consist of layers of triangular cellular structure as its core where it is capable to absorb high impact energy.

The specimen was designed with the dimension of 90 mm x 20 mm x 20 mm following the representative volume element (RVE) method. The RVE method is often used in any material testing such as tensile test as it is effective to analyze the mechanical properties of the material such as Young's modulus, elastic modulus, strain hardening and other properties [11]. Since this study was mainly focus on the material selection of the lattice structure that has a high energy absorption, the parameter of the triangular lattice structure was kept constant, meaning all the specimens of the lattice structure have the same volume. The parameter of the lattice structure was designed according to the work that has been done by Niu et al [9]. Based on their study, it was found that the triangular lattice structure with the length of 4.8 mm, thickness of 1.74 mm and height of 4.57 mm produced 76 percent of relative density which was good for energy absorption and the parameter of the lattice structure was shown in Table 1.

Table 1. The parameters of the triangular lattice structure [9].

Cell shape	Length, L (mm)	Thickness, t (mm)	Height, h (mm)
Triangular	4.8	1.74	4.57

Theoretically, the higher the relative density, the higher the energy absorption. Therefore, the parameters of that lattice structure was chosen. The diagram of a unit cell of triangular structure and the 3D modelling of triangle cellular structures were shown Figure and Figure .

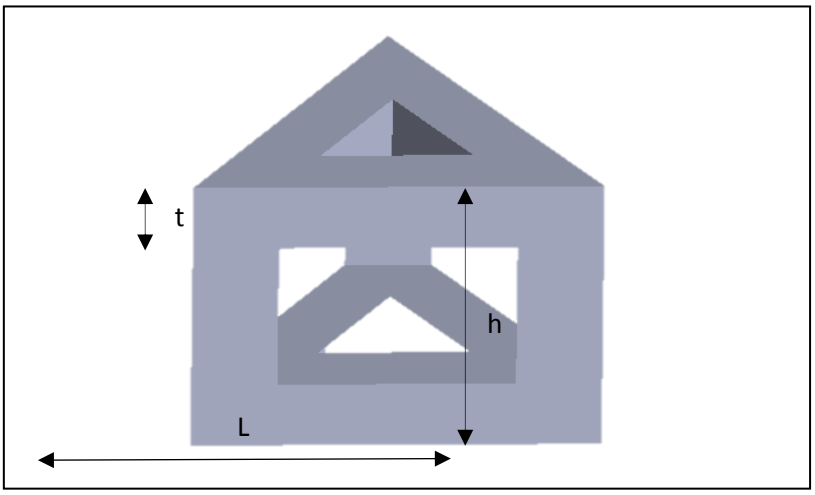


Figure 3**.** A triangular unit cells.

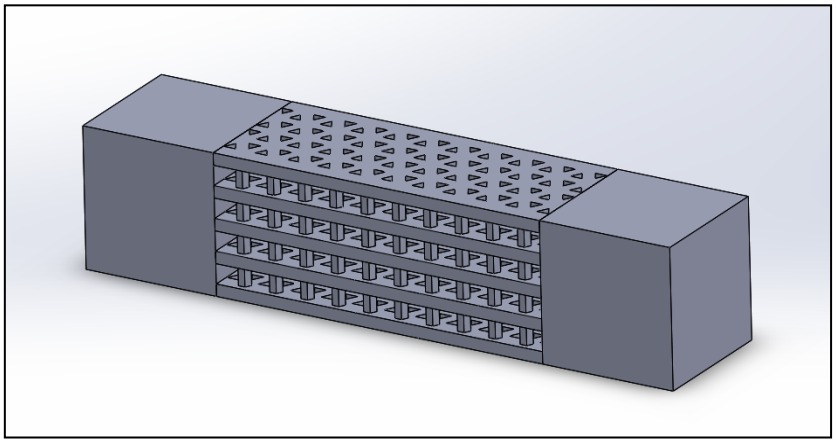


Figure 4. The triangular lattice structure specimen.

The specimen of the lattice structure was created by patterning the triangular unit cells in in-plane direction. Then, the single layer of the triangular lattice structure was then arranged in out-plane direction.

2.2 Material parameters

The 3D-printer materials used in this study were acrylonitrile butadiene styrene (ABS) and polylactic acid (PLA) by Ultimaker and the technical data of these 3D-printed materials were listed in Table . Other than that, the mechanical properties of the cellular structure is also influenced by the relative density (RD) which can be defined by the following formula [17]:

$$Relative\ Density\ (RD) = \frac{\rho^*}{\rho} \times 100\% \qquad (1)$$

where the density of the cellular structure is denoted by ρ^* and it is divided by the wall material's density denoted by ρ. The energy absorption of the material can be determined based on the relative density of that particular lattice structure. As theoretically, the higher the relative density, the higher the energy absorption of the material.

Table 2**.** The mechanical properties of 3D-printed filaments.

Material	ABS	PLA
Tensile Modulus (MPa)	2030 ± 45	2852 ± 88
Tensile Strength (MPa)	29.3 ± 0.8	38.1 ± 0.9
Poisson's Ratio	0.35	0.36
Density (g/cm^3)	1.04	1.26

However, the challenge to the comparative study between these two 3D-printed materials was the unavailable information or data of the mechanical properties of the materials based on the lattice structure design. All these mechanical properties presented in Table was based on the solid 'dog-bone' shaped specimen which was widely used for material testing. This issue can be the proof of limited application and testing for 3D print materials in lattice structure study. Besides, some plastic materials are often being used in injection molding process because it is difficult to 3D print soft, flexible and rubber like plastic materials which can be easily bent under high stress and temperature [12].

2.3 Experimental Preparation

2.3.1 3D Printing

The process of 3D printing begins by drawing a solid 3D model using any computer-aided engineering program such as SolidWorks. Then, the computer-aided drawing (CAD) file was then converted to .STL file format before being sent to the Ultimaker Cura 3.0 software for the preparation of 3D printing model. The setting of the 3D printing machine was shown in Table .

Table 3**.** The setting of 3D printing machine.

Layer height (mm)	0.2
Shell thickness (mm)	1.2
Fill density (%)	100
Print speed (mm/s)	40
Nozzle size	0.4

The triangular lattice structure specimens were fabricated using 3D printing method using the materials that have been described previously. Two different tests were conducted to study the mechanical properties and mechanical behavior of the lattice structure specimen such as tensile test and impact test. Each of the test were repeated for three times in order to observe the average trend of the results. Therefore, about eight specimens for each materials were 3D printed using the dimensions listed in **Error! Reference source not found.**. The 3D printed specimens of the triangular lattice structure shown in

Figure .

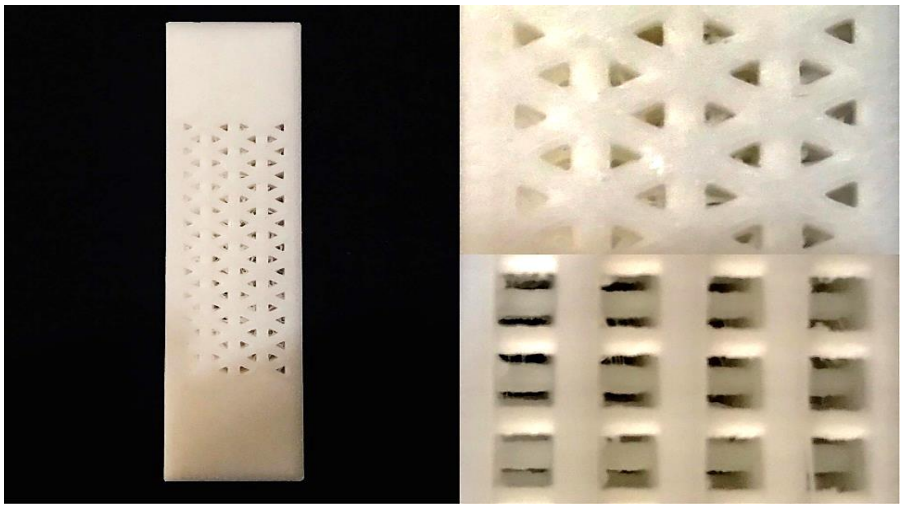


Figure 5. The 3D printed specimens of the triangular lattice structure in-plane and out-plane direction for PLA and ABS material.

2.3.2 Tensile Test

The tensile test was conducted using the Instron 5969 universal testing machine at a room temperature specifically 27^{o}C for all the 3D printed materials. The machine was set up by attaching the jigs at the top and the bottom base of the machine as shown in Figure . The function of the jig was basically to clamp the specimen. The specimen was clamped in between the jigs and it needs to be ensured that the solid end of the specimen was not clamped tightly as it can cause deformation or shearing on the specimen before the testing. All the settings for the tensile test was set using the Bluehill Universal software that compliances with the Instron machine. The software was used to define the type of the testing, the dimension of the specimen, tensile speed and the axial force on the specimen. In this test, the speed was set to 0.25 mm/s.



Figure 6**.** The tensile test set-up.

As the force was applied to the specimen axially, the elongation, yield and the strain hardening of the specimen was observed. All the raw data of the specimens such as stress and strain were extracted directly from the software and the results were tabulated in a graph form. From the stress-strain graph, the effective Young's Modulus of the lattice structure specimen, E^* can be obtained from the gradient of linear elastic region and E* can be determined by using the formula [9]:

$$E^* = \frac{\sigma}{\varepsilon} = \frac{\left(\frac{F_t}{A_0}\right)}{\left(\frac{\Delta L}{L_{Tot}}\right)} \quad (2)$$

where the normal stress and the axial strain are denoted by σ and ε respectively. Besides, the axial uniaxial tension force is denoted by F_t, the cross-sectional area of the cellular structure is denoted by A_0, the tensile elongation is denoted by ΔL and the total length of the cellular structure is denoted by L_{Tot}.

The material of the lattice structure that has high energy absorption or toughness can be determined by the area under the stress-strain curve. Meaning, the larger the area under the stress-strain curve, the higher the energy absorption. Besides, material toughness can be defined as the ability of the material to absorb energy per unit volume before it fractures and it can be defined by using the following formula:

$$\int_0^{\varepsilon} \sigma \, d\varepsilon \quad (3)$$

where the stress is denoted by σ and the strain is denoted by ε. Usually the material toughness require a combination of strength and ductility as the ductile material is elastic and exhibits plastic deformation.

2.3.3 Impact Test

The impact test was conducted using the Gunt WP410 350 Nm impact test machine at room temperature which is 27^{o}C as shown in Figure . This experiment was important for the fundamental experiments as from this test, the amount of energy absorption of the lattice structure specimen can be observed as the impact load with a capacity of 350 Nm (Joule) hits the specimen. Another objective of this experiment was to evaluate the fracture behavior of the material in general whether the material is ductile or brittle.

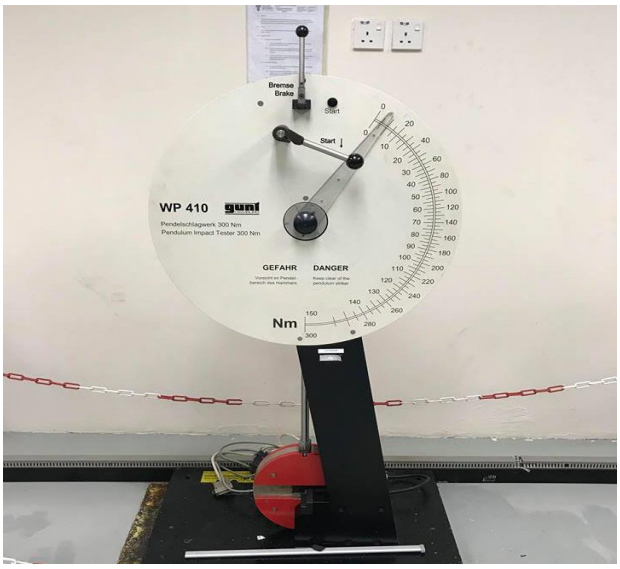


Figure 7**.** Impact tester set-up.

During the experiment, the pendulum hammer is lifted to the pendulum arm and the specimen is then placed at the specimen holder. It must be ensured that top face of the triangular lattice structure specimen is facing towards the pendulum hammer as it gets hit. By pulling out the pin, the pendulum hammer was released and the kinetic energy was transferred to the lattice structure specimen when both were in contact. At this point, the specimen is either bent or shattered by the impact of the hammer operating at 350 Nm (Joule) and the hammer impact speed was at 5.5 m/s. The brake was applied as soon as the specimen gets hit by the hammer and the impact energy can be read directly from the large scale.

In this experiment, the hammer was lifted at maximum height in which the maximum height can be calculated using the equation:

$$h = \frac{v^2}{2g} \tag{4}$$

where height is denoted by h, velocity is denoted by v and the gravitational acceleration is denoted by g which has a value of 9.81 m/s^2.

2.3.4 Finite Element Analysis

The finite element analysis (FEA) was used to simulate the triangular lattice structure specimen model under tension. The most important thing in FEA is to have a fine mesh in order to capture the stress and strain of the specimen at a particular region. Meaning, the finer the mesh, the more accurate the results. However, the fine mesh will results in longer computational time as there will be hundreds, thousands or millions elements that need to be solved. In this study, the combination of tetrahedral and hexahedral mesh elements were used on the geometry of triangular lattice structure specimen as the both combination of hexahedral and tetrahedral mesh elements as shown in Figure were the best choice to achieve an accurate results due to its stability and has robust convergence. From the mesh independence test, it was found that the mesh size of 0.8 mm resulted in more accurate results where it has the skewness of 0.25 and orthogonal quality of 0.84. However, in this study, the ANSYS Workbench student version has limitation on the number of mesh elements where the meshing for structural analysis is limited only up to 300000 elements. Therefore, the mesh size of 0.8 mm which consists about 197392 elements were chose in the simulation of tensile test.

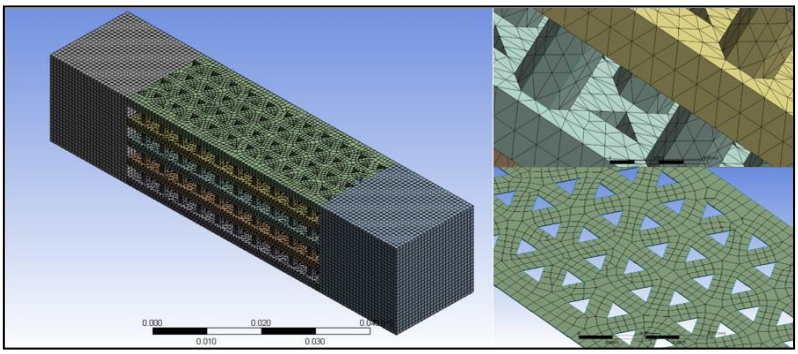


Figure 8**.** The tetrahedral and hexahedral mesh for finite element analysis.

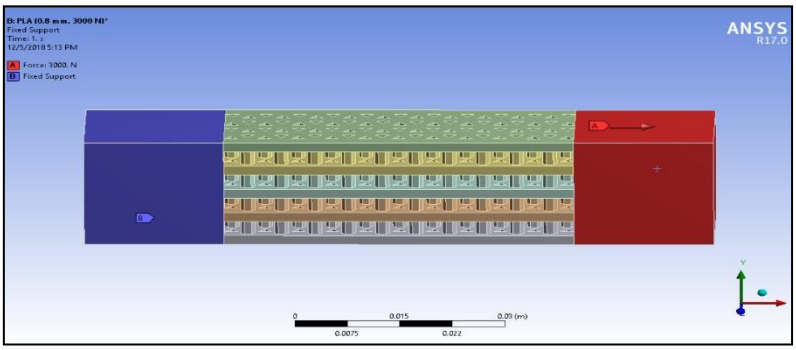


Figure 9**.** The boundary conditions for tensile test.

In the simulation, the force of 3000 N was applied on the most right end side (x-direction) of the specimen as the 3D printed materials as from the tensile testing it was found that the maximum load that the triangular lattice structure specimen can withstand is 3000 N. The left end side of the specimen was set as a fixed support as shown Figure 9. The parameters such as maximum stress and elastic plastic strain were obtained in order to calculate the effective Young's Modulus of the triangular lattice structure, E^*. Not only that, the deformation on the triangular lattice specimen was also observed in the simulation.

3. Results and Discussion

3.1 The Quality of 3D Printing Specimens

The triangular lattice structure specimens were manufactured by 3D printing with the dimension of 90 mm x 20 mm x 20 mm including two solid ends for the tensile test grips as shown in Figure . Three specimens from two different materials were printed with 100 percent infill for each tensile testing and impact testing. All the lattice structure specimens for PLA material were fabricated with good quality except for a few specimens of ABS. There was a few defects on the ABS specimens where some of the lattice struts were chipped off in part build up. This may happen due to the low quality of the ABS filament used or the filament might contains air bubbles. A few of ABS specimens that had manufacturing defect were not used in this study as it might affect the results, only ABS specimens without the manufacturing defect were used in this study. Other than that, another factor that contributes to the manufacturing defect was the Ultimaker 2+ printer machine was not capable to print a flexible or rubber like plastic material like ABS. During the 3D printing using ABS filament, the second layer of the lattice structure cannot be printed or malformed as the ABS layer was not stick

well to the other neighbouring layers and it toppled over during the process. Therefore, the comparative study and testing were done on good quality of PLA and ABS specimens only.

3.2 Tensile Test Results

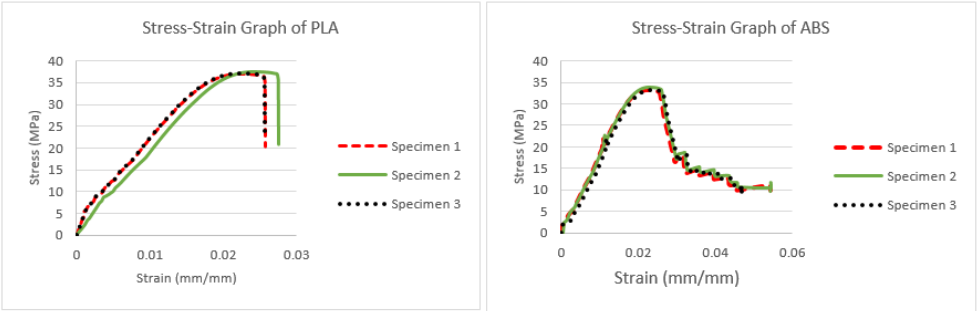


Figure 10**.** The stress-strain curve of PLA and ABS from the tensile testing.

Figure 10 showed the stress-strain curve for each of the PLA and ABS specimens. The trend-line of the stress-strain curve for the 3D printed materials showed the typical tensile behavior where it consisted of the linear elastic, plateau and rupture point. Both 3D printed lattice structure materials showed a regular linear stress strain curve at the beginning of linear elastic region before yielding as presented in Figure . The effective Young's modulus of the triangular lattice specimens can be observed from the linear region where it obeys the Hooke's Law where the stress was directly proportional to the strain. This point of linear region can be called as elastic region where theoretically, the material will return back to its original shape or condition once the load is removed. If the load is still applied to the specimen it will yield and deformation will occurs.

Table 4**.** The effective Young's Modulus, *E** by tensile test for two different types of materials.

Material	Relative Density (%)	E* (MPa)	Ultimate Tensile Strength (MPa)	Elongation (%)
PLA	76	2000.54	37.22	2.4
ABS	76	1785.91	33.08	2.6

Besides, the effective Young's Modulus of the material described the stiffness of the material. The material with the highest value of effective Young's Modulus is stiff and strong. In order to find the effective Young's Modulus, one of the three specimens was chosen (Sample 1) for each materials as shown in Table . The comparisons between the two materials were done by having a constant relative density of 0.76. The relative density is important in the production of lightweight structure as it is the fraction of particular volume taken up from the solid materials for the lattice structure. With fixed relative density, the mechanical properties such as the effective moduli of triangular lattice structure of each 3D printed materials can be observed. Based on Table , it showed that PLA has the highest effective Young's Modulus value of 2000.54 MPa compared to the ABS which has the value of 1785.91 MPa. Thus, it indicates that PLA is stiffer and stronger compared to the ABS material.

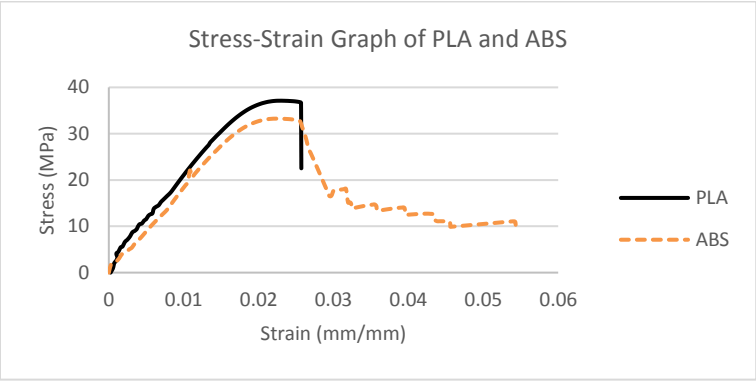


Figure 11**.** The experimental stress-strain graph of PLA and ABS.

Then, the study of the tensile toughness was done by comparing the area under the stress-strain graph for ABS and PLA materials. It was found that ABS material has higher toughness compared to PLA material.

The area under the curve was evaluated using EXCEL where the curve was integrated using the Eq. (3), From the cumulative integral from zero strain to the fracture strain, it was found that the toughness of PLA has a value of 646.61 kJ/m^3 while the toughness of ABS has a value 994.21 kJ/m^3. Thus, it showed that ABS has higher toughness compared to the PLA material. Not only that, the low elastic modulus of ABS which has a value of 1785.91 MPa showed that the ABS specimen was strained further compared to the PLA material before yielding and this allows more energy to be absorbed by the material. Besides, from the stress-strain curve in Figure, it showed that the maximum stress of PLA at fracture was 37.22 MPa with a strain of 0.025 mm/mm while for ABS material, the maximum stress at fracture was 33.08 MPa with a strain of 0.0263 mm/mm.

3.4 Tensile Test Simulation

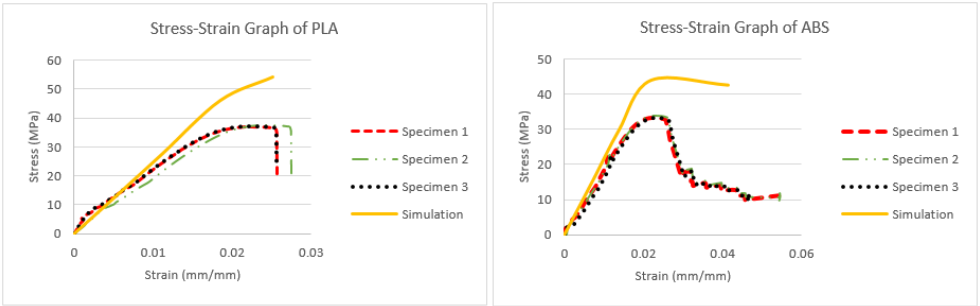


Figure 12**.** The simulation stress-strain graph for PLA and ABS.

The finite element analysis (FEA) was done in order to compare and validate the effective Young's Modulus of the specimens with the experimental results. The linear regression function was applied in the calculation of effective Young's Modulus and it is available in EXCEL. With the usage of 'LINEST' function, the slope of the linear elastic line as shown in Figure can be calculated. Not only that, the Eq. (2) also can be applied in the calculation of Young's modulus and from the calculation, the value was agreed to the value of 'LINEST' function. Therefore, both approach can be used in the effective Young's modulus calculation.

As the relative density of the specimens for each materials were the same, therefore it was reliable and appropriate to compare the effective Young's modulus of both materials directly. The validation results was done as shown in Table and it can be seen that PLA has higher E* compared to ABS as the material was stiffer.

Table 5**.** The comparisons of effective Young's Modulus between the experimental and simulation results.

Material	**Experimental**		**Simulation**		**Error (%)**
ABS	**Relative Density (%)**	**E* (MPa)**	**Relative Density (%)**	**E* (MPa)**	
	76%	1785.91	76%	1976.66	10.68
PLA	76%	2000.54	76%	2508.85	25.4

3.5 Impact Test

Table 6**.** The results of the impact test for PLA and ABS materials.

Material	**Impact Energy Absorbed (J)**
PLA	8
ABS	30

Impact test was done on the ABS and PLA specimens in order to perform quality test and observe the fracture behavior of the materials. The results of the energy absorption for both materials were shown in the Table and it showed that the ABS has high energy absorption where it has the value of 30 Joules compared to the PLA which only resulted 8 Joules of energy absorption. Not only that, it was found that PLA was more brittle compared to the ABS.

4. Conclusion and Future Work

The capability of the 3D printed materials to absorb impact energy was studied numerically and experimentally. Due to the complexity of the triangular lattice structure, investigation was done in order to study the mechanical properties of the 3D printing materials for the lattice structure specimen. Two different 3D printed materials such as ABS and PLA were used for comparisons study in order to choose the best material that was suitable for the high impact absorbed elbow pad. In the future, the usage of high precision and heavy duty 3D printing machine can be used instead of the basic commercial 3D printing machine as it is more reliable to print a soft, flexible and rubber like plastic material such as ABS. From the comparisons study between the two 3D printed materials, the results were summarized as follows.

- The 3D printed material, ABS has higher energy absorption compared to the PLA. It can be seen from the area under the graph of tensile test and impact test result as both agreed that ABS can absorbed more impact energy compared to PLA material.

- PLA can be said as a brittle material because it did not exhibits plastic deformation as seen from the stress-strain graph of the tensile test. From the graph, it showed that PLA failed soon after the ultimate strength (UTS) region.
- As for the ABS, it exhibited plastic deformation or also known as yielding and it can be seen from the stress-strain graph of the tensile test. Therefore, ABS can be considered as a ductile material.
- The low elastic modulus of ABS showed that the ABS specimen was strained further compared to the PLA material before yielding and this allows more energy to be absorbed by the material.

After all, based on the stress-strain curve from the experimental, the Young's modulus and the maximum tensile strength can be observed clearly as the graph displays a typical linear stress-strain behavior. Despite the fluctuation that can be seen on the curve, it still can be considered as a linear. The fluctuation happened due to the slippage and also moving jigs during the testing that cause an inconsistency in data reading. It can be said that the results from this project is reliable. Not only that, the concept and method to determine the mechanical behaviors of 3D printed lattice structure are approachable in this study.

The authors would like to thank Yong Leng Chuan, Norhabibah Mohamad and Hui Leng Choo for continuous guidance, assistance and supervision throughout this research.

Reference

[1] S. Kale, N. Khani, A. Nadernezhad, B. Koc, Modeling and additive manufacturing of biomimetic heterogeneous, *3rd CIRP Conference on BioManufacturing* **65**, 48-55 (2017).

[2] V. Crupi, G. Epasto, E. Guglielmino, Comparison of aluminium sandwiches for lightweight ship structures: Honeycomb vs. foam, *Marine Structures,* **30**, 74-96 (2012).

[3] J. Huang, Q. Zhang, F. Scarpa, Y. Liu, J. Leng, Shape memory polymer-based hybrid honeycomb structures with zero Poisson's ratio and variable stiffness, *Composite Structures,* **179**, 437-443 (2017).

[4] G. Tiwari, T. Thomas, R. P. Khandelwal, Influence of reinforcement in the honeycomb structures under axial compressive load, *Thin-Walled Structures,* **121-112**, 1-8 (2017).

[5] F. Kholoosi, S. A. Galehdari, Design and analysis of a helmet equipped with graded honeycomb structure under impact of flat and Hemi-spherical anvils, *Plasticity and Impact,* **173**, 1299-1306 (2017).

[6] J.F. Vincent, P.Owers, Mechanical design of hedgehog spines and porcupine quills, *Journal of Zoology* **210**, 55-75 (2009).

[7] L. F. B. Hucko, Material Model of Metallic Cellular Solids, *Computers & Structures,* **62**, 1049-1057 (1197).

[8] J. Ju, J. D. Summers, Compliant hexagonal periodic lattice structures having both high shear strength and high shear strain, *Materials and Design,* **32**, 512-524 (2011).

[9] J. Niu, H. L. Choo, W. Sun. S. H. Mok, Numerical study on load-bearing capabilities of beam-like lattice structures with three different unit cells, *Materials: Design and Application,* **1**, 1-18 (2017).

[10] Y. Song, Y. Li, W. Song, K.Yee, K. Y. Lee, V. L. Tagarielli, Measurements of the mechanical response of unidirectional 3D-printed PLA, *Materials and Design*, **123**, 156-164 (2017).

[11] S. Youssef, E. Maire, R. Gaertner, Finite element modelling of the actual structure of cellular materials determined by X-ray tomography, *Acta Materialia*, **53**, 719-730 (2004).

[12] S. Barner, *Mechanical Properties of Additive Manufactured Honeycomb Structures*, (Clemson University, 2015).

[13] A. Karimi, M. Navidbakhsh, Mechanical properties of PVA material for tissue engineering applications, *Material Technology*, **29**, 1-11 (2014).

[14] S.A. Galehdari, M. Kadkhodayan, S. H. Moud, Low velocity impact and quasi-static in-plane loading on a graded honeycomb structure; experimental, analytical and numerical study, *Aerospace & Technology*, **47**, 425-433 (2015).

EURECA 2018 – Conference Paper
Paper number 2ME24

Design and Simulation of Vehicle Simulator Structure

Farid Mohd Bin Aladdin[1], Dr. Seong Chun Koay[1], and Kah Kit Phang[1]

[1]Department of Mechanical Engineering, School of Engineering, Taylor's University. No, 1 Jalan Taylor's, 47500 Subang Jaya, Selangor DE, Malaysia

Abstract. The evolving of technology that is growing rapidly has start to influence researchers into studying the human interaction between machines. Vehicle is one of the complex machine being study by engineers that are interest in optimizing the human comfort level due to the interaction of human exposing to different type of circumstances such as sound and vibration. In the research study, a vehicle simulator structure is design accordingly with the determination to increase human comfort level by having experimentation under a vibration shaker. The static and dynamic factors of the structure is analyzed with the consideration of ergonomics and anthropometric data collected. The development of the design is constructed using Solidworks 2016 and the simulation is run through Ansys workbench 18.2 program. The design of the structure is being gradually enhance by altering the geometric shape with three iterations depending the data acquired from the simulation results. In addition, the type of material and joining between the simulator structure platform and the rigid seat design is discussed. The final outcome of the vehicle simulator structure will achieve its robustness and attain the desire human comfort level.

Keywords: Human comfort; vehicle simulator structure; static & dynamic factors; ergonomic and anthropometric data; design & simulation

1 Introduction

Human has been developing methods to explore the world by moving places to another. One of the invention that has cause an evolution to humankind was vehicle. Vehicle has been used to transport people to a destination in a short period of time and it has display an important factor in human progression and world development. As production of vehicles increasing every year, the aspect of human comfort is being question continuously by both engineers and designers in the development of new type of model. Vehicle seat is one of the major aspect in studying human discomfort. Researchers has conduct one of the studies involving the seating posture of driver. It shows that consistent bad posture of the driver has been mainly the cause of overall discomfort which might lead to musculoskeletal injuries and potentially having permanent damage to human health. In the investigation of multiple cases, whiplash and lower back pain is the type of injuries commonly happen on drivers [1]. Whiplash occurs around the driver's neck due to the sudden change in acceleration and deceleration of force that is uncontrollable which relates to dynamic factors. The lower back pain is due to the constant improper seating posture that leads to continuous discomfort especially for long duration. Therefore, more conducts have been carried out intensively on improving the safety, comfort and effectiveness of the seating system for the driver in vehicle. However, the study of human perception has been always a complex topic as it involves human response system towards machine. A method is needed for analyzing the behavior of human interaction and by developing a vehicle simulator structure, it opens a certain aspect of interest that enable the study of human comfort and understand in designing a better vehicle structure for future vehicle development.

Based on the majority vehicles used in the world, car structure will be taken as an example of model for the research in constructing the vehicle simulator structure with the purpose of study human comfort based on static and dynamic factors [2]. In static comfort, the seat and the structure of the vehicle is analyzed based on its strength depending the geometric shape design. The deformation from the human pressure distributed along the structure is improved without neglecting the ergonomics and anthropometric data obtained from research. As both ergonomic and anthropometric criteria must be applied simultaneously to achieve the expectation of human comfort [3]. Thus, the seating posture of human can be enhance depending the simulation data of the design. However, in real cases, the seat will positively experience constant changes due to the present of mechanical vibration and sound occurring from the surrounding environment. Consequently, dynamic factor is needed to be analyze for human comfort especially for long-term exposure of dynamic condition, it will dramatically affect the performance of the driver.

1.1 Research questions

What are the common injuries drivers frequently experience and what type of consideration requires to design a suitable vehicle simulator structure by increasing human comfort level? The injuries occur in most drivers are due to the uncomfortable seating posture in a certain duration in static and dynamic condition. As to design the right vehicle simulator structure, anthropometric and ergonomic conditions has to implement in order to achieve much comfortable car seats.

1.2 Hypothesis

The increasing of car production by automobile industries has been using seats that are designed statically due improvement on external mechanism of the car suspension which affects the dynamic factor. Thus, dynamic studies on the seat itself is not commonly done in the studies as they tend to optimize the seat with luxury seating cushion. The simulation of vehicle simulator structure allowing the study on dynamic factor in a rigid seat structure designed with proper criteria.

1.3 Project scope

Vehicle simulator structure is design with a justifiable model based on anthropometric data and ergonomics to allow a future research development on improving human comfort in vehicle seat by studying the varies aspect of static and dynamic factors.

1.4 Project objectives

The objective of this project is to design and simulated the vehicle simulator structure in studying human discomfort. As for the type of vehicle, car is chosen for part of the researching by designing the geometric shape that can mimic the surrounding environment of the car driver. The consideration of anthropometric data and ergonomics is used to design the car simulator structure. Also, the seat structure is evaluated with the data obtain from engineering simulation using ANSYS software to justify the design is accurately acceptable.

2 Literature review

The transmission of vehicle vibration to the seated human body brings an interesting topic to researchers. Vehicle simulator structure is mainly constructed with the purpose to study human discomfort and understand the characterization of automotive seat structure towards static and dynamic factors. A study of the characterisation of vehicle seat structural dynamics and effects on

ride comfort has been done by Leon from RMIT University. His research objectives were to understand the structural dynamics of common vehicle seat that may affects human comfort due to vibration [4]. His investigation on the changes in natural frequencies based on the three different specimens seat structure is assess with the current ISO standards measurement procedure. The different cushioned seats from passenger side may diverge the actual data needed in studying the dynamic factor due to the surface pressure and vibration absorption from the foam seat cushion itself.

In another study by Neil and his team, he combined the effect of long-term sitting and whole-body vibration in analyzing the human discomfort for vehicle occupants [5]. The dynamic factor that relates to whole-body vibration is caused by the frequency transferred from vehicle environment to human body. Based on the concept of Ebe's model, the total seat discomfort is dictated by the static factor whenever there is no vibration occurred, but when vibration is input into the seat, the combination of static and dynamic factors is included [6]. In most cases, vehicle environment has a low magnitude of vibration entering the seat due to high quality of vehicle suspension. Thus, optimizing the static factors such as the stiffness, and seat structure can achieve a certain comfort level. The figure below shows the model of responding of vibration magnitude to overall discomfort according to the factors in a period of time.

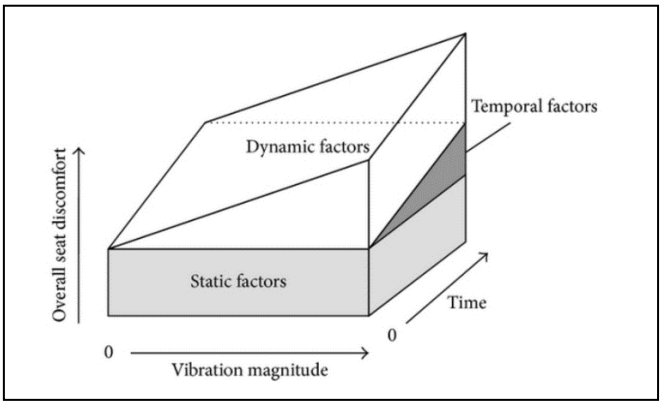


Fig. *1*. Model of vehicle seat discomfort [6].

Consequently, the both static and dynamic factors is taken into thoughts on overall discomfort while designing the vehicle simulator structure. In addition, the sensitivity of human response towards whole-body vibration is between 1Hz to 80Hz [7]. Having frequency out from the range could cause overall discomfort. As the interest of dynamic studies is between 1Hz to 100Hz, the natural frequency of the structure is design to have more than 100Hz. The reason is to ensure resonance doesn't occurred when the conducting dynamic studies on the interest field of frequency is same as the natural frequency of the vehicle simulator structure. In a case where resonance

occurred, human discomfort and health will be at risk while conducting the procedure as well as the vehicle simulator structure which might deform unpredictable.

3 Research methodology

3.1 Overall research design

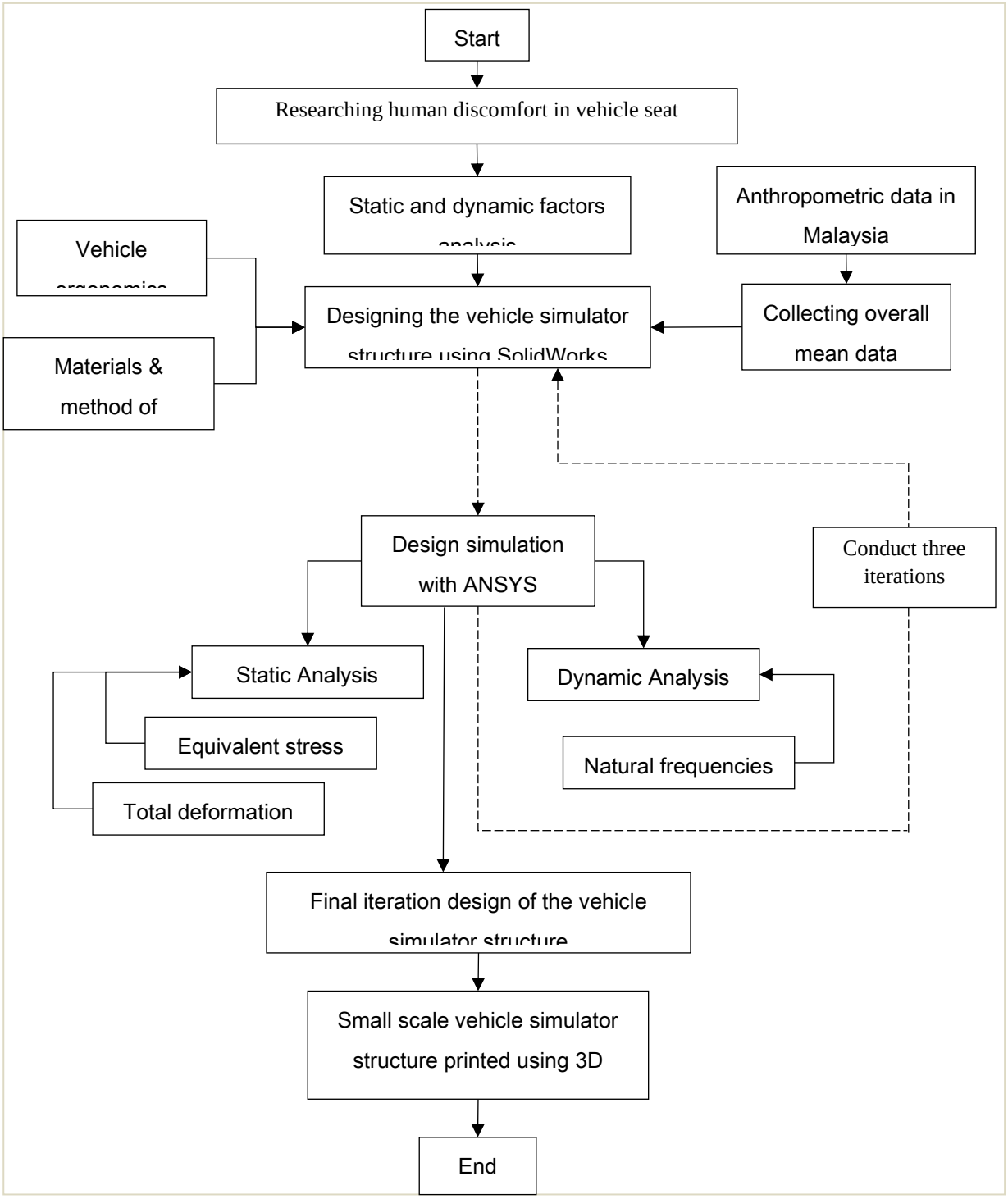


Fig. 2**.** Research design and simulation of vehicle simulator structure.

3.2 Measurement and data collection procedures.

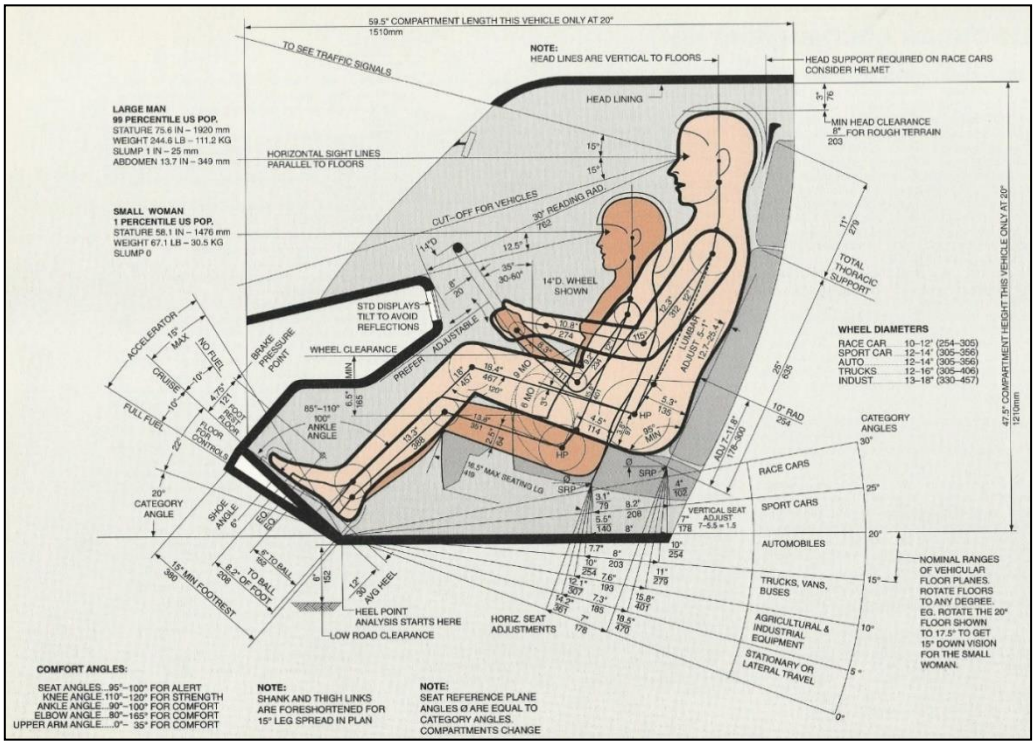


Fig. 3**.** Ergonomics of vehicle design [8]

Ergonomics is part of the study of human efficiency in their working environment. In the process to developing the vehicle simulator structure, relevant data is needed to reference the sketching of a design. As shown in figure 3 above, the vehicle seat design has been conducted by researchers in a way of having ergonomics criteria depending different types of vehicle. Having the dimension and angle able to assist in designing the structure accordingly at first. Due to the vehicle simulator structure will be design rigidly which means no adjustment based on individuals, the measurement of average human body is needed. Unfortunately, the complex and diverse structure of human body from different peoples across the world has cause a limitation towards designing stage.

In the extensive field of anthropometrics data that has been done, the research of this project will be based upon the overall Malaysian citizen to ease on the designing of vehicle simulator structure. The anthropometric database collected from over 1007 Malaysian citizens by a group of researchers at Universiti Kebangsaan Malaysia (UKM) is credited to assist on the vehicle simulator structure design [9]. From the results acquired, the mean data is taken as the anthropometric dimension for designing the structure. The mean data is taken as the average measurement of overall

Malaysian citizen. A rough design will be created with the estimated data from both ergonomics and anthropometric by having the concept of a vehicle environment based upon the driver seat of automobiles.

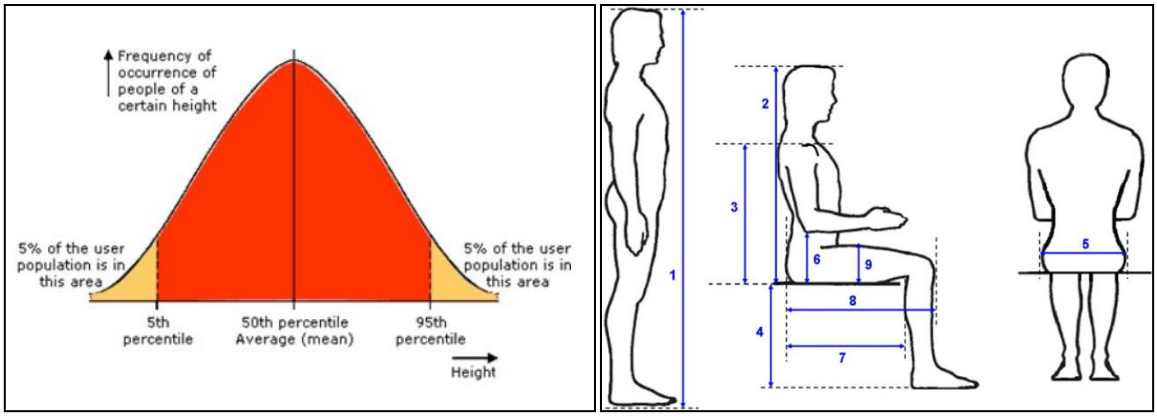


Fig. 4. The normal distribution graph and anthropometric measurement [9].

From figure above shows a normal distribution graph with an explanation of the frequent occurrence of people of a certain height. Thus, the mean value which acquired from the results is the section of 50th percentile. From table 1 below, the needed results of mean data for anthropometric dimension is taken for the requirement of the design structure. In addition, the average mean weight of the overall Malaysian citizen is measured with 60.40 kilogram.

Table 1. Anthropometric data of overall 1007 Malaysian citizen based on figure 5 representation [9].

No.	Average anthropometric dimension	Mean (mm)
1.	Stature	1565.00
2.	Sitting height	792.86
3.	Sitting shoulder height	515.84
4.	Popliteal height	424.80
5.	Hip breadth	378.34
6.	Sitting elbow height	224.66
7.	Buttock to popliteal length	448.60
8.	Buttock to knee length	558.70
9.	Thigh height	160.64
10.	Head length	194.94
11.	Crotch height	789.30

3.3 Equipment used

During the design stage of vehicle simulator structure, Solidworks 2016 is used to create different parts of the structure. This process allows the parts to be created and assemble together depending the right input dimension. The design is then analyze using Ansys workbench 18.2 simulation to understand the behavior of static and dynamic factors. The final iteration that is improved from previous iteration design will be printed out using 3D printer machine with a small scale of 1:10 due to a limitation of size provided by the machine of not exceeding 250mm x 250mm. The purpose of having a small scale is due to the full-scale fabrication process requires extended time to build it.

3.4 Materials and method of assembling

Automobiles have becoming heavier in order to satisfy requirements of comfort, safety and larger interior space for the users. Besides that, automobiles have to meet a strict regulation in reducing the exhaust emission of CO_2 (carbon dioxide) and NO_x (nitrogen oxide) that rises every year. Thus, the reduction of fuel consumption is required for all automobile manufacturers. From various methods in reducing the fuel consumption including having hybrid systems or advanced diesel engines, automotive weight reduction plays an important factor [10].

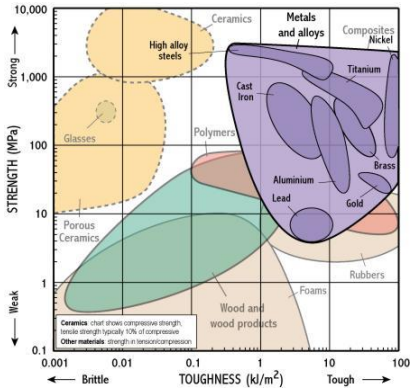


Fig. 5. Strength and toughness of materials [11].

In figure 5, metals and alloys have higher durability based on its strength and toughness. The latest trending of material use in automotive body panels was aluminum alloy because of its lightweight composition. It is affordable method in creating the structure and provide less waste to the pollution as it is recyclable material. Therefore, aluminum alloy is chosen as the material for vehicle simulator structure in obtaining the results of static and dynamic condition. Based on the assembling method, the aluminum alloy sheets are shaped and weld together to form the vehicle simulator structure according to the design. Welding is considered to provide strong joining which

withstand a better static and dynamic changes. Although its irreversible after the assembling, it is chosen with a reason of producing the permanent joints in the direction of preventing failure and improve the efficiency in the joints. However, the rigid seat designed is not permanently connect to the platform of the structure. The interest in studying on different vehicle seat itself can be use in exchange of the rigid seat on the platform. Thus, the rigid seat is design with a locking seat bracket beneath the seat that connects to the platform. The bracket is created with the consideration of having it to be universal with others seat connections.

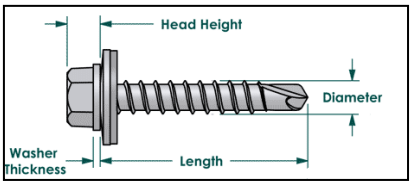


Fig. 6. Grade 8 hex washer head bolt dimension.

In addition, the selection of screw that secure the seat bracket to the platform is analyze. One of the existing bolt that is use in vehicle seat bracket is grade 8 bolts. The purpose of having a built-in washer is to help the distribution of load to a wider area on the platform. Due to the fine thread, it has low loosening tendency compare to coarse thread.



Fig. 7. Two-point seat belt and vibration shaker machine.

Vehicle simulator structure is design for the purpose of testing and experimenting dynamic and static factors under a vibration shaker. It is important to ensure the safety of the user is protected. In figure 7, the two-point seat belt is to control the user in contact with the seat from falling during the researching process on the vibration shaker.

3.5 Types of data analysis

Having the final iteration design, the structure will achieve its durability in relation to the static and dynamic factors based on simulation results. The analysis is conduct using Ansys software.

3.5.1 Static Factor Analysis

The entire vehicle simulator structure will be analyzed to investigate the level of deformation. Changes on the design will be made if the equivalent stress is larger than the tensile strength of the structure. The vehicle simulator structure is analyzed with the presence of human weight and other forces aspect as the form of pressure distributed to the seat structure.

3.5.2 Dynamic Factor Analysis

Vibration in dynamic factor produces frequencies to the entire simulator structure. The interest of study of human comfort is between 1Hz to 80Hz whereas the structure should achieve more than 100Hz of natural frequency to prevent resonance that would collapse the structure.

3.6 Result reporting and limitation.

According to the data analysis, the results is reported in the form of engineering analysis having the proper method and technique to acquire and justify the overall design. However, there is every limitation to where the design is created. In the simulation process of meshing, a fine meshing is recommended. However, there is a numerical problem of size limits for the model due to software license that limit from producing a better result. Besides that, full scale fabrication of the vehicle simulator structure is suspended due to the cost and time constrain. Thus, a small scale of the vehicle simulator structure is printed out for demonstration using 3D printer system.

4 Results and discussion

4.1 Grade 8 bolt and seat bracket design and assembles.

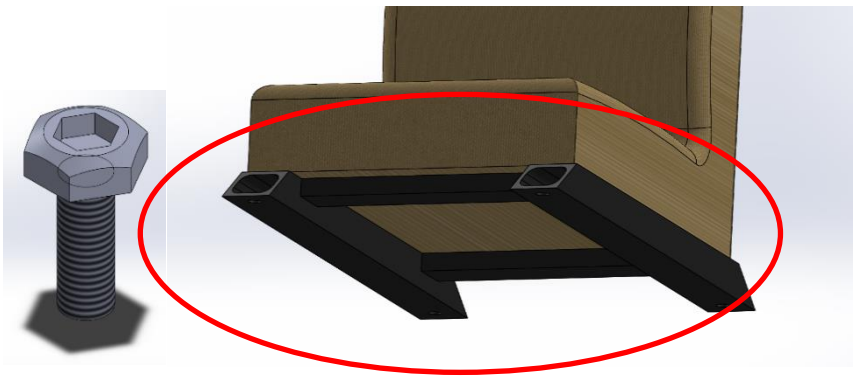


Fig. 8. Grade 8 Bolt and vehicle seat rail bracket design.

The bolt is sketch according to grade 8 bolt specification. Besides that, the seat is design to mimic the vehicle seat with a rail bracket attached below. The seat bracket design is simplified similar as the universal vehicle seat bracket.

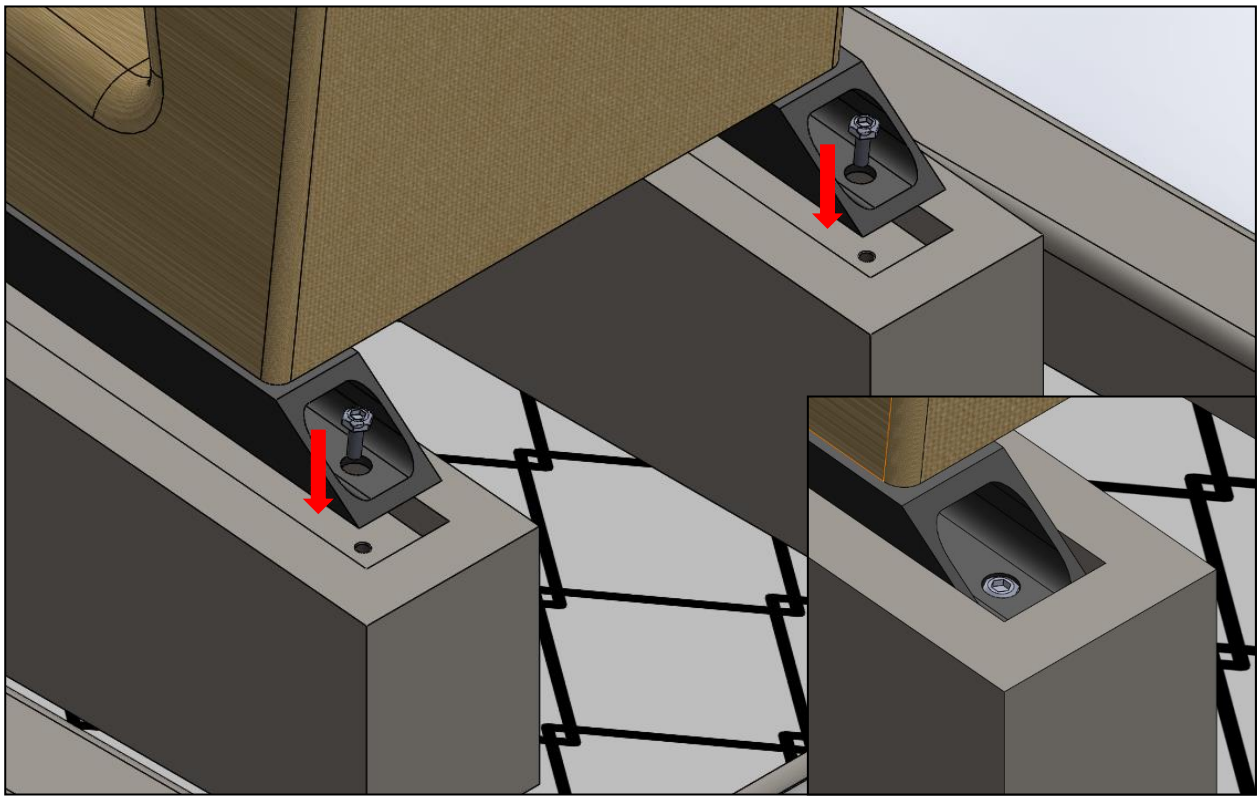


Fig. 9. Method of assembling of the seat bracket and the platform using grade 8 bolts.

A simple connection shown in figure 9 where grade 8 bolts is connected accordingly until it is fully tighten as shown in the side picture in figure 9.

4.2 Designing vehicle simulator structure for automobile in driver seat.

4.2.1 First iteration design and simulation.

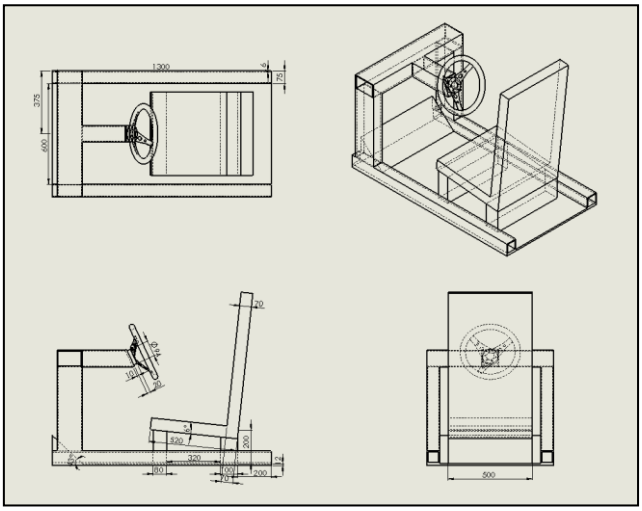


Fig. 10. First iteration design of vehicle simulator structure. (units in mm)

The first stage of design is created based on a list of steel pipe dimensions. The total deformation and equivalent stress of the platform is simulated and results obtained shows a small amount of deformation when the average human weight is set as the pressure applied to the structure.



	Mode	Frequency [Hz]
1	1.	84.275
2	2.	292.58
3	3.	330.57
4	4.	448.56
5	5.	507.81
6	6.	562.79

Fig. 11. Results obtained from the vehicle simulator structure based on dynamic analysis.

From the results shown in figure 11, the natural frequency obtained for first mode is below 100Hz. The design affects the area of study needed on studying human comfort and could possible cause resonance when the frequency supplies is same as the natural frequency.

$$\frac{w}{w_n} = 1\ (resonance) \tag{1}$$

Based on equation (1), resonance occurred when the frequency, w supplied divided by natural frequency, w_n of the structure is equal to 1. Since the natural frequency of the structure is set to be more than 100Hz, the response of amplitude against time will be always be in-phase response.

4.2.2 Second iteration design and simulation.

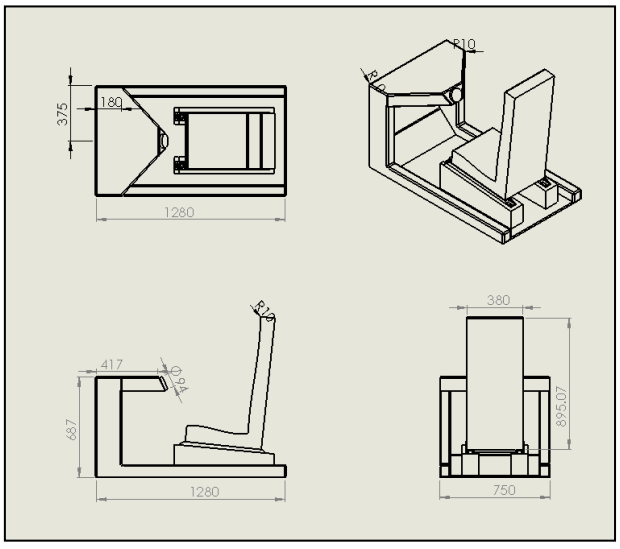


Fig. 12. Second iteration design of vehicle simulator structure. (units in mm)

The structure design changes a lot to meet the requirement of structure improvement based on the analysis obtained. The new assemble between the rigid seat to the platform is reconstruct with a better perception. The additional side walls that cover the seat bracket allowing less tension on the bolts itself.

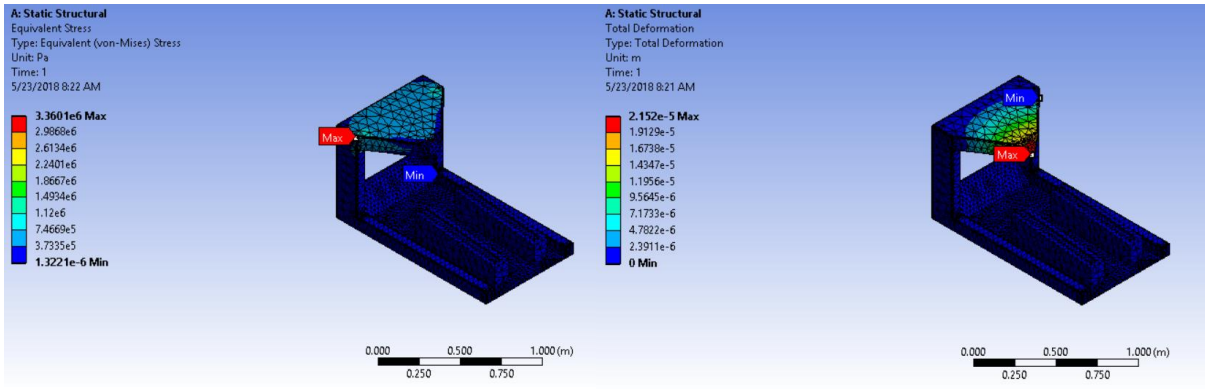


Fig. 13. Second iteration equivalent stress and total deformation of the vehicle simulator structure for platform.

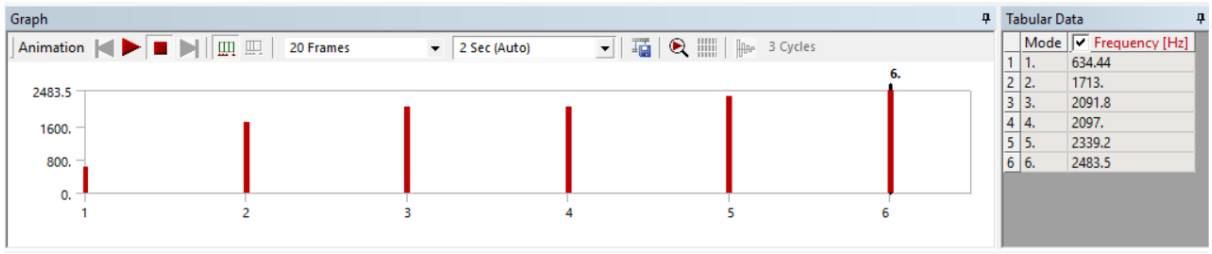


Fig. 14. Second iteration of the natural frequencies from multiple modes due to dynamic factor on the platform.

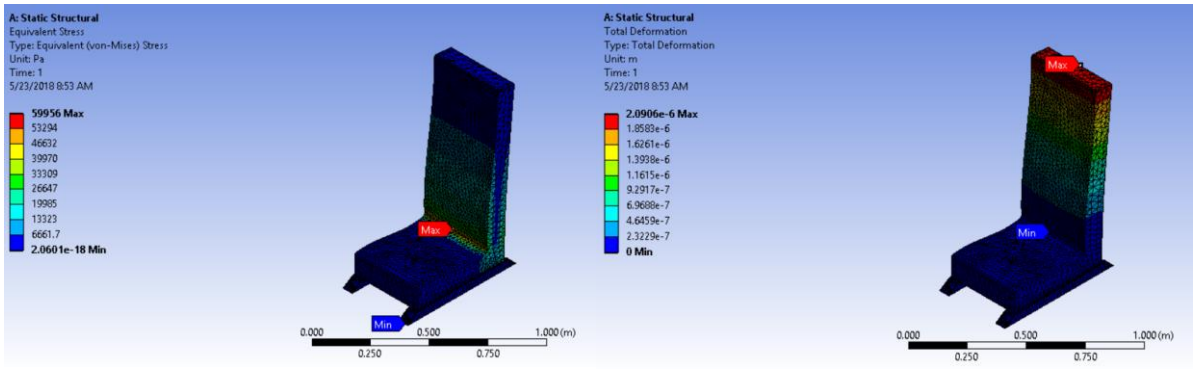


Fig. 15. Second iteration equivalent stress and total deformation of the vehicle simulator structure for rigid seat.

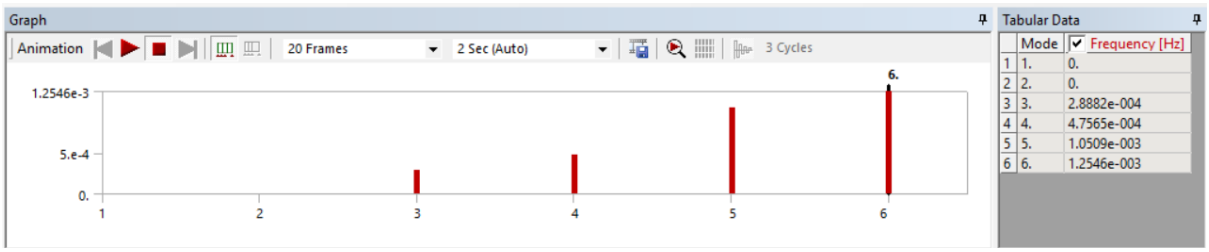


Fig. 16. Second iteration of the natural frequencies from multiple modes due to dynamic factor on the rigid seat.

The low natural frequency values is below the interest of study of human comfort sensitivity which is between 1Hz to 80Hz. Thus, it is concluded that the rigid seat design is safe to be use.

4.2.3 Third iteration design and simulation. (Final design)

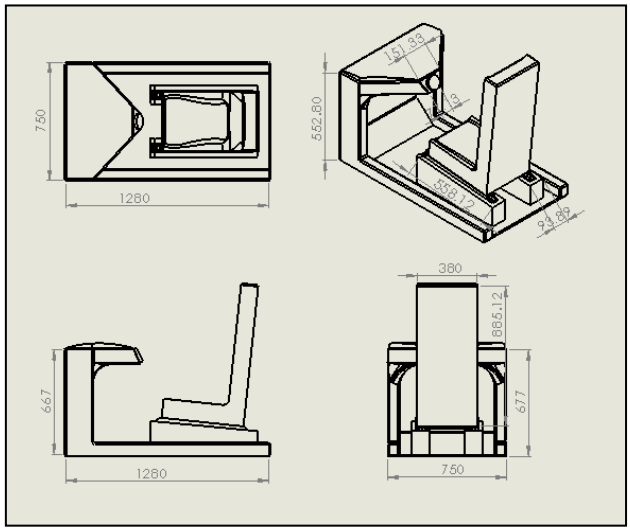


Fig. 17. Third iteration design of vehicle simulator structure. (units in mm)

In consideration to improve the design, the shape of the rigid seat is adjusted to fit the shape of human body structure. From the previous second iteration design, the platform structure is enhanced with a better fillet shape on the area that has higher deformation rate. The method of improvement has been geometrically reshaped according to the results obtain from the previous iteration.

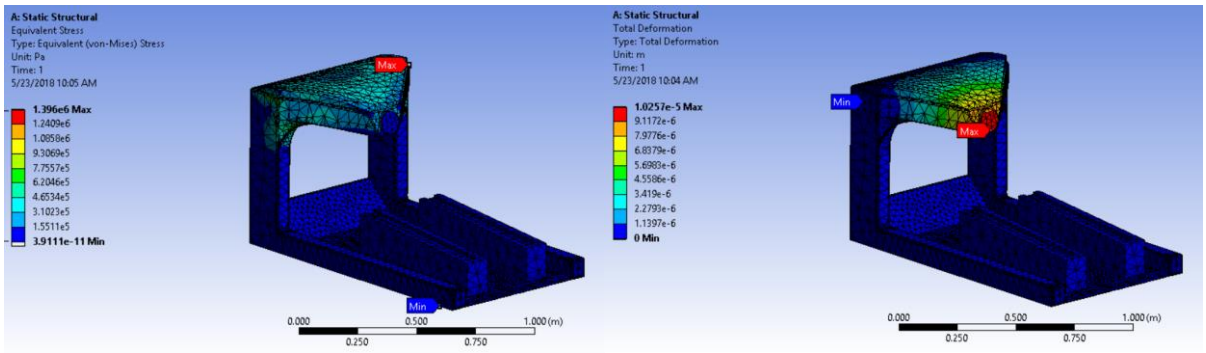


Fig. 18. Third iteration equivalent stress and total deformation of the vehicle simulator structure for platform.



Fig. 19. Third iteration of the natural frequencies from multiple modes due to dynamic factor on the platform.

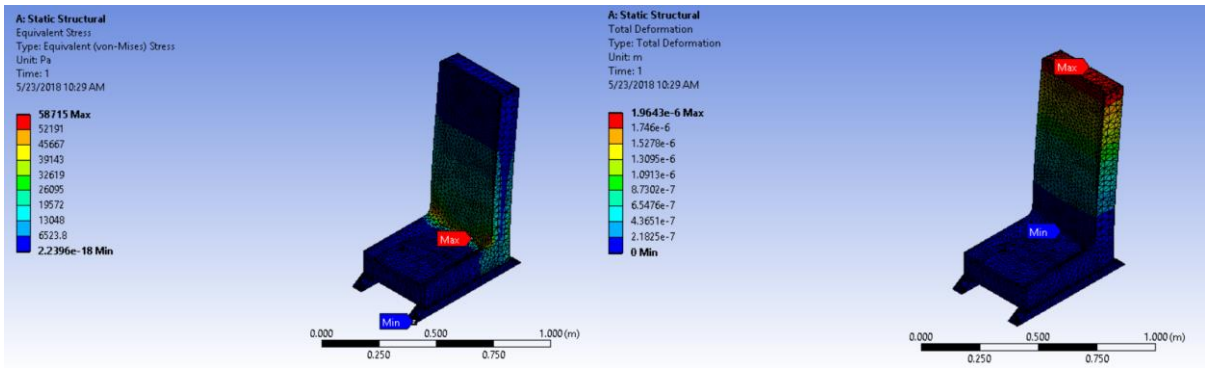


Fig. 20. Third iteration equivalent stress and total deformation of the vehicle simulator structure for rigid seat.

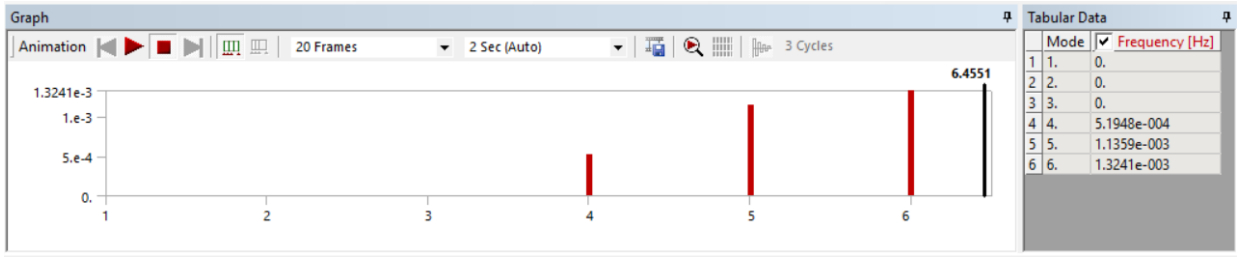


Fig. 21. Third iteration of the natural frequencies from multiple modes due to dynamic factor on the rigid seat.

From figure 21, third iteration rigid seat design has no natural frequency for the first three modes. It might be due to the rigid body mode of high weight structure which has no fluctuation.

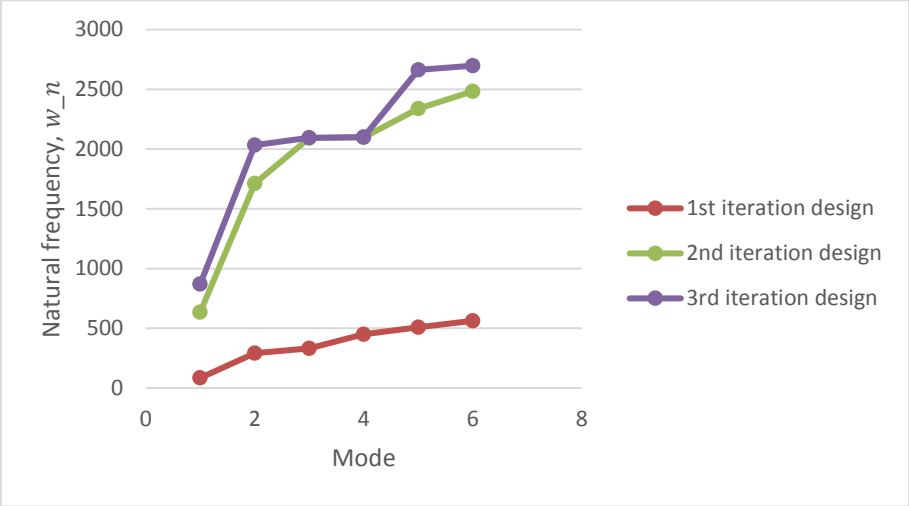


Fig. 22. Natural frequency against the mode graph based on the three iterations design for the platform structure.

4.3 Discussion

The purpose of having three iterations is to develop a consistent modifying process on the structure designed with an objective to improve the structure in term of rigidness and safety conduction during experimentation on vibration shaker. Each iteration requires proper methods and tools to identify the issues of the structure before enhancing it. The simulated results show a fairly improvement towards the design. The total deformation of the vehicle simulator structure has been slightly decreases every iteration. Aluminum alloy has a value $2.8x10^8 Pa$ tensile yield strength. In the comparison to the equivalent stress, the value shows that it didn't exceed the maximum value of the material strength which describes the material failure. It shows that the structure able to withstand without permanent deformation from the pressure that is being applied onto it. Besides that, figure 22 shows the natural frequency obtained from each iteration. The improvement made to increase the natural frequency of the structure has been achieved to a minimum value of 869.2Hz based on the tabulated data in figure 19. The safety factor of the vehicle simulator structure design according to aluminum alloy used is at 201:1 and is determined that the structure is in a safe margin of usage.

5 Conclusion and recommendation

In conclusion, the final iteration design of vehicle simulator structure is considered to be possible for conducting human comfort research. The robustness of the structure is accomplished as it able to

withstand the pressures with small deformation. Unfortunately, the project is restricted with time duration that forces to have only 3 iterations design and simulation. It is recommended that the design is conducted with more than three iterations to enhance the better results gain from simulation. Additionally, fabricating the vehicle simulator structure allows additional testing to be conduct directly from the vibration shaker which shows a better picture in identifying the design details. Lastly, the design of vehicle simulator structure is expected to bring new discovery and changes for the improvement in future vehicle industries to provide better interaction between human and machines.

6 References

[1] A. Jhinkwan, "Design Specifications and Ergonomics Evaluation of Car Seat," *International Journal of Engineering Research & Techonology (IJERT)*, vol. 3, no. 5, pp. 611-613, 2014.

[2] H. P. Wolfel, "Virtual optimization of car passegner seats: Simulation of static and dynamic effects of drivers' seating comfort," *International Journal of Industrial Ergonomics*, vol. 38, no. 5-6, pp. 410-424, 2008.

[3] B. Md Deros, "Fundamental sitting anthropometric and differences among Malaysian Malays, Chinese, and Indians," *Seminar 1 - AMReG 08*, pp. 169-170, 2008.

[4] L. Lo Zhiming, "Characterisation of Vehicle Seat Structural Dynamics and Effects on Ride Comfort," School of Aerospace, Mechanical and Manufacturing Engineering, RMIT University Bundoora East Campus, Australia, 2010.

[5] N. J. Mansfield, "Combined Effects of Long-Term Sitting and Whole-Body Vibration on Discomfort Onset for Vehicle Occupants," *Hindawi Pubishing Corporation*, pp. 1-8, 2014.

[6] K. E. a. M. K. Griffin, "Quantitative prediction of overall seat discomfort," *Ergonomics*, vol. 43, no. 6, pp. 791-806, 2000.

[7] "ergonomicsblog," [Online]. Available: http://www.ergonomicsblog.uk/human-response-to-vibration/. [Accessed 28 August 2017].

[8] ediamond92, "emilyjdiamond," 18 October 2015. [Online]. Available: https://emilyjdiamond.wordpress.com/2015/10/18/ergonomics-and-anthropometrics-2. [Accessed 28 August 2017].

[9] D. Mohamad, "Development of a Malaysian Anthropometric Database," World Engineering Congress, Kuching, Sarawak, Malaysia, 2010.

[10] T. Sakurai, "The latest Trends in Aluminum Alloy Sheets for Automotive Body Panels," *Kobelco technology*, pp. 22-28, 2008.

[11] T. Kobayashi, "Strength and Toughness of Materials," *Springer-Verlag Tokyo*, pp. 141-154, 2012.

EURECA 2018 – Conference Paper
Paper number 2ME25

A Numerical Study to Compare the Antifouling Potential of an Isotropic and an Anisotropic Microtopography

Ramzi Bin Ab Rashid, Felicia Wong Yen Myan

School of Engineering, Taylor's University, Malaysia
ramziab.rashid@gmail.com

Abstract

Biofouling is defined as accumulation of unwanted settlement of micro and macro organism on any surface that has been submerged for a period of time. The phenomenon resulted in adverse effects in various industries especially in the maritime industry. A lot of effort was made to develop antifouling approaches to mitigate biofouling. Surface modification is one of the approaches to prevent biofouling and is advantageous because it is non-toxic and will not harm the environment. Research has shown that the settlement trends of biofouling organisms are dependent on physical distributes of the topographies (i.e. feature size, geometry and surface patterns). Isotropic topography is defined as the surface topography which exhibit assigned pattern of geometries while anisotropic surfaces consist of geometry with scattered and randomly arranged order. There is little evidence to indicate that isotropic surface topographies possess higher antifouling potential as compared to anisotropic surfaces. This project aims to address the gap in the differences of hydrodynamic and physical characteristics around both isotropic and anisotropic topographies with a view on comparison of topography arrangement that would exhibit better antifouling potential. This research consists of two phases which are the topography modelling stage and simulation stage. Computational Fluid Analysis (CFD) will be the main component of the simulation stage where it will be used to simulate the flow on the topographies modeled through CAD Solidworks software. The simulations include the process of meshing, grid dependence analysis and mesh convergences. The parameters that are being focused includes the vorticity, velocity profile, shear strain stress and the wall shear stress. Results obtained from the simulation will then be compared between the respective topography and previous literature results. Upon the completion of the project, the modelled topography should provide an ideal response towards the real conditions of biofouling environment while isotropic topography is expected to shows a better antifouling potential compared to the anisotropic topography.

Keywords: Biofouling, antifouling, surface modification, isotropic topography, anisotropic topography, computational fluid analysis, CFD

1. Introduction

Inhabitation of both micro and macro living organisms on any submerged surface is a natural phenomenon which define the natural biofouling. Biofouling comprises of a variety of form which includes biofilm layer, microfouling and macrofouling and organic foulants. This accumulation of organisms on the submerged surface are variant in terms of sizes ranging from tiny viruses to giant kelps resulting in multi-dimensional community of organism.

Biofouling has been reported to cause a substantial and adverse impacts in the maritime industry. The presence of fouling organism on the hulls of ships were found to result in a significant increase in the frictional drag of ships and vessels as the ship moves through the water [1]. It was reported that a general increase of 40% fuel consumption is resultant from biofouling [2]. In addition to that statistic, the expenses of a one-way trip voyage from San Francisco to Yokohama has increased by 77% as a result of the hull fouling. The ship's hull maintenances become more expensive as dry docking need to be carried more frequent due to the fouling [3].

Biological fouling process are grouped into four main key stages where it covers the conditioning, the initial accumulation of absorbed organics, growth and settlement of pioneer organism, prior to the successive micro and macro fouler [4] The illustration of the biofouling stages are shown in Figure 1.

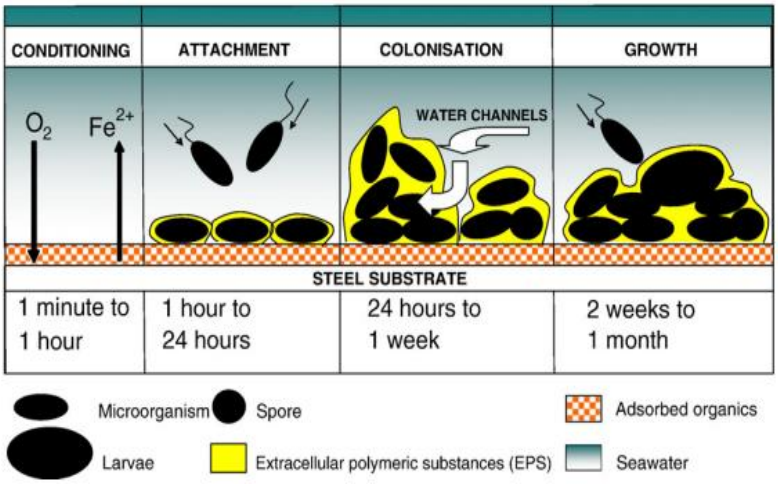


Figure 1: Illustration of biofouling stages [4]

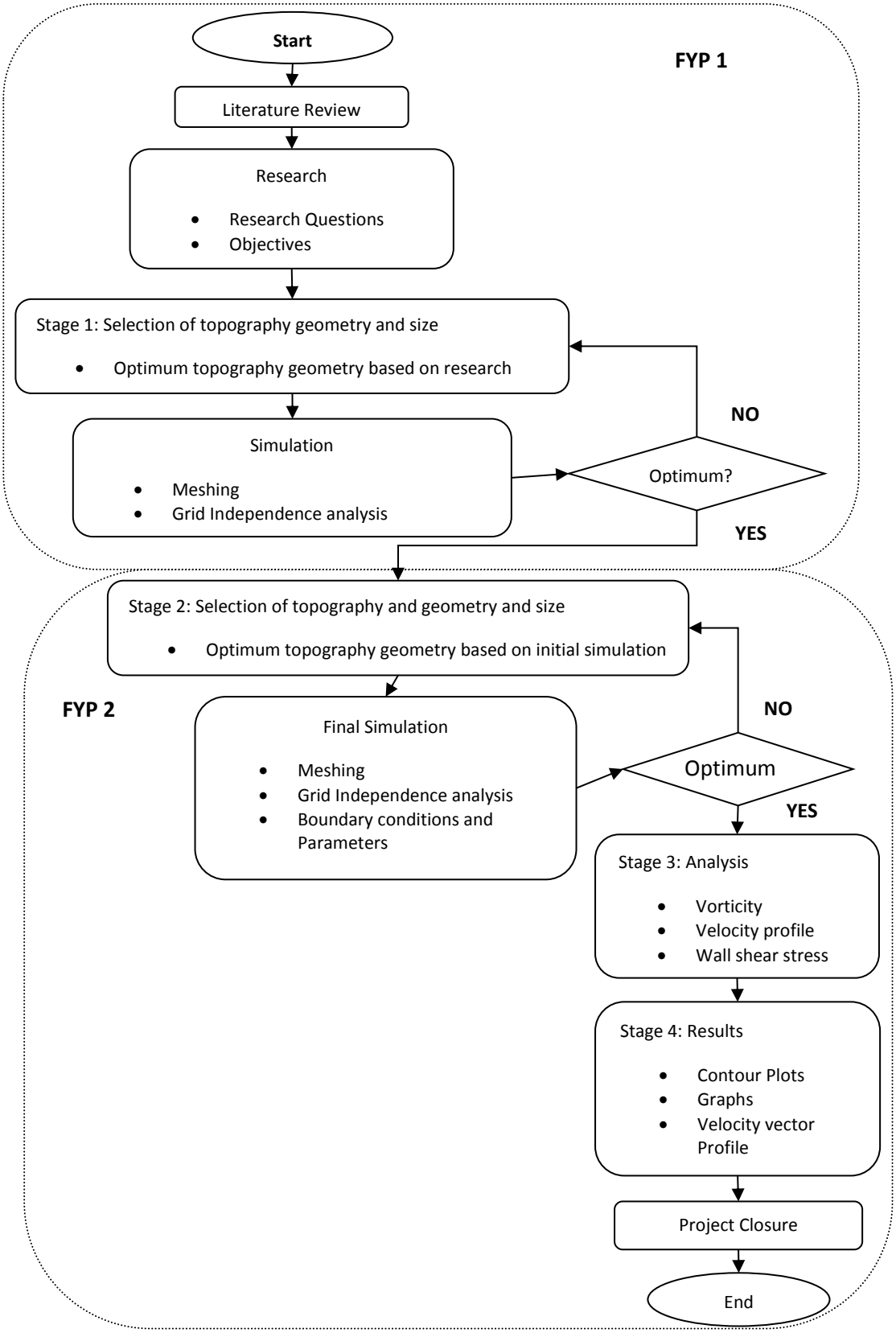
In general, the prevention would be through the mechanical three general approach, which is the application of chemical agent and the surface modification of the structure itself [5]. An example of the mechanical approach would be the detachment of biofouling organisms manually using instrumental approach from the surface itself. In another effort, the chemical approach can be referred of using the chemical agents in exterminating the biofouling organisms from the surfaces. Surface modification approach includes the alteration and modification of either the surface's chemical composition or application of surface topography in discouraging the settlement of biofouling organisms.

To date, the most suitable solution found to tackle this problem is through the application of the Tributyltin self-polishing copolymer paints (TBT-SPC paints) [6]. Unfortunately, after an International convention discussion held on 5 October 2001 which discussed the effect of usage of TBT in the marine biological environment has led to the ban of its usage by the International Maritime Organization (IMO) in 2008. It was found that the use of had an adverse effect on the marine life causing malformations of shell growth around their environment[6] .

Various studies that have been conducted throughout the past decades have shown great number of potential approaches in overcoming the fouling effect. In the meantime, the expensive setup costs of experiments and lab studies has distorted further research of most researcher in this

aspect where structural, apparatus and multi-related issues is crucial for a quality research. Recent studies have found an alternative approach such as Computational Fluid Dynamics (CFD) as an ideal solution to further the research as it offers approximate simulation on the subjects and the functionality of antifouling topographies[7]. The approach on flow analysis studies on the surface topographies provide an alternative for traditional on-site experiments with a better control over the boundaries and reduction of unwanted environmental effects such as predatorial effect of another organism. In addition to that, it also allows us to understand the nature of the surface controls closely before carrying out further on-site researches with a much lower cost of study. In this research, the study focuses on the characterization of patterns over topography and their effect on the topography antifouling potential.

2. Research Methodology



2.1 Geometry Modelling

In modelling the fluid domain for the project, Solidworks 2015 Software was utilized in designing the required three-dimensional (3D) model. The model was set accordingly to a fluid domain dimension of 50mm long, and a 5mm by 5mm cross-sectional area. The fluid domain model can be seen in Figure 1. The topography subsequent design was set to the base of the domain, located 2mm from the outlet of the model with an area of 2mm by 3mm. Based on literature review, Hagen-Poiseuille's theory were followed as the theory suggested that the fluid flow will develop laminar flow in any fluid domain with significant difference in it's length compared to it's cross section size [27]. The pressure drops along the flow induced the development of laminar flow inside the domain.

Geometry and size of the topographies are the main component of this project. Through the literature study that has been made, well circumscribed geometries such as circle, hexagon and others has been showing a greater magnitude of shear-bounded isolated areas when compared to other type of geometry and this is proven through the study conducted by Halder et al. [11]. Thus, for Isotropic geometry, circular pillars were chosen as the geometry whereas fir the anisotropic model, both circular pillars and cube were chosen as the preferred geometry for the project. Based on literature review, it was found that the optimum dimension of topography in controlling biofouling were in between 64 µm to 256 µm [18]. From the definition, isotropic model topography consists of 70 circular pillars located precisely aligned around the 3mm by 2mm topography area while the anisotropic model topography was modelled with both cube and circular pillars geometry placed randomly around the topography area. Subsequently, the fluid domain was set to a 50mm length and 5mm by 5mm cross sectional domain where the topography is placed 2mm from the outlet and 1.5mm distance from each side of the domain wall. The model of each topography is shown in the following Figure 2 to 4.

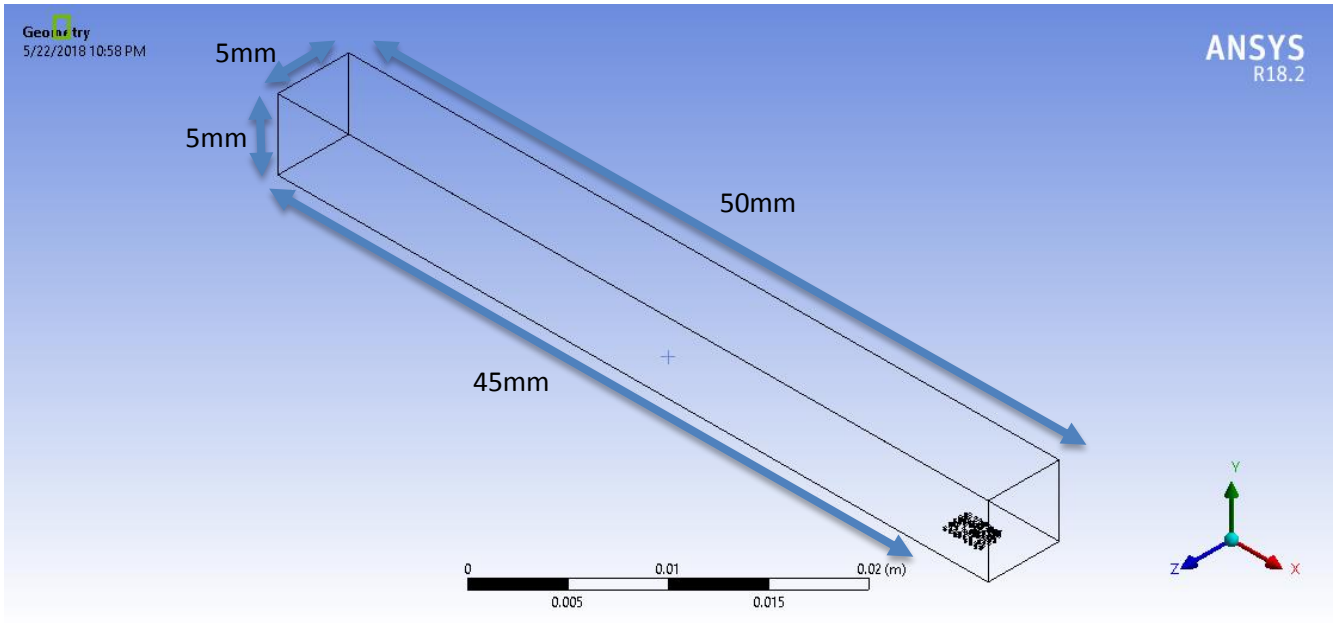


Figure 2. Fluid Domain of Anisotropic topography

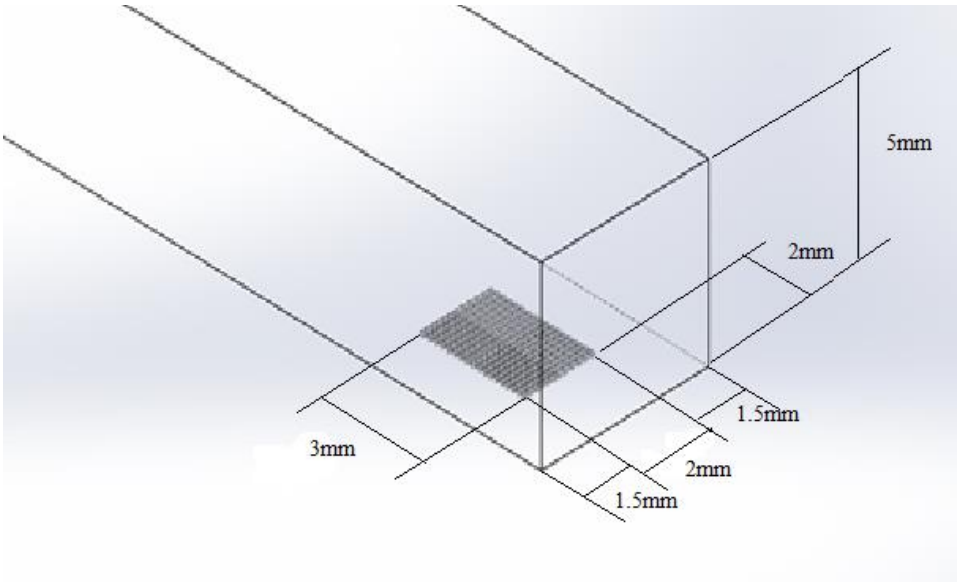


Figure 3. Dimensions of Topography and Fluid Domain

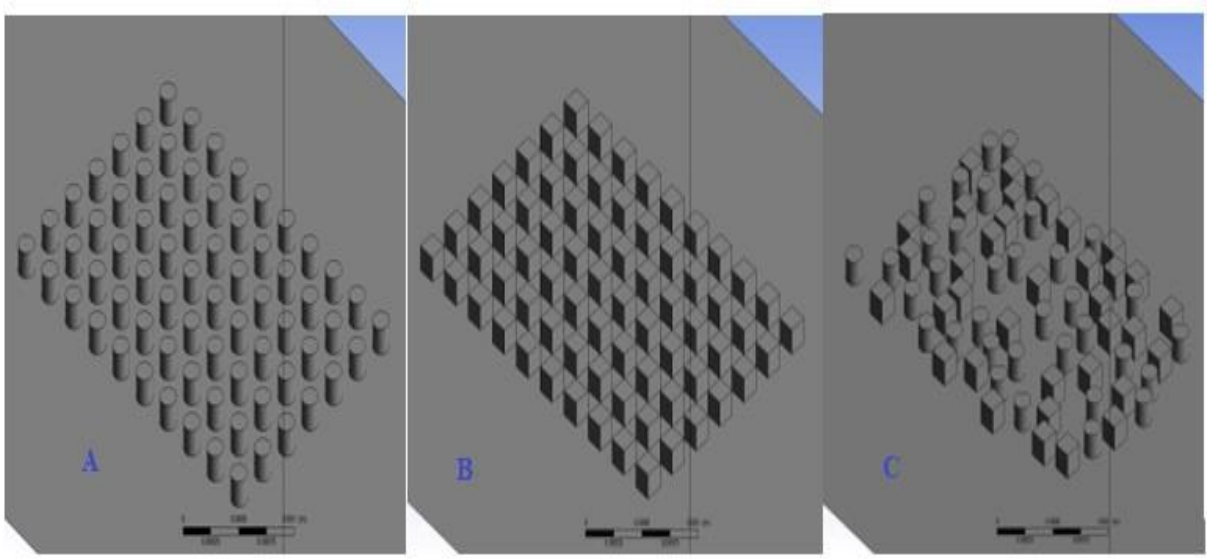


Figure 4. Isometric view of Isotropic cylinder (A), Isotropic cube (B) and Anisotropic topography (C)

2.2 Meshing Method

The main requirement for an excellent result in CFD analysis is to have the best possible mesh of the model. Both of the Isotropic and Anisotropic topography model was modelled using Solidworks 15.0 where the model was then converted into STEP file before transferring the model to ANSYS software. The meshing was done through the meshing module in ANSYS and the mesh was generated through tetrahedron method. In the meshing process, the inflation level was set to 5 layer in which would provide more precise meshing of the model. The mesh is shown in Figure 5 and 6.

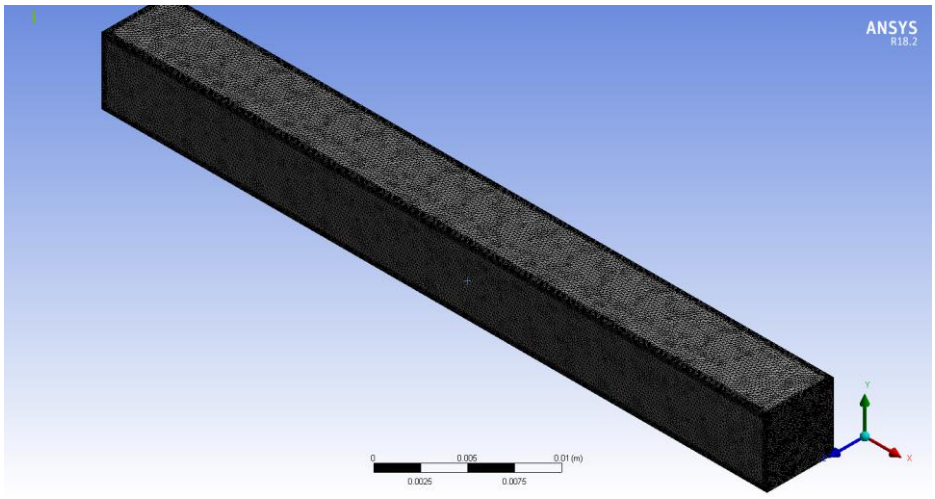


Figure 5. Mesh of Isotropic cylinder topography

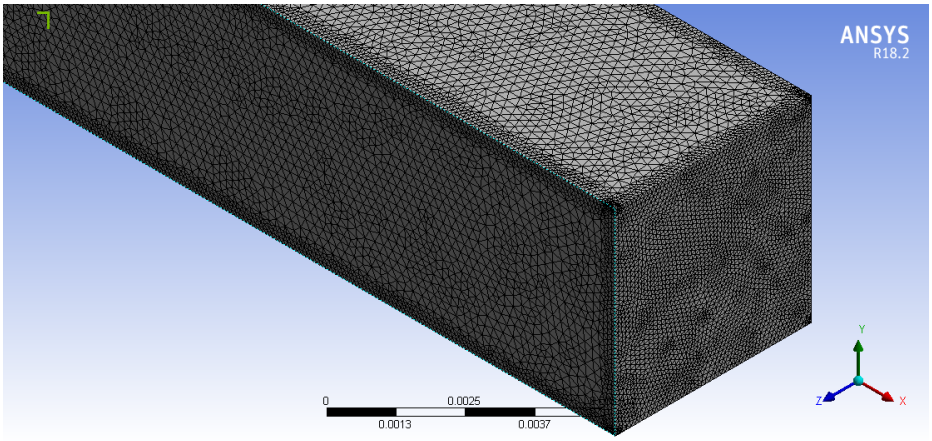


Figure 6. Close up view of mesh around the outlet near the topography placement

In order to gain a higher quality of meshing, face sizing, edge sizing and refinements has been carried out to increase the subsequent topography meshing quality. The maximum mesh size was also set for a few sizes such as 0.00015m, 0.0002m and 0.0005m in which would keep the mesh size much smaller and more decent for the meshing process. These approaches are important to gain knowledge and obtain the optimum number of mesh elements prior to the simulation through the grid analysis process. This will be later explained in the results section. Edge sizing has been carried out to the edges of the domain while all the faces of the geometry inside the topography were all face sized as well. These approach into meshing decreases the size of the meshing element which later enhance the quality of the mesh itself. Thus, more concentrated meshing around the selected entity and edges shall be more precise and accurate for further process. In addition to that, both element quality and skewness of the mesh were taken into account I the meshing process to ensure it reliability. During the simulation also, 10% of the poor mesh were improved using the ‘improve’ function in the setup simulation, where the mesh was once again checked and mesh quality report for the mesh were carried whether it will be possible to get a convergence using the mesh.

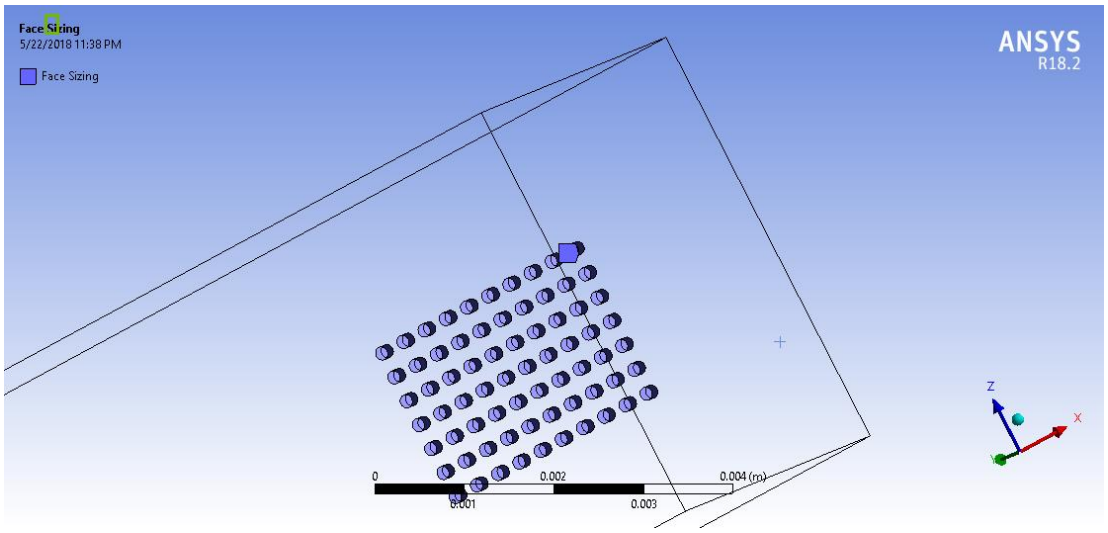


Figure 7. Face Sizing at topography geometry surfaces

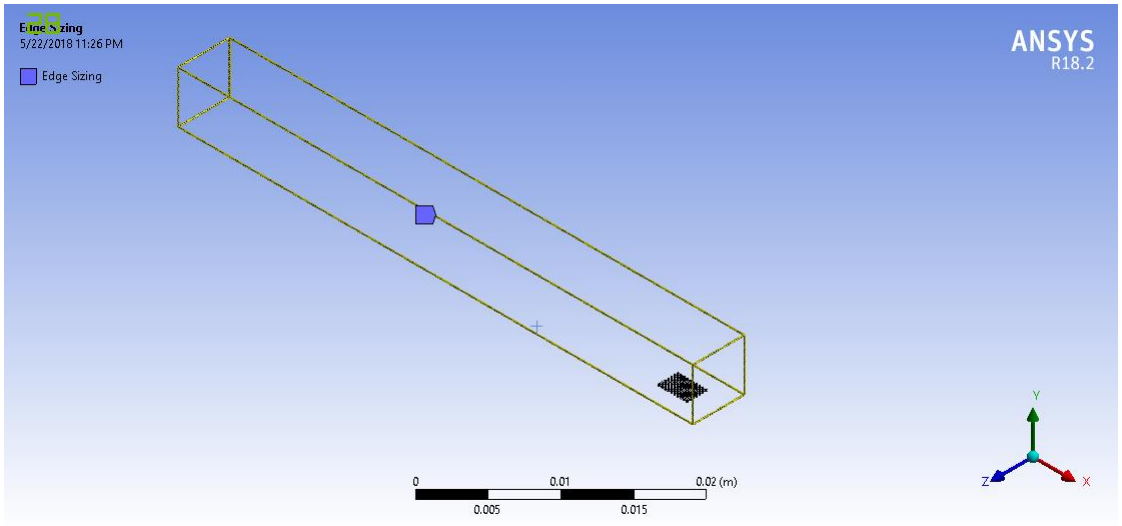


Figure 8. Edge sizing of the domain wall

2.3 Boundary and Parameter Setup

In this research, the main software used for simulation and analyzation of data is ANSYS FLUENT version 18.2. thus, the parameters and boundary condition setup circulate around the need of the software itself. For the model, all parts were labelled accordingly through its function such as Inlet, 'Outlet', 'Wall' and 'Domain Base' accordingly to denotes their presence and position as shown in Figure 9. The parameters taken into account includes the inlet velocity, characteristics of flowing fluid, solid and a few others. In this research, to implement a clearer view of biofouling, water (H_2O) was used as the flowing fluid with a natural density of 998.2 kgm^{-3} and viscosity of 0.001003 $kgm^{-1}s^{-1}$ where it was also available in FLUENT database. Apart from that, the k-ω turbulence model had been used to simulate the flow as according to literature review, this model was able to provide a higher accuracy of the wall shear stress throughout the simulation [12]. In addition to that, the fluid domain wall was set to no-slip condition to enhance the flow. The inlet mass flow rate was set to 0.001$kgms^{-1}$ at the inlet which is quite significant to a research done by Halder et.al (2013), because of significant differences in the size of domain and topography.

For the simulation, the velocity fields and pressure shall be using both the Navier-Stokes equations (Equation 3) and the continuity equation (Equation 4) with the principle of preservation and the conservation of momentum. The velocity vector $\vec{\nabla}$ is showed in Equation 3.

$$\frac{\partial \rho u}{\partial t} + \nabla \cdot \rho u V = -\frac{\partial \rho}{\partial x} + \nabla \cdot (\mu \nabla u) + S_{m,x} \quad (1)$$

$$\frac{\partial \rho v}{\partial t} + \nabla \cdot \rho v V = -\frac{\partial \rho}{\partial y} + \nabla \cdot (\mu \nabla v) + S_{m,y} \quad (2)$$

$$\frac{\partial \rho w}{\partial t} + \nabla \cdot \rho w V = -\frac{\partial \rho}{\partial z} + \nabla \cdot (\mu \nabla w) + S_{m,z} \quad (3)$$

$$\frac{\partial \rho u}{\partial t} + \nabla \cdot (\rho V) = 0 \quad (4)$$

3.Results and Discussion

3.1 Grid Independence Analysis

As mentioned before, meshing is an integral part of this project in order to harness an excellent result and more precise simulation on the subsequent situation. Thus, it is important to have an optimum level of mesh and mesh numbers to both minimizing the period of time required for simulation while obtaining accurate results. In a study conducted by Halder et.al (2016), the mesh elements number was increased in all successive models at the set-up inlet mass flow rate of 0.001 $kgms^{-1}$. Thus, following this reference, the number of both of the topography were increased and analyze to reach optimal level.

In this study, the main parameter in determining the optimum number of mesh elements is the wall shear stress. In calculating the relative error of the mesh refinement, the percentage difference between the refinement were used. The relative error percentage should be lower than 5% for it to be the optimum refinement. The grid independence analysis of this research is shown in Table 1.

Table 1. Grid Independence Analysis of Isotropic and Anisotropic Topography Model

Topography Model				**Optimum Mesh Number**
Isotropic Cylinder	Mesh Refinements	494100 → 1199579	1199579→ 2060531	1199579
	Relative Error (%)	43.59	3.82	
	Mesh Refinements	552987→690139	690139→ 3424666	690139

Isotropic Cube	Relative Error (%)	37.26	1.46	
Anisotropic Surface	Mesh Refinements	314009 → 4544075	4544075 → 4731731	4544075
	Relative Error (%)	17.47	4.06	

3.2 Results

3.2.1 *Hagen-Poiseuille's Theory*

The flow in the simulation follows and supported by the Hagen-Poiseuille's theory. The flow develops starting from the inlet and continue to flow into a parabolic flow before reaching the topography area. In this study, the simulation has shown a good behavior in following the theory where the velocity continued to increase parabolically as it passes through the inlet until reaching the 45mm just right before the topography for both of the model. This can be seen in Figure 9. In this figure, it can be seen that the velocity of the fluid was zero at the wall of the domain whereas the velocity was maximum at the center of the domain itself.

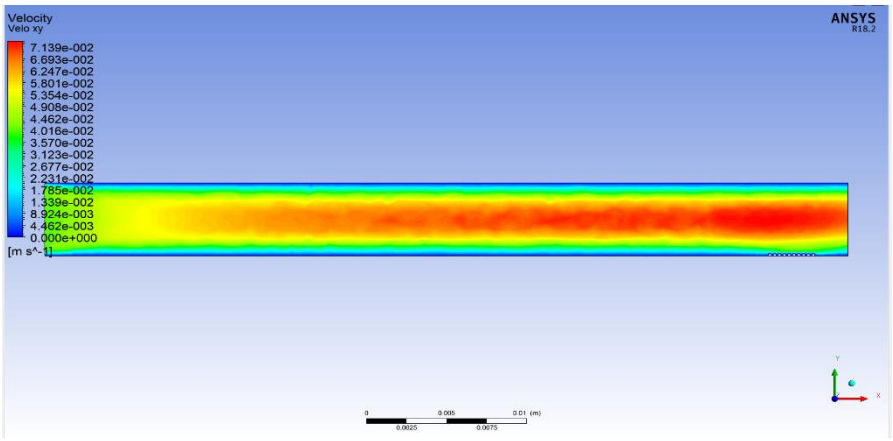


Figure 9. Velocity contour plot of XY plane (z=0)

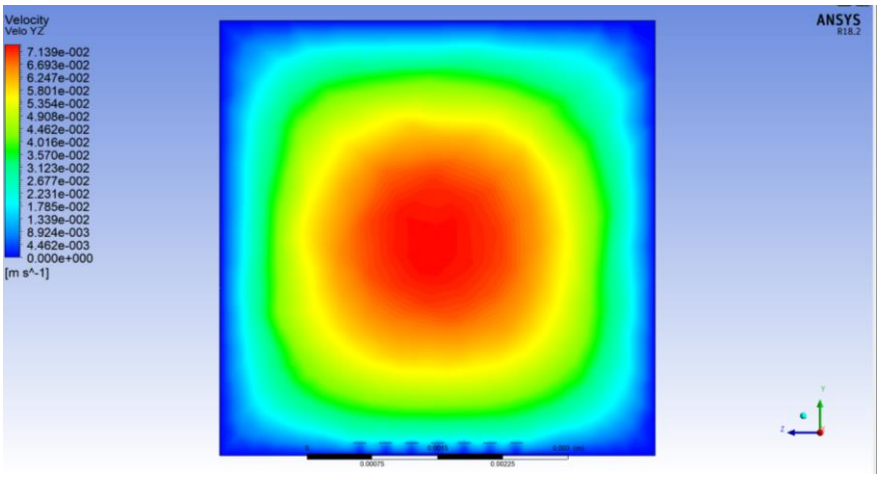


Figure 10. Isotropic cylinder velocity contour of XY plane (z=0)

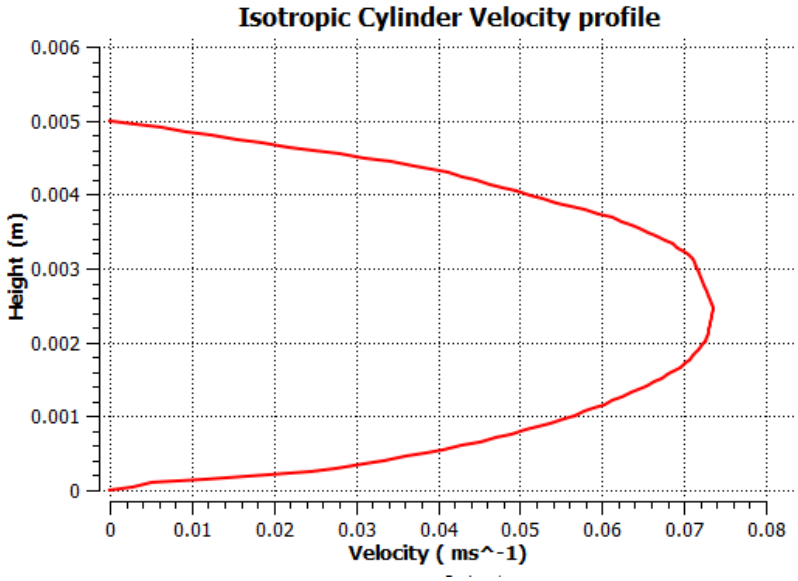


Figure 11. Isotropic cylinder velocity profile at X=45mm

The velocity profile at X=45mm for all three models were identical, showing a parabolic curve and hit the highest velocity at the mid-section height of the domain. The zero velocity found in the Y=0mm and Y=5mm can be related to the no-slip condition given to the fluid domain wall during the simulation.

3.2.2 Velocity Vector and Streamline Plot

Both streamline and the vector plots for the velocity of the flow during simulation were plot to have insight towards their development throughout the process. Streamlines plot for both of the topography has shown a significant difference in the velocity around the topography in which higher velocity flow were more focused towards the upper part and above he geometries in the topography. The presence of a higher velocity concentration towards the surface indicates that it is more likely for biofouling organisms to settle down which would enhance the surface's antifouling potential.

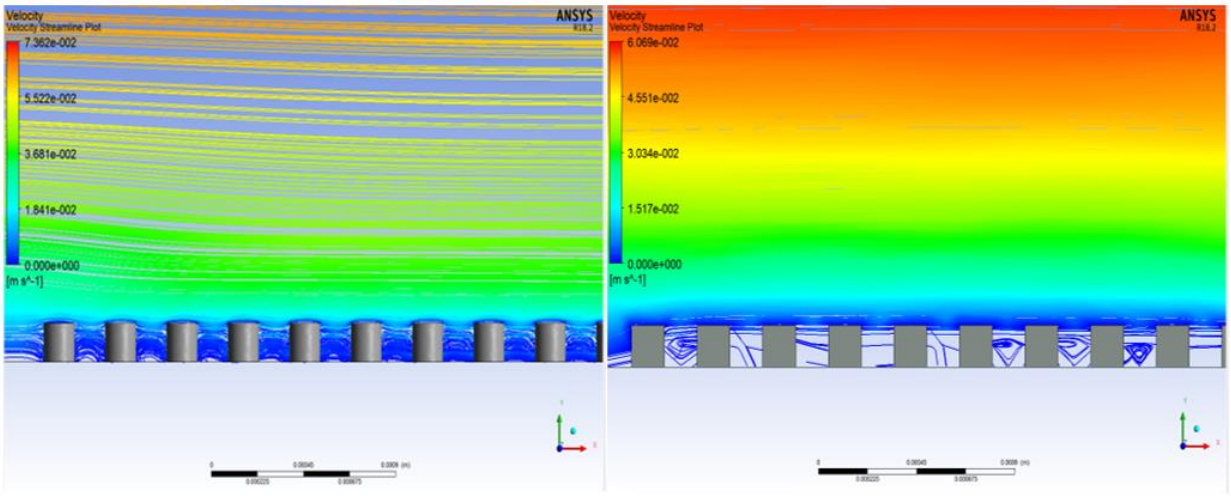


Figure 12.Isotropic cylinder (left) and cube (right)vector streamline plot

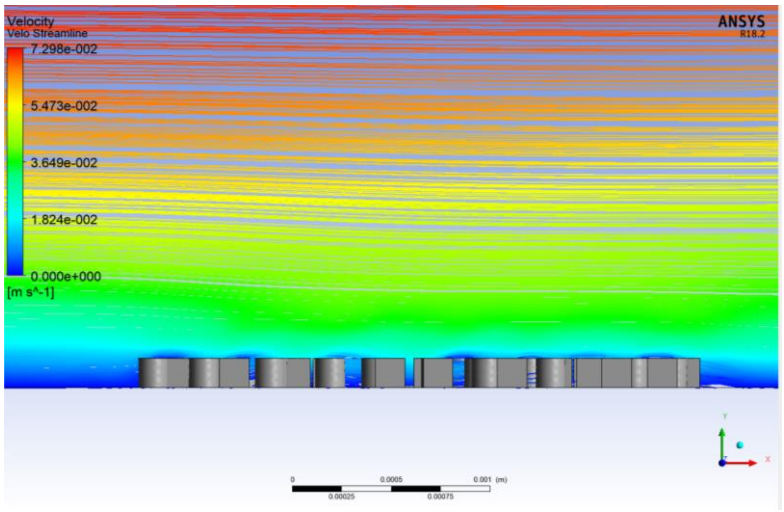


Figure 13. Streamline overview over Anisotropic Topography

Figure 10 show the streamlines of velocity arrow which indicates the concentration and the magnitude of flow velocity of the anisotropic model. The area which is not covered by the arrow would potentially be inhibited by the biofouling agents since there are insignificant magnitude of velocity that will decrease their comfort. In fact, both model shows the same behavior in which for the isotropic model, a few vortices were formed in between the geometry. In terms of significant changes that might happen from the formation of vortices is that these vortices might as well be the transport medium for the biofouling agents to accumulate from the fluid flow in between the topographies.

3.2.3 Wall Shear Stress plot

Previous study on the behavior of biofouling agents towards substrates that are more likely to be inhibited shows that it tends to attract microorganisms to explore them. Exploration can lead to the initial contact between the microorganisms and the surface itself where this situation was proven to be one of the initial indicators for fouling. Thus, it is more likely to control biofouling from happening by first avoiding the first step towards their contact or attachment which would further reduces the tendency of fouling itself. As mentioned earlier, wall shear stress is an important indicator in determining the antifouling potential by the surface in which this statement was also supported by a study conducted by Halder et.al (2013) and Myan et.al (2016). The relation between both of the

statement can be assumed that microorganisms would avowing settling on a surface with a higher shear stress where their initial contact was also reduced through the high shear stress.

Both isotropic and Anisotropic model has shown a relatively different results throughout the flow simulation in which Isotropic model has show a better distribution of wall shear stress compared to the anisotropic topography. In Figure 14 to 16, the isotropic topography has shown a more shear stress distribution contour where anisotropic topography has literally shown not much variations of shear in their geometry walls. Thus, this suggests that isotropic topography would inhibit a higher antifouling potential compared to anisotropic topography. The low appearance of the wall shear stress for both of the topography can be related to the inlet speed which was reduced by a significant margin but would still reliable to distinguish the difference in shear stress between them in the same scenario. This will further improve in the current final phase of improvisation of the study simulation.

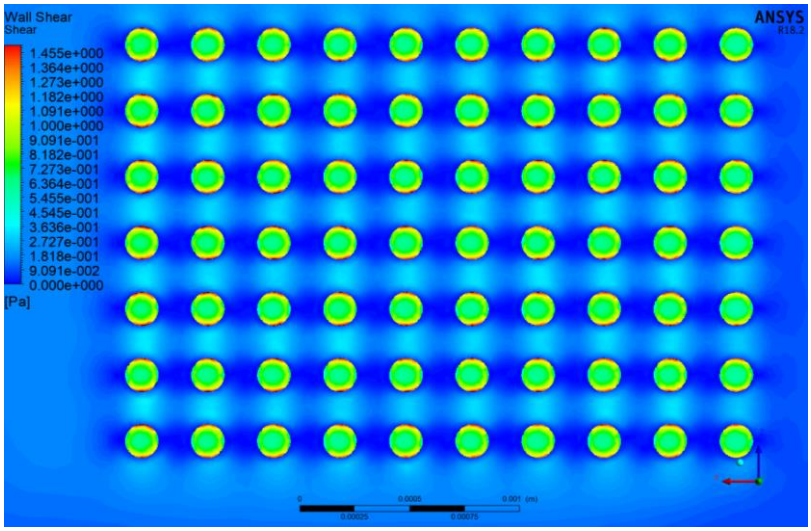


Figure 14. Wall Shear Stress Contour of Isotropic topography

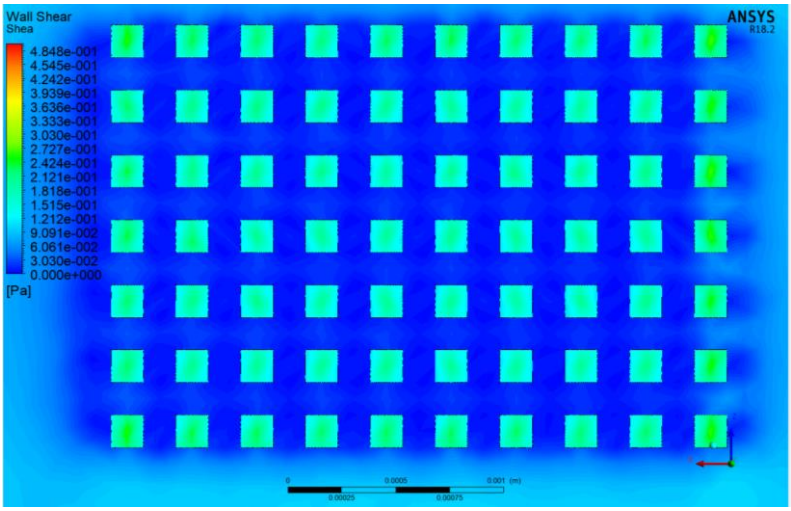


Figure 15. Wall Shear Stress Contour of isotropic cube topography

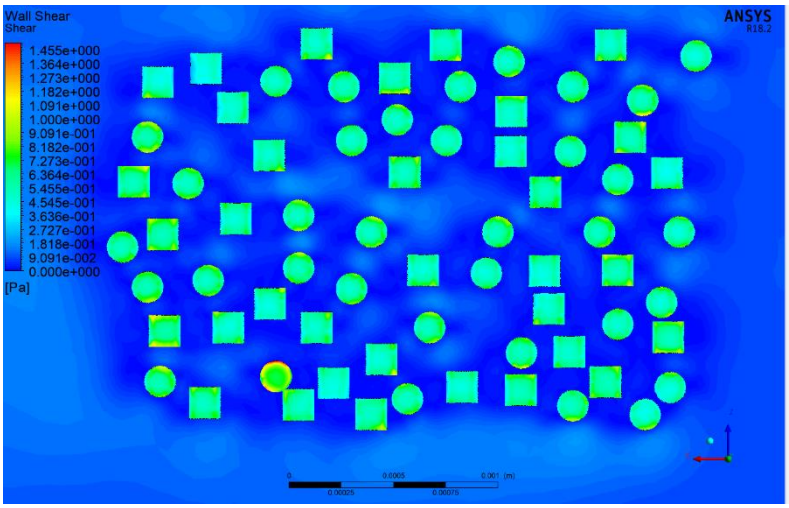


Figure 16. Wall Shear Stress Contour of Anisotropic Topography

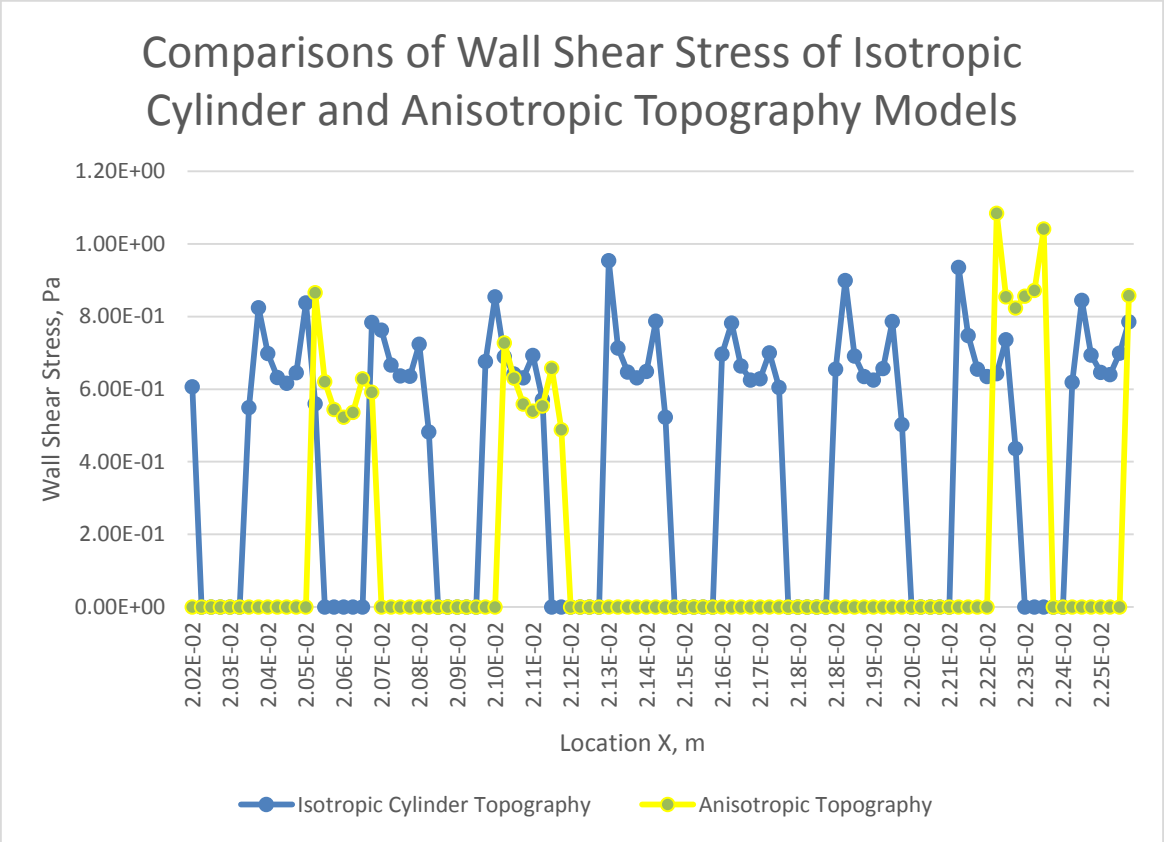


Figure 17. Comparisons of wall shear stress of isotropic cylinder and anisotropic topography models graph

Figure 17 shows the variations of the wall shear stress along a line drawn in the center of both isotropic cylinder and anisotropic cube topography. A relatively similar patterns of wall shear stress were seen in the plot by the isotropic cylinder while the anisotropic topography shows a gap in between them. These gap may induced and encourage more settlement of the microorganisms as the is little to none resistance of wall adhesion through wall shear stress parameter.

4. Conclusion

In a nutshell, the research has been leaning on the usage of both ANSYS 18.2 and Solidworks 2015 in analyzing the potential of Antifouling for both Isotropic and Anisotropic topography surfaces. Through this research, it was found that there are significant differences in biofouling nature between both of the topography where Isotropic topography show a more likely higher antifouling potential compared to the Anisotropic topography which relates to a higher wall shear stress distribution in Isotropic topographies. This study also proved the reliability of Computational Fluid Analysis(CFD) in analyzing the behavior of biofouling agents.

REFERENCES

[1] S. Cao, J. D. Wang, H. S. Chen, and D. R. Chen, "Progress of marine biofouling and antifouling technologies," *Chinese Sci. Bull.*, vol. 56, no. 7, pp. 598–612, 2011.

[2] M. A. Champ, "A review of organotin regulatory strategies, pending actions, related costs and benefits," *Sci. Total Environ.*, vol. 258, no. 1, pp. 21–71, 2000.

[3] A. Abbott, P. D. Abel, D. W. Arnold, and A. Milne, "Cost–benefit analysis of the use of TBT: the case for a treatment approach," *Sci. Total Environ.*, vol. 258, no. 1, pp. 5–19, 2000.

[4] L. D. Chambers, K. R. Stokes, F. C. Walsh, and R. J. K. Wood, "Modern approaches to marine antifouling coatings," *Surf. Coatings Technol.*, vol. 201, no. 6, pp. 3642–3652, 2006.

[5] T. Vladkova, "Surface Modification Approach to Control Biofouling," in *Marine and Industrial Biofouling*, H.-C. Flemming, P. S. Murthy, R. Venkatesan, and K. Cooksey, Eds. Berlin, Heidelberg: Springer Berlin Heidelberg, pp. 135–163, 2009

[6] K. A. Dafforn, J. A. Lewis, and E. L. Johnston, "Antifouling strategies: History and regulation, ecological impacts and mitigation," *Mar. Pollut. Bull.*, vol. 62, no. 3, pp. 453–465, 2011.

[7] F. W. Y. Myan, J. Walker, and O. Paramor, "The interaction of marine fouling organisms with topography of varied scale and geometry: a review.," *Biointerphases*, vol. 8, no. 1, p. 27, 2013.

[8] A. G. Nurioglu, A. C. C. Esteves, and G. de With, "Non-toxic, non-biocide-release antifouling coatings based on molecular structure design for marine applications," *J. Mater. Chem. B*, vol. 3, no. 32, pp. 6547–6570, 2015.

[9] R. A. Braithwaite and L. A. B. T.-A. in M. B. McEvoy, "Marine Biofouling on Fish Farms and Its Remediation," vol. 47, no. Supplement C, Academic Press, 2004, pp. 215–252, 2004

[10] X. Pu, G. Li, and H. Huang, "Preparation, anti-biofouling and drag-reduction properties of a biomimetic shark skin surface," *Biol. Open*, vol. 5, no. 4, pp. 389–396, 2016.

[11] Q. She, R. Wang, A. G. Fane, and C. Y. Tang, "Membrane fouling in osmotically driven membrane processes: A review," *J. Memb. Sci.*, vol. 499, no. Supplement C, pp. 201–233, 2016.

[12] P. Halder *et al.*, "A novel approach to determine the efficacy of patterned surfaces for biofouling control in relation to its microfluidic environment," *Biofouling*, vol. 29, no. 6, pp. 697–713, 2013.

[13] K. M. Berntsson *et al.*, "Reduction of barnacle recruitment on micro-textured surfaces:

Analysis of effective topographic characteristics and evaluation of skin friction," *Biofouling*, vol. 16, no. 2–4, pp. 245–261, Nov. 2000.

[14] M. E. Callow *et al.*, "Microtopographic Cues for Settlement of Zoospores of the Green Fouling Alga Enteromorpha," *Biofouling*, vol. 18, no. 3, pp. 229–236, Jan. 2002.

[15] J. Xu *et al.*, "Investigation of the biofouling properties of several algae on different textured chemical modified silicone surfaces," *Appl. Surf. Sci.*, vol. 311, pp. 703–708, 2014.

[16] L. Xiao *et al.*, "Hot Embossed Microtopographic Gradients Reveal Morphological Cues That Guide the Settlement of Zoospores," *Langmuir*, vol. 29, no. 4, pp. 1093–1099, Jan. 2013.

[17] P. Halder *et al.*, "Microfluidic disturbances on synthetic patterned surfaces and their impact on microorganisms in relation to biofouling control Partha Halder School of Civil , Environmental and Chemical Engineering," *Biofouling*. vol.30, no.6, pp 695-707, 2014.

[18] N. Aldred, A. Scardino, A. Cavaco, R. de Nys, and A. Clare, "Attachment strength is a key factor in the selection of surfaces by barnacle cyprids (Balanus amphitrite) during settlement," *Biofouling*, vol. 26, no. 3, pp. 287–299, 2010.

[19] M. L. Carman *et al.*, "Engineered antifouling microtopographies - Correlating wettability with cell attachment," *Biofouling*, vol. 22, no. 1, pp. 11–21, 2006.

[20] Oxford English Dictionary, "Oxford English Dictionary Online," *Oxford English Dictionary*, 2017. [Online]. Available: http://dictionary.oed.com.

[21] C. Carl, A. J. Poole, M. J. Vucko, M. R. Williams, S. Whalan, and R. de Nys, "Enhancing the efficacy of fouling-release coatings against fouling by Mytilus galloprovincialis using nanofillers," *Biofouling*, vol. 28, no. 10, pp. 1077–1091, 2012.

[22] J. Ballester-BeltrÃ¡n, M. J. P. Biggs, M. J. Dalby, M. SalmerÃ³n-SÃ¡nchez, and A. Leal-EgaÃ±a, "Sensing the Difference: The Influence of Anisotropic Cues on Cell Behavior," *Front. Mater.*, vol. 2, no. May, pp. 1–12, 2015.

[23] M. J. P. Biggs, R. G. Richards, and M. J. Dalby, "Nanotopographical modification: a regulator of cellular function through focal adhesions," *Nanomedicine Nanotechnology, Biol. Med.*, vol. 6, no. 5, pp. 619–633, 2010.

[24] M. Salta *et al.*, "Designing biomimetic antifouling surfaces," *Philos. Trans. R. Soc. A Math. Phys. Eng. Sci.*, vol. 368, no. 1929, pp. 4729–4754, 2010.

[25] Y. S. Khor and Q. Xiao, "CFD simulations of the effects of fouling and antifouling," *Ocean Eng.*, vol. 38, no. 10, pp. 1065–1079, 2011.

[26] K. Efimenko, J. Finlay, M. E. Callow, J. A. Callow, and J. Genzer, "Development and Testing of Hierarchically Wrinkled Coatings for Marine Antifouling," *ACS Appl. Mater. Interfaces*, vol. 1, no. 5, pp. 1031–1040, May 2009.

[27] N. A. Mortensen, F. Okkels, and H. Bruus, "Reexamination of Hagen-Poiseuille flow: Shape dependence of the hydraulic resistance in microchannels," *Phys. Rev. E*, vol. 71, no. 5, p. 57301, May 2005.

EURECA 2018 – Conference Paper
Paper number 2ME26

Design and prototyping of a new economic automatic coconut deshelling machine.

Ryan Jerome Lee, Ghafour Amouzad Mahdiraji

Abstract. The coconut industry is a fairly large industry in Asia with 90% of the world's coconut imports originating from Asia, with Indonesia, Philippines and India topping the charts in that sequence. In Malaysia, coconuts are the fourth most important crop produced in the country behind palm oil, rubber and rice paddy. Despite the importance of the coconuts industry to Asia, some portions of the processing line are still stuck using relatively outdated machinery. One section in particular is the de-shelling station and this makes the job dangerous. The most common method used by the industry is a rotating saw that cracks and pulls the shell of the fruit away from the flesh of the coconut. This outdated machine is extremely dangerous as the operators hand is relatively close to the blade of the saw. One moment of negligence from an unskilled operator may cause the operator to lose a limb as his arm is dragged into the machine. This machine also does not have any fail safe sensors designed to help reduce casualties. This project was conducted with the aim of designing a new semi-automated de-shelling machine to be used in the coconut industry that will reduce the danger factor to the operator. The entire machine must also fulfil several other conditions such as being no less efficient than the old method of de-shelling coconuts and being economically viable in that it will not be extremely expensive. To produce the best prototype, research was done to investigate previous de-shelling methods and the best method to de-shell coconuts. The research was done in 3 phases which was; literature review, site visit and experiments done on coconut samples. From the data obtained, a prototype of a semi-automated coconut de-shelling machine was designed and individual parts were built for testing and refining. Following that, a functioning prototype will be built and refined to produce a proof of concept that can be scaled up to be used in an industrial machine.

1 Introduction

The coconut tree is widely known around the world as the 'tree of life' due to its multifarious uses.[1] For centuries, the coconut palm has been one of the world's major crop plants as it was able to fulfil the basic necessities of life for early settlers; food, drink, fuel and shelter. The fruit of the coconut palm was by far the most important nut in the world as there were a number of products that can be derived from it. The husk can be processed into a fibre known as coir. From immature nuts a fine fibre suitable for coir yarn and from the mature nuts, a coarser mattress and bristle fibres are obtained. The hard shell of the coconut is mainly consumed as burning fuel, either as is or carbonized to form charcoal. Finely ground shells can also be used as filler for thermoplastics which yields a thermoplastic with higher tensile and flexural modulus compared to untreated polymers. [2]

However the fruit of the coconut is by far the more useful resource obtained from the coconut tree. This is because coconut oil is collected from the kernel of the coconut. The coconut oil is a very versatile resource which finds use in various industries from food products to cosmetics.[5] In recent years, coconut products has become trendy due to the fact that the natural composition of coconut oil which are made up of medium chain fatty acids that the body burn for energy rather than store as fats. This discovery has led to coconut oil being the hit trend in the world of weight loss products. Furthermore, coconut oil also contains antiviral, antibacterial and antiprotozoal properties due to the presence of several types of fatty acids. This means food products stored in coconut oil is highly stable towards oxidation and has a longer shelf life. [4]

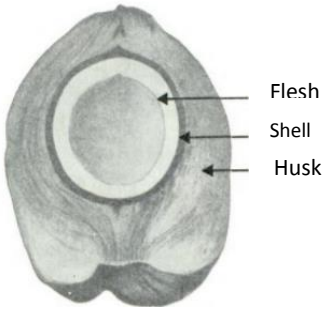


Figure 1: Cross Section of Coconut Fruit.[2]

With its wide range of uses and recent boom in popularity, it is easy to see why the coconut palm has long been considered a cash crop that is widely grown in agricultural based countries. 90% of the world coconuts are grown in Asia, with Indonesia, Philippines and India topping the charts in order. In Malaysia, coconut crops are the fourth most important crop behind palm oil, rubber and rice paddy. However due to recent competitions with palm oil for land has led to a yearly decline of total area of coconut cultivation. Furthermore approximately 63% of coconuts produced locally are used for domestic consumption with the remainder for industrial processing. [1] This trend has led to Malaysia importing husked coconuts from other producing countries such as Thailand, Indonesia and India to be processed in the coconut processing plants before being exported to other countries.

The first stage of coconut processing (which this project is focuses on) is a relatively simple process of de-shelling and pairing the husked coconuts to extract the whole white flesh of the coconut. The coconuts are typically husked in the plantation before being sent to the processing plant to reduce weight and allow for ease of transport. From the plantation, the coconuts are weighted, checked for damage, de-shelled and paired before being sent to the next stage of processing.

The most widely used method of de-shelling coconuts is by utilizing the cracking disk cutter and pin combination that can be seen in Figure 2. This method uses the disks to crack the hard shell of the fruit and pulls the shell away from the flesh of the coconut. From Figure 3, it can be observed that the method used to de-shell the coconut is quite hazardous as the operators hand is close to the open blade. There have been cases where workers being negligent and losing a limb because the saw rotates and pulls the entire arm in before the machine can be stopped. Hence, there is a need to create a machine that will remove the danger factor in this process.



Figure 2: De-shelling Tool.[7]

1.1 Research questions

How can we develop a safe method and efficient to deshell the hard shells from the coconut flesh?

1.2 Research objectives

To design and prototype a new and semi-automated system used to de-shell coconuts to obtain the flesh that is safer and as efficient as the method currently used in the industry

1.3 Hypothesis

Having a semi-automated system will reduce the amount of injuries without lowering the efficiency of the coconut de-shelling process.

1.4 Scope

The scope of this project is only to deshell the coconut, which is to separate the hard shell from the soft flesh of the coconut, without placing the technician/worker in a dangerous situation. The aim of this project is to develop and prototype and semi-automated or fully automated coconut de-shelling machine.

1.5 Contribution to Body of Knowledge

From this project, several factors which cause the coconut shell to separate from the flesh will be obtained, studied and adapted to the heavy industry to improve the deshelling process in the coconut industry. Furthermore a prototype will be developed and tested to obtain a suitable way to safely and efficiently deshell coconuts and harvest the flesh.

2 Literature review

Over the years, many methods have been devised to de-shell coconuts and the simplest method is to simply cut the fruit in half and scrape the flesh out. However in the processing plant, the coconut must be kept as one whole piece with minimal damage to ensure that it is fit to pass through to the pairing and the subsequent processes in the plant. Therefore to accomplish this task, it is important to first understand the challenges faced when de-shelling the coconuts and also investigate the other ways used by the industries to de-shell coconuts and other hard shelled fruits.

The main challenge faced when deshelling coconuts whole is the structure of the coconut. As seen in Figure 1, the coconut is a hollow fruit with a hard shell covering it. This prevents the use of any excessive force on the fruit or else the flesh inside may crack before the shell does. Secondly, the flesh of the coconut is also adhered to the shell of the fruit. This makes it hard to separate the flesh without damaging it.[2] Thirdly during the site visit, I was informed that when the coconuts are imported from other countries, it usually arrives as a mixed batch of several different species of coconuts. This means that the size and shape of the coconut would vary and it would be hard to calibrate a fine tuned automated machine to work with the whole batch.

There are several method devised over the years to deshell coconuts while keeping the fruits whole. The oldest method is by manually cracking the shell with a small pickaxe or axe. However this method is significantly slower than using machines as the worker will have to adjust his/her strength and angle of hitting to avoid injuring himself and also to avoid damaging the coconut flesh. This method of deshelling is still used in some mills but has been largely replaced with the usage of mechanical tools.



Figure 3: Manual De-shelling using Pickaxe.

The most common method, as mentioned above is by using the cracking disk cutter and pin as seen in Figure 2. This method is used in most of the coconut mill in South East Asia and a skilled operator can de-shell up to 200kg of coconuts per hour. This method uses the blades to crack the shell and force the pin into the layer between the flesh and the shell. The constantly rotating blade will pull on the shell forcing it to separate from the flesh that is held back by the pin. This principle also comes in several forms such as replacing the blade with paddles to allow for more traction on the shell as seen in Figure 4. However regardless of the design, it is still extremely dangerous for the operator to use this machine as one moment of negligence can cause the operators hand to be pulled into the machine.



Figure 4: Rotating Paddle and Pin De-shelling Machine. [7]

A slightly more automated method was developed in 1965 by an inventor by the name of Gerald Kleiman. [8] Kleiman's design utilizes 2 prongs which hold the coconut in place and a circular saw which would cut a circular pattern around the fruit as seen in Figure 5, after which a worker would be needed to peel the shells off the fruit.

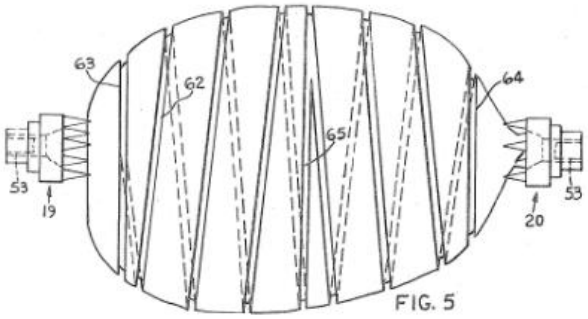


Figure 5: The Kleiman Coconut De-shelling Machine. [8]

The Kleiman designs have since been improved upon by an Italian company specializing in food equipment by the name of ABL Machineries. The ABL design is semi-automated where an operator only need to place the fruits in the machine and collect the fruits after the process has been completed.[9] This new functioning principle of slicing into the shell without cutting into the flesh still required an extra step after the cuts due to the flesh being adhered to the shell. In the original Kleiman design, an operator was required pry the flesh away from the shell using a flexible knife whereas in the ABL design, the coconuts had to be heated in an oven after cutting it and an operator had to pry the flesh from the shell similar to the Kleiman design. This means that these designs are not feasible as the shells would still have to be loaded and unloaded by hand which would decrease the overall efficiency of the mill. Furthermore, these machines are very extremely expensive and the output of the machine does not justify the costs.

There are several methods that can be used to delaminate or remove the adhesion between the flesh and the shell. The most common method is by using heat, traditionally, the coconuts were left to dry out in the sun for 2 to 3 days before a worker deshelled it using a pickaxe. Alternatively, steaming the coconuts whole in a sterilizer would also loosen the adhesion between the flesh and shell.[3] Another method used to delaminate the flesh and shell is by freezing the coconuts whole.

This method causes the water to freeze and subsequently the flesh of the shell to harden, after the coconut has been frozen, heavy impact can be used to break the shell apart with the flesh staying whole. However, freezing massive amounts of coconuts in an industrial level will have an extremely high cost and the subsequent thawing will slow the milling process.

The coconut processing industry in Malaysia imports its fruits from high volume producers such as India and Indonesia. The fruits are husked in the plantation to reduce its weight before being sent over to Malaysia by cargo boats. This means that the husked coconuts spend up to two weeks in a warm container which helps start the delamination process of the fruits but also produce some wastage as there are some fruits which will be damaged in the plantation and eventually decompose in the container.

3 Research methodology

The research method used in this project is a quantitative study where samples are being tested in the lab and the results are observed to develop a suitable method to deshell coconuts. The study would be done in several stages with the first being a site visit followed by sample tests. Using the results from the site visit and sample tests, the initial design of the machine will be developed. Following that, a prototype will be built to produce a proof of concept.

3.1 Site Visit

The site visit was done in week 5, the purpose of the site visit was to observe the actual deshelling process in a coconut mill. The mill in question was Kapar Coconut Industries (KCI) Mill located in Kapar, Selangor. During the site visit it was observed that the mill uses the cracking disk cutter and pin machine to deshell the coconut and the main resource being collected is the coconut flesh with the coconut water as a secondary concern.

From the site visit, it was also observed that while majorities of the processing were done using heavy machinery and requires very little human operators. However the initial processes of cracking, draining and pairing were done by hand or with specialized machinery requiring operators. This was due to the fact that the pre-existing semi-automated machinery for the de-shelling and pairing processes were expensive and slow compared to manual labor. Skilled workers using the cracking disk deshelling machine could crack up to 200kg per hour whereas skilled workers in the pairing process could pair up to 400kg per hour using a relatively cheap fruit peeler. Furthermore, the automated machinery used in the pairing process produced a lot of wastage as it removed a large portion of coconut flesh along with the skin.

Discussions with a supervisor and a manager were done to further understand the mechanics and difficulties in building a semi-automated coconut deshelling machine.

3.2 Sample Tests

3.2.1 Experimental Procedure

Experiment 1: Effects of removing water before heating.

1. 5 samples of coconuts without water and 5 with water were placed into an oven at 70^{o}C.
2. The oven was set to heat up to 100^{o}C.
3. The samples were checked every 15 minutes for 60 minutes.
4. The observations were recorded.

Experiment 2: Heating at constant temperature.

1. The oven was pre-heated at 70^{o}C.
2. 5 samples of coconuts without water were placed into the oven.
3. The samples were removed after 15 minutes.
4. The samples were then cracked open with a hammer to check the state of delamination.
5. Steps 1 to 4 were repeated with duration of 30 minutes, 45 minutes and 60 minutes.
6. Steps 1 to 5 were repeated at temperatures of 80^{O}C, 100^{O}C and 120^{O}C.
7. The observations were recorded.

3.3 Prototype Design

The prototype was designed as seen in Figure 6 based on the existing rotating paddle and pin deshelling tool seen in Figure 2. There are two core components in this design; the first is the rotating blade which functions to bite into the shell to pull it towards the second core component which is the pin which cracks the shell and slips into the coconut to pry the flesh away from the shell. The current coconut deshelling tool design requires a worker to hold the nut against the blade and pin while manually rolling the nut to allow for deshelling across the whole fruit. In this prototype, the two blades are mounted onto shafts set on motors and designed to rotate in opposing directions. There is one pin for each blade which is located approximately 0.5cm from the blades. The opposing forces acting on the coconut will in theory rotate the fruit while deshelling it without requiring a worker to hold it in place. The locations of the pins have to be adjusted to find the location at which the coconut begins to crack when placed in this machine. The motor distance and blade height can be adjusted to allow for more varied tests to be done and obtaining a better range of tests data.

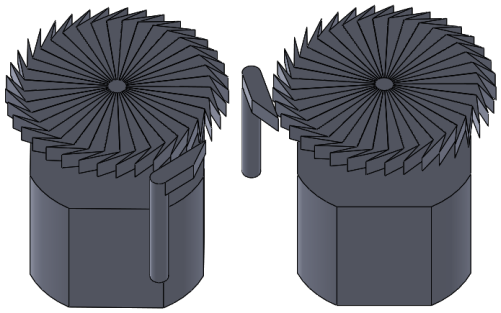


Figure 6: Prototype Drawing Isometric View

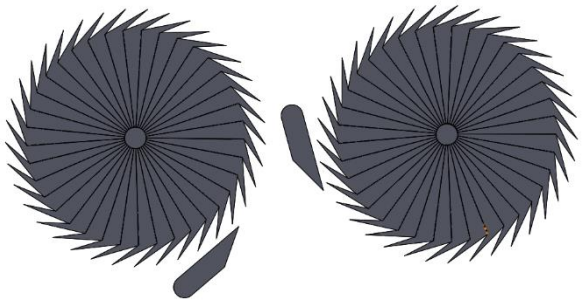


Figure 7: Prototype Drawing Top View

The diameter of the prototype blade was 20cm, with the individual teeth being angled at 30^{o} and 3cm long as seen in Figure 8. The size and shape of the blade is important to ensure that the teeth bite into the shell and pull it towards the pin instead of cutting it like a saw. The center hole of the blade for the shaft was set at 2cm. In the prototype design drawing, the blade is mounted directly onto the motor seen in Figure 9 to produce a simple design of the intended prototype.

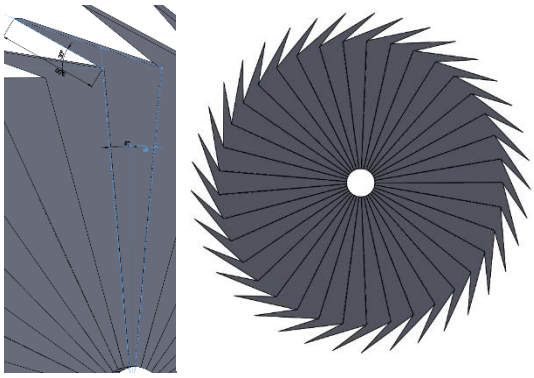


Figure 8: Prototype Blade Drawing

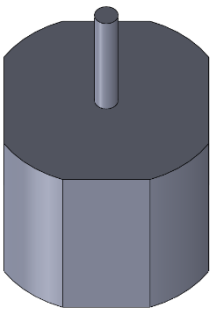


Figure 9: Prototype Motor Drawing

The design of the pin was based on the sample pin obtained from Kapar Coconut Industries seen in Figure 9. This circular pin was used in the deshelling machine and grinded regularly to maintain the sharpness of the tip. The prototype pins were designed to match the height of the blade therefore the height needed to be adjustable for the testing procedures. The porotype pins were also in the shape of an inverted capital L, this is because the blade and pin in the prototype are mounted horizontally not vertically. The length of the pin was set at 8cm with one edge grinded down to form a 30^{0} angle.



Figure 10: Sample Pin

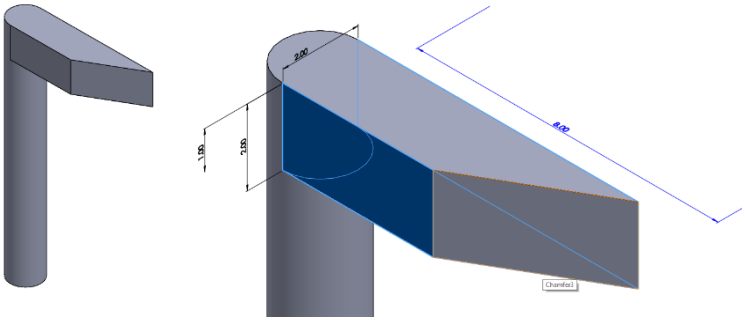


Figure 11: Prototype Pin Drawing

The completed prototype can be seen in Figure 12. The motors used to build the prototype were repurposed 240V universal motors obtained from old washing machines. These motors were suitable because they are able to run on both AC and DC electrical supply and were cheap and readily available. The blades used were loaned from Kapar Coconut Industries. Those blades were designed after being tested on and actual deshelling machine. The blades are mounted on a rotating shaft and are connected to the motor via a fan belt to prevent damage to the motors in the event of stalling. The two blades will rotate in opposite direction with the nut in the between them. The nut is held onto the blades loosely with a piece of wood to allow it to spin. The current prototype does not have the pin as seen in Figure 12. This is to test if the pin is required when there are two blades acting on the coconut. The maximum speed of the two motors used in the prototype was 1000rpm. All the shafts used in the design are threaded and all the components are held together using nuts and washers. This setup allows for easier adjustment of the blades.



Figure 12: Prototype without Pins Top View.

The prototype pins seen in Figure 13 was manufactured in the Taylors workshop by welding two pieces of 2cm diameter solid steel pipes and grinding down an edge using a hand grinder. The manufactured pins did not comply with the exact design of the sample pin as the tools needed were no readily available. As seen in Figure 14, the edge of the pin does not comply with the 30^{o} design and is approximately 45^{o}. The prototype pins were measured and mounted onto the prototype by boring a 2cm diameter hole into the base and inserting the pins into the holes. This method of mounting the pins ensures that the pins will not move when the coconut is forced onto it.



Figure 13: Prototype Pin Side View.



Figure 14: Prototype Pin Edge.



Figure 15: Prototype with Pins

3.4 Prototype Test

3.4.1 Experimental Setup

The experiment was conducted to investigate if the prototype would rotate the coconut in between the blades without manual help and the importance of the pin as seen in Figure 7 in the deshelling process. The experiment was setup as seen in Figure 9, the blades were set to be 15 cm from each other. Both blades were set at 5cm above the base with no height difference between the blades. The samples tested were not heated but the water was drain from the coconuts. The water was drained to prevent water damage to the motors in the event the coconut cracks. The speed was set at the motor maximum of 1000rpm. A smooth piece of wood was used to push and hold the coconut in between the blades.



Figure 16: Experimental Setup

3.4.2 Experimental Procedure

Experiment 3: Effect of one rotating and one stationary blade without pins on coconut.

1. The experiment was set up as seen above.
2. The motors were turned on.
3. A coconut was placed in between the blade.
4. The observations were tabulated and recorded.

Experiment 4: Effect of dual spinning blades on coconut without pins.

1. The experiment was set up as seen above.
2. The motors were turned on.
3. A coconut was placed in between the blade.
4. The observations were tabulated and recorded.

Experiment 5: Importance of pin to deshelling process.

1. The experiment was set up as seen above.
2. The motors were turned on.
3. A coconut was placed in between the blade.
4. The observations were tabulated and recorded.
5. The motors were turned off and the height differences of the blades were set to 5cm by moving both blades by 2.5cm.
6. Steps 1 to 4 were repeated at this new setting.
7. Steps 1 to 6 were repeated with the height difference of the blades at 10cm by moving both blades an additional 2.5cm.

4 Results and discussion

4.1 Experimental results

Experiment 1: Effects of removing water before heating.

State	Time (mins)	Sample				
		1	2	3	4	5
Water	15	No cracks, No delamination	No cracks, No delamination	No cracks, No delamination	No cracks, No delamination	No cracks, No delamination
	30	No cracks, No delamination	No cracks, No delamination	No cracks, No delamination	No cracks, No delamination	No cracks, No delamination
	45	No cracks, No delamination	No cracks, No delamination	No cracks, No delamination	No cracks, No delamination	No cracks, No delamination
	60	No cracks, No delamination	No cracks, No delamination	No cracks, No delamination	No cracks, Partial delamination	No cracks, Partial delamination
No Water	15	No cracks, No delamination	No cracks, No delamination	No cracks, No delamination	No cracks, No delamination	No cracks, No delamination
	30	No cracks, No delamination	No cracks, No delamination	Small cracks, Partial delamination	Small cracks, Partial delamination	Small cracks, Partial delamination
	45	Small cracks, Partial delamination	Small cracks, Partial delamination	Small cracks, Full delamination	Small cracks, Full delamination	Small cracks, Full delamination
	60	Small cracks, Full delamination	Small cracks, Full delamination	Large Cracks, Full delamination	Large Cracks, Full delamination	Large Cracks, Damaged Fruits

Table 1: Results of Experiment 1.

Experiment 2: Heating at Constant Temperature.

Temperature (°C)	Time (mins)	Sample				
		1	2	3	4	5
70	15	No cracks, No delamination	No cracks, No delamination	No cracks, No delamination	No cracks, No delamination	No cracks, No delamination
	30	No cracks, No delamination	No cracks, No delamination	No cracks, No delamination	No cracks, No delamination	No cracks, Partial delamination
	45	No cracks, Partial delamination	No cracks, Partial delamination	No cracks, Partial delamination	Small cracks, Partial delamination	Small cracks, Partial delamination
	60	Small cracks, Partial delamination	Small cracks, Partial delamination	Small cracks, Partial delamination	Small cracks, Partial delamination	Small cracks, Partial delamination
80	15	No cracks, No delamination	No cracks, No delamination	No cracks, No delamination	No cracks, No delamination	No cracks, No delamination
	30	No cracks, No delamination	No cracks, Partial delamination	No cracks, Partial delamination	Small cracks, Partial delamination	Small cracks, Partial delamination
	45	Small cracks, Partial delamination	Small cracks, Partial delamination	Small cracks, Partial delamination	Small cracks, Partial delamination	Small cracks, Full delamination
	60	Small cracks, Partial delamination	Small cracks, Full delamination	Small cracks, Full delamination	Small cracks, Full delamination	Small cracks, Full delamination

100	**15**	Small cracks, Partial delamination	Small cracks, Partial delamination	Small cracks, Partial delamination	Small cracks, Full delaminatio n	Small cracks, Full delaminatio n
	30	Small cracks, Full delamination	Small cracks, Full delamination	Small cracks, Full delamination	Small cracks, Full delaminatio n	Large cracks, Full delaminatio n
	45	Large Cracks, Full Delaminatio n	Large Cracks, Full Delaminatio n	Large Cracks, Full Delaminatio n	Large Cracks, Damaged Fruits	Large Cracks, Damaged Fruits
	60	Large Cracks, Damaged Fruits	Large Cracks, Damaged Fruits	Large Cracks, Damaged Fruits	Large Cracks, Damaged Fruits	Large Cracks, Damaged Fruits
120	**15**	Small cracks, Full delamination	Small cracks, Full delamination	Small cracks, Full delamination	Large cracks, Full delaminatio n	Large cracks, Full delaminatio n
	30	Large Cracks, Full Delaminatio n	Large Cracks, Full Delaminatio n	Large Cracks, Full Delaminatio n	Large Cracks, Damaged Fruits	Large Cracks, Damaged Fruits
	45	Large Cracks, Damaged Fruits	Large Cracks, Damaged Fruits	Large Cracks, Damaged Fruits	Large Cracks, Damaged Fruits	Large Cracks, Damaged Fruits
	60	Large Cracks, Damaged Fruits	Large Cracks, Damaged Fruits	Large Cracks, Damaged Fruits	Large Cracks, Damaged Fruits	Large Cracks, Damaged Fruits

Table 2: Results of Experiment 2.



Figure 17: Small Crack on Coconut.



Figure 18: Large Crack on Coconut.



Figure 19: Full Delamination on Top Portion of Coconut.

Experiment 3: Effect of one rotating and one stationary blade without pin on coconut

Motor Speed	**1000rpm**
Coconut Rotation	Does not rotate at all, blade cuts into the shell similar to a saw.
Shell Cracking	No

Table 3: Results of Experiment 3.

Experiment 4: Effect of using dual rotating blade without pin on coconut

Motor Speed	**1000rpm**
Coconut Rotation	Rotates very quickly when pushed lightly against the blades, does not rotate when forced onto the blades with excessive force
Shell Cracking	No

Table 4: Results of Experiment 4.

Experiment 5: Importance of pin in the deshelling process

	Height Difference Between Blades (cm)		
	0	**5**	**10**
Coconut Rotation	Rotates very quickly when pushed lightly against the blades, does not rotate when forced onto the blades with excessive force	Rotates very quickly when pushed lightly against the blades, does not rotate when forced onto the blades with excessive force	Rotates very quickly when pushed lightly against the blades, does not rotate when forced onto the blades with excessive force
Shell Cracking	No	No	No

Table 5: Results of Experiment 5.

4.2 Discussion

From Experiment 1, it can be observed that when the water is extracted from the fruit before heating, the effects of heating is more prominent. However it is also observed in Table 1 that when the water is left in the fruit, there is less likelihood of the shell cracking in the heating process. This may be due to the lack of a hole in the shell as it was observed that the cracking usually started at the hole that the water is extracted from. The results also show that the coconuts delaminate better when the water has been extracted as only partial delamination occurs after a full hour in the oven. Partial

delamination is the state in which the flesh of the coconut is mostly stuck to the shell after it cracked using a hammer. The flesh does not dislodge from the shell and any excess force applied to remove it only damages the flesh. Thus it is observed from Experiment 1 that after the coconut has been drained, it delaminates faster when heated in the oven.

From Experiment 2, it is observed that 70^{o}C is not hot enough for the coconut to undergo an efficient delamination. At 70^{o}C, the process is very slow with the coconut only undergoing partial delamination after 1 hour. From the trend we can observe that the coconuts will eventually achieve full delamination after an extended period time. From Table 2, we can also observe that by increasing the temperature to 80^{o}C, the results obtained improves as 4 out of 5 samples undergo full delamination after an hour. Full delamination occurs when the flesh separates whole from the shell with minimal force applied after the coconut has been cracked open using a hammer. An example of delamination can be seen in Figure 19 which shows partial delamination of a coconut. In the image it can be seen that the shell has been seperated from the flesh, however there is still a brown layer of skin which covers the flesh. The layer of skin is removed in the pairing station of the process plant.

The results at 100^{o}C showed the best results as all the fruits showed full delamination after 30 minutes in the oven. However, after 30 minutes the flesh of the fruits started being damaged as large cracks form on the flesh and the flesh would be split in half in some cases. The large cracks formed in line with the cracks formed on the shells and the number of damaged fruits increased with time and increased temperature with the trend shown clearly seen when the fruits were heated at 120^{o}C. At 120^{o}C, the fruits have a small window of full delamination before the flesh becomes damaged.

From Table 3, we can observe the results of Experiment 3 which concerns the rotation of the coconut when a dual blade system of deshelling is applied. The results were promising in that when a slight force was applied using a smooth circular wood, the coconut is snagged by the blade teeth which causes it to rotate a full 360^{o}. However, when force is applied, the coconut stops rotating and the fast moving blades bites into the shell and begins to cut it, similar to when using a band-saw to cut the shell.

From Table 4, we can observe the height difference between the two blades does not cause the shells to crack. These results show that even when running a dual blade deshelling machine, the pin is an essential component in the design which cracks the coconut and all for proper deshelling process to occur. The observations of Experiment 4 are also in line with Experiment 3 where when force is applied onto the coconut, the blades function more like band-saws and cuts the shell.

5. Conclusion

The results of Experiment 1 showed that for the easier coconut shell-flesh delamination, the water should be drained before heating. From Experiment 2, it can be observed that for the best results, the coconut should be heated at approximately 100^{0}C for 20 minutes to achieve full delamination without damaging the flesh due to excess heat. When heated to 120^{o}C, there is an increased chance that the flesh would be damaged hence it is best to reduce the heat even though the heating period would be slightly longer. From Experiment 3, it can be concluded that the prototype concept of using dual blades to achieve the function of rotating the coconut on the blade is feasible. Hence eliminating the need for a worker to manually rotate the coconut when using the deshelling machine. Experiment 4 concluded that a pin is required even when dual blades are used, as the results show that without the

pin to crack the shell, the blades function more like a saw and will cut the shell in half instead of cracking it.

In conclusion, the experiments show that to improve the delamination process of the coconut to allow for easier deshelling, the fruits can first be drained and then heated at approximately 100^{o}C for 20 minutes. Following that, a new and improved deshelling method can be developed by using the dual blade and pin system which would negate the need for a worker to hold and rotate the coconut. However, the results also show that the pin is extremely important in the deshelling process.

Future work that can be done is installing two pins into the prototype; one for each blade. The pin must be aligned properly with the blades to ensure that cracking occurs. Future experiments using the prototype with the pins installed can be conducted to obtain the effect of draining and heating; to see if it drastically improves performance and the effect of the position of the blade on the performance of the machine. Using the data obtained from these new experiments, a design for a new industrial machine can be developed and build

6 References

[1]. A. Sivapragasam, "Coconut in Malaysia – Current Development and Potential for Re-vitalization", 2008. [Online] Available : http://www.iipm.com.my/ipicex2014/docs/oral/Session%202B%20Sivapragasam.pdf. [Accessed 10/10/2017].

[2]. Brian E. Grimwood and F. Ashman," The Coconut" in *Coconut Palm Products : Their Processing in Developing Countries*. London: FAO, 1979, pp. 24-33.

[3]. Brian E. Grimwood and F. Ashman," Mechanization in the Manufacture of Desiccated Coconut" in *Coconut Palm Products : Their Processing in Developing Countries*. London: FAO, 1979, pp. 34-36.

[4]. Prakruthi Appaiah et al., "Composition of Coconut Testa, Coconut Kernel and its Oil", Central Food Technological Research Institute, India. 2014.

[5]. Juan A. Hernandez, "Is Coconut the New Gold" in *Caribbean Business*. Puerto Rico: LMH, 2016.

[6]. World Atlas, *The World Leaders in Coconut Production* (2017). [Online] Available : http://www.worldatlas.com/articles/the-world-leaders-in-coconut-production.html. [Accessed 10/10/2017]

[7]. Coconut De-shelling Machine, (2017). [Online] Available : https://dir.indiamart.com/impcat/coconut-deshelling-machine.html. [Accessed 10/10/2017]

[8]. Gerald Kleiman, "Coconut Deshelling Machine" US Patent 3340918 A, Sept 12, 1967.

[9]. ABL Machinery Catalogue, (2017). [Online] Available : http://www.abl-fruit-machinery.com/prodotti/pdf/CatalogoGenerale2006ABL.pdf . [Accessed 10/10/17]

Development Of Mathematical Model For Driveline Abuse Test

Sheldon Vinsent[1] [*], Noor Zafirah Abu Bakar[1] , and Hazlan bin Meera Hussain[2]

[1]Department of Mechanical Engineering,Faculty of Built Environment, Engineering, Technology & Design, Taylor's University Lakeside Campus.
[2]Transmission Engineering, Powertrain Dept., Engineering Division, PROTON HOLDINGS BERHAD
[*]sheldon.vinsent@gmail.com

Abstract. The driveline abuse test is a common and mandatory test among vehicle original equipment manufacturers. The test is conducted when the car is at rest, brakes are released, the clutch is not in the engaged position and first gear is selected. It then proceeds on to the driver accelerating till maximum engine speed is reached. A driveline abuse test is conducted by loading the car with a surplus of torque by engaging the clutch. When this occurs, a transient torque is transmitted to all of the components of the drivetrain. Such components include the clutch, manual transmission, differential, driveshaft and wheels. During the aforementioned test, a PTL is installed into the test in order to minimize the torque applied. Without a peak torque limiter, many of the engine components can potentially be damaged due to the large magnitude of torque. This paper aims to find the torque transmitted throughout all the driveline components during the abuse test as well as to find the correlation between the size of the peak torque limiter, torque reduction and delay. In order to achieve these goals, a mathematical model is developed which incorporates the loss for each driveline component. Once all values are inputted into the mathematical models, a simulation using SIMULINK can be used to observe the torque change. To investigate the mechanism of the peak torque limiter, computational fluid dynamics will be enforced in this project to simulate the oil flow into the slave cylinder which pushes the clutch fork to measure the time taken for the clutch fork to move for a given PTL diameter. The simulation deviated about 20% from the experimental output torque at the wheels.

Keywords: Torque transmissibility, clutch abuse, PTL, driveline

Nomenclature

SYMBOL	MEANING	UNIT
C_{DIFF}	Damper constant of differential	Nms/rad
D	Mean diameter	mm
F_F	Force due to friction	N

F_{PP}	Force applied on the clutch	N
G_{RR}	Rolling friction variable	-
G_{SL}	Sliding friction variable	-
H	Height	m
J_{DRIVE}	Inertia of driveshaft	kg.m3
K_{DRIVE}	Spring constant of driveshaft	Nm/rad
K_{RS}	Replenishment/ Starvation factor	-
K_{S1}	Seal constant	-
K_{S2}	Seal constant	-
M_{RR}	Torque lost due to rolling friction	Nm
M_{SL}	Torque lost due to sliding friction	Nm
N	Clamp Load	N
R_{EQ}	Equivalent radius	m
R_I	Inner radius of friction disc	m
R_O	Outer radius of friction disc	m
$T_{1ST\ GEAR,LOSSES}$	Overall torque lost in the 1st gear	Nm
T_{AR}	Torque lost due to air resistance	Nm
T_C	Torque lost due to friction of flywheel	Nm
$T_{CLUTCH,LOSSES}$	Overall torque lost in the clutch	Nm
$T_{DIFFERENTIAL,LOSSES}$	Overall torque lost in the differential	Nm
$T_{DRIVESHAFT,LOSSES}$	Overall torque lost in the driveshaft	Nm
T_{FC}	Torque lost due to cushioning spring	Nm
T_{GEAR}	Torque lost due to gear meshing with synchronizer	Nm
T_{MESH}	Torque lost due to meshing of 1st gear	Nm
$T_{SYNCHROMESH}$	Torque lost due to synchromesh meshing	Nm
$T_{SYNCHROMESH,LOSSES}$	Overall torque lost in the synchronizer	Nm
W	Mass of gear	kg
X_{TO}	Position of release bearing	m

SYMBOL	MEANING	UNIT
η	Number of contact surfaces	-
μ	Coefficient of friction	-
ρ	Density	kg/m^3
ν	Viscosity	Kg/ms
ω	Angular velocity	m/s
ϕ_{ish}	Inlet shear heating reduction factor	-
ϕ_{rs}	Kinematic replenishment/starvation reduction factor	-
ϕ_{bl}	Sliding loss factor	-
α	Angle of synchronizer engagement	°
$\phi_{differential}$	Displacement of differential	m
$\phi_{driveshaft}$	Displacement of driveshaft	m
$\dot{\phi}_{differential}$	Angular velocity of differential	m/s
$\dot{\phi}_{driveshaft}$	Angular velocity of driveshaft	m/s
$\ddot{\phi}_{differential}$	Angular acceleration of differential	Nms/rad
$\ddot{\phi}_{driveshaft}$	Angular acceleration of driveshaft	Nms/rad

1.Introduction

The automotive industry is one of the largest and oldest industries which dates back to 1808 where François Isaac de Rivaz designed the first car that is powered by an internal combustion engine and this marks origin of the automotive industry [1].With this revolutionary breakthrough which allows individuals to travel long distances in a shorter time, the demand for cars was rising exponentially. As of 2014, 1.2 billion cars are on the road all around the globe and 21.25 million of that are in Malaysia. Moreover, there are an abundance of car companies with research facilities across the world, yet there is still much to know about this man-made product [1].

With the ampleness of cars on the road, it is of dire importance that design of each car is validated through numerous test to withstand adverse conditions. Such test include water wading test which involves moving the car through a body of water while still maintaining its structural integrity and functionality. Moreover, there are emission tests which monitors the amount of fumes the car exhaust is discharging. This test is done in efforts to reduce air pollution. The test of interest in this report is the driveline abuse test which is basically measuring a sudden instance of torque applied to the driveline. This test is of great importance as it realistically reproduce the scenario of a driver suddenly engaging the clutch at times of acceleration and from the results of this test, it can be depicted whether or not the car is viable under that condition [2].

The driveline abuse test is a common and mandatory test among vehicle OEM. The test is conducted when the car is at rest, brakes are released, the clutch is not in the engaged position and first gear is selected. It then proceeds on to the driver accelerating till maximum engine speed is reached. Once this speed has been reached, the clutch is then pressed abruptly [2]. At PROTON, this test is only conducted in an experimental manner meaning that there is no computer-aided analysis software to run the test. Moreover, only the final output torque at the wheels is currently known while the torque readings for the other driveline components are obscured. In addition, the test consumes a lot of time and money if component failure occurs. With all of the drawbacks that have been previously mentioned, it is quite clear that there is a need for a solution. For this reason, PROTON has decided to work together with Taylor’s University in order to rework the abuse test into a simulation where the output torque in each component as well as the abuse factor is known which allows the experimenter to analyse the results to anticipate failure.

In order to identify the transmitted torque among the driveline components, one must fully comprehend the components involved and the flow of transmission. A flow diagram of the driveline is illustrated in Fig. 1.

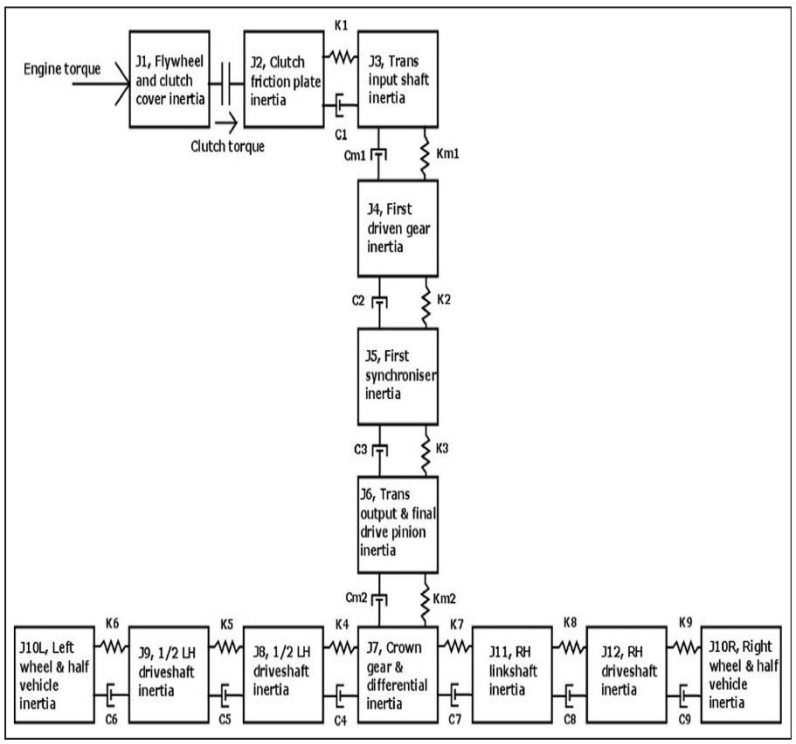


Fig. 1. Flow of torque in the driveline. [2]

During the abuse test, component damage and even breakage is fairly common where the transmission shows first indication of such failure. In efforts to prevent this, a PTL is implemented to delay the torque and this is found to be successful. A PTL is a small contrivance that is inserted before the clutch fork to delay the flow of the chosen oil by restricting the flow path which consequences in less torque being transferred at one instance. **Error! Reference source not found.** shows the PTL mechanism. The green component is the press-in cone and the red component is the orifice which has a hole in the centre. The methodology behind the PTL is that during disengagement, the clutch is released and the oil will force the orifice forward as it flows through the larger diameter section of the PTL. During engagement, the clutch is engaged which results in the oil flowing backwards and the orifice is pulled towards the cone but it flows through the hole as the large diameter is currently blocked.

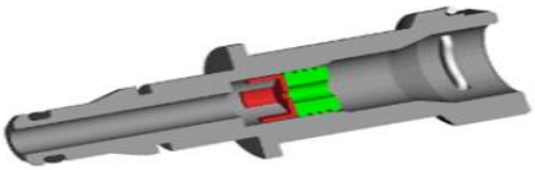


Fig. 2. PTL

Although the purpose of a PTL is established, it is still unknown what is the direct correlation between the size of the PTL and how much torque can be reduced. The only information that is available about the usage of PTL right now is that it restricts the applied torque that cause the torque transferred to be delayed and thus preventing it from reaching its maximum potential. Furthermore, there is no data readily available to correlate a torque vs time graph in furtherance of more comprehensive analysis. For this reason, additional research has to be conducted so that more can be learnt about the behaviour of the PTL [3].

The preceeding predicaments are of great importance and require dire attention however there is still another aspect which has not been accounted for which is development of the author throughout the span of the project. This project is under the Engineering Education Lab research group and it efforts the author to learn efficaciously according to an agenda established by the author. Undertaking a final year project is challenging and there is no experience like it prior to this project. Hence, it can be inferred that gaps exist the overall capability of the student and it will be investigated throughout the period of the study.

The objective of this research is to design and simulate the driveline abuse test in Simulink. A driveline abuse test is conducted by loading the car with a surplus of torque by engaging the clutch. When this occurs, a transient torque is transmitted to all of the components of the drivetrain. Such components include the clutch, manual transmission, differential, driveshaft and wheels. During the aforementioned test, a PTL is installed into the test in order to minimize the torque applied. Without a PTL, many of the engine components can potentially be damaged due to the large magnitude of torque. However, it is not known what the characteristics of the PTL is like. Thus researching and finding out what the relationship between the diameter of the PTL and engagement time is the secondary objective.

In order to develop a simulation and create visualizations of the change in engine torque throughout the driveline, a model has to be constructed first. Journals suggest that modeling the driveline torque losses in a manner of using the measured engine torque and subtracting the factors that affect the torque value is a suitable way to analyze the reduction in torque[4]. This would create a linear graph descending downwards. In contrary, another author dictates that modeling the driveline as a mass-spring-damper (MSD) model is the most appropriate method to simulate the torque change at each component [2]. In this approach as shown in Figure 1, a pre-determined amount of masses signify the inertia values and the spring and dampers represent the movement of each component throughout the shaft. It can be argued that utilizing the MSD method will not produce realistic results as it will generate a torque with respect to time graph which does not accurately relate to transmissibility of torque in the driveline as the torque should not be fluctuating frequently in an actual vehicle. However, a single transient torque value being inputted to the system is the worse alternative as this goes against the engineering design and purpose of a gearbox. In a gearbox, there are two principles known as first and final gear ratio which aims to amplify torque which is most definitely higher than the torque losses which results in the trend of the torque graph to proceed upwards. With this in context, a graph trend with fluctuations will be preferred as to one with no fluctuations at all. Hence, an MSD model is preferred in this project. Despite these two approaches having a different methodology and result, their commonality is that both of them are investigating the change in torque.

In order to study the flow inside of a PTL, CFD has to be done on the fluid domain. A turbulence model which is one or more mathematical equation used to characterize the behavior of the flow. A study dictates that using the standard k-e model to simulate flow in cylindrical domain as the k-e model is known to be reliable and it is suitable for many flows[5] However, another investigation dictates using k-e realizable will be suitable as this would give a more accurate description of the flow [6]. Although both flows are acceptable as they both share the same turbulent kinetic energy equation. However, realizable would be the preferred option as the equation used to solve ε is of an enhanced version as compared to the standard k-e because more velocity gradients are factored in. Also, flows of large separation are not expected for this simulation thus the fact that realizable k-e equation is restricted by the isotropic eddy viscosity assumption will not be of concern. Hence, the realizable k-e will be utilized in the project.

2. Research Methodology

The research that was conducted is a qualitative study. Since Proton Sdn. Bhd manufactures cars of reputable quality since 1983 designed by experienced engineers, a lot of research must be done to meet their calibre. The study will include comprehensive research on driveline components and how the torque is transferred. This has already been done as shown in the literature review. From the obtained findings, a mathematical model will be constructed and finally be implemented into Simulink. Additionally, an insight on how CFD will implemented to study the PTL will be highlighted.

2.1 Mathematical Model

This is the stage that all the conducted research has been building up to. An overall mathematical model was used to calculate the torque loss throughout the whole driveline. A mathematical model is the characterization of a system using mathematical terminology. In order to find the torque values at each component of the driveline, a mathematical model was established for each component of the driveline. The components that was covered in this section are clutch, 1st gear, synchronizer, differential and driveshafts. This was validated with experimental results to evaluate the validity of the model later on.

2.1.1 Clutch

This is the first component of the driveline and there are four models that represent the torque loss in a dry clutch which include factors such as cushioning springs, friction and air resistance. Also, torque capacity will also be discussed. Eq. (1) shows the torque lost due to cushioning spring [5].

$$T_{fc}(x_{to}) = \eta \mu_{clutch} R_{eq} F_{pp}(x_{to}) \quad (1)$$

x_{to} is used to represent the state of the cushioning spring with respect to the position of the release bearing. Thus, when the release bearing is at the maximum distance away from the diaphragm spring, it means that the cushioning spring is flat and compressed as the clutch is engaged.

Eq. (2) displays the torque lost due to friction of the flywheel and friction disc [7].

$$T_c = \mu_{clutch} F_f R_{eq} \eta \quad (2)$$

Lastly, Eq. (3) represents the torque lost due to air resistance [8].

$$T_{ar} = 0.04 \rho_a^{0.8} \nu_a^{0.2} \left(\omega R_{eq}\right)^{1.8} \left(\frac{h}{2R_{eq}} + 0.33\right) \quad (3)$$

Eq. (4) signifies the clutch torque capacity [2].

$$Clutch\ Torque\ Capacity = \eta \mu_{clutch} N \frac{2(R_0^3 - R_i^3)}{3(R_0^2 - R_i^2)} \quad (4)$$

The torque capacity represents the amount of torque that the clutch can withstand. This means even if a higher amount of torque is transmitted to the clutch from the engine, the clutch will only operate at the maximum torque value which is the value of the clutch torque capacity.

2.1.2 1st gear

The loss when engaging 1st gears can be broken down into two sections which is meshing loss and bearing loss. Meshing loss is loss caused by the interaction between gears and bearing loss is related to the movement of the balls or rollers inside the raceways of the bearing.

Eq. (5) are used to find the torque loss for sliding friction and the force of the friction acting on the gear respectively [6].

$$T_{mesh} = \mu_{mesh} w \tag{5}$$

Bearings have three main losses which are rolling, sliding and seal losses. The three models are displayed in Eqs. (6), (7), (8), (9), (10) and (11) are based on [9]–[11].

Eq. (8) demonstrates the torque lost due to rolling.

$$M_{rr} = \phi_{ish}\phi_{rs}G_{rr}(v\omega_{RPM})^{0.6} \tag{8}$$

Eq. (9) displays the formulation of the inlet shear heating reduction factor.

$$\phi_{ish} = \frac{1}{1+1.84\times10^{-9}(\omega_{RPM}d)^{1.28}v^{0.64}} \tag{9}$$

Eq. (10) displays the formulation of the kinematic replenishment/starvation reduction factor.

$$\phi_{rs} = \frac{1}{e^{[K_{rs}vn(d+D)\sqrt{\frac{K_Z}{2(D-d)}}}} \tag{10}$$

Eq. (11) shows the torque lost due to sliding.

$$M_{sl} = G_{sl}\mu_{sl} \tag{11}$$

$$\mu_{sl} = \phi_{bl}\mu_{bl} + (1-\phi_{bl})\mu_{EHL} \tag{12}$$

Eq. (13) demonstrates the torque lost due to seals in the bearings.

$$M_{seal} = K_{S1}d_s^{\beta} + K_{S2} \tag{13}$$

K_{S1} and K_{S2} are dimensionless constants.

2.1.3 Synchronizer

Eq. (14) shows the torque lost due friction of the synchronizer surface which based on [12]. Two coefficients of friction will be inputted here to find the torque lost due to friction for the gears and the synchronizer ring.

$$T_{synchromesh} = \frac{\eta_c\mu_{brass}dF_a}{2sin\alpha} \tag{14}$$

$$T_{gear} = \frac{\eta_c\mu_{gear}dF_a}{2sin\alpha} \tag{15}$$

2.1.4 Differential

The same equations for gear meshing will be implemented. The equations stated earlier are still applicable for tapered roller bearings. However, the values of each variable will be altered.

2.1.5 Driveshaft

The equations stated earlier are still applicable for needle roller bearings. However, the values of each variable will be altered.

2.1.6 Final mathematical model

The equations shown demonstrate the development of the mathematical model. Eqs. (14), (15), (16), (17) and (18) are equations that represent the loss of each component which also formulate the final model.

$$T_{clutch,losses} = T_{fc}(x_{to}) + T_c + T_{ar} \quad (14)$$

$$T_{1st\ gear,losses} = T_{mesh} + M_{rr} + M_{sl} + M_{seal} \quad (15)$$

$$T_{synchronizer,losses} = T_{synchromesh} + T_{gear} \quad (16)$$

$$T_{differential,losses} = T_{mesh} + M_{rr} + M_{sl} + M_{seal} \quad (17)$$

$$T_{driveshaft,losses} = M_{rr} + M_{sl} + M_{seal} \quad (18)$$

As seen in above, Eqs. (15), (17) and (18) are exactly the same model except that the gear losses are not accounted for in the driveshaft due to the constant velocity joint thus there is minimal torque loss there. However, each of them have a different angular speed. For example, the driveshaft will have least angular speed because it is the final component of the driveline while the 1st gear while have the highest angular speed because it is one of the earlier components. Also, three components use different bearings, thus the bearing specifications will differ. The 1st gear uses cylindrical roller bearing, the differential uses a tapered roller bearing and the driveshaft uses a needle roller bearing. Since, all components use a roller bearing, the model remains the same but the torque value at each component will still vary. It is important to note that if T_{engine} is greater than the clutch torque capacity from Eq. (4), then the torque capacity is taken as the new value for T_{engine} because the clutch cannot handle a torque above its capacity. The windage and churning losses for the 1st gear have not been taken into consideration as the PROTON Saga does not use a completely oil-submerged gearbox.

Eq. (19) will be inputted used in the Simulink simulation to create the MSD model to find the peak torque during abuse scenario. Similar models will be used to find the value of torque at different driveline components. The Simulink model shown in Figure 3 represents the Eq. (19).

$$J_{drive}\ddot{\phi}_{drive} = K_{drive}(\phi_{diff} - \phi_{drive}) + C_{diff}(\dot{\phi}_{diff} - \dot{\phi}_{drive}) \quad (19)$$

2.1.7 Simulink

Integrator, gain and summation blocks are used to form the mathematical model and the scope is used to display the graph formed by the model itself. A sin wave block was added to select the computational technique that was used and a step size of 0.00001 seconds was implemented to replicate the transient nature of an abuse scenario as this replicates the instantaneous clutch engagement. This is due to the step size directly translating to the clutch engagement time.

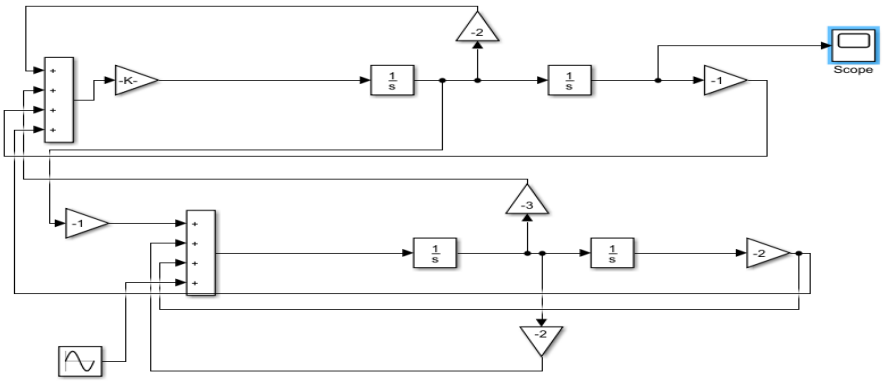


Fig. 3. Simulink model.

With both the clutch engagement time and speed being factored in, the results can now be tabulated.

2.2 Computational fluid dynamics (CFD) on PTL fluid flow

There is not an abundance of journals where the topic of study is PTL. Purchasing several PTL's to conduct an experiment is also not a viable option as it quite expensive. Thus, CFD will be conducted on the oil flow inside several PTL with different diameters. The engagement time which is the duration taken for the brake fluid to flow within the PTL will be the variable that will be analyzed. The results will then be tabulated and visualized in the form of a graph using ANSYS FLUENT and MATLAB. Figure 4 shows the CAD model designed for the fluid domain for CFD.

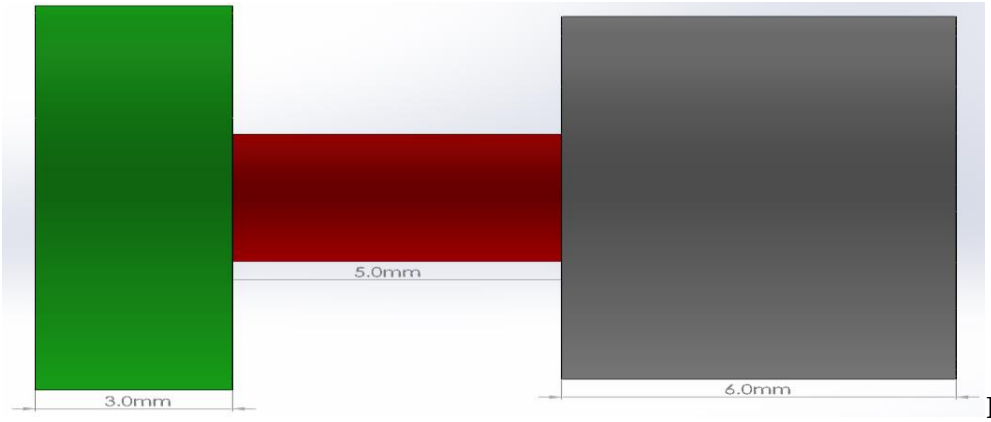


Fig. 4. PTL model.

The fluid domain is of a total length of 14 mm while the red tube is of interest in this investigation as that is the constriction for the flow. The diameter of the red tube that will be investigated is 1,2,3,4 and 5 mm while the grey and green cylinder will be kept at a constant diameter at 8.5mm and 9mm respectively. Moreover, this fluid domain is not hollow so that the flow can be calculated in CFD using the Navier Stokes equations. However, in reality, the PTL is in fact hollow. Figure 5 shows the meshing enforced for this model.

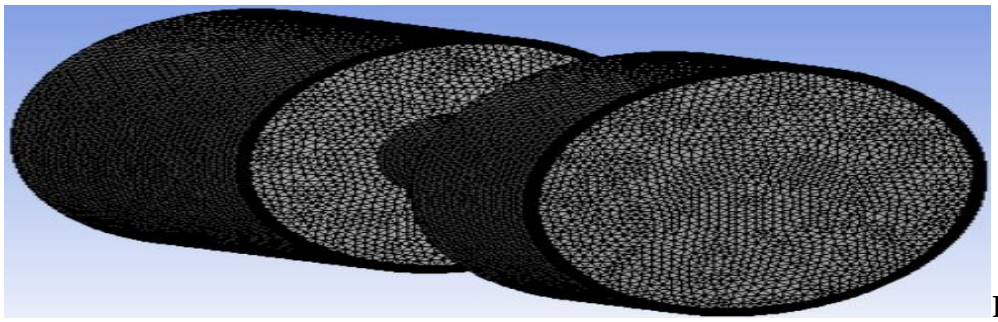


Fig. 5. Meshing of PTL model.

In regards to the global mesh settings, the relevance center was set to fine and the smoothing was set to high. As for the alterations implemented for the local mesh, a body sizing of 0.2mm was implemented and inflation was set at the outer circumference of the cylinder to capture the flow at the boundary layer. Table 1 shows the element count and maximum skewness of the model. Since the skewness is less than 0.98, CFD can be carried out and produce accurate results. Also, a grid independence test was conducted to test which was the optimum element count to product a solution that converges effectively.

Table 1. Mesh metric for PTL.

PTL Diameter (mm)	Max Skewness	Elements
1	0.89776	876408
2	0.89995	882804
3	0.89994	910048
4	0.89998	930112
5	0.89995	963281

The turbulence model used for this simulation is k-ε realizable as it accurately predicts internal flows accurately as the fluid domain has both these characteristics. Moreover, no other turbulence model in the k-ε and k-ω family has the ability to predict this characteristic accurately and time conservative as compared to k-ε realizable. Dot 3 brake fluid was used as the fluid flowing through the domain. It has a density and viscosity of 1030 kg/m^3 and 0.00206 kg/m/s. The inlet velocity, turbulent intensity and viscosity ratio is set to 0.172 m/s, 5 % and 10 respectively. A second order coupled scheme was utilized to tabulate the results and it was initialized as hybrid. It was set to run for 350 iterations. Few sound assumptions have been made in this simulation such as the wall roughness. Wall roughness is not inputted into this simulation thus making the wall ideal and not having any significant frictional effects. Also, the velocity value will be taken at the cell along the outlet at 4.25 mm above the y-axis and this will be assumed as the average overall pressure along the wall. An average value at the wall is not taken as by just simply extracting values from the outlet and dividing the quantity would not give an accurate and reliable result as the finite volume method does not operate this way. Lastly, the PTL is assumed to completely filled with Dot 3 fluid. The type of fluid is verified by PROTON however the amount of fluid that is inside the PTL is assumed to be full as that is the specification of the study and it shall remain constant throughout all experiments.

3. Results

3.1 Obtainment of abuse factor

By utilizing all the equations, the efficiency for each driveline component can be derived as shown in Table 2. It can be seen here that clutch has the most torque loss. This coincides with the theory as the clutch experiences a lot of loss due to friction as heat and sound energy dissipating during the mating of clutch disc and flywheel is one of the main contributor of energy loss which consequence in torque loss.

Table 2. Efficiency of driveline at different RPM.

	Efficiency (%) at different RPM	
Component	1500RPM	6000RPM
Clutch	91.35	95.62
1st gear	93.79	91.67
Synchronizer	99.31	99.04
Differential	98.06	97.87
Driveshaft (Left)	99.51	98.38
Overall	88.07	81.35

After factoring in the overall efficiency into the Simulink model, Figure 6 was tabulated which shows a torque(kNm) against time(ms) relationship. The peak torque value extracted from this graph is 1301Nm. The erratic nature of the graph shows the extent of the abuse that the driveshaft is experiencing. For example, during the time step from 0 to 2.5ms, it can be seen that there is a sudden increase in torque because of the sudden clutch engagement. Using similar models, the torque values of the torque at each component have also been calculated as seen in the Table 3. This torque value is also within a close range to the tabulated value from an equation given by the industry thus this value is reliable.

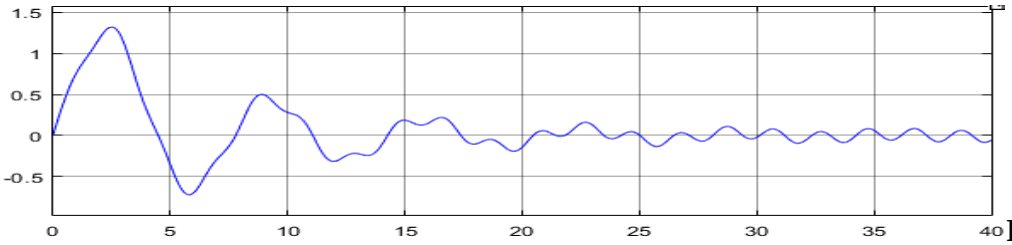


Fig. 6. Peak torque of driveline.

Table 3. Torque of each driveline component at different RPM.

	Torque(Nm) at different RPM	
Component	1500RPM	6000RPM
Clutch	17	113
1st gear	80	480
Synchronizer	65	463
Differential	285	2602
Driveshaft (Left)	135	1301

It also important to note that the torque at the clutch did not exceed the torque capacity which leads to the result from equation (4) being omitted. Also, the torque of the 1st gear exponentially increased because the first gear ratio was multiplied. The abuse factor can then be calculated by dividing the torque at 6000RPM over the torque at 1500RPM which equates to 6.25. This shows that the torque is amplified by approximately 6 times as compared to when the car is moving slowly which is a great increase.

The value obtained from the driveshaft in the experimental version of the abuse test is 1053.67 Nm. This amounts to an error of 19.08%. This error can be due to a number of reasons. Firstly, the efficiency of the driveline is expected to be less than what is calculated as not all the factors have been accounted for because not all losses can be represented in a mathematical model as some may be too complex to be defined this way. Moreover, some factors could not be measured as such equipment is not available and it would not be justifiable to obtain the needed equipment unless it resulted in a substantial increase of accuracy in the readings.

3.2 CFD on PTL

The PTL investigation using CFD was carried to find the time taken for clutch engagement. It shows that PTL with the lowest diameter gives a flow of the highest velocity and torque. The results are shown in Table 4.

Table 4. Relationship between PTL diameter and peak torque

PTL Diameter (mm)	Velocity (m/s)	Time (s)	Peak Torque (Nm)
1	9.45	0.0015	1116
2	4.50	0.0031	1065
3	1.96	0.007	1043
4	1.22	0.011	1017
5	0.775	0.018	1005

A graph was formed based on Table 4 which is Figure 7. Figure 7 shows that there is a linear negative correlation between the diameter and peak torque meaning that the diameter is inversely proportional to the peak torque. This can be justified by observing the flow of the dot 3 fluid in the PTL as when the diameter is smaller, it creates a constriction which will consequence in low pressure creating a rise in fluid velocity thus it accelerates the flow resulting in less time needed for engagement. This phenomenon is known as the Venturi effect and it can be seen in Figure 8.

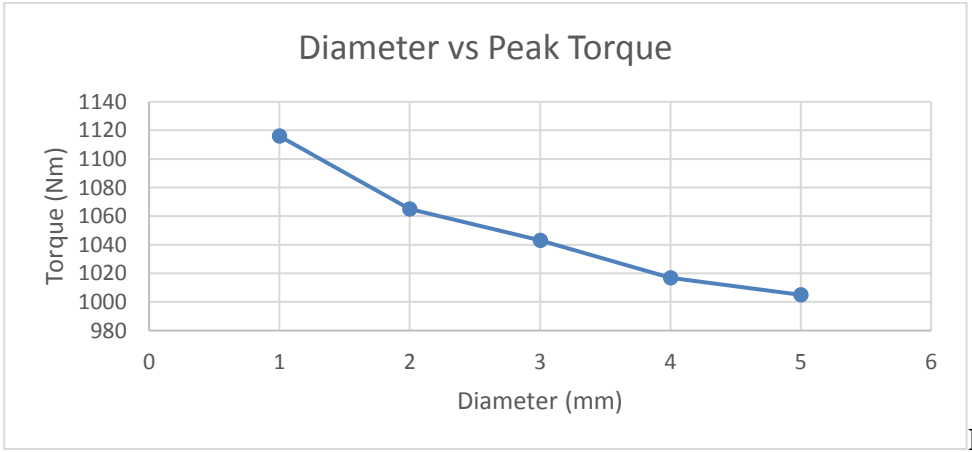


Fig. 7. Graph of diameter vs peak torque.

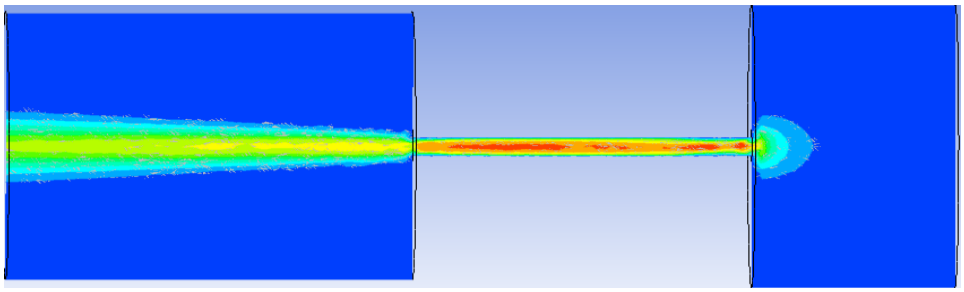


Fig. 8. Velocity contour plot of PTL.

4.Conclusion and Recommendation

The torque at the driveline during an abuse scenario is 113Nm at the clutch, 2500Nm at the 1st gear, 2357Nm at the synchronizer, 2602Nm at the differential and finally 1301Nm at one driveshaft. Moreover, the abuse factor was also calculated which is 6.25 which indicates a large increase as compared to normal operating speed. Additionally, the PTL study has been concluded and it showed that a smaller PTL diameter will result in less time needed for clutch engagement but consequences in a larger peak torque. With the presence of this newly discovered information, the industry is one step closer to forming a simulation that could act as a precursor to the actual experiment as with the torque values, validation for the simulation can be carried out. Also, now the industry knows how much torque is subjected to the driveline which is crucial as the durability of the driveline can be evaluated more effectively now.

There are many more mathematical models that can be implemented in this project. However, the parameters that are associated with aforementioned mathematical models cannot be found theoretically or experimentally with the current time frame. For example, the temperature of the clutch disc affects the coefficient of friction which results in lesser torque transferred throughout the driveline. There is no device that can readily find the temperature of the clutch disc. If time was not a constraint, a setup could be designed with an Arduino Nano and an MLX90614ESF AAA infrared IR temperature sensor module. An Arduino Nano is the most applicable for this scenario as compared to other microcontrollers on the market as space in the clutch is of scarce and the size of the Arduino Nano is small thus allowing it to be inserted inside the clutch cover.

There are also parameters that affect torque transmissibility but could not be factored in because there was no mathematical model that could define the loss. The different lengths of the driveshaft are an example of this. The torque readings could be measured experimentally but torque sensors are very expensive on the market at the moment thus this course of action could not be used as this project has no budget.

When CFD was being done, the assumption that the PTL was completely filled with dot-3 fluid was made while this may not actually be the scenario. With this in context, the effect of omitting this assumption is unknown and could produce a different result. Hence, this is an investigation worth venturing into.

Lastly, the PTL study could not be validated by cross checking with experimental results as each PTL is costly thus an experiment could not be conducted. This consequence in the PTL study not proving reliable result as the author desired. This resulted in the author relying on grid independence test and mesh metrics to validate the accuracy of the simulation. While these mesh metrics and grid independence test aid in convergence of the simulation, it cannot provide full authentication of the input and output from the simulation.

5.Reference List

[1] E. Afify and D. Klett, "Internal Combustion Engines," *Energy Convers.*, pp. 10–26, 2007.
[2] P. Bingham, S. Theodossiades, T. Saunders, E. Grant, and R. Daubney, "A study on automotive drivetrain transient response to 'clutch abuse' events," *Proc. Inst. Mech. Eng. Part D J. Automob. Eng.*, vol. 230, no. 10, pp. 1403–1416, 2016.
[3] M. Zink, R. Shead, and R. Welter, "Clutch Release Systems," *Eff. Br. mindfulness Interv. acute pain Exp. An Exam. Individ. Differ.*, vol. 7th LuK Sy, pp. 27–40, 2002.
[4] J. Berglund, "MASTER â€TM S THESIS Design of a power loss model for vehicle drivetrains."
[5] J. Sodja, "Turbulence models in CFD," *Univ. Ljubljana*, no. March, pp. 1–18, 2007.
[6] J. Hart, "Comparison of Turbulence Modeling Approaches to the Simulation of a Dimpled Sphere," *Procedia Eng.*, vol. 147, no. 0, pp. 68–73, 2016.
[7] G. Pica, C. Cervone, A. Senatore, M. Lupo, and F. Vasca, "Dry Dual Clutch Torque Model with Temperature and Slip Speed Effects," *Intell. Ind. Syst.*, vol. 2, no. 2, pp. 133–147, 2016.
[8] X. Zhang and C. Mi, *Vehicle Power Management: Modeling, Control and Optimization*. 2008.
[9] C. M. C. G. Fernandes, P. M. T. Marques, R. C. Martins, and J. H. O. Seabra, "Gearbox power loss. Part I: Losses in rolling bearings," *Tribol. Int.*, vol. 88, pp. 298–308, 2014.
[10] C. M. C. G. Fernandes, P. M. T. Marques, R. C. Martins, and J. H. O. Seabra, "Gearbox power loss. Part II: Friction losses in gears," *Tribol. Int.*, vol. 88, pp. 309–316, 2015.
[11] C. M. C. G. Fernandes, P. M. T. Marques, R. C. Martins, and J. H. O. Seabra, "Gearbox power loss. Part III: Application to a parallel axis and a planetary gearbox," *Tribol. Int.*, vol. 88, pp. 317–326, 2015.
[12] O. Back, "Basics of Synchronizers," no. December, 2012.

EURECA 2018 – Conference Paper
Paper number 2ME28

Sintered Properties of Stainless Steel-doped Y-TZP Ceramics

Suraj Nair[1], W. J. Kelvin Chew[1*], S. Ramesh[2]*

[1]Department of Mechanical Engineering,

School of Engineering, Faculty of Built Environment, Engineering, Technology and Design, Taylor's University, 47500 Subang Jaya, Selangor, Malaysia.

[2]Centre of Advanced Manufacturing & Material Processing (AMMP), Department of Mechanical Engineering, Faculty of Engineering, University of Malaya, 50603 Kuala Lumpur, Malaysia.

[*]Corresponding Authors:

Surajnair30, KelvinWaiJin.Chew@taylors.edu.my

Abstract

Yttria-tetragonal zirconia are usually known as a type of polycrystalline ceramic dioxide from the transition metal Zirconium. Yttria-tetragonal zirconia has excellent mechanical as well as physical properties, due to this benefit zirconia is well known in the orthopaedics field, where hip replacement using zirconia has shown exceptional wear resistance properties in comparison to other materials. In any case, one of the real constraints of Y-TZP ceramics is its susceptibility to ageing- induced tetragonal to monoclinic stage change when uncovered in steam condition. Y-TZP ceramics production shows a moderate change in stage from tetragonal to monoclinic, beginning at the free surface took after by the development of microcracking and strength degradation. Based on the pressure and ambient temperature, zirconia can exists in 3 crystalline forms such as monoclinic (m), cubic and tetragonal (t).The most stable structure at room temperature with standard pressure would be the monoclinic structure and is the form found in natural deposits. The transformation from monoclinic to tetragonal happens at 1170 ℃ with a 4-5% shrinkage. Further shrinkage happen at 2370 ℃ when the transition from tetragonal to cubic happens. The helpful effect of MnO2 doping on the densification and mechanical properties of commercial 3mol% 3Y-TZP is accounted for. Therefore, the insertion of transition metal oxide like manganese oxide(MnO2) is likely to affect the hydrothermal ageing resistanve if they help sintering at generally at low temperature (i.e.<1300℃) and results is densification with grain development. The point of the present work was to think about the of including little measure of manganese oxide (up to 1wt%) on the densification and mechanical properties of yttria-balanced out zirconia. 3 mol% of yttria-stabilized zirconia powder with about 0.1 wt% total impurities are used. Using wet milling, various amount of high purity manganese oxide is mixed with Y-TZP. To obtain ready to press powders, oven dried was used to remove all fluids in the mixture. At 0.3 MPa and with cold isostatical pressed at 200 MPa, the disc and rectangular bar were compressed. Pressureless sintering was

performed. The hypotheses of this experiment and research is to help the ageing resistance of zirconia ceramics to be improved when co-doped with different dopant and to improve the mechanical properties of Y-TZP with Manganese oxide. From this experiment, it is expected that the knowledge on how to improve the LTD of zirconia to increased. Moreover, further research can be conducted when this experiment produces results that help the characteristics of Y-TZP.

INTRODUCTION

Yttria-tetragonal zirconia are usually known as a type of polycrystalline ceramic dioxide from the transition metal Zirconium. Yttria-tetragonal zirconia has excellent mechanical as well as physical properties, due to this benefit zirconia is well known in the orthopaedics field, where hip replacement using zirconia has shown exceptional wear resistance properties in comparison to other materials. Nevertheless, the risk of the catastrophic fracture is still a concern in this industry.

In dentistry, Zirconia has been broadly received for endosseous implants, ceramics crowns and implant abutments. Due to an expanding demand aesthetically satisfying dental restorations, zirconia-based restorations have become one of the predominant remedial decisions. Y-TZP has strength which is higher than 1 GPa and 6-10MPa m1/2 normally.

In any case, one of the real constraints of Y-TZP ceramics is its susceptibility to ageing- induced tetragonal to monoclinic stage change when uncovered in steam condition. Kobayashi et al. was the first to discover that Y-TZP ceramics production shows a moderate change in stage from tetragonal to monoclinic, beginning at the free surface took after by the development of microcracking and strength degradation. Numerous different laborers have tried to suppress this overwhelmed effect of aging, despite the fact that the basic system that oversees ageing has not been unequivocally settled.

The presentation of zirconia into alumina as a sintering help has for quite some time been practiced for densification of alumina designing pottery. Nonetheless, the idea of toughening alumina ceramics production by scattering zirconia particles in the grid has just has been perceived over the most recent ten years. The presence of a small quantity of zirconia into alumina as a sintering help in the development of a strong arrangement which advances the densification forms by the introduction of lattice defects.

Besides that, many other research were done towards great boundary modification with the use of dopants or sintering additives because it has been perceived that during ageing monoclinic nucleation begins at grain limit districts and spread inwards into the grain. Therefore, little quantity of dopant can advance densification and significantly control the microstructure and to improve the mechanical properties of the sintered Y-TZP body. For an example, research carried out by Kenellopoulous and Gill uncovered that doping Y-TZP with copper dioxide improves the densification of the ceramics through a component including liquid phase because of the low melting point of CuO in ZrO2. In this way, the consideration of transition metal oxides, for instance manganese oxide is probably going to influence the hydrothermal ageing resistance if they help the densification at generally low temperature, beneath 1350oC.

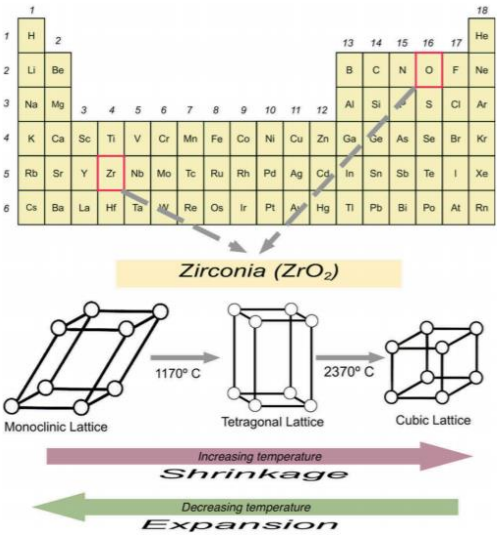


Figure 1: The phases in zirconi

	3Y-TZP	ZTA	Mg-PSZ
Chemical component	Y_2O_3, ZrO_2	Al_3O_2, ZrO_2	MgO, ZrO_2
Crystalline phase	Monophase	Biphase	Biphase
Flexural strength, MPa	800-1300	750-850	700-800
Hardness (GPa, Vicker's)	10-12	12-15	5-16
Fracture toughness	5-10	6-12	8-15

Table 1: Properties of biomedical zirconia

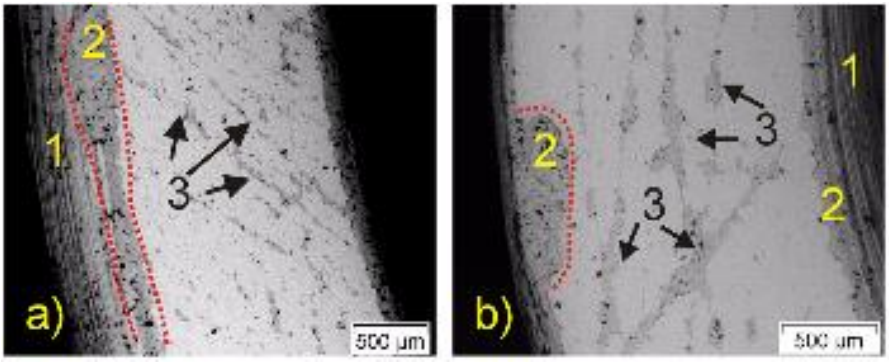


Figure 2: Crack propagation of Y-TZP

RESEARCH METHODOLOGY

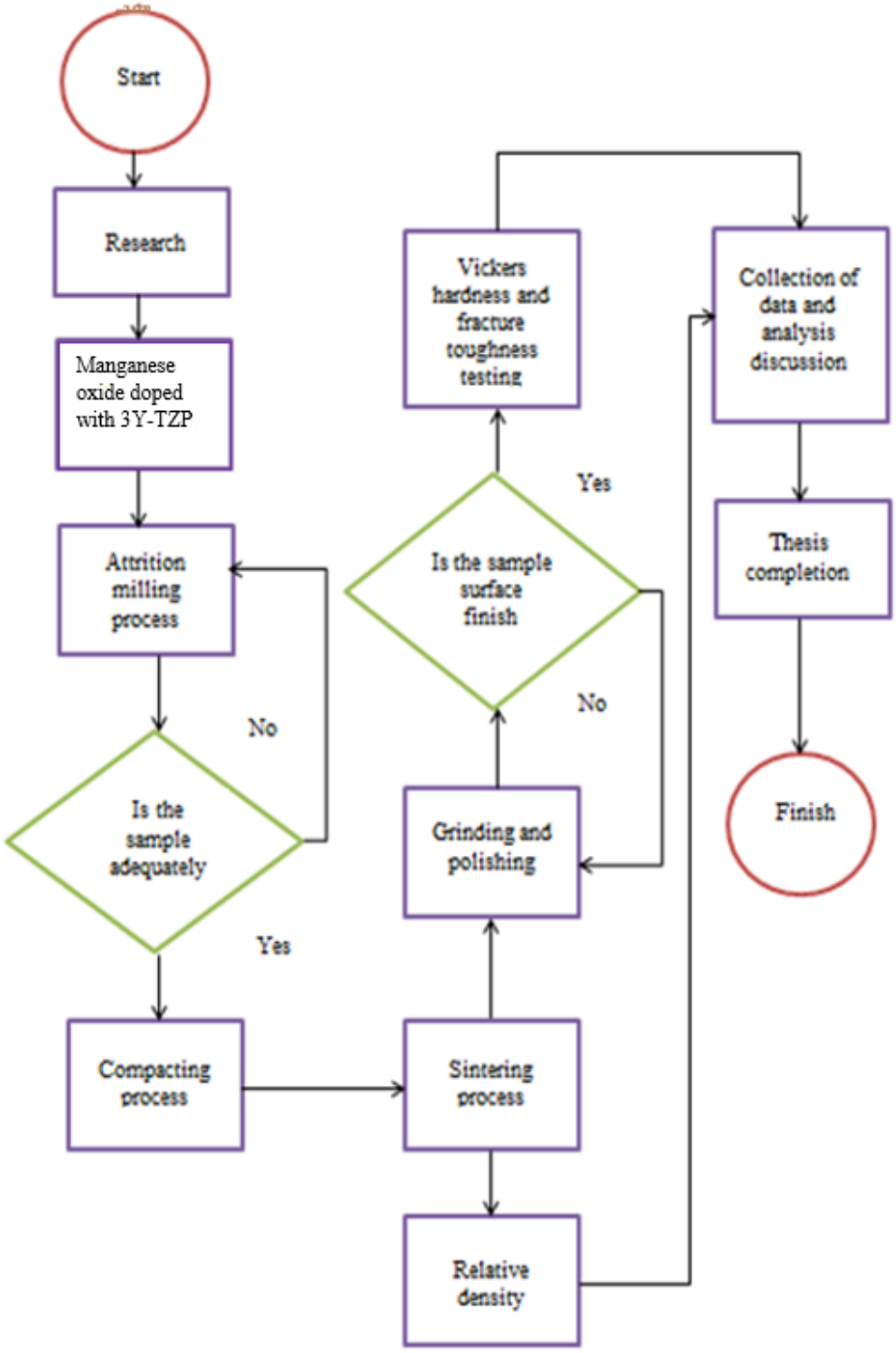


Figure 27: Research methodology flowchart

Powder Preparation

The two main material that has to be acquired in this research project were the 3Y-TZP and manganese oxide. The initial stages of the process is to mix the mixture well with a proper measurement of manganese oxide content. The weight percentage of the manganese oxide were fixed at 0 wt%, 0.05 wt%, 0.1 wt% and 0.5 wt% before mixing it with 3Y-TZP. Moreover, it is important to measure the materials individually before mixing them together. Initially, 100ml of ethanol is

poured into the beaker before pouring manganese oxide and 3Y-TZP respectively. This is because ethanol act as a mixture medium enhancement. The dopant which is manganese oxide is poured first because of its small size breakdown which subsequently makes it easy to disperse.

For the powder preparation process, the Digital Ultrasonic Bath (Powersonic UB-410, Thermoline Scientific, Australia) was used. A beaker is filled up with distilled water and placed inside the Digital Ultrasonic Bath machine for a duration of 15 minutes to undergo intensive mixing. As soon as the mixture is mix thoroughly, it is then placed inside of Laboratory Attritor Mill (01-HD, Union Press, United States) where it undergoes further breakdown on powder mixture for a time spend of 45 minutes and at a spend of 500 rpm. To enhance the milling process, 5mm size of zirconia milling ball was added. To produce a mixture with slurry, a sieve with a measurement of 212 µm was utilized. The Universal Oven (UN 55, Memmert, Germany was used to bake the remaining mixture into a cake like form where the temperature of the oven is set at 60℃ for overnight. Smaller forms of the cake mixture was produce by crushing with the hand tool provided and the mixtures were sieved again with sieve of a measurement of 212 µm to produce a fine final powder composition.

Green Sample Preparation

The machine of Hydraulic Bench Press (HP10-150, RMS Hydro, Malaysia) was used for a firmly packed process of the powder mixture. Where the powder mixture was poured into a circular shaped die which have a total diameters of 20mm. The high pressure bench press was subjected to a pressure of 1000bar for 10 seconds and the purpose of doing so is to obtain a fine green body round tablets. Creating the fine green round tablet with initiated adhesion as the importance of this reflects the production quality before proceeding to the next process of cold isostatic pressing (CIP). At this moment of the process, precaution have to be taken towards the green body round tablets as it is considered in a fragile phase as it is yet to reach and applied with sintering process.

Furthermore, the Cold Isostatic Press (KJYU150, Shanxi Golden Kaiyuan Co., Ltd, China) machine was operated for the CIP process where the green body round tablets were been placed inside a glove as well as placed it again inside desired square shaped container. The CIP process focus to compact the samples in multiple direction and reduced the length of each separated solid. Thus, samples diffusion rate increased and eventually produced superior samples densification. Besides, the reason for the usage of glove here function as security as it prevent the white milky coolant to penetrate the green body round tablets. On the other hand, the container in this case then to be stored under room temperature which in this case aim for neither heat nor pressure to penetrate and ultimately affect the green body round tablets during the pressing process. Presence of potential cracks is highly noticable at the green body round tablets supposed that if there were any existence of heat or pressure that intrude the pressing process. As an overall for this current process stage, the green body round tablets indeed can likewise be referred as green samples.

Sintering Process

For measurement and testing, the samples are compacted and formed into a solid by doing the sintering process. Pressureless sintering was chosen as the type of sintering process that was applied. The sintering process begins with the use of Electric Box Furnace (LT10, LT, Malaysia) where the green samples are placed inside a crucible and stored inside this machine. The sintering temperature varied from range of 1200 ℃, 1350 ℃ and 1500 ℃. The temperature of the furnace was increased at rate of 10℃ per minute till the desired temperature is obtained for a duration of 2 hours. As the heating is completed, the samples is then allowed to cool down with a rate of 10℃ per minute till it approaches room temperature.

Grinding and Polishing Process

Grinding Process

The Polishing & Grinding Machine (GP2V, LT, Malaysia) was used as soon as the sintering process was completed. Each samples were grinded for about two minutes on the machine where a grinding paper is placed and the speed of the machine is set at 50 rpm. There were five different type of grinding paper used (E.g. 120,240,600,800 and 1200) which the surface of the grinding is made of silicon carbide. In addition to that, as the grade of the grinding paper increases, the finer the surface of the paper. The grinding process starts with lowest graded paper as it is the roughest surface area and followed with 240, 600, 800 and 1200 respectively. The results of successful grinding can be seen on the grinded surface of the material where there are visible one direction lines.

Polishing Process

Polishing process will be done on the same machine as the grinding process which was the Polishing & Grinding Machine (GP2V, LT, Malaysia) with the help of polishing clothes and diamond paste. The main purpose of polishing the samples till it reaches a shining or mirror like surface is to obtain an accurate test values for the Vickers hardness testing and fracture toughness testing. There were two different type of diamond paste provided (E.g 1 µm and 6 µm). Moreover, the diamond paste with a larger diamond bit will be used first then followed with 1 µm diamond bit.

Bulk Density Measurement

Using a standard Mettler Toledo Balance AG204 densi-meter and with the help of Archimedes' principle, the bulk density of the dense compact disc (above 95% of theoretical density) can be found. For the immersion medium, distilled water was used. However, for low bulk density (below 95% of theoretical density) , measuring the geometric dimension and sample mass will aid in obtaining the value of the bulk density. This method will have an overestimate value of sample's density because of the water going through the pores of the samples. By using the theoretical density of Y-TZP which is 6.1 Mgm^{-3}, the relative density can be calculate. The formula to calculate the bulk density is as shown below:-

$$\rho = \frac{Wa}{Wa - Ww}\rho w \qquad (1)$$

Where:

ρ = Bulk density of the sample

W_a = Weight of the sample in air

W_w = Weight of the sample in water

ρ_w = Density of distilled water. The temperature effect on

the water density was taken into consideration using the table provided in Appendix B.

Vickers Hardness Determination

The hardness of Y-TZP was discover by using the Vickers hardness test method. In this test, the load is applied gradually, without impact, and the load is held for 10 seconds. The Vickers hardness (Hv) is calculated based on the surface area of the indent using equation:-

$$H_v = \frac{1.854P}{D^2} \quad (2)$$

Where

P = Applied load

D = Average diagonals= $\frac{D_1+D_2}{2}$

Fracture Toughness Determination

The length of the four cracks are measured after each Vickers indentation. The fracture toughness is calculate by using the following formula:-

$$\left(\frac{K_{Ic}\phi}{H_v a^{\frac{1}{2}}}\right)\left(\frac{H_v}{E\phi}\right)^{\frac{2}{5}} = 0.035\left(\frac{L}{a}\right)^{-\frac{1}{2}}$$

where

K_{Ic} = Fracture toughness

H_v = Vickers hardness

E = Young's modulus

a = Half length of the average diagonal

L = Average crack length = $\frac{L_1+L_2+L_3+L_4}{4}$

ϕ = Constraint factor which is taken as 3 [6]

Figure 28: Fracture toughness formula

Results

Bulk density

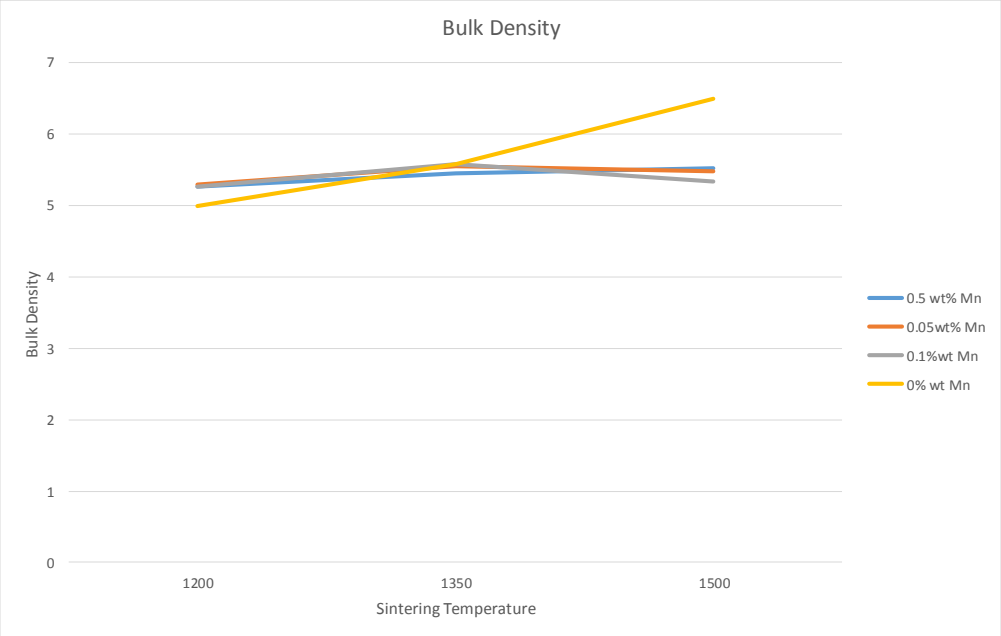


Figure 4: Bulk Density

By referring to the graph above, it can be seen that the lowest bulk density is at 5g/cm2 which has 0 wt% of Manganese oxide and it was sintered at a temperature of 1200℃. As it can be seen that, the bulk density of the 0 wt% increases as the temperature increases from 1200℃ to 1500℃. For the 0.05 wt%, 0.1 wt% and 0.5wt% the bulk density is at around the same range of value which is from 5.26 to 5.55 g/cm2. As the temperature increased, the bulk density of the material of all three of the material increased. For 0.1wt% Mn after the temperature 1350℃, the bulk density dropped gradually till it reaches 1500℃ with a bulk density of 5.36 g/cm2.

Looking at graph, it can be seen that the doped Y-TZP had no improvement in the bulk density value after the temperature of 1350℃. The reason for this to happen is due to the fact that the development of the cubic phase as temperature increases beyond 1350℃, the samples develops cubic phase in the tetragonal phase. It also can be seen that, when the temperature exceeds 1500℃, the zirconia had changes from partially transform to monoclinic or cubic transformation. The samples with undoped manganese oxide shows the optimum benefits from increased temperature as it showed the highest bulk density when it is sintered at 1350℃ and 1500℃. By referring only to the sintering temperature, it can be said at temperatures between 1200℃ and 1350℃, it shows that all samples showed an increased which proves that the optimal temperature for doped 3Y-TZP is from 1200℃ to 1350℃

Vickers Hardness

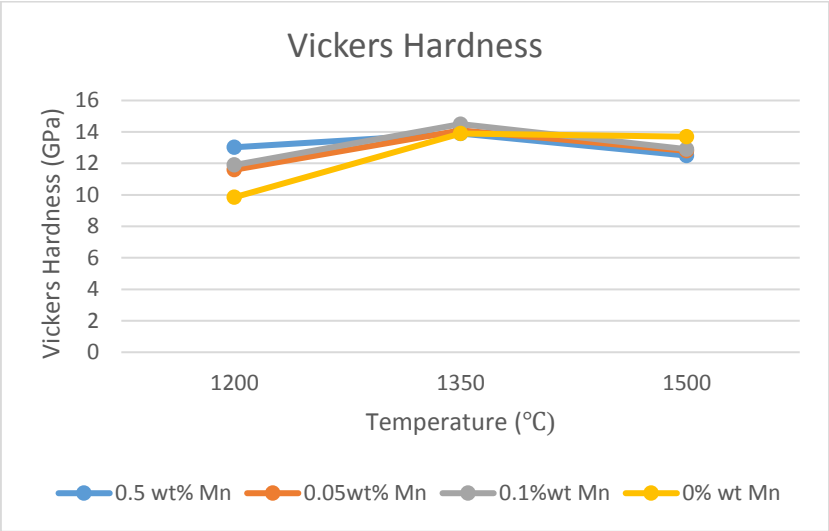


Figure 13: Vickers Hardness

By referring to the Figure 5 above, it shows the effect of sintering temperature and with the addition of manganese oxide towards the Vickers hardness at room temperature. The results shows that there are beneficial effect of adding manganese oxide into 3Y-TZP (i.e. 1350℃). The undoped samples 3Y-TZP showed to have the lowest hardness at 9.85 GPa at 1200℃ and it increased to the maximum value of 13.9 GPa at 1350℃ before the samples decreased to 13.7 GPa as the sintering temperature increases to 1500℃. In comparison, the samples with manganese oxide doped showed higher values compared to the undoped samples when sintered between 1200℃ and 1350℃ as it can be seen in the figure above. For the samples of 0.05wt% and 0.1wt% the hardness trend was identical where it increased at a great rate from ~11.6 GPa and 11.9 GPa respectively when the samples are sintered at 1200℃ to obtained values beyond 14 GPa at a sintering temperature of 1350℃. However, the hardness trend of the two material showed similar trend as the undoped samples where the decreases in hardness was noticed when sintering temperature reached beyond 1350℃.

For the 0.5wt% samples, similar observation was noticed for hardness when sintering temperature increased. The material showed very high hardness at the initial stage of sintering temperature (1250℃) where the hardness value was at 13.03 GPa. As the temperature increased to between 1300℃ to 1350℃, the 0.5wt% obtained a slightly increased value of 13.34 GPa. Although, sintering above 1350℃ caused a negative effect as the hardness of the ceramic decreased. This is due to the increase in cubic phase content in the tetragonal matrix when samples sintered at temperature above 1400℃.

Fracture Toughness

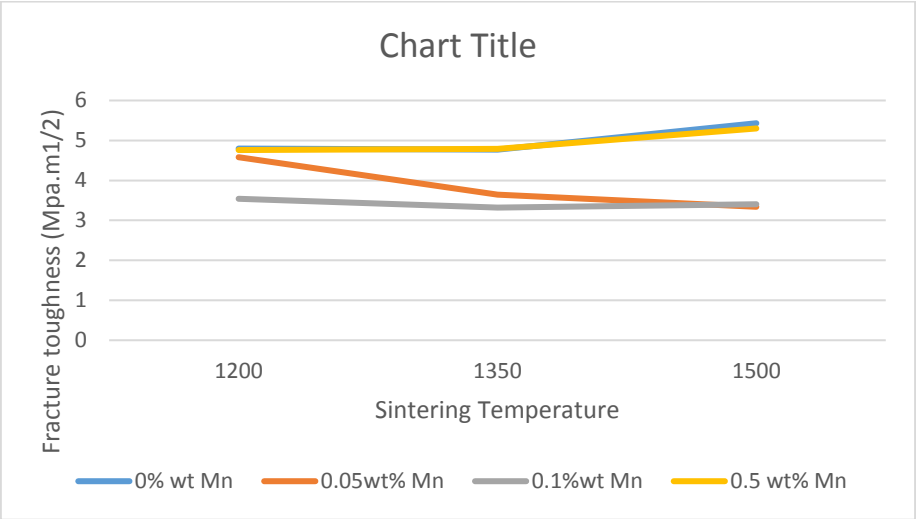


Figure 14: Fracture Toughness

By looking at the graph above, it can be seen that the fracture toughness of the undoped and doped samples. It was found that the 0wt% and 0.5wt% showed similar fracture toughness trend as at 1200℃, both showed to have a fracture toughness of 4.80 MPa.m1/2 and 4.76 MPa.m1/2. As the temperature increased, both showed an increase in fracture toughness where 0 wt% reached the maximum value of 5.43 MPa.m1/2 and the sample of 0.5 wt% obtained a value of 5.3 MPa.m1/2. It can be seen that the optimal temperature for the 0.5 wt% samples was at 1350℃ where the fracture toughness were higher than all the other samples at a value of 4.79 MPa.m1/2. This due to the state of stability of the tetragonal matrix in the zirconia material. Moreover, the 0.05 wt% and 0.1 wt% showed a negative effect as the temperature increased. It can be seen that the 0.05 wt% had a high fracture toughness at the sintering temperature of 1200℃ but as the temperature increased to 1350℃, the fracture toughness rapidly declined. This is due to the cubic phase development in tetragonal matrix hence causing the both the samples to have a decreased value of fracture toughness.

4. Conclusions

The experiment was successfully conducted to investigate the properties of Y-TZP when doped with Manganese oxide. It has been found out that the highest density was obtained by 0%wt Mn with 6.5g/cm2 at the sintering temperature of 1500℃. It was also identified that with the addition of more percentage of manganese oxide, the bulk density of the material increased as well. It shows the more percentage of manganese oxide added, the better the bulk density. Moreover, it showed in the Vickers hardness test that the addition of manganese oxide helps and improves the samples. It was found that the, 0.05wt% and 0.1wt% showed the best improvement at the sintering temperature around 1250℃ and 1300℃ where the Vickers hardness showed the maximum value. Fracture toughness also showed that the addition of the manganese oxide has improvement on 3Y-TZP with only percentage of 0.5wt% and above. During the sintering temperature between 1250℃ to 1300℃, the sample showed the maximum value of fracture toughness. This shows that the addition of manganese oxide has improvement on the 3Y-TZP but only towards a certain extent.

REFERENCE

1. S.Ramesh. 2013. INFLUENCE OF MANGANESE ON THE SINTERING PROPERTIES OF TETRAGONAL ZIRCONIA. [ONLINE] Available at: http://www.ceramics-silikaty.cz/2013/pdf/2013_01_028.pdf. [Accessed 2 November 2017].
2. S.Sivakumar. 2016. DENSIFICATION BEHAVIOR AND PROPERTIES OF IRON OXIDE DOPED Y-TZP CERAMICS. [ONLINE] Available at: http://jestec.taylors.edu.my/Special%20Issue%20eureca%202015_1/paper%2014.pdf. [Accessed 1 November 2017].
3. P. KANELLOPOULOS, C. GILL. 2002. Hydrothermal ageing of yttria-stabilised zirconia, sintered at 1300◦C–1325◦C: the effects of copper oxide doping and sintering time variations. [ONLINE] Available at: https://sci-hub.cc/https://doi.org/10.1023/A:1021047918043. [Accessed 30 October 2017].
4. Sylvain Devillea , Je´roˆme Chevaliera,*, Gilbert Fantozzia , Jose´ F. Bartolome´ b, Joaquı´n Requenab, Jose´ S. Moyab, Ramo´n Torrecillasc , Luis Antonio Dı´azc. 2003. Low-temperature ageing of zirconia-toughened alumina ceramics and its implication in biomedical implants. [ONLINE] Available at: https://ressearch.files.wordpress.com/2013/02/2003-deville-low-temperature-ageing-of-zirconia-toughened-alumina-ceramics-and-its-implication-in-biomedical-implants.pdf. [Accessed 30 October 2017]
5. Duan Chonga Feng, Chou Yong Tana, Ramesh Singha, Andanastuti Muchtarb, Mahendra Rao Somalub, Chui Kim Nga, Boon Kar Yapc, Yee Ching Teha, Yoke Meng Tana. 2016. Effect of Manganese Oxide on the Sinterability of 8 mol% YttriaStabilized Zirconia. [ONLINE] Available at: https://sci-hub.cc/https://doi.org/10.1016/j.matchar.2016.09.001. [Accessed 30 October 2017].
6. S. Ramesh a, *, S. Meenaloshini b , C.Y. Tan a , W.J. Kelvin Chew b , W.D. Teng c. 2007. Effect of manganese oxide on the sintered properties and low temperature degradation of Y-TZP ceramics. [ONLINE] Available at: https://sci-hub.cc/https://doi.org/10.1016/j.ceramint.2007.04.012. [Accessed 30 October 2017].
7. Isabelle Denry a,∗, J. Robert Kelly b. 2007. State of the art of zirconia for dental applications. [ONLINE] Available at: https://sci-hub.cc/10.1016/j.dental.2007.05.007. [Accessed 9 October 2017].
8. Lughi V, Sergo V. 2010. Low temperature degradation -aging- of zirconia: A critical review of the relevant aspects in dentistry.. [ONLINE] Available at: https://www.ncbi.nlm.nih.gov/pubmed/20537701. [Accessed 9 October 2017].

EURECA 2018 – Conference Paper
Paper number 2ME29

Characterization of Co-doped Zirconia

Tan Wei Keong[1], Kelvin Chew Wai Jin[1], and Ramesh Singh[2]

[1]Taylor's University, School of Engineering, Malaysia
[2]Univeristy of Malaya, Faculty of Engineering, Malaysia

Abstract Zirconia is a ceramic with one of its uses being a hip implant. Research has shown that after a period of time, these implants can fail. In order to correct this, a new material should be used instead. The material that is proposed in this study is zirconia co-doped with manganese oxide and alumina. In order to determine the suitability of this new material, the bulk density, fracture toughness and material hardness of the new material will be determined and compared to the material originally used. During the course of the research, there will be 3 stages which are research, experimentation and analysis. Research will first be done to determine the bulk density, fracture toughness, material hardness and ageing resistance of past materials and to find any prior research being done on the current material. Experimentation involves the powder synthesis, green sample preparation, grinding and polishing processes. Analysis will then proceed with determining the bulk density, fracture toughness and material hardness of the sample via the suitable testing methods. In conclusion, the samples show higher bulk densities, fracture toughness and material hardness as the sintering temperature increases until a certain point where it decreases. Not only that, the doped samples also show higher bulk densities, fracture toughness and material hardness compared to non-doped samples.

1 Introduction

Ceramics are inorganic and non-metallic objects. These objects are commonly known to be brittle, hard and heat resistant. Ceramics can be broken down into 2 types which were traditional and advanced ceramics. Advanced ceramics are ceramics that exhibit exceptional properties when compared to traditional ceramics. Because of these properties, advanced ceramics can be used for multiple applications. An example of advanced ceramics that have seen significant usage is zirconia. Zirconia otherwise known as zirconium dioxide is a crystalline oxide that naturally exists with a monoclinic structure. Zirconia can exists in different phases which were cubic, monoclinic, amorphous and tetragonal with each phase having their own unique properties. A form of zirconia that has seen significant use is the yttria-stabilized tetragonal polycrystal (Y-TZP). Y-TZP boasts high mechanical strength, resistance to impact, wear, erosion, chemical and corrosion as well as a low thermal conductivity. An example of this is its usage with medical implants. However, these implants have been known to fail with the cause determined to be its ageing resistance within the human body **[1, 2]**. Therefore, in order to rectify this, another material will need to be used to replace the Y-TZP. A method to create a new material is to dope existing materials with select dopants in order to create a product with stronger properties. Doping is the process of introducing doping agents otherwise known as dopants into the original material for the purpose of changing the original properties and producing an end product with better ones. For this research, zirconia be doped with both manganese oxide (MnO_2) and alumina (Al_2O_3). The factors that will be analysed and compared will be the bulk density, fracture toughness, material hardness, and ageing resistance.

Determining the properties of Y-TZP that was co-doped with both MnO_2 and Al_2O_3 is one of the objectives of this research. In order to do so, preparation of the sample will be required in order to determine the properties. Another method would be to use past references as a baseline for estimation and comparison. A research has been done which uses the same materials that were used in this research. Said research was done to determine the microstructure properties of doped zirconia dental ceramics that were prepared using microwave sintering **[3]**. Besides that, multiple experiments have been done using the zirconia ceramic and varying dopants which include graphene, titania, and scandia **[4-6]**. These research have determined that when zirconia is doped with another substance, the bulk density, fracture toughness and material hardness have shown some improvements. Not only that, the results obtained also point to the fact that sintering temperature also played a part with the properties as most samples that were sintered at higher temperatures exhibiting stronger properties compared to the other samples that were sintered at lower temperatures.

Another factor of observation in this research will be the phases of the ceramic as the phases of the doped ceramic being able to greatly influence the properties of the end product. As stated earlier, zirconia can exists in 4 different phases which were the cubic, monoclinic, tetragonal and amorphous phase. However at relatively low temperatures of 65-400 $^\circ$C, Y-TZP can undergo a phase transformation into the monoclinic phase. This phase transformation is an unfavourable one as Y-TZP in the monoclinic phase tend to exhibit weaker bulk density, fracture toughness and material hardness when compared to it being in the tetragonal phase **[7, 8]**. There have been some research that have been done to determine the effect of dopants on the stability of the zirconia ceramic in tetragonal phase. Results from the research indicate that usage of cerium or yttrium can increase the thermal efficiency which in turn increases the phase stability of the ceramic **[9]**.

Besides that, the ageing resistance of Y-TZP will also need to be determined. As zirconia ceramics have seen wide commercial use, ageing resistance will be an important factor due to it generally determining the longevity of the product **[10]**. In order to test and determine this factor, the Low Temperature Degradation (LTD) test will be used. There have been some research that have been done to determine the ageing resistance of doped zirconia ceramics. The results have shown that the zirconia ceramic exhibited improvements in their ageing resistance with the dopants being Al_2O_3 and MnO_2 **[11]**. Another research using Al_2O_3 and silica (SiO_2) have similarly shown improvements with the ageing resistance **[12]**.

The final factor of observation in this research will be the microstructure of the ceramic. Microstructure analysis will focus on the analysis of the grains of the material. These analysis are done in order to better understand the reaction of the material when placed in specific conditions. Research has been done to determine the change in the microstructure of Y-TZP when it is strained **[13]**. The analysis was done using the Scanning Electron Microscope (SEM) test. Based on the results of that test, it was determined that the average grain size increases with the strain whereas some of the larger grains do not exhibit any changes which would indicate that Y-TZP having strong properties.

2 Experimentation Methodology

Experimentation for this research requires a few steps. The first step being the powder sample preparation. This step can then be broken down into a few more which include the powder synthesis, green sample preparation, sintering, grinding and polishing. Powder synthesis is the process of mixing different powders together to ensure that the desired powder oxides were mixed well and to also ensure that the powder has a sufficient surface area. The powders to be used will be the zirconia, MnO_2 and Al_2O_3 powders. After that, the samples are then made to undergo the green sample preparation processes of pressing and the cold isostatic press (CIP). Pressing is first done to shape the sample and then CIP is done to finish up. CIP is done as it can improve sinterability of the ceramic. After that is done, the samples will then be sintered. The type of sintering to be used in this research is pressureless sintering. The samples will then be sintered at temperatures of 1200, 1350 and 1500°C. The final step will be to grind and polish the samples. Grinding will be done using abrasive papers of grades 120, 240, 600, 800 and 1200. Once the grinding is complete, the samples are then polished using synthetic diamond polishing with grades of 1 and 7 microns.

2.1 Bulk Density

After the sample preparation has been completed, the analysis of the properties will be done. The first of which being bulk density. This density of the samples were done using the water immersion technique based on Archimedes' Principle. This will use a standard Mettler Toledo Balance AG204 densi meter and distilled water measured to be 25°C. For samples with a theoretical density of less than 95% of the theoretical density, the bulk density will then be obtained via the measurement of the geometric dimensions and sample mass. Calculations for the bulk density will use the following equation:

$$\boldsymbol{\rho = \frac{W_a \rho_w}{W_a - W_w}} \quad \textbf{(1)}$$

Where $\boldsymbol{\rho}$ = Bulk density of the sample (kg/m^3)

$\boldsymbol{W_a}$ = Weight of the air sample (N)

$\boldsymbol{W_w}$ = Weight of the water sample (N)

$\boldsymbol{\rho_w}$ = Density of distilled water (kg/m^3)

2.2 Material Hardness

The next analysis was the hardness test which was done using the Vickers Material Hardness test. For the test, the following equation was used:

$$\boldsymbol{H_V = \frac{1.854P}{D^2}} \quad \textbf{(2)}$$

Where $\boldsymbol{H_V}$ = Material hardness (Pa)

$\boldsymbol{P}$ = Applied load (N)

$\boldsymbol{D}$ = Average diagonal of the sample (m)

During the test, the load was lowered slowly onto the sample without impacting it. This was done to ensure that any sudden application of force do not affect the samples being measured. The load of 10 kg was then held in place for at least 10 seconds in order to indent the sample. The indent was then measured to determine the material hardness.

2.3 Fracture Toughness

Once that was done, the next analysis will be the fracture toughness. The following equation was then used :

$$\boldsymbol{\left(\frac{K_{IC}\emptyset}{H_V\sqrt{a}}\right)\left(\frac{H_V}{E\emptyset}\right)^{\frac{2}{5}} = 0.035\sqrt{\left(\frac{L}{a}\right)}} \quad \textbf{(3)}$$

Where $\boldsymbol{K_{IC}}$ = Fracture toughness

$\boldsymbol{a}$ = Length of the average diagonal (m)

$\emptyset$ = Constraint factor which will be taken as 3 **[29]**

$\boldsymbol{E}$ = Young's Modulus

$\boldsymbol{H_V}$ = Material hardness

L = Average crack length (m)

3 Results and Discussion

In the proceeding calculations, the samples that were used will be referred to by their respective sample codes. **Table 1** will show the corresponding sample code based on the weight percentage (wt%) of the dopants used and sintering temperature.

Table 1. Table of sample codes.

Sample Description	Temperature (°C)		
	1200	1350	1500
0.5 wt% MnO_2	A1	A2	A3
0.5 wt% MnO_2 + 0.05 wt% Al_2O_3	A4	A5	A6
0.5 wt% MnO_2 + 0.5 wt% Al_2O_3	M1	M2	M3
Pure Y-TZP	Y1	Y2	Y3

3.1 Bulk Density

Calculations for the bulk density were done using **Equation 1**. During the experimentation, the temperature of the distilled water was measured to be 25°C. Therefore the density of water will be set at 0.99707 g/ml. As the 1 g/ml is equal to 1 g/cm^3, the density of the distilled water will also be 0.99707 g/cm^3. **Table 2** shows the results of the analysis.

Table 2. Table of results for density.

Sample	Weight (g)		Density (g/cm^3)
	In air	In water	
Y1	2.4576	1.9773	5.102
Y2	2.4528	2.0133	5.565
Y3	2.4849	2.0339	5.494
A1	2.4543	1.9988	5.372
A2	2.4486	2.0009	5.453
A3	2.4459	2.0054	5.536
A4	2.4502	1.9982	5.405

A5	2.4525	2.0012	5.418
A6	2.4526	1.9992	5.394
M1	2.4590	2.0050	5.400
M2	2.4578	2.0081	5.449
M3	2.4578	1.9997	5.349

The results were translated to the graph shown in **Figure 1**. In the graph, it can be seen that as the sintering temperature increases, so does the bulk density until it reaches a certain point in which the bulk density decreases instead. This is true for all the samples except for the samples that were doped with only 0.5 wt% of MnO_2. Thus, this proves that sintering temperature does have an effect on the properties of the doped zirconia ceramic. Another matter of note is that there are hardly any differences when the doped ceramics are compared to one another.

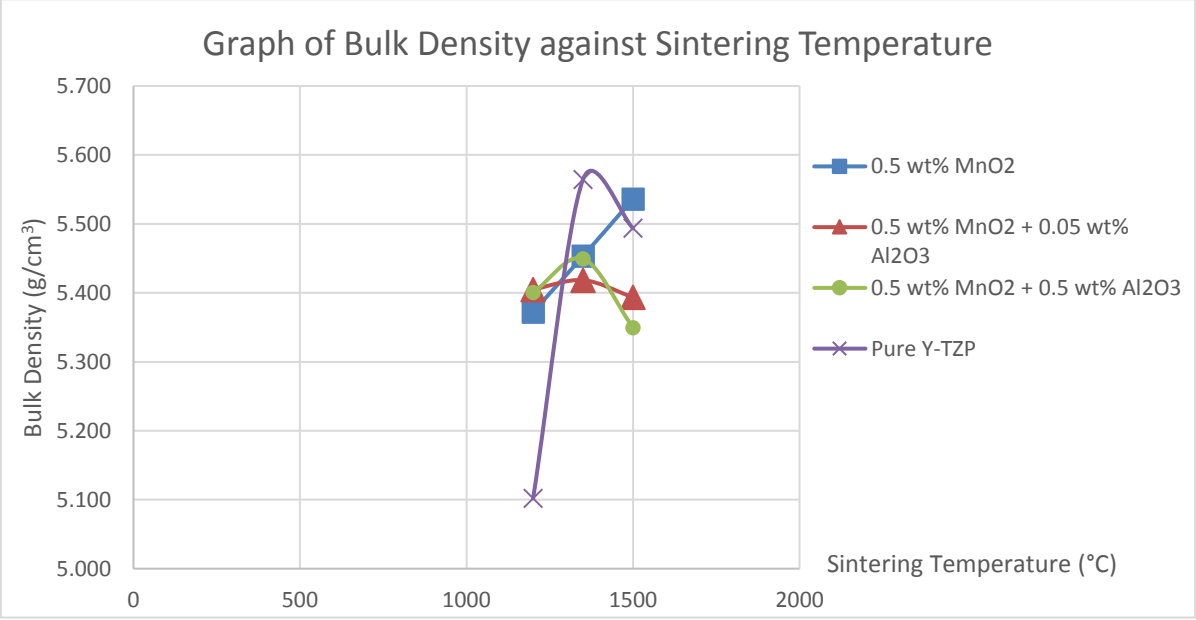


Figure 1. Graph of bulk density against sintering tempera

3.2 Material Hardness

Calculations for the material hardness were done using **Equation 2**. The following **Table 2** shows the results of the analysis.

Table 3. Table of results for material hardness.

Sample	Diagonal (μm)			H_V (GPa)
	1	2	Average	

Y1	134.6	137.2	135.9	9.848
Y2	113.6	114.7	114.2	13.958
Y3	115.0	115.3	115.2	13.717
A1	118.4	117.9	118.2	13.029
A2	116.5	116.5	116.5	13.401
A3	119.4	121.9	120.7	12.495
M1	118.3	117.5	117.9	13.084
M2	116.0	115.3	115.7	13.598
M3	123.6	116.7	120.2	12.599
A4	120.0	116.5	118.3	9.848
A5	117.4	116.6	117.0	13.286
A6	119.4	118.3	118.9	12.876

The results were translated to the graph shown in **Figure 2**. During the analysis, it can be seen that the hardness of the samples that were doped with 0.5 wt% of Al_2O_3 were higher compared to the other samples. Not only that, the hardness of the samples also increased until a certain point before it decreases again. This phenomenon applied to all of the samples. Based on this, it can be determined that as sintering temperature increases, so does the material hardness of the samples until it reaches a certain temperature in which the samples soften instead

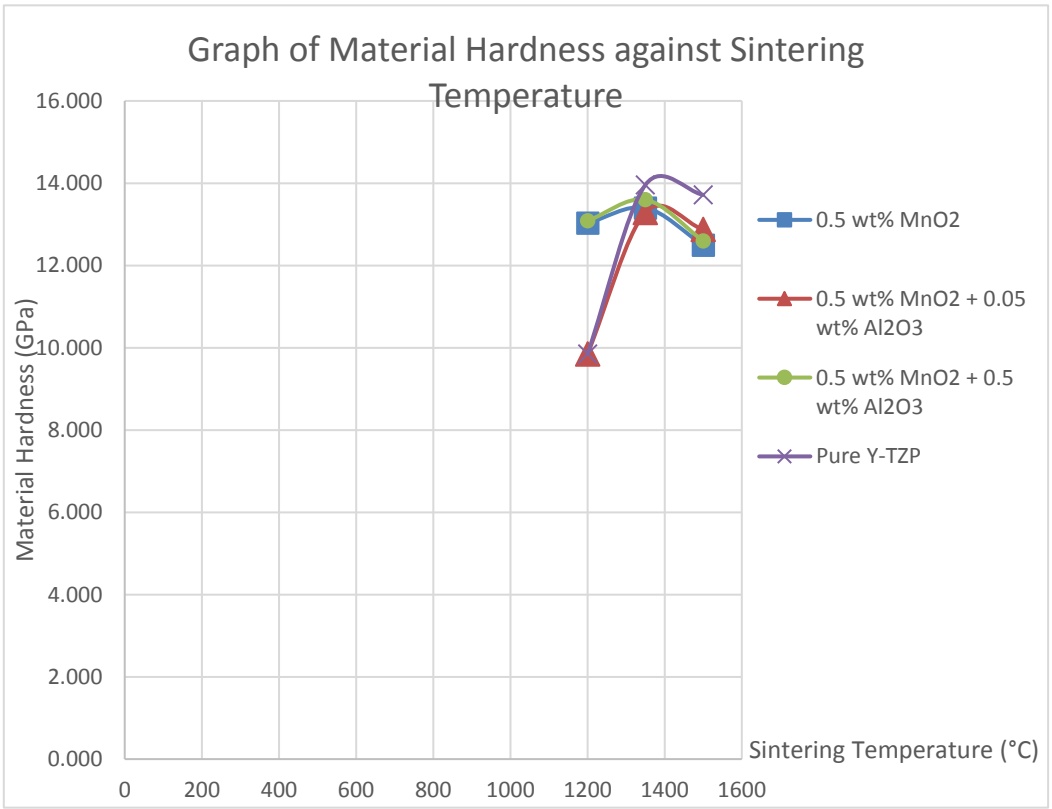


Figure 2. Graph of material hardness against sintering temperature

3.3 Fracture Toughness

Calculations for the fracture toughness were done using **Equation 3**. The following table is the table of results for the analysis of fracture toughness.

Table 3. Table of results for fracture toughness.

Sample	Crack Length (μm)						Average Crack Length (μm)	K_{IC} (Pa$\sqrt{m}$)
	L1	L2	L3	L4	L5	L6		
Y1	82.1	67.8	59.6	71.7	72.7	67.4	70.217	4.821E+09
Y2	76.4	69.4	84.3	82.1	68.4	80.5	76.850	4.772E+09
Y3	60.1	54.5	64.4	57.9	54.9	62.4	59.033	5.436E+09
A1	73.6	73.7	76.7	77.7	76.3	78.8	76.133	4.762E+09
A2	81.2	85.3	66.4	72.1	80.2	68.4	75.600	4.792E+09
A3	70.4	58.7	54.0	64.8	58.0	58.1	60.667	5.312E+09
M1	74.7	72.9	81.0	81.0	81.7	81.7	78.833	4.682E+09
M2	80.3	76.3	64.2	72.8	64.6	68.5	71.117	4.948E+09
M3	66.3	63.3	68.9	66.5	65.3	59.5	64.967	5.138E+09
A4	64.4	57.7	67.5	82.2	80.8	69.4	70.333	4.192E+09
A5	66.1	55.6	63.4	64.5	72.7	67.3	64.933	5.166E+09
A6	60.7	60.9	61.2	76.9	69.4	69.1	66.367	5.094E+09

The results from the table above were then made into the following graph in **Figure** 3. From the graph, it can be observed that as the sintering temperature increases so does the fracture toughness of the samples until a certain point where some samples show a decreasing fracture toughness. Besides that, it can also be observed that the samples that were sintered with 0.05 wt% of Al_2O_3 show generally higher fracture toughness overall throughout the graph.

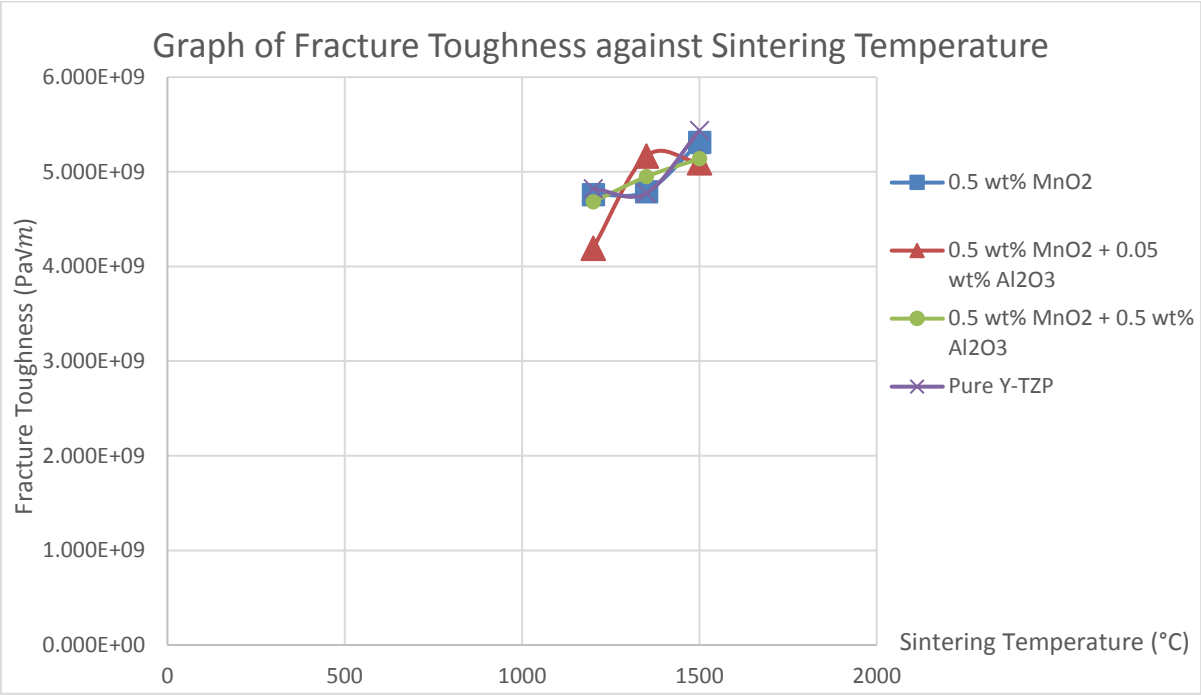


Figure 3. Graph of fracture toughness against sintering temperature.

4 Conclusion

Based on the results of the research, the following conclusions could be drawn.

1. Doped ceramics showed better bulk density, fracture toughness and material hardness when sintered at higher temperatures.
2. The zirconia ceramic co-doped with manganese oxide and alumina showed better bulk density, fracture toughness and material hardness than its original counterpart.

References

1. M. Norton, R. Yarlagadda and G. Anderson, "Catastrophic failure of the Elite Plus total hip replacement, with a Hylamer acetabulum and Zirconia ceramic femoral head", *The Journal of Bone and Joint Surgery*, **84**, 631-635, (2002).
2. F. Traina, M. De Fine, A. Di Martino and C. Faldini, "Fracture of Ceramic Bearing Surfaces following Total Hip Replacement: A Systematic Review", *BioMed Research International*, **2013**, 1-8, (2013).
3. Y. Ai, X. Xie, W. He, B. Liang and Y. Fan, "Microstructure and properties of Al2O3(n)/ZrO2 dental ceramics prepared by two-step microwave sintering", *Materials & Design (1980-2015)*, **65**, 1021-1027, (2015).
4. S. Ramesh, M. Khan, H. Alexander Chee, Y. Wong, P. Ganesan, M. Kutty, U. Sutharsini, W. Chew and A. Niakan, "Sintering behaviour and properties of graphene oxide-doped Y-TZP ceramics", *Ceramics International*, **42**, 17620-17625, (2016).
5. C. Guo, J. Wang, C. He and W. Wang, "Effect of alumina on the properties of ceria and scandia co-doped zirconia for electrolyte-supported SOFC", *Ceramics International*, **39**, 9575-9582, (2013).

6. X. Zeng, Z. Du, C. Schuh, N. Tamura and C. Gan, "Microstructure, crystallization and shape memory behavior of titania and yttria co-doped zirconia", *Journal of the European Ceramic Society*, **36**, 1277-1283, (2016).
7. Z. Wu, N. Li, W. Zhao and J. Yan, "Low Temperature Degradation of Y-TZP Ceramic for Dental Applications", *Advanced Materials Research*, **873**, 241-249, (2013).
8. C. Laberty-Robert, F. Ansart, C. Deloget, M. Gaudon and A. Rousset, "Dense yttria stabilized zirconia: sintering and microstructure", *Ceramics International*, **29**, 151-158, (2003).
9. G. Theunissen, A. Winnubst and A. Burggraaf, "Effect of dopants on the sintering behaviour and stability of tetragonal zirconia ceramics", *Journal of the European Ceramic Society*, **9**, 251-263, (1992).
10. I. Tredici, M. Sebastiani, F. Massimi, E. Bemporad, A. Resmini, G. Merlati and U. Anselmi-Tamburini, "Low temperature degradation resistant nanostructured yttria-stabilized zirconia for dental applications", *Ceramics International*, **42**, 8190-8197, (2016).
11. D. Ragurajan, M. Golieskardi, M. Satgunam, M. Hoque, A. Ng, M. Ghazali and A. Ariffin, "Advanced 3Y-TZP bioceramic doped with Al_2O_3 and MnO_2 particles potentially for biomedical applications: study on mechanical and degradation properties", *Journal of Materials Research and Technology*, (2017).
12. A. Samodurova, A. Kocjan, M. Swain and T. Kosmač, "The combined effect of alumina and silica co-doping on the ageing resistance of 3Y-TZP bioceramics", *Acta Biomaterialia*, **11**, 477-487, (2015).
13. J. Shi, Z. Lu, J. Gao, G. Zhu, L. Li and T. Lai, "Microstructure and micro-mechanical properties of Y-TZP and Y-TZP/Al2O3 composite after superplastic deformation", *Acta Materialia*, **46**, 1923-1932, (1998).
14. Musikant, S., In What Every Engineer Should Know about Ceramics, (Marcel Dekker, Inc., 1991) 104-105.

Android Device Extended Shield

Boon Hock Teh[*]*, Mohammad Hosseini Fouladi, and Mohsen Nabipoor*

School of Engineering, Taylor's University, 47500 Subang Jaya, Selangor, Malaysia

Abstract. With growth of Internet-Of-Things (IoT) applications, it is important and beneficial to utilise smartphone's functionalities to interact with physical world. However, current methods used to achieve that require multiple development platforms and/or more in-depth knowledge of Android development. This research assesses the feasibility of interaction between Android devices and external peripherals in one platform and to design and develop a development platform for users to use. UMFT311EV, a development module for FT311D was used to interface Android devices' USB to peripherals' GPIO and PWM interfaces in this research. The research design of this research involves software development and experimental analysis. After validating feasibility of interacting Android devices with external peripherals, framework of development platform was developed. Libraries and APIs utilising Android and peripherals' functionalities were developed and deployed. Experiments were conducted to test and assess implementations using different Android devices' functions. Comparing results of this research with that of existing platforms, it is concluded that it is feasible to have only one software development platform for interacting Android with external peripherals. Furthermore, technical skills requirement was also lowered with libraries, APIs and a basic app developed and ready for use. However, interface chip used in this research is unsuitable because experiments conducted found GPIO interface was functioning on Android 4.1 but not on newer releases – Android 4.4, 6.0 and 7.1. From Android's official website, Android 4.4, 6.0 and 7.1 represent 58.7% of devices running on Android while Android 4.1 represents only 1.5%.

[*] Corresponding author: tehboonhock@hotmail.com

Introduction

Microcontroller

Microcontrollers are used in various applications [1] and to reduce amount of effort and time working with them, development boards are created. Arduino UNO is an example of development board for ATmega328 microcontroller [2]. Development boards reduce learning curve and allow a wider audience to learn and develop applications using microcontrollers.

Microcontrollers are function specific hence they have limited capabilities [1]. Basic Arduino boards such as Arduino UNO can take input from sensors and produce electrical outputs to control peripherals only. It does not have the functionalities of Wi-Fi, Bluetooth, GPS, display screen, etc. To obtain these functionalities, extra modules or "*shields*" for Arduino or higher end Arduino board is required. Despite many of these functionalities are available in today's smartphones, there is a lack of direct method of harnessing the functionalities of a smartphone to be used to interact with peripherals.

Harnessing Android devices' functionalities

One method available currently requires purchase of a shield or module for Arduino to communicate with smartphones. This method is inefficient because for developers, development needs to be done both on smartphone platform and microcontroller development board platform. Take Android smartphone and Arduino for an example, to utilise the smartphone's functionalities, a smartphone application (henceforth referred as 'app') needs to be developed. This development is done in Java programming language. Next, Arduino libraries to communicate with the app are developed for users to use and this development is done in C/C++ programming language [3]. Hence, any modifications/updates or addition of new features need to go through two development phases and platforms. An example of this approach is by using 1Sheeld shield for Arduino. As seen from their GitHub account (https://github.com/Integreight/), Arduino and Android each have their own repository. Micro:bit is also an example using this method and with the difference of development on this platform is done in Python programming language [4].

Another method available requires users to develop both an app and a program for development board. IOIO-OTG is an example of development using this approach. Although this approach gives users freedom to create and tailor apps to their requirements, it is less beginner friendly. Users are required to understand Android app development which includes Java programming language, XML, SQLite and various Android concepts such as activity lifecycle, layouts, contexts, fragments, intents and many more before learning or doing any hardware related work.

Communication interfaces and Android Open Accessory

Smartphones and tabs cannot interact directly with external peripherals due to difference of communication interfaces. While smartphones support Wi-Fi, Bluetooth and Universal Serial Bus (USB), interacting with external peripherals usually requires other types of interfaces such as general-purpose input/output, pulse-width modulation (PWM), universal asynchronous receiver-transmitter (UART), Inter-Integrated Circuit (I^2C) and Serial Peripheral Interface bus (SPI) [5, 6]. For example, lighting an LED requires GPIO and changing motor speed requires PWM interface. Therefore, an interface device is required for smartphone to interact with external peripherals.

In 2011, Google introduced Android Open Accessory (AOA) – a protocol that allows an Android device to interact with an external USB hardware in accessory mode. This protocol standardises and simplifies connection between Android devices and USB hardware. Several development boards and PCBs such as IOIO-OTG [7, 8], some Arduino boards [9] and FTDI FT311D [6] implemented AOA protocol. This simplifies communication of Android devices with external hardware.

About this research

This research aims at understanding communication interfaces between Android devices and external hardware peripherals, and to study communication interfaces and develop a platform with a readily available app and API libraries for users to develop their own programs in one platform. With evolution of newer Android API Levels, older API Level or code may be deprecated [10]. Figure 0.1 shows some examples of API Levels and their respective Android versions, release names and ABI (application binary interface).

Release Name	API Level	ABI	Target
Oreo Download	27	x86	Android 8.1 (Google APIs)
Oreo Download	26	x86	Android 8.0 (Google APIs)
Oreo Download	26	x86_64	Android 8.0 (Google APIs)
Nougat Download	25	x86	Android 7.1.1 (Google APIs)
Nougat Download	25	x86_64	Android 7.1.1 (Google APIs)
Nougat Download	24	x86_64	Android 7.0 (Google APIs)
Nougat Download	24	x86	Android 7.0 (Google APIs)
Nougat Download	24	x86_64	Android 7.0
Nougat Download	24	x86	Android 7.0
Marshmallow Download	23	x86_64	Android 6.0 (Google APIs)
Marshmallow Download	23	x86	Android 6.0 (Google APIs)
Marshmallow Download	23	x86	Android 6.0
Marshmallow Download	23	x86_64	Android 6.0

Figure 0.1 Android API Levels

A prototype app was developed and installed on four different Android versions: Jellybean (4.1), KitKat (4.4), Marshmallow (6.0) and Nougat (7.0). Then, libraries for developing programs were developed and tested with UMFT311EV board. The program developed is tested on different API Levels to ensure backward compatibility. Finally, real world application projects were experimented to understand and test the feasibility of developed platform.

Android was selected as the smartphone operating system (OS) for the scope of this research due to its open source nature and has the largest smartphone OS market share – over 80% [11, 12]. Access to devices with Android versions mentioned is available during this research. Android Studio, the official IDE for Android development was used for development during this research.

The name given to this research and the app is Fiyepr, pronounced as fai·per.

Methodology

The research design of this research involves software development and experimental analysis.

Software development

Firstly, APIs provided by FTDI for FT311D development and demo apps along with their source code – GPIODemo (Figure 0.1) and PWMDemo (Figure 0.2) were studied and understood via documentations provided on their website (http://ftdichip.com). The apps' source codes were studied and experimented with peripherals to fully understand the APIs before developing an app for this research shown in Figure 0.3.

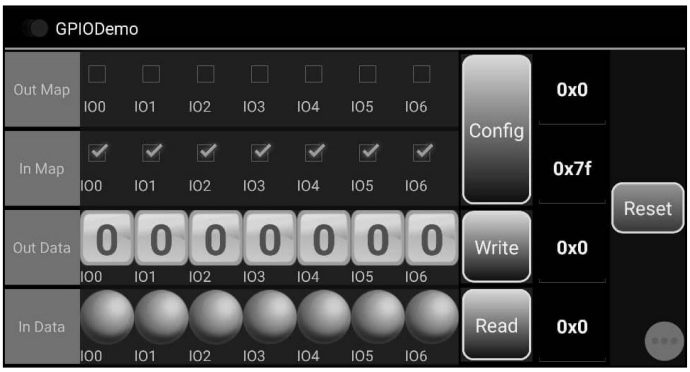


Figure 0.1 GPIODemo app by FTDI

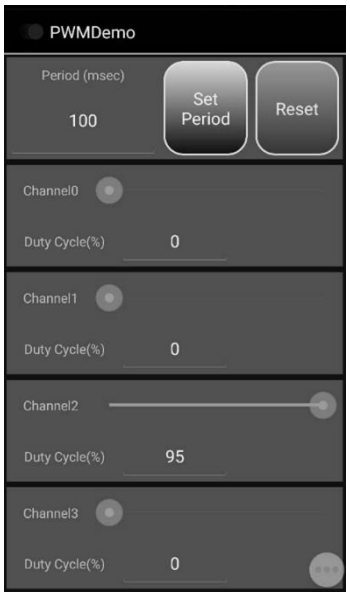


Figure 0.2 PWMDemo app by FTDI



Figure 0.3 Fiyepr app

Next, three main libraries were developed for users to use – GPIOLibrary, PWMLibrary, and GeneralLibrary.

GPIOLibrary contains methods related to GPIO interface. For example, a method called *digitalWrite()* is used set output pin as 'ON' state or 'OFF' state. The method takes two parameters which the first is an *int* value representing the pin number from 0 to 6 and second is an *int* value denoting if pin is 'ON' or 'OFF': any value larger than 0 is denoted as 'ON' and value smaller or equal to 0 is denoted as 'OFF'. The name resembles that of Arduino's for simplicity.

PWMLibrary contains methods related to PWM interface. *analogWrite()* is one of the methods contained in this library. This method takes two parameters: first one is *int* value representing pin number and second one is *int* value ranging from 0% to 95% denoting the duty cycle. 95% is the maximum duty cycle for FT311D [13].

GeneralLibrary contains methods not related to GPIO or PWM such as *delay()*. This method takes a parameter of *int* value representing milliseconds to "pause" the program.

Finally, smartphone's functionalities were explored such as playing sounds and using smartphone's sensors. A sensor library called Sensors was developed to make development easier for users. Experiments were conducted to test code implementations.

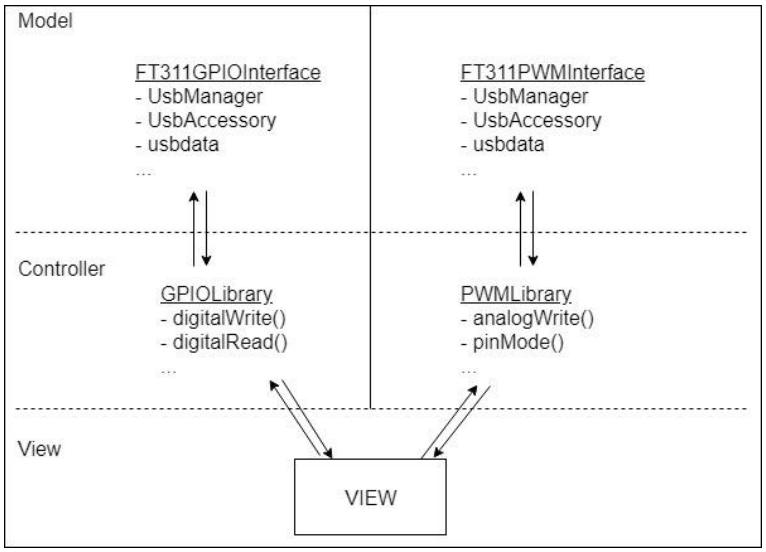


Figure 0.4 MVC architecture in this research

The software architecture in this research follows Model-View-Controller (MVC) architecture. Model objects, controller objects and view objects are separated. Figure 0.4 illustrates two examples in this research. For GPIO functionalities, FT311GPIOInterface class in the model layer contains data such as USB data and file streams while GPIOLibrary serves as the controller to manipulate these data and interact with view layer. The same architecture applied to PWM and sensor code developed.

Experimental analysis

The interface device used in this research is FTDI FT311D chip. This chip bridges Android device's USB port to six different interfaces: GPIO, UART, PWM, I^2C, SPI (slave) and SPI (master) [6]. Due to difficultly working with the chip because of its small size and quotations for PCB printing from vendors are out of research's budget (ranging from over RM 1500 to RM 3000), UMFT311EV shown in Figure 0.5 was purchased and used. It is a development module for FT311D chip [14]. The scope of peripheral interfaces in this research was limited to GPIO and PWM.

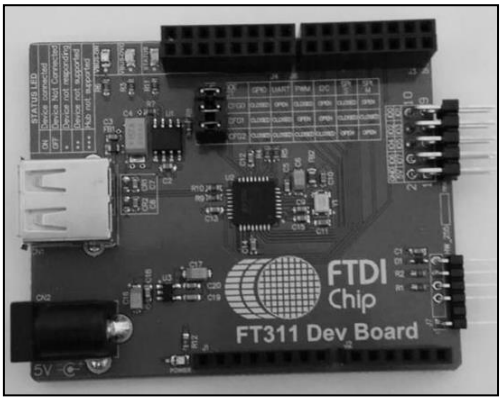


Figure 0.5 UMFT311EV

Code developed were experimented with projects such as blinking LEDs, controlling light intensity and receiving digital inputs from push buttons. Each tests and experiments were carried out on each device mentioned.

When the programs were first tested, the smartphones were found to freeze although the programs were still running fine. After several tests, the error was found to originate from *delay()* method. The program was running on single thread therefore when *sleep()* method was called within *delay()* method, the whole thread paused and caused the smartphones to be irresponsive. With Java's multithreading feature, a new thread was started to allow app's activity process to run concurrently with developed program's process. This allowed phone to remain responsive to user actions while program is running.

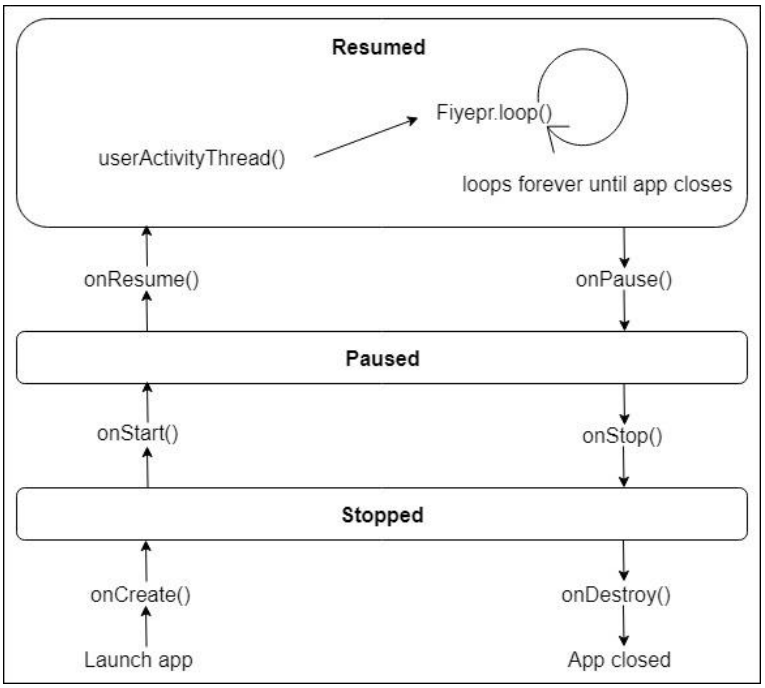


Figure 0.6 Fiyepr's activity lifecycle

Figure 0.6 shows Fiyepr app's activity lifecycle and respective method call before entering new state. These methods are built-in and will be called automatically. When app is in resumed state, it is the app user is currently interacting with. In resumed state, when "CLICK TO RUN" button shown in Figure 0.3 is pressed, a new thread of *userActivityThread* is created and executed. The execution is wrapped in a loop to run forever until *onDestroy()* is called. This allow program to actively change, respond and control peripherals.

To further investigate feasibility of utilising smartphone's features while interacting with external peripherals, two more experiments were conducted. The first experiment was a mini piano. A mini piano shown in Figure 0.7 was built and program for it was developed. This experiment aimed to test ability to receive inputs from external peripherals and produce output, in this case, sound. In this experiment, each key was matched to each input pins of UMFT311EV and unique tones were assigned to each pin. While writing the program for this experiment, it is noted that *Soundpool* constructor was deprecated from API Level 21 onwards therefore new *Soundpool* constructor was required.

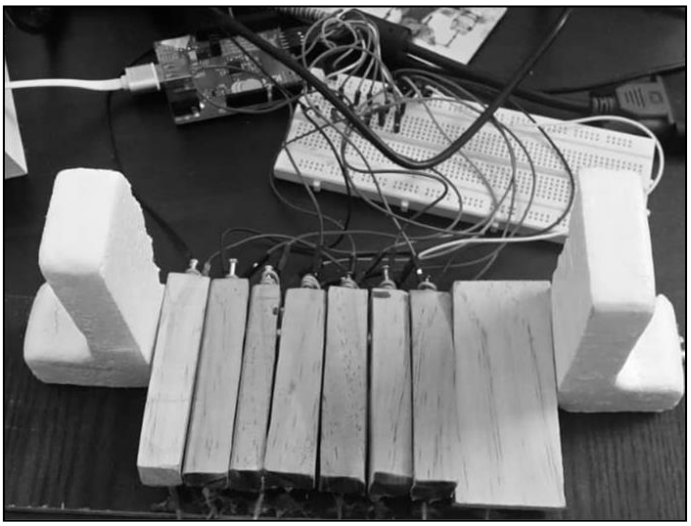


Figure 0.7 Mini piano built for experiment

An experiment to utilise smartphone's sensors was also conducted. In this experiment, basic circuitry and program was developed to control LEDs' intensity using smartphone's accelerometer. Although sensors' values can be obtained simply via *SensorManager* class, the program for interacting with peripherals run on separate thread from the main thread therefore sensor values need to be obtained via implementation of *SensorEventListener* class. This required several methods to be overridden therefore to make development easier for developers using Fiyepr, a library called Sensors was developed.

Results and discussion

Basic implementation of single development platform for smartphone to interact with peripherals was done and proved feasible. However, FT311D can only use one interface at a time hence limiting usages. Furthermore, FT311D's GPIO failed to function on Android 4.4, 6.0 and 7.0. *writePort()* method provided in FTDI's API was throwing error message of "write failed: ENODEV (no such device)". It is a known bug when writing to devices using AOA protocol via *FileInputStream* or *FileOutputStream*[15]. ABI of each device was investigated and found to be similar. Therefore, to solve this, PWM was used to simulate GPIO with 5% duty cycle as 'OFF' and 95% duty cycle (FT311D's max duty cycle) as 'ON'. 94% was used instead of 95% because 95% was found to be unreliable and produced errors.

According to data of Android version distribution as of May 2018 obtained from Android official website [15], the total distribution percentage of Android 4.4, 6.0 and 7.0 which GPIO failed to function is 58.7% while Android 4.1, which GPIO was fully functional represents only 1.5% of total distribution. This further indicated FT311D used in this research is not suitable and other alternatives need to be explored.

With MVC architecture, code for each layer can be easily maintained and reused. Libraries developed also simplified development especially for beginners as they only need to develop their own program in one place – Fiyepr class in Fiyepr.java.

[15] https://issuetracker.google.com/issues/36933798

Table 2 Comparison of technical requirements among different platforms for interacting Android device with external peripherals

Platform	**No. of software development platform (for developers)**	**No. of software development platform (for users)**	**Programming language**	**User need to create app?**
Fiyepr	1 (Android)	1 (Android)	Java	No. Unless custom app required.
1Sheeld (for Arduino)	2 (Android, Arduino)	1 (Arduino)	Java, C/C++	No.
Micro:bit	2 (Android, Micro:bit)	2 (Android, Micro:bit)	Java, Python	Yes.
IOIO-OTG	1 (Android)	1 (Android)	Java	Yes.

Table 2 shows comparison of technical requirements among different platforms. For developers, software development work on Fiyepr is simplified because programs for harnessing an Android smartphone's functionalities and interaction with external hardware are on the same platform – Android. Development work is faster because developers can easily add or update APIs without having to update other platforms.

When developing Android to work with other platforms, a developer needs to understand multiple frameworks and different programming languages, namely Java for Android and for example, C/C++ for Arduino or Python for Micro:bit. For Fiyepr, only Java is required.

Furthermore, with a basic app developed and ready for use, technical skills requirement for users is lowered. Users who do not need custom app with different look or extra buttons can still use various smartphone functionalities as APIs will be developed and provided. For all Fiyepr programs, *Fiyepr* class containing two methods, namely *Fiyepr()* and *loop()* in Fiyepr.java is required (see Figure 0.1). *Fiyepr()* method will execute at the beginning of user's program and it is useful for setting up Fiyepr for the rest of the program such as configuring pins as output or input. *loop()* method executes over and over again until app is closed. This is where code to execute repetitively for user's program should be. The concept of having a method that executes once at the beginning of user's program and one that repeats itself in perpetuity is adopted from Arduino. Arduino has two functions: namely *setup()* that works similar to *Fiyepr()* and *loop()* that works similar to *loop()* in Fiyepr.

While *loop()* in Fiyepr is named similar to *loop()* in Arduino, *Fiyepr()* is used to make use of Java programming's constructor feature – *Fiyepr()* is a constructor method. Constructor methods have the same name as their class and is syntactically the same with a method [16].

```
1   package com.fiyepr.fiyepr;
2
3   import android.content.Context;
4
5   import static com.fiyepr.fiyepr.GeneralLibrary.*;
6   import static com.fiyepr.fiyepr.PWMLibrary.*;
7   import static com.fiyepr.fiyepr.GPIOLibrary.*;
8
9   public class Fiyepr {
10      private final static String TAG = "Fiyepr";
11
12      Fiyepr(Context context) {
13          // code here will execute once at the beginning of your program
14      }
15
16
17      public void loop() {
18          // code here will execute over and over until app is closed
19      }
20
21  }
```

Figure 0.1 Fiyepr class

Lastly, some classes, methods and even the Android API itself may be deprecated with release of newer Android versions. According to Oracle, deprecated software is code that is no longer useful and should no longer be used [17]. Reasons for deprecating an API include security concerns, insignificant for future release and encourages bad practices. A study by Li Li et al. found deprecated Android APIs are regularly cleaned up from framework code base within short period of time therefore developers must respond quickly to these deprecations. Program developed needs to check Android version and use correct implementations to ensure program developed is always up to date with latest Android version and is backward compatible.

Conclusion and future work

This research has proven it is feasible to use one development platform for interacting smartphone with external peripherals. With all development work done in one platform, development can be done faster and codes can be maintained and updated more easily. Libraries and APIs developed are also easy to use with minimal knowledge Android platform required to get started.

A framework of app, libraries and APIs have been developed users to use. For future work, more libraries utilising more Android phone's functionalities such as GPS, Wi-Fi, Bluetooth, infrared sensor, etc. Libraries and APIs for more peripherals such as various sensors should also be developed to make this platform more robust and usable.

The bridge used in this research should also be change to one that is capable of interfacing multiple communication interface simultaneously.

Lastly, documentations and basic tutorials need to be prepared to provide as guides for users to adopt Fiyepr and learn how to use this platform.

References

[1] G. Gridling and B. Weiss, "Introduction to Microcontrollers," Vienna University of Technology, Wien, 2007.

[2] M. Banzi and M. Shiloh, Make: Getting Started with Arduino 3rd Edition, California: Maker Media, Inc., 2015.

[3] B. W. Evans, "Arduino Programming Notebook," 2007.

[4] M. Berry and R. Chambers, "Micro:bit - A Quick Start Guide for Teachers," Hodder Education, London, 2015.

[5] T. DiCola, "Adafruit FT232H Breakout," Adafruit Learning System, 2017.

[6] Future Technology Devices International Limited, “FT311D (USB Android Host IC),” Future Technology Devices International Limited, Glasgow, 2013.

[7] Sparkfun Electronics, “Connecting to the IOIO-OTG,” Sparkfun Electronics, Colorado.

[8] F. C. Serce, A. Erpay, A. Kara, B. Ünal, D. Özgubar, A. B. Öztürk and S. Şekerci, “Design and Development of an Android Accessory,” *International Journal of Electronics and Electrical Engineering*, vol. 3, no. 5, pp. 390-395, 2015.

[9] A. Göransson and D. C. Ruiz, Professional Android Open Accessory Programming with Arduino, Indiana: John Wiley & Sons, Inc., 2013.

[10] B. Phillips, C. Stewart and K. Marsicano, Android Programming: The Big Nerd Ranch Guide, Atlanta: Pearson Technology Group, 2017.

[11] Statista, “Global mobile OS market share in sales to end users from 1st quarter 2009 to 2nd quarter 2017,” 2018. [Online]. Available: https://www.statista.com/statistics/266136/global-market-share-held-by-smartphone-operating-systems/. [Accessed 12 May 2018].

[12] L. Li, J. Gao, T. F. Bissyandé, L. Ma, X. Xia and J. Klein, “Characterising Deprecated Android APIs,” in *Association for Computing Machinery*, Gothenburg, 2018.

[13] Future Technology Devices International Limited, “Software Application Development FT31xD Android Programmers Guide,” Future Technology Devices International Limited, Glasgow, 2013.

[14] Future Technology Devices International Limited, “DS_FT311D_Development_Module: UMFT311EV (USB Android Host Module),” Future Technology Devices International Limited, Glasgow, 2012.

[15] Android, “Distribution dashboard,” Android, 24 May 2018. [Online]. Available: https://developer.android.com/about/dashboards/. [Accessed 11 June 2018].

[16] H. Schildt and D. Skrien, Java Programming: A Comprehensive Introduction, New York: McGraw-Hill, 2013.

[17] Oracle, “How and When To Deprecate APIs,” Oracle, [Online]. Available: https://docs.oracle.com/javase/7/docs/technotes/guides/javadoc/deprecation/deprecation.html. [Accessed 11 June 2018].

EURECA 2018 – Conference Paper
Paper number 2ME31

Optimization Of The Performance Of Vapor Compression Cycle Using Liquid Suction Line Heat Exchanger

THABIT KHALIFA, ALI NAIF, ABDULKAREEM SH. MAHDI AL-OBAIDI

School of Engineering, Taylor's University, Taylor's Lakeside Campus,
No. 1 Jalan Taylor's, 47500, Subang Jaya, Selangor DE, Malaysia

Abstract

Mechanical subcooling and Liquid Suction Line Heat Exchanger (LSLHX) systems are approaches that are shown to improve the performance of Vapour Compression Cycle (VCC). This study is carried out with two main objectives. First, to optimize the heat source and heat sink water volumetric flow rate combination that outcomes in the best performance. In order to evaluate the effect of using subcooling cycle and LSLHX cycle using the optimum flow rate combination. Then, to optimize the heat source and heat sink water volumetric flow rate combination that outcomes in the optimum performance. Lastly, to optimize the system performance through implementing subcooling and LSLHX. At optimum water flow rates basic VCC performance was better than published data. The system performance was improved by 9.98% at the optimum flow rate when solely subcooling was used while deteriorated by 47.42% at full LSLHX.

Keywords: Coefficient of performance, Liquid suction line heat exchanger, Subcooling, Vapour compression cycle.

1.Introduction

Air Conditioning and Refrigeration (ACnR) systems have become an essential need in the recent years due to its importance to carry daily life applications like cooling control and, food and medical preservation. Malaysia is one of the countries that demand ACnR system such as air-conditioners and refrigerators in 99% of its infrastructure; which in return consume 38% of the overall household energy consumption [1]. Many types of researches have been conducted to optimize the energy consumption of the ACnR systems by improving the coefficient of performance (COP) of the systems. COP improvement can be achieved when by improving the Cooling Capacity (CC) and reducing the power consumption. The performance of ACnR systems improvement can be studied experimentally, theoretically or numerically. Theoretical and numerical approaches are, cost and time saving and can be used to describe the system's ideal behaviour [2].

Nomenclatures

$C_{p,water}$	Water heat capacity
h	Enthalpy
$\dot{m}_{ref}$	Refrigerant mass flowrate
$\dot{m}_{Wevap}$	Evaporator water mass flowrate
$\dot{Q}_{evap}$	Cooling capacity
T_{EWI}	Temperature of the inlet of evaporator
T_{EWO}	Temperature of the outlet of evaporator
W_{comp}	Work done by compressor

Abbreviations

EETXV	Eternally Equalizing Thermal Expansion Valve
LSLHX	Liquid Suction Line heat exchanger
VCC	Vapour Compression Cycle
VSC	Variable Speed Compressor

However, experimental analysis describes the system's actual operating behaviour. Multi-staging, subcooling and vapour injection are the main three methods used to improve the performance of the ACnR systems [3]. However, vapour injection and subcooling are considered to be the best methods to improve the (CC) which ultimately improves the COP.

Qureshi and Zubair [4] highlighted, there are four main types of subcooling namely; Ambient, external heat sink, mechanical and liquid suction line heat exchanger (LSLHX). In this study, it was reported, implementing mechanical subcooling improved the system performance by 21%. Pottker and Hrnjak [5] studied the effect of subcooling of VCC system utilizing 4 different refrigerants namely; R410a, R134a, R123yf, and R717 when, subcooling was implemented the performance have increased by 7%, 5.9%, 8.4% and 2.7% respectively. The highest performance improvement was noted with refrigerants with the higher latent heat of vaporization. LSLHX is a heat exchanger that is used in the ACnR systems to transfer heat from the saturated liquid exiting the condenser to the super-heated vapour exiting the evaporator. Besides aiding in increasing the cooling capacity, LSLHX ensures a significant advantage to the system as it gets rid of any liquid form refrigerant flowing through the compressor which correspondingly increases the compressors lifespan.

Domanski and Didion [6] and Aprea et al. [7] studied theoretically the effect of incorporating LSLHX in a basic VCC. The results indicated that the COP of the system increased when refrigerants with high heat capacity, the coefficient of thermal expansion and latent heat of vaporization were used with LSLHX engagement. Also, it was noted that the COP improvement of the LSLHX VCC depended on the type of the refrigerant used. Klien et al. [8] produced a mathematical model to study the effect refrigerants on the VCC with LSLHX considering the pressure drop in the suction line of the LSLHX. It was found that the COP increases when using R134a while decreasing when using R22. On the other hand, Navarro Esbri et al. [9] studied experimentally the effect installing LSLHX on the system's performance using R134a and R1234y. The results showed, when using R1234y the performance dropped by 8.5% while, when using a VCC LSLHX the performance dropped only by 4.25%. Pottker and Hrnjak [10] executed relatively similar study using R134a and R1234y with and without implementing LSLHX. It was found that the performance increased by 9% and 18% respectively when the system was incorporating with a LSLHX. Also, it was noted in this study that the maximum COP is achieved with 9°C of subcooling.

Devecioglu and Oruc [11] studied the effect of the ambient temperature on a LSLHX VCC system with a variable speed compressor utilizing R453A and R22, and without considering the pressure drop in the suction line of the LSLHX. As the LSLHX is engaged, it was noted that the cooling capacity and power consumption of the system increased as a result of increasing the ambient temperature. Additionally, it was found that the cooling capacity with R22 was higher than R453A. On the other hand, the power consumption for R22 application was higher than R453A in the basic VCC system yet negligible when applying LSLHX. Moreover, the average of the performance of the system improved by 28.5% and 26% respectively for R22 and R453A.

One of the most significant drawbacks of adding LSLHX to a VCC is the increment of the power consumption that is supplied to the compressor. This is due to the effect of the pressure drop induced in the suction line of the LSLHX which ultimately reduces the performance of the overall system. Zhang et al. [12] investigated the possibility of replacing R 134a by R1234yf and R1234ze with incorporating with LSLHX. The maximum pressure-drop for R1234yf and R1234ze was 20 kPa and 14 kPa respectively while 17 kPa for R134a. Imran et al. [13] studied LSLHX VCC using R245fa that noted the maximum pressure drop was 8 kPa. Longo et al. [14] used R410 and R32 to study LSLHX VCC which noted the maximum pressure drop was 13 kPa. Longo and Gasparella [14], Yan and Lin [15], Jassim et al. [16] and Huang et al. [17] reported the maximum pressure drop when using R134a was 10 kPa, 27 kPa, 70 kPa and 9 kPa respectively.

Taking into account the total pressure drops, frictional losses contributed up to 90%, while the remaining 10% of pressure losses were due to port, acceleration and gravitational. However, each of refrigerants used outputs in a different value of pressure drop which, influences the overall performance of the system. Also, the range of the maximum pressure drops using the same refrigerant indicates that the conditions applied to the system do greatly influence the performance of LSLHX and LSLHX incorporated VCCs. In addition, the proportionally linear relationship between pressure drop and kinetic energy per volume was reported.

In order to maximize the COP of the VCC, the relationship between the cooling capacity increment due to the subcooling and the increment of power consumption due to the pressure drop has to be optimized. Nevertheless, it is discovered that the operating conditions of the refrigeration system are highly significant to achieve the maximum value of COP. In the industry, VCC systems undergo serval operating conditions. Based on the analysis of previous studies done, the application of LSLHX may be detrimental to the VCC performance under certain system operating conditions or loadings. Hence, there is a need to investigate the behaviour of a VCC cycle that could shift between a basic VCC and LSLHX VCC during on-peak and off-peak loadings respectively. The focus of this study is, first to design and built an experimental VCC that could analyse both basic and LSLHX VCC system at off-peak and on peak loading respectively. Secondly to optimize the heat source and heat sink flow rates, and to validate system performance with published data of identical systems. Lastly, to evaluate the effect of LSLHX engaged in subcooling and full LSLHX operation.

1.2 Research Questions

1. What is the optimum water heat source and heat sink volumetric flow rate combination that outcomes in the best performance?

2. What is the optimum performance of the system through implementing subcooling and LSLHX?

2.Experimental Set-up and Procedure

The design of the experimental setup is utilized through manipulating researches conducted by Navarro-Esbri et al. [9] and Devecioglu and Oruc [11] as depicted in Fig. 1. Water is utilized as the heat source and heat sink in this study where it is piped to flow in the opposite direction of the refrigerant flow of the system. The heat exchange generated using this method is higher than the co-counter flow at a given flow rate. The configuration of the system cycle outputs into different types of cycles like basic, LSLHX and sub-cooling cycle.

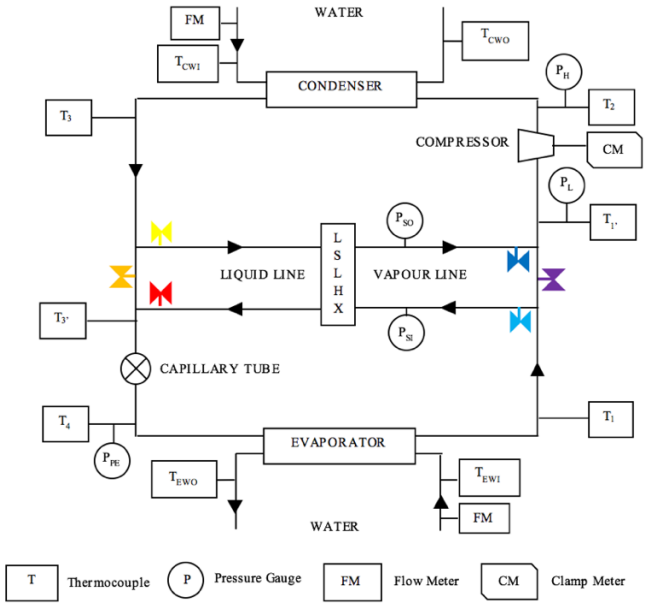


Fig. 1. Schematic diagram of the experiential setup.

The configuration of the working rig is designed to utilize shut-valves to perform the basic cycle, subcooling cycle, and LSLHX cycle separately as shown in Table 3. The actual working rig used in this study is illustrated in Fig. 2. One horse power is used to compress R22 refrigerant into the refrigeration cycle

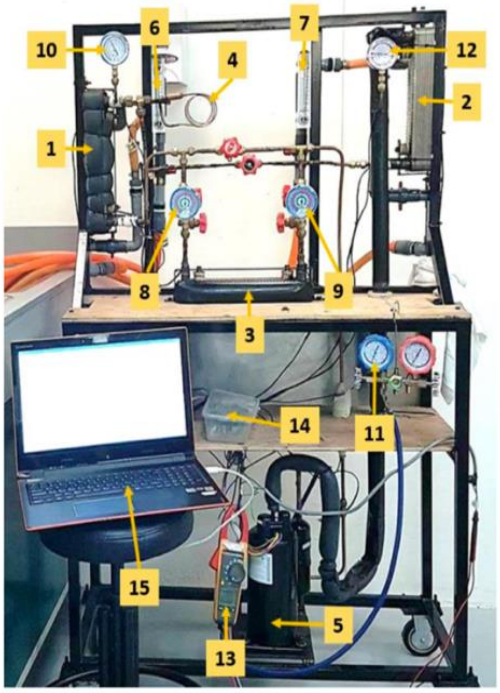
Table 1. Refrigeration cycle configurations.

Cycle	Liquid line			Suction line		
	main	**LSLHX in**	**LSLHX out**	**main**	**LSLHX in**	**LSLHX out**
basic	ON			ON		
LSLHX		ON	ON		ON	ON
Subcooling		ON	ON	ON		

Water flow rate combinations are used to validate the basic vapour compression cycle's performance as seen in Table 2. The flow rate was kept between 1 L/min to 1.5 L/min due to heating load is higher than cooling load however within this range of flow difference, the system was stable. The best performance achieved out of the nine combinations will be considered as the optimum case. Then, the effect of LSLHX will be studied considering the optimum case flow rates.

Table 2. Water flowrate combinations cases.

Condenser water flowrate (l/min)	**Evaporator water flowrate (l/min)**		
	3.5	3.75	**4**
4.5	1 (case A)		
4.75	1.25 (case B)	1 (case A')	
5	1.5 (case C)	1.25(case B')	1 (case ")
5.25		1.5 (case C')	1.25 (case ")
5.5			1.5 (case C")



1) Evaporator
2) Condenser
3) LSLHX
4) Capillary tube
5) Compressor
6) Evap. Flowmeter
7) Cond. Flowmeter
8) Pressure gauge (inlet of LSLHX)
9) Pressure gauge (outlet of LSLHX)

10) Pressure gauge (pre-evap)
11) Pressure gauge (suction)
12) Pressure gauge (discharge)
13) Clamp meter
14) Arduino Uno
15) Computer (data logger)

Fig. 2. Actual experimental setup.

Evaporator - Cooling capacity

The cooling capacity $\dot{Q}_{evap}$ of the system is calculated as given in Eq. (1).

$$\dot{Q}_{evap} = \dot{m}_{Wevap}\, C_{p,water}\, (T_{EWI} - T_{EWO}) = \dot{m}_{ref}\, (h_1 - h_4) \quad (1)$$

Where $\dot{m}_{Wevap}$ is the mass flow rate of evaporator heat source water, Cp_{water} is specific heat capacity of water, T_{EWI} is the evaporator water inlet temperature, T_{EWO} is the evaporator water outlet temperature, $\dot{m}_{ref}$ is the mass flow rate of the working fluid or refrigerant, h_1 is the enthalpy of the working fluid at evaporator outlet and h_4 is the enthalpy of the working fluid at evaporator inlet.

Compressor - Power input

The power input done by the compressor W_{comp} is the product of the potential difference and the current supplied using as in Eq. (2).

$$W_{comp} = VI = \dot{m}_{ref}(h2 - h') \quad (2)$$

Where $\dot{m}_{ref}$ is the mass flow rate of the working fluid or refrigerant, h_2 is the enthalpy of the working fluid at compressor discharge, $h_{1'}$ is the enthalpy of the working fluid at compressor suction, V is the voltage and I is the current consumed by the compressor.

Coefficient of Performance

The coefficient of Performance (COP) is the ratio of the cooling capacity and compressor power consumption, as in Eq. (3).

$$COP = \frac{\dot{Q}_{evap}}{W_{comp}} \quad (3)$$

By substituting Eq. (1) and (2) into Eq. (3), the COP can be also described as in Eq. (4).

$$COP = \frac{\dot{m}_{ref}\, (h_1 - h_4)}{VI} \quad (4)$$

3.Results and Discussion

The system pressure ratio has to be within 3-3.5 to ensure a decent cooling capacity in such refrigeration cycle. The pressure ratios of the water flow rate combinations are depicted in Table 3.

Table 3. Pressure ratios of the basic cycle combinations.

Case	A	B	C	A'	B'	C'	A"	B"	C"
Pressure ratio	3.571	3.289	3.138	3.479	3.293	3.165	3.403	3.338	3.150

As it can be seen from Table 3, all pressure ratios achieved were within the operation range. In cases, A, A' and A" the pressure ratios were slightly higher than the other cases as these cases have 1 l/min flow rate difference. Second highest-pressure ratios appeared in cases B, B' and B" that have 1.25 l/min flow rate difference. While, the lowest pressure ratio occurred at cases C, C' and C", where the flow rate difference was 1.5 l/min. Thus, the pressure ratio drops when increasing the heat source volumetric flow rate difference between the condenser and evaporator.

The performance of the experimental rig was evaluated against the performance outcomes of one horsepower off-the-shelf air conditioner unit used in the study conducted by Rahman and Rahman [18]. In this study, a comparative study between R22 and R290 was performed to study the performance of (VCC) at three different evaporating temperatures such, 16 °C, 19 °C and 22 °C the COPs achieved were 3.18, 3.19 and 3.2 respectively.

3.1.Basic VCC cycle

3.1.1. Power consumption and cooling capacity

Water is used as the heat source and heat sink in this study as opposed to the study conducted by Rahman and Rahman [18]. Cooling capacity and compressor power consumption of the flow rate combinations are compared with the literature as depicted in Fig. 3. The highest cooling capacities were achieved in cases with 1 l/min flow rate these cases are A', A" and A with 2.71 kW, 2.704 kW and 2.68 kW respectively. Also, the second highest cooling capacities were achieved when the water flow rate difference was 1.25 l/min which appeared at cases B', B" and B at 2.669 kW, 2.62 kW and 2.582 kW respectively. While, the least cooling capacities were achieved, when the flow rate difference was 1.5 l/min which, appeared in cases C', C" and C, at 2.548 kW, 2.554 kW and 2.53 kW.

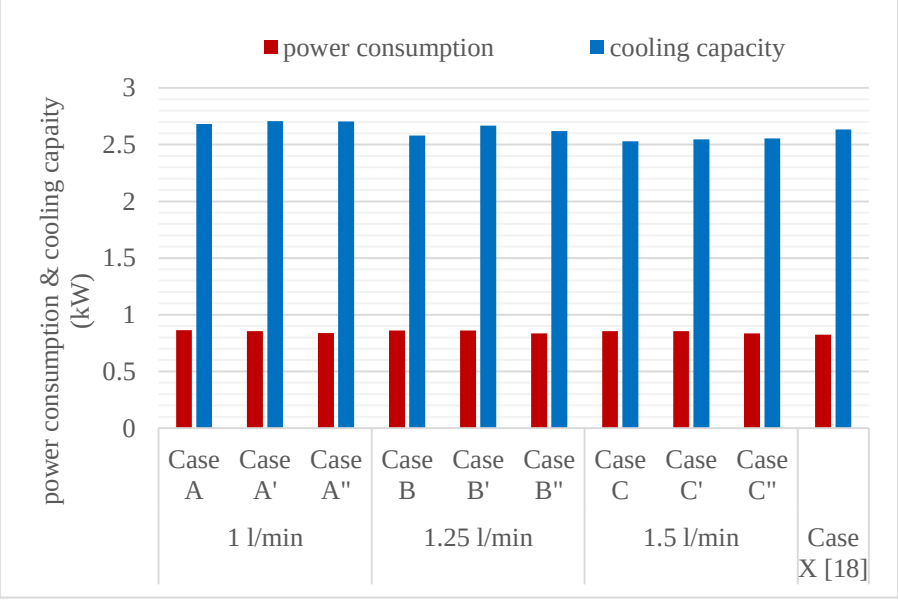


Fig. 3. Basic VCC cooling capacity and compressor power consumption comparison between water flow rate combination cases and Case X [18].

Three flowrate combinations with 1 l/min have successfully achieved higher cooling capacity compared to the literature. Namely, these cases are case A, A' and A" with 1%, 3%, and 7% advantage respectively. On the other hand, the overall power consumption achieved in this study was slightly higher than the power consumption achieved by the literature case X by Rahman and Rahman [18]. However, to explain the rise in power consumption, high flowrate difference consumes high power to stabilize the overall system performance. Nevertheless, the lowest average power consumptions achieved in cases with 1 l/min flow rate followed with 1.25 l/min and 1.5 l/min. Cases C", B" and A", have made the closest agreement to the literature by 98.64%, 98.5% and 98.3% respectively. However, the minor difference in power consumption between the designed working rig and literature may have occurred due to the uncertainties and higher irreversibility in the designed system.

3.1.2. Coefficient of Performance (COP)

COP is the ratio of cooling capacity over compressor power consumption. The value of COP is used to judge the performance of the cooling system in other words, the higher COP value the better the cooling performance. The finest COP values can be achieved when cooling capacity is high while, the compressor power consumption is low. The comparison between the performance of the 9 flow rate combination cases and the literature is illustrated in Fig. 4.

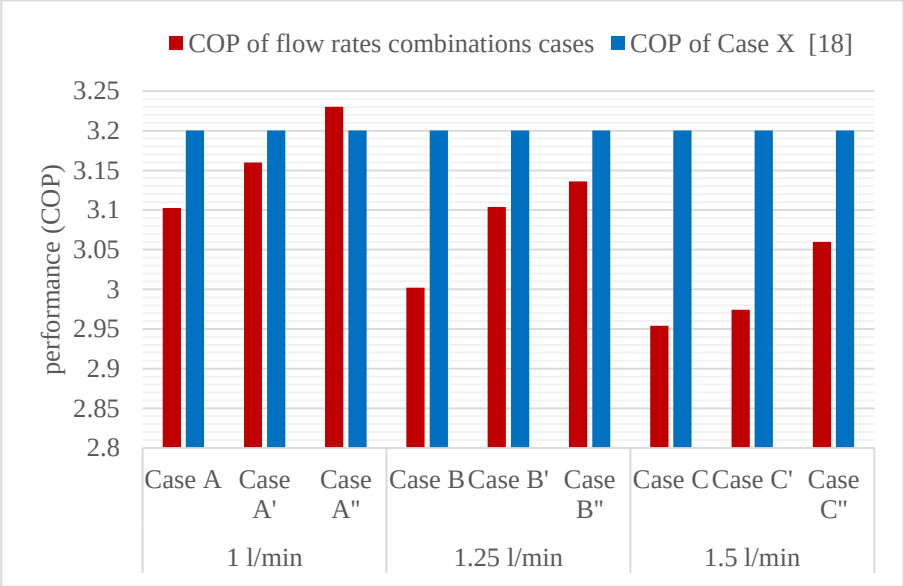


Fig. 4. Comparison between the performance of the flow rate combinations cases and Case X [18].

The highest COPs were achieved by cases with 1 l/min flow rate difference as the best combination case was A" followed by case A' with 3.23 and 3.159 respectively. The second highest COPs were achieved by cases with 1.25 l/min flow rate difference at cases B", B' and B with 3.00, 3.100 and 3.136 respectively. While, the lowest COPs were achieved at cases with 1.5 l/min flow rate difference at cases C", C' and C with 2.953, 2.974 and 3.059 respectively. It is noted that COP significantly improves in each flow rate combination as the water flow rate pumped into the condenser and evaporator of the refrigeration system increased by regular rate. In other words, COP at case A" improves the performance of A' and COP of case A' improves the performance of A; same goes for cases denoted by B and C. However, case A" achieved 3.85% better COP value than case X by Rahman and Rahman [18]. Therefore, case A" with 4 l/min at the condenser and 5 l/min at the evaporator is chosen to be the optimum case of this study as it has achieved the highest COP value compared to other combinations and literature.

3.2.Liquid suction line heat exchanger (LSLHX)

The optimum case or case A" was utilised to study the effect of running full LSLHX and subcooling cycles. However, to study subcooling cycle, refrigerant was permitted to flow as a liquid form in the liquid side of the LSLHX while the suction vapour was permitted to flow in the basic main line. On the other hand, to study the effect of running full LSLHX, both suction and liquid sides of the basic cycle were closed while the suction and vapour lines of the LSLHX were open.

3.2.1. Power consumption and cooling capacity

Comparison between the effect of subcooling cycle and engaging full LSLHX cycle on system's cooling capacity and power consumption is illustrated in Fig. 5. Cooling capacity has improved by 7.14% when subcooling system was implemented while it has dropped by 51.28% when full LSLHX cycle was implemented.

The decline of the cooling capacity of full LSLHX system can be explained by two observations. Dysfunction of expansion, where it was noted that the working fluid enters and leaves the expansion device (capillary tube) at the similar temperature. LSLHX system was oversized to fit one-horsepower system with R22. In other words, the system was not expanding, because it was overly subcooling and the capillary tubes could not endure the capacity of the liquid. However, the compressor power consumption was reduced when implementing subcooling and full LSLHX by 3% and 7.93 % respectively. LSLHX compressor power reduction was more significant than subcooling due to the significantly low in the pressure ratio caused by the dysfunction of the capillary tubes.

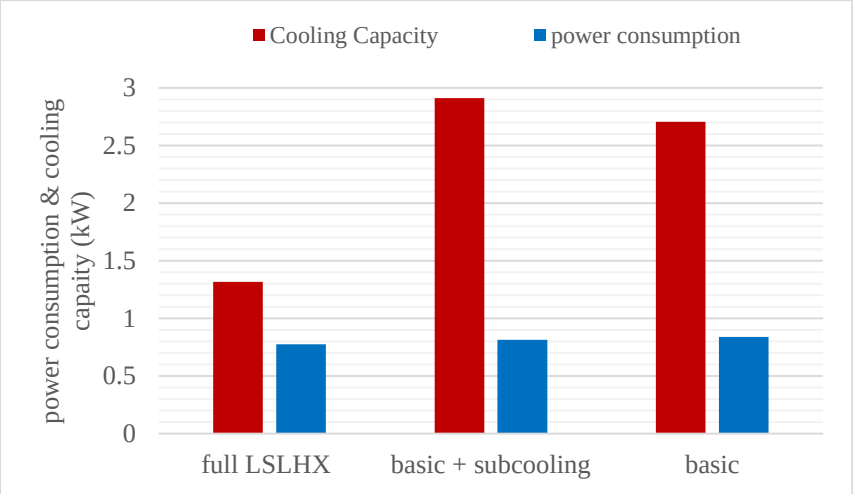


Fig. 5. The effect of subcooling and full LSLHX on the performance based on the optimum case.

3.2.2. Coefficient of performance (COP)

The effect of subcooling and engaging full LSLHX on the COP is illustrated in Fig. 6. Based on the results conducted, when implementing subcooling COP increased by 9.94% while it dropped by 47.42% when engaging the full LSLHX. However, the significant drop in the performance of the full LSLHX cycle was due to the low cooling capacity.

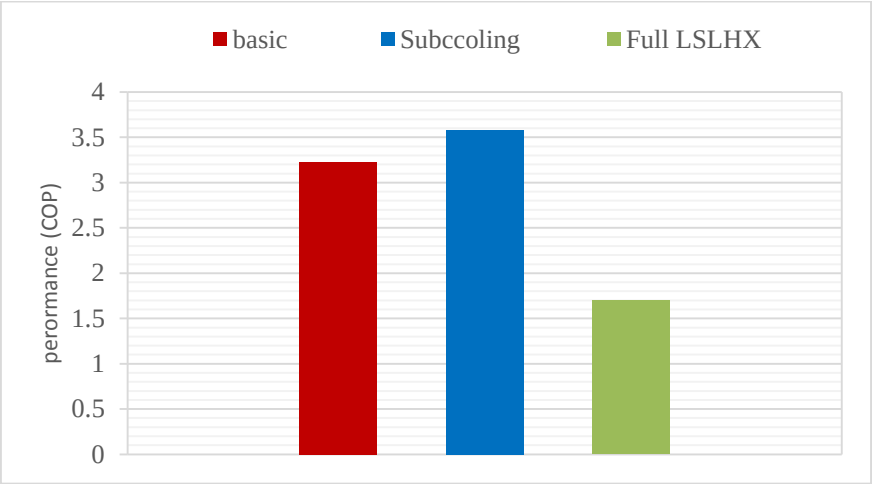


Fig. 6. The effect of subcooling and full LSLHX on the performance based on the optimum case.

To understand the behaviour of the system under 1 l/min flow rate, case A', and case A have been tested using similar approach as case A". When subcooling was applied, both cases A and A' have experienced improvement by 8% and 3.5% respectively. The system performance in case A and case A' have dropped by 50.6% and 47.4% respectively when the full LSLHX has been engaged. Thus, the trend achieved is similar to the optimum case.

Subcooling cycle has significantly improved the performance of the cooling system while full LSLHX cycle was an unstable approach to improve the performance of the system. Qureshi and Zubair [4] and Pottker and Hrnjak [5, 10] have achieved performance improvement when using mechanical subcooling approach as it has increased the cooling capacity and saves energy. On the other hand, the drop in the coefficient of performance at LSLHX cycle can by justified by Domanski and Didion [6] as LSLHX can affect the performance of the cooling system negatively. As the performance of the LSLHX depends highly on the operating condition of the system. In this study, it was found out that to achieve positive results utilizing LSLHX using R22 and R 134a, the difference between condenser and evaporator temperatures must be at least 45 °C and 13 °C respectively. But, the temperature difference achieved in the working rig at the optimum case was 22 °C.

There are several approaches that can be considered to overcome the drawbacks occurred when LSLHX was fully engaged into this system. Firstly, to change the working fluid from R22 to R134a. Considering, R134a operates more significantly at low rangers of temperature can operate better under the low range of temperature difference between the evaporator and condenser. Secondly, to change the expansion device from capillary tube to eternally equalizing thermal expansion valve (EETXV) as it provides the cooling systems with significantly more stable expansion process. And, to replace the constant speed compressor used by variable speed compressor (VCC) as it adopts the changes in capacity, stabilizes the pressure ratio and the overall performance of the system.

4.Conclusion and Future Works

In conclusion, the performance of basic VCC was identified based on cooling capacity and power consumption of 9 flow rate combinations. After that, the COPs of the flow rate combinations were compared to the literature. The highest pressure rations were achieved at achieved at flow rate combinations with 1 l/min flowed by 1.25 L/min and 1.5 L/min. However, case A" has achieved very performance advancement by 3.85% compared to the literature [18] therefore I was considered as the optimum case of this study. The performance of full LSLHX and subcooling cycle solely have been evaluated utilising the case A". the performance was improved by 9.94% at subcooling solely cycle. On the other hand, the performance has dropped to half when full LSLHX cycle was utilised. The significant drop in performance at LSLHX is due to the oversized LSLHX which resulted in over

subcooled liquid that was over the capacity of the expansion device. In favour of improving the performance of LSLHX in future works, an alternative refrigerant to be used like R 134a in the system to achieve the range of the required operating conditions. And, to implement VSC to adopt changes in capacity and to stabilize the pressure ratio and the overall performance. Also, an alternative expansion device to be used such EETXV to stabilize the expansion process and to adopt changes in capacity.

Reference

1. Kubota, T.; Jeong, S.; Hooi, D.; and Ossen, D. (2011). Energy consumption and air-conditioning usage in residential buildings of Malaysia. *Journal of International Development and Cooperation*, 17(3), 61-69.
2. Naif, A.; Al-Obaidi, A.S.M.; and Nassir, M.H. (2015). Effect of evaporator heater power input and refrigerant flow rate on the performance of a refrigerator - Developing empirical models. *Journal of Mechanical Engineering and Automation*, 5(1), 20-28.
3. Park, C.; Lee, H.; Hwang, Y.; and Radermacher, R. (2015). Recent advances in vapor compression cycle technologies. *International Journal of Refrigeration*, 60, 118-134.
4. Qureshi, B.; and Zubair, S.M. (2013). Mechanical sub-cooling vapor compression systems: Current status and future directions. *International Journal of Refrigeration*, 36(8), 2097-2110.
5. Pottker, G.; and Hrnjak, P. (2015). Experimental investigation of the effect of condenser subcooling in R134a and R1234yf air-conditioning systems with and without internal heat exchanger. *International Journal of Refrigeration*, 50, 104-113.
6. Domanski, P.; and Didion, D. (1994). Evaluation of suction-line/liquid-line heat exchange in the refrigeration cycle. *International Journal of Refrigeration*, 17(7), 487-493.
7. Aprea, C.; Ascani, M.; and Rossi, F. (1999). A criterion for predicting the possible advantage of adopting a suction/liquid heat exchanger in refrigerating system. *Applied Thermal Engineering*, 19(4), 329-336.
8. Klein, S.A.; Reindl, D.T.; and Brownell, K. (2000). Refrigeration system performance using liquid-suction heat exchangers. *International Journal of Refrigeration*, 23(8), 588-596.
9. Navarro-Esbrí, J.; Molés, F.; and Barragán-cervera, Á. (2013). Experimental analysis of the internal heat exchanger influence on a vapour compression system performance working with R1234yf as a drop-in replacement for R134a. *Applied Thermal Engineering*, 59(1-2), 153-161.
10. Pottker, G.; and Hrnjak, P. (2015). Effect of the condenser subcooling on the performance of vapor compression systems. *International Journal of Refrigeration*, 50(217), 156-164.
11. Devecioğlu, A.G.; and Oruç, V. (2017). The influence of plate-type heat exchanger on energy efficiency and environmental effects of the air-conditioners using R453A as a substitute for R22. *Applied Thermal Engineering*, 112(517), 1364-1372.
12. Zhang, J.; Desideri, A.; Kærn, M. R.; Ommen, T. S.; Wronski, J.; and Haglind, F. (2017). Flow boiling heat transfer and pressure drop characteristics of R134a, R1234yf and R1234ze in a plate heat exchanger with conditions prevailing in the evaporator of organic Rankine cycle units. *International Journal of Heat and Mass Transfer*, 108(Part B), 1787-1801.
13. Imran, M.; Usman, M.; Yang, Y.; and Park, B.-S. (2017). Flow boiling of R245fa in the brazed plate heat exchanger: Thermal and hydraulic performance assessment. *International Journal of Heat and Mass Transfer*, 110, 657-670.
14. Longo, G.A.; and Gasparella, A. (2007). Refrigerant R134a vaporisation heat transfer and pressure drop inside a small brazed plate heat exchanger. *International Journal of Refrigeration*, 30(5), 821-830.
15. Yan, Y.Y.; and Lin, T.F. (1999). Evaporation Heat transfer and pressure drop of refrigerant R-134a in a plate heat exchanger. *Journal of Heat Transfer*, 121(1), 118.

16. Jassim, E.W.; Newell, T.A.; and Chato, J.C. (2006). Refrigerant pressure drop in chevron and bumpy style flat plate heat exchangers. *Experimental Thermal and Fluid Science*, 30(3), 213-222.
17. Huang, J.; Sheer, T.J.; and Bailey-Mcewan, M. (2012). Heat transfer and pressure drop in plate heat exchanger refrigerant evaporators. *International Journal of Refrigeration*, 35(2), 325-335.
18. Rahman, M.M.; and Rahman, H.Y. (2013). Hydrocarbon as refrigerant for domestic air conditioner: A comparative study between R22 and R290. *Elixir Thermal Engineering*, 53, 11976–1197

EURECA 2018 – Conference Paper
Paper number 2EE01

System Protection Coordination Study For Taylor's University Electrical Distribution System

Chew Ai Chin, Reynato Andal Gamboa*

School of Engineering, Taylor's University, Taylor's Lakeside Campus, No. 1 Jalan Taylor's, 47500, Subang Jaya, Selangor DE, Malaysia
*Chew Ai Chin: aichin.chew@sd.taylors.edu.my

Abstract

System protection coordination studies are important in power system networks to ensure the continuity of service in the system. This paper presents relay coordination and tripping sequence of circuit breakers for Taylor's University using Electrical Transient Analysis Program (ETAP) by choosing appropriate relay and circuit breaker settings after conducting load flow and fault analysis to find the relay pick up current and plug setting multiplier. Two different buses were simulated for three-phase fault to ensure the circuit breakers have proper tripping sequence and timing. The results obtained for transformer 2 load bus MSB 2 have short circuit value of 31.7 kA and tripping time for breakers CB-T2L as primary protection, CB-T2H and CB-IF2 as backup protection are 30.6 ms, 472 ms and 507 ms respectively. For transformer T4 load bus MSB 4, the fault current obtained is 46.8 kA and the tripping time for breakers CB-T4L as primary protection, CB-T4H, and CB-IF2 as back up protection are 30.7 ms, 196 ms and 413 ms respectively. The back-up protection for each protective device is achieved by ensuring appropriate coordination time interval between the protective devices for a more reliable protection. The time-current characteristics curves (TCC) for relays and low voltage circuit breakers were presented to show the interrupting time of the devices based on the current level.

Keywords: Protection Coordination, Circuit Breakers, Protective Relays, ETAP

5.Introduction

Power distributed in a commercial building is used to operate lighting loads, electrically operated devices and motor loads [1]. These loads need to be isolated when a system fault occurs. Faults or short circuit in a power system occurs when larger values of current compared to the normal condition current flow into the system as a result of the short circuit [2]. Some causes of faults are natural disasters, lightning, and faulty equipment. Single phase to ground faults make 70% to 80%, phase to phase to ground faults 17% to 10%, phase to phase faults 10% to 8% and three phase faults 3% to 2% [3]. Faults in any parts of a system should be prevented from happening and must be isolated from the rest of the system as soon as possible for the distribution system to function satisfactorily.

Protective devices are used to accomplish this. A protection devices team is made up of circuit breakers, current transformers, protective relays and a battery system as shown in Figure 1 [4].

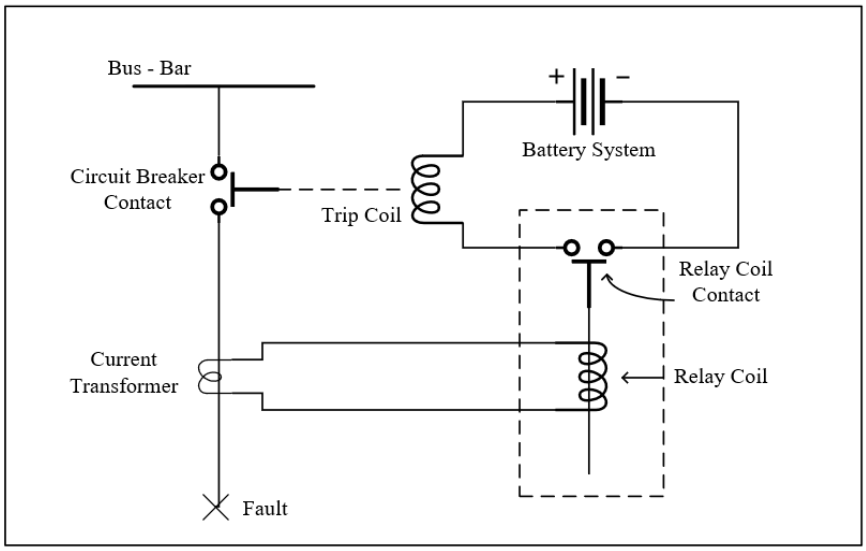


Figure 1. Single Line Diagram of a Protection Team
(Source: Principles of Power System [3])

Taylor's University's Electrical Distribution System (TUEDS) is the subject chosen for this assessment as TUEDS applies for this system protection. TUEDS consists of two substation transformers each with two main feeder loads and protected by power circuit breakers at different locations in the system as shown in Figure 2 [5]. The incoming power supply to TUEDS is 11kV with a frequency of 50Hz. The said system was studied by previous researchers which focused on peak demand control [6] and system performance assessment [5]. One of the major operational control of any distribution system is the correct sizing and setting of protective devices and their respective protection coordination. TUEDS applies a similar protection scheme.

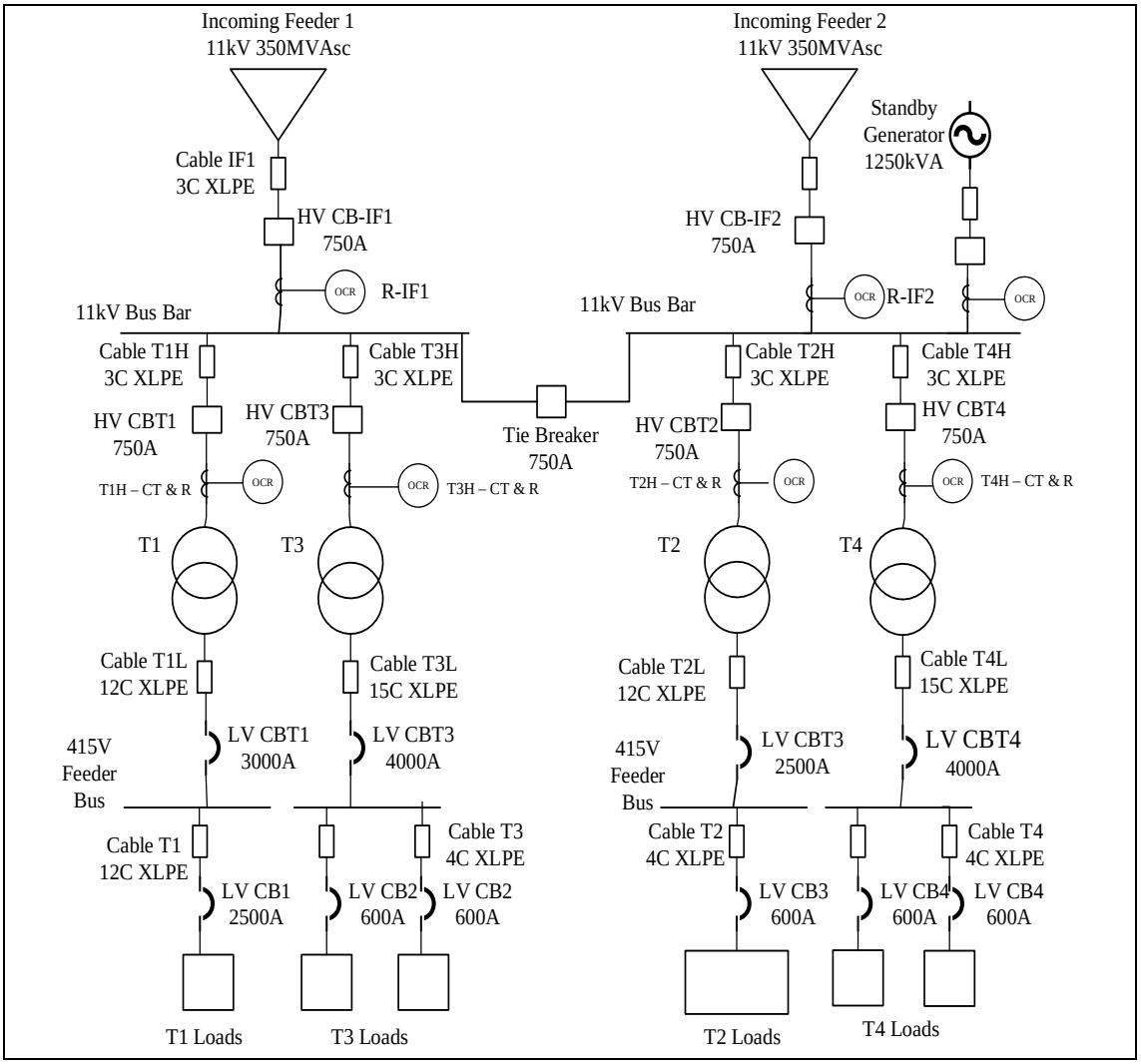


Figure 2. Single Line Diagram of Taylor's University Electrical Distribution System [5]

Proper protective device settings and relay coordination are required to ensure normal system operation at all times. The coordination of protective devices is essential in distribution systems to have least interruptions and restoration time. The effects of faults can be minimized or the whole system will break down [7]. Protective device coordination is a time sequence operation and is carried out to determine the tripping settings of each protective device in a power system so that maximum protection with minimum interruption is provided for all kinds of faults that may occur in the system [8]. This assessment can help prevent equipment failures within a system to prevent the shut down of the whole facility. The simulation of the coordination of protective devices, when subjected to fault conditions at any point in the system was carried out using ETAP software.

For protection system coordination on ETAP, previous researchers conducted the following studies consisting of load flow study, fault analysis, and protective relay coordination. All these researchers conducted protection system coordination using the same methods. Champa [9] *et al.* conducted a study on overcurrent relay coordination of a 33kV radial industrial power plants and presented load flow and short circuit analysis and concluded that

overcurrent relays need to be set properly as they provide correct discrimination and act as primary and back up protection devices. Saini [10] studied overcurrent relay coordination for phase and earth faults using ETAP by conducting load flow and finding the fault current to coordinate the relay settings. Mahapatra [11] *et al* focused on optimum overcurrent relay coordination of a power grid and also conducted load flow and short circuit study to obtain the operating time of the relays for the relays coordination. Patel [12] *et al* conducted relay coordination on ETAP by first conducting load flow and fault analysis to calculate the plug settings (PSM) and time multiplier settings (TMS) for the protective relays. Thangalakshimim [13] studied planning and coordination of relays in the distribution system by conducting load flow and short circuit analysis and used to fault current obtained to find the operating time to set the relay settings. Pho [14] simulated and analysed fault conditions in ETAP to determine the protective device coordination for cable, bus, and transformers and set the relay settings using STAR module to coordinate the TCC curves associated with the protective relays. Thanigaivel [15] *et al* studied the power flow analysis and protection coordination of Sri Muthukumaran Institute of Technology (SMIT) in Chennai, India by collecting data from SMIT and conducting load analysis and fault analysis to find out protective devices that are overloaded and used the fault current calculated to coordinate the protective devices. Time Current Coordination (TCC) curves for a particular portion of the system was drawn to show the coordination of devices and the circuit breakers are coordinated in downstream sequence to avoid blackout conditions.

Previous students of Taylor's University have conducted studies on TUEDS but no study was done to emphasize on the protective device coordination of TUEDS. Other researchers from various institutes used ETAP software to study load flow, fault analysis, and protective device coordination on industrial and commercial buildings to ensure that the buildings have proper protective device coordination. For TUEDS, similar study and analysis as Thanigaivel's [15] *et al* were done. The assessment of protective device coordination for TUEDS was focused on the protective relay and circuit breaker coordination. The objective of this study is to evaluate the settings of the protective devices to determine the tripping sequence of circuit breakers and relays.

6. Research Methodology

The methodology is simplified in the flowchart shown in Figure 3.

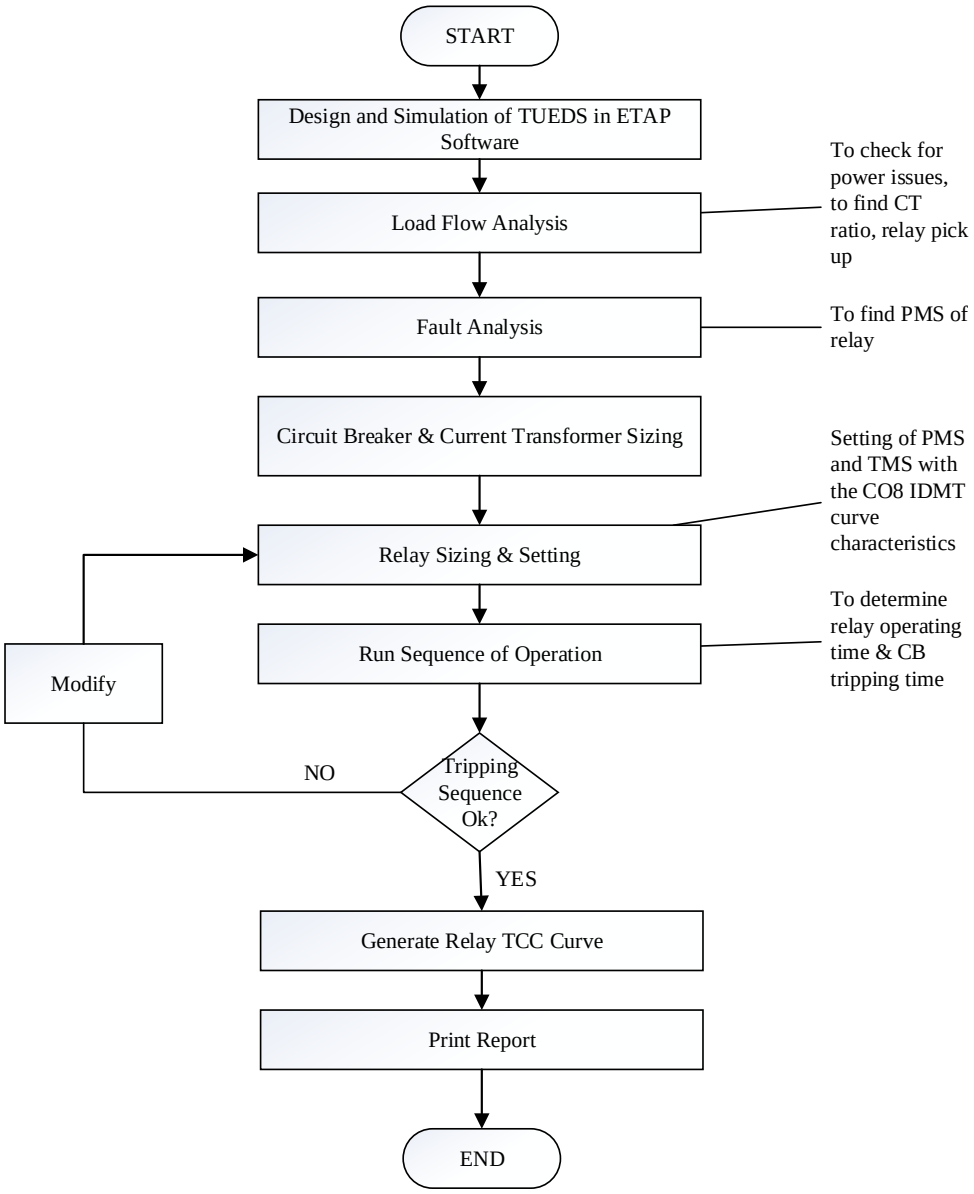


Figure 3. Research Methodology

Load flow and short circuit study are essential in relay coordination. The functional type relays available that will be used are overcurrent relays. Relay coordination is done to check whether the relay is fast and reliable enough to detect the fault at the proper time and send the signal to the circuit breaker. The overcurrent relay shows the relationship between the relay operating time in plug setting multiplier (PMS) and time multiplier setting (TMS) [11]. The overcurrent relay setting for radial distribution system is the PSM and TMS. Load flow study determines the CT ratio and short circuit analysis can decide the PSM setting of the relay. The pick-up current is the minimum current in the relay coil when the relay starts to operate to open the circuit breaker. The rated current through the relay or pickup setting (amps) was found using [12]

$$\text{Pick up} = \frac{\frac{MVA\ x\ 1000}{\sqrt{3}\ x\ rated\ voltage\ (L-L)}}{CT\ ratio} \quad (1)$$

Pick-up current can be used to find the current setting of the relay is needed to adjust the pick-up current to any value that is required. Each relay is associated with a current transformer. The current setting was found using

$$\text{Pick-up current} = \text{rated secondary current of C.T. } x \text{ current setting} \quad (2)$$

Using PSM the TMS of the backup relay can be found. PSM is the ratio of a fault current in the relay coil to the pick-up current.

$$\text{PSM} = \frac{fault\ current\ in\ relay\ coil}{pick-up\ current}$$

$$= \frac{fault\ current\ in\ relay\ coil}{rated\ secondary\ current\ of\ CT\ x\ current\ setting} \quad (3)$$

The TMS is the control to adjust the time of operation of the relay. The time dial setting usually has a calibration from 0 to 1 in the steps of 0.5s. These are multipliers used to convert the time derived from PSM curve to the actual operating time of relay.

$$\text{TMS} = \text{time setting multiplier } x \text{ PSM of the relay from curve} \quad (4)$$

For this study, the TMS for the relays for primary protection devices are set to 1 and back up protection relays are set to 1.5.

The general equation for the CO8 standard inverse definite minimum time (IDMT) overcurrent relay for the operating time, t_{op} of the relay is [16]

$$t_{op} = \frac{0.14\ TMS}{(PSM)^{0.02}-1} \quad (5)$$

The time-current characteristics curve (TCC) for low voltage circuit breakers were produced as the voltage and current for small power systems are too large for the relays to detect directly. High voltage circuit breakers do not have TCC as in large systems the sensing function of the fault is done by the protective relays and the switching function is done by the

circuit breakers to safely interrupt the fault current and the relays TCC characteristics were shown.

7. Results and Discussion

The TUEDS system was designed as shown in Figure 4, Figure 5 and Figure 6 respectively.

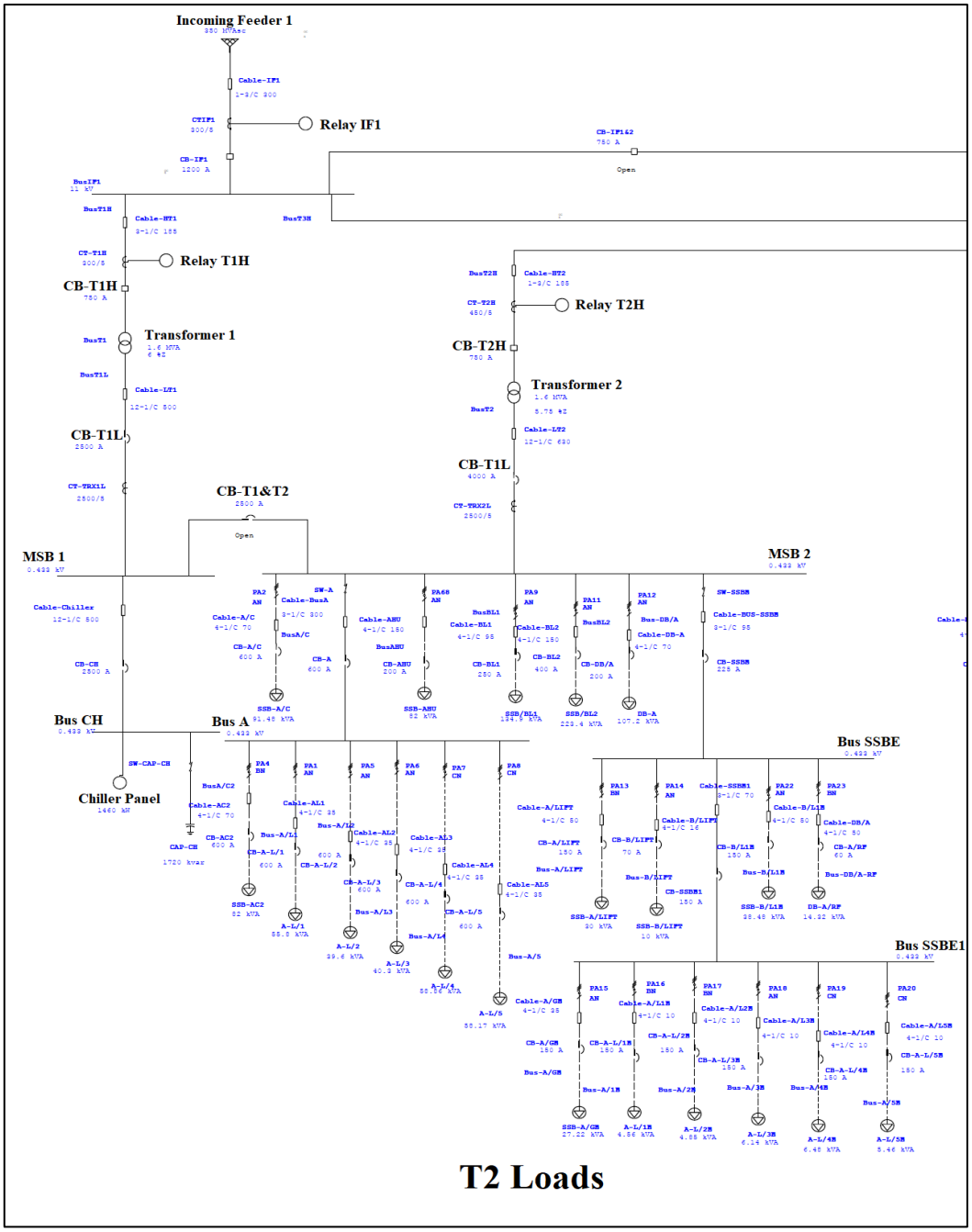


Figure 4. TUEDS System on ETAP – Transformer 1 and Transformer 2 Loads

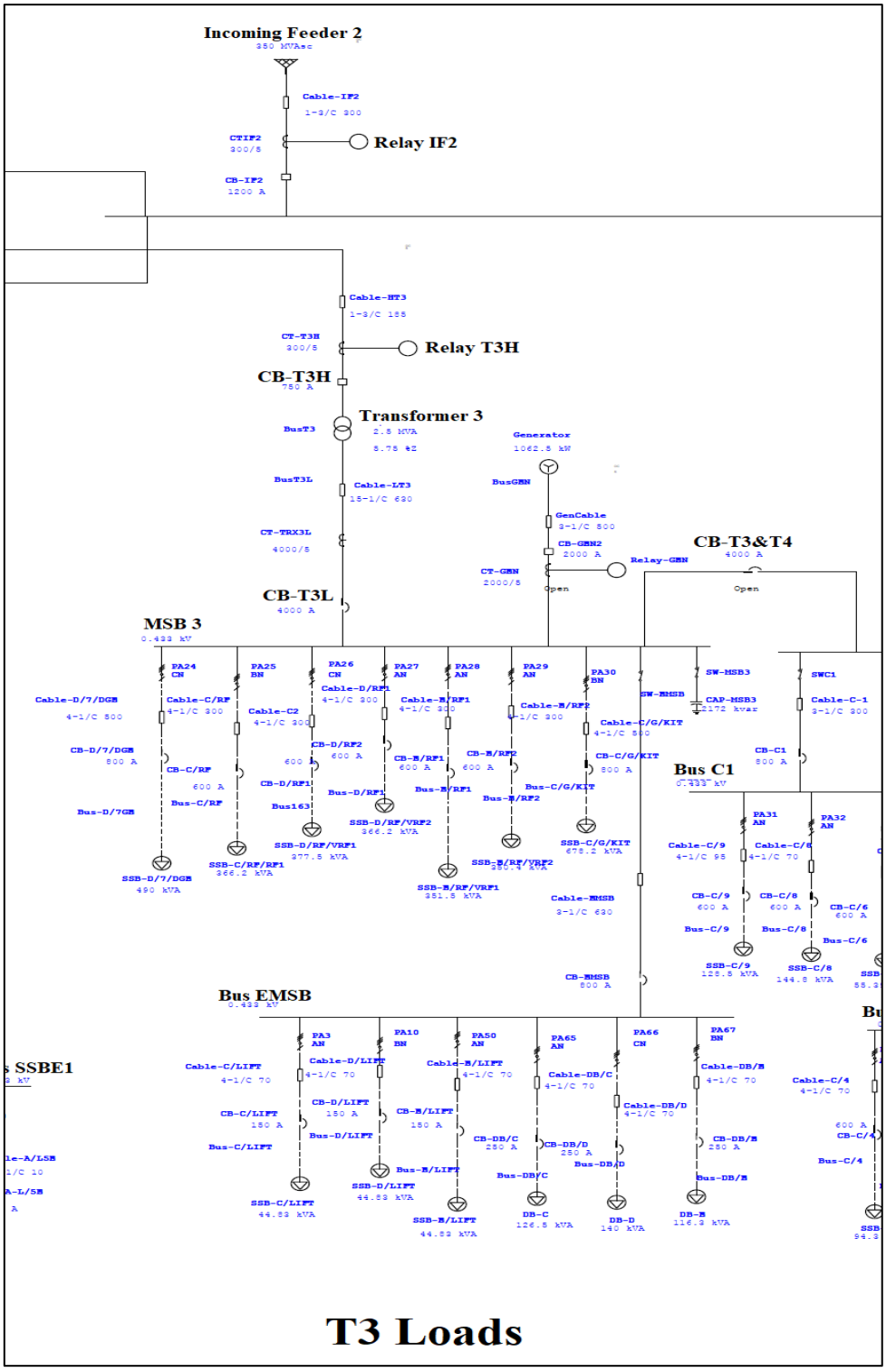


Figure 5. TUEDS System on ETAP – Transformer 3 Loads

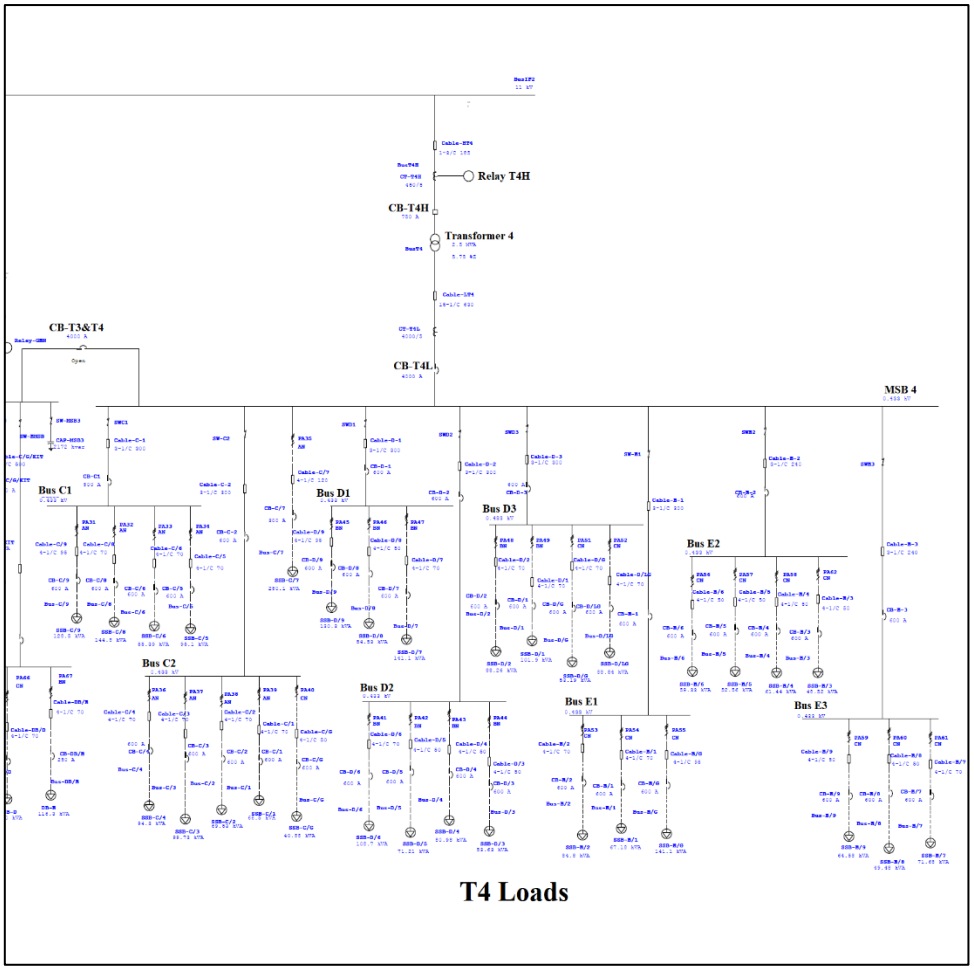


Figure 6. TUEDS System on ETAP – Transformer 4 Loads

After conducting load flow and fault analysis, the CT ratio, relay pickup, PMS, TMS and operating time, t_{op} was calculated using eq 1, 2, 3 and 5 respectively and tabulated in Table 1.

Table 4. Bus Relay Settings

Bus	CB & Relay	Full Load Current (A)	CT Ratio	Max Fault Current (kA)	Relay Pick up/Tap Setting (A)	PMS	TMS	T_{op} (ms)
IF1	IF1	226	300:5	18.37	4	76.54	1	762
IF2	IF2	177.3	300:5	18.37	3	102	1.5	1102
T1	H-T1	87.9	300:5	18.37	2	153	0.5	350
	L-T1	2234	2500:5	-	-	-	-	-

T2	H-T2	47.7	450:5	18.37	5	204	0.5	392
	L-T2	1212	2500:5	-	-	-	-	-
T3	H-T3	141.7	450:5	18.37	2	102	0.5	350
	L-T3	3600	2500:5	-	-	-	-	-
T4	H-T4	129.6	300:5	18.37	3	102	0.5	367
	L-T4	3293	4000:5	-	-	-	-	-

All transformer relays, relays T1H, T2H, T3H and T4H which are closer to the loads have a TMS of 0.5 and the incoming feeder relays, relay IF1 and IF2 have a time dial of 1 so that it operates as fast as possible with minimum interrupting time. For PSM of lesser than 1, normal current is flowing through the circuit and no tripping will occur. When the PSM is more than 1, it indicates that there is fault current flowing through the circuit and the more value of PSM shows the multiples of fault current flowing through the circuit.

The tripping sequence for two buses, MSB 2 and MSB 4 was done to ensure correct tripping sequence during fault at the selected bus. The 3-phase fault is simulated at Bus MSB 2 which consists of loads from transformer 2. The sequence when each breaker trips is shown in Figure 7.

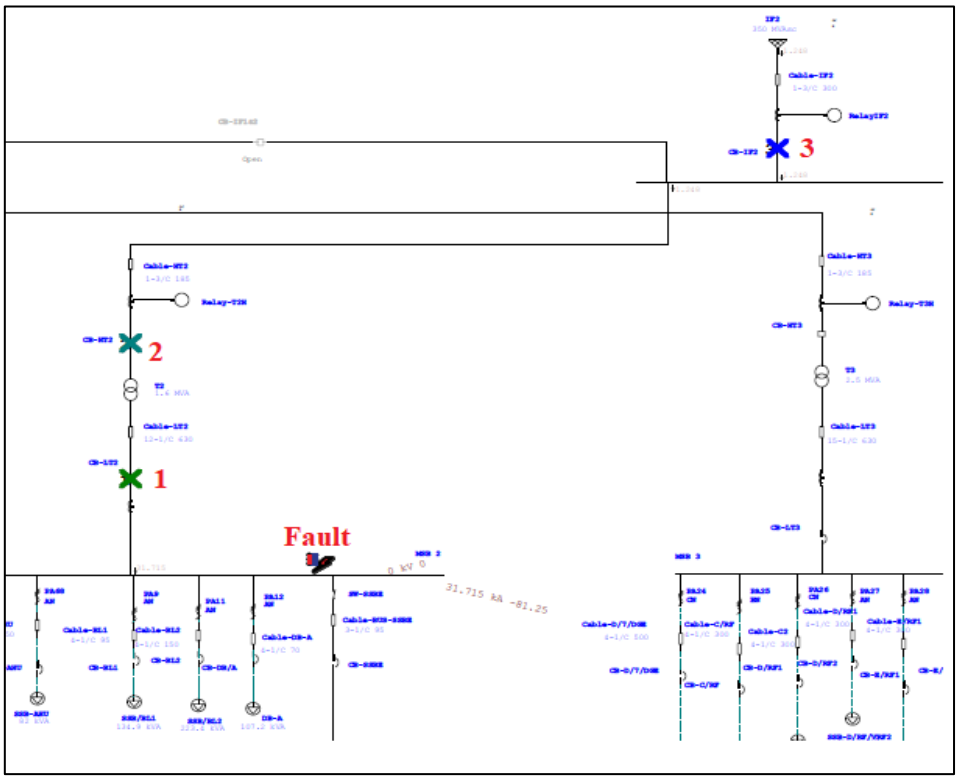


Figure 7. Tripping Sequence for Fault at MSB 2 at Transformer 2

The TCC produced shows how fast the breaker and relay will trip at certain current level. The higher the current, the shorter the time the protective devices will act The TCC curve for a fault at Bus T4 is shown in Figure 8.

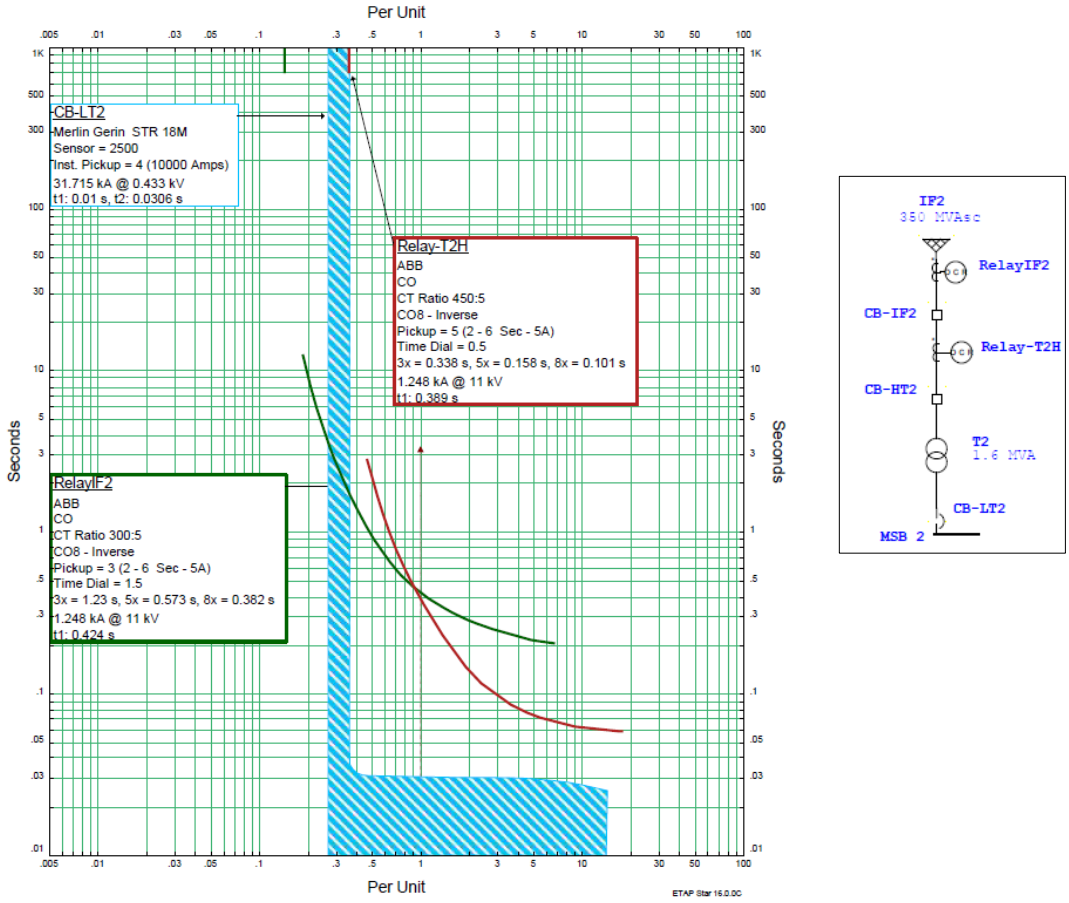


Figure 8. TCC curve for Fault at Bus MSB 2 at Transformer 2

When a fault occurs at MSB 2, CB-T2L will trip first, followed by CB-T2H and then CB-IF2 as they act as back up to CB-T1L. The TCC produced shows how fast the breaker and relay will trip at certain current level. The top part of the TCC shows the overload tripping component of the circuit breaker performance and the bottom part shows the instantaneous trip component of the breaker. The time it takes for the breakers to open completely or called the maximum clearing time will decreases when current increases. Therefore, the higher the fault current the faster the breaker will trip or the higher the current, the shorter the time the protective devices will act. The tripping time for each breaker is tabulated in Table 2.

Table 2. Tripping Time for Fault at Bus MSB 2

Device	Type of Protection	Time (ms)	Fault (kA)	Current

CB-T2L	Primary	30.6	31.7
Relay T2H	Back up	389	1.248
Relay IF2	Back up	424	1.248
CB-T2H	Back up	472	1.248
CB-IF2	Back up	507	1.248

The second tripping sequence was conducted in transformer 4 load bus MSB 4 as shown in Figure 9.

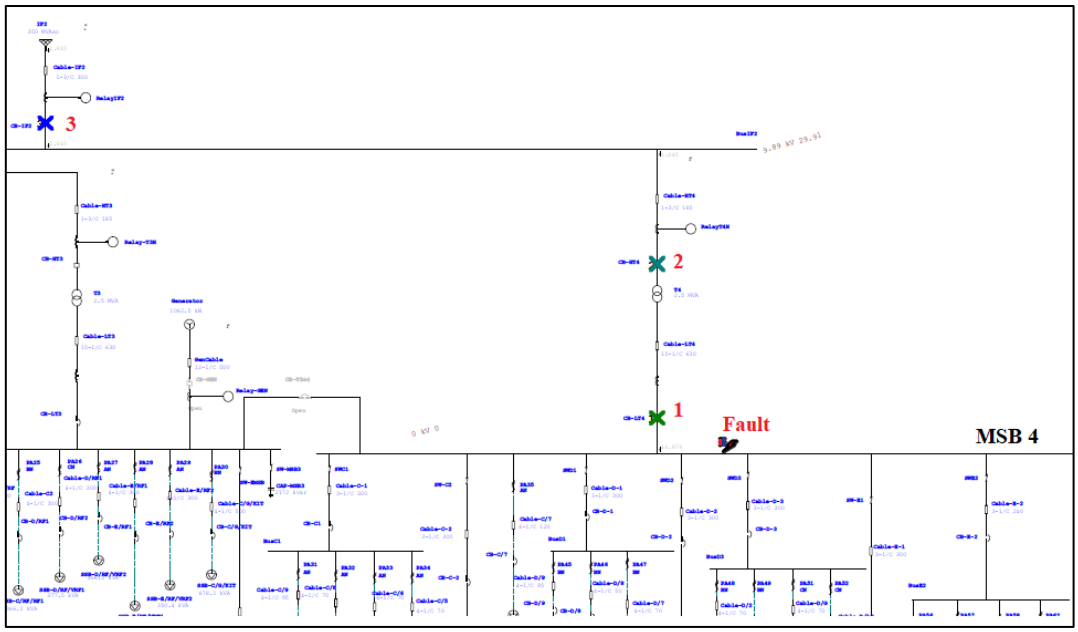


Figure 9. Tripping Sequence for Fault at Bus MSB 4

The TCC produced shows how fast the breaker and relay will trip at certain current level. The higher the current, the shorter the time the protective devices will act The TCC curve for relays and breakers used during a fault at Bus MSB 4 is shown in Figure 10.

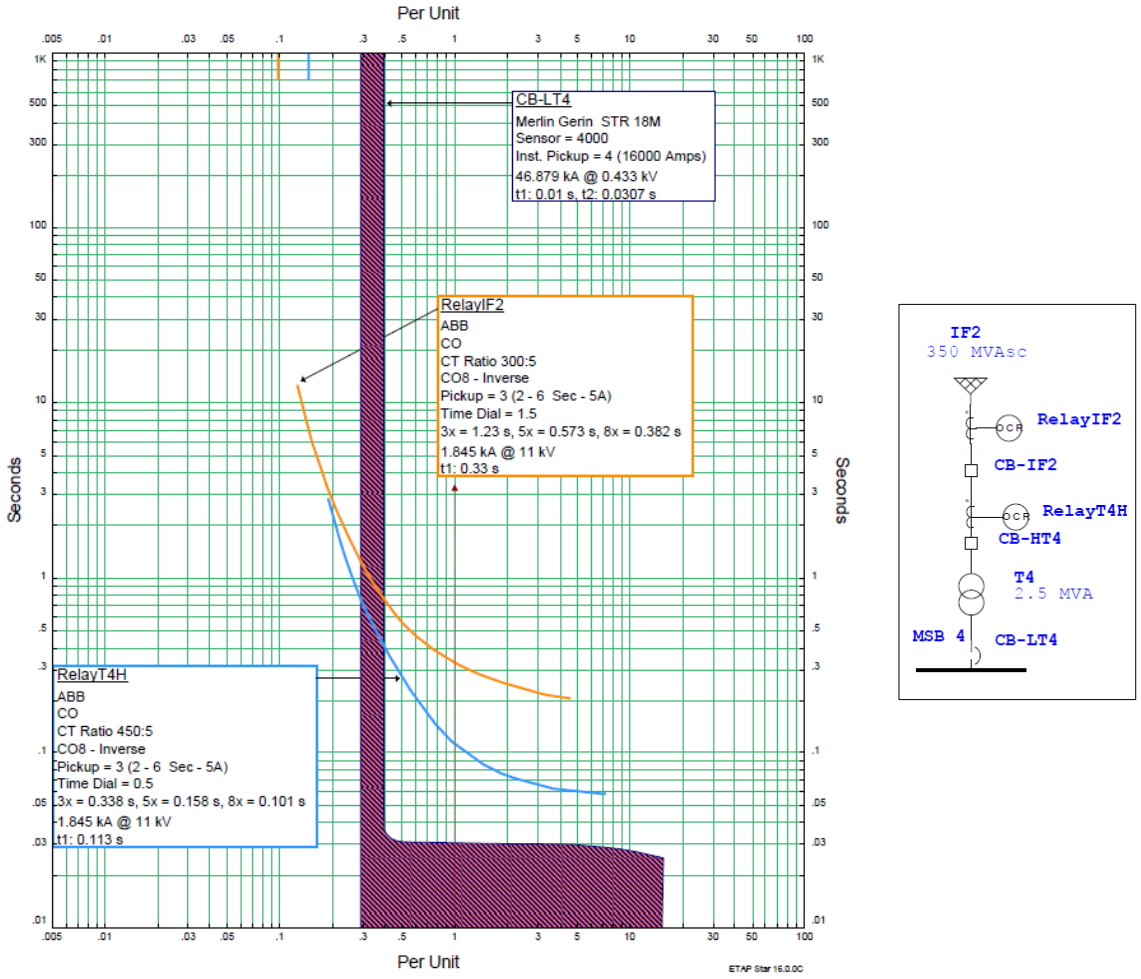


Figure 10. TCC curve for Fault at Bus MSB 4 at Transformer 4

When a fault occurs at MSB 4, CB-T4L will trip first, followed by CB-T4H and then CB-IF2 as they act as back up to CB-T4L. The TCC produced shows how fast the breaker and relay will trip at certain current level. The top part of the TCC shows the overload tripping component of the circuit breaker performance and the bottom part shows the instantaneous trip component of the breaker. The time it takes for the breakers to open completely or called the maximum clearing time will decreases when current increases. Therefore, the higher the fault current the faster the breaker will trip or the higher the current, the shorter the time the protective devices will act. The tripping time for each breaker is tabulated in Table 3.

Table 3. Tripping Time for Fault at Bus MSB 4

Device	Type of Protection	Time (ms)	Fault Current (kA)
CB-T4L	Primary	30.7	46.8
Relay T4H	Back up	113	1.845

CB-T4H	Back up	196	1.845
Relay IF2	Back up	330	1.845
CB-IF2	Back up	413	1.845

Tripping sequence was also conducted at MSB 1 and MSB 3. The tripping time for fault at MSB 1 and MSB 3 are tabulated in Table 5 and Table 6 respectively.

Table 5. Tripping Time for Fault at Bus MSB 1

Device	Type of Protection	Time (ms)	Fault Current (kA)
CB-T1L	Primary	30.9	30.4
Relay T1H	Back up	85.9	1.2
CB-T1H	Back up	169	1.2
Relay IF1	Back up	378	1.2
CB IF1	Back up	461	1.2

Table 6. Tripping Time for Fault at Bus MSB 3

Device	Type of Protection	Time (ms)	Fault Current (kA)
CB-T3L	Primary	31.1	46.9
Relay T3H	Back up	71.1	1.85
CB-T3H	Back up	154	1.85
Relay IF1	Back up	262	1.806
CB IF1	Back up	345	1.806

Coordination for the relay and breaker settings can be further improved by dragging the relay characteristics in the TCC graph. The relay parameters such as PSM and TMS will be changed automatically. The TMS for Relay IF2 was changed to 1.5 as it trips faster than CB-T2H during tripping sequence of fault at MSB 2. The overall circuit breakers and relays TCC curves are shown in Figure 11 and Figure 12 respectively.

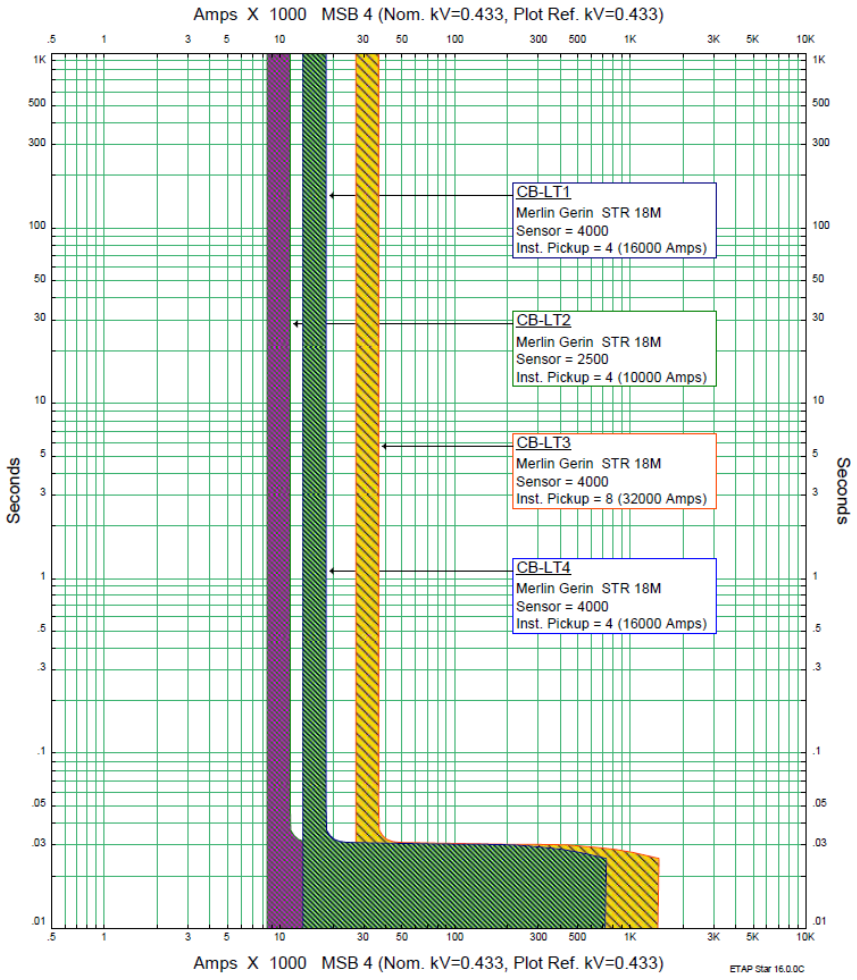


Figure 11. TCC Curve for Circuit Breakers

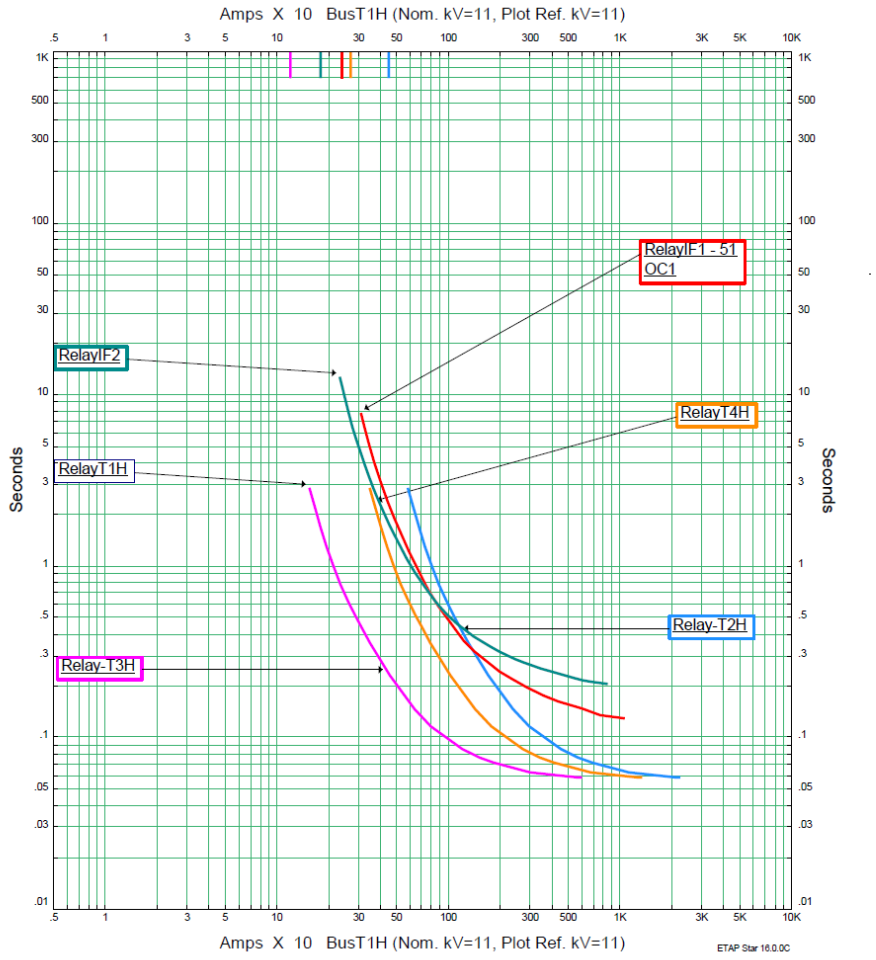


Figure 12. TCC curve for Protective Relays

Relay IF1 and IF2 have a time dial of 1 and 1.5 respectively and relay IF2 has a higher y axis location compared to other relays. Relay T1H to T4H have a time dial of 0.5 and are also in the same y axis location. The x axis which is different due to the pick-up current of each relays. Table 7 shows the relay trip time at multiple pick up currents.

Table 7. Tripping Time for Relays

Relay ID	Curve	OCR			Trip Time at Pick Multiple (ms)						
		Pick up	Primary A	Time Delay	2x	3x	4x	5x	6x	8x	10x
RelayT1H	CO8 - Inverse	2	120	0.5	745	338	215	158	128	101	85.9
Relay-T2H	CO8 - Inverse	5	450	0.5	745	338	215	158	128	101	85.9
Relay-T3H	CO8 - Inverse	2	120	0.5	745	338	215	158	128	101	85.9
RelayT4H	CO8 - Inverse	3	270	0.5	745	338	215	158	128	101	85.9
RelayIF1	CO8 - Inverse	4	240	1	1940	815	513	378	314	249	217
RelayIF2	CO8 - Inverse	3	180	1.5	2960	1230	769	573	477	382	334

8. Conclusion

The major protective device assessment done in this study is the relay and circuit breaker coordination for TUEDS. The load flow analysis was conducted on ETAP to set the circuit breaker and current transformer ratings and fault analysis were conducted to find the maximum fault current at each bus to set the relay pick up current, PMS and TMS for the relays settings. Simulation of faulted part of the system was conducted to check whether there is correct tripping sequence of protective devices and was verified through the TCC curves which also show the amount of time is needed for the breakers to trip at a certain current level. As the short circuit current increases, the time for the breaker to trip decreases. Coordination for the relay and breaker settings can be further improved by dragging the relay characteristics in the graph. The relay parameters such as PSM and TMS will be changed automatically. Protective devices should be selected appropriately to provide the necessary primary and secondary back up protection. For TUEDS system where the load demand is always increasing, protective device coordination study is essential to ensure that there is continuity of power in the system. ETAP software is a very good tool for protective device coordination.

Acknowledgment

The author will like to thank Taylor's University for providing a research environment to study the subject.

References

[1] O. C. Zienkiewicz, R. L. Taylor, "Power Distribution Systems", Vol. 3. pp. 1-152, EATON, Aug. 2017.
[2] A. L. Sheldrake, *Handbook of Electrical Engineering: for Practitioners in the Oil, Gas, and Petrochemical Industry*. John Wiley and Sons Ltd USA, 2003. pp 249 – 266
[3] V. K. Mehta and R. Mehta, *Principles of Power System*, Multicolor Edition. S. Chand Publishing, 1982. pp 395 - 612
[4] Y. G. Paithankar, S. R. Bhide, *Fundamentals of Power System Protection*. New Delhi: Prentice-Hall of India, 2007. pp 11 - 29
[5] T. Ting Yong, "Performance Assessment of Taylor's University Distribution System," Taylor's University, 2017.
[6] A. Nadarajan, "Peak Demand Analysis for the Look-Ahead Energy Management System: A Case Study at Taylor's University," Taylor's University, Kuala Lumpur, 2014
[7] L. Hewitson, M. A. Brown, and B. Ramesh, *Practical Power Systems Protection*. Amsterdam Elsevier, 2008. pp 1 – 7
[8] M. T. Glennon, "Short-Circuit and Protection Coordination Studies," *The Hartford Steam Boiler Inspection and Insurance Company*, 2018 p. 1.
[9] S. Champa, S. R. Vyas, "Protection of Industrial System Using OverCurrent Relay Co-Ordination-Review", Vol. 6, No. 2, Feb. 2017. pp. 923–931
[10] S. Saini, *Overcurrent Relay Coordination for Phase and Earth Faults Using ETAP*. Amity University, Noida, India, pp 1- 4 2014.

[11] S. Mahapatra, D. Debniloy, S. A. Mishra, K. Aditya, "Optimum Overcurrent Relay Coordination of a Power Grid", *Journal of Engineering Research and Applications* Vol.4 Issue 4, pp 39 – 44, April 2014

[12] H. A. Patel, V. M. Sharma, A. Deshpande, "Relay Coordination using ETAP," *International Journal of Scientific & Engineering Research,* Vol. 6, Issue 5, pp 1583-1588, May 2015.

[13] S. Thangalakshmi, "Planning and Coordination of Relays in Distribution System," *Indian Journal of Science and Technology*, College of Engineering Chennai, Vol. 9, no. 31, pp 1 – 7, Aug. 2016.

[14] E. Pho, "Overcurrent Coordination Study",California Polytechnic State University, USA, pp. 1 – 25, 2009.

[15] M. Thanigaivel, A.Rahman, "Power Flow Analysis and Protection Coordination of Real Time System," *International Conference on Explorations and Innovations in Engineering & Technology (ICEIET)*, pp. 57–62, 2016.

[16] V. N. Rajput, T. M. Vala, "Co-ordination of Overcurrent Relay for Chemical Industrial Plant using ETAP." *International Journal of Futuristic Trends in Engineering and Technology*, Vol. 1, No. 2, pp 1 – 5, 2014

EURECA 2018 – Conference Paper
Paper number 2EE02

Study on Effect of Salt Concentration in Heat Transfer Fluid on Performance of Semi-transparent Photovoltaic System

Chong Meng Joe[1], *Aravind CV*[1,*], *Rashmi Walvekar*

[1]School of Engineering, Taylor's University

*aravindcv@ieee.org

Abstract

This paper presents the effect of salt (sodium chloride, NaCl) concentration of heat transfer fluid (HTF) on the performance of solar photovoltaic (PV). HTF is often used in solar collectors where the HTF harnesses solar thermal energy. The experiment was carried out by channelling HTF of concentrations 0 g/L, 10 g/L, 20 g/L and 30 g/L of kitchen salt below a 90W, 100 thin film solar PV of 20 % transparency through a copper tube. The first part of analysis was about the relationship between the solar irradiance, voltage produced by PV and temperature measured. The results showed that increase in salt concentration increased the heat absorption characteristics of HTF. For 30 g/L of salt concentration HTF, the maximum temperature difference achieved was 7.5 °C while for 0 g/L of salt concentration HTF was 6.25 °C. That decreased the temperature of panel and improved the overall efficiency of the system, i.e. solar PV was producing higher voltage of 89.4 V when 30 g/L salt concentration of HTF was used than 0 g/L, which was 87.18 V, at a solar irradiance of 900 W/m^2. The second part of analysis was about the temperature increase of HTF in a closed loop heat transfer within 30 minutes and results showed that using higher concentration HTF could achieve a higher temperature difference, i.e. usage of 30 g/L salt concentration of HTF increased temperature by 3.5 °C while usage of 0 g/L salt concentration increased temperature by only 1 °C. Using HTF with higher salt concentration exhibited good thermal properties which might improve the solar PV system. 30 g/L concentration of salt water would be a good option as HTF as it had approximately the same concentration as sea water which could be found in abundance near the coastline.

1 Introduction

With fossil fuel being a limited source of electricity generation, renewable energies are used as alternatives to reduce dependency on fossil fuel. Solar energy is a low-carbon energy technology where it is more environmental friendly to be used and it has the potential to grow to a large scale. Even though the solar generating capacity has been growing rapidly in recent years, showing great improvements in performance, technology as well as the price, further advances are still needed to enable the solar technology to be more cost-competitive than fossil generation [1, 2].

In the new photovoltaic (PV) era, PV3.0, the solar modules have higher efficiency, making it more cost-competitive in the energy economy. With higher efficiency, the developers can develop a smaller footprint which generates the same amount of power. However, the advancement up till now is still insufficient for the solar systems to be implemented commercially. Research and development is essential to contribute to the advancement in solar technology [3].

Solar energy is still not widely used because generating electricity using solar PV is not economical due to solar technology being expensive and has low production with high capital cost ratio [4]. "Making solar energy economical" has become one of the 14 grand challenges for engineering in the 21st century, listed by the National Academy of Engineering (NAE) with the aim to create an impact to the society and world. This grand challenge emphasizes the importance of making solar energy more affordable to the public in effort of reducing carbon footprint as well as the dependency on fossil fuel [5]. This has inspired the core purpose of this project, which is to contribute to addressing this grand challenge in making solar energy economical.

Solar energy can be harvested in the form of light or heat [6]. Monocrystalline, polycrystalline and thin film PV are normally used to convert light energy to electrical energy while concentrating solar power (CSP) collectors capture the heat energy and store it for heating applications. A relatively new technology is the transparent luminescent solar concentrator (TLSC). It allows light to pass directly through without capturing photons but capture specific nonvisible wavelengths of sunlight instead, making it transparent as infrared and ultraviolet light is not detectable by human eye. This attribute allows it be used for applications where it is hidden in plain sight without obstructing the view for example, on the screen of mobile devices as well as windowpanes of skyscrapers [7]. The major drawback of this technology is that the efficiency of the system is still quite low at about 1%. However, Lunt and his team [7] is confident that they can reach up to 10% efficiency.

To harvest solar energy, the solar PV panels will have to be exposed to sunlight for a long period of time. This increases the temperature of the PV panels. It was noticed that every increase in degree temperature will cause a decrease in efficiency of a PV panel, i.e. approximately 0.45% for monocrystalline/polycrystalline silicon and approximately 0.25% for amorphous silicon [8]. Therefore, combining both solar PV and solar collector produces a photovoltaic-thermal (PVT) collector which generates electricity and at the same time absorb thermal energy. Since the efficiency of solar PV decreases with increasing temperature, the heat of the panel when the solar intensity is high will be used to heat the air/water in the collector which will then be used in some heating applications. That way, the temperature of the solar PV will be reduced, maintaining the electrical efficiency of the overall system.

Generally, heat transfer fluid (HTF) circulates around the solar PV to harvest the solar thermal energy [9]. Hoffman *et al.* [10] suggested vegetable oil to be used as HTF because it had good thermophysical properties. Molten salts are also good option as HTF because they can melt at relatively low temperatures while molten salts with extremely high boiling point can also perform well in operating temperature as high as 800°C because they are thermally stable [9].

Chen *et al.* [11] conducted an experiment using molten salt with silicon dioxide, SiO_2 nanoparticles and they found out that preparing the molten salt nanofluid through high-temperature melting had better thermal stability than being prepared by ultrasonic dispersion. However, the preparation of molten salt nanofluid requires high temperature which may not be convenient in such applications as the heat harvested from the solar energy is not sufficient. Besides, large amount of salt will be needed for the fluid to pass through the solar collector. Seong *et al.* [12] found that 35% sea salt solution had a better cooling performance than water. Since sea water is abundant especially near the coastline, it can be used as HTF for solar panels which are installed near the coastline. The disadvantage of using HTF containing salt is its high corrosive nature to metal alloys [9]. Since most channels are made of metal alloy because it has higher thermal conductivity, the corrosive nature of the molten salts will have to be resolved completely before using molten salts as HTF for commercial applications. Huang *et al.* [13] suggested to use water soluble corrosion inhibitors for suppressing corrosion of copper.

Rikesh [14] conducted an experiment to determine the thermal behaviour of HTF with different kitchen salt concentration placed under a parabolic trough solar collector. It was noticed that 20 g/L salt water achieved higher temperature and higher transmission of heat to the water tank through heat exchanger. Besides, applying insulation, e.g. acrylic foam and polystyrene to concentrator pipe yielded higher thermal efficiencies. It was found that 20 g/L salt water with acrylic foam as pipe insulation had the best thermal efficiency of 4.4% improvement. Rikesh [14] then experimented on using water as HTF in the cooling system of a silicon thin film of 20% transparency as shown in Fig. 27. It was noticed that the experiment stopped at HTF with 20 g/L of salt concentration with the justification of higher salt concentration increased the rate of corrosion. However, the sea water contains about 35 g/L salt concentration and have good cooling effect [12], it became an inspiration to investigate the effect of using higher salt concentration as HTF at least up to 30 g/L, with the vision of using sea water as HTF in bigger projects near the coastline.

Rikesh [14] claimed that the voltage drop of the PV panel due to heat was restored after cooling system was added, making it to have the potential to be used in a hybrid PVT system where heat energy could be used in other applications. In Rikesh's work, it was noticed that the cooling of solar PV increased the electrical output of the PV. However, no experiments were done on the effect of using salt water as HTF on the electrical output of the PV. Also, the solar irradiance was not taken much into account when analyzing the results. Other than that, for the bottom cooling layer, there were 2 ends where one allowed the HTF to be pumped in and the other end allowed the HTF to be pumped out of the layer. Without a proper channel, the HTF would be moving in random motion which might reduce the effectiveness of the system.

The efficiency of the solar PV could be improved from many different factors, e.g. materials fabrication, cooling system, types of HTFs used. For this research, due to budget

constraint, the approach of the research would be focusing on designing a cooling system and utilizing appropriate HTFs. Rikesh's research [14] had become an inspiration to this research which was to utilize both of the findings, i.e. effect of salt concentration on the thermal properties of HTF as well as improvement in electrical output of solar PV after adding a cooling system with HTF of optimal salt concentration, and develop a system which might function more efficiently. Kitchen salt would still be used as the material for HTF preparation because it was widely available and relatively cheaper than other oil-based or nanofluid HTFs.

The research aimed to optimize the electrical output of solar PV via heat removal method using salt solution as HTF with optimal salt concentration.

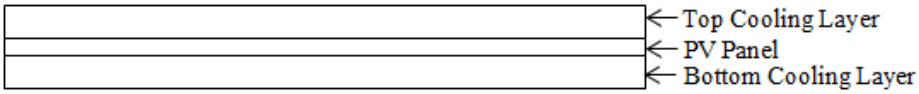


Fig. 27: Rikesh's Experimental Setup on Voltage Regulation [14].

2 Research Methodology

To investigate the effect of salt concentration of salt concentration of salt water as HTF on the performance of a solar PVT collector, the experiment was conducted using HTFs with different concentrations of sodium chloride (NaCl), i.e. 0g/L, 10g/L, 20g/L and 30g/L. The research methodology was as shown in Fig. 28. The experiment was stopped at 30g/L because sea water contains about 35% salt concentration [12]. The HTFs were prepared by dissolving appropriate amount of salt into water. The HTF was channelled below a 90W, 100V semi-transparent PV panel through a copper tube by using a water pump.

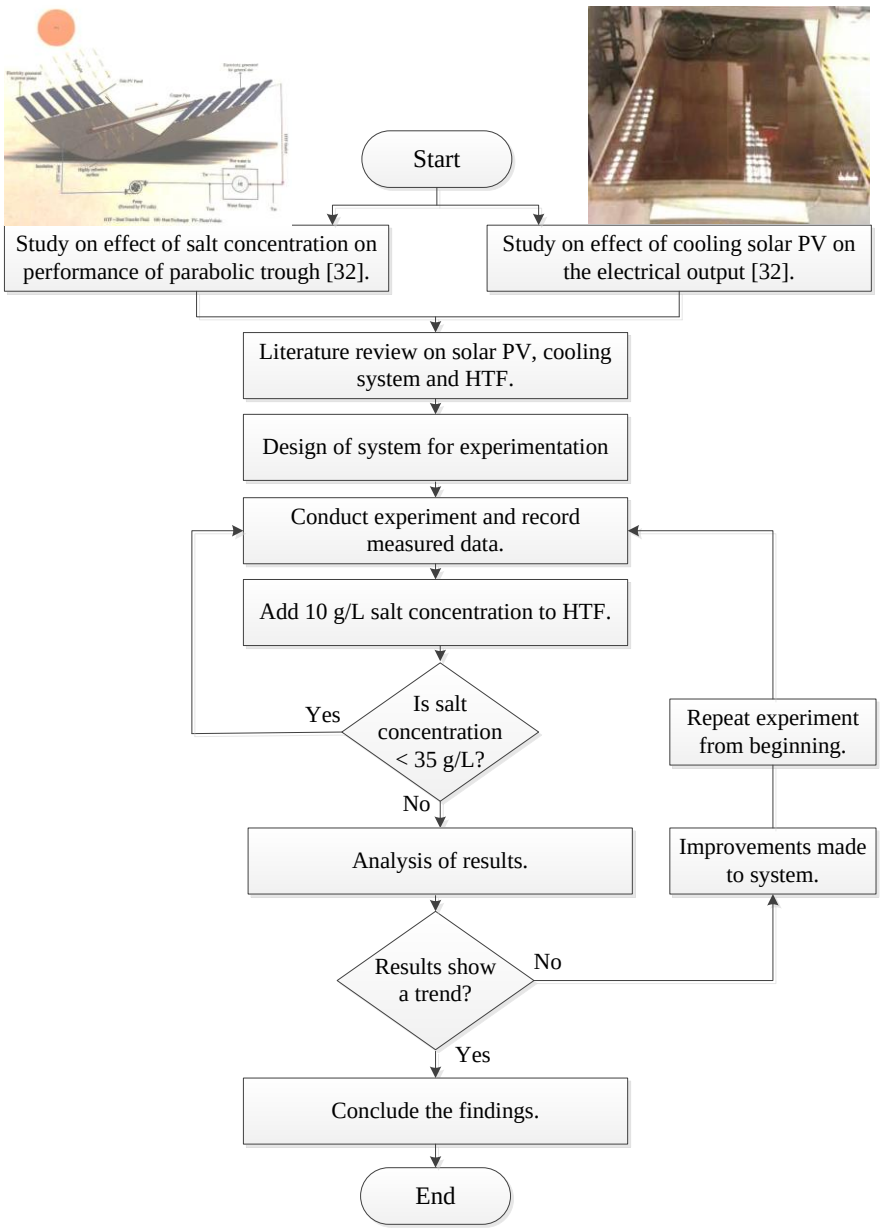


Fig. 28: Research Methodology Flowchart.

2.1 Experimental Setup

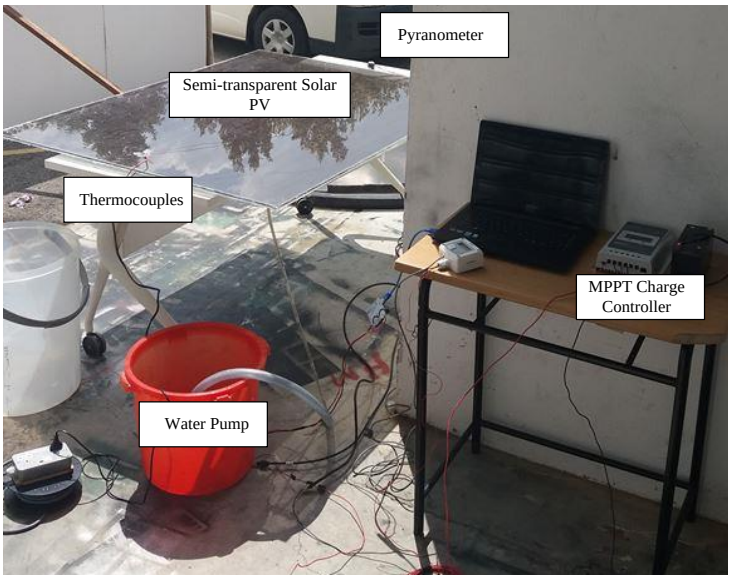


Fig. 29. Experimental Setup.

The experiment was carried out outdoors under natural sunlight and the experimental setup was as shown in Fig. 29. The semi-transparent PV was connected to a maximum power point tracking (MPPT) charge controller. MPPT charge controller is chosen because of its better performance in terms of maximizing the power output of the system by regulating current to and fro the battery [15]. Due to the varying weather condition, a pyranometer was used to obtain the solar irradiance at different time. Thermocouples were also placed at the water inlet, water outlet, top and bottom of the semi-transparent PV panel to measure the temperature of input HTF, output HTF, top of the solar PV panel and bottom of the solar PV panel respectively. In the experiment, the HTF from the outlet was not channelled to the input supply so that the input temperature was maintained at a certain temperature. That way, it was easier to understand the effect of salt concentration of HTF on the heat absorption characteristics of HTF from the solar PV and ultimately the performance of the solar PV.

2.2 Experimental Procedure

Each of the 4 experiments was carried out for at least 1 hour. As the solar irradiance varied from time to time, to determine the effect of salt concentration on the performance of the solar PV, the measurements taken would have to be of approximately constant solar irradiance. However, the measurements taken should be at least 45 minutes after the experiment started, knowing that voltage produced by PV decreased with time. That was to ensure that the effect of salt concentration of HTF on the performance of solar PV after a period of time would be determined and not the initial condition.

Then, the outlet HTF would be channelled back to the inlet source to create a closed loop heat transfer system. That was to determine how fast the HTF of different salt concentrations would heat up within a certain period of time. Each experiment was carried out for 30 minutes.

3 Results and Discussions

The measurements taken were temperature of top of the panel, temperature of bottom of the panel, temperature of HTF at inlet, temperature of HTF at outlet, voltage produced by the PV and solar irradiance.

3.1 Temperature

The temperatures of the input HTF, output HTF, top of panel and bottom of the panel throughout the experiment were measured and recorded as below. The results in Fig. 30(a) and Fig. 30(b) showed that the temperature of top of the panel would be slightly higher than the bottom part of the panel and the difference in temperature was higher in Fig. 30(b) than Fig. 30(a). That trend was not quite applicable for the results shown in Fig. 30(c) and Fig. 30(d) as the temperature of top part of the panel would slightly decrease from time to time. That might be due to the windy conditions during the experimental period which helped cooling the PV, reducing its temperature. As for the temperature of the HTF at the inlet and outlet, Fig. 30(a), Fig. 30(b), Fig. 30(c) and Fig. 30(d) all showed that the outlet HTF was hotter than inlet HTF, indicating heat from the panel was captured by the HTF. The inlet HTF was maintained at a relatively constant temperature while the outlet HTF slightly increased over time.

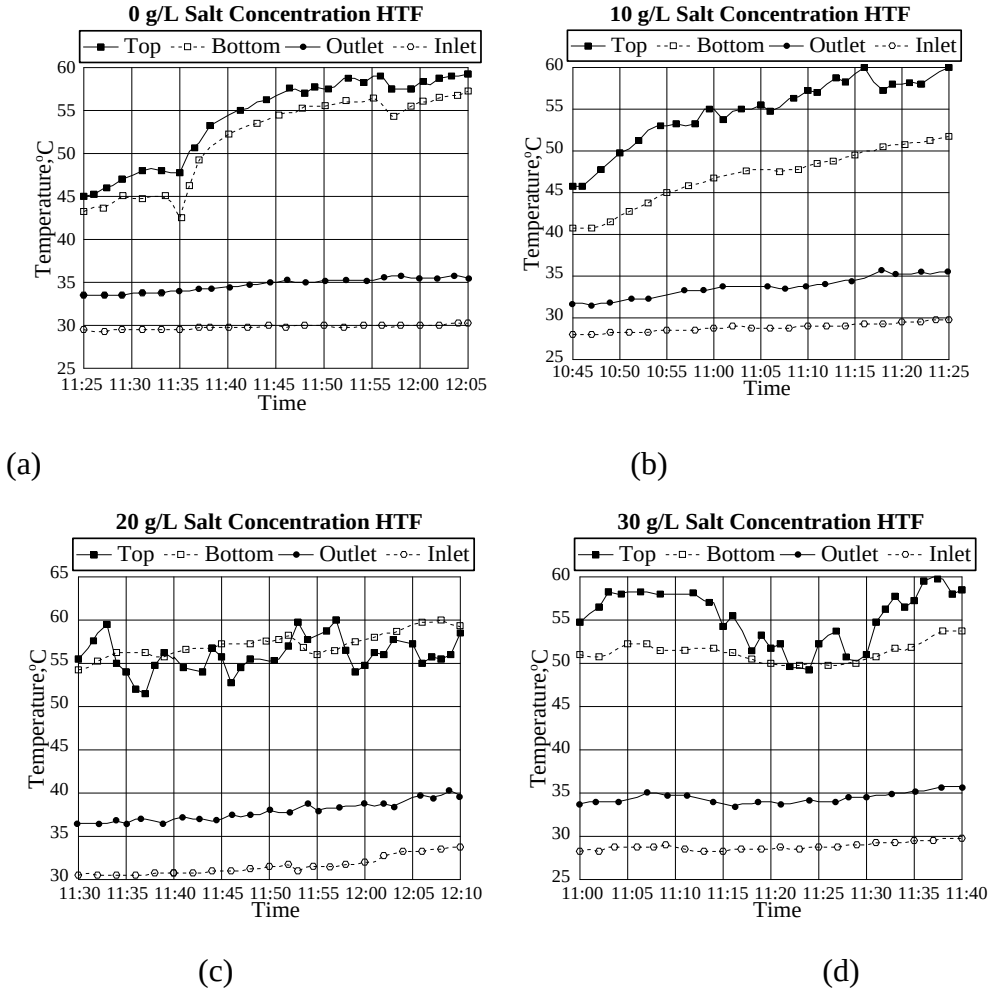


Fig. 30. Graph of Temperature Measurements against Time for 4 Different Salt Concentrations.

Table 5. Maximum Temperature Difference in Each Experiment.

HTF Salt Concentration, g/L	Inlet Temperature, °C	Outlet Temperature, °C	Maximum Temperature Difference, °C
0	29.75	36	6.25
10	29.25	35.75	6.5
20	31.75	38.75	7
30	28.25	35.75	7.5

The maximum difference in temperature of the outlet and inlet HTF was determined and tabulated in Table 5. The results showed that as the salt concentration of HTF increased, the maximum temperature difference between the outlet HTF and inlet HTF also increased. For 0 g/L salt concentration HTF, the maximum temperature difference achieved was only 6.25 °C while the maximum temperature difference achieved for 30 g/L salt concentration was 7.5 °C. That indicated that the increase in salt concentration of HTF also increased the heat absorption of the HTF, harnessing more thermal energy.

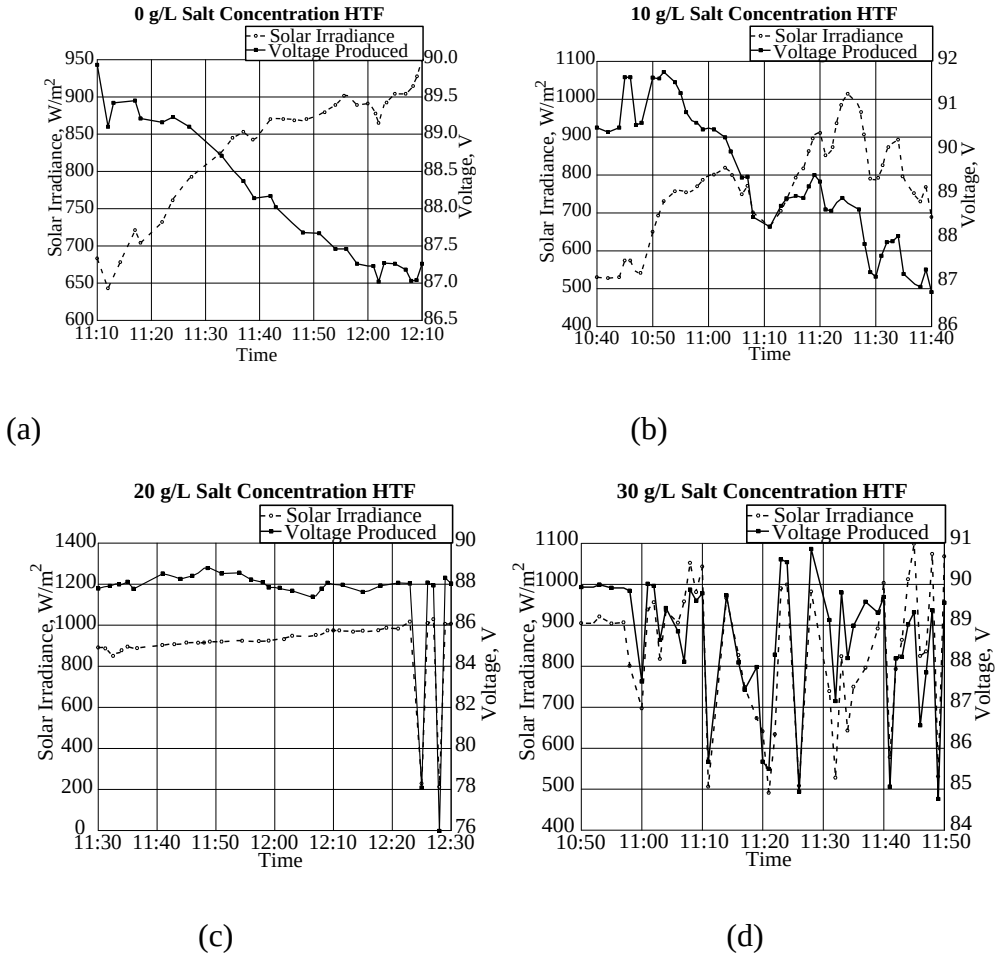


Fig. 31. Graph of Solar Irradiance and Voltage Produced against Time for 4 Different Salt Concentrations.

Table 6. Effect of Salt Concentration on Voltage Produced.

HTF Salt Concentration, g/L	Solar Irradiance, W/ m^2	Voltage Produced, V
0	904	87.18
10	893	88.05
20	903	88.51
30	848	89.4

3.2 Solar Irradiance and Voltage Produced

The effect of solar irradiance on the voltage produced by the solar PV was first analysed under 4 different conditions, which were 0g/L, 10g/L, 20g/L and 30g/L concentration of salt water as HTF. The results were plotted as shown in Fig. 31.

Fig. 31(a) and Fig. 31(b) showed that the voltage produced by the PV decreased over time and it might increase by a little when the solar irradiance was high. The solar irradiance in Fig. 31(c) and Fig. 31(d) was varying quite a lot and therefore the voltage produced by PV would also vary accordingly. The results showed that the voltage produced was proportional to the solar irradiance, it changed as soon as the solar irradiance changed, regardless of the salt concentration in the HTF.

Since the experiments were not carried out at the same time and therefore not under the same condition, i.e. solar irradiance was different for each experiment. The effect of HTF salt concentration on the voltage produced by the solar PV was determined by identifying the voltage produced at a certain solar irradiance, e.g. approximately 900 W/m^2, for each condition after at least 45 minutes after the experiment started and the results were tabulated as shown in Table 6.

It was noticed that at approximately 900 W/m^2 in every experiment after a period of time, the voltage produced slightly increased as the salt concentration of HTF increased from 0 g/L to 30 g/L. In other words, the percentage drop in voltage produced by solar PV over a period of time decreased as the salt concentration of the HTF increased. It was expected that increasing the salt concentration would increase the heat absorption of HTF.

3.3 Closed Loop Heat Transfer System

After 30 minutes of experimental period, the initial temperature and final temperature of the HTF in a closed loop heat transfer system were recorded as shown in Table 7.

It was noticed that with higher salt concentration, the increase in temperature of the HTF was greater as well. The HTF with 30 g/L salt concentration was heated up by 3.5 °C while HTF with 0 g/L salt concentration was only heated up by 1 °C. That once again justified the better thermal characteristics of higher salt concentration HTF as it could take a shorter time to reach a higher temperature.

Table 7: Temperature of HTF after 30 Minutes.

HTF Salt Concentration, g/L	Initial temperature, °C	Final Temperature, °C	Temperature Difference, °C
0	35.75	36.75	1
10	33	35.75	2.75
20	32	35.25	3.25
30	32.25	35.75	3.5

4 Conclusion

The maximum temperature difference between the outlet HTF and inlet HTF increased as the salt concentration of HTF increased, indicating that the more heat was removed from the solar PV by the HTF when the salt concentration increased. When more heat was removed, the decrease in efficiency of the panel would be minimized. Since the solar irradiance varied for each experiment and the voltage produced varied proportionally with the solar irradiance, the voltage produced by the solar PV at a certain solar irradiance after a period of time for all 4 experiments was used for comparison. Therefore, at approximately 900 W/m^2 solar irradiance, the voltage produced was highest when 30 g/L HTF was used, which was 89.4 V, while the voltage produced was lowest when 0 g/L HTF was used, which was 87.18 V. That indicated that the increase in heat absorption by the HTF minimized the decrease in voltage production of the solar PV over a period of time. With greater heat absorption using higher salt concentration, if the outlet HTF was channelled back to the inlet supply as a closed loop heat transfer, the temperature of the HTF would be increased further which could be used for applications such as water heating. The experiment results also showed that the increasing salt concentration of HTF would increase the temperature at of the HTF in a closed loop heat transfer at the end of the experiment. After 30 minutes, the HTF with 0 g/L salt concentration increased in temperature by only 1 °C while the HTF with 30 g/L salt concentration increased in temperature by 3.5 °C. In other words, the HTF with higher salt concentration would heat up faster.

In conclusion, the salt concentration of the HTF improved the performance of the solar PV system. When the salt concentration of HTF increased, the maximum temperature difference between the outlet HTF and inlet HTF would also increase, indicating more heat was transferred away from the solar PV, increasing the electrical output of the solar PV because the temperature of the panel was reduced. With greater electrical output, the overall efficiency of the system could be said to have increased. However, using salt solution as HTF would increase the rate of corrosion of the copper tube as the increase in ions concentration affected rate of oxidation. Further studies on how to reduce the effect of salt solution on the rate of corrosion or substitution to copper tube had to be done to improve the effectiveness of the whole system. The experiment would have to be repeated again to increase the validity of the results as well as testing it with loads, in order to reduce the random errors, especially caused by the weather conditions.

5 Acknowledgement

The authors acknowledge the support for the project from the Taylor's University flagship research grant TUFR/2017/001/01, 2017- 2020.

References

[1] R. Schmalensee, V. Bulovic, and P. Sharp, *The Future Solar Energy - An Interdisciplinary MIT Study*. Massachusetts Institute of Technology, 2015.

[2] G. Boyle, *Renewable Energy: Power for a Sustainable Future*, 3rd ed. Oxford: Oxford University Press, 2012.

[3] W. Li, "PV3.0," *Solar Power World*, November, pp. 34–37, 2017.

[4] N. Gomesh, I. Daut, M. Irwanto, Y. M. Irwan, and M. Fitra, "Study on Malaysian's perspective towards renewable energy mainly on solar energy," *Energy Procedia*, vol. 36, pp. 303–312, 2013.

[5] "Make Solar Energy Economical," *NAE Grand Challenges For Engineering*. [Online]. Available: http://www.engineeringchallenges.org/9082.aspx. [Accessed: 11-Oct-2017].

[6] U.S. Department of Energy, "2016 Renewable Energy Data Book," December 2015, pp. 1–132, 2016.

[7] Y. Zhao, G. A. Meek, B. G. Levine, and R. R. Lunt, "Near-Infrared Harvesting Transparent Luminescent Solar Concentrators," *Adv. Opt. Mater.*, vol. 2, no. 7, 2014.

[8] S. A. Kalogirou and Y. Tripanagnostopoulos, "Hybrid PV/T Solar Systems For Domestic Hot Water And Electricity Production," *Energy Convers. Manag.*, vol. 47, no. 18–19, pp. 3368–3382, 2006.

[9] K. Vignarooban, X. Xu, A. Arvay, K. Hsu, and A. M. Kannan, "Heat Transfer Fluids for Concentrating Solar Power Systems - A Review," *Appl. Energy*, vol. 146, pp. 383–396, 2015.

[10] J. F. Hoffmann *et al.*, "Temperature Dependence of Thermophysical and Rheological Properties of Seven Vegetable Oils in View of Their Use as Heat Transfer Fluids in Concentrated Solar P lants," *Sol. Energy Mater. Sol. Cells*, vol. 178, December 2017, pp. 129–138, 2018.

[11] X. Chen, Y. ting Wu, L. di Zhang, X. Wang, and C. fang Ma, "Experimental Study on The Specific Heat and Stability of Molten Salt Nanofluids Prepared by High-temperature Melting," *Sol. Energy Mater. Sol. Cells*, vol. 176, October 2017, pp. 42–48, 2018.

[12] S. W. Lee, S. M. Kim, S. D. Park, and I. C. Bang, "Study on The Cooling Performance of Sea Salt Solution During Reflood Heat Transfer in a Long Vertical Tube," *Int. J. Heat Mass Transf.*, vol. 60, no. 1, pp. 105–113, 2013.

[13] H. Huang, Z. Wang, Y. Gong, F. Gao, and Z. Luo, "Water Soluble Corrosion Inhibitors for Copper in 3 . 5 wt % Sodium Chloride Solution," *Corros. Sci.*, vol. 123, January, pp. 339–350, 2017.

[14] R. Ramsurn, "Energy Recovery Through Phase Layered Heat Removal Using Sustainable Materials," Taylor's University, 2017.

[15] R. Mayfield, *Photovoltaic Design & Installation For Dummies*. Hoboken, NJ: Wiley, 2010.

EURECA 2018 – Conference Paper
Paper number 2EE03

Design of Double Layered Vertical Axis Wind Turbine combining Lift and Drag force

Chua Chong Zhe[1], Chockalingam Aravind Vaithilingam[1]*

[1]School of Engineering, Taylor's University, Malaysia
chongzhe.chua@sd.taylors.edu.my

Abstract.

Wind is one of the renewable energy that some of the countries used for electricity generation. Many research and studies about design of wind turbine blade have been made for better harvesting wind energy efficiency. Many countries have been investing a lot of time and resources on developing renewable technology in order to reduce carbon emission. Nowadays some countries implement this renewable technology successfully to their electricity power generation system. This paper will be focusing on how design of vertical axis wind turbine blade influence efficiency. Efficiency of blades is related to power coefficient. To increase power coefficient of wind turbine, lift to drag ratio needs to be improved when designing the wind turbine. The design used is twisted Darriues wind turbine and tubercles design for improving power coefficient. The design will be formed using SOLIDWORK software and tested using COMSOL Multiphysics software. COMSOL Multiphysics software is used to analyze the flow around the wind turbine blade. Air flow around conventional design and new design blades will be compared and explained. Simulation results show that the design with tubercles performs better compared to design without tubercles.

1. Introduction

Renewable energy is now a trend to most of the advanced countries. It is the solution to energy and environment problem faced by all countries. Most of the countries have been investing times and money on developing renewable energy technology in order to solve environmental problem and become less dependent on imported energy from other countries. The technology discussed in this paper is related to wind turbine. Most of the common wind turbine used is horizontal axis wind turbine. It is only used in the places that have high wind speed. For places that have low wind speed, vertical axis wind turbine (VAWT) still can provide certain amount of electricity after harvesting wind energy. To maximize efficiency of wind turbine blades, power coefficient which is affected by lift to drag ratio needs to be improved. First, understanding about vertical axis wind turbine and working principle needs to be done.

1.1 Types of wind turbine

There are two types of wind turbines used in this world which are vertical axis wind turbine and horizontal axis wind turbine. Horizontal Axis wind turbine is the one that commonly used in most of the countries due to their wide open areas that can be used to harvest wind energy. Besides, horizontal axis wind turbine only suitable to areas that have high wind speed. Vertical axis wind turbine is normally used in low wind speed areas. [1]

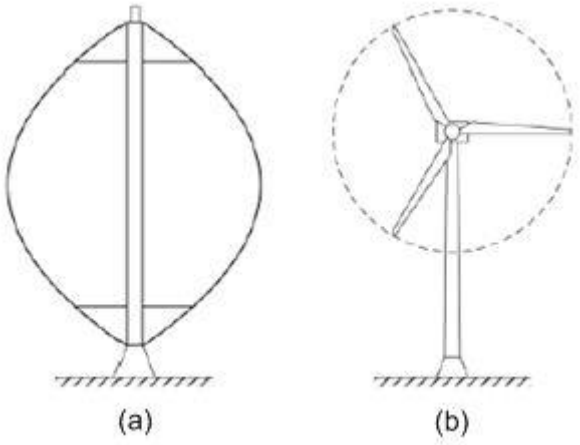


Figure1.1.1: Vertical axis wind turbine (a) and Horizontal axis wind turbine (b)

There are two main types of vertical axis wind turbine which are Darriues [2]and Savonius [3]wind turbine. Darriues wind turbine uses lift force to operate and Savonius wind turbine using the drag force to operate. Both types of wind turbines have their own advantages and disadvantages. Darriues type has high power efficiency but require a self-starting mechanism for it to rotate. Savonius type doesn't require self-starting mechanism but has low power efficiency.[4] By combining these two types, Darriues- Savonius wind turbine[5] is the solution to difficulty of both type wind turbine. It consists of s-shape Savonius vanes and curved aerofoil Darriues blades. Savonius vanes are added to Darriues wind turbine in order to make it self-starting since Darriues is not able to start without an initial net rotational force. It is omnidirectional and doesn't need special mechanism to rotate itself towards wind direction.

In other words, Savonius part will be self-starting mechanism and Darriues part will be provide high power efficiency.

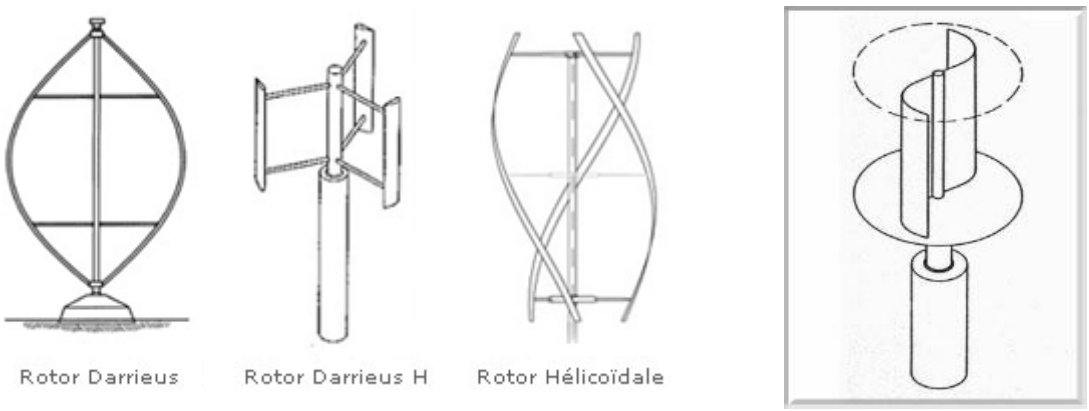


Figure1.1.2: Darrius(left) and Savonius(right) wind turbine

Beside these two types wind turbines, some of the latest vertical axis wind turbine blade design is combining both.[6] The combination of Savonius and Darriues wind turbine is called Darriues- Savonius wind turbine. It consists of s-shape Savonius vanes and curved aerofoil Darriues blades. Savonius vanes are added to Darriues wind turbine in order to make it self-starting since Darriues is not able to start without an initial net rotational force. It is omnidirectional and doesn't need special mechanism to rotate itself towards wind direction. This type of turbine can be used for small and large system to generate electricity. This system normally is chosen whenever low cost is important than efficiency. From the journal about design, development and testing of a combined Savonius and Darrieus vertical wind turbine, it concluded that Darriues Savonius wind turbine should have different assemblies to perform effectively. The journal also mentioned that increase in thickness of aerofoil will improve self-start capability of turbine.[7]

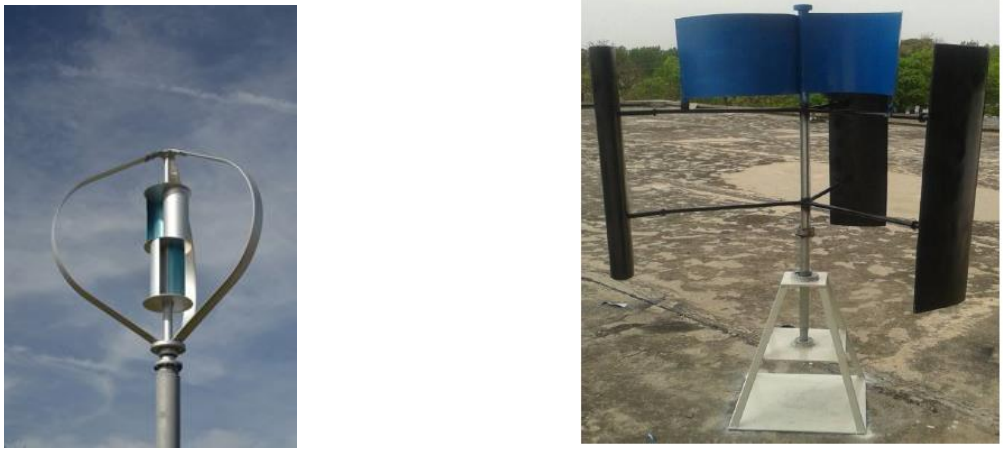


Figure1.1.3: Darriues- Savonius wind turbine (left) Darriues Savonius wind turbine (right) from journal

1.2 Working principle of wind turbine blade

Two aerodynamic forces are involved when wind turbine are operating in an unconstrained fluid which is in air. These forces are drag force and lift force. Drag force is the component in line with the direction of air stream. Lift force is the component that is perpendicular to direction of air stream. Figure below shows the direction of lift and drag forces and the angle of attack which is the angle measured against the chord line of aerofoil.[8]

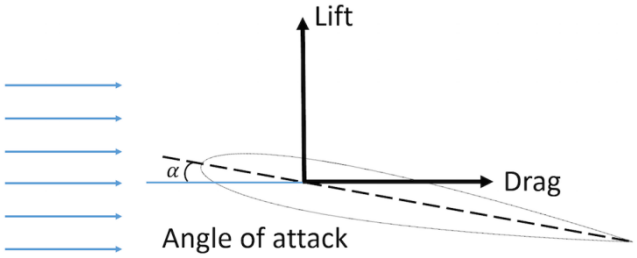


Figure 1.2.1: the direction of lift and drag forces and the angle of attack which is the angle measured against the chord line of aerofoil

The wind energy can be expressed by equation below [1]:

$$P = 0.5pAV^3 \quad (1)$$

Where p is air density, A is area and V is velocity of air.

The efficiency of wind turbine blade is based on power coefficient. It is influenced by the lift and drag coefficients which are are used to calculate maximum lift to drag ratio and find out the efficient setting of angle of attack of the blade when the ratio is maximum. To improve wind turbine, lift to drag ratio should be improved because it relates to power coefficient of wind turbine. lift and drag coefficients are calculated using formula below.

$$\text{Drag coefficient, } C_D = \frac{D}{0.5pV^2A_B} \quad (2)$$

$$\text{Lift coefficient, } C_L = \frac{L}{0.5pV^2A_B} \quad (3)$$

Where D and L are drag force and lift force in newtons, p is the air density in kgm^{-3}, v is the velocity of air approaching aerofoil in ms^{-1}, A_B is the blade area in m^2. These coefficients are measured in wind tunnel at different angle of attack and wind velocities.

1.3 Tubercles design

In order to improve the performance of wind turbine, tubercles design is added into wind turbine. Tubercles design comes from humpback whale flippers. The bumps on the flippers helps whale reduces stall which is increased in drag to make some tight turns. In other words, it allows whale's flipper to attack at higher angle before stall occurs and more lift can be generated. There are researchers have come up with mathematical model that helps explain hydrodynamic edge and the model could improve engineering design such as more stable airplane design and turbines blades that can capture more energy from water and wind because it can provide more lift and reduces drag. [9]

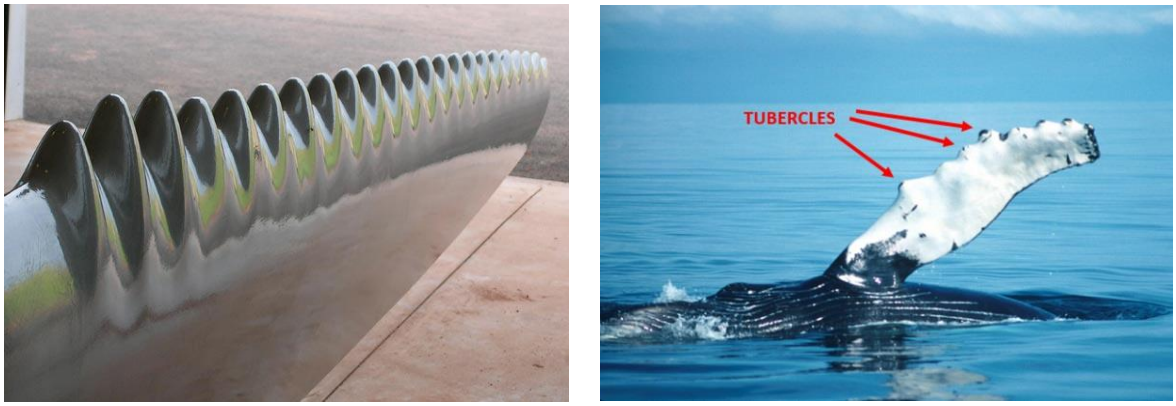


Figure 1.3: tubercles design on wind turbine blade and tubercles on whale flipper

There is a journal mentions about the application of tubercles design. The performance of tubercles on rudder was explained in journal[10]. It helps to generates more lift at the angle more than 22^{o} compared to a smooth rudder at a Reynold number of 200000. This effect diminishes on rudder at higher Reynold number and the tubercles accelerate the onset of cavitation. Tubercles may replace boundary-layer control structures such as flaps and slots that are necessary to prevent stall at the period of high angles of attack. The replacement of these structures could reduce weight of aircraft and increase fuel economy. Besides, there is company combines tubercles and its product. Envira-North System Ltd produced industrial ceiling fans that are modified with tubercles for large buildings. A high-volume, low-speed model with a 24-foot diameter of five blades is reported to be 25% more efficient and consumes 20% less electricity to operate than a 10-blade configuration. In addition, this fan is 20% quieter. Suppression of tonal noise by the addition of tubercles to an airfoil in a low-speed wind tunnel was observed. Tonal noise is most effectively reduced by tubercles of large amplitude and smaller wavelength. WhalePower corporation combine tubercles with wind turbine and result an increase generation of energy. Wind turbine blades with tubercles are able to increase electrical generation at moderate wind speed compared to unmodified blades.

There is a journal[11] discusses about effect of number and size of tubercles. 4 different sizes of tubercles which are 100mm, 125mm, 150mm and 200mm and 3 different numbers of tubercles which are 15, 19 and 23 are tested using CFD software. Table below shows the lift force obtained from different size and number of tubercles.

Table2.6: forces with different size of tubercles and number of turbecles

Number of Tubercles	Size of Tubercles			
	100 mm	125 mm	150 mm	200 mm
15	11.547 N	11.765 N	11.279 N	11.227 N
19	11.287 N	11.240 N	11.171 N	11.026 N
23	11.317 N	11.013 N	11.111 N	11.031 N

The results show that the increase of size tubercles and tubercles leads to decrease in generation of lift. When using 15 tubercles, CFD shows that 125mm tubercles generates maximum lift compared to other combination of size and number of tubercles. The conclusion of journal is tubercles are very useful in generating more lift than the model without it and the trends of results shows that there are optimal size and number of tubercles for different wind turbine model.

Based on article in journal[9], addition of tubercles on VAWT increases lift to drag ratio without sacrificing structure stability of blades. NACA0012 was the airfoil model used in study which did not have highest coefficient of lift and its structure outperforms other model. The effect is analyzed by using FEA analysis. Results from the journals shows that addition of tubercles increases lift and reduces drag when comparing the normal wind turbine blade.

2. Design of vertical axis wind turbine

The vertical axis wind turbine model is designed using SOLIDWORK software. Darriues part is using twisted Dariues blade design and Savonius part is using hyperbolic paraboliad design. Savonius blade isn't arranged in S-shape like conventional s-shape Savonius wind turbine. It has a twisted shape which allows it to capture more energy and overlapped part form by two blades allows the airflow to be directed to other blade in order to accumulate enough drag force for self-starting. Darriues part using twisted Darriues blade in order to increase lift and drag ratio. This shape allows the blades experiences less drag and more lift when rotating.

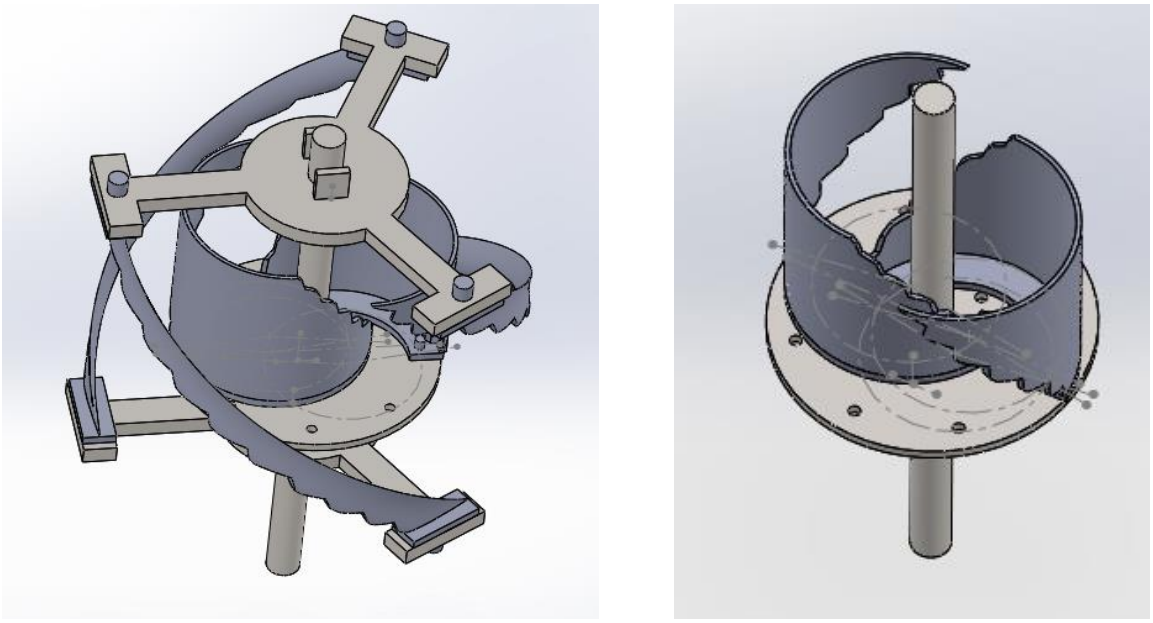


Figure 2.1: New design of Darriues Savonius wind turbine and arrangement of Savonius wind turbine blade

Turbecles design is added to both parts. Based on article shown in journal[12], addition of tubercles on VAWT increases lift to drag ratio without sacrificing structure stability of blades. NACA0012 was the airfoil model used in study which did not have highest coefficient of lift and its structure outperforms other model. The effect is analyzed by using Finite Element Analysis (FEA). Results from the journals shows that addition of tubercles increases lift and reduces drag when comparing the normal wind turbine blade.



Figure 2.2: tubercles design added to frontedge of Darriues blades and edge of Savonius blade.

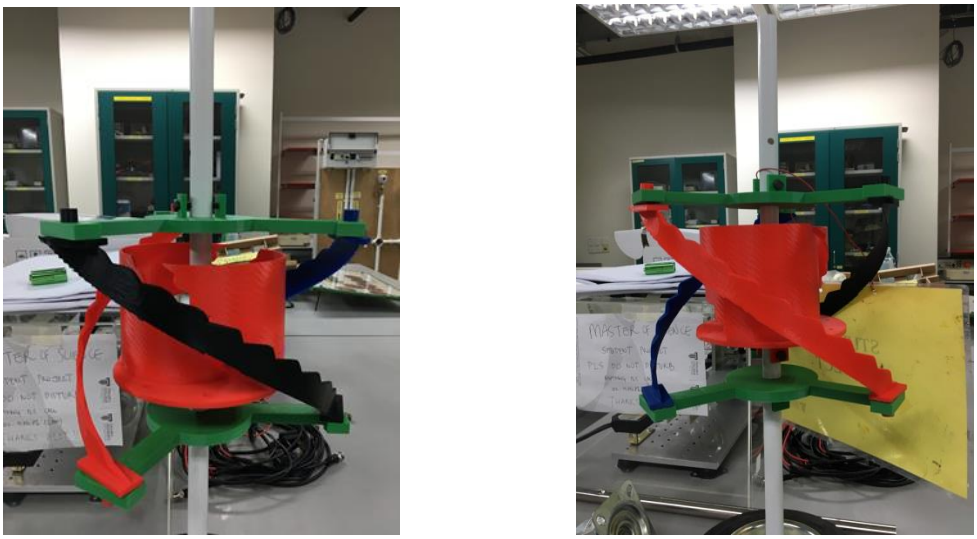


Figure 2.3: prototype based on design of SOLIDWORK software

3. Result and discussion

The model is analyzed by using COMSOL software. The settings of the physics are turbulent flow and turbulence model is low Reynold number k-ε which is suitable for vertical axis wind turbine blades. In the results generated using COMSOL software, stream line will be used to represent and slice to represent the air flow around the blades.

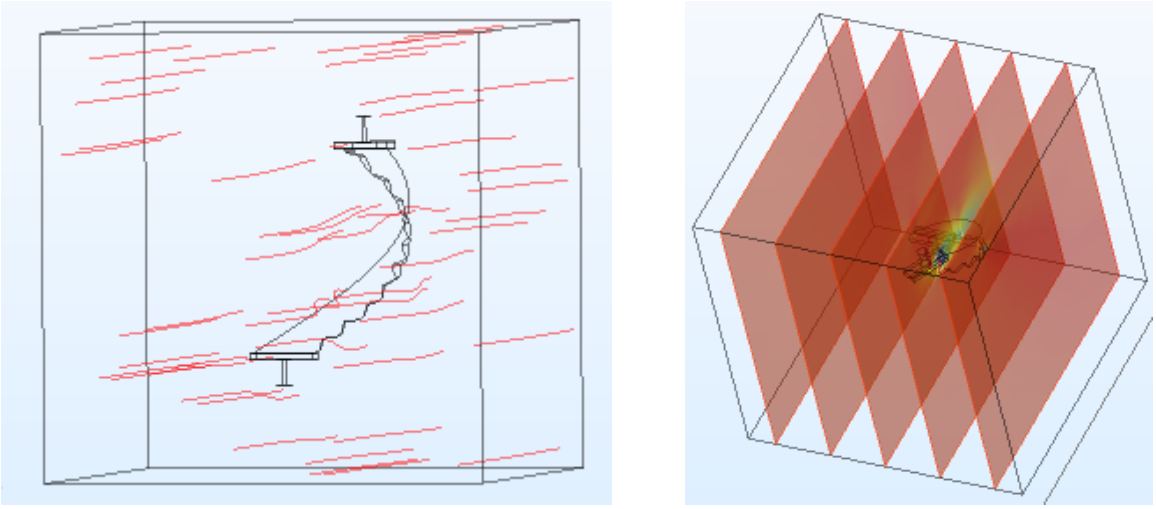


Figure 3.1: air flow around Darrius blade with tuberces in stream line plot and slice plot

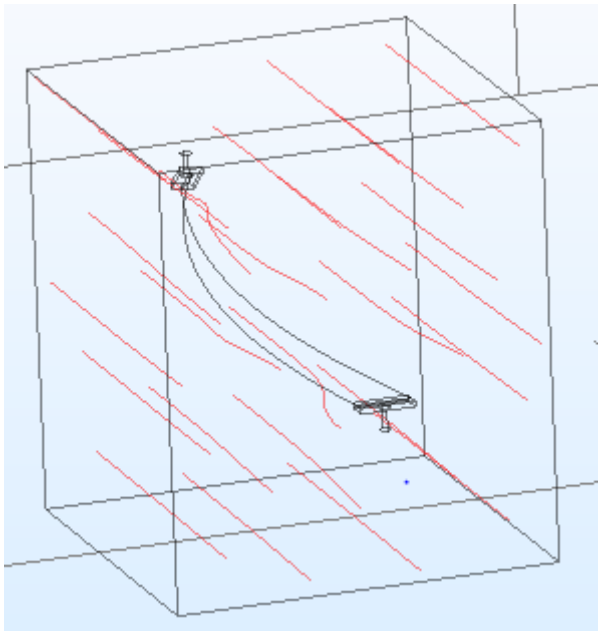


Figure 3.2: Air flow around Darrius blade without tubercles

From the stream line plot, the flow of air stream around tubercles become turbulent when interacting with tubercles. This shows that more lift force is generated to push the turbine blade to rotate. Besides, from the slice plot, the blue area represent the area of the blade experiences maximum drag force and red area represent the area that experience minimum drag force. Based on the result, twisted Darriues blade design and tubercles design has successfully fulfilled their purpose on Darriues wind turbine part. Compared to the Darrius blade without tubercles, from figure 3.2, there is less turbulent flow around the blade. In conclusion, blades with tubercles can perform better than the blades without tubercles.

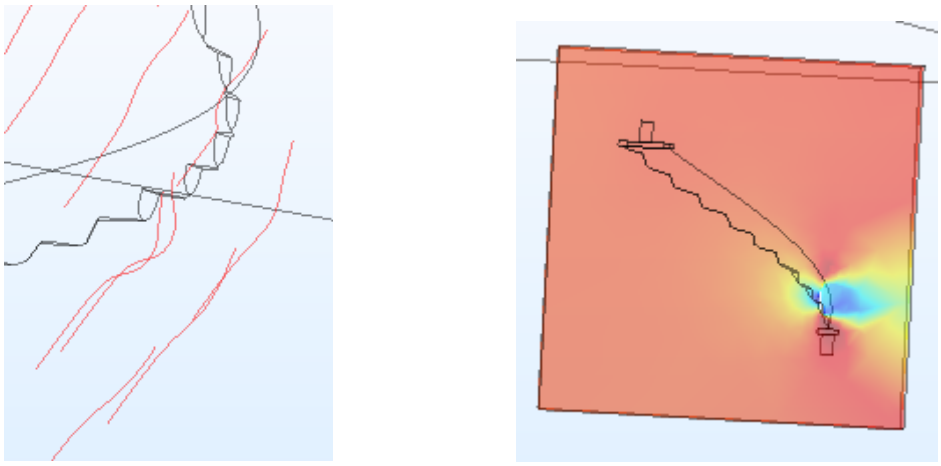


Figure 3.3: streamline plot that shows airflow around tubercles of wind turbine blade and slice plot that shows the drag force experienced by turbine blade.

Based on the result obtained for COMSOL simulation, Savonius blade designed using hyperbolic parabolaid shape is able to create some small vortex which allow the air circulate and produce enough drag to rotate the turbine blade all the time. The edge with tubercles design also able to create turbulent flow that helps darrius part for roataion. Compared to conventional Saconius blade, no tuberlent flow and vortex are formed. The whole blades experinces more

drag force compared to hyperbolic shape. To improve lift to drag ratio, drag needs to be reduced. Drag experinced in hyperbolic parabolaid shape is less compared to conventional blade.

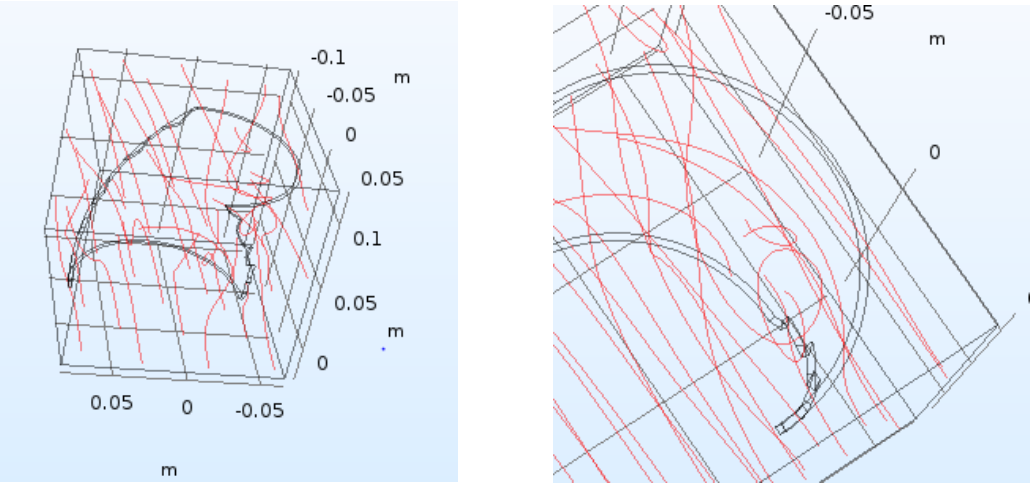


Figure 3.4: air flow around Savonius blade and the vortex created by hyperbolic parabolaid shape

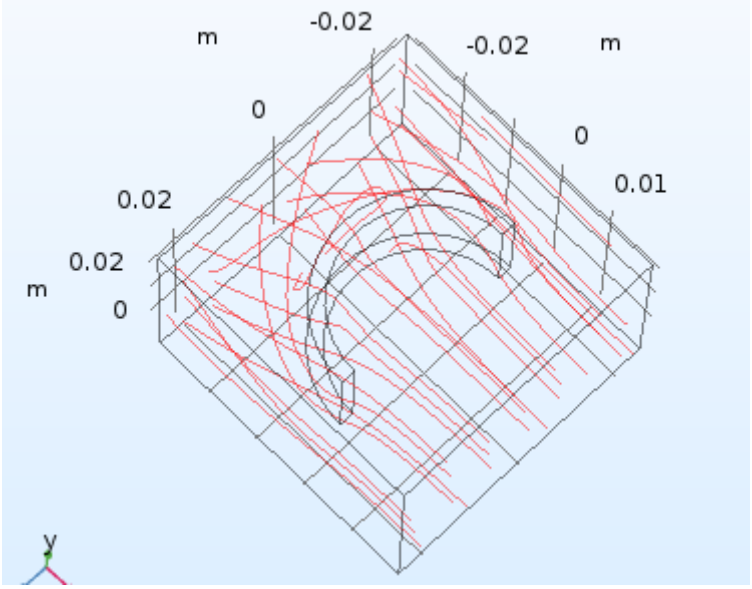


Figure 3.5: air flow around conventional Savonius blade

Drag and lift forces act on blades are computed using COMSOL software. Then by applying the formula found in research, the lift and drag coefficients are calculated. For Savonius part, the drag coefficient of new design is 0.65. Drag coefficient of conventional Savonius design is 0.73. The drag coefficient of new design of Savonius blades is less than conventional Savonius design. In other word, the drag force experienced by the blade is lower in new design of Savonius blades.

For Darrius part, after computing lift and drag coefficient from result of COMSOL simulation, formulas of double stream tube model which is mentioned in journal[13] is applied to calculate power coefficient of Darrius blades. Lift and drag coefficient of new darriues blade design are 0.26 and 0.12. Lift and drag coefficient of conventional twisted blade design are 0.23 and 0.11. The lift to drag ratio of new design is 2.17 and the conventional design is 2.09.

Overall new design performs better than conventional design based on simulation result. The reason is tubercles design on leading edge of Darrius blades improves lift to drag ratio of Darriues blade by generating more lift from the turbulent flow caused by the tubercles.

The coefficients computed from COMSOL software are low due to the forces computed in software are low. The sizes of the blades have been scaled down comparing to standard size of wind turbine and settings of the simulation are low. The wind velocity set was 2.5m/s and the atmospheric pressure is 1atm. Because of the settings and sizes, the values computed are very small.

4. Conclusion

Based on the COMSOL simulation result, tubercles design is able to improve lift coefficient by creating turbulent flow which allows the darriues blades to rotate faster and improve power coefficient. For the Savonius part, hyperbolic parabolaid shape is able to direct the airflow and create vortex. In other words, enough drag force is generated to start the rotation of the blade. In conclusion, the tubercles design and hyperbolic parabolaid design implemented to vertical axis wind turbine is proved to be able to improve the power coefficient of wind turbine by improving lift to drag ratio.

Acknowledgement

The authors would like to acknowledge the support of the project partially by the Taylor's Flagship Research Grant TUFR/2017/001/01, 2017-2020.

5. References

[1] M. Ragheb, "Vertical axis wind turbines," 2013.

[2] D. Lian, J.-H. Lee, and Y.-C. Kim, "Power Prediction of Darrieus Type Wind Turbine Considering Real Air Velocity on the Wind Turbine," *Eur. Wind Energy Conf. Exhib.*, 2008.

[3] S. Jagadish, V. Sai, and T. V. Rao, "Design and Analysis of Vertical Axis Savonius Wind Turbine," vol. 8, no. 2, pp. 1069–1076, 2016.

[4] A. Kadam and S. Patil, "A Review Study on Savonius Wind Rotors for Accessing the Power Performance," *Iosr-Jmce*, no. September 2015, pp. 18–24, 2013.

[5] M. Abid, K. S. Karimov, H. A. Wajid, F. Farooq, H. Ahmed, and O. H. Khan, "Iranica Journal of Energy & Environment Design , Development and Testing of a Combined Savonius and Darrieus Vertical Axis Wind Turbine," vol. 6, no. 1, pp. 1–4, 2015.

[6] R. K. Kavade and P. M. Ghanegaonkar, "Design and Analysis of Vertical Axis Wind Turbine for Household Application," *J. Clean Energy Technol.*, vol. 5, no. 5, pp. 353–358, 2017.

[7] C. Srinivasan, G. Ajithkumar, S. Arul, G. Arulprasath, and T. M. Dharunbabu, "Design of Combined Savonius-Darrieus Wind Turbine," *IOSR J. Mech. Civ. Eng.*, vol. 14, no. 2, pp. 60–70, 2017.

[8] A. Sullivan, “Aerodynamic forces acting on an airfoil,” p. 2, 2010.

[9] C. Seidel, S. Jayaram, L. Kunkel, and A. Mackowski, “Structural Analysis of Biologically Inspired Small Wind Turbine Blades,” *Int. J. Mech. Mater. Eng.*, vol. 12, no. 1, p. 19, 2017.

[10] F. E. Fish, P. W. Weber, M. M. Murray, and L. E. Howle, “The tubercles on humpback whales’ flippers: Application of bio-inspired technology,” *Integr. Comp. Biol.*, vol. 51, no. 1, pp. 203–213, 2011.

[11] N. Conference, O. Recent, D. In, and S. Green, “Design and Analysis of Drag and Lift Vertical Axis,” *J. Chem. Pharm. Sci.*, no. 7, pp. 106–108, 2015.

[12] M. W. Lohry, D. Clifton, and L. Martinelli, “Characterization and Design of Tubercle Leading-Edge Wings,” *7th Int. Coneference Comput. Fluid Dyn.*, pp. 1–11, 2012.

[13] H. E. Saber, E. M. Attia, and H. A. El Gamal, “Analysis of Straight Bladed Vertical Axis Wind Turbine,” *Int. J. Eng. Res. Technol.*, vol. 4, no. 7, pp. 714–723, 2015.

EURECA 2018 – Conference Paper
Paper number 2EE04

Design and Analysis of Wind Powered Generator

Henry Chin Tshun Fan , Aravind CV*

School of Engineering, Taylor's University, 47500 Subang Jaya, Selangor, Malaysia
**aravindcv@ieee.org*

Abstract

With the challenges on inconsistent wind pattern and constant power generation, dynamic power generation is a bigger challenge. With wind speed ranging from 2 m/s to 12 m/s in Malaysia, power generation from horizontal axis wind turbine is nearly impossible. Hence, the direction is turning towards vertical axis orientations recently. The design strategy and analysis of a small axial flux wind generator is presented in this paper. The developed generator has the capability to generate output voltage of 2.4 V at wind speed of 1.9897 m/s which is within the range of wind speed in Malaysia.

1 Introduction

Malaysia is a developing country, electrical energy is one of the important factor to improve the economic growth in Malaysia. The demand of electrical energy must meet the population in Malaysia that is increasing. Malaysia has very rich fossil fuel resources which accelerates power generation development in Malaysia. However, the limitation of fossil fuels may not help the development of power generation infinitely. Thus, Malaysia should put more resources to explore the development of renewable energy (RE).

Wind turbine can be classified based on their orientation axis of wind turbine. There are two main types of wind turbines, which are Horizontal Axis Wind Turbine (HAWT) and Vertical Axis Wind Turbine (VAWT) [1]. Both types of wind turbines convert kinetic energy into mechanical energy. The orientation axis of VAWT is perpendicular to the direction of wind while the rotational axis of HAWT is parallel to the direction of the wind [2]. These two types of wind turbines have their own benefits and drawbacks. The most obvious benefits are HAWT is able to operate with higher efficiency than VAWT under high wind velocity condition while VAWT has the capability to produce higher aerodynamic power than HAWT under low wind velocity condition [3], [1]. The wind powered generator converts mechanical energy (from the rotation of wind turbine's blades) to electrical energy. The generator can be divided into two main types in terms of magnetic flux direction which are axial flux direction as shown in Figure 1 (a) and radial flux direction as shown in Figure 1 (b) [4].

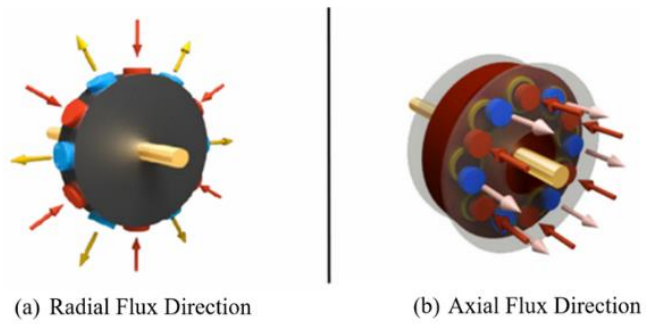


Fig. 1. (a) Radial Flux; (b) Axial Flux Configuration [5].

Most of the conventional wind-powered generator uses the application of radial field magnetic flux direction. In radial flux machine (RFM), magnetic flux flows parallel in the air gap between its rotor and stator while magnetic flux flows perpendicularly in the air gap between its stator and rotor in the axial flux machine (AFM). The structure of AFM usually has larger diameter and shorter axial length compared to conventional machine [6]. Theoretically, AFM operates with higher overall performance compared to conventional machine.

2 Application of generator in the literature

A machine with high rotational speed that has applied the theory of axial field was presented at London Imperial College. This type of machine has successfully started commercial production with the partnership of Turbo Genset Company. Pullen et al described applications of axial flux permanent magnet machine (AFPMM) in hybrid automotive and powertrain with high rotational speed of sixty thousand rpm and it generates rated output power of

approximately of 12 kW to 100 kW [7]. In addition, Holmes et al has done an experiment on a generator with a microfabricated axial flux permanent magnet (PM) micro turbine. The structure of this generator is fabricated with outer diameter of 7.5 mm. At rotational speed of 30000 rpm, this machine is able to generate small power of 2.2 mW [8].

The suitability of axial flux PM (AFPM) in wheel motors is very significant in solar car application due to the high efficiency and light in weight for the structure of AFPMM. Patterson and Spee presents the explanation of design and construction of an AFM in solar car[9]. Besides, Patterson and Spee also did an experimental test on its no load driven test, cogging torque and no load running test. The experimental result shows that the application of AFPM in the motors helps in improving overall performance compared to conventional motors [9]. On the other hand, Lovatte et al optimized the motor of solar-powered vehicle with the application of AFPM with structure of ironless winding and integration of Halbach magnet array. After analysing the experimental results as presented in this paper, AFPM motor has been proved that the overall performance of the solar-power car is better than its previous structure of motor [9].

Caricchi, Solero and Crescimbini et al has published many research papers about the wide application of AFPMM such as an air-cored generator for aircraft, ships and vehicles [10], vehicle wheel motors [11], [12], hybrid vehicles generator [13], and elevator direct drive [14]. Jack, Maddison and Mecrow mixed the application of radial flux and axial flux topologies in a single machine using soft magnetic composite materials. It can be observed that the magnetic flux flows in the motor is concentrated from a large surface area into the armature area. Therefore, high efficiency power can be generated compared to conventional machine [15].

Chan explained about application of AFPM in a single phase machine and alternator with high frequency [16]. From this paper, it can be concluded that AFPMM has larger diameter-to-length ratio and high power-to-weight ratio. The AFPMM machine is very popular in different applications past decades but the operational constraints do not allow to produce very high power in comparison to that of the HAWT.

3 Mathematical Modelling of Wind Powered Generator

3.1 Characteristics of wind turbine

The generated aerodynamic power of wind turbine can be expressed in Equation (1) [17],

$$p = \frac{1}{2}\rho A C_p V^3 \qquad (1)$$

where A is blade's swept area in m^2, ρ is air density kg/m^3, C_p is performance coefficient of wind turbine and V is wind velocity in m/s.

3.2 Design Equations of the AFPMG

3.2.1 Specific Electric Loading

Specific electric loading, ac, also known as current density on the stator surface can be determined as Equation (2) [6].

$$ac = \frac{no.of\ phase\ \times \sqrt{2} \times I_{ph} \times 2N_{ph}}{\pi \times D_{savg}} \qquad (2)$$

where N_{ph} is the number of turns per phase, $\sqrt{2}I_{ph}$ is the peak current and D_{savg} is the average diameter of stator in meter. The average diameter of stator is described as Equation (3) [6].

$$D_{savg} = \frac{D_{so} + D_{si}}{2} \quad (3)$$

where D_{so} is the outer stator diameter and D_{si} is the inner stator diameter in the unit of meter. By arranging Equation (2) [6], the phase current is shown in Equation (4).

$$I_{ph} = \frac{ac \times \pi \times D_{savg}}{No.of\ phases\ \times \sqrt{2} \times I_{ph} \times 2N_{ph}} \quad (4)$$

3.2.2 Specific Magnetic Loading

The specific magnetic loading, B_g with the unit of Tesla, can be determined by Equation (5).

$$B_g = \frac{p\phi}{\pi D_{avg} L_i} \quad (5)$$

where p represents the number of poles and ϕ represents the flux density per pole, D_{avg} determines the average diameter of stator and L_i is the axial length.

3.2.3 Electromagnetic Force Equation (EMF Equations)

The induced electromotive force of an AFPMG can be derived as equation (6) [6].

$$E_{out} = \frac{\sqrt{2}}{2} B_g N_{ph} D_{avg} L_i \omega_m \quad (6)$$

where B_g is the flux density flows in the airgap in Tesla, N_{ph} is the number of turn per phase, D_{avg} is the average diameter of the stator in meter, L_i represents the axial length in meter, k_w is the fundamental winding factor and ω_m is the speed of the rotor in rps.

3.2.4 Output Power of the Machine

The power of the machine is expressed as Equation (7) [6].

$$P = C_o D_{avg}^2 L_i w_m \quad (7)$$

where C_o determines as Equation (8).

$$C_o = \pi \frac{h}{4} B_g k_w k_1 \quad (8)$$

D_{avg} is the average diameter of the stator in meter, L_i represents the axial length in meter, ω_m is the speed of the rotor in rps, h is the number of faces of stator, B_g is the flux density flows in airgap in Tesla, k_w is the fundamental winding factor, $k_1$is the specific electric loading in A-cond/m.

3.3 Application of Design Equations

The design of machine should be started with necessary assumption and apply the parameters as shown in Table 1 into design equation as described in Section 3.2

Table 1. Design Parameters.

Parameter	Symbol	Unit	Value
Radius of Wind Turbine	r	Meter [m]	0.285
No. of poles	P	-	12
Number of stator slots	S	-	10
Radius of Rotor	r	Meter [m]	0.1
Outer diameter of stator	D_{so}	Meter [m]	0.224
Inner diameter of stator	D_{si}	Meter [m]	0.08
Specific Magnetic Loading	B_g	Tesla [T]	0.608
Specific electric loading	ac	Amp.cond./ m^2	9000
Winding Factor	k_w	-	0.5
Number of Turns per phase	N_{ph}	-	370
Number of faces of stator	h	-	2

3.4 Stator and Winding Configuration

In the stator configuration, it consists of 10 slots. Each slot is filled with a coil. All the phases are connected in series as shown in Figure 2 to form a single phase to obtain a single phase output.

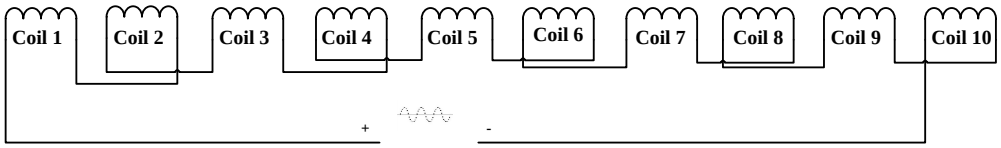


Fig 2: Armature Coil Connection

4 Simulation and Development of AFPMG

4.1 Numerical Analysis of AFPMG

The model as shown in Figure 3 is the structure of AFPMG drawn in numerical tool.

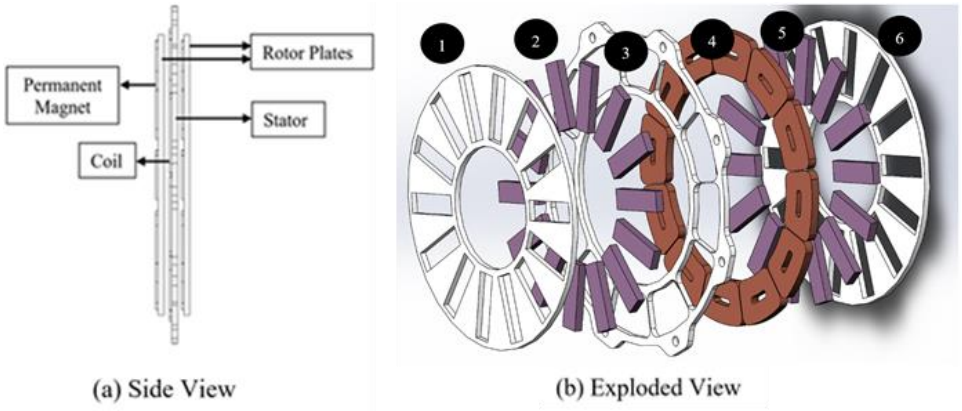


Fig. 3. Design of AFPMG.

As shown in Figure 3, item ‘1’ and ‘6’ are the rotors plates of AFPMG and each plate consists of 12 poles, item ‘2’ and ‘5’ are PMs which are embedded into the poles of rotor plates, item ‘3’ are the coils which are inserted into the frame of the stator (item ‘4’), item 4 is the stator which consists of 10 slots. After designing the model in the numerical tool, the model in Figure 3 is exported into JMAG software for running finite element analysis. The model in Figure 3 was analysed with its magnetic flux density, coil flux linkage and output voltage.

The magnetic flux density of AFPMG simulated from numerical analysis tool is shown in Figure 4.

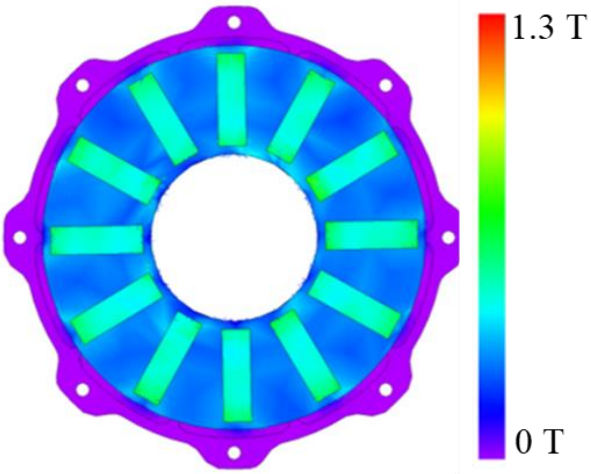


Fig. 4. Contour Plot of Magnetic Flux Density of Rotor Plate.

As presented in Figure 4, different colour represents different strength of the magnetic flux density. It can be observed that the magnetic flux density at different points of the machine is different. It is also observable that the magnetic flux density in the rotor plate is higher than stator. This is because rotor plate is made with ferromagnetic material and there are PMs embedded on the rotor plate. The ferromagnetic material is a type of material which exhibits strong magnetism when magnetic field is applied on it. The location with maximum magnetic flux density is very near to the PM. The minimum flux density occurs in the stator which is very far away from the PM. As PM produces magnetic field itself, the point which is nearer to the PM has higher magnetic flux density, while the point which is further from the PM has lower magnetic flux density.

The PM configuration with theoretical and simulated flux lines is shown in Figure 5.

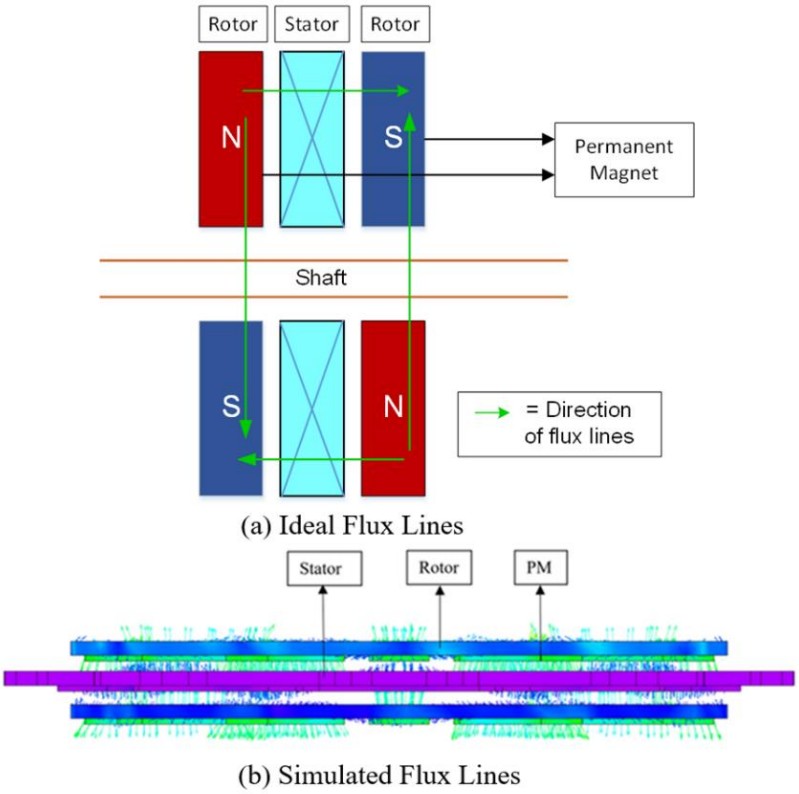


Fig. 5. PM Configuration with theoretical magnetic flux lines and simulated flux lines.

As presented in Figure 5, the PM configuration set in this simulation is NSSN configuration. The magnetic flux flows from the north pole of the magnet through the air gap and coil and lastly reach the south pole of the magnet in the opposite plate. When the rotor plate is rotating, the magnetic flux produced by the PMs embedded in the rotor cuts the conducting loop in the coil and current is induced in the coil. This is because the magnetic force produced by the PM causes the free electrons in the copper wire to move. The free electrons moving in the conductors carry electric charges and this generates alternating current in the copper wire. When the rotor plate is rotating and cutting the coil, a sine waveform of coil-flux linkage is generated in a coil.

4.2 Development of AFPMG

The generator consists of moving parts and static part. The moving parts consist of 2 rotor plates and the static parts consist of one stator frame. Each of the rotor plates consists of 12 poles. Each pole is embedded with NdFeB magnets. Figure 6 shows the materials of the prototype.

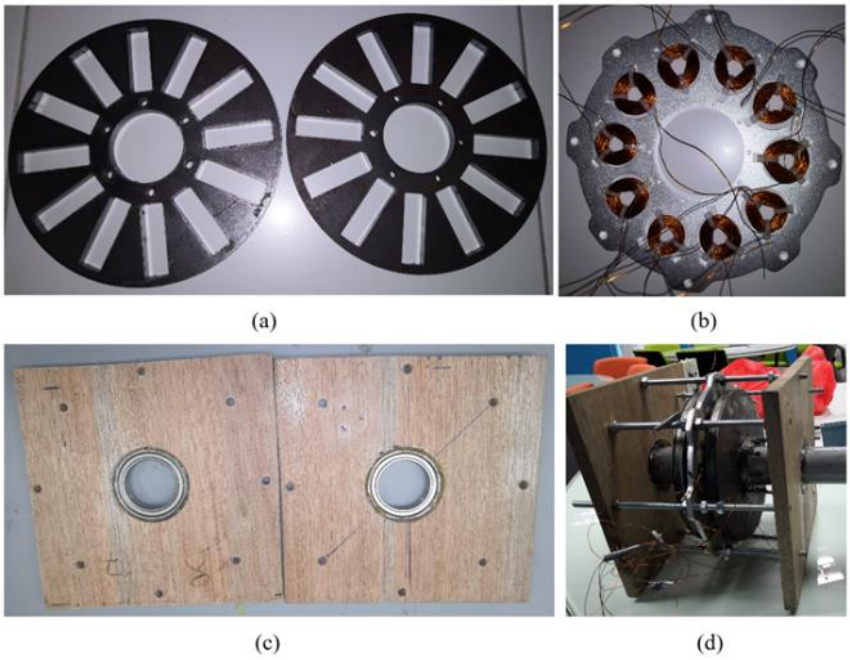


Fig. 6. (a) Rotor Plates; (b) Stator frame and coils; (c) Wooden Board with bearing; (d) prototype of AFPMG.

As shown in Figure 6 (a), the rotor plates are cut with 12 rectangle poles and 6 circle poles. The rectangle poles are developed so that PMs can be embedded into the rotor plate while the 6 circle poles are designed for the holding of two rotor plates in parallel using bolts and nuts. The rotor plate is made with low carbon steel (mild steel). The stator as shown in Figure 6 (b) acts as an aluminium frame for holding the 10 sets of coils (copper wire). The 8 circle poles located near the edge of the frame are used for holding purpose using long steel rods. The wooden board as shown in Figure 6 (c) is embedded with bearing and used for holding the shaft of the generator. The bearing is used to reduce the friction between the moving part (shaft) and static part (wooden board). The assembled prototype of AFPMG is shown in Figure 6 (d).

5 Results and Discussion

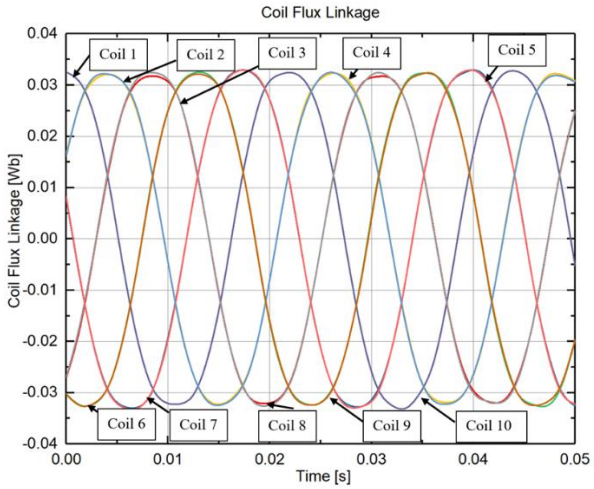


Fig. 7. Simulated Result of Coil-Flux Linkage of AFPMG (combination of all coils).

As shown in Figure 7, two coils of the machine generate the same phase of sinusoidal waveform due to the winding configuration as shown in Figure 2 and the operating speed of the machine, Figure 8 is plotted by extracting a one period of the waveform for one of the coil of the machine.

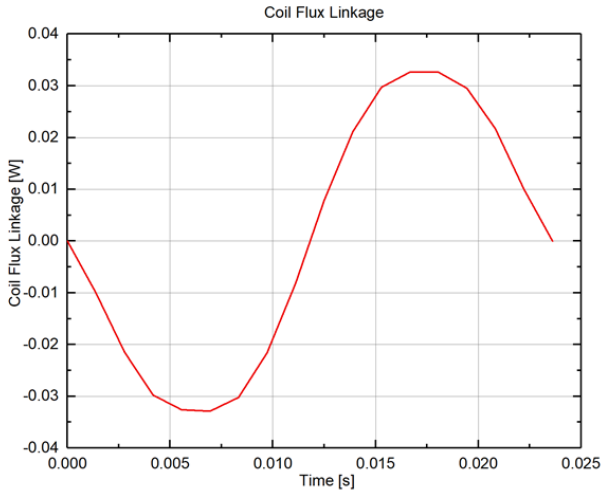


Fig. 8. Simulated Waveform of Coil Flux Linkage for one of the coils in one period.

As shown in Figure 8, the flux linkage in any of the coils completes a cycle of sine waveform in every 0.022 s with the rotational speed of 450 rpm. The design of the machine was used to develop a prototype and the experimental results were used to analyze with the application of wind turbine to investigate the output of the AFPMG according to different wind velocity. The output of developed AFPMG has analyzed its performance with application of wind turbine by considering Equation 9.

$$Rotational\ Speed\ of\ Machine = \frac{speed\ ratio \times v \times 60}{2\pi r} \times 100\% \quad (9)$$

where v is the wind velocity, r is the radius of the wind turbine. The speed ratio as presents in Equation 9 indicates the speed ratio between the rotational speed of wind turbine and the rotational speed of wind-powered generator. By assuming the speed ratio to be 1.2, r to be 0.285 meter, the generated voltage of wind-powered generator is presented in Figure 9.

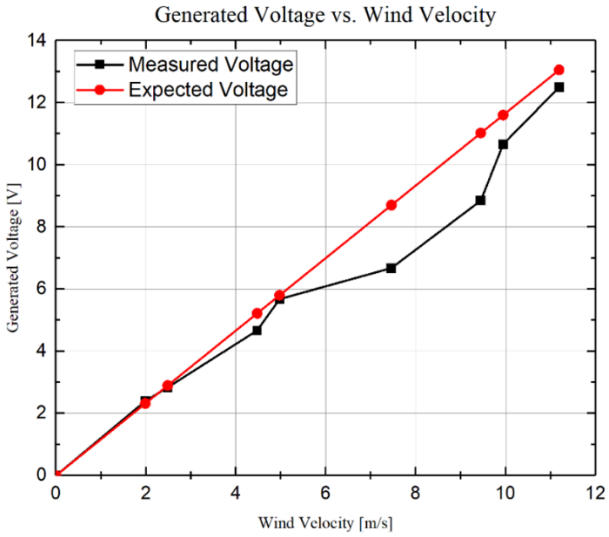


Fig 9. Generated Voltage of developed AFPMG.

By analyzing the operating range of wind velocity as presented in Figure 9, the developed AFPMG generates 2.4 V and 12.5 V at wind velocity of 1.9897 m/s and 11.1919 m/s respectively which are within the range of wind speed in Malaysia. Thus, it has proved that the developed AFPMG can be operated and generate output voltage under low wind speed condition area.

6 Conclusion

This paper has described the design of wind powered generator using theoretical calculation and simulation using numerical tools and construction of AFPMG according to the designed model. This generator is designed with the application of principle of axial field. The structure of generator is a double-rotor-single-stator AFPMG. The design parameters include number of poles and stator, outer and inner diameter of stator, specific magnetic loading and specific electric loading, winding factor, number of turns per phase and number of faces of stator. The simulated model can be observed that the rotor plate has high magnetic flux density and the magnetic flux line flows from one pole of the PM embedded in the rotor plate to another pole of PM embedded at the opposite rotor plate by cutting through the air gap and coil of the machine. The developed wind-powered generator has the capability to generate output voltage of 2.4 V with wind velocity of 1.9897 m/s while with wind velocity of 11.1919 m/s, the generator generates output voltage of 12.5 V. Hence it has proved that, with a wind turbine that meets the speed ratio of 1.2 and radius of 0.285 m, the generator has the capability to generate voltage within the range of wind speed in Malaysia where Malaysia is considered as low wind speed area.

Acknowledgement

The authors acknowledge the support for the project from the Taylor's University flagship research grant TUFR/2017/001/01, 2017- 2020.

References

[1] T. Wei Wei and C. Aravind, "Magnetic Geared Radial Axis Vertical Wind Turbine for Low Velocity Regimes," in *MATEC Web of Conferences*, 2018, vol. 3007, pp. 1–10.

[2] D. A. Spera, *Wind Turbine Technology*. Cencage Learning, 2009.

[3] P. Jain, *Wind Energy Engineering*. McGraw Hill, 2011.

[4] R. Bojoi, A. Cavagnino, A. Miotto, A. Tenconi, and S. Vaschetto, "Radial flux and axial flux PM machines analysis for more electric engine aircraft applications," in *2010 IEEE Energy Conversion Congress and Exposition, ECCE 2010 - Proceedings*, 2010, pp. 1672–1679.

[5] D. Moreels, "Axial Flux vs Radial Flux: 4 Reasons Why Axial Flux Machines have a Higher Power Density," *Magnax*, 2018. [Online]. Available: https://www.magnax.com/magnax-blog/axial-flux-vs-radial-flux.-4-reasons-why-does-axial-flux-machines-deliver-a-higher-power-density. [Accessed: 20-Dec-2017].

[6] Gieras, J. F., Wang, Rong-Jie, Kamper, and M. J., *Axial Flux Permanent Magnet Brushless Machines*. Dordrecht: Springer London, 2008.

[7] D. a. Howey, a. S. Holmes, and K. R. Pullen, "Measurement of stator heat transfer in air-cooled axial flux permanent magnet machines," *Ind. Electron. 2009. IECON '09. 35th Annu. Conf. IEEE*, pp. 1197–1202, 2009.

[8] A. S. Holmes, Guodong Hong, and K. R. Pullen, "Axial-flux permanent magnet machines for micropower generation," *J. Microelectromechanical Syst.*, vol. 14, no. 1, pp. 54–62, Feb. 2005.

[9] D. J. Patterson, G. Heins, M. Turner, B. J. Kennedy, M. D. Smith, and R. Rohoza, "An overview of the compactness of a range of axial flux PM machines," *Proc. - 2017 IEEE Work. Electr. Mach. Des. Control Diagnosis, WEMDCD 2017*, pp. 27–32, 2017.

[10] F. Caricchi, F. Crescimbini, O. Honorati, G. Lo Bianco, and E. Santini, "erformance of coreless-winding axial-flux permanent-magnet generator with power output at 400 Hz, 3000 r/min," *IEEE Trans. Ind. Appl.*, vol. 34, no. 6, pp. 1263–1269, 1998.

[11] F. Caricchi, F. Crescimbini, F. Mezzetti, and E. Santini, "Multistage axial-flux PM machine for wheel direct drive," *IEEE Trans. Ind. Appl.*, vol. 32, no. 4, pp. 882–888, 1996.

[12] L. Solero, O. Honorati, F. Caricchi, and F. Crescimbini, "Nonconventional three-wheel electric vehicle for urban mobility," *IEEE Trans. Veh. Technol.*, vol. 50, no. 4, pp. 1085–1091, Jul. 2001.

[13] F. Crescimbini, A. DiNapoli, L. Solero, and F. Caricchi, "Compact Permanent-Magnet

Generator for Hybrid Vehicle Applications," *IEEE Trans. Ind. Appl.*, vol. 41, no. 5, pp. 1168–1177, Sep. 2005.

[14] F. Caricchi, F. Crescimbini, and O. Honorati, "Modular axial-flux permanent-magnet motor for ship propulsion drives," *IEEE Trans. Energy Convers.*, vol. 14, no. 3, pp. 673–679, 1999.

[15] A. G. Jack, B. C. Mecrow, and C. P. Maddison, "Combined radial and axial permanent magnet motors using soft magnetic composites," *"Electrical Mach. Drives, 1999. Ninth Int. Conf. (Conf. Publ. No. 468),"* vol. 1999, no. 468, p. 25, 1999.

[16] C. H. T. Lee, K. T. Chau, and C. C. Chan, "Comparison of flux-switching machines with and without permanent magnets," *Chinese J. Electr. Eng.*, vol. 1, no. 1, pp. 78–84, 2015.

[17] Yicheng Chen and P. Pillay, "Axial-flux PM wind generator with a soft magnetic composite core," in *Fourtieth IAS Annual Meeting. Conference Record of the 2005 Industry Applications Conference, 2005.*, 2005, vol. 1, pp. 231–237.

Smart City Intelligence Safety Systems On Road (S.C.I.S.S.O.R)

Muhammad Hadi bin Saleh[1,] *,Teh Aun Shih*[216]*, and *Aravind CV*[3]

[1]Electrical and Electronic Engineering, School of Engineering

Taylor's University.

aunshih.teh@taylors.edu.my

Abstract.

Echolocation is a method that uses sound to determine the location of the object in a space. Echolocation is one of the applications of Doppler effect. The technique is used commonly by microbats to help them hunt their prey and navigate in the dark. The bats emit ultrasonic waves and listen for echoes produce by its surrounding. The research is about replicating echolocation of the Microbat system to develop a driver assistance system(DAS) as part of the "Smart City" initiatives. Ultrasonic sensors are used to replicate the echolocation technique. This paper focuses on analyzing the potential of the ultrasonic sensors to be used as DAS. the accuracy of the sensors with an object placed at a different angle at a different distance and the arrangement of the sensors in the shape of a regular polygon to cover a 360° area surrounding it. . The objective of this research is to develop an algorithm that able to spatially map the distance of object surrounding the vehicle to detect a potential hazard and navigate through it. The rethe sult found that, at a shorter distance, the sensors able to detect a signal even if it exceeds the measuring angle. Then, increase in a number of sides of the polygon, increase the area coverage per 360°. In addition. from analyzing the distance vs time and velocity vs time graphs, the location and motion of the object are able to be determined.

1 Introduction

Technological advancement in recent years has fostered development in urbanization which leads to people migrating and converging to cities [1]. This is linked to opportunities towards improving their way of life via better job, education and social life. There will always be positive and negative impacts of urban development but for certain development in the city drives energy needs and increases the demand for natural resources, territorial development and adequate infrastructure [1]. This raises a concern for the sustainability of the environment and increases the need for solutions to alleviate the issues with increasing development. The concept or idea of a 'Smart City" has been receiving wide-spread interest across the world as a strategy to address the issue with the modernization of cities [1, 2]. Creating a Smart City requires a lot of improvement especially development in the infrastructures such as mobility, agriculture, logistics, and communication. Prioritizing which area of infrastructure initiatives for development is not a simple task as not all city have the same characteristic, resources, and problems [2]. In Malaysia for example, transportation has always been a problem due to inefficient public transport, traffic congestion, ineffective traffic light and inconsiderate reckless drivers. Despite that, the number of vehicle on the road is still increasing as Malaysia is experiencing growth in economic, motorization and industrialization [3]. An investigation was done by Malaysian Institute of Road Safety Research (MIROS) shows the main cause of the accidents are due to risky driving, speeding, and fatigue [4]. Table 1 summarises the common causes of accidents and the corresponding number of accidents from the investigation done by MIROS crash reconstruction unit in a 2013 report.

Table 1. Causes of accidents.

Factor	***Number of accidents***
Risky Driving	121
Speeding	93
Fatigue	70
Safety, Health, and Environment	38
Road Defects	36
Driving Under the influence of drugs/alcohol	24
Brake Defects	20
Conspicuousness	18
Tyre Defects	14

Overloading	11

Generally, the accidents can be classified into two categories, accidents that are caused by driver and accidents that are not caused by the driver. Out of 10 major causes, 6 of it are caused by the driver. Thus, this project research is about studying ways to reduce the amount of collision occurring on the by implementing the concept of bat echolocation of a microbat on a vehicle for obstacle avoidance in the form of driving assistance system(DAS).

1.1 Driver Assistance System (DAS)

Research done by T. Sato and M. Akamatsu stated, theoretically driving has a hierarchical structure in which they are strategic, tactical and operational behaviour [5].

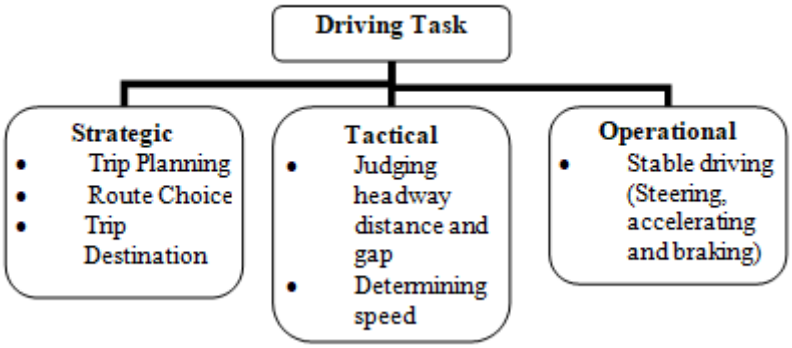


Figure 2. The hierarchical structure of driving behaviour.

Figure 1 shows the essentials behaviour that determines the skills of the driver to control their vehicles. Lacking in one of the behaviour components might cause accidents to occur. As an example, lacking in the strategic level of behaviour such as bad trip planning might lead to reckless lane switching to get to their destination which endangers another vehicle in the process and ultimately leads to bad driving behaviour. In order to improve driver efficiency and behaviour on the road, a lot of drivers use driving assistance system(DAS) to help them navigate the road [6]. The goals are categorized into three types of goals [6].

1. Vehicle dynamics stabilisation
2. Information, warning & Comfort
3. Automated & Cooperative driving.

A good example of DAS which is used by many drivers is the navigation system. Typically presented in a digital map and auditory information, the system will inform the user information such as traffic, route, speed and estimated time arrival which help the driver with the trip. The advanced function existed in the system are expected to enhance road safety and also help the user become more efficient[5]. Different types of DAS either currently in development or in the market use a different type of sensors to achieve stated above. Mainly there are three types of sensors implemented on the vehicle to create a DAS and they are proprioceptive, exteroceptive and sensor network[6]. However, there is a common trend on which sensors are used in the development of the system. As an example, for positioning and

object detection, exteroceptive sensors such as RADAR and LIDAR are used. Adaptive Cruise Control(ACC) is one of the commonly known DAS that uses such sensors in their system [7]. ACC is a system that utilizes this forward sensor to scan area in front of the vehicles. Couple with electronic and drive control the system enable the vehicle to brake and reduce acceleration when necessary [8, 9,12]. Table 2 show list of currently existed DAS technology.

Table 2 Description of commercialise DAS.

Driving Assistance System	**Description**	**Reference**
Adaptive Cruise Control (ACC)	Utilizes a forward-looking sensor to scan area in front of the vehicles. The system uses radar technology, electronic brake and drives control. When engaged the system to react by matching the speed of the vehicle within the sensor range and apply to brake and reduce the acceleration to follow the vehicle at a safer distance	[6, 7, 10]
Lane departure warning system (LDWS)	This system is used to monitor and provide a warning to the driver when the vehicle is changing lanes without using a turn signal. This is to help a drowsy or careless driver. The system detects the position of the vehicle with respect to the lane boundary. The system is build based cameras or vision sensors. A technique such as an edge detection is commonly used to develop the algorithm for lane detection.	[7, 10, 11]
Parking assistance system	The system assisting the driver in checking the rear area of the vehicle to ensure it is clear. There are several version of this system. Typically, the system only provides visual and auditory information to the driver. A more advanced version of this system provides the assistance of steering and auto park the vehicle with help of path planning and tracking algorithm. The system uses a combination of several sensors such as image sensors and ultrasonic sensors.	[12, 13]
Pre-Crash system	It is a type of system that detects and alert the driver to imminent accidents. The pre-crash sensor is primarily used as a radar to detect the object. The system judges the probability of a collision based on the relative speed of the vehicle with respect to the object. The system will decide whether it can avoid the collision or help to mitigate the collision damage by activating the brake assist and pre-crash seat belt	[7, 15]
Traction Control System	Traction control prevents the vehicle from swerving when accelerating on loose surface, reduce engine	[16]

	output until the vehicle can move without the wheels of vehicle skidding. This help improves the stability of the vehicle. The way it works is by applying the brake to the wheel so the differential able to apply power to the other wheel because a conventional differential does not distribute torque usefully to the wheels while skidding. The system uses wheel speed sensor which the speed sensor is an application of the hall effect. Another name of this sensor is hall effect sensor.	

However, the acceptance and attitude by the public regarding DAS are not always positive as some might called it intrusive and distracting [5, 9]. In addition, the unwillingness to let the automated system of the vehicle to take control is deemed as a negative aspect of the DAS. Hence the question of how to develop a system the user can trust that is not intrusive and distracting is raised everytime a DAS is being developed [9].

1.2 Bat Echolocation

Microbats are one of many animals that uses echolocation or biosonar. What makes microbats special is how extensively they used echolocation in comparisons to other types of bats in particular megabat which most of them does not use echolocation [17]. Echolocation is the use of sound wave the determine the location of the object in space [18]. For microbats, echolocation is used mainly to locate their prey or food, roosting crevices even and avoid obstacles in the dark [17, 18]. The bats emit pulses of ultrasonic burst and receive information regarding its surrounding by listening to the echoes of the waves [18, 19]. Specifically, the bat emits a wave with a certain intensity or amplitude and pulse rate while waiting for the received signal intensity from echoes [19]. Obstacle avoidance DAS typically uses waves type of sensors such as ultrasonic, infrared (IR), Radio Detection and Ranging (RADAR) and Light Detection and Ranging (LIDAR). Each with their own advantages and disadvantages, the research focuses on the using the ultrasonic sensors due to its inexpensive price and its ability to work in the dark environment but also object surface detection [20, 21, 22]The research objective is to develop an algorithm for driving assistance system that uses ultrasonic wave echolocation to detect potential hazards in relation to collisions by spatially mapping the distance of surrounding objects enabling the vehicle to navigate around these objects to avoid collisions. The research studies effect of different orientation and arrangement of multiple ultrasonic sensors in the shape of a regular polygon on its ability to spatially map the surrounding objects surrounding it.

2 Methodology

2.1 Platform Selection

The platform for hardware and software to develop the project was determined and chosen based on the availability of resources, cost, and complexity of the platform.

2.1.1 Hardware

Development board, Arduino UNO was chosen from among the other competitors, Raspberry Pi and Beagle Bone. The reason for this selection because the board is inexpensive, less complex and the resources are easy to find. Other hardware decided is the type of sensor which is the ultrasonic sensor.

2.1.2 Software

There are two types of software used to develop this project. One is Arduino internal development environment (IDE) and another is MATLAB. Arduino (IDE) was used to develop the algorithm while MATLAB software was used to aid the project as an analytic tool.

2.2 Bat Algorithm Implementation

Echolocation of microbat is replicated HC-SR04 ultrasonic sensors. Figure 2 illustrates the echolocation concept inspired by the microbats is done on three different conditions which are static object, dynamic object moving away and towards the vehicle.

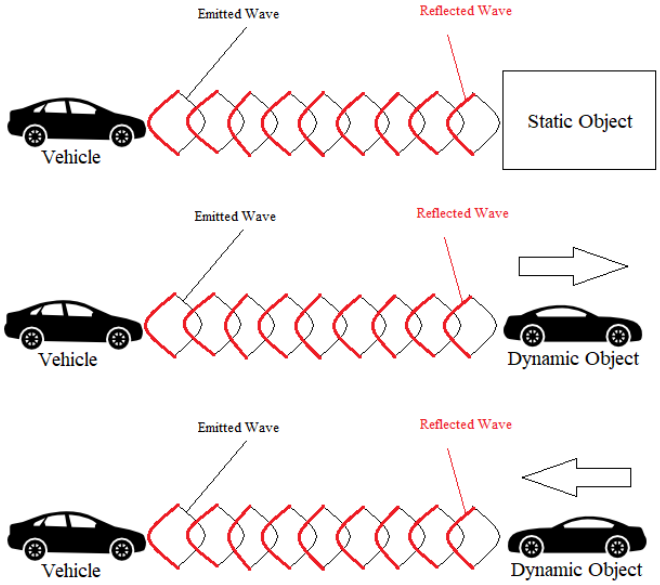


Figure 3. Echolocation on vehicle.

A series of test is done was done on the sensors to help develop the algorithm.

2.2.1 Signal Accuracy

The sensor timing of the sensor is as shown in Figure 3 and according to the datasheet provided by the manufacturer the measuring angle is given as 15° to tieh and area of coverage of a single sensor is as shown in figure 4.

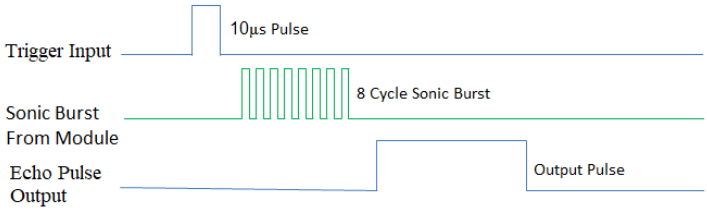


Figure 4: Timing Diagram of ultrasonic sensor.

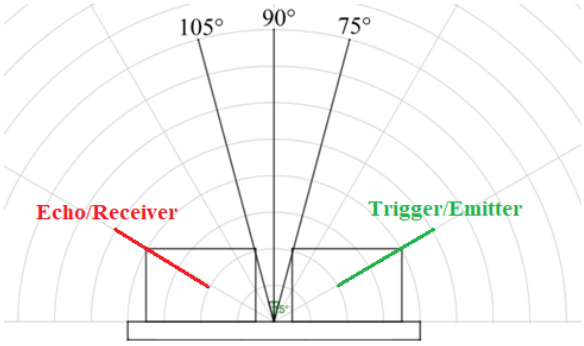


Figure 5. Measuring angle of ultrasonic sensor.

An object is placed at a different angle while facing the sensor starting from 0°, 15°, 30°, 45°, 60°, 75°, 90°, 105°, 120°, 135°, 150°, and 180°. The object is placed at the distance of 0cm, 5cm, 10cm, 15cm, 20cm and 25cm away from the sensor. The distance read by the sensor is recorded. The purpose of this test is to study the effect of the value of the sensor when the object is placed inside and outside of its measuring angle.

2.2.2 Arrangement of sensors

Multiple sensors are arranged in shape of a regular polygon which is a triangle and a square. The prototypes purpose was to study how the sensors react to static and dynamic motion of object.

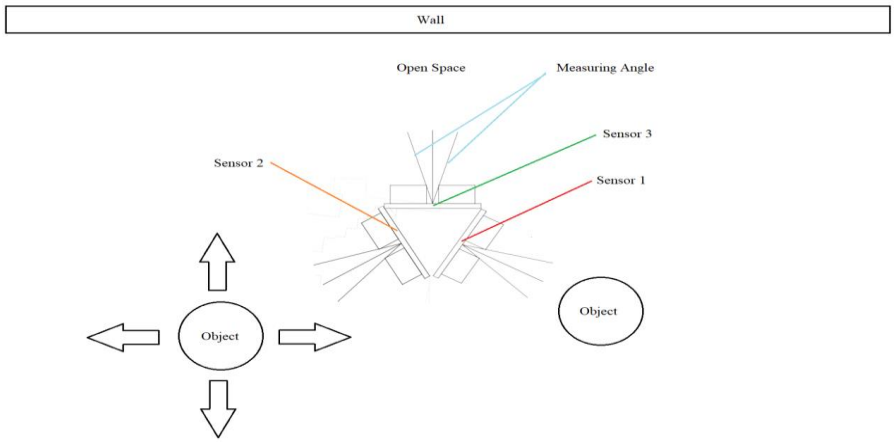


Figure 6. Sensor setup for triangle arrangement.

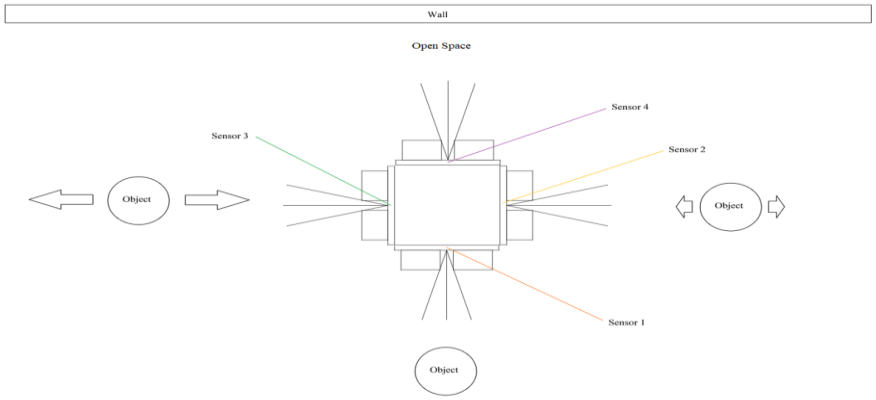


Figure 7. Sensor setup for square arrangement.

Referring to Figure 5 and Figure 6, object with arrows mean the object is moving. For square arrangement, the longer arrow shows a faster rate of movement. Open space means there is no object placed in front of it and it is pointed to the wall. 10 readings are taken from the experiment and recorded to be analyzed using MATLAB software. Each reading has 0.5 seconds interval. The condition at each sensor for a triangle and square arrangement is summarized in Table 3 and Table 4.

Table 3. Condition at each sensor for triangle arrangement.

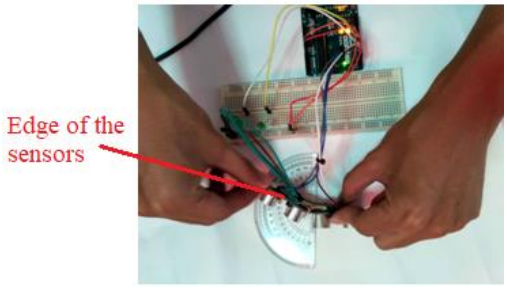
Sensor	**Condition**
1	Open space
2	Static object
3	Moving object

Table 4. Condition at each sensor for square ararngement.

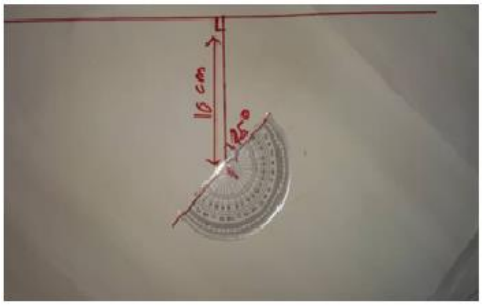
Sensor	**Condition**
1	Static object
2	Moving object at a slower rate
3	Moving object at a faster rate
4	Open space

2.2.3 Sensors Coverage between 2 sensors

The area in which the sensors are not able to cover is the blind spot of sensors. A test to investigate the effect of the arrangement of the sensors with the blind spot of the arrangement was done. Two sensors are arranged at an angle of 60°, 90°, 108°, 120° and 135°. Each sensor is paired with a LED which the LED will light up when the object is detected in front of it and turned OFF otherwise. Refer Figure 7(a) and Figure 7(b) for the arrangement of the setup.



(a) Setting up the angle



(b) Test Setup

Figure 8. Setup for sensor coverage test.

The object is placed at 45° and 10cm away from the edge of the sensors connected as shown in Figure 7(a). Note that the distance is set to 10cm because the result from the accuracy test of the sensors showed the sensor is able to approximately detect an object even it is outside of its measuring angle at this distance for angle 60° and 120°. The object is moved in a straight line and the state of LED is observed. Assuming the object is moved from Sensor 1 to sensor 2, record the distance the object travelled when the state of LED 1 changed from ON to OFF and to the state of LED 2 changed from OFF to ON. The purpose of this is to study the best arrangement of sensors that will give the lowest blind spot area with the minimal amount of sensors used.

2.3 Developing Algorithm

The prototype was built to test the algorithm. The arrangement of sensors made is based on the result obtained from the previous result. The algorithm is designed to be able to spatially map the distance of the object surrounding the vehicle. The Response system or the feedback system of the algorithm is made out of LED which it will respond to the preset condition. The algorithm check for two values which they are distance of object surrounding the vehicle and speed of object in relative to the vehicle. The Response can of the system is as shown in Table 5 and Table 6 for distance threshold and speed threshold respectively.

Table 5. Pre-set response of the algorithm for object distance detection.

Distance threshold, cm	Response of LED
Less than 15	ON
More than 15, less than 20	Blink 2 time

More than 20	OFF

Table 6. Pre-set response of the algorithm for object velocity detection.

Velocity range cm/s	Alert Level	Response of LED
Less than - 50	High	All Blink 5 times
More than - 50, less than 0	Medium	All Blink 2 times
More than 0	Low	OFF

3 Results and Discussion

3.1 Sensor Accuracy

The formula used by the sensor to calculate the distance of the object is given as Eq. 1

$$Distance = \frac{t_{on} * 0.034}{2} \quad (1)$$

where t_{on} is the duration of the trigger pulse.

The result from accuracy testing of the sensor is tabulated and Table 7 is the result of the test.

Table 7. Distance detected by the sensor at different angle and distance.

Angle, θ°	Distance from sensor, cm				
	5	10	15	20	25
0	118	113	118	116	117
15	119	116	119	120	118
30	115	120	116	117	112
45	116	119	117	116	115
60	6	9	116	115	118
75	8	13	16	23	116
90	5	10	15	20	25
105	6	11	16	21	117
120	6	12	115	118	116
135	116	117	118	115	118
150	117	114	116	117	117
175	6	12	115	118	116

180	115	112	114	117	116

From the result in Table 7, at an angle of 90°, the object is able to measure the distance accurately. As the object is placed is placed at either 75° and 105°, the accuracy drops but it is still considered accurate with only a small deviation to its accurate value. However, at the distance of 25cm, the sensors are not able to accurately measures it. This shows the measuring angle of the sensor given by the datasheet is confirmed to be at 15°. This test helps determine the threshold distance for the algorithm which in this case is decided to be at 20cm. Despite the measuring angle is 15°, the sensor still able to detect an object even it is outside its measuring angle as seen at an angle of 60° and 120° but the range is only up to 10cm.

3.2 Static and Dynamic Object

Multiple sensors are arranged into a triangle shape and square shape. These two prototypes are used to test the reaction of the sensors with a different kind of motion of object. Result for triangle arrangement and square arrangement is shown in Table 8 and Table 9 respectively.

Table 8. Reading by each sensors for triangle arrangement.

Time	**Distance, cm**		
	Sensor 1	**Sensor 2**	**Sensor 3**
0.00	189	41	5
0.50	188	41	9
1.00	189	41	29
1.50	188	41	15
2.00	188	41	12
2.50	188	41	6
3.00	188	41	24
3.50	189	41	27
4.00	188	41	35
4.50	188	41	19

Table 9. Reading by each sensors for square arrangement.

Time	**Distance, cm**			
	Sensor 1	**Sensor 2**	**Sensor 3**	**Sensor 4**
0.00	38	5	5	191
0.50	38	9	11	192

1.00	38	26	32	190
1.50	38	50	3	192
2.00	38	48	28	190
2.50	38	36	13	190
3.00	38	16	23	190
3.50	38	3	27	190
4.00	38	10	5	190
4.50	38	26	19	190

Graph of distance versus time and Graph of velocity is plotted for triangle arrangement and square arrangement. Figure 8 and Figure 9 are the graphs plotted for the triangle arrangement while Figure 10 and Figure 11 is the graph plotted for the square arrangement.

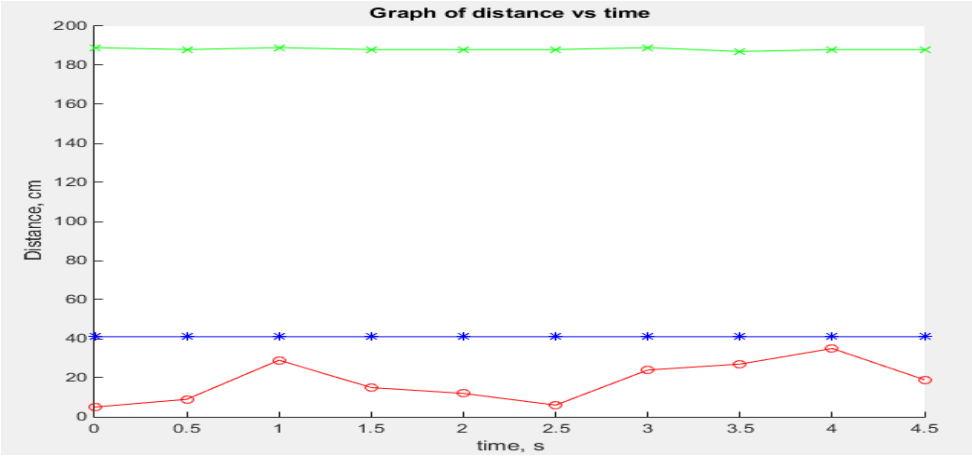


Figure 9. Graph of distance versus time for triangle arrangement.

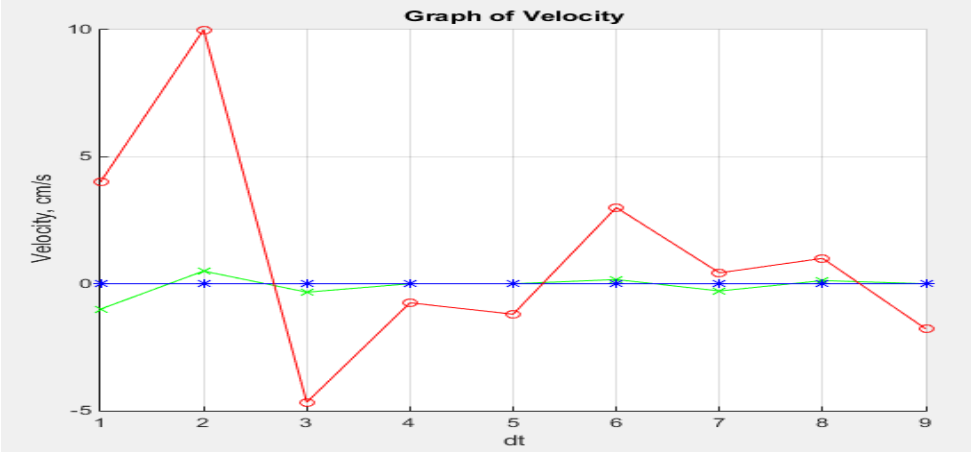


Figure 10. Graph of velocity for triangle arrangement.

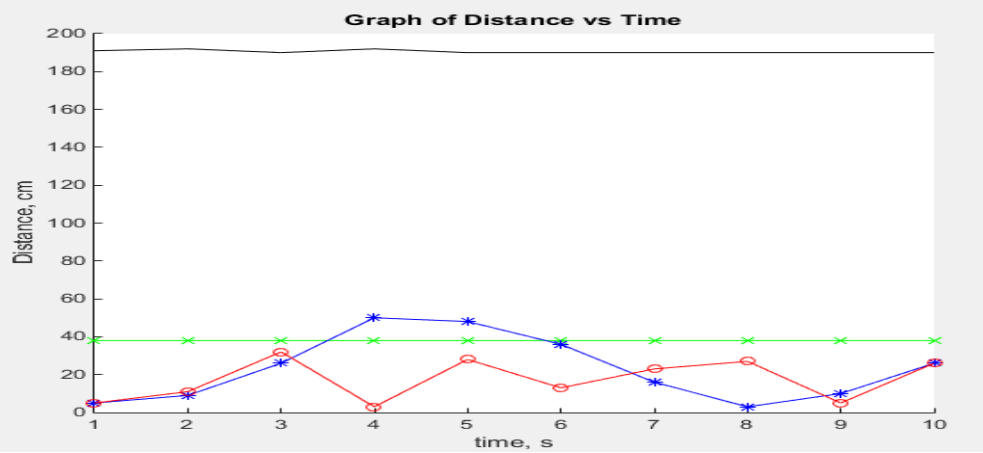


Figure 11. Graph of distance versus time for square arrangement.

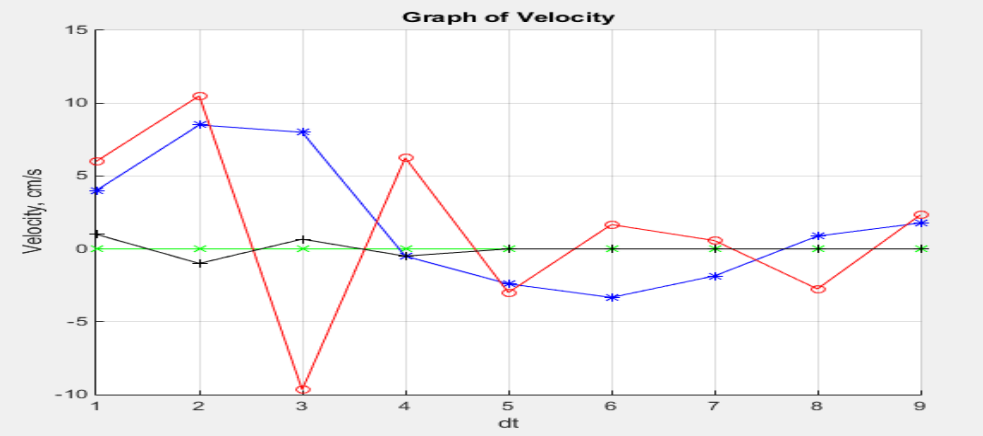


Figure 12. Graph of velocity for square arrangement.

The marker used are 'x', '*', 'o' and '+' for sensor 1, sensor 2, sensor 3 and sensor 4 respectively. From the graphs of distance versus time, for both arrangement, for the static object, the plotline is a straight line. A similar trend can be seen if the sensor is pointed at an open space which it only detects its distance to the wall. However, if the object moved, the plotline gives a gradient as shown in both of the graphs. On top of that, if the object is moved at a different rate, the steepness of the slope or gradient is also different. Since the gradient of

a distance versus time graph is velocity, the velocity of the object near the sensor can be obtained. The magnitude of the slope is the speed while the sign of the velocity is the vector of the object either it is moving away or toward the sensor. A higher magnitude of velocity means the object is moving at a high speed. The positive sign of the velocity indicates the object is moving away while a negative sign indicates the object is moving toward the vehicle. From this analysis, an algorithm is developed to detect the speed and the direction of the object in relative to the vehicle.

3.3 Sensors Coverage between 2 sensors

The arrangement of the sensors is set to cover a 360° area surrounding, but from the sensor accuracy testing, it is shown that the sensor is not able to detect object if the object is more than the measuring angle of the sensors the exception of when the object is placed at angle of 60° and 120° with a length of 10cm. Thus a test was done to investigate the effect of different angle of separation of sensors on the coverage area of the arrangement. Note that the angle separation between sensors is determined base on the interior angle of a regular shaped polygon.

Table 10. Distance taken by the object to switch the state of LED's at a different angle.

Number of sides, n	**The angle of separation between sensors, θ°**	**Distance taken by the object to switch the state of the LED's, cm**
3	60	0
4	90	18
5	108	14
6	120	12
8	135	12

From the result, it is shown that at increase angle of separation between sensors, the distance taken is decreasing. However, when n = 6, the distance is the same as n = 8. From this result, the ideal way to arrange the sensor is to arrange it in a shape of a hexagon.

3.4 Implementing Algorithm

An algorithm was developed and the algorithm can be summarized into a flowchart. Figure 12 is the flowchart of the algorithm.

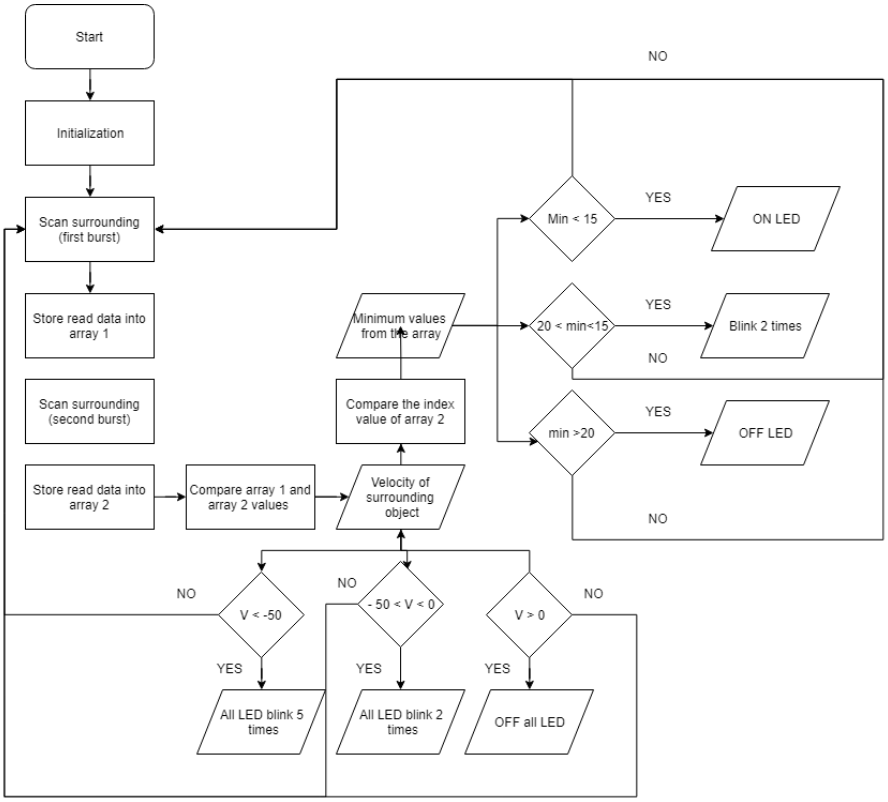


Figure 13. Flow chart of the algorithm

The area in which the sensors can cover is as shown in Figure 13

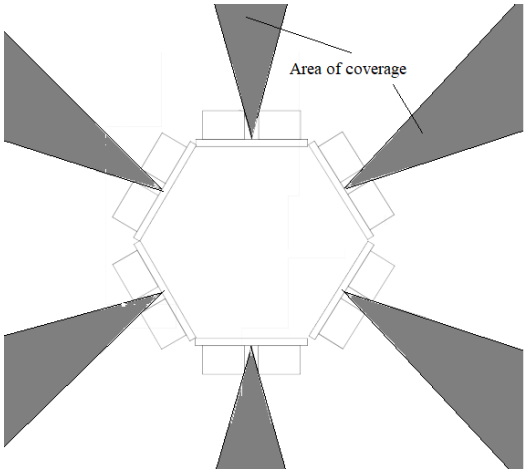


Figure 14. Coverage of the modified prototype.

The algorithm is tested in order to determine the performance of the algorithm. The condition tested to test the algorithm are placing an object in front of each sensor in and out of threshold range, an object approaching towards the vehicle at more than the threshold velocity and the object move away from the vehicle. Each condition is tested 10 times. For the first condition, out of 10 trials, 2 are of it are a false positive. For the second condition, out of 10, 4 are a false positive. Lastly, out of 10 trials, none are false positive.

4 Conclusion

From the accuracy testing, it is shown that the sensor works best when the object is within the measuring angle of the sensor and the accuracy drop as the object is placed at a higher angle especially when more distance is added. However, there are exceptions such as if the object is placed near enough at an angles of 60° and 120°. to Other than that, the plotline of the graph of distance versus time tells two things which they are distance of the object relative to the sensor and also the relative velocity of the object to the vehicle. From plotting the graph of velocity versus time, the speed and the direction of the object relative to the vehicle can be calculated. The magnitude of the velocity versus time graph is the speed which higher magnitude means the higher the speed of the object while the sign of the velocity indicates the movement and the direction of the object. The positive sign indicates the object is moving away from the vehicle while a negative sign indicates the object is moving towards the vehicle. Furthermore, to spatially map the surrounding object, the sensor needs to be able to cover 360° of the surrounding. From the research, it is shown that the best shape or arrangement to cover 360° area is by arranging the 6 sensors in a hexagonal shape.

References

[1] A.Cocchia, "*Smart and Digital City: A Systematic Literature Review*", *Springer International Publishing Switzerland*, p. 19, (2014).

[2] R. Dameri, Smart City Implementation. Cham: Springer International Publishing, pp. 1-10, (2017).

[3] Z. Eusofe and H. Evdorides, "Assessment of road safety management at institutional level in Malaysia: A case study", IATSS Research, vol. 41, no. 4, pp. 172-181, 2017.

[4] Road Safety Plan of Malaysia 2014-2020. Wilayah Persekutuan Putrajaya: Jabatan Keselamatan Jalan Raya, pp. 1-27, (2014).

[5] T. Sato and M. Akamatsu, "Driver Behavior at Intersections", Encyclopedia of Sustainability Science and Technology, p. 359, (2012).

[6] K. Bengler, K. Dietmayer, B. Färber, M. Maurer, C. Stiller and H. Winner, Three Decades of Driver Assistance Systems Review and Future Perspectives. IEE Intelligent Transportation System Magazine, pp. 6-22, (2014).

[7] A. Shaout, D. Colella and S. Awad, "Advanced Driver Assistance Systems - Past, Present and Future", Int. Compunter Engineering Conf, vol., 2011.

[8] I. Akyildiz, W. Su, Y. Sankarasubramaniam and E. Cayciri, "A survey on Sensor networks", IEEE CommunicationMagazines, pp. 102-114, 2002.

[9] K. Brookhuis, D. Waard and W. Hanssen, "Behavioural impacts of Advanced Driver Assistance Systems–an overview", EJTIR, vol. 1, no. 3, pp. 245-253, 2001.

[10] O. Gietelink, J. Ploeg, B. De Schutter and M. Verhaegen, "Development of advanced driver assistance systems with vehicle hardware-in-the-loop simulations", Vehicle System Dynamics, vol. 44, no. 7, pp. 569-590, 2006.

[11] P. Jadhav and U. Jadhav, "Lane Departure Warning System", IJCA, pp. 1-3, 2015.

[12] K. Sakiyama, T. Shimizu and K. Sako, "Parking Assist System", Fujitsu Ten Tech M., vol. 5, pp. 1-9, 2000.

[13] H. Jung, C. Choi, D. Kim and P. Yoon, "System configuration of intelligent parking assistant system", Proc. 13th World Congr. Intell. Transp. Syst. Services., pp. 1-8, 2006.

[14] S. Tokoro, K. Kuroda, T. Nagao, T. Kawasaki and T. Yamamoto, "System configuration of intelligent parking assistant system", Japan, 2002, p. 545.

[15] H. Hayashi, R. Inomata, R. Fujishiro, Y. Ouchi, K. Suzuki and T. Nanami, "Development of pre-crash safety system with pedestrian collision avoidance assist", Japan, 2013, p. 13.

[16] M. Conti, C. Pascal and D. Camillo, "Traction Control System for Motorcycles", Embedded Systems, vol. 2, pp. 1-10, 2009.

[17] X. Yang, "A New Metaheuristic Bat-Inspired Algorithm, in Nature Inspired Cooperative Strategies for Optimization", Springer, no. 284, pp. 65-74, (2010).

[18] Dr. Biology, "Echolocation", ASU - Ask A Biologist, 2018. [Online]. Available: https://askabiologist.asu.edu/echolocation. [Accessed: 21- May- 2018].

[19] M. Ben Ameur and A. Sakly, "FPGA based hardware implementation of Bat Algorithm", Applied Soft Computing, vol. 58, pp. 378-387, (2017).

[20] F. O'Leary, "How Different Driverless Sensors See & Navigate the Road", driverless.wonderhowto, 2017. [Online]. Available: https://driverless.wonderhowto.com/news/different-driverless-sensors-see-navigate-road-0176550/. [Accessed: 07- Jun- 2018].

[21] R. Burnett, "Ultrasonic vs Infrared (IR) Sensors – Which is better?", maxbotic, 2017. [Online]. Available: https://www.maxbotix.com/articles/ultrasonic-or-infrared-sensors.htm. [Accessed: 07- Jun- 2018].

[22] A. S, M. S, D. Bose and K. Ramachandran, "Performance comparison of Infrared and Ultrasonic sensors for obstacles of different materials in vehicle/ robot navigation applications", in OIP Conf. Series : Materials Science and Engineering, 2018, p. 149.

EURECA 2018 – Conference Paper
Paper number PG01

Comparison Of Experimental Thermophysical Properties Of Glycerol And Polyethylene Glycol 600 Based Deep Eutectic Solvents (Dess) With Des And Ils Literature Findings

Amarpreet Singh[1], Rashmi Walvekar[1], Mohammad Khalid[2], Wong Wai Yin[3], TCSM Gupta [4]*

[1] Taylor's University, Jalan Taylor's, Subang Jaya, 47500 Selangor, Malaysia
[2] Research Centre for Nano-materials and Energy Technology, School of Science and Technology, Sunway University, No. 5, Jalan Universiti, Bandar Sunway, 47500 Subang Jaya, Selangor, Malaysia

[3]University Kebangsaan Malaysia, Bangi, 43600 Selangor, Malaysia
[4] Research and Development, Apar Industries Limited, Mumbai, India
[*]Corresponding Author: rashmi.walvekar@gmail.com

Abstract

The research focuses on Deep Eutectic Solvent (DES) which is formed with common salt of Choline Chloride (ChCl) with two different type of hydrogen bond donor (HBD) which are glycerol and polyethylene glycol 600 (PEG). The glycerol based DES was formed with molar ratio 1:2, 1:3, 1:4 and 1:5 whereas the PEG based DES was formed with three components of ChCl:PEG:gly mixture with ratio 1:3:2, 1:4:2 and 1:5:2. The lowest melting point of PEG based DESs were found to be 17.8°C. The viscosities of the DESs were found to be decreasing as the temperature increases. The DESs viscosity were found to be lower than those of ILs and differs slightly with those of literature DES. The densities of the experimented DESs were higher than ionic liquids (ILs). The common factor that determines the physical property of IL and DES is the type component used to form the solvent. DES has an added advantage where varying molar ratio also effects the property which is not the case for ILs. Moreover, DES are more environmental friendly than ILs

Keywords: Deep Eutectic Solvent, Ionic Liquid, Glycerol, Polyethylene glycol.

1. Introduction

IL is relatively new type of chemical that has been discovered for different application and has promising potential for other implication which is rapidly being explored. Currently, ILs have been applied in food science, separation, nanomaterial processing and many other industries. There are various studies conducted on the ability of ionic liquids to perform as lubricant and the results show positive outcome. IL is a type of liquid salt that consist of ions and ions pair which have relatively low melting points. IL compounds have asymmetrical cations and anions structure that allows ILs to have low melting point. The type of anions and cations determine the physical and chemical properties of IL. The common type of cations are imidazolium, ammonium, and pyridinium whereas anions are PF_6, BF_4, and others [1].

There might be plenty of advantages of using ILs but unfortunately there are some disadvantages as well. In the usage of anions such as PF_6 and BF_4 imidazolium salts can lead to reaction with water which results in formation of hydrogen fluoride. The unwanted formation can greatly affect the tribological behaviour of lubricating system [2]. Some ILs showed severe corrosiveness towards copper metal strips when tested at elevated temperatures [3]. The ILs showed different kind of behaviour when tested as lubricant with different type of surfaces. The decomposition of IL in the presence of air and moisture results in corrosion. The occurrence of corrosion on the lubricating surface will reduce the lifespan of the equipment causing failure and increased cost due to replacement of the specific part. This lead to the exploration of DES as the replacement solvent for ILs.

Deep Eutectic Solvent is a type of mixture formed by two or more components which has lower melting point than the individual component. The formation of DES lead to alteration of physical properties of the components which widens the possible application of this solvent. Generally, DES is formed with a quaternary ammonium salt or also known as hydrogen bond acceptor (HBA) and hydrogen bond donor (HBD) which has charge delocalization in the form of hydrogen bonding. The hydrogen bond is formed between halide ion and HBD having lower melting point compared to the individual component [4]. The HBD can be amide, acid, alcohol and other suitable compound that is capable of forming hydrogen bond. DES can be easily produced beginning with simple mixing process and heating which is relatively cheap in order to obtain a eutectic mixture [5]. This cost of synthesising DES is relative low that makes it ideal for as replacement solvent for the conventional solvents. DES has lower melting point than the individual component due to formation of complex anion that decreases the lattice energy [6]. The melting point or freezing point of the DES is achieved by eutectic composition of the two component mixture. Eutectic point is achieved by varying the molar ratio of the salt and HBD.

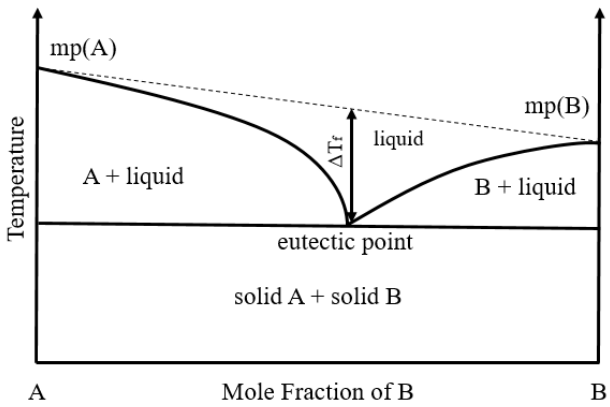


Figure 1 Melting point of component A and B at different mole fractions

From the Fig. 1, the magnitude of interaction between the component A and B determines the lowest freezing point of the DES. The higher interaction between these components at an optimum molar ratio will result in higher difference between the theoretical freezing point temperature and the eutectic temperature [4]. Therefore, each salt and HBD combination have different optimum molar ratio at which the DES has the lowest melting point. In a study by Hayyan et al. (2013), the formation of D-glucose and ChCl DESs were investigated with different molar ratios. There were seven different ratio tested by varying the amount of D-glucose (HBD) to a fixed amount of salt which is choline chloride. The ratio of D-glucose:ChCl (2:1) gave a colourless liquid with the lowest freezing point of 288.15 K which is the eutectic point of the DES. When the D-glucose was added in excess, a white semisolid liquid was observed due to the lack of salt to form hydrogen bond with the glucose resulting in a heterogeneous mixture.

The viscosity of the DES is an important physical property that has to be considered when studying the possible application of the new solvent. Generally DESs have higher viscosity at room temperatures and as the temperature increases the viscosity of DESs decreases [8]. For example, DES as lubricants should poses reasonable viscosity as extremely high viscosity will increase the friction and wear of surface and low viscosity will lead to poor lubrication. High viscosity at low temperature results in energy being wasted and lead to increase in temperature due to heat from the friction. Glycerol that are extensively studied and are known to have high viscosity as well as behave as Newtonian fluids [9]. The research investigates the ability of DESs to replace ILs in future and more environmental benign approach. The study of the comparison will enable commercialisation of DESs in the industry as well as the addition of new type of DES with the formation of PEG based DES. The PEG 600 based DES is novel discovery as no research has been done before and with the respective properties listed will allow wider application of this DES.

2. Experimental

2.1 Materials

Choline Chloride (ChCl) [$HOC_2H_4N(CH_3)_3Cl$] was purchased from Merck with purity 99.0% was used as the common salt for both the DESs. The HBDs used were glycerol and PEG 600. The industrial glycerol [$C_3H_8O_3$] with purity of 97% was purchased together with polyethylene glycol 600 (PEG) [$HO\text{-}(CH_2CH_2OH)_n\text{-}H$] of R&M chemicals from Wataka Trading.

2.2 Preparation & Experiment

Glycerol based DESs were prepared with four different molar ratio whereas the PEG based DESs were prepared with three different molar ratios as shown in Table 1. The glycerol based DESs were formed by mixing the components based on the molar ratio and stirring at 300 rpm at 120°C for a duration of 2 hours where a colourless liquid was formed. The three components PEG based DES was formed by initially adding ChCl in the PEG according to the respective molar ratios and stirred at 300 rpm with heating at 120°C C for 2 hours. Then glycerol was added to the mixture and further stirred with similar condition which was successful in synthesizing PEG based DESs.

Table 1: DESs with different molar ratios

Salt	HBD 1	HBD 2	Molar Ratio	Abbreviation
ChCl	Glycerol	-	1:2	DES 1
			1:3	DES 2
			1:4	DES 3
			1:5	DES 4
	PEG 600	Glycerol	1:3:2	DES 5
			1:4:2	DES 6
			1:5:2	DES 7

In order to measure the moisture content of DESs, Mettler Toledo Karl Fischer was used. The melting point was measured using DSC-60 Plus, Shimadzu which has the range as low as -140°C. The Fourier Transform Infrared Analysis (FTIR) was conducted using the Perkin Elmer Spectrometer 100 with range of 4000 – 650 cm^{-1}. Thermal conductivity was measured as a function of temperature by using the KD2 Pro Decagon Device with uncertainty of ± 5% and jacketed circulating water bath. The thermal conductivity were measured at 25°C, 40°C, 60°C, 80°C and 100°C. The viscosity was measured using Haakee Mars III Rheometer from Thermo Scientific with spindle plate size of P35 Ti L and lower plate TMP 35. The viscosity was measured at 25°C, 40°C and 100°C with two different shear rates of 10 s^{-1} and 500 s^{-1}. The dynamic viscosity was obtained by taking the average viscosity of the two different shear rate at the particular temperature. The density was measured by using the Anton Par DMA 4500 M at temperature of 25°C, 40°C and 90°C. The viscosity was measured at temperature of 100°C which was selected due to limitation of the equipment and as the highest temperature to observe the behavior of DES at extreme temperature whereas the heating element of DMA 4500 M limits the temperature to 90°C to prevent any damage to the U-tube thus the DESs were measured at that particular temperatures.

3. Result & Discussion

3.1 Melting Point

The melting point (T_m) of glycerol based DESs have been reported earlier. In a study done by Tan et al. (2016) found that the freezing point of ChCl:Gly with molar ratio 1:2 was found to be -40°C whereas the individual freezing point of ChCl was reported to be 302°C and for glycerol to be 18°C [11]. Thus, glycerol based DESs are known to have lower melting point than the individual components. From Table 2, the T_m of the PEG based DESs was novel discovery as there has been no results reported on the melting point. It was found that the DES 7 has the lowest melting point at 17.8°C compared to DES 5 and DES 6. This could be due to more hydrogen bonds formation between the salt and HBDs leading to the formation of the eutectic point.

Table 2 Melting point of PEG based DESs

Sample	Molar Ratio			Melting point (°C)
	ChCl	PEG	Glycerol	
DES 5	1	3	2	18.8
DES 6	1	4	2	18.4
DES 7	1	5	2	17.8

From Table 3, it was found that ChCl:glycerol:ethylene glycol DES with molar ratio of 1:2:2 has the lowest freezing point due to highest decrease in lattice energy and highest hydrogen bonding between the components. The ratio 2:1:1 was found to be unstable as turbid white liquid was reported depicting unstable DES formation. This colour indicates that the salt which is the ChCl was added in excess into the mixture and there were insufficient HBDs to form hydrogen bonding [12]. It can be concluded that when forming a stable DES, the molar ratio plays an important role to obtain the lowest melting point. If either the salt or HBD are added in excess, the mixture will be saturated and lack of hydrogen bonding between the compound will result in non-homogenous DES.

When comparing the three components DES between PEG DESs and the ethylene glycol DESs, the ethylene glycol DESs have lower melting point which was found with varying multiple molar ratio of the DES as seen Table 3. Therefore, more extensive study need to be conducted to find out the optimum molar ratio which results in the lowest melting point for the PEG based DESs.

From Table 4, certain glass transition temperature point of ILs were found in the study conducted by Totolin et al, 2013 which showed the variation of glass transition point (Tg) depending on the structure of the ILs [13]. All the ILs were found to have lower Tg than PEG based DES. Unlike DES, ILs are greatly affected by the type cation and anion. Different combination of cation and anion will result in different physical properties. Thus, it is much easier to alternate molar ratio such as in the synthesise of DES without changing the component of the solvent to achieve lower melting or freezing point of desired solvent.

Table 3 Freezing point of Choline chloride, glycerol and ethylene glycol

Molar Ratio			Freezing point (°C)
ChCl	Glycerol	Ethylene glycol	
1	1	1	8.36
1	2	1	-4.28
1	1	2	-18.06
1	2	2	-23.75
2	1	1	-
2	2	1	12.25
2	1	2	22.77

Table 4 Glass Transition point of Ionic Liquids [13]

Sample	Tg (°C)
1-Allylimidazoletributylborane (AIM-TBB)	- 4
1-Ethylimidazoletributylborane (EIM-TBB)	9
1-Butyl-3-methylimidazoliumbis(trifluoromethanesulfonyl)imide(BMIM-NTf2)	-4
Tributylmethylphosphoniumdimethylphosphate (Bu_3MeP-$(MeO)_2PO_2$)	12

3.2 Viscosity

From Figure 2, glycerol has very high dynamic viscosity (0.7058 Pa.s) at room temperature 25°C which rapidly decreases to 0.01710 Pa.s as the temperature increase 100°C. The glycerol based DESs exhibit lower viscosity values compared to pure HBD and has a very small difference at temperature of 100°C. The lowest viscosity was obtained by DES 1 (0.2002 Pa.s) at 25°C followed by DES 3 (0.2440 Pa.s), DES 2 (0.2607 Pa.s), and DES 4 (0.3038 Pa.s). The variation of viscosity at 100°C is small with lowest being DES 3 (0.01271 Pa.s) then DES 1 (0.01339 Pa.s), DES 2 (0.01363 Pa.s), and finally DES 4 (0.01386 Pa.s).

The dynamic viscosity for DES 1 of 0.2002 Pa.s at 25°C was found to different from the reported values of 0.259 Pa.s [14] and 0.281 Pa.s [11] which could be due to the chemical nature of the component used as well as the moisture content [14]. However, increasing molar ratio which increases the dynamic viscosity behavior was observed for ChCl glycerol DES by study done by Abbott et al. (2007) and Chemat et al. (2015). When the molar ratio was increased, abundant HBD were available to form hydrogen bonding. The presence of massive hydrogen bond network leads to lower mobility of free species existing in the DES thus increasing the dynamic viscosity [11] . When more HBDs were added to the DES, the resultant viscosity tends to move closer to the pure HBD component. However in a study conducted by Mjalli et al. (2014) where glycerol HBD was mixed potassium carbonate salt which lead to higher dynamic viscosity than the pure HBD. Therefore, the type of salt used in DES also plays an important contribution towards dynamic viscosity.

On the other hand, it was noted from Figure 3 that viscosity of pure PEG is lower than PEG based DESs. At 25°C viscosity of PEG is 0.1282 Pa.s while increases with DES 7 (0.1686 Pa.s), DES 6 (0.1823 Pa.s) and DES 5 (0.1962 Pa.s). An opposite pattern is observed for PEG based DESs compared to the glycerol based DES. This could be due to the structure of the three components DES formed where the voids in the liquid are smaller at lower molar ratio compared to higher ratio which resulted in higher dynamic viscosity (Y. Liu et al., 2014).

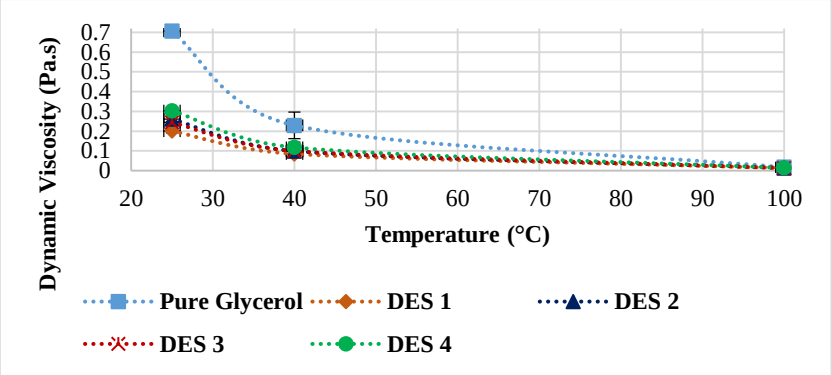


Figure 2 Dynamic viscosity of pure glycerol and DESs with respect to temperature

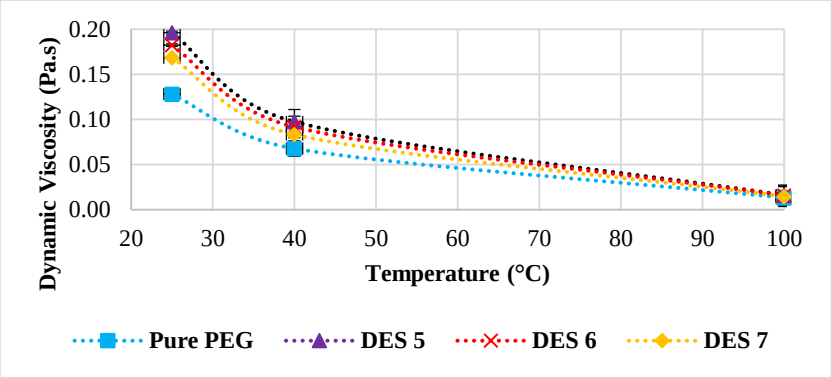


Figure 3 Dynamic viscosity of pure PEG and DESs with respect to temperature

The increment of dynamic viscosity of PEG based DES was similar to the study conducted by Chemat et al. (2015) where three component's DES consisting of ChCl, glycerol and L-arginine exhibited higher viscosity when DES was formed. As the molar ratio was increased, the dynamic viscosity increases because of the increment of the hydrogen bond formation. From the dynamic viscosity information of DES, the suitable application with respect to an optimum molar ratio can be identified and selected. For certain application such as metal electrodeposition, high viscosity is not a desired factor thus DES synthesis is able to alter the viscosity for the application [7].

There are some studies reported on the viscosity of ChCl:Gly DES which shows the variation of viscosity with different molar ratio as shown in Table 5. The lowest viscosity was found for the ratio of 1:2 and as the molar ratio is increased the viscosity was found to be increasing due to the increase of glycerol content. This is similar to the result found with glycerol based DESs where DES 1 with ratio 1:2 has the lowest viscosity at temperature of 25°C. The viscosity of DES 1 was found to be 0.2002 Pa.s which is indeed lower than the viscosity reported in Table 4. The viscosity of DES is influenced by the hydrogen bonding, van der Waals and electrostatic interaction [14]. The increases in HBD content in the eutectic mixture leads to increase in the network of hydrogen bonding between the molecules. This lead to lower mobility of free space within the mixture thus higher viscosity at a given temperature.

From Table 6, the viscosities of PAO and ILs were found in a study done by Espinosa et al. (2013). The ILs viscosity were found to higher than base fluid PAO 6. It was noted among the ILs, the longer the alkyl chain the higher the viscosity. This is because the increase in the chain leads to stronger Van Der Waals forces as well as the presence of hydroxyl group enhances the forces of attraction between the molecules [19]. The ILs viscosity were found to

be higher than those of glycerol and PEG based DESs. The difference is significantly great between these solvents. These DESs are more suitable for application with lower viscosity as in comparison to the mentioned ILs. Extremely higher viscosity can turn out to be an unfavourable property. For example, in lubrication high viscosity will result in higher friction which defeats the purpose of lubrication. Viscosity of the ILs are greatly influenced by the length of alkyl chain whereas in DES the amount of HBD used determines the viscosity.

Table 5 The viscosities of different ChCl:Gly ratios with their respective measuring temperatures

Salt:HBD	Molar Ratio	Viscosity (Pa.s)	Temperature (°C)	Reference
ChCl :Glycerol	1:2	0.376	25	[10]
	1:2	0.281	25	[11]
	1:2	0.259	25	[14]
	1:3	0.450	20	
	1:3	0.376	20	[15]
	1:3.33	0.401	20	
	1:4	0.450	20	
	1:5	0.503	20	
	1:6.67	0.548	20	
	1:10	0.790	20	
	1:20	0.998	20	

Table 6 Viscosities of ILs at 25°C

Sample	Viscosity (Pa.s)	Reference
PAO 6	0.048	
Di-[bis(2-hydroxyethyl)ammonium]adipate (DAd)	1.510	
Bis(2-hydroxyethyl)ammoniumsalicylate (DSa)	1.740	[19]
Bis(2-hydroxyethyl)ammoniumoleate (DO)	1.040	
PAO + 1 wt% DAd	0.047	

3.3 Density

Density of the DESs depends on the type of the HBD and salt as well as the molar ratio. Pure glycerol has the highest density with 1.253 g/cm^3 at 25°C and 1.210 g/cm^3 at 90°C. It is noted from Figure 4 that DES 1 has the lowest density followed by DES 2, DES 3 and finally DES 4 with the highest density when comparing the DESs. All the samples were found to decrease linearly as the temperature increases. As the amount of glycerol (HBD) increases in DES with the molar ratio, higher density was obtained. This is similar in a study found by

Francisco et al. (2013) where increase in molar ratio contributes to reduction in the free space between the molecules thus increasing density.

From Figure 5, the lowest density observed was for pure PEG while all the DES depicting higher density. The highest density at 25°C was measured for DES 6 with 1.135 g/cm^3 followed by DES 5 and the lowest density was DES 7 with 1.132 g/cm^3. The difference between densities of PEG based DESs were found to be smaller compared to glycerol based DESs. However, when compared with temperature, the PEG based DESs have a higher drop in densities with percentage ranging from 4.52% to 4.57%. The glycerol based DESs were found to be lower than pure component whereas the PEG based DESs showed opposite effect with enhancing the density of the PEG based DESs in comparison with the pure HBD component. The enhancement occurred due to the presence of glycerol based component in the DES and in a study done by Hayyan et al. (2013), the eutectic phenomena plays a vital role on the resultant density. The enhancement of density was also found in a study conducted by Abbott et al. (2007), where zinc chloride was used as the common salt with acetamide and urea HBDs showed higher density compared to pure HBD components. The resultant DES density is dependent on the packing or the molecular structure of the DES which can be explain by the hole theory. When the salt and HBD were mixed the average hole radius decreases which contributes to more free space thus increasing the density (Qinghua et al., 2012). Overall, the density of the DES could be easily altered with the type of HBDs and the molar ratio to suit a certain application. The density of PEG based DESs in this study were found to be higher compared to alkylimidazolium dialkyl phosphates ILs which are PEE (1.125 g/cm^3), PBE (1.038 g/cm^3), and POE (1.016 g/cm^3) respectively [23].

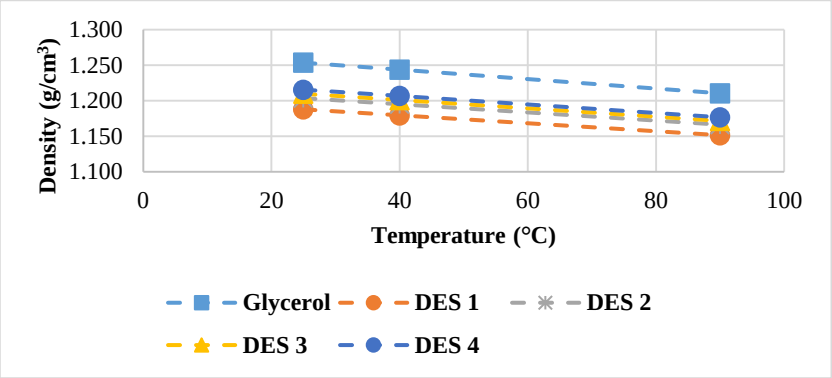


Figure 4 Density of pure glycerol and the DESs

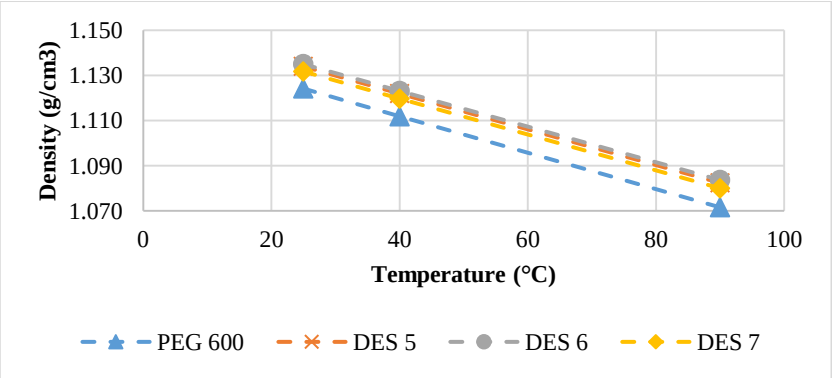


Figure 5 Density of pure PEG and the DESs

The density of DES is strongly dependent on the molar ratio of the HBD and salt which is normally higher than the density of water [8]. The HBD with hydroxyl group have higher density than aromatic group. Moreover increasing the chain length of the HBD decreases the density [24]. In general the density of DES is expected to increase with the increase of relative molar ratio as the structuring effect is expected to be higher. This reduces the free volume or in other words the free motion of molecules [20]. The division of mass over the volume of a liquid gives the density. Thus with increasing the ratio either salt or HBD will actually reduce the free motion of the molecules in the compound which leads to higher density.

In a study conducted by Yusof et al. (2014), the density of Tetrabutylammonium bromide (TBABr) as salt and glycerol as HBD was investigated. The results are shown in Figure 6. The DESs were prepared with five different combination of 75.0%, 80.0%, 83.3%, 85.7% and 90% percentage of HBD in the DES with respect to molar ratio. The highest density was achieved by the 90.0% glycerol for the temperature of 303 K and the densities were found to decreases almost linearly with increasing temperature. This can be justified as the temperature is increased, the cations and anions will vibrate and molecular rearrangement occurs. The molecular rearrangement is caused by the weak interaction between the ions present in DES which results in lower density. The highest molar ratio also has the highest density where 90% glycerol exhibit higher density compared to the other molar ratios.

Besides that, from Figure 7 the density of ChCl:Gly (1:2) and pure glycerol over a range of temperature were observed. The density decreases almost linearly with increasing temperature [11]. The decreasing trend of Figure 7 is similar as in Figure 6 but more steeper in Figure 6. Figure 7 also shows the density of different molar ratios of ChCl:Gly. The densities were taken at a fixed temperature of 293 K and the effect of molar ratio on density could be observed. As the molar ratio increases, the densities were found to be increasing significantly [15]. This is due to the amount of HBD which is glycerol increasing from ratio 1:3 to 1:20. From the density of the experimented glycerol DESs and the literature DESs, increasing the temperature leads to decreasing density. Due to the limitation of densitometer, the experimental density could not be taken at temperature of 20°C.

For lubrication purpose, density plays an important role and the densities of ILs and poly-alpha olefin (PAO) were listed in Table 7. All the densities were found to be lower than of density of the experimental glycerol and PEG based DESs except for ZDDP. The density of ZDDP were found to be higher than DES 1 but lower than the other measured densities. ZDDP is widely used base fluid or additives for the lubrication industry [26]. It can be concluded that glycerol and PEG based DESs exhibited densities that are in the acceptable range to be used as lubricant source. However, extensive studies on other important parameters need to be conducted to analyze the capability of these DESs as potential lubricant.

Table 7 Density of PAO and ILs

Sample	**Temperature (°C)**	**Density (g/m^3)**	**Reference**
PAO 4 base Oil	23	0.80	[26]
trihexyltetradecylphosphoniumbis(2-ethylhexyl)phosphate IL [P66612][DEHP]	23	0.91	
Solution of zincdialkyl-dithiophosphate (ZDDP) in oil	23	1.20	
PAO + IL (1wt%)	23	0.80	

PAO + ZDDP (1wt%)	23	0.80

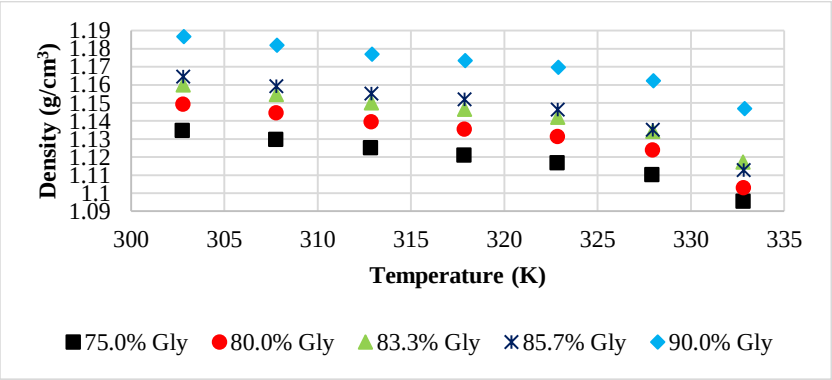


Figure 6 The graph of Density against Temperature of TBABr:Glycerol DESs

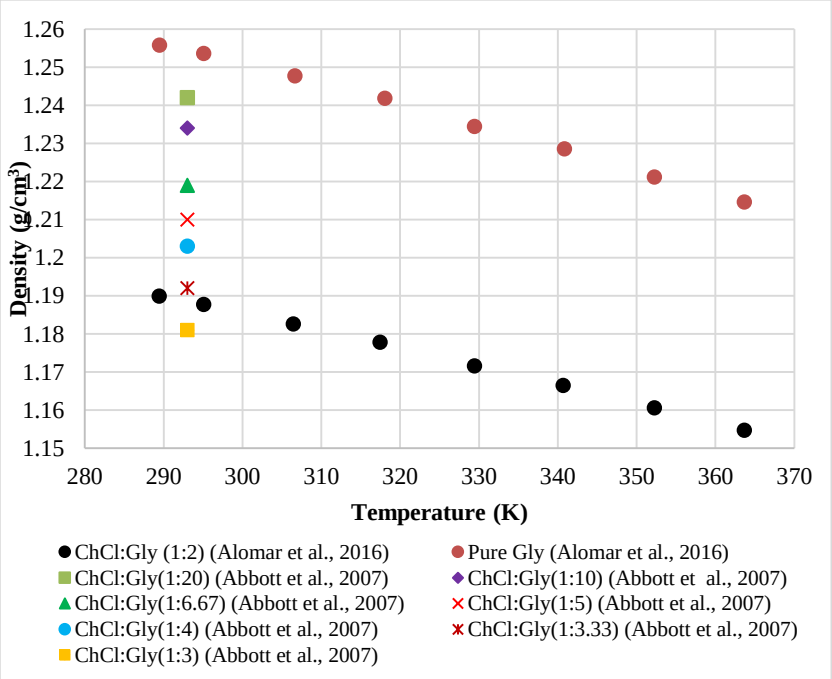


Figure 7 The graph of Density against Temperature of ChCl:Glycerol DESs

4. Conclusion

Glycerol and PEG based DESs properties such as melting point, viscosity and density were experimentally reported. The results found were compared to DESs and ILs data available in literature. For PEG based DESs, there were no reference or literature available because PEG based DESs are relatively new and no studies has been done on PEG 600 based DES. These DES requires extensive research to discover further the properties of the DESs at the same time with different molar ratios. The glycerol based DESs showed similar behaviour but different in values. This could be due to the type of salt and HBD used as well as the purity of the DES component. When compared with ILs, DESs density were found to be higher and viscosity lower. The common factor that affect the physical property of DES and IL is the type of component used. However, with DES there is an addition factor that can be altered which is the molar ratio to obtain specific property. This is not applicable for ILs which makes DES easily tuneable. Overall, the exhibition of the properties reveals that the formation of DES with respect to the type of component used and varying molar ratio results in tailor made capability of the solvent to suit certain application. This novel solvent is much easier produced and cost

effective in comparison with other available solvent in the market as well as environmental friendly.

5. Reference

[1] J. Van Rensselar, "Unleashing the potential of ionic liquids," *Tribol. Lubr. Technol.*, vol. April, 2010.

[2] K. S. Torimoto T, Tsuda T, Okazaki K, "New Frontiers in Materials Science Opened by Ionic Liquids," *Adv. Mater.*, vol. 22, no. 11, pp. 1196–1221, 2010.

[3] N. Dörr, I. Gebeshuber, D. Holzer, H. D. Wanzenböck, a Ecker, a Pauschitz, and F. Franek, "Evaluation of Ionic Liquids as Lubricants," *J. Microengineering Nanoelectron.*, vol. 1, no. 1, pp. 29–34, 2010.

[4] E. L. Smith, A. P. Abbott, and K. S. Ryder, "Deep Eutectic Solvents (DESs) and Their Applications," *Chem. Rev.*, vol. 114, no. 21, pp. 11060–11082, 2014.

[5] A. Abo-Hamad, M. Hayyan, M. A. AlSaadi, and M. A. Hashim, "Potential applications of deep eutectic solvents in nanotechnology," *Chem. Eng. J.*, vol. 273, pp. 551–567, 2015.

[6] A. P. Abbott, G. Capper, D. L. Davies, R. K. Rasheed, and V. Tambyrajah, "Novel solvent properties of choline chloride/urea mixtures.," *Chem. Commun. (Camb).*, no. 1, pp. 70–71, 2003.

[7] A. Hayyan, F. S. Mjalli, I. M. AlNashef, Y. M. Al-Wahaibi, T. Al-Wahaibi, and M. A. Hashim, "Glucose-based deep eutectic solvents: Physical properties," *J. Mol. Liq.*, vol. 178, pp. 137–141, 2013.

[8] B. Tang, H. Zhang, and K. H. Row, "Application of deep eutectic solvents in the extraction and separation of target compounds from various samples," *J. Sep. Sci.*, vol. 38, pp. 1053–1064, 2015.

[9] Y. Shi, I. Minami, M. Grahn, M. Björling, and R. Larsson, "Boundary and elastohydrodynamic lubrication studies of glycerol aqueous solutions as green lubricants," *Tribol. Int.*, vol. 69, pp. 39–45, 2014.

[10] T. Tan, M. Zhang, Y. Wan, and H. Qiu, "Utilization of deep eutectic solvents as novel mobile phase additives for improving the separation of bioactive quaternary alkaloids," *Talanta*, vol. 149, pp. 85–90, 2016.

[11] M. K. Alomar, M. Hayyan, M. A. Alsaadi, S. Akib, A. Hayyan, and M. A. Hashim, "Glycerol-based deep eutectic solvents: Physical properties," *J. Mol. Liq.*, vol. 215, pp. 98–103, 2016.

[12] K. C. Ho, K. Shahbaz, W. Rashmi, F. S. Mjalli, M. a Hashim, and I. M. Alnashef, "Removal of Glycerol From Palm Oil-Based Biodiesel Using New Ionic Liquids Analogues," pp. 98–111, 2015.

[13] V. Totolin, I. Minami, C. Gabler, and N. Dörr, "Halogen-free borate ionic liquids as novel lubricants for tribological applications," *Tribol. Int.*, vol. 67, pp. 191–198, 2013.

[14] S. Khandelwal, Y. K. Tailor, and M. Kumar, "Deep eutectic solvents (DESs) as eco-friendly and sustainable solvent/catalyst systems in organic transformations," *Journal of Molecular Liquids*, vol. 215. Elsevier B.V., pp. 345–386, 2016.

[15] A. P. Abbott, R. C. Harris, and K. S. Ryder, "Application of hole theory to define ionic liquids by their transport properties," *J. Phys. Chem. B*, vol. 111, no. 18, pp. 4910–4913, 2007.

[16] F. Chemat, H. J. You, K. Muthukumar, and T. Murugesan, "Effect of l-arginine on the physical properties of choline chloride and glycerol based deep eutectic solvents," *J. Mol. Liq.*, vol. 212, pp. 605–611, 2015.

[17] F. S. Mjalli, J. Naser, B. Jibril, S. S. Al-Hatmi, and Z. S. Gano, "Ionic liquids analogues based on potassium carbonate," *Thermochim. Acta*, vol. 575, pp. 135–143, 2014.

[18] Y. Liu, Y. Chen, and Y. Xing, "Synthesis and characterization of novel ternary deep eutectic solvents," Chinese Chemical Society, 2014.

[19] T. Espinosa, J. Sanes, A. E. Jiménez, and M. D. Bermúdez, "Protic ammonium carboxylate ionic liquid lubricants of OFHC copper," *Wear*, vol. 303, no. 1–2, pp. 495–509, 2013.

[20] M. Francisco, A. van den Bruinhorst, and M. C. Kroon, "Low-Transition-Temperature Mixtures (LTTMs): A New Generation of Designer Solvents," *Angew. Chemie Int. Ed.*, vol. 52, no. 11, pp. 3074–3085, 2013.

[21] A. P. Abbott, J. C. Barron, K. S. Ryder, and D. Wilson, "Eutectic-based ionic liquids with metal-containing anions and cations," *Chem. - A Eur. J.*, vol. 13, no. 22, pp. 6495–6501, 2007.

[22] S. R. F. ois J. roˆ me Qinghua Zhang, Karine De Oliveira Vigier, "Deep eutectic solvents : syntheses, properties and applications," *Chem Soc Rev*, vol. 41, pp. 7108–7146, 2012.

[23] L. Yong-ming, P. Wei, L. Shuqin, C. Jian, W. Ruigang, and L. Jianqiang, "Mechanical properties and microstructure of a Si 3 N 4 / Ti 3 SiC 2 multilayer composite," vol. 28, pp. 223–226, 2014.

[24] G. Garcia, S. Aparicio, R. Ullah, and M. Atilhan, "Deep Eutectic Solvents: Physicochemical Properties and Gas Separation Applications," *Energy & Fuels*, vol. 29, pp. 2616–2644, 2015.

[25] R. Yusof, E. Abdulmalek, K. Sirat, and M. B. A. Rahman, "Tetrabutylammonium bromide (TBABr)-based deep eutectic solvents (DESs) and their physical properties.," *Molecules*, vol. 19, no. 6, pp. 8011–26, 2014.

[26] J. Qu, H. Luo, M. Chi, C. Ma, P. J. Blau, S. Dai, and M. B. Viola, "Comparison of an oil-miscible ionic liquid and ZDDP as a lubricant anti-wear additive," *Tribol. Int.*, vol. 71, pp. 88–97, 2014.

EURECA 2018 – Conference Paper
Paper number PG02

A Comparative Study of the Effects of Dimples on Aerofoils of Horizontal Axis Wind Turbines at Laminar & Turbulent Flows

*M.K. Lee, *M. Hosseini Fouladi, Satesh N.N., Manish Kumar Singh Domun*

School of Engineering, Taylor's University,

No.1 Jalan Taylor's, 47500, Subang Jaya, Selangor, Malaysia

*mfoolady@gmail.com

Abstract

Increasing environmental pollution has led to an urgent need to examine wind energy as a source of power generation. The purpose of this paper is to compare the performance of various aerofoils used on horizontal axis wind turbines (HAWT) at laminar and turbulent flows. Performance is defined as the ratio of the coefficients of lift to that of drag. The impacts of improving aerodynamic performance of the aerofoil are an increase in the efficiency of the wind turbine as well as a reduction of blade material. A dimple on the surface of an aerofoil is shown to increase its lift, reduce drag and cause a delay of the separation point at the boundary layer for various angles of attack. This paper presents the performance of S833 aerofoil in turbulent flow and the NACA0012 aerofoil in laminar flow. Results show that the best combination of the shape, size and position are spherical dimples of 2 mm diameter positioned closest to the leading edge of the aerofoil and that smaller sized dimples are better than larger ones for increasing aerodynamic performance.

Keywords: Aerofoil, Dimples, Position, Wind Turbine, Performance

1. Introduction

The increasing awareness of environmental pollution caused by burning fuels to harness energy has led many researchers to consider sources of clean energy. The most natural source of clean energy is from wind, which is freely available, though this parameter is a fluctuating quantity. Harvesting wind energy is particularly tempting due to a reduction in size of turbine blading which makes it particularly suitable for homes and small installations. The lift-type HAWT's are commonly used for harvesting the energy from the wind due to their large capacity factor, Goldstein [1] and Ryan and Bollinger [2]. Rotor blade design in terms of its shape and size are based on its aerodynamic performance and materials to fabricate it for high strength and low weight should be readily available, Ma and Zhang [3]. Timmer and van Rooij [4] provided a comprehensive study and design of wind tunnel tests of dedicated aerofoils for wind turbines developed by Delft University of Technology where the effects of vortex generators on various aerofoils were presented. The encouraging trends in the use of wind power is reported in [5] where there was a 104% annual increase in installed wind capacity from year 2000 to year 2010. Efficient harvesting of wind energy using HAWT requires a study of their performance.

Sandesh and Rohan [6] investigated the performance of NACA0012 symmetrical aerofoil using CFD. The performance of asymmetrical aerofoil for wind turbine blade using a single dimple has not been used to perform numerical analysis as a 3D model uses huge memory resources. Furthermore, the study of dimple sizes and their positions on the aerofoil have not been taken into much consideration from previous studies as these parameters have an impact on the coefficient of lift and drag.

This paper deals with increasing the performance of assymetrical turbine blades using single dimple. Spherical dimples are used as literature have shown that they are better vortex generators compared to other shapes such as squares or hexagons

Nomenclature:

AoA = Angle of Attack

C_L = Coefficient of Lift

C_D = Coefficient of Drag

C_L/C_D = Aerodynamic Performance

CFD = Computational Fluid Dynamic

3D = 3-dimension

2D = 2-dimension

Re = Reynolds Number = $\frac{\rho U l}{\mu}$

ρ = fluid density

U = velocity of fluid

l = length of fluid

A = projected frontal area of aerofoil body (m^2)

Drag and lift on aerofoil

The drag equation is:

$$F_D = \frac{1}{2} C_D \rho A U^2 \quad (1)$$

and the lift equation is:

$$F_L = \frac{1}{2} C_L \rho A U^2 \quad (2)$$

The choice of turbulence models and their merits are described below:

1.1 Choice of Turbulence Models

Various turbulence models are available. These augment the Navier-Stokes equations with an additional turbulence eddy viscosity term, but they differ in how it is computed.

1.1.1 Spalart-Allmaras (SA) model

The Spalart-Allmaras model adds a single additional variable for an undamped kinematic eddy viscosity. It is a low Reynolds number model and can resolve the entire flow field down to the solid wall. The model is relatively robust and has moderate resolution requirements. This model does not accurately compute fields that exhibit shear flow, separated flow, or decaying turbulence. Its advantage is that it is quite stable and shows good convergence. Example of computer simulation of axial velocity of wing tip vortex is shown in Figure 1 [7]. This model overdamps the flow in the core of the vertex. The SA model can be modified by adding correction terms to reduce the eddy viscosity in the core of the vortex and significantly improves the simulation of vortex dominated flows.

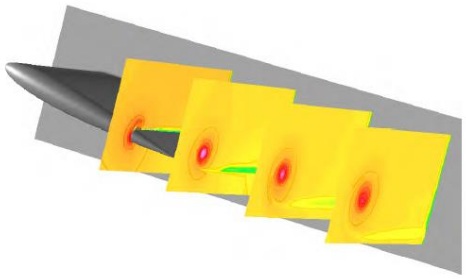


Figure 1: Computer simulation of axial velocity of wing tip vortex of NACA0012 aerofoil using SA model at an angle of attack of 10^0 [7]

1.1.2 k-ε model

The k-ε model solves for two variables: k, the turbulence kinetic energy; and ε (epsilon), the rate of dissipation of turbulence kinetic energy. Wall functions are used in this model, so the flow in the buffer region is not simulated. The k-ε model has good convergence rate and relatively low memory requirements. It does not very accurately compute flow fields that

exhibit adverse pressure gradients, strong curvature to the flow, or jet flow. It does perform well for external flow problems around complex geometries.

The following turbulence models are all more nonlinear than the k-ε model. They can often be difficult to converge unless a good initial guess is provided. The k-ε model can be used to provide a good initial guess.

1.1.3 k-ω model

The k-ω model is similar to the k-ε model, but it solves for ω (omega) — the specific rate of dissipation of kinetic energy. It is a low Reynolds number model, but it can also be used in conjunction with wall functions. It is more nonlinear, and thereby more difficult to converge than the k-ε model, and it is quite sensitive to the initial guess of the solution. The k-ω model is useful in many cases where the k-ε model is not accurate, such as internal flows, flows that exhibit strong curvature, separated flows, and jets.

1.1.4 Low Reynolds Number k-ε model

The low Reynolds number k-ε model is similar to the k-ε model but does not need wall functions: it can solve for the flow everywhere. It is a logical extension of the k-ε model and shares many of its advantages, but generally requires a denser mesh; not only at walls, but everywhere its low Reynolds number properties kick in and dampen the turbulence. It can sometimes be useful to use the k-ε model to first compute a good initial condition for solving the low Reynolds number k-ε model. An alternative way is to use the automatic wall treatment and start with a coarse boundary layer mesh to get wall functions and then refine the boundary layer at the interesting walls to get the low Reynolds number models.

The low Reynolds number k-ε model can compute lift and drag forces and heat fluxes can be modelled with higher accuracy compared to the k-ε model. It has also been shown to predict separation and reattachment quite well for numerous cases.

1.1.5 SST model

The SST model is a combination of the k-ε model in the free stream and the k-ω model near the walls. It is a low Reynolds number model. It has similar resolution requirements to the k-ω model and the low Reynolds number k-ε model, but its formulation eliminates some weaknesses displayed by pure k-ω and k-ε models.

1.2 Effects of dimples

One of the most significant problems faced in aerodynamics is the flow separation which results in a sudden loss in the lift causing a stalled condition. This condition can be devastating for a wind turbine which uses the concept of lift for the rotation of the blade to produce electricity. The separation point has a great impact on the performance of the aerofoil whereby a delay in the separation of the boundary layer should result in an increase of the lift at a high angle of attack. However, Ghoddossi's investigation of six aerofoils [8], shows that there was only a slight improvement of lift coefficient in one of them at high angles of attack as shown in Figure 2, and that further investigation needed to be performed to validate his results. Past studies have shown that a dimpled golf ball travels higher and further than one with a smooth surface as a dimpled surface causes turbulence at low Reynolds number resulting in extra momentum and energy in the boundary layer and hence delaying the flow separation [9]. The

dimples on aerofoil are significant as the angle of attack increases and functions on the same principle as vortex generators [9].

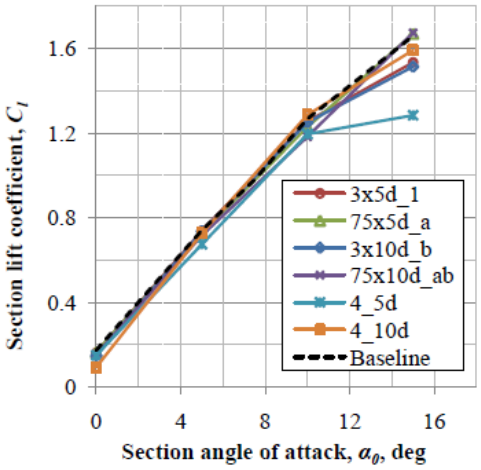


Figure 2: Dimpled section lift coefficients of six NACA 64_1-212aerofoils [8] compared to undimpled (Baseline) aerofoil

2. Methodology

2.1 Modelling of single dimpled aerofoil

The criterion in the selection of an aerofoil for a wind turbine blade is a high lift coefficient and a low drag coefficient. For a Horizontal Axis Wind Turbine (HAWT) of diameter 1 m to 3 m, the family of S833, S834 and S835 aerofoils is most appropriate for inaudible, thick and natural-laminar flow as well as high ratios of lift to drag coefficients. The noise produced by an aerofoil is related to the blade chord thickness and its coefficient of lift to the thickness decreases towards the tip. In addition, the of the rotor [10].

The geometry of the S833 aerofoil from National Renewable Energy Laboratory (NREL), designed using SolidWorks, is shown in Figure 3. The length of the chord is 120 mm with a span is 40 mm. The dimensions of the aerofoil have been scaled downwards compared to the original dimensions of a wind blade aerofoil due to limitations in the educational licence and to reduce computational resources in ANSYS Fluent.

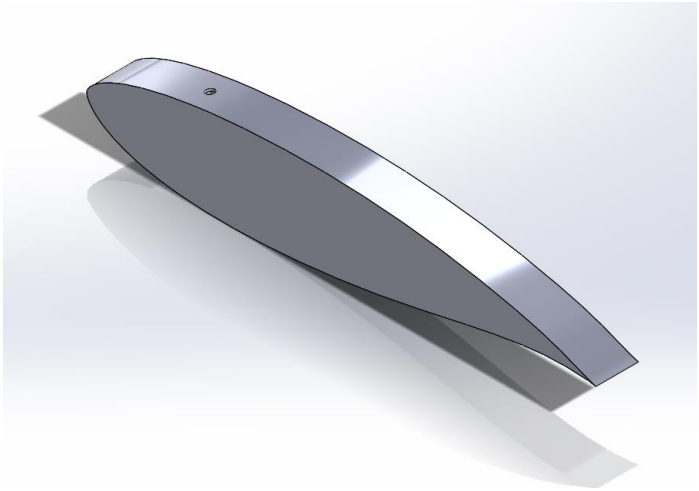


Figure 3: Isometric view of S833 aerofoil

Parameters for aerofoils with spherical dimples of different sizes and locations investigated in this paper are shown in Figure 4. These are used to analyse the effects of the dimple size and its position on their aerodynamic performance. The position of the dimple is measured from the leading edge and is indicated by the ratio of its position to that of the chord length in percentages.

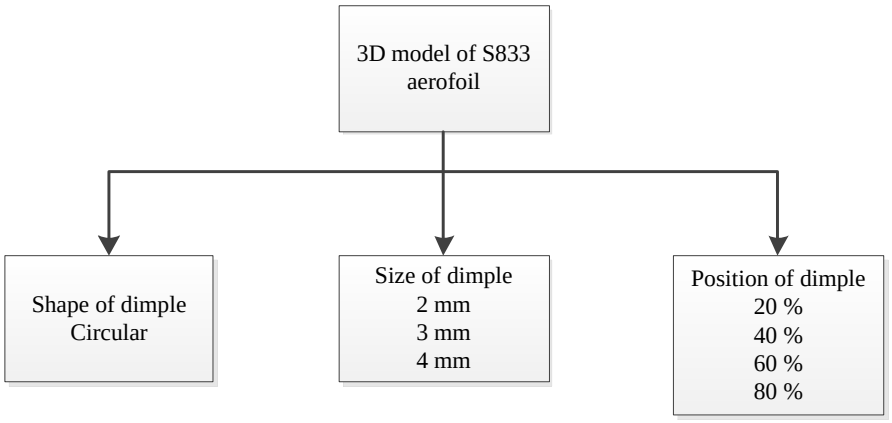


Figure 4: Parameters for S833 aerofoil

Case Study: Numerical modelling and meshing of computational fluid domain and dimple

The model of aerofoil shown in Figure 3 is imported in Design Modeler (DM) to design the computational fluid domain of the aerofoil in the form of a C-shaped. Based on the experiment conducted by Katsumi Aokia [11], it was suggested that the computational fluid domain for numerical analysis should be approximately equal to 25 times the size of the aerofoil. Therefore, the dimensional fluid domain would have the following dimensions 2 m length × 0.8 m width × 1.5 m height to be able to mesh the fluid domain properly to study the fluid at the trailing edge of the aerofoil. The length of the computational fluid domain must be long enough since the area of concern is the wake region caused by the turbulent flow of the aerofoil which affect the coefficient of drag of the aerofoil.

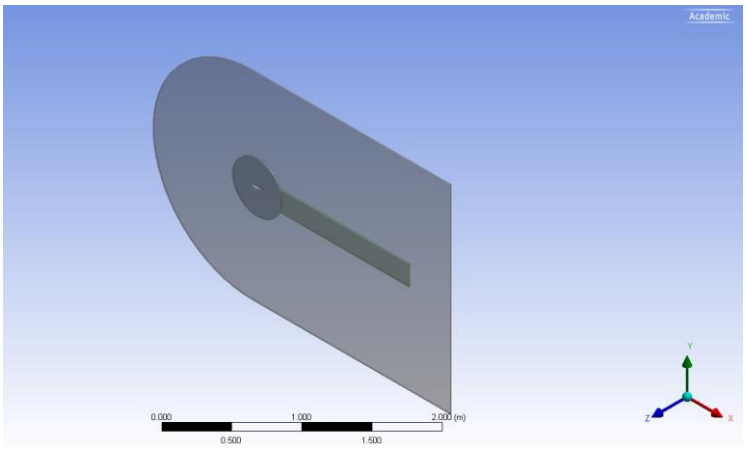


Figure 5: 3D Computational fluid domain

The C-shaped domain is designed and extruded with the aerofoil positioned as shown in Figure 5. A circular and rectangular shape is modelled around the around the aerofoil of dimension 0.5 m and 1 m by 0.2 m respectively. The purpose of this design is to facilitate the process of meshing in the next stage and to define a smaller mesh size in the critical area. A boolean operation is used to finalize the computational fluid domain whereby the aerofoil is subtracted from the C-shaped computational fluid domain since the objective is to study the flow of the fluid over the aerofoil. The computational fluid domain is then sliced over the surface the aerofoil to increase the quality of the mesh. All the bodies are then compressed to form a single part. The inlet surface is defined as the velocity inlet and the outlet as pressure outlet. The aerofoil and dimple surfaces are defined as the aerofoil surface which is used in the simulation to obtain the solution such as the coefficients of lift and drag.

The meshing process is the most critical step in the numerical analysis as the accuracy of results is dependent upon the mesh quality. A good combination of the accuracy, efficiency and ease in generating the mesh in dependent upon the geometry and the different mesh control selected. The two common types of mesh are the tetrahedral and the hexahedral which are selected based on the geometry of the design whereby the tetrahedral mesh require 1.5 times

more memory and calculation compared to the hexahedral. Meshing of the computational fluid domain is shown in Figure 6.

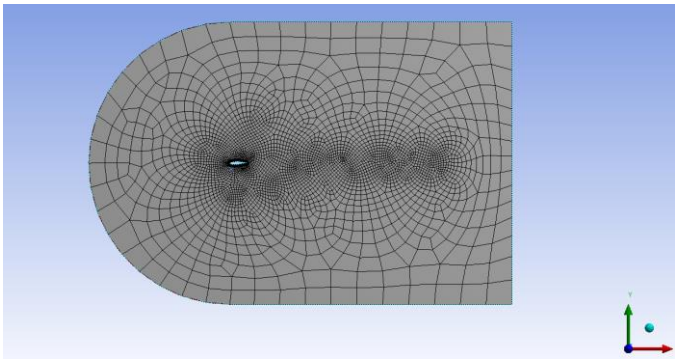


Figure 6: Meshing of computational fluid domain.

Mesh control:

(i) The first mesh control is the sweep method whereby the mesh is mapped from one side of the aerofoil to the other side which is the target surface to achieve identical mesh elements for the entire computational fluid domain.

(ii) The second mesh control is the sizing of the 2 edges of the aerofoil. In this mesh control, the edge of the aerofoil is divided into a finite number of elements of 100 number of divisions. An increase in the number of divisions do not have a great impact on the accuracy of the result and might induce errors due to deformation of the mesh element at the trailing edge of the aerofoil because of its geometry whereas a lower number of division might affect the accuracy of the result.

(iii) The third mesh control is the sizing of the circular and rectangular body. The option is set to body of influence and the two bodies are selected with a growth rate of 1.2 and an element size of 10 mm. This will result in a mesh element of 10 mm with a growth rate of 1.2 in the region around the aerofoil since the objective is to study the effect of the dimple on the aerofoil and at the trailing edge whereby the wake region is formed. Furthermore, the inflation method is selected with the option of total thickness layer of 20 layers with a growth rate of 1.12 at a maximum thickness of 10 mm. This mesh control enables the reduction of computational resources and time for the simulation in the next stage. The inflation control grows the mesh element from the cross-sectional geometry of the aerofoil as shown in Figure 7 to study the boundary layer around the aerofoil.

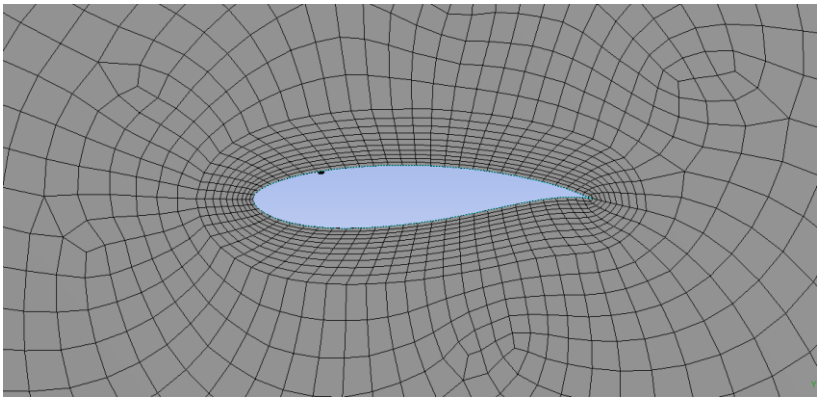


Figure 7: Meshing of aerofoil boundary

The dimple is meshed with the multizone, sizing and inflation control whereby the hexahedral mesh envelopes the surface of the dimple as shown in Figure 8. This enables the creation of a very fine mesh which is mapped to the surface of the aerofoil. These controls allow the study of the boundary layer of the fluid which consist of the viscous layer, buffer layer and the log-law layer.

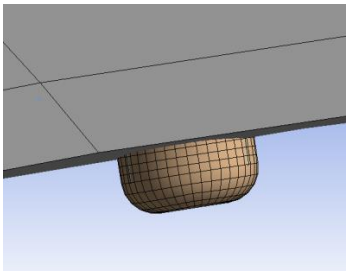


Figure 8: Meshing of dimple

2.1.1 Mesh Quality

The mesh quality is analysed based on the number of nodes and elements, the skewness and the orthogonal quality. For a good quality mesh, the orthogonal quality must be as close as possible to 1 which is defined as a good quality mesh and the skewness should be less than 0.97 which will prevent deviation of the results while performing the iterations. The orthogonal skewness is defined as good when the maximum skewness is close to 0 and bad as the skewness approaches 1 which is the ratio of the angle of span between the mesh elements. If the above criteria are not satisfied, the mesh controls must be redefined and improved with other controls. The average value of the skewness of mesh elements, orthogonal quality of the meshes and types of mesh at different sections of the aerofoil as determined from ANSYS Fluent are shown in Figures 9 to 11 respectively.

The average skewness of 0.251 shown in Figure 9, satisfies the criteria for the mesh quality. The skewness of meshes in the computational fluid domain of the models are checked

to ensure that they are within the acceptable range. The result of the mesh quality showed that the overall percentage of the skewed mesh are at a very low amount of approximately 10 % and it is not in the region of concern being studied.

Statistics	
Nodes	17441
Elements	12913
Mesh Metric	Skewness
Min	1.64518192074364E-03
Max	0.99176396578453
Average	0.251244704096259
Standard Deviation	0.175600557860704

Figure 9: Skewness of mesh

The orthogonal quality of the mesh shown in Figure 10 has an average value of 0.88 and satisfies the above criterion.

Statistics	
Nodes	17441
Elements	12913
Mesh Metric	Orthogonal Quality
Min	0.029920545758705
Max	0.999913873415037
Average	0.889286676525793
Standard Deviation	0.158001995432847

Figure 10: Orthogonal quality of mesh

The types of mesh formed at different sections and number of mesh elements is shown in Figure 11. It can be deduced that nearly all meshes are hexahedral mesh. To determine the location of poor mesh elements, the bar chart with low red quality can be selected. If mesh elements within the vicinity of interest are poor, they can be refined by other mesh controls such as patch conforming, sizing and inflation.

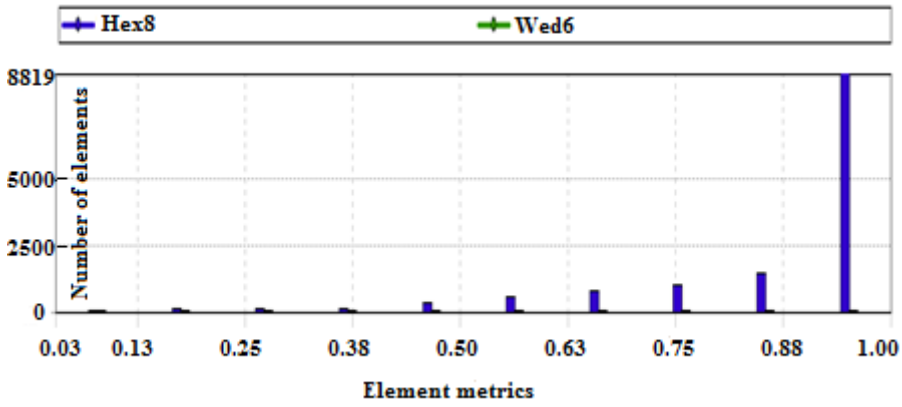


Figure 11: Types of mesh used for grid generation

2.1.2 Boundary conditions and turbulence model

The turbulent model chosen for this study is the Spalart-Allmaras model. This model consists of one transport equation to solve for the kinematic eddy (turbulent) viscosity, Javaherchi [12]. Since the objective of this paper is to determine the effects of dimples on the aerofoil performance based on the the coefficients of lift and drag, the turbulence model of Sparlat-Allmaras is most suitable.

The Spalart-Allamaras is an appropriate turbulent model to study the wall boundary and local shear of the fluid. If the boundary layer of the computational fluid domain is not fine enough, the turbulence model will predict the flow near the boundary wall.The boundary conditions are defined by the inlet velocity of the fluid at 20 m/s at different angle of attack (AoA) and the solution is computed from the inlet. In addition, the solution monitors the coefficient of lift and coefficient of drag at the surface of the. The simulation is carried out for angles of attack from 0 ^{o} - 20 ^{o} at a specific inlet velocity of 20 m/s. The simulation is performed at a constant Reynolds number calculated as follows.

$$Reynold's\ Number = \frac{\rho U l}{\mu} = \frac{1000 \times 20 \times 0.12}{1.789 \times 10^{-5}} = 1.342 \times 10^{5}$$

2.1.3 Flow profile in dimpled aerofoil

The flow of the fluid at different angles of attack in the cross section of the dimple region are as shown in Figure 12. At very low angle of attack the velocity of the fluid in the dimple is not much affected since the flow over the surface of the aerofoil is more dominant and the velocity of the fluid is relatively high. As the angle of attack increases from 5^{o} to 10^{o}, the velocity of the fluid and the impact of the dimple is higher. It can be noticed for angles of attack of 5^{o} and 10^{o}, the velocity of the fluid is approximately 10 m/s in the dimple region. The velocity within the vicinity of the dimple is about 7 m/s. The dimple on the surface of the aerofoil acts a small vortex generator causing the fluid to follow the surface of the dimple forming a circular pattern. The effect is especially noticeable in Figure 12 (d) where the centre of the vortex formed has zero velocity and this results in a change in the boundary layer of the fluid over the surface of the aerofoil.

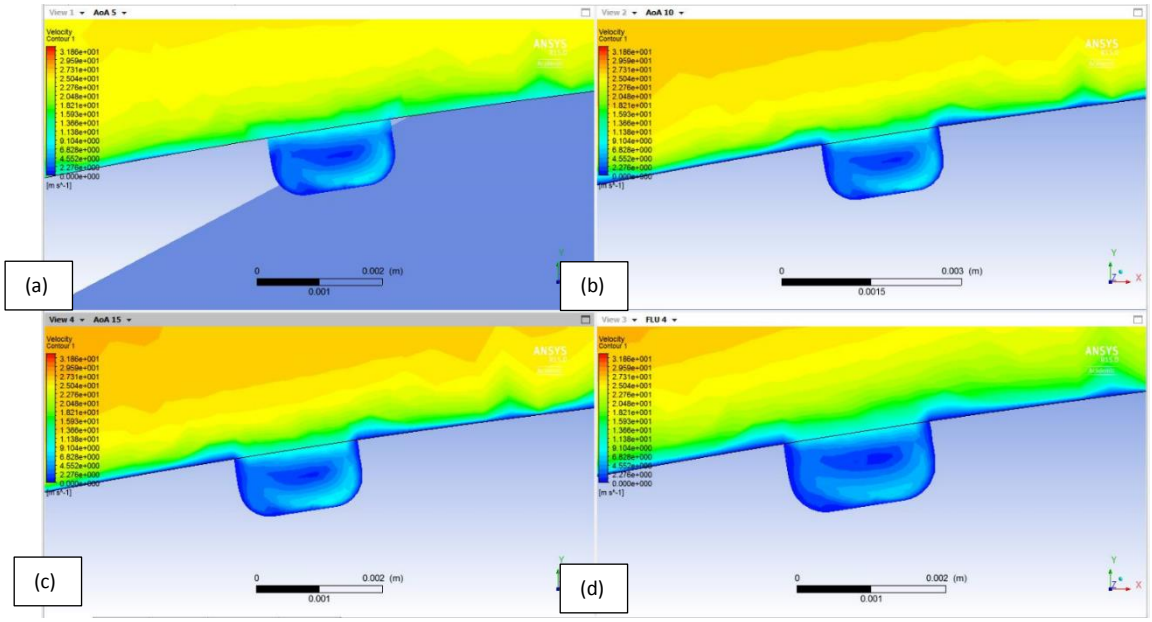


Figure 12: Velocity flow inside dimple

2.2 Modelling of multiple-dimpled aerofoil

Multiple dimples can also be modelled as shown by Rasal and Katwate [6] for laminar flow at free stream velocities of 6 m/s and 8 m/s. At these low velocities, will dimples make any difference to the performance HAWTs? This question can be answered by comparing the aerodynamic performance for laminar and turbulent flows.

Rasal and Katwate [6] modelled NACA0012 aerofoil profile with a chord length of 300 mm, span 250 mm and maximum thickness 36 mm. Outward dimples were prepared on the upper surface of two wooden models. Model 1 had a regular surface without any dimple. Model 2 was an aerofoil with dimple size 1% of chord length and model 3 was an aerofoil with dimple size 2% of chord length. The size of dimpled surfaces varied in percentage of chord length measured from the trailing edge.
NACA0012 profile was made by using *x* and *y* coordinates from NACA data. ANSYS Fluent was used for numerical analysis of this 2D aerofoil. The model was subjected to laminar flow as the free stream velocity was very small (6 m/s and 8 m/s). The tetrahedral type of meshing was used with smallest element size 0.001 m. Results were obtained for NACA0012 with dimple size of 1% and 2% of chord length at an angle of attack of 10^0.

3 Results

3.1 S833 profile with single dimple using Spalart-Allmaras model

3.1.1 Effect of size of dimple

Figure 13 shows that the coefficient of lift is highest for 2 mm dimples up to an angle of attack of 17^0 compared to 3 mm and 4 mm dimples while Figure 14 shows that the coefficient of drag is lowest for 2 mm dimples up to an angle of attack of 20^0. This implies that the aerodynamic

performance (C_D/C_L) of S833 aerofoil is enhanced with the presence of 2 mm diameter inward dimples. This observation is further reinforced as shown in Figure 15 and the aerodynamic performance is maximum at an angle of attack of 10^0

3.1.2 Effect of position of dimple on lift

Dimples positioned at different locations of the chord length demonstrate the same trendline for the coefficient of lift as shown in Figure 16. At low angles of attack between 0^o to 10^o, the coefficients of lift are approximately the same with slight deviation for the dimple positioned at 20% 40 % 60 % and 80. At an angle of attack of 10^o a stall condition occurs for all dimple positions. At high angle of attack of 15^o, dimples positioned at 40 %, 60% and 80 % of the chord length have no significant effect on the lift since the point of separation of fluid has already been achieved and fluid is no more in contact with the aerofoil. The dimple positioned at 20 % of the chord length which is closest to the leading edge demonstrate a better coefficient of lift for all angles of attack as fluid in still in contact with the surface the aerofoil. At an angle of attack of 20^o, the coefficient of lift is increased significantly for all positions of the dimples due to the thick camber of the aerofoil except for the dimple at 80% chord length as it is too close to the trailing edge.

3.1.3 Effect of position of dimple on drag

The trendlines of Figure 17 are approximately identical except for the dimple positioned at 80 % of the chord length. At a low angle of attack of 5^o, the coefficients of drag for dimples positioned at 20%, 40% and 60% of the chord length are similar in magnitude whereas the dimple positioned at 80% of the chord length results in a much lower coefficient of drag. This is because, the dimples position at 20% 40% and 60 % of the chord length cause turbulence along the surface of the aerofoil which affect the smooth flow of the fluid as the flow at low angle of attack is laminar and the point of separation has not been reached. At a low angle of attack of 5^o, the fluid travels over the entire body of the aerofoil and the dimple position at 80% of the chord length cause a delay in the flow separation point and reduces the wake area by recirculation of the fluid at the boundary layer, thus resulting in a lower drag coefficient. As the angle of attack increase to 10^o and 15^o, the coefficient of drag is reduced for the dimple position at 20%, 40% and 60% of the chord length as the flow separation point is closer to the leading edge of the aerofoil that delays the flow separation and reduce the wake area. On the other hand, the dimple positioned at 80% of the chord length increases the coefficient of drag it is no longer effective and fluid is no longer in contact with the aerofoil. As angle of attack increases to 20^o, all drag coefficients increase since the wake region at the trailing of the aerofoil is extensively large and cannot be accommodate by the recirculation of the fluid caused by the dimples.

3.2 NACA0012 profile with multiple dimples using laminar model

Rasal and Katwate [6] showed that aerodynamic performance is higher for dimple size of 1% chord length compared with that for 2% chord length. The performance of this aerofoil with dimple size of 1% chord length is also higher than that of the smooth aerofoil except at an angle of attack of 17^0. The aerodynamic performance is also maximum at an angle of attack of 10^0.

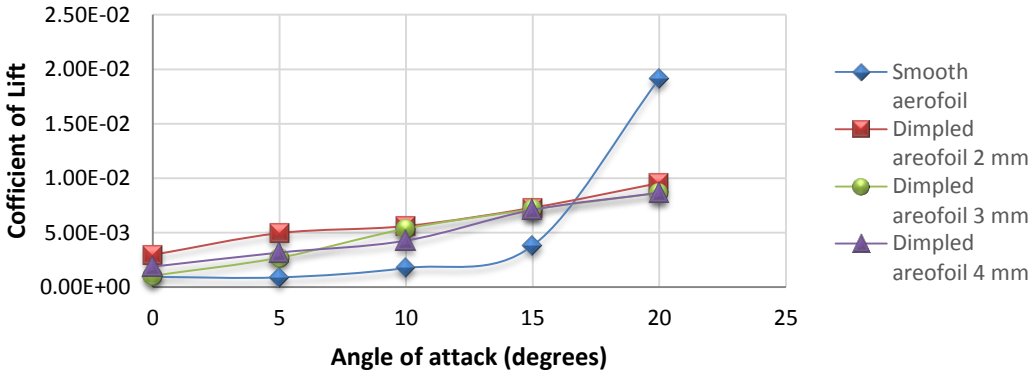


Figure 13: Variation of coefficient of lift for S833 aerofoils of various dimple sizes

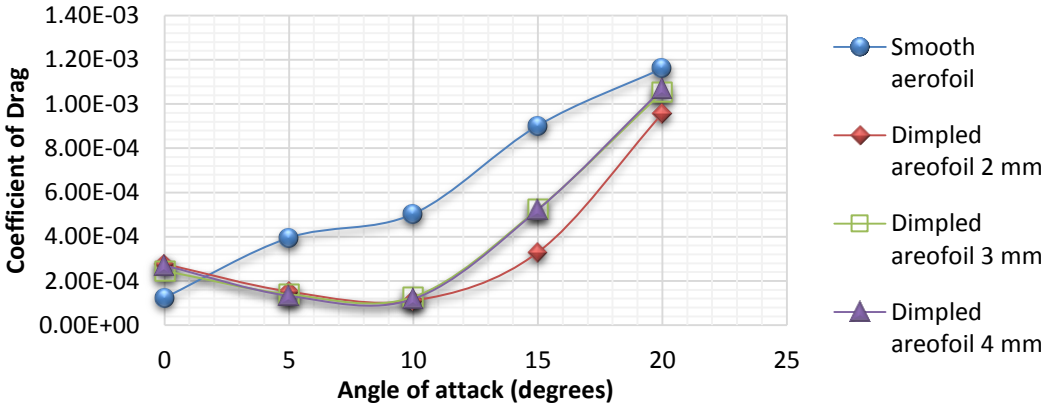


Figure 14: Variation of coefficient of drag for S833 aerofoils of various dimple sizes

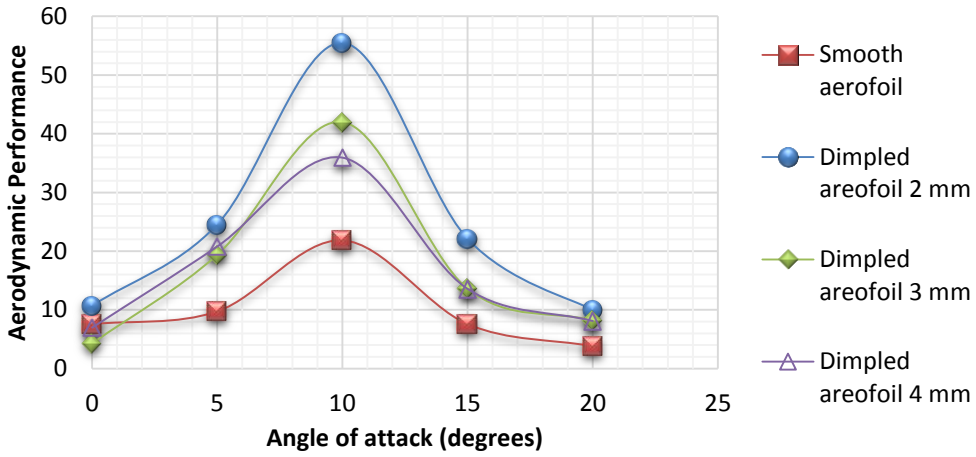


Figure 15: Performance of S833 aerofoil at a constant Reynolds number of 1.342×10^5 using Spalart Allmaras model

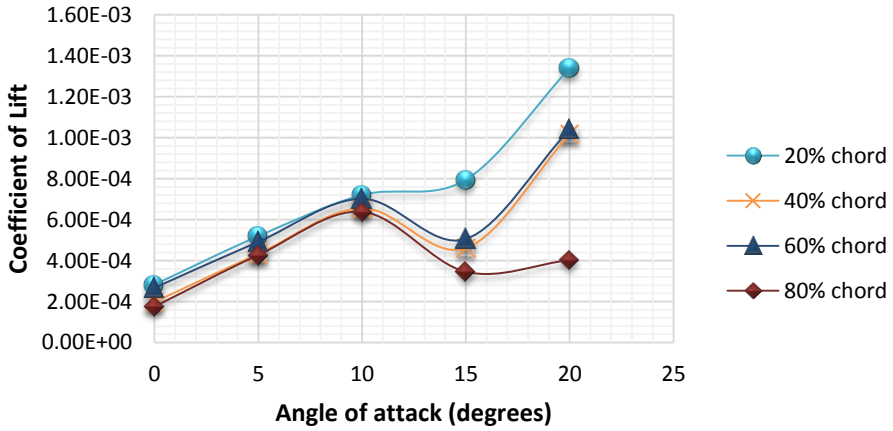


Figure 16: Variation of coefficient of lift for S833 aerofoils of various dimple positions

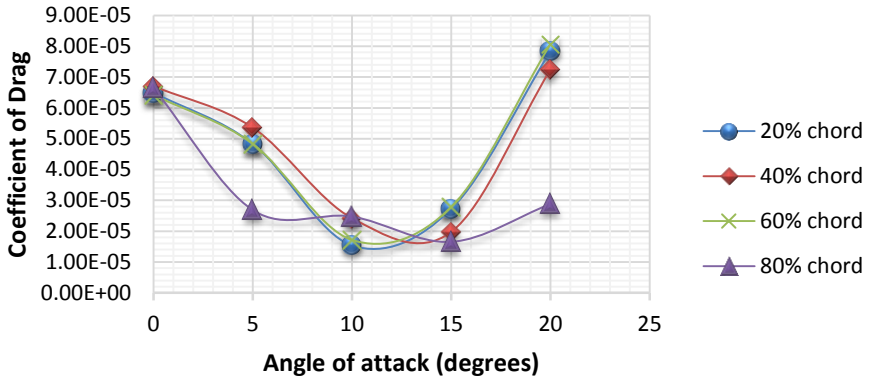


Figure 17: Variation of drag for S833 aerofoils of various dimple position

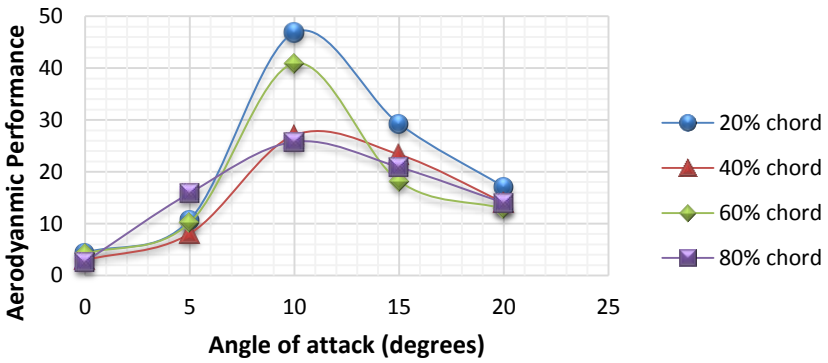


Figure 18: Performance of S833 aerofoils for various dimple positions

4. Discussion

4.1 Single dimple S833 aerofoil using Spalart-Allmaras model

4.1.1 Effect of dimple size and position on aerodynamic performance

Figure 15 shows that at an angle of attack of 0^0, the aerodynamic performance of all aerofoils is approximately equal. All dimpled aerofoils demonstrate better aerodynamic performances

compared to the smooth aerofoil as the angle of attack increases. As the angle of attack increases from 0^0 to 20^0, the dimple size of 2 mm diameter is more effective in increasing the aerodynamic performance compared to other dimple sizes since the change in flow of the fluid in the boundary layer from laminar to turbulent is sufficient to accommodate the recirculation of fluid in the wake region, thus decreasing the drag. The aerodynamic performance is a maximum at an angle of attack of 10^0 since the coefficient of drag is lowest and coefficient of lift is relatively high. Furthermore, at the stall condition where there is a sudden drop in the coefficient of lift at an angle of attack of 10^0, the aerofoil with a dimple size of 2 mm performs better than the other aerofoils.

Figure 18 shows that the dimple positioned at 20% of the chord length results in better aerodynamic performance at high angles of attack compared to dimples positioned at 40% 60 % and 80% of the chord length. The dimple position at 80% of chord length results in better aerodynamic performance at low angles of attack. Therefore, the effect of the position of the dimple is dependent upon the angle of attack. At low angles of attack, the dimple positioned at trailing edge has a better aerodynamic performance since the flow separation point is at the end of the aerofoil and the wake area is also very small. Hence, it reduces the drag produced whereas the lift produced is relatively high for this dimple position resulting in a high aerodynamic performance. The dimple positioned at 20% of the chord length is near the leading edge and results in a significantly higher aerodynamic performance compared to other dimple positions as the flow separation is approximately along the middle of the aerofoil. This results in the change of the boundary layer from laminar to turbulent reducing the wake region by recirculation. The location of this dimple is optimum for the range of angles of attack where maximum lift of the aerofoil takes place due to its thick camber.

4.2 Multiple dimple NACA0012 aerofoil using laminar model

Multiple dimples on NACA0012 aerofoils increase their aerodynamic performance in laminar flow. The maximum aerodynamic performance occurs at an angle of attack of 10^0. Smaller size outward dimples result in higher aerodynamic performance compared to larger size outward dimples. This has also been determined by Bogle *et al*. [13].

5. Conclusion

Maximum aerodynamic performance is obtained using a 2 mm inward dimple as compared to 3 mm and 4 mm inward dimples. Position of dimple nearest the leading edge of the aerofoil increases its aerodynamic performance in turbulent flows. Maximum aerodynamic performance for S833 aerofoil profile occurs at an angle of attack of 10^0.

This paper shows that even a single dimple on the surface of S833 aerofoil can increase its aerodynamic performance in turbulent flow. The results are limited to this aerofoil profile only. Future work on more aerodynamic profiles are required to determine the quantum of increase in aerodynamic performance due to single and multiple dimples in laminar and turbulent flows.

References

[1] L. Goldstein, “A proposal and a theoretical analysis of a novel concept of a tilted-axis wind turbine.,” *Energy*, vol. 84, pp. 247–254, 2015.

[2] R. Wiser and B. Mark, “Wind Energy Technologies and Applications,” *Wind Technologies Market Report*, 2015. [Online]. Available: https://energy.gov/sites/prod/files/2016/08/f33/2015-Wind-Technologies-Market-Report-08162016.pdf. [Accessed: 10-Apr-2018].

[3] P. C. Ma and Y. Zhang, “Perspectives of carbon nanotubes/polymer nanocomposites for wind blade materials.,” *Renew. Sustain. Energy*, vol. 30, pp. 651–660, 2014.

[4] W. A. Timmer and R. P. J. O. M. van Rooij, “Summary of the Delft University Wind Turbine Dedicated Airfoils,” *J. Sol. Energy Eng*, vol. 125, no. 4, pp. 488–497.

[5] “Global Wind Report (GWEC),” 2016.

[6] S. K. Rasal and R. R. Katwate, “Experimental & Numerical Investigation of Lift & Drag Performance of NACA0012 Wind Turbine Aerofoil,” *Int. Eng. Res. J. - Spec. Ed. PGCON-MECH-2017*, pp. 1–5, 2017.

[7] R. H. Nichols, *Turbulence Models and Their Application in Complex Flows Revision 4.01*, 4.01. University of Alabama, Birmingham.

[8] A. Ghoddoussi, “A Conceptual Study of Airfoil Performance Enhancements Using CFD,” M.Sc, Wichita State University, Wichita, 2011.

[9] R. Bhadri, T. Ravi, and S. Srinath, “Aerodynamic effects of dimples on aircraft wings,” *Int. J. Adv. Mech. Aeronaut. Eng. IJAMAE*, vol. 2, no. 2, pp. 169–172, 2015.

[10] D. M. Somers, “‘The S833, S834 and S835 Airfoils,’ , Vols. NREL/SR-500-36340.,” 2005.

[11] K. M, H. O, and A. Katsumi, “Aerodynamic characteristics and flow pattern of a golf ball with rotation,” *The Engineering of Sport 8 - Engineering Emotion*, vol. 2, no. 2. pp. 2431–2436, 2010.

[12] T. Javaherchi, “Review of Spalart-Allmaras Turbulence Model and its Modifications,” University of Washington, 2010.

[13] P. Bogle, A. Pandalkar, S. Takke, M. Yedge, and S. Rasal, “Performance Testing of NACA0012 Aerofoil by Providing Dimple Surface,” *Int. J. Res. Appl. Sci. Eng. Technol.*, vol. 5, no. IV, pp. 1–4, 2017.

A Natural Language Processing Framework For Spoken Dialogue Systems

Praveen Edward James[1], Mun Hou Kit[1], Chockalingam Aravind Vaithilingam[1], Alan Tan Wee Chiat[2]*

[1]School of Engineering, Taylor's University, Taylor's University Lakeside Campus, No. 1, Jalan Taylor's, 47500 Subang Jaya, Selangor, Malaysia.

[2]School of Engineering, Multimedia University, Melaka

*HouKit.Mun@taylors.edu.my

Abstract

Natural Language Processing (NLP) systems are predominantly application specific. Numerous challenges are faced by the researchers when such systems are applied to different tasks like information extraction, controlling smart devices, autonomous navigation and so on. The purpose of this work is to design a generalized NLP system based on a novel NLP framework, which can be customized to any domain. The design involves a three-stage natural language processing framework or system, which combines syntactic generation, semantic extraction and a strong rule-based control. Syntactic generator generates syntax by aligning sentences with Part-of-Speech (POS) tags limited by the number of words in the lexicon. Semantic extractor extracts meaningful keywords from the queries raised. The above two modules are controlled by generalized rules by the rule-based controller module. The system is evaluated under different domains and compared with the Airline Travel Information System (ATIS) database. The results reveal that the accuracy of the system is 92.33% on an average and the ATIS database has an accuracy of 93%. The design process is simple, and the processing time is 2.12 seconds, which is minimal compared to similar statistical models. The system supports a vocabulary of about 700 words and can be used as NLP module in a spoken dialogue system for various domains or task areas.

Keywords: Natural Language Processing; syntactic generator; semantic extractor; domain; intent; lexicon;

1. Introduction

Spoken dialogue systems offer application specific functionality using a speech interface. It includes the following components: speech recognition, natural language understanding, dialogue management, natural language generation and text-to-speech. Software based realizations requires high processing capacity like speed and accuracy and hence they are fulfilled by increasing system capabilities. However, in some cases the increase in performance of these systems are non-linear.

Some of the existing commercial spoken dialog systems are DELL's customer service system [1], Mercury for flight reservation [2] and Let's Go for bus schedules [3]. Luna is a spoken dialog system for call routing application [4]. Spoken dialog systems also facilitate application development using speech in an Integrated Development Environment (IDE) [5].

One of the unique characteristics of a spoken dialogue system is that it is task-specific. The system needs to be constructed based on the general traits of a language, when generalizing the system for multiple tasks. These include grammar, syntactic and semantic rules which are unique to every language.

The proposed system combines three tasks integrating natural language understanding, dialogue management and natural language generation as a single process called natural language processing. Language understanding is process of extracting semantic content from text generated by a speech recognizer. Dialog manager adds additional context and back-end knowledge to rank and choose response information. Natural language generator converts response information into text. The proposed framework tags information source text with Part-of-Speech (POS) or syntactic information. The query text is segmented with semantic identifiers like domain, intent, request and keyword slots for semantic information extraction.

These identifiers are matched with the source text governed by syntactic and semantic rules to acquire response information. This information is processed by a natural language generator to generate response text. These stages are collectively represented as an NLP framework. The framework is then tested on different domains and benchmarked with ATIS dataset. A general spoken dialogue system is shown in Fig. 1.

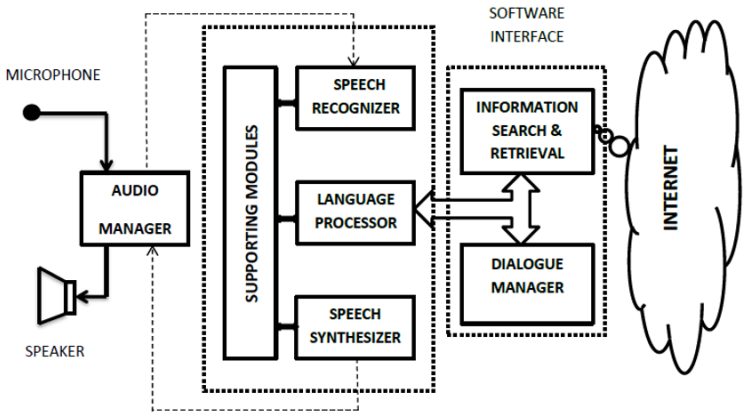


Fig. 1. A Spoken Dialogue System

A pioneer spoken language understanding is the Aircraft Travel Information System (ATIS). It includes phonetic modelling, bigram language model and a probabilistic parser [6]. Lemon and Pietquin proposed a dialog strategy by monitoring the performances of speech recognizer, parser, natural language generator and speech synthesizer [7] using machine learning. This model unfolded the performance capabilities of efficient machine learning

algorithms and formed the basis for designing similar systems. Young *et al*., designed a Partially Observable Markov Decision Process (POMDP) by including a Bayesian model and optimizing through a reward driven process [8]. Practical application of this process requires efficient algorithms and measured approximations and the complexity increases when designed as a general-purpose system.

Long Short-Term Memory (LSTM) networks are utilized for word labelling tasks in spoken language understanding. Experiments on the ATIS dataset have asserted the effectiveness of such systems [9]. Wen *et al*., proposed a natural language generator that learns from unaligned data and optimizes sentence planning and LSTM structure [10]. LSTM based system has long training schedules.

Christen in his work, formulated criteria and procedures to extract semantic information from a dictionary and tag input text [11]. The work combines both syntactic and semantic information and is used in query expansion strategies. Liu *et al*., combined personal information with natural language understanding and target smart communication devices such as Personal Digital Assistants (PDA) [12]. Significant accuracy improvements can be achieved when compared to baseline models.

From the above techniques, two categories of natural language processing (NLP) can be achieved. They are model-based and process-based. Model-based systems are more complex in nature and require abundant resources. When the design is process-based, they use specific algorithms and have better adaptability. The proposed method is process-based that integrates syntactic generation and semantic extractor using rule-based template matching or control to generate response text for text-based queries targeting a specific domain.

The rest of this paper is divided into the following sections; Section 2 describes the proposed model with the core processes involved; Section 3 covers the experiments conducted and the attained results together with the relevant discussions; Finally, section 4 concludes this paper with an insight into the future direction of this work.

2. Proposed System

NLP is an integral component of a spoken dialogue system. There are 2 design strategies namely model-based and process-based. This section highlights the design of a process-based NLP system called the SSR framework. The main building blocks of this framework is shown in Fig. 2.

The functionality of the SSR framework involves acquisition of information and query text, syntactic generation, semantic extraction, lexicon creation, rule-based parser and response generation.

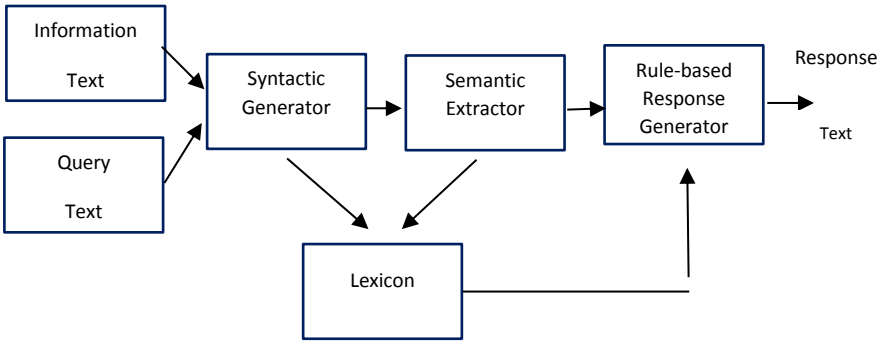


Fig.2. SSR Framework

2.1. Syntactic generation

The syntactic generation process is illustrated in Fig. 3. The information is available in a text file as text sentences.

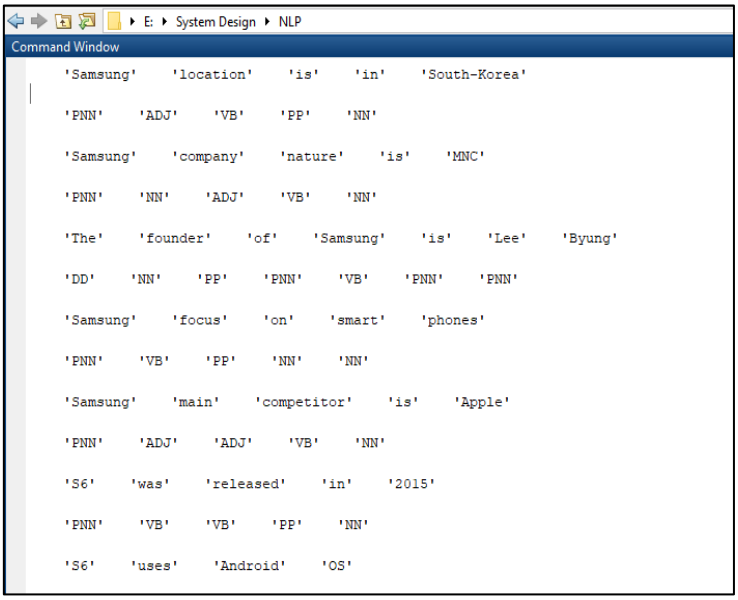


Fig. 3. Syntactic Generation Process

The process involves of splitting the sentence into words and assigning Part of Speech (POS) tags to each word. This necessitates the application of syntactic or grammatic rules to distinguish noun, pronoun, verb, adverb, adjective, article, preposition and so on to the input text and storing the information along with the words in a word dictionary or lexicon. The syntactic tags are generated by comparison with similar sentences which are provided as targets.

2.2. Semantic extraction

This process involves extracting some appropriate words or keywords in a query to identify the task required. A modified slot filling technique is used for this purpose. This process involves extracting keywords based on input determinants, output determinants, index word, domain context and starter words. The query is matched with similar structured text and then the keywords are extracted. The more the semantic constructs, better is the processing accuracy. A simple illustration is provided in Fig. 4.

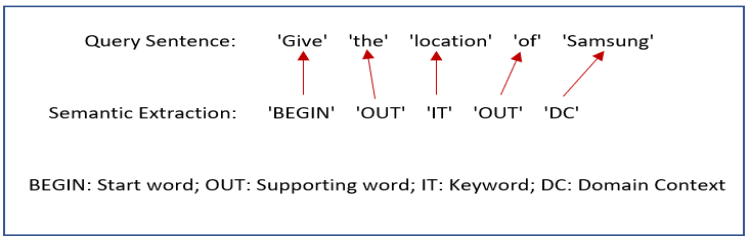


Fig. 4. The Semantic Extraction Process

Based on the syntactic generation and semantic extraction processes, a word dictionary or lexicon is created with a direct mapping between the tags and the words. The lexicon is processed by the rule-based response generator.

2.3. Response Generator

The Response generation is based on formulae which combines a set of syntactic and semantic parsing rules. If an index word in a query is an adjective in the information text, then the adjacent noun is eliminated and the alternate noun and used in the response text. The main objective is to get an appropriate match between the query and the information source. The response extraction process is illustrated in Fig. 5. In this example there are two nouns and based on the keyword location 'Tamil Nadu' is selected for the response.

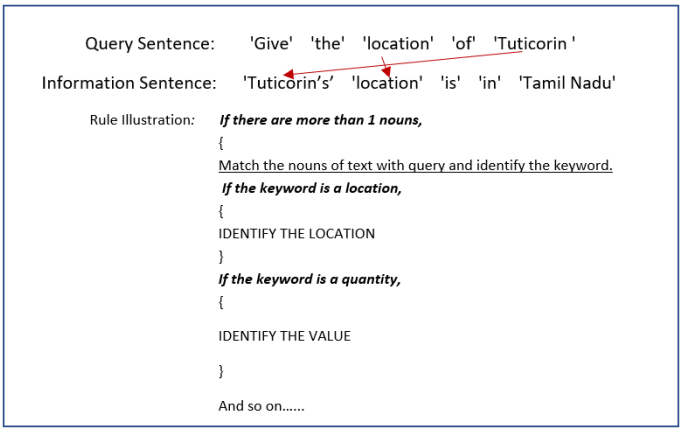


Fig. 5. The Response Generator

All the above processes are integrated into this framework. The broad perspective of this framework can be obtained from the following algorithm.

Step 1: Obtain domain relevant information from the environment as a text file, a database or from internet-based sources.

Step 2: Perform Syntactic generation i.e. the process of obtaining syntactic information from the source.

Step 3: Obtain the query text from the user as a real-time input or from a text file.

Step 5: Apply formulated rules following a hierarchical strategy and adapting a combination of syntactic, semantic and slot-based parsing techniques.

Step 6: Identify and generate response text as the output of the framework.

3. Results and Discussion

A series of experiments are performed, and their results are given below:

3.1. Information Processing

Three sets of text data are used individually for the experiments. Information about Samsung and its product S6 are given in set 1. Information about Taj Mahal, one of the seven wonders of the world are given in set 2. Flight information based on ATIS dataset is given in set 3. The accuracy and processing time are calculated and the values for set 1 are provided in Table 1.

Table 1. Information Processing Application (set 1)

No.	Query and Response	Accuracy (Percentage)	Processing Time (Sec)
1	Q: Give the founder of Samsung A: The founder of Samsung is Lee Byung	100	2.12

2	Q: Identify the focus of Samsung A: Samsung focus on smart phones	90	2.11
3	Q: Which OS is present in S6 A: S6 uses Android OS	100	2.11
4	Q: Give the location of Samsung A: Samsung location is in South-Korea	100	2.11
5	Q: Identify the product released in the year 2015 A: S6 was released in 2015	90	2.13
6	Q: What is the main feature of S6 A: S6 main feature is cost-effective	90	2.11
7	Q: Tell the RAM size of S6 A: S6 RAM size is 3GB	90	2.13
8	Q: How much does S6 cost A: S6 cost is 1000 Ringgits	90	2.13
9	Q: Identify the company nature of Samsung A: Samsung company nature is MNC	90	2.12
10	Q: Who is the main competitor of Samsung A: Samsung main competitor is Apple	90	2.12
AVERAGE		93	2.12

The text sentences used to test the system are directly input as a query and stored in a variable or as a file. They are processed by the framework and the output text is output as speech in combination with a speech synthesizer. Each query is provided 10 times and the number of times the response is generated accurately is used to calculate the accuracy. The averages of accuracy are used for comparison with different datasets.

The results reveal that the accuracy and processing time of set 1 are 93% and 2.12 sec respectively. The accuracy and processing time are calculated for set 2 and 3 and are given in Table 2.

Table 2. Performance Comparison

No.	**Dataset**	**Accuracy (Percentage)**	**Processing Time (Sec)**
1.	Samsung Information	93%	2.12
2.	Taj Mahal Information	91%	2.13
3.	ATIS Information	93%	2.12
AVERAGE		92.33%	2.12

The comparison charts are given in Fig. 6. The system is stable with minor differences when the domain context changes. The values in both charts have minor differences even when the data set changes. Hence the framework can be considered as a general system and can adapt to different applications.

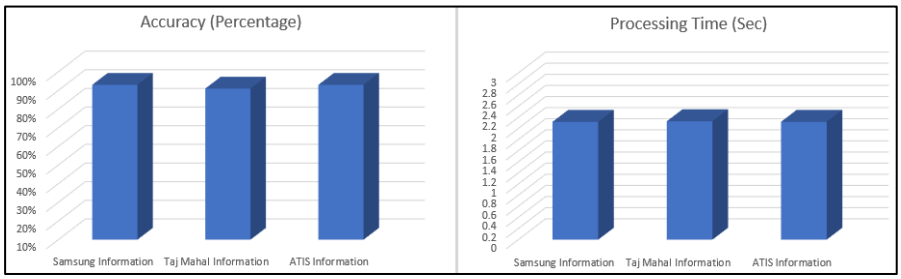


Fig. 6. Accuracy and Processing Time Comparison Charts

The accuracy of an LSTM based state-of-the art based on ATIS dataset is 94.7 [13]. When compared with the results of the average accuracy of the proposed system, it is higher by 2.4%. On the other hand, LSTM systems consume larger resources and have longer processing time. NLP is usually a part of a larger system. The larger systems may have LSTM based processing for more than one task like Speech recognition and NLP. In such cases the system may prove to be cumbersome.

4. Conclusion

In this work, we have developed a novel framework for NLP. The results have shown that it is suitable for spoken dialog systems with medium vocabulary datasets. This process-based system integrates semantic and syntactic parsing, slot-filling and rule-based processing and hence is generalized in nature.

The system trades some accuracy for a simpler design and the processing time is minimal, when compared with model-based systems. State-of-the-art systems can be developed using this framework if more rules are used for controlling deviations from accurate output values. With some unique features, this framework can be adapted to build complex systems in the future.

5. References

[1] Gorin, A.; Riccardi, G.; and Wright, J.H. (1997). How may I help you? *Speech communication*, 23(1): 113-127.

[2] Seneff, S.; and Polifroni, J. (2000, May). Dialogue management in the Mercury flight reservation system. In Proceedings of the 2000 ANLP/NAACL *Workshop on Conversational Systems-Volume 3, Association for Computational Linguistics*, 11-16.

[3] Eskenazi, M.; Black, A.W.; Raux, A.; and Langner, B. (2008). Let's Go Lab: a platform for evaluation of spoken dialog systems with real world users. In *Ninth Annual Conference of the International Speech Communication Association*.

[4] Dinarelli, M.; Stepanov, E.; Varges, S.; and Riccardi, G. (2010, March). The Luna spoken dialogue system: Beyond utterance classification. *In Acoustics Speech and Signal Processing (ICASSP)*, 2010 IEEE International Conference, 5366-5369.

[5] Delimarschi, D.; Swartzendruber, G.; and Kagdi, H. (2014, June). Enabling integrated development environments with natural user interface interactions. In *Proceedings of the 22nd International Conference on Program Comprehension*, 126-129.

[6] Zue, V.; Glass, J.; Goddeau, D.; Goodine, D.; Hirschman, L.; Phillips, M.; and Seneff, S. (1992, February). The MIT ATIS system: February 1992 progress report. In *Proceedings of the workshop on Speech and Natural Language Association for Computational Linguistics*, 84-88.

[7] Lemon, O.; and Pietquin, O. (2007, August). Machine learning for spoken dialogue systems. *In European Conference on Speech Communication and Technologies (Interspeech'07)*, 2685-2688.

[8] Young, S.; Gašić, M.; Thomson, B.; and Williams, J.D. (2013). POMDP-based statistical spoken dialog systems: A review. *Proceedings of the IEEE*, 101(5), 1160-1179.

[9] Yao, K.; Peng, B.; Zhang, Y.; Yu, D.; Zweig, G.; and Shi, Y. (2014, December). Spoken language understanding using long short-term memory neural networks. *In Spoken Language Technology Workshop (SLT)*, 2014 IEEE. 189-194.

[10] Wen, T.H.; Gasic, M.; Mrksic, N.; Su, P.H.; Vandyke, D.; and Young, S. (2015). Semantically conditioned LSTM-based natural language generation for spoken dialogue systems. arXiv preprint arXiv, 1508.01745.

[11] Christen, D. (2013). Rule-Based Semantic Tagging. An Application Undergoing Dictionary Glosses. arXiv preprint arXiv, 1305.3882.

[12] Liu, X.; Sarikaya, R.; Zhao, L.; Ni, Y.; and Pan, Y.C. (2016). Personalized Natural Language Understanding. In *INTERSPEECH*, 1146-1150.

[13] Mesnil, G.; Dauphin, Y.; Yao, K.; Bengio, Y.; Deng, L.; Hakkani-Tur, D.; and Zweig, G. (2015). Using recurrent neural networks for slot filling in spoken language understanding. *IEEE/ACM Transactions on Audio, Speech, and Language Processing*, 23(3), 530-539.

EURECA 2018 – Conference Paper
Paper number PG04

Drying Of *Clinicanthus Nutans* Leaves Using Combined Vacuum-Microwave Method: Drying Kinetics And Antioxidant Studies

*Lisa Y.W. Chua, Bee Lin Chua**

School of Engineering, Taylor's University, Taylor's Lakeside Campus, No. 1 Jalan Taylor's, 47500, Subang Jaya, Selangor DE, Malaysia
*Corresponding Author: BeeLin.Chua@taylors.edu.my

Abstract

Medicinal herbs are recognised as important reservoirs of natural compounds that confer beneficial healing properties. Post harvesting of herbs through drying is important to inactivate any metabolic reactions that may potentially degrade important biological compounds. However, drying of herbs may have unfavourable effects on the bioactive content and antioxidant activity. Selection of a suitable drying method is thus crucial to minimise degradation of valuable compounds responsible for antioxidant activity in herbs. For this reason, vacuum microwave drying (VMD) is introduced in this study as it was proven in past research to have produced food products with high antioxidant capacities. The objective of this study is to determine the influence of various drying methods on the antioxidant activity of *Clinicanthus nutans*. Leaves of *Clinicanthus nutans* were dried using two drying methods, namely convective drying (CD) at 40, 50 and 60 °C and vacuum-microwave drying (VMD) at 240, 360 and 480 W. Overall, vacuum microwave drying at 360 W gave the highest antioxidant activity followed by VMD at 480 W.

Keywords: Drying, *Clinicanthus nutans*, Drying kinetic, Antioxidant activity, Vacuum-microwave drying.

Nomenclatures

W	Watt
M_R	Moisture ratio
M_0	Initial moisture ratio
Mt	Moisture content at time t
M_e	Equilibrium moisture content

Abbreviations

CD	Convective drying
VMD	Vacuum microwave drying
ABTS	2,2'-azinobis [3-ethylbenzothiazoline-6-sulfonic acid]-diammonium salt
TEAC	Trolox equivalent antioxidant capacity
MRP	Maillard reaction products

1. Introduction

Despite the importance of synthetic drugs in improving human health, many research are also focused on finding alternative ways to improve body immune system to counter attack diseases. Medicinal herbs are recognised as extraordinary reservoirs of natural biological compounds that confer for various beneficial healing effects. Phytochemicals in particular are found in medicinal herbs that are known to possess numerous pharmacological activities [1].

Freshly harvested herbs are categorised as perishable commodities as they contain high water content and therefore are prone to unfavourable enzymatic activities and susceptible to microbial growth [2]. The content of phenolic compounds may decrease significantly in raw material during the period between harvesting and processing. Hence, it is essential that fresh herbs are preserved effectively through the removal of moisture that is contained in them and to inactivate enzymatic degradation, chemical and metabolic reactions [3]. Drying is the most common method for post-harvest preservation of medicinal herbs in order to remove moisture to ensure preservation of medicinal properties of plants [4]. However, post-harvesting is a crucial process in the industrial production of medicinal herbs as it may affect the quantitative and qualitative aspects of bioactive constituents present in medicinal herbs [5].

The primary aim of drying involves the reduction of water content to less than 15% to inhibit microbial growth and to prevent biochemical changes while preserving important

constituents in raw herbs with nutraceutical or health-promoting properties [6]. Presently, the most practical and common method used to dehydrate herbs commercially is through convective drying [2]. However, convective drying has low energy efficiency and may not necessary produce medicinal herbs with high retention of bioactive constituents [2]. Convective drying employs surface heating in which moisture evaporation from food material is driven by moisture concentration gradient. Evaporation of moisture from the surface is relatively efficient but, diffusion of moisture from the centre region of food product to the surface is slow and rate limiting, resulting in a low drying rate [4]. A prolonged drying time may lead to high quality deterioration in the final dried product [7]. Hence, convective oven drying may not be suitable for the drying of medicinal herbs due to the abovementioned limitations. At the same time, the degradation of bioactive compounds may also be due to the long exposure of plants to oxygen [8].

Considering the sensitivity of bioactive compounds in plant materials to thermal degradation and oxidation, the development of hybrid drying technologies is imperative to overcome the disadvantages of conventional drying methods as combined drying methods are versatile and the maximization of advantages of two or more drying methods may offer better drying outcomes [2]. VMD is a hybrid drying method that combines microwave heating in a vacuum chamber to create a reduced pressure. In VMD, microwaves penetrates food material, heats up water through dipole rotation and ionic conduction and causes vaporization of moisture at a lower temperature under reduced pressure [6]. This combined drying method is targeted in maintaining or to speed up microwave drying while avoiding high temperatures [4]. In addition to increasing drying rate through volumetric heating, the lower pressures in VMD is able to induce faster evaporation of moisture from plant material at a lower temperature, thereby decreasing possible chemical changes in plant materials by high drying temperatures [9]. Therefore, VMD is aimed to increase drying rate, reduce plant material's exposure to oxygen and reduce drying temperature by the reduction of pressure created from a vacuum chamber.

In order to demonstrate the effectiveness of VMD in improving the retention of bioactive compounds, *Clinicanthus nutans*, a medicinal herb native to Malaysia will be used in this study. *Clinicanthus nutans* (Burm.f.) lindau, or more commonly known as 'Belalai gajah' or 'Sabah Snake Grass' have gained increasing interest among the research community as the leaves extract was reported to possesses promising antioxidant activity [10]. Traditionally, the leaves of *C. nutans* are being used for the treatment of diabetes mellitus, skin inflammations, fever, various cancers, kidney problems, anti-snake venom, among others [11]. Pharmacological activities of *C. nutans* includes antimicrobial, antiproliferative, antitumorigenic, and anti-inflammatory [12].

The objectives of this study includes the identification of the best drying method in producing dried leaves of highest antioxidant activity in addition to studying the drying kinetics of *C. nutans* using CD and VMD.

2. Materials and Methods

2.1. Sample preparation

Clinicanthus nutans was purchased from TKC nursery (Seremban, Negeri Sembilan). Leaves were cleaned before subjected to drying. The bone dry weight of all leave samples were determined by vacuum-oven method with operating temperature of 60°C and a drying duration of 24 h.

The initial moisture content of leaves was determined from Eq. (1).

$$\text{Moisture content} = \frac{\text{Initial weight} - \text{bone dry weight}}{\text{bone dry weight}} \quad (1)$$

2.2. Chemicals

6-hydroxy2,5,7,8-tetramethylchroman-2-carboxylic acid (Trolox), 2,2′-azinobis (3ethylbenzthiazoline-6-sulfonic acid (ABTS), potassium persulfate, HCl, and methanol were purchased from Sigma-Aldrich (Steinheim, Germany).

2.3. Drying process

Approximately 40 g of leaf samples of *Clinicanthus nutans* were subjected to two drying methods. The first drying method was convective drying (CD) and the second was vacuum-microwave drying (VMD). Mass losses of herb samples were monitored and drying was stopped when the mass loss of consecutive samples were 0.05 g or less.

2.3.1. Convective drying (CD)

Briefly 40 g of leaf samples was dried in a convective oven designed and built in the Institute of Agriculture Engineering (Wroclaw, Poland) at temperatures of 40, 50, and 60 °C. The leaf samples of 40 g were spread on a wire mesh tray, which was placed on top of drying chambers. The temperature measurements of drying chambers were ± 1°C.

2.3.2. Vacuum-microwave drying (VMD)

Herbs of 40 g was dried in a vacuum-microwave dryer (Plazmatronika, Wroclaw, Poland) at microwave powers of 240, 360 and 480 W. The herbs were placed in an organic glass container, to prevent any leaching of chemicals and this container was connected to a vacuum system. During the process of drying, the container was rotated at a speed of 6 rpm. Meanwhile, the pressure in the vacuum-drum varied from 4 to 6 kPa. An electric fan equipped at the bottom of the dryer provided an air stream of velocity and temperature of 1 m/s and 22°C, respectively. Rotation of container and airstream were necessities to prevent local over –heating of herbs during the process of drying.

2.4. Extraction of polyphenol compounds for antioxidant activity assay

Approximately 0.3 g of each grounded herb samples were weighed into test tubes. A total of 0.7 mL of 80% aqueous methanol was added with the addition of 1% HCl. The suspension was mixed slightly. Tubes containing the suspension were sonicated for 15 min twice and left at a temperature of 4°C for 24 h. Next, the extract was centrifuged for a duration of 10 min at 15000 rpm, and supernatants were collected at 4 °C to be used within a period of 24 h.

2.5. Antioxidant activity analysis

2.5.1. $ABTS^{\bullet+}$ radical scavenging assay

ABTS radical scavenging assay was used to determine the free radical scavenging activity as described by Re et al., [13] ABTS was dissolved in water to form a concentration of 7 mM. ABTS stock solution was reacted with 2.45 mM potassium persulfate to form ABTS radical cation ($ABTS^{\bullet+}$). The mixture was left to stand in the dark at room temperature for 12–16 h before using in the assay. This solution was diluted with redistilled water to obtain an absorbance of 0.700 ± 0.02 at 734 nm. For the antioxidant activity analysis, 3.0 mL of the diluted radical solution will be mixed with 20 µL of the extracted supernatant. The absorbance was read at 734 nm after 6 minutes. All determinations were performed in triplicates. The results obtained were expressed relative to micromolar Trolox per 100 g of dry weight in terms of Trolox equivalent antioxidant capacity (TEAC).

3. Results and Discussion

3.1. Drying kinetics

Drying kinetics of *Clinicanthus nutans* leaves dehydrated by CD and VMD is as shown in Fig 1.

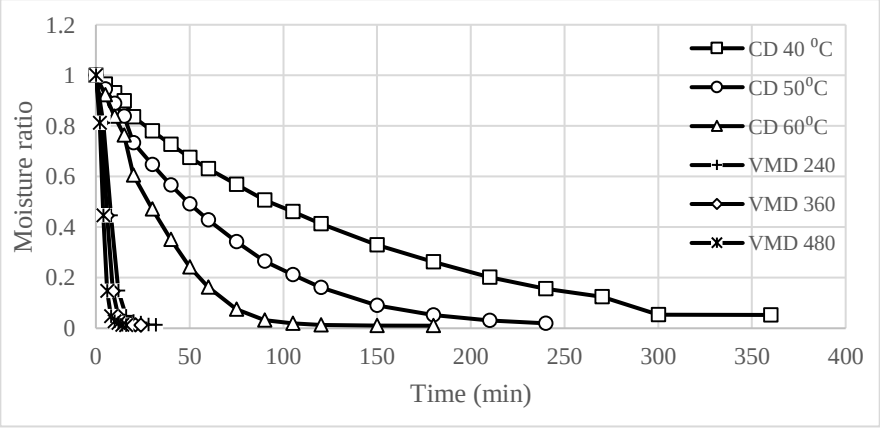


Fig. 1. Drying kinetics of *Clinicanthus nutans* dehydrated by CD method at 40, 50 and 60°C and VMD method at 240, 360 and 480 W.

With reference to Fig 1., during the initial phase of CD, moisture loss is relatively fast however, successive moisture loss was seen to decrease with time and drying starts to be time consuming. The total drying time of CD at 50°C to reach equilibrium moisture content of 0.069

kg/kg db reached ca. 240 min. The drying duration for VMD (240, 360 and 480 W) on the other hand, was much shorter compared to CD, achieving a drying duration of only 32, 24 and 16 minutes, respectively.

The relationship between drying rate and moisture ratio of all drying methods are shown in Fig 2. As expected, the drying rate of VMD at 240, 360 and 480 W were the highest, and drying rates were observed to increase with higher application of microwave power. The volumetric heating of microwave drying is such that microwave energy is able to penetrate the inner regions of leaves structure and heat is produced within by the absorption of microwave energy by water molecules. This is followed by evaporation of water in situ, and subsequent diffusion of internal moisture to the surface as vapour. This happens as the increase of positive steam pressure develops in food, which pushes vapour to the surface once solution within a food reaches boiling point [14].

Drying rate of convective drying at 40, 50 and 60°C were considerably lower compared to VMD and drying rates were observed to increase with the application of higher temperatures. It is noteworthy that although drying temperature was increased by 10 °C, drying rates does not increase greatly. For instance, an increase of 10°C from 40°C to 50°C corresponded to an average 0.0025 min^{-1} increase in drying rate. In the case of VMD, when microwave power was increased from 240 to 360 W, a higher increase in average drying rate of 0.0104 min^{-1} was observed.

It is also to be noted that drying rate for all drying treatments decreased at some point during drying. In the case of VMD, drying rates starts to increase until moisture ratio of 0.8 and decreased thereafter. This decreasing rate period is known as the falling rate period and is characterised by a continuous reducing drying rate. The falling rate period can be divided into two period, first falling rate period, which has higher drying rate than the drying rate of second falling rate period [9]. Regardless of the microwave power applied, it is typical that a higher drying rate is observed at the initial drying period of VMD as the moisture content of leaves is higher initially and this corresponds to a higher dielectric constant. Consequently, a larger microwave power was absorbed by the leave material and more heat was generated. This cause more moisture to be evaporated and therefore drying rate was higher initially. However, when drying continues, the reduction of moisture from leave material subsequently reduces the amount of microwave energy being absorbed, which results in the fall of drying rates observed.

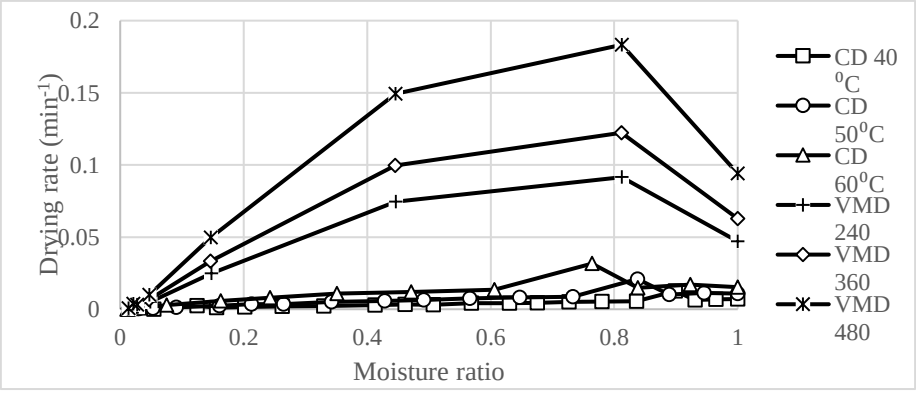


Fig. 2. Drying rate against moisture ratio of *Clinicanthus nutans* dehydrated by CD method at 40, 50 and 60°C and VMD method at 240, 360 and 480 W.

3.2. Antioxidant activity of *Clinicanthus nutans* as affected by drying method

Antioxidant activity of fresh and dehydrated *Clinicanthus nutans* leaves were estimated by using ABTS method, as shown in Table 3. Overall, among the six drying treatments, the highest antioxidant activity was observed for VMD at 360 W followed by VMD at 480 W. CD achieved relatively lower antioxidant activity as the relatively long drying time (360 min at 40 °C) may have given allowance for extensive oxidation to take place. It was also observed that CD at 60°C achieved higher ABTS value compared to CD at 40 and 50 °C, with ABTS values increasing following the increase in CD temperature. A higher hot air temperature employed in CD corresponded to a higher antioxidant value as the time taken for completion of drying process was also reduced. The samples were less exposed to hot temperature at 60°C, and less degradation of heat labile antioxidant compounds occurred.

It is also noteworthy that higher values of ABTS were obtained by CD at 40, 50 and 60 °C and VMD methods at 360 and 480 W compared to fresh samples. This behaviour may be the result of subjecting leave samples to heat treatment, which may lead to the production of new compounds exhibiting higher antioxidant activity. This is an exemplary case of Maillard reaction, which forms various Maillard reaction products (MRPs), possessing antioxidant properties [15].

In the case of VMD, it was also observed that when microwave power was increased, antioxidant activity increased from 240 to 360 W. However, a further increase of microwave power from 360 W to 480 W caused antioxidant capacities to decrease. A possible explanation to this may be because an increase of 240 W to 360 W shortened drying duration from 32 to 24 min. For this reason, samples are therefore less exposed to hot drying temperature. However, when microwave power was increased from 360 to 480 W, the drying duration may have shortened from 24 to 16 min, but at 480 W, a higher temperature was employed which may have caused thermal degradation of compounds responsible for antioxidant activity to a higher extent.

Table 3. The influence of drying method on antioxidant activity of *Clinicanthus nutans*.

Drying method	Antioxidant activity (μM Trolox/100 g dw)
Fresh	1.02
VMD 240 W	0.89
VMD 360 W	2.10
VMD 480 W	1.78
CD 40 °C	1.09
CD 50 °C	1.46
CD 60 °C	1.66

VMD, vacuum-microwave drying; CD, convection drying.

4. Conclusions

Among the different drying methods, VMD showed highest drying rate and the shortest total drying duration while CD showed lower drying rate, which corresponds to a considerably longer drying duration. This study has demonstrated that the best option to dry *Clinicanthus nutans* based on the antioxidant analysis was VMD at 360 W followed by VMD at 480 W. The final conclusion that can be drawn is that VMD is an improved drying method compared to CD as this microwave-assisted drying method produced dried samples of *Clinicanthus nutans* with relatively higher antioxidant activity compared to the more conventional convective drying.

References

[1] A. M. Saxena, J. Saxena, R. Nema, D. Singh, *Phytochemistry of Medicinal Plants - ProQuest*, vol. 1, no. 6. 2013.

[2] J. W. R. Chan, C. H. Chong, and D. K. S. Ng, "Process synthesis and design for extraction of bioactive compounds from *Strobilanthes crispus* leaves," *J. Eng. Sci. Technol.*, pp. 113–137, 2015.

[3] S. D. Sarker, S. D. Sarker, Z. Latif, Z. Latif, A. I. Gray, and A. I. Gray, "Natural Product Isolation," in *Natural Products Isolation*, 2005, pp. 1–25.

[4] K. J. Chua and S. K. Chou, *Emerging Technologies for Food Processing*. 2014.

[5] K. Jalal, M. Rahmat, F. T. Mohammad, and N. Himan, "Influence of Drying Methods , Extraction Time , and Organ Type on Essential Oil Content of Rosemary (*Rosmarinus officinalis* L .)," *Nat. Sci.*, vol. 7, no. 11, pp. 42–44, 2009.

[6] D. Wray and H. S. Ramaswamy, "Novel concepts in microwave drying of foods," *Drying Technol.*, vol. 33, no. 7, pp. 769–783, 2015.

[7] H. Feng, Y. Yin, and J. Tang, "Microwave Drying of Food and Agricultural Materials: Basics and Heat and Mass Transfer Modeling," *Food Eng. Rev.*, vol. 4, no. 2, pp. 89–106, 2012.

[8] A. Michalska, A. Wojdyło, K. Lech, G. P. Łysiak, and A. Figiel, "Physicochemical properties of whole fruit plum powders obtained using different drying technologies," *Food Chem.*, vol. 207, pp. 223–232, 2016.

[9] Á. Calín-Sánchez, A. Figiel, K. Lech, A. Szumny, and Á. Carbonell-Barrachina, "Effects of Drying Methods on the Composition of Thyme (*Thymus vulgaris* L.) Essential Oil," *An Int. J.*, vol. 31, no. 2, pp. 224–235, 2013.

[10] P. Pannangpetch, P. Laupattarakasem, V. Kukongviriyapan, U. Kukongviriyapan, B. Kongyingyoes, and C. Aromdee, "Antioxidant activity and protective effect against oxidative hemolysis of *Clinacanthus nutans* (Burm . f) Lindau," *Songklanakarin J. Sci. Technol.*, vol. 29, pp. 1–9, 2007.

[11] I. N. Zulkipli, R. Rajabalaya, A. Idris, N. A. Sulaiman, and S. R. David, "*Clinacanthus nutans* : a review on ethnomedicinal uses, chemical constituents and pharmacological properties," *Pharm. Biol.*, vol. 55, no. 1, pp. 1093–1113, 2017.

[12] A. Alam *et al.*, "*Clinacanthus nutans:* A review of the medicinal uses, pharmacology and phytochemistry," *Asian Pacific Journal of Tropical Medicine*, vol. 9, no. 4. pp. 402–409, 2016.

[13] R. Re, N. Pellegrini, A. Proteggente, A. Pannala, M. Yang, and C. Rice-Evans, *Re R, Pellegrini N, Proteggente A, Pannala A, Yang M & Rice-Evans C: Antioxidant activity applying an improved ABTS radical cation decolorization assay. Free Rad. Biol. Med. 26, 1231-1237*, vol. 26. 1999.

[14] C. H. Scaman and T. D. Durance, "Combined microwave vacuuum-drying," in *Emerging Technologies for Food Processing*, 2005, pp. 507–533.

[15] A. Wojdylo, A. Figiel, and J. Oszmian, "Effect of Drying Methods with the Application of Vacuum Microwaves on the Bioactive Compounds, Color, and Antioxidant Activity of Strawberry Fruits," in *J. Agric. Food Chem*, pp. 1337–1343, 2009.

EURECA 2018 – Conference Paper
Paper number PG05

Detection Of Time Localised Transition In Meditation EEG Using Discrete Wavelet Transform

Jen Looi Tee, Wei Jen Chew, Hou Kit Mun, Siew Wei Phang*

School of Engineering, Taylor's University, Taylor's Lakeside Campus, No. 1 Jalan Taylor's, 47500, Subang Jaya, Selangor DE, Malaysia
*Corresponding Author: teejenlooi@gmail.com

Abstract

Meditation is a mental exercise of being in a state of relaxed, focused attention. When exiting meditation (self induced or otherwise externally disturbed), a transition Electroencephalogram (EEG) signal was observed. This study extracted the EEG transition feature of the signal between state of meditation and post meditation using Discrete Wavelet Transform (DWT). Wavelet analysis retains both time and frequency information, allowing the transition feature to be easily identified and localised on the time scale. When given a continuous meditation EEG signal as input, results from DWT were applied to detect time localised transition during meditation. Preliminary results demonstrated that the DWT feature extraction model is capable of detecting when a meditation practitioner exited meditation at 90% accuracy based on a meditation EEG dataset recorded locally.

Keywords: Meditation, EEG, Discrete Wavelet Transform, Time Frequency Analysis, Transition Feature Extraction.

Nomenclatures

$A_{1..n}$	Approximate coefficient output from h[n]
B_0	Classifier constant
B_1	Classifier constant
$D_{1..n}$	Detail coefficient output from g[n]
g[n]	Impulse response quadrature mirror filter to h[n]
h[n]	Impulse response of wavelet low pass filter
i	Imaginary number
k	Constant
P_R	Probability of classifier result
t	Time (s)

Greek Symbols

ω	Angular frequency.

Abbreviations

EEG	Electroencephalogram
DWT	Discrete Wavelet Transform
FFT	Fast Fourier Transform
BLR	Binomial Logistic Regression
EU	European Union

1. Introduction

Meditation is a voluntary mental exercise. When performed successfully, it is described as being in a mental-emotional state of relaxation, calmness and wakefulness, as well as detachment from intruding thoughts. Research on meditation has shown numerous physical and emotional benefits have been associated with meditation [1–7].

Further studies on the physiology of meditation using Electroencephalogram (EEG) has shown specific patterns in the human brain associated with meditation. However, most literature discussing EEG analysis on meditation were based upon Fourier analysis methods, which mean the results were all void of time based information. When analysis results carries no time resolution, time sensitive information such as transitions between meditation and non-meditation (pre-meditation, post-meditation, distraction from meditation) were not well defined and examined in literature.

This study examined the transition between meditation and post meditation rest period using time-frequency analysis. Feature of transition (distraction / exit of meditation), localised in time, was extracted using Discrete Wavelet Transform (DWT). Given a signal (continuous in time), the feature extraction model would differentiate when a meditation practitioner was "in a state of meditation" vs "exit from meditation".

Research on meditation [8–9] using EEG analysis has been focused upon analyzing inter-group differences, eg. Long Term Meditation practitioner vs Novice (Control) practitioner, or inter-state differences eg. Meditation vs Rest period. The two most widely applied methods of analysis were frequency sub band power comparison and inter-channel frequency sub band coherency.

The sub band power and coherency analysis were based upon Fourier methods, typically the Fast Fourier Transform (FFT) to extract frequency domain data from the time domain EEG signal.

Fourier based analysis has one shortcoming - the basis of FFT requires the input signal to be stationary, ie. Any frequency components existing within the signal must uniformly present at all times as Fourier analysis is an integral over all time, as shown in Eq. (1).

$$X(\omega) = \int_{-\infty}^{\infty} x(t) e^{-i\omega t} dt \quad (1)$$

The resulting data carries no time information.

However, an EEG signal, being a physiological signal, is non-stationary in nature. The oscillatory frequencies of a recorded EEG signal potentially changes from second to second as physiological and functional state of a person's brain varies from second to second. Hence, in order to apply Fourier Transform to a non-stationary signal, short segments of signals were extracted from the recorded EEG signal. These segments, due to their short length, were treated as quasi stationary and subsequently filtered and analyzed.

As mentioned in Hinterberger's article [10] "The preprocessing of EEG data followed a standard approach - By applying artifact reduction and filtering into spectral bands using Fourier transform", indicated this approach to be the common method currently applied to meditation EEG signal processing. During the segmentation process, each segment is treated as non continuous entity from another segment. Any segment containing artifacts was discarded, with results of accepted segments averaged prior to analysis. This series of actions completely loses the time element of the original signal..

While the final results could be identified as extracted from "known periods of meditation" / "known periods of rest", they do not carry any detailed localized time information, nor transitional information (data variation against time).

On the other hand, the DWT offers a time and frequency estimation of the signal. The frequency components (which are called scales in DWT) are localized in time (called translation in DWT). Due to the fact that EEG is a non-stationary signal, a time varying spectral estimation technique such as wavelet has proven to be popular feature extraction methods [11–15], and is the proposed method for feature extraction in this article.

2. Methodology

This study is based on an experimental setup. Equipment requirement for this study centralizes around the Electroencephalogram. The device used is manufactured by CamNTech, named the CamNTech Actiwave Multichannel Recorder, a class 2a (EU) medical device. It includes the EEG recording device, electrode leads, conductive adhesive paste (for interface between electrode and subject's scalp surface), and a docking interface which links the EEG recorder to a computer. The device comes with a user guide and the operational procedures were clearly described within the Actiwave User Guide [16]. The Actiwave device samples EEG signals at a rate of 128 Hz. Electrode placements followed the international standard 10-20 EEG electrode placement as shown in Fig 1.

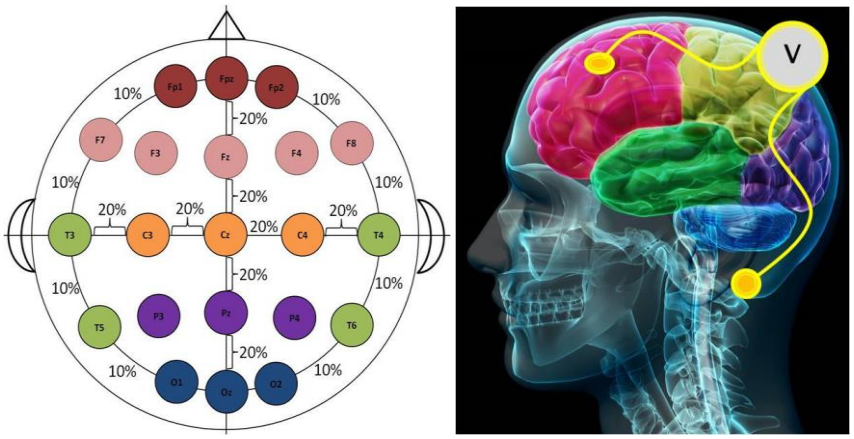


Fig. 1. Standard 10-20 placement of EEG electrode placement map, colour coded to correspond with various brain lobes using the mastoid bone as reference point.

Twenty subjects, aged between 18 - 55, were tasked with performing Focused Attention Meditation guided by an audio recording [17] according to the standard practice of Theta Healing®. Theta Healing® [18], a meditation practice founded by Stibal, who authored a book titled under the same name, stated that the Theta Healing® technique is a meditation process. The sampling frame for this study is drawn from Theta Healing® practitioners from Malaysia, Singapore, and Australia. Data collections were conducted at Theta Healing® seminars, at the respective venue, with permission and prior mutual agreement. Data collection takes place in the late afternoon, after the conclusion of regular seminar activities.

At the beginning of the experiment, the subjects were briefed with the entire procedure, and informed consent was obtained prior to continuing. Subjects remain seated comfortably during the entire measurement. EEG electrodes was placed on the F3 and F4 according to the EEG 10-20 standard placements of electrodes (corresponding to the brain's frontal lobe) of subject. The F3 and F4 points are selected based on previous studies [19], [20], where F3 and F4 were some of the points with noticeable EEG changes observed during meditation activities.

EEG measurements of these two points were recorded during meditation and after the mediation process stops (post meditation rest period). The audio recording guides participants through approximately eleven minute visualization meditation process. At the end of the audio recording, subject was instructed to stop meditation activity. The EEG recording continues for another two minutes, recording post meditation signal. EEG data were then extracted and evaluated.

Each recorded signal $x[n]$was decomposed through a series of filters seen in Fig. 2, called a filter bank. The mother wavelet, $g[n]$ is a half band high pass filter, which decompose the signal and outputs detail coefficients, with D_1 being the Level 1 coefficient. At the same time, the signal $x[n]$ was passed through a half band low pass filter with an impulse response $h[n]$ written as Eq. (2) and $h[n]$ is a quadrature mirror filter of $g[n]$, with the relationship between these two filters written through their respective z-transform as Eq. (3).

$$y[n] = \sum_{k=-\infty}^{\infty} x[k]h[n-k] \quad (2)$$

$$G(z) = zH(-z^{-1}) \quad (3)$$

A_1 is the output of the low pass filter $h[n]$. A_1 is further decomposed through a high pass filter, giving D_2 as the Level 2 coefficient, and so forth.

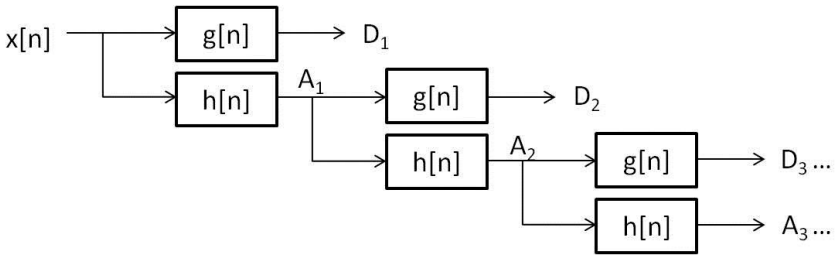


Fig. 2. Discrete Wavelet Transform (DWT) filter bank.

Given the Nyquist principal in data sampling (where the highest discernible frequency content is half of the sampling frequency, which was 128 Hz in this experiment), the raw EEG data sequence would contain frequency components from 0 to 64 Hz. As the Discrete wavelet filter banks are composed of quadrature mirror filters, each decomposition process would halve the frequency content of each level. With Level 1 containing equivalent frequency range of 32 - 64 Hz, Level 2 containing equivalent frequency range of 16 - 32 Hz, and so forth, with the complete equivalent frequencies content seen in Table 1.

Table 1. The equivalent frequencies contained within each decomposition level and corresponding frequency bands.

Wavelet Level	Level 1 (D1)	Level 2 (D2)	Level 3 (D3)	Level 4 (D4)	Level 5 (D5)	Level 6 (D6)	Residual (A6)
Equivalent Frequencies	32-64 Hz	16-32 Hz	8-16 Hz	4-8 Hz	2-4 Hz	1-2 Hz	0-1Hz
Equivalent Freq. Bands	Gamma band	Beta band	Alpha band	Theta band	Delta band	Delta band	Unclassified

In the frequency analysis of neural brainwaves (EEG oscillations), the frequencies information of the EEG signal are typically categorized into frequency bands as Delta (1-4 Hz), Theta (4-8 Hz), Alpha (8-15 Hz), Beta (15-30 Hz), and Gamma (>30 Hz). As there have no conclusive reports of human brain EEG oscillation observed below 1 Hz, this study limits the decomposition to level from level 1 to level 6 (1-64 Hz). The best decomposition level would be selected among these 6 levels.

Once the Wavelet Level was determined, we proceeded to the optimum wavelet/wavelet family selection. In an exhaustive study by Chen [21], where each wavelet member (e.g. symlet 2 to 8) within the wavelet family (e.g. Symlet family), for all families (e.g. Coiflet, Daubechies, Symlets, Discrete Meyer, Haar) were investigated, Chen concluded that for DWT analysis, intra and inter family differences were minimal (e.g. accuracy achieved by all wavelets were between 95% to 97% for UBonn dataset, and between 87.33% to 89% for MIT dataset). Since intra family differences were small, only one member per family (Coiflet,

Daubechies, Symlet, Discrete Meyer, Haar) was selected for inter family comparison in this study.

For validation of wavelet family selection, the Binomial Logistic Regression (BLR) model was chosen as the classifier. Regression models are a family of classifiers or prediction models that predict the dependant variable (expected outcome or output value) based on the independent variable (input value). For this work, the regression model of choice was the Binomial Logistic Regression because the dependent variables were non-continuous nominal values (ie. there are only two possible categories - meditation or transition). A set of training data is required to generate the classification function, shown in Eq. (4). The $P_R(\frac{Y}{X})$ is the probability of the input segment to be a transition or meditation signal.

$$P_R(\frac{Y}{X}) = \frac{e^{(B0+(B1)*X)}}{1+e^{(B0+(B1)*X)}} \quad (4)$$

In summary, the collected data goes through a data processing flow as shown in Fig. 3.

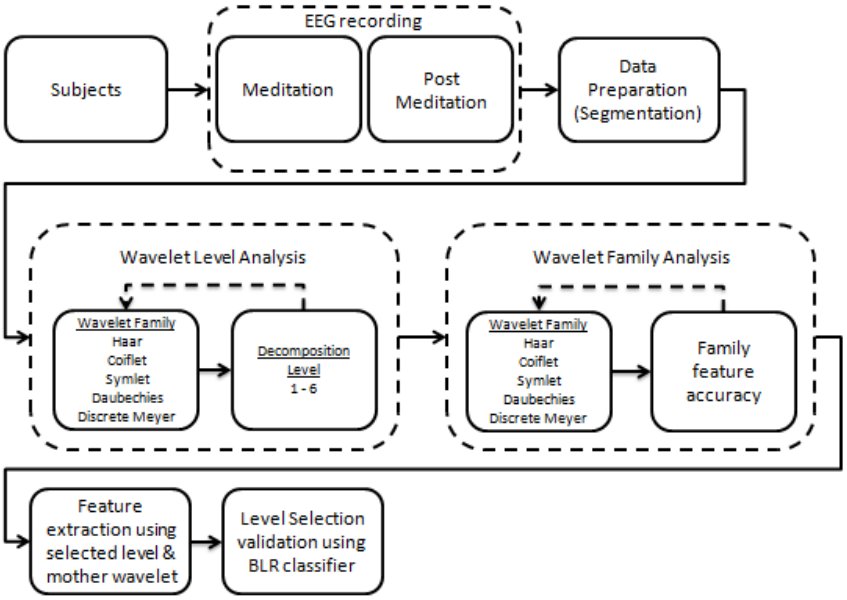


Fig. 3. The experiment framework process flow diagram.

3. Results and Discussion

A total of 20 participants completed participation in the experiment. Following the EEG recording sessions, the EEG data were examined. Each participant was measured at both the F3 and F4 point, yielding two data sequences from each participant, giving a total 40 sets of data sequence. Of the 40 EEG sequences, one sequence was corrupted and 39 EEG data sequences were viable for further processing. For the preliminary study of wavelet levels and family selection, a total of 50 meditation segments and 50 transition segments were extracted from the 39 EEG sequence. An example of the EEG recording is seen in Fig. 4.

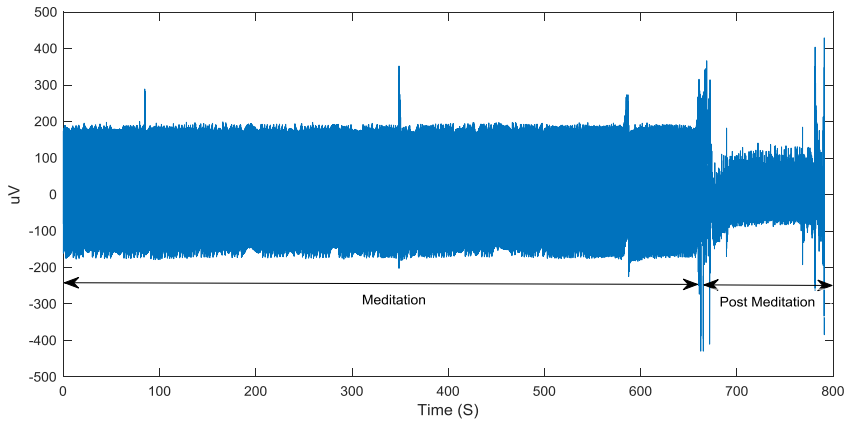


Fig. 4. An example of EEG recording showing meditation signal transitioning into post meditation/rest period.

As shown in the Fig. 4, the meditation session was 11 minutes long, followed by 2 minutes of post meditation recording, with a short period of transition formed in between meditation and post meditation. From each set of data sequence, 10 seconds of meditation data (around the 9 minute mark after the start of meditation) and 9 seconds of transition data (around the 11 minute mark which is the end of the meditation) were extracted. The extracted data were further separated into 9 or 10 segments, with each segment being 1 second long, and consisting of 128 data points (EEG sampling rate of 128 Hz).

Analysis and selection of Wavelet Level

The performance of a wavelet classifier hinges upon the selection of mother wavelet, wavelet decomposition level and feature selection. As indicated by Chen [21], the proper selection of wavelet decomposition level, from which features were selected, carries a high impact on the accuracy of the classifier. The preliminary test of this study seeks to confirm this observation, as well as to determine the optimum decomposition level from which to extract feature for classification.

For decomposition level evaluation, thirty meditation EEG segments and thirty transition EEG segments were randomly selected and processed using DWT, decomposed down to level 6. A sample of a transition segment its respective DWT decomposition (Left: meditation, Centre: transition, Right: Rest) joint side-by-side for visual comparison purposes is shown in Fig. 5.

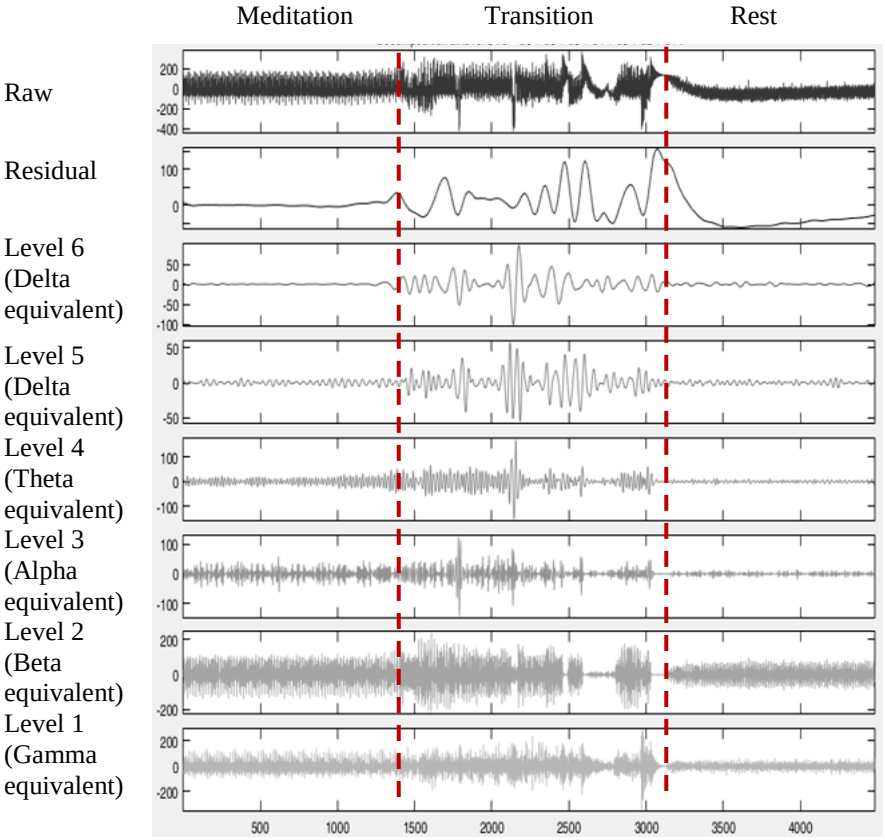


Fig 5. Raw EEG signal and its DWT decomposition showing "Meditation" (left) going through a "Transition" period (middle) into post meditation "Rest" period (right).

When comparing the meditation segment (left) and rest segment (right), higher Level 3 (Alpha band) and Level 4 (Theta band) activity was observed. This was expected and consistent with general findings of higher Alpha and Theta power during meditation in comparison to rest period.

The point of interest, the Transition period segment, displayed high signal volatility in Level 5 and Level 6, measureable as standard deviation (selected feature).

The 30 meditation segments and 30 transition segments were each decomposed using 5 different mother wavelets, one from each of Haar, Symlets, Coiflets, Daubechies, and Discrete Meyer wavelet family, and the standard deviation of each decomposition level of each segment were calculated and analysed. The resulting feature values, in log scale are shown in Figs. 6 to 10.

Results in Figs. 6 to 10 showed that the decomposition level contributed significantly to the variation in extracted feature values. In the raw signal, as well as level 1 to 4, there are no significant feature difference between meditation signals and transition signals across all five wavelets analysis. Higher feature differences between meditation signal and transition signal were observed in level 5, with feature difference between meditation signal and transition signal being the most distinct at level 6, across all five wavelets analysis. The results indicated that level 6 is the most optimum decomposition level for feature extraction with this dataset.

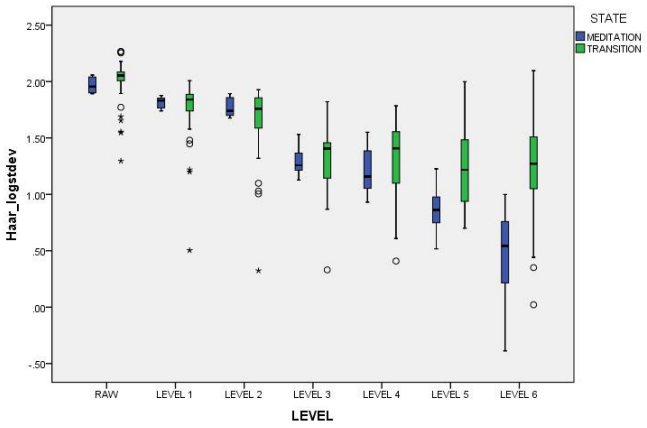


Fig. 6. Meditation vs transition feature analysed using Haar wavelet.

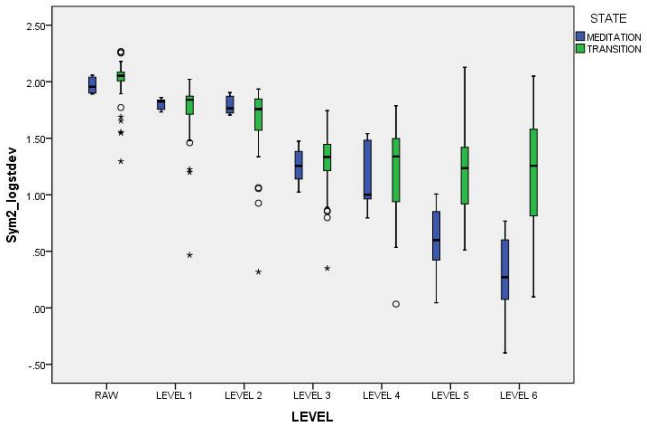


Fig. 7. Meditation vs transition feature analysed using Symlet2 wavelet.

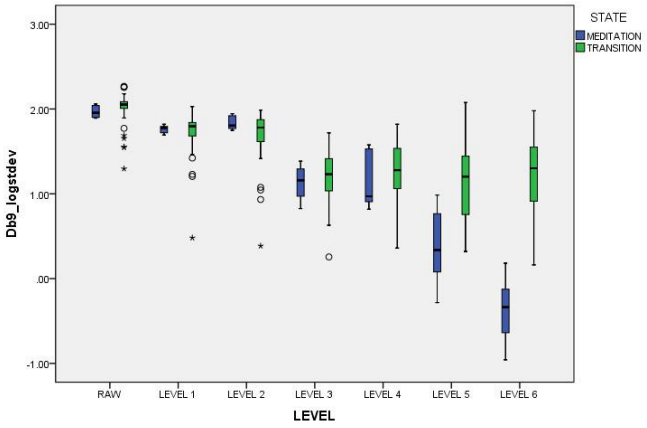


Fig. 8. Meditation vs transition feature analysed using Daubechies9 wavelet.

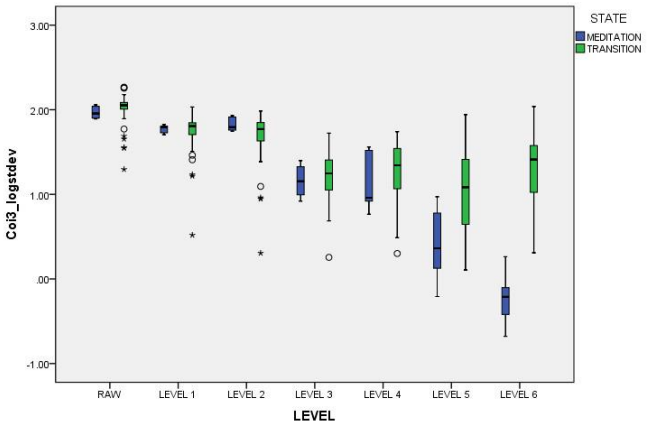


Fig. 9. Meditation vs transition feature analysed using Coiflet3 wavelet.

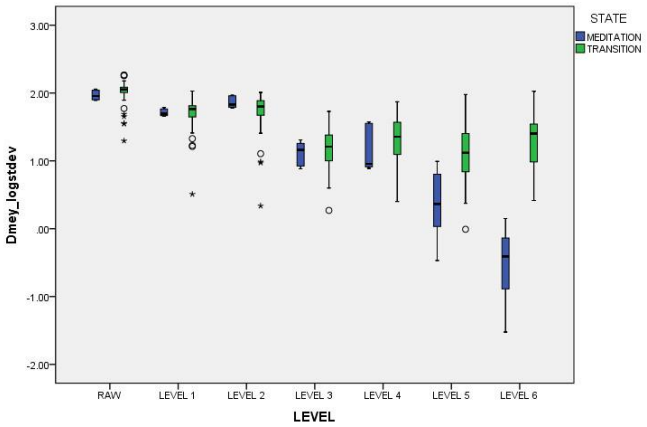


Fig. 10. Meditation vs transition feature analysed using Discrete Meyer wavelet.

Analysis and selection of Wavelet Family

For level 6 comparisons among the five wavelet families, the initial results using 30 samples were inconclusive. The classification accuracy achieved for each family were Haar - 83.3%, Symlet - 85%, Daubechies - 98.3%, Coiflet - 100%, and Discrete Meyer - 100%. The exceedingly high accuracy of Coiflet and Discrete Meyer was due to the distinct difference between level 6 meditation feature and level 6 transition feature seen in figs. 9 and 10. To confirm the superior efficiency of the Coiflet and Discrete Meyer mother wavelet, the sample size was increased to 50 random meditation segments against 50 random transition segments. Results were shown in Fig. 11.

As the sample size was increased to 50, the accuracy achieved by each wavelet pulled close. The result indicated that there were only minor variations among different wavelet families. The inter-wavelet differences pale in comparison to the variation seen among inter-level differences (intra-wavelet).

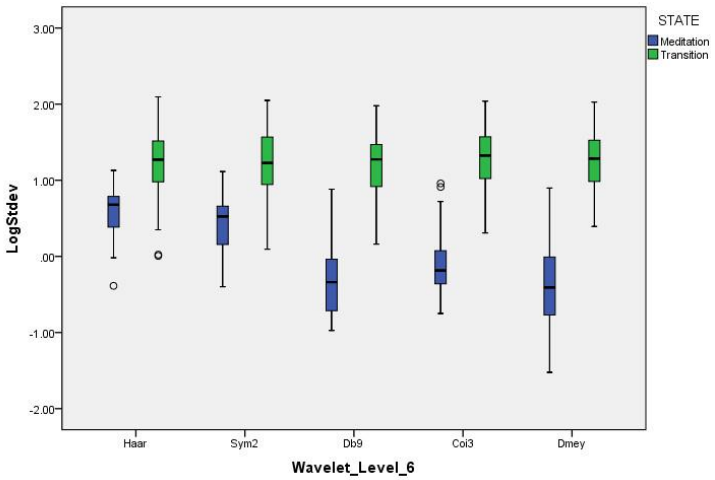


Fig 11. Comparison of Level 6 meditation signal feature vs transition signal feature extracted using different Wavelet Families.

The level 6 feature extracted using each of the five wavelet family was further evaluated using a binomial logical regression classifier. The classification function was able to achieve reasonably high automatic classification accuracy (>86%) across all 5 wavelets, show in Table 2., with accuracy defined in Eq. (5).

$$ACC\ (accuracy) = \frac{\sum True\ Positive + \sum True\ Negative}{Total\ Population} \quad (5)$$

A true positive result is when a transition segment was classified as transition, and a true negative result is when a meditation segment was classified as meditation.

Table 2. The accuracy delivered by respective DWT mother wavelet.

Wavelets	**Haar**	**Symlet**	**Daubechies**	**Coiflet**	**Discrete Meyer**
Accuracy	**87%**	**88%**	**86%**	**90%**	**90%**

From the results, the performance of various mother wavelets was very similar, with the Discrete Meyer and Coiflet wavelet yielding slightly higher accuracy at 90%. Between these two, Discrete Meyer yielded lower average meditation values (bigger difference between meditation and transition values), and was selected as the final wavelet of choice to analyse the entire dataset.

Discussion

EEG feature extracted by DWT was not be significantly affected by choice of mother wavelet, with only a small variation in accuracy observed among different wavelet families. The similarity in performance is owed to the design of the DWT filter bank design that drove a common data decomposition flow using wavelet quadrature filters. The minor difference seen is due to the differences in the mother wavelet's frequency response curve. While each mother wavelet frequency responce curve is a half band filter, the slope of each wavelet filter is ultimately different, resulting in different filtering efficiency between each wavelet family.

Notable wavelet family that provided high accuracy for the meditation dataset of this experiment were the Discrete Meyer and Coiflet.

The sample size of this preliminary study was limited to 50 sample segments. Since the classifier accuracy was affected by the sample size, a bigger sample size is recommended for the generation of the final classifier function.

More importantly, results were highly sensitive to the selection of Wavelet Levels. For DWT EEG processing, the selection of levels is a delicate matter affected by a couple of factors, namely the sampling frequency, decomposition depth (max level) and target frequency component.

Notable differences between meditation signal feature and transition signal feature were observed in Level 5 and 6, with Level 6 carrying the most distinct differences.

4. Conclusion

This study examined and affirmed the key DWT selection criteria for Meditation EEG time frequency analysis. Fourier based studies examined the differences between meditation and rest, but due the lack of time resolution, FFT results could not be used to detect when exactly in time is a practitioner in meditation or otherwise. This study demonstrated DWT as an alternate signal analysis method that is capable of processing time varying, non-stationary signal, with output features localised in time. In short, meditation EEG analysed with DWT contains time and frequency information, a good step forward from the pure frequency content of Fourier analysis.

References

[1] Rosenkranz, M. A.; Lutz, A.; Perlman, D. M.; Bachhuber, D. R. W.; Schuyler, B. S.; MacCoon, D. G.; and Davidson, R. J. (2016). Reduced stress and inflammatory responsiveness in experienced meditators compared to a matched healthy control group. *Psychoneuroendocrinology*, 68, 117–125.

[2] Harinath, K.; Malhotra, A. S.; Pal, K.; Prasad, R.; Kumar, R.; Kain, T. C.; … Sawhney, R. C. (2004). Effects of Hatha Yoga and Omkar Meditation on Cardiorespiratory Performance, Psychologic Profile, and Melatonin Secretion. *The Journal of Alternative and Complementary Medicine*, 10(2), 261–268.

[3] Solberg, E. E.; Holen, A.; Ekeberg, Ø.; Østerud, B.; Halvorsen, R.; and Sandvik, L. (2004). The effects of long meditation on plasma melatonin and blood serotonin. *Medical science monitor : international medical journal of experimental and clinical research*, 10(3), CR96–R101.

[4] Slagter, H. A.; Lutz, A.; Greischar, L. L.; Francis, A. D.; Nieuwenhuis, S.; Davis, J. M.; and Davidson, R. J. (2007). Mental training affects distribution of limited brain resources. *PLoS Biology*, 5(6), 1228–1235.

[5] Jha, A. P.; Krompinger, J.; and Baime, M. J. (2007). Mindfulness training modifies subsystems of attention. *Cognitive, Affective, & Behavioral Neuroscience*, 7(2), 109–19.

[6] Aftanas, L.; and Golosheykin, S. (2005). Impact of regular meditation practice on EEG activity at rest and during evoked negative emotions. *International Journal of*

Neuroscience, 115(6), 893–909.

[7] Hofmann, S. G.; Sawyer, A. T.; Witt, A. A.; and Oh, D. (2010). The effect of mindfulness-based therapy on anxiety and depression: A meta-analytic review. *Journal of Consulting and Clinical Psychology*, 78(2), 169–183.

[8] Cahn, B. R.; and Polich, J. (2006). Meditation states and traits: EEG, ERP, and neuroimaging studies. *Psychological bulletin*, 132(2), 180–211.

[9] Lomas, T.; Ivtzan, I.; and Fu, C. H. Y. (2015). A systematic review of the neurophysiology of mindfulness on EEG oscillations. *Neuroscience and Biobehavioral Reviews*, 57, 401–410.

[10] Hinterberger, T.; Kamei, T.; and Walach, H. (2011). Psychophysiological classifi cation and staging of mental states during meditative practice, 341–350.

[11] Aspiras, T. H.; and Asari, V. K. (2011). Log power representation of EEG spectral bands for the recognition of emotional states of mind. In *Information, Communications and Signal Processing (ICICS) 2011 8th International Conference*. Singapore, 1-5.

[12] Rafiee, J.; Rafiee, M. A.; Prause, N.; and Schoen, M. P. (2011). Wavelet basis functions in biomedical signal processing. *Expert Systems with Applications*, 38(5), 6190–6201.

[13] Tarantino, V.; Bisiacchi, P.; and Sparacino, G. (2009). A wavelet Methodology for EEG Time-frequency Analysis in a Time Discrimination Task. *International Journal of Bioelectromagnetism*, 11(4), 185–188.

[14] Procházka, A.; Kukal, J.; and Vyšata, O. (2008). Wavelet transform use for feature extraction and EEG signal segments classification. *2008 3rd International Symposium on Communications, Control, and Signal Processing, ISCCSP 2008*, 719–722.

[15] Rosso, O. A.; Martin, M. T.; Figliola, A.; Keller, K.; and Plastino, A. (2006). EEG analysis using wavelet-based information tools. *Journal of Neuroscience Methods*, 153(2), 163–182.

[16] Ungless, G. (2014). The Activewave User Guide. Cambridgeshire, UK: CamNTech Ltd.

[17] Stibal, V. (2007). *Abundance Meditation* (CD). Idaho Falls, Idaho: Theta Healing Institute of Knowledge.

[18] Stibal, V. (2013). *Theta Healing (TM)* (6th Ed.). Carlsbad, California: Hay House, Inc.

[19] Wong, W. P.; Camfield, D. A.; Woods, W.; Sarris, J.; and Pipingas, A. (2015). Spectral power and functional connectivity changes during mindfulness meditation with eyes open: A magnetoencephalography (MEG) study in long-term meditators. *International Journal of Psychophysiology*, 98(1), 95–111.

[20] Cahn, B. R.; Delorme, A.; and Polich, J. (2010). Occipital gamma activation during Vipassana meditation. *Cognitive Processing*, 11(1), 39–56.

[21] Chen, D.; Wan, S.; Xiang, J.; and Bao, F. S. (2017). A high-performance seizure detection algorithm based on Discrete Wavelet Transform (DWT) and EEG. *PLoS ONE*, 12(3), 1–21.

EURECA 2018 – Conference Paper
Paper number PG06

Impulsive Force Calibration of a Torsional Thrust Stand using Electrostatic Technique

Lam Jiang Kai[1], Koay Seong Chun[1], Cheah Kean How[2]*

[1]School of Engineering, Taylor's University, Malaysia

[2]School of Engineering and Physical Science, Heriot-Watt University Malaysia

[*]jiangkai21@gmail.com

Abstract

The evaluation of micropropulsion system is a critical process. For this, thrust stands are widely known as an effective method to complete such task. As part of a development in establishing a thrust stand with enhanced measuring capability, this work presents the calibration of a torsional thrust stand for impulsive force using electrostatic calibration technique. Utilising commercially made heat sinks, the calibration system is able to generate repeatable and consistent calibration forces at over three orders of magnitude (10 – 5270 μN). High voltage pulses were also applied to the system, generating calibration impulse bits of 1.3 – 52 μNs. These calibration forces are then used to calibrate the torsional thrust stand for resolving impulsive force produced from any micropropulsion system.

Keywords: Micronewton, Thrust stand, Microthruster, Electrostatic calibration.

1. **Introduction**

Development of nanosatellites (< 10 kg) continues to be highly participated as they are simpler and more cost effective, yet equally functional in space applications [1]. In nanosatellites, microthrusters are used as part of their micropropulsion system responsible for crucial tasks like attitude control, station keeping, drag compensation, and orbital transfer [2]. As such, it is necessary to evaluate the performance of a microthruster accurately.

Forces produced by microthrusters are extremely low (in the order of micronewton). Hence, resolving them requires high-sensitivity measuring instruments. Pendulum thrust stands are widely recognised as an effective instrument for measuring such forces [3]. They are essentially a spring-mass-damper system, whereby a structure holding the microthruster is supported by a torsional spring. The structure oscillates as forces are applied. By analysing the oscillation, the forces produced by microthrusters can be measured. There are three main configurations for pendulum thrust stand, i.e. hanging [4], [5], inverted [6], [7], and torsional [8]–[10], each with their own advantages and limitations [3], [4].

In any case, calibration of thrust stands is necessary. It establishes the relationship between the thrust stand response in terms of displacement and the forces applied. Generally, calibration techniques can be categorised into contact and non-contact. Contact techniques include string-pulley-weight system [4], impact hammer [11], and impact pendulum [12]. These are among the earliest methods used for calibration. Although they are easy to setup, the calibration force produced is comparatively larger than non-contact techniques [13], which is in the order of sub-micronewton and above. In addition, the contact nature of these techniques tends to induce zero drift on the thrust stand.

Non-contact techniques include gas dynamic [13], [14], electrostatic (ES) [11], [15]–[17], and electromagnetic (EM) [9], [18], [19]. Gas dynamic calibrators are reliable in producing calibration forces between nanonewton and sub-micronewton [14]. In contrast, ES calibrators are capable of wider range of calibration forces, typically between hundreds of nanonewton and thousands of micronewton [17]. For EM calibrators, calibration forces are reported at sub-micronewton and above. Both ES and EM also exhibit good consistency and repeatability. However, past survey has shown that ES is more established as a calibration technique compared to EM which is relatively new and requires further research.

As evidenced by the expansion in design configurations and calibration techniques, thrust stand development has been carried out extensively within the past few decades. However, past thrust stands were mostly developed for their specific microthrusters. A single thrust stand with enhanced force measuring range is much needed as it can accommodate the testing of multiple types of micropropulsion systems, hence shortening both time and cost of development. As such, this study aims to calibrate a torsional thrust stand for wider range of impulsive force applications. A pair of aluminium heat sinks is implemented as the ES calibrator in order to produce the range of calibration force needed.

2. **Research Methodology**

2.1 Torsional Thrust Stand Setup

A thrust stand based on torsional pendulum is designed and built. Generally, torsional thrust stand has good balance of high measuring and low vibrational noise sensitivities. The existing thrust stand consists of a 60 cm torsional arm made of U-shaped aluminium beam. It is light weight (210 g) yet mechanically stiff enough to support external loadings (e.g. microthruster). The overall dimension is designed as such in order to ensure its fitment into a facility-provided vacuum chamber, which is expected to be done later in the development. The torsional arm was supported by a single-ended flexural pivot (F-20, C-Flex) that acts as torsional spring. The pivot was clamped and connected to a heavy rectangular aluminium base (3 kg). Four anti-vibration mounts (126-3904, RS Pro) were installed underneath each corner of the base for stability enhancement against external vibration. A strong permanent magnet was placed in close proximity under the torsional arm to induce an eddy current brake in order to dampen the oscillation of the arm. A high resolution (0.5 μm) laser displacement sensor (HL-G103-S-J, Panasonic) was positioned at one end of the torsional arm to measure its deflection. The ES calibrator was installed at the other end of the arm. A transparent acrylic casing was used to enclose the entire assembly in order to minimise the effect of ambient disturbance on the thrust stand response. The actual setup is as shown in Figure 1.

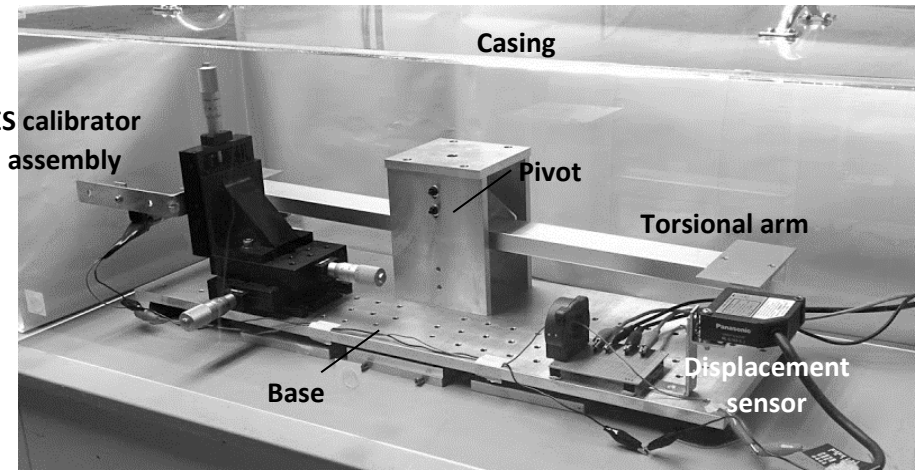


Figure 1. Actual torsional thrust stand setup.

2.2 Electrostatic Calibration System

The calibration process involves installing a calibrator onto the thrust stand, where the calibrator applies an accurately known force or impulse to the torsional arm. The displacement of the arm due to the applied forces is then recorded using the displacement sensor.

Commercially made aluminium heat sinks of various dimensions are widely available on the market at low costs nowadays. Their design characteristics e.g. multiple fins are also suitable for generating a wide range of ES forces, while remaining compact-sized, which is crucial when in use inside the vacuum chamber. As such, in this study, a pair of heat sinks is engaged and used as the ES calibrator, as shown in Figure 2. ES calibration forces are generated when high voltage passes through the engaged heat sinks (two conductive bodies). There are

various parameters of heat sink that affect the generation of ES force, as governed by Equation 1 [15]:

$$F = 2N\varepsilon V^2\left[a - \frac{b}{V}\left(\frac{c+g}{\pi x_0}\right)\right], \quad (1)$$

where F is the electrostatic force generated, N
N is the number of fin pairs,
$\mathcal{E}$ is the permittivity of air in farad per meter, F/m
V is the applied voltage, V
Coefficients a and b are experimentally determined constants,
For c, g and x_0, they are measured in distance, m, as illustrated in Figure 2.

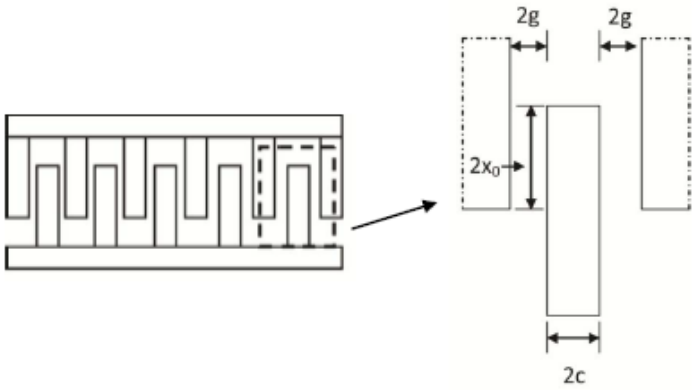


Figure 2. Schematic of engaged heat sink fins. 2c is width of individual fin, 2g is gap between successive fins, and 2x_0 is engagement between fins [15].

Based on the equation, the generation of ES force is more dependent on number of fins N and voltage applied V; whereas c, g, and x_0 are not as critical because the amount of V is typically much higher than them (1/V). Hence, three heat sink pairs, each with different number of fins were procured:

1. 13x11 (total number of fins per heat sink: 143)
2. 7x8 (total number of fins per heat sink: 56)
3. 6x7 (total number of fins per heat sink: 42)

**Note that 13x11 etc. denote the number of fins along the sides of heat sink.*

Each pair is tested with various voltage levels in order to determine the amount of ES force able to be generated. Although not as critical, tests were also conducted to determine the valid range of engagement distance for generating consistent and reproducible force. This serves as a general guideline when installing the calibrator onto the thrust stand.

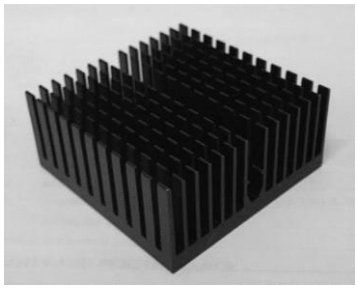


Figure 3. The 13x11 heat sink.

2.2.1 Experimental Setup

To accurately measure the amount and range of calibration forces that the heat sinks can generate, each pair of identical heat sinks is engaged at a distance (5 mm) and various voltage levels (100 to 900 V) are applied across the heat sinks. A high voltage pulser (E-462, Physik Instrumente) is used to provide the needed voltage levels, paired with a function generator (8202, Dagatron) to obtain pulsed signal for generating impulsive force. A high resolution weighing balance (HR250AZ, A&D Weighing) is used to measure the force generated. It has a resolution of 0.1 mg (0.1 mg = 0.981 μN). One of the heat sinks is placed on top of the weighing balance; whereas the other is placed externally and its position can be adjusted using a mechanical stage (PT3/M, Thorlabs). Figure 4 shows the setup. Consequently, a force-voltage graph for each pair of heat sinks tested is produced.

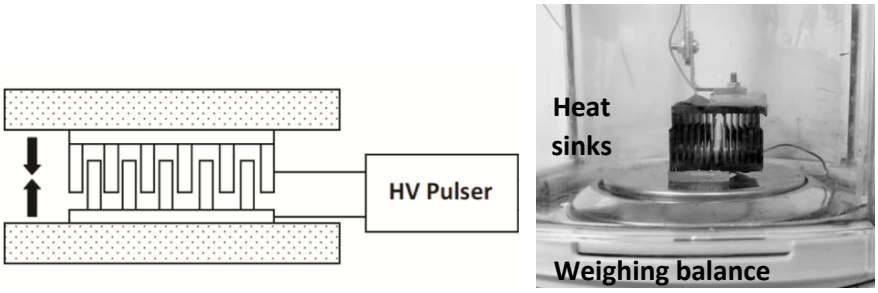


Figure 4. Schematic (left) and actual (right) experimental setup.

To determine the valid engagement distance range of each heat sinks pair, the setup remained the same. The only difference is that the voltage is fixed at 700 V, while the engagement distance between the heat sinks is varied (2 to 16 mm). As a result, a force-distance graph is produced.

2.2.2 Implementation onto Thrust Stand

After the tests, heat sinks pair that achieved the targeted force range with good consistency is installed to the thrust stand for calibration, as shown in Figure 5. One of the heat sink (ground) is fixed to the other end of the torsional arm as opposed to the end with the laser displacement sensor (LDS). The other heat sink (positive) is placed externally and its positioning and engagement are adjusted using the mechanical stage. The measured calibration forces are then applied to the torsional arm, and the corresponding deflections are recorded using the LDS.

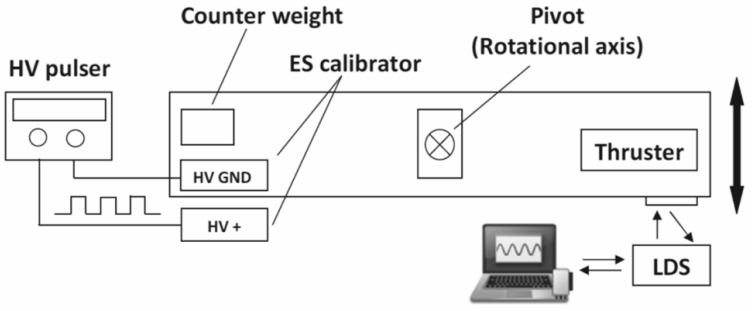


Figure 5. Schematic of ES calibrator installed onto the thrust stand (top view).

3. Results and Discussion

3.1 Electrostatic Force Measurement

Figure 6 shows the ES forces generated by each heat sink pairs at varying voltage levels. As expected, higher number of fins generates higher magnitude of forces. Such a trend is as dictated in Equation 1, where number of fins is directly proportional to ES force generated.

It is noted that ES force generated increases as voltage applied is higher, which is also expected based on Equation 1. Their relationship exhibits good polynomial fit (R-squared values close to 1), which indicates that the forces generated is predictable and reliable.

Based on the results, the use of 7x8 heat sink pair is omitted as its range of forces generated can be covered with the combined use of 6x7 and 13x11 heat sink pairs. This combination provides a range of ES forces that covers up to three orders of magnitude, i.e. 10 – 1130 μN and 140 – 5270 μN, for 6x7 and 13x11 heat sinks, respectively.

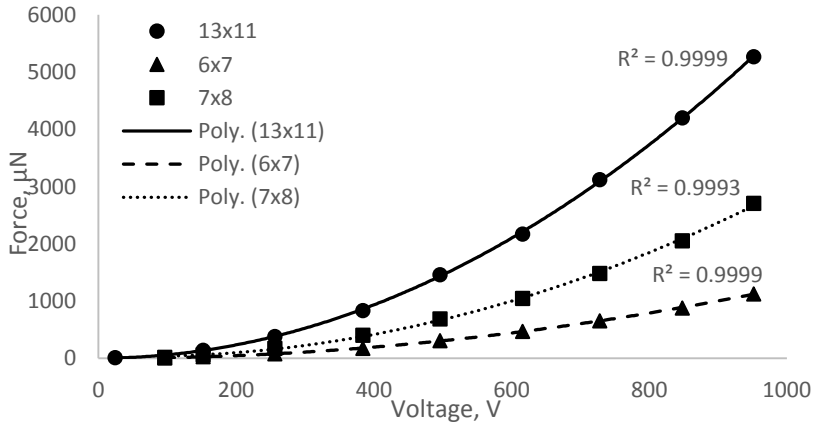


Figure 6. Electrostatic force generated by heat sinks of different dimensions at various voltages.

Figure 7 shows the change in ES force with the engagement distance for both 6x7 and 13x11 heat sink pairs. For the 6x7 heat sink, the ES force generated remains relatively constant and begins to deviate at 9 mm of engagement distance. As for the 13x11 heat sink, the force generated begins to deviate at 7 mm of engagement distance. The 6x7 heat sink has a longer engagement range because of its longer fin length compared to the 13x11 heat sink. As for the

deviation in both cases, investigation revealed that it is due to the tip of the fin getting closer to the base of the opposite heat sink, where surface area increases significantly, causing increased ES interactions.

These results serve as a guide for installing the ES calibrator onto the thrust stand. Based on the results, in order to maintain good repeatability and consistency, the engagement distance is to be kept at 2 – 7 mm, which is plenty and relatively easy to be setup.

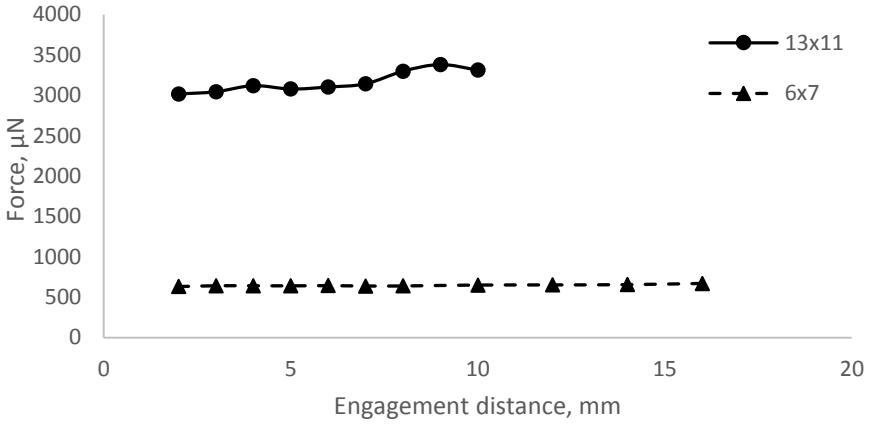


Figure 7. Electrostatic force generated by 13x11 and 6x7 heat sinks corresponding to various engagement distances at 700 V.

3.2 Calibration for Impulsive Force

Calibration for impulsive force was done by applying various impulse bits to the thrust stand. To produce impulse bits, the ES calibrator was connected to the function generator with squared input signals. By adjusting the signal amplitude (amount of voltage) and the pulse time, different levels of calibration impulse bit can be produced.

In order to obtain a linear relationship between thrust stand response and calibration impulse bit applied, the pulse time should be within one-tenth of the natural period of the thrust stand, $1/f_{nat}$ [20]. The natural period, f_{nat} of existing thrust stand was determined to be 1.8 Hz. This implies that the pulse time should not exceed 55 ms to ensure linearity between thrust stand response and calibration impulse bit.

An example of the squared signal is shown in Figure 8, where the pulse width is 46 ms and the output signal amplitude is 700 V. This translates into a calibration impulse bit of 30.2 µNs for 6x7 heat sink and 143.5 µNs for 13x11 heat sink ES calibrator.

It is observed that the output signal has some irregularities such as slightly mismatched rise and fall time of the pulse, and slight overshoot after voltage amplification. They are identified as a limitation due to the equipment used such as the pulser and the signal probe, which in theory may cause some impacts to the calibration results. However, the actual differences are expected to be minute.

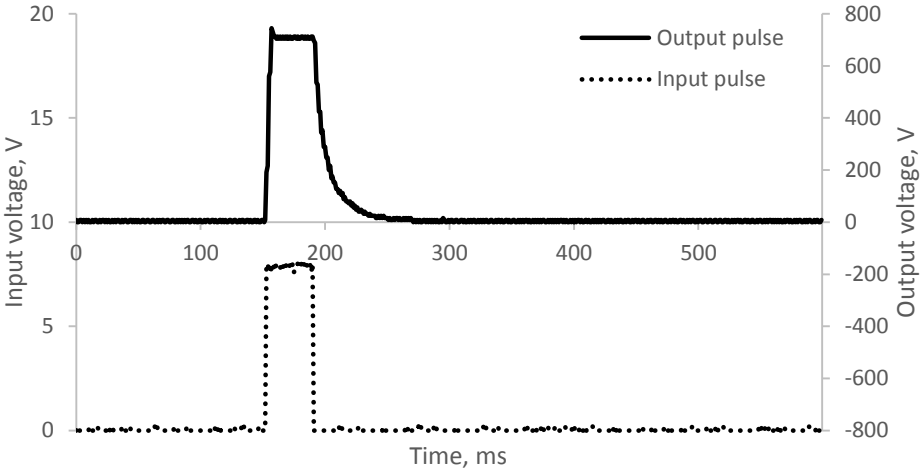


Figure 8. Squared input signal of 46 ms pulse width and its corresponding high voltage output signal.

Nevertheless, impulse bits of 1.3 – 52 µNs were applied to the thrust stand using the 6x7 heat sink ES calibrator. The corresponding response (maximum deflection range) is then recorded using the displacement sensor. Figure 9 shows a typical thrust stand response to a calibration impulse bit of 30.2 µNs. The same impulse bit was repeated within a duration of 14 s. It can be observed that the maximum deflection range obtained (24.2 µm in this case) is consistent. This shows that the control of the pulses is precise. The oscillation pattern is also as expected with no zero drift present, indicating the thrust stand is responding well with the impulse bit applied and the system is stable.

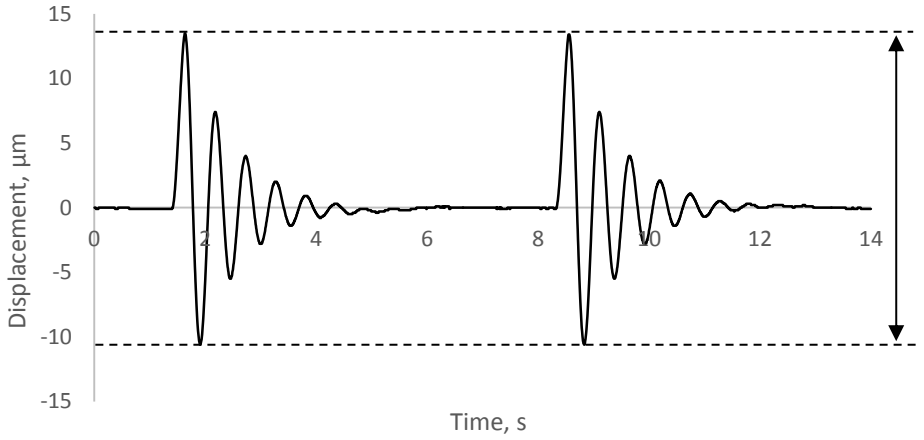


Figure 9. Thrust stand response to impulse bit produced at 700 V and 46 ms pulse width using 6x7 heat sinks. Pointing arrows indicate the maximum deflection range.

Each maximum deflection range corresponding to the applied impulse bit is plotted to produce the calibration curve for impulsive force measurement, as shown in Figure 10. The curve has shown good linearity. With the use of the 13x11 heat sinks, the range of impulse bits can be further extended. As such, more effort is underway. After the calibration, the thrust stand can then be used to measure impulsive forces from pulsed mode micropropulsion systems.

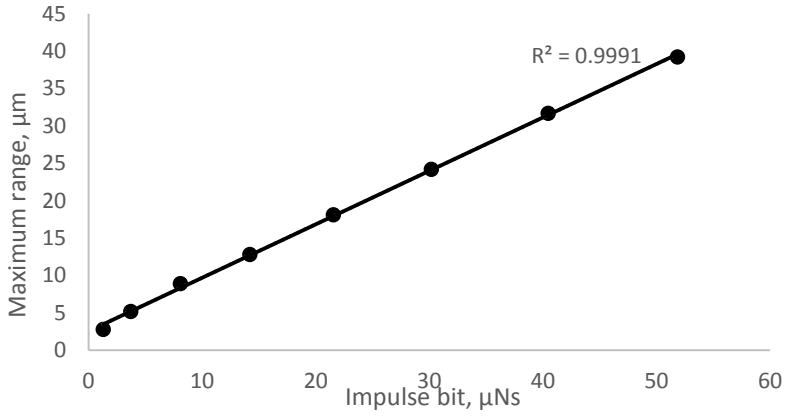


Figure 10. Calibration curve for impulsive force measurement.

4. **Conclusion**

As a conclusion, the existing thrust stand is calibrated for impulsive force applications using the current heat sinks ES calibrator setup. The thrust stand is calibrated to resolve impulsive force in the range of 1.3 – 52 µNs. Furthermore, it is expected that the range can be further extended with the use of bigger heat sinks, so that the force measuring range of the thrust stand is enhanced. Nonetheless, more studies (e.g. the high voltage output pulsed signal generation) need to be done. An error budget needs to be develop as well in order to characterise the performance of the ES calibrator and the thrust stand.

References

[1] W. Shiroma, L. Martin, J. Akagi, J. Akagi, B. Wolfe, B. Fewell, and A. Ohta, "CubeSats: A bright future for nanosatellites," *Cent. Eur. J. Eng.*, vol. 1, no. 1, 2011.

[2] K. H. Cheah and K.-S. Low, "Fabrication and performance evaluation of a high temperature co-fired ceramic vaporizing liquid microthruster," *J. Micromechanics Microengineering*, vol. 25, 2015.

[3] J. E. Polk, A. Pancotti, T. Haag, S. King, M. Walker, J. Blakely, and J. Ziemer, "Recommended Practice for Thrust Measurement in Electric Propulsion Testing," *J. Propuls. Power*, vol. 33, no. 3, pp. 539–555, 2017.

[4] K. A. Polzin, T. E. Markusic, B. J. Stanojev, A. Dehoyos, and B. Spaun, "Thrust stand for electric propulsion performance evaluation," *Rev. Sci. Instrum.*, vol. 77, no. 105108, 2006.

[5] T. Moeller and K. A. Polzin, "Thrust stand for vertically oriented electric propulsion performance evaluation," *Rev. Sci. Instrum.*, vol. 81, no. 11, 2010.

[6] K. G. Xu and M. L. R. Walker, "High-power , null-type , inverted pendulum thrust stand," *Rev. Sci. Instrum.*, vol. 80, no. 55103, 2009.

[7] D. T. Jacobson and D. H. Manzella, "50 KW CLASS KRYPTON HALL THRUSTER PERFORMANCE," in *39th AIAA/ASME/SAE/ASEE Joint Propulsion Conference and Exhibit*, 2003.

[8] H. White, P. March, J. Lawrence, J. Vera, A. Sylvester, D. Brady, and P. Bailey, "Measurement of Impulsive Thrust from a Closed Radio-Frequency Cavity in Vacuum,"

J. Propuls. Power, 2016.

[9] G. Hathaway, "Sub-micro-Newton resolution thrust balance," *Rev. Sci. Instrum.*, vol. 86, no. 105116, 2015.

[10] J. Lun and C. Law, "Direct thrust measurement stand with improved operation and force calibration technique for performance testing of pulsed micro-thrusters," *Meas. Sci. Technol.*, vol. 25, 2014.

[11] A. P. Pancotti, M. Gilpin, and M. S. Hilario, "Comparison of electrostatic fins with piezoelectric impact hammer techniques to extend impulse calibration range of a torsional thrust stand," *Rev. Sci. Instrum.*, vol. 83, no. 35109, 2012.

[12] H. Koizumi, K. Komurasaki, and Y. Arakawa, "Development of thrust stand for low impulse measurement from microthrusters," *Rev. Sci. Instrum.*, vol. 75, no. 3185, 2004.

[13] N. P. Selden and A. D. Ketsdever, "Comparison of force balance calibration techniques for the nano-Newton range," *Rev. Sci. Instrum.*, vol. 74, no. 5249, 2003.

[14] A. J. Jamison, A. D. Ketsdever, and E. P. Muntz, "Gas Dynamic Calibration of a Nano-Newton Thrust Stand," *Rev. Sci. Instrum.*, vol. 73, no. 10, pp. 3629–3637, 2002.

[15] K. H. Cheah, K. S. Low, Q. V. Tran, and Z. Lau, "Development of an Electrostatic Calibration System for a Torsional Micronewton Thrust Stand," *IEEE Trans. Instrum. Meas.*, vol. 64, no. 12, pp. 3467–3475, 2015.

[16] A. H. Yan, B. C. Appel, and J. G. Gedrimas, "MilliNewton Thrust Stand Calibration Using Electrostatic Fins," in *47th AIAA Aerospace Sciences Meeting*, 2009.

[17] S. Chen and S. Pan, "A force measurement system based on an electrostatic sensing and actuating technique for calibrating force in a micronewton range with a resolution of nanonewton scale," *Meas. Sci. Technol.*, vol. 22, no. 45104, 2011.

[18] H. Tang, C. Shi, X. Zhang, Z. Zhang, and J. Cheng, "Pulsed thrust measurements using electromagnetic calibration techniques," *Rev. Sci. Instrum.*, vol. 82, no. 35118, 2011.

[19] Z. He, J. Wu, D. Zhang, G. Lu, Z. Liu, and R. Zhang, "Precision electromagnetic calibration technique for micro-Newton thrust stands," *Rev. Sci. Instrum.*, vol. 84, no. 55107, 2013.

[20] B. C. D. Souza and A. D. Ketsdever, "Investigation of time-dependent forces on a nano-Newton-second impulse balance," *Rev. Sci. Instrum.*, vol. 76, no. 15105, 2005.

EURECA 2018 – Conference Paper
Paper number PG07

Experimental And Theoretical Investigation On Displacer Topology Of A Low Temperature Gamma -Type Stirling Engine

Kun Yong Ng, Edwin C. Y. Chung, Satesh N. Namasivayam, Douglas K. T. Tong*

School of Engineering, Taylor's University, Taylor's Lakeside Campus, No. 1 Jalan Taylor's, 47500, Subang Jaya, Selangor DE, Malaysia
*Corresponding Author: ChinYau.EdwinChung@taylors.edu.my

Abstract

Stirling engine is an engine that convert heat energy to mechanical motion from the expansion and compression of fluid. Among the three types of Stirling engine, the Gamma type is the most suitable for low temperature heat source. However, low temperature heat source generates lower output power according Carnot cycle. To improve its performance, displacer topology is modified to optimizes the thermodynamic flow of working fluid in the Stirling engine. This paper discusses the effect of five displacer designs on the performance of a Gamma type Stirling engine. The preheating temperature for the engine is 100ºC with an initial filling pressure of 1 bar at various operating speed are investigated. The experimental results are compared with theoretical thermodynamic equations and Schmidt theory. The results showed that the Stirling engine prototype generated a maximum shaft power of 63.3 W at an operating speed of 472 rpm with work done at 10.72 J per cycle. It is possible to increase the engine shaft power by 47.4 W through reducing the dead volume by 2.8 dm^3. The concave shape displacer has an increase of 15.9% shaft power compared to the flat shape displacer. Based on the experimental results, placing the concave shape of the displacer toward the heat source would increase the shaft power by 5.2% compared to placing the concave shape at the other side of displacer.

Keywords: Stirling Engine, Displacer topology, low temperature

1. Introduction

Stirling engine convert heat energy and generates mechanical energy from the expansion and compression of the working fluid. Unlike internal combustion engines, it only operates with the fossil fuel. Stirling engines can be operated by any type of heat source such as biomass, solar geothermal etc. It is a closed system that produces no waste or any harmful gases from the energy sources.

Stirling engines are typically used for waste heat recover systems because it unable to generate a high output power instantly unlike the internal combustion engine. By using Stirling engines to recover heat from the flue gas of a power plant, a 30% savings in fuel consumption was suggested from the simulation with TRNSYS and GenOpt [1]. Gamma type Stirling engine has been found that to have the highest efficiency in terms of recovering waste heat [2].

Glossary

A	Amplitude, m
c_v	Specific heat at constant volume, J/kg K
c_p	Specific heat at constant pressure, J/kg K
C_r	Compression ratio, Vmax/Vmin
D_d	Diameter of the displacer, m
D_p	Diameter of the piston, m
D_{dl}	Diameter of the displacer length, m
m	Mass of working fluid, kg
$\dot{m}_C$	Mass flow rate of compression, kg/rad
$\dot{m}_D$	Mass flow rate of dead volume, kg/rad
$\dot{m}_E$	Mass flow rate of expansion, kg/rad
P	Pressure, Pa
R	Gas constant, $Jmol^{-1}K^{-1}$
S	Engine Power Stroke, m
S_{ca}	Spherical cap angle, °
S_{ch}	Spherical cap height, m
T_D	Temperature of the working fluid in the dead volume, K
T_H	Temperature of the working fluid in the hot component, K
T_L	Temperature of the working fluid in the cold component, K

T_R	Temperature of the working fluid in the regenerator, K
V_C	Volume of the compression, m^3
V_D	Volume of the total dead volume, m^3
V_{DC}	Volume of the compression dead volume, m^3
V_{DE}	Volume of the expansion dead volume, m^3
V_E	Volume of the expansion, m^3
V_{max}	Maximum volume of the working fluid, m^3
V_{min}	Minimum volume of the working fluid, m^3
V_R	Volume of the regenerator, m^3
V_{SC}	Piston swept volume, m^3
V_{SE}	Displacer swept volume, m^3
W_{ideal}	Work done based on ideal adiabatic equations, J
W_{sch}	Work done based on ideal Schmidt analysis, J
α	Phase angle, °
κ	Isentropic expansion factor, (Cp/Cv)
κ_a	Isentropic expansion factor of atmospheric air
κ_{H_2}	Isentropic expansion factor of hydrogen
κ_{He}	Isentropic expansion factor of helium
π	Mathematical constant, 3.14159
θ	Crank angle, °
$\emptyset$	Diameter, m
v_p	Velocity of piston, m/s
ω	Angular velocity, rad/s

The performance of Stirling engines is based on the temperature gradient between the hot side cylinder and the cold side cylinder. The higher the temperature differences, the higher output power according to the Carnot theorem. It also has higher thermal efficiencies than Rankine cycle based systems [3]. High temperature difference Stirling engines have higher output power, but the cost of the materials is high as it needs to withstand the high temperatures and pressures. This research focuses on low temperature difference Stirling engine (LTDSE) as most waste heat from daily appliances are in the low temperature range.

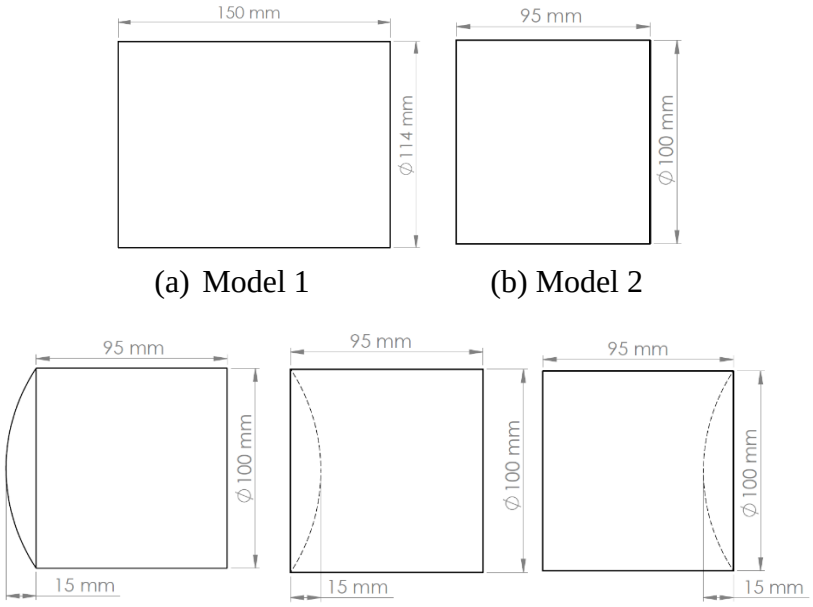
The displacer is a piston located on the hot side cylinder of gamma type Stirling engine. It is the first component of Stirling engine that separates the high temperature working fluid to the low temperature working fluid inside the system. Another component is the connector in between the hot side and cold side cylinder, which is usually integrated with a regenerator. This regenerator is used to absorb heat from the working fluid as it traverses from the high to the low temperature regions and to preheat it as it traverses in the opposite direction. It helps to maintain the temperature difference of both sides while the engine is operating and this indirectly reduces the dead volume of the system as this dead volume has a negative impact on the power output from the system [4]–[7].

A regenerator that integrates into displacer is called moving regenerator where it moves together with the displacer [8]. For moving regenerators, using low porosity wire mesh is suitable for high-speed Stirling engine whereas regenerators with high porosity wire mesh is suitable for low-speed Stirling engine [9]. The displacer gap in between the cylinder and the displacer influences the flow and the heat transfer of working fluid. These energy losses are influenced by the enthalpy pumping (leakage flow between both sides) and the shuttle heat transfer (displacer) motion between the hot part and cold part. The suggested minimum displacer gap is between 50 microns and 70 microns with the speed between 25 Hz and 35 Hz [10]. This displacer gap is normally in between 0.6 mm to 1 mm [11]–[14].

Another type of displacer design for Stirling engine has no mechanical connection to the power piston [15]–[19]. This was invented by William Beale in 1964 and is named as the Free Piston Stirling engine (FPSE). It has minimum mechanical losses as compare to crankshaft driven Stirling engine. The piston of FPSE is connected to a spring and a linear alternator to generator electricity.

Based on the above review, the output power of Stirling engine is improved by changing the shape and the configuration of the displacer. However, the displacer top and bottom shapes are yet to be explored. Hence, this research intends to study the impact of the spherical displacer top and the displacer bottom.

The objective of this study is to determine the impact of displacer topology to the output power of LTD gamma type Stirling engine. 5 variations in displacer topology are investigated as shown in Fig. 1. Model 1 and model 2 are designed to understand the impact of changing the displacer length and diameter. The model 1 has the diameter clearance gap of 3 mm to the hot component cylinder whereas model 2 has diameter clearance gap of 10 mm to the hot component cylinder. Model 2 to model 4 are designed to investigate the impact of changing the shape of the displacer top. Model 2 and model 5 are designed to learn the influence of changing the shape of the displacer bottom. To integrate spherical cap design that has a spherical cap height of 0.015 m into the displacer, the displacer length of model 2 to model 5 is set to be 0.095 m. The models are: (a) Flat-flat (Ø 0.114 m), (b) flat-flat (Ø 0.1 m), (c) Convex-flat, (d) Concave-flat, and (e) flat-concave as shown in Fig. 1.



(a) Model 1 (b) Model 2

(c) Model 3 (d) Model 4 (e) Model 5

Fig. 1. Investigated topology of displacer (Geometry and dimensions).

2. Stirling engine test rig characteristics

A gamma type Stirling engine prototype was built for this study as shown in Table 1. The displacer and power piston are connected to crankshaft with a 90° phase angle difference. On the hot side, the cylinder is heated by a Bunsen burner as the heat source for the system. All parts are made of aluminium except the linear bearing rod which was made of carbon steel. The detail design of 5 various model are provided in Table 2.

Table 1. Characteristic of the gamma Type Stirling engine

Engine Specifications	Value
Power stroke	0.09 m
Inner diameter of the hot component cylinder	0.12 m
Inner diameter of the cold component cylinder	0.09 m
Inner diameter of the connecting tube	0.01 m
Length of the hot component cylinder	0.25 m
Length of the connecting tube	0.03 m
Compression ratio	1.26 m
Working fluid	air
P	101325 Pa

T_H	100 ºC
T_L	24 ºC

Table 2. Displacer model specifications

	Model 1	Model 2	Model 3	Model 4	Model 5
Topology	Flat-flat	Flat-flat	Convex-flat	Concave-flat	Flat-concave
D_d (m)	0.114	0.100	0.100	0.100	0.100
D_{dl} (m)	0.150	0.095	0.095	0.095	0.095
S_{ca} (°)	0	0	33.4	-33.4	-33.4
S_{ch} (m)	0	0	0.015	-0.015	-0.015
V_D (dm^3)	1.175	3.982	3.921	4.043	4.043

3. Instrumentation

The speed of the flywheel is measured by Tachometer. The working fluid temperature was measured using micro thermocouple by placing it inside the Stirling engine and connecting it to a Multimeter. An electrical engine is used to control the Stirling engine operating speed for various speed testing in a range from 170 rpm to 470 rpm [20]. The power consumption of the electrical engine is measured by a power meter. The operating speed of the electrical engine is controlled using a variable ac supply at the range from 70 V to 100 V with interval of 10 V for each model.

Each experiment was subjected to a fifteen to twenty minutes preheating stage to ensure that the working fluid had reached the desired operating temperature before applying a twelve minutes Stirling engine run time. The Power Meter, Tachometer and Multimeter readings were recorded when the temperature of working the fluid has reached the desired temperature. Seven readings were recorded from each experiment during the twelve minutes run time with each case being repeated twice.

4. Mathematical modelling

An ideal adiabatic equation for Stirling engine is derived based on the Ideal gas law, the Second Law of Thermodynamics, the isothermal equations of Stirling engine and the Carnot theorem. The equation is given below.

$$W_{ideal} = - m c_v (T_H - T_L) (\kappa - 1) \ln\left(\frac{V_{max}}{V_{min}}\right) \quad (1)$$

Note that there are 5 parameters that directly influence the output power of the system. These 5 parameters are the mass of working fluid, m, specific heat capacity at constant volume, c_v, temperature differences, isentropic parts and the volumetric ratio of the engine. Hence, this

explains that the work done is increased when the initial pressure is increased as the mass of the working fluid is increased. The heat capacity can be increased by integrating the regenerator to the system. Temperature differences depend on the heat source temperature. The higher temperature of heat source, the higher will be the temperature difference, and hence the higher the work done by the system. Volumetric ratio depends on power stroke and dead volume of Stirling engine. The higher the volumetric ratio, the higher the work done by the system. The volumetric ratio is increased by increasing power stroke and reducing dead volume of Stirling engine. Helium as a working fluid performs better than atmospheric air and hydrogen as $\kappa_{He} = 1.630$ for helium gas whereas $\kappa_a = 1.402$ and $\kappa_{H_2} = 1.410$ for atmospheric air and hydrogen respectively.

In this study, the Schmidt analysis was used to study mass balance of working fluid in the system. The assumptions made for this study's gamma type Stirling engine mathematical model are as follow:

1. The working fluid in the system is an ideal gas
2. The working fluid is ideal homogeneous mixed in each working fluid volume.
3. The heat exchange of isothermal compression and isothermal expansion are assumed ideal heat exchange.
4. The system has perfect regeneration where no heat losses in the regenerator. The temperature profile of regenerator is linear and constant.
5. No leakage of working fluid.
6. The engine works in constant operation speed with a sinusoidal motion.
7. Pressure drop in between hot and cold component is not considered.

The working fluid volume in the Stirling engine is divided into five parts, V_E, V_{DE}, V_R, V_C, V_{DC} as shown in Fig. 2.

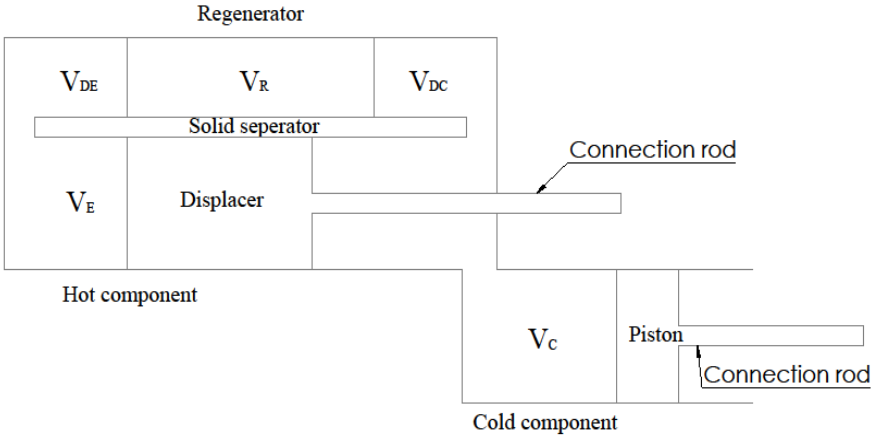


Fig. 2. Simplified γ type Stirling engine

The working fluid volume in the hot part and the working fluid volume in the cold parts is stated in below,

$$V_E = \frac{V_{SE}}{2}\,[1 - \cos(\theta)] \tag{2}$$

$$V_C = \frac{V_{SE}}{2}\,[1 + \cos(\theta)] + \frac{V_{SC}}{2}\,[1 - \cos(\theta - \alpha)] \tag{3}$$

Since the Stirling engine prototype is a γ type Stirling engine, the phase angle, α is equal to 90° and θ is the crank angle. The maximum volume is when θ is 270° whereas the minimum volume is when θ is 90°. V_{SE} and V_{SC} represent the expansion and compression swept volume respectively. The dead volume represents the clearance volume in the expansion and compression space and this includes the connection in between hot and cold components. The total dead volume in the system is hence written as follows.

$$V_D = V_{DE} + V_R + V_{DC} \tag{4}$$

The temperature in the hot and the cold component are T_H and T_L respectively. The temperature of the regenerator is in between the temperature gradient of the hot and cold component. The temperature of regenerator, T_R and the temperature of total dead volume, T_D are defined in following equations,

$$T_R = (T_H - T_L)\left[\ln\left(\frac{T_H}{T_L}\right)\right]^{-1} \tag{5}$$

$$T_D = (V_{DE} + V_R + V_{DC})\left[\left(\frac{V_{DE}}{T_H} + \frac{V_R}{T_R} + \frac{V_{DC}}{T_L}\right)\right]^{-1} \tag{6}$$

The total mass of working fluid is the sum of the expansion, compression and the dead volume working fluid mass as shown in below.

$$m = \frac{P}{R}\left(\frac{V_E}{T_H} + \frac{V_D}{T_D} + \frac{V_C}{T_L}\right) \tag{7}$$

The total mass of working fluid in the system is redefined by substituting the Eq. (2) and Eq. (3) into Eq. (7) as shown in below.

$$m = \frac{PV_{SE}}{2RT_L}\left\{K_1 - \left[\left(\frac{T_L}{T_H} - 1\right)\cos(\theta) + \frac{V_{SC}}{V_{SE}}\cos(\theta - \alpha)\right]\right\} \tag{8}$$

$$K_1 = \frac{T_L}{T_H} + \frac{2V_D}{V_{SE}}\frac{T_L}{T_D} + 1 + \frac{V_{SC}}{V_{SE}} \tag{9}$$

Eq. (8) is the general equation used to calculate the total mass of working fluid. The specific total mass of working fluid can be calculated by substituting instantaneous crank angle and phase angle. The pressure-volume diagram of the system is plotted based on equations below. Rearranging Eq. (8) with trigonometry identity rule, the pressure of the system is defined as follows.

$$P = 2\,mR\,T_L\left\{V_{SE}\,K_1\left[1 - \frac{C_1}{K_1}\cos(\theta - \beta)\right]\right\}^{-1} \tag{10}$$

$$C_1 = \sqrt{\left[\left(\frac{T_L}{T_H} - 1\right) + \left(\frac{V_{SC}}{V_{SE}}\right)\cos(\alpha)\right]^2 + \left(\frac{V_{SC}}{V_{SE}}\sin(\alpha)\right)^2} \tag{11}$$

$$\beta = \tan^{-1}\left\{\left(\frac{V_{SC}}{V_{SE}}\sin(\alpha)\right)\left[\left(\frac{T_L}{T_H} - 1\right) + \left(\frac{V_{SC}}{V_{SE}}\right)\cos(\alpha)\right]^{-1}\right\} \tag{12}$$

P_m represents the average pressure of a complete Stirling cycle. To calculate the average pressure of the working fluid, integrate Eq. (10) with the crank angle from 0 to 2π, then multiply to 1/2π and solved it using Dwight's Tables of Integrals. The average pressure is presented as follows.

$$P_m = 2\ m\ R\ T_L \left[V_{SE}\ K_1 \left(\sqrt{1 - \left(\frac{C_1}{K_1}\right)^2} \right) \right]^{-1} \quad (13)$$

The maximum pressure occurs when the total volume is at minimum and the minimum pressure occurs when total volume is at maximum. Hence, the maximum pressure is obtained while $\cos(\theta - \beta) = 1$ whereas the minimum pressure is obtained while $\cos(\theta - \beta) = -1$ as shown in below,

$$P_{max} = P_m \left(\sqrt{1 - \left(\frac{C_1}{K_1}\right)^2} \right) \left(1 - \frac{C_1}{K_1}\right)^{-1} \quad (14)$$

$$P_{min} = P_m \left(\sqrt{1 - \left(\frac{C_1}{K_1}\right)^2} \right) \left(1 + \frac{C_1}{K_1}\right)^{-1} \quad (15)$$

The total work done is the sum of work done of expansion and compression. Differentiating Eq. (2) and Eq. (3) with the crank angle to find the changing rate of expansion and compression volume, then integrating the work done for each crank angle from 0 to 2π as shown in below,

$$W_{sch} = \int_0^{2\pi} \left\{ mR\ T_L \left[\frac{V_{SC}}{V_{SE}} \sin(\theta - \alpha) \right] \left[K_1 (1 - \frac{C_1}{K_1} \cos(\theta - \beta)) \right]^{-1} \right\} d\theta \quad (16)$$

Based on ideal gas law, then substitute Eq. (2) and Eq. (3) for expansion mass and compression mass, then differentiating to crank angle respectively with quotient rule. The mass flow rate of expansion, compression and dead volume are given below,

$$\dot{m}_E = \frac{V_{SE} C_2}{2T_H} \left(\sin(\theta) - \frac{C_1}{K_1} [\sin(\beta) + \sin(\theta - \beta)] \right) \quad (17)$$

$$\dot{m}_C = \frac{V_{SE} C_2}{2T_H} \left\{ -\sin(\theta) + \frac{V_{SC}}{V_{SE}} \sin(\theta - \alpha) + \left(\frac{V_{SC}}{V_{SE}} - 1 \right) \left(\frac{C_1}{K_1} \sin(\theta - \beta) \right) - \frac{C_1}{K_1} \sin(\beta) - \frac{C_1}{K_1} \frac{V_{SC}}{V_{SE}} \sin(\beta - \alpha) \right\} \quad (18)$$

$$\dot{m}_D = \frac{V_D C_2}{T_D} \left(\frac{C_1}{K_1} \sin(\theta - \beta) \right) \quad (19)$$

Where $C_2 = P_m \left(\sqrt{1 - \left(\frac{C_1}{K_1}\right)^2} \right) \left[R \left(1 - \frac{C_1}{K_1} \cos(\theta - \beta) \right)^2 \right]^{-1}$

Based on Eq. (10) to calculate the pressure of the system and plot it against with the total volume, then compare with ideal adiabatic equation Stirling cycle as shown in Fig. 3. The Schmidt theory predicted the output power more accurately compared to ideal adiabatic equations as shown in Table 1. Schmidt theory considers more factors compare to ideal adiabatic equation such as the temperature of regenerator and dead volume.

The mass flow rate of each components is calculated separately through the mathematical model equations. The working fluid mass flow rate of expansion, compression and dead volume are calculated based on the Eq. (17) to Eq. (19) as shown in Fig. 4. The sign of the mass flow rate shows the direction of the working fluid flow direction. When the mass flow rate of the expansion working fluid increase, the mass flow rate of the compression working fluid decrease and vice versa. The average pressure of the system influences the mass

flow rate of working fluid. The higher the mass flow rate, the more energy is being transferred and contributes to higher power output from the system. The mass flow rate of compression working fluid has a similar trend to the heat flow rate against the crank angle [21]. Hence, the compression piston in the low temperature component produces higher output power compare to expansion displacer in high temperature component. The expansion mass flow rate has the same trend as the pressure drop in the system [22]. The expansion mass flow rate increase at the beginning of the cycle when the working fluid undergoes expansion, then the pressure increases and flows to compression component.

The main pressure drop in this Stirling engine is the connection between the hot and cold component cylinder. It is considered as the dead volume of the system and the diameter of this connector cylinder is smaller than the hot and cold component cylinder. Pressure drop happened when the working fluid flowed through various diameter tubes and due to frictional flow on the cylinder wall. This pressure drop has negative impact on the engine performances [23]. When the working fluid flows to the cold component cylinder, the pressure force on the surface of power piston increases and generates power as shown in Fig. 5. It is a typical trend of shaft power for gamma type Stirling engine [24].

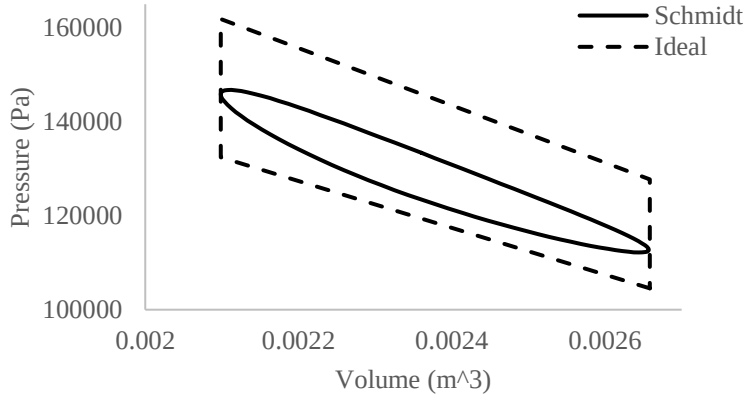


Fig. 3. P-V diagram of the Stirling engine

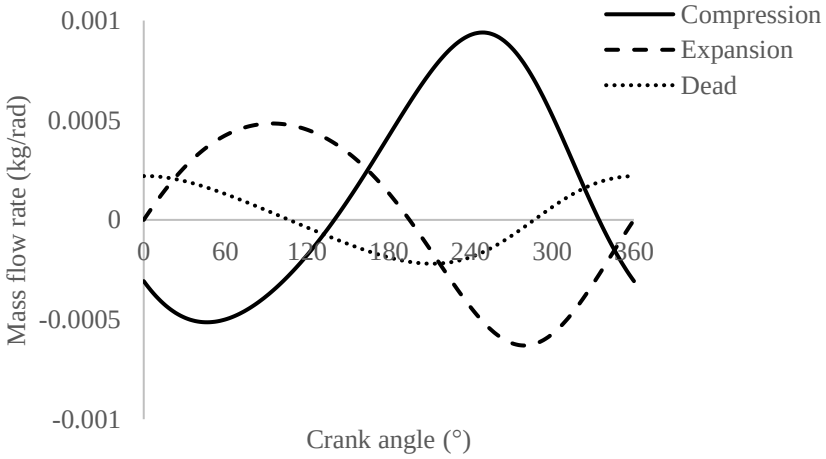


Fig. 4. Mass flow rate of working fluid

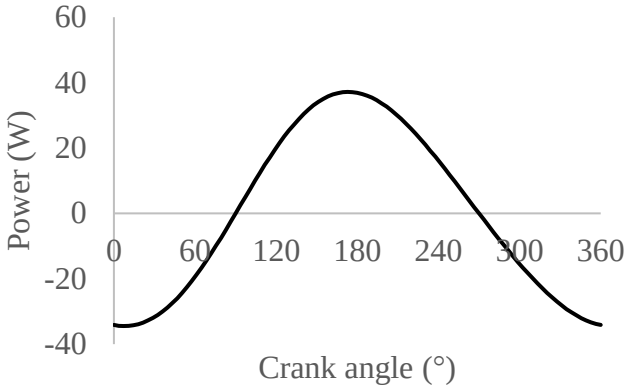


Fig. 5. Output power against crank angle [24]

5. CFD Simulation

ANSYS Fluent turbulent transient model with dynamic mesh is used for this study to verify the mathematical model equations and the experiment results. The 3D Fluent simulations were performed using an asymmetry of a 2D mesh drawing. To minimize error of dynamic mesh, the mesh cell size is defined to 1 mm x 1 mm and the quality of mesh is 1.0. It is the same mesh cell size throughout the mesh drawing.

The simulation setups are pressure-based solver, transient time with a time step interval of $6x10^{-4}$ seconds, Viscous (SST k-ω) and dynamic mesh. The dynamic movement is input into CFD through user defined file (UDF) by using C coding. The coding states the power piston and displacer movement velocity of the system. The velocity equation for power piston is provided as follows.

$$v_p = A\omega\sin(-\frac{\pi}{2} + \omega t) \quad (20)$$

ω is assumed to be based on the operating speed of 435 rpm. The output power of the system is measured through the integration of the pressure on the power piston surface and the pressure change on the displacer. Since the time step interval is $6x10^{-4}$ seconds, the actual physical time is about 5 minutes and takes weeks to complete. The last complete Stirling cycle result is being considered as the results if it converges.

For the boundary condition, the top of displacer's cylinder wall is set to 150°C with 6 mm thickness of aluminium. The heat flux on displacer's cylinder is set to 3255 W/m^2. The other walls such as connector, power piston and cold component cylinder are set to natural convection. The simulation neglect mechanical friction losses, mechanical joint losses, manufacturing defects of each components, engine vibration, momentum force by flywheel, unbalance force of power piston and counter weight.

Table 3 shows the comparison of output power from ideal adiabatic equation, Schmidt theory, CFD simulation and experimental result. The Ideal Stirling cycle predicted the maximum achievable power based on working fluid thermodynamic behaviour. The Schmidt theory estimated the average output power by separating the working fluid inside Stirling engine into 5 volumes as shown in Fig. 2. The output power is estimated through integrating

the work done of working fluid at every crank angle as shown in Eq. (16). CFD simulation includes pressure shuttle loss, momentum flow, dynamic turbulent, friction loss in pipe, heat loss to surrounding, thermal equilibrium between hot and cold working fluid. Hence, the output power is much lower compare to Ideal Stirling cycle and Schmidt theory. The error propagation of ideal Stirling cycle and Schmidt theory are calculated based on assumption of heat source temperature of 150 ± 2°C with operating speed of 386 ± 5 rpm. The experimental error is calculated based on standard deviation of the experimental results with the heat source temperature of 150°C.

Table 3. Comparison of output power

	Ideal	Schmidt	CFD simulation	Experiment
Power (W)	181.0 ± 5.2	52.8 ± 1.1	54.5	55.3 ± 11.5
Operating speed (rpm)	386 ± 5	386 ± 5	435	386 ± 82.0

6. Results and discussion

The temperature of the Stirling engine is normally measured on the surface of the hot component cylinder using a k-type thermocouple [25] or an infrared thermometer [26] or measuring the flame temperature [13]. In this study, a micro thermocouple is placed inside the hot cylinder to measure the temperature of the working fluid. To minimize error in predicting the indicated power, the operating temperature is considered instead of initial preheated temperature throughout this study [20]. There is a temperature differences of 10ºC to 15ºC between the operating temperature and the initial preheating temperature. In this study, operating temperature is considered as the error is minimized. For Ideal Stirling cycle, the average power error has reduced from 42.2 W to 32.8 W as shown in Table 4. For Schmidt theory, the average power error has reduced from 3.42 W to 1.94 W as shown in Table 5.

Table 4. Comparison of operating and initial temperature using Ideal Stirling cycle

Model	Experiment power output (max) (W)	Based on operating temperature (W)	Error (W)	Based on initial temperature (W)	Error (W)
1	63.3	86.7	23.4	99.8	36.5
2	16.0	51.4	35.5	59.2	43.3
3	16.0	57.7	41.6	66.4	50.4
4	27.8	59.2	31.4	68.2	40.4
5	22.9	54.8	31.9	63.1	40.3

Table 5. Comparison of operating and initial temperature using Schmidt theory

Model	Experiment power (average) (W)	Based on operating (W)	Error (W)	Based on initial (W)	Error (W)
1	42.6	25.6	-17.0	29.3	-13.2
2	3.52	5.65	2.10	6.50	3.00
3	0.61	6.42	5.80	7.38	6.80
4	2.20	6.43	4.20	7.39	5.20
5	-8.57	5.94	14.5	6.83	15.4

The Stirling engine test rig is tested with the temperature at 65ºC, 100ºC and 135ºC for model 2 as shown in Fig. 6. Based on the results, the higher the heating temperature, the higher the shaft power which fulfil to the Carnot theorem and Ideal gas law. When the working fluid absorbs more heat energy, the higher the pressure increase, the higher the output power by the system. The Schmidt theory has accurately predicted, with the error of ± 2%, and the Ideal Stirling cycle shows the maximum achievable power from the system. The similar trend can be found in other researchers' result although the design of Stirling engine is not completely the same [9], [27]. The details of their Stirling engines are provided in Table 6. For the following results, the predicted output power from Ideal Stirling cycle is calculated based on Eq. (1) whereas Schmidt is based on Eq. (16).

Table 6. Detail of reference Stirling engine

	Chen [9]	Karabulut [11]	Cheng [25]	Aksoy [26]	Sripakagorn [30]
Type	gamma	beta	beta	beta	beta
Fluid	air	air	air	helium	air
P (bar)	2	1.4	4	5	1
C_r	-	1.65	1.57	1.65	1.61
S (m)	0.05	0.06	0.035	0.079	0.037
D_p (m)	0.0256	0.07	0.07	0.069	0.074
Heat Source	≈ 250°C	≈ 200°C	650°C	1000W	≈ 400°C

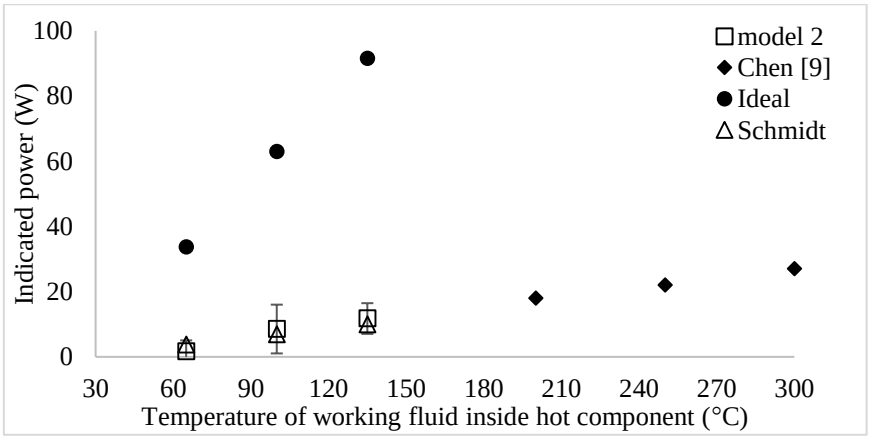


Fig. 6. Engine performance at various temperature

Model 1 has a displacer diameter of 113 mm and a gap of 3 mm to the cylinder wall. The displacer top and bottom are both flat. The result shows that the higher the operating speed

of the engine, the higher the shaft power as shown in Fig. 7. It has similar behaviour as the Ideal Stirling cycle, Schmidt theory as well as other researchers' results [9], [25]. The average work done per cycle is 7.23 J. The higher operating speed, the higher number of cycle per second, the higher output power.

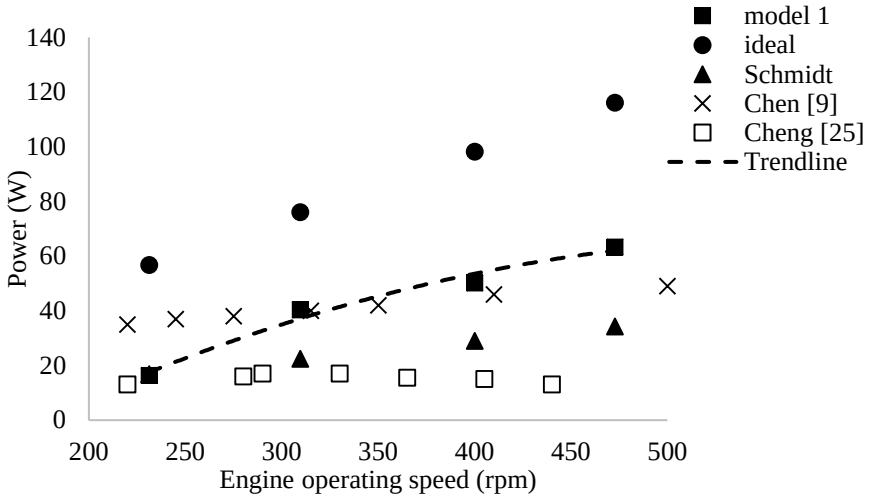


Fig. 7. Model 1 performance against operating speed

Model 2 has a displacer diameter of 100 mm and a gap of 10 mm to the cylinder wall. The displacer top and bottom are both flat. Model 2 has similar design as model 1. The differences between these two models are the diameter of the displacer and the dead volume of the engine. The smaller the displacer diameter, the higher the dead volume, the smaller the swept volume of the displacer, hence the lower the shaft output power. The expansion pressure of the working fluid acting on the displacer surface is much lower because the displacer diameter is much smaller as compare to the model 1. The gap of 10 mm between the displacer and the cylinder has allowed the working fluid flows through the displacer without providing work done to the system. The differences in output power between models 1 and 2 is 47.3 W whereas the theoretical different is 35.3 W. The results of model 2 are less consistence compare to model 1 due to the different of dead volume. Dead volume of model 1 is 1.175 dm^3 whereas the dead volume of model 2 is 3.98 dm^3. When the operating speed increases, the shaft output power does not increase like the prediction of Ideal Stirling cycle and Schmidt theory. This similar behaviour is found in other researchers' finding at this operating speed of Stirling engine as shown in Fig. 8 [25], [26].

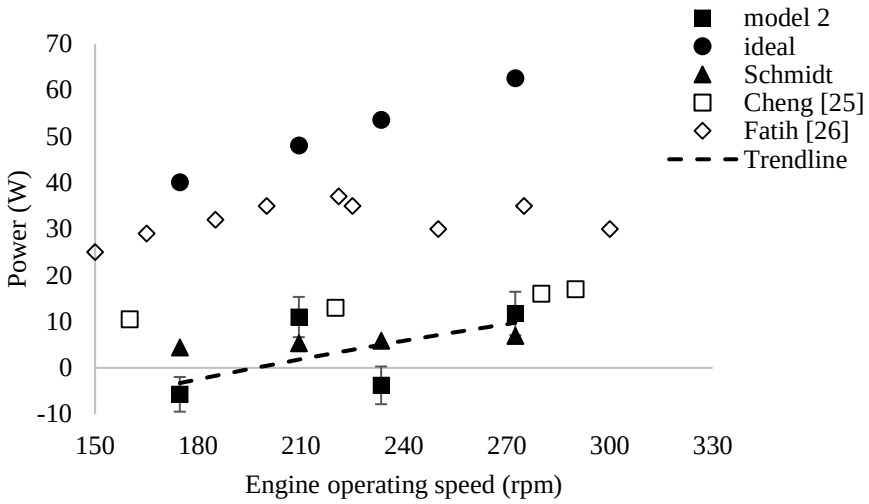


Fig. 8. Model 2 performance against operating speed

Model 3 and model 4 have the same displacer diameter and the gap to the cylinder wall like model 2. The different between these 3 models is the shape of the displacer top that is closer to the heat source. The displacer of model 3 is a convex shape whereas model 4 is a concave shape. The output power range from these models are close to each other as shown in Fig. 12. The result for model 3 shows that the higher the operating speed, the lower the output power. Although it behaves differently to the theoretical prediction as shown in Fig. 9, but these trend has been identified by other researchers for low temperature range experiment [26]–[28]. Stirling engine that operates under 300°C has possibility to have this trend as it has been tested from 200ºC to 400ºC [9].

The main reason of this down trend is due to the expansion force of the working fluid is not being harvested completely at higher operating speed. The expansion force of the working fluid acts on the surrounding cylinder wall instead of acting on the top surface of the displacer. The shape of the displacer and cylinder toward the heat sources is different. The cylinder is in flat shape whereas the displacer is convex shape. The expansion of the working fluid flows through the gap between displacer side wall and the cylinder wall instead of pushing the displacer top surface which generates output power. Hence, the higher the operating speed, the lower output power. At the higher operating speed with this convex shape displacer, the Stirling engine is mainly driven by electrical motor instead of the work done by the working fluid in the system. The engine consumed more energy to operate than lower operating speed because the engine speed is against the work done of the working fluid in the system as shown in Fig. 9.

From these 3 models, the results show that the topology of displacer impacts the output power of Stirling engine. The maximum output power of model 4 has the highest performance compare to model 2 and 3 as predicted based on Ideal Stirling cycle and Schmidt theory as shown in Table 7. A small portion of the working fluid in the hot component cylinder remains in the concave shape of the displacer when it undergoes expansion. Hence, the working fluid in the hot component retains more heat energy and maintaining the temperature gradient. During the compression stage, lesser heat energy is used to reheat the working fluid when it flows back from cold component cylinder and it reduces the impact of thermal equilibrium in the system.

Both model 3 and 4 have the same design to keeps the heat energy in the hot component, but the working fluid flow patterns are different for these two models. The vortex turbulent flow of working fluid occurred at the top edge of the displacer for model 3 whereas it is occurred at the top centre of the displacer for the model 4. The location of the vortex turbulent flow influences the amount of expansion force being harvested by the displacer of the system. Under constant pressure, the higher the surface area, the higher the force acting on the displacer. Hence, the more output power from concave shape as the surface area of concave shape is larger than the flat shape as shown Fig. 12. Based on the Fig. 8 and Fig. 10, the concave shape displacer produces higher output power than the flat shape displacer especially at higher operating speed.

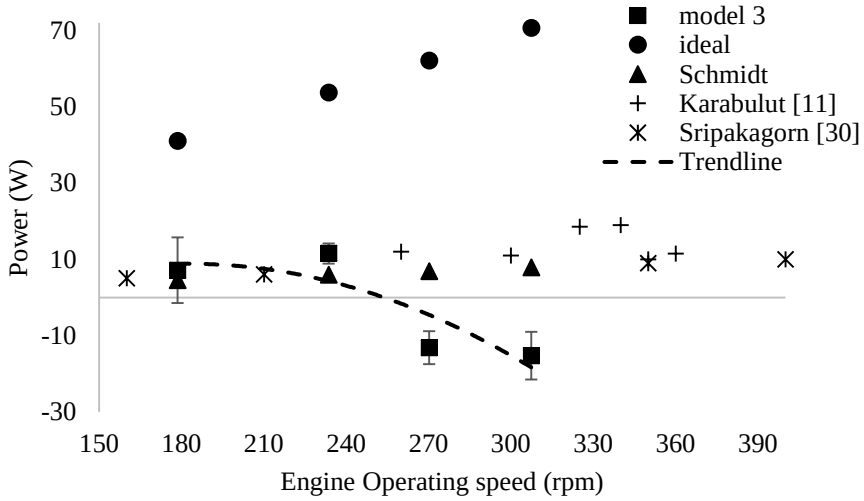


Fig. 9. Model 3 performance against operating speed

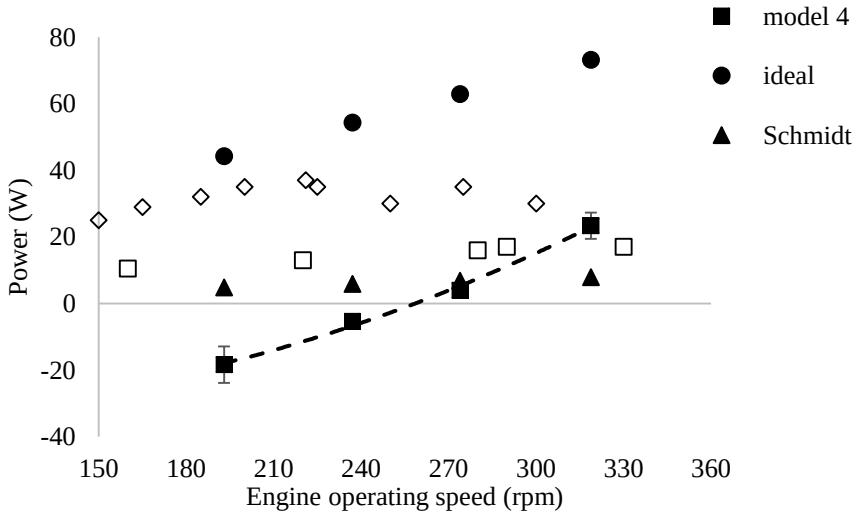


Fig. 10. Model 4 performance against operating speed

Model 4 and 5 have the same displacer design. The main differences between these two models is the concave shape position in the displacer. Model 4 concave position is near to the heat source whereas model 5 concave position is away from the heat source. Based on the experimental results for model 5 shows that the trend is the power is increased at lower

operating speed and decrease at higher operating speed [20], [24], [25], [29]. The optimal operating speed for model 5 is around 256 rpm with 2.27 W average output power as shown in Fig. 11.

Based on the results from model 4 and 5, the concave shape near to the heat source has positive impact whereas the concave shape on another side has negative impact. The concave shape that near to the heat source is harvesting same moment force as the power piston. Since the power piston and the displacer are connected to the same crank shaft, the one with same moment force direction increase the shaft power and the one with opposite moment force direction decrease the output torque. Hence, model 5 has lower shaft output power compare to model 2 and 4 as shown in Fig. 12 and Table 7.

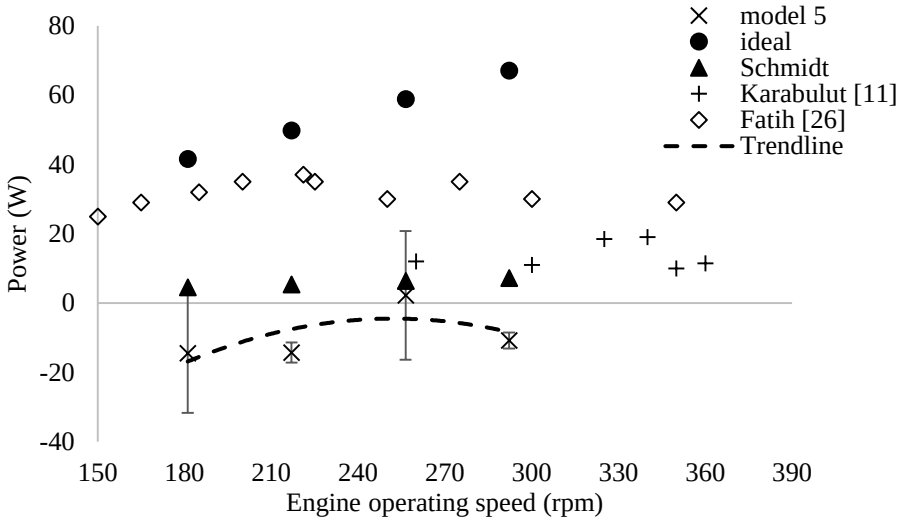


Fig. 11. Model 5 performance against operating speed

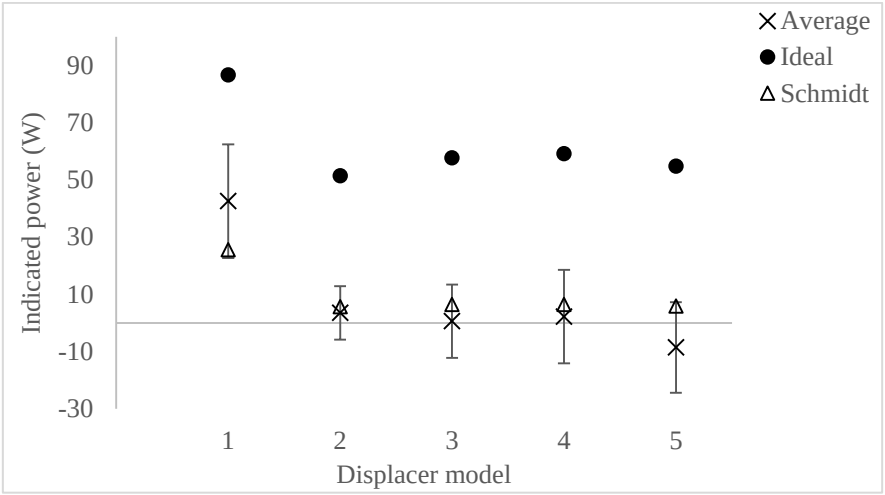


Fig. 12. Engine performance of all models

Based on the maximum shaft power from all models, model 1 has the highest shaft power among all model as shown in Table 7. Model 1 has much lower dead volume as compare to all other models as shown in Table 2. The dead volume of model 1 is 1.18 dm^3 whereas model 2 to 5 are around 4 dm^3. The theoretical Ideal Stirling cycle and Schmidt theory predicted

model 3, 4, 5 have higher output power than model 2 as shown in Table 7. The maximum power of Stirling engine models has similar trend as theoretical prediction. However, the average power does not align with theoretical prediction. Based on the experiment results, the prediction from Schmidt theory are more reliable compare to the Ideal Stirling cycle. When increasing the area to collect more expansion by integrating concave or convex shape, the dead volume is increased directly proportionally. However, the dead volume decreases the output power as shown in the experimental results of model 1 and 2.

Table 7. Experimental power output of all models

Model	Maximum power (W)	Ideal (W)	Average power (W)	Schmidt (W)	Average operating Speed (rpm)
1	63.3	86.7	42.6	25.6	353
2	16.0	51.4	3.52	5.65	224
3	16.0	57.7	0.612	6.42	251
4	27.8	59.2	2.20	6.43	258
5	22.9	54.8	-8.57	5.94	239

7. Conclusion

In this study, various displacer designs and its performances were investigated. The results showed that the model 1 that has a displacer with flat shape, length 0.15 m and Ø 0.114 m generates a maximum shaft power of 63.3 W when at an operating speed of 472 rpm. Based on model 1 and 2 that has a displacer with flat shape, length 0.095 m and Ø 0.1 m results, the engine shaft power is possible to increase by 47.4 W through reducing the dead volume by 2.8 dm^3. The dead volume is reduced by increasing the displacer diameter and displacer length. Furthermore, the smaller the gap between the displacer and cylinder, the higher the output power.

Comparing the results from model 2 to 4, topology of the displacer of the Stirling engine impacts the output power of the system. Among these three models, concave shape displacer has positive impact on the output power of the system. The model 4 concave shape displacer has increased 15.9% shaft power compare to model 2 flat shape displacer. The vortex turbulent flow at the centre of the concave displacer top has higher output power compare to the vortex turbulent flow at the edge of the convex displacer top.

Based on experimental results for model 4 and 5, which have same amount of working fluid inside the engine, but the concave configuration is different. Theoretically, these models should have the same output power. However, according to the experimental results, placing the concave shape toward the heat source would increase the shaft power by 5.2% compare to concave shape on another side of displacer. The higher the pressure force acting on the displacer surface that toward the heat source, the higher the output power is generated. This is because the direction of the pressure force acting on this surface is the same pressure force direction acting on the power piston at the cold component. Hence, it magnifies the output power of the system. On the other hand, pressure force that acting on another side of displacer is reducing the output power as the direction of pressure force is against the system.

Although the experiment results show that the concave shape improves the maximum output power, but further investigation on the various concave angle is needed. Moreover, the combination of concave and convex shape of displacer and power piston would further improve the shaft output power. The vortex turbulent flow by the concave and convex shape should be considered when predicting the output power. The dead volume of the Stirling engine should be minimized to obtain higher output power.

References

[1] A. Cacabelos, P. Eguía, J. L. Míguez, G. Rey, and M. E. Arce, "Development of an improved dynamic model of a Stirling engine and a performance analysis of a cogeneration plant," *Appl. Therm. Eng.*, vol. 73, no. 1, pp. 608–621, 2014.

[2] M. J. Dadi, "Review Article The most efficient waste heat recovery device: A gamma type Stirling engine," *International Journal of Advanced Engineering Technology,* Vol. 3, no. I, pp. 189-195, 2012.

[3] D. J. Shendage, S. B. Kedare, and S. L. Bapat, "An analysis of beta type Stirling engine with rhombic drive mechanism," *Renew. Energy*, vol. 36, no. 1, pp. 289–297, 2011.

[4] B. Kongtragool and S. Wongwises, "Thermodynamic analysis of a Stirling engine including dead volumes of hot space, cold space and regenerator," *Renew. Energy*, vol. 31, no. 1, pp. 345–359, 2006.

[5] P. Puech and V. Tishkova, "Thermodynamic analysis of a Stirling engine including regenerator dead volume," *Renew. Energy*, vol. 36, no. 2, pp. 872–878, Feb. 2011.

[6] J. Araoz, M. Salomon, L. Alejo, and T. H. Fransson, "Non-ideal Stirling engine thermodynamic model suitable for the integration into overall energy systems," *Appl. Therm. Eng.*, vol. 73, no. 1, pp. 203–219, 2014.

[7] I. Tlili, Y. Timoumi, and S. Ben Nasrallah, "Analysis and design consideration of mean temperature differential Stirling engine for solar application," *Renew. Energy*, vol. 33, no. 8, pp. 1911–1921, 2008.

[8] W.-L. Chen, K.-L. Wong, and Y.-F. Chang, "A numerical study on the effects of moving regenerator to the performance of a β-type Stirling engine," *Int. J. Heat Mass Transf.*, vol. 83, no. 1, pp. 499–508, 2015.

[9] W.-L. Chen, K.-L. Wong, and H.-E. Chen, "An experimental study on the performance of the moving regenerator for a γ-type twin power piston Stirling engine," *Energy Convers. Manag.*, vol. 77, no. 1, pp. 118–128, Jan. 2014.

[10] M. T. Mabrouk, Kheiri, and M. Feidt, "Displacer gap losses in beta and gamma Stirling engines," *Energy*, vol. 72, no. 1, pp. 135–144, Aug. 2014.

[11] H. Karabulut, H. S. Yücesu, C. Çınar, and F. Aksoy, "An experimental study on the development of a β-type Stirling engine for low and moderate temperature heat sources," *Appl. Energy*, vol. 86, no. 1, pp. 68–73, 2009.

[12] C. Cinar, S. Yucesu, T. Topgul, and M. Okur, "Beta-type Stirling engine operating at atmospheric pressure," *Appl. Energy*, vol. 81, pp. 351–357, 2005.

[13] J. Araoz, E. Cardozo, M. Salomon, L. Alejo, and T. H. Fransson, "Development and validation of a thermodynamic model for the performance analysis of a gamma Stirling engine prototype," *Appl. Therm. Eng.*, vol. 83, no. 1, pp. 16–30, 2015.

[14] C. Çinar and H. Karabulut, "Manufacturing and testing of a gamma type Stirling engine," *Renew. Energy*, vol. 30, no. 1, pp. 57–66, Jan. 2005.

[15] E. Ataer, "Numerical analysis of regenerators of free-piston type Stirling engines using Lagrangian formulation," *International Journal of Refrigeration*, vol. 25, no. 1, pp. 640–652, 2002.

[16] S. Kwankaomeng, B. Silpsakoolsook, and P. Savangvong, "Investigation on Stability and Performance of a Free-piston Stirling Engine," *Energy Procedia*, vol. 52, no. 1, pp. 598–609, 2014.

[17] Q. Yang, E. Luo, W. Dai, and G. Yu, "Thermoacoustic model of a modified free piston Stirling engine with a thermal buffer tube," *Appl. Energy*, vol. 90, no. 1, pp. 266–270, Feb. 2012.

[18] B. Jia, Z. Zuo, G. Tian, H. Feng, and P. Roskilly, "Development and validation of a free-piston engine generator numerical model," *Energy Convers. Manag.*, vol. 91, no. 1, pp. 333–341, 2015.

[19] S. H. Zare and H. Bahreman, "A novel active free piston Stirling engine : Modeling, development, and experiment," *Appl. Energy*, vol. 199, no. 1, pp. 400–415, 2017.

[20] J. Bert, D. Chrenko, T. Sophy, L. Le Moyne, and F. Sirot, "Simulation, experimental validation and kinematic optimization of a Stirling engine using air and helium," *Energy*, vol. 78, no. 1, pp. 701–712, Dec. 2014.

[21] A. Sowale, A. J. Kolios, B. Fidalgo, T. Somorin, A. Parker, L. Williams, M. Collins, E. Mcadam, and S. Tyrrel, "Thermodynamic analysis of a gamma type Stirling engine in an energy recovery system," *Energy Convers. Manag.*, vol. 165, no. 1, pp. 528–540, 2018.

[22] I. Barreno, S. C. Costa, M. Cordon, M. Tutar, I. Urrutibeascoa, X. Gomez, and G. Castillo, "Numerical correlation for the pressure drop in Stirling engine heat exchangers," *Int. J. Therm. Sci.*, vol. 97, no. 1, pp. 68–81, 2015.

[23] S. Suman, M. K. Khan, and M. Pathak, "Performance enhancement of solar collectors—A review," *Renew. Sustain. Energy Rev.*, vol. 49, no. 1, pp. 192–210, 2015.

[24] R. Gheith, H. Hachem, F. Aloui, and S. Ben Nasrallah, "Experimental and theoretical investigation of Stirling engine heater: Parametrical optimization," *Energy Convers. Manag.*, vol. 105, no. 1, pp. 285–293, 2015.

[25] C.-H. Cheng, H.-S. Yang, and L. Keong, "Theoretical and experimental study of a 300-W beta-type Stirling engine," *Energy*, vol. 59, no. 1, pp. 590–599, Sep. 2013.

[26] F. Aksoy, H. Karabulut, C. Çınar, H. Solmaz, Y. Ö. Özgören, and A. Uyumaz, "Thermal performance of a Stirling engine powered by a solar simulator," *Appl. Therm. Eng.*, vol. 86, no. 1, pp. 161–167, 2015.

[27] B. Kongtragool and S. Wongwises, “Performance of a twin power piston low temperature differential Stirling engine powered by a solar simulator,” *Sol. Energy*, vol. 81, no. 7, pp. 884–895, Jul. 2007.

[28] B. Kongtragool and S. Wongwises, “A four power-piston low-temperature differential Stirling engine using simulated solar energy as a heat source,” *Sol. Energy*, vol. 82, no. 6, pp. 493–500, Jun. 2008.

[29] R. Gheith, F. Aloui, and S. Ben Nasrallah, “Determination of adequate regenerator for a Gamma-type Stirling engine,” *Appl. Energy*, vol. 139, no. 1, pp. 272–280, Feb. 2015.

[30] A. Sripakagorn and C. Srikam, “Design and performance of a moderate temperature difference Stirling engine,” *Renew. Energy*, vol. 36, no. 6, pp. 1728–1733, 2011.

EURECA 2018 – Conference Paper
Paper number PG08

Mathematical Modelling Simulation Analysis Of A Photovoltaic Thermal System

Mohammad Taghi Hajibeigy[*1], Rashmi Walvekar[2] and Chockalingam Aravind Vaithilingam*[1]

[1]Electrical and Electronic Engineering, School of Engineering

[2]Chemical Engineering, School of Engineering

Taylor's University, 47500 Subang Jaya, Selangor, Malaysia

Abstract. This paper analyses the heat response data collected from a PVT system, under normal conditions, with steady water acting as a coolant. Experimental and simulation values were compared and analyzed in this paper. The thermal response of the PVT system depends solely on the irradiation of sunlight. Therefore, the thermal energy output of the PVT system varies according to the solar irradiation. In this experiment, the PVT thermal response was measured via Thermocouple sensors mounted in each layer of the PVT system, which included solar panel, aluminum thermal plate, and Heatsinks. A charge controller was connected to the output of the PV to regulate the charging process for a battery so that the electrical output can also be affected by the thermal response of the solar panel. The amount of solar irradiation was calculated based on the reading from the Pyranometer and the surface area of the PV. The setting of the Pyranometer and the thermocouples to measure the PV thermal value and the ambient temperature was set to ten seconds each, which was read using a data logger.

Keywords: Hybrid PVT, thermal energy, heat transfer, thermal collector, photovoltaic

1 Introduction

Solar is one of the clean, renewable and sustainable sources of energy which has to be harvested everywhere on the earth special places which have extended the sunshine around the year like Malaysia. This source of energy can be harvested by Photovoltaic Thermal (PVT) which can contribute to the energy consumption of the household or industry. In regards to utilize the combination of thermal and photovoltaic systems, the technology has been there for a while now, but not much work has been done to improve on it. PVT's have to start to attract more interest in the solar energy sector due to increasing demands for renewable energy source [1]. A PVT can harvest both electrical and thermal energy since the PV by itself alone only can retain up to 20% maximum and the majority of the energy around 70% is wasted via thermal [2]. The low efficiency of the PV can be further improved by harvesting the thermal portion of the Sun radiation on the PV system and collected such energy in a thermal tank for the future usage. A suggested approach is to come up with a mathematical modelling of the system, simulate using MATLAB/Simulink, analyze the gathered data, evaluate the efficiency as a means to transfer the thermal energy collected in a container under the PV and suggest improve efficiency of the system and build the best model according to the results that been approached. This research is the specific mathematical modelling for the proposed system which can be accustomed based on the different types of materials and fluid as a coolant are used. Further, the obtained mathematical model could be simulated to better understand the contribution of each parameter to the overall effect of the system's efficiency.

Solar panels work perfectly only in certain weather condition, but since the weather is always changing and the solar panels are used in different climate all over the world, most panels do not operate under ideal conditions. Understanding how the solar panels react to these different conditions is essential for engineers to develop a solution accordingly [3]. With this knowledge, a design can be introduced to improve the efficiency of solar panels that operate in non-optimal conditions. This study was undertaken to employ water in the container as a coolant in the PVT system. PV cells when its strike with a sunlight basically generates electricity, however, silicon PV cells tend to convert only small part of the radiation to electricity while the rest result in heating of the solar panels. As PVT system, there is heat transfer from the cells to the thermal plate or tubes to the coolant underneath. The heating of the coolant reduces the temperature of the PV cells, therefore increasing their efficiency when the solar cells are exposed to a high temperature and radiation conditions. The hybrid PVT has a pump and storage tank but in this paper, only one part was shown and studied while the water is steady to analyze the behaviour of heat transfers. Figure1 exhibits the general idea of the PVT system principle.

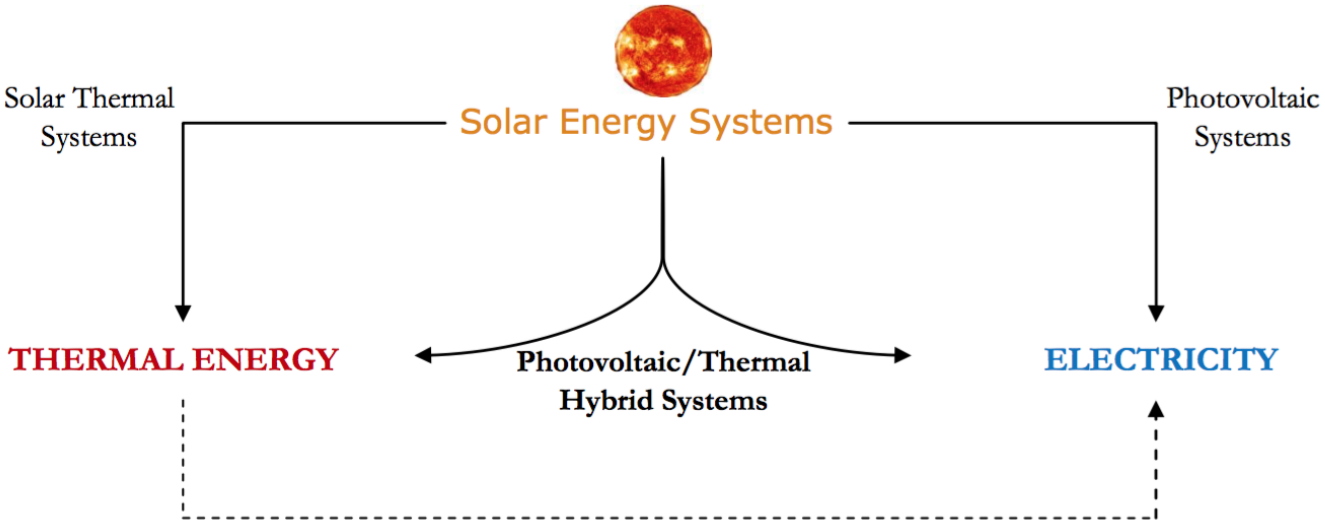


Fig. 1. Overview of solar energy systems [4].

2 Mathematical modelling of the photovoltaic system

The modeling is divided into 6 different stages, the aim of the modeling is to simulate how the temperature on the photovoltaic panel affects the thermal energy in each stage starting from the heat from the sun to the different layers of the hybrid collector all the way to the heat transfer from the heat exchanger to the water in the tank, this will let the user simulate how much energy is being wasted and how much energy is turning into useful energy such as electrical energy and energy to heat up the water in the tank. Figure 2 shows the principles of the photovoltaic system.

All the steps of the simulation are shown briefly below:

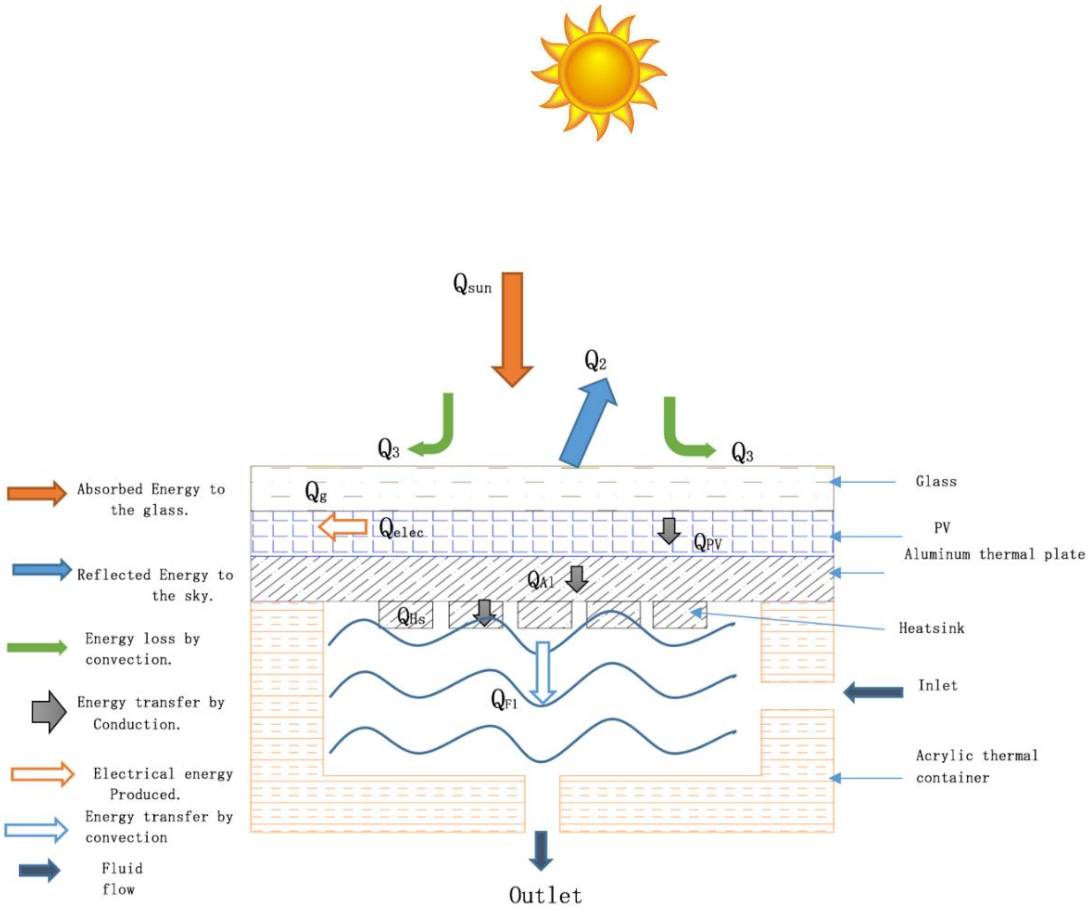


Fig. 2. Principles of a photovoltaic system.

The overall project flow is shown in the flowchart in Figure 3.

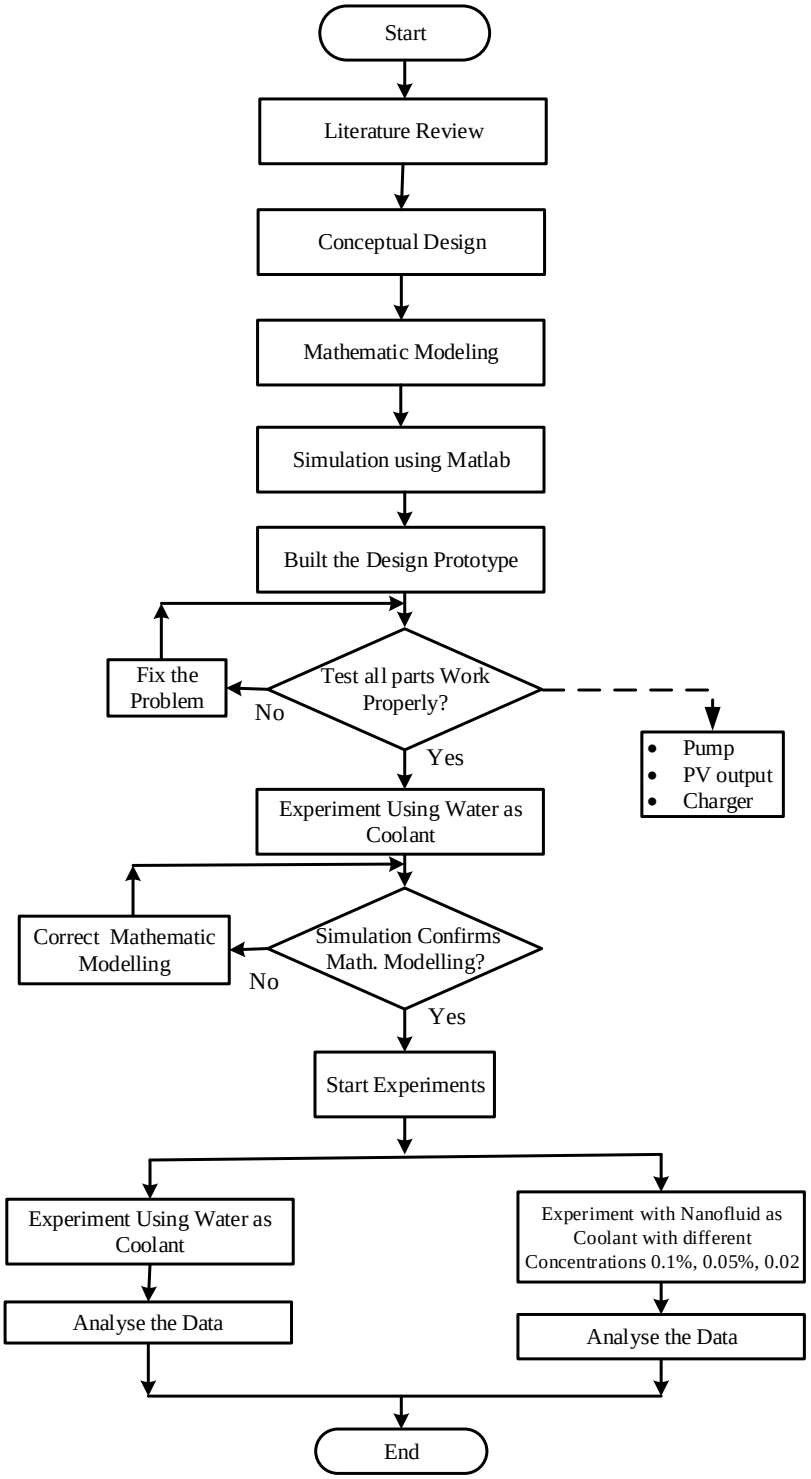


Fig. 3. Flowchart of the overall work on the research.

The Heat transfer from the Sun to the different layers of the Hybrid collector:

2.1 Heat transfer from the Sun to the PV [5].

$$Q_{PV} = Q_{Sun} - (Q_2 + Q_3 + Q_{elec}) \quad (1)$$

[The net energy of the PV]

$$Q_{Sun} = \varepsilon g * \alpha_{PV} * S * A_{PV} \quad (2)$$

[Sun energy projected to the surface of the PV]

$$Q2 = \varepsilon g * \sigma * Ag * (Tg4 - Tamb4) \quad (3)$$

[Irradiation Energy reflected to the sky]

$$Q_3 = \frac{\Delta T}{\frac{1}{(h_{amb} * Ag)}} \quad (4)$$

[Energy transfer by convection to the environment]

$$h = 2.56 * Wv + 8.55 \quad (5)$$

[Convective heat transfer effected by the wind speed]

$$Q_{elec} = \frac{Q_{sun} * \eta_{ref} * e^{[\beta(T_{PV} - T_{ref})]}}{\alpha_{PV}} \quad (6)$$

[Electrical energy produced by the PV]

$$Q_{PV} = \varepsilon_g * \alpha_{PV} * S * A_{PV} - [\varepsilon_g * \sigma * A_g * (T_g^4 - T_{amb}^4) + \frac{\Delta T}{\frac{1}{(h_{amb} * A_g)}} + \frac{Q_{sun} * \eta_{ref} * e^{[\beta * (T_{PV} - T_{ref})]}}{\alpha_{PV}}] \quad (7)$$

2.2 Heat transfer from the PV to the Aluminum thermal plate [6], [7].

Figure 4 shows the connection of the PV with the aluminum thermal plate through thermal glue.

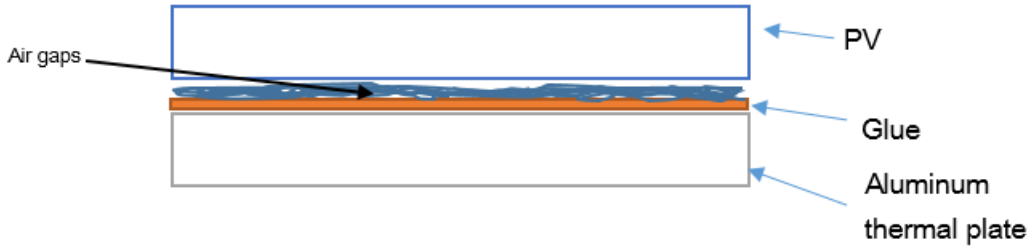


Fig. 4. Representation of PV, Aluminum and glue.

In here there are 2 heat losses by conduction in the glue and by convection due to the air gaps. However, these losses can be negligible but can be calculated as shown below:

$$Q_{Al} = Q_{PV} - (Q_{RAl} + Q_{cnv_Al} + Q_{cnd_gl}) \quad (7)$$

[The net energy of the Aluminum thermal plate]

$$Q_{RAl} = \frac{\Delta T}{R_{Al}} \quad (8)$$

[Resistive transfer energy of the Aluminum thermal plate]

$$R_{Al} = \frac{b_{Al}}{K_{Al} * A_{Al}} \quad (9)$$

[Thermal resistance of the Aluminum thermal plate]

$$Q_{RAl} = \frac{\Delta T * K_{Al} * A_{Al}}{b_{Al}} \quad (10)$$

$$Q_{cnv_Al} = h_{amb} * A_{Al} * (T_{Al} - T_{amb}) \quad (11)$$

[The heat loss by convection due to the uniform Aluminum thermal plate with PV]

$$Q_{cnd_gl} = K_{gl} * \frac{A_{gl}}{b_{gl}} * (T_{gl} - T_{Al}) \quad (12)$$

[The heat loss by convection through the glue in between the PV and the Aluminum thermal plate]

$$Q_{Al} = \varepsilon_g * \alpha_{PV*} S * A_{PV} - [\varepsilon_g * \sigma * A_g * (T_g^4 - T_{amb}^4) + \frac{\Delta T}{\frac{1}{(h_{amb} * A_g)}} + \frac{Q_{sun} * \eta_{ref} * e^{[\beta(T_{PV} - T_{ref})]}}{\alpha_{PV}} [\frac{\Delta T * K_{Al} * A_{Al}}{b_{Al}} + h_{amb} * A_{Al} * (T_{Al} - T_{amb}) + K_{gl} * \frac{A_{gl}}{b_{gl}} * (T_{gl} - T_{Al})] \quad (13)$$

2.3 Heat transfer from the Aluminum thermal plate to the Heatsink [8].

Figure 5 shows the Heatsink used in the experiment. It was used to extract the heat from the top layer aluminium plate and transferred to the coolant which it is submerged into it. The heatsink is made of aluminum metal that is anti-rust with good heat transfer capability where thermal energy is dissipated away from the device, thus allowing regulation of the device's temperature at optimal levels.

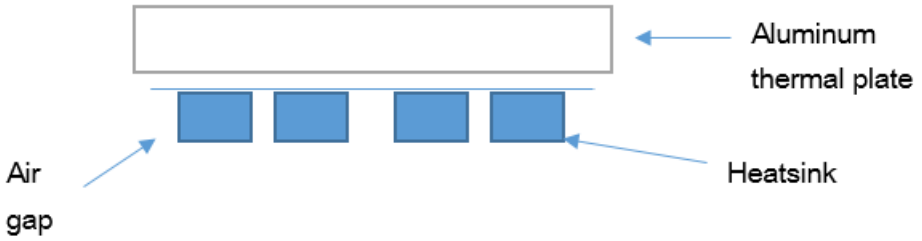


Fig. 5. Representation of Aluminum and heat sink.

$$Q_{HS} = Q_{Al} - (Q_{RHS} + Q_{cnv_cont_air}) \quad (14)$$

[The net energy transfer from the Aluminum plate to the Heatsink]

$$Q_{RHS} = \frac{\Delta T * K_{HS*} A_{HS}}{L} \quad (15)$$

[Resistive transfer energy of the Heatsink]

$$Q_{cnv_cont_air} = h_{cont_air} A_{Al} * (T_{Al} - T_{cont_air}) \quad (16)$$

[Heat loss to the air gap from the Aluminum thermal plate and the Heatsink]

$$Q_{HS} = \varepsilon_g * \alpha_{PV*} S * A_{PV} - [\varepsilon_g * \sigma * A_g * (T_g^4 - T_{amb}^4) + \frac{\Delta T}{\frac{1}{(h_{amb} * A_g)}} + \frac{Q_{sun} * \eta_{ref} * e^{[\beta(T_{PV} - T_{ref})]}}{\alpha_{PV}}] - [\frac{\Delta T\, K_{Al} * A_{Al}}{b_{Al}} + h_{amb} * A_{Al} * (T_{Al} - T_{amb}) + K_{gl} * \frac{A_{gl}}{b_{gl}} * (T_{gl} - T_{Al})] - [\frac{\Delta T * K_{HS*} A_{HS}}{L} + h_{cont_air} * A_{Al} * (T_{Al} - T_{cont_air})] \quad (17)$$

2.4 Heat transfer from the Heatsink to the Fluid [9].

$$Q_{Fl} = Q_{HS} - (Q_{cnv_cont_air} + Q_{cnd_cont}) \quad (18)$$

[The net energy transfer from the Heatsink to Fluid]

$$Q_{cnv_cont_air} = h_{cont_air} * A_{HS} * (T_{HS} - T_{cont_air}) \quad (19)$$

[Heat loss from the Heatsink to the air of the container]

$$Q_{cnd_cont} = K_{arc} * A * (T_{arc} - T_{amb}) \quad (20)$$

[Heat loss by conduction throw the thermal container to the ambient outside the thermal container].

This loss can be negligible since the container is insulated with a high reflector to 97%, the heat loss will be only 3%.

$$Q_{Fl} = \varepsilon_g * \alpha_{PV} * S * A_{PV} - [\varepsilon_g * \sigma * A_g * (T_g^4 - T_{amb}^4) + \frac{\Delta T}{\frac{1}{(h_{amb} * A_g)}} + \frac{Q_{sun} * \eta_{ref} * e^{[\beta(T_{PV} - T_{ref})]}}{\alpha_{PV}}] - [\frac{\Delta T \, K_{Al} * A_{Al}}{b_{Al}} + h_{amb} * A_{Al} * (T_{Al} - T_{amb}) + K_{gl} \frac{A_{gl}}{b_{gl}} * (T_{gl} - T_{Al})] - [\frac{\Delta T * K_{HS} * A_{HS}}{L} + h_{cont_air} * A_{Al} * (T_{Al} - T_{cont_air})] - [h_{cont_air} * A_{HS} (T_{HS} - T_{cont_air}) + K_{arc} * A_{arc} * (T_{arc} - T_{amb})] \quad (21)$$

2.5 Heat transfer from the Fluid to the heat exchanger [10].

Figure 6 shows the orientation of the copper pipe used as a heat exchanger.

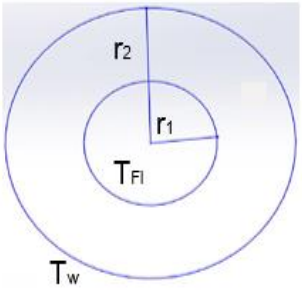


Fig. 6. The diameters of heat exchanger pipe.

$$Q_{ex} = Q_{Fl} - \frac{\Delta T}{Q_{cnd_pi} + Q_{conv_pi} + Q_{conv_pi_in}} \quad (22)$$

$$Q_{cnd_pi} = \frac{2\pi * L * kpmid}{ln(\frac{r1}{r2})} * (T_{FL} - T_{amb}) \quad (23)$$

[Heat loss by conduction in the pipe material]

$$Q_{cnv_pi} = h_{amb}*2\pi *r2*L*(T_{Fl} - T_W) \quad (24)$$

[Heat loss by convection of the pipe's outside layer]

$$Q_{conv_pi_in} = h*Fl*2\pi*r_1*L*(T_{FL} - T_W) \quad (25)$$

Energy of Heat exchanger (Q_{ex})

$$Q_{ex} = \varepsilon_{g*}\alpha_{PV*} S*A_{PV} - [\varepsilon g*\sigma_{Ag}*(T_g^4 - T_{amb}^4) + \frac{\Delta T}{\frac{1}{(h_{amb*}A_g)}} + \frac{Q_{sun*}\eta_{ref*}e^{[\beta(T_{PV}-T_{ref})]}}{\alpha_{PV}}] - [\frac{\Delta T* K_{Al}*A_{Al}}{b_{Al}} + h_{amb}*A_{Al}*(T_{Al} - T_{amb}) + K_{gl}*\frac{A_{gl}}{bgl}*(T_{gl} - T_{Al})] - [\frac{\Delta T*K_{HS}*A_{HS}}{L} + h_{cont_air*}A_{Al}*(T_{Al} - T_{cont_air})] - [h_{cont_air*}A_{HS*}(T_{HS} - T_{cont_air}) + K_{arc}*A*(T_{arc} - T_{amb})] - [\frac{2\pi*L*K_{Pi_mid}}{ln(\frac{r1}{r2})}*(T_{Fl} - T_{amb}) + h_{amb}*2\pi*r2\,(T_{Fl} - T_{amb}) + h*Fl*2\pi*r1*L*(T_{Fl} - T_W)] \quad (26)$$

To complete the calculation we need to find h_{Fl}. The most important step in heat convection calculations is the determination of the appropriate heat transfer coefficient. The higher the fluid velocity is, the higher the heat transfer coefficient will be.

$$h_{Fl} = \frac{Nu*K}{D} \quad (27)$$

[Reynolds number]

$$Re = \frac{\rho*Fl_v*D}{\mu} \quad (28)$$

When the value of the Reynolds number for pipe flow is less than 2100, the flow is streamlined and regular and is called laminar. Above Re = 2100, the flow is highly chaotic and irregular and is said to be turbulent.

The Prandtl number is defined as

$$Pr = \frac{\mu*Cp}{K} \quad (29)$$

For Laminar Flow in tubes, the following correlation applies:

$$Nu = 3.66 + \frac{0.0668*\left(\frac{D}{L}\right)Re*Pr}{1+0.004*\left[\left(\frac{D}{L}\right)Re*Pr\right]^{2/3}} \quad (30)$$

For Turbulent Flow in tubes, we have

$$Nu = 0.023 * Re^{0.8}\ pr^n \quad (31)$$

where n = 0.4 for heating and n = 0.3 for cooling.

2.6 Heat transfer from the heat exchanger to the water [11], [12].

$$Q_w = \frac{\Delta T}{Q_{cnd_Cp}+R_{conv_Cp}+R_{conv_Cp_in}} \quad (32)$$

[Energy transfer from the exchanger to the water in the tank]

$$Q_{cnd_Cp} = \frac{2\pi*L*K_{Cp_mid}}{ln(\frac{r_1}{r_2})}(T_{Fl} - T_W) \quad (33)$$

[Heat loss by conduction by copper pipe material]

$$Q_{conv_Cp} = hW*2\pi*r_2*L*(T_{Fl} - T_W) \quad (34)$$

[Heat loss by convection by the outside layer of the copper pipe copper pipe]

$$Q_{conv_Cp_in} = h*Fl_2 * \pi * r_{1*} L*(T_{Fl} - Tw) \quad (35)$$

$$Q_W = \left[\frac{2\pi*L*K_{Cp_mid}}{ln(\frac{r_1}{r_2})} + h\mathbf{w}*2\pi*r_2*\mathbf{L} + h_{Fl}*2\pi*r_1*\right]*(T_F - T_w) \quad \mathbf{(36)}$$

Figure 7 shows the diagram of the experimental setup.

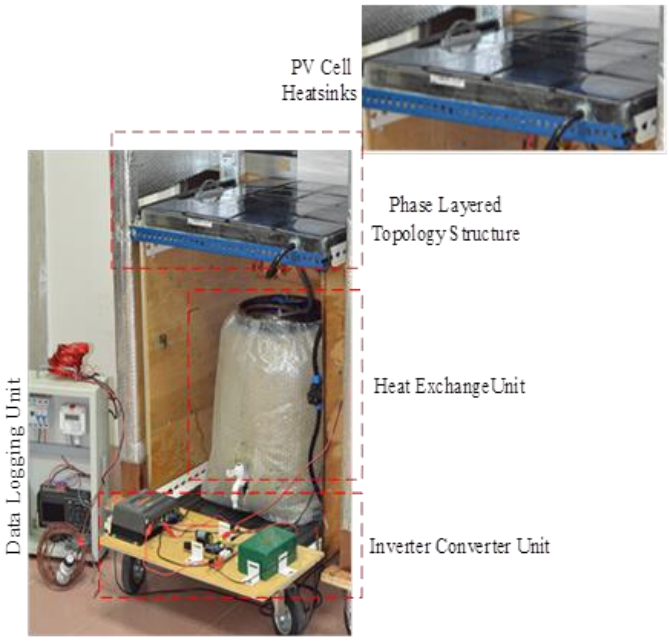


Fig. 7. Proposed System with Data Logger and Charge Controller.

3 Experimental Verification

This experiment investigates the thermal energy transfer in the PVT system to identify the system behaviour according to the solar irradiation since the heat transfer of the system layers, in this case, depending solely in the irradiation. Also, the solar panel temperature is important to know which affect the electrical output power and lead to reduce the efficiency [5]. However, water is employed in the thermal container without any circulation as a start in this experiment.

The pyranometer is a device that used to measure solar irradiance on a flat surface which can measure the solar radiation flux density (W/m2). The pyranometer is directly connected to the data logger to accurately track the solar irradiation.

The data logger is an electronic device which records data over time or in relation to a location with a sensor. The frequency of capturing data can be set from 1 sec to minutes' range. The duration of the capturing data can be set as the user desired from minutes to hours. For this particular case, the data logger was set to capture the data every 10 seconds for 3 hours. The data obtained was saved in a USB drive which was placed in the data logger and later transferred to the computer for analysis.

The thermocouple is a sensor which used to measure the ambient temperature in conjunction with recording the irradiance of Sun at the same time. These data, irradiance of Sun and ambient temperature were saved in the same thumb drive and later transferred to a computer for analysis.

In this simulation, MATLAB software was employed for further analyzing the data obtained and to calculate the heat transfer of the PVT and the efficiency in relation to the solar irradiance and ambient temperature.

3 Results and discussion

The data that has been taking from the temperature sensors and the pyranometer, later on, be used by MATLAB to be further analyzed. The Figures below are the outputs of this experiment and the simulation. Figure 8 shows the solar radiation used in the experimental portion of the research.

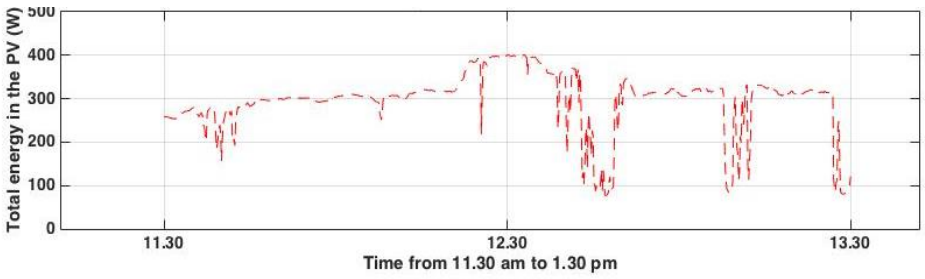


Fig. 8. Solar radiation.

Figure 9 indicates that the behaviour of the temperature in each layer depending solely on the solar radiation as shown in

Figure1. However, the surface of the thermal aluminum plate is bent and deform because of the heat generated while welding the Heatsinks so it's not symmetry with the solar panel which leads to some heat loss also the thermal glue in between which has 2% loss and that explain the gap in between the thermal aluminum plate and the PV panel.

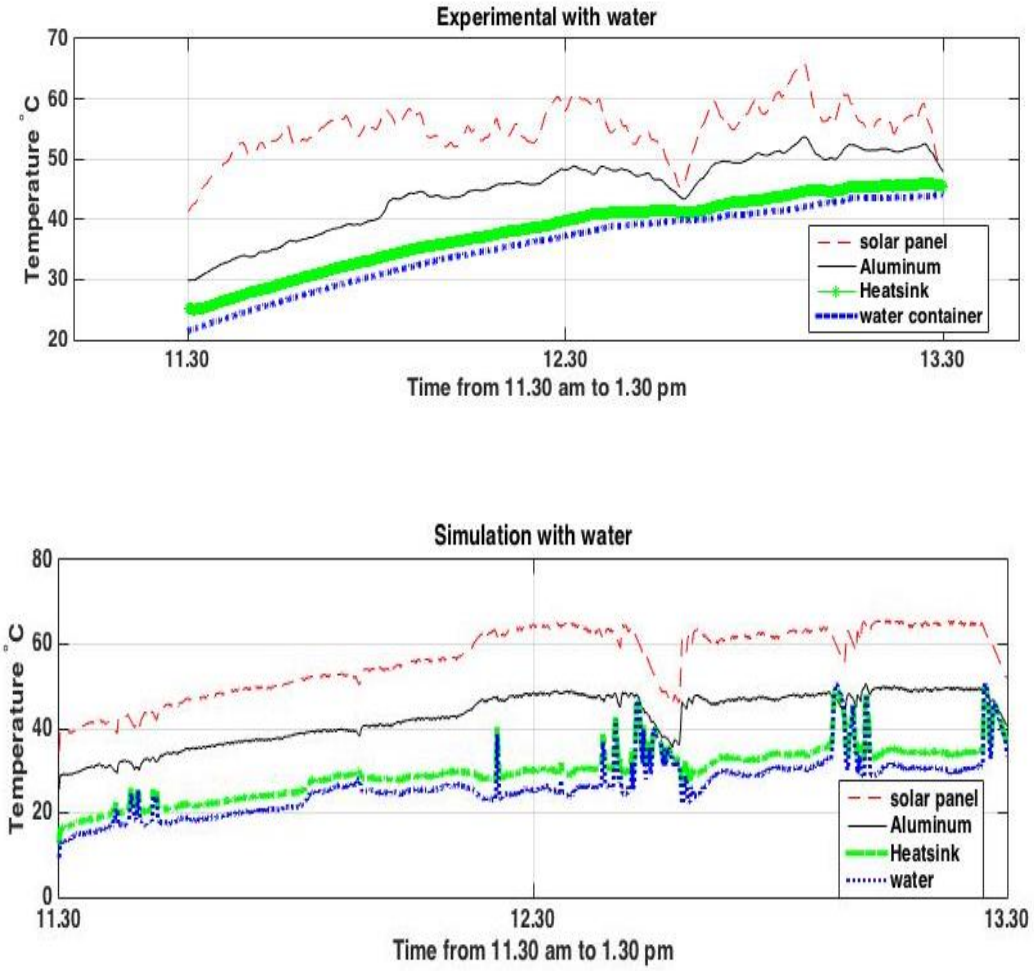


Fig. 9. Simulation and experimental of PV/T layers heat transfer.

Heat is characterized as the type of energy that is exchanged between two systems by ideals of a temperature contrast. Figure 9 shows the thermal energy be transferred by radiation from the sun to the PV. The thermal energy is rising in some points which indicate the PV is gaining energy and reached around 220W.

Figure 10 shows a comparison between experimental and simulation analysis of each layer's temperature in the PVT system. The layers in sequence solar panel, aluminum thermal plate, heat sink and water in the container. Figure 10 shows that the aluminum, heatsink and water container temperature are very much alike, hence confirm the mathematical modelling of the system. There are slight different which requires further enhancement of the mathematical model.

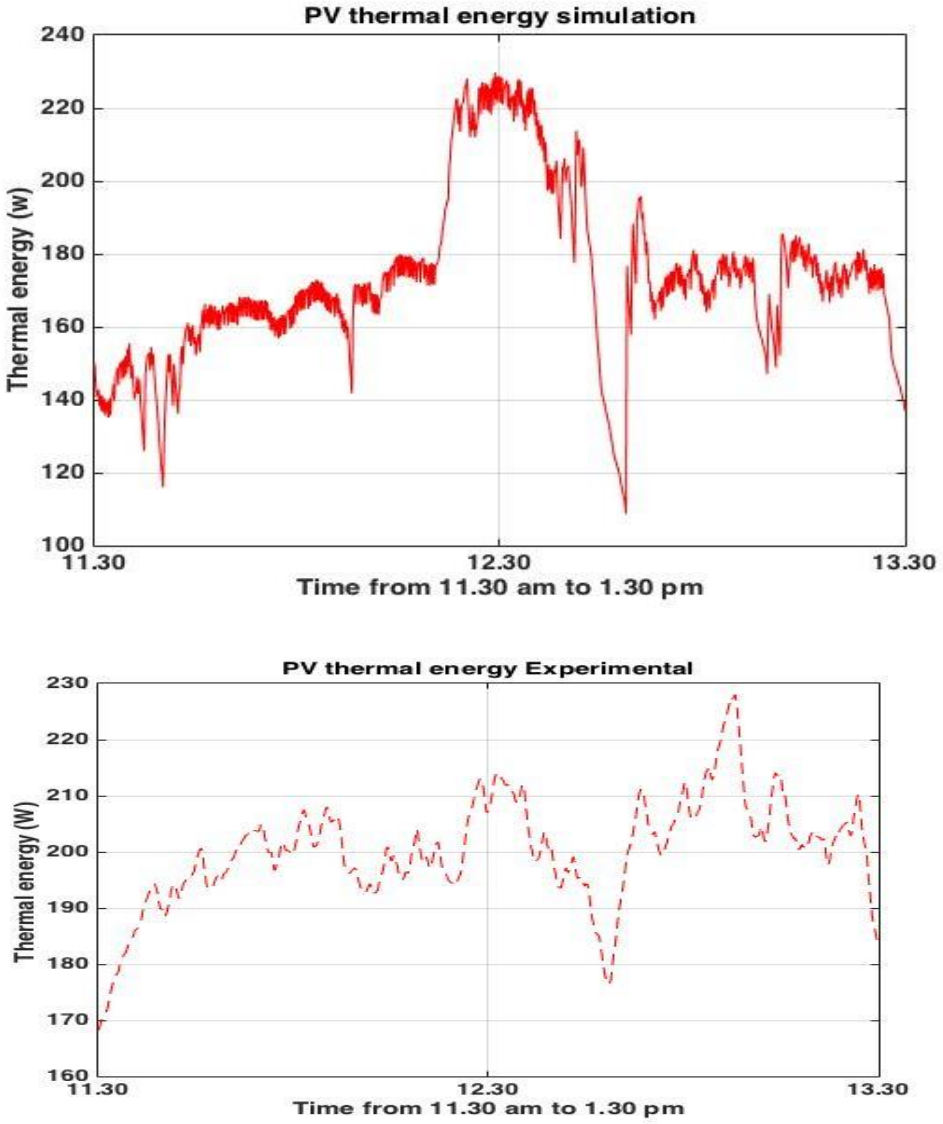


Fig. 10. Simulation and experimental of thermal energy.

Noticing a drop of the thermal energy between 12 pm to 13 pm, that's can be explained as the panel cooling down by losing heat to the other layer of the PVT system which is the thermal plate. Moreover, the thermal plate reached a maximum energy of 300 W result of the interaction between the PV and the thermal plate. Spontaneously, heat flows from a hotter body to a colder one. This heat transfer process between the PV panel and the thermal plate called conduction since there are two plates attached to each other. The drop in some points can be explained that

the thermal energy is transferred out of the plate to the Heatsinks under the plate.

The graph shows the different energy level for each layer, the thermal energy from the photovoltaic will be transferred to the water while travelling between each layer it can be seen that there will be a certain amount of energy lost due to convection and conduction between layers as shown in Figure 11. The total heat loss of the system can be calculated by comparing the thermal energy of the PV shown in 2.1 to the thermal energy of the water shown in 2.7. From the calculation below, it can be seen that 16.2% of the thermal energy of the PV has been captured as a useful energy. The mathematical modelling and the simulation of the system can show where the improvement of the system in terms of thermal and electrical efficiency is needed.

$$\frac{68 - 57}{68} X\ 100 = 16.2\ \%$$

In general, the electrical efficiency of PV will drop 0.4% per ℃ when the temperature of PV is above 27 ℃. According to an article published by civic solar [13], [14] heat can reduce electrical output efficiency by 10-25%, thereby removing the thermal energy of the system the electrical efficiency can be improved. It can be inferred that by capturing more thermal energy the electrical efficiency of the system can be improved.

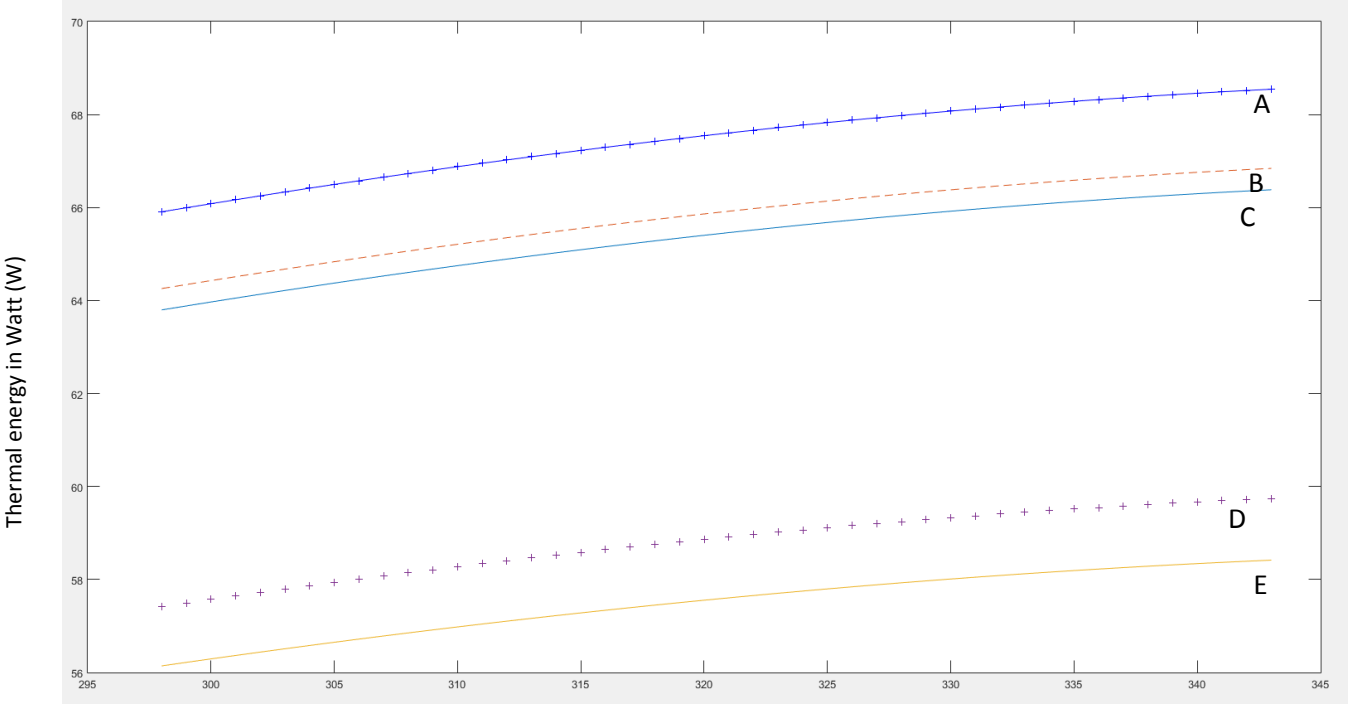


Fig. 11. Thermal energy simulation of the proposed PVT system.

- A: Thermal energy of the photovoltaic system
- B: Thermal energy of Aluminum plate
- C: Thermal energy of Heat Sink
- D: Thermal energy of Heat exchanger

- E: Thermal energy of water

4 Conclusion

The sensible and viable use of solar energy is a critical way which can manage the worldwide vitality crisis at present. Photovoltaic (PV) cell, which changes over sun radiation to electricity, with no structure for mechanical thermal interlink. So the study on enhancing the productivity of solar panel is exceptionally essential. This paper showed the thermal response of the PVT system layers and how much the solar panel can absorb heats when the temperature rises. Finding a way to make the thermal energy transfer faster in each layer can help to improve the efficiency of electrical and thermal output, hence fast heat transfer can maintain a steady temperature. With this knowledge, a design can be produced to improve the efficiency of solar panels that operate in non-optimal conditions. However, this study will be continued to employ a nanofluid to improve furthermore the heat transfer in the PVT system.

References

[1] Owusu, P. and Asumadu-Sarkodie, S. (2016). *A review of renewable energy sources, sustainability issues and climate change mitigation*. Cogent Engineering, 3(1)

[2] R. N. Schock, A. Adegbululgbe, J. Fenhann, I. Konstantinaviciute, W. Moomaw, H. B. Nimir, B. Schlamadinger, C. Turner, Y. Uchiyama, N. Wamukonya, X. Zhang, O. R. Davidson, P. R. Bosch, R. Dave, and U. Kingdom, "Energy Supply," 2007.

[3] Akadiri, P., Chinyio, E. and Olomolaiye, P. (2012). Design of A Sustainable Building: *A Conceptual Framework for Implementing Sustainability in the Building Sector*. Buildings, 2(2), pp.126-152.

[4] Kumar Moluguri, N., Rama Murthy, C. and Harshavardhan, V. (2016). Solar Energy System and Design - Review. Materials Today: Proceedings, 3(10), pp.3637-3645.

[5] Cooper, P. (1972). Some factors affecting the absorption of solar radiation in solar stills. Solar Energy, 13(4), pp.373-381.

[6] Hilbert, S., Hänggi, P. and Dunkel, J. (2014). Thermodynamic laws in isolated systems. Physical Review E, 90(6).

[7] Lotfi, A. (2014). Numerical Analysis of Heat Transfer for Cooling of Photovoltaic Cells. PAMM, 14(1), pp.501-502.

[8] Hammami, M., Torretti, S., Grimaccia, F. and Grandi, G. (2017). Thermal and Performance Analysis of a Photovoltaic Module with an Integrated Energy Storage System. Applied Sciences, 7(11), p.1107.

[9] Ventola, L., Chiavazzo, E., Calignano, F., Manfredi, D. and Asinari, P. (2014). Heat Transfer Enhancement by Finned Heat Sinks with Micro-structured Roughness. Journal of Physics: Conference Series, 494, p.012009.

[10] Zhou, X., Li, X., Cheng, K. and Huai, X. (2018). Numerical Study of Heat Transfer Enhancement of Nano Liquid-Metal Fluid Forced Convection in Circular Tube. Journal of Heat Transfer, 140(8), p.081901.

[11] Baliga, B. and Azrak, R. (1986). *Laminar Fully Developed Flow and Heat Transfer in Triangular Plate-Fin Ducts*. Journal of Heat Transfer, 108(1), p.24.

[12] Sharma, A. and Cogley, A. (1982). *Numerical Techniques in Radiative Heat Transfer for General, Scatterin*g, Plane-Parallel Media. Numerical Heat Transfer, Part B: Fundamentals, 5(1), pp.21-38.

[13] CivicSolar, Inc. (2018). *How Does Heat Affect Solar Panel Efficiencies?* [online] Available at: https://www.civicsolar.com/support/installer/articles/how-does-heat-affect-solar-panel-efficiencies.

[14] King, D., Kratochvil, J. and Boyson, W. (2018). *Temperature Coefficients for PV Modules and Arrays: MeasurementMethods, Difficulties, and Results. Sandia National Laboratories*.

6 Appendix

Table 8: Parameters in the modelling

εg	Emissivity (glass)	0.95	dimensionless
αpv	Absorption (PV)	0.75	dimensionless
Apv	Area (PV)	0.2485	m2
σ	Boltzmann Constant	1.38E-23	J/K
Ag	Area (Glass)	0.2485	m2
Tg	Temp. (Glass)	298	K
Tamb	Temp. (Ambient)	298	K
Wv	Wind Speed	0	m/s
hamb	Heat Transfer Coe.	8.55	W/m2k
ηref	reference efficiency	0.15	dimensionless
β	Volumetric Therm. Expansion	0.0034	K^-1
Tpv	Temp. (PV)	298	K
R_Al	Thermal Resistance of Al	9.06339E-05	K/W
b_Al	Thickness of Al	0.005	m
K_Al	Thermal Cond. Of Al	222	W/mK
A_Al	Area of Alum. Plate	0.2485	m2
T_Al	Temp. (Al Plate)	298	K
K_TP	Thermal Cond. Of Therm. Paste	5	W/mK
A_TP	Area of Therm. Paste	0.2485	m2
B_TP	Thickness of Therm. Paste	0.001	m
T_TP	Temp. of Therm. Paste	298	K
T_HS	Heat Sink Temp	298	K
K_HS	Heat Sink Conductivity	222	W/mK
A_HS	Heat Sink Area	0.2485	m2
L_HS	Length of Heat Sink Fins	0.047	m
h_cont_air	Thermal Cond. Of Air in Container	0.024	W/mK
A_HS	Area of Heat Sink	0.2485	m2
T_cont_air	Temp. Of Air in Container	298	K
K_arc	Conductivity of Acrylic	0.2	W/mK
A_arc	Area of Acrylic	0.2485	m2
T_arc	Temp. of Acrylic	298	K
Kpmid	Thermal Cond. Of Pipe (nylon)	0.25	W/mK
r1	Inner Diameter nylon tube	0.01	m
r2	Outer Diameter nylon tube	0.012	m
T_Fl	Fluid Temp	350	K
T_W	Water Temp	298	K
L	Length of Nylon Pipe	1	m
K_CP_mid	Thermal Cond. Of Pipe (Copper)	386	W/mK

r1_CP	Inner Diameter copper tube	0.01	m
r2_CP	Outer Diameter copper tube	0.012	m
L_CP	Length of Copper Pipe	2	m
h_W	Thermal Cond. of Water in Container	0.6	W/mK
h_Fl	Thermal Cond. Of Fluid	0.6	W/mK

Table 9: Nomenclature and subscripts.

Nomenclature	
ΔT	Temperature difference (k)
A	Surface area (m^2)
Nu	Nusselt number (dimensionless)
Pr	Prandtl number (dimensionless)
Re	Reynolds number (dimensionless)
Q	Heat transfer (w)
Q_{RHS}	Resistive transfer energy of the Heatsink
S	Solar radiation (w/m^2)
K	Thermal conductivity (w/mK)
L	Length (m)
T	Temperature (K)
T_{Fl}	Temperature of fluid (K)
Tw	Temperature of water (K)
b	Thickness (m)
h	Heat transfer coefficient (w/m^2K)
Fl_V	The fluid velocity l*(m/s)
D	Characteristic length (m)
Cp	The heat capacity (J/kg °C)
Q_{ex}	Energy of Heat exchanger
Q_{cnd_pi}	Energy of pipe by conduction
Q_{cnd_cont}	Energy of container by conduction
Q_{RAl}	Resistive transfer energy of the Aluminium
Q_W	Energy of water
Q_{conv_Cp}	Convection energy of copper pipe
Q_{HS}	Energy of Heatsinks
Q_{elec}	Electrical Energy
Q_{PV}	Energy of PV

Greek symbols	
β	Volumetric thermal expansion coefficient (dimensionless)
α	Absorption coefficient (dimensionless)
μ	The viscosity (Pa.s) = $(N \cdot s)/m^2$ = $kg/(s \cdot m)$
ε	Emissivity (dimensionless)
σ	Boltzmann constant (w/mk)
ρ	density (kg/m^3)
εg	(Emissivity of glass)
Subscript	
Al	Aluminum thermal plate
HS	Heatsink
Fl	Fluid in the container
w	Water in the tank
arc	Acrylic thermal container
PV	PV panel
amb	Ambient
Wv	Wind velocity
Pi	Rubber pipe
Cp	Copper pipe
gl	Glue
conv	Convection
cnd	Conduction
g	Glass
ex	Heat exchanger
mid	Middle part of the pipe
in	Inside the pipe
A_g	Surface area of glass

EURECA 2018 – Conference Paper
Paper number PG09

External Cathodic Protection For Above Ground Storage Tank Using Controlled Sacrificial Anodes

Muhammad N. Jawad, Ghafour Amouzad Mahdiraji[*]*, Mohammad Taghi Hajibeigy*

School of Engineering, Taylor's University, 47500, Subang Jaya, Selangor, Malaysia

[*]Email: ghafouram@gmail.com

Abstract

Controlled Sacrificial anode cathodic protection and coating give the optimum protection against corrosion for tank grounded sandy soil. This project presents an experimental study for designing controlled sacrificial anode system for the external tank bottom where the tank is placed above ground. Two sets of water tanks have been designed one with conventional cathodic protection (CP) that the current flow from the anode and the potential of the tank set naturally without any control system. The second tank is designed with a manual current control system includes a variable resistor. The potential of the conventional tank compared to the reference point shows – 1510 mV with a current flow of 252 µA when the system is in ON state, which offers a potential of around – 992 mV in OFF condition. This potential is higher than the minimum potential requirement of – 850 mV for normal corrosion control, thereby, it results a short anode lifetime. In the second tank, the proposed current control system is set to produce more optimum potential and current flow of – 1079 mV and 101.1 µA in ON condition, which results an OFF potential of – 867 mV, a voltage just above the minimum potential requirement. The results show by using the proposed controlled cathodic system, the anode lifetime can be increased by about 2.5 times compared to the conventional method, which can significantly improve the conventional corrosion control system.

Keywords: Corrosion, Corrosion control system, Cathodic protection, Anode current control, Petroleum tank, Sacrificial anodes

1. Introduction

Cathodic protection (CP) is a technique for protecting the metals from corrosion in the environment such as in soil or water. CP is used to protect buried pipelines, ships, marine's jetties, tanks and any metals in contact with soil and water. The main function of using CP is to reduce the potential difference between cathodes and anodes. This reduction process is due to the polarization of cathodes to the potential of most active anodes [1].

The main reason for the corrosion is electrochemical reaction driven by a potential difference between anodes and cathodes, which have contact with the electrolyte such as soils or water. Cathodic protection process can be applied to any metallic structure, which has contact with the electrolyte. The main benefit to apply cathodic protection is to protect steel structures immersed in water or buried in soil. CP can be used to protect reinforced concrete from corrosion. The corrosion process means the removal of electrons of the metal and the consumption of those electrons by some other reduction and reaction such as oxygen or water. Corrosion is one of the most important problems encountered by the owners and operators of the underground, offshore, submerged and other metallic structures exposed to an electrolyte. If the corrosion is not controlled, it can lead to large costs in repairing or facility replacement. Even great costs can be incurred from environmental damage, injuries and fatalities. The corrosion costs billion USD annually, so CP system can lead to reducing corrosion rate and saving costs [2]. However, traditional sacrificial anodes arrangements cannot perform optimum as the current flow in the system varies inherently without any control, which leads to losing the anodes material very fast, thereby, a short anode lifetime. In addition, the uncontrolled potential will cause high potential in some area of the tank, which causes non-uniform current distribution. This phenomenon also can cause of hydrogen evolution at the cathode surface that may cause mechanical failures. Furthermore, it may cause coating disbondment, which in that case, the CP current will not reach to the tank metal to perform proper protection [6].

This study proposing a new cathodic protection that offers full current and voltage control of CP system. This is performed by placing appropriate variable resistors in the cathodic system to optimize the current and voltage in the CP system. A comparative experiment is designed including two water tanks first, conventional CP system without any current control and second, a tank with the proposed CP system. The detail of CP criteria and methodology are presented in Section 2 and 3, respectively. Comparison of the two tanks performance is analyzed in Section 4 followed by Conclusion section.

2. Criteria for Cathodic Protection

Although the basic theory of CP is simple (impressing DC current on a structure to reduce the corrosion rate), the obvious question that arises is: How do achieve adequate protection on a buried or immersed structure? The answer to this question is that various criteria have been developed over the years that permit a determination of whether adequate protection is being achieved. Those criteria are more common by measuring the potential between the structure and the electrolyte. The measurement permits a rapid and reliable determination of the degree of protection attained. Basically, potential criteria are used to evaluate the changes in structure potential with respect to the electrolyte that is caused by CP current flowing to the structure

from surrounding soil or water. The potential of a structure at a given location is commonly referred to as the structure-to-electrolyte potential. The structure-to-electrolyte potential can be measured by measuring the voltage between the structure and a reference electrode placed in the electrolyte directly over the structure. The most common reference electrode used for this purpose is a copper/copper sulfate reference electrode (CSE). The potential is referred to as an "ON" potential when the measurement is taking after applying CP system. The "OFF" potential is referred to as an "instant OFF" potential or polarized potential if the measurement is made after the interruption of all current sources. This is when the measurement of the structure-to-electrolyte potential made immediately following the interruption of the cathodic protection power source [3].

Following shows the criteria for CP system [4]:

- Criteria 1: At least a potential of – 850 mV is required when cathodic protection applied with respect to copper/copper sulfate reference electrode. The voltage drops across the structure-to-electrolyte must be considered in this case.
- Criteria 2: At least – 850 mV as polarized potential with respect to copper/copper sulfate reference electrode is required.
- Criteria 3: A minimum polarized potential of 100 mV should exist between copper/copper sulfate reference electrode and structure. In addition, when the third criteria are chosen, the natural potential (E_{CORR}) of the structure should be measured in order to ensure the structure is protected when the polarized potential of 100 mV between copper/copper sulfate reference electrode and structure has been measured to satisfy this criteria, based on the following equation:

$$\Delta_{E100} = E_{OFF} - E_{CORR} \quad (1)$$

Δ_{E100} is the minimum polarized potential of 100 mV, E_{OFF} is OFF potential of the structure, and E_{CORR} is the natural potential of the structure or corrosion potential. If the structure meets one of the above criteria it means that the structure is cathodically protected. But under some conditions these criteria may not be sufficient such as the presence of sulphite bacteria or high temperature and dissimilar metals [5].

3. Materials and Method

This section introduces the main procedure of experimental and designing of the controlled sacrificial anode system for the external tank. One of the important element is to take care of the potential difference between the cathode and the environment. Therefore, the potential difference value need to be measured with respect to a reference electrode. Cathodic potential criteria are used as a recommended minimum potential requirement for controlling external corrosion of water tank.

This study is designed with two tanks both with the same dimensions of 20 cm diameter and 22 cm height made of a similar material of mild steel. Both tanks are manually painted with epoxy of Samurai paint which it can be used to protect steel from fast corrosion and provide a smooth uniform surface. Both tanks are made in the same time and painted in the same day. The tanks are designed to be placed above ground at the sandy soil as shown in Figure 1.

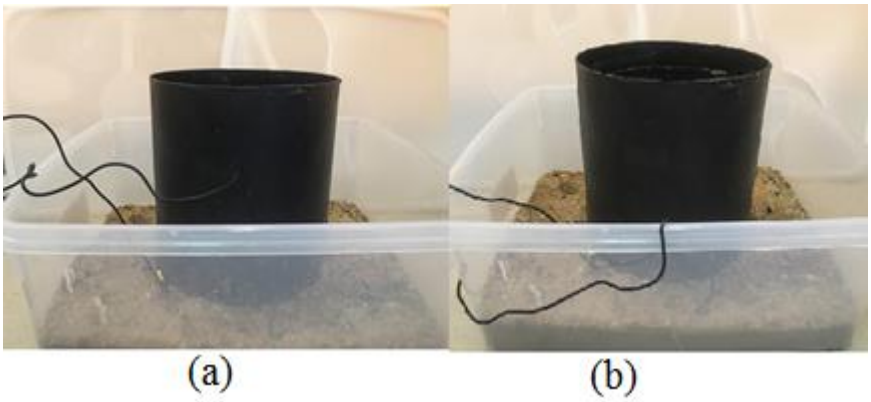


Figure 1 Two tanks (a) tank with conventional cathodic protection, (b) tank with controlled cathodic protection

Both tanks have cathodic protection system. One has a conventional cathodic protection and the other one has a new protection that is proposed in this study. The cathodic material used in both tanks is ribbon Magnesium anodes installed in sandy soil under the tank. For the design chemometric factors for external protection, 2 cm gap is chosen between the ribbon anodes and the tank metal to make sure that the current reaches the entire bottom. This establishes a setup similar to the ground-bed technique.

In the tank with conventional CP system, the current flows from the anode via the soil to the tank body naturally, the CP system in the second tank is proposed to be controlled using a variable resistor. Figures 2 and 3 show the electrical circuit of the conventional and the proposed tank system, respectively. In order to measure the current, switch S1 should be at 'ON' condition while switch S2 at 'OFF' condition. In this case, the current will flow from the anode to tank bottom and the ammeter will measure the CP current. Thereby, the tank to soil potential in 'ON' condition is measured in reference to the copper/copper sulfate electrode. The porous plug of the electrode is in contact with the soil, the negative voltmeter lead is connected to the reference electrode while the positive lead is connected to the tank test point as shown in Figures 2 and 3. The 'OFF' potential will be measured when switch S1 at 'OFF' condition. A similar approach for current control has been used previously for pipeline system [10], but never used for tank application. In the proposed method, the current flow is controlled based on the minimum desired potential of the tank body.

In this study, a protection period of 60 years is considered for tank bottom protection for the conventional protection method. Considering this protection period, the anode volume is calculated with the length of 9 cm, 15 cm, and 9 cm and a separation of 6.92 cm that are connected in parallel [9]. In the proposed system, a variable resistor is used to control the anode current flow to the tank. The variable resistor will be connected in series to the anode circuit as shown in Figure 3. By using the variable resistor, the minimum cathodic protection current can be achieved. The current can be measured when switch S1 is closed and switch S2 is opened.

It is very important to measure the current output of the anodes and to control that current in order to achieve the optimum level of protection with low consumption of anodes, which will lead to increase lifetime of the cathodic material and to prevent excessive electrical stress on the coating. The potential set point should not exceed – 0.9 V versus a saturated copper/copper sulfate reference electrode. In this study, all the measurements of voltage and current and adjustment of the variable resistor are manually done. All these advantages expected to be achieved by using the new arrangement of installing the controlled ribbon Magnesium anodes. The measurement for both tanks has been recorded in four different points, Point A to D, on the ground around the tank bottom as illustrated in Figure 4.

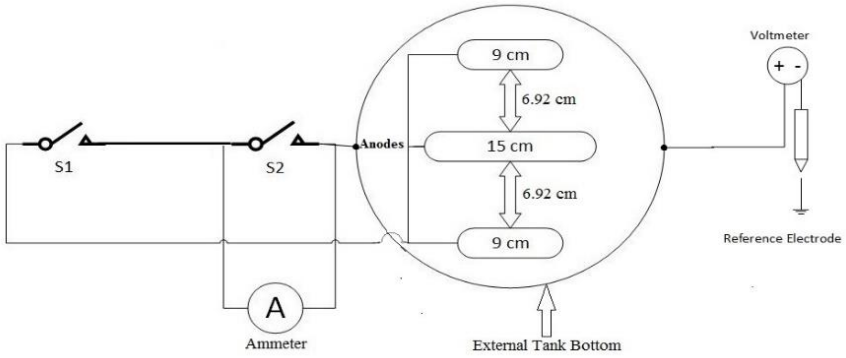


Figure 2 Electrically connection of uncontrolled external protection tank bottom.

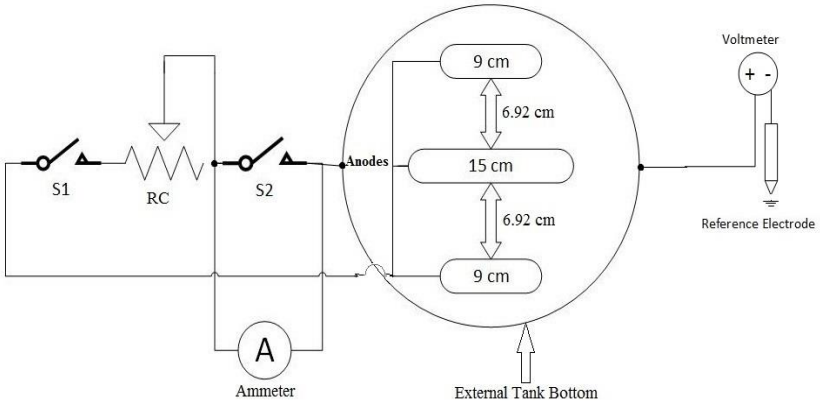


Figure 3 Electrically connection of controlled external protection tank bottom

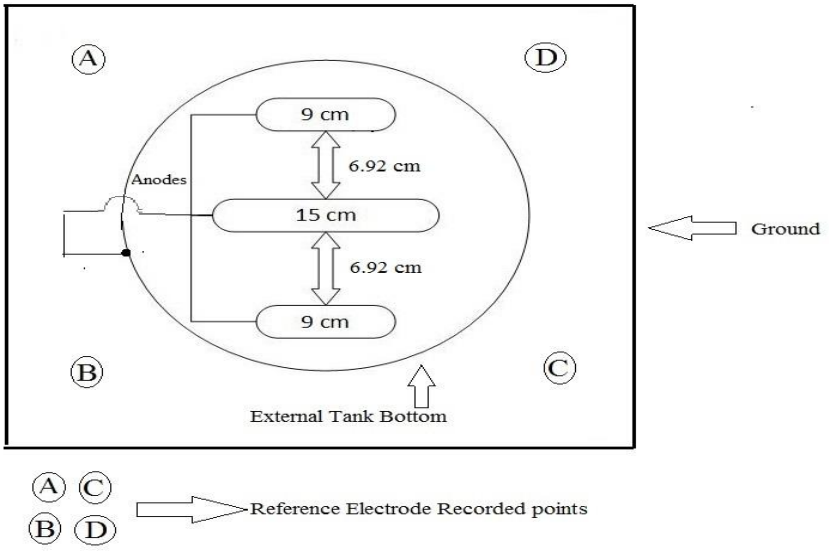


Figure 4 The measurement points for controlled and uncontrolled CP system

4. Results

Initially, the CP system may need less current compared to later time as its age increases, because coating's resistance of the tank decreases greatly with age and directly affects structure-to-electrolyte resistance. Controlling output current of sacrificial anodes will lead to have an optimized system by providing a number of benefits to anode lift time, and uniform potential distribution. The high potential can cause hydrogen evolution at the cathode surface that may cause coating mechanical failures, which required additional current to be supply to exposed area in the tank. furthermore, hydrogen evolution may cause electrical shielding due to coating disbondment, which in that case, the CP current will not reach to the tank metal to perform proper protection.

Conventional CP System

The potential of the external tank bottom for the conventional CP system has been measured with respect to copper/copper sulfate reference electrode as the results shown in Table 1. The measurements have been done for four different places around the tank bottom (as shown in Figure 4) to see if all the tank bottom are protected as well as the voltage distribution uniformity across the tank bottom. The results show that the potential in OFF condition for all the four measurement points are above the minimum voltage requirement for protection, which is – 850 mV. Thereby, the protection across the tank bottom is expected. However, there is no way to control and optimize the amount of this potential as the amount of current delivers by the anodes changes naturally depending on the soil resistivity and coating efficiency.

Table 1 External potential and current in ON condition and potential in OFF condition measured at four points for the tank with conventional CP system

Condition	**ON Potential**		**OFF Potential**
Reading Points	**External Potential [V]**	**External Current (μA)**	**External Potential [V]**
A	– 1.510	252	– 0.992
B	– 1.448	246	– 1.048
C	– 1.474	252	– 1.039
D	– 1.510	246	– 1.034

CP System with Current Control

For external tank bottom-controlled system, the potential has been measured by using copper/copper sulfate at four measurement points about the same area as what is measured for the conventional tank. Table 2 shows the result of potential for ON and OFF condition and the current flow for ON condition for the four points. It should be noted that the results presented in Table 2 is recorded after the variable resistor is set to the optimum condition to achieve the minimum protection potential and current. The results show that all the four measurement points are considered as protected as the potential in OFF condition is above – 850 mV.

Comparing the results in the conventional method and the proposed method, although both of them satisfy the protection requirement, however, the current flow in the proposed method is minimized to 101.1 μA, which is about 2.5 times less than what the conventional system is consumed. Thereby, it is expected that the tank with controlled CP system can has a lifetime of about 2.5 times greater than the conventional CP system.

Table 2 External potential and current in ON condition and potential in OFF condition measured at four points for the tank with conventional CP system

Condition	**ON Potential**		**OFF Potential**
Reading Points	**External Potential (V)**	**External Current (μA)**	**External Potential (V)**
A	– 1.079	101.1	– 0.867
B	– 1.078	101.1	– 0.868
C	– 1.079	101.1	– 0.870
D	– 1.078	101.1	– 0.868

5. Conclusion

This study proposed a new CP system that offers full control of the sacrificial anodes current in order to optimize performance of the CP system. In this study, two experimental water tanks one with conventional CP system without any current control and the other one with current control system. Both systems have provided full protection across the tank bottom. However, the proposed CP system with current control has provided the minimum external potential required for protection. The results show that the current consumed by the proposed CP system is about 2.5 times lower than the conventional system. With such current control optimization, the lifetime of the anodes in controlled CP system can be increased by 2.5 times compared to the conventional system. The proposed CP system optimization would be very useful for oil and gas industries as well as water supplier companies.

Acknowledgement

The authors would like to acknowledge the Flagship Grant No. TUFR/2017/001/05 that partially supported this project.

References

[1] Kenneth S. Okiongbo, Edirin, 2012, Investigation of Soil.

[2] Rana. Hussain, 2012, Cathodic Protection of Storage Tank.

[3] Peabody A, W. "Control of pipeline corrosion." Criteria for cathodic protection, 24-25. NACE Press, 1967.

[4] Peabody A, W. "Control of pipeline corrosion." Criteria for cathodic protection, 2nd edition, 49-55. NACE Press, 1967.

[5] Winstion Revie.r. " Oil and Gas Pipelines: Integrity and Safety." Microbiologically Influenced Corrosion, 2nd edition, 394. Wiley, 2015.
[6] Peabody A, W. "Control of pipeline corrosion." Over- Protection of Coated Lines, 2nd edition, 28. NACE Press, 1967.
[7] Peabody A, W. "Control of pipeline corrosion." Cathodic Protection with Impressed Current 23-24, 2nd edition, NACE Press, 1967.
[8] API Recommended practice 575, "Cathodic Protection of underwater structure,

American Petroleum Institute, Second Edition (1997).
[9] Nace international 'Cathodic protection specialist course manual' CP4, (2011).
[10] Guri E.Nustad , (2003) . Resistor Controlled Cathodic Protection for Stainless Steels in Chlorinated Seawater. Online access at (https://forcetechnology.com/-/media/force-technology-media/div-5-energy-materials-and-welding/reports-whitepapers articles/resistor-controlled-cathodic-protection-for-stainless-steels-in-chlorinated-seawater.pdf)

EURECA 2018 – Conference Paper
Paper number PG10

Investigation On Polarization Losses In A Direct Carbon Fuel Cell Operating On Oil Palm Mesocarp Fiber Biochar

Nida Jafri[1], Yoon Li Wan[1], Wong Wai Yin[2], Veena Doshi, Cheah Kean How[3]*

[1]Discipline of Chemical Engineering, School of Engineering, Taylor's University Malaysia, No.1 Jalan Taylors, 47500, Subang Jaya, Selangor DE, Malaysia.

[2]Fuel Cell Institute, University Kebangsaan Malaysia, 43600 UKM Bangi, Selangor DE, Malaysia.

[3]School of Engineering and Physical Sciences, Heriot-Watt University Malaysia, 62200 Putrajaya, Malaysia.

*Corresponding Author: LiWan.Yoon@taylors.edu.my

Abstract

The performance of a solid oxide electrolyte based Direct Carbon Fuel Cell (DCFC) was evaluated based on the existing mathematical model of Tafel equation which was used to simulate the performance of the DCFC. The model takes into account the electrochemical reaction dynamics, mass-transfer and the electrode processes. The fuel sources were derived from Oil Palm Mesocarp Fibre (OPMF) and commercially available Activated Carbon (AC). The power density for OPMF biochar was superior (2.82 $mWcm^{-2}$) than that obtained for AC fuel (2.11 $mWcm^{-2}$). The main polarization losses occurring in the cell components were determined. The results indicated that the anode activation polarization was the major potential loss occurring in the circuit. The activation polarization loss was the highest for AC, followed by untreated mesocarp fibre biochar & alkali treated mesocarp fibre biochar. The results showed that the pre-treatment of the biochar was able to increase the surface oxygen functional groups while reducing the ash content. These factors are believed to have contributed towards increasing the electrochemical reaction area and reducing the activation polarization loss. The novelty of the work lies in the pre-treatment process which makes the biochar a superior fuel over commercially available AC fuel.

Keywords: Direct carbon fuel cell, solid oxide electrolyte, Oil palm mesocarp fibre, Biochar, Modelling, Polarization losses.

1. Introduction

DCFC has recently gained importance because it presents an attractive way of biomass utilization for clean energy production. The DCFC includes three main components: anode, cathode and electrolyte. The overall process of generating electricity by a DCFC system is relatively simple compared to other fuel cell technologies and does not require expensive preparation of any gaseous fuel.

Nomenclature

E^o	theoretical potential
F’	faraday’s constant (96,487 C mol^{-1})
G	gibbs-free energy (J)
J	current density (Am^{-2})
j_0	exchange current density (Am^{-2})
*j*c	current density in the electrode phase (Am^{-2})
j_{lim}	limiting current density (Am^{-2})
*j*s	current density in the electrolyte phase (Am^{-2})
*j*0	exchange current density (Am^{-2})
I	current (A)
n	numbers of electrical charge transfer in an electrochemical reaction (mole)
P_{CO2}	partial pressure of CO_2 in gas phase (Pa)
P_{O2}	partial pressure of O_2 in gas phase (Pa)
R	resistance ($\Omega\ m^2$)
R’	gas constant (8.314 J mol K^{-1})
*R*c	resistance in the electrode phase ($\Omega\ m^2$)
*R*ct	charge transfer resistance ($\Omega\ m^2$)
*R*ce	resistance of all components except for anode ($\Omega\ m^2$)
*R*s	resistance in the electrolyte ($\Omega\ m^2$)

T	temperature (K)
V_{cell}	cell voltage (V)
V_N	open circuit voltage (V)
V_0	open circuit voltage at standard state (V)

Greek Symbols

β	apparent charge transfer coefficient
η	polarization loss (V)
η_{act}	activation polarization (V)
η_{con}	concentration polarization (V)
η_{ohm}	ohmic polarization (V)

Superscript

act	activation
an	anode
cat	cathode
con	concentration
ohm	ohmic

This cell is an interesting system because it can use a diverse variety of fuels such as, coal, biomass, waste fuel, and all kinds of hydrocarbons. These solid fuels carry high energy densities in regards to both volumetric and mass densities [1, 2, 3].

DCFCs are categorized into the molten carbonate DCFC, the solid oxide DCFC, and the hybrid DCFC [4]. DCFC systems face issues like low power density, poor fuel supply system, and low durability. In an attempt to explain the issues, researchers have led experimental and numerical research into DCFCs mainly exploring the anode mechanism for

the DCFC and DCFC modeling. Modeling research can be a useful tool to understand the reaction mechanism between the solid fuel, electrolyte, and electrode, and to improve the fuel cell system design.

In a DCFC operated on solid oxide based- electrolyte, the major voltage losses occurring are due to (i) activation polarization at the anode (ii) activation polarization at the cathode (iii) ohmic polarization (iv) concentration polarization at the anode (v) concentration polarization at the cathode [5, 6, 7]. The activation polarization and concentration polarization depend largely on the anode interlayer thickness. Using a thick anode interlayer would allow for more active sites of the three phase boundary (TPB), thereby decreasing the voltage loss due to activation polarization at the anode [8, 9]. This also helps in increasing the mechanical strength of the anode interlayer However, the process can result in issues related to transportation limitation where the fuel gas can hardly penetrate the thick anode interlayer.

Liu et al. [10] studied on simulating the influence of packed-bed anode on DCFC cell performance. They reported that the low reactivity of graphite fuel was caused by high anode activation polarization. The reaction rate of solid carbon with operating temperature was considered as one of the important parameters. The carbon particle size together with the height of the packed bed largely affected the cell performance as these parameters were linked to the effective surface area and transportation path.

Zhang et al. [11] studied the polarization losses in a packed-bed anode DCFC with a molten carbonate electrolyte and graphite. They reported that the polarization losses were a result of electrode kinetics, ionic resistance of the cell components, and transportation process of reactants and products.

Zhang et al. [12] worked on the numerical model of a fluidized bed electrode DCFC. They reported that the activation polarization and ohmic polarization were the main dominant losses over concentration polarization.

The modeling studies done so far on the DCFC have primarily considered pure solid carbon, such as graphite, carbon black, and activated carbon, because of the irregular properties of coal and biomass. Thus, the surface properties of coal, which forms the triple-phase boundary between the electrode and the molten electrolyte (where the electrochemical reaction takes place), such as the existence of oxygen-functional groups, surface pores, and ash content, were not taken into account in the simulation of anode polarization. Although, these surface properties have played an important role in the DCFC experimental research [13-15].

Chemical pre-treatment using either acid or alkaline has been found as a potential technique for lignin degradation [16]. According to Damisa et al., [17] removal of lignocellulose crosslinks leads in the increase of porosity and internal surface area of the lignocellulose by decreasing the crystallinity and degree of polymerization. Pre-treatment

using NaOH has shown to facilitate the breakdown of lignin in order to increase the surface area prior to pyrolysis. In a recent study, empty fruit bunch was treated with three different concentrations of NaOH (i.e. 5 wt%, 15 wt% and 25 wt %) and the pre-treatment lead to the swelling of lignocellulosic compound, thus increasing the surface area [18]. In addition, the pretreatment of the biomass and upgrading of the bio-oil have improved its quality by reducing or even eliminating undesired products.

The objective of this study is to model the polarization losses for the DCFC single cell. The purpose is to determine and simulate the various polarizations in relation to the experimentally obtained power densities. A commercial software MATLAB^{TM} is adopted for this purpose.

2. Experimental method

2.1 Material preparation

The Oil Palm Mesocarp Fibre (OPMF) samples used in this study was collected from an oil palm plant in Sri Ulu Langat in Dengkil, Selangor, Malaysia. The Activated Carbon (AC) samples were procured commercially from Sigma Aldrich (M) Sdn Bhd. OPMF sample was washed with distilled water to remove dirt particles and other unwanted materials. It was then placed in an oven (UN75, Memmert, USA) at 105 ºC for 24 h for moisture removal (ASTM D2867-09). After the drying process, OPMF biomass was grinded with the help of a grinder (JK-SG-160, KGC Scientific) and sieved into a particle size of 0.5-2.0 mm using a sieve shaker (RX-812-1, Tyler). The OPMF samples were kept in a desiccator prior to usage. Alkali pre-treatment with 2.0M NaOH (99.9 %) was then carried out on 20 g of oven dried OPMF samples. The samples were stirred at 100 °C for 24 h before being washed with distilled water [18]. Pre-treated and washed OPMF samples were dried again in the oven (UN75, Memmert, USA) following the same ASTM D2867-09 standard at 105 ºC for 24 h for moisture removal. The OPMF sample was then subjected to pyrolysis at 500 °C to be converted to fine biochar. The research involved using two types of fuel derived from OPMF biomass and one commercially available AC fuel. The nomenclature and descriptions are summarized in Table 1.

2.2 Chemical analysis

All fuel samples were chemically characterized by means of elemental analysis (C, H, N, S and O wt% content) in a CHNS elemental analyzer (Vario MACRO Cube CHNS, Germany). Proximate analysis (volatile matter, ash and moisture content) was carried out using thermogravimetric analyser (STA 6000, Perkin Elmer) and done with the help of carrier gas nitrogen (N_2) at a flow rate of 20 ml min^{-1}.

Table 1: Nomenclature of different fuels used in the study

Fuel	Description
AC	Activated Carbon, commercially supplied by Sigma Aldrich used without any pre- treatment or pyrolysis.
UMF	Untreated OPMF pyrolyzed at 500 °C

MF_2.0	OPMF pre-treated with 2.0M NaOH and pyrolyzed at 500 °C

2.3 DCFC fabrication and electrochemical testing

An optimal design of the configuration of DCFC reactor was developed to evaluate the activity of the fuels under different conditions, as detailed in Fig. 1. The DCFC setup was supplied with commercial button cell from Ningbo SOFCMAN Energy**,** Technology Ltd., Co. China. The cathode of the DCFC was made up of Lanthanum strontium manganite *(*LSM*)* which is an oxide ceramic having a thickness of 25 µm. The anode material was made up of Nickel-Yttria stabilized zirconia (Ni-YSZ) having a thickness of 400 µm which provided the conductive surface for effective oxygen anions transportation. The electrolyte was made up of ceramic material, Yttria-stabilized zirconia (YSZ) with a thickness of 15 µm. Silver wires were used as electrical contacts on the electrodes. The electrochemical cell units were placed between the two ceramic cylindrical tubes.

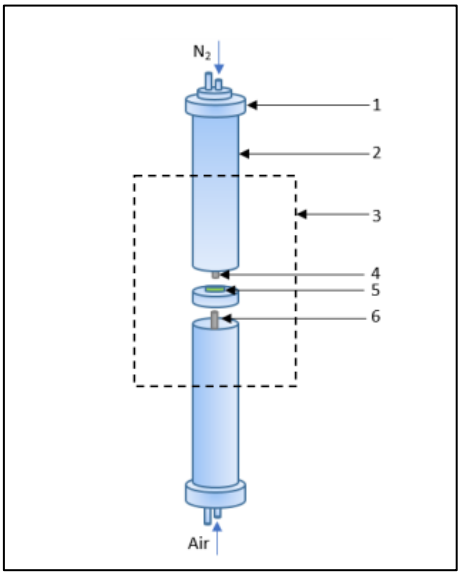


Fig. 1: Setup of Direct Carbon Fuel Cell. 1: flange, 2: ceramic tube, 3: furnace, 4: anode current collector, 5: biochar placed on top of button cell, 6: cathode current collector.

Fig. 1 shows the design and the schematic components of the DCFC. 0.1 g of OPMF biochar was placed on the cathode side of the button cell (cell surface area of 1.743 cm^2). The vertical furnace was set to run to a temperature of 800 °C with a ramping rate of 10 °C min^{-1} and the temperature was maintained at 800 °C for 2 hrs. Nitrogen gas was supplied into the system through the anode and cathode side at 200 and 600 ml min^{-1} respectively. The gas supply at the cathode end was switched with oxygen about 10 min before the system reached 800 °C with a flow rate of 600 ml min^{-1}. The electrochemical testing was performed at a temperature of 800 °C after the Open Circuit Potential (OCP) reached a steady state. The anode side was purged with N_2 gas (constant flow rate of 200 ml min^{-1}, STP) and the anode side was purged with O_2 gas (constant flow rate of 600 ml min^{-1}, STP). The OCP was recorded during

the experimental run using a Potentiostat (model Gamry Interface 1000). The electrochemical impedance spectroscopy (EIS) of the DCFC was calculated at a temperature of 800°C with a ramping 10 °C min^{-1} in the frequency range of 100 KHz to 0.1 Hz. The current-voltage (*I-V*) curve of the run was evaluated through electrochemical workstation with a scan rate of 10 mV s^{-1} [19, 20].

3. Mathematical model

The DCFC comprises of an anode, cathode, and a solid oxide based electrolyte that exists between the two electrodes as shown in Fig. 1. OPMF biochar and AC are employed as the fuels which are supplied to the electrolyte at the anode. In this work, Yttria-stabilized zirconia (YSZ) was used as the electrolyte.

The elemental carbon in the fuel contains high energy density and is oxidized electrochemically with the following reactions occurring in the electrodes [21, 22]:

Anode: $C + 2O^{2-} \rightarrow CO_2 + 4e^-$ (1)

Cathode: $O_2 + 4e^- \rightarrow 2O^{2-}$ (2)

Overall: $C + O_2 \rightarrow CO_2$ $E^o = 1.02$ V (3)

Solid carbon is directly introduced into the anode compartment and electrochemically oxidized to CO_2 at high temperature generating electrical power. The overall cell reaction is given by Eq. (3).

MATLAB 2014b software is used to simulate the electrochemical reaction of the DCFC. Numerical modeling is conducted to analyze the electrochemical reactions in the DCFC system.

The electrochemical potential mainly comprises of four components: Open Circuit Voltage (OCV), activation polarization, ohmic polarization, and concentration polarization. Therefore, the voltage of the electrochemical reaction is written can be written as shown in Eq. (4).

$$E_{Cell} = E_N - \eta_{act} - \eta_{ohm} - \eta_{con} \quad (4)$$

3.1.Open circuit voltage

The open circuit voltage V_N is calculated by Nernst equation and is expressed as-

$$V_N = V^0 + \frac{R\prime T}{nF\prime}\ln\left(\frac{p_{o_2} p_{co_2,cat}^2}{p_{co_2,an}^3}\right) \quad (5)$$

$$V^0 = \frac{\Delta G^0}{nF\prime} \quad (6)$$

3.2.Activation polarization

When current flows through a cell circuit, the voltage decreases. This drop in voltage is called as the polarization loss η, and is caused by different phenomenon which includes charge transfer η_{act}, ion concentration gradient η_{con}, and circuit Ohmic resistance η_{ohm}. Therefore, the cell voltage η_{cell} is calculated by subtracting these polarization losses from the open circuit voltage

$$V_{cell} = V_N - (\eta_{act,an} + \eta_{act,cat} + \eta_{ohm} + \eta_{con,an} + \eta_{con,cat}) \quad (7)$$

In order to calculate the activation polarizations for anode and cathode, respectively, the general Bulter–Volmer equation was used-

$$j = j_o\{\exp\left(\beta \frac{nF'\eta_{act}}{R'T}\right) - \exp\left(-(1-\beta)\frac{nF'\eta_{act}}{R'T}\right)\} \quad (8)$$

The apparent charge transfer-coefficient β value is usually assigned as 0.5 for fuel cells [24]. The anode exchange current density $j_{0,an}$ is related to the charge transfer resistance R_{ct} and is given by-

$$j_{0,an} = \frac{R'T}{nF'R_{ct}} \quad (9)$$

and

$$R_{ct} = 30.79 + 1.48 * \exp(-\frac{T}{28.58}) \quad (10)$$

$$j_{o,cat} = j^o_{o,cat}(p_{co_2})^{r_1}(p_{o_2})^{r_2} \quad (11)$$

3.3. Ohmic polarization

The current flowing through the electrolyte phase is expressed as-

$$j_{s,i} = j(1 - 2\pi(\frac{x}{D_c - 1})) \quad (12)$$

and the current flowing through the electrode phase is-

$$j_{c,i} = 2\pi j(\frac{x}{D_c - 1}) \quad (13)$$

The resistances occurring in the other parts is expressed as-

$$R_{ce} = \frac{A}{p_{o_2}^{0.67}}\exp\left(\frac{B}{T}\right) + C_R + D\exp(\frac{f}{T}) \quad (14)$$

where p_{O2} equals the partial pressure of oxygen at the cathode surface, C_R is a constant referring to the Ohmic resistance of the contacts, D is a kinetic parameter and is proportional to the electrolyte amount of the matrix. The complete Ohmic polarization can be written as-

$$\eta_{ohm} = jR_{ce} + \eta_{ohm,an} \quad (15)$$

$$\eta_{ohm,an} = \sum_{i=1}^{N_s} j_{s,i}R_{s,i} + \sum_{i=1}^{N_s} j_{c,i}R_{c,i} \quad (16)$$

4. Results and discussion

4.1. Proximate and ultimate analysis of fuels

Table 2 shows the results of proximate and ultimate analysis of all the fuels used in the study. As evident from the table, it can be seen that the volatile matter content increases from AC to UMF and MF_2.0 sample. The AC sample has the highest ash and sulfur contents, which could result in performance degradation in the DCFC. In contrast, MF_2.0 has the highest volatile matter and oxygen content, which is anticipated to contribute to a higher reactivity of this fuel which leads to to a higher carbon conversion and better electrochemical performance [23, 24].

Table 2. Proximate and ultimate analysis of the fuels used in the study

	MF_2.0	**UMF**	**AC**
Elemental analysis			
C (wt %)	73.07	77.40	96.42
H (wt %)	1.36	1.97	0.61
N (wt %)	6.77	2.96	0.00
S (wt %)	0.05	0.24	0.61
O (wt %)	18.73	17.43	0.20
Proximate analysis			
Ash (wt %)	0.35	0.42	2.16
Moisture (wt %)	7.85	4.69	5.29
Volatile matter (wt%)	75.90	44.19	-

4.2. DCFC performance

Table 3 depicts the impact of carbon type on DCFC performance, in terms of cell voltage, developed current and power density outputs at 800 °C. The best performance was shown by the MF_2.0 sample, which displays a maximum power density of 2.82 $mWcm^{-2}$ at 800 °C. Under the same conditions, power density values are obtained with the UMF and AC samples, following the order MF_2.0 > UMF > AC.

Regarding the influence of fuel properties on the DCFC performance, it is well established that sulfur and ash have a negative impact on the electrochemical performance. On the other hand, the oxygen content and volatile matter contribute towards enhanced power outputs. It is reported that about 2–6 wt% sulfur in carbon fuels results in the degradation of cell performance due to anode corrosion [23]. Similarly, it is reported that at higher over-potentials, a sharp drop in the developed current is observed. This occurs due to the passivation of electrodes by dissolved coal ashes [25].

Summarizing the above points, it can be said that the inferior DCFC performance of AC sample in comparison to the MF_2.0 sample, could be attributed to its higher impurities content and volatile matter content. On the other hand, MF_2.0 sample exhibits better performance, due to its low ash content (particularly sulphur content) and high volatile matter content.

Table. 3. Obtained experimental values in DCFC for the fuels & their respective ash content

Samples	Op. Temp. (°C)	OCP (V)	Current Density (mAm^{-2})	Power Density ($mWcm^{-2}$)	Ash (%)
Raw_OPMF	-	-	-	-	8.58
AC	800	0.82	3.44	2.11	2.16
UMF	800	0.81	2.87	2.32	0.42
MF_2.0	800	0.82	6	2.82	0.35

4.3. Activation polarization

The activation polarization loss is dominant at low current densities and is an irreversible voltage loss where the reactants must overcome the activation energy levels to start the electrochemical reaction [26]. After the activation energy level is crossed, the electrons are transported at the interface between the electrode, solid fuel and the electrolyte.

The anode and cathode activation polarizations are shown in Fig. 2(a) and (b), respectively. The value of anode activation polarization is higher than cathode activation polarization under similar temperature and current density range. The activation polarization occurring in the cell circuit accounts for the most serious loss. The loss is the highest in the case of the AC fuel, followed by UMF fuel and MF_2.0 fuel as seen in Fig. 2(a).

The current flowing across both the electrodes is denoted by the sum of the forward and reverse current flows [27]. This current flowing in both the directions is referred to as exchange current density and is considered as the major factor affecting the activation loss. This exchange current density directly influences the electrochemical reactions and cell performance. The performance of the cell is increased when the exchange current density is higher because the activation polarization (η_{act}) has to decrease in order to satisfy the required current (j). The exchange current density increases as the cell temperature increases. The number of electrons (n) in the reaction mechanism is fixed at 4 in this study, as shown in Eqs. (1–4). The value of transfer coefficient denoted by α ranges from 0 to 1 depending on the reactive ratio between the anode and the cathode. In this study, the reactivity of both the electrodes is anticipated to be equal (α was fixed at 0.5 for both sides) [28].

It is interesting to note that the alkali-treated OPMF biochar has a higher oxygen concentration than AC and UMF fuels used in the study. The activation polarization loss is smaller for OPMF biochar as compared to the other two fuels as seen in Fig 2(a) & 2(b). It is established in literature that the presence of surface oxygen molecules improves the oxidation reaction rate of carbon [29, 22]. An increased number of oxygen functional groups may also contribute towards improving the wettability between solid carbon fuels and electrolytes, thus increasing the reaction area [30].

As shown in Fig. 2(b), the cathode activation polarization is much lower as compared to the anodic activation polarization shown in Fig. 2(a) across the whole current density range. Typically, cathodic activation polarization arises due to the flat-plate electrode and electrode material. The silver wire used as the electrode in this work carries high conductivity and acts as a good wetting material with the solid oxide electrolyte. This wetting process makes for a high number of active sites on the electrode. The oxygen gets absorbed at the electrode surface and gets dissociated at the triple-phase boundary between the silver electrode metal, gas, and solid oxide based electrolyte. This phenomenon causes higher oxide ions to be formed, and the reaction of CO_2 and oxide ions occurs near the triple-phase boundary [31]. Thus, silver shows low polarization loss and acts as a good wetting material.

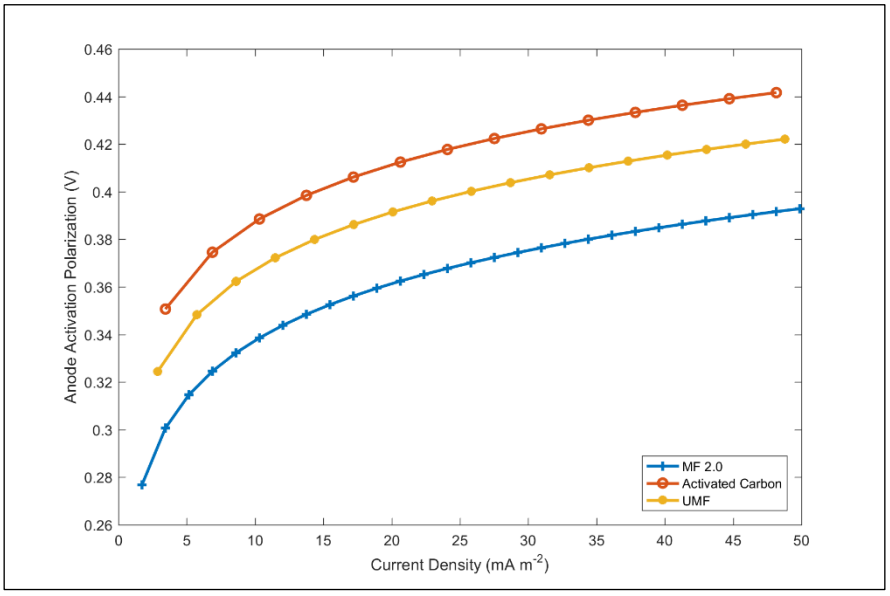


Fig. 2(a). Anode activation polarization loss vs. current density at 800 ^{o}C

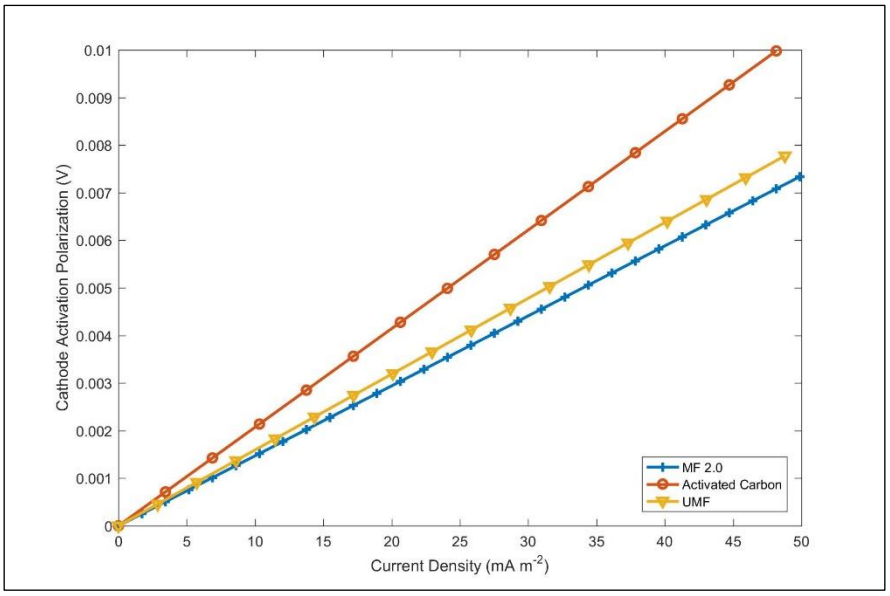


Fig. 2(b). Cathode activation polarization loss vs. current density at 800 ºC

4.4. Ohmic polarization

Ohmic polarization occurs because of the resistance to ion and electron flows in the cell [1, 26]. It is caused by the resistances inside the cell and it obeys Ohm's law. The total resistances present in the cell include the resistance in the anodic compartment (Ran) and the resistance in the cathodic compartment (Rcat). The voltage losses due to ohmic polarization for fuel cells operating on low current densities is usually small as compared to the activation polarization loss. At low current densities, the activation loss is dominated.

Fig. 3 shows the ohmic polarization of the three fuels used in the study. The results show that the ohmic polarization loss is close to the activation polarization loss of the anode and much higher than the activation polarization loss of the cathode. The highest loss is recorded for AC fuel, followed by UMF and MF_2.0 fuel. It ought to be noted that the ohmic resistance comprises of the electrolyte resistance and contact resistances between carbon particles and anode, and between carbon particles and current collectors. In a DCFC set-up, the carbon fuel itself is capable of acting as a current carrier in addition to the silver mesh used. The number of contact points between the fuel and anode along with the char conductivity can have an influence on the overall ohmic resistance [32]. It is likely that lower levels of impurities such as Si, Fe, Ca and Mg in MF_2.0 fuel in comparison to AC and UMF fuel would have contributed to the detected lower ohmic resistance for MF_2.0 by allowing better contact between fuel particles with fewer insulating phases.

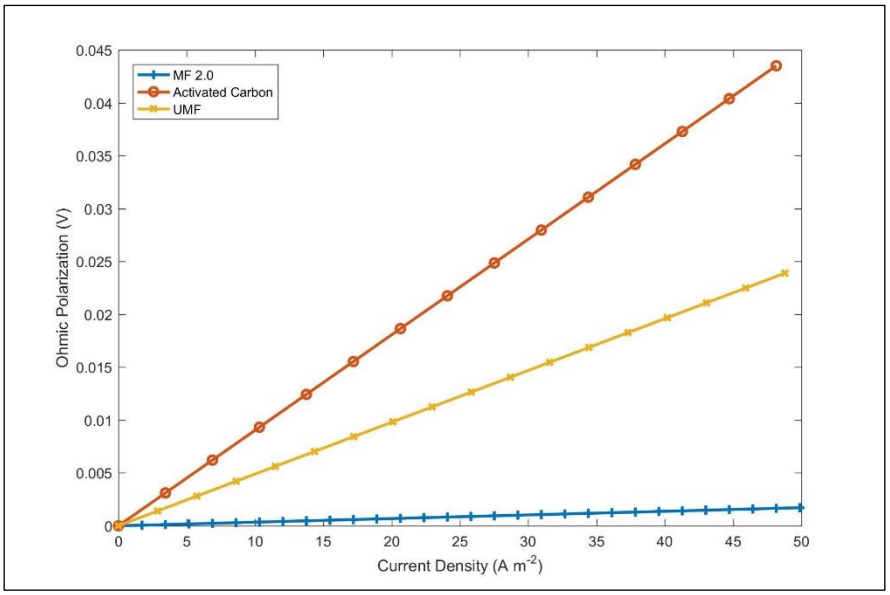


Fig. 3. Ohmic polarization loss vs. current density at 800 ^{o}C

5. Conclusions

The performance of a DCFC was studied. Some concluding observations from the investigation are given below.

- The major voltage loss in the DCFC occurs due to the activation polarization for all the three carbon fuel samples. However, the highest loss was recorded for AC fuel and the lowest loss for MF_2.0 fuel.
- The MF_2.0 fuel has a higher oxygen concentration than AC and UMF fuels used in the study. The presence of surface oxygen molecules improves the oxidation reaction rate of carbon. An increased number of oxygen functional groups may also contribute towards improving the wettability between solid carbon fuels and electrolytes, thus increasing the reaction area and reducing the activation polarization loss.
- The cathode activation polarization is much lower as compared to the anodic activation polarization for the fuel samples. This is due to the silver wire used as the electrode in this work which carries high conductivity and acts as a good wetting material with the solid oxide electrolyte.
- The ohmic polarization loss is close to the activation polarization loss of the anode and much higher than the activation polarization loss of the cathode. The highest loss is recorded for AC fuel, followed by UMF and MF_2.0 fuel.
- It is likely that lower levels of impurities such as Si, Fe, Ca and Mg in MF_2.0 fuel in comparison to AC and UMF fuel would have contributed to the detected lower ohmic resistance for MF_2.0 by allowing better contact between fuel particles with fewer insulating phases.

- The alkali pre-treatment of the OPMF biomass was able to reduce the ash content while increasing the oxygen content. These factors are likely to reduce the voltage losses occurring in the circuit.

Future work

Further experimental work is required to be done at different operating temperatures of DCFC to test the suitability of the present model at low current densities. As the polarization losses are directly dependent on the temperature, hence different range of temperatures should be explored to compare the losses occurring in the cell circuit.

References

[1] Elleuch, A., Sahraoui, M., Boussetta, A., Halouani, K.; and Li, Y. (2014). 2-D numerical modeling and experimental investigation of electrochemical mechanisms coupled with heat and mass transfer in a planar direct carbon fuel cell. *J. Power Sources.* 248, 44–57.

[2] Elleuch, A., Yu, J., Boussetta, A., Halouani, K.; and Li, Y. (2013). Electrochemical oxidation of graphite in an intermediate temperature direct carbon fuel cell based on two-phase electrolyte. *Int. J. Hydrogen Energy.* 38, 8514–8523.

[3] Ahn, S., Eom, S., Rhie, Y., Sung, Y., Moon, C., Choi, G.; and Kim, D. (2013). Application of refuse fuels in a direct carbon fuel cell system, *Energy.* 51, 447–456.

[4] Giddey, S., Badwal, S.P.S., Kulkarni, A.; and Munnings, C. (2012). A comprehensive review of direct carbon fuel cell technology. *Prog. Energ. Combust*. 38, 360–399.

[5] Zhao, F.; and A.V. Virkar. (1996). Dependence of polarization in anode-supported solid oxide fuel cells on various cell parameters. *Journal of Power Sources*, 141(1): p. 79-95.

[6] Gong, W., et al. (2014). Parameter identification of an SOFC model with an efficient, adaptive differential evolution algorithm. *International Journal of Hydrogen Energy*, 39(10): p. 5083-5096.

[7] Zhu, W., Ding, D.; and Xia, C. (2008). Enhancement in Three-Phase Boundary of SOFC Electrodes by an Ion Impregnation Method: A Modelling Comparison. *Electrochemical and Solid-State Letters*, 11(6): p. B83-B86.

[8] Dusastre, V.; and J.A. Kilner. (1999). Optimisation of composite cathodes for intermediate temperature SOFC applications. *Solid State Ionics*, 126(1–2): p. 163-174.

[9] Fukunaga, H., et al., (2002). The relationship between overpotential and the three phase boundary length. *Solid State Ionics*, 86–88, Part 2(0): p. 1179-1185.

[10] Liu, Q., Tian, Y., Xia, C., Thompson, L.T., Liang, B.; and Li, Y. (2008) Modeling and simulation of a single direct carbon fuel cell. *J. Power Sources.* 185, 1022–1029.

[11] Zhang, H., Chen, L., Zhang, J.; and Chen, J. (2014). Performance analysis of a direct carbon fuel cell with molten carbonate electrolyte. *Energy*. 68, 292–300.

[12] Zhang, J., Jiang, X., Piao, G., Yang, H.; and Zhong, Z. (2015). Simulation of a fluidized bed electrode direct carbon fuel cell. *Int. J. Hydrogen Energy*. 40, 3321–3331.

[13] Li, C., Lee, E., Kim, Y.; and Lee, D. (2014). Enhancing triple-phase boundary at fuel electrode of direct carbon fuel cell using a fuel-filled ceria-coated porous anode. *Int. J. Hydrogen Energy*. 39, 17314–17321.

[14] Li, C., Yi, H., Jalalabadi, T.; and Lee, D. (2015). Thermal decomposition of alkane hydrocarbons inside a porous Ni anode for fuel supply of direct carbon fuel cell: effects of morphology and crystallinity of carbon. *J. Power Sources.* 294, 284–291.

[15] Li, C., Yi, H.; and Lee, D. (2016). On-demand supply of slurry fuels to a porous anode of a direct carbon fuel cell: attempts to increase fuel-anode contact and realize long-term operation. *J. Power Sources* 309, 99–107.

[16] Mosier, N., Wyman, C., Dale, B., Elander, R., Lee, Y. Y.; and Holtzapple, M. et al. (2005). Features of promising technologies for pre-treatment of lignocellulosic biomass. *Bioresource Technology*. 96, 673-86.

[17] Damisa, D., Ameh, J. B.; and Umoh, V. J. (2008). Effect of chemical pre-treatment of some lignocellulosic wastes on the recovery of cellulase from Aspergillus niger AH3 mutant. *African Journal of Biotechnology*. 7:2444-50.

[18] Amin, N. A. S., Misson, M., Haron, R., Kamaroddin, M. F. A., Omar, W. N. NW.; and Haw, K. G. (2012). Bio-oils and diesel fuel derived from alkaline treated empty fruit bunch. *International Journal of biomass & renewables*. 1, 6 – 14.

[19] Elleuch, A., Boussetta, A., Yu, J., Halouani, K.; and Li, Y. (2013). Experimental investigation of direct carbon fuel cell fuelled by almond shell biochar: Part I. Physicochemical characterization of the biochar fuel and cell performance examination. *International Journal of Hydrogen Energy.* 38, 16590-16604.

[20] Li, X., Zhu, Z., Marco, R.D., Bradley, J.; and Dicks, A. (2010). Evaluation of raw coals as fuels for direct carbon fuel cells. *Journal of Power Sources*. 195(13), 4051-4058.

[21] Hackett, G.A., Zondlo, J.W.; and Svensson, R. (2007). Evaluation of carbon material for use in direct carbon fuel cell. *Journal of Power Sources.* 168, 111-118.

[22] Li, X., Zhu, Z., Chen, J., Marco de, R., Dicks, A., Bradley, J.; and Lu, G. (2009). Surface modification of carbon fuels for direct carbon fuel cells. *Journal of Power Sources. 186,* 1-9.

[23] Cherepy, N.J., Krueger, R., Fiet, K.J., Jankowski, A.F.; and Cooper, J.F. (2005). Direct conversion of carbon fuels in a molten carbonate fuel cell, *J. Electrochem. Soc.* 152, A80–7.

[24] Kaklidis, N., Kyriakou, V., Garagounis, I., Arenillas, A., Menendez, J.A., Marnellos, G.E.; and Konsolakis, M. (2014). Effect of carbon type on the performance of a direct or hybrid carbon solid oxide fuel cell. *RSC Adv.* 4, 18792–18800.

[25] Vutetakis, D.G., Skidmore, D.R.; and Byker, H.J. (1987) Electrochemical oxidation of molten carbonate-coal slurries. *J. Electrochem. Soc.* 134, 3027–3035.

[26] Elleuch, A., Boussetta, A.; and Halouani, K. (2012). Analytical modeling of electrochemical mechanisms in CO_2 and CO/CO_2 producing direct carbon fuel cell. *J. Electroanal. Chem.* 668, 99–106.

[27] Hosoi, T., Yonekura, T., Sunada, K.; and Sasaki, K. (2015). Exchange current density of SOFC electrodes: theoretical relations and partial pressure dependencies rate-determined by electrochemical reactions. *J. Electrochem. Soc.* 162, F136–F152.

[28] Chan, S.H., Low, C.F.; and Ding, O.L. (2002). Energy analysis of simple solid-oxide fuel-cell power systems. *J. Power Sources.* 103, 188–200.

[29] Li, X., Zhu, Z.H., Marco, R.D., Dicks, A., Bradley, J., Liu, S.; and Lu, G.Q. (2008). Investigation of chemical and electrochemical reactions mechanisms in a direct carbon fuel cell using olive wood charcoal as sustainable fuel. *Ind. Eng. Chem. Res*. 47, 9670–9677.

[30] Hao, W., He, X.; and Mi, Y. (2014). Achieving high performance in intermediate temperature direct carbon fuel cells with renewable carbon as a fuel source. *Appl. Energy*. 135,174–181.

[31] Nguyen, H.V.P., Kang, M., Ham, H., Choi, S., Han, J., Nam, S., Hong, E.; and Yoon, S. (2014). A new cathode for reduced-temperature molten carbonate fuel cells. *J. Electrochem. Soc*. 161, F1458–F1467.

[32] Adam, C. R., Sarbjit, G., Aniruddha, K., Sukhvinder, P.S. B., Sankar, B.; and Bradley, P. L. (2014). Direct carbon fuel cell operation on brown coal. *Applied Energy*. 120, 56–64.

EURECA 2018 – Conference Paper
Paper number PG11

Load Bearing Simulation On Lumbosacral Disc In Pre And Post-Operated Thoracic Scoliosis Patients

P. Mohankumar, Yong Leng Chuan, Anis Suhaila Shuib, Shajan Koshy*

School of Engineering, Taylor's University, Taylor's Lakeside Campus, No. 1 Jalan Taylor's, 47500, Subang Jaya, Selangor DE, Malaysia
*Corresponding Author: mohankumar.palaniswamy@sd.taylors.edu.my

Abstract

Scoliosis is a musculoskeletal disorder seen all around the world. It affects both the alignment of vertebra and disc. Scoliosis can be treated conservatively with a cast and brace or surgically with spinal instrumentation. During planning for surgical instrumentation, several factors need to be considered. Among those, biomechanical changes in the non-scoliotic vertebra and disc are important. This is vital in determining the future degenerative changes of the spine. For this reason, in this study we developed a finite element model of the lumbosacral joint using CT scan files to find the total deformation and equivalent static strain of the lumbosacral disc between pre and post-operative thoracic scoliosis patients. From our results, it is evident that there is a structural change in the vertebral alignment followed immediately after corrective surgery. The correction in alignment of scoliotic spine bring changes to the biomechanical functionality and load bearing capacity of the lumbosacral intervertebral disc before and after surgery.

Keywords: Thoracic scoliosis, Lumbosacral disc, Finite element analysis, Load, Strain.

Nomenclatures

L_5	Fifth lumbar vertebra
m	Meter
N	Newton
S_1	First sacral vertebra

Abbreviations

CDB	Coded Database
CoG	Center of Gravity
DICOM	Digital Imaging and Communications in Medicine
EES	Equivalent Elastic Strain
LoG	Line of Gravity
NIOSH	National Institute for Occupational Safety and Health
TD	Total Deformation

1. Introduction

Human vertebral column consists of 24 articulating and 9 fused vertebrae (7 cervical, 12 thoracic, 5 lumbar, 5 fused sacral and 4 fused coccyx vertebrae), which totals to 33 vertebrae. An intervertebral disc, held together by ligaments and joints, separates the column formed by the articulating vertebra with the adjacent vertebra. This result in the formation of curves during weight bearing. Scoliosis is a deformity of the vertebral column, in which the spine is abnormally twisted and curved to the sides. Globally scoliosis is one of the most common musculoskeletal disorder affecting paediatric age group with a prevalence of 2-3%. When examining the spine from back, a scoliotic spine will appear 'C' shaped (single curvature) or 'S' shaped (double curvature). It can be treated conservatively with a cast or brace or surgically with spinal instrumentation. Opting for surgical intervention depends upon various factors such as etiology, severity, cardiopulmonary involvement, Cobb's angle and age. During spinal instrumentation surgery, surgeons fuse the scoliotic vertebrae using metal implants. Since the alignment of vertebrae is affected in scoliosis, the Center of Gravity (CoG) and Line of Gravity (LoG) are also affected. In an anatomical standing posture, the CoG and LoG lies anterior to sacrum bone (S_2). Whereas, in scoliosis patients, the CoG and LoG is deviated depending on the configuration of the spine. This level of deviation can be roughly understood by measuring

the coronal balance, sagittal balance, thoracic trunk shift, thoracolumbar and lumbar sagittal alignment.

A study done by Damavandi *et al*., [1] on head and trunk mass and center of mass position estimations in able bodied and scoliotic girls concluded that the pre-operative scoliotic girls have greater pelvic forward tilt and trunk inclination compared to normal subjects. Whereas, another study done by Park *et al*., [2] on the effect of scoliosis angle on sway on center of gravity found that the whole-body balancing ability in the pre-operative scoliosis patients is significantly different from normal persons. This explains the importance of pelvic tilt, center of gravity and trunk inclination in maintaining a proper posture. In scoliosis patients, since the trunk posture is altered or shifted to one side, it in turn provides more pressure to the lumbar region on the side of scoliosis curve [3]. Using image processing [4], a study conducted by Hajizadeh *et al*., [5] on developing a 3D multibody model of the scoliotic spine with lateral bending motion for comparison of ribcage flexibility concluded that the load at lumbar joints in scoliosis model were higher when compare to the normal subjects.

2. Literature Review

Vertebral column is connected with pelvis and lower limbs forming a continuous plane for weight transmission and support for the body in bipedal gait and posture of humans. Pelvis is made up of the hip bones and sacrum. Femur bone of thigh forms an articulation with the acetabulum to form hip joint. Weight from the head, arm and trunk are passed through vertebral column and transferred to the lower limbs through sacrum and sacroiliac joint. (refer Fig. 1) Intervertebral discs play a major role in transferring load from one vertebra to other. It acts as a shock absorber.

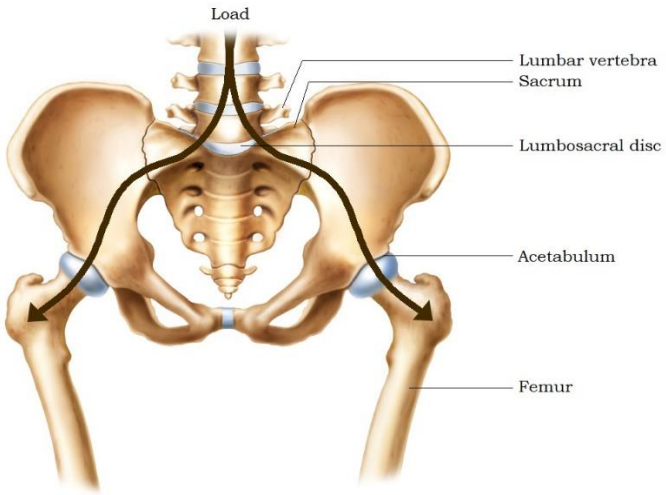


Fig. 1. Weight distribution [19].

Pressure within the center of disc is never zero, because of the pre-existing tension even when the disc is unloaded. Physical property of intervertebral disc allows it to withstand a considerable amount of load, even when the load is applied for an extended period of time. Normal intervertebral disc is an anisotropic structure [6]. National Institute for Occupational Safety and Health (NIOSH) guidelines for manual (1994) lifting concluded that the joint between fifth lumbar vertebra (L_5) and first sacral vertebra (S_1) is the joint of greatest lumbar

stress during weight lifting. Study done by Spoor *et al.* found that 20% reduction in vertical sacroiliac joint shear resulted in 70% increase in sacroiliac joint compression force [7]. In normal subjects, vertebral column is arranged linear in frontal, transverse plane and angular in sagittal plane. Although, in a scoliotic spine, vertebral column is arranged angular in all the three planes. Since it is often accompanied by some amount of lateral twist in the spine (kyphosis). When scoliosis patients undergo corrective surgery, surgeons focus on correcting the scoliosis curve (vertebrae causing scoliosis curve), implant Harrington rod made up of stainless steel or titanium along the course of the expected normal vertebral curve and screw the vertebrae to it using pedicle screws. Thus, rearranging the vertebral column to a new or normal position.

During scoliosis correction, surgeons correct the scoliosis angle by using manual pressure, implants and bone graft. Manual pressure is to adjust and correct the scoliotic curve, surgical implant is to fix the corrected vertebra in its anatomical position & prevent it from scoliotic recurrence, and bone graft is to fuse the corrected scoliotic vertebrae & heal it as a single fused vertebra. Some claim that most of the curve is reduced because of the manual pressure and on the other hand, some claim its due to the vertebral fusion and metal implants. A study done by Trobisch *et al*., [8] on postoperative trunk shift in Lenke 1 and 2 curves concluded that the postoperative trunk shift is common after surgery for adolescent idiopathic scoliosis. But it occurs only in 13.6% of patients and 65% of trunk shift is in fact iatrogenic (caused by surgeon). If the curve is corrected only by manual pressure, implants can take over the vertebral fusion. Then need for fusing the vertebrae will be a questionable debate. Even after spinal instrumentation, due to the sudden change in the configuration of spinal column, patients feel a disturbance in their balance. A study by Abreu *et al*., [9] on the influence of surgical treatment of adolescent idiopathic scoliosis on postural control supports this theory. They concluded that the scoliosis patients have a large CoP oscillation compared to age matched healthy adults. Even after surgery, oscillation is decreased on the initial 90 days. But later, it remained larger than before surgery. Also, another study done by Nohara *et al*., [10] on lumbar disc degeneration in patients with adolescent idiopathic scoliosis with spinal fusion claims that 48% of disc degeneration occurs at Lumbosacral junction (L_5-S_1) and segments adjacent to fused vertebrae has only 8% of chance. If the abnormal curve (scoliosis) leads to an altered coronal balance, sagittal balance, thoracic trunk shift, thoracolumbar and lumbar sagittal alignment, then after treating the scoliosis, these parameters should, by right return to normal or at least close to normal. This raises a query whether scoliotic vertebral fusion also affects the non-scoliotic vertebrae (vertebrae not involved in the scoliotic curve) of spine. Hence, in order to validate this, in this study, we find the total deformation and strain of the lumbosacral intervertebral disc between the pre and post operated thoracic scoliosis patients. The objectives of this study are to find whether the manual correction during corrective surgery bring any immediate changes to the structure of spine and to find whether correction in alignment of thoracic scoliotic spine bring any changes to the biomechanical functionality and load bearing capacity of the lumbosacral intervertebral disc before and after surgery.

3. Methodology

Prevalent of scoliosis is 1 to 2% in adolescence. Among those 1 to 2%, determining the patients with same side thoracic scoliosis who underwent corrective surgery is a tiresome work and the

availability of such kind of data is exceptional. Hence, this study was observational cross-sectional study. Sampling method followed was convenient sampling.

3.1. Data collection

Data collection was done at Government General Hospital, Chennai, India. Proper consent was obtained from radiology department before collecting data. Since bone fusion gets complete by 6 to 9 months [11], CT scan data of patients who underwent thoracic scoliosis correction not more than 2 months and with the age group between 10 to 20 years were selected for this study. 2 patients fulfilled the above-mentioned criteria. Radiographs were taken with patients in lying position. As during standing, patients might tilt their pelvis unknowingly. Radiographs were obtained in DICOM format. Baseline assessment like age, sex, date of surgery and date of scan were noted. Patients data are provided below. (refer Table 1).

Table 1. Patient Details.

Gender	Age	Pre-operative Scan	Date of Surgery	Post-operative Scan
M	19	12-01-2016	19-01-2016	26-02-2016
M	16	08-02-2016	26-02-2016	03-04-2016

3.2. Method

Obtained DICOM files were imported into image segmentation software Materialise, version 12.0. Two separate masks were created for bones and disc, where the fifth lumbar vertebra (L_5), sacrum and lumbosacral disc are selected, and the other parts were cropped out. Segmented images of L_5, sacrum and lumbosacral disc are then converted into a surface mesh and later into a solid volume. This solid volume is uniformly meshed with 4 node tetrahedral and maximum edge length of 2 mm. (refer Fig. 2). Meshed volume is exported to FEA solver program ANSYS version 18.0 as CDB file. The same procedure is followed for both the patients pre and post-operative data sets.

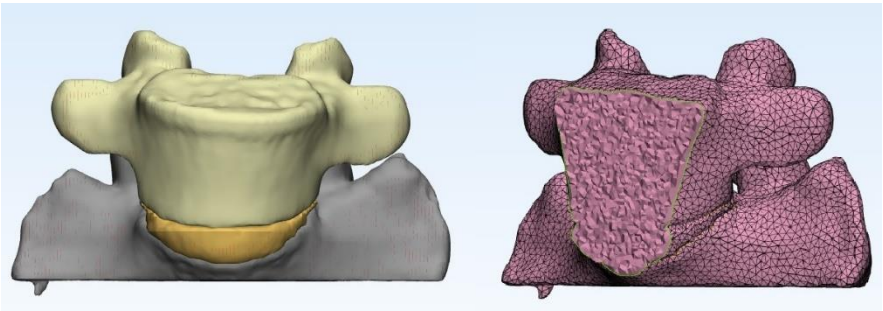


Fig. 2. Meshed Lumbosacral Joint.

The exported model (CDB file) is opened with Ansys Workbench module. A static structural analysis is set to run. Since the aim of this study was to find only the structural change between pre and post-operative, the property of bone and disc were assumed to be isotropic. The isotropic material properties of bone and disc were attained from literatures [12] [13]. Sacrum was set as a fixed support and a predetermined weight of force was applied on the L_5 vertebra. In our previous study [14], it was found that on a normal standing position, an average

adult weighing 65 kgs with normal lumbosacral angle of 30° would exert a net force of 196 N on the lumbosacral disc. Hence, same 196 N force was applied on this model.

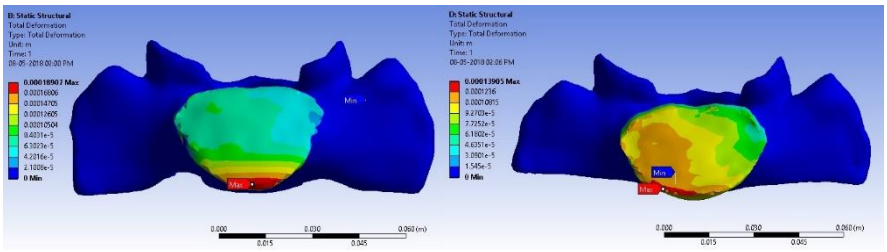
4. Results and Discussion

Results of applying 196 N force on the lumbosacral disc between pre and post-operative models showed us that there is a difference between them. Before correction, total deformation and equivalent elastic strain of the lumbosacral disc was found to be 0.00020242 m and 0.03153 m/m. Whereas, after correction and before complete fusion of the scoliotic vertebrae, the total deformation and equivalent elastic strain of the lumbosacral disc was found to be 0.00013905 m and 0.018143 m/m. (refer Table. 2)

Table 2. Results. TD – Total Deformation, EES – Equivalent Elastic Strain.

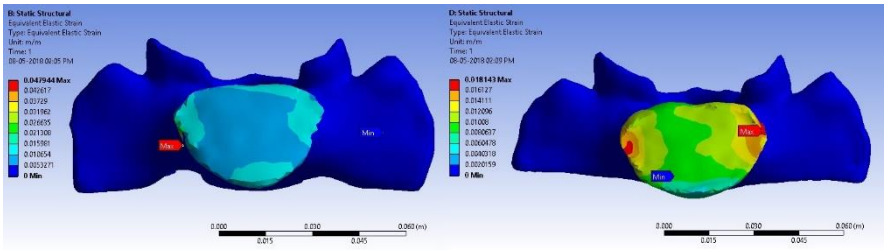
	Patient 1		**Patient 2**	
	Pre-operative	**Post-operative**	**Pre-operative**	**Post-operative**
Nodes	65755	58247	80705	74583
Elements	385584	326962	470451	435291
TD	0.00020242 m	0.00011567 m	0.00018907 m	0.00013905 m
EES	0.03153 m/m	0.019186 m/m	0.047944 m/m	0.018143 m/m

In both the cases, it was evident that the area of total deformation and area of equivalent elastic strain in pre and post-operative disc had changed. In pre-operative lumbosacral disc, the maximum area of total deformation was on the anterior aspect of the disc. Much force was concentrated on the anterior and had an uneven distribution. Whereas, in post-operative, the maximum area of total deformation was on the antero-lateral aspect of the disc and the force of 196 N was evenly distributed to a certain extent. (refer Fig. 3) We noticed the same level of changes in the equivalent elastic strain as well. In pre-operative it was found that the maximum strain was on the lateral aspect of the disc (right side). In post-operative, maximum strain was found nearly on both the sides (lateral) on top (superior) of the disc. (refer Fig. 4) It is important to note that both the patient had a right sided scoliosis.



(a) Pre-operative **(b) Post-operative**

Fig. 3. Total Deformation of Lumbosacral disc.



(a) Pre-operative **(b) Post-operative**

Fig. 4. Equivalent Elastic Strain of Lumbosacral disc.

A laboratory model designed to reliably produce disc rupture under physiologically reasonable stresses involved loading a cadaveric lumbar spine specimen for 6.9 hours under 1334 N compression in 7° flexion with lesser than 3° of rotation. Disc tear occurred in 10 of 14 specimens [15]. However, the study did not specify which side of the disc it was torn. In another study [16], it was reported that, during application of tension, failure is routinely observed at the disc end plate, junction between disc and vertebral body, with forces ranging from 863 N at cervical and 3000 N at lumbar. Vertebral bodies fail to compression at 3000 N in cervical and at 5000N in lumbar region. These results support our findings, as the strain analysis showed a maximum strain on either side of the top of the disc.

Earlier, a study by Karami *et al*., [17] on the assessment of coronal radiographic parameters of the spine in the treatment of adolescent idiopathic scoliosis concluded that precise attention to the coronal balance in pre-operative is vital in prevention of post-operative decompensation. During the scoliosis correction surgery, surgeons perform osteotomy, place bone grafts in the course of scoliosis curve and fuse the vertebrae together. With the help of metal implants, bone graft and bone regeneration, curve correction occurs promptly. Another study by Ameri *et al*., [18] on natural history of coronal balance after spinal fusion in adolescent idiopathic scoliosis revealed that the first 12 months after posterior spinal fusion is the spontaneous improvement period for coronal balance. Following that period of time is less likely.

5. Conclusions and Recommendations

Our results showed that, the total deformation and equivalent elastic strain of lumbosacral disc as 0.00020242 m and 0.03153 m/m. Whereas, after correction and before complete fusion of the scoliotic vertebrae, it was found to be 0.00013905 m and 0.018143 m/m. Furthermore, a mesh convergence analysis shall be done with greater sample size to substantiate the above-mentioned results. From our results, it is evident that there is a structural change in the vertebral alignment followed immediately after corrective surgery. The correction in alignment of scoliotic spine bring changes to the biomechanical functionality and load bearing capacity of the lumbosacral intervertebral disc before and after surgery. This helps in improvement of the functional capacity of the individual and thus helps in reducing the morbidity due to the deformity before correctional surgery.

References

[1] Damavandi, M.; Dalleau, G.; Stylianides, G.; Rivard, C.H.; and Allard, P. (2013). Head and Trunk mass and center of mass position estimates in able-bodied and scoliotic girls. *Medical Engineering & Physics*, 35, 1607-1612.

[2] Park, J.Y.; Park, G.D.; Lee, S.G.; and Lee, L.C. (2013). The Effect of Scoliosis Angle on Center of Gravity Sway. *Journal of Physical Therapy Science*, 25(12), 1629-1631.

[3] Mohankumar, P.; and Leong, W.Y. (2014). Mechanical Properties of the Human Vertebrae Between Normal, Post Corrective and Post-Operative. *IEEE International Symposium on Robotics and Manufacturing Automation*, Kuala Lumpur.

[4] Mohankumar, P.: and Leong, W.Y. (2015). Medical radiographic image processing using edge detection mechanism. *International conference of science, technology, engineering and mathematics*, Kuala Lumpur.

[5] Hajizadeh, K.; Gibson, I.; and Liu, G. (2013). Developing a 3D Multi-Body Model of the Scoliotic Spine with Lateral Bending Motion for Comparison of Ribcage Flexibility. *International Journal of Advanced Design and Manufacturing Technology*, 6(1), 25-32.

[6] Jensen, G.M. (1980). Biomechanics of the Lumbar Intervertebral Disk: A Review. *Physical Therapy*, 60, 765-773.

[7] Pel, J.J.M.; Spoor, C.W.; Pool-Goudzwaard, A.L.; Hoek van Dijke, G.A.; and Snijders, C.J. (2008). Biomechanical analysis of reducing sacroiliac joint shear load by optimization of pelvic muscle and ligament forces. Annals of Biomedical Engineering, 36(3), 415-424.

[8] Trobisch, P.D.; Samdani, A.F.; Pahys, J.M.; and Cahill, P.J. (2011). Postoperative trunk shift in Lenke 1 and 2 curves: how common is it? and analysis of risk factors. *European Spine Journal*, 20, 1820-1828.

[9] Carvalho de Abreu, D.C.; Gomes, M.M.; Rocha de Santiago, H.A.; Pereira da Silva Herrero, C.F.; Porto, M.A.; and Luiz, H. (2012). What is the influence of surgical treatment of adolescent idiopathic scoliosis on postural control?. *Gait & Posture*, 36, 586-590.

[10] Nohara, A.; Kawakami, N.; Seki, K.; Tsuji, T.; Ohara, T.; Saito, T.; and Kawakami, K. (2015). The effects of spinal fusion on lumbar disc degeneration in patients with adolescent idiopathic scoliosis: a minimum 10-year follow-up. *Spine Deformity*, 3, 462-468.

[11] Bradford, D.S.; Tay, B.K.B.; and Hu, S.S. (1999). Adult Scoliosis: Surgical Indications, Operative Management, Complications and Outcomes. *SPINE*, 24(24), 2617-2629.

[12] Haiyun, L.; and Zheng, W. (2006). Intervertebral disc biomechanical analysis using the finite element modelling based on medical images. *Computerized Medical Imaging and Graphics*, 30, 363-370.

[13] Noriyasu, H. (2011). Theory and Applications of CT Imaging and Analysis. Retrieved May 2, 2018, from https://www.intechopen.com/books/theory-and-applications-of-ct-imaging-and-analysis.

[14] Mohankumar, P.; Leong, W.Y.; Cheah, K.H.; and Yong, L.C. (2018). Engineering concepts in analysing lumbosacral load in post-operative scoliotic patients. *Journal of Engineering Science and Technology*, 13(4), 1058-1069.

[15] Aminoff, M.J.; and Daroff, R.B. (2003) *Encyclopedia of the Neurological Sciences* (2nd ed.). New York: Elsevier.

[16] Humzah, M.D.; and Soames, R.W. (1988). Human intervertebral disc: structure and function. *The Anatomical Record*, 220, 337-356.

[17] Karami, M.; Maleki, A.; and Mazda, K. (2016). Assessment of Coronal Radiographic Parameters of the Spine in the Treatment of Adolescent Isiopathic Scoliosis. *Archives of Bone and Joint Surgery*, 4(4), 376-380.

[18] Ameri, E.; Ghandhari, H.; Nabizadeh, N.; and Hesarikia, H. (2014). Natural history of coronal balance after spinal fusion in adolescent idiopathic scoliosis. *Shafa Orthopedic Journal*, 1(2), 12-16.

[19] Morris, S. (2018). Pelvic discomfort in pregnancy. Retrieved May 8, 2018, from http://www.drmorris.com.au/pelvic-discomfort-in-pregnancy/.